Constitution of the deep transition zone and lower mantle shown by diamonds and their inclusions

Mark T. Hutchison

Thesis submitted for the degree of
Doctor of Philosphy

University of Edinburgh
September 1997

Declaration

Except where specific reference is made to other sources, the work presented in this thesis is the original work of the author, and has not been previously submitted for a degree at this, or any other university or institute of learning .

Mark T. Hutchison September 1997

Acknowledgements

Firstly, my sincerest thanks go to my long-suffering supervisors, Ben Harte and Jeff Harris, who have coped valiantly under a sea of paper. Their advice throughout my research, both practical and esoteric, has been greatly appreciated. Ben is particularly thanked for those moments of base-touching and for bringing me up to speed and, indeed, Jeff, for pointing out the crocodiles.

Furthermore, I owe a great debt to the plethora of experts who have lent their skills to the success of this project. The value of our discussions has often more than equalled the value of the numbers themselves and in this regard, particular thanks are due to Catherine McCammon, Pan Conrad and Pierre Cartigny. Also gratefully acknowledged are John Craven, Pete Hill, Mike Hursthouse, Mark Light, Rus Hemley, Stuart Kearns, Simon Burgess, Simon Parsons, Robert Gould, Stuart Boyd, David Fisher, Ross Angel, Nancy Ross, Eric Condliffe, David Robson, Postman 'Harrry' Pat, Yvonne Cooper and Louise Kerr.

The text itself has been significantly improved following reviews by Ben Harte, Jeff Harris, Catherine McCammon, Steve Haggerty, Pierre Cartigny, Paula McDade, John Craven, Mike Hursthouse and my examiners, Ian Main and Violaine Sautter. Furthermore, I am deeply indebted to the library staff and Kevin Murphy of the Min. Soc. for advice on abbreviation and for hard to get references.

Throughout, I have tapped into that pulsating mass that is the academic community. In this regard, particular thanks are due to Yingwei Fei and Ian Main for riding the mathematical wave with me. Also thanked are Tetsuo Yagi, Barry Dawson, Malcolm McCallum, Peter Deines, Luciano Secco, Gabriella Salviullo and Marc Javoy for perusing my data and Thomas Stachel, Valerie Malavergne, Donald Sutherland, Oded Navon, Wayne Taylor, Maya Kopylova, Tom Sharpe, Ray Burgess, Ian Parsons, Simon Harley, Roz Smith and Al Duba for more general discussion.

Also acknowledged are The South African Mail and Guardian, the Australian Gold Bulletin, Asia Precious, New England Bride Inc., Diamondcutters Inc., Best Diamond Value Inc. Greenberg Jewelers Inc. and the Royal Museum of Scotland for information discussed in section 1.4.1.

The final moments have been eased hugely by my 'team-thesis' of serving wenches. In particular Paula 'sorted' McDade, Mimi 'snotty' Hill and Amanda 'I think you should just scan it' Voase; my relief surpasses description.

At the 6th IKC and beyond......: Julia Tsybulchik (for being wonderful), Kevin Leahey (for amongst other things, outrageously provoking the procurement of official papers), Tanya Makeeva (for her Russian dress-sense and fear of sharks), Dean Robson (for sharing our mafia booty and that 'where has the road gone' moment), Pavel Grib (Russian humour?), Jessica Carvalho (quality Lambada,

stunning fish impersonations and Japanese-proximal vodka control), Steve Haggerty (toasts and mafia advice), Barry Dawson (my *HUGE* birthday vodka), Jeff Harris (trans-continental bribery supplies), the people who put all the bilberries in the forest near Magadan, Sandra Ishawood (of Barclaycard, for bailing on my behalf) and the bloke from Rent-a Wreck for giving me a home, are all remembered fondly.

My thesis represents the culmination of eight years in what has to be one of the most wonderful cities I know. I would like this work to be dedicated to those who have made living here such an enjoyable experience, especially to Neil Saunders (my fellow sufferer) and Mimi Hill (my bean); also to Lucy Ketchin (for mutual understanding), Mark Cleasby, Anthony Taylor (for keeping me tonaly correct), Alison Graham, Kerry Barber, James Allen, Jo Critchley (for cooking tips), Nick Hazel (for being a great example of writing-up skills), Brigid Smith, Corinne Barber, Hannah Jonathan, Elaine Johnston, Sarah Macintyre, Ian Snape (for my intro. to E's), my fellow DJ's past and present (Ian Macintyre, Jim Moyle, Helen King, John Baines, Marathon-Man) and the punters and kiddies at Eternal, Rock Night, Iniquity, Undead Can Dance, Tushratta and Incarnate. Also thanked are the Department of Geology and Geophysics and, laterally, J.T., for supplying me with accommodation.

During the period of my writing-up many people have suffered (or sighed with relief) over my hermit-like existence (Neil Saunders, Dave Carruthers, Lorna Walker, Brigid Smith, Mary Jane Addinall, Marc and Karen Greenberg...........). Their patience is gratefully appreciated. I intent to make up for the neglect by doing some extra dangerous things on the end of a rope with Dave and in the pub with Neil.

In the end, I did fraternise in the department; thanks go to Paula for making the experience a richer one for me and introducing a little more 'team-diamond' to Edinburgh. Laterally, I have become indebted to my office-mates for allowing me to make ours the least desirable part of the department (apparently): Jason Smith (for giving us more oxygen), Tim Brand (for his computer and his -ness), Al Matthewson (for being, well, Al), Amanda Voase (for....everything....: for being the most organised woman in the world and for doing the dishes, making me coffee, flapping and squeeking, for sharing 'that Ben moment', for introducing me to Finland - 'land of lakes', for helping me keep up my record of trashed hire cars, for winning the prize of 'most original use of a cleavage' and, not least, for quite THE most spectacular early morning backward-mapping of a particularly fluid-rich granulite), Bob the Sheep and Julie.

My thesis would be a far paler second-best without my Granny and Aunt Cath. Thank you for my laptop and thank you for years of love.

My deepest love and affection as always goes to my Mum, Dad, Gavin and Fiona and to Mimi who was a constant friend and 'support'.

Abstract

Diamonds from the São Luiz alluvial deposit, Brazil, have been found to occlude syngenetic inclusions whose associations are evidence for formation in the mantle transition zone and lower mantle (Wilding, 1990; Harte and Harris, 1994). These diamonds represent the most extensive sample of deep mantle available to date, and have been subjected to detailed study. Five principal associations are identified.

One association involves orange garnet inclusions (with diopside and pyrrhotite) which contain a significant pyroxene component in solid-solution (majorite component) indicating formation in the transition zone (Akaogi and Akimoto, 1977). Trends of major element composition against Si content are most consistent with formation within the deepest regions of the transition zone where equilibrium with perovskite structured $CaSiO_3$ (CaSi-Pvk) is envisaged (Irifune and Ringwood, 1987).

The remaining associations all involve MgO - FeO (fPer) and are also believed to have been in equilibrium with $CaSiO_3$ composition inclusions. The association of fPer and $(Mg,Fe)SiO_3$ (LM I) is understood to have formed at pressures of >24 GPa (Yagi et al., 1978), within the lower mantle, where $(Mg,Fe)SiO_3$ adopts a perovskite structure (MgSi-Pvk) at pressures above the breakdown of $(Mg,Fe)_2SiO_4$ ringwoodite. Indeed, all the broadly pyroxene composition phases recovered in association with fPer are envisaged to have formed with perovskite structures. The LM I association also includes grains of broadly pyrope-almandine composition with high Fe^{3+} content ($Fe^{3+}/\Sigma Fe = {\sim}0.7$) and very low Ca (<0.15 wt% CaO) and depleted rare earth element (REE) concentrations consistent with equilibrium with REE-phyllic CaSi-Pvk. This new mineral is shown to adopt a tetragonal $I\bar{4}$-2d structure and is referred to provisionally as ‘TAPP’ (tetragonal almandine-pyrope phase). Given the propensity for MgSi-Pvk to adopt the entirety of the likely lower mantle Al_2O_3 budget within its structure at depths over 820 km (e.g. Kesson et al., 1995), and the stability of an Al_2O_3-involving association at depths of 720-820km (Irifune et al., 1996), TAPP is believed to form in aluminous bulk compositions in the depth region, 670-720km. A deeper association of fPer, aluminous and Fe^{3+}-rich MgSi-Pvk and Al_2O_3 (ruby) from São Luiz diamonds forms a third (LM II) association.

The remaining two associations have characteristics indicative of formation in the deepest regions of the transition zone. An association (LM III) of low Ca-garnet with a small majoritic component, a previously unrecorded C2/c structured Al-Ca-Na-Fe^{3+}-rich magnesium silicate (with 11, 5 and 6 wt% Al_2O_3, CaO and Na_2O respectively) and fPer is reported. Trace element compositions of this garnet are found to be transitional between majoritic garnet (Harte, 1992) and TAPP. The final association, found in a single diamond involves a $(Mg,Fe)_2SiO_4$ composition inclusion, fPer and TAPP (UM/LM

association), and is suggestive of formation within the range 460-720km depending on bulk composition (Jeanloz and Thompson, 1983). Also identified from São Luiz is the first recorded sapphire inclusion in diamond.

Change in cell parameters on release of two fPer inclusions (one from Guinea, West Africa) have been measured and interpreted on the basis of expected mantle geotherms and physical properties of compressibility and expansivity. Depths of formation of ~300km are inferred which, on correction due to the fractured and plastically deformed nature of the diamond hosts, extend to within the lower mantle. The very low Fe^{3+} content of fPer and the large Fe^{3+} content of aluminous MgSi-Pvk inclusions additionally support formation at high pressure (McCammon et al., 1995 and McCammon, 1997). Furthermore, the presence of significant quantities of magnesioferrite as inclusions in many fPer inclusions is consistent with the high Fe^{3+} content of associated phases and indicates relatively oxidised conditions of formation. Partitioning of Fe, Ni and Mg between fPer and MgSi-Pvk is indicative of high temperature (>2000K) within the lower mantle which suggests a steep thermal gradient at 670km and hence a thermal boundary layer between the upper and lower mantle. This observation, in addition to indications from associations of a compositional distinction between upper mantle and lower mantle, supports separate régimes of mantle convection.

The diamonds themselves show cathodoluminescence patterns indicative of a complex interplay of growth and resorption. Transition zone stones show a range in nitrogen content from <15 to 311ppm, and are highly aggregated indicating a long, high temperature history. Lower mantle stones are even more deficient in nitrogen (mostly Type II diamond), and show a very tight clustering of $\delta^{13}C$ composition around -5‰. Given ranges of up to 9‰ within single stones, precipitation under fluctuating conditions within a homogeneous reservoir is concluded. Values for $\delta^{15}N$ of -6 and -5.2‰ have been obtained for an upper / lower mantle boundary sourced stone.

Thermoelastic modelling is applied to a variety of deep mantle phases and it is concluded that, with a thermal boundary between upper and lower mantle, there exists a narrow depth region just below 670km where many phases, (particularly diamond) are gravitationally stabilised. Diamond moving within the circulatory system of the lower mantle will, therefore, tend to pond in this region. Exhumation from the deep mantle is believed to have been relatively swift due to the lack of: re-equilibration of composite grains; complete exsolution of majoritic garnet; and recombination of magnesioferrite with fPer. A régime of transportation by upwelling mantle plume is envisaged. The dominance within thin cratonic areas amongst world-wide locations of deep mantle diamonds is also discussed. This observation is interpreted in terms of thin cratonic areas being suitably reduced to stabilise diamond at shallow depths, unlike in oceanic settings where diamond burns to form CO_2. Additionally, the crust in thin cratonic regions is not suitable for formation of lithospheric diamond and so the deep population of stones is not outnumbered by shallow sourced diamonds.

Glossary

ATP	**A**tmospheric **T**emperature (298K) and **P**ressure (0 GPa)
bleb	A feature of relatively high back scattered electron intensity in ferropericlase. Blebs are defined in the current study to be either spots of no more than 0.8 µm in diameter or elongate features no more than 0.8 µm in width and up to ~10 µm in length. Blebs are taken as being distinct from larger features of high BS-intensity in fPer such as the veins and inclusions seen in BZ66 and BZ238B.
boundary effect	The effect of a thermal boundary between upper and lower mantle whereby mantle phases experience little volume change on ascent (section 7.1.2).
BS(E)-	Back scattered (electron). Refers to back scattered electrons imaged using either the electron microprobe or scanning electron microscope.
BSE	Bulk silicate earth
BZ	Prefix to sample numbers adopted for some diamonds and their inclusions involved in the present study and previous work by Wilding (1990) and Harte, Harris and Watt (1993, *personal communication*). Refers to the locality of São Luiz, **B**ra**Z**il.
CaSi-Pvk	Either presently or originally perovskite (Pm3m) structured phase of essentially $CaSiO_3$ composition. Examples within the present study are grains BZ97, BZ115 and BZ252A.
Cc	Continental crust
CM	Ca-rich phase identified by Gasparik (1990) in run products in the $CaSiO_3$-$CaMgSi_2O_6$ system at pressures over 14.5 GPa.
Cor.	Corundum
cpx	Clinopyroxene: a structural implication is intended unless specifically stated otherwise (often by sufficing with the term ‘composition’).
crud	Inclusions which, either by their friable behaviour, extreme softness, brown mottled appearence, association with oxidised fracturing in diamond or very poor electron probe totals, are interpreted as being either contaminant, epigenetic in origin or products of secondary alteration.
DAC	Diamond anvil cell
deep mantle	The mantle transition zone and lower mantle
EPMA	Electron probe microscope analysis
flat	Diamond which has been polished on two parallel sides (BZ251-BZ258).
FTIR	Fourier Transform Infra-Red Spectroscopy
grain	Refers to a crystalline material recovered from diamond, either an entire inclusion, or a discrete body which, by means of its compositional characteristics, and relevent observations throughout the diamond breaking process, can reasonably be assumed to be a fragment of what once was a single inclusion. An example of the latter meaning being the two grains BZ259A1 and BZ259A2 which were recovered as fragments of an original single inclusion.
Grt	Garnet: a structural implication is intended unless specifically stated otherwise (often by sufficing with the term ‘composition’).

GU	Prefix to sample numbers adopted for some diamonds and their inclusions involved in the present study. Refers to the locality of the Kankan district, **GU**inea.
heavy elements	High mass elements, Pb, Th and U, measured on some inclusions by ion-probe
HFSE	High field strength elements. (e. g. Hf, Ta, Y, Zr, Nb)
I.R.	Infra-Red
JH	Prefix to sample numbers adopted for some diamonds and their inclusions involved in the present study. Refers to a group of the samples obtained by **J**eff **H**arris from São Luiz, Brazil.
LILE	Large ion lithophile elements (e. g. Rb, K, Ba, Sr)
LM	Lower mantle or lower mantle association. This association comprises all inclusions released from diamond of a type which are known, at least in some cases, to coexist with fPer from the same diamond but have not been released from diamond additionally hosting Types I, II and III MgSi-Pvk (otherwise such inclusions would have been assigned to the LM I, LM II or LM III associations).
LM I	Lower mantle I association. This association consists of all syngenetic included material which has come from the same diamond host as a Type I MgSi-Pvk.
LM II	Lower mantle II association. This association consists of all syngenetic included material which has come from the same diamond host as a Type II MgSi-Pvk.
LM III	Lower mantle III association. This association consists of all syngenetic included material which has come from the same diamond host as a Type III MgSi-Pvk.
majorite	$MgSiO_3$ composition adopting a garnet (Ia3d) structure
majoritic garnet	$(Ca,Mg,Fe)_3Al_2Si_4O_{12}$-$(Ca,Mg,Fe)SiO_3$ solid solution composition garnet (Ia3d) structured phase
material	Either individual mineral grains or rocks as, for example, are entrained into plumes.
MgSi-Grt	Garnet (Ia3d) structured phase with the same compositional range as MgSi-Pvk
MgSi-Ilm	Ilmenite ($R\bar{3}$) structured phase with the same compositional range as MgSi-Pvk
MgSi-Pvk	Perovskite (Pbnm or Pm3m) structured phase of essentially enstatite composition + / - quantities of Al, Fe, Na and Ca. The term encompasies all inclusions of Type I, II and III pyroxene composition as defined in section 2.2.1.5.
MORB	Mid-Ocean Ridge Basalt
opx	Orthopyroxene: a structural implication is intended unless specifically stated otherwise (often by sufficing with the term ‘composition’).
P/T	Pressure and temperature
prim-	primitive
quenching effect	The effect of pressure release before full thermal relaxation (as seen in rapid exhumation) wherebye mineral phases experience a molar volume greater than that under atmospheric conditions (ATP) (section 7.1.2).
REE	Rare earth elements (e. g. La, Ce, Pr, Nd, Sm, Eu, Gd, Tb, Dy, Ho, Er, Tm, Yb, Lu)
R’ite	Ringwoodite (Cubic Fd3m spinel-type structured $(Mg,Fe)_2SiO_4$ phase)
sB	Superphase-B (e.g. Gasparik and Drake, 1995)
SEM	Scanning electron microscopy or scanning electron microscope

St’ite	Stishovite
standard set	The list of LILE, REE, HFSE and heavy elements from which trace elements are routinely chosen for determination on São Luiz inclusions by the University of Edinburgh / NERC Cameca ion microprobe (appendix 9).
stone	A commonly accepted term to refer to diamond, particularly prevelent in industrial scenarios. It is adopted here as a useful alternative to the word ‘diamond’ in order to aid the flow of the text.
TAPP	Tetragonal almandine-pyrope phase. A working acronym for the new $I\bar{4}2d$-structured phase obtained as inclusions from São Luiz diamonds.
Type I (Px)/ (MgSi-Pvk)	Refers to a pyroxene of enstatite-ferrosilite composition with less than 5 wt% Al_2O_3, 0.5 wt% Na_2O and 0.1 wt% CaO. Inclusions of this type are interpreted as being part of a lower mantle association and are believed to have adopted a perovskite structure on genesis.
Type II (Px)/ (MgSi-Pvk)	Refers to a pyroxene of composition with greater than 5 wt% Al_2O_3, between 0.5-2 wt% Na_2O and 0.1-2 wt% CaO recovered as inclusions from São Luiz diamonds. Inclusions of this type are interpreted as being sourced within the lower mantle and are thought to have adopted a perovskite structure on genesis.
Type III (Px)/ (MgSi-Pvk)	Refers to a pyroxene of enstatite-ferrosilite composition with greater than 5 wt% Al_2O_3, greater than 2 wt% Na_2O and greater than 2 wt% CaO recovered as inclusions from São Luiz diamonds. Inclusions of this type are interpreted as being sourced within the lower mantle and are thought to have adopted a perovskite structure on genesis.
TZ	The transition zone association consisting of inclusions of majoritic garnet, pyrrhotite and associated (diopsidic) pyroxene composition grains.
UM/LM	The upper mantle / lower mantle association consisting of inclusions of olivine, fPer and TAPP composition from BZ243.
W’ite	Wadsleyite - orthorhombic Imma structured $(Mg,Fe)_2SiO_4$ phase
yr	year

Contents

APPENDICES

Chapter 1 Introduction

Diamond is a truly remarkable mineral which, aside from its clear aesthetic and commercial value, has an invaluable role to play in our understanding of the earth and, by extrapolation, in our comprehension of planetary states in general. Historically, diamond has both provided an important means of study of the state of the cratonic mantle lithosphere and asthenosphere through observations of its included material and through the diamonds themselves. Such study has been an invaluable adjunct to data provided by other directly observable mantle material: mantle xenoliths, mantle rocks exposed at the earth’s surface (ophiolite belts and, in continental settings, localities such as the Rhondda Massif, Benni Bouserra and Kokchetav), magmatic distillates of the mantle such as MORB, OIB, kimberlites and lamproites. The deeper into the earth we hope to sample, however, the more we have to rely upon diamond to provide material for study. Indeed, the unique nature of diamond's chemical and physical resistance to alteration places it as, arguably, the *only* means by which deep earth material, particularly from the transition zone and lower mantle, can be supplied to science for study: the word ‘diamond’, appropriately enough, comes from the Greek ‘adamas’ meaning unconquerable. Until recently, the deepest known diamonds were sourced from ~200 km, as determined by use of geothermobarometry on coexisting included phases (see Meyer, 1987). This situation changed with the identification of transition zone sourced majoritic garnets from Monastery (R.S.A.) diamonds (Moore and Gurney 1985) pushing sampling depths to ~ 480km (Moore et al., 1991); the only other transition zone material being a few rare xenoliths from Jagersfontein (Haggerty and Sauter, 1990). Such depths are still well short of the lower mantle. The first lower mantle material was discovered in 1984 with the identification of a MgO-FeO (fPer) inclusion from Orrorroo (Australia) (Scott-Smith et al., 1984). Subsequently, lower mantle material has been observed from eight localities worldwide (section 2.2.1.4) of these, by far the most important is the São Luiz alluvial diamond mine in Matto Grosso, Brazil.

This thesis presents the most comprehensive study of São Luiz diamonds and their inclusions to date. It follows on from the work of Wilding and Harte, principally on transition zone material (Wilding 1990 and Harte, 1992) and the work of Harris, Watt and Harte (Watt et al. 1994 and Harte and Harris 1994).

Section 1.1 Philosophy of Study

The principal aim of the present study has been to provide as comprehensive a picture as possible of the truly unique São Luiz diamonds, and has necessitated the employment of a wide variety of analytical techniques. In addition, the present work attempts to provide a synthesis and interpretation of all contemporary knowledge of both São Luiz material and deep mantle diamonds in general.

This philosophy has resulted in a rather unconventional research plan. The bulk of the study involves work directly undertaken by myself; diamond break-out, sample preparation, electron probe and ion microprobe analysis, Fourier transform Infra-Red spectroscopy, some X-Ray diffraction, some scanning electron microscopy, bulk δ^{13}C analyses. In addition, a number of lines of enquiry have been followed by specialists in particular analytical techniques and wherever possible, an active part in this work has been undertaken by myself. These specialists include McCammon (Bayreuth, Mössbauer), Hursthouse and Light (ESPRC, Cardiff, XRD), Parsons, Gould and Blake (Edinburgh, Chemistry, XRD), Cartigny (Paris, δ^{15}N and δ^{13}C analysis), Conrad and Hemley (Carnegie Institution, Washington, XRD), Angel and Ross (UCL, FTIR and XRD), Rogerson (Edinburgh, SPM), Forsyth (Edinburgh, AFM), Findlay and Jeffreys (Edinburgh, SEM) and Condliffe (Leeds, SEM). This invaluable assistance is acknowledged, where appropriate, in the text.

In addition to presenting data from inclusions broken out by myself, many diagrams presented herein, involve published data from non-São Luiz sources and both published and unpublished data from São Luiz from previous work. Where this is the case, due attention is drawn. In addition, the thesis involves some work undertaken on a small number of lower mantle inclusions from Guinea; it is expected that this locality may be the next major source of deep seated diamonds available for study and, at present, further work is being undertaken by Stachel and Harris.

Although it is clear that the material presented is of great scientific interest, it is important to note that the total volume of sample is small, the lower mantle material available comprising approximately 1x10^{-23} % of that volume of the earth. Every attempt has been made, however, to keep sight of this throughout the following discussion. The reader would do well to do the same whilst, in addition, keeping in mind that at the very heart of geological study is the value of the raw material.

➠

Section 1.2 São Luiz alluvial diamond deposit

Material involved in the present study was supplied by Sopemi Ltd (Brazil) via the Diamond Trading Company (London). Samples are referred to throughout by numbers prefixed by BZ (Brazil) and JH (Jeff Harris) where suffices are adopted according to the methodology described in appendix 3.1.

The São Luiz alluvial diamond deposit lies centrally within the continent of S. America in Mato Grosso State, Juina Province, Brazil[1], figure 1.2_1. The principal deposit is located within channels, palaeo-channels, flats and terraces of the Rio Cinta Larga, a tributory of the Rio Aripuanã. A number of secondary deposits lie in the Rio Cinta Larga catchment area, namely the Rio Vinte e Um, Rio Mutum, Igarapé Porcão, Rio Juininha and Rio Juina-Mirim[2] (Watkins, J. (SOPEMI), 1997, *personal communication*).

The location of the magmatic source of the deposit is not known, although there are a number of Mesozoic kimberlites recognised in the Juina area (Tompkins, 1992), some of which lie upstream on the Aripuanã river. None of the kimberlites are being mined, but, given that the alluvial diamond production of Juina Province is significant, ~ 10 Mcarats per year (Teixeira, N. (RTZ Mineracao), 1997 *personal communication*), it is likely that the kimberlites do have some diamond potential. Little has been published on the detailed geology of the area although it is suspected that localised, extensive surveying *has* been carried out. At present, research is being undertaken on the geochemistry, field relations and diamond prospectivity of Juina kimberlites by Teixeira (RTZ, Mineracao).

From a general geological point of view, Brazil has three major cratonic regions (figure 1.2_2) two of which fit with African cratonic regions on reconstructed plate distribution (figure 1.2_3). The three Brazilian cratons are:

- The Amazonico Craton which contains the Guiana Shield to the north and the Gaupore Shield to the south. It is within the broad outline of the Amazonico Craton that the São Luiz deposit is located.

---

[1] More specifically, it can be found approximately 560 km NW of the state capital Cuiabá, 37 km W of Juina township. The principal deposit is centred on a longitude of -59° 05´ 50´´ West and latitude of -11° 23´ 33´´ South. It is located on Brazilian 1:250 000 Map SC21-Y-C, Juina at coordinates x = 271015, y = 873620 (Jeff Watkins (SOPEMI), 1997, *personal communication*).

[2] River names can be translated as follows: Rio São Luis; River of St. Louis; Rio Aripuanã, Aripuena (State) River; Rio Cinta Larga, River of the wide basin (or curve); Rio Vinte e Um, River 21; Rio Mutum, Mutum river; Igarapé Porcão, Braided river; Rio Juininha, Little river of Juina; Rio Juina-Mirim, River of Juina-Mirim.

- The São Francisco Craton, to the east of the country which is considered to be the western portion of the Congo Craton.
- The São Luis Craton, which lies around the coastal town of São Luis, and is considered to be the southern portion of the West African Craton. This name has no relationship with the São Luiz of the present study.

Additionally, a small craton (Rio de la Plata Craton) has been identified in the south of the country.

Brazilian kimberlites (Svisero, 1995) have been identified as lying along a series of lineaments, figure 1.2_2, a common observation for kimberlitic distribution (eg. Hoal et al., 1995). All these lineaments were re-activated during the triggering of Atlantic spreading and saw a degree of volcanic activity (Tompkins, 1992). Juina kimberlites lie on a lineament trending at ~ 125° across Brazil towards Rio de Janeiro[3]. This lineament contains another nine kimberlite clusters in addition to that of Juina (figure, 1.2_2). The type of volcanism along the lineation appears to vary according to basement type with kimberlitic volcanism within the bounds of the Amazonico craton and volcanism dominated by dunites and lamprophyres within the Parana Basin. Although the Juina kimberlites lie within the *general bounds* of the Amazonico Craton they, as indeed all other Lineament 125° AZ kimberlites, are not truly cratonic. In fact the Juina kimberlites and the three other kimberlitic fields nearby, all lie within a mobile belt, the Rio Negro-Juruena Mobile Belt, bounding the stable core of the craton, what is termed the Central Amazonico Province, figure 1.2_4. This mobile belt is believed to have an island arc affinity (Carrington, 1990 *personal communication to Wilding (1990)*) caused by docking of the Central Amazonico Province with basement rocks to the south west and has a metamorphic age of approximately 1450-1750 Ma. It has been remobilised during the Proterozoic presumably as it is the most obvious point of weakness within the cratonic area.

➠

---

[3] The other two lineaments being the Transbrasilien Lineament trending at approximately 30° from Fortaleza and containing three kimberlite fields and the Blumenau lineament within the Parana Basin and containing one kimberlite field. The Blumenau lineament has been found to extend into Angola and Zaire on reconstruction of the S. American and African plates.

Section 1.3 The diamond deposits of Guinea

Material involved in the present study was supplied through the Diamond Trading Company (London). Samples are referred to throughout the text by numbers prefixed by GU (Guinea) where suffices are adopted according to the methodology described in appendix 3.1.

Guinea has a modest yet significant diamond production. Geologically, it occupies part of the West African Craton[1] which extends into Sierra Leone, famous as the source of the world's third largest gem diamond (the 969.8 carat 'Star of Sierra Leone'). Historically, diamonds have been available on the market from suppliers in Conakry, the capital city of Guinea. However, the sources of material on this market are poorly constrained and probably include some illegally imported stones from Sierra Leone. Recently, however, stones have become available from Kankan, a locality inland where the source area is far better constrained (Harris, 1996, *personal communication*). It is from this supply source that the Guinean diamonds considered herein were obtained.

Archean granitoids and Archean and Proterozoic supracrustal metamorphic rocks form the well exposed basement of this part of the West African craton (cf. Hurley et al., 1971). Kimberlite intrusions are fairly prolific (eg. Rombouts, 1987), but the diamond grade varies considerably. For the Kankan area, Sutherland (1993) presents the characteristics of the kimberlite dykes of the upper drainage basin of the Mandala River (~8°30'N ~9°30'W), figure 1.3_1, and their associated alluvial diamond deposits. He describes diamonds under 24 subdivisions, involving floodplain, terrace, pediment and slope from 8 localities. Although no detailed study has been made of the inclusion parageneses from the Mandala basin, the diamond characteristics show striking similarities to features of lower mantle sourced stones from São Luiz and Guinea[2] described in sections 5.1 to 5.3. These similarities, in terms of quantity of plastically deformed, dodecahedral or irregular, pitted, inclusion-rich stones, may not be entirely coincidental. Amongst nearby Guinean sources, there is much variability; some appear to be distinctly different e.g. Benko (Rombouts, 1987), indeed throughout Guinea and Sierra Leone striking variations between very proximal deposits are commonplace; others, however, show strong similarities with Mandala Basin material (Sutherland, D. (Placer Analysis), 1994 *personal communication*).

---

[1] Sierra Leone, Guinea, Liberia and the Côte d'Ivoire all encompass the central part of the West African craton.

[2] Morphology; octahedra and macles rarely exceed 6%, the dominant forms being dodecahedra intermediate and irregular (often ~ 70%): plastic deformation is very extensive (40 - 90 %): pitting is common (45 - 90 %) and stones are overwhelmingly colourless or brown (Sutherland, 1993).

Section 1.4 Diamond from a social perspective

Section 1.4.1 Historical interest in diamond

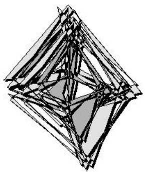

The first diamond discoveries were probably made in alluvial deposits in India around 800 B.C. The recorded history of diamond appears much later and can be found in the works of Plato and Ptolemy of Alexandria. The source of Indian alluvial diamonds has never been found, supplies largely dried up in the 18th century. Up until the late 19th century, Brazil had become the most prolific producer of diamonds worldwide, however, at this point, diamonds were discovered in South Africa.

One of the first South African finds was on land owned by Deiderik and Johannes De Beers who sold their property soon after, due to the subsequent influx of miners. In 1888, and incorporating the old De Beers land, the De Beers Mining Company was formed by Cecil Rhodes. Under its present ownership of the Oppenheimer family it is, by far, the largest player in the worldwide diamond market.

Diamonds are now described from Brazil, Guyana, Argentina, Colombia, U.S.A., Canada, Finland, Norway, Russia, Sakha, Kazakhstan, China, India, Sri Lanka, Sierra Leone, Ivory Coast, Angola, Guinea, Zaire, Botswana, South Africa, Lesotho, Zimbabwe, Namibia and Australia. The most recent finds have been in the Canadian Northwest Territories (Fipke et al., 1995) and Norway (Reuter, 1996). Of the plethora of works on the major localities, particularly from Southern Africa and Russia, the reader's attention is drawn, in particular, to Harris (1991), Dawson (1980), papers in Nixon (1979) and the volumes of the six International Kimberlite Conferences.

Throughout history, diamonds have been regarded with awe, respect and, above all, desire: a testiment to diamond's unique nature. Traditionally, diamonds have been a token of love, although, until the 20th century, they have been solely playthings of the wealthy. A diamond was the gift of Archduke Maximilian of Austria to Princess Mary of Burgundy in 1477 (reputedly she was the first woman to wear a diamond ring) and in 1773 the light-blue Orloff stone[1] was given to Catherine the Great of Russia by Prince Gregory Orloff. Indeed, in England in the 1500's diamond rings were known as scribbling rings as they would be used to scribble romantic pledges on window-panes.

The properties which have sparked such interest in diamond are obvious; hardness, brilliance, colour and rarity; but it is perhaps also for these reasons that some cultures have adopted a quite different approach to this remarkable mineral. In China diamond has been regarded as being unlucky and,

---

[1] Originally the eye of an idol in a Brahman temple, this stone was stolen by a French soldier.

considering the wars, murders and generally unpleasant behaviour which have surrounded diamonds, such relegation is perhaps not surprising:

The Darya-i-Nur, a flawless, transparent pink stone of approximately 175-195 carats, was stolen during the Persian attack of Delhi in 1739. It now resides amongst the crown jewels of the ex-Shah of Iran. The Koh-i-Noor stone (meaning: ‘mountain of light’), whose recorded history dates back to 1304, was taken as a spoil of war by the Mogul Sultan Babur in the 16th century. When one of its subsequent owners, the Shah Nadir, was murdered, it was taken to Afghanistan where it was given to Ranjit Singh of Punjab in exchange for military help. It resided for just a short time in Indian hands, however; the British demanded it as indemnity during the Sikh wars. It now resides as a 108.93 carat stone in the British crown jewels. The Pigot, named after Lord Pigot, Governor of Madras who purchased it in 1775, was bought by Ali Pasha, Viceroy of Egypt in 1818. During a fracas in his palace, the Viceroy was mortally wounded by the Sultan of Turkey, but the sultan failed to get his hands on the stone as, on the Viceroy’s dying command, the stone was smashed by one of his guards. Furthermore, a single diamond had a profound effect on the course of European history. Napoleon used a 140.5 carat stone as collateral for loans to finance his military efforts. Perhaps the most legendary of unlucky stones, however, is the Hope diamond. It currently resides in the Smithsonian Institute, partly because its history was so disaster-ridden that many buyers refused to consider the stone’s offer for sale in 1949. It is thought that this remarkable blue stone, was cut from the Blue Travernier, formerly part of the French crown jewels and stolen during the French Revolution. This stone had been brought to Europe from India in 1642 and was purchased by and cut for Louis XIV of France. As the Hope diamond, named after its 1830 buyer, it saw two bankruptcies, one suicide, one accidental death and a family break-up.

Amongst other stones of note are:

- The Cullinan; the largest recorded stone; originally 3106 carats and, in fact, a broken fragment from a larger stone. It was found during an inspection at the Premier mine in 1905 and named after the Premier Diamond Company’s chairman. It was purchased by the Transvaal government and given to Britain’s Edward VII in 1907. The stone was cut by Joseph Asscher of Amsterdam into 9 major and 96 minor stones; the largest being the Star of Africa, 530.2 carats and the Cuillinan II, 317.4 carats.
- The Regent; regarded as one of the most perfectly cut large stones. It was brought to England by William Pitt, another Governor of Madras and sold in 1717 to the Duke of Orleans. It now resides in the Louvre.
- The Excelsior: this high clarity blue-white stone was found in 1893. It was cut into 21 stones of which the largest is 69.80 carats.

- The 232-carat Star of Yakutia, from Mir, Sakha
- The 342-carat XXVI Party Congress, from Udachnaya, Sakha

In addition to being used as an excuse for conflict, diamonds have also been used as a *means* of conflict. Diamond powder was regarded as being deadly poisonous. The Turkish Sultan Bajazet was believed to have been murdered by his son who slipped powdered diamond into his food. Benvenuto Cellini cheerfully considered himself to have cheated death because his murderer’s lapidary had swapped the diamond he had been given as a murder weapon for powdered glass! Pope Clement VII died after being fed 14 spoonfulls of crushed gemstones as an attempted cure for his failing health; it was thought that the diamond was the cause of death. Carbon is certainly considered to be a carcinogen although contemporary beliefs of the detrimental physiological properties of diamond lie more as a possible asphixiant than a toxin.

It is not in keeping with the remainder of this work to end discussion on an aspect of diamond on a negative note. With this in mind it should be noted that diamonds have been regarded as being a cure for mental illness, a talisman to ward off evil spirits, lightning and pestilence, and a surity of success in the law courts. From a scientific standpoint, I shall attempt to show that they can also be regarded as efficient messengers from the deep earth.

Section 1.4.2 General diamond characteristics

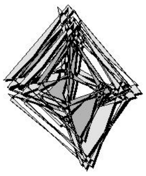

In terms of gem quality stones, the four C's are used as the indicators of quality. These are colour, clarity, cut and carat, where the cut is the only man-made factor involved in a diamond's value[1].

Colour: The colour of diamond, from a popular perspective, is purely a matter of aesthetics. Public tastes change but, due to the strong historical definitions of value, combined with the direction of 20th century marketing, pure, colourless, stones have, until recently, commanded the highest prices. The terminology of diamond colour used by the gem trade, table, 1.4_1, reflects this. Colourless stones are, however, not the only stones. Black, white, brown, blue, yellow, pink and red stones; of differing hue and saturation are in current production. In some respects, the historical preference for colourless[2] stones, with their 'virginal' connotations is quite appropriate because any colouration represents some form of deviation from pure Fd3m carbon. Thus:

- Black stones are graphitised, surficially or internally; due to radiation damage or unfavourable physical conditions. Such stones are termed 'boart'.
- White colouration arises from trapped CO_2 (Harris and Gurney, 1979).
- The colour of brown stones arises from plastic deformation, section 5.3.2.
- Substitiutional boron absorbs the red part of the visible spectrum, giving rise to blue stones.
- Single substituted N is responsible for the yellow colouration of some stones.
- The origin of the colour of rare, pink and red stones is, as yet, unclear, although plastic deformation has been a suggested mechanism.

Table 1.4_1 The traditional colour classification scale for gem-quality diamonds. In addition, categories for 'fancy' or coloured stones are in use.

C/less			Nr. colourless				Ft. Yellow			V. Light Yellow					Light Yellow							
D	E	F	G	H	I	J	K	L	M	N	O	P	Q	R	S	T	U	V	W	X	Y	Z

Some coloured stones can be far rarer, however, than the purest of colourless stones. At present, the public is being persuaded to buy such coloured gems and the market value is now reflecting the diamond industry's success. Intense pink or 'pigeon-blood red' stones, of which only six stones

---

[1] Various techniques, for example, heat treating, are employed to improve the colour of stones; most dealers, however, will not handle such material.

[2] In the distant past, preference was dictated mostly by availability; large stones were more often colourless but coloured stones were equally valued. Henry VII of England's gift to Agnes Sorrell in 1477 was a five-carat pink stone of unknown source; rare now; unique then.

above 3 carats have ever been tendered for sale, command prices of \$1 million per carat, compared to \$15,000 for a D-class flawless stone. Intense pink stones have been offered for invited viewing once a year in Tokyo, Hong Kong and Geneva since 1985, and Perth and London since 1996 (Jackson, 1996). Brown, yellow (cognac and champagne), and blue stones (particularly for use as semi-conductors) also have their market niche.

Clarity: The clarity of a stone is dependent on a number of factors:

- Its intrinsic purity of colour (or lack of colour) which is dependent on the distribution of impurities.
- Deformation of any kind, either in the form of fractures or plastic deformation, detracts from a gem-stone's value.
- Macroscopic impurities such as graphitisation, voids relating to fibrous growth and, in particular, mineral inclusions, have enormous scientific value; the latter being at the core of this thesis. It is perhaps justifiable that inclusion-filled stones now have value as 'nature's imperfections'; indeed when it comes to rarity, diamonds containing TAPP inclusions (section 2.2.1.3.3) are rarer than the famed pigeon-blood red stones from Argyle. It is tempting to view marketing of inclusion-filled diamonds as a shrewd mechanism for boosting the value of certain stones.

The classification of diamond clarity is outlined in table 1.4_2 and is based on a combination of reasonable eyesight and the 10x magnification of a jewler's 'loupe'. The scale runs from FL (the cleanest stones) to I_3 (the most flawed gem-quality stones). Diamonds of better quality than VVS are termed 'loupe-clean' whereas stones containing inclusions which are not visible with the naked eye are those better than SI_2.

Table 1.4_2 Classification of the clarity of gem-quality diamond.

FL	Flawless	SI_1	Small inclusions / slight internal faulting
IF	Some surface blemishes	SI_2	Small inclusions / definite faults
VVS_1	V. v. small inclusions, v. diff. to find	I_1	Inclusions easily visible to the x10
VVS_2	V. v. small inclusions, difficult to find	I_2	Inclusions just visible to the naked eye
VS_1	V. small inclusions / sl. scratches	I_3	Inclusions easily visible to the naked eye
VS_2	V. small inclusions / external defects		

Cut: The term 'cutting' is a misnomer in relation to the diamond industry. It is certainly true to say that pulsed laser bursts are used in some circumstances to 'cut' stones but, for gemmological purposes, stones are either cleaved or polished[3]. Diamond ‘cutting’, in fact, is relatively recent. The first records of diamond polishing comes from 14th century India but for at least two hundred years subsequently, diamonds were not, generally, ‘cut’; they retained their value despite only partially exhibiting their brilliance. The queen of Hungary had a celebrated crown of uncut stones fashioned in approximately 1074. The first commercially orientated cutting centres were set up in Antwerp in 1550 (trading having started there in 1447), indeed Antwerp can still be considered the home of the diamond trade. Even after stones became more prized when cut or faceted, it was not until the early 20th century, when the theory of optical refraction was applied to diamond faceting in detail, that stones were cut routinely for optimum brilliance. An example of poor pre-20th century faceting comes from Hyderabad in India. The Great Mogul diamond was cut under the orders of the Shah Jehan (who also ordered the building of the Taj Mahal). It was so badly cut that instead of paying the lapidary he was heavily fined. Faceted stones which have brilliance below present standards are often, therefore, pre-1900 in age.

Diamonds are faceted to achieve the greatest possible reflection of incident light. The angle of facet depends, therefore, on the critical angle of refraction, a special case of Snell’s Law, equation 1.4_1 as illustrated in figure 1.4_1. The interrelation of facets depends on the ultimate overall shape desired. The most popular, and indeed, most brilliant, shape is termed the round-brilliant. Other shapes are: hearts, pears (eg. Cullinan I), marquise, ovals, trillions, emeralds, princesses and radiants, figure 1.4_2.

$$\sin i = n \qquad \text{Equation 1.4\_1}$$

where: i is the angle of incidence of a ray within diamond on the diamond / air boundary such that total internal reflection takes place: n is the refractive index of diamond which depends on, amongst other factors, N content and is equal to 2.417 (Peter, 1923) for pure II diamond.

The most important features of a cut stone are the table and the depth, figure 1.4_3. For a brilliant-cut stone the *depth%* and *table%*, as defined by equations 1.4_2 and 1.4_3, must lie within the ranges 57-63% and 58-65% respectively[4].

$$depth\% = 100\,\text{x}\,\frac{depth\ (\text{mm})}{average\ girdle\ diameter\ (\text{mm})} \qquad \text{Equation 1.4\_2}$$

$$table\% = 100\,\text{x}\,\frac{longest\ table\ measurement\ (\text{mm})}{average\ girdle\ diameter\ (\text{mm})} \qquad \text{Equation 1.4\_3}$$

---

[3] Diamonds are polished with diamond powder in light oil against a steel lap (scaife). The stone is lowered close enough to the skaife to allow for contact between the stone and the diamond powder but not too close as to permit contact between the stone and the steel.

[4] Some dealers demand tighter constraints. As, commonly, ~65% of a stone’s weight is lost on cutting, however, and, in some cases more value is gained on increased weight than is lost on decreased brilliance, these constraints are sometimes deliberately flaunted.

Carat: The carat is a measurement of weight defined as 0.2 g. Its origin is from the carob seed, which was used in Egypt and the Middle East as a standard unit due to its remarkably constant size and weight. The carat is subdivided into ‘points’: 100 points comprising one carat.

As the density of diamond is, for the purposes of the gem-industry, constant, the carat is also a useful measure of size, particularly within suites of stones of constant shape. Figure 1.4_4 is a scale representation of the size of brilliant-cut stones. Although a useful scale for industry purposes, the carat has no scientific value and is thus not considered further herein.

➠

Section 1.5 Diamond studies

From a geological point of view, the study of diamond itself provides an opportunity to glean inferences on the conditions of the environment surrounding its formation (e.g. P, T, fO_2, isotopic composition of source material, its speed of growth) and any factors which have affected its state subsequent to growth (the role of shear as manifest by plastic deformation or fracture, fluctuations in fO_2 as manifest by absorption or re-precipitation).

The observations whereby such inferences can be obtained can be subdivided into two main categories; physical characteristics and compositional characteristics.

➠

Section 1.5.1 Physical characteristics

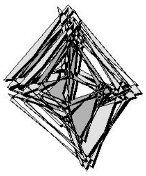

Crystallography and Morphology: Diamond is cubic (space group Fd3m) with a cell edge of 3.567 Å at ATP (Skinner, 1956). It grows in one of two general directions: (111) giving rise to an octahedral morphology or (100) giving a cubic morphology.

- Most diamonds exhibit a dominantly octahedral morphology, general conditions of pressure and temperature of formation being within the stablility field of preferred (111) growth.
- The cubic morphology is adopted by diamonds growing at low T (Giardini and Tydings, 1962) as shown on figure 1.5_1. As a result, rather than being xenocrystal, as inferred for the majority of diamonds, naturally occurring cubic diamonds are thought to have formed at relatively shallow depths (~100 km in the cratonic lithosphere), in some cases associated with their kimberlite or lamproite hosts. Indeed, commonly, diamonds are found exhibiting cubic overgrowths on octahedral cores eg. Mbuji Mayi (Boyd et al., 1987). Entirely cubic stones are rare, comprising typically < 1 % of the sample from any one mine (Harris, 1992).

Additional forms of diamond[1] occur as a result of specific ambient conditions:

- Resorption of cubic stones produces tetrahexahedra and octahedral stones form dodecahedra.
- Rapid growth, thought to be related to kimberlitic fluids (Arima et al., 1993) gives rise to fibrous stones and fibrous coats to existing stones eg. from Botswana, Angola, Sierra Leone, Yakutia and the Northern Territory of Australia (Boyd et al., 1992), Zaire and Mbuji Mayii (Boyd et al., 1987) and Mbuji Mayii (Javoy et al., 1984).
- Individual stones which have < 50 % identifiable morphology are termed irregular.
- Twinning occurs giving rise to macles, of which some rare stones are tetrahedral in morphology (Moore, 1990).
- The term carbonado is adopted[2] for some rare aggregated stones.

---

[1] Although a number of carbon allotropes are known, e. g. graphite and buckminsterfullerine (C_{60}), perhaps most worthy of particular mention is londsdaleite (Frondel and Marvin, 1967). This is a hexagonal polymorph of diamond which, unlike other C allotropes shares some of diamond's exceptional physical characteristics. It is a high pressure, low temperature phase found in meteorites (Frondel and Marvin, 1962) and impact zones (Hough et al., 1995).

[2] The origins of carbonado are still a matter for much debate. So far, they have only been found in placer deposits, prompting a tendency to induce mechanisms of formation completely unrelated to a magmatic event e. g. large impact metamorphism (Smith and Dawson 1985), transformation of subducted organic carbon to diamond (Robinson, 1978) or radiation damage of coals (Kaminskii 1987). The most recent study of carbonado, using stones from the Central African Republic (Kagi et al 1994), would favour a scenario secondary to kimberlite / lamproite eruption. Kagi et al (1994) favour radiation induced fusion of seed stones; seed stones having been identified by their aggregated N content including platelets. This aggregation would suggest that seeds were formed at conditions of high temperature and thus in the normal lithosphere setting expected for the formation of diamond in general (see section 1.3.2.2. for a detailed discussion of N aggregation). Very intense laser induced photoluminescence is characteristic of carbonado. This is indicative of radiation damage and, in addition to the abundance of crustal mineral inclusions, would suggest annealing of the seeds in a crustal setting.

Additional properties: Diamond is well known for its exceptional physical properties, particularly its hardness. In addition, it has the lowest electrical conductivity and highest thermal conductivity, melting point and refractive index recorded. Table 1.5_1 summarises some of the important physical constants obtained for diamond. Furthermore, diamond is highly resistent to chemical attack. At low temperatures oxidising agents represent the only means of compromising the chemical sanctity of diamond; diamond oxidises in air at ~ 900 K. At higher temperatures a number of molten metals are highly carbonophilic; examples are tungsten, tantalum, iron, nickel and cobalt.

Table 1.5_1 Physical properties of diamond

Hardness (Moh)	10	Thermal conductivity	~2000 $Wm^{-1}K^{-1}$ (II)
Hardness (Knoop)	9000 $kgmm^{-1}$ (111)	Resistivity	> 10^{18} ohm m
Bulk modulus	4.42×10^{11} Nm^{-2}	Dielectric constant	5.70 (300K)
Thermal expansion	0.02844×10^{-4} K^{-1}	Refractive index	2.41726 (589.29nm)

For full expansions and discussion see references in Field *Ed.* (1979, 1992)

Section 1.5.2 Compositional characteristics

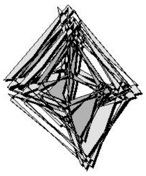

Although principally composed of carbon, diamond exhibits a wide compositional variation. In particular, the isotopic composition of carbon making up diamond has been found to vary (and shows a larger range than most other minerals or magmatic rocks, section 1.5.2.1) and has been used to infer both the mechanisms and conditions of diamond formation and the composition of the source region. Non-carbon species are also found to be present in diamond. These occur as two general types;

- Those occurring as inclusions, both macro- and microscopic (down to those comprising a few unit cells occupying defects).
- Those occupying lattice sites replacing carbon atoms in the diamond structure itself.

Consideration of the nature of inclusion phases and classification will be discussed separately in section 1.6. Of the elements found as impurities in diamond, by far the most common is nitrogen, in fact so much so, that the state of N occupying lattice sites forms the basis of one of the major classification schemes of diamond (section 1.5.2.2). In addition to N, however, some 69 elements have been detected as impurities in diamond; B, He, O, Na, Cr, Fe, Mg, Al, Si, Ca and Pt having been found in quantities > 100 ppm (see Bibby, 1984 for detailed discussion). It is hard to say to what extent these elements are incorporated in sub-microscopic inclusions rather than in lattice sites, certainly for the elements of atomic radius differing substantially from carbon, the former scenario is more likely. It should be noted, however, that some elements adopt very significantly smaller radii with increasing pressure (e. g. see Moore et al., 1991 for a discussion of the role of Na in majoritic garnets). Of the elements listed above, B, He and O as well as N, can, often, be considered to occupy lattice sites.

Section 1.5.2.1 Carbon isotopic content of diamond

Besides ^{12}C, the most common isotope of carbon is ^{13}C, occurring in cosmic concentrations as 1.11 atomic % of total C (Nier, 1950). The carbon isotopic content of materials is most commonly presented in terms of the parameter δ^{13}C where:

$$\delta^{13}C = \left[\frac{\left({}^{13}C / {}^{12}C \right)_{\text{sample}}}{\left({}^{13}C / {}^{12}C \right)_{\text{standard}}} - 1 \right] \text{x1000} \qquad \text{Equation 1.5\_1}$$

The standard material used is usually the Pee Dee Belemnite from the Pee Dee formation, South Carolina, U.S.A. (Craig, 1957) and δ^{13}C is expressed in parts per thousand (‰).

Observations: Early pioneering work on the determination of carbon isotopes in diamond was carried out by Nier and Gulbransen (1939). The carbon isotopic characteristics of diamonds from a large number of sources worldwide have now been determined. Of over 1300 analyses collated for the present study, the range in values obtained was found to be from -34.4[1] (Sobolev et al., 1979) to 1.98[2] (van Heerden, 1993).

As figure 1.5_2 demonstrates, this range in composition is greater than that exhibited for carbon isotopes in other mantle derived material (van Heerden, 1993) and is almost exactly the same as that observed for meteorites (Deines and Wickman, 1973). The range does not, however, spread to the extremely depleted values of some sediments (Kirkley et al., 1991).

In terms of the distribution of data, δ^{13}C values for diamond cluster strongly around a value of ~ -5 ‰, similar to that of OIB, MORB, carbonatites and kimberlites. Indeed the similarity of the mode of δ^{13}C values around this value for a wide range of mantle derived material, has led to the acceptance of the range δ^{13}C = -5 to -7 ‰, as being the original (primordial) and representative mantle compositional range. Unlike other mantle carbon sources, however, diamond shows a marked negative skew in its distribution (figure 1.5_3). The first of the highly depleted δ^{13}C values was obtained by Smirnov et al. (1979).

The distribution of δ^{13}C values seen in figure 1.5_3, is not globally constant. The carbon isotopic characteristics of stones from Dokolwayo (Daniels, 1991), for example, does mirror the global trend.

---

[1] This value was obtained from a polycrystalline diamond intergrowth of unknown paragenesis from the Mir pipe, Yakutia.

[2] This value was obtained from a Hunan stone of unknown paragenesis.

Other localities, however, yield different characteristics. Star diamonds (Hill, 1989) show a restricted range in values clustering closely around $\delta^{13}C$ = -5 ‰, whereas Argyle stones (Jaques et al., 1989) show a distinctly positive skew with a mode at $\delta^{13}C$ = ~ -12 ‰.[3].

Explanation of $\delta^{13}C$ variation: Three explanations can be envisaged for the presence of $\delta^{13}C$ values outwith the primordial mantle range:

- The true primordial range of $\delta^{13}C$ in the mantle is, in fact, not as restricted as often cited; areas exist in the mantle which have bulk $\delta^{13}C$ values relatively depleted or enriched compared to the range -5 to -7 ‰ (a view supported by, amongst others, Deines et al., 1993)[4].
- There exist a number of processes by which carbon isotopes can be fractionated.
- There exists a mechanism whereby depleted or enriched material can be taken into the mantle, for example, by means of subduction.

Given that diamond is envisaged to be precipitated in an environment involving fluid, it would seem inevitable that some explanation of the excessive range in $\delta^{13}C$ values in diamond should be attributed to its particular mechanisms of growth; in particular to fractionation due to the presence of a fluid[5] phase (Deines, 1980). Growth of diamond from a homogeneous $\delta^{13}C$ source, in the absence of fluid (but in the presence of melt), *can* produce a variation in $\delta^{13}C$, because of fractionation between growth faces. The range of fractionation, however, in a fluid absent phase is likely to be small and close to 1‰ (Deines, 1980 and Polyakov and Kharlashina, 1995). In the presence of fluid, fractionation occurs depending on the fluid species involved. Diamond is expected to precipitate within fluid comprising various proportions of the components, C, H and O and a number of diamond precipitating reactions can be envisaged. Deines (1980) concluded that only reactions involving CO_2 and CH_4 were plausible under mantle conditions, CO being expected to be present in insignificant quantities. Deines (1980) modelled the precipitation of diamond under conditions of 4.5 GPa, 1793 K using an initial source $\delta^{13}C$ value of -5 ‰. As diamond is *enriched* in $\delta^{13}C$ compared to CH_4 by ~ 1 ‰, he found that reactions involving methane, e. g. the dehydrogenation of methane:

$$CH_4 \leftrightarrow C + 2H_2 \qquad \text{Equation 1.5\_1}$$

---

[3] These differences, as will be discussed in the following paragraphs, have a strong correlation with paragenesis type.

[4] This can be the *only* explanation of any $\delta^{13}C$ heterogeneity if the *total* carbon in a particular source rock is converted to diamond. Certainly, if diamond is a stable phase, carbon will be strongly partitioned into crystallising diamond, however, C can be accommodated within a number of crystalline substances and, in particular, melt and other fluid phases. The total conversion of carbon to diamond, however, is not considered particularly relevent to natural diamond precipitation régimes.

[5] Here, the term fluid is used, in particular, to refer to C-H-O fluid. Fractionation involving melt is low.

largely cause a slight, $\delta^{13}C$ = ~ 3 ‰, negative skew in distribution centring around the initial $\delta^{13}C$ value of the fluid. In contrast, as diamond is *depleted* in $\delta^{13}C$ compared to CO_2 by ~ 4 ‰, precipitation of diamond by reduction of CO_2:

$$CO_2 \leftrightarrow C + O_2 \qquad \text{Equation 1.5\_2}$$

produces distributions with a shift in mean $\delta^{13}C$ of ~ 5 ‰ and a positive skew. Figure 1.5_4 shows the form of distributions which Deines (1980) obtained.

It should be noted, however, that the particular end-result of fractionation depends, of course, on the relative proportions of other species involved and whether, in fact, precipitation occurred under conditions of equilibrium and in open or closed systems.

Fluid fractionation may provide a satisfactory explanation for the range in $\delta^{13}C$ values for some individual diamonds (eg. Javoy et al., 1984). Although neither distribution modelled by Deines (1980), figure 1.5_4, necessarily, mirrors the distribution of $\delta^{13}C$, many discrepancies can be accounted for by varying physical conditions. For some stones, however, the range of $\delta^{13}C$ is too large (Javoy et al., 1984) to be explained by simple fractionation. In particular, variation of $\delta^{13}C$ in coated stones is explained by the coat forming in altogether different physical conditions from the core (Boyd et al., 1987). Within individual pipes, the range of $\delta^{13}C$ compositions in diamonds, even accounting for variation in pressure and temperature conditions (Deines, 1980) is often greater than can be explained by fractionation from a single source $\delta^{13}C$ value. Javoy et al. (1986) invoked degassing of CO_2 as a mechanism for enhancing fractionation, however, his fractionation factors have been disputed (Mattey et al., 1990). Another factor must, therefore be added to explanation of $\delta^{13}C$ ranges within many diamond populations. Source mixing is the proposed model for the ranges obtained from diamonds from: Finsch and Premier (Deines et al., 1984): Roberts Victor (Deines et al., 1987): Jagersfontein and Koffiefontein (Deines et al., 1991): a single diamond from Koffiefontein (Harte and Otter, 1992) and Letseng-la-Terai (McDade and Harris, 1996).

When we consider diamonds on the basis of their paragenesis (section 1.6), we see that neither peridotitic (figure 1.5_5), websteritic (figure 1.5_6), nor coated stones (figure 1.5_7) contribute significantly to the negative distribution of $\delta^{13}C$ values for diamond. On the other hand, diamonds of the eclogitic (figure 1.5_8) and sulphide (figure 1.5_9) parageneses[6] (plus a number of stones of unknown paragenesis, figure 1.5_10) do show significant depleted $\delta^{13}C$. Eclogitic stones from Dokolwayo (Daniels, 1991) have a distribution very similar to the global eclogitic distribution, whereas Argyle (Jaques et al., 1989) and Sloan (Otter, 1989) eclogitic diamonds have a pronounced peak at depleted values. It should be kept in mind, however, that not all diamond sources involving eclogitic diamonds yield heavily depleted carbon isotopic contents. Eclogitic diamonds from Ellendale (Jaques et al., 1989), Star (Hill, 1989), and, to an extent, Premier (Deines et al., 1989) all yield $\delta^{13}C$ values clustering around -5 ‰.

Certainly, the bulk composition of source rocks for eclogitic diamonds is quite different from that of peridotitic and coated diamonds, simply on the basis of inclusion chemistry. It would be reasonable to suggest, therefore, that, for at least eclogitic diamonds with highly depleted carbon isotopic content, the source of carbon has a different isotopic content from that of peridotitic source material rather than having to invoke an unusual mechanism of formation. The same is also probably true for sulphide and websteritic paragenesis stones.

---

[6] As described in section 1.4.

Section 1.5.2.2 Nitrogen in diamond

Nitrogen is the most widespread and abundant impurity in diamond. Its abundance, however, is highly variable. Values of the order of 5500 ppm have been recorded whereas, type II diamonds typically have nitrogen contents below 20 ppm (Bibby, 1982). Furthermore, in type IIb diamonds, nitrogen content is so low, <0.2 ppm that the presence of boron is not wholly compensated for; such crystals are p-type semiconductors.

Two particular aspects of nitrogen are considered important in addition to its concentration. These are the isotopic characteristics of nitrogen and its state of aggregation. Details of these two factors are discussed in the following sections, 1.5.2.2.1 and 1.5.2.2.2.

Section 1.5.2.2.1 Aggregation of N in diamond and Infra Red absorption characteristics

The presence of nitrogen in diamond causes absorption in the one-phonon region of the Infra-Red spectrum (Kaiser and Bond, 1959). The energy of absorption is dependent on both the concentration and distribution of nitrogen impurities and is usually measured using Fourier Transform Infra-Red Spectroscopy (FTIR).

Observations: A number of different absorptions can be identified and these give rise to the common classification system used for diamond.

- Diamonds exhibiting no absorption in the one-phonon region are termed Type II[1, 2].
- Diamonds exhibiting absorption in the one-phonon region are termed Type I which is further subdivided:
  - A broad absorption around 1150 cm^{-1} classifies a stone as Type Ib
  - Diamonds exhibiting *additional* absorption at 1282 cm^{-1} are termed IaA
  - Absorption at 1175 cm^{-1} gives rise to IaB[3] diamonds. In detail, pure IaB diamonds tend to show a plateau between 1310 cm^{-1} and 1230 cm^{-1} (over the position of IaA absorption) a maximum peak at 1175 cm^{-1} with a shoulder at 1100 cm^{-1} and a spike at the Raman energy of 1332 cm^{-1} . Occasionally, local absorption also occurs at 1365 cm^{-1} (B' absorption), and at 1370 cm^{-1} (D absorption).

Figure 1.5_11 represents the typical absorption characteristics of N-rich stones of differing aggregation state and incorporates the typical absorption characteristics of carbon in the two-phonon region present in all diamond spectra. In addition, table 1.5_2 summarises the classification scheme outlined above.

---

[1] The designation of a stone as Type II has, historically, been a hazy matter. Although the implication is that Type II stones are free from nitrogen impurity, such a conclusion depends on the analytical threshold and uncertainty of the technique used to determine concentration from IR absorption. Up until five years ago, the minimum threshold for determination of N content in diamond from FTIR was ~ 30 atomic ppm. This value refers to the general supply of stones ie. not those which have been specially cut, polished, orientated and scrupulously cleaned for analysis. Diamonds described as Type II using apparatus developed over five years or so ago, can, therefore be considered to have less than 30ppm N. More modern apparatus (eg. the Nicolet Magna-IR™ 750 Spectrometer used in the present study) which can measure down to ~10 atomic ppm nitrogen give rise to a definition of Type II as referring to stones with ≤10 atomic ppm nitrogen. For most studies of nitrogen, such indistinction of classification is relatively unimportant because diamonds containing ≤30 ppm nitrogen are rare. Low N stones comprise a significant proportion of the present study, however. Indeed, similarly sourced stones from other localities yield low nitrogen concentrations. For example, K30 and K34 fPer bearing diamonds from Koffiefontein are classified as Type II and stone K33 yields 33 ppm N (Deines et al., 1991). Care has, therefore, been taken to classify the meaning of Type II for the present and related studies in the following text, section 5.5.2.1.

[2] Additionally, absorption at 0.305, 0.348 and 0.364µm (in the 3 phonon region) is observed for some rare blue diamonds. This is attributed to the presence of B which appears, naturally, in concentrations up to ~ 0.25 ppm: such stones are termed Type IIb.

[3] Diamonds exhibiting characteristics of IaA and IaB absorption are termed Type IaAB.

Table 1.5_2 Diamond classification on the basis of FTIR one-phonon absorption characteristics.

Classification	One-phonon absorption	N aggregation	Notes
Ib	Broad 1150cm^{-1} peak	Single-substituted N	
IaA	1282cm^{-1} peak	Pairs of N	
IaB	1175 & 1332 cm^{-1} peaks	4 N atoms + vacancy	Often with D and B’
II	No absorption	Generally ≤ 30 at. ppm N	
IIb	2460 & 2790 cm^{-1} peaks	Single-substituted B	

Explanation: Much work has been undertaken on the interpretation of the one-phonon absorption. It has been concluded that, certainly at relatively low P, T conditions (~ 5 GPa)[4], N singly substitutes for carbon in diamond. It is this accommodation which gives rise to Ib absorption (Kaiser and Bond, 1959). It is thermodynamically preferable, however, for nitrogen to exist in higher forms of aggregation, ie. pairs and certain types of clusters. Nitrogen atoms migrating through the diamond lattice due to the movement of defects will tend to rest longer when they become adjacent to additional N atoms. This scenario leads to IaA absorption where N exists as pairs (Davies, 1976) and, on further aggregation, IaB absorption, where four nitrogen atoms cluster around a vacancy[5],[6] (Lousber and van Wyk, 1981). Additionally, D and B’ absorptions are considered to be due to aggregations of tens to thousands of C and N atoms displaced by the stabilisation of vacancies on formation of B centres and forming strings or plates (Evans and Phaal, 1962 and Woods, 1985): D is also termed ‘platelet absorption’. Platelet size is dependent on the concentration of nitrogen; high concentrations of nitrogen will aggregate quickly thus forming many short platelets whereas on slower growth, where nitrogen concentrations are lower, platelets will accumulate to greater lengths (Woods, 1985).

It is now possible to quantify the type and abundance of nitrogen impurity in diamond because FTIR spectra can be deconvoluted. Specifically, total N content and % A, % B and % D components of aggregation can be determined from FTIR analyses. Boyd et al. (1994 and 1995) present the most complete description of the quantification methodology to date.

Factors involved in the progression of aggregation: The progression of aggregation that a N containing stone is expected to experience is Ib to IaA to IaAB to IaB, with the starting state depending on the initial aggregation. The degree to which this progression proceeds has been found

---

[4] It is not known whether or not diamond formed at extreme conditions of temperature accommodates nitrogen, initially, in an aggregated state. Certainly the presence of *some* IaA signature in lower mantle sourced stones from the present study, section 5.5.4 and 5.5 would suggest that high states of aggregation even at lower mantle conditions require some period of time to evolve before becoming flly IaB stones. High temperature may still, however, favour missing out the Ib - IaA step. This interpretation further compromises the effectiveness of quantitiative determination of temperature and residence time for aggregated stones.

[5] Absorption at 24000 cm^{-1}, in the visible spectrum, is interpreted as being due to 3 N atoms surrounding a vacancy. Such aggregation is termed N3.

[6] There is observed to be a progression from Ib to IaA to IaB on addition of thermal energy and / or time (Evans and Harris, 1989), which emphasises the migrational and relative stability aspects of aggregation.

to depend on a number of factors; notably temperature, time and total N content and has been quantified in terms of %IaA, %IaB and %Ib by Evans and Harris (1989). Although it may seem that the determination of N aggregation could, therefore, be a useful tool in dating stones if their conditions of formation are known, the progression of aggregation is highly temperature dependent and is also significantly affected by plastic deformation: a factor whose effect is poorly understood. In practice, therefore, given the uncertainties in not only the formation temperature but temperature *history* of even the best constrained stones, in addition to the unknown role of other factors, e. g. N3 centres[7], platelets, pressure, initial aggregation, plastic deformation, defects etc., it is considered here that any quantification of residence time or temperature history is inappropriate. Indeed, this is especially true for stones of the present study whose temperature histories are subject to large uncertainty. It should be kept in mind, however, that consideration of the role of temperature and time in aggregation still has an important role to play. Indeed aggregation state represents a useful tool in indicating, *qualitatively*, the likely history of a suite of stones and it is from this qualitative viewpoint that the aggregation of stones in the present study will be considered, section 5.5.2.1.2.

➠

---

[7] On progression from IaA to IaB, the intermediary formation of N3 centres have not been observed (Evans and Harris, 1989). Given, however, that the conditions of formation of N3 centres are not known, their role cannot be considered mutually exclusive from IaA to IaB aggregation in all natural systems.

Section 1.5.2.2.2 Nitrogen Isotopic content of diamond

In addition to ^{14}N, a second nitrogen isotope occurs in significant quantities naturally; ^{15}N. Some of the earliest work on nitrogen isotopic content of diamond was conducted by Javoy et al. (1984) who studied the nitrogen isotopic content of coated diamonds from Mbuji Mayi. Subsequent work has been undertaken by, amongst others, Boyd et al. (1988, 1992), vanHeerden (1993), Boyd and Pillinger (1994), Cartigny et al. (1996), and the present study (section 5.4.2.2.1). In a similar fashion to carbon, nitrogen isotopic contents are typically expressed in the delta notation, of the form of equation 1.5_1, as $\delta^{15}N$. For nitrogen, the standard used is atmospheric nitrogen.

Observations: Despite being a light element, as nitrogen is a *trace* element in diamond, it has significant potential to be fractionated isotopically, certainly more so than carbon, section 1.5.2.1. Most initial work on $\delta^{15}N$ was undertaken on coated stones where a range from +7.7 ‰ to -8.7 ‰ was found (Boyd et al., 1992). Furthermore, $\delta^{15}N$ values in coats were generally found to be more depleted than cores of individual stones (Boyd et al., 1987, 1992). For non-coated stones, the $\delta^{15}N$ range comprises +16.6 ‰ (Boyd and Pillinger, 1994) to -34.5 ‰ (Cartigny et al, 1996). The distribution of over 450 $\delta^{15}N$ values from the literature and the present study, was found to be largely Gaussian with a mean of 0.57 ‰ (figure 1.5_12). Little work has been undertaken to study the role of paragenesis on nitrogen isotopic content of diamond, indeed the distribution of all stones analysed is dominated by the signature of stones of unknown paragenesis (figure 1.5_13). Available data (van Heerden, 1993 and Cartigny et al., 1996) indicate a more *enriched* range amongst eclogitic stones, 13.6 ‰ to -4.6 ‰[1], with a mean of 2.97 ‰ (figure 1.5_14) and a slightly *depleted* distribution for coated stones (figure 1.5_15) centring on a mean of -2.19 ‰ and exhibiting a positive skew. Peridotitic stones (figure 1.5_16), on the other hand, have a mean of 0.8 ‰ and a range close to the global range.

Source of nitrogen isotopic signature: The generally accepted scenario for the evolution of the Earth's atmosphere is that it evolved from degassing of the upper mantle on formation of the crust. One would expect, by balance, that the mantle has a $\delta^{15}N$ composition intermediary between crustal material and the atmosphere. As the atmosphere is defined as having a $\delta^{15}N$ value of 0 ‰, and the nitrogen isotopic content of such crustal material as organic matter in sediments, ammoniacal nitrogen in metasediments and S-type granites, all have positive values for $\delta^{15}N$ (as discussed in Boyd and Pillinger, 1994), slightly positive $\delta^{15}N$ values are expected for mantle material. However, the first extensive study of $\delta^{15}N$ compositions of diamonds (Javoy et al., 1986), yielded *negative* $\delta^{15}N$ values for coated diamonds. Javoy et al. (1986) assumed that these values were representative of the

---

[1] Cartigny et al's (1996) value of -34.5 ‰ was for an eclogitic stone from Fuxian.

bulk mantle and invoked a number of complex models to redress the anomaly. Javoy's (1995, *personal communication*) preference appears to be that a secondary, positive $\delta^{15}N$ is required in order to redress the balance. This positive reservoir may be C1 chondrites, which have largely enriched $\delta^{15}N$ values (Kung and Clayton, 1978). The only additional nitrogen bearing materials known, which yield significantly depleted $\delta^{15}N$ values, are enstatite chondrites (Kung and Clayton, 1978). Javoy et al. (1986) suggests that this is the source of negative $\delta^{15}N$ in diamond and it follows, therefore, that the bulk composition of the mantle diamond source is of enstatite chondrites. The coated stones which Javoy et al. (1984) use for their model, however, are unrepresentative of the diamond population (compare figure 1.5_15 with 1.5_12). Indeed, coated stones, in contrast to more enriched eclogitic and peridotitic material, on the basis of, amongst other factors, inclusion chemistry, exhibit more similarity with their host kimberlite than with typical mantle material. vanHeerden (1993), having observed that the diamond population generally has *positive* $\delta^{15}N$ values suggested that if these values are taken as being representative of the mantle, the simple degassing model from a positive $\delta^{15}N$ reservoir used to explain atmospheric evolution, works. On the other hand, there *may* be indications from the $\delta^{15}N$ distribution of São Luiz material, section 5.4.2.2.1, that there are parts of the deep mantle where a relatively depleted mantle reservoir exists.

It is irrefutable that the diamond population does have a significant scatter in $\delta^{15}N$ values, figures 1.5_12 - 1.5_16. Fractionation can provide a suitable explanation for this observation. There are indications that significant nitrogen isotope fractionation can occur on diamond formation (Boyd et al., 1994). Indeed, unlike for carbon isotopes, significant fractionation has been found to occur between growth zones (Boyd and Pillinger, 1994 and Boyd et al., 1988). A fractionation of ~ 4.5 ‰ $\delta^{15}N$ was measured bewteen nitrogen on {100} compared to {111}. The influence of fluid fractionation has not been studied but is likely to be significant. Fractionation can, therefore, still be considered a plausible mechanism for the cause of nitrogen isotopic variation in diamond.

Section 1.5.2.3 Additional Impurities

A comprehensive review of impurities in diamond can be found in Bibby (1982) and, in particular, an excellent discussion of gases in diamond can be found in Ozima (1989). More recently, technical advances have allowed for improved precision and the ability to analyse smaller sample sizes. Results obtained using recent advances can be found in Blaçic et al. (1992), Hart et al. (1993), Mathez et al. (1993) and Verchovsky et al. (1993).

Requirements: Particular emphasis has been placed on an attempt to measure the isotopic proportions of radiogenic elements, in particular, the noble gases. Results obtained so far give a starting point for calculations of mantle evolution and can be compared with more recently sourced material such as MORB to investigate the evolution of systems such as the mantle / atmosphere. In order to obtain useful results, however, there are two main requirements:

- Precision of measurement at the ppm or even ppb level.

  Analytical techniques successfully employed have tended to be nuclear (giving good resolution and high count rates allowing for high precision); neutron activation analysis (NAA) (eg. Luther and Moore, 1964) and micro-activation using ^{3}He (e. g. Mathez et al., 1993). In NAA, the decay of artificially heavy isotopes of the element to be analysed is measured. An example of such a reaction followed is $^{10}B(n,^{7}Li)^{4}He$. For micro-activation, a typical reaction would be $^{16}O(^{3}He,p)^{18}F$ where ^{18}F decays to ^{18}O by positron emission, a reaction which can be monitored. For samples where abundances of the trace elements of interest are high, however, more direct techniques such as combustion mass spectrometry (eg. Verchovsky et al., 1993) have been adopted. Combustion does have its problems. It introduces minute quantities of atmospheric gases which add uncertainty to any results obtained. For minerals other than diamond, release of volatiles by melting is the most commonly adopted approach to avoid this problem. However, with the melting point of diamond above 4200K (Van Vechten, 1973), melting is an unrealistic approach. This problem has been successfully avoided, due to the breakthrough observation that volatile release may go very close to completion on graphitisation of diamond (Kaiser and Bond, 1959). This technique, where applicable, is now widely employed.
- Confidence as to the ability of diamond to retain its impurities.

  Studies of diffusion of gases in diamond have been the most extensive and show the following broad results. Two modes of degassing tend to occur in step-heating experiments. The first, a fast diffusion usually involving a small quantity of trapped gas occurs at low temperatures (up to 1973 K). This is thought to involve gases caught in defects. The second mode occurs at higher temperature (above 2073 K) and is very slow, of the order of 10^{-17} cm^{2}s^{-1} for He (Ozima, 1989),

> which is relatively mobile compared to other elements, for example Ar (Fukunaga et al., 1987). The variability of diffusion values obtained is huge but, even so, the general consensus appears to be that diffusion is sufficiently low to retain heterogeneity at reasonable mantle temperatures for times approaching the age of the Earth (Ozima, 1989). Such results allow for reasonable confidence that trace element compositions are representative of composition on crystallisation of diamond.

As far as results and inferences obtained from the study of impurities in diamond are concerned, these are best tackled individually.

Oxygen: Where O appears to be present as a lattice occupying component (i.e. not residing in, for example, sub-microscopic silicate inclusions), concentrations obtained from diamonds from a variety of sources yield values ranging from 10-100 ppm (Mathez et al., 1993).

Helium: Helium isotopic compositions (^{3}He/^{4}He) of ~ 2 x 10^{-4} have been determined for a number of diamonds (Takaoka and Ozima, 1989). This value is higher than the planetary ratio of 1.4 x 10^{-4} (Ozima, 1989). Since the value of the ^{3}He/^{4}He ratio is expected to have decreased with time, assuming that the diamond value is representative of mantle material, this would indicate that the planetary ratio adopted is not indicative of the bulk earth. A solar composition, in line with observations by Anderson (1989), section 4.2, with a ratio of ~ 4 x 10^{-4} is suggested, therefore, as being more representative of the bulk earth. Some problems arise, however, due to the possible formation of ^{3}He by cosmogenic means. Unless cosmogenic signatures can be removed, alluvial diamonds and stones in the upper 50m of kimberlite bodies are unsuitable for meaningful helium ratios in this context (Verchovsky and Begemann, 1993)[1].

Argon: The high ^{40}Ar/^{36}Ar ratio determined for some diamonds would suggest that subducting slab material was not a significant component in their source region (Bibby, 1982).

Hydrogen: Hydrogen is commonly found in diamond and can be identified by its absorption at 3107cm^{-1} in the infra red (Kiflawi et al., 1996). In some cases, hydrogen is an important catalyst in the crystallisation of diamond (section 6.1.1).

➠

---

[1] This problem may be surpassable by the adoption of step-heating techniques. Cosmogenic ^{3}He may be released at lower temperature than primordial ^{3}He.

Section 1.5.3 Interrelation of compositional and physical characteristics

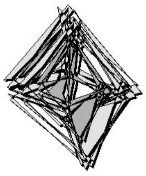

The study of the interrelationships of compositional and physical features of diamond has been followed extensively in the literature. Definitive conclusions have not, however, been particularly forthcoming. More than anything, it is clear that the lack of consistency in the interrelationship of determined variables (such as $\delta^{15}N$, $\delta^{13}C$, N content) is indicative of a high degree of complexity relating to the mechanisms of diamond growth.

Carbon and nitrogen isotopes: The range in $\delta^{13}C$ and $\delta^{15}N$ compositions for both suites of stones and individual diamonds is such that a large number of analyses are required in order to say anything meaningful about the distribution of isotopes. The same is true when interrelations of carbon and nitrogen isotopes are considered. Although the distributions of $\delta^{15}N$ look reasonably well grouped from figures 1.5_12 - 1.5_16, for individual stones and sources, the range of values is large. van Heerden (1993) observed large variations in $\delta^{15}N$ for Argyle plates showing homogeneous $\delta^{13}C$ content, Javoy et al. (1984) found a positive correlation of $\delta^{15}N$ against $\delta^{13}C$ for a population of stones from Mbuji Mayi whereas van Heerden (1993) observed an opposite trend. Apparent discrepancies could, perhaps, be solved by discriminating between sources and diamond type. Plotting *all* available data on the basis of paragenesis, figure 1.5_17, shows that perhaps some trends can be identified:

- For all analyses, irrespective of paragenesis, it is clear that the variation in $\delta^{15}N$ values is almost double that of $\delta^{13}C$ values[1]. Furthermore, it is only within the field of least depleted carbon isotopic content, $\delta^{13}C$ of ~ -8 ‰ to ~ -3 ‰ ('mantle' values) that strongly negative values of $\delta^{15}N$ (< -10 ‰) appear. Depleted $\delta^{13}C$ stones, as a general rule, have positive $\delta^{15}N$ values. The distribution of all analyses is strongly mirrored by the behaviour of stones of unknown parageneses as this population involves diamonds from a variety of sources and, presumably, mineralogies.
- The eclogitic suite of stones, predominantly involving data from Australian stones (van Heerden, 1993), generally represent the common carbon-depleted eclogitic diamonds ($\delta^{13}C$ ~ -10 ‰). Values for nitrogen are, typically, positive and, although no particular trend is obvious, it is perhaps noteworthy that the only negative values for nitrogen isotopic content lie amongst the more depleted $\delta^{13}C$ stones.

---

[1] The differences in mass between ^{15}N and ^{14}N compared to ^{13}C and ^{12}C are not significant. As discussed previously, section 1.3.2.2.2, nitrogen, being a trace element is subject to greater fractionation than carbon.

- The stones of peridotitic paragenesis which have been measured for nitrogen isotopic content are, perhaps, a little unrepresentative of the global population. As discussed before, *Argyle* peridotitic diamonds, of which figure 1.5_17 is predominantly composed, are unusually depleted in carbon isotopic content. Interestingly, unlike the eclogitic stones analysed, there does appear to be a significant trend in $\delta^{15}N$ against $\delta^{13}C$; the less depleted the carbon isotopic content the more depleted the nitrogen isotopic content.
- Coated stones show the opposite trend to peridotitic stones: increasing enrichment in $\delta^{13}C$ is matched by increasing enrichment in $\delta^{15}N$.

Clearly, more analyses are required for particular trends of nitrogen isotopic content of diamond against carbon isotopic content, to be assured. Extensive work is being carried out presently by Cartigny and Harris (following from Cartigny et al., 1996). At present though, it can be said that the inter-relationship of $\delta^{15}N$ with $\delta^{13}C$ *may* provide a means for distinguishing parageneses (van Heerden, 1993).

Interrelationship of nitrogen characteristics: vanHeerden (1993) observed an increase in nitrogen content and nitrogen aggregation state with enrichment in $\delta^{15}N$ content for some Argyle 2 mm diamonds. However for some other stones he found a trend of *decreasing* nitrogen content with increasing $\delta^{15}N$, a similar observation being made by Boyd et al. (1988). vanHeerden (1993) also observed that eclogitic stones from Argyle have lower nitrogen content and are more highly aggregated than peridotitic stones. This cannot, however, be regarded as a global trend. Some interrelationships are a little clearer, however. For example, coated stones tend to have higher nitrogen contents. Such stones are envisaged to have grown quickly and, as such, kinetic factors rather than equilibrium factors have been relatively more important. Impurities such as N are more likely to be accommodated under such a scenario. Furthermore, the centres of plates studied by, for example, vanHeerden (1993) often have higher nitrogen content and higher $\delta^{15}N$ values. This is consistent with fractional crystallisation where nitrogen, and particularly ^{15}N, behaves compatibly with diamond (Boyd et al., 1994).

Relationship of colour and morphology to $\delta^{13}C$ composition: Extensive study has been made, (e.g. Deines et al., 1984, 1987, 1989, 1991, 1993) into the significance of visually observable characteristics of diamonds in terms of their $\delta^{13}C$ composition (for discussion see Harris, 1992). Colourless diamonds from Bellsbank appear to be more enriched in $\delta^{13}C$ than coloured stones, although the correlation is extremely variable (Deines, 1980). Furthermore, Deines (1980) does suggest that there is a rough correlation between shape and carbon isotopic content from Premier (dodecahedral diamonds are more depleted in $\delta^{13}C$ than octahedra and macles). Generally, however, amongst Premier diamonds, Deines (1980) found no significant relationships between shape, colour and carbon isotopic content. This observation reflects the worldwide concensus that shape and colour usually appear to have little to do with composition.

Relationship of mineral chemistry to isotopic content: In a broad sense, the relationships between $\delta^{13}C$, $\delta^{15}N$ and inclusion chemistry have been previously discussed in sections 1.5.1, 1.5.2.2 and 1.5.3 in so much as paragenesis type has been linked to $\delta^{13}C$ and $\delta^{15}N$ content. The reader is referred to Deines et al. (1984, 1987, 1989, 1991, 1993) and Deines and Harris (1995) for discussion for individual localities and the review of Kirkley et al. (1991) for worldwide sources.

➠

Section 1.5.4 Formation of diamond

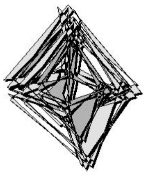

Details of the formation *mechanisms* of diamond will be discussed from a chemical point of view in section 6.1.1 and on an atomistic scale in section 6.1.2. It is the role of the present section to discuss, in a broad sense, the traditional view for the formation of diamond within a geological framework, in particular, concerning the source regions which account for 99% of diamonds mined at present. The reader will be able to compare and contrast the following discussion with that of the scenario proposed specifically for the formation of the diamonds from São Luiz and Guinea in section 6.3.

Two key observations have been made by workers in the field of diamond formation. Firstly, diamond is a high pressure phase stable at conditions in excess of 4.8 GPa at 1400 K (Kennedy and Kennedy, 1976), figure 1.5_18. Secondly, on Earth, primary sources of diamond have been observed predominantly in kimberlites and lamproites in cratonic or craton related settings[1] (for further discussion of locations of diamond sources see section 7.5.3). These two observations have led workers to believe that the source of diamond for which we have examples at the Earth's surface is thickened continental mantle lithosphere (e.g. Haggerty, 1986) and, perhaps, in some cases, sub-cratonic asthenosphere. Here, the P,T conditions of a low geotherm favour formation of diamonds at depths of ~ 100km (in the thickest cratonic areas) assuming adequate carbon to facilitate the sourcing of diamond. In addition, the conditions of oxygen fugacity are thought to be favourable for diamond stability (the role of fO_2 on diamond formation will be discussed in detail in 6.2.1). A useful discussion of the growth of diamond in such a setting is provided by Haggerty (1986). Figure 1.5_19, being his figure 2, illustrates the different régimes for particular types of diamond as far as morphology and type are concerned. According to Haggerty (1986), diamonds do not, generally, form in the asthenosphere because of high fO_2, but will form in the lithosphere in differing forms according to conditions of pressure and temperature: low aggregated nitrogen-bearing cubes forming at shallow depths with an increasing tendency towards more aggregated nitrogen and octahedral shaped stones with increasing depth. Included material is dictated by the host mineralogy, either, broadly, eclogitic or peridotitic (section 1.6). Additionally, the diamond content of the kimberlite or lamproite body (this is found to differ widely, Harris, 1992) will be due to the complex interplay of a number of factors: the region of the Earth from where such magmatism is sourced, the oxygen fugacity of the kimberlitic melt, the scale of residence of kimberlite before final eruption (if any) and the mechanism of kimberlite emplacement[2] and its relationship with host rock tectonics.

---

[1] Rarely, diamonds have been also been found in a variety of other earth-bound settings calling for different explanations for their formation from those discussed in this section. Briefly, these stones are found in ultra high-pressure metamorphic rocks e.g. Kokchetav, Kazakhstan (Sobolev and Shatsky, 1990) and China (Shutong et al., 1992) and as graphitised diamonds in the Rhonda massif of S. Spain and its African counterpart, Beni Boussera (Pearson et al 1989, 1993 and Davies et al 1993). In addition, diamond has been recovered from impact craters (Hough et al 1995) and in ophiolitic settings (Kaminsky et al., 1986).

[2] Diamond is found to float in melts of certain compositions (Suzuki et al., 1995). This fact will, likely, have some bearing on the diamond productivity of even rapidly emplaced magmas, like kimberlites.

An additional formation model is proposed by Kesson and Ringwood (1989), figure 1.5_20. They prefer a subduction origin where, rather than being precipitated from a fluid, diamond is formed from melt produced on dehydration of the slab. Eclogitic diamonds are envisaged to be primary precipitations from the melt whereas peridotitic diamonds evolve from percolation of these melts into surrounding peridotitic rock. Kesson and Ringwood (1989) therefore propose that E-type stones will predate P-type stones sourced from the same subduction event. Although this may be a wholly feasible model for the explanation of some diamond, it does not serve to explain, for example, the range in carbon isotopic signatures observed in most populations.

Xenocrysts or phenocrysts?: An additional question arises. Is the diamond we see in kimberlites and lamproites merely sampled by eruptives, i.e. xenocrystal, or is it a product of crystallisation from the melt, i.e. phenocrystal? It appears that the answer to this question can be ‘yes’ on both counts:

Experimentation has shown that given a volatile rich kimberlite melt, providing carbon is present, diamond will grow (Arima et al., 1993). In addition, fibrous diamonds show a plethora of included material of phases found as phenocrysts in kimberlite (e.g. Javoy et al 1984). The state of N aggregation of these diamonds as dominantly IaA (Boyd et al 1987 and 1992) or, rarely, Ib (terms discussed in 1.5.2.2), imply short residence times of low temperature between diamond formation and exhumation to the Earth's surface (Evans and Harris 1989); again compatible with a phenocrystal origin. Fibrous morphology implies rapid growth, and because fibrous diamonds usually exhibit a cubic morphology (e. g. Boyd et al., 1994), low temperatures of formation are implied (see figure 1.5_1). All these features are compatible with a phenocrystal origin, or at least an origin closely related to the event causing low degree melting or metasomatism triggering kimberlite or lamproite formation (Boyd et al 1994). In addition to fibrous diamonds, a phenocrystal origin has been implied for the formation of some true micro-diamonds[3]. Fibrous and cubic diamonds, although being the dominant type from some sources (eg. Mbuji Mayi in Zaire, Javoy et al 1984) are not representative of most diamonds currently in production, which are octahedral or dodecahedral in morphology and have features which would imply a xenocrystal origin:

Features of the majority of diamond (such as morphology, nitrogen aggregation and isotopic ratios in their inclusions) strongly indicate ages greater than those of their host kimberlite or lamproite and are, thus, xenocrysts. The vast majority of diamonds are non-cubic in dominant morphology and reasonably aggregated IaAB or IaB: such stones must have formed at reasonably high temperature (>1400 K assuming a pressure of 4.5 GPa) and have resided in the lithosphere for a considerable

---

[3] The definition of micro-diamond, strictly, is a diamond which has grown to a size no greater than 1mm in maximum dimension. Because of the tendency to adopt a simple size classification for diamond, there are many examples in the literature of diamonds being referred to as micro-diamonds simply because they are smaller than 1mm; many of these stones could be broken fragments of larger stones.

length of time, c. 97 Ma[4] (for 25% IaB aggregation of 1000 ppm N)[5]. More compelling evidence comes from the dating of groups of inclusions from a number of diamonds. Most notably ages of 1930 Ma for lherzolitic garnet and cpx inclusions from Premier in the Kaapvaal Shield (Richardson et al., 1984), 3200 - 3300 Ma for sub Ca-garnets from Bultfontein (Kimberley) and Finsch (Richardson et al., 1994), 990 Ma from eclogitic garnet and cpx from Orapa (Richardson et al., 1990) and 1158-1542 for eclogitic cpx from Argyle (Burgess et al., 1992) have been recorded. All these ages are significantly older than their kimberlite sources (see references in Harris, 1992).

The present consensus is, therefore, that although most diamonds are clearly much older than their magmatic hosts, diamond survives, in most cases (sections 7.5.1 and 7.5.3) in kimberlite or lamproitic melts (albeit eventually metastable in relation to graphite). Furthermore, under certain conditions, diamond xenocrysts can act as seeds for the precipitation of more diamond (kimberlite and lamproite both being carbon rich) and new crystals can form in the melt (Arima et al., 1993). It is important to keep this framework in mind when considering the form of relationships of ultradeep diamonds, as discussed in this work, with their kimberlite sources. This draws into discussion possible régimes of ultra-deep kimberlites (eg. Haggerty, 1994) and will be considered in detail in section 7.3.3.

Formation conditions: The development of geothermometers and geobarometers appropriate for application to inclusion assemblages has led to the determination of formation conditions for diamonds from a large number of localities[6]. Details are reviewed in Finnerty and Boyd (1987) and Harris (1992). The most commonly adopted thermometers are: garnet-olivine (O'Neill and Woods 1979), garnet-cpx (Mori and Green, 1985) and opx-cpx (Lindsley and Dixon, 1976), for peridotitic inclusions, and garnet-cpx (Ellis and Green, 1979; Powell, 1985 and Krogh, 1988) for eclogites. Two barometers, garnet-cpx (Nickel and Green, 1985) and opx-garnet (MacGregor, 1974) are adopted for peridotites. Assuming a pressure of 5 GPa, temperatures of formation range from 1173 - 1773 K. On average, eclogitic diamonds appear to originate from regions of hotter geotherms than peridotitic diamonds in that temperature ranges assuming the same pressure span to higher values for eclogitic inclusion pairs. There is significant overlap, however, and exceptions occur, Roberts Victor eclogitic stones, for example, appear to be have a cooler source than peridotitic stones (Harris, 1992). Often, diamonds of different paragenesis from the same locality are indistinguishable by means of temperature.

---

[4] This calculation involves large temperature related uncertainty and should be treated with caution. See section 1.5.2.2.1 for discussion of calculations.

[5] Such stones could still be phenocrysts, simply residing in a magma chamber for significant time to aggregate.

---

[6] Determination of the range of formation conditions of diamond has important implications for clarifying the histories of continental evolution (e.g. Gurney, 1990).

Section 1.6 Inclusions in diamond

In addition to atomic and molecular impurities, diamonds commonly contain inclusions of crystalline material of various sizes from a few unit cells to the macroscopic scale. Reviews of the occurrence of inclusions in diamonds are given by Harris and Gurney (1979), Meyer (1987), Gurney (1989), Harris (1992), van Heerden et al. (1995). Included material was first reported as early as 1645 by John Evelyn. Since then, and including those discovered in the present study, at least 56 different phases have now been described as inclusions in diamond, table 1.6_1. Inclusions can be classified into two[1] principal categories (Meyer, 1987).

- Epigenetic inclusions are defined as crystals which have grown from external sources into fracture systems of their diamond hosts. This definition also includes provision for pseudomorphic replacement of pre-existing inclusions. Inclusions can easily be classified as epigenetic if their stability field is significantly outwith that of diamond[2]; for example serpentine; although any phase, can, of course, be incorporated into a fracture system at a date subsequent to diamond formation.
- Syngenetic inclusions, on the other hand, have grown simultaneously with their occluded diamond, have a common phase field and, often, an imposed morphology is evident.

Epigenetic inclusions give valuable insights into the compositions of fluids (for example kimberlitic magma) associated with diamond at different points during their lifetime. Indeed, a number of inclusions released from stones in the present study are likely to have an epigenetic origin. Examples of epigenetic inclusions in this study are the biotite, plagioclase and albite inclusions from BZ239, section 2.2.1.9. The particular aim of the present study, however, is to investigate aspects of the nature of the deep earth; transition zone and lower mantle. In order to attempt this through study of inclusions, it is imperative, therefore, to consider *syngenetic* inclusions only.

---

[1] Meyer (1987) defines a third, ‘protogenetic’ category for inclusions which have formed *before* the occluded diamond. Such inclusions, in most cases, are difficult to separate from a syngenetic classification.

[2] The stability field of Cr-spinels (Cr-poor chromite) is outwith that of diamond (although $FeCr_2O_4$ chromite lies within diamond stability) and yet Cr-spinel (~ 65 wt% Cr_2O_3 up to 8 wt% Al_2O_3, Meyer, 1987) is a common inclusion in otherwise inclusion-free stones. There is much debate as to whether diamond grows naturally under metastable conditions (e.g. Angus and Hayman, 1988) which may be a reasonble explanation for the observation of seemingly syngenetic Cr-spinel inclusions. This is still a rather open question.

Table 1.6_1 Summary of epigenetic and syngenetic inclusion phases with syngenetic inclusions subdivided into paragenesis type.

Epigenetic	**Harzburgitic**	**Lherzolitic**	**Websteritic #**	**Eclogitic**
Serpentine	Sulphide ‡	Sulphide ‡	Sulphide ‡	Omphacite
Graphite *	Py-alm garnet	Py-alm garnet	Py-alm garnet	Py-alm garnet
Haematite	*>2 wt%* Cr_2O_3 ☯	*>2 wt%* Cr_2O_3 ☯	*up to 1 wt%* TiO_2	*<2 wt%* Cr_2O_3 ☯ *
Kaolinite	Olivine $Fo_{>92.5}$	*R of lherz. trend †*	*Mg # 0.55-0.80*	Kyanite
Acmite	Cr-spinel ¢	Olivine $Fo_{90-92.5}$	Olivine $Fo_{<90}$	Sanidine
Richterite	Mg-Ilmenite ¢	Cr-diopside	Cpx	Quartz *
Perovskite	Zircon ¢		Opx $En_{<90}$	Rutile
Mn - Ilmenite	Native iron ¢			Ruby
Spinel	Diamond ¢			Ilmenite
Xenotime	Clouds ¢			Chromite
Sellaite				Clouds
Goethite				
Fluids §				
Staurolite				
Sulphur *				

Sulphide ‡	**Majoritic garnet**	**Ferropericlase**	**Unknown**
Pyrrhotite *	Majoritic garnet *	TAPP *¥	Phlogopite
Chalcopyrite	Pyrrhotite *	Type I Px *	Biotite *
Pentlandite	Diopside *	Type II Px *¥	Muscovite
Heazlewoodite		Type III Px *¥	Amphibole
Pyrite		fPer *	Magnetite
Monosulphide s.s.		Wollastonite *¥	Apatite
Cubanite		Corundum ♣*	Moissanite *
		Quartz *	Sapphire *¥
			Calcite
			Glass þ

All terms are compositional, no structural information is necessarily implied. Data adapted from Harris (1992) table 9.3. # Deines et al. (1993) ☯ Gurney (1984) § Schrauder and Navon (1994) ♣ Var. ruby recovered in the present study is believed to be part of the ferropericlase association þ Wang et al. (1994) and Wilding (1993, *personal communication*) * Discovered in diamonds from the present study. ¥ Unique to the present study. ‡ According to Deines and Harris (1995) only 20% of sulphides could have formed in equilibrium with olivine; hence the proposal for an additional sulphide paragenesis. † For definition of the lherzolite trend see section 1.6.1.1. ¢ Classified under the general peridotite paragenesis. McDade and Harris (1996) obtained a calcite inclusion from diamond from Letseng-la-Terai which had strong syngenetic characteristics. Daniels et al. (1996) record a staurolite inclusion in a diamond from the Dokolwayo kimberlite; given their interpretation of this inclusion as being of crustal origin possibly subducted before diamond occlusion, this inclusion is protogenetic.

Syngenetic inclusions can be subdivided into a number of different parageneses. These parageneses are associations of phases which make up particular mantle rock types. Occasionally, several phases from one particular paragenesis are seen found within the same diamond. Indeed certain phases have been assigned to a particular paragenesis purely on basis of such association e. g. native Fe (Sobolev et al., 1981). Historically, 7 paragenesis types have been coined; eclogitic, harzburgitic, lherzolitic, wehrlitic, sulphide[3], websteritic[4] and unknown. Of these, the wehrlitic paragenesis is only loosely defined (McCandless et al., 1989) and is rarely used and the unknown paragenesis is a temporary classification for phases which cannot be confidently incorporated within other parageneses. Due to the findings of the present study, a number of phases which have previously been incorporated in the unknown paragenesis have been incorporated into two new paragenesis types. Table 1.6_1 summarises the phases discovered as inclusions in diamond on the basis of paragenesis type including the present study.

The particular compositional details of the parageneses types harzburgitic, lherzolitic, websteritic, sulphide and eclogitic are discussed in the following sections; 1.6.1-3 and the fPer and majoritic garnet parageneses[5] are discussed in section 2.3.

As previously mentioned, the classification scheme largely arises from similarities between inclusion types and the parageneses found in mantle rock types. In detail, there are often marked chemical differences between the compositions of diamond-sourced and xenolith-sourced phases.

---

[3] There has been much debate recently (e.g. Deines and Harris, 1995) over whether the sulphides should be classified as a separate paragenesis or as part of a general peridotitic paragenesis (involving harzburgitic, lherzolitic, websteritic). Sulphides are the most common inclusion in diamond and often occur outwith an association with other phases. Indeed they come from diamonds which have stable isotope characteristics distinct from other parageneses (Eggler et al., 1991 and Deines and Harris, 1995), compare figure 1.3_9 with figures 1.3_5 - 1.3_10.

[4] Harzburgitic, websteritic and lherzolitic paragenesis are commonly combined as a peridotitic paragenesis although many features of the websteritic paragenesis suggest that it is transitional between peridotitic and eclogitic parageneses.

[5] The fPer paragenesis is interpreted as having a lower mantle origin and the majoritic garnet as having a transition zone origin, section 4.4.2. These parageneses are so-called because fPer and majoritic garnet can be considered indicators of such depths of origin.

Section 1.6.1 Peridotitic parageneses

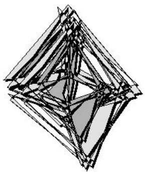

Although this paragenesis can been subdivided, it is sometimes useful to retain the classification for general discussion, especially as much previous work makes no attempt to subdivide inclusion type further. Sulphides aside, peridotitic inclusions make up the majority of crystalline material included in diamond (e.g. Harris, 1992)[1]. The fact that peridotitic inclusions dominate is particularly interesting due to the fact that diamondiferous peridotite nodules are exceedingly rare[2]. This fact alone is enough to indicate that the source of peridotitic inclusions is different from that of mantle peridotites appearing at the earth's surface in, for example, kimberlites. Indeed, when we look to the compositional details of peridotitic inclusions compared to peridotitic minerals from other sources, we observe striking differences. This is true across the board from both lherzolitic, websteritic and harzburgitic subivisions. For example, in terms of CaO and Cr_2O_3 compositions, Richardson et al. (1984) show that Finsch garnet inclusions have a distinctly harzburgitic composition whereas garnets from associated peridotitic nodules are distinctly lherzolitic. This distinction presumably has an explanation in the form of different source areas for diamonds and nodules and, indeed, garnet concentrates which yield intermediary compositions, probably come from intermediary localities.

The most prolific phases in the peridotitic parageneses are garnet, olivine, cpx and opx. Extensive measurement of compositional details of each of these phases included in diamond has been carried out (eg. Meyer and Boyd, 1972, and reviewed in Harris, 1992; Harris and Gurney, 1979 and Meyer, 1987). figures. 1.6_1 - 1.6_3 summarise much of the compositional findings so far obtained.

Garnets: The chemistry of garnet inclusions varies more amongst peridotitic parageneses than amongst other phases. This is often due to the source rock bulk composition lying away from a garnet composition; small changes in bulk composition are, therefore, reflected in large changes in the composition of garnet. The most commonly adopted method of subdivision of peridotitic garnet is on the basis of the Cr_2O_3 wt% / CaO wt% plot. Peridotitic diamond inclusions are found to plot in two general areas: a field of low CaO incorporating a range of Cr_2O_3 contents and a band of increasing Cr_2O_3 with CaO starting at ~4 wt% CaO, 2 wt% Cr_2O_3[3] (where values vary from pipe to pipe), figure 1.6_1. In terms of thermodynamics, the presence of a field, rather than a line in compositional space, is indicative of the presence of an additional degree of freedom and thus a loss of one component in the system. Consideration of the phase diagram comprising Al_2O_3, $CaSiO_3$ and

---

[1] On the basis of individual localities, however, this generalisation does not hold true; some kimberlites show a predominance of other parageneses; the Argyle mine, for example has a strong eclogitic dominance.

[2] Jaques et al. (1990) describe a diamondiferous peridotite xenolith from Argyle.

[3] Eclogitic garnets plot in a third field, CaO-rich but with Cr_2O_3 contents, arbitrarily below 2 wt%, section 1.4.2.

$MgSiO_3$ (Boyd, 1970) shows that most mantle peridotitic bulk compositions lie, either in a phase field involving garnet, cpx and opx (a lherzolitic assemblage), or else on a reaction line comprising garnet and opx (a harzburgitic assemblage)[4]. On the basis of a three component lherzolitic field, at fixed pressure and temperature, the composition of garnet is invariant, however in the harzburgitic region, the composition of garnet is variable but of lower Ca-content. Because natural systems do not simply involve the three components, $CaSiO_3$, $MgSiO_3$ and Al_2O_3 (Cr_2O_3, for example, is, of course, an important component), lherzolitic garnets will have more than one degree of freedom; the important point, however, being that harzburgitic garnets will have *one more* degree of freedom than lherzolitic garnets. These observations serve to explain the distribution of peridotitic garnet inclusions in diamond. Harzburgitic inclusions plot in a field at relatively low Ca contents whereas, lherzolitic inclusions plot, essentially on a line in Cr_2O_3 / CaO space (called the lherzolitic trend); any variation from simply a straight line to higher Cr contents can be attributed to higher conditions of pressure and / or temperature (Brey, 1991). Due to their higher Cr contents, inclusions of the harzburgitic garnet are purple whereas, the presence simply of Fe causes the deep red colouration of lherzolitic garnets. Additionally, websteritic garnets can be distiguished from garnets of other parageneses because of a high TiO_2 content, up to 1 wt% and, like eclogitic garnets have an orange colour. Table 1.6_2 presents typical compositional details for garnet inclusions of the peridotitic paragenesis in addition to websteritic garnets transitional with the eclogitic paragenesis. Figure 1.6_2 shows the compositional differences between peridotitic garnets and eclogitic garnets.

Table 1.6_2 Typical compositions of peridotitic and websteritic garnet and opx inclusions in addition to eclogitic garnet and cpx.

wt%	**P-Garnet‡**	**W-Garnet ‡**	**E-Garnet ♥**	**E-Cpx ♥**	**P-Opx ‡**	**W-Opx ‡**
SiO_2	41.8 (0.07)	40.3 (0.51)	39.9 (0.48)	54.9 *(0.51)*	56.9	55.0 (0.66)
TiO_2	0.1 (0.06)	0.7 (0.24)	0.5 (0.14)	0.5 *(0.16)*	0.0	0.1 (0.03)
Al_2O_3	19.5 (0.40)	19.4 (0.28)	22.3 (0.35)	9.5 *(3.31)*	0.8	0.6 (0.16)
Cr_2O_3	6.0 (0.55)	3.4 (1.36)	0.1 (0.04)	0.1 *(0.04)*	0.3	0.5 (0.76)
FeO	6.1 (0.14)	13.5 (3.26)	16.6 (1.55)	5.4 *(1.32)*	4.6	11.9 (2.24)
MnO	-	-	0.4 (0.11)	0.1 *(0.04)*	-	-
MgO	21.4 (0.47)	17.3 (1.85)	11.8 (2.10)	10.7 *(2.51)*	35.9	30.2 (1.52)
CaO	4.7 (0.78)	4.2 (0.97)	7.9 (2.40)	13.3 *(1.97)*	0.6	0.8 (0.16)
Na_2O	0.0 (0.0)	0.0 (0.02)	0.1 (0.09)	4.8 *(1.37)*	0.1	0.1 (0.03)
K_2O	-	0.0 (0.0)	-	0.3 *(0.23)*	-	0.0 (0.00)

‡ Deines et al. (1993) ♥ Data from Orapa diamonds (Deines et al., 1993). Figures in brackets refer to standard deviation of 1σ. P- Peridotitic W- Websteritic

Olivines: Harzburgitic olivines tend to be more Mg-rich (~Fo_{94}) than lherzolitic olivines (~Fo_{92}). In comparison to both paragneses, however, websteritic olivines exhibit a significant Fe enrichment; being typically of $<Fo_{90}$ composition.

---

[4] At conditions of 3 GPa, 1473 K.

Enstatites: Like olivines, the harzburgitic enstatites are commonly more Mg-rich (En_{96}) than lherzolitic enstatites (En_{94}), average compositions are summarised in table 1.6_2. Websteritic enstatites, in comparison are significantly Fe-rich, being typically around En_{85} in composition.

Clinopyroxenes: The lherzolite paragenesis is typified by Cr-rich diopsides. These have Cr_2O_3 contents of ~3 wt % and tend to be Mg-rich ~19 wt % oxide (Deines et al., 1991). Figure 1.6_3 shows the compositional range of peridotitic cpx inclusions compared to eclogitic inclusions in terms of the pyroxene quadrilateral. The harzburgitic paragenesis, by definition, does not include a cpx phase.

The websteritic paragenesis: Gurney et al. (1984) made the first discovery of inclusions with chemistry transitional between eclogitic and peridotitic compositions from Orapa. They discovered an assemblage of garnet, opx and cpx involving an unusual combination of high Fe and Cr content from eight diamonds from the Orapa kimberlite. Subsequently, websteritic inclusions have been observed from Monastery (Moore and Gurney, 1989) and by Deines et al. (1993) from Orapa and by McDade and Harris (1996) from Letseng-la-Terai.

➠

Section 1.6.2 Eclogitic paragenesis

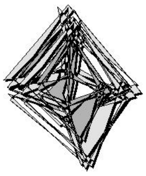

Garnets: Eclogitic garnets plot in a quite distinctive compositional field from peridotitic garnets. They are more Ca rich and, in addition, have more Fe and less Mg than peridotitic inclusions. The distinction is best elucidated by a Ca - Mg - Fe cation plot, figure 1.6_2. In addition, their Cr_2O_3 contents are < 2 wt% which puts them on a quite separate compositional field on a Cr_2O_3 / CaO (figure 1.6_1) and Na contents are often significant. Like websteritic garnet inclusions, they exhibit an orange colour. Average compositions from Deines et al. (1993) are presented in table 1.6_2.

Clinopyroxenes: Eclogitic cpx inclusions are omphacitic. Compared to typical omphacites, however, they have elevated K contents; K_2O ~ 0.26 wt %. When plotted in the pyroxene quadrilateral, they occupy a distinct field from peridotitic cpx being relatively Fe-rich, $Di_{80-60}Hd_{20-40}$ (figure 1.6_3). Average compositions from Deines et al. (1993) are presented in table 1.6_2.

Section 1.6.3 Sulphide inclusions

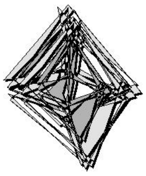

A wide range of sulphides have been recovered as inclusions from diamond, table 1.6_1. These are, generally, Fe-Ni-Cu-sulphides, figure 1.6_4. Most sulphide inclusions are composites of several phases and have bulk compositions consistent with ‘ from an original monosulphide phase (as discussed in Harris, 1992) and summarised in figure 1.6_5.

Monosulphide solid solution from South African diamonds shows a range of Fe:Ni ratios clustering around 8 - 10 wt % NiO (Deines and Harris, 1995) with pyrrhotite, chalcopyrite, pentlandite, pyrite and cubanite being the most common phases forming composite inclusions (Harris, 1992). On the basis of major element chemistry and carbon isotopic content, Deines and Harris (1995) conclude that most sulphide inclusions could not have crystallised in coexistence with olivine: they propose a separate paragenesis for most sulphide inclusions. Perhaps it is not surprising, therefore, that despite the proliferation of sulphide inclusions, it is uncommon to observe them in coexistence with silicates, especially olivine. In terms of sulphur isotopic content, Eldridge et al. (1991) found that for African sulphide inclusions in diamond, sulphur isotopic contents differed significantly from other mantle material. Indeed sulphur isotopic values were found to have affinities with sedimentary signatures. Eldridge et al. (1991) cite this observation as evidence for a subducted component amongst the source of lithospheric diamonds. Rudnick et al. (1993), however, found no significant difference between sulphide isotopic composition of Siberian diamonds and ‘average’ mantle although they do, however, cite the highly variable Pb isotopic compositions as evidence for mixing.

Section 1.6.4 Occurrence and significance of inclusion type

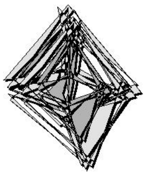

Commonly, both peridotitic and eclogitic inclusions are recovered from a single locality but in widely differing proportions. The Argyle mine, for example exhibits a dominance of eclogitic inclusions whereas for the Finsch mine, around 98% of stones are peridotitic (Harris and Gurney, 1979; Richardson et al 1984). Even within parageneses, the occurrence of individual phases varies in proportion (eg. Harris, 1992). This relative abundance[1] can be interpreted as reflecting the petrology of the diamond source régime.

It is often accepted that peridotitic material is fairly representative of the mantle in general, the particular compositional differences between peridotitic inclusions in diamond and phases in peridotitic xenoliths arising from the fact that peridotitic diamonds are sourced from, generally, greater depths than peridotite xenoliths (geothermometry supports this, Finnerty and Boyd, 1987): peridotitic diamonds, clearly from suitable depths for diamond stabilisation; peridotite xenoliths from shallower depths. Eclogite formation models tend to either involve cumulate or melt products of magmatic events in the mantle, removal of a trondjhemite-tonalite-granodiorite component to leave an eclogitic restite (Ireland et al., 1994), or else involve metamorphism or metasomatism of initially crustal material (e.g. Taylor and Neal, 1989). Kesson and Ringwood (1989) would attest that eclogite arises from the partial melting of subducted former serpentinite slab on dehydration; such a model is becoming increasingly popular. For reviews of the petrology of mantle xenoliths, the reader is referred to the detailed discussions of Harte and Hawkesworth (1987) and Ringwood (1989).

---

[1] Care must be taken over the significance of relative abundance of different phases included in any diamond population. This is because a sampling bias is difficult to avoid and as Gurney et al. (1986) have shown, abundances of paragenesis type vary with diamond size. Often in studies of inclusion material, emphasis is put on identifying and setting aside particular phases. In addition, some inclusions offer themselves for study due, for example, to their obvious colour. In contrast, other inclusions, especially colourless ones, may be unrepresented in a sample population due to the difficulty involved in identifying them. In the present study, much effort has been put into locating specific, unusual inclusions for study from a restricted size range; no attempt is made herein, therefore to read any significance into the relative proportion of phases recovered.

Chapter 2 Inclusion Chemistry

The determination of details of the chemistry of São Luiz and Guinean diamond inclusions has been a multi-stage process. Chapter 2 initially describes the important considerations of the break-out process (section 2.1) with methodology being detailed in appendix 1. Details of the major and minor element chemistry (as determined by EPMA) are presented in section 2.2 with subsequent classification being summarised in section 2.3. Trace element characteristics of selected inclusions have been determined by ion microprobe and are presented in section 2.4 and the details of oxidation state of iron as determined by Mössbauer spectroscopy are presented in section 2.5. Visual observations are reported throughout the chapter where they relate to points of chemistry (sections 2.2.1.9, 2.2.2 and 2.2.1.3.2 discuss BS-imaging features of BZ83, composite grains and majoritic garnets respectively and section 2.1 and appendix 2 include data on epigenetic inclusions). In addition, a detailed visual study of textures in fPer inclusions has been undertaken and is discussed in the section 2.6.

Section 2.1 Inclusion break-out

The unique nature and limited population of São Luiz and Guinean stones called for both a particularly carefully considered and undertaken inclusion release procedure. Presently, there are two methods of inclusion release which are adopted by practitioners; combustion and fracturing. The earliest attempts to determine the nature of impurities in diamond adopted the combustion approach (Dumas and Stas, 1840 and Davy, 1814) where wet chemical methods were employed to determine the composition of ash produced on combustion. Combustion is a method still favoured by some workers notably Shimizu (Shimizu and Sobolev, 1995). Such a technique has the particular advantage that inclusion material is wholly separated from its diamond host; in theory, all included material can be recovered and is often instantly recognisable as such as it is the only material left after inclusion release. Additionally, the morphology of inclusions tends to be retained by adopting combustion, rather than fracturing, where there is a risk of breaking the inclusions in addition to the diamond. There are a number of fundamental disadvantages with the combustion technique, however, which make it unsuitable for the present study. Firstly combustion destroys the diamond host thus precluding δ^{13}C, δ^{15}N, N concentration and FTIR analyses. In addition, any combustible inclusion material eg. graphite, included diamond[1] and some sulphides would be lost. Perhaps most concerning, however, is that adopting a combustion approach brings into question the authenticity of the recovered material. Specifically, heating the inclusions in an oxygenated environment may prompt diffusion of volatile species, resetting of exsolution textures and potentially provide sufficient activation energy to revert any high P,T polymorphs still remaining after exhumation to their ATP stable state. It is concluded that adopting combustion to release inclusions involves an unnecessary risk of undoing the excellent work which diamond often offers in providing a chemically and physically protective seal for its inclusions. These risks, in addition, are not wholly hypothetical. For example the 'downtown' feature of Sr heterogeneity in Yakutian garnet inclusions analysed by Shimizu and Sobolev (1995) may well be an artefact of release by combustion[2]. Diffusion of Sr in garnet is faster (1.0 x 10^{-8} cm^{2}s^{-1}) than many elements (Burton et al. 1995) and heating to 1000 K could serve to explain the inhomogeneities observed by Shimizu and Sobolev (1995) particularly if elevated Sr had been previously introduced into the system via fractures (Burton, 1997 *personal communication*).

---

[1] Inclusions of diamond within diamond have been recorded from a number of sources eg. Letseng-la-Terrai (McDade and Harris, in preparation) and China (Wang et al., 1994).

[2] An alternative explanation may be that the Sr heterogeneity is not, as Smimizu and Sobolev (1995) attest, a diffusion profile at all, but a completely separate Sr-rich grain boundary phase. Certainly the garnet presented in Shimizu and Sobolev (1995) does not show a smooth diffusion profile, but a sharp step close to the inclusion edge characteristic of a grain boundary with a separate phase. The other heterogeneous stones Shimizu and Sobolev (1995) refer to, however, may be smoother.

In this study, therefore, I have chosen to adopt the approach of diamond fracture for the release of inclusions. Full details of methods and apparatus are presented in appendix 1

Diamond fracture is not a method free of its own problems, these tend, however, to be related to the skill and care of the operator rather than involving damaging effects out of his or her control. Specific difficulties involve the identification of inclusion material, as distinct from:

- **Crud**[3] which may have percolated and crystallised into fractures. Crud looks cruddy, however, in order to minimise the possibility of discarding useful material, all material which could, at least partially, be primary was picked out and mounted for polishing. As a result, some of the grains mounted and numbered as inclusions are clearly not primary (appendices 1 and 2), as indicated by poor electron probe totals, extreme friability or inability to take a polish.

- **Diamond** Specific problems involving diamond fragments are that their irregular relief results in them often looking anisotropic. In addition, they occasionally exhibit colour (either intrinsically or due to crud, particularly along fracture systems) and, even when fragments are colourless, confusion can arise between identification as diamond, as opposed to colourless inclusions. Some of the key grains in the study of São Luiz material are colourless inclusions so particular attention has to be applied to this point in practice. With care and experience the problem can be adequately resolved; colourless inclusions tend to look like individual crystals, even if the morphology is commonly that of diamond and thus can be distinguished from fragments of the single crystal host. In addition, analysis in cross-polars can be instructive as flat faced grains which show anisotropy cannot be diamond. In a similar fashion to the philosophy adopted for the separation of crud, a prudent approach was adopted. As the reader will see (appendix 2) however, only two diamond shardsc (from JH6) were picked out: due to their resistence to polish they were quickly identified as such.

---

[3] As defined in the glossary

- **Crusher material** A less easily resolvable problem involves crusher material contamination. As will be discussed in section 2.2.1.7, native iron has been described as inclusions in diamond (Meyer and McCallum, 1985 and Sobolev, 1981) so any iron recovered cannot necessarily be written off as being crusher metal. Careful electron probe analysis of unknowns and definite crusher shards have in the present case, resolved this problem.

- **Glass** Glass from the crusher windows is easily recognised as it tends to form long shards, is of even thickness and clearly isotropic.

Section 2.2 Major and minor element analyses of São Luiz and Guinean inclusions determined by electron microprobe

The polished samples of potential inclusion material were analysed for major and minor elements using the Cambridge Instruments MkV and Cameca Camebax electron microprobe apparatus (EPMA) of the University of Edinburgh Dept. of Geology and Geophysics. Operating conditions and correction procedures are outlined in appendix 8. Results obtained are considered under two frameworks; inclusion type analysis (section 2.2.1) and composite grain studies (section 2.2.2). All electron probe analyses are presented in appendix 3.1, averaged analyses for each inclusion being presented according to association in appendix 3.2.

Section 2.2.1 Inclusion type analysis

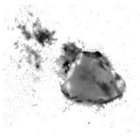

A total of 14 different phases have been identified as syngenetic inclusions from São Luiz diamonds[1]. These are olivine, quartz, mantle lithosphere garnet, majoritic garnet, TAPP ($I\bar{4}2d$ mineral of roughly pyrope-almandine composition, section 3.3.1), ferropericlase ([Mg,Fe]O, often termed magnesiowüstite in the literature[2]), upper mantle clinopyroxene, Type I, II and III pyroxene (see section 2.2.1.5 for classification), $CaSiO_3$, Al_2O_3 (var. ruby and sapphire), pyrrhotite + haematite. In addition to these phases, moissanite (SiC) and a high-Al phase of uncertain composition have been described from São Luiz (Wilding, 1990). Native iron has been observed in work undertaken by Harris and Watt (1993, *personal communication*). As will be described later, section 2.2.1.8, these grains are thought to be contaminant from the crusher material.

---

[1] It should be noted that, at this stage, the reader should be wary of inferring any structural implication relating to the phases listed. In this chapter, mineral names are used to infer composition only, thus simplifying classification. Although likely to conform to their ATP structures, some grains may, in fact, still exist as high pressure polymorphs. This consideration is discussed in detail in chapter 3.

[2] The term ferropericlase (commonly abbreviated to fPer) is adopted herein, rather than the more commonly adopted term, magnesiowüstite because, with one exception, all these grains are magnesium rich (i.e. closer to the periclase end-member). Neither term, however, is strictly correct, the International Mineralogical Association (I.M.A.) approved terms being the rather unwieldy ferroan periclase and magnesium wüstite.

Section 2.2.1.1 Inclusions of olivine composition

Three olivines have been extracted from São Luiz diamonds. Two (BZ111 and BZ117B) were found by Wilding (1990), and one (BZ243C) during the present study. All three olivines are relatively Mg-poor, Mg/(Mg+Fe) varies from 0.87 - 0.91, compared to olivines from mantle xenoliths (Mg/(Mg+Fe) being typically ~0.89 - 0.95) and olivine inclusions in diamond from other sources (Harris and Gurney, 1979, Mg/(Mg+Fe) being typically ~0.92 - 0.94). Ni occurs as ~0.35 wt% and Cr and Mn contents are low (MnO ~0.1 wt% and Cr_2O_3 ~0.2 wt% for BZ243C and <0.04 wt% for BZ111 and BZ117B).

Section 2.2.1.2 Silica inclusions

Five silica inclusions have been found as inclusions in São Luiz diamonds; two from the work of Wilding (1990), BZ99 and BZ103 and three from the present study; BZ235D, BZ239D and BZ239F. The compositions of these grains are unremarkable; being essentially just SiO_2. The only significant minor element appears to be Fe comprising ~0.2 wt% in BZ103, BZ239D, BZ239F and ~0.08 wt% in BZ235D. All three silica grains recovered in the present study have a milky amorphous character to them which could be interpreted as being characteristic of epigenetic silica. Alternatively, an amorphous nature may be indicative of these grains having undergone rapid polymorphic transition from stishovite to quartz[1] and thus have become polymineralic on a fine scale. As discussed by Wilding (1990), BZ99 and BZ103 have a clear colouration and strong crystalline morphology: it is likely that at least *these* two grains are syngenetic.

---

[1] BZ239 silica inclusions would thus be consistent with reasonably Fe-rich fPer BZ239A and BZ239G in a lower mantle association, section 4.4.2.4.

Section 2.2.1.3 *Inclusions with garnet-like compositions*

Inclusions which fall into the broad compositional field of garnet occur in the São Luiz sample. Three very distinct compositional types have been identified of which the third has been shown to have a structure distinct to true garnet (Harris et al., 1997, section 3.3.1):

- Grosspaldite (grossular - pyrope - almandine) garnets
- Majoritic garnets
- Tetragonal almandine pyrope phase (TAPP) inclusions

➠

Section 2.2.1.3.1 Grosspaldite garnets

This suite of garnets has been discussed at length by Wilding (1990) and consists of grains yielding normal quantities of Al and Si relative to O: namely 2 Al and 3 Si cations per 12 O anions. Wilding (1990) terms these garnets Group I and recovered a total of 20 from São Luiz diamonds. Two grains are involved in the present study : BZ237C from São Luiz and GU3B from Guinea. Both grains have a very slightly majoritic component (they involve an excess of Si of less than 3.1 cations per 12 O anions) and otherwise, are compositionally quite distinct from each other.

GU3B: GU3B has a chemical composition consistent with Wilding's (1990) Group I garnets and coexists with a pyroxene similar to those found with Group I garnets by Wilding (1990). It is strongly grossular enriched ($Gr_{32}Py_{42}Al_{16}$). Additionally, GU3B has a significant TiO_2 component, ~1.67 wt%. In terms of silica content it is marginal in composition between grosspaldite and majoritic garnet, and, in particular has a far smaller majoritic component than the majority of majoritic garnets recovered in the present study (section 2.2.1.3.2).

Figure 2.2_1 summarises the compositional field of São Luiz grosspaldite garnets from Wilding (1990) in terms of a Cr_2O_3 / CaO plot used to subdivide garnets of upper mantle composition. Included is GU3B which clearly lies within the limits of Wilding's Group I field.

BZ237C: BZ237C has an unusual chemistry which sets it apart from both Wilding (1990) Group I inclusions and the other 'garnet' composition inclusions involved in this study. Unlike Group I and majoritic garnets the CaO content is only ~ 1.72 wt%, CaO. However, this is also significantly more calcic than TAPP grains, (section 2.2.1.3.3). In terms of Fe and Mg cations, its composition is pyrope$_{87}$-almandine$_{13}$, intermediary between TAPP and majoritic and Group I compositions. In addition, BZ237C contains ~ 3.0 wt% Cr_2O_3, a value comparable to TAPP but significantly more than majoritic or Group I grains. The coexistence of BZ237C with a pyroxene (BZ237A, see section 2.2.1.5.5) which is also considered unique in terms of other pyroxene grains, lends support to the consideration of inclusions from BZ237 being part of a separate association (section 2.3).

Section 2.2.1.3.2 Majoritic garnets

Terminology: Garnets are termed ‘majoritic’ if, compositionally, they lie along the solid solution series between garnet, $X_3Y_2Si_3O_{12}$ and pyroxene, $XSiO_3$. Where X is primarily Ca, Mg and Fe and Y is Al. Garnets of this type are commonly orange in colour and can be recognised compositionally, by an excess of Si and deficiency of Al in comparison to ‘normal’ garnet. Naturally-occurring majoritic garnets throughout the literature have between 3.10[1] and ~ 3.43[2] Si cation per 12 O anions and between 1.95 and ~ 0.96 Al cations per 12 O anions.

Dominant composition: Wilding (1990) identified 14 majoritic garnets which he termed Group II garnet. In addition, the present study has yielded a further 6 majoritic garnets from São Luiz; BZ215C, BZ216A1, BZ217A, BZ218A, BZ223A, BZ223B and 1 from blebs within Guinean inclusion GU3B: GU3B itself, with 3.08 Si cations per 12 O anions falls short of being defined as a majoritic garnet. The 6 São Luiz grains exhibit between 3.11 and 3.18 Si cations per 12 O anions and show a wide range in Ca, Mg and Fe contents. Table 2.2_1 summarises the compositions of the majoritic grains in terms of grossular, pyrope and almandine components and Si content.

Table 2.2_1 Compositions of majoritic garnets recovered from São Luiz and Guinea discovered as part of the present study with marginal grain GU3B included for comparison.

Sample	BZ215C	BZ216A1	BZ217A	BZ218A	BZ223A	BZ223B	GU3B	GU3BDk*
Gr	0.39	0.35	0.08	0.19	0.40	0.39	0.32	0.35
Py	0.36	0.48	0.65	0.48	0.34	0.34	0.42	0.43
Al	0.25	0.17	0.27	0.34	0.26	0.26	0.26	0.22
Si/12 O	3.11	3.14	3.18	3.14	3.18	3.16	3.08	3.36

* Dark blebs in GU3B. Gr: grossular, Py: pyrope, Al: almandine

Plotting the seven grains along with the Group II majoritic garnets of Wilding (1990) shows a consistency in composition between the two studies, figure 2.2_2. Compositional details are also very similar to those of majoritic garnets obtained from diamonds from Monastery (Moore and Gurney, 1985 and Moore et al., 1991).

Compositional heterogeneities: BS-electron imaging of the seven samples discussed above was carried out on the Cameca Camebax electron microprobe of the University of Edinburgh, Department of Geology and Geophysics. Samples BZ216A1, BZ217A, BZ218A, BZ223A and GU3B, showed small patches of relatively light or dark BS-reflectivity, often towards the edge of the grains (textures

---

[1] Garnets exhibiting between 3.1 and 3.0 Si cations per 12 O anions are not generally termed majoritic because such ‘excess’ of Si could alternatively be attributed to analytical uncertainty.

[2] Sample A1-24 from Moore and Gurney (1985). A value of 3.36 was recorded for the majoritic inclusions in GU3C.

in BS-images of BZ215C were concluded to be due to topography[3]). These features are only resolvable at the highest contrast capability of the electron microprobe and so represent only a small contrast in mean atomic mass. In order to determine the composition of the blebs, analyses were carried out by electron microprobe analysis and EDS. The analyses obtained (appendix 3.1) were often poor as a result of the following:

- ♦ Patches often occur at the edge of the grain where the polish is often poorer and the surface slopes.
- ♦ Patches are very small (<2µm in diameter) thus involving host material in the analysis.

The analyses were, however, good enough to give indications of the identity of phases present.

BZ216A1: BZ216A1 showed a relatively dark bleb (~ 3 µm) well into the grain in addition to a few small dark areas at the edges, figure 2.2_3. Electron microprobe analyses on both areas gave poor totals of ~94% (appendix 3.1). However the high SiO_2 (47.8 and 54.3 wt%) and Na_2O (6.2 and 5.0 wt%) suggest that the blebs are of a jadeitic composition which is consistent with a lower mean atomic weight and thus lower BS-reflectivity. Comparing the analyses BZ216A1Dk-1, BZ216A1Dk-2 (from appendix 3.1) and BZ216A1 (from appendix 3.2), there is possibly a transition in composition from BZ216A1 to BZ216A1Dk-2 to BZ216A1Dk-1 which can be explained in terms of analysis BZ216A1Dk-1 being predominantly made up of jadeitic material whereas BZ216A1Dk-2 comprises a significant proportion of host majoritic garnet.

BZ217A: Dark areas can be seen in BZ217A close to the edge of the specimen (figure 2.2_4). These look very similar to those of BZ215C but electron microprobe analyses (appendix 3.1) show them to have compositions broadly similar to blebs in BZ216A1. The blebs in BZ217A incorporate at least 6 wt% Na_2O and appear to be jadeitic diopside.

BZ218A: BZ218A appears to be homogeneous in BS-imaging except for a fragmented edge which could be indicative of a grain boundary (figure 2.2_5). This edge yields Na on an EDS analysis, and the electron microprobe analysis (appendix 3.1) shows Si contents typical of pyroxenes. Although the Na_2O content of ~2% is smaller than dark areas in *other* grains the analysis total is poor and it is considered likely that this area is jadeitic diopside. Indeed, the predominance of Mg over Fe over Ca is consistent with the host, appendix 3.2.

BZ223A: BS-imaging of BZ223A shows marked inhomogeneities as seen in figure 2.2_6. There are a number of light spots ~2 µm in diameter; two areas of dark BS-reflectivity; a patch at one end; two features with tails near the light blebs.

The dark areas, in terms of their morphology, are reminiscent of charging spots. Electron microprobe analyses, although giving low totals, would appear to correct to a typical majoritic garnet SiO_2

---

[3] In BZ215C and BZ223B no analyses inconsistent with the host composition were obtained. In BZ215C a network of interwoven

content. However there is higher than usual Na for the garnet so it is possible that these minute blebs are jadeitic diopside masked by their Ca, Mg, Fe majoritic garnet host.

The light areas are puzzling. They yield a relative abundance of Mg over Fe over Ca but with relatively high Fe and, although yielding analyses with a total deficit of around 10 wt%, fall at least 10% short in SiO_2 to make up even a garnet composition. Their Al_2O_3 content is high, at least 25 wt%. The composition of the blebs cannot be solved with the data available but three possibilities are envisaged:

- The light areas are an exsolved phase of Al, Fe spinel. Analyses of BZ223AL-1 and BZ223AL-2 can be interpreted as incorporating both a majoritic garnet host component and an Al, Fe spinel.
- The light areas are an exsolved phase approximating to a $(Ca,Mg,Fe)_2(Al,Si)_2SiO_7$ composition (gehlenite) of the type recorded by Liu (1978). In terms of seven oxygen cations, analyses BZ223AL-1 and BZ223AL-2 (appendix 3.1) would fit such a composition providing that some Si fits in the Al site. Because of the poor nature of these analyses, however, any such conclusion should be treated with caution.
- The light areas are hydrated blebs. Certainly the low totals and the irregular cation calculation, appendix 3.1, would be consistent the presence of fluid, however this feature is more likely to be due to the size and topography of the area analysed. One may expect this to lower the mean atomic weight and thus produce *dark* BS-reflectivity (although a very significant fluid content would have to be present in order to be detectable by BS-EPMA), however, such an effect could be counteracted by the observed excess Fe in the blebs. It is believed that such an explanation is the least likely of the three scenarios.

GU3B: Some dark flecks appear towards one end of the sample and are reminiscent of topography, figure 2.2_7. Electron microprobe analyses obtained, for one bleb in particular, however, were good, appendix 3.1. Like the host, the composition of the blebs is of a Mg, Ca, Fe majoritic garnet but, instead of the 3.08 Si cations per 12 O anions of the host, the blebs have 3.36 Si cations per 12 O anions. With 45 wt% SiO_2 and 13.6 wt% Al_2O_3, the blebs can be said, therefore, to be highly majoritic, which is consistent with their relatively low BS-reflectivity.

Summary and discussion: Observations on majoritic garnets from the present study yield four different types:

- Homogeneous majoritic garnet: BZ215C and BZ223B
- Majoritic garnet hosts with dark blebs of jadeitic diopside; BZ216A1, BZ217A, BZ218A

---

dark blebs, ~1 µm across at the edge of the grain appeared to be due to topography.

- A majoritic garnet host (BZ223A) with dark blebs of jadeitic diopside and light blebs of an unknown phase, possibly an Al, Fe spinel composition; a $(Ca,Mg,Fe)_2(Al,Si)_2SiO_7$ phase; or else a fluid rich phase
- A slightly majoritic garnet (GU3B) with dark blebs of highly majoritic composition

Wilding (1990) observed some of the above features in majoritic garnets from São Luiz. Of his 14 Group II garnets, he identified BS-inhomogeneity within 11[4] and of these he observed 5 textural subdivisions all involving a jadeitic pyroxene + / - normal-Si garnet.

Source of dark areas in majoritic garnet: A process of exsolution is best invoked to explain the textural and compositional features of dark areas in the majoritic garnets of the current study because at the proposed depths of formation of the majoritic garnet association (section 4.4.2.2) a full solid solution between pyroxene and garnet is envisaged.

Jadeitic diopside composition exsolving from a majoritic host is indicative of an originally more majoritic inclusion.

Highly majoritic blebs exsolving within a slightly majoritic host, purely in compositional terms, would suggest an original grain with an intermediary majoritic composition. Such exsolution would indicate a solvus within majoritic compositions which has not been observed, section 4.3.1. An alternative explanation arises from the observation that GU3B came from the same diamond as the jadeitic diopside GU3C. It could be that these grains are different parts of a composite grain[5], in which case the blebs of highly majoritic garnet could be remnants of the original grain before exsolution of slightly majoritic garnet and jadeitic diopside composition.

The details of the phase relations in the majoritic and jadeitic systems are dealt with in section 4.3.1 and the present discussion will be expanded in light of this in section 4.3.2.

Source of light areas in BZ223A: If, as suggested, the light blebs in BZ223A are of Al-Fe spinel or $(Ca,Mg,Fe)_2(Al,Si)_2SiO_7$ composition (e. g. Liu 1978), it could be that they have exsolved from an original majorite grain in a similar fashion to the exsolution of jadeitic diopside from majoritic garnet. Certainly with 3.18 Si cations per 12 O anions and due to the fact that light blebs are widespread throughout the sample, this may be considered possible.

---

[4] He termed these Group IIB as opposed to the 3 Group IIA grains which yielded a homogeneous BS-image.

[5] Guinean inclusions from GU2 and GU3 were supplied already released from their diamond hosts. No information on inclusion association is known.

Section 2.2.1.3.3 TAPP grains

In addition to the other types of 'garnet' recovered from Luiz some of inclusions have been recovered which fall into a third category. They are termed TAPP (tetragonal almandine-pyrope phase) which has a structural implication as discussed in section 3.3.1.

Three grains falling into the TAPP category were recovered in the study by Harte and Harris (1994). These grains are BZ205A, BZ206B and BZ207A. In addition, a further seven grains of TAPP, have been identified during the present study, namely, BZ238A, BZ240B, BZ243A, BZ244B, BZ259A1, BZ259A2, BZ265A. Of the TAPP inclusions, three occurred alone in diamond and five co-existed with separate inclusions of ferropericlase (including one case where TAPP was also in direct contact with a (Mg,Fe)SiO_3 inclusion). In another case, lacking ferropericlase, TAPP was in contact with a Mg, Al, Na silicate.

The TAPP crystals are of apple green colour and 30-100 μm in diameter. They exhibit either a distinct cubo-octahedral morphology, or in one case, BZ259A, an elongate and tabular form.

Table 2.2_2 Site allocation for cations in TAPP grains in terms of garnet and TAPP structure ¥.

Sample	**205A**	**206B**	**207A**	**238A**	**240B**	**243A**	**244B**	**259A ***
Garnet								
Si in Si site	2.94	2.92	2.81	2.91	2.94	2.95	2.91	2.97
Ti + R3 in Si	0.06	0.08	0.19	0.09	0.06	0.05	0.09	0.03
Ti + R3 in Y	2.00	2.00	2.00	2.00	2.00	2.00	2.00	2.00
Na + R2 in X	2.92	2.90	3.03	2.88	2.92	2.92	2.91	2.95
Ti + R3 in X	0.08	0.10	-0.03	0.12	0.08	0.08	0.09	0.05
TAPP								
Si in Si1	1.00	1.00	1.00	1.00	1.00	1.00	1.00	1.00
Si in Si2	1.94	1.92	1.81	1.91	1.94	1.95	1.91	1.97
Al in Si2	0.06	0.08	0.19	0.09	0.06	0.05	0.09	0.03
Mg in M1	0.93	0.84	0.82	0.89	0.93	1.00	0.92	0.98
Fe^{3+} in M1	0.07	0.16	0.18	0.11	0.07	0.00	0.08	0.02
Al^{3+} in M2	1.88	1.82	1.49	1.84	1.88	1.94	1.86	1.89
Cr^{3+} in M2	0.13	0.12	0.07	0.17	0.13	0.13	0.15	0.13
Mn in M2	0.05	0.03	0.02	0.05	0.04	0.05	0.06	0.04
Ti^{3+} in M2	0.00	0.00	0.22	0.00	0.00	0.00	0.00	0.00
M2	2.06	1.97	1.81	2.06	2.05	2.13	2.07	2.07
Mg in M3	1.69	1.89	1.81	1.73	1.73	1.54	1.72	1.81
Fe^{2+} in M3	0.22	0.11	0.38	0.18	0.20	0.30	0.19	0.09
Ni, Na, K in M3	0.03	0.03	0.01	0.03	0.03	0.02	0.02	0.03
M3	1.94	2.03	2.19	1.94	1.95	1.86	1.93	1.93

¥ - Compositional details of BZ265A are not included, identification as TAPP for this grain was made by in-situ XRD (section 3.3.1.3), * - averaged from BZ259A1 and BZ259A2

All nine inclusions for which compositional details have been determined, have very similar compositions with the exception of BZ207A which, although relatively Fe-Ti rich, is consistent with the stoichiometry of the other grains, table 2.2_2. The composition of TAPP is similar to pyrope-almandine garnet although the Mg/(Mg+Fe) (typically close to 0.93) is unusually high for naturally occurring garnets. The CaO content at <0.15 wt% is much lower than that generally found in garnets from peridotite and eclogite xenoliths from the upper mantle. Indeed, plotting the compositions of the nine grains on a Cr_2O_3 / CaO wt% diagram, TAPP clearly occupies a compositional field of its own[1], figure 2.2_8. The TAPP compositions notably show normal garnet Si:Al ratios without evidence for a majoritic type of substitution.

Cation totals are normalised to 8 cations per 12 O anions and are assigned to sites on the basis of full occupancy on M1 (which is supported by crystallochemical evidence, section 3.3.1.2). BZ265A is ommited from the table as identification as TAPP followed in-situ structural analysis (section 3.3.1.3) rather than EPMA.

---

[1] TAPP also shows distinctive features of ferric iron content (section 2.5.1.2) and trace element characteristics (section 2.4.3.2).

Section 2.2.1.4 fPer inclusions

A total of 41 inclusions of a composition lying along the solid solution series periclase (MgO) - wüstite (FeO) have been recovered from São Luiz. Of these, 12 are detailed in Wilding (1990) and 7 were recovered by Harris (1993, *personal communication*), the rest being retrieved as part of the present study. In addition, 2 samples from Guinea have been recovered in the present study.

A few samples of fPer diamond inclusions have, additionally, been recorded from the literature, these are often referred to as 'magnesio-wüstite'. Table 2.2_3 summarises the locations of worldwide sources of fPer inclusions and includes both published and unpublished data.

Analyses: The range in composition of fPer inclusions from São Luiz is greater than that of any other phase recovered. In terms of Mg#[1], compositions range from 0.38 (BZ66) to 0.85 (BZ251A). The distribution is negatively skewed, figure 2.2_9.

Table 2.2_3 Occurrence of fPer inclusions in diamond worldwide

Locality	Number of fPer	Locality	Number of fPer
São Luiz (BZ)†	41	Koffiefontein (RSA) ¥	4
Guinea ‡	12*	River Ranch (ZIM)¢	1
Letseng-la-terai (LES) 💣	1	Monastery (RSA)¤	1
Sloane (USA)¥	1	Orrorroo (AU)♥	2

* Guinea has yielded 2 definite samples from the present study in addition to 10 possible inclusions from unbroken diamonds. More material has come to light through work by Stachel and Harris (1996, *personal communication*).
BZ- Brazil, LES- Lesotho, USA- Colorado, U.S.A., RSA- Republic of South Africa, ZIM- Zimbabwe, AU- Australia.
† Present study; ‡ Present study + Stachel and Harris (1996, *personal communication*); 💣 McDade and Harris (1995); ¥ Moore et al. (1986); ¢ Kopylova et al. (1995); ¤ Moore and Gurney (1986); ♥ Scott-Smith et al. (1984).

The two Guinean inclusions analysed for the present study broaden the distribution towards the Mg-rich end; GU2A and GU4A1 both having Mg# of 0.87. In terms of literature data, the distribution is expanded yet further. The single inclusion of fPer from Monastery (Moore and Gurney, 1986) is exceptionally Fe-rich, Mg# being 0.13; whereas inclusions from Orrorroo (Scott-Smith et al., 1984), Koffiefontein and Colorado (Moore et al., 1986) lie at the Mg-rich end; the Colorado fPer has a Mg# of 0.88. Full analyses of published fPer compositions from the literature are presented in table 2.2_4 and are incorporated into the histogram, figure 2.2_9.

---

[1] Based on cations and Fe as Fe^{2+} from appendix 3.2.

Table 2.2_4 Compositions of fPer inclusions from the literature

	E5-1¥	**A262***	**K30***	**K33***	**K34***	**ORR6A‡**	**ORR4A‡**	**A100 ***	**Al-40 ***
SiO_2	n.d.	0.00	0.08	0.09	0.13	0.00	0.00		
TiO_2	n.d.	0.00	0.00	0.00	0.00	0.00	0.00		0.17
Al_2O_3	n.d.	0.00	0.00	0.00	0.07	0.01	0.00	0.10	0.17
Cr_2O_3	0.50	0.57	0.49	0.52	0.67	0.16	0.23	0.84	
FeO	22.27	19.80	21.70	20.50	20.30	21.13	22.92	19.40	93.00
MnO	0.04	0.19	0.15	0.16	0.17	0.15	0.16	0.32	0.32
NiO	n.d.	1.41				1.20	1.10		
Na_2O		0.30	0.29	0.25	0.20			0.07	
MgO	73.57	78.10	77.30	76.80	76.90	77.70	76.75	78.70	7.29
CaO	0.07	0.00	0.00	0.05	0.03	0.00	0.00	0.04	
K_2O				0.06					
Total	96.45	100.37	100.01	98.43	98.47	100.35	101.16	99.47	100.95
Cations									
Si	0.000	0.000	0.006	0.007	0.010	0.000	0.000	0.000	0.000
Ti	0.000	0.000	0.000	0.000	0.000	0.000	0.000	0.000	0.019
Al	0.000	0.000	0.000	0.000	0.006	0.001	0.000	0.009	0.022
Cr	0.031	0.033	0.029	0.031	0.040	0.009	0.013	0.049	0.000
Fe^{2+}	1.410	1.193	1.315	1.258	1.245	1.279	1.387	1.174	8.110
Fe^{3+}	0.036	0.031	0.034	0.032	0.032	0.033	0.036	0.030	0.601
Mn	0.003	0.012	0.009	0.010	0.011	0.009	0.010	0.020	0.030
Ni	0.000	0.084	0.000	0.000	0.000	0.072	0.066	0.000	0.000
Na	0.000	0.043	0.042	0.036	0.029	0.000	0.000	0.010	0.000
Mg	8.515	8.604	8.565	8.615	8.624	8.597	8.488	8.705	1.217
Ca	0.006	0.000	0.000	0.004	0.002	0.000	0.000	0.003	0.000
K	0.000	0.000	0.000	0.006	0.000	0.000	0.000	0.000	0.000
Total	10.000	10.000	10.000	10.000	10.000	10.000	10.000	10.000	10.000
Mg#	0.86	0.88	0.87	0.87	0.87	0.87	0.86	0.88	0.13

¥ River Ranch (Kopylova et al., 1995) ‡ Orrorroo (Scott-Smith et al., 1984); * Koffiefontein (Moore et al., 1986); Cation values are calculated on the basis of 10 O anions and normalised to 10 cations. Fe^{3+} is calculated from ratios determined by Mössbauer analysis in São Luiz material, section 2.5.2, where ratios of $Fe^{3+}/\Sigma Fe$ used = 0.025 for all samples except for A1-40 where a value of 0.069 is employed.

In terms of minor elements, Ni, Cr and Mn are particularly important with Al and, occasionally Na being present in small, yet significant concentrations. Throughout all fPer inclusions (including data from the literature from other localities) there appears to be a close positive correlation of Ni with Mg content, figure 2.2_10. In terms of Cr content, Cr also appears to be more abundant in Mg-rich fPer although the correlation, figure 2.2_11 is poor, most likely as a result of the larger error on Cr concentrations. Indeed, plotting Ni + Cr against Mg#, figure 2.2_12 shows a good correlation. Exceptions to the trend are BZ66 and BZ205C, which show anomalously high Cr contents and BZ250C which shows an anomalously high Ni content.

Elements, Al, Ti and Na also show general positive correlations with Mg#. This is summarised in terms of Na + Ti + Al cations in figure 2.2_13. However, rather than following a linear trend, fPer compositions bound against a maximum for a particular, Mg#. This behaviour is likely due to the small concentrations involved and, thus large errrors. Again, BZ66 appears to be highly anomalous.

Discussion: A large range in Mg# is often interpreted as due to some form of fractionation process involving melt. As will be discussed in section 4.4.2, the relationship in trace element content against Mg# for fPer and the likely association of most grains with CaSi-Pvk is strong evidence to support such an interpretation. Indeed, the range in fPer in contrast to other phases would suggest that fPer is the liquidus phase. Normally, one would expect to see Al, Ti and Na to increase with evolution of, for example, a crystalising melt, cf. figure 2.2_13, however, in the presence of coexisting pyroxene, particularly Type II and Type III, sections 2.2.1.5.3 and 2.2.1.5.4 one would expect any crystallising melt to become quickly depleted in Al, Na and Ti.

➡

Section 2.2.1.5 Inclusions with pyroxene-like compositions

A total of 14 inclusions of pyroxene stoichiometry have been recovered from São Luiz during the present study and that of the series BZ201 - BZ214 (Harte and Harris, 1994). In addition one pyroxene inclusion, GU3C has been recovered from Guinea. These inclusions can easily be subdivided in terms of major element chemistry, figure 2.2_14.

BZ213A: BZ213A lies in a compositional field on its own compared to other pyroxene stoichiometry inclusions recovered from São Luiz. It is particularly Ca-rich, ~ 19 wt%. In terms of the pyroxene quadrilateral it plots as a Ca-deficient $Di_{91}Hd_8$. Its Cr_2O_3, Na_2O and Al_2O_3 contents are all fairly low, 0.73, 0.72 and 1.15 wt%, respectively, especially compared to the TZ Group, classified in the following. In terms of upper mantle composition, whether BZ213A can be considered eclogitic or lherzolitic is a little ambiguous. With low Na content it is certainly not a typical eclogitic omphacite but with the exception of slightly high Mg, it does still fit within the range of eclogitic compositions defined by McCandless and Gurney (1989). Cpx of this type are, in some instances, seen in association with eclogite xenoliths (eg. Reid et al., 1973 and Milashev et al., 1963) so BZ213A may be in association with cpx of the TZ Group. There are, however, no exceptions to BZ213A fitting a Group 2 lherzolitic cpx composition of Stephens and Dawson (1977) and lherzolitic cpx of Hervig et al. (1986); indeed Dawson (1997, *personal communication*) would prefer this mineral to be classified as a fairly Cr-poor Group 2 lherzolitic cpx[1]. As will be discussed in section 4.4.2, however, the favoured interpretation is that BZ213A has an altogether different source from TZ Group cpx.

In terms of cation assignments, the slight deficit of Si can be accommodated by a small amount of Al. M1 is satisfied by the remaining Al, all Fe, Cr and a large proportion of Mg. The remaining Mg is assigned to M2 along with Ca, Ti, Ni, K, Na and Mn and is presented in table 2.2_5 along with data from the TZ group described as follows.

BZ209A, BZ209B, BZ218B and GU3C (TZ[2] Group): Although GU3C is slightly more Ca-rich than, BZ209A, BZ209B and BZ218B, they are considered as a single group due to their general compositional similarity and their association with majoritic garnets (section 2.3). Inclusions of the TZ group are essentially diopsides with a significant jadeite component, i. e. omphacites (significant Al occupies M1 and Na occupies M2). In the case of GU3C there appears to be a slight excess of Si. Little Mg is required to occupy the M2 site in order to achieve full occupancy (table 2.2_5). As figure 2.2_14 shows, the group plots at around $Jadeite_{29-50}Augite_{71-50}$ where the augite component has a composition of around $Diopside_{79-83}Hedenbergite_{21-17}$, appendix 3.2. Cr is present in small quantities

---

[1] This interpretation corresponds to that on the basis of trace elment concentrations, sections 2.4.5.1 and section 2.4.7.

as ~ 0.1 wt% oxide and Ni and Mn are almost entirely absent. All inclusions from the TZ Group occupy the same compositional field as Wilding's (1990) Group II pyroxenes recovered from São Luiz and can be considered to be well within the eclogitic Group II[3] cpx compositional field of McCandless and Gurney (1989).

Table 2.2_5 Cation assignments for BZ213A and for TZ association pyroxenes

		Transition Zone (TZ) Association			
	BZ213A	BZ209A	BZ209B	BZ218B	GU3C
Si in Si1	1.980	1.997	1.999	1.981	2.011
Al in Si1	0.020	0.003	0.001	0.019	0.000
Si site total	**2.000**	**2.000**	**2.000**	**2.000**	**2.011**
Mg in M1	0.841	0.557	0.553	0.586	0.660
Al in M1	0.029	0.256	0.272	0.255	0.187
Fe^{2+} in M1	0.100	0.148	0.163	0.091	0.152
Fe^{3+} in M1	0.009	0.035	0.009	0.067	0.000
Cr in M1	0.020	0.003	0.003	0.001	0.001
M1 site total	**0.999**	**1.000**	**1.000**	**1.000**	**1.000**
Ca in M2	0.724	0.572	0.587	0.618	0.738
Ti in M2	0.006	0.024	0.022	0.015	0.012
Ni in M2	0.003	0.001	0.001	0.001	0.000
K in M2	0.000	0.023	0.012	0.002	0.000
Mg in M2	0.212	0.061	0.060	0.030	0.071
Na in M2	0.051	0.316	0.315	0.332	0.166
Mn in M2	0.004	0.003	0.003	0.002	0.002
M2 site total	**1.000**	**1.000**	**1.000**	**1.000**	**0.989**

Fe^{3+} content calculated on the basis of cation and charge balance after Ryburn et al. (1976).

Type I MgSi-Pvk: BZ120C, BZ207C and BZ251B are exceptionally pure (Mg,Fe)SiO$_3$ and are referred to as Type I. They are all essentially Enstatite$_{96-99}$Ferrosillite$_{4-1}$ in composition[4] with very low Ca and Na; all <0.1 wt% as oxide. Al and Ti are present in small quantities at ~ 1 - 3 wt% oxide and 0.2 wt% oxide respectively. It should be noted that Type I pyroxenes plot at the Al end of figure 2.2_14 only because Al is *relatively* abundant compared to Na and Ca; its presence is small compared to other pyroxene groups.

All inclusions of Type I pyroxene exhibit a small deficiency of Si which can be satisfied by Al, table 2.2_6. The remaining Al is assigned to M1 along with Mg and Fe. If there is an M2 site (see discussion in section 3.3.5) then it is comprised almost entirely of Mg. It should be noted, however, that for this and Type II and Type III MgSi-Pvk, assignments represent a reference model. Phases are expected to have originally adopted perovskite-type structures (section 3.3.5).

---

[2] TZ (Transition Zone) refers to the expected location of origin for the group involving BZ209A, BZ209B, BZ218B and GU3C. The reasoning behind this will be discussed in detail in section 4.4.2.

[3] TiO$_2$ is a little high for both Group I and Group II, it matches the latter, however, more closely.

[4] Calculated on the basis of Mg and Fe^{2+}; Fe^{3+} contents are very high in Type I pyroxene, section 2.5.3.

Table 2.2_6 Cation assignments for Type I, II and III pyroxenes

	Type I			**Type II**			**Type III**			
	120C	**207C**	**251B**	**210B**	**241B1**	**241B2**	**237A**	**242B**	**246A**	**259B**
Si in Si1	1.961	1.935	1.961	1.757	1.875	1.832	2.000	1.914	1.888	1.957
Al in Si1	0.039	0.065	0.039	0.243	0.125	0.168	0.000	0.086	0.112	0.043
Mg in M1	0.843	0.679	0.865	0.661	0.524	0.574	0.475	0.406	0.435	0.483
Al in M1	0.011	0.044	0.015	0.162	0.294	0.237	0.345	0.431	0.378	0.375
Fe^{2+} in M1	0.107	0.218	0.087	0.037	0.038	0.039	0.023	0.029	0.033	0.027
Fe^{3+} in M1	0.027*	0.055*	0.022*	0.110†	0.113†	0.118†	0.070†	0.086†	0.98†	0.080†
Cr in M1	0.012	0.004	0.011	0.031	0.031	0.032	0.087	0.048	0.056	0.036
Ca in M2	0.002	0.002	0.002	0.024	0.023	0.026	0.190	0.164	0.174	0.200
Ti in M2	0.006	0.005	0.004	0.001	0.000	0.000	0.000	0.001	0.001	0.000
Ni in M2	0.000	0.001	0.000	0.000	0.000	0.000	0.000	0.000	0.000	0.000
K in M2	0.000	0.000	0.001	0.000	0.000	0.000	0.000	0.000	0.000	0.001
Mg in M2	0.984	0.988	0.992	0.879	0.813	0.855	0.368	0.443	0.450	0.378
Na in M2	0.004	0.005	0.002	0.070	0.053	0.059	0.422	0.313	0.307	0.405
Mn in M2	0.005	0.009	0.004	0.027	0.035	0.037	0.014	0.038	0.058	0.033
M2 Total	**1.011**	**1.020**	**1.005**	**1.001**	**0.924**	**0.977**	**0.995**	**0.959**	**0.991**	**1.018**

† Fe^{3+} content calculated on the basis of $Fe^{3+}/\Sigma Fe = 0.75$ (section 2.5.3). * Fe^{3+} content calculated on the basis of $Fe^{3+}/\Sigma Fe = 0.20$ (section 2.5.3).

Type II MgSi-Pvk: An additional suite of inclusions (BZ210B, BZ241B1 and BZ241B2) differs from Type I pyroxene primarily in terms of Al content. These grains are termed Type II, and all contain ~ 10 wt% Al_2O_3. Projecting onto the pyroxene ternary, the composition of Type II inclusions lies at $\text{Diopside}_{98}\text{Hedenbergite}_2$. Cr, Mn, Na and Ca contents are also all significantly higher than Type I pyroxenes, being around 1.2, 1.1, 0.9 and 0.6 wt% oxide respectively. Compared to Type I, Ti contents are significantly lower, ~ 0.02 wt% oxide.

In terms of cations, Type II pyroxenes have a distinct deficit of Si which can be accommodated by ~ 50% of Al cations, table 2.2_6. The remaining Al cations account for the deficiency of Fe and Mg compared to Type I, and are assigned to M1 along with Mg, Fe and Cr. M2 comprises, predominantly Mg with Na, Mn and Ca.

Type III MgSi-Pvk: An additional distinct suite (comprising BZ237A, BZ242B, BZ246A and BZ259B) are termed Type III and are similar in composition to Type II pyroxene except that both Ca and Na are present in significant quantities, ~ 5 wt% CaO and 6 wt% Na_2O. This shift in composition is offset by a decrease in the amount ferro-magnesium component although the relative abundances of Fe and Mg remain unchanged from Type I and Type II pyroxene (Type III Mg/(Mg+Fe) = 0.97). Al also resides in Type III pyroxenes at ~ 11 wt% oxide.

In terms of cations, unlike Type II pyroxenes, Type III pyroxenes show little Si deficit, table 2.2_6. Almost all Al, therefore can be considered to occupy the M1 site. Mg is chosen to partition between M1 and M2 in almost equal proportions, the remaining M2 being made up principally of Ca and Na.

Section 2.2.1.6 CaSiO$_3$ composition inclusions (CaSi-Pvk)

Three inclusions of a CaSiO$_3$ composition have been recovered from São Luiz diamonds: BZ97 and BZ115 from work by Wilding (1990) and BZ252A from the present study. The compositions of all three inclusions are of exceptionally pure CaSiO$_3$ compared to wollastonite from other localities (Deer et al., 1983); the only significant minor elements being Al, Mg and Fe: all at oxide concentrations of no more than 0.16 wt%. Ti, Cr, Mn, Ni and Na were also detected but at concentrations hardly discernable from background at < 0.05 wt %.

In terms of cations, (appendix 3.2) the Ca site is fully satisfied in all cases, any deficit appears on Si. Minor elements Al and Fe can be considered to substitute for Si, with Fe on this site likely to be predominantly the smaller cation, Fe^{3+}; an observation which is consistent with large Fe^{3+} content of other São Luiz inclusions (section 2.5).

➠

Section 2.2.1.7 Alumina inclusions

A total of six inclusions of alumina composition have been recovered from São Luiz: BZ214A from the work of Harris, Watt and Harte (1993, *personal communication* and Watt et al., 1994) and BZ227A, BZ228A, BZ229B, BZ241Acor[1] and BZ241C from the present study.

In terms of visual characteristics and major element characterisation, these can be subdivided into three types:

- Sapphire. Deep sky blue inclusion BZ227A comprises small amounts (0.6 - 0.1 wt%) of Fe, Si, Mg and Ti in addition to Al. Minor quantities of Cr, Ni, Na and Ca were additionally detected.
- Ruby. Blood red inclusions BZ214A, BZ241C and BZ241Acor[2] owe their colour to the presence of some 8 wt% Cr_2O_3. Si, Fe, Mg and Ti oxides comprise ~ 0.6-0.07 wt% and minor quantities of other elements were detected but in quantities within error of the background.
- Corundum. White inclusions BZ228A and BZ229B (originally observed as being blue and indicative of BZ229B being contaminant) were found to yield only Ti (0.14 wt% for BZ228A and 0.75 wt% for BZ229B) and, perhaps, a little Mg as minor components.

All minor elements are found to compensate for deficits in Al cation concentrations (appendix 3.2).

In terms of Cr content, and colour, ruby grains are clearly distinct from the other inclusions of alumina composition. Concentrations of minor elements are so low, however, that in order to be sure of the classification scheme proposed above for sapphire and corundum, more analytical precision was required. It was deemed to be the role of the ion microprobe to confirm the above classification, section 2.4.2.

A single corundum containing 3.05 wt% TiO_2 as the only significant impurity has been recorded from a Monastery diamond (Moore and Gurney, 1986). Compositionally, this grain is quite distinct from São Luiz Al_2O_3 inclusions.

---

[1] BZ241Acor is an additional grain which was found within the same pip as BZ241A fPer after polishing. Ion microprobe analysis, section 2.4.2, confirms this grain to be a fragment of inclusion BZ241C. Ideally this inclusion should be termed BZ241C2 but the previous nomenclature is retained to avoid confusion over the pip name as opposed to inclusion name.

[2] EPMA analyses were not obtained from BZ241Acor, confirmation as alumina composition is on the basis of EDS analysis.

Section 2.2.1.8 'Inclusions' of native iron

One grain, BZ208A, which was recovered amongst fragments from the breaking of BZ208 (Harte, 1993, *personal communication*), has a composition of what is, essentially, native iron, table 2.2_7. Native iron has been reported as inclusions in diamond (Sobolev et al., 1981 and Meyer and McCallum, 1985). Due to the fact, however, that fragments of the steel crusher, commonly, appear amongst the products of diamond fracturing (section 2.1) it was considered important to compare the compositions of BZ208A with the crusher material and iron grains from the literature. BZ208A, crusher fragments Fe1, Fe2 and Fe3 and electron microprobe standard iron were analysed by EPMA. Average analyses were computed using the best[1] analyses and are presented in table 2.2_7. The analyses of standard iron (FE) yielded good EPMA totals: confidence could thus be applied to measurements of unknown material.

Table 2.2_7 Electron microprobe analyses of native iron crusher material, 'inclusion' BZ208A, iron standard material and inclusions from Sloan and Yakutian diamonds.

Sample **Analyses ***	**Crusher †** 8	**BZ208A** 3	**FE (Standard)** 2	**Yakutia** 5	**Sloan** -
Si	0.243	0.253	0.005		0.271
Ti	0.000		0.000		0.000
Al	0.041	0.040	0.010		0.011
Cr	0.430	0.463	0.000	0.116	0.123
Fe	96.717	96.680	99.625	98.24	100.7
Mn	0.309	0.303	0.010	0.016	0.372
Ni	0.091	0.087	0.000	0.166	0.000
Mg	0.011	0.013	0.015		0.054
Co	0.144	0.170	0.175	0.12	
Ca					0.093
Cu				0.15	
Total	97.987	98.010	99.840	98.676	101.62

Yakutian analyses are averaged from the compositions of inclusions MP-412, MP-689, Ac-88, Ac-196 and Mn-8 from Sobolev et al., 1981. Sloan analyses are converted from oxide values from McCallum (1996 *personal communication*). * Number of analyses used in calculation of average composition (unknown for Sloan inclusion). † Crusher material composition was constructed from analyses of grains Fe1, Fe2 and Fe3.

There is no significant difference between the composition of the crusher material and that of 'inclusion' BZ208A. We can conclude, therefore that BZ208A is a contaminant and not a inclusion from diamond.

In contrast, both Meyer and McCallum (1985) and Sobolev et al. (1981) are confident that their inclusions are syngenetic. Indeed, McCallum (1996, *personal communication*), cites that the Fe recovered from Sloan appeared to be a single crystal (although with a rather deformed morphology)

---

[1] Given the presence of C in the crusher steel, analyses totalling greater than 97.5 wt% were deemed appropriate to be incorporated into the average for each sample.

and came from a diamond which was identified as containing a grey inclusion before breaking. In contrast to BZ208A, comparison of crusher material with Sloan and Yakutian inclusions, shows a marked difference despite the fact that the Sloan stone yielding native iron was broken using a similar crusher as the present study. Details of the procedure for release of the Yakutian inclusions have not been ascertained. However, given the similarity of Sloan and Yakutian Fe, it would seem most likely that both Sloan and Yakutian material *are* syngenetic. It should be noted that neither the Sloan or Yakutian inclusions have Ni contents approaching those of Fe:Ni alloy observed to occur as blebs in BZ66 (section 2.6.1.2).

➠

Section 2.2.1.9 Additional phases

Sulphides: Six grains, BZ215A, BZ221A2, BZ222A, BZ222B, BZ222C and BZ231A, were recovered from four stones and were mounted in Araldite®. They were found to be of similar composition lying within a restricted range in Fe (0.89 - 0.98 cations) per S anion. Also present are small quantities of Ni together with some Cu and Co (appendix 3.1). These compositions are consistent with the six grains being pyrrhotite. Pyrrhotites tend to be partially non-stoichiometric, ranging in composition Fe_xS from $x = 0.875$ to 1, so the small quantities of Ni, Cu and Co may, either partially make up the cation deficit, or else exist as minute grains of pentlandite and chalcopyrite (sulphides commonly seen in association with pyrrhotite as diamond inclusions; Harris, 1992).

Moissanite: Two moissanite (SiC) composition inclusions, BZ98 and BZ118A have been recorded by Wilding (1990) from São Luiz. They are reported to be typified by high, 150 wt%, electron microprobe totals when oxygen to give SiO_2 is added to the analysed amount of Si. In addition, 6 similar grains were obtained in the present study; BZ219C, BZ223D, BZ230B, BZ230D, BZ232B and BZ235C. These grains all give similar analyses, appendix 3.1, ranging from 153.6 to 158.4 Si calculated as SiO_2 and between 0.09 and 0.46 wt % Al calculated as Al_2O_3. The six grains all have a striking deep blue colour and range in size from ~100 to 40 µm.

SiC is a ubiquitous polishing and grinding material used in mineral preparation laboratories. The possibility that moissanite grains could be contaminant must, therefore, be carefully addressed. There is a concensus that moissanites recorded from a number of diamond sources are contaminant: Sloan moissanite (Otter and Gurney, 1989) has been proved to be laboratory contaminant and there is also doubt as to the validity of the Monastery sample (Moore and Gurney, 1989) due to its retrieval in the same laboratory. Wilding (1990) appears to be confident that BZ98 and BZ118A are syngenetic inclusions: he cites their faceted single crystal morphology as negating the possibility of BZ98 and BZ118A being contaminant. Indeed the appearence of faceted faces on a grain 'released' from an Argyle stone (Jaques et al. 1986) has been used to suggest that syngenetic moissanite inclusions occur within diamond from this source also. Study of carborundum grit used in the University of Edinburgh, Department of Geology and Geophysics shows that although many grains show obvious features of rounding and conchoidal fracture, many grains are single crystals showing clear growth faces and sharp interfacial angles. It is concluded, therefore, that single crystal morphology cannot be used as evidence to support a syngenetic origin for moissanite crystals.

Table 2.2_8 Comparison of 'inclusion' moissanite (Incl.) with polishing carborundum (Carb.)

	Si	Ti	Al	Cr	Fe	Mn	Ni	Na	Mg	Ca	Total
Incl.	156.4	0.01	0.26	0.01	0.00	0.01	0.01	0.01	0.01	0.01	156.7
Carb.	149.9	0.01	0.34	0.01	0.04	0.01	0.01	0.01	0.01	0.01	150.4

Inclusion data is averaged from 7 analyses, appendix 3.1, from grains BZ219C, BZ223D, BZ230B, BZ232B and BZ235C and presented as wt% calculated as oxide for each element. Averaged data for Carb includes two good analyses from two grains.

Of the six grains involved in the present study, no moissanite grains were recovered from diamonds which appeared to have blue inclusions before breaking. Furthermore, as well as grains showing clear faces, smaller, irregular grains make up the population; similar, again, to polishing carborundum. Stronger evidence that the six moissanite grains of the present study are contaminant comes from their compositional determination. EPMA Analyses were carried out on carborundum grains used for polishing in the laboratory; these yielded no significant compositional difference from the six 'inclusions', averaged in table 2.2_8, which, amongst themselves showed little compositional variation. None of these points are enough to conclude that the six moissanite grains involved in the present study *are* contaminant but it is considered that the likelihood is strong.

Magnetite: BZ83 was reported to be a fPer inclusion which yielded poor EPMA totals (Harte, 1991 *personal communication* following analysis by Harris, 1991) and was not considered further at that time. Observations carried out at the University of Leeds, on potential fPer inclusions by BS-SEM (section 2.6.1) included an analysis of BZ83. BS-imaging showed that BZ83 is a composite grain comprising two parts with numerous 1 - 4 µm, circular, dark BS-intensity features within the lighter half of the grain. These are located, predominantly, away from the grain boundary, figure 2.2_15. In addition to the scratches on the polished surface, it would appear that there is also an undulose variation in BS-reflectivity within the light BS-area. EDS-SEM measurements were obtained and showed that the dark areas contained Fe with some Ti, Al and Mn whereas the light areas contained principally Fe with some Mg.

BZ83 was investigated further by a combination of BS-EPMA imaging and EPMA analysis. Two analyses were obtained from each of the light and dark portions of BZ83 in addition to one analysis from the largest of the dark circular patches. Full analyses obtained are presented in appendix 3.1. All analyses gave low totals where Fe was originally calculated solely as FeO. Such totals may be indicative of a high Fe^{3+} content and totals of 93 - 98% are considered typical of magnetite analyses. The Fe^{3+} content has been estimated[1] following the method outlined in appendix 8, results being presented in appendix 3.2. It was found that the dark blebs yielded essentially the same composition as

---

[1] As discussed in section 2.5. for most minerals, the determination of Fe^{3+} content by EPMA can be considered very crude and should, wherever possible, be backed, or even better, substituted, by some other means of analysis, eg. Mössbauer analysis. In the case of minerals such as magnetite where there are significant quantities of both Fe^{3+} and Fe^{2+} present, the errors involved are significantly smaller and results can, therefore, be treated with more confidence.

the dark half of the grain[2]; BZ83DkBl-1 being equivalent to BZ83Dk-1 and BZ83Dk-2. Assigning cations to their most likely sites (table 2.2_9) gives the following compositional details:

- The dark portion of BZ83 is a magnetite with the A-site partially occupied by Fe^{3+} balanced by Al^{3+} and the B-site involving Fe^{2+}, Ti^{4+}, Mn^{2+} and Mg^{2+}. The Fe^{2+} / (Fe^{2+} + Fe^{3+}) value for the dark portion is 0.342.
- The light portion of BZ83 is a magnetite with full Fe^{3+} occupancy on the A-site and partial Fe^{2+} occupancy on the B-site which is balanced by Fe^{3+}, Mg^{2+} and a small amount of Mn^{2+}. The light portion is more Fe^{3+}-rich, with Fe^{2+} / (Fe^{2+} + Fe^{3+}) = 0.306.

Table 2.2_9 Site occupancy for cations in dark and light areas of BZ83 based on 4 oxygen anions.

	A-Site		**B-Site**					
	Fe^{3+}	**Al^{3+}**	**Fe^{3+}**	**Fe^{2+}**	**Mg^{2+}**	**Ti^{4+}**	**Mn^{2+}**	**O^{2-}**
Dark	0.95	0.05	0.93	0.97	0.04	0.04	0.02	4.00
Light	1.00	0.00	0.99	0.88	0.10	0.00	0.03	4.00

No association with another phase can be assigned to inclusion BZ83; it was the only inclusion recovered from its host diamond. No paragenesis can therefore be assigned. It should be noted, however, that the fPer inclusions recovered from São Luiz, with the possible exception of BZ66, section 2.6.1.2, are likely to represent a bulk composition plotting partially into the Fe^{3+} portion of the Fe^{3+} - Fe^{2+} - Mg^{2+} compositional field, section 2.5.2. If the source of BZ83 involves a spinel phase (magnesio-ferrite), it can be considered that BZ83 represents a source region partially more oxidised than that sourcing fPer inclusions. This can be considered a reasonable suggestion, particularly in light of the high Fe^{3+} contents recorded for many São Luiz inclusions, section 2.5.

Epigenetic phases:

Biotite: BZ239 yielded a single biotite grain as a composite with silica, BZ239D. It was found to contain ~17 wt% Al_2O_3, 7 wt% K_2O and has a Mg# of 0.50, appendix 3.1. It is highly unlikely that biotite would remain stable at conditions of diamond stability and so can be considered epigenetic.

Feldspar Group Minerals: Wilding (1990) reports an inclusion (BZ106[3]) of composition $Ca_2Al_2SiO_7$,. His analysis gives a good total but calculation on the basis of 7 oxygen anions does not give a reasonabe cation total. This analysis is far more consistent with a composition of anorthite, $CaAl_2Si_2O_8$, (table 2.2_10).

---

[2] Allowing for some contribution of light-BS component in analysis BZ83Dk-1 due to the small size of the feature.

[3] This inclusion has been lost so no further details could be obtained.

In addition to BZ106, one composite grain (BZ239E) of albite and andesine has been recovered in the present study. The albite has a composition of An_8 and the andesine has a composition of An_{44}. This may represent a peristerite intergrowth exsolved from a single An_{26}. Although BZ239E looks pristine the association of this composite grain with a quartz / biotite[4] composite, BZ239D, and a milky[5] quartz grain, BZ239F, in the same diamond, suggests an epigenetic origin. This conclusion is supported by the observation of the stone before breaking (appendix 1), which showed that it was highly deformed and yielded evidence of surface colouration (other patches of the stone from where fPer inclusion BZ239G was recovered, appeared to be pristine). On breaking, BZ239D and BZ239F were reported to look epigenetic.

Table 2.2_10 Composition of BZ106 (Wilding, 1990)

	BZ106 wt%		BZ106 per 8 O
SiO_2	43.6	**Si**	2.02
TiO_2	0.01	**Ti**	0.00
Al_2O_3	35.8	**Al**	1.96
FeO	0.42	**Fe**	0.02
MnO	0.01	**Mn**	0.02
Na_2O	0.04	**Na**	0.00
MgO	0.01	**Mg**	0.00
CaO	19	**Ca**	0.94
K_2O	0.25	**K**	0.01
Total	100.0	**Total**	4.98

BZ228D: A large, 200 x 200 x 160 µm, pseudo-spherical, white, amorphous (both in terms of appearence and structure, section 3.3.6) grain (BZ228D) was recovered from BZ228. Its physical features are classically reminiscent of a secondary inclusion. As it was recovered whole, however, it was decided that it merited further study and turned out to be valuable as its features are indicative of what to avoid in terms of searching for syngenetic unaltered inclusions.

After a structural determination by Gandolfi camera XRD (section 3.3.6), the grain was mounted in Araldite® and polished. Investigation by BS-EPMA, showed that it is hollow, figure 2.2_16. No quantitative analysis of the rim could be obtained due to the friable nature of the material, EDS analysis over the area of the grain showed, however, a strong S Kα peak, significant Ca Kα, Ca Kβ, Si Kα and Cl Kα peaks and the presence of some P Kα and Cu Kα. Reducing the analysis field to exclude counts from Araldite®, significantly reduced the count rate but also the presence of Cl, Cu and P: these components are expected, therefore to have arisen from the Araldite® itself and from pip

---

[4] Although there are some arguements to suggest a stability field for feldspars deep into the mantle (section 4.4.1) biotite is considered most likely to be an epigenetic phase.

brass. The count rate for the inclusion material was not sufficient to suggest that BZ228D is simply some mix of sulphide and silicate; it is likely that there is also a significant hydrous component: BZ228D is clearly not a syngenetic inclusion.

Sulphur: BZ235 yielded what appeared to be two fragments (BZ235B1 and BZ235B2) of a single metallic grey, tabular crystal. Initial EPMA analyses for the standard set of elements, as an oxide (appendix 3.1) yielded only very minor components of Al, Fe, Mn, Ni and Na. Determined as a sulphide, however, it gave totals of ~112% with minor Cu and Ni amongst the standard sulphide element suite of Fe, Co, Ni, Cu, Zn and S. BZ235B1 and BZ235B2 are, ostensibly, native sulphur. Although the grains themselves looked in good condition they came from a clearly oxidised stone and so, therefore, are considered to be epigenetic.

---

[5] The important observation here is the milky colour. As discussed previously, section 2.2.1.2, milky amorphous quartz grains are indicative of an epigenetic origin in contrast to clear well-crystalised grains of SiO_2, BZ99 and BZ103 (Wilding, 1990) which are more likely to be syngenetic.

Section 2.2.2 Compositional studies of composite grains

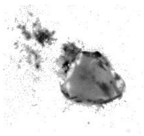

Three composite grains of deep mantle origin have been recovered during the present study:

- BZ241B1,C, a composite of Type II pyroxene and a ruby
- BZ237A6,C, a composite of Type III pyroxene and a partially majoritic garnet
- BZ259A2,B, a composite of a TAPP and a Type III pyroxene

In addition, a forth composite (reported by Harte and Harris, 1994) has been further investigated in this study:

- BZ207A,C, a composite of a TAPP and a Type I pyroxene.

Such touching grains are of particular importance because they were presumably in equilibrium at the time of diamond occlusion. They allow a useful comparison with non-touching grains in an assessment of how exhumation has affected composition and what the equilibrium compositions on diamond formation were (section 4.5).

A compositional study was undertaken on the grains mentioned above. This adopted two pathways:

- EPMA mapping in terms of four elements on each of BZ237A6,C, BZ241B1,C and BZ259A2,B
- EPMA point analyses in traverses across the boundaries exposed in each of BZ207A,C, BZ237A6,C, BZ241B1,C and BZ259A2,B

Section 2.2.2.1 EPMA mapping of composite grains

Allowing for topographic effects and at the resolution of the analyses (1 µm), there is no evidence of compositional gradients across the grain boundaries of any of the three composite grains studied.

BZ237A6,C: On the polished surface, the Type III pyroxene, BZ237A6 occupies a significant triangular portion at one end and a long thin tail at the other whilst the garnet portion, BZ237C, occurs as a band running diagonally across the grain. EPMA maps of the sample surface were made for the elements; Fe, Al, Cr and Si.

All four maps (figure 2.2_17) contain a diffuse signature, principally towards the tail, which corresponds to an undulose topography, particularly one deep scar, which was observed visually[1]. This effect is seen most markedly in Al.

The garnet, BZ237C is picked out strongly by a large contrast in Fe and Al with the pyroxene, BZ237A6. The contrast in Si is less, although quite evident and opposite in nature to Fe and Al. However, for Cr, there appears to be very little difference between the garnet and pyroxene composition grains.

BZ241B1,C: On the polished surface, a grain boundary lies across the middle of the composite inclusion. EPMA maps of the sample surface were made for the elements; Fe, Al, Cr and Si (figure 2.2_18).

Marked contrasts appear in all four element maps and contain, to varying degrees, a diffuse signature which corresponds to an undulose topography. The ruby, BZ241C is picked out strongly by a large excess of Al and, to a lesser extent, Cr compared to the pyroxene. Fe and Si are much more prominent in the pyroxene (BZ241B1). Within BZ241B1, there appears to be a further grain boundary, evident in Fe and, to a lesser extent, in Cr. The additional detail which appears in Al, however, combined with a visual inspection of the grain, allow one to conclude that this effect is due to topography: in this portion of the inclusion the grain slopes into the Araldite®.

BZ259A2,B: On the polished surface, the grain boundary lies transversely across the middle. EPMA maps of the sample surface were made for the elements; Fe, Al, Cr and Mg. All four maps (figure 2.2_19) contain a diffuse signature which corresponds to an undulose topography, particularly at the edges of the grain and around a deep gash in the TAPP, BZ259A2. This effect is seen most markedly in Al and Mg.

---

[1] Subsequent to EPMA mapping, BZ237C was subjected to ion microprobe analysis, section 2.4.5.1, the present topography of the surface is different from that shown in figure 2.2_17.

Marked contrasts appear between the TAPP and pyroxene compositions are seen in all four element maps. The TAPP, BZ259A2 is picked out strongly by an excess of Cr, Al, Mg and, to a lesser extent, Fe compared to the Type III pyroxene, BZ259B.

➠

Section 2.2.2.2 EPMA transects across composite grains

BZ207A,C: Seven EPMA analyses were carried out on BZ207A (pyroxene composition) and nine were carried out on BZ207C (garnet composition), appendix 3.1. BZ207A,C is a small grain and it has an area of ion microprobe damage near to the grain boundary. Two good analyses were obtained for BZ207A and four on BZ207C, all of these analyses lay on the central axis of the grain, away from the edges and the grain boundary (the low take-off angle of the Camebax makes the apparatus particularly sensitive to rounding problems). It was considered unwise to attempt to polish away the ion microprobe pit in order to improve the quality of the surface due to the risk of losing such a small grain.

BZ237A6,C: Eleven EPMA analyses were conducted on BZ237A6 and ten were conducted on BZ237C. Due to rounding problems only seven analyses on BZ237A6 and five on BZ237C were considered good enough to incorporate into average analyses. Most good analyses were obtained from restricted, well polished, areas and so a good range of distances from the suture was not forthcoming. Within these small areas, no significant compositional variation could be found. Between areas of good polish, the only compositional variations were seen in Si content. This was found to match variation in analysis total and so it can be concluded that any detected variation in the composition of BZ237A6 and BZ237C in relation to the suture is an artefact of the polishing process rather than due to compositional zonation in the specimen.

BZ241B1,C: Due to the problems encountered for BZ207A,C it was decided to attempt to improve the polish on BZ241B1,C. The grain surface was roughened with 6 μm diamond paste and subsequently polished down with 1 μm paste. Eleven analyses were undertaken on the pyroxene portion, BZ241B1, none of which yielded particularly good totals (appendix 3.1) due to the grain beginning to break up (appendix 3.1).

BZ259A2,B: BZ259A2,B is the largest of the composite grains and its original polish was found sufficient to yield good EPMA analyses. The grain boundary, at this stage, however, had been eroded during the inital polishing and so good analyses could not be obtained closer than 5 μm from the boundary. In order to address this problem, the grain was re-polished; succesful analyses being obtainable down to 2 μm from the boundary. The grain was still found to have rounded at the edges so such areas were avoided. Effort was made to analyse points in a random order, ie. not consistently approaching or retreating from the suture line, so as to avoid compositional artefacts caused by drift in analytical conditions. In total 51 points were analysed and because of rounding problems and general surface topography, some analysis points gave poor totals, both high and low. The distribution of total values did not vary with position from the grain boundary. Plotting analysis total against wt% SiO_2 (figure 2.2_20) shows a good positive correlation: the quality of analysis, therefore, significantly effects the values for individual oxides obtained. With this in mind, analyses with totals between 97% and 101% only, were used in plotting. Even in this range, however, as figure 2.2_20 shows, there is a good, positive correlation between EPMA totals obtained and the wt% of the more abundant elements: Si, Mg and Al. For the purposes of eliminating any potential bias this could produce on the data, cation values were re-calculated from oxide wt% values normalised to give 100% totals and plotted against distance from the grain boundary calculated as outlined below[1].

Calculation of distance from analysis point to grain boundary: The analysis points were recorded by hand onto a photograph of the grain to enable measurements of the distance of each analysis point from the polished surface to the grain boundary.

The boundary slopes towards the pyroxene (both the upper and lower sutures can be seen through the transparent grain). This means that an analysis on the pyroxene side, a certain distance from the suture, would be closer to the boundary than an equivalent point on the garnet side. Correction must be made for this. Furthermore, the boundary also slopes towards one edge of the grain so a calculation of the true distance from the analysis point to the boundary must involve, not only the distance, p, from the upper suture line (figure 2.2_21) and an estimate of the slope of the boundary, but also a distance, r, from one side of the grain. Assuming that 5 μm of the original 40μm grain has been polished away, this gives an angle of dip of 54.01° on the one side of the grain and 47.72° on the other. The distance from the analysis point to the boundary, *q*, can therefore be given by Equation 2.2_1:

$$q = p\sin\left[\frac{r(54.01 - 47.72)}{61.38}\right] + 47.72 \qquad \text{Equation 2.2\_1}$$

which simplifies to:

$$q = p\sin[0.1025r + 47.72] \qquad \text{Equation 2.2\_2}$$

Na, Ca, K, Ni and Ti, show no indication of gradation towards the suture even though analyses were successfully obtained at 2 microns from the boundary (the closest that can be achieved without overlap). There does exist, however, a striking compositional gradient for Mg and Fe, particularly on the garnet side. As figure 2.2_22 shows, there appears to be an increase in Mg and decrease in Fe

---

[1] In practice, no significant difference, between using normalised values and simply plotting distance against wt% was found.

away from the boundary into the garnet. Correspondingly, the Mg # increases from the boundary, into the garnet from 0.912 at 3 µm to 0.92 at a distance of 30 µm. On the pyroxene side, both iron and magnesium are seen to increase in concentration towards the boundary. Si shows a slight increase in cation abundance from deep in the garnet to the suture, figure 2.2_22, and a very slight decrease from deep in the pyroxene to the suture. Al, if anything, shows an slight increase in abundance from the garnet to the suture.

➠

Section 2.3 Coexisting phases and mineral associations

Table 2.3_1 Summary of associations defined in terms of inclusions from São Luiz and Guinea.

Association[¢]	**Phase**	**Inclusion**				
U.M.	Diopside	BZ213A				
T.Z.	Pyrrhotite	BZ215A*	BZ221A2	BZ222A,B	BZ222C	BZ231A
	Diopside	BZ209A	BZ209B	BZ218B*	GU3C	
	Maj-Grt	BZ218A*	BZ215C*	BZ216A1	BZ217A	BZ223A,B
		GU3B	GU3BDk			
L.M.	fPer	BZ67	BZ70	BZ73	BZ74	BZ76
		BZ103	BZ116B†	BZ201A	BZ205B*	BZ205C*
		BZ206A*	BZ226D1	BZ233C	BZ238B*	BZ239A
		BZ239G	BZ245A	BZ245B	BZ250C	BZ255A
		BZ260D	BZ260E	JH2A	JH7A1	JH11A1
		JH12A1	JH17A1	GU2A	GU4A1	
	Magnetite‡	BZ83L	BZ83Dk			
	TAPP	BZ205A*	BZ206B*	BZ238A*	BZ240B	BZ244B
	CaSi-Pvk	BZ97	BZ115	BZ252A		
L.M. I	fPer	BZ120A*	BZ207B*	BZ251A*		
	I MgSi-Pvk	BZ120C*	BZ207C#	BZ251B*	BZ254[a]	
	TAPP	BZ207A#				
L.M. II	fPer	BZ210A*	BZ241A*			
	II MgSi-Pvk	BZ210B*	BZ241B1#	BZ241B2*		
	Ruby	BZ214A¥	BZ241Acor§	BZ241C#		
L.M. III	fPer	BZ242A*				
	III MgSi-Pvk	BZ237A6*Φ	BZ237A1-8	BZ242B*	BZ246A	BZ259B#
	TAPP	BZ259A1*	BZ259A2#			
	Low Ca-Maj-Grt	BZ237C*Φ				
L.M. / U.M.	fPer	BZ243B*				
	Olivine	BZ243C*				
	TAPP	BZ243A*				
Unknown	Sapphire	BZ227A				
D''	fPer	BZ66#				
	Fe:Ni	BZ66L#				

Inclusions occupying each association are those for which good EPMA analyses have been obtained and include inclusions released in the present study (BZ214-BZ260), and those from Wilding (1990) and Harte, Harris and Watt (1993, *personal communication*) on which some work has been carried out as part of the present study.

¢ Association names refer to source regions as discussed in section 4.4.2: U.M., Upper mantle; T.Z., Transition zone; L.M., general lower mantle association; L.M. I, lower mantle association in association with Type I pyroxene, section 2.2.1.5.2; L.M. II, lower mantle association in association with Type II pyroxene, section 2.2.1.5.3; L.M. III, lower mantle? association in association with Type III pyroxene, section 2.2.1.5.4; L.M. / U.M., 670 km region; D'', possibly related to the D'' layer of the core - mantle boundary. † Wilding (1990) refers to this inclusion as occuring in association with a CaSi-Pvk; this cannot be verified as the grain has been lost. * Occurs from the same stone as a different phase from the same association. # Occurs as a composite (touching) grain with a different phase from the same association. § See section 2.4.7. ‡ Magnetite is only assigned to the L.M. association tentatively, section 2.2.1.9 and section 4.4.2. ¥ No coexisting phases were found with BZ214A, assignment to the LM II association is on the basis of similarity of this grain with BZ241C and BZ241Acor. Φ These grains may be considered transitional in composition. The garnet, BZ237C, has a composition transitional between majoritic garnet and TAPP and the pyroxene, BZ237A, although ostensibly Type III is not entirely consistent with other Type III inclusions. [a] Good analyses could not be obtained for BZ254 due to a poor polish, however, EDS spectra suggests that BZ254 is of an enstatite composition and thus belongs to the LM I association.

The compositional aspects of individual phases occurring as inclusions, section 1.4 and section 2.2, are a crucial part of any study of diamonds and their relationship to their source environment. However, the key to determining the location of these source regions lies, primarily, with the mineralogical *association* of inclusions within them. Such observation goes far to constraining the environment of genesis in a framework of pressure, temperature and fO_2. Commonly, the mineral phases recovered from São Luiz and Guinean diamonds are highly unusual and, in some cases they, and their associations are unique compared to those recorded from other sources (section 1.4). From observations of which syngenetic phases occur from which diamonds (appendix 2) a number of separate associations can be drawn up incorporating São Luiz and Guinean material. These associations are presented in table 2.3_1. The reader will observe that each association is given a name which may not have any connection with the discussion up to this point. These titles refer to the source region which is inferred by each association and is discussed in detail in section 4.4.

Section 2.4 Trace element analyses of São Luiz inclusions by ion microprobe

A total of 69 analyses on 36 inclusions were carried out using the Cameca ims 4f ion microprobe of the University of Edinburgh / NERC. Operating conditions, calculation procedures and errors are outlined in appendix 9.1. All analyses obtained within the present study are presented in appendix 4.1 as concentrations in wt ppm. Averaged values for each grain calculated from analyses presented in bold in appendix 4.1 and, normalised to C1 chondrite, are presented in appendix 4.2 which also contains averaged values for each phase. These averaged phase compositions also include averaged trace element data referred to in Harte et al. (1994).

➠

Section 2.4.1 Trace element characteristics of olivine inclusions

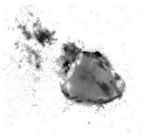

Two olivines from São Luiz have been analysed by ion microprobe. One analysis was undertaken on BZ243C and, in addition, one analysis was performed by Harte (1993, *personal communication*) on BZ111: the average olivine composition presented in appendix 4.2 incorporates both of these analyses.

A chondrite normalised distribution (figure 2.4_1), shows that São Luiz olivine contains very little in the way of any trace elements. Subsequently the scatter in the data obtained is large. Values for LILE and REE measured are typically around 0.1 x C1 with K content being particularly low, < 0.01 x C1. The one exception is a spurious value for Yb obtained from analysis of BZ243C at 4.5 x C1, believed to be due to an electrical spike during the reading of Yb on one cycle (Yb for BZ243C is omitted from the average olivine composition calculated). The HFSE show a trend in increasing C1 normalised value from Y to Nb.

Similar trace element compositions are observed in olivine from other geological settings[1] (e.g. Hutchison et al., 1995). Furthermore, the trend in HFSE seen for BZ243C is the same as that seen in olivines from Monastery (Hutchison et al., 1995). The one dissimilarity lies with the LREE. São Luiz material shows a hump over La and Ce which is not observed from other sources. Given the scatter in the data and the large errors involved, however, no great significance is attached to this observation.

---

[1] Because of the scarecity of trace elements in olivines, little data appears in the literature; Hinton and Craven (1997, *personal communication*) however, would support this attestation from experience.

Section 2.4.2 Trace element characteristics of Alumina inclusions

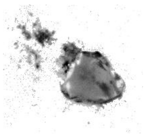

Grains of alumina from São Luiz have been analysed for trace elements belonging to both the standard set (appendix 9) and for additional elements which could substitute into the corundum $R\bar{3}c$ structure. From the literature, corundums commonly contain significant quantities of transition elements and platinum group elements (e.g. Schreyer et al., 1981 and Kerrich et al., 1987). Many of these additional elements are difficult to analyse on the ion microprobe because of strong interference, particularly with oxides and hydrides of aluminium present, and as a result of poor ionisation. The additional masses chosen for analysis were: ^{40}Ca, ^{48}Ti, ^{52}Cr, ^{56}Fe, ^{58}Ni, ^{69}Ga, ^{74}Ge, ^{85}Rb, ^{88}Sr, ^{89}Y, ^{90}Zr, ^{93}Nb and ^{208}Pb and the methology adopted for estimate of concentration is presented in appendix 9. The particularly wide assessment of compositions of the Al_2O_3 inclusions was carried out in order to determine if any distinctions might exist between and amongst the different inclusion types (particularly as two diamonds yielding ruby inclusions, BZ214 and BZ241, have different carbon isotopic content) and to determine if particular trace elements might indicate different parageneses.

Analyses were carried out on all six corundum grains, namely, BZ214A, BZ227A, BZ228A, BZ229B, BZ241Acor and BZ241C; two analyses being carried out on each of BZ227A and BZ228A. It was found that three distinct types of corundum could clearly be identified on the basis of this study, which confirm the groupings on the basis of EPMA, section 2.2.1.7:

- Group I, comprising of BZ227A
- Group II, comprising of BZ214, BZ241Acor and BZ241C
- Group III, comprising of BZ228A and BZ229B

The analyses for the most distinctive and abundant elements[1] in Al_2O_3 are presented, according to the above groups, in figures 2.4_2 to 2.4_4.

Group I: BZ227A contains the smallest concentration of trace elements. Both analyses show a generally steady decrease in concentration with increasing atomic number of the order of 10 to 0.00001 ppm. Peaks occur within this trend, however, at Ti, Fe and Ge at ~ 10, 10 and 0.1 ppm respectively.

Group II: With increasing atomic number, ruby type grains show a decrease in relative concentration of the elements analysed, from of the order of 10 ppm to 0.00001 ppm with a relatively flat trend

---

[1] Of trace elements from the standard set, only 6 elements were detected at levels above background in BZ214A (appendix 4.1). These elements were Rb, Sr, Yb, Pb, Y and Zr all of which lay significantly below chondritic values ranging between 0.001 x C1 for Sr and 0.63 x C1 for Pb.

between Ge and Pb. Within this trend, a distinctive peak occurs at Cr (which particularly distinguishes ruby from other corundums) with minor peaks at Ga, Sr and Zr at ~ 100, 0.1, 0.01 and 0.01 ppm respectively. No significant difference between analyses of BZ214A, BZ241C and BZ241Acor was observed.

Group III: Group III grains also show a general decrease in concentration with increasing atomic number to Ge. The range, compared to the other groups, however, is greater, 100 - 0.00001 ppm. In addition there appears a broad hump over Sr, Y, Zr and Nb with concentrations of up to ~ 1 - 10 ppm.

The groupings based on trace elements successfully mirrors the early classification (section 2.2.1.7).

As with EPMA results, section 2.2.1.7, the grain (BZ241Acor) which appears in the same pip as fPer inclusion, BZ241A, fits into Group II (ruby group). An origin from within diamond for the Group I and Group II grains is unquestionable; having been observed before diamond break-out and, in the case of BZ241C and BZ241Acor, being part of a composite grain; the possibility of contaminant can be ruled out. Grains BZ228A and BZ229B are indistinguishable and, additionally, constitute a separate group from the other corundum grains: explanation of their presence, however, is a more complex issue. Being present in directly successive break-outs (although, granted, on separate days) and being unexpected[2], the possibility of contamination must be addressed. Al_2O_3 is a commonly used abrasive in labs such as the one used for the break-out of BZ228 and BZ229. Extensive consultation with users of the lab suggested that Al_2O_3 had not been used in the recent past. If it had been, what would have been used would have been 0.25 µm white powder and not the 50 µm white coloured grains discussed here. It would seem unlikely, therefore, that BZ228A and BZ229B could be contaminant from Al_2O_3 polishing powder but even so, it is noteable that BZ229B is recorded as being blue on release from diamond but appears to be distictly white subsequent to polishing. It is considered advisable to treat these grains with caution. Perhaps fortunately, although inherently interesting, their significance within a petrological framework is difficult to assess: no other inclusions were recovered in association with any of these grains.

➠

---

[2] BZ228 yielded three tiny green flecks which were mounted as BZ228A1,2,3 and BZ229 yielded two blue shards mounted as BZ229B1,2. All grains appeared questionable and were not expected to be corundums (Appendix 1).

Section 2.4.3 Trace element analyses of inclusions of broadly garnet composition

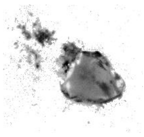

Trace element concentrations (appendix 4.1) were measured within the present study on a single majoritic garnet (BZ237C) and on five TAPP grains (BZ205A, BZ206B, BZ207A, BZ243A and BZ259A1). In addition, analyses have been undertaken on majoritic inclusions by Harte (1992) and Wilding (1990); and TAPP by Harte (1993, *personal communication*).

Section 2.4.3.1 Trace element characteristics of majoritic garnets

BZ237C was chosen for trace element analysis,[1] because it has characteristics which make it distinct from grains analysed by Harte (1992) and Wilding (1990). Firstly, it is only slightly majoritic (although has inclusions within it which have a large majoritic component, section 2.2.1.3.2) and secondly, it is associated with a Type III pyroxene rather than a TZ Group pyroxene.

Trace element concentrations were found to be generally low, never exceeding 4 x C1 (figure 2.4_6). Amongst the LILE analyses Ba, at 0.06 x C1 is more abundant than Sr at 0.01 x C1. HFSE concentrations were particularly low with an increasing trend from Y to Nb; all below 0.4 x C1. Amongst the REE, within error, a sharp increase in REE concentrations from La, 0.23 x C1 was found with a mound over Sm (2.99 x C1) and Eu. From Tb onwards, concentrations tailed off to a chondritic plateau.

Comparison with earlier majoritic garnet analyses from Harte (1992) is made in figure 2.4_6. Values for LILE are comparable between the two groups. For HFSE and REE from BZ237C, however, concentrations are lower than majoritic garnets throughout (with the exception of La, Ce and Nd in BZ19) and do not show the same shoulder over Sm and Eu. Comparison with trace element concentration of TAPP (section 2.4.3.2, figure 2.4_6) shows that BZ237C has a composition intermediary between majoritic garnet and TAPP.

---

[1] It was confirmed by BS-EPMA, as figure 2.4_5 shows, that the analysis was succesfully obtained from the BZ237C rather than the Type III MgSi-Pvk portion (BZ237A6), particularly, as the sputtered sample measured was collected from the central portion of the analysis pit.

Section 2.4.3.2 Trace element characteristics of inclusions with TAPP composition

A total of 18 analyses were carried out on five separate TAPP inclusions, BZ205A, BZ206B, BZ207A, BZ243A and BZ259A1. Chondrite normalised trace element concentrations are presented in figure 2.4_7 along with an averaged value comprising data from BZ205A, BZ206B and BZ259A1.

BZ205A, BZ206B, BZ207A and BZ259A1 all contain LILE concentrations around 0.1 x C1, showing broadly similar values for Rb, Ba and K and a dip in Sr. Absolute concentrations are slightly higher than majoritic garnets. The trend in REE concentrations is particularly clear for BZ206B (figure 2.4_7) with a dominant plateau of MREE-HREE values. The overall *pattern* is similar to that of majoritic garnets (section 2.4.3.1 and Harte, 1992) as is the trend in HFSE from Y up to Zr and down to Nb. The most distinctive feature of the four TAPP grains is that absolute concentrations of REE and HFSE are far lower than majoritic garnets (down to 0.01 x C1): a feature which is probably linked to their coexistence with CaSi-Pvk (section 4.4.2.4). Analyses for BZ207A were found to exhibit a large scatter and, in particular, concentrations of Hf, Ta, Zr and Nb were very high (> 100 x C1). These anomalies are believed to be due to the exceptional small size of the grain, its close proximity to Type I MgSi-Pvk composite BZ207C and electrical spikes during analysis. BZ207A analyses are, therefore, not included in the averaged TAPP composition presented (figure 2.4_7).

In contrast to the other TAPP compositions, the concentration of REE in BZ243A is relatively high, showing a peak over Sm (33.79 x C1) similar to BZ237C (BZ243A is thus not included in the calculated average TAPP composition). Apart from a high value for La, 28.14 x C1, the increase in REE concentrations is steep across the LREE from chondritic at Ce. Throughout the rest of the REE, the trend is far shallower showing a hump across Sm and Eu and a broad rise towards Lu. Values for HFSE stradle the chondritic with a rise in concentration from Y to Nb. Although in terms of major element concentrations (section 2.2.1.3.3), BZ243A is wholly compatible with the TAPP compositional field, in terms of trace elements, this inclusion compares more favourably with majoritic garnets. Indeed, BZ243A shows more similarity with majoritic garnet compositions than BZ237A (section 2.4.3.1).

These compositional characteristics are not entirely surprising. BZ243A, although TAPP in major element composition, does not occur in the same association as other TAPP grains (section 2.3), it coexists with an olivine composition grain (BZ243C) and a fPer (BZ243B). Having a majoritic trace element composition would suggest that BZ243A has not crystallised in association with the REE-hungry CaSi-Pvk (section 2.4.5) and is strong evidence to support the assumption that the paragenesis which BZ243A occupies lies at the upper and lower mantle boundary, as discussed in section 4.4.2.

Section 2.4.4 Trace element characteristics of fPer inclusions

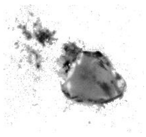

A total of 21 analyses were carried out on 12 fPer inclusions from São Luiz, appendix 4.1. The averaged value presented in appendix 4.2 incorporates 6 analyses by Harte and Craven (1993, *personal communication*) on BZ66, BZ67, BZ70, BZ73, BZ74 and BZ120.

Figure 2.4_8 shows the chondrite normalised values obtained for fPer inclusions. There is a marked scatter in the data, particularly over the REE. This is due to the fact that fPer contains very little in the way of trace elements. Long counting times and a large number of analyses have been sufficient, however, to obtain some useful data.

LILE concentrations are low; chondritic values for Rb, a large range of Ba values from less than 0.01 x C1 to one analysis above chondritic. The majority of analyses show a decrease in chondrite normalised concentration of Sr compared to Ba. Amongst the REE, the trend would appear to increase towards HREE, although, given the scatter, this can be considered to be speculative. Values average to being chondritic throughout but each element shows a scatter over, typically, an order of magnitude[1]. Amongst the HFSE, Hf is generally low, the averaged value being high due to a result from BZ205B, Ta appears to be chondritic. Y is significantly depleted, compared to the other HFSE: Zr varies over two orders of magnitiude around 0.5 x C1 as does Nb.

---

[1] Scatter of this magnitude can be considered to be within error, appendix 9.

Section 2.4.5 Trace element analyses of inclusions of pyroxene composition

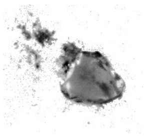

Trace element concentrations were measured within the present study on U.M., Type I, Type II and Type III pyroxene inclusions, appendix 4.2. In addition, analyses have been undertaken on Type I pyroxene BZ120 by Harte (1993, *personal communication*).

Section 2.4.5.1 Trace element characteristics of upper mantle pyroxene

A total of four analyses were undertaken on BZ213A. Chondrite normalised analyses are presented in figure 2.4_9.

Amongst LILE, Sr is particularly enriched in BZ213A at ~ 44 x C1, in contrast to Ba which is highly depleted at 0.03 x C1; K lies at intermediary concentrations. REE are enriched markedly above chondrite with a trend rising from La, ~ 12 x C1, to Nd, ~ 30 x C1 and then decreasing to Er, ~ 1 x C1. Special attention was paid to the measurement of Eu. Of the four analyses obtained Eu concentrations were not found to be inconsistent with the trend of neighbouring REE, no Eu anomaly was, therefore, found. Yb concentrations were found to be high, ~6 x C1 and although such high values occurred for only two of the four analyes, in the absence of any surrounding data, it is not clear whether this point can be considered spurious or not. Of the HFSE, Y, Zr and Nb were all analysed. Values are close to chondritic for Y and Nb; Zr is relatively enriched at 3.28 x C1.

➠

Section 2.4.5.2 Trace element characteristics of Type I, Type II and Type III pyroxenes

Ion microprobe analyses were carried out on Type I pyroxene, BZ207C, Type II pyroxenes, BZ210B and BZ241B2 and Type III pyroxenes, BZ237A, BZ246A and BZ259B, appendix 4.1. Averaged values for Type I pyroxene include one analysis by Harte (1993, *personal communication*) on BZ120, of the Wilding (1990) suite.

The scatter in trace element concentrations for all types of pyroxene is large (figure 2.4_10). The best constrained data are for Ba, Sr, LREE and HFSE. Throughout, concentrations of K, Ba, Sr and REE are low (~ 0.1 x C1 for Type I[1], ~ 0.01 - 0.1 x C1 for Type II[2] and ~ 0.8 x C1 for Type III). Additional similarities between pyroxene type involve a fairly flat REE trend subsequent to a rise from La to Nd for Types I and II. Furthermore, Y is highly depleted relative to Zr and Nb. Features distinctive of inclusion type are as follows:

Type I MgSi-Pvk: HFSE, Zr, Hf, Nb, Ta are enriched in increasing magnitude over chondrite, ~1 to ~ 10 x C1. Y is highly depleted at ~ 0.01 x C1, the Zr / Y ratio being 133 where incorporation of BZ120, see above, brings the average down to 53. Heavy elements Pb and Th occur at ~ 3.6 and 0.25 x C1 respectively.

Type II MgSi-Pvk: Amongst the HFSE, values for Y and Zr only, were obtained; the Zr / Y ratio ranges from 58 - 109, the average lying at 80.

Type III MgSi-Pvk: The averaged value for Type III pyroxene is highly biased by large values for BZ259B. For BZ259B, Sr is particularly enriched, ~ 3.5 x C1 and REE values lie along a largely chondritic trend, although, Tm, Yb and Lu are more abundant at ~ 2 x C1. Amongst the HFSE, Hf is particularly abundant, ~ 7 x C1, whereas Y, Zr and Nb all lie below chondrite. BZ259B has a Zr / Y ratio of ~ 5. The characteristics of trace element concentrations of the additional Type III pyroxenes, BZ237A and BZ246A, generally mirror those of BZ259B[3], yet at lower concentrations. Zr / Y ratios, excepting BZ259B, range from 21 to 112 which gives an average for all Type III pyroxenes of 29.

---

[1] With the exception of one value at Sm, ~ 2 x C1.

[2] With the exception of a very large value, ~ 17 x C1 for Yb from analysis of BZ210B and a very low value for Er from BZ241B2. Given the trend in rare earths of ~ 0.1 x C1, the presence of Lu in BZ210B at ~ 0.1 x C1 and the presence of Yb in BZ241B2 of ~ 0.1 x C1, these values can be considered anomalous.

[3] Except that the other Type III pyroxenes do not show the same enrichment in Sr and extreme HREE.

Section 2.4.6 Trace element characteristics of $CaSiO_3$ composition inclusions (CaSi-Pvk)

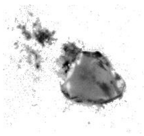

Analyses were undertaken on BZ97 and BZ115 (appendix 4.1) by ion microprobe. Chondrite normalised analyses are presented in figure 2.4_11.

The range in concentration of LILE for CaSi-Pvk was found to be large. Rb was not detected in any analysis, K is low (<0.1 x C1), Ba has values around 0.1 x C1. Sr is highly enriched (~ 100 x C1). REE concentrations in CaSi-Pvk are far higher, ~ 100 x C1, than in any other São Luiz phase measured. The trend in REE rises from La, ~ 200 x C1 to Ce, ~300 x C1 and then steadily decreases to Lu, ~ 60 x C1. In addition there is a small Eu anomaly (~ 33% greater, normalised to chondrite, than neighbouring elements), and a deficit involving Er, Tm and Yb in comparison to Lu. HFSE are also enriched, particularly Y, ~ 86 x C1 with Hf, Ta and Zr ranging from 2 - 50 x C1. Heavy elements are depleted, Pb less so than U and Th; values range from 5 - 0.3 x C1.

Section 2.4.7 Discussion of trace element characteristics of inclusions from São Luiz

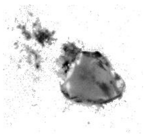

CaSi-Pvk inclusions: Inclusions of a $CaSiO_3$ major element composition are clearly highly enriched in trace elements, particularly REE, Sr and Y. Such trace element characteristics are most compatible with the CaSi-Pvk inclusions from São Luiz crystallising with a perovskite structure:

- Perovskite itself ($CaTiO_4$), is known for its capability of acting as a sink for REE, particularly LREE and indeed perovskite structured minerals have been synthesised with REE as major components, eg. $La_{2-x}Ba_xCuO_4$, (Maeno et al., 1994). Analyses have been undertaken by a number of authors on samples of perovskite from kimberlites and alnöites (Boctor and Boyd, 1979 and Campbell et al., 1997 and analyses summarised in Mitchell and Reed, 1988). All trace element analyses are broadly similar to the results obtained from the CaSi-Pvk inclusions although concentrations from perovskite are significantly larger (typically of the order of 10^5 to 10^2 times chondrite). The literature shows a range in compositions of trace element compositions of perovskite. Some analyses exhibit trends which match those observed from CaSi-Pvk from São Luiz. In particular, all analyses from Benfontein, Monastery and De Beers (Boctor and Boyd, 1979) and a number of analyses in Mitchell and Reed (1988) show an excess in Ce over La. Furthermore, all analyses in Boctor and Boyd (1979), including samples from Bellsbank show an excess in Lu over Yb. In *contrast* to São Luiz CaSi-Pvk, all samples from Boctor and Boyd (1979) show a deficit in Y and a number of samples in Mitchell and Reed (1988) show low Sm. Additionally, there is no evidence in the literature to support a Eu anomaly in natural perovskites.

- Experimental investigation has also been made into the tenacity for trace elements in CaSi-Pvk. Perovskite structured phases of a $CaSiO_3$ composition were synthesised from REE doped starting materials by Kato et al. (1988). Although concentrations are not comparable, as they used doped samples, CaSi-Pvk was found to accommodate most of the REE in comparison to coexisting phases[1].

Inclusions of broadly garnet composition:

BZ237C: The fact that BZ237C is both compositionally distinct from other majoritic garnets, section 2.2.3.2, and belongs to a different paragenesis, section 2.3, goes far to explaining the spurious trace element characteristics of the inclusion.

---

[1] Details of partitioning are discussed in detail in section 4.5.1.4.

The lower REE, Sr and Y concentrations, compared to other majoritic garnets are all consistent with BZ237C coexisting with CaSi-Pvk. This conclusion is consistent with the general lack of majoritic component in BZ237C[2] and the fact that BZ237C has significantly less CaO (1.72 wt%) compared to majoritic garnets (which commonly contain up to 15 wt%). However, unlike the TAPP grains believed to coexist with CaSi-Pvk, CaO and trace element concentrations in BZ237C are not as low. It is concluded that the LM III paragenesis, to which BZ237C belongs, probably contains less CaSi-Pvk than LM I and LM II parageneses.

TAPP: The differences between TAPP and majoritic garnet trace element compositions can be best explained by incorporating observations of the trace element characteristics of CaSi-Pvk (section 2.4.5). Combining the trace element concentrations of TAPP and CaSi-Pvk in a ratio of 6:1 gives a concentration which falls within the majoritic field of Harte (1992), figure 2.4_12. The fit is not exact, however, in particular, the resulting composition has a steeper REE trend than majoritic garnet. This can be accounted by the accommodation of trace elements in diospide coexistin with majoritic garnet.

fPer inclusions: The low trace element concentrations of fPer inclusions are certainly consistent with crystallisation with CaSi-Pvk[3], since values are low for all elements. It is also considered likely, however, that the trace element characteristics of fPer inclusions are controlled by structural factors: fPer is simply not of an appropriate structure to accommodate large amounts of trace elements.

Pyroxene composition inclusions:

Upper mantle pyroxene BZ213A: BZ213A exhibits a striking similarity, both in terms of trend and absolute values of trace element concentrations, to mantle pyroxenes from a variety of localities. Analyses from both mantle megacrysts and cpx in xenoliths are compared with BZ213A in figure 2.4_13 and include data from Hutchison et al. (1995), Harte et al. (1991), Caporuscio and Smyth (1990) and Shimizu (1975). Amongst REE, two types of trend can be seen in figure 2.4_13;

- A fairly flat REE pattern tailing off towards HREE reflected in samples from Matsoku (Harte et al., 1991), Monastery (Hutchison et al., 1995 and Harte et al., 1991), Thaba Putsoa (Shimizu, 1975 and Harte et al., 1991) and Mothae (Shimizu, 1975).
- A more fractionated REE trend falling steeply in concentration towards HREE reflected in samples from Liquobong (Shimizu, 1975), Bultfontein (Shimizu, 1975), Bobejaan (Caporuscio and Smyth, 1990), Roberts Victor (Caporuscio and Smyth, 1990).

---

[2] Majoritic garnets lose their majoritic component at depths approaching 22 GPa, section 4.4.1.

[3] Also see section 4.5.1.3.

These trends reflect, in general, the contrast between eclogite and peridotitic asociations, however it should be noted that in eclogites the slopes of trends can vary hugely with bulk composition (Harte and Kirkley, 1997).

BZ213A more closely resembles the second trend. In terms of concentration, Roberts Victor samples are generally more depleted than BZ213A: the samples which best match BZ213A are the cpx from Bobejaan (Bellsbank, Caporuscio and Smyth, 1990) and Shimizu's (1975) granular lherzolite cpx from Liquobong and Bultfontein. Temperature estimates for xenoliths from these localities are fairly unexceptional for mantle material, ~ 1200 - 1400 K (Finnerty and Boyd, 1987 and references in Bishop et al., 1978); granular lherzolites are generally considered to be sourced at lower temperatures than sheared lherzolites (see Harte and Hawkesworth, 1987 for discussion). BZ213A, is not associated with any additional phase. Given the similarity in trace element data to granular lherzolites and, in terms of major element composition to cpx from Bultfontein (Wilding, 1990) and other lherzholitic cpx, section 2.2.1.5.1, it can be considered most likely that BZ213A is part of a lherzolitic paragenesis.

Type I, Type II and Type III pyroxenes: The low REE and Y concentrations and the excess of Ba over Sr[4] for pyroxenes from Type I, Type II and Type III are all consistent with these pyroxenes crystallising in equilibrium with CaSi-Pvk (and thus, adopting perovskite structures themselves, section 4.4.2). Furthermore, the relative excess of REE and smaller Zr / Y ratio of Type III pyroxenes would suggest that less CaSi-Pvk is present in the LM III paragenesis. This observation is completely in line with the trace element characteristics of BZ237C, as discussed above, which suggest crystallisation in association with some CaSi-Pvk but in smaller quantities than crystallisation involving TAPP. Interestingly Type III pyroxene contains significantly more Na than Type I and Type II pyroxene, yet is more REE enriched. This trend is the opposite of that seen in cpx from mantle xenoliths (Caporuscio and Smyth, 1990), making Type I, II and III pyroxenes yet more inconsistent with an interpretation as being part of typical upper mantle paragenesis.

---

[4] With the exception of BZ259B.

Section 2.5 Mössbauer Study of inclusions

Of great interest is the state of oxidation of the deep Earth. As will be discussed in section 6.1.2, oxygen fugacity, fO_2, is a fundamental parameter in the stability of diamond and any determination of fO_2 in the mantle has more broad implications relating to mantle evolution and recycling, section 8.3. The most common element which will readily adopt more than one state of oxidation is iron; existing as ferrous (Fe^{2+}) or ferric (Fe^{3+}). Subsequently, the oxidation state of Fe is commonly used as an indicator of fO_2. There has been much discussion over whether the electron probe can be used to successfully calculate the state of iron oxidation in a sample. This debate has resolved around two methodologies:

- Electron probe analyses are initally calculated on the basis of common oxides of each element in question, Fe being calculated as FeO. Theoretically, any presence of Fe^{3+} will therefore result in an artificially low analysis total. If this defecit is attributed to the presence of Fe^{3+}, then its contribution can be calculated (appendix 8 and Ryburn et al., 1976). For some phases, such calculations may work reasonably well[1] but, in general, determination of Fe^{3+} by this technique must be viewed as extremely crude. There are a number of reasons: any deficit in totals may, additionally, be attributed to the presence of volatiles such as OH^-, or more reduced states of additional elements such as Cr. The assumption that an analysis should total exactly 100% is questionable, as it depends strongly on analytical conditions: calculation of Fe^{3+} incorporates, inherently, the error involved in every other element analysed.
- Fe^{3+} will produce a very slightly different spectrum of X-Rays than Fe^{2+} due to its differing electron environment. Determination of this shift can be attributed quantitatively to the presence of Fe^{3+} (eg. Höfer et al., 1993 and 1994) and a similar technique by Bajt et al., 1994). In practice, however, few facilities are set-up to operate on this basis as a matter of routine and errors are inherently large.

Further techniques, currently in their infancy, are X-Ray photoelectron spectroscopy (XPS, discussed in Raeburn et al., 1995) and electron energy-loss near edge structure (ELNES, being developed in Bayreuth, Poe et al., 1997).

A far better method for measuring the concentration of Fe^{3+} is Mössbauer spectroscopy. The Mössbauer effect occurs because gamma rays of a particular energy will be absorbed and re-emitted by specific nuclei in a solid without energy loss from recoil. The energy of absorbed radiation is dependent on the electronic environment of the nucleus which, in turn, is dependent on the environment of the specific element involved. This means that by measuring the absorption of gamma rays in a sample, the oxidation state and structural setting of Mössbauer active components in a

---

[1] For example magnetites, section 2.2.1.9.

sample can be measured. The Mössbauer effect is very similar to the principles involved in crystal field theory, the theory which describes the splitting of energy levels in electron clouds and explains, for example, the absorption of light in transition elements. The key difference is the fact that the Mössbauer effect is a nucleur phenomenon.

Few nuclei are particularly useful for Mössbauer analysis. Isotopes must have sufficiently large nucleur transitions to give energetic enough gamma emission, but not too large as to create radiation damage in the sample. Additionally, decay must be dominantly by gamma emission and for practical purposes the emmitor must be reasonably abundant. Over 100 Mössbauer transitions are known, amongst which, those in ^{57}Fe are the most commonly used.

Although there is no net change in the energy of the nucleus analysed, because absorption is *linearly* directed (in the direction the beam), whereas the emmision adopts *random* directions, the net effect on the transmitted gamma beam is one of absorption[2]. For analysis of absorption over a range of energies, rather than designing a source incorporating a frequency range, which is not practically possible, a spectra is obtained by a single energy source and application of the Doppler effect. The sample is oscillated towards and away from the source, thus exposing the sample to a range of energies. The Mössbauer spectrum produced is commonly, therefore, presented as absorption against velocity in mm/s.

Spectra are then deconvoluted into spectra due to each contributory component. Three key observations are made for each deconvoluted spectra ; isomer shift, quadropole splitting and magnetic splitting as summarised in figure 2.5_1.

- Isomer shift (I.S.) is the shift in energy due to valence state, spin state and coordination of surrounding atoms. For example, the isomer shift for high-spin Fe^{3+} compounds is lower than for high-spin Fe^{2+} compounds due to the smaller electron density at the nucleus in the latter compounds.
- Ground states are, in addition, split, where the electron density of the nucleus' environment is anisotropic. This splitting is termed quadrupole splitting (Q.S.); the magnitude of which can be utilised to determine the degree of distortion of a particular coordination.
- A hyperfine magnetic field will cause further splitting, for example ^{57}Fe in magnetite will adopt six peaks rather than the two observed in pyroxenes.

Spectra are considered to be deconvolutable unambiguously. Although there has been some discussion criticising the shortcomings of deconvolution methodogy (eg. Rancourt, 1994), these problems are not considered significant for the current study (McCammon, 1996 *personal communication*).

---

[2] Some Mössbauer techniques are specifically aimed at measuring scattered, ie emmitted radiation. This technique is particularly useful in investigating surface properties.

As far as interpretation of spectra are concerned, there are two important practical points. Firstly, for Fe, the effect of valence outweighs that of the geometry of the atomic environment. This means that Fe^{2+}, no matter in what coordination, will not generally overlap Fe^{3+} in isomer shift / quadrupole splitting space, figure 2.5_2 (after Burns and Solberg, 1990). Secondly, the area of absorption is approximately proportional to the concentration of the species involved and so, measuring the deconvoluted peak areas from a Mössbauer analysis will yield the relative proportion of Fe^{3+} to Fe^{2+} in a sample.

The interested reader will find reviews by Hawthorne (1988), McCammon et al. (1991) and McCammon (1995) useful as a more detailed description of Mössbauer analysis.

Mössbauer apparatus has historically been designed to measure large samples. The inclusions involved in this study are too small to be measured by conventional techniques. Recent advances, however, have resulted in the development of a Mössbauer milliprobe (McCammon et al., 1991, McCammon, 1994). A high intensity, >2000 mCicm^{-2}, source, finely collimated by Pb shielding, is utilised in conjunction with a Ta mask allowing transmission through an aperture of as little as 50 µm in diameter. The sample distance is reduced, in comparison with conventional techniques, to < 5mm.

A total of ten inclusions: fPers; BZ66, BZ67, BZ73, BZ238B and BZ251A: TAPP; BZ238A, BZ243A: Type II Pyroxene; BZ210B; Type I Pyroxene; BZ120C and BZ251B, were analysed by Dr. Catherine McCammon at the Bayerisches Geoinstitut, Universität Bayreuth using 14.4 keV gamma rays. Criteria for the choice of specimens were: large size (BZ73 and BZ67[3]); peculiarity in terms of composition (BZ238B and BZ66, section 2.2.1.4 and section 2.6.1.2); mutual association (BZ251A and BZ251B and BZ238A and BZ238B); and representative range (BZ73 and BZ67: BZ73 is homogeneous on BSE inspection whereas BZ67 yields a fine texture of bright scattering, section 2.6.1.1). Results were obtained for nine of the ten samples; BZ120C being lost probably in the preparation process. BZ251A and BZ251B were analysed within their occluding diamond (BZ251), other samples were prepared by removing a slice ~0.5 mm in thickness, from the top of each pip containing the inclusion to minimise the thickness of transmitting medium[4]. Data are discussed in McCammon et al. (1995a, 1996a and 1997) and the following sections. In addition, McCammon et al. (1995b) have undertaken a study of two São Luiz majoritic garnets.

---

[3] BZ67 and BZ73 are approximately 400 and 450 µm in diameter, respectively.

[4] Only a slight absorption in gamma transmission is caused by Araldite®, however, due to the small size of the inclusions, and, in some cases, low iron content, any steps to maximise transmission are considered desirable.

Section 2.5.1 Mössbauer study of garnet composition inclusions

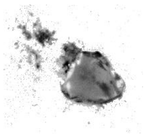

Section 2.5.1.1 Mössbauer study of majoritic garnet

The presence of Fe^{3+} is very significant in two majoritic garnets from São Luiz analysed by McCammon et al. (1995b) and is within the range of that probably present in majoritic garnets from diamonds from other sources. Calculation on the basis of EPMA for majoritic garnets recovered from Monastery diamonds (Moore and Gurney, 1985) yields values for $Fe^{3+} / \Sigma Fe$ of 0.02 - 0.31.

Little experimental work has been undertaken on the role of Fe^{3+} in garnet. Woodland and O'Neill (1993), however, did show that with increasing Fe^{3+} content over Al, a garnet composition became favoured above an assemblage of spinel + garnet, particularly at higher pressure. This work is consistent with a high pressure origin for São Luiz majoritic garnets.

➠

Section 2.5.1.2 Mössbauer analyses of TAPP

Analyses on BZ238A and BZ243A each took approximately 2-3 weeks to complete due to their small iron content and size (~50 µm). Like majoritic garnets, the content of Fe^{3+} in TAPP inclusions is high (figure 2.5_3). The two spectra obtained are very similar, which would rule out any extreme effects due to orientation. Table 2.5_1 summarises the data obtained.

In addition to the large amount of Fe^{3+}, the striking feature of the Mössbauer spectra is the quadrupole splitting of Fe^{2+}. Despite the composition of TAPP being very similar to pyrope - almandine, section 2.2.1.3.3, Fe^{2+} does not show the degree of quadrupole splitting which would be expected for occupancy of dodecahedral [12] sites. Indeed QS values for Fe^{2+} in BZ238A and BZ243A are consistent with octahedral [6] coordination (see figure 2.5_2). Furthermore, QS values for Fe^{3+} are more consistent with tetrahedral [4] coordination than octahedral [6] coordination. The two TAPP grains analysed, therefore provide information consistent with a new structure distinct from garnet (see section 3.3.1 for full structural determination).

Table 2.5_1 Summary of Mössbauer analyses of TAPP

(a) Deconvolution data

Sample	**I. S. Fe^{3+}**	**Q. S. Fe^{3+}**	**I. S. Fe^{2+}**	**Q. S. Fe^{2+}**
BZ238A	0.15(8)	0.57(15)	1.03(19)	2.39(39)
BZ243A	0.17(2)	0.69(3)	1.10(3)	2.04(6)

(b) Compositional data

Sample	**FeO wt %**	**Fe^{3+} / Σ Fe**
BZ238A	4.98	0.74(8)
BZ243A	5.19	0.66(8)

Figures in parenthesis refer to the standard deviation of the last digit.

Section 2.5.2 Mössbauer analyses of fPer inclusions

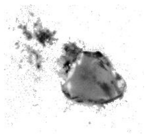

Each analysis took approximately one day to complete. The results of Mössbauer analyses are presented in figure 2.5_4 and are summarised in table 2.5_2.

Table 2.5_2 Summary of Mössbauer analyses of fPer inclusions

Sample	ΣFe / (ΣFe+Mg)$_{cations}$	Fe^{3+} / Σ Fe
BZ66	0.64	0.07(2)
BZ67	0.46	0.02(2)
BZ73	0.30	0.02(1)
BZ238B	0.17	0.03(3)
BZ251A	0.15	0.00(2)

Data from McCammon et al. (1995) and McCammon (1995, *personal communication*).

The first striking feature of the results is the exceptionally small amount of Fe^{3+} which São Luiz fPer inclusions contain (any variation in Fe^{3+} content may be related to the presence of Na). As figure 2.5_2 shows, the Mössbauer spectra of all four inclusions show little deviation from an ideal Fe^{2+} quadrupole split pattern, the small deviation at low values of isomer shift being due to the presence of a little Fe^{3+}. There is a small peak on the probability distribution of quadrupole splitting on BZ66 and BZ238B at values around 2.5 mms^{-1}. This peak was initially suggested to be due to the presence of a small amount of silicate (McCammon, 1995 *personal communication*). Given the presence of FeNi in BZ66, section 2.6.1.2, and the anomalous features in BZ238B, FeNi may be a reasonable alternative explanation. Fe adopts a [8] coordination in taenite; consistent with a high value for Q.S..

It is clear, even from visual inspection of figure 2.5_4, that BZ66 and BZ238B contain the most[1] Fe^{3+}. At conditions of ATP, pure Fe_xO will only be stable with at least Fe^{3+} / O^{2-} = 0.132, figure 2.5_5 (McCammon et al., 1995). Experimentation has shown that at higher temperatures, and more importantly, higher pressures (McCammon et al., 1995; Srecec et al., 1987; Speidel, 1966), the stability field of Fe_xO shrinks towards lower Fe^{3+}. The oxygen-rich boundary with Fe_xO + magnetite is believed to move to lower Fe^{3+} contents on the stabilisation of a high pressure polymorph of magnesioferrite (McCammon et al., submitted and figures 2.5_5 and 2.5_6). These observations are true throughout the fPer solid solution series and the implication for high pressure fPer inclusions is that those lying towards the oxygen rich end should exsolve to fPer + magnesioferrite on decompression. Observations by SEM and TEM on fPer grains from São Luiz (section 2.6.1.1), provide an indication that this process is occurring in some São Luiz material, section 2.6.1.1. Quantitatively, values for Fe^{3+} / O^{2-} for fPer inclusions from São Luiz lie just below the lowest values

---

[1] Some of this 'Fe^{3+}' may be attributed to the presence of silicate but it should also be noted that BZ66 in particular has a particularly high Na_2O content (~ 1 wt%, appendix 3.2).

which are expected for pressures of 18 GPa and temperatures of 1273 K (McCammon, 1995). This observation represents important independent evidence supporting formation of São Luiz fPers at depths greater than the transition zone. As the minimum Fe^{3+} content of fPer is virtually independent of conditions of fO_2 at high pressure (McCammon, 1995) any doubt as to conditions of fO_2 in the deep earth will not compromise a conclusion of lower mantle formation.

Plotting Fe^{3+} / O^{2-} against $\Sigma Fe / (\Sigma Fe+Mg)_{cations}$ (figure 2.5_5) yields a fairly smooth curve through the non-anomalous grains[2], BZ73 and BZ66, similar to those of the fPer + Fe / fPer phase boundaries of figure 2.5_6. Although there is little crystal chemical evidence to suggest that Fe^{3+} / O^{2-} is a strong function of depth there is little evidence to refute it. The observation of a restricted range of Fe^{3+}/O^{2-} compositions may imply a relatively limited range of depths of formation of the samples analysed. Indeed this range can be crudely calculated. We can assume an exponential dependence of minimum Fe^{3+} / O^{2-} on depth (as Fe_xO is unlikely to achieve complete stoichiometry), and can assign 18 GPa and 1273K to a depth[3] of 514 km, using the PREM mapping of depth to pressure (equation A14_15), and 0.1 MPa and 298 K to a depth of 0.1 km for $\Sigma Fe / (\Sigma Fe+Mg)_{cations} = 1.0$. If we also assume that at some arbitrary high pressure, say 5000km, Fe^{3+} / O^{2-} = 0, we have three conditions to satisfy, table 2.5_3.

Table 2.5_3 Conditions for fitting of an exponential relationship to the dependence of Fe^{3+} / O^{2-} on depth.

Depth (km)	0.1	514	5000
Fe^{3+} / O^{2-}	0.132	0.058	0

From figure 2.5_5, for Fe^{3+} / O^{2-} we can estimate bounds on $\Sigma Fe / (\Sigma Fe+Mg)_{cations} = 1$ of between 0.0345 and 0.0394. Applying the exponential fit (figure 2.5_7) yields a range in 'depth' of ~800 to 1100 km. This calculation is based on only two data points and, thus, is subject to large errors. Particularly at low values of Fe^{3+} / O^{2-}, the dependence of depth on Fe^{3+} / O^{2-} is large. What is important, however, is the conclusion that because the calculated depth is of the order of the *upper* rather than *lower* reaches of the lower mantle, it is unlikely that the range in non-anomalous fPer inclusions subjected to the present study are sourced from a range of depths down to the base of the lower mantle. Any variation in Mg/(Mg+Fe), therefore, is more likely to be a result of crystallisation than depth stratification and supports the interpretation of trace element data on fPer (section 4.5.1.3).

---

[2] BZ66 clearly does not fit on the same trend as BZ67, BZ73 and BZ251A, on the other hand, BZ238B, in terms of this correlation is not particularly anomalous, incorporation of BZ238B into the following calculations does not significantly affect the conclusions.

[3] A temperature of 1273K is grosely under-estimated for this depth, considering both Geotherm 1 and Geotherm 2 (section 4.2). The significance of the present calculation, however, is related principally to the range in 'depths' implied rather than their absolute value.

Section 2.5.3 Mössbauer analyses of pyroxene inclusions

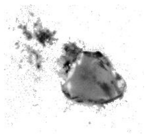

Figure 2.5_8 and table 2.5_4 summarise the Mössbauer data collected on Type I pyroxene (BZ251B) and Type II pyroxene (BZ210B). Analyses took approximately a week to complete.

Table 2.5_4 Summary of Mössbauer analyses of Type I pyroxene, BZ251B and Type II pyroxene, BZ210B.

(a) Deconvolution data

Sample	I. S. Fe^{3+}	Q. S. Fe^{3+}	I. S. Fe^{2+}	Q. S. Fe^{2+}
BZ210B	0.13(1)	0.56(2)	1.20(2)	2.30(4)
BZ251B	0.20(11)	0.30(22)	1.16(5)	2.23(9)

(b) Compositional data

Sample	FeO wt %	Fe^{3+} / Σ Fe
BZ210B	5.14	0.75(3)
BZ251B	3.80	0.20(6)

Figures in parenthesis refer to the standard deviation of the last digit

A number of observations are striking:

- Values for QS of Fe^{2+} are closer to being consistent with a pyroxene structure (~2.22 mm s^{-1}, Dowty and Lindsley, 1973) than a MgSi-Pvk structure (1.58 mm s^{-1}, McCammon et al., 1992). This implies that neither BZ210B nor BZ251B retain the perovskite structure they would be expected to have in the lower mantle and is consistent with independent and full structural determination of BZ210B (section 3.3.5).
- Like the TAPP and majoritic garnet grains, the Fe^{3+} content of BZ251B and, in particular, BZ210B is very high. This observation ties in well with other compositional observations.

The high Fe^{3+} contents of BZ251B and BZ210B are also consistent with experimental determinations and considerations of crystal chemistry.

For Type I pyroxene compositions (e.g. BZ251B), experimental work (McCammon et al., 1996a) has shown that MgSi-Pvk can accommodate significant quantities of Fe^{3+} at high pressure, the amount of which varies with fO_2. Experiments conducted on $Mg_{0.95}Fe_{0.05}O_3$ at 24-25 GPa, 1923 K, showed that, at its low fO_2 stability, $Fe^{3+}/\Sigma Fe$ of 0.05 was accommodated whereas at high fO_2 the sample contained in excess of 0.1 $Fe^{3+}/\Sigma Fe$. The presence of larger amounts of Fe^{3+} in BZ251B, can be explained in terms either of high fO_2, or, more likely, higher pressure.

The Al content of BZ210B (Type II pyroxene) is high and shows a slight deficiency in Si and Mg which can be explained in terms of a substitution Al and Fe^{3+}:

$$Mg^{2+} + Si^{4+} \leftrightarrow Al^{3+} + Fe^{3+} \qquad \text{Equation 2.5\_2}$$

As Table 2.5_5 shows, the results of Mössbauer analysis are entirely consistent with such an interpretation.

Table 2.5_5 Comparison of cation concentrations of Si, Mg, Al, Fe^{2+} and Fe^{3+} for BZ210B, BZ251B and $En_{90}Fs_{10}$

Sample	(Si / 6 O)	(Mg / 6 O)	(Al / 6 O)	(Fe^{3+} / 6 O)	(Additional cations / 6 O)
BZ210B	1.76	1.54	0.40	0.11	0.16
BZ251B	1.96	1.86	0.05	0.02	0.09
$En_{90}Fs_{10}$	2	1.8	0	0	0.2

In the presence of Al, experimental results record large amounts of Fe^{3+} and, in contrast to low-Al MgSi-Pvk, suggest that $Fe^{3+}/\Sigma Fe$ is less dependent on fO_2 (McCammon, 1997).

➠

Section 2.5.4 Summary of Mössbauer data

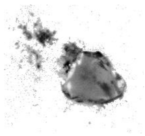

As far as lower mantle phases, TAPP, fPer and Type II pyroxene, are concerned, at first glance there would appear to be an inconsistency in the data obtained. On one hand, fPer yields extremely low quantities of Fe^{3+}, whereas both TAPP and, in particular Type II pyroxene, yield large amounts of Fe^{3+}. As discussed previously, sections 2.5.1-3, experimental work has an answer to these observations. fPer with minimal Fe^{3+} could coexist with relatively high Fe^{3+} in TAPP and Type I and II pyroxenes provided that fPer coexists with magnesioferrite (Fe^{3+}-rich oxide)[1]. As will be seen later, section 2.6.1, there is good evidence for this coexistence being the case. Additionally the presence of FeNi alloy in BZ66 and, questionably, in BZ238B, section 2.6.1.2, is entirely consistent with a low Fe^{3+} content in the host.

The salient points from Mössbauer studies of São Luiz samples are as follows:

Majoritic garnets

- Majoritic (TZ) garnet contain large amounts of Fe^{3+} (McCammon et al., 1995b)

TAPP

- TAPP inclusions contain large amounts of Fe^{3+}, ~75% of total Fe.
- Mössbauer data would suggest that Fe^{2+} occupies octahedral [6] sites and Fe^{3+} occupied tetrahedral [4] sites; in line with the interpretation of TAPP as a new tetragonal $I\bar{4}2d$ phase (section 3.3.1).

fPer

- fPer inclusions exhibit very little Fe^{3+}, <7% of total Fe; strong evidence to suggest a formation at pressures equivalent to the lower mantle (and particularly under high fO_2 as indicated by the presence of magnesioferrite, section 2.6.1).

MgSi-Pvk

- Type I and Type II MgSi-Pvk both contain large amounts of Fe^{3+}, (~20% and 78% of total Fe respectively)
- Mössbauer data are consistent with BZ210B and BZ251B presently adopting a C2/c structure
- Type II MgSi-Pvk represents a substitution of $Fe^{3+} + Al^{3+} \leftrightarrow Mg^{2+} + Si^{4+}$ with Type I MgSi-Pvk.

---

[1] Very little magnesioferrite would be required to be in association with fPer in order to redress the balance of ferrous - ferric iron content This fact alone means that any spinel phase within fPer for which Mössbauer data has been obtained would have an absorption spectra which would be masked by the background of the fPer host. In addition, spinel has a magnetic component and so any absorption would appear as six peaks rather than a doublet (four peaks would lie within the velocity range measured). What this means is that a spinel phase, if present in fPer, would be very unlikely to appear on Mössbauer analyses.

Section 2.6 SEM and TEM analyses of fPer inclusions

Secondary electrons, those reflected on impingement of an electron beam on a sample, have an intensity which is dependent on the atomic mass of the sample. This means that imaging of back scattered electrons provides a useful means of identifying composite grains, inclusions, exsolution features etc. where an atomic mass difference is present.

Wilding (1990) noticed that BS imaging of certain fPer grains using the Cameca Camebax e-probe of the University of Edinburgh showed bright flecks or blebs on polished surfaces. These observations were followed up by Harte (1993, *personal communication*), who examined samples BZ66, BZ67, BZ70 and BZ73 by the back scattered electron technique on SEM apparatus specially set up for enhanced BSE imagery at the University of Manchester[1]. Harte observed that two of these fPers, BZ66 and BZ73 showed no well defined areas of contrasting BSE intensity, whereas BZ70 showed bright flecks and BZ67 showed a combination of bright flecks and more elongate linear features.

It was decided that a full invesigation of fPer inclusions, in order to assess their BS-characteristics, was required. This has taken three paths:

- Initial BS-imaging was carried out on 31 inclusions[2] reported as being fPer from amongst the Wilding (1990) suite (BZ- numbers < 200), the BZ201-BZ214 suite and the suite of stones broken in the present study: BZ215-BZ265. Three Guinean fPer inclusions were also imaged. Analyses were undertaken using the SEM facilities of the University of Leeds[3]. The apparatus was operated by Dr. Eric Condliffe with assistance by myself. In addition to samples either containing ‘blebs’ or no variation in BS-image some samples were found to show additional features. These additional features are discussed in section 2.6.1.2.
- One sample, BZ67, was polished and analysed by transmission electron microscopy (TEM) and analytical TEM (ATEM). Analysis for crystal structure (TEM) was carried out by Dr. Martin Lee at the University of Edinburgh, Department of Biochemistry and for chemical composition (ATEM) at the Institute for Occupational Medicine (Edinburgh).
- Diamond BZ257 was broken subsequent to all other analyses of fPer. The electron microprobe was used to investigate an inclusion fragment (BZ257A3) for the existence of blebs.

➠

---

[1] The absolute difference in BS-intensity of the bright and dark areas of fPer inclusions is not great. This means that great care must be taken in optimising the contrast and brightness of the image produced from BS-analysis in order to observe any features present. For this reason, detailed work was carried out using BS-SEM at Manchester rather than continuing with BS-EPMA at Edinburgh where the system is not optimised for such work.

[2] In addition to inclusions giving good EPMA analyses, grains giving poor EPMA analyses were also included in the BS-SEM study.

[3] Like the Manchester facility, the facility at Leeds is well optimised for BS-imaging.

Section 2.6.1 Observation of ‘blebs’ in fPer inclusions

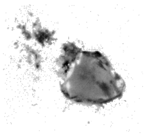

Of the 37 inclusions studied[1], 34 showed clean polished surfaces and gave EDS spectra consistent with identification as fPer.

Including the observations made by Harte, (1993, *personal communication*), of 31 São Luiz inclusions, 9 contain small (sub-micron sized) bright areas on BS-SEM (termed ‘blebs’), such as shown in figure 2.6_1. None of the 3 Guinean inclusions showed evidence for blebs (eg. figure 2.6_2). Table 2.6_1 summarises observations from both studies.

Table 2.6_1 Summary of all São Luiz and Guinean fPer inclusions imaged under BS-SEM with the number of images taken as part of the present study and notes on the features observed.

Inclusion	Photo[*]	Blebs	Comments	Inclusion	Photo[*]	Blebs	Comments
BZ66¥	3	???	3μm bright spots	BZ239G	1	No	S
BZ67[†]	0	Yes	E + Veins	BZ241A	1	No	S
BZ70¥	2	Yes	Spots	BZ242A	2	No	S
BZ73[†]	0	No	S	BZ245A	1	No	S
BZ74	3	Yes	E	BZ245B	1	No	Tartan
BZ76	1	No	S	BZ250C	3	Yes	E + Sp
BZ83	*2*	*No*	*Ti-mag/FeO ??*	BZ257A3‡	0	Yes	S
BZ103	1	No	S	BZ260D	2	No	S
BZ116B	1	No	S	*BZ260E*	*0*	-	*Not found*
BZ201A	2	Yes	E + Top.	JH2	1	No	S
BZ205B	1	No	S	*JH6A1*	*1*	*No*	*Crud*
BZ205C	1	Yes	Sp	JH7A1	1	No	S
BZ206A	1	No	S	JH11A1	1	No	S
BZ207B	1	No	S	JH12A1	3	No	S
BZ210A	1	No	S	JH17A1	4	Yes	Sp
BZ226D	2	Yes	Sp	GU2A	1	No	S
BZ233C	1	No	S	GU4A1	1	No	S
BZ238B	1	No	P, S	GU4F	1	No	S
BZ239A	1	No	S				

Inclusions in italics are not fPer. * Photographs recorded as part of the present study. ¥ Observed by Harte (1993, personal communication) and subsequently studied at Leeds. † Observation by Harte (1993, *personal communication*). S- Scratches were the only surface feature to appear on BS-SEM observation. Sp- Bright spot-shaped blebs of ~0.5 μm were observed. E- Bright elongate blebs varying in length from 1 to 10 μm and of ~0.5 μm width were observed. P- The sample was observed to be highly pitted. ‡ Analysed subsequently by BS-EPMA. ??? BZ66, although exhibiting bright BS areas does not show blebs sensu stricto.

---

[1] These figures include BZ257A3, analysed by BS-EPMA subsequent to work at Leeds and Harte’s (1993, *personal communication*) analyses of BZ67 and BZ73 which, unlike BZ66 and BZ70 were not repeated in this study.

The blebs can be classified into two types which appeared in varying proportions amongst the samples:

- Spots of ~0.5 µm in diameter (rarely as large as 1 µm eg. BZ50C). For some grains, notably JH17A1, spots appeared to group into short, ~1 µm to ~10 µm lines (figure 2.6_3).
- Elongate features, no wider than ~0.5 µm but with lengths between ~1 µm and ~10 µm. Elongate blebs were found generally to be fairly straight, any change in direction being at approximately 135°. For some samples, BZ70, BZ74 (figure 2.6_1) and BZ201A, in addition to elongate blebs, veins of the same BS-SEM intensity as blebs were observed to stretch across the width of the sample.

At one extreme, BZ226B (figure 2.6_4), spots predominate; the ratio of Σ elongate blebs / Σ spots for one image taken at x3190 magnification is 0.0451. At the other extreme, BZ74, this ratio is 1.268 for an image taken at x3190 magnification (figure 2.6_1).

In order to draw any conclusions from the above observations, four main points have to be tackled:

- Are the blebs compositionally distinct features within the fPer grains themselves, or are they a secondary feature; simply surface contaminant or an artefact of surface topography?
- What is the relationship between the spots and elongate blebs?
- If the blebs are features of the fPer grains themselves what are the details of their composition?
- Is there any relationship between the observation of blebs and the composition of their fPer hosts?

Blebs in fPer: intrinsic or secondary features?: Although BS-SEM imaging predominantly responds to changes in atomic mass of the sample analysed, topography on the sample surface can also have an influence on the image obtained. This question can be addressed by comparing secondary electron (SE) and BS-SEM images: SE-SEM images respond only to topography. Long linear features (concluded to be scratches) and a common, dull, random, diffuse intensity variation appeared in both BS-SEM and SE-SEM images. Blebs, however, where present, appeared only in BS-SEM images and are therefore not a feature of surface topography.

Surface contaminant, was found to be present in most fPer grains. This takes the form of flecks of gold from ion microprobe analyses, dust and brass from the polishing procedure. Although, in general, because of their small size, the composition of blebs could not be determined by EDS, gold and brass could be ruled out because of their significantly higher intensity on BS-SEM. In addition, blebs appear both on ion-probed and non-ion probed (eg. BZ226D) grains. Specks, which appeared both on the sample and on the Araldite®, interpreted to be dust, were typically found to be larger (~2 µm) than spots and never elongate in shape. The concentration of such dust specks was also found to be greater within grooves, for example in BZ250C, (figure 2.6_5); consistent with such an identification. It can confidently be assumed that blebs are not, in general therefore, surface contaminant.

The relationship between spots and elongate blebs: Due to the varying proportions and the tendency for some groups of spots to be aligned, it would appear that the two types of blebs are linked. Additionally, where elongate blebs predominate, elongate blebs show some consistency in alignment (figure 2.6_1) which was quantified by measurement of the lengths and orientations of all elongate blebs photographed. This data was biased on the basis of length[2] whereby the value for orientation for each elongate bleb was incorporated into the final data set for each photograph *x* number of times where *x* refers to the length of the bleb measured in mm from the photograph[3]. Histograms of biased elongate bleb orientation are presented in figure 2.6_6 and show two key features:

- Most BS-SEM analyses show a preferred orientation of elongate blebs especially for sections where there exists a predominance of elongate blebs over spots (compare figure 2.6_6b with 2.6_6g). One exception is the high magnification (x3190) image obtained from BZ226D (figure 2.6_6.h) which shows a very strong preferred orientation despite showing relatively few elongate blebs.
- Where there is a preferred orientation of elongate blebs, there is generally a crude indication that there are two preferred directions, one strong one and one minor one, at approximately 90° to each other (BZ74, BZ70, BZ201, BZ226D, figures 2.6_6a-d,h).

These observations suggest that the blebs are acicular grains of a higher average atomic mass than fPer. The relative predominance of spots against elongate blebs is determined by the angle of polishing where the acicular grains have some form of preferred orientation. Spots are, therefore, lateral sections, whereas elongate blebs are longitudinal sections; lines of spots occur where either sinuous blebs cut through a flat surface or a sinuous polished surface cuts through straight blebs at a small angle.

Composition of blebs: Blebs are too small for single grain analysis by EPMA (analysis sizes are ~ 2 μm in diameter) and are very much on the limit of the resolution of EDS using SEM. EDS spectra *were* obtained from some samples, but even for BZ250C for which one spot was found with a diameter of 1 μm, no obvious difference was found between the composition of blebs and host although there may have been an indication of a slight shift towards Fe enrichment compared to the host (appendix 3.1). The fact that blebs are observed features with BS-SEM, however, means that they *have* to be of a

---

[2] It was found that even without incorporation of this biasing procedure, the same conclusions discussed, as follows, could be logically reached.

[3] i.e. a 1.4 mm elongate bleb with an orientation of 124° sent the value 124 to the final data set for the image in question 14 times.

different composition to their hosts and so the lack of a significant difference with EDS analysis can be interpreted as a limit of the analytical technique rather than a suggestion that no difference exists.

There would appear to be only one technique available at present with sufficient resolution to allow for determination of the composition of these blebs. This technique is transmission electron microscopy (TEM). Here, the sample in question is ion-thinned to a thickness appropriate for the transmission of elecrons through the sample. This thickness depends on the media to be analysed but for geological material is typically of the order of 0.1 μm. Three types of analysis can be carried out using TEM; observational, structural and compositional:

TEM has the advantage of far higher resolution over SEM. Features which can be picked out are grain boundaries and inclusions down to sizes of the order of 10 nm or less and indeed, depending on the operating conditions and quality of the sample, individual lattice planes can be observed. In addition, crystal structural determination (crystal system and space group) of samples down to a few unit cells in size can be made. A TEM fitted with an EDS for X-Ray analysis also allows for compositional data to be obtained from samples of very small size.

BZ67 was succesfully thinned such that small plateaux on the edges of holes in the sample were of suitable thickness for TEM. Under the higher resolution of the TEM technique, it was clear that these blebs are crystalline grains within the fPer host of a square cross section and occasionally containing within them additional small, 0.1 μm grains with a possibly cubic morphology (figure 2.6_7). Diffraction patterns were obtained from three grains and were observed to be of cubic symmetry (figure 2.6_8). These patterns were subsequently measured (Lee, 1996 *personal communication*). No internal standard was available for the calibration of diffraction patterns obtained and so some offset between raw d-spacings obtained and those of the standard material representing the actual structure of the blebs could be expected. Even so, it was found that the d-spacings obtained gave a good match with spinel structured Fd3m magnetite (the Fe end of the magnesioferrite solid solution series) and, by using the standard magnetite d-values as a calibrant[4] the fit was seen to further improve, see table 2.6_2.

ATEM data were also obtained for BZ67. As for the results obtained by EDS, little difference in composition between host and blebs was found. Data obtained are summarised in Table 2.6_3. If anything, there does appear to be a slight shift to higher Fe and Ni and lower Mg content in blebs compared to the host. This is in agreement with analysis incorporating a bleb on BZ257A3, appendix 3.1, although, with this analysis, no shift in Ni was detected. Although there is still some question as to

---

[4] One diffraction line is chosen as the calibrant, in this case (200) at 4.20 Å for magnetite. The closest raw d-spacing to 4.20 Å from the unknown is set to this value and all additional raw data multiplied by the appropriate correction factor (in this case 4.20 / 4.18).

how much influence the host has, in EDS spectra obtained for blebs, even on the resolution of ATEM, it would appear that, the composition of blebs is similar to their host. This conclusion is consistent with the observation that the difference in back scattering between blebs and host under BS-SEM is very subtle.

Table 2.6_2 Diffraction data for three blebs (8081, 8087, 8089) in BZ67 determined by TEM

8081 d (Å)	**8087 d (Å)**	**8089 d (Å)**	**Magnetite d (Å)**	**(hkl)**	**8081 d (Å)**	**8087 d (Å)**	**8089 d (Å)**
4.16		4.18	**4.20**	(200)	4.20*		4.20*
	2.92		**2.97**	(220)		2.97*	
2.51		2.51	**2.53**	(311)	2.53		2.52
	2.06		**2.10**	(400)		2.10	
1.90		1.90	**1.93**	(331)	1.91		1.90
1.40		1.42	**1.42**	(531)	1.41		1.43
	1.31	1.32	**1.33**	(620)		1.33	1.33
		1.26	**1.27**	(622)			1.27
		1.11	**1.12**	(642)			1.12
	0.92		**0.96**	(662)		0.94	

* Set as calibrant line using magnetite as the standard; all additional lines being corrected by the same factor. Data obtained from Lee (1996, *personal communication*)

Table 2.6_3 Compositional data obtained for blebs, inclusions in blebs and host from BZ67

Element	**Host**	**Bleb 1**	**Bleb 2**	**Bleb 3**	**Minor bleb**
Mg	43.47	40.76	41.54	33.60	38.08
Fe	56.39	58.71	58.35	67.15	58.79
Ni	0.14	0.54	0.12	n.d.	3.13
Mg #	0.43	0.41	0.42	0.33	0.39

Data are presented as atomic Mg and Fe per 100 O anions. Mg# is simply the ratio Mg to Mg + Fe. Analyses consisted of measurement of Fe $K\alpha$ and Mg $K\alpha$ radiation only. Cr and Ni content of BZ67 is very low and outwith the reolution of the ATEM employed.

Relationship of the occurrence of blebs to composition of fPer hosts: As mentioned previously, of the 31 fPer grains analysed from São Luiz, 26% exhibit blebs. The full range of Mg# for São Luiz is 0.850 (BZ251A) to 0.363 (BZ66). As table 2.6_4 shows, the range in Mg# of fPer grains exhibiting blebs is almost as great. Additionally, almost the full range in Cr and Ni contents are incorporated within bleb containing fPer inclusions. It would appear, therefore, that there is no relationship between the composition of host and the occurrence of blebs.

Table 2.6_4 Range in Mg # for fPer inclusions from São Luiz exhbiting blebs.

Sample	BZ257A3	BZ70	JH17A1	BZ74	BZ201A	BZ205C	BZ226D	BZ67	BZ250C
Mg #	0.743	0.711	0.697	0.640	0.636	0.629	0.563	0.543	0.461

Summary: To summarise so far, it would appear that a minor, yet significant proportion of fPer inclusions, spanning almost the entire range of fPer compositions contain inclusions visible by BS-SEM. These inclusions are either of the form of small acicular grains, ~0.5 x 10 µm, narrow (~0.5 µm) veins, or more formless larger (~4 µm) patches. Acicular grains appear to have a single preferred orientation within their fPer hosts and occasionally show an additional orientation at appoximately 90° to the main trend: probably a function of host structure. The compositional characteristics of inclusions in fPer are of a higher iron content than their fPer hosts. The structure of blebs in BZ67 is consistent with that of spinel structured magnetite (and throughout the magnesioferrite solid solution series). This observation constitutes strong evidence to suggest that the blebs observed in fPer are magnesioferrite.

Section 2.6.2 Additional visual characteristics of fPer inclusions

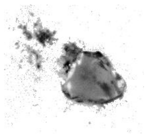

As part of the study of fPer inclusions for the existence of blebs, two inclusions, BZ66 and BZ238B, although not exhibiting blebs in the sense defined herein, did yield interesting detail on BS-SEM analysis.

BZ66: BZ66 shows a large number of roughly circular patches ranging from 1 to 4 µm across in addition to a few elongate patches ~1 µm in width by ~2 µm in length and of a brighter BS-intensity than blebs seen in other grains, figure 2.6_9. There also appear to be a number of small (0.5 µm) circular blebs too small to analyse.

EDS analyses were undertaken at Leeds for the host and the large patches, figure 2.6_10. EDS analysis successfully obtained from one of the larger inclusions showed the inclusion to be significantly more iron rich than its host, figure 2.6_10b cf. figure 2.6_10a. In addition, Ni was found to be a significant component of the inclusion, being absent within the accuracy of the EDS in the fPer host: and Mg, in contrast, was found to be absent.

Electron microprobe analyses were carried out and were found to confirm the SEM-EDS observations, table 2.6_5. Four analyses were obtained from blebs of varying sizes. They span a range in composition involving varying Fe, Mg, Ni, Na and Mn from FeNi alloy to a composition approaching that of the host; and thus represent different amounts of host signature contributing to each analysis. From analysis, BZ66L-1, in particular, it can be concluded that the large blebs in BZ66 are FeNi alloy comprising an Fe/Ni ratio of ~4:1

Table 2.6_7 Electron probe analyses of BZ66 fPer host and BZ66 large inclusions (BZ66 L-*x*).

	BZ66 L-1		**BZ66 L-3**		**BZ66 L-2**		**BZ66 L-4**		**BZ66 Host**	
	wt%‡	*cation*	wt%‡	*cation*	wt%‡	*cation*	wt%‡	*cation*	wt%‡	*cation*
Fe	96.2	*7.93*	81.4	*7.21*	84.3	*7.16*	75.6	*6.39*	73.6	*6.17*
Ni	25.4	*2.01*	28.7	*2.45*	28.4	*2.32*	16.1	*1.31*	0.10	*0.01*
Cr	0.29	*0.02*	0.45	*0.04*	0.41	*0.03*	0.71	*0.06*	1.06	*0.08*
Na	0.00	*0.00*	0.00	*0.00*	0.08	*0.02*	0.59	*0.12*	1.05	*0.20*
Mn	0.10	*0.01*	0.24	*0.02*	0.16	*0.01*	0.53	*0.04*	0.80	*0.07*
Mg	0.06	*0.01*	1.44	*0.23*	2.23	*0.34*	13.9	*2.09*	23.13	*3.46*
Total*	122.1		112.4		116.2		107.6		99.9	

The inclusion is markedly richer in Fe and Ni content and relatively deficient in Cr, Na, Mn and Mg.
* Totals comprise all elements including minor elements not presented in this table, see appendix 3.1 for full analyses. Analyses were carried out on the Cameca Camebax electron microprobe of the University of Edinburgh operating at 20kV, 20nA.
‡ Calculated as wt% oxide. As FeNi contains no oxygen, however, wt% totals are higher than 100%.

BZ238B: BZ238B shows a single, elongate, bright area in BS-SEM which is approximately 1.5 µm in length, figure 2.6_11. Comparison of secondary electron and BS-imaging of this inclusion would suggest that it is protruding above the surface of the fPer host at one side, indicating that it may be of greater hardness than its host. EDS spectra were collected using the Leeds SEM facility from the BZ238B fPer host and this single inclusion, figure 2.6_12a,b. Fe content was seen to be slightly larger in the inclusion than in the host. In addition, the inclusion appeared to have a larger Ni content and a substantially larger Cr content than the host.

An attempt was made to determine the composition of the feature on BZ238B accurately by electron microprobe. On obtaining a BS-image of BZ238B on the University of Edinburgh Cameca Camebax apparatus, however, it was found that the feature in question was no longer present. As mentioned previously, it was seen to be protruding from the surface and was, therefore, likely to have been lost in transit or during the electron microprobe preparation process.

Comparison of bright BS features: The features observed in BZ66, BZ238B and other fPer inclusions discussed in section 2.6.1.1 have a number of similarities. They also, however, exhibit a number of fundamental differences. The salient points in question are summarised in table 2.6_8.

Table 2.6_8 Summary of salient features pertaining to blebs in fPer and the patches observed by BS-imaging in BZ66 and BZ238B.

	Blebs	BZ66 patches	BZ238B grain
Size	≤0.5µ width by ≤10µm	1.5 - 4 µm	2 µm
Shape	Spots or thin flecks	Spots or lozenges	Lozenge
Fe content	> host	» host	> host
Ni content	> host	» host	> host
Cr content	unknown	< host	» host
Mg content	< host	« host	< host
Mn	unknown	< host	> host

As far as visual features are concerned, the patches in BZ66 are broadly similar to the grain in BZ238B, both being fundamentally different from the blebs seen in other fPer grains.

In terms of composition, the anomalous Cr content of BZ238B sets it aside from the blebs or BZ66 features. It could be argued that this is simply an anomalous analysis but this can be considered unlikely because the SEM-EDS was working well within normal parameteres at the time. The general trends in the composition of inclusions in BZ66 and blebs, in comparison to their hosts, is the same. Quantitatively, however, the analyses are fundamentally different; BZ66 patches being, clearly, FeNi alloy whereas the spectra obtained from flecks in BZ67 are consistent with them still being oxides. It could still be argued, however, that each analysis of blebs in BZ67 incorporates a significant host component. It can be conceded that there may be *some* host contribution from material below each bleb but a significant contribution is considered unlikely for a number of reasons:

- The window through which EDS spectra were obtained from blebs was approximately 200 nm in width, significantly smaller than the 500 nm size of the blebs. EDS analyses involved transmitted X-Rays from an area which, on the surface, was entirely bleb material.
- The width of the bleb grains from which analyses were obtained was observed to be no smaller than 500 nm. As they give cubic X-Ray diffraction patterns it is likely that they have a depth of ~ 500 nm. Since, in order to allow transmission of the incident electron beam, the sample must be ~100 nm in thickness it is unlikely that significant host material lies under the grains analysed.

A further argument can be invoked to support the BZ66 patches being different from the fPer bleb material; that of structural determination. As has been argued, the diffraction data obtained for BZ67 blebs are consistent with them adopting a Fd3m magnetite structure. The data are not consistent, however, with the structure of FeNi alloy:

There are four different known polymorphs of FeNi alloy relevent to geological conditions. These are taenite, kamacite, awaruite and an unnamed tetragonal phase. Awaruite is a predominantly Ni-rich alloy and so is not relevent to the present discussion. The unnamed tetragonal phase, being tetragonal, has a structure (Mehta et al., 1980; Ramsden and Cameron, 1966 and Takahashi et al., 1968) completely inconsistent with structural determination of BZ67 blebs. Taenite and kamacite[1], on the other hand are both Fe enriched and are both cubic (Ramsden and Cameron, 1966): taenite has a fcc unit cell whereas kamacite has a bcc unit cell. The principal diffraction lines for taenite and kamacite are presented, in comparison with BZ67, in table 2.6_9.

Although there is some coincidence of diffraction lines, the general fit is poor (cf. the good fit with magnetitie, table 2.6.2). This is true no matter what ratio of FeNi is employed, Takahashi et al. (1968) found only a 0.1% variation in principal cell parameter for taenite at ATP with between 0 % and 10.5 wt% Ni; a similar result was found by Ramsden and Cameron (1966) for kamacite: strong evidence, again to support the opinion that the large patches in BZ66 are not the same as the blebs found in other fPer grains discussed in section 2.6.1.1.

As far as whether the FeNi in BZ66 is taenite, kamacite or in the form of the tetragonally structured phase is unclear given the lack of structural data for BZ66 patches. It is known that kamacite exsolves from taenite at low temperatures giving rise to the Windmenstaten structure (Aladag and Gordon, 1969) and, relative to the hcp tetragonal phase, the body centred cubic kamacite, is stable at lower pressure (Takahashi et al., 1968); below ~8 GPa, 296K. If the patches in BZ66 had exsolved low pressure kamacite, these would not have been detected given the resolution of the BS-imaging

---

[1] Taenite is also termed γ-Fe:Ni whereas kamacite is also termed α-Fe:Ni

performed on B66. The question of the detailed structural nature of BZ66 patches can be considered unresolved as yet.

Table 2.6_9 Comparison of diffraction lines from BZ67 with principal diffraction lines (>I_{rel} =10) for taenite and kamacite from three meteorites (Ramsden and Cameron, 1966).

BZ67	**Taenite [1]**	**Taenite [2]**	**Kamacite [3]**	**Kamacite [2]**
d (Å)	**d (Å)**	**d (Å)**	**d (Å)**	**d (Å)**
	7.05			
			4.40	
		4.24		
4.17				
	3.52			
		3.34		
				3.04
2.92				2.95
	2.84	2.88		
2.51		2.52		
			2.10	
2.06	**2.07**		**2.03**	**2.03**
				1.97
1.90				
	1.79			
			1.49	1.48
1.41			1.44	1.44
1.32				
1.26	1.23			
			1.17	1.17
1.11	1.08			
				1.02
0.92				

Lines in bold are the principal lines (I_{rel} = 100) for each spectra. Localities are: [1] Twin City, [2] Linville and [3] Carlton

Source of BZ66 patches: BZ66 is, by far, the most iron rich fPer recorded from São Luiz or Guinea, Mg # = 0.363; in this respect it is anomalous, as it would also appear to be due to its incorporation of FeNi blebs[2]. Referring to the other fPer grains, it has been indicated that the range in composition may not be related to depth but to the degree of crystallisation (section 2.5.2). The immediate conclusion as to the source of FeNi in BZ66, however, could be the core - mantle boundary; a significantly greater depth than suggested for other São Luiz and Guinean fPer inclusions (section 4.4.2). A number of observations would support such a source:

---

[2] It should be noted that Wilding (1990) refers to FeNi alloy patches in fPer from São Luiz. He reports that a good analysis was obtained from one grain and cites observtion of FeNi in ten others. However he neither presents it nor refers to its source. As, of the Wilding material, BZ66 shows the only patches of a size analysable by EPMA, it is likely that it was from this inclusion that he obtained his good analysis. As he conducted no higher resolution analyses it can be concluded that his remark that Fe:Ni alloy patches occur in fPer inclusions, stems from a combination of this analysis and the observation of blebs in other grains. As has been discussed here, these features are not the same.

- The core is generally thought to comprise FeNi alloy with additional minor components (Stevenson, 1981).
- FeNi alloy has been reported from meteroites thought to be equivalent to source body cores (e. g. Ramsden and Cameron, 1966)
- There is evidence to support vigorous chemical reaction in the D’’ layer between what is ostensibly core Fe and mantle $MgSiO_3$ (Knittle and Jeanloz, 1991 and Wysession, 1996). This is thought to follow the reaction:

$$Mg_xFe_{1-x}SiO_3 + 3[(1-x)-s]Fe = xMgSiO_3 + sSiO_2 + [3(1-x)-2s]FeO + [(1-x)-s]FeSi \qquad \text{Equation 2.6\_1}$$

  and produces compositions of enstatite, quartz, fPer and FeSi. If the reacting Fe was to contain significant Ni, it could be quite conceivable that textures involving spherical blobs of FeNi reactant within fPer product would be produced as is seen for BZ66. Indeed there has been some argument that FeNi melt would have difficulty separating from silicate melt (Ballhaus and Ellis, 1996); this zone is probably highly intermixed. It is also particularly noteworthy that equation 2.6_1 refers to an essentially Mg-free fPer product consistent with the composition of the BZ66 host.
- Diamond has been found in association with FeNi alloy (Vinogradov et al., 1968 and Bashir et al., 1996) in meteorites.
- It is a popular conception that upwelling mantle plumes, often manifest at the earth’s surface have a source in the D’’ layer (Hofmann and White, 1982; Richards et al. 1989; McKenzie and section 4.1). A mechanism of transfer of material from the D’’ layer to the surface is thus quite conceivable.

Although the evidence is strong to support a D’’ layer source for BZ66, it is not, however, the only explanation. The presence of FeNi within Fe-rich fPer may simply represent either exsolution or crystallisation in highly reducing conditions at some other, unknown, location, cf. figure 2.5_7. Indeed, Malavergne et al. (1995) report the presence of FeNi alloy in the run products of experiments undertaken on olivines with composition of $(Mg_{0.78}Fe_{0.20}Ni_{0.02})_2SiO_4$. At 15 GPa, 1773 K[3] they observed run products of wadlseyite in association with $Fe_{0.71}$:$Ni_{0.29}$, whereas, at 40 GPa, 1773 K[4] the FeNi observed in association with fPer and an amorphous silicate phase had a composition of $Fe_{0.8}Ni_{0.2}$. The indications from experimentation are that FeNi of the same composition of patches in BZ66 is stable in association with fPer at upper lower mantle pressures: whether or not the reducing conditions required for such stability are present in the upper lower mantle is another question. Furthermore, both Urakawa (1991) and Malavergne et al. (1995) present evidence to suggest that Ni becomes increasingly less siderophile with depth. Partitioning of Ni between fPer and FeNi alloy for BZ66 are more coincident with values obtained at low pressures than under core conditions. Experimental results should be treated with caution, however. FeNi was seeded into the starting

---

[3] Temperature was determined purely by observation of grain size of run products. It is, therefore, subject to large uncertainty.

[4] *ibid.*

composition of Malavergne et al. (1995) and the presence of an amorphous silicate could be cited as evidence for a lack of equilibrium in their experiments[5].

---

[5] Another explanation being that the silicate had not retained its structure on quenching as occurs with CaSi-Pvk.

Section 2.6.3 *Genesis of high BS-intensity features in fPer inclusions*

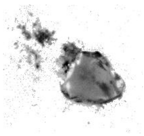

Some aspects of the compositional phase relationships of the *ferrous* iron-rich end of the system MgO, FeO, Fe_2O_3 have been previously discussed (section 2.5.2). With significant bulk *ferric* iron content, however, it can be seen from the phase relations (McCammon et al., 1995; Srecec et al., 1987 and Speidel, 1966), figure 2.5_7, that there exists a field where fPer coexists with grains adopting compositions along the magnesioferrite solid solution series (Fe_3O_4 - $MgFe_2O_4$). The structure of this solid solution series at ATP is cubic (of spinel Fd3m type). In addition, grains of magnesioferrite coexisting with fPer will exhibit a smaller Mg # (where Fe is adopted as total Fe) than their hosts. Compositions of coexisting pairs of fPer and magnesioferrite can be calculated using tie lines and are presented in table 2.6_8 for the end members periclase and wüstite in addition to three fPer inclusions BZ238B, BZ67 and BZ66. The general compositional similarities of inclusions in fPer (section 2.6.1) to those expected for magnesioferrite coexisting with fPer, table 2.6_8[1] additionally support the conclusion that the inclusions observed in fPer are magnesioferrite and consideration of phase relations in the $FeO-Fe_2O_3-MgO$ system explain their origin.

Table 2.6_8 Predicted values for $Mg/(Mg+\Sigma Fe)$cations for magnesioferrite coexisting with three fPer inclusions for which compositional details of inclusions have been obtained.

	Periclase	BZ238B	BZ67	BZ66	Wüstite
fPer	1.000	0.828	0.430	0.363	0.000
Magnetite s.s.	0.333	0.167	0.143	0.083	0.000

The presence of magnesioferrite inclusions in fPer solves an uncertainty relating to the Mössbauer characteristics of fPer paragenesis[2] inclusions. As has been discussed in detail in section 2.5.4, fPer inclusions contain very *little* ferric iron whereas other lower mantle phases (Type II pyroxene and TAPP) contain very *large* quantities of ferric iron. Both observations are characteristic of the behaviour of these phases at high pressure irrespective of fO_2 (McCammon, 1997 and McCammon et al., in press). However, the presence of blebs of Fe^{3+}-rich magnesioferrite suggests that the *bulk* composition of the host is relatively O-rich.

---

[1] Given that all compositional determinations of blebs and larger inclusions presented in this subsection are likely to incorporate a compositional component of the host, it is expected that the actual compositions of inclusions in fPer are even more iron rich than determined. This is more in line with predicted values for magnesioferrite solid solution.

[2] The fPer paragenesis, as described in section 2.3, is believed to have a lower mantle origin, section 4.3.

The question still remains as to why only some fPer inclusions yield evidence for blebs and other types of inclusion. This can be answered in one of three ways:

i) Inclusions of magnesioferrite in inclusions not exhibiting blebs may simply be too small to be detected by BS-SEM. Such particularly small inclusions should show up on TEM observation and, indeed the existence of 0.1µm inclusions in BZ67 would suggest that this is a feasible argument.
ii) fPer inclusions may form in two generally distinct régimes; one involving relatively oxidised conditions and a coexistence with ferric iron rich TAPP and MgSi-Pvk and a different régime involving relatively reduced conditions and a coexistence with different phases e. g. Fe metal (Sobolev et al., 1981 and Meyer and McCallum, 1985).
iii) Magnesioferrite may not have exsolved due to the restrictive nature of the diamond host

Suggestion ii) is considered to be least likely because most fPer inclusions containing blebs have been recovered from diamonds without associated silicate phases whereas those fPer inclusions not exhibiting blebs often occur in association with other fPer paragenesis phases. Indeed a case in point is BZ205. This stone yields a TAPP inclusion and two fPer inclusions. One (BZ205B) appears to be in equilibrium with the TAPP (section 4.4.2) whereas the other (BZ205C) appears to be in disequilibrium with TAPP. It is the *dis-equilibrium* fPer, however (BZ205C) which contains blebs whereas BZ205B does not. This is in contradiction to suggestion ii). Furthermore, the lack of exsolution of majoritic garnets and re-equilibration of composite grains provides corollary with suggestion iii) and, as section 7.1.4 shows, large internal pressures are imposed by São Luiz diamonds.

Chapter 3 Structural features of inclusions from São Luiz and Guinean diamonds

In Chapter 2 the compositional characteristics of the Sao Luiz inclusions have been considered. Discussion of individual minerals, however, was grouped under names which were not intended to imply a particular crystal structure. The structural features of a particular composition are, however, of fundamental importance. Many of the mineral grains obtained from São Luiz and Guinean diamonds at the conditions of pressure and temperature proposed for their formation (Chapter 4), would have structures different to their ATP polymorphs. The most obvious example being the Type I, II and III pyroxenes (section 2.2.1.5) which we would expect to have been stable in the lower mantle as perovskite structured phases (here called MgSi-Pvk).

Entrapment in diamond can provide a mechanism for retention of the chemical sanctity of the included mineral (section 7.2.1). The question which arises here is whether diamond occlusion also allows retention of the *structure* of the included material? Clearly, discovery of a perovskite structured $MgSiO_3$ inclusion, for example, would be additional compelling evidence for a lower mantle origin. In fact, even if the cell parameters of included material were to be found to be elevated above ATP values, then such an observation would go part of the way to inferring a depth of formation. This latter consideration is discussed specifically in section 7.1.

Subsequent to a pilot study by Angel and Ross (Angel, 1993 *personal communication*), detailed structural studies of some São Luiz and Guinean inclusions, both in-situ and released from diamond, were undertaken using a Gandolfi camera at the University of Edinburgh. Where additional detail, corroborative evidence or separate information unsuited to Gandolfi camera analysis was required, material was distributed for study elsewhere.

Section 3.1 Techniques adopted for structural analyses

A total of six techniques involving five laboratories were employed (where operating conditions and some aspects of theory are discussed in appendix 10). With the exception of Fourier Transform Infra-Red (FTIR) analyis, all techniques adopted were single crystal X-Ray diffraction analyses. Studies conducted were:

- **UCL XRD:** Single crystal X-Ray Laue diffraction using MoKα at University College London and conducted by Dr. R. Angel and Dr. N. Ross.
- **UCL FTIR:** Fourier transform infra-red analysis (FTIR) at University College London and conducted by Dr. R. Angel and Dr. N. Ross.
- **Edinburgh Gandolfi-XRD:** Single crystal X-Ray diffraction using a Gandolfi camera provided by the Royal Museum of Scotland, and using MoKα and CuKα radiation at the Department of Chemistry, University of Edinburgh.
- **Edinburgh XRD:** Single crystal X-Ray diffraction using MoKα at the Department of Chemistry, University of Edinburgh and conducted by Dr. S. Parsons and Dr. R. Gould: having the advantage of provision for full structural determination.
- **ESPRC XRD:** Single crystal X-Ray diffraction using MoKα at the ESPRC facility, Department of Chemistry, University of Wales Cardiff and conducted by Prof. M. Hursthouse and Mr. M. Light: having the advantage of provision for full structural determination of small (30 μm) samples.
- **Carnegie XRD:** Single crystal X-Ray diffraction microanalysis using beamline X17C of the National Synchrotron Light Source at Brookhaven National Laboratory, and conducted by P. Conrad and Prof. R. Hemley of the Geophysical Laboratory, Carnegie Institute, Washington having the advantage of provision for full structural determination of very small (10 μm) samples.

Section 3.2 Subjects of structural analysis

Structural data were obtained for a total of 18 single crystal inclusions, 19 diamonds incorporating included material, 1 inclusion-free diamond sample (JH2) and 1 standard sample ($NH_4O_2.H_2O$). Analyses conducted on inclusion material are summarised in table 3.2_1.

Table 3.2_1 Summary of material investigated for structural data.

Name	Location	Method	Notes	Name	Location	Method	Notes
GU4	**Edinburgh**	**Gandolfi**	**fPer in-situ**	**BZ253**	**UCL**	**FTIR**	**Pyroxene in-situ**
GU4A1	**Edinburgh**	**Gandolfi**	**fPer**	**BZ253**	**UCL**	**XRD**	**Opx in-situ ¤**
JH2	**Edinburgh**	**Gandolfi**	**Diamond**	**BZ253**	**Carnegie♣**	**XRD**	**Cpx + Grt in situ**
JH2A	**Edinburgh**	**Gandolfi**	**fPer**	BZ254	UCL	FTIR	Pyroxene ? in-situ
JH7A3	**Edinburgh**	**Gandolfi**	**fPer**	BZ255	UCL	FTIR	Poor transmission
JH11A2	**Edinburgh**	**Gandolfi**	**fPer**	BZ255	UCL	XRD	Garnet ? in-situ ¤
JH12A2	**Edinburgh**	**Gandolfi**	**fPer**	BZ256	UCL	FTIR	Nothing detected
JH17A3	**Edinburgh**	**Gandolfi**	**fPer**	**BZ256**	**Carnegie♣**	**XRD**	**fPer + wollastonite**
BZ205A	Edinburgh	Gandolfi	TAPP	BZ257	UCL	FTIR	Poor transmission
BZ206B	Edinburgh	Gandolfi	TAPP	BZ257	Edinburgh	Gandolfi	fPer ? in-situ
BZ227A	**Cardiff**	**ESPRC**	**Corundum**	**BZ257**	**Carnegie♣**	**XRD**	**fPer ¤ + cpx in-situ**
BZ228D	**Edinburgh**	**Gandolfi**	**Amorphous**	**BZ257A1**	**Edinburgh**	**XRD**	**fPer ¤**
BZ240B	**Edinburgh**	**Gandolfi**	**TAPP**	**BZ257A5**	**Carnegie♣**	**XRD**	**fPer**
BZ241B2	**Cardiff**	**ESPRC**	**Opx (Pbca) ¤**	**BZ258**	**UCL**	**FTIR**	**Pyroxene in-situ**
BZ242B	**Cardiff**	**ESPRC**	**Cpx (C2/c)**	BZ265	Edinburgh	Gandolfi	TAPP ? in-situ
BZ243C	Cardiff	ESPRC	Olivine	**BZ265**	**Carnegie♣**	**XRD**	**TAPP ¤ in-situ**
BZ244B	**Cardiff**	**ESPRC**	**TAPP**	BZ266	Edinburgh	Gandolfi	fPer ? in-situ
BZ249A	**Edinburgh**	**XRD**	**Diopside**	BZ267	Edinburgh	Gandolfi	fPer ? in-situ
BZ251	**UCL**	**FTIR**	**Px in-situ**	BZ268	Edinburgh	Gandolfi	fPer ? in-situ
BZ251	**UCL**	**XRD**	**Opx in-situ**	BZ269	Edinburgh	Gandolfi	fPer ? in-situ
BZ252	UCL	FTIR	Multi ? in-situ				

All phase names presented have a structural implication, eg. cpx indicates a C2/c pyroxene structure. Determinations in bold refer to analyses where structural confirmation of the phase(s) present was achieved. ? - Uncertain phsae determination by diffraction or visual observation. For example, for BZ266, this stone appears to contain a fPer inclusion but analysis by Gandolfi camera failed to produce any non-diamond diffraction lines. ¤ Split diffraction peaks, poor crystallographic fit or identification multiply orientated sub-grains suggests that these grains are polycrystalline. ♣ Carnegie refers to analysis undertaken at Brookhaven by workers of the Carnegie Institution.

Full details of each analysis are discussed according to phase in section 3.3.

Section 3.3 Results of structural analysis

Section 3.3.1 Investigation of the structure of the tetragonal-pyrope almandine phase (TAPP)

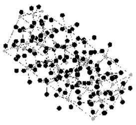

Due to the unique chemical composition of the ‘garnet’ like inclusions, TAPP, discussed in section 2.2.1.3.3, it was considered essential to attempt to determine the structure of at least some of these inclusions. Structural information was obtained for three inclusions:

- BZ240B, analysed in Edinburgh by Gandolfi Camera XRD
- BZ244B, analysed at the ESPRC facility, Cardiff by XRD
- BZ265A, as part of a study of diamond BZ265, analysed at Brookhaven by XRD

The results of these analyses are summarised in the following sections.

Section 3.3.1.1 Gandolfi camera X-Ray diffraction of TAPP

Due to analytical problems encountered, as outlined in appendix 10, analysis of the TAPP inclusion in BZ265 and single crystals BZ205A and BZ206B, yielded no structural information. A single 408 hour exposure of BZ240B (film D55), however, was successful.

Film D55 was significantly fogged because of the long period of exposure. Two lines were, however, clearly recognisable. These lines appear at distances of 15.424 +/- 0.006 and 25.13 +/- 0.006 mm from the axis of analysis. According to equation A10_1, these values correspond to d-values of 2.6480 +/- 0.001 and 1.6334 +/- 0.0004 respectively. Although two lines are clearly not sufficient to determine either space group or crystal system, a comparison with table 3.3_1 shows that d-spacings of BZ240B are neither coincident with d values for pyrope-almandine garnet nor with MgSi-Pvk. BZ240B, although having a generally pyrope-almandine composition, does not, therefore, adopt a garnet or perovskite structure. Comparison with table 3.3_3, however, shows that the lines appearing on D55 *do* correspond to diffraction from (204) and (400), in TAPP, section 3.3.1.2. Diffraction from (228), (211) and (206), which should have the same intensity as (400), table 3.3_3, are not observed because they occur in fogged areas of the film.

Although it was not proven at the time of analysis, the measurement of BZ240B was the first indication of the structure of what was later determined as being a new phase; TAPP, section 3.3.1.2.

Table 3.3_1 d-spacing and intensity for main reflections of pyrope, almandine and MgSi-Pvk for comparison with d-spacings from BZ240B.

$Mg_3Al_2Si_4O_{12}$ Ia3d (Pyrope)					**$Fe_3Al_2Si_4O_{12}$** Ia3d (Almandine)					**$MgSiO_3$** Pbnm (Perovskite)				
I (%)	**d-value**	**h**	**k**	**l**	**I (%)**	**d-value**	**h**	**k**	**l**	**I (%)**	**d-value**	**h**	**k**	**l**
6.56	4.6753	2	1	1	7.91	4.7051	2	1	1	0.9	3.9261	1	0	1
1.66	4.0489	2	2	0	1.95	4.0747	2	2	0	9.14	3.4485	0	0	2
6.35	3.0607	3	2	1	6.13	3.0802	3	2	1	23.1	3.4298	1	1	0
55.12	2.863	4	0	0	53.57	2.8813	4	0	0	9.36	3.071	1	1	1
100	2.5607	4	2	0	100	2.5771	4	2	0	24.58	2.4646	0	2	0
33.61	2.4416	3	3	2	31.04	2.4571	3	3	2	100	2.4318	1	1	2
23.14	2.3376	4	2	2	21.81	2.3525	4	2	2	18.58	2.3877	2	0	0
24.67	2.2459	4	3	1	24.36	2.2602	4	3	1	0.48	2.3209	0	2	1
11.42	2.0908	5	2	1	10.93	2.1042	5	2	1	3.43	2.1901	1	2	0
2.59	2.0244	4	4	0	2.55	2.0374	4	4	0	9.82	2.1489	2	1	0
6.56	1.8578	5	3	2	6.82	1.8696	5	3	2	9.16	2.0874	1	2	1
11.09	1.8578	6	1	1	11.26	1.8696	6	1	1	20.89	2.0714	1	0	3
6.12	1.8107	6	2	0	5.99	1.8223	6	2	0	17.33	2.0516	2	1	1
0.43	1.7671	5	4	1	0.32	1.7783	5	4	1	11.12	2.0051	0	2	2
1.74	1.6885	6	3	1	1.82	1.6993	6	3	1	6.46	1.9631	2	0	2
14.49	1.653	4	4	4	14.57	1.6635	4	4	4	11.97	1.9097	1	1	3
0.43	1.6196	5	4	3	0.61	1.6299	5	4	3	8.85	1.8488	1	2	2

Calculation of values was undertaken using computer programme XPOW 2.0 adapted from Downs et al. (1993) and using crystallographic data for pyrope and almandine (Armbruster et al., 1992) and MgSi-Pvk (Horiuchi et al., 1987).

Section 3.3.1.2 ESPRC X-Ray Diffraction of TAPP, BZ244B

Cell data, site occupancy and thermal parameters in addition to bond lengths and angles determined for sample BZ244B[1] are presented in table 3.3_2. Structural determination shows that BZ244B is profoundly tetragonal with space group $I\bar{4}2d$. It contains 3 independent oxygen sites in general positions, two distinct tetrahedral 'silicon' sites, both with 2-fold symmetry, and three other cation sites; M1 has 4-fold symmetry and a 'capped' tetrahedral environment, with four short and four long M1-O bonds, whilst M2 and M3 have 2-fold symmetry, with octahedral co-ordination. The Si tetrahedra are not linked together, so that BZ244 is an orthosilicate[2]. On the basis of independent sites, it can be described by the formula: $(M1)_1$ $(M2)_2$ $(M3)_2$ $(Si1)_1$ $(Si2)_2$ $(O1)_4$ $(O2)_4$ $(O3)_4$ which can be simplified to $(M1)(M2)_2(M3)_2Si_3O_{12}$. Figure 3.3_1 shows the structure of BZ244B viewed down different zone axes.

Using the chemical data for major elements (appendix 3.2) coupled with known crystallochemical behaviour, and the results of many least-squares refinement trials and bond-valence calculations, cation assignments were made as follows:

i) The two types of Si sites were modelled to achieve full occupancy by mixing in approximately 4.5% Al. Ferric iron was considered as a possibility for balancing the Si deficiency in the Si sites but was not consistent with the observed bond lengths.

ii) Six crystallochemically controlled model configurations were considered for the siting of the remaining Al^{3+}, the Mg^{2+} and the transition metal elements. The best refinement placed Al^{3+}, Cr^{3+} and Mn^{2+} in the smaller octahedral site M2; Fe^{2+} into M3; Mg^{2+} distributed between predominantly the octahedral M3 site and the 'capped' tetrahedral M1 site; Fe^{3+} solely in the 'capped' tetrahedral site M1. This assignment is supported by values for isomer shift and quadrupole splitting for Fe^{2+} and Fe^{3+} calculated on the basis of the Mössbauer analyses (McCammon et al., 1996).

---

[1] BZ244B was chosen for analysis subsequent to the loss of BZ240B.

[2] The open structure and edge sharing of the M2 octahedron with one of the Si tetrahedra are concerning as these features are not characteristic of high pressure phases. A possible alternative solution to the structure could be as a twinned garnet however the crystallographic data do not satisfy such a model for all cell dimensions (Angel, R. 1997 *personal communication*). It remains possible that TAPP may represent a different form of microstructure and this possibility is currently being investigated by Conrad, P. (Carnegie Institution). Any microtextured garnet, however, is not consistent with the independent results of Mössbauer analysis (section 2.5.1.2) which show that no amount of Fe occupies a [12]-coordinated site of the type seen in garnet. At this stage no alternative model fits the described crystallographic data as well as the described structure.

The full site allocations are given in table 3.3_2, but the broad result of this refinement using principal cations gives a formula of $(\mathrm{Mg, Fe^{3+}})[\mathrm{Al, Cr. Mn}]_2\{\mathrm{Mg, Fe^{2+}}\}_2\mathrm{Si_3O_{12}}$ where (), [] and {} indicate M1, M2 and M3 sites respectively.

The chosen model leaves small deficiencies at all M sites, and so some minor switching of cations could be possible. The refinement results, however, can be judged to be quite satisfactory according to all normal criteria (e. g. R values, thermal parameters). In view of such a good fit and of the constraints applied, in terms of analytical results and cation charge sums, the proposed model must be close to the actual structure. Some of the bond lengths are relatively long, but it is quite possible that expansion of the crystal structure has occurred following the release of the specimen from its diamond enclosure, and any extraneous bond elongation could be expected to be taken up by BZ244 under its natural conditions of high pressure and temperature[3].

It is concluded from the structural and compositional charactersitics of BZ244B that this is an example of a previously unknown phase. This phase is allocated the name TAPP (tetragonal almandine-pyrope phase). Given that BZ244B occupies a group of grains which exhibit strong structural, and compositional similarities, section 3.3.1.1, section 3.3.1.3 and section 2.2.1.3.1, this name is allocated to the group in general.

On the basis of the structural details obtained for BZ244B, a powder pattern can be calculated for comparison with additional grains (such as BZ240B, section 3.3.1.1). Values for d-spacing and relative intensity for TAPP are thus presented in table 3.3_3 and figure 3.3_2 which, in addition, shows the clear structural difference between TAPP and garnet structured pyrope - almandine.

---

[3] Observations of expansion on release from diamond have been made for ferropericlase inclusions, section 7.1.4.

Table 3.3_2 Crystallographic data for BZ244B, tetragonal almandine-pyrope phase (TAPP)

(a) Unit cell and analysis data

Crystal System	Tetragonal	**Formula Weight**	417.36
Space Group	I$\bar{4}$2d (no. 122)	**Calculated Density (Mgm^{-3})**	3.580
a dimension (Å)	6.526(4)	**Data/Parameters**	6.8
c dimension (Å)	18.182(9)	**R**	0.039
Reflections	1581	**Rϖ**	0.071
Independent Reflections	322 I > 4σ	**μ (mm^{-1})**	1.854 mm^{-1}

(b) Positions and thermal parameters *

Atom **	Site	x	y	z	U_{11}	U_{22}	U_{33}	U_{12}	U_{13}	U_{23}
M(1)	4a	0	0	0	3(1)	3(1)	10(2)	0	0	0
M(2)	8d	0.2600(4)	0.2500	0.1250	9(1)	7(1)	4(2)	0	0	0(1)
M(3)	8c	0	0.5000	-0.0227(1)	5(2)	5(2)	6(1)	-2(2)	0	0
Si(1)	4b	0.5000	0.5000	0	8(2)	8(2)	6(2)	0	0	0
Si(2)	8d	-0.1508(4)	0.2500	0.1250	8(2)	7(2)	10(2)	0	0	1(1)
0(1)	16e	0.0186(7)	0.2794(7)	0.0573(2)	7(3)	8(3)	9(2)	-3(3)	-2(2)	2(2)
0(2)	16e	-0.2621(8)	0.0374(6)	0.1011(2)	13(3)	10(2)	10(2)	6(3)	-2(2)	4(2)
0(3)	16e	0.4370(7)	0.2954(7)	0.0460(2)	8(3)	16(4)	6(2)	6(2)	1(2)	-2(2)

(c) Interatomic distances (Å) and angles (°)

M(1)-O(1)	2.109(5)	(x4)	M(1)···O(2)	2.521(5)	(x4)
M(2)-O(1)	2.004(5)	(x2)	M(2)-O(2)	1.925(4)	(x2)
M(2)-O(3)	1.866(5)	(x2)	M(3)-O(1)	2.052(5)	(x2)
M(3)-O(2)	2.124(5)	(x2)	M(3)-O(3)	2.014(5)	(x2)
Si(1)-O(3)	1.630(5)	(x4)	Si(2)-O(1)	1.664(5)	(x2)
Si(2)-O(2)	1.625(5)	(x2)			

O-M(1)-O	104.3(1), 120.4(2)	O···M(1)···O	86.48(1), 122.05(2)
O-M(2)- O^{cis}	103.7(3), 90.8(2), 88.7(2), 89.9(2), 87.9(2), 92.8(2), 76.5(3)	O-M(2)-O^{trans}	179.2(4), 166.3(2)
O-M(3)-O^{cis}	93.7(2), 103.6(2), 89.4(3), 79.6(2), 84.1(2), 87.7(2), 95.4(3)	O-M(3)-O^{trans}	155.7(3), 175.8(2)
O-Si(1)-O	118.3(3), 105.2(1)	O-Si(2)-O	126.8(4), 101.7(2), 113.2(2), 96.4(3)

The structure was determined via direct methods (SHELX-86 (Sheldrik, 1990)) and refined by the least-squares program SHELX-93 (Sheldrik, 1993). * All atoms refined with anisotropic thermal parameters. The anisotropic displacement factor exponent takes the form; - 2pi^2 [$h^2a^{*2}U_{11}$+...+$2hka^*b^*U_{12}$]. ** M(1) = Mg^{2+} 0.19025, Fe^{3+} 0.0465; M(2) = Al^{3+} 0.44000, Cr^{3+} 0.0380, Mn^{2+} 0.01425; M(3) = Mg^{2+} 0.46975, Fe^{2+} 0.02025; Si(1) = Si^{4+} 0.2500 ; Si(2) = Si^{4+} 0.4787, Al^{3+} 0.02125

Table 3.3_3 d-spacing and intensity for main reflections of BZ244B.

TAPP I$\bar{4}$2d BZ244B

I (%)	**d-value**	**h**	**k**	**l**	**I (%)**	**d-value**	**h**	**k**	**l**
1.32	6.1423	1	0	1	0.17	1.865	2	0	8
3.73	4.5455	0	0	4	3.85	1.8011	3	2	1
0.85	4.4409	1	0	3	0.79	1.7343	3	2	3
2.34	4.1148	1	1	2	6.56	1.7057	3	1	6
0.16	3.263	2	0	0	1.03	1.6916	1	1	10
14.82	3.1765	1	0	5	0.23	1.6677	3	0	7
3.88	3.0712	2	0	2	4.13	1.6611	2	1	9
20.26	2.8816	2	1	1	**19.06**	**1.6315**	**4**	**0**	**0**
100	**2.6507**	**2**	**0**	**4**	5.19	1.6204	3	2	5
10.98	2.6295	2	1	3	21.79	1.6192	2	2	8
4.66	2.533	1	1	6	1.16	1.6058	4	0	2
0.22	2.4133	1	0	7	2.83	1.6023	1	0	11
0.67	2.3073	2	2	0	0.00	1.5883	2	0	10
2.22	2.2761	2	1	5	0.4	1.5768	4	1	1
4.94	2.2728	0	0	8	0.1	1.5356	4	0	4
20.68	2.2205	2	0	6	0.61	1.5314	4	1	3
0.39	2.1599	3	0	1	2.59	1.5278	3	1	8
2.42	2.0637	3	1	0	2.46	1.5166	3	3	2
3.49	2.0574	2	2	4	1.5	1.5152	0	0	12
6.03	2.0474	3	0	3	7.05	1.485	3	2	7
2.91	2.0125	3	1	2	2.51	1.4803	3	0	9
5.13	1.9403	2	1	7	2.24	1.4593	4	2	0
0.00	1.9299	1	0	9	3.05	1.4513	4	1	5
1.21	1.8791	3	1	4	1.2	1.4408	4	2	2
1.67	1.8668	3	0	5	1.93	1.4383	2	1	11

Highlighted lines refer to reflections obtained from BZ240B, section 3.3.1.1. Calculation of values was undertaken using XPOW 2.0 adapted from Downs et al. (1993).

Section 3.3.1.3 Micro-X-Ray diffraction of TAPP, BZ265A at Brookhaven

Micro-diffraction provides the third independent line of evidence to support a $I\bar{4}2d$ structure for TAPP. BZ265 is a large, colourless diamond clearly exhibiting a green inclusion (BZ265A) towards one end. Initial investigation of this stone using synchrotron source X-Ray micro-diffraction yielded 28[1] lines which matched the predicted pattern calculated for TAPP, BZ244B (see table 3.3_3). Initial calculated cell parameters of a = 6.53 Å and c = 18.158 Å with a value of $\sigma = 0.0073$ match well the refined cell parameters of a = 6.526(4) and c = 18.182(9) Å for BZ244B (section 3.3.1.2). This initial analysis was carried out with a large beam and non-centred chi circle. With a smaller, 17 x 20 µm, beam the identity of BZ265A as being of TAPP structure was confirmed. Refined cell parameters being almost identical at: a = 6.53 Å and c = 18.158 Å.

---

[1] Of these, 19 lines gave the best R value and were used in the determination of cell parameters.

Section 3.3.1.4 TAPP as a unique phase

Unlike the other phases recovered in the initial study of Sao Luiz diamonds, TAPP has not been observed in high pressure and high temperature experiments designed to investigate the composition of the deep Earth nor has it been observed to occur naturally.

Several experimental studies (Ahmed-Zaïd and Madon, 1995; Irifune and Ringwood, 1993; Ito and Takahashi, 1987; Ahrens and Graham, 1972; Liu, 1975; Takahashi and Ito, 1987) have found evidence of an aluminous phase distinct to garnet, but these new phases have not been fully characterised. It is notable that, as figure 4.4_42 demonstrates, none of these phases yield structural data which correspond well to TAPP.

The term 'tetragonal garnet', however, has appeared several times in the literature. It is important to clarify here the distinct differences between TAPP and minerals referred to as 'tetragonal garnet'. These 'tetragonal garnets' have structures similar to that of TAPP in that they have independent Si tetrahedra however thay have stronger affinities to garnet in that they do not have highly elongate and are, in fact, pseudo-cubic. As examples, Ringwood and Major (1967) worked on $CdGeO_3$ and $CaGeO_3$, Akimoto and Syono (1972) indexed $MnSiO_3$ as tetragonal, Fujino et al. (1986) refined this structure and Griffen et al. (1992) reported a natural, pyralspite$_{75}$-grandite$_{25}$ garnet which yielded a tetragonal structure. From X-Ray diffraction determinations undertaken at high pressures and temperatures, Sawamoto (1987), working within a restricted range of pressures (17-24GPa) and temperatures (1650°C and above) with an $MgSiO_3$ composition, determined a phase which best fitted a tetragonal structure. Also, Yagi et al. (1992) synthesised an $MgSiO_3$ 'tetragonal garnet' at 2200°C, 20GPa identified using a similar determinative technique. An extension away from the pure end-member composition of the $MgSiO_3$ phase, involving Fe, was investigated by Matsubara et al. (1990).

Predicted phase relations involving TAPP are discussed in section 4.4.2.4.

Section 3.3.2 Investigation of the structure of alumina inclusion BZ227A

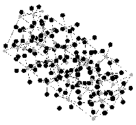

The transition of $R\bar{3}c$ corundum structured Al_2O_3 to Pbna Rh_2O_3(III) structured Al_2O_3 is found to occur at pressures of 90 GPa (equivalent to 2071 km) for a temperature of 0 K (Marton and Cohen, 1994; Cyann et al., 1990). This pressure is likely to be rather extreme, even for the inclusions studied here. Nevertheless, a structural determination of BZ227A was considered pertinent for three reasons:

- It is not implausible to envisage some São Luiz diamonds forming at depths significantly within the lower mantle, particularly in light of the compositional aspects of BZ66 possibly indicative of core proximity (section 2.6.1.2). With pressures at the core / mantle boundary of 136 GPa, the transition in structure of Al_2O_3 to Rh_2O_3(III) may occur in the lower mantle.
- A disadvantage in the LAPW technique[1] (Marton and Cohen, 1994 and Cyann et al., 1990) lies in the fact that calculations were performed at 0 K[2]: the effect of applying a geologically relevent temperature is not known. The possibility, therefore, cannot be ruled out that the transition of $R\bar{3}c$ structured Al_2O_3 to Pbna Rh_2O_3(III) may occur at depths relevent to the source of some São Luiz stones.
- BZ227A is the first sapphire to be recorded as an inclusion in diamond.

---

[1] Linearized augmented plane wave method, section 7.1.1.

[2] Applying temperature of greater than 0K involves an unreasonable increase in the complexity of calculation and thus computer time involved.

Section 3.3.2.1 ESPRC X-Ray diffraction of alumina, BZ227A

Table 3.3_4 Structural data for BZ227A, sapphire

(a) Unit cell and analysis data

Crystal System	Hexagonal	**Formula Weight**	102.21
Space Group	R$\bar{3}$c (no. 167)	**Calculated Density (Mgm^{-3})**	3.960
a dimension (Å)	4.773	**Data/Parameters**	4.4
c dimension (Å)	13.035	**R**	0.0442
Reflections	273	**Rϖ**	0.0951
Independent Reflections	47 I > 4σ	**μ (mm^{-1})**	1.359 mm^{-1}

(b) Positions and thermal parameters *

Atom **	Site	x	y	z	U_{11}	U_{22}	U_{33}	U_{12}	U_{13}	U_{23}
M(1)	12	0	0	0.3523(2)	2(2)	2(2)	0(3)	1(1)	0	0
O(1)	18	0.3066(7)	0	0.2500	2(2)	3(2)	0(4)	1(1)	0(1)	0(1)

(c) Interatomic distances (Å) and angles (°)

M(1)-O(1)#1	1.859(2)	M(1)-O(1)#2	1.859(2)
M(1)-O(1)#3	1.859(2)	M(1)-O(1)#4	1.979(3)
M(1)-O(1)	1.979(3)	M(1)-O(1)#2	1.979(3)
O(1)#1-M(1)-O(1)#2	101.19(9)	O(1)#1-M(1)-O(1)#3	101.19(9)
O(1)#2-M(1)-O(1)#3	101.19(9)	O(1)#1-M(1)-O(1)#4	86.39(3)
O(1)#2-M(1)-O(1)#4	164.2(2)	O(1)#3-M(1)-O(1)#4	90.76(7)
O(1)#1-M(1)-O(1)	164.2(2)	O(1)#2-M(1)-O(1)	90.76(7)
O(1)#3-M(1)-O(1)	86.38(3)	O(1)#4-M(1)-O(1)	79.61(12)
O(1)#1-M(1)-O(1)#2	90.76(7)	O(1)#2-M(1)-O(1)#2	86.39(3)
O(1)#3-M(1)-O(1)#2	164.2(2)	O(1)#4-M(1)-O(1)#2	79.61(12)
O(1)-M(1)-O(1)#2	79.61(12)		

The structure was determined via direct methods (SHELX-86, Sheldrick, 1990) and refined by the least-squares program SHELX-93 (Sheldrick, 1993) * All atoms refined with anisotropic thermal parameters. The anisotropic displacement factor exponent takes the form; - $2pi^{2}[h^{2}a*^{2}U11+...+2hka*b*U12]$ ** M(1) = Al^{3+} 0.32985, Fe^{2+} 0.0015, Si^{4+} 0.00116, Mg^{2+} 0.00066, Ti^{4+} 0.00016

273 reflections were collected over θ = 5.84° to 24.03°. With a goodness of fit on F^2 = 1.020, it was found that BZ227A adopts a normal hexagonal corundum R$\bar{3}$c structure (figure 3.3_3). Table 3.3_4 summarises the results of this structural determination.

From the structural data obtained for BZ227A, table 3.3_4, predicted powder lines can be calculated. As table 3.3_5, and its graphical representation, figure 3.3_4 shows, these lines appear to be very similar to literature values.

Table 3.3_5 d-spacing and intensity for main reflections of BZ227A and standard Al_2O_3 corundum

Al2O3 R$\bar{3}$c BZ227A sapphire					**Al2O3** R$\bar{3}$c				
I (%)	**d-value**	**h**	**k**	**l**	**I (%)**	**d-value**	**h**	**k**	**l**
62.85	3.4907	0	1	2	65.96	3.48	0	1	2
100	2.5591	1	0	4	100	2.5509	1	0	4
46.35	2.3865	1	1	0	47.33	2.3795	1	1	0
0.41	2.1725	0	0	6	0.35	2.1652	0	0	6
97.06	2.0917	1	1	3	98.15	2.0854	1	1	3
1.53	1.9701	2	0	2	1.58	1.9642	2	0	2
49.23	1.7453	0	2	4	49.82	1.74	0	2	4
95.45	1.6065	1	1	6	97.94	1.6014	1	1	6
2.3	1.5512	2	1	1	2.43	1.5466	2	1	1
3.25	1.5193	1	2	2	3.36	1.5148	1	2	2
7.45	1.5159	0	1	8	7.18	1.5108	0	1	8
37.91	1.4088	2	1	4	38.24	1.4045	2	1	4
56.64	1.3778	3	0	0	57.24	1.3738	3	0	0
1.1	1.3401	1	2	5	1.16	1.336	1	2	5
1.56	1.2796	2	0	8	1.43	1.2754	2	0	8
16.39	1.2432	1	0	10	16.74	1.239	1	0	10

Calculation of values was undertaken using XPOW 2.0 adapted from Downs et al. (1993) and using crystallographic data for corundum (Newnham and DeHaan, 1962).

Section 3.3.3 Investigation of the structure of fPer inclusions

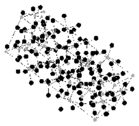

Structural details within the periclase-wüstite solid solution series have been presented in the literature (Skinner, 1956; Hazen, 1976b; Simons and Seifert, 1978; Sumino et al., 1980; Jackson and Neisler, 1982; Sreçec et al., 1987; Richet et al., 1988; Richet et al., 1989; Jackson and Khanna, 1990; Fei et al., 1992; Reeber, 1995; Mao et al., 1996). It might be presumed, therefore, that little would be gained from a detailed structural determination of single fPer inclusions. Indeed, unlike phases of, for example, $MgSiO_3$ composition, it is not envisaged that the fPer inclusions involved in this study would have undergone any phase change throughout their history. Phase changes have been determined for pure Fe-fPer (wüstite) and for all pressures and temperatures likely to be relevent to depths down to ~2100 km, FeO is stable in the NaCl (B1) structure (figure 4.4_22). It is not thought that the addition of Fe^{3+} and Mg to this system would significantly change the depth of transition to the NiAs (B8) structure.

There are two reasons, however, why structural study of fPer inclusions has been undertaken:

- By using single crystals, the structure of almost stoichiometric fPer can be investigated:

  There exists an important difference between much of the fPer presented in the literature and the fPer from São Luiz (and by inference, Guinean fPer inclusions). As Mössbauer analyses have shown (section 2.5.2), São Luiz fPer inclusions contain very little Fe^{3+}. However, fPer employed in the determination of cell parameters presented in the literature are synthesised at low pressure (references in figure 3.3_5). Because of the necessity for significant Fe^{3+} to be present in order to stabilise fPer under crustal and atmospheric conditions of pressure and temperature (e. g. Sreçec et al., 1987), synthetic samples, therefore, contain significant Fe^{3+}. This results in non-stoichiometry of the solid solution series, reflected in a non-linearity in the relationship between Mg# and unit cell parameter (figure 3.3_5). Towards the iron end, increasingly larger amounts of Fe^{3+} are required to stabilise the fPer structure; charge being balanced by the presence of vacancies and oxygen fugacity being buffered by the presence of iron (such phase relationships are summarised in figure 2.6_11). The fPer grains in this study represent a good opportunity to investigate the influence of Fe^{3+} and impurity content (such as Ni) on cell volume in the fPer series in addition to gaining inferences on the value of cell volume for stoichiometric FeO. Such values are important for modelling aspects of lower mantle density.
- Taking measurements from in-situ and subsequently released inclusions allows investigation of elevated internal pressures (section 7.1). fPer is considered to be the ideal avaliable phase for such investigation:

- Its behaviour under varying conditions of pressure and temperature is significantly different from diamond.
- Its visual features are such that it can often be easily identified in-situ.
- It is a particularly common inclusion type in São Luiz and Guinean diamonds.
- It is considered to be a good indicator, in the parageneses considered herein, of a lower mantle source and thus, potentially, high confining pressure, section 4.4.1.
- Being cubic in structure, it has only one cell parameter which can, thus, be easily measured.

In light of the above points, study of ferropericlase inclusions were made as follows:

- FTIR of diamonds BZ255, BZ257, BZ258 containing in-situ fPers at UCL.
- X-Ray Diffraction of BZ255 containing an in-situ fPer, BZ255A at UCL.
- Gandolfi X-Ray diffraction of diamonds (GU4, BZ257, BZ266, BZ267, BZ268, BZ269) containing fPer inclusions in-situ and on single crystal fPer inclusions (GU4, JH2A, JH7A3, JH11A2, JH12A2, JH17A3).
- X-Ray micro-diffraction of BZ257 and BZ256 (containing in-situ fPer, BZ257A and BZ256A) and of BZ257A5; a fragment of the released fPer inclusion at Brookhaven.
- X-Ray diffraction at Edinburgh of BZ257A1, a further fragment of released fPer inclusion BZ257A.

Section 3.3.3.1 Gandolfi camera X-Ray diffraction of fPer grains

Table 3.3_6 presents the data obtained. It was found that values for N (appendix 10) for which N was directly proportional to $\sin^2\theta$ (obtained from diffraction angles) corresponds to a face centred cubic structure[1] in accordance with the accepted structure of fPer solid solution as Fm3m. Values of unit cell parameter, a, were found to lie between 4.22 and 4.28 Å, depending on composition, consistent with the published ATP conditions of the end members periclase (Scacchi, 1841) and wüstite (Shenk and Dingmann, 1927) as 4.213 and 4.307 Å respectively.

Figure 3.3_6 shows the comparison of the variation in cell parameter against Mg content obtained from São Luiz and Guinean inclusions measured at ATP[2] with synthetic fPers from the literature. This plot also includes data from BZ257A presented in section 3.3.3.3. Unlike the synthetic data, fPers from São Luiz and Guinea, lie on a straight line with values of *a* for, in particular, Fe-rich fPer, being greater than published values. The data describe the variation of cell parameter against Mg/(Mg+Fe) as:

$$a = -0.1092\left(\frac{Mg}{Mg+Fe}\right)_{cations} + 4.3365 \qquad \text{Equation 3.3\_1}$$

The linearity in cell parameters obtained for the study of fPer inclusions is indicative of stoichiometry and, as such, is further evidence[3] to suggest that fPer inclusions are highly depleted in Fe^{3+}. Such a composition is interpreted as being due to formation of São Luiz and Guinean fPer at conditions of high pressure and can be viewed as further evidence to suggest a deep origin for fPer paragenesis diamonds.

Additionally, table 3.3_6 shows that there exists a change in cell parameters between GU4(fPer) and GU4A; the same inclusion analysed both within and without of its diamond host. Indeed, comparison of analysis of BZ257(fPer) and BZ257A, sections 3.3.3.2-3 also shows an increase in unit cell parameter from accommodation within to without diamond. A quantitative observation of this nature has important implications for indicating a depth of formation for these stones and will be discussed in the appropriate framework in section 7.1.2.

---

[1] Systematic ommisions in the F-centred structure are such that planes involving either all odd or all even Miller indices produce a net diffraction. This means that diffraction from (111), (200), (220), (311), (222), (400), (331), (420) etc. only are seen. This is in contrast to the primitive unit cell where all planes produce a net diffraction and the body centred cell where the sum of Miller indices must yield a positive value.

[2] ie. data for GU4A and BZ257A (section 3.3.3.2 and 3.3.3.3) measured in-situ are omitted, values for cell parameter obtained being artificially low due to internal pressure.

[3] Also consider Mössbauer data discussed in section 3.3.3.

Table 3.3_6 Data obtained for diffraction lines for fPer inclusions.

		JH11A2 (D26)		**JH17A3 (D23)**		**JH7A3 (D22)**		**JH12A2 (D54)**		**JH12A2 (D25)**	
N	**hkl**	2θ / 10	$\sin^2\theta$	2θ / 10	$\sin^2\theta$	2θ / 10	$\sin^2\theta$	2θ / 10	$\sin^2\theta$	2θ / 10	$\sin^2\theta$
3	**111**	1.6552	0.0207	1.6435	0.0204	1.6690	0.0211	1.6613	0.0209	1.6598	0.0208
				1.6747	0.0212						
4	**200**	1.9102	0.0275	1.8986	0.0272	1.9048	0.0274	1.9050	0.0274	1.9180	0.0278
				1.9251	0.0280	1.9544	0.0288	1.9314	0.0281		
8	**220**	2.7168	0.0552	2.7179	0.0552	2.7152	0.0551	2.7134	0.0550	2.7242	0.0555
				2.7426	0.0562	2.7450	0.0563	2.7305	0.0557		
11	**311**	3.2017	0.0761	3.2116	0.0765			3.2072	0.0763	3.2153	0.0767
12	**222**	3.3390	0.0825	3.3610	0.0836			3.3539	0.0832	3.3613	0.0836
16	**400**										
19	**331**							4.2700	0.1325		
20	**420**										
24	**422**							4.8164	0.1665		
Mg #		0.5140		0.6970		0.7400		0.7260		0.7260	
m			145.05		143.76		142.30		143.96		143.67
a (Å)			**4.2797**		**4.2606**		**4.2538**		**4.2636**		**4.2593**
R^2			1.0000		0.9997		1.0000		1.0000		1.0000

		JH12a2 (D21)		**JH2A (D 28)**		**GU4 (D29) §**		**GU4 (D30) §**		**GU4A (D35)**	
N	**hkl**	2θ / 10	$\sin^2\theta$	2θ / 10	$\sin^2\theta$	2θ / 10	$\sin^2\theta$	2θ / 10	$\sin^2\theta$	2θ / 10	$\sin^2\theta$
3	**111**	1.6614	0.0209	1.6555	0.0207			1.6681	0.0210	1.6410	0.0204
								1.7106	0.0221	1.6754	0.0212
4	**200**	1.9061	0.0274	1.9200	0.0278					1.9054	0.0274
		1.9349	0.0282							1.9337	0.0282
8	**220**	2.7329	0.0558	2.7286	0.0556	2.7322	0.0558	2.7192	0.0553	2.7297	0.0557
						2.7778	0.0576	2.7751	0.0575	2.7463	0.0563
11	**311**	3.2223	0.0770	3.2152	0.0767					3.2364	0.0777
12	**222**	3.3627	0.0837	3.3569	0.0834	$m\alpha_1$	143.42	$m\alpha_1$	144.49	3.3734	0.0842
16	**400**			3.9072	0.1118	$m\alpha_2$	138.85	$m\alpha_2$	138.66		
19	**331**			4.2611	0.1320	$a\alpha_1$	4.2470	$a\alpha_1$	4.2628		
20	**420**			4.3784	0.1390	$a\alpha_2$	4.2040	$a\alpha_2$	4.2011	4.4062	0.1407
24	**422**			4.8224	0.1669						
Mg #		0.7260		0.7607		0.8679		0.8679		0.8679	
m			143.25		143.73						142.35
a (Å)			**4.2531**		**4.2602**	**av**	**4.2255**	**av**	**4.2320**		**4.2397**
R^2			0.9999		1.0000		1.0000		0.9998		0.9999

2θ / 10 is simply the position of each diffraction line measured in cm from the exposed film, m is the gradient of the plot of N against $\sin^2\theta$ with R being the appropriate fitting value, a is the cubic cell parameter. Where two diffraction lines are obtained for one value of N, this corresponds to splitting due to the presence of $K\alpha_1$ and $K\alpha_2$ radiation, otherwise $K\alpha$ is used for calculation. Errors on diffraction line measurement are estimated as approximately 0.003° 2θ which imposes a ~0.2% error on final unit cell parameters. All analyses are for single crystal inclusions released from their diamond hosts with the exception of § fPer cell parameters measured in-situ (i.e. within occluded diamond).

Section 3.3.3.2 Micro-X-Ray diffraction of fPer at Brookhaven

BZ257 was found to contain a fPer inclusion, BZ257A. 20 diffraction peaks from a single analysis of a 15μm wide volume, gave a cell parameter of 4.2374 Å. Furthermore, analyses taken from different areas of the grain showed a range of cell dimensions (4.237 Å, 4.237 Å, 4.24 Å and 4.242 Å) and orientations indicative of twinning, a multi-grain state or marked lattice distortion. An analysis conducted on the surface of the fPer and incorporating what appeared to be a minute green inclusion yielded peaks corresponding to lines (240), (020), (111) and (220) of fPer in addition to diffraction probably from the associated pyroxene (section 3.3.5.3). Diffraction lines consistent with the presence of magnesioferrite and graphite (observed as a film over the inclusion surface) were also detected.

The association of fPer inclusions with a pyroxene (possibly Al-rich) would suggest a lower mantle source for BZ257.

BZ257 was subsequently broken and the fPer inclusion, BZ257A, recovered in 5 pieces (appendix 1). X-ray diffraction of BZ257A5 yielded a cell parameter of 4.2437(3) Å. A further fragment, BZ257A1 was measured in Edinburgh, section 3.3.3.3.

X-Ray diffraction of BZ256 also gave a positive identification for fPer.

➠

Section 3.3.3.3 X-Ray diffraction of fPer, BZ257A1 at Edinburgh

BZ257A1, produced eight strong diffractions which gave a good fit to a NaCl structure (the structure adopted by (Mg,Fe)O) of cell dimension, 4.2489 Å. Additional minor peaks, ~ 1/20th of the major peak intensity, were, also identified which indexed to a unit cell of double this cell dimension. These reflections neither fitted taenite nor magnesioferrite structures and are interpreted as being due to some ordering of Mg and Fe onto distinct sites (Parsons, 1997 *personal communication*).

➠

Section 3.3.4 ESPRC X-Ray diffraction of olivine inclusion, BZ243C

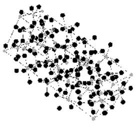

Olivine compositions undergo three structural changes within the upper mantle before breaking down into (Mg,Fe)O + (Mg,Fe)SiO_3 bounding the lower mantle. With decreasing depth these polymorphs are ringwoodite[1], (Cubic Fd3m), wadsleyite[2] (Orthorhombic Imma) and olivine (Orthorhombic Pbnm). As the transition from wadsleyite to olivine occurs at shallow depth, ~390 km (figure 4.3_4), such behaviour means that olivine inclusions are fairly likely to retain a high pressure structure[3] and are thus worthy of study.

BZ243C is a particularly interesting olivine in that it yields an unusually low Mg# and occurs in the same diamond as an inclusion of TAPP (BZ243A) and fPer (BZ243B). BZ243C was then chosen for structural analysis using the ESPRC facility at the University of Wales Cardiff. Unfortunately, however, no diffraction was obtained from this small (60 x 40 x 30 µm) grain.

---

[1] Often, incorrectly, termed γ-olivine, or γ-spinel.

[2] Often, incorrectly, termed β-olivine of modified spinel

[3] Although information on the activation energy of the back-transformation of wadsleyite or ringwoodite to olivine is not available, it is not considered likely to be as small as that pertaining to the back transformation of MgSi-Pvk to enstatite (Knittle and Jeanloz, 1987).

Section 3.3.5 Structural investigation of pyroxene composition phases

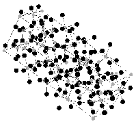

Amongst lower mantle phases, phases of broadly pyroxene composition have invoked the most discussion. In particular, the adoption of a perovskite structure for an exceptionally wide range of compositions within the lower mantle, has received a large degree of interest in the literature (Navrotsky and Weidner, 1989). The nature of the perovskite structure allows for the adoption of large quantities of trace elements (section 2.4.5); indeed perovskite itself, $CaTiO_3$, is well known for its incorporation of exceptionally high REE concentrations (Mitchell and Reed, 1988)[1]. The identification of a pyroxene composition phase adopting a perovskite structure from São Luiz or Guinea would be exceptionally important, representing proof of a lower mantle origin[2].

Pyroxene compositions invoke additional structural interest. Enstatite (i.e. Type I composition) has an orthorhombic Pbnm structure at ATP but undergoes transformation to a C2/c clinopyroxene sructure at ~10 GPa for reasonable mantle temperatures (Akaogi et al., 1987; Gasparik, 1989 and Angel et al., 1992), figure 4.4_1. As will be discussed in detail in section 4.3.1, the compositional field in which pyroxenes adopt an orthorhombic structure at low presssure is fairly large. The system $MgSiO_3$ - Al_2O_3 has been investigated by Boyd and England (1964), Boyd (1970) and Anastasiou and Seifert (1972) under lithospheric conditions (figure 3.3_6). With increasing temperature, below the liquidus, increasing amounts of Al (up to 16 wt%) are accommodated within a single Al-enstatite orthorhombic structured phase, where Al is incorporated onto both M and T sites by the substitution $AlAlSi^{-1}Mg^{-1}$ (Boyd and England, 1964). It is within this solid solution series that the compositions of Type II pyroxenes (section 2.2.1.5) lie. Furthermore, natural samples of aluminous hypersthene of composition very similar to Type II pyroxenes are recorded from the Sutam River gneiss, Russia (Brovkin et al., 1975). These have an orthorhombic (Pbca) structure. Increasing pressure promotes the breakdown of Al-enstatite to less aluminous enstatite + garnet but results of Anastasiou and Seifert (1972) suggest that a monoclinic phase may be stabilised at intermediate pressure and high temperature, of the conditions perhaps in the final stages of volcanic transportation.

The situation for Type III composition phases is less clear. No pyroxenes of similar composition have been found in the literature as a comparison for structural data. Furthermore, material of Type III composition has not been investigated experimentally. Inferences can, perhaps, be made from similar systems. In the jadeite-enstatite system, for example, figure 4.4_17, at reasonable mantle temperatures there exists a compositional field incorporating the enstatite end member where, with increasing

---

[1] Furthermore, from an industrial point of view, perovskites are of importance. Superconducting properties have been discovered so far for $LaBaCuO_4$-Pvk and Sr_2RuO_4-Pvk (Maeno et al., 1994).

[2] From a practical point of view, however, the likelihood of identifying a lower mantle sourced perovskite structured phase is very low. Certainly, stabilization of perovskite structure within diamond would be the most likely scenario in which to find such structure

pressure, up to 18 mol% $NaAlSiO_3$ can be accommodated within an orthorhombic structure (Gasparik, 1989). At pressures above that of the reaction of albite + forsterite ↔ cpx (observed by Gasparik (1989) at 2 GPa, 1473 K), any additional $NaAlSiO_3$ in the system will result in the formation of two pyroxenes, the strongly NaAl rich pyroxene adopting a monoclinic structure and a composition of approximately $MgNaAlSi_2O_6$. It is not until ~10 GPa that a pyroxene with less than 50 mol% $NaAlSiO_3$ will transform to a monoclinic structure. The situation is similar with substitution of $CaMgSi_2O_6$ (Gasparik, 1990 and Gasparik, 1989), figure 4.4_14. In contrast, Salviulo et al. (1997) report a *monoclinic* (C2/c) structure for $(Ca_{0.77}Na_{0.08}Mg_{0.06}Fe_{0.08})(Mg_{0.66}Al_{0.11}Fe_{0.13})(Al_{0.20}Si_{1.80})O_6$ from the Western Ross Embayment, Antarctica. Although the composition is not identical to Type III pyroxenes, it is perhaps more comparable than the experimental data discussed.

The present study: In light of the possibility that high pressure polymorphs of pyroxene composition grains may be observed for São Luiz material, a study of the structural characteristics of pyroxene grains both in-situ and released from diamond was undertaken.

---

retained at atmospheric pressure, but the activation energy of the back transformation of perovksite to enstatite structure has been found to be very small (Knittle and Jeanloz, 1987).

Section 3.3.5.1 X-Ray diffraction of pyroxenes at UCL

Following an initial indication by FTIR that pyroxenes may be present in four of the eight diamonds investigated at UCL, three were chosen for detailed X-Ray diffraction analysis. Of these diamonds, one, BZ251 provided good reflections (inclusion BZ251A was subsequently identified as a Type I pyroxene). BZ253, however, provided a poor unit cell, perhaps an indication of it being polycrystalline, and BZ255 yielded nothing. Analyses obtained indicate that the two pyroxene structures obtained are orthorhombic, not monoclinic. Table 3.3_7 summarises the cell parameters obtained for BZ251 and BZ253.

Table 3.3_7 Cell parameter and unit volume data obtained for BZ251 and BZ253 pyroxene inclusions in-situ.

Sample	**a (Å)**	**b (Å)**	**c (Å)**	**V (Å^3)**
BZ251	18.219 (1)	8.795 (1)	5.1809 (1)	830.2 (1)
BZ253	18.20 (3)	8.79 (1)	5.172 (2)	827 (1)

➠

Section 3.3.5.2 ESPRC X-Ray diffraction of pyroxenes, BZ241B2 and BZ242B

BZ241B2: Initial structural determination of BZ241B2 (Type II pyroxene) proved to be problematic, data obtained gave a poor fit to any reasonable pyroxene structure. It was concluded that this was due to the grain being polycrystalline. Further analysis was attempted on a fragment broken from BZ241B2. This subsequently proved successful: a full structural determination was obtained based on 2817 reflections. This shows that BZ241B2 adopts an orthorhombic Pbca structure; full data being presented in table 3.3_8.

As outlined in section 3.3.5, for the composition of BZ241B2, Pbca represents an ATP structure. Table 3.3_9 of calculated powder data and figure 3.3_7, clearly show the similarity between the structure of BZ241B2 and Pbca pyroxene of similar composition (Brovkin et al., 1975). The orthorhombic structure of BZ241B2 is interpreted as being due to reversion from an original perovskite-type structure via the intermediate C2/c polymorph on exhumation.

BZ242B: A full and successful structural determination of Type III pyroxene BZ242B (of Na-Al enstatite composition) was obtained based on 787 reflections. This shows that BZ242B adopts a monoclinic C2/c structure; data being presented in table 3.3_10. Figure 3.3_8 illustrates the distortion of BZ242B from the orthorhombic system.

Table 3.3_8 Structural data for BZ241B2, Type II pyroxene.

(a) Unit cell and analysis data

Crystal System	Orthorhombic	**Formula Weight**	207.97
Space Group	Pbca (no. 61)	**Calculated Density (Mgm^{-3})**	3.325
a dimension (Å)	8.740(11)	**Data/Parameters**	7.26
b dimension (Å)	5.203(11)	**R**	0.0368
c dimension (Å)	18.27(2)	**Rϖ**	0.0642
Reflections	2817	**μ (mm^{-1})**	1.804 mm^{-1}
Independent Reflections	661 I > 4σ		

(b) Positions and thermal parameters *

Atom**	Site	x	y	z	U_{11}	U_{22}	U_{33}	U_{12}	U_{13}	U_{23}
M(1)	8c1	0.3460(2)	0.1356(4)	0.6240(1)	3(1)	7(1)	7(1)	0(1)	2(1)	0(1)
M(2)	8c1	0.5202(2)	-0.3589(4)	0.6205(1)	15(1)	11(1)	17(2)	-3(1)	-2(1)	-2(1)
T(1)	8c1	0.6580(2)	-0.0436(4)	0.7290(1)	9(1)	7(1)	5(1)	0(1)	0(1)	1(1)
T(2)	8c1	0.3370(3)	-0.1954(4)	0.4741(1)	7(1)	9(1)	8(1)	0(1)	2(1)	-1(1)
O(1)	8c1	0.3360(5)	-0.1926(10)	0.5642(3)	4(3)	13(3)	11(3)	3(3)	-4(3)	3(3)
O(2)	8c1	0.5125(5)	0.3062(10)	0.5667(3)	9(3)	8(3)	21(4)	3(3)	4(3)	3(3)
O(3)	8c1	0.1616(5)	-0.0350(9)	0.6823(3)	7(3)	13(3)	9(3)	0(3)	2(3)	0(2)
O(4)	8c1	0.4960(5)	-0.0370(9)	0.6900(3)	10(3)	12(3)	7(3)	1(2)	0(2)	-5(3)
O(5)	8c1	0.7747(5)	0.1771(10)	0.6981(3)	16(3)	11(3)	10(4)	-5(3)	-1(2)	3(3)
O(6)	8c1	0.3031(5)	0.1083(11)	0.4471(3)	15(3)	16(4)	8(4)	10(3)	-1(2)	1(3)

(c) Interatomic distances (Å) and angles (°)

M(1)-O(4)	1.994(5)	M(2)-O(2)#3	2.002(7)	T(1)-O(5)	1.637(5)
M(1)-O(3)#1	2.019(6)	M(1)-O(4)	2.112(6)	T(1)-O(3)#7	1.621(6)
M(1)-O(3)	2.126(5)	M(2)-O(5)#5	2.293(6)	T(1)-O(5)#5	1.666(6)
M(1)-O(2)	2.001(6)	M(2)-O(1)	2.097(5)	T(2)-O(2)#6	1.617(5)
M(1)-O(1)	2.029(7)	M(2)-O(3)#4	2.154(6)	T(2)-O(6)#4	1.670(6)
M(1)-O(1)#1	2.128(6)	M(2)-O(6)#6	2.368(6)	T(2)-O(1)	1.646(5)
		T(1)-O(4)	1.586(5)	T(2)-O(6)	1.681(7)

O(4)-M(1)-O(2)	92.2(2)	O(2)-M(1)-O(3)	177.3(2)	O(5)#5-M(2)-O(6)#6	76.6(2)	O(2)#6-T(2)-O(1)	117.9(3)
O(2)-M(1)-O(3)#1	85.6(2)	O(1)-M(1)-O(3)	83.5(2)	O(2)#3-M(2)-O(4)	169.1(2)	O(1)-T(2)-O(6)#4	107.3(3)
O(2)-M(1)-O(1)	97.0(2)	O(2)-M(1)-O(1)#1	95.1(2)	O(2)#3-M(2)-O(3)#4	82.1(2)	O(1)-T(2)-O(6)	106.5(3)
O(4)-M(1)-O(3)	90.5(2)	O(1)-M(1)-O(1)#1	92.6(2)	O(4)-M(2)-O(3)#4	87.1(2)	O(4)-T(1)-O(5)	112.7(3)
O(3)#1-M(1)-O(3)	93.8(2)	O(2)#3-M(2)-O(1)	95.3(2)	O(1)-M(2)-O(5)#5	150.4(2)	O(4)-T(1)-O(5)#5	100.5(3)
O(4)-M(1)-O(1)#1	172.5(2)	O(1)-M(2)-O(4)	83.7(2)	O(3)#4-M(2)-O(5)#5	106.7(2)	O(5)-T(1)-O(5)#5	105.9(3)
O(3)#1-M(1)-O(1)#1	83.7(2)	O(1)-M(2)-O(3)#4	82.3(2)	O(1)-M(2)-O(6)#6	91.0(2)	O(2)#6-T(2)-O(6)#4	104.0(3)
O(3)-M(1)-O(1)#1	82.3(2)	O(2)#3-M(2)-O(5)#5	113.6(2)	O(3)#4-M(2)-O(6)#6	171.3(2)	O(2)#6-T(2)-O(6)	110.1(3)
O(4)-M(1)-O(3)#1	94.9(2)	O(4)-M(2)-O5(#5)	69.0(2)	O(4)-T(1)-O(3)#7	117.8(3)	O(6)#4-T(2)-O(6)	111.0(2)
O(4)-M(1)-O(1)	88.6(2)	O(2)#3-M(2)-O(6)#6	104.2(2)	O(3)#7-T(1)-O(5)	108.3(3)		
O(3)#1-M(1)-O(1)	175.6(2)	O(4)-M(2)-O(6)#6	86.7(2)	O(3)#7-T(1)-O(5)#5	110.9(3)		

The structure was determined via direct methods (SHELX-86, Sheldrick, 1990) and refined by the least-squares program SHELX-93 (Sheldrick, 1993) * All atoms refined with anisotropic thermal parameters. The anisotropic displacement factor exponent takes the form; - $2pi^2[h^2a^{*2}U_{11} +...+2hka^*b^*U_{12}]$.

Table 3.3_9 d-spacings for main reflections of BZ241B2 and Al-rich hypersthene

Al-rich hypersthene * (Pbca)				**BZ241B2** (Pbca)			
d value	**h k l**	**d value**	**h k l**	**d value**	**h k l**	**d value**	**h k l**
18.22	0 0 1	4.009	1 1 2	9.135	0 0 2	2.8755	1 0 6
9.11	0 0 2	3.9493	2 0 2	6.3151	1 0 2	2.8292	1 1 5
8.765	1 0 0	3.9447	0 1 3	4.5675	0 0 4	2.7756	3 0 2
7.8986	1 0 1	3.644	0 0 5	4.37	2 0 0	2.6994	2 1 4
6.3162	1 0 2	3.5972	1 1 3	4.3426	1 1 1	2.6015	0 2 0
6.0733	0 0 3	3.5539	2 0 3	4.0481	1 0 4	2.5755	0 2 1
5.188	0 1 0	3.4229	0 1 4	4.0156	1 1 2	2.5177	3 1 1
4.992	1 0 3	3.3648	1 0 5	3.9421	2 0 2	2.5167	1 1 6
4.9897	0 1 1	3.3479	2 1 0	3.6039	1 1 3	2.502	0 2 2
4.555	0 0 4	3.2928	2 1 1	3.3463	2 1 0	2.4983	2 0 6
4.5082	0 1 2	3.1884	1 1 4	3.2915	2 1 1	2.4705	1 2 1
4.4645	1 1 0	3.1581	2 0 4	3.195	1 1 4	2.4678	2 1 5
4.3825	2 0 0	3.1424	2 1 2	3.1576	2 0 4	2.4562	3 0 4
4.3363	1 1 1	3.0367	0 0 6	3.1421	2 1 2	2.4489	3 1 2
4.261	2 0 1	2.9819	0 1 5	3.045	0 0 6	2.4054	1 2 2
4.0418	1 0 4	2.9319	2 1 3	2.9327	2 1 3	2.3924	0 2 3

Calculation of values was undertaken using XPOW 2.0 adapted from Downs et al. (1993) and using crystallographic data for BZ241B2 (table 3.3_8) and * natural $(Mg_{1.46}Al_{0.20}Fe_{0.28})(Si_{1.83}Al_{0.17})O_3$ aluminous hypersthene adapted from Brovkin et al. (1975), a = 8.765, b = 5.188, c = 18.220.

As outlined in section 3.3.5, for the composition of BZ242B, it is unclear whether the C2/c structure is the stable ATP state or whether this is a high pressure structure analogous to the trasformation of enstatite. Table 3.3_11 and figure 3.3_9, being calculated powder data, clearly show the differences between C2/c BZ242B, C2/c $NaAlSiO_3$ and C2/c Ca-Al-Na pyroxene (Salviulo et al., 1997). These differences cast further doubt on whether pyroxenes from the literature can be used to predict the ATP-stable structure of BZ242B composition.

What can be concluded is that the monoclinic structure of BZ242B has reverted from an original perovskite-type structure, due to the low energy of this back-transformation (Jeanloz and Knittle, 1987), however whether it retains a structure intermediate between this and its ATP structure is unclear.

Table 3.3_10 Structural data for BZ242B, Type III pyroxene.

(a) Unit cell and analysis data

Crystal System	Monoclinic	**β (°)**	108.33(4)
Space Group	C2/c (no. 15)	**Formula Weight**	418.20
a dimension (Å)	9.587(4)	**Calculated Density (Mgm^{-3})**	3.344
b dimension (Å)	8.699(6)	**Data/Parameters**	6.57
c dimension (Å)	5.247(4)	**R**	0.0516
Reflections	787	**R_{ϖ}**	0.1024
Independent Reflections	309 I > 4σ	**μ (mm^{-1})**	1.811 mm^{-1}

(b) Positions and thermal parameters *

Atom**	Site	x	y	z	U_{11}	U_{22}	U_{33}	U_{12}	U_{13}	U_{23}
M(1)	4	0	0.9049(6)	0.2500	15(2)	15(3)	26(3)	0	14(2)	0
M(2)	4	0	0.2847(6)	0.2500	18(3)	21(3)	12(3)	0	2(2)	0
Si(1)	8	0.2933(3)	0.0924(4)	0.2456(7)	12(2)	10(2)	22(2)	1(2)	10(2)	0(2)
O(1)	8	0.1137(7)	0.0860(9)	0.1368(14)	10(4)	22(4)	19(5)	10(4)	12(3)	-3(4)
O(2)	8	0.3674(9)	0.2554(9)	0.3261(15)	30(5)	25(5)	32(5)	1(4)	13(4)	-16(4)
O(3)	8	0.3546(8)	0.0078(11)	1.0264(18)	24(4)	48(6)	39(6)	-11(4)	15(4)	-29(5)

(c) Interatomic distances (Å) and angles (°)

M(1)-O(2)#1	1.946(10)	M(1)-O(2)#2	1.946(10)	Si(1)-O(2)	1.583(8)
M(1)-O(1)#3	1.981(7)	M(1)-O(1)#4	1.981(7)	Si(1)-O(1)	1.635(6)
M(1)-O(1)#5	2.105(9)	M(1)-O(1)#6	2.105(9)	Si(1)-O(3)#13	1.624(10)
M(2)-O(1)#8	2.222(8)	M(2)-O(1)	2.222(8)	Si(1)-O(3)#14	1.653(9)
M(2)-O(2)#9	2.215(8)	M(2)-O(2)#10	2.215(8)		
M(2)-O(3)#11	2.461(10)	M(2)-O(3)#12	2.461(10)		

O(2)#1-M(1)-O(2)#2	96.1(5)	O(2)#1-M(1)-O(1)#3	93.0(3)	O(1)#8-M(2)-O(1)	77.8(4)	O(1)#8-M(2)-O(2)#9	88.3(3)
O(2)#2-M(1)-O(1)#3	90.1(3)	O(2)#1-M(1)-O(1)#4	90.1(3)	O(1)-M(2)-O(2)#9	77.5(3)	O(1)#8-M(2)-O(2)#10	77.5(3)
O(2)#2-M(1)-O(1)#4	93.0(3)	O(1)#3-M(1)-O(1)#4	175.4(5)	O(1)-M(2)-O(2)#10	88.3(3)	O(2)#9-M(2)-O(2)#10	161.9(5)
O(2)#1-M(1)-O(1)#5	90.7(3)	O(2)#2-M(1)-O(1)#5	171.1(3)	O(1)#8-M(2)-O(3)#11	137.6(3)	O(1)-M(2)-O(3)#11	119.3(3)
O(1)#3-M(1)-O(1)#5	95.3(3)	O(1)#4-M(1)-O(1)#5	81.2(3)	O(2)#9-M(2)-O(3)#11	131.5(3)	O(2)#10-M(2)-O(3)#11	65.5(3)
O(2)#1-M(1)-O(1)#6	171.1(3)	O(2)#2-M(1)-O(1)#6	90.7(3)	O(1)#8-M(2)-O(3)#12	119.3(3)	O(1)-M(2)-O(3)#12	137.6(3)
O(1)#3-M(1)-O(1)#6	81.2(3)	O(1)#4-M(1)-O(1)#6	95.3(3)	O(2)#9-M(2)-O(3)#12	65.5(3)	O(2)#10-M(2)-O(3)#12	131.5(3)
O(1)#5-M(1)-O(1)#6	83.1(4)	O(2)-Si(1)-O(3)#13	111.3(5)	O(3)#11-M(2)-O(3)#12	75.9(3)	O(2)-Si(1)-O(1)	117.3(4)
O(3)#13-Si(1)-O(1)	108.2(4)	O(2)-Si(1)-O(3)#14	103.3(5)	O(3)#13-Si(1)-O(3)#14	106.6(3)	O(1)-Si(1)-O(3)#14	109.5(4)

The structure was determined via direct methods (SHELX-86, Sheldrick, 1990) and refined by the least-squares program SHELX-93 (Sheldrick, 1993) * All atoms refined with anisotropic thermal parameters. The anisotropic displacement factor exponent takes the form; - 2pi^2[h^{2}a*^{2}U$_{11}$ +...+2hka*b*U$_{12}$]. ** M(1) = Mg^{2+} 0.232, Fe^{2+} 0.029, Al^{3+} 0.215, Cr^{3+} 0.024, Ti^{4+} 0.0005; M(2) = Mg^{2+} 0.193, Na^{+} 0.157, Ca^{2+} 0.082, Fe^{2+} 0.029, Mn^{2+} 0.019; Si(1) = Si^{4+} 0.957, Al^{3+} 0.043

Table 3.3_11 d-spacing and intensity for main reflections of BZ242B and standard $NaAlSiO_3$ jadeite.

BZ242B **Type III Na-Al-pyroxene** C2/c					**$(NaAl)Si_2O_6$** C2/c					**Natural Ca-Al-Na pyroxene ♥** C2/c				
I (%)	**d-value**	**h**	**k**	**l**	**I (%)**	**d-value**	**h**	**k**	**l**	**I (%)**	**d-value**	**h**	**k**	**l**
1.61	6.2883	1	1	0	5.12	6.1961	1	1	0	2.96	6.4355	1	1	0
0.91	4.5503	2	0	0	1.66	4.4891	2	0	0	100	4.6704	2	0	0
1.7	4.397	-1	1	1	13.16	4.3469	-1	1	1	0.22	4.4395	0	2	0
11.82	4.3495	0	2	0	20.65	4.281	0	2	0	19.58	4.418	-1	1	1
2.32	3.5472	1	1	1	1.18	3.5362	1	1	1	3.45	3.6535	1	1	1
26.18	3.2762	0	2	1	13.4	3.2451	0	2	1	62.75	3.3395	0	2	1
19.16	3.1441	2	2	0	10.91	3.0981	2	2	0	0.42	3.2177	2	2	0
100	2.9655	-2	2	1	100	2.9168	-2	2	1	10.52	2.9904	-2	2	1
28.3	2.88	-3	1	1	27.33	2.827	-3	1	1	0.3	2.9382	3	1	0
46.43	2.8644	3	1	0	43.64	2.8251	3	1	0	7.65	2.896	-3	1	1
1.25	2.7628	1	3	0	0.24	2.7199	1	3	0	3.8	2.8214	1	3	0
5.59	2.548	-2	0	2	3.96	2.5228	-2	0	2	0.05	2.559	-1	3	1
21.02	2.5202	-1	3	1	0.58	2.4954	-1	1	2	2.89	2.5467	-2	0	2
0.16	2.5096	-1	1	2	39.1	2.4876	0	0	2	5.18	2.5341	0	0	2
36.86	2.4904	0	0	2	17.46	2.4841	-1	3	1	1.35	2.5304	-1	1	2
26.32	2.431	2	2	1	33.16	2.4138	2	2	1	19.93	2.5063	2	2	1
0.2	2.3237	1	3	1	1.07	2.2996	1	3	1	0.89	2.381	1	3	1
0.35	2.2751	4	0	0	0.07	2.2445	4	0	0	0.49	2.3352	4	0	0
0.12	2.2368	-3	1	2	0.01	2.2046	-3	1	2	0.16	2.2924	3	1	1
12.26	2.215	3	1	1	13.97	2.2019	3	1	1	1.43	2.2333	-3	1	2
0.03	2.1985	-2	2	2	0.56	2.1735	-2	2	2	0.06	2.2198	0	4	0
0.02	2.1748	0	4	0	15.71	2.1582	1	1	2	0.08	2.2165	1	1	2
6	2.1612	0	2	2	9.04	2.1509	0	2	2	1.22	2.209	-2	2	2
12.74	2.1603	1	1	2	0.03	2.1405	0	4	0	6.58	2.2008	0	2	2
17.21	2.1022	-3	3	1	12.32	2.0661	-3	3	1	6.22	2.1452	3	3	0
4.88	2.0961	3	3	0	6.24	2.0654	3	3	0	0.35	2.1286	-3	3	1
5.42	2.0813	-4	2	1	5.96	2.044	-4	2	1	1.56	2.105	-4	2	1
9.14	2.0269	-4	0	2	6.31	1.9924	-4	0	2	0	2.0667	4	2	0
0.67	2.016	4	2	0	0.39	1.9879	4	2	0	0.02	2.0333	0	4	1
16.05	1.9931	0	4	1	18.7	1.9662	0	4	1	1.21	2.023	-4	0	2

♥ Pyroxene of composition, $(Ca_{0.77}Na_{0.08}Mg_{0.06}Fe_{0.08})(Mg_{0.66}Al_{0.11}Fe_{0.13})(Al_{0.20}Si_{1.80})O_6$.similar to Type III although with significantly more Ca and less Mg and Fe (Salviulo et al., 1997). Calculation of values was undertaken using XPOW 2.0 adapted from Downs et al. (1993) and using crystallographic data for jadeite from Clark et al. (1969).

Section 3.3.5.3 Micro-X-Ray diffraction of pyroxenes at Brookhaven

Of the four diamonds analysed, pyroxene structures were identified from BZ253 and BZ257. Provisional[1] cell parameters were obtained for two cpx structured grains in BZ257. Structural data are summarised in table 3.3_12.

Table 3.3_12 Summary of cell parameter and volume data for pyroxene grains examined in-situ within stones BZ253 and BZ257.

Sample	**a (Å)**	**b (Å)**	**c (Å)**	**β (°)**
BZ257	9.635	8.988	5.344	103.945
BZ257♣	9.797	8.717	5.34	105.109

♣ Inclusion on the fPer / diamond boundary

Cpx lines present in diamond BZ257 appear to be sourced from both a green grain located on the polished face-side of the main fPer inclusion as well as from a separate inclusion. The possible cpx on the fPer / diamond boundary is extremely small (<10 μm). The analytical area (~11 x 17 μm) showed a strong Ba fluorescence, as yet unexplained, and yielded four diffraction lines which match diffraction from fPer planes (240), (020), (111) and (220). The presence of fPer lines suggests an overlap of the analytical volume with the adjoining fPer. The pyroxene lines obtained from BZ257 are consistent with a low Ca, relatively Fe rich pyroxene and an Al- rich pyroxene with low Ca. Due to the coexistence of this pyroxene with fPer and the similarity of BZ257 data to cell parameter data of BZ242B (section 3.3.5.2) it is likely that the latter interpretation is correct: BZ257 pyroxene is likely to be a Type III pyroxene. It would, thus, be reasonable to suggest that BZ257 is a lower mantle stone.

---

[1] An orientation matrix was not applied.

Section 3.3.6 Additional observations on structural investigations

BZ228D: A white amorphous-looking grain was recovered from BZ228 (section 2.2.1.9) and was studied by Gandolfi camera X-Ray diffraction. Two analyses were undertaken each for 48 hours using MoKα radiation. Given the large size of the grain (200 x 200 x 160 µm), if it was crystalline, it would have been expected to yield some diffraction for exposure times of this length. As both films were found to be blank on development, it was concluded that not only does BZ228D look amorphous, crystallographically, it *is* amorphous. This inclusion is, thus, thought to be secondary.

BZ249A: Inclusion BZ249A was studied by X-Ray diffraction at Edinburgh and found to have a monoclinic C2/c pyroxene structure (table 3.3_13). Although this grain was lost before compositional data could be obtained by EPMA, thermal parameters and site occupancies conform to a diopside composition of approximately $CaMg_{0.7}Fe_{0.3}Si_2O_6$ (rather than of the composition of, for example, BZ242B of section 3.3.5.2). It can be considered likely that BZ249A is a diopside of a similar type to BZ209A, BZ209B, BZ213A and BZ218B (appendix 3.2).

Additional phases in BZ253: X-Ray diffraction of BZ253 at Brookhaven yielded diffraction consistent with two grains; one a C2/c pyroxene (section 3.3.5.3) and the other a Ia3d garnet.

Additional phases in BZ255: Angel and Ross (1993, *personal communication*) reported a number of split diffraction peaks from a dark inclusion in BZ255. By the 2θ values and angular relationships, it was clear that the inclusions were under significant strain (Angel, 1997 *personal communication*). At the time, it was suggested that the diffraction was due to two garnet structured phases in close proximity and of different compositions. However, the diffraction peaks were weak and the splitting of lines made centering the specimen difficult. Following subsequent polishing, the only obvious inclusion in BZ255 was found to be a fPer (by EPMA); neither a pyroxene nor a garnet. Certainly, fPer and garnet structures are both cubic, although the unit cell edge of garnet is approximately 3 times that of fPer. The preferred explanation for the anomalous X-Ray diffraction of BZ255, however, is that the diffraction *was* due to fPer where interpretation was masked by the high distortion due to extreme strain. There is strong independent evidence to support the belief that most diamonds from São Luiz have been subjected to significant distortion, (section 5.6), it could follow that the inclusions themselves are distorted and, certainly, as measurements discussed in section 7.1.4. show, they are, at least, under strain. Additionally, like BZ255, the fPer grain BZ257A *appeared* to be a single crystal. However, high resolution investigation (section 3.3.3.2) showed a cluster of slightly misaligned fPer grains and on release from diamond the grain split easily into a number of fragments (appendix 1).

Additional phases in BZ256: In addition to the identification of fPer in BZ256 (section 3.3.3.2), a wollastonite structured inclusion has also been identified. At the time of writing, a full structural determination was not forthcoming. It should be noted, however, that this is a very important result. Although chemical arguements (section 4.4.2) support $CaSiO_3$ composition inclusions (BZ97, BZ115 and BZ252A) forming in equilibrium with fPer association inclusions, structural confirmation of $CaSiO_3$ coexisting with fPer in BZ256 would mean that this is the first diamond identified which provides proof of such a mutual association.

Table 3.3_13 Crystallographic data for BZ249A

(a) Unit cell and analysis data

Crystal System	Monoclinic	**Formula Weight**	464.68
Space Group	C2/c (no. 15)	**Calculated Density (Mgm^{-3})**	3.506
a dimension (Å)	9.751	**Data/Parameters**	6.8
b dimension (Å)	8.914	**R**	0.047
c dimension (Å)	5.264	**Reflections**	1153
μ (mm^{-1})	3.57 mm^{-1}	**Independent Reflections**	387 $I > 4\sigma$

(b) Positions and thermal parameters *

Atom **	Site	x	y	z	U_{11}	U_{22}	U_{33}	U_{12}	U_{13}	U_{23}
Ca	4	0.0000	0.6995	0.7500	81	138	92	0	-7	0
		0.0000	0.0002	0.0000	8	9	9	0	6	0
Mg	2	0.0000	0.9070	0.2500	33	72	38	0	-2	0
		0.0000	0.0002	0.0000	9	10	10	0	6	0
Fe	2	0.0000	0.9070	0.2500	33	72	38	0	-2	0
		0.0000	0.0002	0.0000	9	10	10	0	6	0
Si	8	0.2124	0.4074	0.7690	28	75	60	0	10	-4
		0.0001	0.0002	0.0002	7	8	7	6	5	6
0(1)	8	-0.1160	0.9129	0.8570	43	114	61	-5	15	15
		0.0003	0.0004	0.0006	17	19	18	15	14	15
0(2)	8	-0.1487	0.5173	0.9946	49	98	61	7	1	-5
		0.0003	0.0004	0.0007	15	18	17	15	13	15
0(3)	8	0.1348	0.7498	1.1794	83	142	64	34	22	12
		0.0004	0.0004	0.0007	17	20	20	15	14	15

(c) Interatomic distances (Å)

Ca-O(1)	2.359(4)	(x2)	Fe-O(1)	2.126(4)	(x2)
Ca-O(2)	2.723(4)	(x2)	Fe-O(1)_$1	2.070(3)	(x2)
Ca-O(3)	2.339(4)	(x2)	Fe-O(3)	2.049(4)	(x2)
Mg-O(1)	2.070(3)	(x2)	Si-O(1)	1.610(3)	(x1)
Mg-O(1)_$1	2.126(4)	(x2)	Si-O(2)	1.674(4)	(x1)
Mg-O(3)	2.049(4)	(x2)	Si-O(3)	1.588(4)	(x1)

The structure was determined via direct methods and refined by the least-squares program Siemens SHELXTL-5.03. * All atoms refined with anisotropic thermal parameters. Thermal parameters are presented as x 10^4. The anisotropic displacement factor exponent takes the form; $-2pi^2$ $[h^2a^{*2}U11+...+2hka^*b^*U12]$. ** Structure conforms to $Mg^{2+} = 2.80$, $Fe^{2+} = 1.20$, $Ca^{2+} = 4.00$, $Si^{4+} = 8.00$ per 24 O.

Section 3.4 Summary of structural determinations

Two frameworks have been employed in the study of São Luiz and Guinean inclusions:

- Study of released inclusions
- Study of inclusions in-situ

Results:

- Determination of a new phase, TAPP. This has a composition similar to pyrope-almandine garnet, but with a profoundly tetragonal, $I\bar{4}2d$, structure. It contains 3 independent oxygen sites in general positions, two distinct tetrahedral 'silicon' sites, both with 2-fold symmetry, and three other cation sites; M1 has 4-fold symmetry and a 'capped' tetrahedral environment, with four short and four long M1-O bonds, whilst M2 and M3 have 2-fold symmetry, with octahedral co-ordination. The Si tetrahedra are not linked together, so that TAPP is an orthosilicate. On the basis of independent sites, it can be described by the formula: $(M1)(M2)_2(M3)_2Si_3O_{12}$. TAPP grains have been discovered both within and released from, the diamond host.
- The first recorded sapphire inclusion in diamond was found to adopt a $R\bar{3}c$ corundum structure.
- A Pbca structure was determined for a highly aluminous (~10 wt% Al_2O_3) pyroxene (Type II).
- A C2/c structure was determined for a highly aluminous (13 wt% Al_2O_3) Na and Ca-rich pyroxene of, otherwise, enstatitic composition (Type III) released from diamond.
- Cell parameters for Fe^{3+} deficient fPer inclusions have been determined over the compositional range Mg# = 0.87 to 0.52. In contrast to literature data which involve Fe^{3+}-rich fPer grains, cell parameters are found to exhibit a linear trend with composition from d = 4.3365 Å for FeO to d =

- Structural study has revealed diffraction lines consistent with magnesioferrite structure, in association with a single fPer inclusion. This result is in agreement with the results of TEM study of blebs in fPer.
- The expansion of cell parameters on release from diamond was measured for two fPer inclusions. These were found to be 0.63% and 0.77%, which, following calculations in section 7.1.5, represent a minimum depth of formation of ~ 300 km. This figure does not account for pressure release due to deformation of the diamond host, a factor which is considered likely to add at least 400 km to the formation depth implied.

- Structural study of many inclusions suggests that they are polycrystalline which is consistent with reversion from high pressure structure and is thus indicative of a deep origin.
- A $CaSiO_3$ composition inclusion has been identified in coexistence with a fPer inclusion. This observation confirms chemical evidence (section 4.4.2) which suggests that similar $CaSiO_3$-bearing diamonds have formed in equilibrium with fPer associations.

➠

Chapter 4 The nature of mantle regions as seen through study of São Luiz inclusions

The chemistry and coexistence of inclusions from São Luiz (and Guinean) diamonds, as discussed in Chapter 2, provides guides to determination of their depth of formation, as well as a unique opportunity to glean information on the composition of depths throughout a significant portion of the transition zone and lower mantle. In particular, the discovery of lower mantle material in diamonds can go some way to answering some of the burning questions in the Earth Sciences. What is the composition of the Earth and, in particular, do the upper and lower mantle have different compositions? These questions are inexorably linked with an understanding of the mechanisms of planetary formation and early planetary history.

Chapter 4 commences with a background discussion of mantle compositions, geotherms and convective state (sections 4.1 - 4.3) and uses this information in conjunction with high pressure and temperature experimental data to consider the origin of the São Luiz and Guinean inclusions (section 4.4). Inferences on bulk mantle composition in terms of both major and trace elements are also drawn. The fit of particular partition coefficients and extent of recrystallisation of coexisting phases are used to infer the degree to which equilibrium has been achieved or attained (section 4.5) and under what physical conditions. In addition, the little partitioning data for Liquid / Crystal for high pressure and temperature mineral phases which is available from the literature is applied to inclusion trace element data to infer the composition of coexisting liquids (section 4.6). States of mantle oxidation (section 4.7) are also discussed using the Mössbauer data presented in section 2.4. The reader will find that this has close links with fO_2 as determined by the diamonds themselves presented later in section 6.3.

Section 4.1 Bulk compositions of the mantle

The following discussion presents some of the contemporary views on the composition of the Earth and provides a framework of bulk compositional data for comparison with diamond inclusion associations.

Sun's (1982) model: The model of Sun (1982) incorporates data from ultramafic mantle nodules and mafic and ultramafic magmas of varying age in order to make predictions of the composition of the primitive mantle. As Sun's (1982) modelling relies heavily on observations on upper mantle material, any extrapolation to bulk mantle composition involves the assumption that the upper and lower mantle are undifferentiated. Elements are discussed on an individual basis, the key observations being that compatible and moderately incompatible elements, in addition to siderophile elements, have shown no significant secular variation since ~ 3.5 Byr: inferred to be the time of core formation. Additionally, estimates of primitive mantle composition from batch melting and primitive nodules shows some differences with C1 chondrites, even for refractory lithophile element values (~ 1.1 x C1).

Ringwood's (1989) pyrolite model: Ringwood makes the observation that, although relatively infertile rocks such as peridotite and eclogite make up a significant portion of, in particular, the continental lithospheric mantle, basaltic magmatism has been, and still is, a common occurrence on the Earth's surface. Clearly, there must exist an extensive body of more primitive, fertile rock which is capable of producing MORB-like melts. Such material is termed 'pyrolite' and is envisaged to dominate the mantle below the oceanic crust as well as comprising a significant portion of the upper mantle below the continents. The composition of pyrolite is estimated by using the observation of a geochemical continuum amongst peridotites (eg. Jagoutz et al., 1979): peridotites containing the most CaO and Al_2O_3 are envisaged to have undergone the least melt extraction and are thus considered to be close to pyrolite in composition. Interestingly, the abundance of involatile elements in pyrolite thus calculated, is very similar to their abundances in C1 chondrites. Furthermore, removing core and volatile components from C1 chondrites produces an even better match with pyrolite with the exception of the fact that C1 chondrite contains too much Si[1], see table 4.1_1. Supporters of the pyrolite model cite the similarity between pyrolite and C1 as suggesting that the whole silicate Earth (including the lower mantle) is composed of a pyrolite composition (ie. devolatilised, siderophile element depleted, C1 chondrites).

Anderson's (1989) solar model: The pyrolite model *assumes* that C1 chondrites are likely candidates for the building blocks of the primitive Earth: Ringwood (1989) cites the similarity of C1 chondrites with the hypothetical pyrolite composition as support for such an assumption. Unfortunately, the source of C1 chondritic meteorites is poorly understood. Indeed, we do not know how representative chondrites are of the asteroid belt, let alone of the material which formed the Earth (Hamilton, 1993) and, furthermore, there have been indications that ordinary chondrites of which we have examples, may have only come from three parent bodies (see Hamilton, 1993 for references). A better estimate for bulk Earth composition would be the non-volatile composition of the Sun because ultimately, the Sun and terrestrial planets arose from the same source within the pre-solar nebula. C1 chondrites, historically, have been used instead, because of the large uncertainties in our measurements of solar composition. Recent advances in measurement of the Sun's photosphere and corona, however, have been made. These suggest that the content of, in particular, Ca and Fe, is higher than that of the so-called 'cosmic' abundance determined from C1 chondrites. This enriched Ca and Fe is not consistent with peridotitic or pyrolite (MORB) source compositions. Anderson (1993), therefore, suggests that there is a compositional divide between true primitive Earth and the asthenospheric reservoir source of MORB, the natural boundary between these two régimes being the upper / lower mantle boundary. The outcome, in terms of composition is that the lower mantle is more pyroxene-rich (Fe and Si enriched) than the upper mantle which appears to fit a more olivine-rich composition.

A number of independent lines of evidence support the solar composition model:

- Evidence from helium isotopes suggests that a solar component is, indeed, relevent to the deep Earth (Honda et al., 1993). ^{4}He/^{3}He ratios for some OIB material (involving a possible lower mantle origin) are not only elevated above MORB, but are even higher than the ratio obtained from C1 chondrites and approach those observed in the Sun’s photosphere.
- Seismic studies suggest that a more pyroxene-rich (‘solar’) bulk composition in the lower mantle would better fit the observed lower mantle seismic velocities (Anderson, 1977).
- Komatiites, are regarded as being the closest approximation to melt of primitive mantle material because they are ancient and formed at very high temperature (up to 1900K). Their high Mg content suggests that they are sourced from a complete melting of olivine (unlike present-day basalts) (Cheadle, 1996 *personal communication*). They would, thus, have incorporated the melt products of Al and Ca bearing phases also (which have lower melting points than olivine). Komatiites should, therefore, retain the Ca/Al ratio of their source which at the stage of their formation would have been a largely undifferentiated Earth. It is striking, therefore, that the Ca/Al ratio, as well as the Fe content of komatiites is remarkably similar to solar values.

---

[1] This excess Si is assumed to be removed along with volatile components.

Javoy's (1995) integral enstatite chondrite model: Javoy (1995) relies heavily on isotopic and redox arguments. He cites that the only primitive meteorites which have isotopic and redox compositions comparable with the Earth are the enstatite chondrites (specifically the EH subgroup). The oxygen isotopic composition of the Earth's mantle and the Moon are very similar and differ significantly from all other solar system bodies, with the exception of enstatite chondrites (^{17}O and ^{18}O for Earth, Moon and EH chondrites coincide to better than 0.2‰, Clayton and Mayeda, 1984). Oxygen isotopes are considered to be the most reliable, compared with He, H and C, as they are not expected to be significantly fractionated on evaporation, however Javoy (1995) also suggest that isotopic evidence from diamonds is consistent with an enstatite chondrite model (Javoy et al., 1986). Assuming that enstatite chondrites are, indeed, representative of the bulk Earth, Javoy (1995) follows a series of calculations to remove, firstly, a primitive upper mantle (PUM) component leaving a core + lower mantle component and, secondly, to remove a core component, leaving a lower mantle composition. The PUM composition is asssumed to be, essentially, pyrolite, and the core-lower mantle system is assumed to make up 81.8% by mass. The resulting lower mantle composition obtained is presented in table 4.1_1 and is fairly similar to that of the solar composition of Anderson (1989) in its abundance of Fe although Si content and Ca/Al ratios are more similar to C1 chondrites.

The similarity of oxygen isotopic composition of the Earth with EH chondrites is compelling evidence to support the use of EH chondrites for modelling the Earth. It is considered here that it is perhaps a more likely Earth composition than C1 chondrites given that C1 chondrites seem to be be sourced from the asteroid belt (which lies between Mars and Jupiter). Although modelling of planetary accretion (Wetherill, 1994) suggests that the provenance of terrestrial planets is likely to incorprate the range 0.5 to 2.5 AU^2 (well beyond the range of the asteroid belt), Wetherill (1994) also attests that there exists a correlation between final heliocentric distance and *average* provenance. Mars is far more likely to have a C1 chondrite bulk composition than the Earth. It should be noted, however, that the carbon isotopic evidence from diamond which Javoy (1995) cites in his compositional model, relies on measurements made from coated stones. Such stones are unrepresentative of the diamond suite. Additionally, EH chondrites are very reduced: having very little or no oxidised iron. Such an observation contrasts markedly with the particularly large concentration of Fe^{3+} in inclusions from São Luiz diamonds, section 2.5.

Allègre et al.'s (1995) PRIMA model: Allègre et al.'s (1995) model also strongly relies on meteoritic considerations. As distinct from other models, however, no assumption of a particular chondritic corollary is made; only that the Earth follows meteoritic *compositional trends* (as Jagoutz et al., 1979). In addition (Ringwood (1989) model), Si is not regarded as behaving purely as a lithophile element, a certain degree of solution of Si into the core is allowed for. Allègre et al. (1995) assumes that the Earth has chondritic trends of non-volatile elements, the upper mantle and lower mantle have the same composition and the core comprises some 10-15 wt% of light elements. Calculations rely on a single important point: the ratios of strictly lithophile elements in the bulk Earth are the same as those of the mantle: and proceed as follows. Ratios of lithophile elements are determined for the most primitive of xenoliths (assumed to be primitive mantle and, according to the definition of Ringwood (1989), pyrolite). Ratios involving *non-lithophile* elements are then calculated by finding the intersection of lithophile element ratios with the chondritic trend. This procedure is carried out for all elements of interest which are then converted to weight percent using known values for lithophile elements in primitive mantle. The composition of the core is then determined by difference.

Representative bulk compositions: Table 4.1_1 summarises the major element compositions of ten rock types envisaged as being candidates for material penetrating into or comprising, the lower mantle. The reader will observe that Allègre's primordial mantle, PRIMA has essentially the same bulk composition as pyrolite (Jagoutz et al. 1979). All ten are used as a basis for comparison with the compositional data recovered from the present study of diamond inclusions and notably involve both crustal, established upper mantle rocks, and hypothesised bulk silicate Earth and lower mantle compositions. Representative cation values for each composition are presented in Table 4.1_1.

Table 4.1_1 Cation bulk compositions

	1 Pyrolite *	**2** PRIMA ‡	**3** C1 ∞	**4** Solar ¥	**5** Lherzolite †
Si	27.3	27.9	30.2	27.9	27.0
Al	2.9	2.9	2.6	2.3	1.5
Mg	34.6	34.0	32.3	30.2	38.4
Fe	4.0	3.8	1.6	8.1	4.2
Ca	2.3	2.1	1.8	2.3	1.2
Na	0.4	0.0	0.0	0.0	0.0

	6 prim-MORB ♣	**7** Harzburgite ♥	**8** Sediment ¤	**9** Eclogite ¢	**10** LM §
Si	29.9	26.3	37.4	28.6	31.6
Al	11.6	0.4	11.5	13.2	1.5
Mg	9.1	41.9	2.5	11.1	24.3
Fe	4.0	4.4	2.7	5.9	8.3
Ca	8.4	0.3	2.2	4.9	1.1
Na	2.3	0.0	1.3	2.4	

Cations are normalised to 100 O anions and are calculated from wt% data presented by: * Jagoutz et al. (1979), ‡ Allègre et al. (1995), ∞ Anderson and Bass (1986), ¥ Anderson (1989), † Maaloe and Aoki (1977), ♣ Green et al. (1979), ♥ Michael and Bonatti (1985), ¤ North American Shale Composite of Gromet et al., (1984) representing a bulk crustal composition, ¢ Kushiro and Aoki (1968), § Javoy (1995). Numbers in bold refer to bulk composition number used throughout relevent figures.

---

[2] 1 Astronomical Unit (AU) = 149.60 x 10^6 km, which is the average distance between the Earth and the Sun and is the basic unit of distance within the solar system.

Section 4.2 Mantle Geotherms

The reader will doubtless be familiar with the determination of geotherms within two frameworks[1]:

- Oceanic settings: for alkali basalts, values for the partitioning of, in particular, trace elements, between crystallising phases and basaltic melt, can indicate the degree of melting and thus the potential temperature (e.g. Fitton and James, 1986). For MORB and OIB, basalt chemistry can predict lithosphere thickness and potential temperature (White and McKenzie, 1989 and Ellam, 1992) and depth of formation (Latin and Waters, 1991).
- Continental settings: where experimentally determined geothermometers and geobarometers (O'Neill and Woods 1979; Mori and Green, 1985; Lindsley and Dixon, 1976; Ellis and Green, 1979; Nickel and Green, 1985; MacGregor, 1974) are used to determine the pressure and temperature of formation of coexisting phases in mantle and crustal xenoliths (Finnerty and Boyd, 1987) and inclusions in diamond (see Harris, 1992).

As more data on the temperature dependence of elastic properties of mantle phases is determined, it will be increasingly possible to obtain a direct, although non-unique, estimate of mantle temperature simply from measurement of the seismic velocity profile of the Earth. We are not, however, at this stage yet; at present, determinations of whole Earth geotherms lie within the realms of more indirect modelling.

As more data on the temperature dependence of elastic properties of mantle phases is determined, it will be increasingly possible to obtain a direct measure of mantle temperature simply from measurement of the seismic velocity profile of the Earth. We are not, however, at this stage yet; at present, determinations of whole Earth geotherms lie within the realms of more indirect modelling.

Modelling aproaches: Workers in this field have adopted a number of different approaches lying between two end-members:

- Models assuming adiabatic heatflow where temperatures are fixed at particular depths by reference to phase relations assumed to account for specific seismic discontinuities.

---

[1] It would appear that the deep sourced diamonds discussed here have been brought up to the surface in magmatic events, they would not have experienced any of the nuances of the geotherms modelled in these two frameworks: being quenched from high temperature, essentially, at low pressure. As such, no further discussion of cratonic geotherms is considered relevent. The interested reader is referred to the references presented.

- Models assuming particular physical properties and régimes of mantle convection, constrained by core/mantle and surface temperature only.

The Debye model (Brown and Shankland, 1981): From a thermodynamic point of view, temperature can be predicted with depth using a so-called Debye model. The Debye model predicts entropy from seismically determined S and P wave velocities, estimated mean atomic weight and compressional and transverse Debye temperatures[2]. From calculation of entropy at an estimated boundary temperature, temperature with increasing depth can be calculated assuming constant entropy. Brown and Shankland (1981) use this model and a first order approximation of adiabatic heat-flow to calculate temperature with depth. Their preferred boundary temperature at the upper/lower mantle boundary is 1873K based on experimental work on the break-down of ringwoodite to fPer + MgSiPvk at 22GPa. They assume no thermal boundary at this stage. From their calculation of density, they then calculate the difference in this density from that predicted by the Adams-Williamson equation (appendix 14) to investigate the effects of a non-adiabatic component. Their findings suggest that within the lower mantle an assumption of adiabatic heat flow is reasonable. In the upper mantle, however, most likely due to phase transitions, there appears to be a significant deviation from an adiabatic component.

Fluid dynamics models (Ritcher and McKenzie, 1981) and Solheim and Peltier (1992): Ritcher and McKenzie (1981) accept the geochemical evidence supporting a layered mantle (section 4.3) and investigate the physical conditions of mantle material which can both satisfy such criteria and the observed average surface heat flow of 4.2 x 10^{-2} Wm^{-2}. In terms of mantle viscocity and Rayleigh number, based on laboratory experiments, their findings are discussed in section 4.3. In addition, Ritcher and McKenzie (1981) attempt a quantification of the mantle geotherm. They use equations of fluid dynamics and related heat flow on 2-dimensional models involving a variety of boundary conditions. Application to the Earth involves dimensionalising the temperatures involved in their calculations, and combining a conductive surface lid, upper mantle heated from below and an internally heated lower mantle. Their results suggest that a temperature difference of around 500 K would be required between the upper and lower mantle in order to satisfy the initial assumptions of convection type and surface heat flow. By a similar technique to that adopted by Ritcher and McKenzie (1981), Solheim and Peltier's (1992) absolute temperature estimates are lower. However, on invoking a phase change at 670 km involving the physical properties of the breakdown of ringwoodite, they too observe a significant thermal boundary. Indeed, Solheim and Pelier (1992) favour the exisence of such a boundary dependent on constraints of time.

---

[2] The Debye temperature is a constant used in lattice dynamics, expressed in units of Kelvin, which is related to vibrational frequency by Planck's constant, Boltzman's constant and pi. It is one of a number of useful variables in lattice dynamics which aims to express elastic, thermal and structural properties of crystalline solids in a unified theory. Further discussion is presented in section 7.1.1.

Adiabatic heat flow model (Jeanloz and Ritcher, 1979): Jeanloz and Ritcher (1979) observe that adiabatic heat flow (e.g. Dziewonski et al., 1975) does not join the fixed points in temperature-pressure space which correspond to the interpretation of seismic discontinuities at 400 km, 670 km and 2900 km as breakdown of wadsleyite, ringwoodite and transition into the Fe core, respectively. They conclude that superadiabatic heat flow must be present within the Earth. On the basis of heat flux calculations, and using a value for surface heat flux of 5.85 x 10^{-2} Wm^{-2}, slightly higher than that adopted by Ritcher and McKenzie (1981), Jeanloz and Ritcher (1979) invoke a 100km thick thermal boundary at the base of the mantle to satisfy the lowest possible estimates of core surface temperature (2800K). A layer of such thickness has been identified and termed the D'' layer (eg. Jeffreys, 1937 and Kendall and Silver, 1996). Furthermore, Jeanloz and Ritcher (1979) advise that an additional thermal boundary layer, possibly at the base of the upper mantle, should also be invoked to satisify what were considered at the time to be more likely estimates of core surface temperature (3200 - 3500K). Since Jeanloz and Ritcher's (1979) work, more intermediary estimates of ~3000K for core surface temperature are favoured (e.g. Duba (1992) and Boehler (1993)) and are summarised in figure 4.4_24. Such temperature estimates are still in line with some thermal boundary at 670 km and, furthermore, it is interesting to note that the estimates of the thermal boundary at 670 km by Jeanloz and Ritcher (1979) are margionally higher than more recent estimates.

Précis of calculated geotherms: Eleven geotherms penetrating into the lower mantle predicted by ten authors are presented in figure 4.2_1 and here, despite some minor variations, two models of mantle geotherm can be clearly seen. One incorporates a thermal boundary at 670km in depth and the other lacks such a boundary.

- Models involving a thermal boundary layer (red in figure 4.2_1) in general, involve temperatures bounding 1700K throughout the upper mantle with a slight temperature increase around the 400 km seismic discontinuity (~ 14 GPa). Temperatures throughout the lower mantle straddle the 2500K mark. Additionally, with the exception of Spiliopouos and Stacey (1984), all authors advocate a *gradational* temperature change for the thermal boundary layer over a significant pressure interval corresponding to depths between 670 and 740 km.[3]
- Models lacking a thermal boundary layer (blue in figure 4.2_1) differ largely in the details of temperature against pressure in the region of the mantle lithosphere. As discussed previously, the thermal state of this area is not considered particularly relevent to erupted material such as the diamonds involved in the present study. From the base of the lithosphere (~ 5 GPa) temperature

---

[3] Appendix 14 and, in particular, equation A14_5 presents the accepted relationship betwen pressure and depth for the Earth's mantle.

is seen to rise smoothly from ~ 1500K and only reaches 2000K deep into the lower mantle (40 GPa +). The reader will note, however, that one particular geotherm does involve unrepresentatively low temperatures; that of Solheim and Peltier (1992). Their approach is purely mathematical and so is likely to be particularly sensitive to uncertainties in the few boundary conditions employed. It should be noted that their results are likely, however, to lie within the errors of other workers and so their data is incorporated into the following calculations.

Adopted geotherms: As a basis for calculation and observation, two model geotherms have been constructed. Details of the methodology adopted follow.

- Geotherm 1, involves a thermal boundary layer between the upper and lower mantle and comprises data from Wang (1972), Spiliopoulos and Stacey (1984), Jeanloz and Ritcher (1979) and Ritcher and McKenzie (1981). Furthermore, Geotherm 1 involves a relatively small decrease in temperature, compared to Geotherm 2, over the final few GPa from the Earth's surface. Such behaviour is typical of slowly rising magmatic bodies.
- Geotherm 2, involves no thermal boundary and comprises data from Solheim and Peltier (1993), Verhoogen (1980), Anderson (1982), Brown and Shankland (1981), Gasparik (1990) and Jeanloz and Ritcher (1979). Furthermore, Geotherm 2 involves a relatively large decrease in temperature, compared to Geotherm 1, over the last few GPa from the Earth's surface. Such behaviour is characteristic of rapid exhumation.

Both geotherms are presented in tabulated form in table 4.2_1 and graphically in figure 4.2_3 and it is these values of pressure and temperature which are used in conjunction with estimated bulk compositions to relate to phase relations discussed in section 4.4, and thermoelastic calculations undertaken in section 7.1.2.

Methodology: The methodology for the construction of Geotherms 1 and 2 is as follows. Data for each of the two geotherms was obtained from the papers outlined above either directly (ie. from tables presented by the authors) or indirectly (from measurement of figures presented). The individual data series were then subjected to piecewise interpolation as polynomial series to degrees for each segment appropriate to a best fit of >98%. For example, the data of Ritcher and McKenzie were fitted to four equations: polynomials of degree 1 for the ranges 6.5-23 and 28-40 GPa (both corresponding to an R^2 fit of 1) and polynomials of degree 3 for the ranges 0-6.5 and 23.5-28 GPa (corresponding to R^2 fits of 1 and 0.982 respectively). From the series of polynomial fits for each geotherm model, values of temperature were calculated at pressure intervals of 1GPa. For the data of Brown and Shankland (1981), Wang (1972) and Verhoogen (1980), extrapolation to 40 GPa was applied. The two average Geotherms 1 and 2 were then obtained simply by calculating an average temperature for each 1 GPa increment using values from each relevent work. In the case of Geotherm 2, due to the use of data from Verhoogen (1980) up to only 7 GPa, such an average calculation produced a drop in temperature at 8GPa, this problem was addressed simply by interpolating a 8 GPa value from data calculated for 7 and 9 GPa. A similar drop in temperature resulted for 27 and 28 GPa due to the application of data from Gasparik (1990) available up to 27 GPa. This was addressed in a similar fashion to that of 8 GPa.

Table 4.2_1 Temperature at selected values of pressure for Geotherms 1 and 2.

Pressure (GPa)	Geotherm 1	Geotherm 2	Pressure (GPa)	Geotherm 1	Geotherm 2
0	273	273	21	1865	1835
1	658	1048	22	1917	1847
2	1013	1286	23	1946	1861
3	1221	1386	24	2043	1899
4	1410	1452	25	2248	1912
5	1557	1507	26	2320	1922
6	1640	1553	27	2384	1924
7	1656	1594	28	2473	1927
8	1662	1600	29	2492	1931
9	1669	1607	30	2498	1939
10	1674	1628	31	2504	1947
11	1679	1648	32	2510	1954
12	1687	1674	33	2516	1961
13	1697	1701	34	2522	1968
14	1708	1725	35	2529	1974
15	1785	1748	36	2537	1980
16	1806	1769	37	2547	1986
17	1816	1785	38	2553	1993
18	1822	1799	39	2559	1999
19	1829	1812	40	2566	2006
20	1836	1824			

Temperatures are in Kelvin. Geotherm 1 includes a thermal boundary layer between 22 GPa (corresponding to the 670km discontinuity in the Earth) and 27 GPa whereas Geotherm 2 has no such boundary. Geotherms 1 and 2 are calculated according to the procedure outlined in the text.

Section 4.3 Mantle convection

The convective state of the mantle continues to be a subject of intense debate. A debate which has centred over the argument as to whether the mantle convects as a single unit (whole mantle convection) or whether the upper and lower mantle convect separately (2-layer convection).

Clearly, there is *some* difference between the upper and lower mantle; the terms upper and lower mantle were coined due to the observation of a discontinuity in the velocities of seismic waves travelling across 670 km in depth, (Johnson, 1967). However, the burning issue is, is this seismic discontinuity, more tangibly, an actual impediment to vertical transport and an indication that upper and lower mantle are fundamentally different (both in terms of composition and physical properties)? Increasingly, it is becoming clear that, the question cannot be answered without consideration of the additional variables of time and volume of material to be transported. Although two separate schools of thought still exist, many of their contrary arguments are not entirely comparable; dealing, as they do, with different timescales and quantities of rock.

The 670km discontinuity: Firstly, what causes the 670 km discontinuity in seismic velocities?:

- A change in bulk composition between upper and lower mantle

  It has been difficult to test this possibility without directly observable material, although the diamond inclusions which are the subject of the present study can be considered to shed some light on this question (section 4.4.2). Those attempting to tackle the compositional question have, primarily, relied upon source region modelling. This uses mantle partition coefficients to calculate a source composition from magmatic rocks (in particular MORB) and, by mass balance, estimates the volume of source region required to have been the residue from crust formation from either a bulk silicate Earth (BSE) or meteoritic composition (eg. C1 chondrites). Such an indirect approach incorporates large uncertainties in liquid/mineral partition coefficients and bulk compositions. However, it is generally[1] concluded that about 1/3 of the volume of the mantle[2] (Anderson and Bass, 1988) is required to have formed Cc and depleted the residue to the degree observed. Such calculations favour two distinct layers bounding at ~670 km in depth.
- Conversion, with increasing pressure, to high density polymorphs and assemblages of upper mantle phases would cause a jump in seismic velocities and rheological parameters.

  Birch (1952) was first to tackle the hypothesis that the 670 km discontinuity is due to phase transitions in mantle minerals. He used calculations based on the elastic properties of mantle

---

[1] Birch (1961) used a moment of inertia approach to estimate a mean atomic weight throughout the mantle and found this to be fairly constant throughout. In light of contemporary data, however, his conclusions must be regarded with caution.

[2] Although Sun and McDonough (1989) suggest that mass balance *may* require upwards of 50% of mantle to be depleted.

minerals as were known at the time and, although founded on poor data, his conclusion that the breakdown of olivine composition to fPer and $MgSiO_3$ is consistent with the seismic anomaly at 670 km remains fundamentally the same as that of today (early experimental evidence was supplied by Ringwood, 1970). Recent advances in experimental petrology (section 4.4) in the measurement of physical properties and phase relations in mantle systems, in addition to numerical approaches (section 7.1.1) under relevent conditions of pressure and temperature, has revolutionised our ability to understand the deep Earth and the nature of the 670 km discontinuity in particular. Results show that, although we cannot be sure of the composition of the mantle, strikingly, no matter what reasonable composition we consider, phase transitions abound around the 22 GPa mark (~670 km in depth), section 4.4.1.

It is the contemporary view that the 670 km discontinuity corresponds to a region of phase transformations and there are indications that compositional differences also are involved. Given the degrees of uncertainty which exist, however, we cannot conclude any state of mantle *convection* without further evidence[3]. This evidence falls within three general frameworks. A purely physical approach of modelling viscous flow in mantle-type systems, an observational geophysical approach and a geochemical approach. Useful reviews can be found in Davies and Richards (1992), Olson et al. (1990) and Ringwood (1989): the following discussion aims to present the salient points.

Physical Modelling Approach: The modelling approach to address the question of mantle convection has taken two routes. A purely mathematical and a practical experimental approach.

Experimental approach: Tanks of viscous fluid[4] subjected to basal heat flux (eg. Richter and McKenzie, 1981) can be made to produce different styles of convection (and plume flow e.g. Campbell et al., 1989). Richter and McKenzie (1981) found that whether two-layer or single layer convection occurred in glycerine-water tanks depended on the combination of both thermal and density difference Rayleigh numbers[5] of the fluid layers. Large density differences promoted *layering*, whereas, if the density difference was small, *mixing* would occur. Temperature dependence was such that if the temperature was too low, no motion occurred, and if the temperature was too high, even large density differences could not prevent mixing. Fluid tank experiments have much value in their ability to act as a springboard for looking for observations of particular convective phenomena. Due to their large scaling problems and the fact that the topography of such experiments

---

[3] As the following discussions will show, there is compelling evidence from São Luiz associations of a bulk compositional difference (section 4.4.2.5) of sufficient density (section 4.4.2.7) and thermal contrast (section 4.5.1.2) between upper and lower mantle, to promote separate convection.

[4] Which approximate to physical properties of mantle material, scaled down in terms of time and volume.

[5] The Rayleigh number is a constant for a fluid system which is particularly valuable in indicating the propensity for convection. Essentially, it is a ratio of bouyancy force, which favours convection (in terms of gravitational acceleration, thermal expansivity and temperature and depth difference), and viscocity drag, which inhibits convection (in terms of kinematic viscocity and thermal diffusivity). For a both internally and externally heated body, the critical Rayleigh number for convection is of the order of 2000.

cannot mimic the 3-D framework of the Earth, they cannot be reliably used to answer questions of mantle flow.

Mathematical modelling: Mathematical modelling uses viscosity and temperature profiles considered pertinent to the Earth in order to assess time dependent motion of mass. Techniques have been constricted in the past by computational limitations to 2-D rectangular sections (Richter and McKenzie, 1981; Çadek et al, 1994; Steinbach and Yuen, 1994; Nakakuki et al, 1994) and 2-D circular sections (Solheim and Peltier, 1993) however, modelling on 3-D cuboid torroidal/spherical volumes (eg. Bunge et al, 1996) has recently been achieved; the latter case being, clearly, most analogous to the Earth. The results of numerical modelling have both simulated whole mantle convection (Çadek et al 1994), layered convection (Richter and McKenzie, 1981; Bunge et al 1996) *and* partially layered convection (Solheim and Peltier, 1993) in addition to modelling particular types of plate motion such as the buckling observed in some tomographic studies. Differing conclusions perhaps indicate that the system is critical, small physical variations causing a switching in convective style. The consensus of mathematical modelling work appears to be that the larger a thermal anomaly the greater the likelihood that it can cross the 670km boundary. Additionally, a common feature is the catastrophic collapse of ponded material with so-called 'flushing' events periodically sweeping large masses into the lower mantle. Particular controversies involve uncertainties in the values and distributions of physical parameters (particularly viscosity). If one was to take a cynical approach one could envisage the picking of reasonable values for these parameters which would fit any preferred convective model.

A further mathematical approach investigates the need for a thermal boundary layer (and thus, separate convection) at 670 km and is discussed in the context of mantle geotherms (section 4.2). Jeanloz and Richter (1979) and Elasser et al. (1979) tend to conclude that a situtation involving both a thermal boundary layer at 670 km in addition to one in the D″ layer is not essential to explain surface heat flow, but may be preferred. Again, however, any conclusion is dependent on many uncertainties such as the size of the D″ layer and the specific value of core/mantle boundary temperature.

Geophysical approach: The geophysical approach has been principally within a seismic framework. The velocity of seismic waves through a body, depends on its temperature; cold bodies, comprising minerals with higher elastic potentials, propagate waves through them at a greater velocity. Two seismic approaches have been followed: a residual sphere approach and, more recently, a tomographic approach. Two scales are investigated:

- Locally, by attempting to trace the paths of large, cold, downward travelling plates through the mantle, in an attempt to determine whether or not they penetrate the 670 km discontinuity.

- Globally, by attempting to detect cells of upwelling, hot and downwelling, cold material.

Residual Sphere approach on a local scale: The residual sphere approach involves the collation of arrival time data, measured by a spread of Earth-based seismometers for deep earthquakes located in the area of interest. Given the magnitude and location of each earthquake, and using a starting model of a homogeneously stratified Earth, arrival times for appropriate downward dipping waves (less than 60° deviation from vertical) are then calculated. The difference in travel times between observation and prediction are then calculated and plotted on a spherical projection according to the angle of the ray path: i.e. in a similar fashion to the plotting of focal mechanisms. Any residual (deviation from prediction) indicates an inhomogeneity of seismic wave velocity somewhere along the raypath and most likely near to the earthquake. The shape and inclination of such inhomogeneity can be inferred from the distribution of residual arrival times. An earthquake located well within the sphere of influence of a downwelling slab would plot as a negative residual band across the centre of the spherical projection at an angle to north depending on its strike. As the technique images *downwards*, an earthquake located at the bottom of a slab would show no residual. Using data from ~600 km deep earthquakes around the Japan Trench, however, Creager and Jordan (1984), *did* see residuals consistent with further downflowing cold slab material. Slab penetration depth models which fitted best their observed residuals, involved penetration to greater than 1100 km, well into the lower mantle[6]. From these results it was inferred[7] that the mantle could not be regarded as a simple two-layer convective system as was assumed at the time.

Tomographic approach on a local scale: The technique of mantle tomography for observing seismic anomalies has developed with the advent of super-computing techniques. Arrival times for tens of thousands of earthquakes from hundreds of stations stretching back some twenty years have been collated. These data are compared to predictions based on homogeneous spherically symmetrical Earth models, to determine mantle seismic heterogeneities on both a whole-Earth and more localised slab-sized scale. Resolution is still poor: ~100 km laterally and 50 - 200 km vertically and deviations of slowness (the inverse velocity scale which is commonly used) are small (~0.1 to 1% and usually ~0.5% for the lower mantle). Even so, some studies appear to show clear penetration of material into the lower mantle. Furthermore, as image quality has improved such that interpretation is less a matter of personal preference, it would appear that subducting plates exhibit a wide range of behaviour with respect to the 670 km boundary. Some plates pond on the 670 km discontinuity, others are deviated along the boundary, whereas, others still, penetrate (with differing degrees of

---

[6] It is difficult to image to greater depth for earthquakes of upper mantle depth because emanating waves fan out and, eventually, will no longer propagate significantly within the slab.

[7] The technique of residual sphere analysis, however, is not without its problems; signatures from close to individual seismic stations could produce residuals of the type seen, particularly, as is the case for some of the older seismic data, if the spread of teleseismic stations is poor and involves a poor spread of location type, i.e. cratonic, oceanic etc. In an attempt to address this problem, Ding and Grand (1994) have used their own shear wave arrivals for two earthquakes sharing the same epicentre but with different focal depths to investigate the Kurile subduction zone. Their results show similar penetration below 670km.

deviation) across 670 km. For example, the subducted Marianas plate appears to have buckled into tight folds at 670 km (Davies and Richards, 1992) where different parts of the same plate behave differently[8] on reaching a depth of 670 km (eg. van der Hilst 1995). Additional it appears that slow moving plates tend to penetrate the lower mantle, whereas fast plates appear less likely to (van der Hilst, 1995). This scenario would appear to fit the thermodynamics of a 670 km boundary determined by the endothermic break-down of olivine composition to fPer and enstatite composition although this has been contested recently, as discussed later. The reaction will occur at a greater depth in a cold plate than in the surrounding mantle (eg. Ito and Takahashi 1987) and so may act against subduction of cold material for approximately 60 kilometres of the upper mantle (assuming a temperature difference of 200K). In the case of fast moving plates, sufficient time to allow equilibration on subduction may not be forthcoming, the depth of elevated bouyancy for such plates would, therefore, be greater thus further inhibiting subduction.

One major problem is common to all of the above discussion: seismic tomography studies in the mantle respond principally to *temperature* anomalies. In order to reach the conclusion that, rather than their temperature extensions, the *slabs themselves* penetrate into the lower mantle, one must assume that what is imaged with tomography is the actual cold plate. Modeling has shown that, under certain conditions, conduction rather than penetration could occur (Ellsworth and Schubert, 1988). However, the lower mantle is still considered to be a viscous fluid over geological timescales. Employing expected values of viscosity (some 30 times, or more, that of the upper mantle; Hager and Richards, 1989; King and Masters, 1992), if one was to expect a downfalling plate to stop at 670 km and conduct with its surroundings, one would expect a hot band to be stabilised below the cold plate. Such observations are not made. Additionally, using thermodynamic considerations, Stacey (1995) is adamant that “tomographic velocity models are not simply explicable as thermal effects”. Furthermore, the fact that the lower mantle is considered to be more viscous than the upper mantle would act at least to considerably slow down a down-flowing plate. If the *plate itself* was to penetrate 670 km, then mass balance dictates that it must thicken up. Although resolution is such that imaging into the lower mantle can, to some degree, still be said to be speculative, it does appear that plates penetrating 670 km do thicken up (Davies and Richards, 1992). Further evidence to support plate, rather than thermal penetration, comes from comparison of tomographic images with the predicted

---

[8] This differing of behaviour within a plate has been interpreted as being linked to ‘roll-back’ of the subduction zone. The surface manifestation of subduction zones tends to propagate against the direction of the subducting plate to varying degrees even within the same plate. In the case of the Izu-Bonin-Mariana subduction, the Izu-Bonin part of the Pacific plate has experienced a large degree of roll-back. Here, the plate is interpreted as being laid along the 670km discontinuity as the subduction zone proceeds in the opposite direction. Where the force of the downgoing plate is directed less sinuously, such as the case in the Marianas, subduction is seen to penetrate the 670km boundary and roll-back is observed to be less significant (van der Hilst and Seno, 1993 and van der Hilst, 1995). A similar interpretation fits the observations of the Tonga-Kermadec trench system (van der Hilst 1995) although this is an anomalous system due to its young age and complex history of surface plate movement (Isacks and Molner 1971). It would appear that roll back and 670km penetration is a ‘chicken or egg’ type debate. Either this interpretation implies that the plate behaves on subduction according to the surface movement of the plates or roll-back is dictated by the specific resistance of subduction into the lower mantle, i.e. if a plate buckles it produces roll-back (eg. Hawkins et al., 1984). Since, as has been concluded for oceanic settings, plate movement is not forced by influx of material at ocean ridges rather it is propagated by plate-pull (McKenzie and Jarvis, 1980), the latter interpretation is favoured.

location of long-ago subducted slabs (eg. Çadek et al 1994). Using values for expected subduction rate (involving an order of magnitude slowing in the lower mantle) and angle of subduction, and assuming non-deviation at 670 km, the present location of the old sub-N. American Pacific plate has been calculated (Grand, 1994). This was found to fit a fast anomaly at a location in the lower mantle below the eastern seaboard of the U.S.A. which would have quickly dissipated had it been a solely thermal relic.

Tomographic approach on a global scale: Whole Earth imaging looks at an altogether different scale from that of individual slabs. Seismic tomography has imaged velocity anomalies varying over some 4 % in bodies of dimension 500 km +. (eg. Hoernle et al 1995). Furthermore, such anomalies often appear to extend across the 670 km region thus supporting whole mantle convection on a large scale (eg. Cadek et al 1994). As for the subducting slab debate, there appear to be both a range of observations either supporting cross 670 km flow or supporting ponding; no doubt the end product is dependent on the physical conditions pervasive in differing regions. In terms of origin, Stacey (1995) would argue that such if tomographic features are purely thermal, such large temperature differences would lead to larger geoid anomalies than observed and unreasonably rapid convection. Thus Stacey’s reasoning would suggest that some large scale convective movement occurs across the 670 km discontinuity.

Another key discriminant of mantle convective régimes is that of radial flow. If radial flow is found to slow at around 670 km, this would be good evidence for two convective régimes. Radial flow can be determined by using accepted tomographic models of shear wave velocity, inverting to density maps and applying to models of viscosity with depth. Morgan and Shearer (1993) found that radial flow exhibited no decrease near to 670 km. In addition, although some dynamic topography can be resolved in velocity at 670 km, such topography is thought by these authors to be too little by two to four times to prevent whole-mantle convection.

Additional lines of evidence: A further geophysical technique used in resolving the mantle convection question has involved geoid anomalies. Thoraval et al. (1995) feel that there is strong evidence from dynamic topography for localised layering of convective flow. The shorter wavelength inhomogeneities predicted from tomographically observed mantle density variations, would create localised geoid anomalies which do not fit with observation. Most tomographic models do not, however, involve density anomalies affecting topography on mantle boundary zones; the resolution of Earth-scale tomography being too poor. For the 670 km zone, as it is believed to involve an endothermic phase change, a negative topography would be produced by downwelling (cold) material (e.g. Schubert et al., 1975). This, in turn, would affect the short wavelength geoid. Thorval et al. (1995) predict a corrected geoid on the basis of expected topography and find that such correction fits geoid observations far better than uncorrected tomographic observation[9]. In fact, they apply their technique, specifically to the Izu-Bonin-Mariana subduction system and, unlike an uncorrected tomographic system, where all slabs would descend into the lower mantle, the Izu-Bonin buckles, whereas the Mariana appears to penetrate directly; in line with seismic evidence (eg. Creager and Jordan 1984).

In all, it would seem that subducting plates are subjected to a play-off between factors encouraging and discouraging penetration below 670 km.

Geochemical approach: The question of mantle layering, and thus, convection, has been addressed by using both observational and experimental determination of bulk composition and finer details of stable isotope and trace element composition. Such methodology has at its root the question of; subsequent to core formation, has the mantle evolved as a single body or has it evolved in largely separate régimes? It should be noted that such debate adopts, yet again, a different timescale and, therefore, direct comparison with results from plate modelling and whole Earth tomography should be treated with caution.

Trace element approach: Historically, OIB has been assumed to have a lower mantle source and MORB an upper mantle source. In theory, differences between them, could reflect compositional differences between upper and lower mantle. Recently it has become clear that this is not a realistic approach. Some authors have inferred a source for OIB in the central, enriched portions of upper mantle convecting cells (e.g. Herzberg, 1984 using Nd, Sr and Pb systematics). Noble gas measurements (eg. Hart and Zindler 1988) suggest that OIB and MORB are very separate sources, some OIB sources being less strongly degassed than MORB and thus more primitive but this may only mean that OIB is commonly sampling a *less evolved* region of the mantle rather than the *lower* mantle. In general, the study of radiogenic signatures of OIB has shown a wide compositional range often indistinguishable from MORB. Plotting radioisotopes of Nd, Pb and Sr for a wide variety of OIB and MORB samples (Davies and Richards, 1992), would suggest the mixing of at least five different source regions. Such observations suggest that the mantle is fundamentally heterogeneous and one cannot hope to look to simplistic scenarios such as OIB as a 'primitive' i.e. lower mantle, sourced material and MORB as a depleted upper mantle material. Indeed, simply from looking at a plot of Nb/U against Nb (eg. Hofmann, 1986), OIB does not lie between MORB and C-chondrites. An additional problem with OIB material, is the role of contamination. OIB is commonly employed for study of hot-spot material rather than CFB, because of the danger of crustal contamination of the latter. The role of sea-water in the former, however, represents an significant unknown quantity.

---

[9] In detail, Thorval et al.'s (1995) correction procedure over-shoots the observed short wavelength geoid anomaly values, providing values smaller than observed. This, they feel could be accounted for by a slight negative topography at the 400 km discontinuity.

By a separate approach, O'Nions et al. (1979) use values of Nd, Ar and Sr isotopes and Jacobsen (1988) uses Sm-Nd, Lu-Hf and Rb-Sr systematics from chondrite for bulk Earth (elements unaffected by core formation) and measurements from sea-water and crustal materials for estimates of crustal composition. By mass balance, both studies find that a 0.5 by volume mantle source for the crust fits their observations most satisfactorily[10]. Further work has been undertaken by Snyder et al. (1993) who observe that measurements of Nd and Sr systematics in Yakutian diamondiferous eclogites (all sampled from the upper mantle) indicate two trends of radiogenic evolution. This observation is consistent with an early (4 Ga) departure from predicted bulk Earth radiogenic evolution which, by difference would suggest no prior differentiation such as would separate upper from lower mantle.

An additional trace element approach regards noble gases. It has been observed that the $^{40}Ar/^{39}Ar$ ratio for MORB is much greater than that of sea water and the atmosphere which suggests early degassing of ‘MORB’; a popular Earth evolution model supported by workers such as Javoy (1995). An elevated ratio is not, however, observed for OIB. This suggests that the OIB reservoir has behaved differently from the MORB reservoir. Furthermore, OIB shows a range of $^{3}He/^{4}He$ ratios substantially enriched in ^{3}He[11] which are primitive Earth characteristics. As described above, however, whether the OIB source area can be considered to be associated with the lower mantle remains unclear. What is clear from geochemical studies of mantle material, is that the mantle is heterogeneous, not just in a thermal sense, as tomography indicates, but also in a compositional sense.

Bulk chemical approach (experimental): Perhaps the primary chemical argument regarding the state of mantle convection, and, specifically, penetration of subducting slabs below a depth of 670 km centres around the breakdown of ringwoodite to MgSi-Pvk + fPer. Whether or not this reaction is the sole reason for the 670 km discontinuity or not is not the issue here. What is important is that this reaction almost certainly occurs in the region of 670 km in depth. How it affects subducting slabs has been a matter of debate. The reaction is endothermic (Ito and Takahashi, 1989; section 4.4.1.1) and so is expected to occur at greater depth within cooler material such as subducting slabs. Intuitively, and this is the conclusion reached by workers up until recently, one would expect the relative bouyancy of unreacted slab material to act *against* subduction (the opposite being true for the exothermic conversion of olivine to wadsleyite around 400 km). However, as has been argued by Solheim and Peltier (1993) the latent heat release has a greater positive influence on subduction than the negative effect of deflection of the phase boundary. Another factor encouraging

---

[10] This is a fairly contestable point, however. Some authors (eg. Hart and Zindler, 1988) would attest that the assumption of any particular BSE isotopic ratio is a 'weak link'. Additionally, mass balance calculations assume that continental crust is the only enriched reservoir (MORB being its compliment). Kimberlite, OIB, and other alkali basalts may also indicate a source region complimentary to MORB and thus, suggest a larger depleted MORB source than the above calculations predict (Anderson, 1981).

[11] Indeed it is the enrichment of ^{3}He above even ‘planetary’ quantities which lead Honda et al. (1993) to conclude that the Earth has a solar composition.

subduction from a mineralogical perspective is that. being cold, plates are rigid and thus more likely to continue on their upper mantle trajectories. Furthermore, Karato et al. (1995) believe that garnet resists plastic deformation (a view contested by Cordier et al., 1996), which implies that if slabs involve significant garnet they could be considered more rigid still.

A longer timescale, Earth evolution approach, favours two layer convection. The largest density contrast between melt and common ferromagnesian minerals appears to occur in two zones in the Earth; near to the surface and in the range 650-700 km (Herzberg, 1984). If it can be assumed that the Earth was mostly molten after core formation then clearly, in a transitional period between supersolidus convection and present day viscosity (probably around 3.5 Ga when the first crustal material separated; Herzberg, 1984), separation of density contrasting phases would be quite conceivable. Following this argument, chemical stratification of the Earth around the upper mantle/lower mantle boundary would have been likely. Ferromagnesian minerals such as olivine composition and the lower mantle assemblage of fPer + MgSiPvk would have separated from a more Fe-rich Si-poor melt supporting separate mantle convection in the early Earth. If such a simple thought process is continued to the present day, one can imagine that with cooling, the mantle Rayleigh number would be smaller at present (higher viscosity) favouring, even more, mantle stratification (cf. Ritcher and McKenzie, 1984), a point, however, that Solheim and Peltier (1993) would contest.

Bulk chemical approach (observational): Another supporter of chemical stratification of the mantle and thus, predominantly, two-layer convection is Anderson (1989). His model of a solar composition for the lower mantle is discussed in detail in section 4.1 and centres upon the adoption of a solar composition rather than a C1 chondrite composition for the Earth.

Comparing densities obtained from seismic studies with those calculated for lower mantle assemblages based on an estimated upper mantle bulk composition, Jeanloz and Knittle (1989) come firmly down on the side of a compositionally stratified mantle. They feel that the observed lower mantle is at least 2.6 % more dense than what would be expected from a lower mantle of upper mantle bulk composition. Such an argument inherently involves uncertainty over upper mantle composition and thermal state. Jeanloz and Knittle (1989) use a model where there is no significant thermal boundary at 670 km[12]. If they were to have employed a thermal boundary mantle geotherm, however (see section 4.2) their estimates of lower mantle density would have been even lower; invoking a bigger discrepancy with observation. This would suggest, therefore, that there is strong validity to their work.

---

[12] However, as discussed later, Price et al. (1989) using the same data are more in favour of layering.

A further conclusion regarding compositional difference comes from work by Duffy and Anderson (1989). They match observed S and P-wave velocities for the whole Earth with predicted values for mantle phases. As is clear from their figures 5 and 6, significant components of stishovite and corundum are required to balance input from CaSiPvk, fPer and MgSiPvk in order to provide a bulk composition in the lower mantle which fits observation: the upper mantle seismic variation is satisfied purely by mixing ferromagnesian minerals.

Other authors prefer a non-stratified Earth. Using the assumption that 'primitive' peridotite xenoliths can be used as representative of the silicate Earth, Allègre et al. (1995) determine the composition of the core by the method outlined in section 4.1. They then conclude that since their predicted iron content for the core fits with seismic observations, then their assumption that the lower mantle does not have a higher iron content than the upper mantle, must be correct.

Summary and conclusions: Clearly the debate of mantle layering and convection is far from solved. The actual state of mantle convection appears to lie in neither the 2-layer nor the 1-layer camp. In addition to the individual problems inherent in the multitude of techniques used to infer mantle state, there is the problem, as alluded to previously, that the results of different techniques are not always comparable; dealing as they do with differing volume and time scales and indeed different snapshots into the evolution of the planet.

A fair summary of the present concensus is exemplified by the following. From the point of view of phase relations, Price et al. (1989) argue that the gradient of the negative Clayperon slope governing the breakdown of ringwoodite to fPer + MgSiPvk would on its own act as only a weak barrier to subduction however, in addition, a density difference of about 2.5% is predicted. Price et al (1989), therefore, recognise the role of plate penetration whilst envisaging, on the whole, merely a *leaky* mantle. Whatever, the method of reasoning, the important point here is the conclusion. The 670 km zone, on the timescale of plate motion, does represent a significant boundary to cross movement. In some circumstances, however, material, if forced enough, or accumulated for long enough, *can* penetrate into the lower mantle. The corollary is true as will be seen in discussion of mantle plumes, section 7.3.1, in that, given sufficient thermal energy or gravitational instability, material can flow upward through the 670 km boundary[13]. Under such a time-scale, convection is likely to be dominated by a two layer mantle régime. On longer timescales, however, it would appear that there is some large scale mass movement across 670 km but not on the scale of true mantle mixing. The lower mantle and upper mantle for most cases can be regarded as distinct but 'leaky' layers.

---

[13] The very existence of lower mantle sourced diamonds as discussed herein is strong evidence for cross 670 km transport.

Section 4.4 Phase relations in mantle systems and the source of São Luiz and Guinean diamonds

A total of 9 mineral associations have been identified on the basis of coexisting phases from São Luiz diamonds[1] (section 2.3). In order to identify the probable depth of formation for these associations, one must look to the results of experimental petrology and mathematical modelling. It has only been relatively recently that the technical ability (experimental and computational) to emulate conditions at pressures and temperatures of the lower mantle, the region from which, as will be discussed in section 4.4.2, many of the São Luiz and Guinean diamonds are sourced, has become available. Numerical techniques are described in connection with the determination of physical properties of minerals in section 7.1.1, the following outlines the salient points of experimental approaches.

The diamond anvil cell (DAC) revolutionised high pressure-temperature research when it appeared in the 70's and now allows pressures and temperatures up to 200 GPa, 4000K (eg. Boehler 1993) to be achieved. Early work included that of Liu (1974, 1975, 1976a,b and 1978), Liu and Ringwood (1975), Yagi et al. (1978) and Bell et al. (1978). Present techniques are reviewed in Angel et al. (1992). Pressure calibration is accurate[2] but even with the most up to date laser technology, uncertainties in temperature are large (often ~800K, see, for example, Kesson et al., 1995), as are temperature gradients; indeed some workers (eg. Malavergne et al., 1997) rely on grain size of run products as a better indicator of temperature than laser power! The problem of temperature inaccuracy is being addressed by some workers (Zerr and Boehler, 1994) by the use of CO_2 lasers rather than the more traditional YAG laser. However an additional problem is that diamond anvils and, thus, sample sizes, are small.

Recent advances in multi-anvil techniques initially developed in the 60's by workers such as Ringwood (1967) have appeared. In the past, multi-anvil experiments have been limited by the unsuitability of the technique for in-situ measurements and by the low temperatures and pressures[3] attainable. Most multi-anvil experiments run at lower mantle pressures fall short in temperature by 200K, or more, below even the coolest of likely geotherms (as can be seen from mantle geotherms plotted on the multitude of phase diagrams presented in section 4.4.1). The development of higher grade tungsten carbide, however, allows for more extreme physical conditions to be emulated (eg. 30 GPa, Kato et al., 1995 and 22 GPa, ~2500K, Gasparik, 1990) and, more recently, sintered diamond

---

[1] Inclusions from Guinean diamonds fit into two of these associations.

[2] Although some doubt as to the reliability of ruby as a calibrant at extremely high pressures (> 90 GPa) has been raised, due to the discovery of a phase transition at around this pressure (Cynn et al., 1990)

[3] Up until the late 1980's pressure attainable were of the order of 22 GPa.

polyhedra as a pressure transmitting medium (eg. Chopelas et al., 1994, Yagi et al., 1994, Funamori et al., 1996 and Kato et al., 1996) has allowed for the use of laser heating and in-situ X-Ray techniques. It would seem likely, therefore, that at shallow lower mantle pressure, the most reliable future results will appear from multi-anvil techniques.

The fact that significant advances have been made in terms of our understanding of the deep Earth, through experimental petrology, is unquestionable. Given the shortcomings outlined above; the inevitable result of working at the practical limits of the science; careful consideration is applied before drawing particular conclusions. For example, experiments conducted at a particular pressure cannot, necessarily, be assigned to particular depths if temperature is inappropriate and questions regarding the presence or absence of particular phases in the mantle cannot, necessarily, be answered if bulk compositions are inappropriate.

In the following sections, a summary of the results of published phase determinations in a number of systems is presented (section 4.4.1). Appendix 12 summarises the details of starting materials, apparatus, run products, run product determination and physical conditions involved in over 100 experiments used to compile the phase diagrams discussed. The reader will find reference to this database useful in assessing the uncertainties involved in individual experiments and their relevence to mantle conditions. Conclusions are subsequently compared with compositional data from deep mantle inclusions in section 4.4.2.

➠

Section 4.4.1 *Phase relations in the earth's transition zone and lower mantle*

The following sections outline only the particular details of mantle phase relations which are considered relevent to the conditions of mantle pressure and temperature. For additional information, the reader is directed to the accompanying phase diagrams compiled from the literature. Sources of data are given on phase diagrams on which are plotted Geotherms 1 and 2 where applicable.

Section 4.4.1.1 The system MgO - FeO - SiO_2

Phase relations involving enstatite composition: Figure 4.4_1 presents phase relations determined for the end member $MgSiO_3$ in terms of pressure and temperature. Transitions along Geotherm 1 and Geotherm 2 comprise:

- orthorhombic $MgSiO_3$ (opx) to C2/c monoclinic structured $MgSiO_3$ at ~7 GPa (1500K).
- C2/c monoclinic structured $MgSiO_3$ breaks down to modified spinel structured Mg_2SiO_4 olivine polymorph (wadsleyite) + stishovite at approximately 18 GPa (1600K).
- At approximately 20 GPa (1600K), the free energy of ilmenite structured $MgSiO_3$ (MgSi-Ilm) becomes lower than the assemblage of wadsleyite + stishovite thus stabilising this phase[1].
- MgSi-Ilm[2] breaks down to MgSi-Pvk[3] at approximately 25 GPa (1650K).

  At still lower temperatures, a phase field involving spinel structured Mg_2SiO_4 (ringwoodite)[4] + stishovite appears.

All the above polymorphic transitions have positive slopes in P/T space (with the exception of the stabilisation of MgSi-Ilm which appears to be largely independent of temperature[5]). Indeed, in terms of transition pressure, all transitions are *significantly* temperature dependent. This means that, if one assumes, that any of these phases are stable within a mantle bulk composition, where they occur in terms of depth, depends strongly on the position of the geotherm. Figure 4.4_1 incorporates representation of the two model geotherms, of section 4.2. It would appear that even incorporating a thermal boundary, in the $MgSiO_3$ system, temperatures are likely to be too low to stabilise majorite (MgSi-Grt).

Phase relations involving enstatite - ferrosilite composition: The addition of Fe has a profound effect on a number of phase relations involving $MgSiO_3$ (figure 4.4_2). Experimental determinations (see figure 4.4_2) have involved temperatures of the order of 1273 - 1373 K which are patently too cold to be directly applicable to mantle conditions. However, they serve well to demonstrate the influence of Fe on the system.

Approaching pressures of 24 GPa, phase relations are particularly complex. The addition of significant FeO begins to stabilise MgO-FeO (fPer). Firstly, for $FeSiO_3$ composition at 16 GPa

---

[1] On the basis of numerical modelling, Navrotsky (1987) would argue that the free energy of wadsleyite + stishovite is smaller than that of MgSi-Ilm in only a restricted field at lower temperature, figure 4.4_1.

[2] MgSi-Ilm has recently been observed occuring naturally in meteorites by Sharp et al. (1997) and subsequently by Tomioka and Fujino (1997).

[3] The first occurrence of MgSi-Pvk was recorded from the Tenham meteorite by Tomioki and Fujino (1997).

[4] First discovered experimentally by Ringwood and Major (1966), the name being proposed by Binns et al. (1969).

(1273K) the assemblage ringwoodite + stishovite breaks down to fPer + stishovite. With increasing Mg content, this transition occurs at increasingly higher pressure, and the phase field of fPer + stishovite + ringwoodite shrinks. It breaks down altogether with the stabilisation of MgSi-Ilm at > 80 mol % MgO and is bounded at high pressure by the final breakdown of olivine composition on the stabilisation of MgSi-Pvk. The stabilisation of MgSi-Pvk is relatively independent of Fe content. and occurs at 20 GPa (1273K) however occurs at increasing pressure with increasing temperature (figure 4.4_1). Up to 10 mol% FeO can be completely accommodated within MgSi-Pvk at ~ 30 GPa which increases with pressure such that at 80 GPa, $Mg_{0.25}Fe_{0.75}$Si-Pvk is stable (a tendency which may be reversed at yet higher pressure). With the addition of further Fe, fPer and stishovite is stabilised such that, finally, for bulk compositions involving ~60 mol % $FeSiO_3$ (20 GPa, 1273K), MgSi-Pvk is no longer stable.

Figure 4.4_3 summarises, in more detail, the temperature effects on phase relations of the $MgSiO_3$ - $FeSiO_3$ system over the 20 - 22 GPa region. High temperatures (~2200K, 20 GPa, above Geotherm 1) are required to invoke stabilisation of MgSi-Grt (majorite) which is inhibited by the presence of Fe. Furthermore, Kato (1986) found the *structure* of majorite to be dependent on Fe content. Below ~ 20 mol % FeO, although broadly of a garnet-type structure, majorite is pseudo-cubic (tetragonal), it is only with the addition of significant Fe that a higher symmetry (cubic) structure is stabilised.

Phase relations involving forsterite composition: Olivine composition phases are stable throughout a very large range of pressure and temperature (figure 4.4_4), corresponding to depths throughout the upper mantle. Throughout this range, Mg_2SiO_4 exists as three polymorphs; olivine, modified spinel-structured Mg_2SiO_4 (wadsleyite) and spinel-structured Mg_2SiO_4 (ringwoodite). Transitions between these phases are exothermic and for reasonable upper mantle conditions, (Geotherm 1 and Geotherm 2) occur at 14 GPa and 17 GPa, respectively. It is only at pressures of around 25 GPa (1700K) that Mg_2SiO_4 finally breaks down following the reaction:

$$Mg_2SiO_4 \text{ (ringwoodite)} \leftrightarrow MgSiO_3 \text{ (MgSi-Pvk)} + MgO \text{ (periclase)} \qquad \text{Equation 4.4\_1}$$

This reaction is endothermic and therefore occurs at greater depth in colder material. It is this reaction that is considered by many to be the major cause of the seismic discontinuity at ~670 km, and the behaviour of this reaction in P/T space which has important implications for subduction. These considerations have already been discussed in depth in section 4.3.

Phase relations involving forsterite - fayalite composition: The transition of olivine to ringwoodite (figure 4.4_5) is partially dependent on Fe content; increased Fe favours the stabilisation of

---

[5] Although some estimates suggest an negative slope for the transition of MgSi-Ilm to MgSi-Pvk.

ringwoodite such that the transition occurs at 7 GPa (1273K) for Fe_2SiO_4 compared to 11 - 13 GPa (1273K) for $(Mg_{0.75}Fe_{0.25})_2SiO_4$[6]. As seen from discussion of phase relations in the $(Mg,Fe)SiO_3$ system, wadsleyite is only stable in the presence of low Fe content, < 35 mol %. The breakdown of ringwoodite at high pressure follows the Mg,Fe version of reaction 4.4_1 for Mg_2SiO_4 > 65 mol % or:

$$(Mg,Fe)_2SiO_4\ _{\text{(ringwoodite)}} \leftrightarrow (Mg,Fe)O\ _{\text{(fPer)}} + (Mg,Fe)O\ _{\text{(fPer)}} + SiO_2\ _{\text{(stishovite)}} \qquad \text{Equation 4.4\_3}$$

where two fPers of differing composition are stabilised (Mg_2SiO_4 < 45 mol %).

The pressure of stabilisation of MgSi-Pvk was found by Jeanloz and Thompson (1983) to be strongly dependent on Fe content. Experiments at higher temperature, however, (Katsura and Ito, 1989) show a sharp decrease in dependence on Fe content such that at 1873K, the breakdown of ringwoodite to MgSi-Pvk + fPer occurs at 23.5 GPa irrespective of Fe content. These conditions of pressure and temperature fall within the range of conditions proposed for depths of ~ 670 km for both Geotherm 1 and Geotherm 2, consistent, therefore, with the breakdown of ringwoodite to fPer + MgSi-Pvk occurring at the upper - lower mantle boundary.

The breakdown of ringwoodite to an assemblage involving stishovite, commences at successively lower pressure for increasing Fe content such that a phase field involving ringwoodite, stishovite and fPer exists down to ~ 17 GPa (1273K).

Phase relations in the system MgO - FeO - SiO_2: Figure 4.4_6 presents isobaric snapshots at 1273 K for the ternary system MgO - FeO - SiO_2 from 8 GPa to 45 GPa. Noteworthy observations are:

- The transformation of coesite to stishovite between 8 and 10 GPa. As figure 4.4_7 shows, for 1273K, the reaction coesite ↔ stishovite occurs at ~ 9.3 GPa (Yagi and Akimoto, 1976).
- Phase relations in the MgO - FeO -SiO_2 system are particularly complex in the range 19 - 24 GPa. At pressures above 24 GPa (1273K), however, throughout lower mantle pressures, the entire system can be described in terms of relative proportions of only three phases: fPer, stishovite and MgSi-Pvk.
- Most importantly, no matter what bulk composition within MgO - FeO - SiO_2 is considered, fPer cannot coexist with a $(Mg,Fe)SiO_3$ composition phase at pressures below 21 GPa. Even then the composition of fPer coexisting with MgSi-Pvk is significantly Fe-rich, >50 mol % FeO. It is not until the final breakdown of ringwoodite at ~ 24 GPa (1273K) (23.5 GPa at 1873K, i.e. the

---

[6] Comparing Fei et al. (1991) with Jeanloz and Thompson (1983) suggests that this transition is not as significantly effected by temperature as the reaction olivine ↔ wadsleyite.

upper-lower mantle boundary, Katsura and Ito, 1989, figure 4.4_5) that a range of Mg content involving Mg-rich fPer can coexist with MgSi-Pvk.

Figure 4.4_8 serves to summarise the available data in terms of ternary relations in MgO - FeO - SiO_2 space at higher temperatures. Also included are plots of bulk mantle composition which suggest that in terms of MgO - FeO - SiO_2, the mantle is best described in terms of the system $Mg_{0.95}Fe_{0.05}SiO_3$ - $Mg_{0.55}Fe_{0.45}SiO_3$ - $(Mg_{0.95}Fe_{0.05})_2SiO_4$ - $(Mg_{0.55}Fe_{0.45})_2SiO_4$.

➠

Section 4.4.1.2 The role of Al and Ca on mantle phase relations

Al under transition zone conditions: Ringwood (1969) discovered that significant amounts of $MgSiO_3$ (enstatite composition) can be dissolved in $Mg_3Al_2Si_3O_{12}$ (garnet composition) at pressures exceeding ~ 10 GPa. This so-called 'majoritic solid solution' has been subsequently investigated in detail (eg. MacGregor, 1974; Babuska et al., 1978 and Irifune and Ringwood, 1987 and references in figure 4.4_9). At higher pressures, the extent of the compositional field of majoritic garnet rapidly extends to involve more enstatite component to a maximum of ~ $En_{90}Py_{10}$ (16 GPa, 1573K, Akaogi et al., 1987). How this behaviour varies with temperature is not entirely clear. At low temperature, increasing enstatite component can be accommodated in garnet with increasing temperature (figure 4.4_9). However, work by O'Neill and Jeanloz (1994) at significantly higher, yet uncertain, temperature, suggests that only a maximum of 60 mol % enstatite component can be accommodated (24 GPa, ~ 2300 K). Given the extreme conditions and the temperature uncertainty involved in the latter experimental work, it is likely that the former conclusions of expanding solubility with increasing temperature are more trustworthy. At any rate, the maximum solubility of enstatite in garnet decreases on the stabilisation of olivine composition phases + stishovite on the breakdown of pyroxene composition.

Al under lower mantle conditions: Early experimental work on pyrolite and MORB starting compositions (Irifune and Ringwood, 1987; Ito and Takahashi, 1987; Takahashi and Ito, 1987; Liu, 1975 and Ahrens and Graham, 1972) indicated occurrence of an Al-rich phase in runs conducted at lower mantle pressure which could not be identified. More recently, Al has been shown experimentally, to be incorporated into perovskite structured $(Mg,Fe)SiO_3$ (Irifune, 1994; Kesson et al. 1995), figure 4.4_9; although other workers (O'Neill and Jeanloz, 1994; Ahmed-Zaïd and Madon, 1995; Yagi et al. 1996 and Irifune et al., 1996) suggest that a separate Al-rich phase coexists with a mildly aluminous perovskite structured $(Mg,Fe)SiO_3$. All these experiments involve some degree of uncertainty, whether in the measurement of run conditions of pressure or temperature or the relevence of particular starting materials or bulk composition.

Shallow lower mantle depths: At shallow lower mantle depths, there is a strong case for the presence of an additional Al-rich phase. Irifune et al. (1996) observed a restricted phase field of MgSi-Pvk + majoritic garnet around 25 GPa, giving way to a single MgSi-Pvk field at higher pressures. With increased Al content (~20 mol % Al_2O_3 and above), majorite breaks down to additional MgSiPvk + corundum (figure 4.4_9). Interestingly Yagi et al. (1996) conducted experiments on pyrope composition at conditions corresponding to those where Irifune et al. (1996) identified the presence of the MgSiPvk + corundum field. Yagi et al. (1996) concluded that their run products involved a MgSi-Pvk of composition of Al-depleted pyrope and a corundum structured phase which they concluded had a composition of partially Al-enriched pyrope. The compositional details of their run products were conducted, however, using EPMA analysis. Due to run products being of a grain size significantly smaller than the EPMA analysis size, the composition of components was determined by extroplation from the trend of a variety of analyses (Yagi, *personal communication* 1996). In terms of the Al-rich component, this extroplation could equally have been made to Al_2O_3 composition rather than Al-enriched pyrope. In conclusion, it is only Yagi et al.'s (1996) *interpretation* of their run products which is inconsistent with the work of Irifune et al. (1996).

In terms of the presence of Fe, this has been investigated by O'Neill and Jeanloz (1994)[1]. They found that with increasing Fe content, majoritic garnet is stabilised in preference to MgSi-Pvk, figure 4.4_10. Their results, however, are qualitative.

Deeper into the lower mantle: The presence of an additional Al-phase at higher pressure has been hotly contested. As figure 4.4_11 demonstrates, however, the experimental work which supports some stabilisation of Al at *very* high pressure (~ 50 GPa) into a phase other than MgSi-Pvk is flawed. O'Neill and Jeanloz (1994) suggest that some Al is accommodated within ruby at pressures of ~ 50 GPa. Ruby, however, was used as a pressure calibrant in these experiments and so is present in the starting material. Given the short run times and large temperature gradients in DAC work of this type, one would not expect to react all starting materials. Indeed it is highly unusual for diffraction peaks of starting materials not to be present in the run products of DAC experiments. Ahmed-Zaïd and Madon (1995) encounter similar problems with starting materials. Given that other experimental work (Kesson et al., 1995) shows that pyrope composition starting materials simply adopt a perovskite structure at 50 GPa and do not involve additional phases, this is considered most likely to be the correct scenario. In terms of the effect of temperature, given the large uncertainties involved, it can only be said that higher temperature is likely to favour stabilisation of more aluminous MgSi-Pvk.

The role of Ca:

$CaSiO_3$: By itself, $CaSiO_3$ undergoes a number of phase transitions through mantle conditions (figure 4.4_12). Following a transition from wollastonite to walstromite structure and subsequent breakdown to Ca_2SiO_4 + $CaSi_2O_5$, Gasparik et al. (1994) found that perovskite structured

---

[1] Although their results are questionable in terms of the accommodation of Al into MgSi-Pvk at high pressure, it is not considered that this effects their conclusions on the role of Fe.

$CaSiO_3$ (CaSi-Pvk) was stabilised[2] at ~12 GPa. This is a significantly lower pressure than the stabilisation of MgSi-Pvk (figure 4.4_1).

$CaSiO_3$ - Al_2O_3: With the addition of Al_2O_3 to $CaSiO_3$, phase relations under transition zone - lower mantle conditions (figure 4.4_13) are broadly similar to those of $MgSiO_3$ - Al_2O_3, the significant difference being the absence of olivine-type phases and the appearence of a peroskite structured phase at lower pressure. Unlike in the $MgSiO_3$ - Al_2O_3 system, however, the garnet structure gives way to a perovskite structure at significantly *higher* pressure (30 GPa, Liu 1979) (cf. results from Akaogi et al., 1987, figure 4.4_9 for $Ca_{50}Mg_{50}$).

$CaSiO_3$ - $CaMgSi_2O_6$: With the addition of Ca to $MgSiO_3$, the decomposition of orthorhombic pyroxene to C2/c monoclinic pyroxene at ~ 10 GPa (1923K, Gasparik, 1990) is not significantly affected, figure 4.4_14a. Bulk compositions of greater than ~ 8 mol % $CaMgSi_2O_6$ simply result in the stabilisation of a separate diopside phase, the Ca content of which rises with increasing pressure; especially on the decomposition of Ca-poor orthorhombic pyroxene at ~ 10 GPa (1973 K). Rising temperature (figure 4.4_14b) however, produces the opposite effect. The phase diagram of $MgSiO_3$ - $CaMgSi_2O_6$ is dominated at high pressure by the stability of CaSi-Pvk (~ 17 GPa, 1973 K) although at intermediary pressures and for Ca-rich compositions Gasparik (1990) identified an additional Ca-rich phase he termed the ‘CM-phase’.

Al and Ca in the mantle: Figure 4.4_15 serves to summarise the role of the presence of Al and Ca for reasonable mantle compositions following the work of Ito and Takahashi (1987a) and Irifune and Ringwood (1987). The majoritic garnet field expands rapidly with pressure in transition zone conditions but on increasing pressure following the stabilisation of CaSi-Pvk (or Ito and Takahashi’s (1987a) unquenchable Ca-rich phase), it contracts in terms of its Ca-content. On final reaction of majoritic garnet to MgSi-Pvk Al is accommodated within an Al-rich phase which, following work by Irifune et al. (1996) and possibly Yagi et al. (1996) is considered most likely to be corundum. At subsequently higher pressure, all Al is accommodated within MgSi-Pvk which, in terms of Ca content, coexsits with CaSi-Pvk. Indeed, Gasparik (1989 and 1990) suggests that, even in complex systems, the composition of CaSi-Pvk remains close to $CaSiO_3$.

---

[2] In addition, Gasparik (1994) identified a low P, high T polymorph of $CaSiO_3$ termed parawollastonite.

Section 4.4.1.3 The role of Na on mantle phase relations

Limited study has been made specifically on the role of Na in mantle systems; the most detailed work (up to 22 GPa) being undertaken by Gasparik (1989 and 1990). However, Na clearly is an important element in some regions sourced by São Luiz diamonds, given its significant presence in São Luiz inclusions, particularly Type III pyroxene and in majoritic garnets.

The addition of Na to an enstatite composition and the addition of Al to $Na_2MgSi_5O_{12}$ have been investigated in a restricted pressure range for 1873K (Gasparik, 1990), figures 4.4_16a and 4.4_16b. As figure 4.4_16c of phase relations in the $CaMgSi_2O_6$ - $NaAlSi_2O_6$ system shows, on the stabilisation of perovskite structured $CaSiO_3$ (CaSi-Pvk), Na, Al, Ca and Mg can no longer be accommodated within a single pyroxene. Above ~ 18 GPa (1873K), Ca is strongly partitioned into CaSi-Pvk and coexists with garnet structured pyroxene. With the addition of a jadeite component, this phase relation remains the same; all jadeite component is accommodated within MgSi-Grt; until the bulk composition of the system comprises more than 50 mol % jadeite. With a further increase in jadeite component, the little remaining Ca is stabilised within a single Na, Al, Ca, Mg garnet-structured phase. Although phase relations at pressures above 21 GPa have not been constrained, given the propensity for CaSi-Pvk to remain pure in composition (Gasparik, 1989 and 1990) and the transition from MgSi-Grt to MgSi-Pvk, it could reasonably be expected that on the stabilisation of MgSi-Pvk, all reasonable amounts of Na could be accommodated within MgSi-Pvk in a similar fashion to the incorporation of large amounts of Al (except, presumably by a different substitution mechanism).

Phase relations involving enstatite - jadeite composition: Figure 4.4_17 summarises phase relations determined at 1473K, 1773K and 1923K in the system $MgSiO_3$ - $NaAlSi_2O_6$ where temperatures investigated do have some direct relevence to conditions expected to occur in the mantle.

From 2 GPa, up to ~ 14 GPa all Na and Al can be accomodated within pyroxene sructures. Increasing amounts of jadeite component, 5 - 20 mol %, can be accommodated within orthopyroxene with increasing pressure until the transformation of orthorhombic structured to C2/c monoclinic structured pyroxene occurs at ~ 11 GPa. Unlike orthopyroxene, cpx can accommodate less and less Na and Al with increasing pressure. From bulk compositions of Jd_{50} to Jd_{100}, all Na and Al is accommodated within a single jadeite solid solution.

At pressures above ~ 14 GPa, providing at least some Na and Al is present, pyroxenes adopt a garnet structure. Indeed examination of figure 4.4_17 shows that the stabilisation of garnet structured pyroxene (MgSi-Grt) occurs at rapidly falling pressure with the introduction of even small amounts of jadeite component: as shown in figure 4.4_1, MgSi-Grt is stabilised at ~ 17 GPa (1923 K), for a composition of $MgSiO_3$, however, the introduction of ~ 5 mol % jadeite causes a fall in stabilisation pressure of ~ 3.5 GPa. With increasing pressure, all Na and Al can be accommodated within a garnet structure with the exception of particulary Mg - rich compositions which stabilise MgSi-Ilm. Consideration of figure 4.4_2 would suggest, however, that the addition of significant Fe would destroy the relative stability of MgSi-Ilm, *all* Mg, Fe, Na and Al being, most likely, contained within a garnet structure. Additionally, comparing figure 4.4_17 with figure 4.4_3 and figure 4.4_9 clearly shows that the addition of Na separately, does not adversely affect the stability of a garnet structure strongly stabilised to lower temperatures with the addition Al. Na, Al-rich majorites are thus quite conceivable phases for the upper mantle.

➠

Section 4.4.1.4 Additional components

Phase relations involving feldspar compositions: Perhaps surprisingly, feldspar composition phases are stable at pressures and temperatures corresponding to significant depths into the upper mantle (figure 4.4_18). Whether these compositions exist in the Earth, however, depends strongly on the bulk compositions involved.

Both $KAlSi_3O_8$ and $CaAl_2Si_2O_8$ have some stability at high pressure (Gautron and Madon, 1994 and Urawaka et al., 1994). Above ~ 10 GPa, for $CaAl_2Si_2O_8$ composition, some anorthite reacts to form kyanite + CaSi-Pvk however a certain amount of hollandite-structured anorthite polymorph remains stable. Under similar conditions, for a $KAlSi_3O_8$ composition, a phase of hollandite structure is stabilised. Indeed, the hollandite structure remains stable even on the addition of significant Na content, up to 50 mol % $NaAlSi_3O_8$ component (figure 4.4_18d); additional Na stabilises a Ca-ferrite structured $NaAlSi_2O_6$ composition phase + stishovite (Yagi et al., 1994).

The role of Fe^{3+}: Fe^{3+} has been discussed in detail in section 2.5 and 2.6 in the system FeO - Fe_2O_3 - MgO and for pyroxene and garnet compositions. In general, increasing pressure promotes the solution of Fe^{3+} into both MgSi-Pvk and garnet compositions. In contrast the minimum amount of Fe^{3+} which is required to stabilise fPer decreases with increasing pressure.

➠

Section 4.4.1.5 The role of fluid

Little work has been undertaken on the role of C-O-H-N fluid in the phase relations of rocks at lower mantle and transition zone conditions. Given the presence of diamond, it is likely that some fluid is present, however, how much is present and of what composition is a matter of debate. Concerning subducting slabs, the most likely fluid transport mechanism into the deep mantle, it is hotly contested as to whether any fluid is retained at lower mantle depths (Zhang and Zindler, 1993; Keppler, 1996).

Experiments have been undertaken to synthesise hydrous versions of a number of phases at high pressure, this has been successful for a number of minerals (Smyth, 1987; Mackwell and Kohlstedt, 1990; Li and Jeanloz, 1991; Young et al., 1993; Smyth, 1994). Whether the phases in question really are stable under the physical and *bulk compositional* conditions of the Earth, however, is unclear althought the presence of deep earthquakes may be indicative of a fluid presence (Raleigh and Paterson, 1965; Thompson, 1992 and Silver et al., 1995).

Gasparik and Drake (1995) ran experiments on a pyrolite bulk composition at 23 GPa. They introduced F as their main fluid component, this being used in preference to water, which would have reacted with their sample vessels. Their results are summarised in figure 4.4_19. Not surprisingly, they found that the liquidus temperature is profoundly decreased with the introduction of small quantities of fluid. Indeed with the introduction of small amounts of fluid, a phase additional to MgSi-Pvk was encountered in run products. This phase was termed super phase-B (sB) and was observed to partition Mg in preference to Ca into its structure. With the addition of more than ~8 mol% $(Ca,Mg)F_2$, Gasparik and Drake (1995) found that all MgSi-Pvk had disappeared leaving a field of CaSi-Pvk and sB. As figure 4.4_19 shows, however, at 23 GPa, sB is stable at temperatures which are likely to be too low, even for the low temperature geotherm, Geotherm 2. sB may only be relevent, therefore, to particularly cool mantle material, such as subducted slab, but only where transformation to perovskite structured phases has occurred and suitable fluid remains present.

It is considered possible for some fluid to reach the lower mantle. If ringwoodite can be considered analogous to wadsleyite (which has a structure only slightly modified from ringwoodite, section 3.3.4) it is possible that ringwoodite could accommodate significant amounts (perhaps up to 3.3 wt% H_2O) of fluid (compare Smyth, 1987 and Smyth, 1994 for wadsleyite with Macwell and Kohlstedt, 1990 for olivine). One can, therefore, envisage a hydrous component being sustained within an olivine composition phase through the transition zone which, on the breakdown of olivine composition, stabilises its own phase. It is not known, however, how the variation in pressure and the presence of significant Al and Fe, as seen commonly for São Luiz and Guinean material, would affect the stability of a separate hydrous phase.

Section 4.4.1.6 Phase relations involving complex systems

Study of phase relations in simple one, two and three component systems, provides the detailed framework essential in producing accurate predictions of phase relations in the more complex systems of natural rocks. This method of producing a comprehensive framework involving a large number of elements is extremely laborious so a number of workers have adopted the approach of modelling mantle mineralogical changes for specific expected bulk compositions.

Phase relations in peridotite, continental crust, chondritic mantle, MORB, primitive MORB, pyrolite and argillaceous and siliceous sediment, have all been studied either along mantle geotherms, or for a range of pressures and temperatures. As with simpler uni, binary and ternary component systems, the results and conditions of relevent experiments are summarised in appendix 11.

Peridotite: Phase relations determined on peridotite (Ito and Takahashi, 1987, figure 4.4_20a), are essentially the same as those of olivine composition (figure 4.4_4) with the additional detail that, at transition zone pressures, the liquidus phase is of an olivine composition and subsequently majorite at higher pressures. At lower mantle pressures, MgSi-Pvk is the liquidus phase. In terms of the relative proportion of phases present (figure 4.4_21h) olivine polymorphs, not surprisingly, comprise 50% in terms of molar proportions, the remainder being majoritic garnet with a small Ca-poor cpx component. At pressures of ~20 GPa, CaSi-Pvk is stabilised, which, on gradual breakdown of majorite, increases in importance. Due to the relatively Fe-poor composition of the peridotite employed, Ito and Takahashi (1987) observed an almost instantaneous breakdown of ringwoodite to fPer + MgSi-Pvk.

Eclogite: Following experimental work on the dissolution of pyroxene in garnet on a simple three component system, Ringwood (1969) attempted to assess the relevence of this transformation to natural rocks. He used an eclogitic starting material which he took up to conditions of 18 GPa (~1673K) and, indeed observed that majoritic garnet was a stable and dominant phase.

Pyrolite: Results for pyrolite (Irifune and Ringwood, 1987 and Irifune, 1994), figures 4.4_21c and d, are essentially the same as for peridotite except with a larger olivine composition component. Additionally, the presence of greater Fe and Al content in pyrolite, results in a depth range for the conversion of ringwoodite to fPer + MgSi-Pvk and, in the case of Irifune and Ringwood (1987) the stabilisation of an Al-phase which is probably a disequilibrium product relating to corundum.

MORB compositions: MORB compositions have been studied by Irifune and Ringwood (1987 and 1993), figures 4.4_21a and 4.4_21b. In terms of transition zone conditions, given the relative SiO_2 rich nature of MORB over peridotite and pyrolite, majoritic garnet is the most significant component in addition to a small amount of stishovite. Run conditions of Irifune and Ringwood (1987) were too low to stabilise MgSi-Pvk, although, even at higher pressures, Irifune and Ringwood (1993) found an absence of MgSi-Pvk. Importantly, majoritic garnet was found to extend significantly into the lower mantle in association with CaSi-Pvk, and Al-phase and stishovite. Certainly the stability of stishovite rather than MgSi-Pvk is consistent with an SiO_2-rich system, cf. figure 4.4_6, but only providing the Fe content is high enough. Although the phase has not been constrained, it is likely that the Al-phases of Irifune and Ringwood (1987 and 1993) are MgSi-Pvk with significant Al component.

Chondritic mantle: Ohtani (1987) investigated phase relations in chondritic material, figure 4.4_20c, up to ~ 22 GPa. Liquidus phase were observed to be the same as for peridotite. In terms of subsolidus relations, Ohtani (1987) found that all components could be accommodated within wadsleyite and majoritic garnet in the transition zone up to 20 GPa.

Sediments: The fate of subducting slabs and thus, potentially, sedimentary material, is the subject of much interest at present (section 4.3). With this in mind, Irifune et al. (1994) conducted a study of the phase relations involving argillaceous sediment, siliceous sediment and an average continental crust (figures 4.4_20b, 4.4_21e, 4.4_21f and 4.4_21g) although only under upper mantle conditions. Assemblages are observed to be dominated by majoritic garnet, stishovite and products of compression of feldspar compositions (figure 4.4_18).

Section 4.4.1.7 Melting relations

Even with a thermal boundary layer, conditions along likely, steady-state, mantle geotherms, are too cold to involve melting for any compositions except those involving significant fluid phase (figure 4.4_19). Given the strong evidence for mantle plumes (section 7.3.1) it is quite plausible that volumes exist in the mantle at temperatures significantly elevated above the average geotherm. Even anhydrous melting, therefore, could be quite relevent in certain restricted depth ranges, such as the base of the lithosphere and the upper mantle / lower mantle boundary.

Within the upper mantle, temperatures along averaged geotherms are only elevated close enough to melting curves at the base of the lithosphere (see, for example, figures 4.4_1, 4.4_4, 4.4_12 and 4.4_18) to make anhydrous melting without added thermal energy possible. The liquidus phase is likely to be olivine.

Within the lower mantle, a thermal gradient must be invoked to come close to conditions suitable for melting. In this case, fPer is the likely liquidus phase[1] providing that the Mg content is high enough. The melting point of (Mg,Fe)O (figure 4.4_22) is significantly greater than that of CaSi-Pvk (figure 4.4_12) (and Fe, figure 4.4_24) which, in turn is greater than that of MgSi-Pvk (figures 4.4_1 figure 4.4_23). The presence of Fe in MgSi-Pvk appears to significantly lower the melting point (compare Heinz and Jeanloz, 1987 to Ohtani, 1983, figure 4.4_23). The presence of fPer on the liquidus is likely to have a profound effect on the composition of this phase should a component of melt be involved, see section 4.4.2.

➡

---

[1] A view supported by Herzberg and Zhang (1996) on melting of peridotite at high pressure.

Section 4.4.2 The source of São Luiz and Guinean diamonds

Compositional aspects of inclusions from São Luiz and Guinean diamonds are discussed in relation to the state of knowledge on phase relations relevent to the deep earth (section 4.4.1), likely bulk compositions (section 4.1) and expected conditions of pressure and temperature (section 4.2). Reference can be made to section 2.3 and the reference sheet for details of associations.

Section 4.4.2.1 The UM association

Wilding (1990) discusses at length a number of non-majoritic calcic garnets and associated diopsides obtained as inclusions from São Luiz which he assigns to a Group I. A single inclusion, BZ213A has been recovered (Harris, 1993 *personal communication*) subsequent to the work of Wilding (1990) which falls into the same compositional field. As discussed in section 2.2.1.5, the major element compositional characteristics of BZ213A fall within the compositional field of Group 2 lherzolitic cpx of Stephens and Dawson (1977), indeed, in terms of trace element characteristics (section 2.4.5.1 and 2.4.7) this can be further constrained to cpx of granular lherzolite type. Given that the garnets of this association have no majoritic component, their formation is consistent with formation at depths of less than 250km.[1] Furthermore, on the basis of calculation of Mg / Fe partitioning between coexisting phases following Ellis and Green (1979) and assuming a pressure of 5 GPa, Wilding (1990) calculated an average temperature of formation of 1685 K ($1\sigma = 112$ K) which is margionally higher than temperatures recorded for granular lherzolite assemblages by Finnerty and Boyd (1987) but not unexceptional. It would be resonable to conclude that the inclusion BZ213A (section 2.2.1.5) and the cpx and garnets of Wilding (1990)'s Group I were formed in the upper mantle at lithospheric depths on a continental geotherm and within a lherzolitic bulk composition. For purposes of comparison, throughout the text, this association is, therefore, termed the upper mantle (UM) association (see section 2.3 and reference sheet).

---

[1] Compare the pressure of onset of pyroxene solution in garnet, figure 4.4_9 and the relationship of pressure with depth of table A14_1.

Section 4.4.2.2 Source of majoritic garnet association inclusions (TZ association)

Majoritic garnet is an example of a phase which was synthesised (Ringwood, 1967) prior to its discovery in nature (as a natural phase in veins in the Coorara meteorite, Smith and Mason, (1970)). Subsequent discoveries have been in shock veins in a chondritic meteorite from Sixiangkon (Chen et al., 1996), in eclogite xenoliths from Bellsbank and Obnazhënnaya (Jerde et al., 1993)[1] and Jagersfontein (Haggerty and Sauter, 1990) and as inclusions in diamonds from Monastery (Moore and Gurney, 1985 and Moore et al., 1991) and São Luiz (Wilding, 1990 and the present study).

As majoritic garnet is a stable phase only at pressures in excess of ~ 8 GPa (section 4.4.1.2), within the MgO - FeO - CaO - Na_2O - Al_2O_3 system, the presence of natural majoritic garnet can, therefore, be cited as evidence of an origin within the Earth's transition zone (hence the terminology 'TZ' for the majoritic garnet association). Furthermore, as the degree of solid solution between garnet and pyroxene within the upper part of the transition zone increases with pressure, measurement of the composition of majoritic garnet can be used to infer a specific depth of formation (assuming a particular temperature). Irifune and Ringwood (1987) observe variations with pressure of Si, Mg and Al in garnets in synthetic pyrolite minus olivine composition (figure 4.4_25) to be consistent with majoritic substitution and employ their results in the construction of a geobarometer. Moore et al. (1991) applied this barometer to majoritic garnets from Monastery diamonds and inferred a range of pressures of formation between 6.8 and 15.4 GPa. Haggerty and Sauter (1990) infer pressures of formation of 12 - 13 GPa from reconstituted majoritic garnet compositions from analyses of coexisting cpx and garnet.

Study of figure 4.4_25, however, shows that once reaching a plateau at ~16 - 20 GPa, majoritic garnets in the pyrolite system[2] lose their majoritic component. This observation is interpreted on the basis of the stabilisation of Ca into CaSi-Pvk above 15 GPa (figure 4.4_12), and the enstatite component into MgSi-Pvk (figures 4.4_9, 4.4_21c and 4.4_21d). Depth of formation cannot, therefore, be assigned unambiguously on the basis of measurement of the Si component in majoritic garnet. However, because phases coexisting with majoritic garnet through the range 10 - 15 GPa are quite different from those in the range 20 GPa and above, majoritic garnets forming in the two régimes can, potentially be discriminated between. The differing parageneses are reflected most

---

[1] In contrast to the other majoritic garnet occurrences mentioned, Jerde et al.'s (1993) samples are predominantly pyroxene in bulk composition (closer to the majorite end-member). As processes involved in garnet exsolution in pyroxene and pyroxene exsolution in garnet are not necessarily symetrical, Jerde et al.'s (1993) samples cannot be compared directly to those of Chen et al. (1996), Moore and Gurney (1985), Moore et al. (1991), Wilding (1990) and the present study.

strongly in the behaviour of Mg / Fe and, to an extent, minor elements such as Na and Ca. An unambiguous depth of formation can, therefore be obtained by plotting majoritic garnet cation values against each of two depths determined by Si content. Provided the sample set incorporates a reasonable range in formation depth the correct depth range can be determined by comparison of the trends in major elements concentration with the trends of figure 4.4_25. This methodology is applied to majoritic garnet suites from the literature and from São Luiz inclusions.

Majoritic garnets from Jagersfontein eclogitic xenoliths: Majoritic compositions have been obtained by recombination of compositional data from exsolved garrnet and cpx from two xenoliths (Haggerty and Sauter, 1990). From the data presented, three data points for unaltered garnet data and two discrete points, one for each xenolith, are available for assigning to particular pressures on the basis of Si content. This is too little data to base a definitive interpretation on, as figure 2.2_26a and 2.2_26b show. However, the trends in majoritic garnet composition are more consistent with an interpretation of formation in the range 10-15 GPa, than at higher pressure. Ca decreases quite linearly with decreasing Si content and there is no indication of a dip in Mg content with increasing Fe content.

Majoritic garnets from Monastery diamond inclusions: The dataset shows significant scatter, however, a number of trends can be discerned. Importantly, a strong negative topography in the trend of Mg content corresponds to a positive topography in the trend of Fe content over mid-values of Si content. Figure 4.4_27a plotted with an *increase* in Si content indicative of a rise in pressure does *not* compare well to figure 4.4_25, whereas figure 4.4_27b plotted with a *fall* in Si content indicative of a rise in pressure does compare well with figure 4.4_25. In addition, a rise in Na content appears at intermediate Si contents, in all, consistent with an origin over pressures in the range of 20 - 25 GPa. No unequivocal conclusion can be reached given the scatter of the dataset and the lack of information on coexisting phases. However, as an inclusion of fPer has been recovered from a Monastery diamond, (Moore and Gurney, 1989) clearly *some* stones have an origin at pressures of the order of 20 GPa.

Majoritic garnets from São Luiz and Guinean diamonds: The dataset of the present study is not extensive. However, comparison of figure 4.4_28a and figure 4.4_28b with figure 4.4_25 yields a number of salient points. Na, shows a maximum in concentration at intermediary Si content and although the scatter in Mg and Fe content is large, there is an average minimum in Mg content corresponding to an average maximum in Fe content at intermediary Si concentrations. Both observations are more consistent with an interpretation of formation in the pressure range 20-25

---

[2] Although the bulk compositions of natural systems are not necessarily equivalent to pyrolite, the principal phases coexisting with majoritic garnet are likely to be the same (figure 4.4_21, with the exception of highly siliceous rocks, for example, sediments).

GPa. Adding the São Luiz, majoritic garnet dataset of Wilding (1990) provides a more substantial database from which to draw conclusions (figures 4.4_29a and 4.4_29b). Mg shows a marked dip in cation concentrations at intermediary Si values which is mirrored by a slight positive topography to Fe content. Furthermore, Ca shows a sharp rise with inferred pressure of formation in the range 20-22 GPa, and Na shows a slight hump at intermediary Si values, in good comparison with figure 4.4_25. Compositional data, therefore, strongly suggest that majoritic garnets from São Luiz have, predominantly formed in the deep transition zone, ~ 550 km +.

Bulk major element composition of the TZ association: Figures 4.4_30 - 4.4_32 express the composition of all non-Wilding (1990) inclusions from the TZ association, in terms of Si, Mg and Fe; Al+Ti+Cr, Ca+Na and Mg+Fe+Mn and Si, Al+Ti+Cr and Mg+Fe+Mn cations respectively. Tie lines are drawn between phases obtained from single diamonds. Bulk compositions 1-10 of section 4.1 are also plotted for comparison. Majoritic garnet BZ215C, coexisting with pyrrhotite BZ215A, falls in a group of slightly more Ca-rich majoritic garnet than BZ218A, coexisting with diopside BZ218B. Majoritic garnet GU3B, coexisting with diopside GU3C represents a more intermediary composition.

The TZ association is Fe and Mg-poor compared to peridotitic and primordial compositions, indeed for all major elements, the TZ series has most compositional similarity with eclogite and primitive MORB compositions of section 4.1. As table 4.1_1 demonstrates, eclogite and primitive MORB are closely similar in composition, although Ca content of MORB is higher, whereas Fe and Al are margionally depleted. Amongst majoritic garnets, in particular, from the TZ association, Ca is highly variable (figure 4.4_31) on this basis it is hard to conclude whether an eclogitic or primitive MORB composition is more appropriate. It should also be noted at this stage that it is important to keep in mind that, although it is not surprising that a combination of majoritic garnet and diopside is consistent with an eclogitic bulk composition, if any olivine was to be present, a true description of the bulk source rock would be peridotitic. It has been attested by Sautter et al. (1991) that significant regions of the transition zone will involve garnetite layers within peridotite. It could be argued that the TZ association is either sourced from these thin garnetite layers, and is thus not a true reflection of the bulk transition zone, or else that the TZ association does in fact include olivine and thus represents a peridotitic bulk composition. Although it is conceded that there is a sampling bias to the diamonds studied, olivine is an easily recognised inclusion and, if it is a part of the TZ association would have been recorded (neither Wilding, 1990, nor the present study reports olivine in association with majoritic garnet). Furthermore, it would seem unlikely that the only transition zone material sampled in the São Luiz and Guinean suites is from unrepresentative garnetite layers. It is believed, therefore that the TZ association, *is* in fact sourced from a dominantly eclogitic or primitive MORB composition region. If, as attested above, the TZ association is source predominantly in the *deep* transition zone, it may represent an accumulation of denser garnet-rich material sourced from subducted slab, the shallower transition zone (unsampled), may by difference, therefore, be predominantly peridotitic. Such a scenario represents a less mixed version of Sautter et al.'s (1991) model.

The proportion of phases required to make eclogitic and primitive MORB bulk compositions corresponding to that of Kushiro and Aoki (1968) and Green et al. (1979) (section 4.1) have been calculated. GU3C diopside, GU3B majoritic garnet (which lies centrally within the TZ compositions) and pyrrhotite BZ215A were used as the most representative compositions for the associated phases of the TZ association. Bulk compositions and component compositions were converted to wt% by element[3] and varying proportions were chosen until a best fit was obtained (table 4.4_1). It was found that a marginally better fit between the TZ association and the eclogitic bulk composition of Kushiro and Aoki (1968) was attained than that for primitive MORB; both fits being within 4%.

Table 4.4_1 Proportion of phases from the TZ association required to fit eclogitic and primitive MORB compositions

	Majoritic Garnet (GU3B)	Diopside (GU3C)	Pyrrhotite (BZ215A)
Eclogite	70%	29 %	1 %
primitive MORB	49.5 %	50 %	0.5 %

In summary, the association of majoritic garnet, diopside and pyrrhotite from São Luiz and FEG is indicative of an origin at depths greater than 250 km and possibly, for at least some inclusions, within the range 550 - 690 km and with a bulk composition of either primitive MORB or eclogite.

Bulk trace element composition of the TZ association: Bulk trace element concentrations for the TZ association were calculated by combining average trace element analyses of average majoritic garnet and diopside from appendix 4.2 in proportions highlighted in table 4.4_1. Trace element information for pyrrhotite was not incorporated due to lack of appropriate data. Such omission, however, is not expected to significantly influence the final trace element composition calculated due to the small proportion of pyrrhotite proposed and its expected lack of significant trace element concentrations. There is little significant difference in trace element characteristics between eclogitic and primitive MORB combinations (figure 4.4_33). Both reconstituted rock types show a significant depletion in HREE and relative depletion of LILE compared to LREE (such characteristics are features of OIB). However, applying the full range of majoritic garnet trace element compositions presented by Harte (1992) gives rise to some bulk compositions more depleted in LREE giving rise to a flat trend throughout REE. This observation in combination with the flat HFSE trend (figure

---

[3] Rather than wt% oxide. This allows for the incorporation of the pyrrhotite component.

4.4_33) is more characteristic of MORB. Furthermore, the absolute concentration of trace elements in reconstituted TZ association material is depleted throughout, compared to both OIB and MORB. Such an observation may not be considered particularly surprising. If the TZ association was either a potential host for MORB, or else a restite, a resulting melt would be more enriched.

Section 4.4.2.3 Source of the UM/LM association; BZ243

The occurrence of olivine and fPer from a single diamond could be explained in terms of each phase being included within the diamond at different depths; ie. a non-equilibrium assemblage. Experimental work in the MgO-SiO_2-FeO system (Jeanloz and Thompson, 1983), however, has shown that there is a restricted range of pressure, temperature and composition[1], for which an olivine composition[2] (ringwoodite phase) is stable in the presence of fPer (figures 4.4_2, 4.4_5 and 4.4_6). The inclusions of BZ243 are quite consistent with formation in the restricted pressure range of ~20-24 GPa, 1373 K (the upper / lower mantle boundary); higher pressures being relevent to elevated temperature. The depth of origin inferred by association is also supported by details of inclusion chemistry. The trace element characteristics of TAPP from BZ243 (section 2.4.3.2) are found to differ from those determined for TAPP grains from the LM I paragenesis. BZ243 TAPP concentrations are much higher and are similar to those of majoritic garnet (section 2.4.3.1). Such high trace element concentrations indicate that the BZ243 association does not involve large amounts of CaSi-Pvk which strongly partitions trace elements within the lower mantle (section 2.4.6) and thus supports a shallower depth of origin. Furthermore, as phase relations indicate that CaSi-Pvk is also stable within a restricted range of depths in the *upper* mantle (figures 4.4_12 and 4.4_16), except where Ca-content is low, the BZ243 association is indicative of formation within a Ca-poor environment. Indeed, it is observed that like other TAPP inclusions from São Luiz, the Ca-content of BZ243A is very low. Given the indications of a transitional origin between the upper and lower mantle for BZ243, the association released from this diamond is thus termed the upper / lower mantle (UM / LM) association.

The inclusions of BZ243 are plotted in terms of cation concentrations on three ternary diagrams, figure 4.4_34 - 4.4_36. In terms of bulk composition, there is little similarity between the UM / LM association and the North American Shale Composite sediment, primitive MORB and eclogite compositions considered. This is particularly noteworthy considering the coincidence of the TZ association with primitive MORB and eclogite. Of the remaining bulk compositions, it is hard to say which the association best fits: none appear to suit the BZ243 assemblage accurately. Olivine, fPer and TAPP compositions are all Si-poor relative to pyroxene compositions and CaSi-Pvk is not expected to be present in significant quantities to redress the balance. The relatively Si-rich compositions of Javoy's (1985) lower mantle composition and C1 chondrite, therefore are considered

---

[1] Given sufficiently Si-poor conditions, ie. with a bulk composition more Si-depleted than (Mg,Fe)SiO_3, the pressure and temperature range of olivine compositions in association with fPer are substantially increased, figure 4.4_6.

[2] An olivine composition phase forming at pressures of 20 - 24 GPa, would adopt a ringwoodite structure. Potentially, such a structure would be retained throughout exhumation, indeed ringwoodite has been discovered as occurring naturally as small purple crystals in meteorites (Binns et al., 1969 and Smith and Major, 1970). It is unfortunate, therefore, that, as section 3.3.4 discusses no stuctural data was forthcoming from BZ243A.

to be poor candidates. In terms of Fe content, Fe enrichment is not especially strong, although there is a significant difference between the Mg # of peridotitic, PRIMA and pyrolite compositions of section 4.1 and the BZ243 assemblage. What can be said is that, due to the presence of TAPP, unless present in very small quantities, a significant Al component is present in the source rock. In all, a best fit bulk composition would appear to be some combination of Anderson (1989)'s solar model and Ca-poor component such as harzburgite. The proportions of TAPP, fPer, olvine and CaSi-pvk compositions required to make up bulk compositions of harzburgite and solar composition are presented in table 4.4_2. These were calculated using compositions of BZ243A, BZ243B, BZ243C and BZ252A in terms of cation concentrations, each inclusion composition being normalised to a total of 100 oxygen anions.

Table 4.4_2 Proportions of LM / UM phases required to give a best fit to solar and harzburgitic bulk compositions

	CaSi-Pvk (BZ252A)	**TAPP (BZ243A)**	**fPer (BZ243B)**	**Olivine (BZ243C)**
Solar	2 %	40 %	10 %	48 %
Harzburgite	2 %	30 %	10 %	58 %

Solar composition from Anderson (1989), Harzburgite composition from Michael and Bonatti (1985)

The convergence of calculated bulk composition to both solar and harzburgite standard compositions were found to be reasonable but not exact, indeed it was difficult to achieve a low enough Al content to fit a harzburgite and a high enough Ca to fit the solar composition and yet retain a good enough fit for other cations; again, indicating that the LM / UM association has some Al and a little Ca. Table 4.4_3 presents the bulk compositions of the LM / UM association in terms of the proportions outlined in table 4.4_2.

Table 4.4_3 Predicted bulk composition of LM / UM association in terms of cations

cations	**Fit to solar composition**	**Fit to harzburgite composition**
Si	22.6	22.6
Al	5.00	6.66
Mg	39.0	36.8
Fe	6.33	5.96
Ca	0.69	0.70
Na	0.15	0.16

Cations normalised to 100 oxygen anions

Bulk trace element composition of LM / UM association: Bulk trace element compositions have been constructed by combination of trace element analysis (appendix 4.2) in combinations to make major element compositions of harzburgite and solar composition. Two calculations were undertaken for each rock type; one using data for average CaSi-Pvk, BZ243A, BZ243B and BZ243C; the other, giving a fuller data set, using averaged trace element data for TAPP, fPer, Olivine and CaSi-Pvk. Results are presented in figure 4.4_37 and show that the final trace element concentrations show similar trends and values throughout (with the exception of low heavy elements in harzburgite calculated using data from the analyses of BZ243 inclusions. This depletion of heavy elements is simply an artefact of them not having been measured, appendix 4.1). It is particularly interesting that despite the major element composition, trace element characteristics remain pretty much unaltered; such an observation invokes confidence that calculated trace element conpositions are close to the true composition of the LM / UM association. Trace element trends and values coincide very well with MORB, even down to the trend in HFSE. It should be noted, however, that the final composition is highly sensitive to the proportion of the highly trace element enriched phase CaSi-Pvk.

Section 4.4.2.4 The LM I association

The LM I association is defined in terms of minerals coexisting with type I pyroxene (section 2.2.1.5). Where these minerals, fPer, TAPP and CaSi-Pvk[1], appear as inclusions within diamonds *not* occluding type I pyroxene, they are classed under the general term 'LM association' but are also incorporated into the present discussion as their compositions are considered to be entirely consistent with an association with type I pyroxene. It should be noted, however, that a number of grains could equally be assigned to the LM II, LM III or even the UM / LM association. Exceptions are TAPP within the LM II association[2], and any significant quantity of CaSi-Pvk in the UM / LM association (section 4.4.2.3).

The fundamentally important aspect of the LM I association is the coexistence of inclusions of enstatite composition and fPer as seen in BZ120, BZ207 and BZ251. As discussed in section 4.4.1.1 and represented by figure 4.4.6, such an assemblage is stable only at pressures of 23.5 - 24.5 GPa or greater (1873 K, 1373 K, figure 4.4_5) and, being largely independent of temperature (figure 4.4_5) is compelling evidence for a depth of formation of greater than 650 - 680 km i.e. within the lower mantle. Hence the adoption of terminology: 'lower mantle I' (LM I) and 'lower mantle' (LM) association.

Bulk composition: Figures 4.4_38, 4.4_39 and 4.4_40 represent the compositional characteristics of the LM and LM I associations in terms of cation concentrations. In terms of Mg and Fe content, the compositional range of MgSi-Pvk is far more restricted than that of fPer (figure 4.4_38) and is consistent with experimental work by, amongst others, Kesson and Fitzgerald (1991). Such an observation suggests a bulk composition closer to MgSi-Pvk than fPer. Small variations in bulk composition explaining large variations in fPer composition, however, are probably not the only explanation as there is a significant variation in trace element compositions across the fPer major element compositional spectrum (section 4.5.1.3); indicative of fractional crystallisation.

Inspection of figure 4.4_38 shows that there appear to be *two* groups of composition; TAPP and / or MgSi-Pvk coexisting with Mg-rich fPer and TAPP and / or MgSi-Pvk coexisting with Fe-rich fPer. These two distinct groups may indicate regions of differing bulk composition and / or physical conditions of the type emphasised by figure 4.4_8 and possibly reflect differing stishovite saturation (figure 4.4_5). Indeed SiO_2 has been reported to coexist with fPer in São Luiz diamonds (section

---

[1] CaSi-Pvk, has not definitively been found to coexist with fPer or MgSi-Pvk. It is confidently asserted to belong to the LM association, however, due to consideration of its phase relations (section 4.4.1.2), trace element characteristics of other LM association phases (section 2.4) and indications from X-Ray diffraction of BZ256 of an association with fPer (section 3.3.6).

[2] Al is believed to reside solely within Al_2O_3, section 4.4.2.5.

2.2.1.2 and Harte and Harris, 1994). It should be noted, however, that the range of fPer compositions from São Luiz diamonds is continuous and spans a wide range in composition from Mg/(Mg+Fe) of 0.38-0.85 cations. Kesson and Fitzgerald (1981) cite the more restricted Mg-rich compositions of Koffiefontein and Orrorroo fPer inclusions as evidence for a consistency of composition, between upper and lower mantle. Such Mg-rich compositions are present in but unrepresentative of, the São Luiz suite. Kesson and Fitzgerald's (1981) attestation of lower mantle composition does not, therefore apply to São Luiz sampled lower mantle. In terms of ternary plots, the LM and LM I associations are consistent with the bulk composition of all considered rocks (section 4.1) but it is notable that the range in Mg # observed for coexisting phases is more Fe-rich than the compositional fields of C1 chondrite and harzburgite. Indeed Fe content appears to be transitional between compositions of pyrolite and PRIMA and solar and LM compositions (section 4.1).

Al is certainly present in the system, in the form of TAPP, but this does not mean that an eclogitic or primitive MORB composition can be invoked; if anything, these compositions are too Fe-rich, relative to Mg and contain too much Na. There is strong evidence to support a significant presence of CaSi-Pvk, given the trace element compositions of the other phases (section 2.4.6) although it is unclear whether there is enough present to maintain the elevated Ca/Al ratio that a solar composition requires. Consideration of the trace element budget of CaSi-Pvk, TAPP and majoritic garnet (section 2.4.7 and figure 2.4_12) suggests that CaSi-Pvk and TAPP may appear in a proportion close to 1:1, bulk compositions of the LM I association are fitted to a solar composition with this in mind (table 4.4_4). Compositions for inclusions, BZ120A, BZ120C, BZ252A and BZ238A were utilised being representative compositions. It was found that, not only is the fit good, but a value close to the Ca / Al ratio of a solar composition can be emulated; results are tabulated in table 4.4_4. However, even with a relatively Fe-rich fPer (e.g. BZ120A), it was not found possible to reproduce an Fe content as high as in a solar composition. A conclusion that the LM I and LM associations come from bulk compositions somewhere transitional between those of a solar composition and a peridotitic composition is considered most suitable. Furthermore, it may be that the majority of inclusions incorporating the LM and LM I association are sourced at shallow depths in the lower mantle, indeed along with the preferred source for the LM / UM (section 4.4.2.3) and LM II associations (section 4.4.2.5) there is a likelihood that most São Luiz, and, especially, the more Mg-rich inclusion hosting, FEG diamonds are sourced in a region bounding the upper and lower mantle.

Table 4.4_4 Proportion of phases from the LM and LM I associations required to fit a solar composition.

	CaSi-Pvk (BZ252A)	**fPer (BZ120A)**	**MgSi-Pvk (BZ120C)**	**TAPP (BZ238A)**
cations	10 %	12 %	66 %	12 %

Rarer, Fe-rich compositions, particularly of fPer do, however, exist and the presence of SiO_2 inclusions, if assigned to the LM paragenesis (section 2.2.1.2) would suggest that more Fe-rich bulk compositions, within the phase field SiO_2 **-** (Fe,Mg)O **-** $(Mg,Fe)SiO_3$ (cf. figure 4.4_6) do exist in the lower mantle. Compositions of this nature, in association with an Al-phase would be closer to a solar composition and are likely to be denser than Fe-depleted material. Thus it would appear likely that at greater depth, the bulk composition of the lower mantle is more like a solar composition. As sections 4.4.2.5 and 4.4.1.2 describe, TAPP probably has a restricted depth range, the Al bearing phase with further increasing depth being corundum and then Al-saturated MgSi-Pvk; such deeper material is seen within the LM II association, section 4.4.2.5.

Bulk trace element composition of LM I association: A bulk trace element concentration for the LM I association has been calculated using trace element data for average fPer, CaSi-Pvk, TAPP and Type I pyroxene (appendix 4.2) in proportions outlined in table 4.4_4 to give a solar major element composition. Results, presented in figure 4.4_41, show that the bulk trace element composition of LM I calculated, shows an OIB trend. Absolute values are more depleted than OIB, however, as the trace element budget is very sensitive to the proportion of CaSi-Pvk, this depletion could easily be corrected for. Such coincidence with OIB may suggest that the LM I association material has a similar genesis; i.e. melt from the same source material. Given the evidence to support an association of São Luiz material with plume material, which also has an OIB association (section 7.3.1) such an explanation for the genesis of LM I material may be considered quite reasonable. It should be kept in mind, however, that the partitioning between the same source rock and the melt it produces at different depths, is likely to be quite different; due to changing temperature, pressure and phases present. The consistency between LM I material and OIB, may, therefore, be quite coincidental unless OIB is produced at depths equivalent to the source of LM I material. Additionally, it is the case that the major element compositions of the LM I association are not coincident with OIB.

The CaSi-Pvk Eu anomaly: As discussed in section 2.4.6, a small positive Eu anomaly was detected in CaSi-Pvk grains. Two possibilities exist to explain such an anomaly:

- The positive Eu anomaly in CaSi-Pvk is a reflection of a bulk excess of Eu in the host rock. Such a characteristic could be taken as evidence for the host rock having undergone crystallisation of a Eu-phyric phase of which the most common is feldspar. As feldspar is only stable at relatively shallow depths (section 4.4.1.4) a subduction origin could reasonably be invoked. In this case a similar Eu anomaly should be found in associated phases.
- The positive Eu anomaly in CaSi-Pvk is a reflection of the peculiarities of the structure of CaSi-Pvk, making it particularly accommodating of Eu. Naturally occurring perovskite does not show any preference for Eu (as discussed in section 2.4.7) however that is not to say that neither does

CaSi-Pvk under lower mantle conditions. Eu adopts a wider range of oxidation state than its neighbouring REE, so peculiarities of lower mantle oxidation may enhance its potential in CaSi-Pvk. Unfortunately no information is forthcoming to enable an assessment of the likelihood of such behaviour, the only trace element study of CaSi-Pvk (Kato et al., 1988) did not involve Eu. If CaSi-Pvk does partition Eu preferentially into its structure, a negative anomaly would be expected within associated phases.

Despite particular attention being paid to the accurate measurement of Eu in related phases (appendix 9), no significant Eu anomaly was detected. Given the small quantities of REE in phases other than CaSi-Pvk, however, any anomaly would most likely be within analytical error. It cannot definitively be said, therefore, what the origin of the Eu anomaly in CaSi-Pvk is. However, given the discrepancy between basaltic composition and that of the LM I association, a structural origin to the anomaly may be considered more reasonable than a subduction related origin.

Phase relations and the stability of TAPP: Clearly, the presence of fPer, MgSi-Pvk and CaSi-Pvk are quite consistent with the predicted phase relations for the lower mantle (sections 4.4.1.1 and 4.4.1.2). Within the LM I and LM assemblages, however, rather than being contained within phases predicted by experimental petrology (figure 4.4_9), Al appears within TAPP. There is much strong evidence to support a lower mantle origin for this phase. Firstly, TAPP is intimately associated with other phases of the fPer paragenesis, both occurring within the same diamonds, and in the case of BZ207A and BZ259A as composites with Type I and Type III MgSi-Pvk grains respectivly. Additionally, the low concentraion of REE in TAPP (section 2.4.3.2) is consistent with crystallisation in equilibrium with CaSi-Pvk. Three key issues remain to be addressed; whether TAPP is a *primary* phase in this lower mantle association or a retrogressive relict formed under decompression (Harris et al., 1997); why it is not observed by experimental petrology and within what particular regions of the lower mantle is TAPP stable?

TAPP as a lower mantle phase: Lower mantle minerals and high pressure phases are characteristically of a high density, containing cation sites with large co-ordination numbers (Ito and Takahashi, 1987). The calculated density of TAPP at atmospheric pressure (3.580 gcm^{-3}) is marginally less than that of a garnet structured phase of similar composition at 3.634 gcm^{-3}. Furthermore, coordination in the new phase, with its three 4-fold, four 6-fold and one distorted 8-fold ('capped' tetrahedron) sites per formula unit (section 3.3.1.2), suggests a relatively open structure compared to normal garnet which has three distorted 8-fold, two 6-fold and three 4-fold sites. However, in the absence of any values of bulk modulus or compressibility for TAPP it is uncertain how its density will compare with garnet at depth in the earth. If TAPP has a relatively high compressibility, then its density might become greater than that of garnet at high pressure.

Furthermore, it should also be noted that the garnet structure is extremely widespread across the range of upper mantle and crustal pressure-temperature conditions and compositons. Thus, if retrogression of a separate very high pressure phase of pyrope-almandine composition occurred, it seems most likely that it would have given rise to the garnet rather than the TAPP structure.

Compositional details of TAPP are consistent with initial crystallisation with its present structure, the virtual absence of Ca in TAPP is a reflection of it not having a suitable site for Ca or any other large ion; because the 'capped' tetrahedral M1 site (section 3.3.1.2) has a significantly smaller volume than the [8] site in garnet.

TAPP, experimental petrology and lower mantle phase relations: Despite the mention of ‘unknown Al phases’ in a number of high pressure experiments (Irifune and Ringwood, 1987; Ito and Takahashi, 1987; Takahashi and Ito, 1987; Liu, 1975 and Ahrens and Graham, 1972), none of these phases are TAPP. As figure 4.4_42 shows, there is no similarity between powder diffraction peaks calculated for TAPP (section 3.3.1.2) and those obtained from X-Ray diffraction of run products involving ‘unknown Al phases’. It is likely that these run products are the products on non-equilibration. The absence of TAPP within the run-products of experimental petrology is not believed to be problematic, however. Athough the results of experimental petrology can be considered invaluable in providing a basis for comparison of natural materials, they can, in no way, be considered to be a substitute. Particularly for experiments emulating lower mantle conditions, there are many practical problems to overcome in achieving equilibrated products and the characterisation of phases in very fine-grained run products can be very difficult (section 4.4). TAPP stability could quite conceivably, therefore, have been missed; both in terms of appropriate bulk composition and physical conditions[3]. Indeed as the following discussion of the likely stability range of TAPP will show, this scenario can be considered to be quite likely. Given the dominance of high coordination sites and subsequent high density of the perovskite structure, in addition to its prevelence in many experiments designed to investigate lower mantle phase relations, it can be considered that the perovskite structure dominates the lower mantle. Indeed, results of experimental petrology suggest that under significant pressure (~ 50 GPa), corresponding to depths well into the lower mantle, and within all reasonable mantle bulk compositions, perovskite structured $MgSiO_3$ will likely accommodate all available Al_2O_3 (at least up to 25 mol% e.g. Kesson et al., 1995) even in the presence of significant Fe (up to 90 mo% $Fe_3Al_2Si_4O_{12}$, Kesson et al., 1995) and possibly Na_2O (section 4.4.1.3). What this implies, therefore, is that TAPP is unlikely to be a *deep* lower mantle host for Al_2O_3. In addition, for low Al_2O_3 bulk compositions such as common mantle peridotites, it

---

[3] Many of the experimental runs which have been carried out on obviously appropriate bulk compositions, such as those on the same compositions as pyrope-almandine garnet, have been undertaken using an actual garnet as starting material (Irifune et al., 1996; Miyajima et al., 1996; Kesson et al., 1995; Ahmed-Zaïd and Madon, 1995 and O’Neill and Jeanloz, 1994), and under the short run times of these difficult experiments, metastable persistence of the garnet may have hindered the nucleation and growth of TAPP.

would appear that MgSi-Pvk will additionally accommodate all available Al_2O_3 through shallower depths up to the lower mantle / upper mantle boundary (figure 4.4_9). Within such bulk compositions, therefore, TAPP is not believed to be the Al-bearing lower mantle phase. Experimental petrology has shown, however, that there *are* ranges of compositions and physical conditions under which aluminous phases additional to MgSi-Pvk are stabilised (e.g. Miyajima et al., 1996, Irifune et al., 1996); these correspond to shallow lower mantle depths (670 - 800 km) for relatively aluminous compositions (e.g. > 5 mol% Al_2O_3 in $MgSiO_3$) corresponding from, for example, solar to basaltic compositions (section 4.1). These are discussed in detail in section 4.4.1.2. but, briefly, involve either corundum or majoritic garnet. Majoritic garnet has a wide stability range throughout the upper mantle and into the upper few tens of kilometres of the lower mantle, whereas corundum is stable, particularly for significantly Al_2O_3-rich compositions, through a significant range of depths in the lower mantle (e.g. Irifune et al., 1996). The most likely region for the stabilisation of TAPP, therefore, would be between the phase fields of MgSi-Pvk + corundum and MgSi-Pvk + majoritic garnet in a range of basic bulk composition in the $MgSiO_3$-Al_2O_3 system of $(MgSiO_3)_{90}(Al_2O_3)_{10}$ - $(MgSiO_3)_{75}(Al_2O_3)_{25}$.as indicated in figure 4.4_43. Under such circumstances TAPP, like garnet (Irifune and Ringwood, 1993), may be expected to lead to relatively low densities for basic rocks compared with peridotites. In terms of mantle dynamics (Irifune and Ringwood, 1993; Anderson, 1989; Ringwood, 1975 and Irifune and Ringwood 1987), TAPP may play an important part in the development of density differences between subducted basic compositions and peridotitic compositions, which will affect their relative segregation and circulation in the mantle. Basalt may be stripped off from subducted lithosphere at 670 km depth.

Section 4.4.2.5 Source of the LM II association

The key difference between the LM I and LM II associations is the role of Al. In contrast to LM I where Al is present in TAPP, no TAPP grains are found in association with type II pyroxene. Here, Al is contained within the pyroxene itself, up to some 11 wt% (section 2.2.1.5) and in ruby (section 2.2.1.7). Under *lithospheric* conditions, significant solid solution exists between $MgSiO_3$ and Al_2O_3. With increasing temperature below the liquidus, up to 16 wt% Al_2O_3 can be accommodated within enstatite (Boyd and England, 1964). With increasing pressure, however, the assemblage of garnet + Al-enstatite is favoured. This is because the near identical molecular weights for enstatite and corundum mean that the difference in density across this substitution is very small (Skinner and Boyd, 1964) and, relatively, garnet is a far denser phase. These observations may suggest that Type II pyroxenes *could* have formed under very high temperature, low pressure conditions (1675 K, 3 GPa). However, this is inconsistent with association of aluminous pyroxene composition with Al_2O_3 and fPer.

Study of figures 4.4_9 and the phase relations for TAPP proposed in figure 4.4_43 suggests that without even the need for a change in bulk composition, the LM II association could simply evolve from a higher pressure and / or temperature of formation than the LM I association (i.e. depths within the lower mantle and hence the name lower mantle II (LM II) association). Increasing pressure within relatively Al_2O_3-rich compositions (Al_2O_3 in $MgSiO_3$ of between 14 and 25 mol%, figures 4.4_11 and 4.4_43) causes movement from the ‘garnet’ or TAPP + MgSi-Pvk to the MgSi-Pvk + Al_2O_3 phase fields. Indeed, as detailed in section 4.3, Duffy and Anderson (1989) strongly favour the presence of Al_2O_3 in association with CaSiPvk, fPer and MgSiPvk in order to fit seismic observations of the lower mantle. In detail, the Al content of MgSi-Pvk increases at the expense of quantity and proportion of $MgSiO_3$ component in majoritic garnet until, at the phase boundary (26 GPa, 1773K, Irifune et al., 1996), MgSi-Pvk has ~14 mol% Al_2O_3 and coexists with pyrope ($Mg_3Al_2Si_4O_{12}$). Pyrope then disproportionates to corundum (Al_2O_3) and Al-rich MgSi-Pvk which, on further pressure increase accommodates more Al_2O_3 (which is consistent with the high Al_2O_3 content of Type II MgSi-Pvk) until all corundum is dissolved[1]. At this point (31 GPa, 1773K, Irifune et al., 1996) all the Al_2O_3 in the system is accommodated within aluminous MgSi-Pvk. Indeed it is pertinent to note that the compositions of BZ210B and BZ241B2 are very similar to aluminous

---

[1] Al^{3+} has a lower atomic weight than Si^{4+} and, in octahedral coordination, a larger ionic radius. Adding Al onto the Si (VI) site of MgSi-Pvk would, therefore, produce a lower density phase and thus may be considered to be indicative of lower pressure than alumina-free MgSi-Pvk. Such an argument does not take into account, however, associated phases. The important point for the stabilisation of aluminous MgSi-Pvk at higher pressure than Al-MgSi-Pvk + Al_2O_3 and alumina-free MgSi-Pvk + garnet is that corundum and garnet are *relatively* less dense phases. In other words, putting Al into MgSi-Pvk in order to stabilise corundum instead of garnet results in a higher density bulk composition just as bulk compositions composed of only aluminous MgSi-Pvk are more dense than those in association with corundum.

MgSi-Pvk synthesised with corundum at 27 GPa and 1773K by Irifune et al. (1996)[2]. The type II association can, therefore be placed within a depth region of ~720 - 840 km in relatively aluminous bulk compositions.

As phases of the LM II association surround a garnet composition (figures 4.4_44 - 4.4_46), indications of the bulk composition of the LM II association are consistent with the aluminous composition inferred from phase relations. In terms of proposed mantle bulk compositions *none* of the compositions considered in section 4.1 is particularly consistent with the LM II association; all are either too ferro-magnesium depleted, or are too Ca and Al-poor. Additionally, none have a similar, significant, Na content. Perhaps the most similar composition is the solar composition proposed by Anderson (1989) but, like the LM I association, it proved impossible to find an exact fit. Furthermore, there would appear to be significant differences in the bulk compositions of LM I and LM II associations. Unlike the LM I association, unless ruby is present in extremely small quantities, the LM II association probably represents a mixture between a solar composition and a more *Al-rich*, Fe depleted composition, yet, like LM I, still relatively Fe-rich compared to mantle peridotites; the presence of significant Cr in ruby suggests that there is some affinity within the LM II association with a peridotitic host rock composition. Table 4.4_5 summarises the preferred combination of phases giving a composition close to a solar composition yet involving a significant aluminous component enriched in Na.

Table 4.4_5 Relative proportion of phase required to make an Al, Ca rich solar composition

	CaSi-Pvk (BZ252A)	**fPer (BZ241A)**	**MgSi-Pvk (BZ241B1)**	**Ruby (BZ241C)**
cations	5 %	20 %	74 %	1 %

It cannot be said that LM I and LM II assemblages are strong evidence for a particular bulk composition for the lower mantle, such as the solar composition suggested by Anderson (1989). Although as the previous discussion and section 4.4.2.4 suggest, there are marked similarities and any uncertainty may be more due to the restricted sample sizes than any real deviation from predicted composition. What is particularly noteworthy, however, is that not only do the LM I and the deeper sourced LM II associations differ in terms of bulk composition with each other, they are both significantly different from upper mantle material. This is a particularly important result because it provides evidence to support a fundamentally different composition between the upper and lower mantle. Provided that the density contrast is large enough (which, as 4.4.2.7 discusses, is believed to be the case) such compositional difference can be cited as evidence to support mantle segregation and, thus, two-layer convection.

---

[2] Results of run E734 using a $MgSiO_3$ + 25 mol% Al_2O_3 starting material. Pressure and temperature errors are estimated at 1 GPa and 100K.

Bulk trace element compositions of the LM II association: There is little significant difference between the trace element composition of LM I and LM II material, calculated on the basis of solar major element composition (figure 4.4_47). If anything, LM II composition is depleted throughout the REE due, principally, to the expected relative paucity of CaSi-Pvk in LM II material. As for the LM I association, LM II shows a coincidence with OIB composition.

Section 4.4.2.6 Source of the LM III association

The LM III represents an altogether different association from LM I and LM II:

- The LM III association, and, particularly that for BZ259, yields trace element concentrations higher than those obtained for LM I MgSi-Pvk (section 2.4.5.2). Furthermore, the associated low Ca-majoritic garnet has trace element concentrations, section 2.4.3.1, lying midway between TAPP in LM I associations, section 2.4.3.2, and majoritic garnets, section 2.4.3.1. Both observations may suggest that the LM III association may form near the boundary of CaSi-Pvk stability.
- Like LM II, type III pyroxene is significantly Al enriched, although at yet higher values ~ 12 wt% oxide. The Na content of type III pyroxene, however, is substantial, ~ 6 wt% oxide.
- Both TAPP and low Ca-majoritic garnet are observed to be in association with the same composition of pyroxene.

The presence of low Ca, partially majoritic, garnet in the LM III association, would suggest an origin in the very shallow lower mantle (cf. figures 4.4_25 4.4_9) and hence the name lower mantle III (LM III) association. Indeed the suggestion that LM III involves the boundary of the stability limit of CaSi-Pvk, may also appear to support this conclusion. Phase relations suggest that CaSi-Pvk is stabilised at shallow depths, figure 4.4_12, however, so a further explanation must be invoked for its diminished presence. One explanation would be that the system is Ca-depleted, indeed the low Ca content of the majoritic garnet, BZ237C would support this conclusion. There is probably an additional compounding factor and that is the role of Na. As discussed in section 4.4.1.3, Na is stabilised within a garnet structured pyroxene at pressures of ~20 GPa rather than within CaSi-Pvk, Na, therefore inhibits the stability of CaSi-Pvk.

Indeed, Na may also provide an explanation for the increased Al content of MgSi-Pvk compared with LM I and LM II associations. All experimental evidence points to *increased* pressure inducing the solubility of Al in MgSi-Pvk, figures 4.4_9 - 4.4_11, yet we have just stated that the LM III association forms at a *lower* pressure certainly than LM II. These observations would appear to be at odds with each other. Phase relations involving Na have not been studied at pressures high enough to address the issue in a definitive manner, however, study of figure 4.4_16a shows, that the presence of significant Na in $MgSiO_3$, significantly lowers the pressure of formation of MgSi-Grt (majorite). If perovskite structured $MgSiO_3$ behaves in a similar fashion, the presence of Na would reduce the pressure required to stabilise Al-rich MgSi-Pvk.

Bulk composition: In terms of bulk composition, there are obvious differences between the LM III association and other São Luiz and FEG associations. Firstly, Na is clearly a more significant component. Comparison of figures 4.4_48 - 4.4_50 (ternary diagrams for LM III) with figures 4.4_30 - 4.4_32 (ternary diagrams for the TZ association) show striking similarities. The main differences are:

- the presence of fPer instead of pyrrhotite
- TAPP or low Ca, partially majoritic, garnet instead Ca-majoritic garnet
- low Ca, Na-rich pyroxene instead of diopside

Both associations may have affinities with eclogitic and primitive MORB compositions, although the LM III slightly less so.

The question still arises, is the LM III association simply a Ca-poor, Na-rich version of the TZ association or is it a *deeper sourced* Ca-poor, Na-rich version? Certainly, if the TZ association is sourced at the lower limit of pyroxene solution in garnet then the answer is yes, the LM III association is sourced at significantly greater depth. If, as preferred (section 4.4.2.2) the TZ association is formed predominantly at the upper limit of pyroxene solubility in garnet the answer is less clear. The presence of TAPP and the lower majoritic component in the majoritic garnet which does appear in the LM III association all suggest that it has a deeper origin, although, arguably, the stability of these phases may simply be increased to lower pressures by the change in composition. The fact that the composition of LM III appears to be transitional between the dominantly eclogitic or primitive MORB composition of the TZ associations and the Al- and Fe- rich compositions of the LM I and LM II associations, would perhaps further favour a source slightly deeper than TZ, perhaps coincident with the upper mantle / lower mantle boundary.

Proportions required to make eclogitic, primitive MORB and solar compositions from LM III are presented in table 4.4_6. As suggested by the ternary diagrams, figures 4.4_48 - 4.4_50, no combinations fit any of the proposed bulk mantle compositions particularly well.

Table 4.4_6 Proportions of phase from the LM III association required to fit mantle compositions

	fPer (BZ242A)	Type III pyroxene (BZ242B)	TAPP (BZ259A1)
Solar	15 %	65 %	20 %
primitive MORB	1 %	55 %	44 %
Eclogite	1 %	50 %	49 %

Solar composition (Anderson, 1989), Primitive MORB (Green et al., 1979) Eclogitic composition (Kushiro and Aoki, 1968)

Compared to a solar composition, Al and Na are too high and Mg, and particularly Fe, are too low in the LM III association. In contrast, compared to primitive MORB and eclogitic compositions, Mg is too high and Fe and Ca are too low in the LM III association. The fits to eclogitic and primitive MORB compositions are far better than that to the solar composition.

Bulk trace element composition of the LM III association: Bulk trace element concentrations in proportions equivalent to solar, eclogite and primitive MORB compositions have been calculated for the LM III association. Results are presented in figure 4.4_51. Amongst the other associations for which bulk trace element compositions have been calculated, the LM III association is most coincident with that of the LM / UM association; the others being quite different. The main difference probably lies with the fact that LM III is not expected to involve CaSi-Pvk: similarly, CaSi-Pvk, is thought to be a minor phase in the UM / LM association. The REE trend of LM III is very flat, with the exception of a slight excess of Tm and Yb, and, in all, mirrors the composition of MORB.

➠

Section 4.4.2.7 Deep mantle inclusions; phase relations over the upper mantle / lower mantle boundary and mantle convection

The individual associations recovered from São Luiz and Guinean diamonds have been discussed separately in sections 4.4.2.1 - 4.4.2.6. The present section aims to summarise the conclusions and compare and contrast the differing associations with a view to predicting likely mantle convective régime.

The multitude of separate lines of evidence regarding the compositional characteristics and associations of deep mantle inclusions within São Luiz and Guinean diamonds strongly suggests that the majority are sourced from a fairly narrow volume comprising the upper part of the lower mantle, the upper mantle / lower mantle boundary itself and an region of the deep transition zone. In addition, material indicative of a deeper origin in the lower mantle is rarely present, as well as a few stones sourced in the mantle lithosphere and shallower regions of the transition zone. It is hard to say how globally representative of the compositions of the mantle regions from which São Luiz and Guinean inclusions are sourced are, however, there does appear to be both a compositional transition with depth, in addition to a distinct compositional difference involving material whose origin is most likely from the lower mantle compared to the upper mantle. Upper mantle material (UM) sampled has a lherzolitic composition with some eclogitic similarity whereas transition zone material (TZ) is *strongly* eclogitic. Deep transition zone material is either ecolgitic (yet Na-rich and deficient in Ca) and possibly involves a solar component (LM III) or else involves a mixture of solar component and an Al-poor harzburgitic component (UM / LM). Lower mantle material (LM I) has a strong solar affinity with increasing Al content with depth (LM II). The increase in solar bulk composition affinity with penetration into the lower mantle provides a striking indication of a compositional difference between upper and lower mantle. Whether such a compositional difference can be said to promote layered mantle convection in the mantle depends on the magnitude of the associated density contrast and is discussed later in this section. Figure 4.4_52 serves to summarise the expected phase fields within which the São Luiz and Guinean associations lie, projected onto a diagram of $MgSiO_3$ - Al_2O_3 bulk composition[1]. In addition, figures 4.4_53 - 4.4_55 aim to summarise the compositional differences between associations. Unlike figures discussed in section 4.4.2.1 - 4.4.2.6, all associations are incorporated onto each ternary diagram, which, although adding to the complexity of the resulting diagrams does allow for direct comparison of association fields. The reader should note the similarity between the TZ and LM III associations and the transition through UM / LM compositions, to the true lower mantle associations LM I and LM II. Indeed the similarity in compositional affinities of transition zone-related associations (TZ, UM / LM and LM III) compared to LM-related associations

---

[1] This diagram is dimensionalised in terms of pressure and temperature following discussion of phase relations in section 4.4.1.1 and 4.4.1.2 and arguments over the need for a thermal boundary discussed in section 4.5.1.2.

(LM I and LM II), does not end with major element characteristics. Trends in calculated trace element concentrations appear to suggest affinity with OIB for transition zone material and MORB for upper mantle / lower mantle boundary material compared to OIB for lower mantle material. Such a similarity with OIB for lower mantle material may be coincidental but also may act to support the evidence of a lower mantle component within OIB discussed in section 7.3.1.

Density contrast between predicted São Luiz: Price et al. (1989) and Jeanloz and Knittle (1989) argue that a density contrast of greater than ~ 3% would be required for the upper and lower mantle to convect separately. Within certain limitations, the density of rock types which the São Luiz and Guinean associations represent can be calculated: the proportions of phases in each association have been inferred (sections 4.4.2.1 - 4.4.2.6), the ATP densities of most relevant phases are published (table 4.4_7) and the relative volume change for these phases over expected mantle geotherms is calculated (section 7.1.2) following the methodology presented in section 7.1.1. A density contrast for the natural sample can, therefore, be inferred.

Table 4.4_7 Atmospheric temperature pressure densities for mantle phases used in calculation of expected rock densities

Diopside	Hedenbergite	Majorite	Pyrope	Almandine	Grossular	CaSi-Pvk
3.279	3.656	3.513	3.565	4.312	3.600	4.252
MgSi-Pvk	FeSi-Pvk	Periclase	Wüstite	Mg-R'ite	Fe-R'ite	Corundum
4.107	5.164	3.585	5.956	3.563	4.848	3.986

Values from references in Smyth and McCormick (1995) except for CaSi-Pvk (Mao et al., 1989) and FeSi-Pvk from appendix 13.

Methodology: In order to investigate any density contrast across the upper mantle / lower mantle boundary, ATP densities for phases used in bulk composition modelling calculations (sections 4.4.2.1 - 4.4.2.6) were interpolated from densities published for end-member compositions. Densities for each phase at 670 km in depth were then calculated by application of relative volume change using conditions of pressure of 24 GPa and temperature of 1899K[2]. Densities for each rock type modelled for each association were subsequently calculated by combining the calculated density for each phase in the proportions summarised in tables 4.4_1 to 4.4_6. Calculated densities are presented in table 4.4_8 and resultant density contrasts are summarised in table 4.4_9.

---

[2] From Geotherm 2 (section 4.2).

Table 4.4_8 Summary of calculated densities for deep mantle rocks at 670 km depth using data from São Luiz assemblages.

Association	**TZ**	**TZ**	**LM/UM**	**LM/UM**
Bulk composition	Eclogite	prim-MORB	Solar	Harzburgite
Density	3.979	3.875	4.006	4.006

Association	**LM III**	**LM III**	**LM III**	**LM I**	**LM II**
Bulk composition	Solar	prim-MORB	Eclogite	Solar	Solar
Density	4.297	4.199	4.175	4.354	4.384

Bulk compositions are modelled for each assemblage using inclusions highlighted in the following tables: TZ, table 4.4_1; LM/UM, table 4.4_2; LM I, table 4.4_4; LM II, table 4.4_5; LM III table 4.4_6

Table 4.4_9 Selected density contrasts between mantle associations modelled to fit a variety of bulk rock compositions

	TZEcl	**TZpM**	**LM/UMs**	**LM/UMh**	**LM IIIs**	**LM IIIpM**	**LM IIIe**	**LM I**	**LM II**
TZEcl	-								
TZpM		-							
LM/UMsol	0.68	3.37	-						
LM/UMh	0.68	3.37		-					
LM IIIs	7.98	10.87	7.26	7.25	-				
LM IIIpM	5.53	8.36	4.82	4.82		-			
LM IIIe	4.94	7.74	4.23	4.23			-		
LM I	*9.43*	12.35			1.33	3.69	4.27	-	
LM II								0.68	-

pM- primitiveMORB; Ecl- eclogite; s- solar; h- harzburgite
Density contrasts are calculated as the percentage increase of (horizontal column density - vertical column density)/vertical column density e.g. the italicised figure 9.43 is calculated by the formula Density contrast = 100x((LMI - TZEcl)/TZEcl).

Limitations: A number of key limitations are inherent in the above calculations:

- Thermoelastic constants for a number of phases are unknown (TAPP, Type II and Type III MgSi-Pvk). Values for garnet and Type I MgSi-Pvk, respectively, are adopted for TAPP and Type II/III MgSi-Pvk.
- Thermoelastic constants of end-member compositions rather than phases of the composition of the inclusions of interest are often unknown. Parameters are interpolated from end members following the methodology in section 7.1.1.
- It is questionable how accurately calculated proportions of phases in each association relate to their source rocks.

All these limitations have relevance for the accuracy of calculated density. In terms of uncertainties in thermoelastic behaviour, however, deviations from real densities are expected to be minor and, given the range of rock types modelled for each association, calculated densities are expected to go some way to bracketing the actual rock type. The importance of the conclusions are not so much in the values of calculated density contrasts but in their magnitude.

Results: The key result is that there is a large density contrast (9.4 - 12.3 %) between modelled transition zone (TZ) source rock and lower mantle (LM I) source rock. Indeed, no matter what the bulk composition of either rock type, there is likely to be a significant density difference between the two. Phases of the LM I association generally have greater densities than phases of the TZ association at 670 km in depth and the least dense phase (TAPP) of LM I is considered to be a lower bound estimate (thermoelastic data for the shallower depth polymorph, garnet, are adopted for TAPP). Additionally, given the greater compositional variation amongst majoritic garnets compared to diopsides, a high density, garnet dominated TZ rock is considered unlikely. The density contrast between TZ and LM I material is primarily controlled by the stabilisation of the high density perovskite structured phases in the LM I association. What can be concluded from these calculations, therefore, is that the contrast between the density of lower mantle material and transition zone material is likely to be significantly greater than 3 % and thus (following the evidence of Price et al., 1989 and Jeanloz and Knittle, 1989) can be cited as evidence for layered mantle convection.

Density contrasts between other associations compound the conclusions of depth of formation, on the basis of phase relations, discussed in sections 4.4.2.3 - 4.4.2.6 and summarised in figure 4.4_52. As table 4.4_9 shows, both LM III and UM/LM associations are transitional in density between true transition zone material (TZ association) and true lower mantle material (LM I association). Additionally, the LM II association yields a higher density than the LM I association[3].

➠

---

[3] This contrast is very small and is probably within error and is a reflection of the fact that at 670 km the LM I association is still stable. With greater depth the contrast is seen to expand (at 768 km the contrast increases to 0.70 %) consistent with the stabilisation of LM II at depth.

Section 4.5 Equilibration of São Luiz and Guinean inclusions and element partitioning

As section 4.4 has demonstrated, details of the assemblages recovered from São Luiz and Guinean diamonds correspond well with the results of experimental petrology. Many of these diamonds yield assemblages of inclusions which can only be stable in the lower mantle or transition zone. The chemical sanctity of diamond as an occluding phase for São Luiz and Guinean inclusions is discussed in detail in section 5.3.1.2. In most cases, one can be assured that once inclusions have been trapped inside diamond, their composition does not change. As many inclusion associations are not touching, some degree of uncertainty still remains as to whether the assemblages outlined in section 2.3, are in equilibrium. It can be envisaged that inclusions within a single diamond are incorporated at different stages of diamond growth; perhaps even under different physical conditions and / or relating to different bulk ambient compositions. Rickard et al. (1989) found evidence for disequilibrium amongst Koffiefontein inclusions and Moore and Gurney (1989) made similar observations on Monastery material. Furthermore, Griffen et al. (1988) found evidence for disequilibrium amongst coexisting garnets and pyroxene from within a number of Western Australian diamonds. Their conclusions suggest diamond growth over a considerable period of time, in many cases, and, given the intensely complex cathodoluminescence observed for São Luiz diamonds (section 5.6), the same is likely to be the case for São Luiz stones. Indeed Harte et al. (1996b) report two different compositions of fPer coexisting with TAPP in BZ205. A study of major element equilibration is, therefore, merited.

Perusal of ternary diagrams for the São Luiz and FEG associations (figures 4.4_30 - 4.4_50) shows that where sufficient examples of coexisting phases are in evidence for cross comparison, the trends in tie lines, in general, are consistent with equilibrium formation. This is particularly striking between Type I MgSi-Pvk, and fPer and TAPP and fPer (figure 4.4_38).

Exceptional disequilibrium: As well as being particularly exemplary of equilibrium associations, figure 4.4_38, however, also contains the most notable apparent exceptions: BZ207 and BZ205. As discussed in section 4.5.2, bulk compositional differences and possible slight re-equilibration of the composite grain BZ207A,C can easily explain its inconsistent behaviour with other coexisting inclusions and yet still indicate equilibium. In the case of BZ205, the fact that the TAPP grain (BZ205A) coexists with two fPer inclusions of widely differing Mg# is clearly unique to this particular stone. As figure 4.4_5 shows, there does exist a region in compositional space where two fPer compositions coexist. For olivine bulk compositions, this lies at dominantly Fe-rich compositions; even more so and at a higher pressure for a pyroxene system (figure 4.4_2). Although some shift in the stability fields is expected on addition of additional components, it is hard to envisage a shift appropriate to account for the *intermediary* Mg# composition of reconstituted BZ205. It is difficult, therefore, to reconcile the features of BZ205 without invoking disequilibrium. It is concluded that one or other, or both, fPer inclusions were incorporated within the growing stone within different regions of the deep mantle. It should be noted that the disequilibrium features of BZ205 are exceptional.

So, in general, equilibrium conditions can confidently be assumed. Section 4.5.1, deals with some of the finer details of equilibrium partitioning and applies this data to obtaining information on mantle conditions and inclusion source. Secondly, section 4.5.2, addresses the special case of equilibration within composite phase inclusions.

Section 4.5.1 Partitioning studies

In addition to the experimental work which has been carried out in order to constrain the relative stability of phases pertaining to different conditions in the mantle, work has also been undertaken specifically to constrain the behaviour of individual elements between these phases. One of the key observations has been that the partitioning of elements is dependent not only on the structures of the host phases but also on the bulk composition[1] and ambient conditions of pressure and temperature. It should be noted at this stage that partitioning of trace elements is *not*, however, dependent on elemental concentration (Beattie, 1993): trace element partitioning obeys Henry's Law.

The state of the science for much upper mantle material, especially pertaining to the lithosphere, is such that partition coefficients have been sufficiently constrained to allow accurate pressure and temperature estimates for the formation conditions of many assemblages (eg. Ellis and Green, 1979; Lindsley and Dixon, 1976; Mori and Green 1985 and Harley, 1984).

For the transition zone and lower mantle, however, results at this stage tend to be more qualitative. Experimental work on transition zone and lower mantle partitioning can be subdivided into two parts:

- Partitioning involving the liquid phase (Hauri et al., 1996; Trønnes et al., 1992 and Kato et al., 1986)
- Partitioning involving subsolidus phases (McCammon et al., 1996; Dalton and Wood, 1993; Fei et al., 1991; Kesson and Fitzgerald, 1991 and Kato et al., 1986)

For twin element partitioning between phases, the exchange distribution coefficient, K_D, is most commonly adopted, where:

$$K_D = \frac{\left(x_i / x_j\right)^{\text{phase I}}}{\left(x_i / x_j\right)^{\text{phase II}}} \qquad \text{Equation 4.5\_1}$$

where x_i and x_j are the concentrations of the elements in question.

---

[1] This also includes an influence of oxygen fugacity.

Also occasionally adopted, is the Nernst distribution coefficient which is expressed in terms of a single element:

$$D_i = C_i^{\text{Phase I}} \Big/ C_i^{\text{Phase II}} \qquad \text{Equation 4.5\_2}$$

where Ci is the concentration of element i in Phase I and II.

Attention must be paid to whether equation 4.5_1 and equation 4.5_2 are calculated on the basis of wt% or cation values.

➠

Section 4.5.1.1 Fe / Mg partitioning between fPer and olivine composition

Experimental results: Fei et al. (1991) present the results of a total of 36 successful experiments designed to investigate the partitioning between fPer and both the polymorphs of olivine, and its breakdown product to MgSi-Pvk. Run conditions ranged from 2 GPa, 1473 K to 26 GPa, ~ 1673 K and involved starting compositions of varying proportions of olivine and fPer over a range of compositions. The main thrust of their research was aimed at accurately constraining phase relationships in the MgO - FeO -SiO_2 system for the transition zone and lower mantle[1], an important by-product being, however, a comprehensive determination of partition coefficients and associated pressures and temperatures.

Fei et al.'s (1991) results show that Fe partitions preferentially into the fPer phase compared to olivine, wadsleyite, ringwoodite and MgSi-Pvk. This partitioning is particularly strong for fPer / olivine and fPer / MgSi-Pvk and increasingly less so for fPer / wadsleyite and fPer / ringwoodite.

The effect of temperature and pressure was determined independently for fPer / olivine: an increase in either parameter was found to favour partitioning of Fe into fPer with temperature being the dominant control. Conditions of pressure and temperature were not varied for runs involving wadsleyite. Given that a combined rise in temperature and pressure, however, produced a similar shift in partitioning for fPer / ringwoodite, it can be supposed that pressure and temperature rises enhance the tolerance for Fe of fPer throughout the olivine system.

Application to inclusions from São Luiz and FEG: Plotting the ΣFe/(ΣFe+Mg) for BZ243B (fPer) against BZ243C (olivine composition), figure 4.5_1, and comparing with data presented in Fei et al. (1984) shows that BZ243 inclusions lie between the data obtained for partitioning between Fe and Mg for fPer / olivine and fPer / ringwoodite. Three possible explanations can account for this behaviour:

i) BZ243B formed in equilibrium with BZ243C adopting an olivine structure but at conditions of pressure and temperature significantly lower than 2 GPa, 1473K.
ii) BZ243B formed in equilibrium with BZ243C adopting a wadsleyite structure but at conditions of pressure and temperature lower than 15 GPa, 1773K.

---

[1] As discussed in detail in section 4.4.1.

iii) BZ243B formed in equilibrium with BZ243C adopting a ringwoodite structure at conditions of pressure either greater than 20 GPa at 1873K or at greater temperatures[2].

Given that both scenarios i) and ii) require conditions of pressure and temperature of formation well removed from any likely mantle geotherm and that it is not considered likely that fPer is a stable phase in any mantle composition at these conditions, it is considered that scenario iii) is most likely[3]. Indeed elevated conditions of temperature or pressure above 20 GPa and 1873K correspond well to both Geotherms 1 and 2, section 4.2. Given the inference that temperature is the dominant factor and significantly increasing pressure would see a break-down of olivine composition, it would seem particularly likely that BZ243 formed at conditions similar to those of Geotherm 1 (section 4.2).

➠

---

[2] Fei et al.'s (1991) experiments were undertaken using a multi-anvil cell. Although they do not present estimates of the error in temperature measurement, similar apparatus usually involves errors of the order of 10 - 50K (e. g. Ito and Takahashi, 1987b). Given, additionally, the small errors in EPMA analysis (grain sizes of run products were usually far larger than the electron beam diameter) it can be attested that the position of the point for BZ243B/C lies outwith error of the mixing lines of figure 4.5_1.

[3] It is expected that TEM could provide further evidence for an original ringwoodite structure for BZ243C in terms of its microstructure (Sautter, V. 1997 *personal communication*).

Section 4.5.1.2 fPer - MgSi-Pvk partitioning and thermal state of the upper mantle / lower mantle boundary

Experimental results of Fe / Mg partitioning: Although the data has little variation, it would appear that the association of fPer with *MgSi-Pvk* produces quite a different effect from that with olivine composition (section 4.5.1.1).

Combining data from Fei et al. (1991), Yagi et al. (1979), Guyot et al. (1988) and Ito et al. (1984), for the system fPer / MgSi-Pvk, increasing pressures in the 20 GPa region, produces a small relative increase in Fe content of fPer. At pressures above ~35 GPa, however, Guyot et al. (1988) and Kesson and Fitzgerald (1991) found no further change in Fe / Mg partitioning between fPer and MgSi-Pvk with pressure. Their results at 40 GPa agree with those of Malavergne et al. (1995). Table 4.5_1 summarises the K_D values[1] for Fe / Mg partitioning between fPer and MgSi-Pvk for a variety of pressures and by various authors and figure 4.5_2 presents their results graphically.

Table 4.5_1 K_D values for Fe / Mg partitioning between fPer and MgSi-Pvk as determined by various authors.

Pressure	25 (GPa)	30 (GPa)	35 (GPa)	40 (GPa)	50 (GPa)	75 (GPa)
K_D*	6.0	4.1		3.5	3.5	3.5
K_D¤	6.62					
K_D¥			4.67			
K_D‡				3.0		
K_D†	2.0 - 3.4	4.6 - 8.0				
K_D§		4.0				
K_D¢	7.0 - 8.1					

* Guyot et al. (1988) 1100-2500 K; ¤Ito et al. (1984); ¥Bell et al. (1979); ‡ Malavergne et al. (1995) 1773 K; † Kesson and Fitzgerald (1991) 1873 K; §Yagi et al. (1979) 1173 K; ¢Calculated from Fei et al. (1991) 1673 K.

The larger range in values obtained by Kesson and Fitzgerald (1991) reflect the larger compositional range of phases studied. It is interesting to note that their values, particularly for ~25 GPa are substantially lower than those obtained by other authors. This is likely to be partially due to the fact that their data is based on a wt% calculation compared to the cation calculations made by other authors (cf. data in table 4.5_2). The *dominant* reason for their lower values, however, is likely to be due to temperature. Fei et al. (1991) suggest an increase in K_D with decreasing temperature. Temperature uncertainties are very large for work carried out using laser heating, and although

---

[1] None of the papers mention specifically whether K_D values have been calculated on the basis of wt% or cations. Fei (1997, *personal communication*) confirms that all his calculations were on the basis of cation values calculated assuming all Fe is present as Fe^{2+}. Additionally, Malavergne (1997, *personal communication*) confirms that calculations in Guyot et al. (1988) and Malavergne et al. (1995) were also on the basis of mol%.

Kesson and Fitzgerald (1991), quote run conditions of 1873K, using the same type of laser operating at the same conditions, Guyot et al. (1988), quote temperature errors of around 750K. It should also be noted that the 1773 K quoted by Malavergne et al. (1995) was determined on the basis purely of grain size and, is thus, also subject to large errors. Since their value for partitioning is consistent with those of other workers quoting the same general temperature, their estimate of 1773K is likely to be reasonably correct.

Given the observations based on experimental data and the strong likelihood that no matter what geotherm is proposed, relative pressure rise will always be greater than relative temperature rise, it can be expected that partitioning of Fe and Mg between fPer and MgSi-Pvk through a significant portion of the lower mantle can be expected to be independent of depth.

Considering the effect of composition in more detail, phase determinations in the FeO - MgO - SiO_2 system show that a wide range of Fe / Mg composition fPer coexists with a very restricted range in Fe / Mg composition MgSi-Pvk, (Bell et al., 1978 and Kesson and Fitzgerald 1991, figure 4.4_6, section 4.4.1.1). In terms of the phase boundary in pressure temperature space, temperatures of experiments are largely inadequate to provide an accurate extrapolation along Geotherm 1 of section 4.1, however, broadly, the most Fe-rich fPer coexisting with MgSi-Pvk varies from Mg# = 0.65 at 670 km to 0.4 at 1600 km in the SiO_2-free system and 0.45 at 670 km to 0.2 at 1600 km in the SiO_2-present system (Yagi et al., 1978, figure 4.4_3). This observation has implications for the interpretation of São Luiz and Guinean inclusions and will be discussed in the following subsection.

Application to inclusions from São Luiz and Guinean: Clearly the MgO-SiO_2-FeO system is rather restricted compared to how we perceive lower mantle bulk composition. However, if we constrain our application of this work to the LM I paragenesis, we restrict[2] the complicating factors principally to Fe^{3+}. The role of Fe^{3+} is not entirely clear. Certainly work by McCammon (McCammon et al., 1997 and section 2.5) suggests that the Fe^{3+} content of most deep sourced São Luiz inclusions is rather substantial. The Fe^{3+} content of BZ251A (Type I MgSi-Pvk, section 2.5) is consistent with this generalisation although is not as significant as in Type II MgSi-Pvk. All experimental work on partitioning discussed above has measured elemental concentrations either by ATEM or by EPMA analyses inferring phase compositions by extrapolation[3]; neither technique incorporates a means of

---

[2] Type I pyroxene is, essentially (Mg,Fe)SiO_3 and CaSi-Pvk, if, indeed, it is stable as part of this paragenesis, does not involve Mg or Fe.

[3] Grain sizes of run products are, typically, smaller than the analytical beam of the EPMA. This means that each analysis incorporates a variable but finite component due to both phases present. The average composition of each phase is estimated by collecting compositional data from a large number of points on the sample, plotting the unknown of interest against some reference ratio (eg. Si / (Si + Mg)) and reading off the unknown having been extrapolated such that the reference ratio corresponds to each of the phases present. For example, Si / (Si + Mg) should equal 0 for fPer and 0.5 for MgSi-Pvk based on cations. This method is widely employed for experiments run at high pressure; in the system presently subject to discussion the method is employed by Fei et al. (1991), Kesson and Fitzgerald (1991), Guyot et al. (1988) and Malavergne et al. (1995).

discriminating oxidation states of Fe; all Fe being measured as total Fe. Certainly the conditions of oxygen fugacity involved in experimental work are likely to be different from that pertaining to São Luiz material, however, if Fe is presented as total Fe, some meaningful comparisons can be drawn.

Run conditions (Fei et al. 1991; Ito et al., 1984 and Yagi et al., 1979) are only marginally cooler than Geotherm 2 proposed for the lower mantle, section 4.2, and so we would expect partitioning of Mg / Fe between fPer and MgSi-Pvk inclusions to yield similar values to the work outlined above. If, however, conditions of formation were significantly hotter (e.g. Geotherm 1, section 4.2), one would expect Fe to be less preferentially partitioned into fPer (perhaps yielding similar values to those obtained by Kesson and Fitzgerald, 1991). Thus by measuring the composition of coexisting fPer and MgSi-Pvk inclusions we can make an informed estimate as to the temperature conditions in the lower mantle.

Table 4.5_2 presents partition coefficients calculated for coexisting Type I MgSi-Pvk and fPer from BZ207 and BZ251. These data are plotted along with the results of experimental data in figure 4.5_3.

Table 4.5_2 Partition coefficients for coexisting Type I pyroxene and fPer inclusions from São Luiz.

	BZ207B/C	**BZ251A/B**
$(\Sigma Fe_{wt\%}\#)^{fPer}$	0.440	0.239
$(\Sigma Fe_{cation}\#)^{fPer}$	**0.306**	**0.150**
$(\Sigma Fe_{wt\%}\#)^{MgSi\text{-}Pvk}$	0.220	0.095
$(\Sigma Fe_{cation}\#)^{MgSi\text{-}Pvk}$	**0.141**	**0.055**
$(Fe_{cation}\#)^{MgSi\text{-}Pvk}$	0.116	0.045
$K_D\Sigma Fe_{wt\%}$	2.00	2.52
$K_D\Sigma Fe_{cation}$	***2.17***	***2.73***
$K_D Fe_{cation}$	2.60	3.27

ΣFe represents total Fe (both Fe^{3+} and Fe^{2+}). Fe# defined as $Fe^{2+}/(Fe^{2+}+Mg)$ (unless Σ is specifically applied) where Fe^{2+} calculated using a value of $Fe^{''+}/\Sigma Fe$ of 0.80 for Type I MgSi-Pvk (determined from BZ251B, section 2.5.3). K_D defined as section 4.5.1 for fPer / Type I MgSi-Pvk. Numbers in bold are plotted on figure 4.5_3. Numbers in bold italics are plotted on figures 4.5_4 and 4.5_5.

It can be clearly seen from figure 4.5_3 that both BZ251 and BZ207 coexisting phases plot to the right of the mixing lines presented in the literature. Following the arguments outlined above, this can be explained in terms of formation at pressures equivalent to those employed experimentally but at higher temperatures (also compare table 4.5_1 with 4.5_2). Indeed as Kesson and Fitzgerald point out, K_D values for inclusions from Koffiefontein inclusions and Orrorroo inclusions are also consistent with their experimentation and thus, high temperature equilibration.

Malavergne et al. (1997) present an additional means of approaching the same question of the physical conditions of fPer / MgSi-Pvk equilibrium. Using crystal field theory, they present two models for K_D values between fPer and MgSi-Pvk: one based on data from Shen et al. (1994), here termed Model 1; and the other based on data from Keppler et al. (1994), here termed Model 2. Their models incorporate expected partitioning data over a significant region of lower mantle pressure and temperature space and are plotted in figures 4.5_4 and 4.5_5. In addition to the data of Malavergne et al. (1997), figures 4.5_4 and 4.5_5 also incorporate the positions of Geotherm 1 and Geotherm 2 (section 4.2) and partitioning data from São Luiz samples. For Model 1, the hotter geotherm, Geotherm 1, appears to be far more appropriate to the partitioning seen for São Luiz material. For Model 2 the situation is less clear cut, if anything, favouring Geotherm 2. However, it should be noted that the presence of Al in MgSi-Pvk could force more partitioning of Fe into fPer thus also favouring Geotherm 2.

As far as Fe / Mg partitioning is concerned, all coexisting Type I / fPer inclusions can be considered to be in equilibrium. Indeed the fact that BZ251A and BZ251B being wholly isolated grains, lie on the same distribution curve, figure 4.5_3 as BZ207C and BZ207B, where BZ207C is in contact with a TAPP, BZ207A, would suggest that the composition of BZ207A/C has not redistributed its components subsequent to formation. This data is, therefore, in line with the observations of touching phases in general from São Luiz, section 2.2.2. We can say with confidence that the majority of fPer inclusions described from São Luiz and Guinea are consistent with formation in equilibrium with MgSi-Pvk. This conclusion is consistent with even the Fe-rich inclusions although in order to have formed in equilibrium with MgSi-Pvk they would have to have formed at significant depth, or certainly under different bulk composition. The one exception, perhaps, is BZ66 which may have formed, alternatively, in association with SiO_2 or, as described in section 2.6.1.2, at far greater depth.

Cr_2O_3, MnO and NiO partitioning: Kesson and Fitzgerald (1991) determined values for D for Cr_2O_3, MnO and NiO for fPer against MgSi-Pvk over a range of pressures. Within the large range of values obtained for each run, they found no variation of partition coefficients with pressure. Data are presented in table 4.5_3 and compared with results from coexisting fPer and MgSi-Pvk from BZ207, BZ251 and Koffiefontein stone A262 (Rickard et al., 1989).

Table 4.5_3 Nernst distribution coefficients of wt% Cr_2O_3, MnO and NiO between fPer and MgSi-Pvk for BZ207, BZ251 and Koffiefontein pair A262.

	Cr_2O_3	**MnO**	**NiO**
Kesson and Fitzgerald 1991	1.05 - 6.5	1.1 - 5.4	1.2 - 19
BZ207B / BZ207C	3.40	1.43	30.0

BZ251A / BZ251B	0.85	1.57	416.7
A262 (Koffiefontein)	1.58	1.73	70.5

Koffiefontein data from Rickard et al. (1989) and this work.

From table 4.5_3 it is clear that MnO and Cr_2O_3 partitioning for natural samples is consistent with data obtained by Kesson and Fitzgerald (1991).

All values of partitioning of NiO obtained from natural samples are inconsistent, however, with Kesson and Fitzgerald's (1991) data[4]: NiO content of the enstatite composition A262 from Koffiefontein having been determined by EPMA at Edinburgh as 0.02 wt%. An explanation for this discrepancy could be that the runs performed by Kesson and Fitzgerald (1991) involved highly reducing conditions controlled by doping with Fe:Ni:Cr alloy. As Malavergne et al. (1995) show, Ni is significantly partitioned into Fe:Ni alloy compared to fPer, especially under low lower mantle pressures, thus highly reducing conditions would result in lower NiO partition coefficients for fPer against MgSi-Pvk than in the absence of Fe:Ni. Similarly, values for NiO partitioning in BZ207, BZ251 in addition to the Koffiefontein material strongly suggests an *absence* of Fe:Ni in the LM I paragenesis, consistent with the rejection of Fe:Ni alloy as an explanation for 'blebs' in fPer inclusions (section 2.6.1) and the high Fe^{3+} content of TAPP and Type I MgSi-Pvk (section 2.5.1.2).

In a similar fashion to Fe / Mg partitioning, Malavergne et al. (1997) present K_D values through pressure / temperature space for Co / Mg and Ni / Mg partitioning. Results for Ni / Mg partitioning (Co has not been measured on São Luiz material) are presented in figures 4.5_6 and 4.5_7. Compared to Fe / Mg partitioning, Malavergne find that Ni is even more strongly partitioned into fPer. Ni contents of São Luiz inclusions from BZ207 and BZ251 are generally rather low, particularly in MgSi-Pvk, however, K_D values can still be calculated and are found to be less extreme than both Models 1 and 2 of Malavergne et al. (1997), even accounting for a small excess of Ni going into the magnesioferrite phase, $K_{DNi/Mg}^{BZ207B/BZ207C} = 16.9$ and for $K_{DNi/Mg}^{BZ251B/BZ251A} = 5.58$. These results, within error, are far more consistent with the higher temperature Geotherm 1. High temperature could be cited as evidence for crystallisation in either a hot lower mantle (involving a thermal boundary between upper and lower mantle) or else within the elevated temperature environment of a mantle plume. As São Luiz inclusions involve a significant range of depths of formation, outwith the expected volume of plume initiation, and, given the implication that diamond will have ponded on the upper mantle / lower mantle boundary over significant periods of time (section 7.1.2) it is believed that the former scenario is the case. Geotherm 1 temperatures are therefore believed to

---

[4] In their discussion Kesson and Fitzgerald (1991) find no inconsistency between inclusion material and expeimentally determined partition coefficients. Their calculation for NiO partitioning, however, was not based on values for the coexisting Koffiefontein inclusions which they refer to but rather on a range of separate inclusions not necessarily in mutual equilibrium: NiO had not been determined for Koffiefontein MgSi-Pvk at this time.

reflect the *ambient* conditions of temperature in the upper mantle / lower mantle boundary region; any association of deep mantle diamonds with a mantle plume (section 7.3.1) is envisaged to be only of *transportation* of previously crystallised diamond.

Relevance to bulk composition: Kesson and Fitzgerald (1991) and Malavergne et al. (1995) have compared their partitioning data to the one fPer - enstatite diamond inclusion pair reported from the literature: A262 from Koffiefontein (Rickard et al., 1989). They correctly conclude that if fPer and MgSi-Pvk are the major phases in the lithology represented by the Koffiefontein diamond A262, and the individual stones from Orrorroo (Scott-Smith et al., 1984) and Sloan (Otter and Gurney, 1989), then Fe / Mg partitioning is coincident with a bulk composition of pyrolite and not, for example a chondritic mantle. Furthermore Kesson and Fitzgerald (1991) cite Cr_2O_3, MnO and NiO as being consistent with a pyrolite composition. Given the question of NiO partitioning discussed above, I would merely question the validity of their NiO partitioning rather than their conclusion that Koffiefontein inclusions are consistent with a pyrolite composition. For some São Luiz and Guinean diamonds, there also appears to be a consistency with a pyrolite bulk composition. However, it is clear from the São Luiz inclusions that the range in compositions of fPer and MgSi-Pvk shown by Orrorroo, Sloan and Koffiefontein stones is not *representative* of the lower mantle sourced by São Luiz diamonds. Indeed, for São Luiz sourced lower mantle pyrolite is by no means a particularly relevant solution (section 4.4.2.4).

➠

Section 4.5.1.3 Deep mantle phases / Liquid

Experimental work: Experimental investigation into the partitioning of elements between transition zone and lower mantle phases and melt has been undertaken by a number of authors: Kato et al. (1988), Gasparik and Drake, (1995), Trønnes et al. (1992).

fPer against liquid: fPer inclusions, given their range in major element concentration, section 2.2.1.4, and the large number of ion microprobe analyses obtained, represent the only São Luiz material studied herein for which an estimate of trace element variation with major element concentration can be made. Figures 4.5_8 to 4.5_11 presents trace element data against Fe # [1] for all fPer inclusions for which data is available, including analyses by Harte and Fitzsimons (1993, *personal communication*).

For all trace elements, the trend in concentration against Fe # is essentially the same: a sharp fall in concentration amongst the Mg-rich fPer inclusions followed by a steady, shallower, fall with increasing Fe content. In detail, this trend is particularly strong[2] for: Sr (amongst LILE), all REE and Y and Zr (amongst HFSE). It was suggested in section 2.4.4 that the low values of trace elements in fPer were likely to be influenced by structural controls. If this were *purely* the case, however, given the linear decrease in cell parameter with Fe content, one would expect a similar linear decrease in large cation content. Although structural factors are still considered to play an important role, the sharp fall-off in trace element contents with increasing Fe # is better explained by fPer crystallising from a melt where the trace element retaining phase crystallises early, but not immediately. Here, crystallisation is reflected in increasing Fe # reflecting increasing evolution. This interpretation assumes that variation in fPer composition is a function of crystallisation rather than depth, following interpretation of the Mössbauer data in section 2.5.2.

Amongst the São Luiz material, the most significant trace element containing phase is CaSi-Pvk (section 2.4.6). Melting experiments involving CaSi-Pvk for pyrolite and primitive MORB (Kato et al. 1988), showed the liquidus phase to be of a majoritic garnet composition at pressures equivalent to shallow lower mantle depths. CaSi-Pvk was *then* found to crystallise followed by MgSi-Pvk: observations which are in line with the above interpretation of trace element evolution in fPer. The composition of liquid coexisting with lower mantle assemblages is discussed in section 4.6.

---

[1] Fe # calculated using total Fe and cation values.

[2] There is not enough data amongst heavy elements to provide a full assessment.

Section 4.5.1.4 Trace element partitioning

Trace element partitioning data allows for the estimation of trace element compositions of an unavailable phase where one half of the pair is available for study. On anticipation of more lower mantle material being forthcoming from other localities, table 4.5_4 presents some partitioning data for key trace elements calculated from data presented in appendix 4.2. Also included is the little available experimental data for MgSi-Pvk and majoritic garnet determined by Kato et al. (1988). As table 4.5_4 shows, this data is quite distinct from MgSi-Pvk / TAPP partitioning forthcoming from São Luiz inclusions and is further evidence to support the initial crystallisation of TAPP and its distinction from garnet. Majoritic garnet partition coefficients, for example with liquid, as discussed in section 4.5.1.3 cannot, therefore, be applied to TAPP.

Table 4.5_4 Trace element partition coefficients for lower mantle region assemblages from São Luiz inclusions in addition to experimental data.

LM/UM	**Ba**	**Sr**	**La**	**Ce**	**Nd**	**Sm**	**Eu**	**Ho**	**Yb**	**Hf**	**Y**	**Zr**
TAPP/Olivine ‡	11.7	2.61	222	3.48	78.7	220	280		3.85		8.13	15.2
TAPP/fPer ‡	0.117	0.319	25.8	1.44			1.79	23.1	31.8		1.39	0.826
CaSi-Pvk/TAPP ‡	0.309	478	6.98	244	31.8	8.36	16.0	15.7	2.95	0.259	403	34.4
LM I												
MgSi-Pvk/TAPP	0.143	1.08	0.004	0.689	1.22	0.018		0.054	0.209	0.733	26.1	13.0
Mpv/Maj. 1673K *			1.50			1.50			1.30	6.00	0.50	5
Mpv/Maj. 2173K *						1.40			1.70	18.0	2.20	15
MgSi-Pvk/fPer	0.033	0.135	0.038	0.566	1.20	0.102		0.200	0.599	2.45	14.5	17.7
CaSi-Pvk/TAPP	1.09	2240	40.8	1500	193	61.9	119	38.7	12.9	0.506	2760	55.3
LM II												
MgSi-Pvk/fPer	0.026	0.103	0.038	0.094	0.073		0.037	0.163	8.07		0.06	0.611
MgSi-Pvk/Ruby		35.8							130		2.87	42.05
CaSi-Pvk/MgSi-Pvk	9.85	2720	9230	13100	2620		3770	877	4.57		25400	123.4
LM III												
MgSi-Pvk/TAPP	0.778	55.7	0.119	1.19	0.576	0.484	0.245	0.098	0.242	0.335	0.558	0.819
MgSi-Pvk/fPer	0.182	6.97	1.01	0.980	0.564	2.78	0.288	0.361	0.696	1.12	0.309	1.11
MgSi-Pvk/ Maj	2.40	163	2.54	1.60	0.634	0.740	0.194	0.380		6.74	2.087	13.9

* Experimental data from Kato et al. (1988). All data use average inclusion data except where indicated by ‡: using data from BZ243 and averaged CaSi-Pvk
Maj.- majoritic garnet

Section 4.5.2 Equilibration in composite inclusions

Previous sections, within chapter 2, have discussed the compositional characteristics of both isolated and composite inclusions. In particular, a number of compositional studies have been attempted to obtain information on any effects of re-equilibration within touching grains, sections 2.2.2.1 and 2.2.2.2. The present section aims to discuss whether there is a case to support any re-equilibration having occurred within touching grains; conclusions being discussed in terms of exhumation mechanisms in section 7.3.4.

LM I Association composite: As figure 4.4_38 shows, both BZ207A (TAPP) and BZ207C (Type I pyroxene) are compositionally dissimilar from other LM I and LM association inclusions. BZ207C is Si and Mg-poor and Al and Fe-rich relative to other Type I pyroxenes. Furthermore, although no non-touching, *Type I* association TAPP grains have been identified, in comparison with TAPP grains in general, BZ207A is Si, Al, Cr, Mn, Na and Ca-poor and Fe and Ti-rich. The deviations from the norm in BZ207C are not matched by deviations in BZ207A, specifically, TAPP grain BZ207A does not show the corresponding majoritic garnet characteristics which such compositional behaviour in BZ207C might suggest. Compositionally, clear trends in non-touching grains are not particularly forthcoming (figure 4.5_12) so it is difficult to say whether BZ207 lies off any particular trend. It cannot be said unequivocally, therefore, that no re-equilibration has occurred in the composite grain. However, re-equilibration in terms of what phase relations would suggest for such composition, i.e. to majoritic garnet and its breakdown products (figure 4.4_9) has certainly not occurred. This lack of decomposition may be a function of the structure and thermodynamics of TAPP but there are additional factors of exhumation rate and the compressive effect of the diamond host which are likely to be involved (section 7.3.4).

LM II Association composite: BZ241B is significantly more Si and Mn-rich and Na-depleted than non-composite Type II pyroxene, BZ210B. None of these elements are expected to be accommodated within ruby, however, so compositional differences between BZ241B and BZ210B cannot be explained in terms of re-equilibration of BZ241B1,C. Indeed, the ruby BZ241C, additionally, has a higher Si content, in addition to higher Fe, than non-composite ruby BZ214A. The only conceivable diffusible element, apart from Al, which would be expected to communicate between ruby and pyroxene is Cr but the Cr contents of neither the ruby BZ241C nor the Type II pyroxene, BZ241A can be considered anomalous compared to non-touching grains. Furthermore, as EPMA mapping shows (section 2.2.2.1), there is no identifiable compositional gradient within phases of the BZ241B1,C composite, so no particular re-equilibration appears to have occurred. Such a lack of compositional readjustment can be explained in terms of a lack of any driving force due to the details of the ruby structure, however, perusal of figure 4.4_9, will show that an association of ruby and Al-rich MgSi-Pvk would be expected to react with falling pressure to form garnet and ruby or majoritic garnet, depending on bulk composition, given sufficient time or temperature. In the case of BZ241B1,C, such regression has clearly not occurred.

LM III Association composites: Although little compositional variation is found amongst the Type III pyroxenes, the two composite grains, BZ237A and BZ259B, show slightly higher Si and Na content and lower Fe and Al content than the two non-composite grains BZ242B and BZ246A. In itself, this could be due to re-equilibration. Amongst the Type III association, neither of the coexisting garnet-type phases, the TAPP grain (BZ259A) or the majoritic garnet (BZ237B) have similar non-composite phases with which to draw comparison. Amongst the majoritic garnets in general, however, BZ237C is particularly Si and Na-poor and Al-rich; which certainly mirrors the compositional characteristics of Type III pyroxene BZ237A. It is not entirely clear whether the compositional features of BZ237C are indicative of some form of re-equilibration from majoritic garnet, certainly low Na content in majoritic garnet has been cited as indicative of lower pressure (e.g. Moore et al., 1991 and Irifune et al., 1994). However, it is questionable whether comparison with other majoritic garnets is reasonable considering that, as discussed in section 4.4.2.6, there is strong evidence in the unusual compositional characteristics of the BZ237 system (for example the particularly high Mg-content and low Ca content of BZ237C) to invoke a region of formation differing from normal majoritic garnets. Such compositional details are, in fact, consistent with phase relations determined relating to majoritic garnets at upper mantle / lower mantle boundary conditions. Given the slight shift in composition of BZ237A from non-composite Type III pyroxenes, it can be concluded that some slight re-equilibration has occurred. It would also appear that re-equilibration has occurred throughout the whole composite grain given the lack of any compositional gradient detected by EPMA mapping (section 2.2.2.1) or spot analyses (section 2.2.2.2). No matter what the region of formation of BZ237A6,C, however, re-equilibration has not gone to the extreme which could be expected. Given decreasing pressure and enough time, one would expect BZ237C to lose all of its majoritic component in a similar fashion to ex-majoritic garnets discussed by Haggerty and Sauter (1990) and Jerde et al. (1993).

The composition of BZ259B shows no significant difference with other TAPP grains in general although, again, it is questionable whether such comparisons are relevant given the different conditions of formation which are likely (section 4.4.2.6). Like BZ237, the compositional distinction of BZ259A from non-composite Type III pyroxenes may be indicative of some re-equilibration and, again, this would appear by EPMA mapping to be pervasive (section 2.2.2.1). Further details of the compositional variation within BZ259A2,C has, however been achieved, section 2.2.2.2.

As section 2.2.2.2 highlights, Na, Ca, K, Ni and Ti, show no indication of a gradation towards the grain boundary. This observation can be explained in one of three ways:

- Diffusion has occurred, but it has proceeded to completion: equilibrium has been reached in terms of the amount of each element which will happily be accommodated within each structure at equilibration conditions.
- No diffusion has occurred simply because the change in crystal structure during exhumation has not significantly changed the relative site sizes and thus altered partitioning of these elements between the two phases.
- No diffusion has occurred because insufficient time or thermal energy has been added to the system to exceed the diffusion activation energy for each species.

By the very low abundance of Ti and Ni in both phases, the low Ca, and Na in TAPP and the relatively low Cr in the pyroxene, it is likely that the latter is the case i.e. kinetic factors have prevented diffusion.

The compositional gradient for Mg and Fe, particularly on the TAPP side (figures 2.2_22a and b), can be explained by slower diffusion of both species in the TAPP[1] as compared to pyroxene. Considering a coupled substitution of $FeMg_{-1}$, Mg slowly migrates out of the garnet and it quickly diffuses through the pyroxene producing a shallow gradient. At the same time, the potential gradient for Fe in both phases favours Fe diffusion into TAPP but, due to the relatively slow diffusion rate of Fe in garnet, a certain amount backs up at the boundary while waiting to diffuse in. This is, however, a simplified model as the compositional gradient of Mg, in particular in TAPP, is not concave as would be expected by simple diffusion in a homogeneous matrix. This may be due to defects influencing local diffusion throughout the grain.

The slight Si increase from deep in the garnet to the suture (figure 2.2_22d) can be explained by slower diffusion in the TAPP. A first glance would indicate that such a trend could be considered indicative of majoritic substitution in grains which have inhabited the transition zone for a time. However, in this case, if anything, the TAPP is significantly Si undersaturated: if, as is likely, BZ259A2 adopts a TAPP structure we would not expect to see any majoritic substitution. There seems to be no corresponding negative substitution to balance Si mobility. The increase in Al from TAPP to the suture (figure 2.2_22e) is particularly puzzling. Certainly the unusually high Al content of the pyroxene may indicate transferral of Al cations but the TAPP shows quite a normal Al content

---

[1] The diffusion coefficients for Fe and Mg in TAPP are unknown. Certainly compared to pyroxene, garnet diffusion is faster, however if TAPP is a higher pressure phase (less open structure) than garnet, an interpretation of slower diffusion in TAPP may be reasonable.

at 23 wt% and anyway, we would, therefore, expect a decrease in Al towards the boundary on the garnet.

Clearly, although some elements of the diffusion of cations in BZ259A2,B can be explained by simple $FeMg_{-1}$ substitution and the relative suitability of particular sites to particular cations, there appear to be complications. These are unlikely to be fully resolved at present as little is known about the particular aspects of diffusion of cations in TAPP of this structure. As far as the degree to which re-equilibration has occurred, clearly it has neither proceeded to completion nor has it involved any profound chemical re-organisation. The lack of significant compositional change of BZ259A2,B could be a reflection of the structural characteristics of TAPP, however, even though phase relations relating to TAPP have not been proven, it would seem likely that given enough time and / or thermal input, TAPP and Type III pyroxene would react to form majoritic garnet and then exsolve to pyroxene and garnet in a similar fashion to phases presented in figure 4.4_9.

Summary: There are indications that re-equilibration has occured for some composite grains (BZ237A6,C, BZ259A2,B and possibly BZ207A,C) however, the evidence is far from clear. The important point to consider is that although *structural* reversion is likely to have occured (c.f. discussion in section 3.3) none of the composite assemblages have re-equilibrated to the assemblages which phase determinations would predict. The reasons for the lack of re-equilibration are discussed in section 7.3.4.

➠

Section 4.6 Liquids in equilibrium with São Luiz associations

Section 4.4.2 has touched upon the bulk trace element budgets of different inclusion associations. For lower mantle material, there is an indication of a bulk OIB affinity. It has been suggested that OIB is primarily plume sourced material which has an origin, at least in part, within the lower mantle (section 7.3.1). Although it is certainly not clear whether any OIB *melt* has actually been produced in the lower mantle and specifically how much fractionation has occured between plume source and OIB magma, it would still seem pertinent to investigate the possibility of lower mantle association inclusions being a source for OIB. Little liquid / crystal partitioning data is available for transition zone and lower mantle material. As section 4.5.1.3 discusses, liquid / crystal partitioning data has been determined for trace elements by Kato et al. (1988) between majoritic garnet, CaSi-Pvk, MgSi-Pvk and melt. It is questionable just how useful such partitioning data is for the current study. Partitioning is dependent on pressure and temperature conditions as well as bulk composition, indeed paritition coefficients determined for CaSi-Pvk involve a basaltic composition, rather than the ultrabasic composition more likely for lower mantle associations (section 4.4.2.4). Furthermore, it is doubtful whether majoritic garnet partitioning can be applied to TAPP. As table 4.5_4 shows the partition coefficients for trace elements calculated between São Luiz Type I pyroxene and TAPP bear no resemblence to the partitioning of Kato et al.'s (1988) MgSi-Pvk and majoritic garnet. The run conditions of Kato et al. (1988) are, however, considered to be quite relevent to lower mantle conditions (unlike many high pressure experiments, their temperatures do not fall short of expected mantle geotherms) and bulk compositions are, at least, basic. An attempt to calculate an equilibrium liquid coexisting with the LM I association has, therefore, been attempted.

Involving phases in equilibrium, one would expect the same liquid composition to be achieved from different phases in the same system. The trace element characteristics of the liquid in equilibrium with CaSi-Pvk does not appear to be the same as that with Type I MgSi-Pvk, figure 4.6_1. Considering the shortcomings of the partitioning data available, however, this cannot be considered surprising. Indeed, partitioning data for Type I MgSi-Pvk are too sparse to make any meaningful inferences for REE, although it should be noted that the trends in LILE do mirror those of OIB but at significantly lower concentrations. Due to the dominant trace element characteristics of CaSi-Pvk, this phase provides the best opportunity for gleaning the composition of equilibrium liquid. For CaSi-Pvk, because of the particularly large values for CaSi-Pvk / liquid for LREE, the resulting liquid has a flat REE trend, very similar to MORB rather than OIB. Trace element concentration is only partially elevated above MORB being closer to primitive MORB and komatiite concentrations. Such a similarity would suggest that São Luiz and Guinean diamonds associated with CaSi-Pvk may represent the deep host rock associated with early earth magmatism (see Xie and Kerrich, 1994). As described above, however, results must be treated with caution.

Section 4.7 Mantle oxidation through studies of São Luiz inclusions

Due to the rarity of natural samples, little is known regarding the oxidation state of the transition zone and lower mantle. Before the appearance of São Luiz material, the closest inferences were taken from extrapolation of conclusions regarding the bounding regions of the earth. The lower mantle was considered to be largely reducing due, in part (with the assumption that the core and lower mantle are in equilibrium) to the fact that the core models best to a composition made up of native iron. The occurrence of native iron (Meyer and McCallum, 1985 and Sobolev et al., 1981), moissanite and fPer (Moore et al., 1986) inclusions within deep sourced diamonds, was seen to support a reduced deep earth. As discussed in detail in section 7.2.2, the upper mantle, as described by xenolith material, appears to have a particularly inhomogeneous oxidation state (e. g. Haggerty, 1990; Ballhaus et al., 1990; Arculus and Delano, 1987). In general with depth, and, particularly within the asthenosphere, reducing conditions appear to dominate (e. g. Daniels and Gurney, 1991 and Taylor et al., 1994), indeed Taylor et al. (1994) suggest that some form of redox melting may occur across the 400 km discontinuity; a possible source for deep earthquakes. The highest pressure, most primitive MORB's are the most reduced of magmatic material (Ballhaus et al., 1991), an observation which, combined with data form OIB discussed in section 7.2.2, suggest a deep mantle reducing source. From these aforementioned considerations, therefore, it has often been assumed that the deep earth tends to be reduced. Experimental evidence comes from O'Neill et al. (1993) who use Mössbauer data on experimental run products involving transition zone phases. They agree that the transition zone is a relatively reduced region, close to metal saturation, however suggest that it is bordered by a more oxidised lower mantle.

The inclusion material from São Luiz provides an important opportunity to infer the oxidation state of the transition zone and lower mantle. At first glance, the presence of moissanite, section 2.2.1.9, which can, however, be considered questionable, and sulphide, section 2.2.1.9, could be cited as being indicative of reducing conditions. Sulphide is the most common inclusion in diamond but is far from being a dominant phase in mantle xenoliths; its presence can be attributed more to the particular equilibrium conditions of the crystallisation of diamond rather than, necessarily, as an indicator of pervasive fO_2 in host rocks. Furthermore, the occurrence of the oxides fPer and corundum as inclusions cannot, *per se*, be attributed to oxidising conditions because, as discussed in section 4.4, their presence is more attributable to density considerations and the relative stability of silicates at conditions in the deep earth. Indeed, even the consideration of the results of Mössbauer data, section 2.5, must be considered in the context of relative stability of Fe^{2+} and Fe^{3+} in the phases concerned.

Transition zone oxidation state from São Luiz material: As presented in section 2.5.1.1, the Fe^{3+} content of majoritic garnets from São Luiz is high: this may seem to be an indication of high oxygen fugacity in the transition zone. Experimental data carried out by O'Neill et al. (1993) at conditions of 18 GPa, 1973 K, however, showed that in equilibrium with Fe and SiO_2 (reducing conditions), majorite contained substantial Fe^{3+}, $Fe^{3+}/\Sigma Fe = 0.1$. This value can be taken as a minimum for the amount of Fe^{3+} required to stabilise majorite. Extrapolation to the Al-rich system of which São Luiz majoritic garnets are part, involves some uncertainty. However, if majoritic garnet behaves in a similar fashion to its Al-free end member, the high Fe^{3+} content of transition zone garnet inclusions can only be cited as being inconsistent with a *highly* reduced source.

A further indication suggests that the fO_2 of transition zone regions is not particularly oxidised. This is the high Cr content (0.19 wt% Cr_2O_3) of olivine from the UM / LM association (BZ243C). This value may seem small but olivines, typically, yield particularly small concentrations of Fe^{3+}. Since the coupled substitution of $Fe^{3+}{}_2Al_{-1}Cr_{-1}$ is expected to occur in olivines, high Cr_2O_3 indicates particularly low Fe^{3+} content.

Lower mantle oxidation state from São Luiz inclusions: Even more so than transition zone inclusions, on the whole, lower mantle inclusions yield remarkably large concentrations of Fe^{3+}, section 4.5. TAPP contains ~ 0.75 $Fe^{3+}/\Sigma Fe$ and pyroxenes contain increasing Fe^{3+} content with Al content (~ 0.2 - 0.75 $Fe^{3+}/\Sigma Fe$ with 1 to 10 wt% Al_2O_3). The thermodynamic preference for Fe^{3+} of TAPP is not known, however McCammon (1997) has undertaken experimental work on the stability of Fe^{3+} in pyroxenes at lower mantle conditions. She shows that perovskite structured $(Mg,Fe)SiO_3$ with 3.3 mol% Al, synthesised under relatively oxidising conditions (Re - ReO_2) at 25 GPa, ~1873 K, contains Fe^{3+} as 50% of total iron. Furthermore, McCammon (1997) suggests that the presence of Al stabilises Fe in perovskite structured $(Mg,Fe)SiO_3$. which is consistent with the compositional variations of São Luiz inclusions (figure 4.7_1). Preliminary indications from experimentation (McCammon, 1997 *personal communication*) also suggest that, like majorite, even at conditions of low fO_2, Fe^{3+} content of perovskite structured $(Mg,Fe)SiO_3$ is high. High Fe^{3+} in Type I and Type II pyroxenes is not, therefore, necessarily evidence for high fO_2 in the lower mantle.

Similarly, the exceedingly low Fe^{3+} concentration in fPer from São Luiz inclusions ($Fe^{3+}/\Sigma Fe$ = ~0.05), section 2.5.2, as for other inclusions, has an explanation in the thermodynamics of the phase rather than in the oxygen environment. Experimentation has shown, as discussed in section 2.5.3, that only at pressures corresponding to the lower mantle (or under exceptionally reducing conditions) can fPer be stable with as low a Fe^{3+} content as seen for São Luiz inclusions (McCammon et al., 1995)[1]. Furthermore, under lower mantle conditions, the Fe^{3+} content of fPer remains consistently low irrespective of fO_2 (McCammon et al., 1995), as any Fe^{3+} is be stabilised within a separate magnesioferrite phase. Low Fe^{3+} content of fPer cannot be cited, *per se*, therefore, as evidence for reducing conditions.

A further characteristic of São Luiz inclusions allows something more definitive to be said about lower mantle oxidation state, this is the presence of magnesioferrite within fPer inclusions. As discussed in section 2.6.1, fPer inclusions have been found to contain variable and, often, significant quantities of magnesioferrite grains. Such an observation would indicate that the ambient conditions in the lower mantle source of São Luiz inclusions is variable in oxidation state and in many cases moderately oxidising. This is because, although the *maximum* amount of Fe^{3+} in fPer is believed also to fall with pressure (figure 2.5_5), particularly on the stabilisation of a high pressure phase of magnesioferrite the phase boundary of fPer and fPer + magnesioferrite is still believed to represent an oxidised environment (McCammon et al., 1997). Indeed the fact that 'blebs' of magnesioferrite have not been dissolved into fPer at ATP may be an indication of bulk O content being to the magnesioferrite side of the phase boundary at low pressure. This indicates a *particularly* oxidised source (figure 2.5_6). It should be kept in mind that there are other interpretations of a lack of dissolution, i.e. the lack of a kinetic driving force at low temperature and the elevated internal pressure imposed by the diamond host.

One, as yet, unanswered question is whether or not fPer grains which do not indicate a presence of magnesioferrite by SEM are indeed devoid of the phase (having dissolved into the fPer at low pressure or originating in a reduced régime). Magnesioferrite in such grains may, simply, be too fine grained to be resolvable. It is not clear, therefore, whether or not fPer without visible magnesioferrite can be cited as evidence for a relatively reduced source.

---

[1] Incidentally, this result is yet further evidence for a lower mantle origin for LM I and LM II associations from São Luiz diamonds: it is only under conditions of lower mantle pressure that high Fe^{3+} in $(Mg,Fe)SiO_3$ can exist in equilibrium with low Fe^{3+} in fPer.

Chapter 5 Diamond characteristics

As introduced in section 1.3, extensive work has been undertaken on upper mantle diamond samples in terms of morphology (Harris et al., 1986); colour (Harris, 1992); fracture (DeVries, 1975); plastic deformation (DeVries, 1975 and Weidner et al., 1994); carbon isotopic composition (Nier and Gulbransen, 1939; Deines, 1980; Boyd, 1989; Kirkley et al., 1991; Harte and Otter 1992 and van Heerden et al., 1995); nitrogen content (Deines et al., 1984, 1987, 1989, 1991, 1993); nitrogen aggregation (Evans and Harris, 1989; Boyd et al., 1994, 1995); nitrogen isotopic composition (Javoy et al., 1984; Boyd, 1988 and Boyd and Pillinger, 1994); cathodoluminescence (Otter et al, 1991 and Taylor et al., 1995a,b) and FTIR of non-nitrogen elements (Knot et al., 1994). For the purpose of comparison, all of the above details have been investigated within the population of diamonds from São Luiz[1].

Appendix 1 and sections 5.1 - 5.3, describe the colour, morphology, fracture and plastic deformation characteristics of all stones from Sao Luiz series BZ215 - BZ272 and JH7 - JH17 in addition to the Guinean stone, GU4. For the purposes of producing meaningful statistical analyses, all lower mantle-type stones are grouped within a single population, rather than employing the subdivisions of lower mantle associations outlined in section 2.3. Furthermore, it should be kept in mind that the observations made for the São Luiz population cannot, necessarily, be taken as being representative of the diamond population of the kimberlite source or even the alluvial deposit. Some sampling bias may have been introduced into the present study as preference was given during collection to inclusion-bearing material (Harris, 1993 *personal communication*). Cathodoluminescence characteristics of selected stones are discussed in section 5.6. In addition to visual observations, δ^{13}C, δ^{15}N and FTIR were determined on stones from the BZ215 - BZ272 series and on some fragments of diamond from BZ201 - BZ214 and the Wilding (1990) suite, BZ1 - BZ117. Results obtained are discussed in sections 5.4 and 5.5. Such work was undertaken on two sets of diamonds:

Broken and unbroken stones (section 5.4):

- Shards from the aforementioned *broken* stones were examined by Fourier Transform Infra-Red Spectroscopy (FTIR) for N content and aggregation, plus any other IR active species (section 5.4.2.1) at the Laboratoire de Geochimie et des Isotopes Stables of the Universitaire de Paris VII.
- Subsequently in the same laboratory, all analysed samples were burned for δ^{13}C analysis (section 5.4.2). In addition, dependent on FTIR results, some fragments were chosen for determination of

---

[1] In addition, study has been made of the single Guinean stone, GU4.

δ^{15}N composition and N content by combustion (section 5.4.2.2). In which case, the released gas was *first* measured for δ^{15}N and *then* for δ^{13}C. Analyses were conducted by Pierre Cartigny.

- FTIR spectra were also obtained from a number of *unbroken* stones from the BZ215-BZ272 suite at the Diamond Trading Company Research Centre in Maidenhead (section 5.4.2.1).

FTIR results, spectra showing some evidence of nitrogen content and analytical methods are documented in appendix 6. Results of δ^{13}C and δ^{15}N determination are presented in appendix 7 with methods being discussed in appendix 11.

Diamonds polished to expose inclusions to the surface (section 5.5): In addition to whole diamonds, two parallel faces were polished onto each of eight diamonds (BZ251-BZ258), containing a representative sample of suspected lower mantle inclusions[2]. Polishing was carried out in order to clearly view the inclusions and the nature of the physical environment within the host diamonds. In addition, these surfaces allowed the cathodoluminescence characteristics of these diamonds to be determined. Subsequently, five diamonds showing both a range of inclusion type and, in addition, the strongest and most complex of cathodoluminescence patterns were further polished to expose inclusions on one of the flat surfaces. Four of these, BZ251, BZ252, BZ254, BZ255, polished successfully whilst the fifth (BZ258), failed to polish because of an orientation too close to (111); the hardest direction in diamond and the one which cannot be polished. The four ‘flats’ were subsequently analysed by:

- ion microprobe of the University of Edinburgh / N.E.R.C. for δ^{13}C (section 5.5.1).
- FTIR Spectrometer for the collection of FTIR spectra (section 5.5.2.1). Analyses were obtained at the Diamond Trading Company Research Centre, Maidenhead, from cuboid volumes close to ion probe pits. The deconvoluted FTIR spectra yielded values for N aggregation state and total nitogen (ppm) and the presence of additional absorption was noted.
- ion microprobe of the University of Edinburgh / N.E.R.C. for absolute N content (section 5.5.2.2).

FTIR analyses and methods are documented in appendix 6. Ion microprobe methods are outlined in appendix 9.2 and data obtained are summarised in appendix 5.

---

[2] Of these, five were later confirmed by EPMA to contain inclusions from lower mantle associations (see section 2.2.1).

Section 5.1 Morphology

The present sample of inclusion-bearing diamonds from São Luiz are either octahedral, dodecahedral, irregular or macled; the single Guinean stone studied, GU4, is dodecahedral, appendix 1. No cubes are recorded. Table 5.1_1 summarises the percentage occurrence of different morphologies according to mantle association and in terms of the total population.

Table 5.1_1 Distribution of morphology amongst Sao Luiz diamonds of the series BZ251-BZ272 and JH7 - JH17

	São Luiz	**L.M. †**	**T.Z. ‡**	**Other ¥**
Dodecahedral	28%	19%	38%	33%
Octahedral	18%	12%	25%	22%
Irregular	41%	54%	0%	41%
Macle	13%	15%	38%	4%
Number of stones *	61	26	8	27

* Statistics omit stones BZ253, BZ256 and BZ265 which were still at the Carnegie Institution at the time of writing. † Stones of fPer associations from São Luiz. ‡ Stones of transition zone paragenesis from São Luiz. ¥ Stones of upper mantle and unknown parageneses from São Luiz. Unbroken stones are assigned to the 'other' suite unless a positive identification of LM or TZ paragenesis has been made by XRD (e.g. BZ257) or EPMA (e.g. BZ251).

Except for the eight transition zone diamonds, irregular stones are particularly common, an observation in keeping with the facts that:

i) a large percentage of the population of diamonds are pitted and exhibit trigons, section 5.3.1.1

ii) dodecahedral stones comprise a significant proportion of the population: dodecahedral morphology is regarded as being an intermediary stage between octahedral and irregular morphologies.

In all cases, dodecahedra are significantly more common than octahedra. Indeed 100% of colourless stones show either evidence of resorption; surface pitting, etch features such as trigons or stepped morphology or, plastic deformation: all features which can be regarded as factors in causing a stone to become less octahedral in morphology. In terms of comparison between source areas, it should be noted that the ratio of dodecahedra to octahedra is margionally higher for lower mantle sourced stones than transition zone sourced stones.

The occurrence of macles appears to be variable but significant, throughout.

The general morphology distribution of worldwide populations of diamonds is variable, as summarised in table 5.1_2.

Table 5.1_2 Summary of distribution of diamond morphology from a number of worldwide localities

	Dodecahdra	**Octahedra**	**Irregular**	**Macles**	**Aggregates**	**Cubes**
Argyle *	<5 %	<5 %	55 %	25 %	10 %	0 %
Ellendale *	35 %	<3 %	40 %	15-20 %	<5 %	0 %
Mandala Basin ¢	major	minor				
Orapa ‡	6 %	11 %	39 %	11 %	8 %	25 %
Premier ¥	4 %	76 %	-	20 %	-	-
DeBeers ¥	47 %	45 %	-	7 %	-	-
Finsch ¥	69 %	29 %	-	3 %	-	0 %
Roberts Victor ¤	0 %	8 %	16 %	61 %	8 %	0 %

¢ Calculated from Sutherland (1993) and Sutherland (1997, *personal communication*) ¤ Calculated from Deines et al. (1987), ¥ Tolansky (1973), ‡ Calculated from Deines et al. (1993), * Harris (1992)

Comparison of tables 5.1_1 and 5.1_2 shows, that São Luiz stones and stones from the Mandala Basin in Guinea which *may* be allied to the present Guinean sample, have unusually high proportions of irregular and dodecahedral stones over octahedral stones: a proportion which may be due to the great depth of origin of these diamonds.

Morphology of other lower mantle and transition zone diamonds: Morphology information for three fPer bearing diamonds from Koffiefontein are described in Deines et al. (1991). One stone was irregular, one was dodecahedral and the third was an octahedral stone. Five majoritic garnet bearing diamonds from Jagersfontein are also described in Deines et al. (1991). Two were irregular, one was a triangular macle, one an octahedron and the fifth a flattened dodecahedral macle. The majoritic garnet bearing diamond from Ghana (Stachel and Harris, 1996) was a dodecahedron (Stachel, 1997 *personal communication*).

Section 5.2 Colour

Colourless and, in particular, brown diamonds are dominant in the sample population of São Luiz stones, as discussed in appendix 1. In addition, there is a very small proportion of cloudy diamonds. The single Guinean stone studied was colourless. Table 5.2_1 presents the percentage occurrence of different colourations.

Table 5.2_1 Distribution of colour amongst São Luiz diamonds

	São Luiz	**L.M. †**	**T.Z. ‡**	**Other ¥**
Colourless	41%	35%	50%	44%
Cloud	2%	0%	0%	4%
Brown	57%	65%	50%	52%
Number of stones *	61	26	8	27

* Statistics omit stones BZ253, BZ256 and BZ265 which were still at the Carnegie Institution at the time of writing. † Stones of fPer association from São Luiz. ‡ Stones of transition zone association from São Luiz. ¥ Stones of upper mantle and unknown associations from São Luiz. Unbroken stones are assigned to the 'other' suite unless a positive identification of LM or TZ association has been made by XRD (e.g. BZ257) or EPMA (e.g. BZ251).

Comparison of colourations of populations of diamonds should be treated with caution as most populations exhibit a colour dependence on the basis of diamond size (Harris, 1997 *personal communication*). General statements are considered, however, to be valid. With the exception of Argyle diamonds, such a high percentage of brown stones is unusual, see table 5.3_3. Furthermore, the dominance of brown stones is particularly strong amongst lower mantle association stones compared to those amongst the transition zone sourced population. The brown colouration of diamonds is believed to be synonymous with plastic deformation, an interrelation discussed in more detail in section 5.3.2.

Clouds are generally associated with micro-inclusions of CO_2 (eg. Schrauder and Navon, 1993). Certainly such a species is not considered incompatible with a *possible* deep origin for the single cloud, BZ227, which yielded a sapphire inclusion. It may be that this stone is not, however, a true cloud; the cloudy appearence being a result of fine surface pitting as observed commonly throughout the São Luiz material, section 5.3.1.1 and, in particular for BZ249 and BZ250, appendix 1.

General colour comparisons with other lower mantle and transition zone diamonds: Two of the fPer bearing Koffiefontein stones were brown, the third was found to be colourless (Deines et al., 1991). Additionally, all five majoritic garnet bearing stones from Jagersfontein were colourless (Deines et al., 1991) as was the single Ghanan stone occluding majoritic garnet (Stachel, 1997 *personal communication*).

Section 5.3 Deformation features

Diamond is a highly durable mineral, even so, under the appropriate conditions, it will deform. Indeed, it is perhaps not surprising, given the proposed lower mantle and transition zone source for many of the diamonds in the present study (section 4.4.2) that a large proportion of São Luiz stones show evidence of deformation.

The deformation can be divided into brittle deformation and plastic deformation, manifestations being described in sections 5.3.1 and 5.3.2, respectively. As, however, a detailed study of internal fracture systems and plastic deformation features was completed on São Luiz diamonds, an outline of the theory of deformation is firstly presented.

Theory of deformation: All materials respond to stress by deformation. Up to certain values of stress, crystalline materials deform elastically. As the name implies, the removal of this stress results in a relaxation to the original morphology. The amount of stress required for a particular strain depends on the material and the isotropic pressure is described by the bulk modulus, section 7.1.1. Above a stress threshold (termed the 'strength' of the material) the material will be subject to failure. Although the absolute strength of an ideal material can be calculated from *ab initio* considerations, this is a purely academic exercise, which has little relevence to the behaviour of natural materials. All materials fail at considerably lower values of strain than that predicted by molecular modelling[1]. The reason for 'premature' failure is that natural materials are not perfect and the stress at which a sample fails depends, therefore, not only on the material it is made of, but also on the details of its internal structure. What this means in terms of the present study, is that, in order to attempt any quantification of the processes which led to deformation, *theoretical* diamond strength is an upper bound[2]. The strength of diamond, to be useful, must be determined by *practical* means or at least be calculated by a method such as that of Hertz (described in Field, 1979) and, even so, whether such a determined value can be applied to material from the present study is questionable. Indeed, investigators of diamond strength, have obtained a wide variety of indentor induced stresses at failure e.g. 1050 - 1800 kgmm^{-2} (Field, 1979).

At conditions of constant ambient pressure and temperature, solids fail by one of two quite distinct mechanisms: plastic flow or brittle fracture. Whether a material fails by slip along atomic planes (plastic deformation) or propogation of fractures (brittle deformation), depends on the temperature and, to some extent, the ambient pressure; plastic deformation being favoured at high temperature

---

[1] Commonly, materials fail at around 10% of their ideal strength.

and low pressure. There is, however, no clear boundary between plastic and brittle deformation because they really only differ in terms of scale. From the point of view of the present study, where chemical integrity of inclusions is considered, a fundamentally important difference does exist. Diamond deforming by plastic deformation, where slip is on a molecular scale, will not allow penetration of foreign material, i.e. the diamond remains coherent, whereas brittle deformation, simply because it operates on a macroscopic scale, allows the opportunity for secondary infiltration.

The strength of diamond: Indentor experiments undertaken at room temperature have been re-calculated by Field (1979) and found to yield values for diamond stresses at failure of between 1050 and 1800 kgmm^{-2} (1.05 - 1.8 x 10^{9} Nm^{-2}). Additionally, he observed that strengths of octahedra were significantly smaller than cubes. At room temperature, such deformation was found to be dominated by brittle behaviour, Evans and Wild (1965) suggest that temperatures in excess of 2100 K for Type Ia stones and 1900 K for Type II stones are required before significant plastic deformation occurs. DeVries (1975) attempted to quantitatively constrain the observation of plastic deformation lamellae in framesites (a non-gem diamond type). In order to investigate plastic deformation, his experiments were specifically designed to *inhibit* brittle deformation. Diamonds were surrounded by fine diamond powder and subjected to pressures and temperatures in the range 1073 - 1873 K and 0.5 - 6 GPa. DeVries (1975) observed that at below 1173 K, he was unable to cause deformation. Small increases in temperature above this value, however, rapidly reduced the strength of the stones studied. Above 1473 K, diamond strength had fallen to a sufficiently low value to make any further increase in temperature virtually ineffectual. A further observation which DeVries (1975) made was of delamination on the release of pressure. This may be a consideration for the behaviour of natural diamonds because they are likely to have undergone fairly rapid pressure quenching on eruption. DeVries (1975) found that, in order to recover the diamonds intact, octahedra had to be aligned such that the <100> axis was parallel to the press axis otherwise surface tension with the surrounding media acted along the {111} cleavage planes to delaminate and, often, fracture the stones. Weidner et al. (1994) conducted broadly similar experiments, this time on powdered diamond in a DAC. The strain in the diamond fragments manifested itself by a shift in the (111) line which was measured by XRD. Using an appropriate value for Young's modulus a stress could be determined. During compression to 10 GPa at room temperature, strain was found to be proportional to pressure indicating elastic deformation. At room temperature, the strength of diamond must, therefore be greater than 10 GPa. Subsequent increase in temperature to 1273 K, again, showed no indication of brittle or plastic deformation. In accordance with the results of DeVries (1975) above 1273 K, diffraction peaks were found to become symetrical, indicating that the fragments of diamond which were supporting the total load to this point had deformed to spread the

---

[2] Lawn and Wilshaw (1975) predict a value of stength in shear of 12.1 x 10^{10} Nm^{-2} along {111}.

load evenly over the whole sample. Furthermore, Weidner (1994) found that increasing temperature reduced the yield strength considerably. TEM analysis of all deformed runs showed an increase in dislocation density of at least three orders of magnitude higher than the starting material and, as no grain size reduction was observed after deformation it is concluded that all deformation, even at low temperatures, is manifest predominantly by plastic deformation. It would appear that DeVries (1975) need not have attempted specifically to inhibit brittle deformation. The results of deformation testing of diamond in terms of temperature are presented in figure 5.3_1.

Indicators of deformation in diamond: Brittle deformation can easily be identified by the observation of fractures, either by the naked eye or by higher resolution techniques. Identification of plastic deformation, however, merits closer attention.

Features of Plastic Deformation: Plastic deformation in diamond is manifest by small scale movement along slip planes and can be recognised in a number of ways:

- By a series of very fine parallel lines in the diamond cleavage plane. Such features are particularly noticable on the rounded edges of dodecahedral stones.
- By a trail of negative trigons (terminology described below) running across octahedral faces parallel to cleavage.
- By commonly occuring on brown diamonds[3], some of which may have a distinct streaking if the deformation occurs in zones.
- Through cathodoluminescence which clearly picks up plastic deformation as fine lines of contrasting CL intensity across affected stones. An example is the image of diamond BZ251, figure 5.6_3.
- Through FTIR measurements. Intensely plastically deformed diamonds tend to inhibit the D-absorption, the result of platelet formation (Chinn et al., 1995). The reason for this absence is akin to mechanisms of work hardening in the brittle régime, plastic deformation being impeded by platelet formation (Evans, 1976).

Trigons: When crystal dislocations interact with the surface of a stone this produces a weakness which can be exploited by chemical attack. There are numerous diamond surface features which result from exploitation of such dislocations. Some take the form of polyhedral depressions in the surface of the stones centred around the dislocation intersection. These depressions are either hexagonal in morphology or triangular. The triangular depressions are called trigons and appear on octahedral faces. They have an orientation either mirroring the shape of the face on which they lie

---

[3] The amount of plastic deformation which a diamond has to experience in order to adopt an obvious brown colouration is not known. The presence of plastically deformed, colourless stones, however, suggest that the onset of plastic deformation does not coincide with the onset of brown colouration: this appears later.

(positive trigons) or inverted by 180° (negative trigons). Orientation depends on the ambient conditions of oxygen partial pressure and temperature, under which they form (Yamaoka et al., 1980), figure 5.3_2, descibed by the equation:

$$\log PO_2 = \frac{-9.0x10^4}{T} + 63 \qquad \text{Equation 5.3\_1}$$

where PO_2 is the partial pressure of oxygen (kbar) and T is temperature in Kelvin

Most geological environments within the stability of diamond lie within the negative trigon stability field; indeed trigons observed on natural diamonds[4] are negative.

Observation of diamond characteristics, therefore, provides important additional information on the mechanism of diamond deformation. As platelets are observed to inhibit plastic deformation, it can be concluded that whether a diamond will deform plastically or not depends, not only on the physical conditions of temperature and pressure, but the details of the internal structure of the stone: Evans and Wild (1965) found that a stress of 5-6 x 10^8 Nm^{-2} (0.5-0.6 GPa) at conditions of 2100 K, atmospheric pressure easily deformed a Type II stone through a large angle, whereas even on application of *double* the stress on a Ia stone rich in platelets, no plastic deformation was produced. Presumably, however, if the conditions of temperature and shear are extreme enough, no amount of platelet formation will be enough to halt deformation (section 6.3.3).

---

[4] 15% of São Luiz diamonds from the present study had trigons. The occurrence amongst lower mantle stones was higher (22%). Orientation into lines was not, however, observed.

Section 5.3.1 Observations of brittle deformation in diamond

Brittle deformation, in particular, offers the opportunity for communication between inclusions and the environment outside of their host diamonds. In order to be certain that the compositions of inclusions represent their initial compositions, it is important for the study of inclusion materials to be confident that communication between inclusion and the extra-diamond environment has *not* taken place subsequent to encapsulation. With this in mind, study has been made of features of brittle deformation by a visual observation of fracture systems for the entire sample and for selected stones by high resolution techniques at the University of Edinburgh (section 5.3.1.2). Particular attention has been paid to how far crack propagation extends from inclusions, how wide cracks are and pursuit of evidence of crack infiltration by non-diamond material and crack closure. BZ251, BZ252, BZ253 and BZ254 and, as a means of comparison, a fragment of diamond JH11(df) which had fracture systems propogated at conditions of ATP (during the process of inclusion release) were chosen for study using the following techniques:

- Back scattered electron probe microscopy (BS-EPMA) and energy dispersive electron probe microscopy (EDS-EPMA) at the Department of Geology and Geophysics on the Cameca Camebax electron microprobe using standard operating conditions (appendix 8)
- Scanning electron microscopy (SEM) at the Department of Biological Sciences, SEM facility operated by Drs. Chris Jeffreys and John Findlay using an accelarating voltage of 10kV. Both secondary electron (SE) and back-scattered electron (BS) images were obtained.
- Atomic force microscopy (AFM) at the Department of Biological Sciences SEM facility on a Digital Instruments Nanoscope III demonstrated by Dr. Nicola Forsyth.
- Scanning probe microscopy (SPM) at the Department of Physics on a Nanovision SPM demonstrated by Mr. David Rogerson.

Section 5.3.1.1 Visual observation of fracture systems

A large number of stones (at least 34 of 61) involved in the present study have features indicative of brittle deformation. Large fractures showing discolouration, small inclusion related fractures and large inclusion related fractures, are all observed. The occurrence of each of these features has been recorded according to association type[1] and locality and is presented in table 5.3_1.

Table 5.3_1 Summary of visible signs of brittle deformation in São Luiz and FEG stones classified according to paragenesis.

	São Luiz	**L.M. †**	**T.Z. ‡**	**Other ¥**
External I	15 %	13 %	12 %	17 %
Internal	55 %	39 %	38 %	72 %
External II	3 %	9 %	0 %	0 %
Number of stones *	61	26	8	27

External I fractures are fracture zones which are seen to reach the surface of the diamond but do not involve the inclusion(s) of interest. External II fractures are fracture systems which show comunication between the diamond surface and the inclusion(s) of interest. These fractures often show a brown oxidised colouration. Internal fractures are systems which are seen to be wholly encapsulated within the stone. † Stones of fPer association from Sõ Luiz. ‡ Stones of transition zone association from Sõ Luiz. ¥ Stones of upper mantle and unknown associations from Sõ Luiz. This suite includes unbroken stones for which a positive identification of association has not been made by XRD (unlike BZ257) or EPMA (unlike BZ251). * Statistics omit stones BZ253, BZ256 and BZ265 which were still at the Carnegie Institution at the time of writing.

There appears to be some variation between sources for each of the brittle deformation features described herein, table 5.3_1, but the broad characteristics remain constant:

- Throughout, few stones exhibit large fractures which run to the surface of the diamond; even fewer also incorporate inclusions. This observation is perhaps unsurprising as such stones are likely to be very weak and few would survive transportation. This observation has important connotations for the sanctity of inclusion chemistry as discussed in section 7.2.
- A significant proportion of diamonds exhibit internal fracturing, in particular, surrounding inclusion systems. The presence of such fracture systems is not entirely surprising considering the differences in expansion behaviour of inclusions relative to diamond on exhumation, section 7.1.2. This observation has significance for the calculation of formation depths from the relaxation of inclusion cell parameters, section 7.1.3.1. It is important to additionally note, that the proportion of stones exhibiting obvious *brittle* deformation is not as high as those exhibiting *plastic* deformation, (section 5.3.2).

---

[1] In order to make the results statistically meaningful, stones of association LM I, LM II, LM III, LM/UM and LM are all tabulated under LM.

As far as the differences between source depths are concerned; the fPer association stones show a greater degree of brittle deformation than the majoritic garnet stones. This observation is consistent with the interpretation of the fPer association being sourced at greater depth than the majoritic garnet association. Deeper sourced stones will have been likely to have undergone a longer and more traumatic history. In addition, their included material will have been subject to a greater relative change in volume compared to the diamond's volume change thus excerting greater internal pressure and potential for fracturing during conditions favourable to brittle deformation.

Section 5.3.1.2 Observation of diamond fracture systems at high resolution

Initial SEM analysis was undertaken on slabs subjected to neither ultrasonic cleaning nor carbon coating, in order to avoid unnecessary contamination of fracture systems. Images were obtained despite some charging problems[1], however it was found that inclusions showed unnacceptibly high levels of diamond polishing contaminant (1/4 µm cubes) and other debris. Slabs were thus treated to a short (10 second) ultrasonic clean in petroleum spirit with a view to removing as much contaminant from the polishing process[2] as possible without, however, removing any more primary fracture infill. Slabs were subsequently lightly carbon coated.

Figure 5.3_3 presents the number system employed to identify specific fractures on the surface of the slabs analysed. Fractures were observed to be associated with all inclusions polished to the surface and because of hardness differences, the inclusion surfaces are lower than that of the diamond (e.g. figure 5.3_4). In addition, the quality of polish appears to vary: BZ255A shows a very good smooth polished surface; BZ251A, BZ251B and BZ252A show areas of good polish and poor polish; the very small portion of BZ254A exposed has a very poor polish.

Fracture characteristics:

JH11(df): Observation of JH11(df) by SEM shows that fracturing at ATP is strongly controlled by the diamond's cleavage. Step fractures on the broken surfaces of shards follow two distinct directions at approximately 65° to each other (figure 5.3_5) and have sharp edges and imperceptibly sharp terminations (figure 5.3_6). These observations are consistent with fracture propogation of synthetic diamond at ATP examined by Field (1979).

BZ251: The fractures associated with BZ251A (figure 5.3_7) appear from the apices of the inclusion whereas, in addition, for BZ251B two fracture planes follow the diamond inclusion interface into the stone (figure 5.3_8). BZ251A and BZ251B show very sharp boundaries against the growth faces. They have angles consistent with a steep diamond / inclusion interface with the polished surface except for the non-fractured side of BZ251B which appears to have a shallower interface. The sharpness of inclusion / diamond boundaries is in contrast to the fractures which are commonly sinuous. There appear to be a range of fracture types:

- Fractures with blunt (4 µm) terminations, e. g. fracture 4 of figure 5.3_3 (figure 5.3_9).

---

[1] In order for a stable image to be obtained, the incident electron beam must have a suitable earth through the sample. As diamond is an exceptionally good electrical insulator, a carbon coat on the sample would have been desirable. This was not applied in the first instance in order to collect information from as uncontaminated a surface as possible.

- Fractures with sharp terminations, e. g. fracture 5 (figure 5.3_9).
- Fractures showing augen features, e. g. fracture 7 (figure 5.3_10) and fracture 3 (figure 5.3_11).

As both fracture 4 and fracture 5 have the same orientation it can be concluded that there is no structural control to fracture termination type. The sinuosity of some fractures is symptomatic of plastic deformation subsequent to brittle fracture. In addition, the differing degrees of augen fractures and blunt terminations would indicate that healing of older fractures has taken place; perhaps as a consequence of plastic deformation. In fact, due to the range of fracture type, it can also be concluded the BZ251 has been subject to a number of deformation events with at least one plastic deformation event being sandwiched between more brittle behaviour. It would also appear that the most recent deformational event has been within the régime of brittle behaviour. The question still arises, however, as to the *mechanism* of fracture healing and the degree to which non-diamond material has infiltrated fracture systems.

BZ252: BZ252 shows one main sinuous fracture system cutting across the stone with the main inclusion, BZ252A at its centre. The longest fracture (fracture 1 of figure 5.3_3) was followed through the stone until it disappeared to a thickness beyond the resolution of the SEM (< 0.01 μm) before the edge of the stone. In addition, to one side of the inclusion, there exists a radial ‘spiders-web’ network of straight fractures terminating against two more sinuous fractures (figure 5.3_12). The fractures exhibit the same range of features as in BZ251: sinuous, straight, sharp terminations, blunt terminations and augen features. It can be concluded that BZ252 has undergone, like BZ251, a series of deformation events, the most recent being within a régime of brittle formation and with plastic deformation healing a previous brittle event.

BZ254: BZ254 exhibits a pseudo-radial cluster of fractures centred on what appear to be two closely-spaced inclusions deeper in the stone. There are four main fractures and a number of smaller fractures (figure 5.3_3); the central area showing an irregular topography (figure 5.3_13). Separated from the main fracture cluster, there is a single curved fracture. Like the stones discussed previously, the fractures show a range in morphology: blunt and sharp terminations, sinuous and straight character. Two relationships are particularly striking:

- One of the main fractures, fracture 1 terminates bluntly just before (20 μm) the isolated fracture, fracture 7 (figure 5.3_14).
- The sharp terminating fractures tend to be shorter and thinner than the blunt terminating fractures.

---

[2] The matrix of the diamond paste is soluble in petroleum spirit.

These observations would indicate that BZ254 has undergone at least one period of brittle fracture followed by plastic deformation and was finally deformed under a brittle régime. Fractures 1 and 7, by their sinuous and slightly augen nature both started their propagation before the final plastic deformation stage. Fracture 7, however, existed before the final propagation of fracture 1; teminated presumably as its damage zone reached fracture 7. The sharp fractures, 6 and 5 and the extension of fracture 3, were likely produced during the final, brittle, deformation whereas, the other fractures, due to their width and inclination are likely multiply-worked and older.

BZ255: BZ255A appears to be a very well polished inclusion (figure 5.3_15). It has a single, slightly sinuous, feature emanating from the sharpest apex which terminates imperceptibly within the diamond approximately 100 µm from the inclusion. It appeared very difficult to resolve and it could be that rather than being a fracture, it is merely a step down in the diamond surface in a similar fashion to figure 5.3_5.

Fracture healing: The healing of fractures can be envisaged within two frameworks:

- On the application of stress, a fracture can be envisaged to simply ‘zip-up’. Here, the fracture heals from the termination backwards and hanging-bonds recombine. Such a process would be facilitated by plastic deformation allowing relatively large gaps to be closed albeit, commonly in an irregular fashion.
- Fractures could be healed by the precipitation of additional diamond from a diamond-bearing fluid.

Two methods have been employed to test these two frameworks: cathodoluminescence and $\delta^{13}C$ determination. It is likely that any newly precitated diamond would show-up as a band of differing cathodoluminescence intensity or wavelength. Additionally, if re-precipitation was to have occurred in a region of depths shallower than the lower mantle[3], it is possible that healing diamond would have a different $\delta^{13}C$ signature from the host stone[4].

The extensions of fracture systems within the four slabs do not show CL patterns distinct from the general pattern of the host diamonds (figures 5.6_3, 5.6_5, 5.6_6 and 5.6_7). In addition, there is no evidence from $\delta^{13}C$ analysis for BZ251 (section 5.4.1, figure 5.5_1 and appendix 5.2.2) to suggest

---

[3] The lower mantle, as discussed in section 5.3.2 and 5.4.2 appears to have a constant value for $\delta^{13}C$ close to -5 ‰.

[4] What this means is that if a healed fracture were to show a different $\delta^{13}C$ signature from the host, ie. ≠ -5 ‰, then this would imply healing by infiltration. The presence of a $\delta^{13}C$ signature equal to the host, however, does not *preclude* healing by infiltration.

any fracture healing by additional diamond. It can be concluded, therefore, that it is more likely that fractures have healed purely by zipping, facilitated by plastic deformation.

The question of fracture infiltration: Back scattered electron imaging is sensitive to variations in the atomic mass of the analysed material. The technique, therefore, represents a method by which to estimate the types of material infiltrating fractures.

BZ251A, BZ251B and BZ255A exhibit small (0.5 µm), irregular patches, of high BS-reflectivity material; particularly on the inclusion / diamond boundary and along some fractures (e. g. figure 5.3_16). The degree of contrast in BS-reflectivity in comparison to diamond or the inclusion material is consistent with this material being of atomic mass high; equal to Fe or In. It is concluded that this material is either mounting indium or polishing steel not removed in the cleaning process: a conclusion supported by EDS analysis. Even on high magnification, e. g. fracture 7 at x2500 (figure 5.3_17) there appears to be no other material infilling fractures. These observations are compounded by e-probe analyses. Additionally, some fine grained (<1 µm) regular shaped grains with a low BS-intensity appeared in both the fracture systems and central area of BZ254A; these are believed to be diamond grit.

BS-imaging of BZ254A showed far less contrast with the diamond than in the other slabs. Combined with the small irregular nature of the central surface, the observation of two inclusions deeper into the stone and poor electron-probe totals obtained for BZ254A (section 2.2.1.5) it can be concluded that the BZ254A is only partially exposed on the surface the other inclusion lying deeper within the stone. For BZ255, the possible fracture was very difficult to detect on BS-imaging and was seen to terminate well before the secondary electron image. This observation is a strong indication that material existing in this possible fracture is controlled by the fracture width (or step depth); the material occupying the possible fracture has not, therefore, been precipitated along it, but forced into it during or subsequent to polishing: any *precipitated* material would not have a minimum size threshold.

In general, most inclusions showed only peaks in EDS spectra consistent with elements from the inclusion phases. particularly for BZ254A and BZ252A; BZ252A, for example, shows a very clean EDS spectra of Si and Ca (area a of figure 5.3_3). More specifically:

- Si X-Rays for some samples (BZ252A) show a few counts per second (cps) over the diamond surface but with a marked increase in concentration over the area of the inclusion. Others (BZ251B) show Si X-Rays entirely confined to the inclusions themselves and not the fractures. As any low-Si background is a general feature, not being restricted to, for example, fracture systems, it can be concluded that, where present, the background is a contamination from the cleaning process; perhaps a greasy residue.

- Imaging Ca X-Rays for BZ252A produces counts solely from the area of the exposed CaSi-Pvk inclusion. There is a little Ca present in fracture 3, however as it penetrates very slightly into the fracture it can be concluded that what is being detected is the edge of the inclusion sloping into the stone. Due to the range in intensity of SEM imaging of BZ252A (figure 5.3_18) any interpretation of the actual extent of the exposed inclusion would appear a little ambiguous. Ca imaging, however, provides a clear answer to this; the extent of the exposed inclusion being outlined on this basis in figure 5.3_3.
- Imaging Fe X-Rays on BZ251A shows that Fe does occupy the fractures as well as the inclusion. Counts are recorded both from high reflectivity specks and throughout the fractures in general. Because *Mg* X-Rays, however, are not found to penetrate into fracture systems this material is concluded to be polishing steel and *not* fPer. For BZ252, Fe X-Rays show a concentration around the edges of the inclusion; particularly in areas f and g.
- For BZ251 (figure 5.3_19), BZ252 (figure 5.3_3) and BZ254 (figure 5.3_13), In and Fe were the only elements detected in fractures (e.g. by EDS in fractures 9 and 10 and from scans In, Si and Fe in augen fracture 11). Additionally, BZ252 showed the presence of a light dusting of Fe and In across the diamond.
- EDS findings further support the findings of single wavelength imaging and are summarised in figure 5.3_3. In addition, some Si is detected from areas f, h and very slightly into fractures 2 and 6 of BZ251A; it is possible that this is an additional phase (perhaps simply of SiO_2 composition) occupying the inclusion / diamond boundary[5].

At higher magnification, SPM and AFM, images were obtained for BZ251A and BZ251B. It can clearly be seen from the AFM image (figure 5.3_20) that there appears to be a periodicity to the surface topography of inclusion BZ251B; highs appear at intervals of 8.0 µm (figure 5.3_21). In addition, 1/4 µm flecks, likely to be diamond grit are common (figure 5.3_22). Similar features are seen within area h of BZ251A by SPM (figure 5.3_23). Even at these high magnifications, no indication of the crystal morphology and regular growth features of precipitated material could be detected, strong evidence, again for a lack of epigenetic infiltration along fracture systems in the stones analysed.

---

[5] Additional phases occupying this region are not unheard of: there have been some indications from X-Ray analysis of BZ257, section 3.3.5.3, that a minute (<10 µm) cpx structured inclusion occupied the boundary between the main fPer inclusion and the diamond. In addition, Wang et al. (1994) reported a multiphase inclusion from a Fuxian diamond. The main inclusion is an olivine which incorporates microinclusions of diamond and graphite and is surrounded by glass and graphite plates.

Summary:

- No evidence could be found to support infiltration of epigenetic material along fracture systems, down to a magnification of at least x2500.
- No evidence could be found to support movement of primary inclusion material along fractures, down to a magnification of at least x2500.
- All material additional to included material yielded features of atomic number contrast, size, morphology, EDS spectra and secondary X-Ray wavelength, consistent with either mounting indium, polishing steel (Fe) or polishing diamond grit only.
- BZ251A shows an indication that an additional phase, possibly SiO_2 in composition, occupies part of the inclusion / diamond boundary.
- BZ251B shows a regular, ~8.0 µm, periodicity of surface topography. This may be a relict of the polishing process or, alternatively, may have a structural origin.
- All four diamond slabs show a variety of fracture features quite different from those propogated at ATP. These are interpreted as being consistent with a varied history of deformation. Sinuous, bluntly terminated and augen fractures indicate that the stones were subjected to plastic deformation subsequent to an earlier, brittle event. The appearence of straight, well defined and sharply terminating fractures indicates, however, that the final stage of deformation was within a brittle régime.
- It is considered likely, that, although the diamonds in question have undergone a turbid history, their inclusions have, on the whole, remained in-tact and chemically unaltered by factors outwith the occluded diamond. This conclusion is supported by indications of equilibrium chemistry dominating coexisting inclusions (section 4.5).

Section 5.3.2 Plastic deformation

Of the stones involved in the present study, a large number (47 stones of 61) show features of plastic deformation. The percentage occurrence of brown stones and those showing plastic deformation lines visually or by CL are classified according to occurrence in table 5.3_2. The single Guinean diamond was colourless and plastically deformed.

Table 5.3_2 The occurrence of brown stones and plastic deformed diamonds from São Luiz.

	São Luiz	L.M. †	T.Z. ‡	Other ¥
Brown	57 %	65 %	50 %	52 %
p.d.	77 %	74 %	75 %	79 %
Brown + p.d.♥	89 %	76 %	100 %	100 %
C/less + p.d.♣	60 %	56 %	50 %	67 %
Number of stones *	61	26	8	27

† Stones of fPer association from São Luiz. ‡ Stones of transition zone association from São Luiz. ¥ Stones of upper mantle and unknown association from São Luiz. This suite includes unbroken stones for which a positive identification of association has not been made by XRD (unlike BZ257) or EPMA (unlike BZ251). ♥ The percentage of brown stones which are, additionally, plastically deformed. ♣ The percentage of colourless stones which are, additinally, plastically deformed. * Statistics omit stones BZ253, BZ256 and BZ265 which were still at the Carnegie Institution at the time of writing.

Table 5.3_2 shows that both brown and plastically deformed diamonds comprise large proportions of the São Luiz diamonds studied. Indeed, almost all brown stones are plastically deformed. This is true irrespective of inclusion association (and thus source area, section 4.3) and concurs with the global observation of Harris (1992) that the brown colouration is a result of plastic deformation.

As summarised in table 5.3_3, the percentage of brown and plastically deformed diamond varies from locality to locality. Compared to the seven South African localities outlined in table 5.3_3, stones from the present study have a far higher proportion of brown and plastically deformed stones. Similarly high incidences of brown diamonds are recorded from Argyle and amongst populations obtained from the Mandala basin of Guinea (Sutherland, 1993) which is within the likely source area of the Guinean sample described herein. Amongst lower mantle and transition zone diamonds from other localities, one of the two brown fPer occluding stones from Koffiefontein showed visual evidence for plastic deformation, the colourless stone showed none (Deines et al., 1991). Additionally, none of the majoritic garnet occluding stones from Jagersfonetin showed visual evidence for plastic deformation (Deines et al., 1991).

São Luiz fPer paragenesis stones appear to be more plastically deformed than majoritic garnet association stones. This observation can be considered to be consistent with a deeper, lower mantle, source for the fPer association[1] Indeed, the high proportion of brown and plastically deformed stones in the present study is consistent with an unusually deep origin or, at least, a more traumatic history than most diamond populations recorded.

Table 5.3_3 Relative proportions of brown and plastically deformed stones compared to total population for selected worldwide localities.

Locality	Craton	% Brown stones	% Plastically deformed stones
Ellendale 4 *	Kimberley	20	-
Argyle *	Kimberley	80	-
DeBeers *	S. African	5.4	14.6
Dutoitspan *	S. African	13.3	21.7
Bultfontein *	S. African	6.0	13.1
Wesselton *	S. African	16.7	25.3
Finsch *	S. African	19.8	28.2
Premier *	S. African	16.4	24.6
Koffiefontein *	S. African	4.4	12.8
Mandala Basin ¤	N.W. African	High	69.1

* From Harris (1992) ¤ Calculated from data in Sutherland (1993), his figure 8 and Sutherland (1997, *personal communication*).

➠

---

[1] The same conclusion arises from the observation that fPer paragenesis stones have more evidence for brittle deformation than majoritic garnet association stones.

Section 5.4 Chemistry of diamond fragments and unbroken stones

Section 5.4.1 Bulk $\delta^{13}C$ detemination of broken stones

Figure 5.4_1 shows that the population of data collected (appendix 7) has a negatively skewed distribution with a mean of -6.25 ‰, median of -5.09 ‰ and standard deviation of 2.53 ‰. More instructively, $\delta^{13}C$ is also shown plotted on the basis of inclusion association in figures 5.4_2 - 5.4_6.

The LM association: As far as LM association stones are concerned figure 5.4_2, $\delta^{13}C$ shows a very tight distribution; values ranging from -3.47 to -5.57 ‰ with a mean of -4.89 ‰, median of -4.87 ‰ and standard deviation of 0.48 ‰. The correlation shows a slight positive skew (figure 5.4_2). Grouping all fPer association diamonds[1] together gives a wider distribution of $\delta^{13}C$ between -3.47 and -11.56 ‰ with a mean of -5.20 ‰ and median of -4.96 ‰. The standard deviation of the population is 1.32 ‰. The correlation shows a strong negative skew.

The Wilding (1990) suite: $\delta^{13}C$ analyses for diamonds reputedly of the LM association of Wilding (1990) are presented against the LM association from the series BZ210-BZ214 and BZ214 - BZ272 of figure 5.4_2, figure 5.4_3. Doubt has been cast on the validity of the Wilding suite, particularly in relation to accidental mixing of sample labels (Harris and Harte, 1993 *personal communication*). This means that one cannot be certain that fragments from a particular bottle relate to the inclusions mounted on the pips carrying the same sample number. The present study of $\delta^{13}C$ and the study of N by FTIR, section 5.4.2.1 for these Wilding (1990) samples was undertaken in order to attempt to assess the validity of Wilding numbering. Study of figure 5.4_3 shows that the Wilding (1990) diamond fragment sample is clearly inconsistent with all other inclusions thought to be of the LM association from Sao Luiz and Guinea[2]. This discrepancy places further doubt on the Wilding (1990) suite and, as will be discussed with reference to FTIR data, section 5.4.2, it was felt necessary to ignore Wilding (1990) data *of this type* in the present study.

UM / LM association: UM/LM diamond, BZ243, yields a $\delta^{13}C$ of -5.34 ‰.

LM I association: Three LM I diamonds are known; BZ207, BZ251 and BZ254. BZ207 was found to have a bulk $\delta^{13}C$ value of -5.00 ‰. BZ251 and BZ254 are discussed in detail in section 5.5.1, however, averaging 20 and 16 ion microprobe analyses yields $\delta^{13}C$ values of -4.09 ‰ and -5.05 ‰ respectively.

---

[1] Diamonds of LM, LM I, LM II, LM III and LM / UM association

[2] Figs. 5.4_2 and 5.4_3, as well as comprising 22 data points from the present study, incorporate 6 points from the BZ201 - BZ214 suite as determined by Dr. Stuart Boyd (Boyd, personal communication 1996). Samples used being BZ201, BZ202, BZ205, BZ206.

LM II asociation: For LM II diamonds, incorporating one value from each of BZ210 and BZ214 as determined by Boyd (1996, *personal communication*), three points are available. It is impossible to infer a particular distribution from such data but it can be observed, at least, that the range in $\delta^{13}C$ is wide; values range from -11.56 to -4.9 ‰. It should be noted that the ruby yielding BZ214 gave a value of -11.56 ‰, whereas the ruby / Px II yielding BZ241 gave a value of -5.30 ‰.

LM III association: Five data points exist for LM III stones figure 5.4_4, again too few to present meaningful statistical information although, interestingly, the mean appears at -5.69 ‰. $\delta^{13}C$ for this suite varies from -4.70 to -8.31 ‰.

Majoritic garnet (TZ) association: TZ diamonds show a wider range in $\delta^{13}C$ than so far encountered figure 5.4_5[3]; values varying from -12.42 to -4.63 ‰ with a mean of -8.17 ‰, median of -7.90 ‰ and standard deviation of 2.61 ‰. The sense of any non-Gaussian distribution is hard to assess indeed it could even be argued that the transition zone diamonds represent two different populations; one involving diamonds of $\delta^{13}C = \sim -12$‰ (BZ209 and BZ222) and one involving the remaining stones clustering around $\delta^{13}C = -5$ ‰.

UM association: The single UM diamond yielded a $\delta^{13}C$ value of -5.27 ‰. (as determined by Boyd, 1993 *personal communication*).

Diamonds of unknown paragenesis: As far as the stones of unknown paragenesis, figure 5.4_6, incorporating 6 values from BZ203, BZ204, BZ208, BZ212 as determined by Boyd are concerned, the range in $\delta^{13}C$ is, again, large; -12.96 to -4.20 ‰. Here, however, values cluster strongly towards the negative end of the distribution, 4 out of 8 lying more negative than $\delta^{13}C = -8$ ‰. The mean lies at -6.41 ‰, median at -4.99 ‰ with a standard deviation of 2.85 ‰.

Guinean diamond GU4: GU4A yielded a $\delta^{13}C$ value of -5.11 ‰.

Comparison of São Luiz and Guinean data with deep diamonds from other localities:

Lower mantle association diamonds: Prior to this study, the principal $\delta^{13}C$ values obtained from lower mantle diamonds are the fPer bearing stones from Koffiefontein (Deines et al., 1991, table 5.4_1). The results show the same tight clustering around -5 ‰ observed for São Luiz diamonds. More recently, a $\delta^{13}C$ analysis of a fPer bearing diamond from Letseng-la-Terrai, Lesotho

---

[3] Figure 5.4_5 includes a single $\delta^{13}C$ analysis from majoritic garnet bearing stone BZ209 determined by Boyd (1993, *personal communication*).

(McDade, 1994 *personal communication*) gave a δ^{13}C value of -3.87 ‰. Figure 5.4_7 presents this data and compares it with the results fom São Luiz and Guinean diamonds.

Table 5.4_1 δ^{13}C values for fPer association diamonds from Koffiefontein

Sample	δ^{13}C	Sample	δ^{13}C
K30	-4.99	K34	-5.04
K33	-5.15		

Data from Deines et al. (1991)

Transition zone association diamonds: The distribution of carbon isotopic content of Jagersfontein diamonds yielding majoritic garnets (Deines et al., 1991) is depleted in a similar way to the transition zone association diamonds from São Luiz. The degree of depletion between the two localities, however, is distinct: Jagersfontein diamonds range from δ^{13}C = -18.94 to -24.39 ‰, and Jagersfontein diamonds show a clearer negatively skewed distribution. Data from Jagersfontein are summarised in table 5.4_2 and presented in comparison with São Luiz data in figure 5.4_8.

Table 5.4_2 δ^{13}C values for majoritic garnet association diamonds from Jagersfontein

Sample	δ^{13}C	Sample	δ^{13}C
J22	-20.19	J27	-22.20
J23	-18.94	J32	-19.43
J25	-24.39		

Data from Deines et al. (1991)

Section 5.4.2 Nitrogen characteristics of broken and bulk stones

Section 5.4.2.1 FTIR analysis of broken and bulk stones

Lower mantle association characteristics: Of the diamonds from the suites BZ201 - BZ214 and BZ215 - BZ272, which showed a lower mantle association[1] , 96% were determined to be Type II on the basis of FTIR (26 of 28 stones). Even when analyses were performed on a number of different locations on a number of fragments from a particular stone, Type II characteristics were found throughout. The two exceptions, BZ226 (of LM association) and BZ237 (of LM III association) were both found to be highly aggregated IaB diamonds (containing 2% and 5% IaA respectively) containing significant platelets and variable amounts of nitrogen. Of fifteen analyses undertaken on five BZ226 fragments, two spectra showed an indication of nitrogen which, on deconvolution, yielded concentrations of 67 and 222 ppm[2], the rest were Type II[3]. In addition, values of 152 and 145 ppm N were obtained for BZ237.

The Wilding (1990) suite: Fragments from five diamonds from the Wilding (1990) fPer association were subjected to FTIR analyses. In contrast to the results of FTIR analyses on fPer association stones from the suites BZ201 - BZ214 and BZ214 - BZ272, three of these stones showed a significant nitrogen presence and one, BZ76 gave a spectrum which showed a significant proportion of IaA (deconvolution yielded 45% IaA, 55 % IaB). Furthermore, Wilding (1990) quotes a nitrogen content of over 800 ppm and ~ 70% IaA for his analysis of fragments from BZ76. Clearly, in a similar fashion to the determination of δ^{13}C for a number of Wilding (1990) fragments, section 5.4.1, apparently fPer yielding diamonds from the Wilding suite are inconsistent with the compositional characteristics of fPer yielding diamonds from the current study and the study of Harris, Watt and Harte (BZ201-BZ214). The conclusion that the sample numbers on phials containing diamond fragments from the Wilding (1990) suite do not correspond to the numbering system of the inclusions, section 5.4.1, is supported on the basis of nitrogen character. Nitrogen characteristics of Wilding (1990) data are not, therefore, considered further.

UM / LM association: Two fragments of diamond BZ243 yielding olivine, fPer and TAPP composition grains, section 2.3, yielded Type II spectra.

Majoritic garnet (TZ) association: Of the nine TZ association diamonds analysed, BZ209, BZ215 and BZ217 showed evidence for the presence of nitrogen; all Type IaAB with significant platelet absoption (1370 cm^{-1}). The remaining six were classified as Type II. Of two analyses undertaken on a fragment from BZ215, one spectrum was deconvoluted succesfully and yielded 289 ppm N with

---

[1] 27 stones broken and analysed in Paris and 1 stone, BZ257, analysed as a bulk stone but proven to contain a fPer by XRD, section 3.3.3.2.

[2] Both spectra were poor, however; errors in these values are likely to be large.

[3] Variation of nitrogen within a stone has been observed from other localities, indeed large amounts of nitrogen can be found in patches for stones which, otherwise are Type II; vanHeerden (1993) found 13 Type II FTIR stones which contained varying amounts of N from 10 to 555 ppm by mass spectrometry on burning.

71% of nitrogen as IaB. Thirteen analyses were conducted on three fragments of BZ217, four spectra were deconvoluted and exhibited a range in nitrogen content from 90 - 127 ppm with nitrogen aggregated as between 42 and 66 % IaB. Two spectra obtained by Boyd (1995, *personal communication*) on fragments of BZ209 gave values from nitrogen concentration of 311 and 252 ppm.

UM association: Two fragments of BZ213 were subjected to a single FTIR analysis by Boyd (1995, *personal communication*), one yielded a Type II spectrum whereas the other yielded a IaAB spectrum with a minimal Raman energy absorption and strong platelet absoprtion at ~ 1370 cm^{-1}. Deconvolution indicated a total of 252 ppm N with 72 % aggregated as IaB.

Diamonds of unknown paragenesis: Diamonds of unknown paragenesis analyses as broken fragments showed a range in nitrogen concentration of Type II to 212 ppm with a minimum of 92% IaB aggregation from nitrogen containing spectra (BZ235). Sapphire bearing diamond BZ227A was determined to be Type II for analysis of one fragment whereas a second fragment yielded a poor IaB spectrum indicating the presence of 71 ppm N.

Of the fourteen *unbroken* stones, eight showed Type II spectra or small amounts of highly aggregated (predominantly IaB) nitrogen (this includes all the diamonds which appear to contain fPer inclusions). Four stones which appeared to contain sulphide inclusions, showed significant IaA absorption (52 - 68 % IaB) and concentrations between 24 and 71 ppm N. These observations are consistent with those from transition zone diamonds described above. The two final diamonds contain large quantities of nitrogen and occlude what appear to be an orange majoritic garnet (BZ262) and (BZ272) an assemblage of a harzburgitic (purple) garnet and a cpx (green). BZ262 yielded a large 93.6 % IaB spectrum indicating the presence of 935 ppm N and showed significant platelet absorption. BZ272 yielded a 56.1% IaB spectrum indicating the presence of 336 ppm N and yielded a smaller, yet significant platelet peak and absorption at ~ 1370 cm^{-1}. The similarity between the nitrogen characteristics of these two stones and diamonds from the transition zone and upper mantle is consistent with the visual identification of their inclusions.

FTIR spectra of comparable stones: Two out of the three fPer bearing diamonds from Koffiefontein studied by Deines et al. (1991) are Type II, the third yielded a 100% IaB spectra with 33 ppm nitrogen; observations in line with the findings from São Luiz stones and the single Guinean diamond studied herein. Four of the five majoritic garnet occluding diamonds from Jagersfontein studied by Deines et al. (1991) yielded Type II spectra, the fifth was found to be a IaAB diamond with 97.7% IaB and 65 ppm nitrogen. Again these observations are consistent with the findings from São Luiz diamonds.

Section 5.4.2.2 Nitrogen composition by bulk analysis

Philosophy of study: Combustion determination of nitrogen was considered important for two reasons:

- The absence of nitrogen absorption in *FTIR spectra* does not, necessarily, imply an absence of nitrogen in a particular sample. It is possible that nitrogen can be accommodated within diamond in such a form as to not cause absorption in the infra-red. Such non IR-active nitrogen has been described in the literature where N resides in what are termed 'voidites' (Hirsch et al., 1986). Voidites are defect cavities within the diamond lattice where nitrogen resides in solid form. Given the high confining pressures of inclusions in São Luiz and Guinean diamonds (section 7.1.4) such a form of nitrogen is a plausible reason for the absence of nitrogen in some FTIR spectra. In order to test such a hypothesis, combustion of some diamond was considered essential. With this in mind, fragments of three diamonds, BZ207, BZ226 and BZ227, were chosen because FTIR indicated that these stones were Type II or, at most, only had very small absorption which could not be deconvoluted.
- Determination of $\delta^{15}N$ composition of São Luiz diamonds was considered an important adjunct to $\delta^{13}C$ determination and FTIR work and, as discussed in section 1.5.2.2.2 provides useful information for the consideration of planetary evolution. Due to the paucity of nitrogen bearing diamonds, in terms of FTIR spectra, throughout the São Luiz sample, the choice for bulk nitrogen determination was limited. A single diamond, BZ237, was chosen from the LM III association in addition to two TZ association diamonds, BZ215 and BZ217, an unknown association stone BZ235 and three stones from the Wilding (1990) suite, labelled BZ76, BZ81 and BZ116.

Nitrogen content: For the samples analysed, nitrogen was found to vary between 63 and 392 ppm, with three fragments having nitrogen below the detection limit[1] (~ 10-20 ppm). Bulk measurements of total nitrogen content for the twelve diamonds correlate well with FTIR analyses of the same fragments. Particularly given the errors involved and that, as noted in section 5.5.2.2, nitrogen content of diamond plates was found to be significantly variable: FTIR analyses involve only small volumes compared to the whole sample which is analysed by combustion. For full comparison of these data see appendix 6 and appendix 7.

- Boyd (1993, *personal communication*) detected some nitrogen in a fragment of BZ207. A separate fragment, however, yielded a Type II spectrum during the present study (N content <

---

[1] $\delta^{15}N$ composition could not be determined on these fragments.

10-20 ppm). On combustion of this fragment, no nitrogen was detected. The genuine bulk nitrogen content of the BZ207 fragment analysed must, therefore, have been < 131 wt ppm.

- Three spectra obtained for fragment BZ226-2 from diamond BZ226 showed a minute quantity of IaB nitrogen which could not be deconvoluted. Combustion showed that the bulk sample contained no nitrogen within error of this method (< 22 wt ppm).
- Two fragments of BZ227A yielded Type II spectra. One fragment, on combustion revealed the presence of 74 ppm N whereas for the other fragment, nitrogen was below the detection limit of the combustion line (< 39 wt ppm).

The similarity of FTIR and combustion determined nitrogen content suggests that no significant nitrogen is present in non IR-active states in the São Luiz diamonds analysed. Stones revealing Type II spectra, may show some variation in nitrogen content on a local scale (cf. section 5.5.2.2) but as a whole can be considered to contain less than 10 - 20 ppm N (the detection limit of the FTIR apparatus employed).

δ^{15}N composition:

Wilding (1990) suite: The three Wilding (1990) diamond fragments exhibited variable δ^{15}N compositions ranging from a particularly depleted value of -10.6 ‰ (BZ116) to a significantly enriched value of + 3.1 ‰ (BZ81). BZ116 gave a value of +0.2 ‰. As discussed in sections 5.4.2.1 and 5.4.1, these values cannot be assigned to particular parageneses.

LM III association: Two fragments of the single N-bearing LM III association diamond, BZ237, gave the same δ^{15}N value (-6.0 and -5.2 ‰) within error. These values lie at the more depleted end of the so-far determined global distribution (see figures 1.3_12 - 1.3_16).

TZ association: Both majoritic garnet bearing diamonds yielded positive values for δ^{15}N; BZ215 gave a value of 1.3 ‰, whereas BZ217 yielded a value of 1.2 ‰. These values lie close to the mean of eclogitic diamonds from Australia (vanHeerden, 1993), figure 1.3_14.

Diamonds from unknown associations: Diamond BZ235 (occluding sulphur and silica inclusions, section 2.2.1.9) yielded a δ^{15}N value of -1.2 ‰, whilst the sapphire-bearing diamond, BZ227 yielded a value of -0.3 ‰.

Section 5.4.3 Additional atomic species within São Luiz diamonds

Elements additional to aggregated nitrogen and intrinsic carbon can be IR-active. In particular, C-H stretching and bending modes and CO_2 cause absorption within the range of I.R. wavelengths determined for diamonds in the current study. C-H bending causes absorption at 2840 and 2905 cm^{-1} (Krot et al., 1994), C-H stretching has been found to both cause absorption in natural as well as synthetic diamonds at 3107 cm^{-1} (Woods and Collins, 1983 and Kiflawi et al., 1996) and CO_2 absorption occurs[1] at 2376 cm^{-1} (observed by Schrauder and Navon, 1993). Typical spectra depicting these absorptions in addition to diamond lattice absorption are shown in figure 5.4_9. The observations are summarised under the ‘comments’ column of appendix 6.2.

All of the above absorptions have been recorded for São Luiz diamonds and are found to be particularly common. For the present study, CO_2 absorption is interpreted as being due to insufficiencies in the correction procedure for atmospheric CO_2 and is therefore not related to the diamonds themselves (Cartigny, 1997 *personal communication*). C-H absorption, however, is believed to be due to bonded hydrogen.

There appears to be no relationship between the presence of C-H bending and inclusion association or nitrogen concentration. Some Type II stones exhibit C-H bending absorption (e.g. BZ206) whereas others do not (e.g. BZ218). At the other extreme, some nitrogen rich stones (> 70 ppm N) show C-H bending absorption (e.g. BZ217) whereas others do not (e.g. BZ227). The only *reasonable* consistency appears to be that Type II stones do not show C-H stretching absorption, with the exception of a small peak for a fragment of BZ239. A similar result was obtained in a study by Woods and Collins (1983). On a population of Ia stones, they found C-H stretching absorption in all spectra but never in Type II stones.

---

[1] CO_2 absorption also occurs at 650, 3620 and 3752 cm^{-1}.

Section 5.5 Chemistry of polished diamond ‘flats’

Section 5.5.1 Determination of δ^{13}C

Points were chosen to investigate possible compositional variations related to the variation of cathodoluminescence intensity observed for each stone and to determine whether any compositional differences related to proximity of inclusions.

Analysis pits were observed to be only slightly elliptical. One representative pit from BZ251 (figure 5.5.1) was imaged using a Nanovision scanning probe microscope (SPM) to assess the likelihood of incursion into deeper CL zones. The pit was found to be of the order of 30 µm wide and only 250 nm deep and so one could be confident of the entire analysis being restricted to the same cathodoluminescence zone even in the case of CL boundaries being steeply inclined[1].

The four plates show a range in δ^{13}C values exhibiting a negative skewed distribution with a mean of -4.28, standard deviation at 1σ of 1.82 and a median of -3.99, figure 5.5_2. Considering the plates individually:

BZ251: Twenty analyses were undertaken concentrating on a comprehensive study of a large area surrounding the two exposed inclusions as well as a traverse extending to the stone edge. Figure 5.5_3 shows the distribution of δ^{13}C values within this area. There appears to be no consistent variation in carbon isotopic values in relation to either distance from the inclusions or to the edge of the stone[2]. The single analysis undertaken at the termination of blunt fracture 4 of figure 5.3_3, yielded a δ^{13}C value (-6.29 ‰) cannot be considered anomalous, particularly with errors of 1 ‰ (1 σ). The values obtained for BZ251 range from -2.25 to -6.60 ‰ with a mean of -4.09 ‰, median of -4.01 ‰ and standard deviation of 1.23 ‰. Figure 5.5_4 plots this distribution which can be seen to be slightly negatively skewed.

BZ252: Sixteen points were analysed, mostly clustering around the inclusion but with some around the main fracture and across to one edge of the plate. The distribution of carbon isotopic content (figure 5.5_5) shows that there is no consistent pattern (within error) either around the inclusions or across the stone. BZ252 shows a wide range in δ^{13}C varying from -1.34 to -9.57 ‰ with a mean of -3.47 ‰, median of -3.18 ‰ and standard deviation of 1.95 ‰ and a slight negative skew (figure 5.5_6). Compared to the rest of the data, however, the value of -9.57 ‰ is very much an outlier, the

---

[1] In order for an analysis to impinge on an additional CL zone the angle of incidence of the CL zone with the slab surface would have to be <1.4° for an analysis coming within 10µm of the surface expression of the zone edge. Should this be the case, zone boundaries would be observed as particularly indistinct which was not observed to be the case for the four slabs analysed.

[2] As the stone is most likely broken, even if a concentric zonation in carbon isotopic content was to have been present it would not be observed to converge to what is now the centre of the stone.

remaining range being -1.34 to -5.10 ‰ giving a mean of -3.06 ‰, median of -3.03 ‰ and standard deviation of 1.19 ‰. This single anomalous point lies close to, but not on, the main fracture (fracture 1 of figure 5.3_3). An analysis undertaken at the termination of fracture 1($\delta^{13}C$ = -5.10 ‰), lies within the range of distribution.

BZ254: Sixteen points were analysed, clustering around the inclusion and involving a traverse across the stone. Although the lowest value obtained ($\delta^{13}C$ = -1.30‰) lies at the edge of the stone, the distribution of $\delta^{13}C$ values throughout BZ254 show no obvious trends (figure 5.5_7). BZ254 shows the widest range of $\delta^{13}C$ with values from -1.30 to -10.24 ‰ with mean of -5.05 ‰, median of -4.91 ‰ standard deviation of 2.09 ‰ and, again, a slight negative skew (figure 5.5_8). If the outliers of -1.30 and -10.24 ‰ are not considered, the distribution is far tighter, being very similar to that of BZ251 and, as we shall see, BZ255. This restricted range lies from -3.18 to -7.90 ‰ with a mean of -4.95 ‰, median of -4.91 ‰, standard deviation of 1.43 ‰ but still with a slight negative skew. The single analysis undertaken at the termination of fracture 1 (of figure 5.3_3) yielded a value of $\delta^{13}C$ = -5.51 ‰; both within a single standard deviation from the mean using the full data set and the restricted data set outlined above.

BZ255: Nine points were analysed on BZ255; clustering mainly around the inclusion but also covering a traverse to a point close to the edge of the polished surface (figure 5.5_9). A consistent trend of decreasing $\delta^{13}C$ value was observed from a point into the stone from the inclusion, to the edge. This range, however, lies within estimated errors. Figure 5.5_10 shows a range of $\delta^{13}C$ from -3.08 to -7.23 ‰ with a mean of -4.78 ‰, median of -4.37 ‰, standard deviation of 1.40 ‰ and with a negative skew.

Section 5.5.2 Nitrogen analyses of polished plates

Section 5.5.2.1 FTIR analysis for Nitrogen in polished plates

BZ251: Spectra obtained in the main sample chamber showed nitrogen to be present in small quantites aggregated as IaB. Due to the crude step size employed in order to achieve high enough intensities, spectra were not deconvoluted. At a higher resolution, ten spectra were obtained, nine of which showed a small presence of nitrogen entirely aggregated as IaB, whereas a tenth spectrum showed no indication of nitrogen (Type II). Concentrations were found to range from 34.9 - 115.0 ppm.

BZ252: Five spectra were collected from BZ252. A single spectrum showed that no nitrogen was present (Type II); all additional spectra being Type IaB. Concentrations were found to range from 40.2 ppm to 69.4 ppm.

BZ254: A single spectrum was obtained from the central region and gave no indication of any nitrogen (Type II); nitrogen content must be at least < 20 ppm.

Comparison with other work: Variation of nitrogen content in diamonds has been reported elsewhere; vanHeerden (1993) found 13 Type II FTIR stones which contained varying amounts of N from 10 to 555 ppm by mass spec on burning. Furthermore, Boyd et al. (1987, 1992 and 1994) observed varition within cores of coated stones by combustion and Harte and Otter (1992) observed a 6.44 ‰ variation within a single CL zone of a Koffiefontein diamond by ion microprobe. Indeed, given the obvious heterogeneity in cathodoluminescence of the polished flats (section 5.6.2) such heterogeneity in nitrogen is not considered surprising. The details of the interrelationship will be discussed in section 6.4.3.

Section 5.5.2.2 Determination of nitrogen content by ion microprobe

Samples BZ251, BZ252, BZ254 and BZ255 were analysed for N content according to the methodology outlined in appendix 9.2. Points were chosen for analysis in order to provide comparison with $\delta^{13}C$ measurements (by sampling as close to $\delta^{13}C$ pits as possible whilst keeping within the same cathodoluminescence zone). Additionally, compositions were determined across the full range of cathodoluminescence intensity for points involving inclusion related features, such as factures.

In all cases, nitrogen distribution appears to correlate well with cathodoluminescence (section 5.6.1); higher nitrogen contents corresponding to brighter CL. These relationships are discussed in detail in section 6.4.3.

BZ251: BZ251 exhibits the widest range of nitrogen content ranging from 0.1 to 260 wt ppm (figure 5.5_13). In general, higher nitrogen concentrations appear towards the area bounded by the two exposed inclusions with some lower concentrations occurring towards the edge of the stone.

BZ252: The nitrogen conten is, again, variable (figure 5.5_14) although of lower concentration than BZ251. With the exception of one analysis containing 635 ppm, BZ252 was found to contain between 0.1 and 217.2 wt ppm nitrogen. Of these, all high concentrations cluster around the area of the exposed inclusion and towards the straight (broken) edge of the stone. Low concentrations are found bordering the rounded edge of the stone. The value of 635 ppm was obtained from analysis of a volume incorporating a portion of fracture 5 (of figure 5.3_2).

BZ254: As figure 5.5_15 shows, BZ254 in general, contains very little nitrogen. An exception is one value of 149.4 wt ppm. Otherwise, all analyses detected < 3 wt ppm of nitrogen. No apparent trend in distribution of nitrogen with location on the polished surface is discernible, although the value of 149.4 ppm was obtained from fracture 2 (of figure 5.3_2).

BZ255: As for BZ254, the nitrogen content of this polished surface was found to be low throughout (figure 5.5_16). All values obtained show less than 10 wt ppm nitrogen. No consistent trend in distribution with location was observed.

Discussion: Values for nitrogen content determined by ion microprobe (figures 5.5_13 and 5.5_14) are closely coincident with results of FTIR analyses (figures 5.5_11 and 5.5_12). Any discrepencies are interpreted as being due to the more averaged nature of FTIR results.

The unusually high local concentrations obtained for BZ252 and BZ254 were found to be associated with analyses obtained along fractures. Atmospheric nitrogen is thought to have been present in large concentrations amongst polishing material trapped within these fractures, thus making such data spurious (Craven, *1997 personal communication*).

➠

Section 5.6 Cathodoluminescence

Cathodoluminescence (CL) is the term for the phenomenum of visible light emission due to electron incidence with a solid media. Davies (1979) provides a comprehensive discussion of cathodoluminescence in diamond.

Briefly, pure diamond does produce cathodoluminscene but not within the visible part of the spectrum. The presence of defects, particularly those associated with aggregated nitrogen and plastic deformation has a most profound effect on the cathodoluminescence spectra of diamond within visible wavelengths. Cathodoluminescence of IaA and IaB aggregated diamond has a characteristic sky-blue colour, the intensity of which appears to be strongly dependent on the presence of platelets (which are dominated by nitrogen, Lang, 1979). The presence of N3 centres promotes yellow-green cathodoluminescence, synthetic Ib diamond are characterised by green cathodoluminescence (e.g. the synthetic stone SYNAT used as a standard for SIMS analysis, sections 5.5, figure 5.6_1), radiation damaged diamonds have canary-yellow CL and pink, purple and orange CL appear to be caused by the presence of CO_2 (Chinn et al., 1995). Intermediary colouration probably arises as a result of contributions of a number of CL active agents, for example plastically deformed CO_2 bearing diamonds show brown CL (Chinn et al., 1995).The *intensity* of cathodoluminescence is dependent on the *concentration* of defects. For many diamonds, as nitrogen is by far the most dominant impurity, variation in catholdoluminescence intensity can be attributed to variation of nitrogen content in such stones.

The particular beauty of cathodoluminescence imagery of diamond, lies in the fact that, depending on the potential of the incident beam, the depth of sample responsible for CL emission is of the order of a few tens of microns. This means that CL images provide information on the degree of inhomogeneity of a very thin slice of material[1]. Such precision means that any inhomogeneity present can be detected to a far greater degree than techniques such as FTIR or optical absorption, which average through the thickness of the sample. In addition, as CL is caused by a multitude of different factors, it can be used to detect even small inhomogeneities whether due to nitrogen, diamond defects, microfractures, or radiation damage; as such, however, the technique has the disadvantage of not being quantitative.

As the details of ambient conditions in terms of stress field and composition (for example nitrogen content) vary throughout a diamond's growth history, cathodoluminescence presents an ideal means

---

[1] Providing the sample is mounted in a suitably absorbant medium, such as indium, internal reflections along the edges of the sample are minimised.

to image the morphology of growth of individual stones provided impurities are present. Cathodoluminescence images of natural stones are, often, fairly simple. Most stones grow either by adopting an octahedral or cubic morphology (reflecting the ambient growth conditions, section 1.5.1), sometimes varying between the two throughout their formation (e. g. Boyd et al., 1988). Usually, stones exhibit concentric CL patterns, consistent with growth outwards from a central point and CL intensity or wavelength often varies in a step-wise fashion[2]. Observations of this nature have been made on, for example, diamonds from Bultfontein (Wilding, 1990 and figure 5.6_2), Yakutia (Taylor et al., 1995a) and Kaal Vallei (Taylor et al., 1995b). Occasionally, the growth history of certain stones is particularly complex. Taylor (1994, *personal communication*) observed a cusp in the CL image of a stone from a Yakutian diamond which he interpreted as the former location of an inclusion which had dissolved out of the stone; the hole having subsequently been re-filled with diamond. Evidence of resorption (cross-cutting relationships of CL zones) has been detected amongst stones from Premier, Koffiefontein, Bultfontein and Finsch (Otter et al., 1991) and stones from George Creek (Chinn et al., 1995) show particularly irregular zonations and unusually coloured CL patterns. CL patterns of São Luiz stones (section 5.6.1), although low in intensity also show particularly complex zonation.

Cathodoluminescence images were obtained from each of the diamond flats (BZ251, BZ252, BZ254 and BZ255 in particular detail) mounted in indium in a steel block. The instrumentation used was a CITL CCL 8200 Mk3A source combined with Nikon Optiphot optics of the Department of Geology and Geophysics. Operating conditions employed were <800 μA and 12-15 kV at 8 Pa.

---

[2] The time period of growth may not, necessarily, be stepwise. Breaks in CL intensity or, indeed wavelength, may simply be due to the fluid reservoir from which the diamond precipitates reaching saturation in, for example, nitrogen, catastrophically falling and then rising again in a similar fashion to the formation of Leizegang rings in silica precipitation such as gives rise to agates (Moxon, 1991).

Section 5.6.1 Cathodoluminescence characteristics of São Luiz diamonds

The cathodoluminescence of all eight slabs was low in intensity. Variation between and within slabs, however, was found to be highly complex. Both diffuse and step-wise zonation was observed, but only for BZ253, BZ255 and BZ258 was any evidence of simple concentric growth found.

Diamonds polished to expose inclusions: Cathodoluminescence images of plates BZ251, BZ252, BZ254 and BZ255 are presented in figures 5.6_3 - 5.6_7 respectively.

BZ251: BZ251 shows the strongest CL intensity of all eight slabs (figure 5.6_3). The colour is a deep blue throughout; variations in intensity, however, expose a complex pattern. BZ251 appears to have had an area broken from one side; the far side from which the two inclusions are most proximal. The CL image is overlain by a series of closely spaced parallel lines in a single direction across the entire imaged surface. In detail, CL is relatively bright around the edge of the stone and, in particular, in an irregular patch occupying an area from the edge of the stone towards the centre and comprising the two exposed inclusions BZ251A and BZ251B. Three particularly dark blue patches are distributed around the area of the inclusions on the polished surface. The dark and light areas are relatively homogeneous in their intensity but are bounded with areas of intermediary intensity by ragged edges and, in places, apparently random distributions of sharp CL intensity change orientated in three general directions. The intermediary intensity areas can be subdivided into two areas:

- one involving the inclusion occupying portion of the stone shows a ‘zig-zag’ patterns of close spaced (5 μm) lines of varying CL intensity (figure 5.6_4)
- the other, occupying the far side of the stone from the inclusions, shows a gradual change in CL intensity.

BZ252: The exposed inclusion, BZ252A lies towards the middle of the polished surface. The single straight edge bounding the slab would suggest that this one side of the stone has had a fragment broken away from it. In terms of CL, BZ252 exhibits a deep blue colouration throughout (figure 5.6_5). Three areas of particularly high intensity are observed:

- a band around the edge of the stone involving the entire perimeter, with the exception of the broken surface.

- a semi-circular shape bounded to one side by particularly intense CL against the single large fracture across the middle of the stone and merging into the background CL on the other side.
- a complex area of straight edged sharp changes in CL intensity in two general directions.

The three bright areas lie amongst a generally dark and diffuse CL; the intensity being particularly low in two subparallel segments on the far side from the broken edge.

BZ254: The two inclusions whose associated fracture systems are exposed on the polished surface, lie partially towards one corner of the roughly square section. The CL intensity is low throughout the stone and blue in colour (figure 5.6_6). Areas of greater intensity lie around the edge of the stone and in a small number of broad, parallel bands across the surface of the stone. Within these bands and, indeed, throughout the stone as a whole, there appears to be some form of step-wise zonation with sharp boundaries and sub-parallel edges. The periodicity of changes in CL of this nature is not on such a fine scale as observed in areas of BZ252 and, in particular in BZ251. The two inclusions appear to occupy an area of particularly low intensity. The boundary of this area is fairly ragged and involves two separate orientations of subparallel lines. Within this darker area, CL intensity appears to be relatively homogeneous with the exception of the fracture systems themselves which are picked out by intense CL.

BZ255: The shape of the diamond suggests that it has either been broken, or smoothly eroded. The single inclusion exposed (BZ255A) lies to one side of the stone close to the longest edge. BZ255 shows a deep blue CL the intensity of which is the lowest of all eight polished slabs (figure 5.5_7). Two particularly dark areas are evident:

- an irregular shaped area surrounding the inclusion and exhibiting a relatively diffuse boundary.
- a second elongate irregular shaped area towards the middle of the polished face.

Within both dark areas, variation in CL is relatively diffuse. Throughout the remainder of the stone, is an indication of concentric octahedral growth involving a series of reasonably sharp edged bands of oscillating CL intensity in two principle directions. The centre of the concentric feature appears to coincide almost exactly with the location of the exposed inclusion BZ255A and has greatest intensity towards the edge of the stone.

Additional polished flats:

BZ253: Two large inclusions lie within one half of this roughly elliptical sectioned stone. The CL colouration of BZ253 is blue throughout, however, in comparison to other stones, it exhibits a slight purplish tinge. The pattern of CL is exceptionally complex and intensity varies markedly (figure 5.6_8). The stone can, roughly, be divided into two halves where one half contains the two inclusions. The inclusion bearing section, in general, is darker and has a rather smoothly varying intensity. There are, however, a series of interwoven subparallel bands of dark and lighter intensity. The second half of the stone exhibits a complex CL zonation which is stepped and appears, in general, to be concentric about a point off the edge of the stone. Intensity is greatest towards the centre, although a number of thinner, light bands appear towards the edge of the concentric feature. This concentric behaviour is not a constant feature of the second half of the stone, however: an area of dark CL impinges from the inclusion bearing portion across half of the outer edge of the concentric feature.

BZ256: The CL intensity of BZ256 is low throughout the surface of the stone and of a deep blue colouration. Because of the depth of the colour, little inhomogeneity could be detected, any present varying smoothly rather than displaying the sharp boundaries seen within other stones.

BZ257: A single large inclusion resided in the centre of BZ257 before breaking. The CL intensity of the stone was found to be variable in blues. Variation, in CL, however, was found to be diffuse: lacking any sharp boundaries and any obvious concentric or step zonation. The fracture systems around the large inclusion were picked out by intense white CL (figure 5.6_9).

BZ258: BZ258 is a large stone exhibiting a complex blue CL pattern of generally low intensity (figure 5.6_10). A single large inclusion lies very near to one polished surface: numerous dark flecks occur throughout the stone. At first glance, the CL pattern appears to be completely random: composed of a jigsaw pattern of sharply bounded dark areas. Superimposed on this, however, is some indication of stepped concentric zonation across a significant portion of the stone centred at a point close to one edge. In addition, the far edge of the stone shows a ‘zig-zag’ pattern similar to that seen for BZ251 although of a wider periodicity and involving more diffuse boundaries.

➠

Section 5.6.2 Interpretation of cathodoluminescence characteristics of São Luiz diamonds

The complex cathodoluminescence of the São Luiz diamonds are interpreted as being symptomatic of multiple histories of growth, resorption, fracture, plastic deformation and intergrowth of stones. A number of particular features, in addition, are interpreted as being artefacts of the preparation.

Fracture systems: Fracture systems are picked out particularly strongly around inclusions in BZ252, BZ254 and BZ257 by intense CL. Cathodoluminescence intensity is known to be instigated by defects on a molecular scale by the set up of donor acceptor pairs. Such defects are likely to be associated with the edges of fracture systems and provide a suitable explanation for the high CL intensity of fractures in São Luiz stones. Fracture systems, in addition, however, act as planes of reflection for light; indeed fractures are often very obvious on optical examination. A significant proportion of the CL intensity associated with fractures is likely, therefore, to be a result of internal reflection and is especially true for fractures such as the large single fracture in BZ252 which penetrates into the stone most likely beyond the depth of primary cathodoluminescent activity.

Fine parallel lines in BZ251: The series of fine lines in CL images of BZ251 (e.g. figure 5.6_3) are interpreted as being saw marks from the cutting of the diamond flat.

High CL intensity borders: The higher average cathodoluminescence which borders BZ251, BZ252 and BZ254 are considered likely to be due to internal reflection against the diamond / indium boundary[1]. The exceptionally high refractive index of diamond means that a larger range of angles of incidence will cause internal reflection (figure 1.2_1) than for any other crystalline material. Although mounting in indium is found to significantly reduce internal reflection resulting from light impinging on the rough boudaries of the stone, indium is a light coloured metal and does reflect light fairly efficiently.

Growth history: Clearly, some stones, BZ253, BZ255 and BZ258, show indications of concentric growth as is typical of diamonds from worldwide sources, section 5.6. Furthermore, some of the stepped features in BZ251 and BZ252 may have been, at one stage, concentric in morphology. It is likely that at least for some diamonds, initial growth was within a reasonably stable growth environment analogous to the conditions of growth of lithospheric diamonds. Given the broken edges of a number of stones, particularly BZ251, BZ252 and BZ254, the fact that the centre of the

---

[1] This conclusion is supported by measurements of nitrogen concentration. As discussed in section 5.5.1.2, nitrogen exhibits a strong positive correlation with CL intensity with the exception of the edges of BZ251, BZ252 and BZ254 which, although showing higher CL intensity exhibit low nitrogen content.

concentric feature in BZ253 lies outwith the stone and, in all case, any concentric zonation is truncated, it would appear that all stones, following initial growth, were subjected to a period of resorption followed by reprecipitation of lower intensity CL. The ragged edges to some features, BZ251 and BZ254, intense zig-zag features, BZ251 and BZ258 and the parallel fine lineations observed across, BZ255 and, in particular, BZ251 are all interpreted as being characteristic of plastic deformation; boundaries being offset on a fine scale by slip and on a larger scale, concentric zonation being radically realigned.

Relationship of growth features to inclusion location: Given that inclusions occupy both areas of light, e. g. BZ251, and dark, e. g. BZ255, CL intensity and are either associated with concentric zonation, BZ255 or in altogether different areas of the stone, e. g. BZ253, it would appear that inclusions have been incorporated within precipitating diamond during all stages of growth. Without detailed study of the cathodoluminescence characteristics of each stone, therefore, with the exception of touching inclusions, multiple inclusions recovered from diamond cannot be considered *a priori* to have been accommodated at the same time or even in the same location. In order to be certain of equilibrium, study of the chemistry of coexisting grains such as discussed in section 4.5.1 is considered to be essential.

Section 5.7 Summary of diamond characteristics

Amongst the diamonds from São Luiz are found a particularly high proportion of brown coloured stones, almost all of which exhibit visually observable features of plastic deformation. Even amongst colourless stones, the occurrence of plastic deformation is high, indeed all show some form of deformation whether manifest by the presence of plastic deformation lines, fractures, trigons or surface pittting. Furthermore, the population involves a particularly high proportion of irregular and dodecahedral stones at the expense of octahedral forms. In terms of source region, the incidence of brown, irregular and obviously deformed stones is higher for lower mantle sourced stones than for shallower transition zone sourced diamonds. Cathodoluminescence and high resolution imaging suggests that as well as having undergone complex growth histories, the deformation of São Luiz stones has been a multi stage process early brittle deformation events sandwiching events of plastic behaviour. In all cases studied, final deformation appears to have been brittle. Detailed study by EPMA, high resolution microscopy and SIMS yields no evidence for secondary material, with the exception of preparation residues, infiltrating into fracture systems down to a resolution of a least x2500. In general, the chemical sanctity of included material can be considered assured.

Lower mantle sourced diamonds: Amongst the lower mantle sourced stones, nitrogen contents are generally low, <100 ppm, indeed, in terms of bulk composition, most stones are Type II (<20 ppm N). They are also highly aggregated > 90% IaB. On a fine scale within individual stones, nitrogen, where present is found to vary where variation is more marked within individual stones than in the population as a whole. δ^{15}N values are depleted ~ -6 ‰. In terms of carbon isotopic concentration, lower mantle sourced stones cluster strongly around δ^{13}C values of -5 ‰, with the exception of a single ruby occluding stone which yields a value of -11.56 ‰.

Upper mantle sourced diamonds: Transition zone sourced stones, in addition to the few shallower sourced diamonds, again, exhibit low concentrations of nitrogen. Nitrogen concentration is not, however, as low as for lower mantle stones and in some cases is as high as ~300 ppm. In terms of nitrogen aggregation, all stones show significant presence of IaB absorption; values for IaB tending to be around 70+ %. δ^{15}N values are variable and positive. Carbon isotopic content of transition zone stones, although exhibiting a cluster around δ^{13}C = -5 ‰, are also, in some cases, significantly depleted compared to lower mantle sourced stones. Values of down to -12.42 ‰ have been found and a single sapphire occluding diamond of unknown origin was found to yield a δ^{13}C value of -4.99 ‰.

➠

Chapter 6 The nature of mantle regions as seen through study of São Luiz diamonds

Chapter 6, firstly (section 6.1), presents the current thinking on the formation of diamond further to introductory comments made in section 1.2.3 and, as an explanation of worldwide diamond carbon isotopic content, in section 1.3.2.1. Details of the compositional and physical charactersitics of São Luiz diamonds (in addition to the single available Guinean stone) presented in chapter 5, are subsequently discussed on the basis of current knowledge (sections 6.2 and 6.3). By approaching diamond characteristics in terms of source areas (from associations discussed in chapter 4), the present chapter aims to present a picture of how these deep diamonds formed, and what their formation can say about the state and evolution of mantle regions.

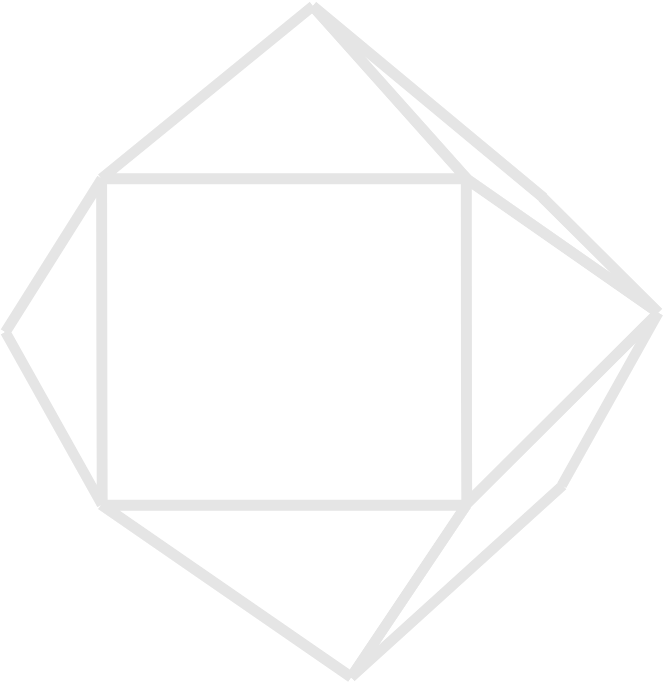

Section 6.1 Mechanisms of diamond formation

The traditional concept of diamond formation as far as context in thickened cratonic roots has been discussed in section 1.2.3. There are, however, two additional factors in the formation of diamond which need to be considered aside from its pressure / temperature stability.

- In order to glean information on the state of the source region of crystallising diamond, it is important to consider the stability of diamond in terms of oxygen fugacity (fO_2). Extrapolation is therefore made (section 6.1.1) from the reaction mechanisms used to explain the carbon isotopic signatures of diamonds (section 1.5.2.1) to the fluid conditions which can be envisaged to promote such reaction mechanisms. Additionally, an attempt is made to envisage how fluid conditions, and thus diamond reaction mechanisms, are likely to change with varying physical conditions; particularly those relevent to the deep mantle.
- Discussion of the growth of diamond on an *atomistic* scale and the role of geologically relevant catalytic mechanisms, additionally, represents an important means to explain a number of characteristics of the stones in the present study. Such points are discussed in section 6.1.2.

Section 6.1.1 *Diamond Stability in terms of fluid species*

As far as pressure and temperature are concerned, the stability of carbon and its polymorphs is well established (Kennedy and Kennedy, 1976 and Wedlake, 1974). Within the boundaries of all reasonable mantle geotherms (section 4.2) and at depths greater than 200 km, it is the diamond form of carbon which is the stable polymorph. It is a reasonable assumption, therefore, that where carbon exists in its elemental state, throughout the whole of the mantle transition zone and lower mantle, it adopts a diamond structure. Diamond is remarkably resistent to mechanical alteration due, in part, to its extreme hardness (section 5.3), its ability to retain hugely elevated internal pressures (section 7.1.4; Schrauder and Navon, 1993 and Navon, 1991) and the very slow diffusion rates for elements in its structure (section 1.3.2.3; Ozima and Zashu, 1988 and Honda et al., 1987). Generally, also, it is highly resistent to chemical alteration, and so, with these features in mind, although a very rare sight, the occurrence of deep sourced diamonds at the earth's surface can be considered to be quite plausible.

Diamond is not, however, infallible. The often quoted phrase ‘a diamond is...forever’ is unfortunately not true, in the chemical sense. Observations show that diamond will burn in air at ~900K (appendix 11), it is metastable at ATP (Kennedy and Kennedy, 1976) and will graphitise at ~2173K in vacuum (Kaiser and Bond, 1959). Under certain conditions of oxygen fugacity, diamond has the theoretical potential of undergoing a number of reactions including the following: $C + O_2 = CO_2$ (the CCO buffer), $C + 2H_2O = CH_4$ (the C-H_2O buffer) or $Mg_2SiO_4 + C + O_2 = MgSiO_3 + MgCO_3$ (the EMOG/D buffer). Indeed, crossing such reaction boundaries in the reverse direction, provides a means for the *formation* of diamond[1].

The mechanism by which diamond forms, is dictated by the physical conditions of pressure and temperature, the oxygen fugacity, which is controlled by the bulk ambient chemistry, and the fluid components available. Most diamond is believed to form from the fluid phase which, in geologically relevent settings, can be described in terms of the components C-O-H. Much work has been undertaken regarding the relative stability of phases within the C-O-H system at differing physical conditions. Particularly notable research has been undertaken by Deines (1980), Saxena and Fei (1987) and Frost and Wood (1997).

---

[1] Haggerty (1986) discusses the possibility that graphite soot in earth’s genetic material (or as a high pressure vapour deposit) can account for some of the diamond budget of the mantle; such soot being accumulated and transformed to diamond due to pressure. Although this may be an important seed material for new diamond, it is clear that diamond does also grow in the mantle by mechanisms other than polymorphic transformation. Amongst the evidence is the incorporation of included material and the fact that some diamonds are seen to be resorbed; if resorption can take place, it can, equally be envisaged that growth takes place.

Using a thermodynamic approach and iterating between fugacity coefficients and mole fraction, Deines (1980) was able to calculate the mole fractions of species in the C-O-H system over a range of pressures (3 - 6 GPa), temperatures (~873 - 2273 K), fO_2 (log fO_2 of 0 to -40) and H_2O saturation (XH_2O of 0.9 to 0.1) conditions. Figure 6.1_1 shows phase relations in the C-O-H system for fluids in equilibrium with elemental carbon for a variety of temperature and pressure conditions. Nowhere within geologically reasonable conditions is CO found to be a dominant phase; elemental carbon is present with either CO_2, H_2O or CH_4 (with some H_2). Figure 6.1_2, summarises the fields of dominant carbon-bearing species in terms of temperature, fO_2 and XH_2O (mole fraction of H_2O). In more oxidised environments, CO_2 is the dominant species, whereas in more reduced environments, CH_4 is the dominant carbon-bearing species. The position of the reaction boundary of $C + O_2 = CO_2$ correlates well with results by Frost and Wood (1997), taken up to higher pressure (7.7 GPa), and reasonably with EOS measurements by Saxena and Fei (1987). Elemental carbon (diamond or graphite) is stabilised at intermediate fO_2, largely between FMQ-1 and IW buffers. Deines (1980) found that an increase in temperature forced elemental carbon stability to higher fO_2 and reduced the stability range. Additionally, elemental carbon stability was found to be compromised in the presence of increasing proportion of H_2O component in the fluid and by decrease in pressure. Interestingly, Zhao et al. (1997), however have been able to synthesisze diamond under hydrothermal conditions at pressures of 0.14 GPa and 1073 K.

The implication which can be taken from the phase relations in the C-O-H system at mantle pressures and temperatures, therefore, is that within the range of mantle fO_2 (section 7.2.2) diamond can either be envisaged to precipitate by reactions of reduction of CO_2 (or burn in the presence of oxygen):

$$C + O_2 = CO_2 \qquad \text{Equation 6.1\_1}$$

oxidation of methane:

$$C + 2H_2O = CH_4 + O_2 \qquad \text{Equation 6.1\_2}$$

or, where CO_2 and CH_4 are present in comparable proportions, by the reaction:

$$CO_2 + CH_4 = 2C + 2H_2O \qquad \text{Equation 6.1\_3}$$

How such reactions affect the stable isotopic contents of thus precipitated diamonds is discussed in section 1.3.2.1.

The origin of precipitating diamond fluids: Some detail is, therefore, forthcoming, on phase relations in the C-O-H system. Comparison of the phase relations with calculated fO_2 for various earth régimes (section 7.2.2) should therefore, give an indication of the likely diamond precipitating reactions in these regions where C-O-H are present (and not bound to, for example, carbonates). The question still arises, however, as to where any available C, O and H originate.

Liu (1984) suggested that, in the case of diamond forming by the breakdown of CO_2, the reactant is sourced from subducted material. Much research has been levied upon the presence of CO_2 and the relative stability of carbonate in the mantle, particularly due to the abundance of carbonate in kimberlites and CO_2 in OIB. For example, experimental work by Dalton and Wood (1995) suggested that CO_2 could only be produced by oxidation of carbonate at an fO_2 greater than FMQ-0.5, under pressure conditions of the upper mantle. This restricts the stability of free CO_2 to only specific oxidised environments within the mantle. Such an observation would appear to be at odds with the fact that carbonate bearing xenoliths are exceptionally rare. Canil (1990) addressed this problem, however, by running experiments which showed that the stability field of carbonate shrinks markedly at low pressure. Carbonate-bearing peridotite xenoliths, therefore, cannot be expected to survive exhumation although as Dalton and Wood (1993) point out, carbonate is stabilised to lower pressure in the lherzolitic system than in the Fe-free equivalent. What this discussion highlights, therefore, is that carbonate in subducting slab can be considered stable at depths throughout the upper mantle. At such times as oxidation is allowed to take place, however, CO_2 can be released; on transport to a more reducing environment of differing lithology, diamond may be precipitated (e.g. Kirkley et al., 1991). Kesson and Ringwood (1989) similarly promote a subduction model but one which involves diamond precipitation from a melt (rather than a fluid) in a H_2O-rich environment. There exist a number of opponents to subduction models for the formation of diamond, for example, Boyd (1988) forsees a difficulty in the exchange of mantle carbon for diamond.

Zhang and Zindler (1993) have made a particular study of carbon and nitrogen in the earth. Firstly, they estimate from noble gas isotopic compositions that the initial CO_2 content of the earth was smaller than that inferred by measurements from meteorites. Comparison of primordial values with the present depletion suggests that CO_2 is less depleted than, for example ^{3}He, despite having similar solubilities within mantle material. This means that, either extensive CO_2 has been recycled by subduction, or else the initial form of carbon was more reduced and thus less likely to degass. Zhang and Zindler (1993) prefer the former model, principally because the latter would appear to be at odds with the large number of Archean carbonates. Most of the degassable CO_2 in the earth is still in the earth's degassable mantle. As far as nitrogen is concerned, however, nitrogen flux into the atmosphere has remained almost constant since the Archean; N_2 does not appear to be extensiely recycled although a small degree of subduction may go on. These conclusions have important implications for the source of deep mantle carbon and nitrogen and will be discussed in section 6.2.

Section 6.1.2 The atomistic growth of diamond and the presence of N and H in São Luiz diamonds

The social value of diamond is such that more study has been levied upon mechanisms of its formation than any other mineral. With reference to its formation, much work has been carried out in order to address the question of under what conditions of P, T, fO_2 and catalyst presence can diamond be formed. Such study has been both within a geologically relevant framework (e. g. Deines 1980, section 6.1.1) and, as discussed in the present section, a more industrially applicable framework. Indeed, in terms of the atomistic growth of diamond, study has *only* been within the industrial framework. As will be discussed, however, some of the pertinent points can be transferred to consideration in a geological setting because many arguments involve parameters independent of conditions of formation, such as bond energies.

The industrial framework has involved the metastable growth of diamond at low pressure using CH_4 / H_2 mixtures (termed carbon vapour deposition, CVD) (eg. Angus and Hayman 1988, Klages 1994) and the catalytic use of Ni in diamond growth at high pressure and temperature (Bundy et al., 1955 and Wakatsuki and Takano 1987).

In order to find clues as to the atomistic mechanisms for *natural* diamond growth, one must first consider the state of crystal terminations. Any crystal must have atoms on its surface not bonded to nearest neighbours of the Type expected by its normal structure, i.e. carbon atoms on the surface of a diamond will not be bonded to more than 3 other carbon atoms. Such a scenario involves a charge imbalance which must be somehow addressed. There is much evidence to suggest that, in the case of diamond, these 'hanging bonds' are usually satisfied by hydrogen (Lander and Morrison 1963) and, in fact, it has been found that the presence of hydrogen acts not only, as described subsequently, as a means to satisfy hanging bonds, but also an essential factor in at least some mechanisms of diamond formation and an important means of suppression of graphitisation (Angus and Hayman 1988).

Frenklaech et al. (1994) have studied the role of hydrogen in the formation of synthetic diamonds. They have shown theoretically, that under certain conditions, hydrogen will act as an efficient catalyst. Their discussion is based around a framework of CVD. Diamond, like most crystalline materials grows through a propagation of steps, in this case involving (111) and (100) (Arima et al., 1993 presents a macroscopic corollary). Frenklaech et al. (1994) hypothesise that the growth of diamond propagates in a fashion utilising the difference in bond energy between covalent C-C bonds and ionic C-H bonds. Hydrogen on the surface of a growing diamond will easily be removed and replaced by radicals of the fluid species, in this case CH_3 or C_2H_2. Once bonded into the system of diamond lattice carbon atoms, however, electron transfer will allow for the removal of hydrogen from the added radical. Essentially, a CH_2 group will be added to a diamond dimer and will bridge groups of bonded carbon atoms. This is the process of addition of carbon into the diamond lattice.

The theoretical approach of Frenklaech (1994) is supported by observation. On an empirical level, this interdependence of hydrogen, hanging bonds, carbon bearing radicals and diamond growth is clear. In order to quickly precipitate high quality diamonds, high concentrations of, not only methyl radicals, but also hydrogen atoms, must be attained (Klages 1995). Additionally, in nature, the supposed *catalytic* role of hydrogen would explain why few diamonds exhibit much bonded hydrogen (Bibby 1982). However, some diamonds *do* exhibit body hydrogen (Woods and Collins, 1983; Kiflawi et al., 1996 and the present study, section 5.4.3). The presence of such hydrogen suggests that in natural systems, reactions *similar* to that of Frenklaech et al. (1994) may, indeed, apply. In cases where significant hydrogen is found, a mechanism of rapid growth thus trapping 'escaping' catalytic hydrogen would be applied. Here, the thermodynamic preference for the expulsion of a *relatively* energetically unstable species such as H, is outweighed by the kinetic effects of rapid growth; a similar argument is used in conjunction with variable reservoir concentrations, for variations in N concentration in diamond (e.g. van Heerden, 1993). Furthermore, a similar mechanism for the incorporation of B into diamond can be envisaged[1].

It should be kept in mind, however, that in nature, the presence of radicals encountered in such abundance in CVD processes is not considered likely; they are due to the high temperatures involved ~ 2200K. They will, however, still be present in a geological setting, although in concentrations such that, instead of producing the formation rates of 10's of microns per hour achieved in CVD (Klages, 1995) diamond will precipitate at a much slower rate. Indeed it has been observed that, provided the substrate temperature is greater than 1100-1250 K, low for most natural settings of diamond formation (and certainly so for the diamonds considered in this study), enough thermal energy is available to impart mobility to adsorbed species and allow such reactions as just described to take place (Angus and Hayman 1988). The relevance of this work to the present study is that it illustrates the important role of carbon bearing species rather than, simply, carbon, in the crystallisation of diamond, and provides a fairly direct comparison with how the CH_4 precipitation reaction (equation 6.1_3) may proceed in nature.

In addition, from this point, it is easy to see how reactions involving CO_2 and other carbon bearing species may undergo similar reaction mechanisms. Indeed CVD diamond has been grown using

---

[1] It should be noted that such stepwise bridging reactions can be used only to explain bonded atoms, not reactions involving vacancies, interstitial atoms or atoms of radically different radii from carbon. The latter being, clearly, incorporated at a molecular level in structural defects.

oxygen bearing species such as OH^- (Bachmann et al., 1991) and there is evidence that yet other species can catalyse the formation of diamond in geological settings. It is interesting to note that, amongst lithospheric diamonds, sulphides are by far the most common inclusion Type. Perhaps in a similar way to the use of Ni to catalyse the formation of synthetic stones (Bundy et al 1955), the abundance of sulphide inclusions is indicative of metal sulphides catalysing the growth of natural diamond (Marx, 1972). Furthermore, although likely to be both a dominant lower mantle phase, and, by its easy identification, subject to positive sampling bias, the predominance of *fPer* in lower mantle stones, may be indicative of a similar catalytic role for (Mg,Fe)O in the lower mantle.

Study of the growth of industrial diamond is still very much in fashion and the geologist can therefore expect a continued flux of new data on the atomistic level from which more inferences transferable to a geological setting will be obtainable.

São Luiz diamonds: Infra-red absorption characteristics of stones in this study (section 5.4.3) support the presence of significant bonded H. Furthermore, there appears to be no systematic relationship between the occurrence of bonded H, and source area. Evidence from CL suggests that São Luiz diamonds have undergone complex growth and resorption (section 5.6). Given the sporadic, but occasionally significant presence of bonded H, it would appear that São Luiz diamonds have seen significantly differing *rates* of growth: the H-bearing stones having grown quicker. Additionally, the fact that H is *not* seen in the FTIR spectra of Type II stones, (with the exception of BZ239 which may still contain some, patchy, nitrogen) suggests that the catalytic role of H in diamond formation requires the presence of N. Such a requirement could be thermodynamically controlled: N-H radicals may be more important in nature than Frenklaech et al.'s (1994) model considers. Alternatively, it may be that, under the conditions of São Luiz diamond growth, N-free reservoirs contain no hydrogen either. H and N are both particularly volatile species, far more so than carbon. It can be envisaged that on degassing of a potential diamond-bearing reservoir, if N was to be lost, so would H: the latter scenario as an explanation for a lack of H in Type II stones, can, therefore, be considered particularly likely. Whatever the correct explanation, however, the interplay of N and H is not restricted to deep diamond growth; Woods and Collins (1983) also found that H was never present in natural Type II stones from their suite of samples.

Section 6.2 Formation reactions of deep mantle diamonds and mantle carbon and nitrogen content: inferences from São Luiz stones and deep mantle diamonds from other localities

As section 6.1.1 has discussed, because of the extent of present knowledge of the phase relations of appropriate fluids, a framework for the formation of *lithospheric* diamonds exists. How this knowledge can be extrapolated to conditions of formation of deep mantle stones, is an important question. A question which, however, is difficult to answer.

In order to calculate fluid phase relations, values for the equilibrium constant for appropriate reactions, which are, in turn, dependent on the fugacities of reacting species, must be known. Such values are known to reasonable accuracy for conditions of pressure and temperature up to around 8 GPa and 2000 K: conditions which fall significantly short, particularly in terms of pressure, of those expected to pervade the source regions of the deep mantle diamonds considered in this current study. Since the work of Deines (1980), advances have been made in the measurement of fugacities to more extreme conditions (e.g. the work of Saxena and Fei, 1987 on CO_2 to 100 GPa). The dataset is not complete, however, so all that can be said, at present, from a theoretical point of view, involves extrapolation from low pressure data. Considering the trends, in terms of P and T, of the reaction boundaries of diamond with CO_2 and CH_4 (figure 6.1_2) it could be inferred that in the deep mantle, diamond stability would be pushed to increasingly oxidised environments, with increasing pressure, in favour of association with CH_4. CO_2 would only be present in particularly oxidised conditions. What the phase relations suggest, therefore, is that diamond may be considered more likely to form in the deep mantle by the decarboxylation of methane than the reduction of CO_2. However, prediction is subject to large uncertainty and it should also be kept in mind that the stability of the various fluid phases considered will also be highly dependent on lithology.

Rather than pursuing the line of prediction further, the São Luiz diamonds themselves can be considered to hold a key to understanding the likely precipitation mechanisms and, thus, stable fluid phases present in the deep earth. If the same trends in fractionation of isotopes of carbon by particular diamond precipitating reactions as described for lithospheric conditions (section 1.3.2.1) can be ascribed to deep mantle conditions, the carbon isotopic content of São Luiz diamonds can be used to infer reaction mechanisms. Such an assumption can be considered to be reasonable; varying conditions of temperature and pressure can be expected to alter the *magnitude* of fractionation: increase in pressure and temperature can both be expected to decrease fractionation (Deines, 1980).

However, as partitioning is dictated by features of diamond crystallography (which is not expected to alter with depth) the *sense* of fractionation can be considered to hold true, irrespective of depth.

Transition zone diamonds: It is not clear whether the TZ diamonds with $\delta^{13}C$ around -12‰ constitute a negative skew to the overall distribution of TZ diamonds (figure 5.4_5) or constitute a separate source. If the former scenario is the case, the distribution of $\delta^{13}C$ from transition zone diamonds from São Luiz would support precipitation from CO_2 (c.f. figures 1.5_4 and 5.4_5). Certainly the negatively skewed distribution centring around $\delta^{13}C$ of ~ -18 ‰ for transition zone diamonds from Jagersfontein (Deines et al., 1991 and figure 5.4_8) can also be considered indicative of precipitation from CO_2-rich fluid rather than CH_4. Both São Luiz and Jagersfontein ranges, however, are likely to be outwith fractionation from a single source for each locality, especially given the high pressures and temperatures involved. If the extrapolation from low pressure data in the C-O-H system discussed previously can be relied upon, an interpretation of precipitation from CO_2 would, therefore, support transition zone diamond formation in a particularly oxidised environment.

Furthermore the São Luiz diamonds are significantly less depleted in ^{13}C than Jagersfontein stones (figure 5.4_8). Such differences in the absolute conmpositions of $\delta^{13}C$ suggests that the transition zone contains areas of markedly differing $\delta^{13}C$ composition incorporating both the fields of typical lithospheric peridotite compositions (figure 1.5_5) and depleted eclogite (figure 1.5_8). Wilding (1990) suggested that variation in $\delta^{13}C$ compositions reflects a depth stratification in the upper mantle with decreasing $\delta^{13}C$ composition with increasing depth. Although this may be true on a large scale, there is no relationship between Si-content of majoritic garnets and $\delta^{13}C$ composition of occluding diamond from the present study. Variations in composition more likely reflect local bulk compositions and the vagaries of precipitation mechanism and physical conditions. In terms, simply, of $\delta^{13}C$ composition, variation of $\delta^{13}C$ reservoirs can be attributed to the influx of subducted material (generally depleted, figure 1.3_2). Indeed, in terms of modelling (section 6.1.1) by Zhang and Zindler (1993), it is almost a pre-requisite that subducted carbon is still a major component of the degassable mantle. They make no comment of exactly what proportion of the earth is degassable (involved in subduction-related recycling), however, even invoking two layer convection, section 4.3, transition zone material can be expected to see some subducted component.

The generally low nitrogen for transition zone diamonds could be cited as evidence for rapid growth, where there is no kinetic mechanism for favouring nitrogen capture. Certainly temperatures are high, which would favour rapid growth, however they are not significantly higher than that of the formation conditions of lithospheric diamonds. A more likely explanation would be that the nitrogen content of the transition zone is simply smaller than that of shallower regions of the earth. As Zang and Zindler (1995) point out, there is no mechanism for, or evidence of, recycling of nitrogen back into the mantle and, additionally, primordial nitrogen is believed to have been significantly degassed. As for carbon, nitrogen does show some variation in terms of its concentration, again, reflecting significant heterogeneity. With the interplay of upwelling material and subducting material, the transition zone can be expected to be particularly heterogeneous compared to higher levels of asthenospheric mantle. It would appear that transition zone diamonds support such a scenario.

Lower mantle association diamonds: The profound clustering of carbon isotopic values from lower mantle sourced São Luiz diamonds around $\delta^{13}C$ of -4.5 to -5 ‰ (figure 5.4_2) appears to be global: lower mantle association stones from Koffiefontein, Guinea and Letseng-la-Terai (figure 5.4_7) show the same distribution. Such a cluster can be considered strong evidence for a uniform carbon isotopic content in the lower mantle, (particularly as the Type III MgSi-Pvk-bearing stone ($\delta^{13}C$ = -8.31‰, BZ246) yielding $\delta^{13}C$ values most distinct from the general cluster, has a likely origin on the upper mantle / lower mantle boundary, section 4.4.2.6). As no skew in the distribution of lower mantle diamond $\delta^{13}C$ is seen, no particular reaction mechanism is implied (the Gaussian distribution is probably due to the small fractionation of carbon isotopes at high pressure and temperatures). As is commonly found for other localities (e.g. van Heerden, 1995), there is more of a variation in $\delta^{13}C$ values within individual stones than the population as a whole. Errors in the determination of $\delta^{13}C$ in diamond flats are large (section 5.5.1) however, a negative skew in the distribution of all flats analysed, centred around $\delta^{13}C$ of -3.5 ‰ (figure 5.5_2) lies outwith error. Such a distribution can be considered to support diamond precipitation by reduction of CO_2 with the greater range in $\delta^{13}C$ values than in bulk stones arising from local variations of $\delta^{13}C$ content and the unknown effects of disequilibrium and growth zone fractionation[1]. Even under lithospheric conditions, precipitation of diamond from CO_2 is indicative of at least a moderately oxidised environment (e. g. Deines, 1980). If the extrapolations to lower mantle conditions discussed above can be employed, the $\delta^{13}C$ distribution of São Luiz flats would indicate precipitation in an even more oxidised environment than CO_2-precipitated lithospheric diamonds. Such a conclusion is consistent with features of diamond *inclusions* where the presence of magnesioferrite in fPer (section 2.6.1) supports crystallisation within a relatively oxygen-rich environment. The fact that average composition of stones is so constant despite the variation *within* individual stones can be considered to be a testiment of the very localised distribution of compositional variation. Either the lower mantle is particularly well mixed or else there is no mechanism for large scale fractionation.

The nitrogen content of lower mantle stones is even smaller than that of transition zone diamonds and this lack of nitrogen is constant throughout the lower mantle suite analysed. If, as believed (section 4.5.1.2) there is a large temperature increase into the lower mantle, the argument of high temperature induced rapid growth precluding nitrogen, could be invoked to explain its absence. A preferred model, however, is that there simply is little nitrogen available within the lower mantle. Indeed the transition in nitrogen contents downward from higher values in lithospheric diamonds, to transition zone diamonds, to lower mantle diamonds, can be considered to be quite consistent with degassing of nitrogen in the earth. Furthermore, as discussed for carbon isotopic content, the general homogeneity compared to local heterogeneity (i.e. within single stones) is indicative of an interplay of fractionating growth mechanisms but within a well mixed reservoir. A well mixed lower mantle is a hot lower mantle (favouring a thermal boundary between upper and lower mantle), or at least is one which has not seen a constant large influx of external material over time. The compositional characteristics of lower mantle diamonds, therefore, would suggest that the lower mantle can be considered to be largely independent of the upper mantle. This observation supports the evidence from inclusion assemblages of a compositional difference between upper and lower mantle *rocks* (section 4.4.2.5) with the presence of a thermal boundary (sections 4.5.1.1 and 4.5.1.2), and of an appropriate density contrast to support separate convection (section 4.4.2.7).

---

[1] Given the complex growth histories of the São Luiz stones, variation of carbon isotopic content within individual diamonds cannot be considered surprising.

Section 6.3 Formation environment of São Luiz diamonds

Section 6.2 has discussed the reaction mechanisms which are believed to have given rise to São Luiz diamonds. The following sections aim to present these mechanisms in a more general framework and answer the questions; how restricted was the environment of formation and from where did the constituents of São Luiz diamonds from different regions originate?

Section 6.3.1 *Processes affecting nitrogen content and stable isotope ratios*

Section 1.3.2.1 and 6.1 have described how a number of different chemical reactions can be invoked to explain the formation of diamond. Because partitioning between reactant and product depends on the reaction involved, measurement of compositional aspects of São Luiz diamonds has led to conclusions regarding the specifics of fluid species involved in the formation of these stones (section 6.2). An additional factor, however, is important in the formation of diamond and it is this which affects the *degree* of fractionation. This additional factor is the communication environment in which the diamond forms and four régimes can be envisaged; precipitation by fractional crystallisation, equilibrium crystallisation in open and closed systems and source region mixing. In theory these environments can be distinguished by using models based on carbon and nitrogen isotopic content and nitrogen content of diamond.

Indicators of crystallisation process, as discussed in this section, are applied to compositional data from São Luiz diamonds in section 6.3.2 in a similar fashion to investigation of other diamond suites (eg. van Heerden, 1995). For diamond suites recorded in the literature, it has been found that in practice, the processes which affect the nitrogen content and stable isotope signatures of diamonds are poorly understood because although end-member processes can be clearly envisaged, it would appear from study of natural samples, that, commonly, an *interplay* of processes must be invoked to explain the carbon and nitrogen characteristics of natural diamonds.

São Luiz diamonds provide an interesting combination of both complex and simple chemistry. As discussed in chapter 5, São Luiz diamonds have undergone complex histories of growth and deformation subsequent to growth. Furthermore, both within individual diamonds and in the population as a whole, heterogeneities in terms of nitrogen concentration and carbon isotopic content have been identified. At the same time, however, São Luiz diamonds are all highly aggregated and have low nitrogen contents; these points are particularly true for lower mantle stones. Furthermore, fPer association diamonds show a remarkable clustering of carbon isotopic content around $\delta^{13}C = -5$ ‰, whereas some majoritic garnet association stones are more depleted. There would appear, therefore, to be a strong case for attempting a qualitative investigation of growth régime.

Compositional characteristics of diamonds under varying conditions of growth:

Rayleigh condensation (fractional crystallisation): Fractional crystallisation can be expressed in terms of the following identity:

$$\frac{R_v}{R_{v0}} = F(\alpha - 1)$$ Equation 6.3_1

where *Rv* and *Rvo* are the isotopic ratios in the residue and source respectively, *F* is the degree of fractionation , i.e. the fraction of carbon remaining in the residue, in the case of diamond formation, and α is a constant known as the fractionation factor.

The degree of fractionation of a fractionable component (for example, $\delta^{13}C$ in diamond), unlike for equilibrium crystallisation, is theoretically infinite and is controlled by the degree of crystallisation and the fractionation factor. As figure 6.3_1 demonstrates, crystallisation must be large, however, (small *F*) to start producing a large fractionation.

The fractionation factor, α, is related to the equilibrium constant of the reaction in progress which, in turn, is heavily temperature dependent and, in addition, is subject to a small pressure influence. Equation 6.3_2 outlines the fractionation factor / temperature relationship:

$$\ln\alpha = \frac{K}{T^2} + K$$ Equation 6.3_2

where K is the equilibrium constant, T is temperature and α is the fractionation factor

Equilibrium constants for the fractionation of nitrogen in diamond are not known. Approximations are available for the fractionation of carbon isotopes (Friedman and O'Neill, 1977); the likely limiting fractionation is of the order of a few per mille (‰). These values, however, are not considered applicable to temperatures of formation likely for São Luiz material; at higher temperatures, fractionation will be smaller. Because of the uncertainty of appropriate parameters, especially at conditions of São Luiz diamond formation, in addition to the small sample size, it is not considered appropriate to quantitatively model the growth of São Luiz diamonds. Comparison, however, with compositional trends expected from fractional crystallisation, can be attempted *qualitatively*. In order to assess whether a diamond, or population of diamonds has undergone fractional crystallisation, an indicator of the fractionation factor *F* is required. As nitrogen behaves as a compatible element in diamond, crystallisation can, therefore, be monitored by the ratio of N/N_{max}[1]. As F → 0, $N/N_{max} \rightarrow 0$. If carbon isotopic content varies with N/N_{max} in the same fashion as figure 6.3_1, the diamond(s) in question can be considered likely to have formed under conditions of fractional crystallisation. van Heerden (1993) was successful in identifying a fractional crystallisation origin for a number of Argyle diamond plates. Similar work by Boyd et al., (1987), however, showed no evidence of fractional crystallisation on coated stones, a result which is not surprising

---

[1] Note that the modelling only works if diamond crystallisation has occurred in a closed system where nitrogen genuinely does behave compatibly and nitrogen content varies linearly with crystallisation.

as there is strong evidence to suggest that the coats formed in a completely different régime from the cores (section 1.3).

Equilibrium crystallisation: Because no material is removed from the system on equilibrium crystallisation the bulk isotopic content of the system will be constant throughout crystallisation. Two particular environments can be envisaged:

- Diamond crystallising in a small reservoir will have an initial isotopic content offset from the reservoir composition by a factor appropriate to the precipitating species. For example, diamond precipitating from CH_4 will have an initial $\delta^{13}C$ value of 4‰ less than the reservoir (section 1.32.1). In order to achive equilibrium, however, the final precipitating diamond will have an isotopic content of an equal value but in opposite sense from the mean. For precipitation from CH_4, therefore, final precipitating diamond will have a $\delta^{13}C$ value of 4‰ *more* than the reservoir.
- For an infinite reservoir, precipitating diamond will adopt a composition displaced from the reservoir value by a factor appropriate to the reacting species throughout crystallisation. For example, therefore, diamond precipitating from CH_4 will have a constant $\delta^{13}C$ value throughout crystallisation, of 4‰ less than the reservoir.

Source mixing: Mixing in a two component system can be expressed by the hyperbolic equation:

$$\mathrm{A}x + \mathrm{B}xy + \mathrm{C}y + \mathrm{D} = 0 \qquad \text{Equation 6.3\_3}$$

where A, B, C and D are coefficients describing the degree of fractionation on mixing and x and y are the variables relating to to the end member states. For single variable relationship such as $\delta^{13}C$ against nitrogen content, coefficient B is equal to zero.

Two component mixing can be identified on diamond crystallisation by a linear trend of isotopic composition against reciprocal nitrogen content. In terms of carbon and nitrogen isotopic ratios, van Heerden (1993) suggests a three component model to explain variability in compositions of Argyle and Ellendale diamonds.

Kinetic fractionation: The mathematics of kinetic fractionation are exceedingly complex. Preliminary results, however, suggest that isotopic fractionation induced kinetically is small; Boyd and Pillinger (1994) observe small but significant fractionation in nitrogen isotopes between octahedral and cubic growth zones in synthetic diamonds; this is unlikely to be significant at high temperature.

Section 6.3.2 Formation environment of São Luiz diamonds

Diamond plates: Nitrogen ion microprobe analyses were chosen to correspond to carbon isotopic points (section 5.5.2.2). Prior to nitrogen analysis, the diamond flats were observed under cathodoluminescence and it was verified that nitrogen points adjacent to carbon points were, as intended, within the same cathodoluminescence zone. According to the methods outlined in section 6.3.1, data obtained from analysis of polished diamond plates have been investigated for evidence of growth under conditions of fractional crystallisation and source mixing. $\delta^{13}C$ values for each of the four plates were plotted against 1/N and N/N_{max} and are presented in figures 6.3_2 - 6.3_9. Errors are large (1σ standard deviation is plotted on graphs presented) which makes interpretation of the data difficult, indeed arguably, if 2σ standard deviation is considered, many plates show total variations within this error (~ 95% confidence).

BZ251: $\delta^{13}C$ does not show a smooth fractionation trend using nitrogen as an indicator of crystallisation: any correlation can be considered to be crude (figure 6.3_2). Indeed, it would appear the trend in nitrogen concentration against $\delta^{13}C$ changes sense at mid-nitrogen concentrations, a feature which is perhaps indicative of two stages of growth (N concentration does correlate well with CL). The most depleted carbon does correlate with the lowest nitrogen contents which is in line with the diamond precipitating from a CO_2-rich fluid, section 6.2. In terms of $\delta^{13}C$ against 1/N, an indicator of two component mixing, no linear trend can be identified, figure 6.3_3. This is true even on omission of the particularly low nitrogen concentration data. As BZ251 contains the greatest amount of nitrogen of the four plates analysed, the poor fits for either a mixing or fractional cryatalisation model provoke little hope for a clear answer for the other plates:

BZ252: Even on omission of the nitrogen in fractures for BZ252 no reasonable correlation for $\delta^{13}C$ against N/N_{max} (figure 6.3_4) or for $\delta^{13}C$ against 1/N (figure 6.3_5). The most depleted carbon does, however, correlate with the lowest nitrogen contents.

BZ254: Observations of BZ254 are not as negative as those of BZ252: on omission of the nitrogen in fractures there is perhaps a correlation for $\delta^{13}C$ against N/N_{max} (figure 6.3_6). The most depleted carbon does correlate with the lowest nitrogen contents and a smooth curve of the form of figure 6.3_1 can be considered to be crudely present. No linear trend for $\delta^{13}C$ against 1/N is observed (figure 6.3_7).

BZ255: BZ255 shows no correlation of $\delta^{13}C$ against N/N_{max} (figure 6.3_8) or 1/N (figure 6.3_9). Like the other plates, however, the more depleted carbon isotopic compositions correspond to low nitrogen contents.

Equilibrium crystallisation: As seen in chapter 5, the $\delta^{13}C$ composition of all diamond flats cluster around a value of $\delta^{13}C$ = -5 ‰ with tails towards more depleted values. If the reservoir value can be considered to be -5 ‰, closed system equilibrium crystallisation can be discounted. Furthermore, although the cluster around $\delta^{13}C$ = -5 ‰ is tight for individual diamonds, it is not tight enough to support open system equilibrium crystallisation. As discussed above, none of the four plates show any evidence for simple two component mixing. Fractional crystallisation is considered a possible explanation for growth of the São Luiz plates studied, at least so far as more depleted carbon isotopic content corresponds to low nitrogen contents. As seen, in particular for BZ251, there is evidence to suggest at least two stages of growth. Given the multiple growth events indicated by the complex cathodoluminescence characteristics of all diamond plates (section 5.6.2) it can be reasonably concluded that São Luiz diamonds, at least those of a lower mantle source, have experienced multiple growth histories possibly within a régime of fractionational crystallisation.

The bulk sample: Figures 6.3_10 - 13 present $\delta^{13}C$ and $\delta^{15}N$ against 1/N and N/N_{max} respectively where N_{max} is taken as the São Luiz population maximum (721ppm from BZ226, used as the $\delta^{13}C$ N_{max} and 338.1 from BZ116 as the $\delta^{15}N$ N_{max}); fPer bearing diamonds are shown by a separate symbol. Neither for fPer bearing diamonds nor for the population as a whole is there a strong indication of a linear trend for isotopic values against 1/N. Additionally, no fractionation curve for isotopic values against N/Nmax is in evidence. Both simple fractional crystallisation and source mixing can be discounted as an explanation for both the diamond population as a whole, in addition to diamonds of a lower mantle origin. Given the multi-stage growth histories, this can perhaps, be considered unsurprising. It would seem to be the case that São Luiz diamonds have grown in a number of régimes of fractional crystallisation involving complex fractionation processes; processes for which little is presently known.

The interrelationship of $\delta^{15}N$ and $\delta^{13}C$ composition: Section 1.3.2.2.2 discussed theories on the $\delta^{13}C$ and $\delta^{15}N$ bearing reservoirs in the earth in terms of the isotopic compositions of diamond; in particular Javoy et al.'s (1986) proposal that the negative $\delta^{15}N$ contents of some diamonds suggest that a $\delta^{15}N$ depleted reservoir must exist in the deep earth. Although, due to the rarity of N-bearing stones, the number of $\delta^{15}N$ analyses for São Luiz diamonds is small, some comment can be made in relation to Javoy et al's (1986) theories. Firstly, the transition zone association diamonds yield positive values for $\delta^{15}N$ and lie within the bounds of C1 chondrite composition. Transition zone diamonds, therefore, suggest that there is no need to invoke an enstatite chondrite model for the source of transition zone material. As discussed above, the possibility of a subduction zone origin for transition zone material cannot be discounted and so it can be considered that the results of transition zone diamond analysis are not inconsistent with Javoy et al's (1986) model where a veneer of C1 chondrite material is invoked. The single definite lower mantle stone (BZ116, whose origin is questionable, aside), BZ237, yielded two analyses showing depleted δ^{15}N values. Such values lie outwith the C1 chondrite compositional field but within the enstatite chondrite field (figure 6.3_14) and could be thus considered to support Javoy's (1986) enstatite chondrite model. It should be noted, however, that BZ237 is not as highly depleted in δ^{15}N values as Javoy et al. (1986) favour. This, indiscrepency can be tackled in one of two ways. BZ237, being of LM III association, is likely to have an origin on the lower mantle / upper mantle boundary, section 4.4.2.6; true lower mantle material may be more depleted. Alternatively, if the composition of BZ237 is representative of the lower mantle as a whole, a model of bulk earth composition involving a more significant C1 component than Javoy et al. (1986) would favour, would be preferred.

➠

Section 6.3.3 *Interpretation of additional features of São Luiz diamonds*

The relationship of platelets to plastic deformation: There has been discussion in the literature of the interrelationship of plastic deformation and platelet formation (e. g. Chinn et al., 1995). In particular, samples from the literature support the view that the presence of platelets inhibits plastic deformation. A study of the interrelationship in São Luiz diamonds is merited.

Transition zone sourced diamonds BZ215 and BZ217 show strong platelet absorption; both stones are colourless, however BZ215 exhibits visual evidence of plastic deformation. Two unbroken, possible TZ association diamonds (BZ262 and BZ272) both showed significant platelet absorption and, in addition, were observed to be plastically deformed. BZ262 is colourless and BZ272 is brown. Furthermore, BZ269 and BZ272 (of unknown association) both showed platelet absorption with BZ272 being brown and plastically deformed and BZ269 being colourless and showing extensive trigon presence.

Although there are some exceptions, it is notable that a large number of platelet containing diamonds are also plastically deformed. Such a relationship contrasts with the observations of shallower sourced diamonds by Chinn et al. (1995, section 5.3), the implication being that some deformed stones from São Luiz have undergone unusually extreme degrees of deformation. Indeed, following the work of Evans and Wild (1965), it would appear that some São Luiz diamonds have undergone shear stresses of greater than 0.5 - 0.6 GPa (1200 K). Such shear stresses may be related to mechanical stress due to the interplay of convective régimes on the upper mantle / lower mantle boundary. Such an interpretation is compounded by the observation that the association of platelets and plastic deformation is particularly strong for lower mantle-related material. It should also be noted, however, that the instance of plastically deformed stones with platelets from transition zone stones suggests that large shear stresses may also be present in shallower mantle regions.

Relationship of cathodoluminescence intensity to nitrogen concentration: As has been discussed in section 5.5.2.2, there exists a *qualitative* relationship between strong cathodoluminescence intensity and high levels of nitrogen. This intensity has been measured *quantitatively* for areas centred on ion microprobe nitrogen analysis points using the spot metering of a Nikon Optiphot attached to the cathodoluminescence instrument of the Department of Geology and Geophysics, University of Edinburgh. Intensity measurements were collected from areas approximating 50 µm in diameter ensuring that chamber pressure, and electron beam conditions remained constant throughout the analysis of each stone. Intensity data were collected as exposure in seconds recommended for each spot which is inversely proportional to light intensity. For each flat, exposure data were converted to cathodoluminescence intensity by taking reciprocals. Reciprocal exposure was plotted against nitrogen content for each flat: the results confirm the visual observations and are presented in figures 6.3_15 - 6.3_19.

The correlation between cathodoluminescence intensity and nitrogen concentration was found to be steep and linear at low concentrations falling off such that at higher values, nitrogen was found to be almost independent of cathodoluminescence. The same correlation was found for each individual flat, although less so for BZ254. For example, for BZ252, following a rise in cathodoluminescence intensity of a factor of 5 over the first 25 ppm N concentration, the rise in luminosity falls to only a further 50% increase over the next 175 ppm. Anomalously high cathodoluminesce was observed for four points on BZ252 (figure 6.3_17) all of which correspond to what has been interpreted (section 5.6.3) as internal reflection from the main fracture across this stone.

Cathodoluminescence in diamond is dependent not only on aggregated nitrogen, but also can be due to hydrogen species and donor-acceptor pairs along dislocations (Yamamoto et al., 1984). The São Luiz diamonds are both deformed and, on occasion indicate the presence of hydrogen, so it is expected that dislocations and impurities contribute to the cathodoluminescence intensity. Variations in these additional factors will be far more influencial at lower concentrations of nitrogen, thus producing the observed greater CL intensity dependence on nitrogen at low concentrations.

The question of Nitrogen in voidites: As discussed in section 5.4.2.2, attention was paid to whether the absence of nitrogen absorption in FTIR spectra which is commonly observed in São Luiz diamonds is due to very small nitrogen content or else nitrogen existing in a non-I.R. active state (such as in voidites). Comparison was made of the total nitrogen content by combustion with nitrogen as determined by FTIR. It can be concluded that no significant nitrogen is present in non IR-active states in the São Luiz diamonds analysed. Stones revealing Type II spectra, may show some variation in nitrogen content on a local scale (cf. section 5.5.2.2), but certainly, as a whole can be considered to contain less than 10 - 20 ppm N (the detection limit of the FTIR apparatus employed).

Chapter 7 Exhumation

Having been formed at depths spanning the transition zone and into the lower mantle, in order to have reached the surface of the earth, the diamonds involved in this study have clearly travelled a great distance. They have, therefore, been exposed to a wide range of pressures and temperatures; conditions likely to be significantly more extreme than those inflicted upon the majority of known diamonds. It is the purpose of this chapter to attempt to infer some of the history of exhumation of the São Luiz and Guinean stones. Previous chapters have presented and discussed characteristics of the diamonds and their relationship to their inclusions and the inclusions themselves in terms of cathodoluminescence (section 5.6) deformation (section 5.3) inclusion equilibration (section 4.5) and diamond compositional characteristics (sections 5.4, 5.5 and 6.6). Chapter 7 attempts to consolidate these separate observations into a coherent framework combined with detailed thermoelastic explanation of the internal pressures observed for a number of inclusions, section 3.3.3. Particular attention is paid to preferred mantle convection models and current models of mechanisms for the exhumation of deep earth material; superkimberlites, plumes and entrainment into convective systems.

Section 7.1 Internal pressure

Two of the striking characteristics of diamond are its highly incompressible nature (McSkimin and Bond, 1972) and its small thermal expansion (Skinner, 1956) compared to other minerals. During the syngenetic encapsulation of an inclusion by diamond, the volume of the included material and the volume of the space it occupies in diamond can be regarded as being the same. Given the physical properties of diamond just mentioned and taking the diamond / inclusion partnership from its conditions of formation at high pressure and temperature to the earth's surface, the inclusion will attempt to expand at a greater rate than its diamond host. Assuming that this excess expansion is at least partially resisted by the diamond, one would expect the inclusion to be subject to a restricted volume, alleviated on, or soon after, breaking of the stone. Indeed, internal pressure has previously been recorded for diamond inclusions by a variety of techniques (Harris et al., 1970 and Schrauder and Navon, 1993), section 7.1.4. If the physical properties of diamond and the included material are sufficiently known, a depth (assuming a particular geotherm) can be assigned to the inclusion / diamond system, simply by measuring the change in cell parameters on release of an inclusion. If the diamond was to have suffered *no* non-elastic deformation subsequent to inclusion encapsulation[1], then this depth would be a measure of the depth of formation of the diamond / inclusion system. Otherwise, the calculated depth represents the minimum, depth of formation which can be converted to a true depth of formation if the degree of deformation accommodating expansion can be determined. Such a technique has potentially great importance for this current work given the inferred lower mantle origin of some of the stones (section 4.4.2), and is herein applied to two fPer inclusions (GU4 and BZ257) for which cell parameter change on release from diamond has been measured (section 3.3.3).

Firstly, an appropriate physical framework must be constructed in order to assess the meaning of any observation. This framework is presented in sections 7.1.1 and 7.1.2. The models constructed, with appropriate corrections, are applied to structural observations of the São Luiz and Guinean stones in section 7.1.4.

---

[1] As has been discussed, section 5.3, and has been observed, sections 5.3.1, 5.3.2 and 5.6, an assumption that the diamond host has not undergone some form of deformation is not reasonable. Even so, however, some indication of the extent of deformation can be estimated and appropiate corrections applied, section 7.3.

Section 7.1.1 Thermoelastic poperties of minerals

Introduction: In order to assess the significance of internal pressures of included material in diamond, the relative volumes of mantle phases, including diamond, must first be calculated along reasonable mantle geotherms. Such a calculation depends, essentially, on two quantities; thermal expansivity (dealt with later, equation 7.1_27)[1] and compressibility (or bulk modulus, equation 7.1_1)[2].

$$K = -V\frac{dP}{dV} \qquad \text{Equation 7.1\_1}$$

where K is the bulk modulus, V is volume and P is pressure, where units of volume are unimportant and the units of K and P are the same.

These parameters vary significantly by both first and second order[3] with both temperature and pressure (see Duffy and Anderson, 1989). So for each phase, values of α (where α is the volume thermal expansivity (K^{-1})), $d\alpha/dP$, $d\alpha/dT$, $d^2\alpha/dP^2$, $d^2\alpha/dT^2$, $d^2\alpha/(dPdT)$, K_0, dK_0/dP, dK_0/dT, d^2K_0/dP^2, d^2K_0/dT^2 and $d^2K_0/(dPdT)$, (where T is temperature (K), P is pressure (GPa) and K_0 is the isothermal bulk modulus [GPa^{-1}]) should, ideally, be known. Many of these parameters, even for upper mantle phases are poorly constrained, reference to appendix 13 will show that even for the basic values of α and K_0 there exist a range of values; suitable values for derivatives are often unknown. In practice, therefore, some estimation and assumption must be invoked.

It is not considered the purpose of this discussion to dwell particularly on the methods employed in the determination of elastic properties of mineral phases, Price et al. (1989) provide a useful discussion of first principles approaches. Additionally, the interested reader may find appendix 12 and references in appendix 13 useful as a database. It is considered instructive, however, in order to assess the reliability of data employed, to consider a few broad points.

Methodology for determination of thermoelastic constants: The elastic properties of relevent phases have been determined by two general approaches:

- **Experimental determination:** Techniques employed are discussed in the context of determination of phase relations in section 4.4.

---

[1] Thermal expansivity (K^{-1}) relates relative volume (or cell parameter) change to temperature change and bulk modulus (in, e.g. GPa) relates relative volume change to pressure decrease.

[2] Bulk modulus is the most commonly used parameter being, simply, the inverse of compressibility.

[3] Further derivatives apply insignificant variations to practical applications.

- **First principles physical approaches:** Theoretically, the physical properties of any crystalline material can be determined by the solution of the Shrödinger equation. For silicates, however, because of their complexity, such calculation lies outwith the reach of modern computational techniques. A way round this problem is to envisage only molecular fragments of silicates and *ab-initio* solutions to the equation; the so called Hartree-Fock method. Recent calculations on mantle minerals have been conducted by Bouaziz and D'Arco (1993), Sherman (1993a,b) and D'Arco et al. (1991, 1993 and 1994).

  An alternative to quantum methods is an atomistic approach using methods such as linear augmented plane wave analysis (LAPW) to describe the charge density and potential surface within a unit cell (eg. Cohen, 1991). More simple, yet more approximate than quantum approaches, atomistic approaches represent the way forward at present; the huge computational burden they still involve, aside.

  Despite the successes, however, first principles approaches have the significant drawback that modelling is carried out at 0K and any extrapolation to atmospheric, let alone mantle, temperatures is rather speculative. For example, D'Arco et al. (1993) estimate the relative stability of phases at mantle pressures whilst keeping temperature at 0K: application to geological questions must be considered with extreme caution.

  In order to address this problem, some workers have adopted an empirical approach; empirical in that they utilise potential models constucted on the basis of experimental results and, therefore, can accommodate temperature dependent information. This method has proven its worth as a predictive tool of ambient condition bulk properties of minerals (eg Cohen, 1987 cf. Yeganeh-Haeri, 1989) but, in that it ignores anharmonic vibrational effects important at high temperature, still has drawbacks as a predictive tool for mantle conditions.

Adoption of thermoelastic constants: Extensive review of the literature has revealed approximately 150 separate works on determination of elastic properties of mantle phases. Values are presented in appendix 13, according to general compositional type, eg. (Mg,Fe)SiO_3 and subdivided according to structure eg. (Mg,Fe)SiPvk, (Mg,Fe)Si-Ilm, (Mg,Fe)Si-Grt etc. and then particular composition eg. MgSiPvk, FeSiPvk etc. Values to be used in calculation were chosen according to the following criteria and are presented in table 7.1_1:

- Where only one value for a particular parameter and particular composition of a phase was available, this was chosen directly.
- Where a number of values for a particular parameter were available, the spread of data was scrutinised thoroughly.

- ◊ Where outliers existed, they were removed from the dataset if they were the result of outdated methods (eg. shock-studies for determination of bulk modulii) or a particular problem could be identified with the determination.

- ♦ Parameters for intermediate compositions were obtained, where necessary, by extrapolation between end members or adoption of the values appropriate to the nearest end-member available; ideal solid solution being assumed.

Such a database provides the values required for modelling the behaviour of included material. In order to apply these correctly to a determination of the behaviour of volume with pressure and temperature, however, a consideration of the physics behind the elastic properties of crystalline solids must be pursued:

Thermodynamic framework: The physical properties of minerals are described by what are termed equations of state (EOS); commonly presented in both integral and differential form to varying orders, in addition to series expansions to suit particular applications. Discussion of the thermodynamic basis for theories governing thermal and elastic variables and, in particular, their higher order derivatives is presented in Stacey (1995).

Approximation factors: Often EOS involve parameters which aim to approximate the behaviour of more than one parameter into a single variable. Examples are:

- ♦ The Grüneisen parameter γ[4] defined in terms of lattice dynamics as:

$$\gamma = \left(\frac{-\partial \bar{\Omega}}{\partial \ln V} \right)_T$$ Equation 7.1_2

where $\bar{\Omega}$ is the average lattice vibrational frequency, T is temperature in K and V is volume

or in terms of bulk physical properties:

$$\gamma = \left(\frac{\alpha_v K_s}{\rho C_v^2} \right)$$ Equation 7.1_3

where ρ is density, C_v is the volume heat capacity, α_v is the volume thermal expansivity and K_s the adiabatic bulk modulus

---

[4] The Grüneisen parameter is found to be particularly useful for two reasons. It is a dimensionless quantity of order unity which acts to simplify many EOS expressions. More importantly, it relates thermal expansion to the elastic constants of a phase and so acts as a most useful predictive tool in modelling temperature sensitive settings such as the earth's mantle. Additionally the temperature dependence of γ is small, typically $d\ln\gamma/dT \approx 2.5 \times 10^{-5}K^{-1}$ which means the Grüneisen parameter is a good approximating tool (Stacey, 1995): consideration of temperature derivatives of γ being unnecessary.

Table 7.1_1 Values for physical constants adopted for calculation in the present study

	Struct.	**Opx***		**Ilmenite**		**Pvk ¥**		**Pvk**	
	Units	$MgSiO_3$	***Ref.***	$MgSiO_3$	***Ref.***	$MgSiO_3$	***Ref.***	$FeSiO_3$	***Ref.***
K_{0T}	GPa	122.8	*>4GPa*	190.9	*Av Pvk + Opx*	259	*2,8-10,13,15,16,20-22,26-29*	258.6	*33,34*
K_0'		5.6	*>4GPa*	4	*Ass MgAlSi-Pvk*	4.02	*2,8-10,16,17,20-22,24-29*	3.9	*19,33,34*
K_0''	GPa^{-1}	-1.6	*52*	-0.077	*Ass CaSi-Pvk*	-0.077	*Ass CaSi-Pvk*	-0.077	*Ass CaSi-Pvk*
δ		6	*1 & 5*	5.7	*Inter Opx + MgSi-Pvk*	5.4	*26-28*	5.4	*Ass MgSi-Pvk*
A_1	K^{-1}x10^{-4}	0.2722	*1,2,4*	0.244	*50*	0.2627	*2,18,23,28*	0.2627	*2*
A_2	K^{-2}x10^{-8}	0.2694	*2*	0	*50*	1.5198	*2*	1.5198	*2*
A_3	K	-0.5588	*2*	0	*50*	-0.0429	*2*	-0.0429	*2*
V_0	A^3	832.49	*53*	262.54	*54*	162.56	*8,9,13-16,22*	167	*Extrap 8*
ρ	Kgm^{-3}	3.2	*3*	3.795	*7*	4.11	*12*	5.164	*Calc 5,19,34*
MV	cm^3/mol	31.32+ 1.63xFe	*1,2,5*	26.35+ 0.5xFe	*5*	24.5	*2,19,26-28*	25.55	*5,19,34*

	Struct.	**Garnet**		**Pvk**		**Olivine**		**Olivine**	
	Units	$MgSiO_3$	***Ref.***	$CaSiO_3$	***Ref.***	Mg_2SiO_4	***Ref.***	Fe_2SiO_4	***Ref.***
K_{0T}	GPa	163	*1,39*	275	*1-4,6,7,9-12*	128.5	*2,3*	137.9	*11*
K_0'		4.25	*1,39*	4.25	*1-4,6-12*	5.28	*2,3*	4	*11*
K_0''	GPa^{-1}			-0.077	*6*	-0.05	*7*	-0.05	*Ass forsterite*
δ		4.75	*1,40*	5.4	*Ass MgSi-Pvk*	4	*1,2*	5.5	*1*
A_1	K^{-1}x10^{-4}	0.249	*1,40*	0.14	*7*	0.3091	*2,3,6*	0.266	*3*
A_2	K^{-2}x10^{-8}	0.39	*40*	0.119	*Calc 7*	0.8504	*3*	0.8736	*3*
A_3	K	-0.5521		0	*Assumed*	-0.5824	*3*	-0.2487	*3*
V_0	A^3	1515	*39,41*	45.27	*4,6,8,11*	289.56	*39*	307.42	*39*
ρ	Kgm^{-3}	3.543	*Extrap 2-5,8,9 in Grt & 40*	4.15	*4,5*	3.21	*Extrap 4,7,13*	4.38	*Extrap 4,7,13*
MV	cm^3/mol	28.5	*Calc 1*	27.5	*Calc V0*	43.73	*2,3*	46.28	*16*

	Struct.	**W'ite**		**W'ite**		**R'ite**		**R'ite**	
	Units	Mg_2SiO_4	***Ref.***	Fe_2SiO_4	***Ref.***	Mg_2SiO_4	***Ref.***	Fe_2SiO_4	***Ref.***
K_{0T}	GPa	173	*2,3*	173	*Ass Mg-w'ite*	215	*2,3,22,23.25*	197	*26*
K_0'		4.15	*2,3*	4	*21*	4.15	*2,3,22-24*	4	*26*
K_0''	GPa^{-1}	-0.05	*Ass Fo*	-0.05	*Ass Fo*	-0.05	*Ass Fo*	-0.05	*Ass Fo*
δ		3	*2*	3	*Ass 2*	3	*2*	3	*Assumed*
A_1	K^{-1}x10^{-4}	0.2891	*2,3*	0.2319	*21*	0.2458	*2,3*	0.2455	*29*
A_2	K^{-2}x10^{-8}	0.6885	*3*	0.7117	*21*	0.5298	*3*	0.3591	*29*
A_3	K	-0.5767	*3*	-0.243	*21*	-0.5702	*3*	-0.3703	*29*
V_0	A^3	538.14	*40*	573.6	*Calc 1,21*	524.56	*41*	558.26	*42*
ρ	Kgm^{-3}	3.473	*18,19*	4.855	*Extrap 18,19*	3.559	*25*	4.848	*42*
MV	cm^3/mol	40.52	*1,2,3*	43.19	*1,21*	39.6	*1,2,3*	42.02	*1 & 28*

	Struct.	**fPer**		**fPer**		**Diamond**		**Cor.**	
	Units	MgO	***Ref.***	FeO	***Ref.***	C	***Ref.***	Al_2O_3	***Ref.***
K_{0T}	GPa	161.7	*2.3.4.23.24.29*	168	*3,11,14,19, 22,25-28*	513.9	*Ass 2,3*	258.4	*1,6*
K_0'		4.09	*3,4,23,24*	3.687	*3,26-28*	4	*Ass 2*	4.08	*1,6,7*
K_0''	GPa^{-1}	-0.03	*4*	-0.03	*Ass 4*	0	*Assumed*	-0.023	*1*
δ		3.03	*1*	3.03	*Ass 1*	3.9	*Assumed*	5	*12*
A_1	$K^{-1}x10^{-4}$	0.3671	*2,8,9*	0.1688	*14*	0.02884	*4*	0.2276	*13*
A_2	$K^{-2}x10^{-8}$	0.9283	*2*	0.204	*14*	1.057	*4*	0.4198	*13*
A_3	K	-0.7445	*2*	0.019	*14*	-0.002665	*4*	-0.0897	*13*
V_0	A^3	74.71	*Calc 8*	81.35	*Calc 30*	45.38	*5*	251.34	*Calc 1,6,7*
ρ	Kgm^{-3}	3.583	*4-6,10*	5.85	*Extrap 4-7,10,12,13*	3.511	*2,3*	3.99	*3,5*
MV	cm^3/mol	11.25	*1 & 2 & 3 & 8*	12.25	*1 & 3 & 14*	3.4168	*4*	25.58	*Calc 8*

	Struct.	**St'ite**		**Garnet**	
	Units	SiO_2	***Ref.***	$Mg_3Al_2Si_4O_{12}$	***Ref.***
K_{0T}	GPa	313	*2-6,8-16*	166	*1*
K_0'		4.26	*2-6,9-11,13,14,16*	4.5	*1*
K_0''	GPa^{-1}	0	*Assumed*	-0.28	*21*
δ		3	*5*	6.15	*1,7*
A_1	$K^{-1}x10^{-4}$	0.151	*2,5*	0.288	*15*
A_2	$K^{-2}x10^{-8}$	1.35	*2*	0.2787	*15*
A_3	K	0	*2*	-0.5221	*15*
V_0	A^3	46.43	*3,4,9-11,14*	1501.9	*18*
ρ	Kgm^{-3}	4.29	*7 & 8*	3.568	*Ex 2-5,8,9 & 40 in $MgSiO_3$*
MV	cm^3/mol	14.01	*1*	113.21	*1*

Data are obtained following the methodology outlined in the text based on values from the literature summarised in appendix 13. All references refer to appendix 13 and are subdivided according to chemistry, for example, reference 5 for $MgSiO_3$-Pvk can be found under the Pyroxene composition heading in appendix 13. Where models involve an intermediary composition, for example $Mg_{0.9}Fe_{0.1}SiO_3$, thermoelastic constants are obtained by linear interpolation.
K_{0T}- Bulk modulus at atmospheric pressure and 298K: K_0'- Pressure derivative of K_{0T}: K_0''- Second pressure derivative of K_{0T}: δ- Anderson-Grüneisen parameter, equation 7.1_5: a_{1-3}- components in the temperature expansivity equation 7.1_15: mV- molar volume: ρ- density: V_0- cell volume. Ass- Assumed from: Inter- Interpolated from: Ex- Extrapolated from: Calc- calculated from: Phase name abbreviations follow those in the glossary: * Clinopyroxene structured $MgSiO_3$ values are similar (see Jeanloz and Thompson, 1983): ¥ Perovskite structured Al-MgSi-Pvk yields very similar values (see Kesson et al., 1994)

furthermore, the thermodynamic Grüneisen parameter can be defined in terms of an adiabatic temperature profile:

$$\gamma = \left(\frac{\alpha K_s}{\rho C_p} \right)$$ Equation 7.1_4

where C_p is the heat capacity per unit mass.

- Debye temperature (θ_D) is related to the Einstein temperature θ_E and relates lattice vibrational energy to temperature on the basis of atomic constraints.

- Anderson-Grüneisen parameter:

This, again, is a useful parameter for expressing the interrelationship of expanisivity with bulk modulus. It is considered independent of temperature for materials at temperatures above their Debye temperature and is defined according to the following identity (Anderson, 1967):

$$\delta_T = -\frac{1}{\alpha K_T} \left(\frac{\partial K_T}{\partial T} \right)_P$$ Equation 7.1_5

where δ_T is the Anderson-Grüneisen parameter

EOS types: Different types of equations of state exist incorporating variables depending on what parameters are available and what is to be studied; all involve approximations in order to be useable as reasonable predictive tools. They tend to be of two types; those incorporating easily measurable parameters such as cell volume and its response to pressure and temperature; and those delving into a more first principles approach involving lattice vibration frequencies.

The simplest relevent EOS is the 'universal' EOS (as discussed in Jeanloz, 1988). Here P and V are related through K_0 and dK_0/dP in the equation:

$$P_{(V/V_o)} = 3K_{0T} \left(1 - \left(\frac{V}{V_o} \right)^{1/3} \right) \left(\frac{V}{V_o} \right)^{-2/3} e^{\left[\frac{3}{2} \left(\left(\frac{dK}{dP} \right)_{0T} - 1 \right) \left(1 - \left(\frac{V}{V_0} \right)^{1/3} \right) \right]}$$ Equation 7.1_6

based on the cohesive energy of a condensed system varying only as a function of particle spacing. It has many applications in materials science but is not reasonably applicable to phases with significant internal degrees of freedom (materials which respond to strain by bond distortion etc.) such as are common in geology.

Finite strain theories, on the other hand adopt the approach that strain is defined such that it is invariant with respect to rotation of crystal axes. Earlier finite strain theories were Lagrangian, ie. they predicted deformation relative to an un-deformed state, later, theories such as Birch-Murnaghan adopted a Eulerian approach, ie. deformation is predicted relative to the deformed state; this latter approach is considered more valid for prediction of phases under significant strain as found in geological settings. Birch-Murnaghan expressions involve combinations of pressure, bulk modulus, expansivity, temperature and density or volume such as the 3rd order Birch Murnaghan expression[5]:

$$P = 3K_0 \left\{ \left(\frac{3K'_0 - 16}{8} \right) \left(\frac{\rho}{\rho_0} \right)^{5/3} - \left(\frac{3K'_0 - 14}{4} \right) \left(\frac{\rho}{\rho_0} \right)^{7/3} + \left(\frac{3K'_0 - 12}{8} \right) \left(\frac{\rho}{\rho_0} \right)^{3} \right\} \qquad \text{Equation 7.1\_7}$$

Other common EOS involve γ for example the Mie-Grüneisen EOS. In fact some EOS are derived from purely empirical observations such as the Grover-Getting-Kennedy formulation (GGK) (Grover et al., 1973).

All these above EOS have been applied to geological problems in the past but are rather simplistic as they either ignore temperature dependence altogether or else assume linear dependence of key variables when they patently do not exist (eg. assumption of $dK_0/dT = 0$ for garnet; Liu et al., 1990).

Geologically relevent EOS: Various hybrids have been formulated specifically for the purposes of geophysical calculations. An early approach (e.g. as employed by Harris et al., 1970) combined isothermal and isobaric EOS of a similar form to:

$$K_T \approx K_{0T} + \left(\frac{\partial K}{\partial T} \right)_P \left(T - T_0 \right) + \frac{1}{2} \left(\frac{\partial^2 K}{\partial T^2} \right)_P \left(T - T_0 \right)^2 + \ldots.. \qquad \text{Equation 7.1\_8}$$

In order to provide a framework for utilising the commonly adopted schemes of determining pressure dependence of cell parameters at room temperature and temperature dependence of cell parameters at 0 GPa, Jeanloz and Knittle (1989) developed an EOS of their own. They combine an Eulerian finite strain EOS (of the type highlighted above) with an anharmonic description of the thermal properties of the phase concerned. Such a method avoids the restrictions imposed by EOS relying on 0K physical

---

[5] A problem still remains in that finite strain theories consider isothermal bulk modulus (K_T), appropriate to low T whereas it has been argued that a more appropriate model for the earth could be considered to involve the adiabatic bulk modulus (K_s). Differences in the two parameters can, to some extent be avoided in earth systems by simply substituting K_s at the boundary condition for K_0; in such a case $K_0 \neq K_T$ (T=0, P=0). Jeanloz (1988) reviews the working differences between Lagrangian and Eulerian strain EOS and finds that, generally, for materials whose dK/dP range from 4 to 6; as do all mantle materials considered here; there is little difference in prediction for small compressibilities. As discussed in section 4.2, adiabatic temperature variation cannot be assumed, particularly around the upper mantle / lower mante boundary, furthermore, use of isothermal bulk modulus can only be considered a problem if temperature dependence is not considered, in the present study, such corrections are made as discussed as follows.

properties. Their EOS involves only isothermal bulk modulus, its pressure derivative, ATP molar volume and the Debye temperature and Grüneisen parameter γ.

Involving, as they do, different approximations, the various high-temperature EOS available do not necessarily give the same results for, for example, volume along a geotherm. A good example of this, as alluded to before, can be seen in the work of Jeanloz (1988) where 3rd order Birch-Murnaghan, Universal and GGK EOS are compared and Fei et al. (1992) where high temperature Birch-Murnaghan, Mie-Grüneisen and Anderson EOS are compared. Indeed it would appear that different EOS tend to fit different types of material, depending on the degree of covalent bonding etc. Theoretically, therefore, an EOS should be chosen to fit the particular phase in question. In practice, however, the mantle phases considered here have similar bonding characteristics, being essentially ionic with some covalent influence between O and nearest neighbour atoms; it would be safe to assume that one single EOS would be relevent for all calculations[6]. Of the models invoking both high pressure and high temperature predictions, expressions have been chosen which involve variables constrained for all the phases of interest. It has been concluded that a temperature dependent variation on the 3rd Order Birch-Murnaghan EOS of the form employed by Fei et al. (1992) is most suitable:

$$P_{(V,T)} = P_{(V,300K)} + P_{Th} \qquad \text{Equation 7.1\_9}$$

where symbols adopt their usual meanings and:

$$P_{(V,300K)} = 3f(1+2f)^{5/2} K_{T0}(1-\zeta_1 f) \qquad \text{Equation 7.1\_10}$$

Where

$$f = \frac{1}{2}\left[\left(\frac{V_0}{V}\right)^{2/3} - 1\right] \qquad \text{Equation 7.1\_11}$$

And

$$\zeta_1 = \frac{3}{2}\left(4 - \left(\frac{\partial K}{\partial P}\right)_{0T}\right) \qquad \text{Equation 7.1\_12}$$

P_{Th}, the thermal pressure, can be defined in terms of a variety of functions, for example:

The Anderson Thermal Pressure Model:

$$P_{Th} = \int_{300}^{T} \alpha K_{T(V_0,T)} dT + \left(\frac{\partial K_T}{\partial T}\right)_v \ln\left(\frac{V_0}{V}\right)(T-300) \qquad \text{Equation 7.1\_13}$$

---

[6] Additionally, given the uncertainties of the parameters employed, most suitable EOS are likely to lie within error of each other.

Where

$$K_T = K_{0T} + \left(\frac{\partial K_T}{\partial T}\right)_P (T - 300)$$

Equation 7.1_14

α, of course, is not constant; varying with temperature; and is commonly expressed:

$$\alpha = \alpha_1 + \alpha_2 T + \alpha_3 T^{-2}$$

Equation 7.1_15

A more classical approach to P_{Th}, appropriate to shock wave studies is the Mie-Grüneisen relation:

$$P_{Th} = \frac{\gamma}{V}\left[E_{(T,\theta_D)} - E_{(300K,\theta_D)}\right]$$

Equation 7.1_16

where γ can be defined in terms of Equations 7.1_1-3 and the $E_{(X)}$ terms of harmonic internal energy are defined in terms of the product of a constant based on the Debye temperature, θ_D and the gas constant, and a thermodynamic term (Fei et al., 1992).

Perhaps the most useful approach for the current study is the Birch-Murnaghan high T EOS (desribed by Fei et al., 1992). This approach avoids the use of the parameter P_{Th} where, in equation 7.1_9, V_0/V is substituted by $V_{(0,T)}/V_{(P,T)}$, K_0 is substituted by K_T and K'_0 is substituted by K'_T such that:

$$K_T = K_{0T} e^{-\delta_T \int_{300K}^{T} \alpha dT}$$

Equation 7.1_17

Where α can be expressed following Equation 7.1_15. Differentiating, gives:

$$\left(\frac{dK}{dP}\right)_T = \left[\left(\frac{dK}{dP}\right)_{0T} + \delta_T\left(e^{\delta_T \int_{300K}^{T} \alpha dT} - 1\right) - K_{0T}\left(\frac{\partial \delta_T}{\partial P}\right)_T \int_{300K}^{T} \alpha dT\right]\psi$$

Equation 7.1_18

Where:

$$\psi = e^{-\delta_T \int_{300K}^{T} \alpha dT}$$

Equation 7.1_19

and:

$$\left(\frac{\partial \delta_T}{\partial P}\right)_T \equiv \left(\frac{\partial^2 K_T}{\partial P^2}\right)_T$$

Equation 7.1_20

Additionally, the integral,

$$\int_{300}^{T} \alpha \partial T$$ Equation 7.1_21

can be expanded to give

$$\alpha_0(T-300)+\frac{1}{2}\alpha_1\left(T^2-300^2\right)-\alpha_2\left(T^{-1}-\tfrac{1}{300}\right)$$ Equation 7.1_22

Following the substitutions of equations 7.1_11, 12, 17 - 22 outlined above into Equation 7.1_10, for any combination of pressure and temperature for a particular phase, a value of $V_{(0,T)}/V_{(P,T)}$ can be calculated. Due to the fact that the resulting identity, of the form:

$$X = f(1+2f)^{5/2}(1-\zeta_1 f)$$ Equation 7.1_23

Where:

$$X = \frac{P}{3K_T}$$ Equation 7.1_24

is a polynomial of factor five, an explicit solution for $V_{(0,T)}/V_{(P,T)}$ cannot be found analytically; equation 7.1_23 must be solved numerically. The function was investigated in two forms:

$$f(1+2f)^{5/2}(1-\zeta_1 f)-X=0$$ Equation 7.1_25

And

$$f(1+2f)^{5/2}(1-\zeta_1 f)\Big/X = 1$$ Equation 7.1_26

Using reasonable constants for ferropericlase (table 7.1_1) it was found that inputing a range of *f* into the LHS of both equations 7.1_25 and 7.1_26 gave, respectively, only one solution of zero (figure 7.1_1) and one solution of unity (figure 7.1_2); the behaviour of V_0/V for differing mathematial solutions and pressure and temperature conditions is presented in figures 7.1_3 and 7.1_4. The graphs show that no ambiguity exists on any reasonable numerical solution of equation 7.1_23. For this study, it was decided to solve equation 7.1_23 numerically by converging on a *zero* solution, i. e. using the form of equation 7.1_25; such a solution can simply be obtained by the construction of a short iterative programme or by the use of a calculation package such as Microsoft Excel 5.0™.

Solution of $V_{(0,T)}/V_{(P,T)}$ for a particular pressure and temperature for a specific phase is still, however, short of what is required. In order to obtain values for $V_{(0,300)}/V_{(P,T)}$, $V_{(0,T)}$ must be calculated explicitly. To do this, theory of the thermal expansion of mineral phases at constant pressure must be called upon. We can use the relationship:

$$V_{(0,T)} = V_{(0,300)} e^{\int_{300}^{T} \alpha dT}$$ Equation 7.1_27

where substitution of α by equation 7.1_15 applies. Thus we now have $V_{(0,T)}/V_{(P,T)}$, $V_{(0,T)}$ and $V_{(0,300)}$. So $V_{(0,300)}/V_{(P,T)}$ can be calculated:

$$\frac{V_{(0,300)}}{V_{(P,T)}} = V_{(0,300)} \frac{V_{(0,T)}}{V_{(P,T)}} \frac{1}{V_{(0,T)}}$$ Equation 7.1_28

Section 7.1.2 ***Calculation of elevated internal pressures***

Section 7.1.1 has presented a framework (summarised in figure 7.1_5) for the description of cell volume for any phase under conditions of varying pressure and temperature. This framework is now applied to phases of interest to the present study and, in particular, to their behaviour on ascent to the Earth’s surface. Incorporating data from table 7.1_1, values for $V_{(0,300)}/V_{(P,T)}$ along Geotherms 1 and 2 (section 4.2) for nine phases of interest have been calculated. Table 7.1_2, of fPer of composition $(Mg_{0.7}Fe_{0.3})O$ along Geotherm 1, is presented as an example of the stages in the calculation of $V_{(0,300)}/V_{(P,T)}$. For the purposes of estimating the relevence of any internal pressure with respect to depth, pressure is converted to depth (figure 7.1_6) according to the method outlined in appendix 14 and, in particular, equation A14_15.

Table 7.1_2 Parameters involved in the calculation of $V_{(0,300)}/V_{(P,T)}$ for fPer of composition $(Mg_{0.87}Fe_{0.13})O$ (GU4A1) along Geotherm 1

P	T	d	$\psi(\alpha_1-\alpha_3)$	K’	K_T	ζ_1	$P/3K_T$	f	V_A	V_B	V_C
0	300	0	1.00	4.037	162.5	-0.055	0.000	0.000	1.000	76.21	1.000
2	1013	61	0.92	4.079	149.9	-0.118	0.004	0.004	1.013	78.13	1.012
4	1410	121	0.88	4.099	142.2	-0.149	0.009	0.009	1.027	79.42	1.015
6	1640	180	0.85	4.109	137.7	-0.164	0.015	0.014	1.041	80.23	1.011
8	1662	238	0.84	4.110	137.3	-0.165	0.019	0.018	1.054	80.31	1.000
10	1674	295	0.84	4.111	137.0	-0.166	0.024	0.022	1.066	80.35	0.989
12	1687	351	0.84	4.111	136.7	-0.167	0.029	0.026	1.078	80.40	0.979
14	1708	406	0.84	4.112	136.3	-0.168	0.034	0.030	1.090	80.47	0.969
16	1806	460	0.83	4.116	134.4	-0.173	0.040	0.034	1.102	80.84	0.962
18	1822	514	0.83	4.116	134.1	-0.174	0.045	0.037	1.114	80.90	0.953
20	1836	566	0.82	4.117	133.8	-0.175	0.050	0.041	1.125	80.95	0.945
22	1917	618	0.81	4.119	132.2	-0.179	0.055	0.044	1.136	81.26	0.938
24	2043	669	0.80	4.123	129.7	-0.185	0.062	0.049	1.149	81.75	0.934
26	2320	719	0.76	4.130	124.1	-0.196	0.070	0.054	1.165	82.89	0.934
28	2473	768	0.74	4.133	121.0	-0.200	0.077	0.058	1.179	83.54	0.930
30	2498	816	0.74	4.134	120.5	-0.200	0.083	0.061	1.190	83.65	0.923
32	2510	864	0.74	4.134	120.3	-0.201	0.089	0.065	1.200	83.70	0.915
34	2522	911	0.74	4.134	120.1	-0.201	0.094	0.068	1.210	83.75	0.908
36	2537	958	0.74	4.134	119.8	-0.201	0.100	0.071	1.220	83.82	0.901
38	2553	1004	0.74	4.134	119.4	-0.201	0.106	0.074	1.230	83.89	0.895
40	2566	1049	0.73	4.134	119.2	-0.202	0.112	0.077	1.240	83.95	0.889

This table is displayed as a representation of the values and trends in the parameters employed. Actual calculation was undertaken in 1 GPa steps and using more significant figures for each parameter. Parameters are those involved in equations 7.1_9 - 7.1_12 and 7.1_17 - 7.1-28 where, in particular, P - pressure in GPa; T - temperature (K); d - depth (km); K’ - dK/dP; V_A - $V_{(0,T)}/V_{(P,T)}$; V_B - V(0,T); V_C - $V_{(P,T)}/V_{(0,300)}$

General observations: Figs. 7.1_7-15 show relationships of $V_{(0,300)}/V_{(P,T)}$ to depth for diamond, fPer, corundum, orthopyroxene, MgSi-Pvk, CaSi-Pvk, olivine, wadsleyite, and ringwoodite respectively.

For both Geotherms 1 and 2, figures 7.1_7-15 show that for all phases, the overall effect of pressure is greater than that of temperature in dictating the molar volumes of mantle phases. In other words, even though the deep earth is substantially hotter than the surface, promoting expansion, mineral phases have smaller molar volumes due to the dominant effect of compression due to elevated pressure. This, in general, even applies for the hotter geotherm, Geotherm 1.

In greater detail, however, it can be seen that, in the case of Geotherm 1, the relatively high temperatures involved give rise to a range of depths in the shallow lower mantle where mineral phases will experience little molar volume change or in some cases a slight contraction on exhumation. Here the effect of contraction on reduction of temperature comes close to balancing expansion due to release of pressure, and, herein, is referred to as the 'boundary effect'. At shallow depths (< 100 km), and for rapid exhumation (where pressure is released before significant cooling, as exemplified by Geotherm 2), calculation shows that here the effect of temperature is dominant to the extent that mantle phases expand to greater volume than ATP volume. Indeed, although to a lesser extent for slower exhumation, most mantle minerals would appear to experience a molar volume elevated above $V_{(0,300)}$ in the final stages of exhumation, here referred to as the 'quenching effect[1]'. These are the observations of the general trends. Comparison of Figs. 7.1_7-15, however, show that different phases behave differently in the magnitude of their relative volume changes as well as the relative importance of temperature and pressure effects: ultimately dictated by values of bulk modulus and thermal expansion.

Phase specific observations: Strikingly, diamond (figure 7.1_7) shows very little change in molar volume along both geotherms compared to all other phases. At shallow depths, if exhumation is slow enough to equilibrate temperature on decompression, diamond will experience almost no volume change at all; on rapid decompression, such as in an eruption, expansion to greater than ATP volume will occur but, again, on a smaller scale than for other phases. Furthermore, calculation on the basis of a thermal boundary between upper and lower mantle (Geotherm 1) suggests that, if such a boundary exists (as is favoured by the present study, section 4.5) there will be a maximum volume (and thus a local density minimum) at around 720 km. This means that a diamond residing at ~ 720 km will suffer an increase in density on both ascent and descent and so, once diamond reaches this area, it should tend to stay there[2]. Thermoelastic modelling, therefore, reveals a mechanism for the accumulation of diamond around the lower mantle / upper mantle boundary.

---

[1] This quenching effect has important implications for the final stages of the history of exhumation of diamonds containing inclusions. What it means is that on eruption, not only is the internal pressure on inclusion on host at its greatest (being the furthest removed position from equilibrium) an additional 'kick' on the host is supplied by the quenching effect. Much of the fracturing, and indeed the break-up of stones is liable to occur during these final stages of a diamond's subterrigenous history.

[2] Density contrasts are not the only factors affecting the convective régime. As Liang et al. (1994) have concluded, under particular conditions of elemental and thermal diffusive coupling, convection may still occur irrespective of density contrasts. Such behaviour, however, is more likely to be a factor relevent to melts and, even if the overall régime is still one of circulation, albeit, restricted, materials behaving in the same fashion as diamond are envisaged to be relatively gravitationally stabilised.

The next least compressible minerals considered are corundum and the perovskite structured phases. Corundum (figure 7.1_8) has a smaller thermal expansivity than diamond and so the boundary effect is less marked for corundum. There would still, however appear to be a depth range showing a negative density / depth gradient although significantly smaller than that of diamond. The final stages of exhumation, no matter how slow, will most likely see a relative expansion to greater than ATP volume. Amongst the perovskite structured phases, the lack of boundary and quenching effects in CaSi-Pvk is particularly striking (figure 7.1_9); diamond aside, CaSi-Pvk has the smallest thermal expansivity, 1.4 x 10^{-5} K^{-1}, of any of the phases modelled. In contrast, MgSi-Pvk (figure 7.1_10) shows pronounced boundary and quenching effects; MgSi-Pvk will have a propensity to stabilise at depths close to the top of the lower mantle in the presence of a thermal boundary, and, as comparison with figure 7.1_11 shows, compressibility is greater than its low pressure orthopyroxene polymorph.

fPer is fairly compressible (figure 7.1_12) and, with a thermal expansivity of ~ 3.41 x 10^{-5} K^{-1} shows significant boundary and quenching effects. It would appear that fPer also has a possible stabilisation depth close to the top of the lower mantle.

In the olivine composition system, comparison of figures 7.1_13 - 15 shows that successively higher pressure polymorphs are characterised by smaller compressibility and greater thermal expansivity. Furthermore, in the event of any ringwoodite stabilised in the lower mantle in, for example subducted slab or particularly Mg-rich systems (figure 4.4_5) there would appear to be a region of gravitational stability close to the top of the lower mantle in the presence of a thermal boundary.

Summary: Of the phases studied, with rapid final exhumation, diamond, CaSi-Pvk, opx, olivine, wadsleyite, ringwoodite, corundum, fPer and MgSi-Pvk, show increasing relative expansion above ATP volume. MgSi-Pvk and fPer bearing diamonds will be the most likely to undergo fracture, given enough internal pressure build-up on eruption[3]. Additionally, for possible lower mantle phases, given the details of compressibility against expansivity, CaSi-Pvk, corundum, fPer, ringwoodite, MgSi-Pvk and diamond, show an increasing likelihood of experiencing gravitational stability in a zone close to the top of the lower mantle, should a thermal boundary exist between upper and lower mantle.

Modelling of phase transitions

Methodology: Diamond, fPer and corundum are not observed to undergo any phase transitions through the range of pressure and temperature conditions relating to exhumation from, at

---

[3] Indeed, most fracturing is thus likely to occur during the final stages of eexhumation.

least the upper half, of the lower mantle. In contrast, however, phases of $(Mg,Fe)SiO_3$ and $(Mg,Fe)_2SiO_4$ composition, have been observed to undergo phase transitions (section 4.4.1). Whether, inclusions of these compositions do, when encalpsulated in diamond, revert from high pressure polymorphs, depends on a number of factors: the activation energy of the reaction, the ambient thermal régime, the duration of ascent and the confining pressure of the diamond host. Given that perovskite structures have not been identified from São Luiz or Guinean inclusions (section 3.3) such transformations *are* believed to take place.

To investigate the effect of phase transitions on volume change with depth, two thermoelastic models of the type outlined for single phases have been constructed. One involves $(Mg_{0.87}Fe_{0.13})_2SiO_4$ composition (figure 7.1_16) and transitions from ringwoodite to wadsleyite to olivine[4] and the other involves $(Mg_{0.9}Fe_{0.1})SiO_3$ composition (figure 7.1_17) undergoing transformation from MgSi-Pvk to MgSi-Ilm to monoclinic structured $(Mg_{0.9}Fe_{0.1})SiO_3$. Both models introduce phase transitions at conditions of pressure and temperature following discussion in section 4.4_2 (figures 4.4_4 and 4.4_1). It should be noted that no calculation is made on the basis of the hypothesised breakdown of MgSi-Ilm to stishovite + wadsleyite before recombination to cpx. This phase field lies in a particularly restricted depth range (figure 4.4_1), and so is even less relevent to Fe-bearing systems (figure 4.4_2). Calculations were undertaken on the basis of an arbitrary unit volume for the initial included phase, at 670 km for olivine composition and 1050 km for pyroxene composition.

Results: Because the thermoelastic constants of olivine composition polymorphs are so similar, exhumation from 670km shows a smooth expansion up until the very final stages (figure 7.1_16). Diamonds containing olivine composition inclusions would have no particular reason not to revert to low pressure polymorphs on exhumation providing sufficient activation energy was available. On the other hand, because of the significant change in expansion gradient through the pyroxene composition the diamond host will experience rapid increases in internal pressure on phase transformation (figure 7.1_17). This contrasts with the smooth behaviour of diamond expansion (figure 7.1_7) which will, therefore, act to resist back-transformation. From a chemical perspective, however, the activation energy of back transformation of MgSi-Pvk to orthopyroxene is particularly small (Knittle and Jeanloz, 1987), which acts in favour of stabilisation of low pressure polymorphs. How these opposing effects relate to each other in terms of relative importance is unclear but it does appear that MgSi-Pvk at least to clinopyroxene is quite possible on theoretical grounds.

---

[4] It should be noted that such calculations of volume change in the olivine system assume constant composition as would be relevent to diamond inclusions. In the earth's mantle, however, it is likely that the transition from olivine to wadsleyite in the presence of garnet involves an Fe-enrichment in the olivine composition phase (section 4.4.1). This compositional shift should be accounted for when applying volume change to bulk rock calculations.

Section 7.1.3 Previous indications of elevated internal pressures of diamond inclusions

A number of authors have observed elevated internal pressures of diamond inclusions (Harris et al., 1970; Navon, 1991; Schrauder and Navon, 1993) in addition, Liu et al. (1990) has alluded to the phenomenum. Results obtained show a large range of internal pressures presumably due to differing degrees of both brittle and plastic deformation of the stones involved in addition to differing depths of formation.

Harris et al. (1970) conducted a study of two garnet inclusions. By a series of step-heating experiments combined with in-situ X-Ray diffraction and knowledge of the thermoelastic properties of garnet, they found initial elevated pressures of 0.2 GPa. On heating to 873 K, internal pressures were found to increase to 1.5 GPa for one inclusion (D1) and 0.7 GPa for the other (D2). It was concluded that, as D2 did not produce the expected increase in elevated pressure with temperature, the diamond encompassing this inclusion had undergone some degree of non-elastic deformation.

Liu et al. (1990) investigated the state of an eclogitic garnet inclusion in diamond using Raman shift in a DAC arrangement. In this case they found that the inclusion in question was not subject to any internal pressure. Their interpretation of this observation was that a garnet / diamond system would be subject to no internal elevated pressure at ATP if the system had formed at between 150 and 280 km [1] with temperature slightly below their expected geotherm.

The lack of extreme internal pressure exhibited by the inclusions discussed above may have two causes. All inclusions studied are relatively large compared to their diamond hosts, therefore allowing reasonable opportunity for inclusion termination sourced fractures to penetrate to the diamond surface. Secondly, compared to lower mantle sourced diamonds, the fracturing of the mantle lithosphere diamond hosts during the last stages of exhumation (section 7.1.2) comprises a far larger proportion of distance of exhumation: much internal pressure build up will have been relieved by this process.

Navon (1991), in contrast, investigated the I. R. absorption of micro-inclusions in 25 coated stones from Zaire and Botswana. He observed a shift in I. R. wavenumber of quartz inclusions corresponding to an internal pressure of ~ 1.5 - 2.2 GPa and by utilising calculations of molar volume for CO_2 and H_2O suggested formation pressures of 4 - 7 GPa.

---

[1] No information is given regarding whether the garnet in question has a majoritic component or not.

Schrauder and Navon (1993) found even larger elevated pressures. Investigation of the I. R. spectra of a brown stone from an unknown locality (Navon, 1997 *personal communication*) showed a shift in the CO_2 line indicative of 5 GPa of elevated internal pressure. In this case, no inclusion was observed visually, prompting the suggestion that the I. R. absorption was due to micro-inclusions of solid CO_2.

Clearly diamond can, therefore, retain its structural integrity in response to such large internal pressures. Just how much the diamond structure can take depends on the volume ratio of diamond to inclusion as well as a miriad of additional factors including the stress régime the system has undergone, the nature of defects adopted on genesis etc. The following section aims to investigate how much stress São Luiz and Guinean stones have been subjected to.

➠

Section 7.1.4 Internal pressures imposed on fPer inclusions

The cell dimensions of two fPer inclusions, BZ257A and GU4A, have been determined both within and without of their diamond hosts (section 3.3.3); significant expansion on release being found in both cases. In addition, their compositions have been determined by EPMA (section 2.2.1.4). Table 7.1_3 summarises the findings.

Table 7.1_3 Summary of change in cell parameters of fPer inclusions on release from diamond

	BZ257A	**GU4A**
Cell dimension within diamond (Å)	4.2374	4.2288*
Cell dimension after release (Å)	4.2463‡	4.2397
Composition	$Mg_{0.743}Fe_{0.257}O$	$Mg_{0.868}Fe_{0132}O$.

‡ Average of two analyses, one by micro-diffraction (Carnegie Institution) and one by XRD (Chemsitry, Edinburgh) * Average of two analyses by Gandolfi camera (Edinburgh)

Internal pressure: Application of the cell parameter expansion data to elastic models of fPer of the compositions of BZ257A and GU4A at 300 K, following the methodology of section 7.1.1, is presented in figures 7.1_18 and 7.1_19. The change in cell parameter for GU4A implies an internal pressure of 1.29 +/- 0.38 GPa, whereas change in cell parameter of BZ257A implies an internal pressure of 1.05 +/- 0.30 GPa. Both calculated internal pressures lie below the predicted yield strength of diamond at 300K of >10GPa (section 5.3) although growth defects may be propogated at lower pressures.

Depth of formation initially assuming no diamond expansion on exhumation: The measured cell parameter change can be applied directly to the predicted behaviour of fPer along Geotherms 1 and 2, if it is assumed that diamond has values for K_{0T} of 0 GPa and α_1 of 0 K^{-1} (figures 7.1_20 and 7.1_21). Such calculation implies formation depths of 280 +/- 12 km (Geotherm 1) and 266 +/- 13 km (Geotherm 2) for GU4, and 256 +/- 8 km (Geotherm 1) and 243 +/- 8 km (Geotherm 2) for BZ257A. Such an assumption of the physical properties of diamond is, clearly, invalid: the diamond host *will* have undergone some expansion on exhumation (figure 7.1_7) however small, thus making the real depths of formation greater than those aforementioned. The behaviour of diamond in this fashion can be corrected for.

Correction for diamond expansion: Volume change of mineral phases discussed in section 7.1.4, have been calculated on the basis of an assumption of unit volume at 300K, 0 GPa. Some modification is required, therefore, to enable application of this data to inclusion *systems* such as fPer in diamond, where, at some depth greater than 0 km, the diamond encapsulation depth, the volume of the inclusion is equal to the space provided by the diamond. Here, the volume of the hole will behave, on exhumation, according to the properties of diamond. In other words, the correction of diamond expansion on internal pressure imposed by fPer, requires a unit volume to be set at the depth of formation both for diamond and for the included phase. Calculations of the ratio of diamond / fPer for hypothetical fPer inclusions in diamond formed at depths at ~30 km intervals (1 GPa steps) from 768 km to 0 km, for each of Geotherms 1 and 2 and for GU4A and BZ257A, have been made (figures 7.1_22-25). All diamond hosts will undergo some maximum internal pressure imposed by fPer at ~120 km, released to an extent by the quenching effect on further exhumation. For fPer-diamond systems formed at depths of over ~250 km the pressure maximum reached is greater than subsequent relaxation and so fPer / diamond systems formed at 250 km and over will still retain an internal pressure on the earth's surface (diamond / fPer at 0 km < 1 for figures 7.1_22 - 7.1_25). Inclusions of fPer encapsulated at shallower depths than this will be influenced more by the temperature decrease than the pressure decrease on exhumation (diamond / fPer at 0 km > 1 for figures 7.1_22 - 7.1_25). Applying the volume change ratios of $V_{\text{in-situ inclusion}}$ / $V_{\text{released inclusion}}$ which is equivalent to the ratio V_{hole} / $V_{\text{released inclusion}}$ or V_{diamond} / V_{fPer} to figures 7.1_22-25, shows depths of formation of 324 +/- 18 km (Geotherm 1) and 318 +/- 21 km (Geotherm 2) for GU4A and 286 +/- 15 km (Geotherm 1) and 278 +/- 15 km (Geotherm 2) for BZ257A.

A simpler calculation can also be adopted to gain the same result, but with the disadvantage, however, of not showing the detail which stepwise calculations of different depths of formation as discussed above reveals. Given the volume change data for each phase discussed in section 7.1.2, and the assumptions that the ratio of $V_{\text{released inclusion}}$ / $V_{\text{in-situ inclusion}}$ is equivalent to the ratio $V_{\text{released inclusion}}$ / V_{hole} (where V_{hole} is equal to $1/V_{\text{diamond at formation depth}}$), this means is that the depth of formation of the diamond fPer system can be found by the intercept of the ratio $V_{\text{released inclusion}}$ / $V_{\text{in-situ inclusion}}$ with the relationship $[V_{(P,T)}/V_{(0,300)}]_{\text{fPer}}/[V_{(P,T)}/V_{(0,300)}]_{\text{diamond}}$ against depth i. e. data for graph 7.1_20 divided by data for graph 7.1_7. Figures 7.1_26 and 7.1_27, present such a calculation for the GU4 and BZ257 diamond-fPer systems where $V_{\text{released inclusion}}$ / $V_{\text{in-situ inclusion}}$ and thus calculated formation depths are shown.

These depths can be regarded as the minimum possible depths of formation in terms of thermoelastic properties[1]: diamonds incorporating fPer inclusions at depths any shallower than these values could not have accumulated enough internal pressure to result in the observed inclusion volume changes. The true depth of formation will be greater still, however, as the diamonds have not just expanded elastically, but have also undergone permanent deformation. A further correction must, therefore, be made for internal pressure release due to such deformation.

---

[1] Phase relations of course, as discussed in section 4.4.2, support a greater depth of formation.

Correction due to diamond host deformation: Both São Luiz diamonds and the Guinean stones studied have, clearly, undergone significant deformation (section 5.3). Indeed some inclusion-related fracturing was observed before inclusion release for both BZ257 and GU4 (appendix 1). The depth of formation of the two fPer-bearing stones BZ257 and GU4 *must*, therefore, have been greater than the depth values discussed previously. Quantification of the degree of deformation and, in particular, the amount of inclusion expansion which has been allowed by deformation is, however, far from being clear.

First of all, a quantifiable source had to be located; many stones show visual evidence of inclusion associated fracture and plastic deformation which could not, however, be conveniently measured. The SEM and CL images obtained for polished flats represent the most obvious means for quantification of fracture related expansion and, although, in no way statistically representative of the population as a whole, qualitatively, these stones appeared to be no more or less deformed than diamonds of lower mantle associations, in general. Three approaches were taken in order to attempt to quantify the amount of inclusion expansion accommodated by diamond fracture: the measurement of displacement of cathodoluminescence bands, the measurement of displacement of inclusion edge and the measurement of increase in inclusion area.

Displacement of cathodoluminescence band: Cathodoluminecence images of polished flats BZ251-BZ258 were examined in detail. No shift in cathodoluminescence band along any of the exposed fractures was detected at a magnification of up to x60. Some of the rough edges to CL patches discussed in section 5.6 are, however, interpreted as being due to plastic deformation. The average displacement of such edges in the central zone of BZ251 (figure 5.6_3) was measured as a ratio against the width of the affected zone in the same direction. Converting this linear expansion to volume expansion by taking the cube of the data yielded an equivalent volume expansion of 1.062. It should be noted that BZ251 showed CL indications of plastic deformation more strongly than most stones; an appropriate value for use in calculations for BZ257 and GU4 may be lower.

Increase in inclusion area: It was observed from BZ251A (figure 5.3_7) and BZ251B (figure 5.3_8) that the edges of the inclusions exposed on the surface of the diamond flat do not follow the regular morphology which would be expected by the imposition of diamond form on the included phases. Significant embayments into fracture zones and, in particular for BZ251B, saw edges, were observed. These are interpreted as regions of expanded inclusion material by means of diamond deformation. The areas of projected initial inclusion boundary, and a conservative estimate of expanded inclusion boundary, given that EDS did *not* reveal included material extending into fracture zones (section 5.3.1.2) were measured for BZ251A and BZ251B (figure 7.1_28). Area expansion was converted to volume expansion by taking the root, cubed, of expanded and initial areas and constructing ratios. It was found that estimates indicated an expansion due to fracture of x1.037 (BZ251A) and x1.070 (BZ251B).

Displacement of inclusion boundary: It was observed that a portion of the inclusion / diamond boundary of BZ252A is displaced outwards from the inclusion edge and is bounded in a v-shape by two obvious fractures extending into the inclusion (figure 7.1_28). This feature resembles the outward movement of a keystone and is interpreted as being due to inclusion expansion induced, diamond fracture. The width of the inclusion both involving and not involving this ‘keystone’ were measured and converted to volume displacement by taking the cube of each length measurement and constructing a ratio. Such a calculation involves the assumption that the keystone displacement occurs in three dimensions around the inclusion; a questionable assumption which means that the estimated volume expansion calculated as 1.249, may be considered to be high.

It should be reiterated that the calculated fracture related expansions, are considered to be subject to large errors. It is, however, notable that three independent calculations come up with similar answers. Given that BZ257A and GU4A were chosen so as to show as little obvious internal fracturing as possible, it is felt that a conservative estimate of expansion[2] due to diamond fracturing of x1.037 be applied.

Investigation of the influence of fracture on internal pressure of inclusions: A similar iterative aproach as the correction due to diamond expansion was adopted for further correction due to diamond fracture. Two scenarios for the release of internal pressure due to fracture can be envisaged: gradual deformation throughout exhumation and a single deformation event at the depth of maximum internal pressure (~91 km, figures 7.1_22-25). Given the complexities of CL patterns of São Luiz diamonds (section 5.6) it is considered likely that deformation has occurred in stages throughout exhumation. It is also considered likely, that, given the kinetics of fracture propagation, a significant proportion of internal pressure build-up was released in a single event at shallow depth. The effect of a total of x1.037 non-elastic deformation related expansion of diamond host over a variety of depths has been investigated using data relevent to a hypothetical inclusion diamond system using a GU4A fPer composition. Three models were constructed with a total expansion of x1.037 applied in the same way as the diamond expansion correction: one with x1.037 expansion due to deformation at 91 km, one with x1.037 expansion at 295 km and a third model with x1.018 expansion at both 91 km and 295 km. Comparison of figures 7.1_ 29-31 (Geotherm 1) shows that the depth of formation which would be implied by a particular change in inclusion volume on release

---

[2] Non-conservative estimates quickly give unreasonably large depths of formation.

from diamond is irrespective of where deformation occurs. Correction for non-elastic deformation on GU4A and BZ257A systems can, thus, proceed without concern over the locations of deformation events. Figure 7.1_32 shows the calculation of formation depth for GU4A based on Geotherm 2.

Results for fPer inclusions: Inclusion expansion on release for GU4A (figures 7.1_29 and 7.1_32) and BZ257A (figures 7.1_33 and 7.1_34) are applied to the above volume change calculations corrected for estimated diamond non-elastic deformation in addition to the elastic diamond expansion correction. Formation depths of 728 +/- 34 km (Geotherm 1) and 666 +/- 26 km (Geotherm 2) for GU4 and 628 +/- 22 (Geotherm 1) and 617 +/- 18 km (Geotherm 2) for BZ257A are required in order to explain the observed change in cell parameters. Due to the uncertainties in non-elastic deformation related expansion, the real significance of such depth values lies not so much in the values themselves but in the fact that they lie near and into the lower mantle. Given that the non-elastic deformation factor employed is considered to be conservative, depths of formation are likely to be greater. The elevated pressures and associated fracturing by inclusions of BZ257 and GU4 can be considered to be strong evidence for a lower mantle source for these diamonds and, by extrapolation, diamonds of the same association. Furthermore, the ability of diamond to withstand large internal pressures and its tendency, when it does deform, to deform by plastic deformation (section 5.3) adds further confidence to the contention that São Luiz and FEG inclusions have largely remained chemically unaltered since formation.

➠

Section 7.2 Integrity of diamond system through exhumation

It is only due to the remarkable qualities of diamond durability, both chemically (section 1.3.1) and physically (section 5.3), that we have the opportunity to directly observe lower mantle minerals. The likelihood of chemical alteration outwith diamond and the fact that lower mantle phases would always be expected to revert to their atmospherically stable forms (Knittle and Jeanloz, 1987) would preclude lower mantle material surviving transit outwith occluding diamond.

Diamond is not, however, infallible. Studies, whose results have been presented in previous sections, have addressed concerns over the possibility of inclusion alteration. What factors must be considered? Without permitting release mechanisms, large pressures can build up around inclusions when diamonds, due to their small expansion relative to other minerals, are exhumed (section 7.1.4). Any release of pressure, however, (section 5.3.1 and section 7.1.4) will also be accommodated by fracture or plastic deformation. As has been observed, the Säo Luiz and Guinean diamonds studied show high instances of plastically deformed stones compared to other suites of diamonds (section 5.3.2). Such deformation, being on an atomic scale, will not compromise the security of the included mineral phase, what one must be careful of is the role of fracture. Fracture can be dealt with on a simple level; infiltration of material into fracture systems can occasionally be clearly seen and commonly, diamonds which are observed thus, yield inclusions which are clearly altered. These can then be easily discarded from a study of wholly syngenetic inclusions. Furthermore, fracturing weakens the diamonds it affects. One could say that, if fracturing exists to a degree that the integrity of the inclusions is compromised, then the inclusion will either appear to be so, or else not be in existence to sample; the stone having disintegrated. The latter part of this argument can be applied to the observation that exceptionally large stones often contain few inclusions; inclusions weaken stones which leads to fracture which is likely to be catastrophic, which reduces the size of the stone. One must, however, also be careful to consider a less extreme case; that where, hypothetically, fracturing occurs and the inclusion is subject to discrete alteration. One could, in fact, envisage fracturing, re-equilibration, at some intermediate depth even followed by fracture infill.

Despite these concerns, testament to the sanctity of diamond has been found in the present study. Aside from stones which have obviously altered inclusions (appendix 1) and despite detailed study, no evidence of fracture infill and inclusion alteration has been found. Studies have involved cathodoluminescence (sections 5.3.1.2 and 5.6) and fracture observation (section 5.3.1.2) in addition to δ^{13}C determination.

So it can be confidently stated that certain diamonds have travelled, relatively intact from the transition zone and the lower mantle to the Earth's surface (diamonds from this study and by inference stones discussed in Otter and Gurney, 1984; Scott-Smith et al., 1984; Moore et al., 1986 and Moore and Gurney, 1986). This observation alone has relevance to the mantle plume debate (section 7.3.1) and mechanisms of mantle convection (section 4.3) and provokes a particularly puzzling question. If diamonds grow in the deep mantle, and, as tomography (Olson et al., 1990), and mathematical considerations (Solheim and Peltier, 1993) suggest, the deep mantle is well mixed, why then do diamonds not occur in OIB which is likely to have, at least in part, a lower mantle origin? The key to this question lies in the oxidation state of regions of the upper mantle and their interaction with diamond stability. Section 6.1.1 has discussed what is known regarding diamond stability in terms of P, T and fO_2. The following discussion attempts to apply this knowledge to what is known of the P, T and fO_2 conditions of regions of the upper mantle.

Mantle Oxidation: Attempts to determine the state of mantle oxidation have taken a number of different paths; thermodynamically based calculations, experimental work and petrological observation. Useful summaries are provided by Arculus and Delano (1987), Haggerty (1990) and Ballhaus (1993). The discussion aims to present the salient points and follows the use of buffering terminology commonly employed to indicate conditions of oxygen fugacity. In order of increasing fO_2, the iron-wüstite (IW), wüstite-magnetite (WM), fayalite-magnetite-quartz (FMQ) and nickel-nickel oxide (NNO) buffers are referred to.

Modelling studies of fluid speciation: Mantle fO_2, although buffered by the composition of the solid phase, is dominated by fluid species present. As the system C-O-H encompasses all the fluid phases expected to dominate the mantle, study of this system can be considered to go some way to the prediction of conditions of mantle fO_2. Experimental calculations of fluid compositions at high pressure and temperature on the system C-O-H have been undertaken for low fO_2 conditions (buffered by iron-wüstite) (Jakobsson and Oskarsson, 1990), low pressure (Frost and Wood, 1997) or have involved extrapolation from shock-wave data (Saxena and Fei, 1987). Comparing experimental and mathematically determined studies shows that, for mantle conditions, experimental results tend to predict slightly higher concentrations of H_2 and lower values for C_2H_6 compared to thermodynamic modelling. Additionally, the concentration of CO under comparable conditions shows a decrease in concentration with increasing T according to experimentation; a result which is contested by calculation. However, CO occurs in very low concentrations resulting in large errors. Indeed, it is likely that shortcomings are inherent in both theoretical and experimental methods for determining fluid speciation. Certainly within the theoretical régime, due to sparse thermodynamic data, calculations at high P,T conditions are often based on extrapolation (eg. Holloway, 1987). It is suggested, therefore, that only generalisations as to stability of multispecies fluids in the C-O-H system can be made with confidence. Fortunately, indirect means of predicting mantle fO_2 can be avoided as there is also available, extensive petrological evidence to provide inferences on the state of oxidation in different parts of the mantle.

Petrological studies: A major conclusion of studies into mantle oxidation is that the mantle exhibits a range of oxidation states from saturation with Fe-Ni phase (low fO_2) to an upper limit involving the oxidation of carbon above FMQ (Haggerty, 1990, figure 7.2_1) based on calculations on naturally occurring Cr-Spinels (Ballhaus, 1993). Conclusions of specific studies are detailed below and figure 7.2_2 serves as a summary of regions of varying mantle oxidation.

Heterogeneous equilibria between garnet, olivine and pyroxene from peridotite nodules suggests a derivation from relatively oxidised source regions, FMQ to WM (Luth et al., 1990). Notably, a single sample of off-craton high T xenolith from Gibeon, South Africa, yields a more reduced value of fO_2 (FMQ -2.5). Although based on a single measurement, this may have a bearing on the nature of occurrence of off-craton diamonds which will be discussed in more detail later (section 7.3). An extensive study by Ballhaus et al. (1991), using their ol-opx-Cr spinel based oxygen geobarometer on a variety of mantle xenoliths provides an additional and separate database. They find that abyssal peridotites and peridotite xenoliths lie close to FMQ for most degrees of evolution, being slightly lower, FMQ -1 for low Cr/Cr+Al spinel xenoliths. Additionally, measurements on symplectites in upper mantle peridotites by Field and Haggerty (1994) suggest fO_2 conditions of FMQ to FMQ -1. Alternatively, studies of volatiles in diamond have yielded evidence of CH_4 suggesting a source close to IW (Deines, 1980): this may be representative of deeper mantle. Furthermore, Haggerty (1990) present the possibility of two oxidised zones (~ NNO); a metasome layer at mid-depths in the cratonic lithosphere and a zone following the asthenosphere / lithosphere boundary and probably related to pre-kimberlite metasomatism. It would appear that mantle oxidation state does vary but, in general, lies within the range of FMQ to IW. The question still arises, however, as to what happens when pressure decreases and melt and metasomatism occurs.

Volcanic and metasomatised settings: The consensus seems to be that geochemical enrichment processes in the upper mantle are oxidising (Ballhaus, 1990). Studies of volcanic gases (eg. Ringwood, 1979) yield values close to FMQ although using such measurements to infer mantle composition may lead to error due to fractionation on degassing. For example, the mantle itself may be less oxidised due to errors in extrapolation as a result of CO or H_2 loss (Ballhaus et al., 1991). Mid-Ocean Ridge Basalts (MORB), again, typically lie close to FMQ, (Christie et al., 1986) although show a fairly wide scatter (Ballhaus et al., 1991). Most interestingly, enriched MORB samples are more oxidised than depleted MORB, suggesting a modern oceanic lithosphere lies more towards FMQ +1 than primitive oceanic lithosphere. Furthermore, Ballhaus et al. (1991) find that arc basalts are typically much more oxidised, between FMQ +1 to FMQ +3 (~ NNO) due, presumably, to the large amount of water in such systems. Kimberlites, as determined by spinel-ilmenite intergrowths (Haggerty and Tompkins, 1983), again seem to be close to FMQ for particular equilibration temperatures but based on calculations throughout magma ascent, can be much more reduced (FMQ -2) (McMahon and Haggerty, 1984). As such, they represent the least oxidised of all magmatic material measured. Metasomatised peridotite samples seem to become increasingly oxidised with increasing degree of metasomatism (Ballhaus et al., 1991). Importantly for this study, in particular, based on measurements of Fe in spinel phenocrysts in basalts (Sun and McDonough, 1989 and Ballhaus, 1990), OIB tend to lie in the vicinity of FMQ +0.5 to FMQ +2 which, with the exception of island arc tholeiites (IAT), places them as the most oxidised of common melts. As such, such melts are incompatible with graphite stability; lying within the carbonate-CO_2 stability field (section 6.1.1).

There is some debate as to whether spinel phenocryst measurements can be used to interpolate into the mantle (fractionation, decompression and degassing may cause partitioning) and, indeed, there is some evidence to suggest a difference in values of fO_2 between basalts and associated xenoliths (Haggerty, 1990). The mechanism of any alteration is not the issue here; we are concerned particularly with the possible environments where diamond stability is compromised. The observation that IAT and OIB are oxidised prompts the question of, from where does this component arise? The obvious answer for IAT is a subducting slab, and it is not coincidental that the most oxidised basalt melts, IATs, are directly related to melting of subducting material. Perhaps it is also not coincidental that the second most oxidised basaltic melt, OIB, is associated with upwelling material (Storey et al., 1992). As discussed in section 7.3.1, there is evidence to suggest that OIB, in addition to being comprised of primitive material, may also involve a large component of subducted material. Furthermore, there is likely also to be a component of oceanic water in the upper reaches of the volcanic system, as suggested by the differences between fO_2 calculated on the basis of basalts and with those of the aforementioned basalt-hosted xenoliths.

Discussion: There has been much discussion along the lines that most diamonds inhabit deep rooted lithosphere (penetrating the diamond stability field) where repeated recycling has resulted in a highly depleted root with relatively low fO_2 (e.g. Haggerty, 1990). Occurrences of transition zone and deeper diamonds clearly adds an additional facet to diamond source areas. As studies of mantle oxygen fugacity discussed above have shown, the mantle, although variable in oxidation state, is generally reduced enough to allow diamond stability (figure 7.2_1). Furthermore, it is clear that it is mainly within the environment of *melting or fluid involved processes* (metasomatism), that oxidation can be considered high enough to dissolve diamond (Haggerty, 1986 and Haggerty, 1990). In particular it is OIB and IAT which have oxygen fugacities unsuitable for the stabilisation of carbon either as graphite or diamond. The deviation of fO_2 away from that appropriate to diamond stability (figure 7.2_3) occurs, for most melts, at relatively shallow depth (although for IAT the *source area* may even be outwith the stability of carbon). So even though deep diamonds may be stable, or at least suffer only a little resorption throughout most of the mantle, if they are entrained into a system of basaltic melting, they are very unlikely to survive[1]. Any diamond entrained into OIB will be burnt off as CO_2 and, indeed, such ex-diamond may be responsible for the high CO_2 contents measured from OIB (eg. Javoy et al., 1986). This means that it is not surprising that, even though OIB may involve primitive material from the deep mantle, diamond is not found to be present.

Kimberlite, in contrast, represents a quite different scenario from the other magmas discussed. The unique characteristics of generation and composition of kimberlitic melts, combined with the colder geotherm characteristic of cratonic regions, means that on ascent, kimberlite magma becomes more *reduced* and, in general terms keeps within the field of diamond stability (McMahon and Haggerty, 1984). This is why we see diamond in some kimberlites. Indeed, not only is diamond likely to survive final exhumation within kimberlite, there is evidence to suggest that diamond will, in fact, crystallise in kimberlite melt (Arima et al., 1993)[2]. The reader must, however, be wary of concluding that kimberlite is an ideal transportation medium for diamond as not all diamonds from kimberlite are pristine. Resorption is a common observation (eg. Hildebrand and Gurney, 1995) particularly when elevated temperatures are involved. The kimberlite sills of the Benfontein locality in South Africa, for example, which crystallised from a particularly hot melt, yield highly resorbed stones (McMahon and Haggerty, 1984) and, indeed, many deep mantle stones show characteristics of resorption (Sutherland, 1993 and thus study, section 5.1[3]). Although such resorption *may* be prior to kimberlite entrainment, it is also entirely consistent with the suggestion that the kimberlite carriers of resorbed stones lie at the boundary of elemental carbon stability in terms of fO_2, as shown in figure 7.2_4. Another important factor in terms of diamond survival within kimberlite as compared with, for example, OIB, is that of exhumation velocity. As section 7.3.3 discusses, kimberlite melt transportation is believed to be extremely fast compared to other compositions of eruptive magma. Even if oxidation state *were* unfavourable for diamond survival in kimberlites, entrained diamonds would be subjected to such conditions for a far shorte time than in OIB, thus promoting diamond survival.

Conclusions: The extensive database of fO_2 for lithospheric and asthenospheric régimes suggests that, despite significant heterogeneities, diamond is stable throughout much of the deep upper mantle. It is when melting and the interaction of a fluid phase, particularly H_2O, is involved, that fO_2 increases rapidly to the extent that diamond stability is compromised. Certain areas of the earth, therefore, can provide an environment in which diamond can quickly be resorbed. As, furthermore,

---

[1] As it is the presence of significant fluid which is responsible for elevated fO_2, it is considered likely that diamond will exist within OIB at depths below the influence of circulatory water.

[2] A process which is likely to be facilitated by the presence of diamond seed grains.

[3] 50% of Sõa Luiz diamonds involved in the present study show evidence of fine surface pitting (of the LM association sample, 52% show this feature).

pressure decrease has a detrimental effect on the stability of diamond at high fO_2 conditions, it is particularly likely that diamonds will burn within H_2O incorporating magmas at shallow depth; e.g. within OIB and IAB settings. It is only in the case of areas of kimberlite melting, where CO_2 dominates the fluid phase and relevant geotherms have shallow gradients, that diamond can usually be considered stable in a melt-related environment and thus survive final exhumation. It is for these reasons that the *presence* of diamonds in the deep mantle (transition zone and lower mantle), such as those from São Luiz, can be considered to be not inconsistent with the *absence* of diamond in most deep mantle associated magmas once they have reached the Earth’s surface.

Section 7.3 Processes of exhumation

It is attested that many São Luiz and Guinean diamonds have formed at great depth: depths within the transition zone and lower mantle. Furthermore, there exists strong evidence to suggest that many diamonds, particularly those with deeper sources, have been subjected to a complex history of deformation, resorption and reprecipitation (chapter 5). The question which naturally follows is, what process brought these diamonds to the surface?

Neither the magmatic source of São Luiz nor Guinean diamonds has been definitively located (sections 1.2 and 1.3). Both suites come from diamondiferous kimberlite-rich areas, however, and, in the case of the Brazilian stones, kimberlites have been identified upstream from the São Luiz alluvial deposit. It is quite reasonable to suppose, therefore, that both São Luiz and Guinean diamonds have been brought to the Earth's surface within kimberlite. Indeed, as has been discussed in detail in section 7.2, *whatever* the mechanism for exhumation to the base of the lithosphere, in order for diamonds to survive the last stages of exhumation, final transport within a kimberlite (or lamproite) magmatic host is almost a prerequisite. A kimberlite association does not *per se* represent an explanation for exhumation from the lower mantle, however: the question of exhumation through the bulk of the mantle can still be considered unanswered.

A number of mechanisms can be envisaged as transportation for lower mantle and transition zone diamonds through the bulk of the mantle:

- Transporation within a plume (section 7.3.1)
- Entrainment in the convective system of the upper mantle (section 7.3.2)
- A Haggerty (1994) 'superkimberlite' (section 7.3.3)

The differing models of deep diamond exhumation are presented in figure 7.3_1.

Section 7.3.1 Mantle Plumes and plume-instigated kimberlite magmatism

Three principal questions must be posed before invoking mantle plumes as a possible mechanism for the exhumation of deep mantle diamonds. What evidence is there to support the existence of mantle plumes in the first place? Can they reasonably be considered to transport material from the deep transition zone and lower mantle through the upper mantle? How does a plume exhumation mechanism fit with final exhumation via kimberlite magmatism?

Evidence for mantle plumes: A number of lines of evidence have led geologists to hypothesise the existence of large masses of material of elevated temperature upwelling through the mantle; so-called ‘mantle plumes’.

- Isolated areas of anomously large scale volcanic activity, continental flood basalts (CFB) and oceanic flood basalts (OFB), have been identified at apparently random positions over the surface of the earth.
- These extensive volcanic regions are found, commonly, to lie at the termination of chains of volcanic islands and seamounts comprising ocean island basalt (OIB). Dating of volcanics from seamounts and volcanic islands in such chains, shows an increase in age towards areas of CFB and OFB.
- Large geoid anomalies are associated with ocean island volcanism.

Modelling the process of oceanic-ridge vulcanism suggests that the typical 7km thickness of MORB is indicative of a mantle potential temperature of ~ 1530 K[1]. In contrast, however, both the huge rates of outpouring of CFB and the mineralogy of OIB, suggest that such magmatism is fed by mantle melting temperatures elevated above ‘normal’ mantle by ~ 200 K (White and McKenzie, 1989). What causes such elevated temperature?

Two hypotheses are proposed:

- Plumes don't exist and CFB are a result of some other process.

  It has been suggested that CFB results from meteoritic impact instantaneously thinning the crust and, in some cases, puncturing the lithosphere. This would undoubtedly result in massive extrusive volcanism due to decompression melting. It seems implausible, however, that meteorites coincidentaly impact with sites associated with hot spot chains. Certainly, if CFB has a

---

[1] Where the mechanical boundary layer is thinned by a factor (β-factor) of 50.

meteoritic cause, it is not clear how associated volcanic chains could last for the 100's of Ma that they appear to survive for. Additionally, no geological evidence of cratering in areas of CFB's has been found and, similarly, there is no evidence of hotspot activity related to known cratering events. It is apparent that several aspects of the geochemistry of CFB suggests that they have a subcrustal origin but it seems unlikely, that wholesale extraction of melt from the lower lithosphere, which is thought to consist of cold, anhydrous, granular peridotite, is possible. Furthermore lithosphere material is, in general[2], already depleted and so would not produce normal basalt (section 4.1).

- Plumes do exist and their initial impact on the lithosphere is manifested as CFB.
  Given the arguments against an alternative magmatic triggering, it seems inevitable that internal heat source must be envisaged for CFB production. Additionally, it seems likely, therefore, the same mechanism can also explain the presence of intrinsically linked ocean island basalts (OIB).

Given the scale of CFB and OFB activity compared to OIB volcanism, the heat souce is envisaged to involve a large, initial body; so-called plume head; quickly giving way to a more temporally extensive, narrow, heat source, the so-called plume tail. Accepting that internally sourced areas of enhanced temperature account for the presence of CFB, OFB and OIB, their initiation is now considered.

Initiation: mechanisms and source: There has been some debate as to whether plumes form at the core/mantle boundary or at the 670km discontinuity, or even the 400km discontinuity. Seismic tomography suggests that the major downwelling currents in the upper mantle are continuous but upwelling currents are not (e. g. Olson et al., 1990 and van der Hilst, 1995). As discussed in section 4.3, however, the resolution of mantle tomography is not sufficiently refined to detect narrow upwelling bodies.

Calculations appear to favour a core / mantle boundary source. Richards et al. (1989) argue that the distance of upwelling required to give sufficient momentum to enable quantities of melt of comparable size to CFB and OFB to be extruded, is consistent with evolution only from depths of the order of the core / mantle boundary. However because of uncertainties over values for mantle viscocity an upper mantle / lower mantle boundary source cannot be discounted.

In order to induce plume formation, a superdiabatic thermal boundary layer must exist in the source region; a scenario which is almost certainly relevent to the core / mantle boundary and is relevent to

---

[2] It is envisaged that metasomatism can enrich granular peridotites enough to produce small volume alkali melts but there is no evidence to suggest that such a process can go on to produce such large volumes of magma, especially over short periods of time: the entire Deccan flood basalts province is believed to have formed in 2Ma.

the upper lower mantle boundary provided a thermal boundary exists between the two (section 4.2 and as favoured by results from partitioning in São Luiz inclusions, section 4.5.1.2). Such a superadiabatic gradient may be unstable enough to cause initiation of hot rising material. The exact mechanism of this is a highly contentious issue; almost all experiments both mathematical and in viscous fluid tanks of plume propagation skip this consideration by injection of low viscocity fluid; an exception is the work by Olson et al. (1988). In this work they consider the effect of pulse heating in two dimensions. Because the fluid they considered had a temperature dependent viscosity, this pulsed heating from below was seen to form plumes but it must be kept in mind that the approximations used for this study were rather drastic; 2-dimensional modelling assuming constant rheology; furthermore it is not clear how the core would subject the lower mantle to *pulsed* heating. Nevertheless, their results show good correlation with the form of plumes envisaged from more direct plume injection experiments.

Entrainment of material during plume ascent: Geochemically, determining the make-up of plume material, even through relatively thin oceanic lithosphere, has proved to be highly problematic. This appears, in part, to be due to the fact that significant volumes of rock are incorporated into a plume during its ascent, but in varying quantities, from plume to plume, and over time (e.g. Menzies, 1992). In general, major element compositions suggest a primitive source (Campbell and Giffiths, 1990). Not surprisingly, most deviation from such compositions are seen for CFB where extensive interaction with the lithosphere has doubtless occurred (e.g. Saunders et al., 1992).

A crustal component: Of the earth's large igneous provinces (which are sourced from plume heads), CFB's show much geochemical inhomogeneity, whereas basalts from oceanic igneous provinces (OFB) have geochemical characteristics more similar to OIB than CFB (Saunders et al., 1992). Furthermore, there exists geochemical evidence from CFB to suggest that their inhomogeneity is due to incorporation of a significant crustal component[3]. It can be concluded, therefore, that plume head material *sensu stricto*, does not contain significantly more lithospheric component than plume tail material until such time as a plume head has to penetrate thick, heterogeneous[4], continental lithosphere and crust. That is not to say, however, that incorporation of material throughout ascent is unlikely. Indeed as will be discussed in terms of ascent velocity (section 7.3.4) the incorporation of a

---

[3] Trace element characteristics commonly point to crustal contamination, although this is never wholly pervasive. A large variation in εNd/ð^{87}Sr is observed amongst flood basalts but, to be explained solely by crustal contamination, would require an unreasonable 60% input (Carlson, 1991). An alternative method by which crustal signatures could be incorporated, is contamination of the mantle by subducted crust occupying the 670km layer. Amongst the evidence for a subduction component in OIB is the slight Eu anomalies detected in some EM-type OIB (Sun and McDonough, 1989). A method capable of distinguishing between these two scenarios involves Nd, Sr and Pb isotopes. Mantle contamination would result in large shifts of Nd, Sr and Pb isotopic compositions without producing the shift in oxygen that crustal contamination would cause. Due to the fact that crust does not have a standard composition, however, the argument only works in one direction. Volcanics with a mantle oxygen signature of ð^{18}O =5.4-6.9, (Harmon et al., 1987), therefore, *cannot* be cited as evidence of a lack of crustal contamination, however values outside this range *can* be cited as evidence for contamination. There is little data on ð^{18}O from OIB or CFB's; the few values obtained lying around 9 ‰: which supports most entrained material being incorporated into upwelling plumes on interaction with the crust.

certain amount of material on ascent represents an important aid to bouyancy and is thus considered a pre-requisite of plume propogation.

Mantle components: In terms of upper mantle and mantle lithosphere contamination, observations of high incompatible element concentrations have been made for many flood basalts. If the isotopic geochemistry of CFB's is closely related to lower lithosphere composition, one might expect a close geochemical correlation between mantle xenoliths and CFB's. However, this is not the case (Menzies, 1992). So perhaps these observations are indicative of a deeper component within the plume's initial material. Another feature noted from CFB's is that depleted material (δ^{87}Sr « 0.7045) occurs amongst events placed in the Palaeozoic, whereas enriched CFB (δ^{87}Sr»0.7045) are Phanerozoic. It is thought that there has not been much evolution through geological time in the lower mantle, but the upper mantle, and most importantly, the lithosphere, have evolved. Such observation can be considered to be evidence to support entrainment throughout ascent; especially the head.

In more detail, a variation in the type of magmas extruded within CFB provinces is observed to progress from early picritic, Mg-rich lavas with lithospheric trace element characteristics, to tholeiitic lavas, towards basalts with MORB characteristics. An interpretation of such time progression is that the picrites, which represent a tiny fraction of the erupted material, represent high degree melting of the shallow lithosphere by the plume impact. Later volcanism is dominated by plume material itself and subsequently, as the plume head material runs out, increased asthenosphere input leads to MORB like lavas (Carlson, 1991). An alternative explanation is provided by Campbell and Griffiths (1990) where the different types of melt represent the hot central part of the plume, main body and increasingly entrained material-rich region. Picrites from the Deccan, (Mahoney, 1988) and Karoo, (Ellam and Cox, 1989) have the strongest lithospheric signatures of any flood basalts, however, supporting the former proposal.

On the basis of evidence from plume-related volcanism discussed above, it can be considered quite plausible, therefore, that diamonds residing in the lower mantle and transition zone material could be entrained into upwelling plumes providing the plumes were sourced deep enough. Indeed, as the bulk of plume material involves the material from the source region which makes up the head, any plume will contain a sampling bias towards the initial source area. Diamond, in fact, is considered *particularly* likely to be entrained into upwelling low density material, compared to other phases, because of its exceptionally low compressibility. The density of diamond at ATP (3.50 - 3.53 gcm^{-3}) lies within the range of ATP density of upper mantle phases. Under conditions of the deep mantle

---

[4] Both compositionaly and structurally.

diamond will have significantly lower density than associated phases (see, for example, figure 7.1_22 and discussions in section 7.1). Indeed melting experiments conducted on peridotite seeded with diamond at conditions of 20 GPa, 2633K and 16 GPa, 2543K show that diamond floats in such molten material (Suzuki et al., 1995). Additionally, it is possible that there may exist a diamond-phyric region which accumulated as a crust on the top of the lower mantle. Such a contention is supported by the modelling discussed in section 7.1_2 where, in the event of a thermal boundary existing between the upper and lower mantle, there exists a region of inverted density / pressure for diamond at such depths, figure 7.1_7. If diamonds from this study *were* entrained in plume systems, the mineralogy of deep sourced inclusions from São Luiz and Guinean being mainly indicative of formation within zones stradling the upper mantle / lower mantle boundary would suggest that the associated plume had a similar source depth. Such an incorporation, however, does not preclude a relationship with deeper sourced upwelling material. In a similar fashion to the formation of kimberlite magmatism on incubation of plume material on the lithosphere, which will be discussed later, lower mantle / upper mantle boundary sourced plumes could form as a result of incubation of core / mantle sourced plumes.

Plumes and kimberlite magmatism: Study of plumes has, understandably, focussed on their direct surface manifestations; OIB, CFB and OFB. Because of the unfavourable oxygen fugacity of magmatism associatied with such manifestations however, diamond entrained into plumes which have ‘made it’ to the surface will have been burnt. What, however, of failed plumes? The initial plume impact and the extension which often is observed to result, appears to be a pained process. The highly directional influence that even the thin oceanic lithosphere has on the position of plume tail magmatism and that thicker continental lithsophere has on head impact, testifies to the difficulties involved in a plume breaking through the lithosphere[5]. It is quite conceivable that many, unseen, plumes fail to penetrate the lithosphere, particularly those which impact on thickened crust, such as is seen associated with cratons[6]. Furthermore, it is clear from the proliferation of crustal and

---

[5] There is much evidence that plume material is channelled into pre-existing thin spots (Thompson and Gibson, 1991). The centroids of vulcanism in some CFB provinces are not coincident with the hotspot positions calculated back from magnetic anomalies. This may be due to channeling of the plume head by thinspots or due to incubation (Harry and Sawyer, 1992). In the Deccan there is this lack of coincidence but it should be kept in mind that there have been a total of three known CFB events during the history of India which could have substantially weakened the lithosphere here; magmatic feeder channels perhaps acting as planes of weakness. Also the S. Atlantic centre was 600km away from the thickest of the Parana CFB's and the Iceland plume site was in C. East Greenland, 800km away from the thickest of the NATP magmatism, (Kent et al., 1992). Granted, this may be partly a function of palaeotopography, to an extent, and the size of the plume head, but it does not explain the asymetry. Perhaps this is why we see occasional continental breakup associated with plumes if magmatism is often forced into the weakest zones. There is often much vulcanism apparent before the main CFB events, 15Ma previous from the Karoo and 10Ma from Gondwana breakup (Kent et al., 1992); this points to incubation. The position of the Yellowstone plume, however, lay (at 60Ma) 500km from the main igneous centres but, since the two centres are in opposite directions from the calculated centre this supports a thinspot rather than an incubation explanation. If the hotspot was to have impacted 10Ma before eruption we should see some initial events offset further to the S.W. Furthermore, even thin oceanic lithosphere has a control on the location of surface vulcanism; hence the occurrence of discrete volcanic centres over time, eg. the Hawaiian chain, rather than a continous line of volcanism.

[6] It is probably no coincidence that CFB research shows similar head size for different events; presumably big plumes are needed to instigate continental rifting no matter what the lithosphere structure. Initial work (Kidd, 1973) showed evidence of 150 hotspots (thermal anomalies), most of which were thought to be still active, mostly manifest on the African plate which hasn't moved greatly with respect to its hotspots for a substantial period of time. Many of these hotspots show no evidence of rifting to any extent and, even though present workers would dispute such a high number (White and McKenzie, 1989) it seems that there are just as many

intermediary components in plume magmatism[7], that the host material through which plumes pass is significantly affected by their passage. Indeed there is evidence for incubation of plume heads on the lithsophere causing melting over a significant time period. Plumes which do not finally break through the lithosphere will still have the same profound heating effect on the material they impact with. Plume impacts on thick continental lithosphere should, at least, produce partial melting: melting of a type which could form kimberlite magmatism, given the appropriate host rock (Dawson, 1980). Indeed Green and Guerguen (1974) proposed a model for kimberlite magmatism triggering by some form of upwelling diapir and Wylie (1980) suggests that some form of thermal triggerring to kimberlite magmatism is mandatory. In order for kimberlite magmatism to be instigated amongst continental mantle lithosphere, it is believed that not only is a thermal induction of low degree melting required but also, some form of fertilisation of the host rock, section 7.3.2. Fertilisation need not be related *per se* to plume impingement although the resulting elevated heat flow could be envisaged to promote the movement of any metasomatising fluid. Geochemical preparation of continental lithsopheric mantle for hosting kimberlite magmatism could have occurred at any time before plume impingement and, given the commonplace ocurrence of kimberlites in cratonic regions, is probably fairly pervasive. A plume model can also be regarded as attractive from the point of view of diamond accumulation. Pervasive mantle diamond population need not be assumed, diamonds could be sourced from a fairly localised volume (the plume head protolith) and, being retained within the plume and resulting kimberlitic magmatism, kept as a concentrated population.

Location of deep diamonds in terms of surface manifestation: There are intricacies of the surface manifestations of deep diamonds additional to their absence in OIB (section 7.2) which have yet to be answered. Deep mantle sourced diamonds are found in areas related to cratons however, as table 7.3_1 summarises, they are not found in *central* cratonic settings (related to thickened lithosphere and the areas of classic lithospheric diamond production). Rather, deep mantle diamonds are dominantly found either on craton edges (eg. Otter and Gurney, 1989) or in mobile belts within (such as São Luiz) or between, cratons.

There is very little direct evidence of the particular peculiarities of off-craton oxidation state but the evidence that does exist (Luth et al., 1990) suggests that the asthenosphere in this area may be more reduced than cratonic setttings. This may further enhance the chances of deep sourced diamonds getting, at least, to the base of the lithosphere. Furthermore, the lithology of craton-edge or near-craton regions, as in regions of thick craton, is still considered to involve favourable conditions of fO_2, even on small scale melting, for the preservation of diamond. Chemically, therefore, craton

---

hotspots associated with extensive rifting as none at all. The reason for this is considered, as explained, to be due to the nature of the lithosphere above the hotspot and the size of the plume (Duncan and Richards, 1991; Müller, 1993; Saunders et al., 1992; White and McKenzie, 1989).

[7] Particularly amongst the early stages of plume history, CFB.

edge-settings can be considered to behave similarly to thick cratons in terms of their likelihood of diamond preservation. Further to this, there are structural and mathematical arguments supporting the *particular* occurrence of deep diamonds within craton edge régimes:

Cratonic settings where most diamonds are found, lie directly above thickened lithosphere so if deep stones were to infiltrate this system, then they would be hugely outnumbered by lithospheric stones. Deep diamonds could be, and are, found within such settings, such as Monastery (Moore and Gurney, 1989), but the number of such occurrences can be expected, and, indeed is found to be, exceedingly rare[8]. Mobile belts and craton-edge settings do not experience appropriate conditions for the formation of diamond: their lithospheric roots lie outwith the stability field of diamond. Any lithospheric mantle diamonds occuring in these regions would have to have been imported from elsewhere (thickened cratonic cores). As a result of the viscous nature of the lithosphere and the contention that deep cratonic sourced explosive kimerlites are likely to travel vertically than sideways, few lithospheric diamonds are expected to reach craton edges or mobile belts. Supporting this argument is the observation that most craton edge kimberlites are non-diamondiferous (eg. Dawson, 1980). This lack of lithospheric stones should allow for a greater percentage ocurrence of deep stones, in the event that they are brought to such settings. Additionally, the rheological contrast between the cratonic lithosphere and the asthenosphere can be considered an ideal conduit for percolating plume flow. Particularly in the case of mobile belts, their fractured nature would make them favourable as a conduit for magmatism and entrainment. This argument is analogous to many aspects of the debate of mantle plumes penetrating the lithosphere, as discussed above. The fact that the surface manifestation of plume impact commonly has a component of horizontal displacement from the supposed location of lithosphere impact, has proved a matter for questioning plate movement histories (White and McKenzie, 1989). This observation is, however, more likely to be due to the particular local distribution of mechanically exploitable lithosphere, (Thompson and Gibson, 1991). Similarly, why else do OIB manifestations appear as discrete volcanic centres e.g. in the case of Hawaii? Less powerful plumes such as are envisaged to carry deep diamonds can be considered *even more* likely to exploit such transport paths rather than punching significantly into the lithosphere. So even deep diamond bearing plumes impacting on craton keels, if they are energetically incapable of penetrating such areas can be considered likely to propogate along the craton base to where it is thin enough for resulting kimberlite to penetrate to the surface.

The differing scenarios of diamond production and plume propogation in relation to craton and off-craton settings discussed above are presented in figure 7.3_2.

---

[8] Inclusions from Monastery diamonds are well documented (Moore and Gurney, 1989) and yet only a single fPer inclusion has been recovered from this locality (Moore and Gurney, 1986).

Table 7.3_1 Documented occurrences of lower mantle sourced diamonds based upon studies of diamond inclusions.

Locality Ÿ	Area Type #	fPer	MgSiPvk	CaSiPvk	TAPP	Other
São Luiz *	Mobile belt (Rio-Negro Jupuena)	37	9	3	8	9
Guinea °	Off-craton? (N.W. African)	12	0	0	0	0
Letseng-la-terai ✈	Mobile belt (Lesotho)	1	0	0	0	0
Colorado †	Off-craton (Colorado)	1	0	0	0	0
Koffiefontein ¢	Off-craton (S. African)	4	1	0	0	0
Zimbabwe ¤	Mobile belt (Limpopo)	1	0	0	0	0
Monastery ¥	Cratonic (S. African)	1	0	0	0	0
Orrorroo §	Off-craton (Kimberley)	1	0	0	0	0

Ÿ Lithospheric setting from Dawson (1980) and additional references; * Present study and Tompkins (1992), see section 1.2; ° Present study and Sutherland (1993), see section 1.3; ✈ McDade and Harris (1994) † Otter and Gurney (1989): ¢ Moore et al. (1986), Koffiefontein lies some 50km from Jagersfontein which is also a source of deep diamonds (majoritic garnet association, Moore and Gurney, 1985); ¤ Kopylova et al. (1995); ¥ Moore and Gurney (1989); § Scott-Smith et al. (1984); # Craton names in parentheses; ? The location of the kimberlite source of Guinean diamonds studied herein is not known although it is considered likely to lie in the south of Guinea and, thus, in an off-craton setting.

Summary and Conclusions: The plume model, instigating kimberlitic magmatism, is considered the most likely for the transportation of São Luiz and Guinean diamonds to the Earth's surface. The popular views of plume formation and transportation are consistent with entrainment of deep Earth material and the velocities envisaged for transportation are consistent with equilibrium compositional charactersitics of São Luiz inclusions (section 7.1.4). In addition, alternative models, as discussed in section 7.1.2 and 7.1.3, invoke significant problems.

Plumes are likely to be sourced by thermal perturbations in the deep Earth; those penetrating the lithosphere being most likely sourced at the core / mantle boundary, whereas lower mantle / upper mantle boundary sourced plumes, particularly those impinging on thickened lithosphere, are most likely to produce melting at the base of the lithosphere before slowly dying. It is plumes such as the latter which are most likely to have carried São Luiz and Guinean diamonds to the base of the lithosphere, as most entrained plume material, particularly in the head, comes from the region of plume source. Following initiation, plumes rise through the mantle with a ~ 250km diameter head and thin tail, additionally incorporating some upper mantle component followed by lithospheric material; hence the occurrence of diamonds from sources from a wide range of depths amongst the São Luiz suite. The surface manifestation of the resulting plume impact on the lithosphere, if any occurs, and indeed, whether crustal breakup occurs or not, can be considered to be very much dependent on the local lithospheric structure and the size of the plume. In areas where crust is old and thick, increased incubation timescales are required[9]. Any diamonds entrained in surface-

---

[9] This period can be shortened when seperate plate driven forces facilitate rifting on upwelling.

breaking plumes will burn due to the unfavourable conditions of oxygen fugacity. In particular, for São Luiz and Guinean diamonds, plumes act primarily as carriers for material *to the base of the lithosphere* wherebye incubation causes localised melting and diamondiferous kimberlite magmatism on previously or syngenetically fertilised lithosphere.

Deep diamonds are rarely seen in cratonic setting despite fO_2 conditions being favourable, due to being completely outnumbered by the deep lithosphere diamonds seen in cratonic kimberlites. The only régime left, therefore, is the off-craton or mobile belt setting where there is a less direct route to deep lithosphere but fO_2, unlike in oceanic settings, is still favourable for diamond stability.

Section 7.3.2 *Entrainment into mantle convection and kimberlite magmatism*

An alternative explanation for the exhumation of deep mantle diamonds involves entrainment into the circulatory system of the mantle and accumulation at the base of the lithosphere; final exhumation being via kimberlitic magma. Kimberlite genetic models are introduced for completeness.

São Luiz and Guinean diamonds, circulatory entrainment and kimberlite magmatism: It is encouraging, from the point of view of entrainment of deep mantle material such as São Luiz and Guinean diamonds, that contemporary kimberlite genesis models involve some interaction between the asthenosphere and the lithosphere (see following discussion). Deep sourced diamonds entering the circulatory system of the asthenosphere could, conceivably, be incorporated into the enrichment event forming kimberlitic protolith. As discussed in section 6.1.1, however, diamond is not stable within an unlimited range of fluid compositions. A fluid rich in enough CO_2 to fertilise depleted harzburgite may be required to be even more CO_2 rich than kimberlite. Depending on conditions of pressure and temperature this could compromise the integrity of incorporated diamond. Additionally, although temperature fluctuation and fluid flow is a likely pervasive scenario for the mantle, in particular along the asthenosphere / lithosphere boundary, it is hard to imagine sudden kimberlite magmatism forming without a particular thermal perturbation (England and Houseman, 1984). Furthermore, unless some mechanism can be envisaged for concentrating deep sourced diamonds in the area of kimberlitic protolith at the time of kimberlite genesis, deep sourced diamonds must be pervasive throughout the asthenosphere[1]; otherwise, the likelihood of finding deep sourced diamonds at all in the resulting kimberlite would be negligible. Convective (and thus slow) ascent is, additionally, incompatible with the chemistry of coexisting inclusions from São Luiz (section 7.3.4). It is on the basis of these arguements that a plume transportation model for deep source diamonds (section 7.3.1) is considered more favourable. Diamond does not have to be pervasive, it does not have to be involved in the fertilisation of kimberlite protolith and, additionally, an appropriate heat source for magmatism is supplied.

Kimberlite genesis: Three hypotheses for kimberlite genesis are discussed by Dawson (1980). The first involves ascent of melt formed deep in the asthenosphere (Harris and Middlemost, 1969). On ascent, incompatible elements are continuously enriched in the liquid until the ambient temperature is low enough such that only the volatiles and particularly incompatible elements lie above the

---

[1] That is not to say, however, that pervasive deep sourced diamonds within the asthenosphere is considered implausible. Certainly, carbon is the fourth most abundant element and no other carbon bearing phase is considered paricularly likely for hosting of carbon in the asthenosphere.

solidus. Such material is considered to be kimberlite and is believed to be capable of explosive volcanism. Dawson (1980) discounts this model, particularly, on the basis that such volcanism should be far more pervasive than is observed and that it does not account for the two component make-up of natural kimberlites. A second model suggests that melting of garnet peridotite results in the formation of a picritic melt (and dunitic residue) which, subsequently, on fractional crystallisation could produce eclogite and a final residue of Si-poor alkali liquid resembling kimberlite (O'Hara and Yoder, 1967). This model can be refuted on the basis that garnet peridotite does not contain sufficient K_2O, TiO_2, CO_2 and P_2O_5 to allow for concentration to the levels seen in kimberlite. Dawson's (1980) preferred model involves small degree melting of a more appropriate kimberlite host rock. Phlogopite carbonate garnet lherzolites have been identified which can be considered ideal for the formation of kimberlite by small degree melting: the essential kimberlite components of K_2O, TiO_2, CO_2 and P_2O_5 are present in significant quantities; the presence of mica could account for the peculiar trace element characteristics of kimberlites. Furthermore, a small degree melt produced from such material, would have the appropriate fluid properties and explosive volcanic potential. Phlogopite carbonate garnet lherzolite xenoliths are rare in the nodule record, however, equally, kimberlites can hardly be regarded as common rocks. Where the phlogopite carbonate peridotites come from still has to be addressed. Wyllie (1980) would attest that such material appears as a consequence of kimberlite magmatism, in addition, more recent refinements to the kimberlite genesis model have called upon mechanisms of external enrichment of more common rock types. For the genesis of what is termed Type IA kimberlites (those sourced from central cratonic areas), Girnis et al. (1995) propose a strongly depleted harzburgite host enriched by deep seated CO_2 rich asthenospheric melts as the kimberlite source. Contemporary and detailed reviews of the subject are presented by Eggler (1989) and Wyllie (1989).

Section 7.3.3 Superkimberlites

Haggerty (1994) proposed an interesting model specifically designed at attempting to explain the exhumation of deep diamonds. At the heart of his proposal, unlike the plume model proposed in section 7.3.1, is the contention that diamonds are associated with kimberlitic-type magmatism throughout their exhumation: not solely during passage through the lithosphere.

Haggerty (1994) argues that there is a close correlation between intense kimberlite activity, basaltic magmatism and superchrons[1]. Particular peaks in kimberlite magmatism appear around 300 Ma (Permian - Pennsylvanian) and 100 Ma (Cretaceous) (references in Haggerty, 1995)[2]. Both time-periods correspond to periods of geomagnetic quiescence. In addition, the Cretaceous period witnessed intense basaltic magmatism (e. g. the Ontong-Java related ‘superplume’ of Larsen (1991)). The interplay of these observations is cited by Haggerty (1994) as evidence for a relationship between kimberlite magmatism and plume events triggered at the core / mantle boundary. Kimberlitic melts have been modelled to form at depths of the transition zone (Ringwood et al., 1993) The preferred model of Haggerty (1994), however, is that proto-kimberlites which are, essentially, komatiitic in composition, can be formed at depth into the lower mantle, related to instability at the core / mantle boundary. True kimberlitic components (CO_2, H_2O, LREE, LILE and HFSE enrichment) will only be adopted on impact with the lithosphere.

Haggerty’s (1994) model represents a hybrid between the models of section 7.3.1[3] and 7.3.2[4]. Indeed the only difference between the Haggerty (1994) model and the plume model of section 7.3.1 may lie in the use of the term ‘kimberlite’: if proto-kimberlite is simply ‘normal’ plume material, then the models are identical. Otherwise, as argued in section 7.3.1, plume triggering represents an attractive explanation not only for supply of the heat required for kimberlitic magmatism but also for the transport of deep diamonds, however, the plume material itself need not bear any compositional

---

[1] Periods of dominantly constant magnetic field sense.

[2] Although age distribution may be biased by sampling: older kimberlites are less likely, for example, to be located simply because of erosion or burial processes.

[3] Plumes represent a transferral mechanism of deep diamonds to the base of the lithosphere wherebye they are taken up by kimberlite magmatism triggered by plume heating on previously fertilised lithosphere.

[4] Diamonds are brought to the lithosphere by normal mantle convection and entrained in kimberlites magmatism.

relationship to kimberlite. Whether true kimberlite material sourced from the deep mantle occurs or not in nature, it is not believed to be a relevent proposal for transportation of São Luiz or Guinean diamonds over the entire distance from their origin to the earth’s surface. Kimberlite magmatism, due to its high volatile content, is believed to propogate extremely rapidly (of the order of ms^{-1}, Wyllie, 1980 and Dawson, 1980). It is unlikely, therefore, to incorporate significant quantities of material subsequent to its initial formation: contrary to the observation that mineral phases from a large range of depths are found in the diamonds presented herein.

Section 7.3.4 Rate of exhumation

Rate of propogation of plumes convective systems and kimberlite magmatism: Given the velocity of kimberlite propagation (Wyllie, 1980 and Dawson, 1980), the rate determining step to any effects of ascent, therefore, is the mechanism of pre-kimberlite transport.

Richards et al. (1989) have made extensive calculations based on data from many of the world's CFB provinces. By calculating CFB volumes from published data and roughly integrating over the time of extrusion from radiometric dating, they have calculated eruption rates ranging from ~0.75 to >1.5 km^3yr^{-1}. Because the geometry of the continental lithosphere is thought be significantly less homogeneous than the oceanic lithosphere, it can be assumed that the CFB rates are more a function of continental lithosphere constraints whereas OIB eruption rates reflect the velocity of transport and size of hotspots. The rate of travel of plumes is generally, therefore, best calculated by considering the eruption rates at OIB centres. Richards et al. (1989) undertook similar calculations as performed on CFB centres on OIB centres using present eruption rates[1] of 0.02 to 0.04 km^3yr^{-1}. Such surface flow rates have been incorporated in mathematical modelling and scaling of viscous fluid tank experiments in order to understanding the propagation of plumes of hot mantle material. Calculations (Whitehead and Luther, 1975 and Richards et al., 1989) based on Stoke's Law predict that a plume rising from 3000 km, with a surface lava flow[2] of $0.04km^3yr^{-1}$, would take 28 Ma to reach the lithosphere. Such a timescale is well within the range of stable hotspot activity but, if most of the plume material is incorporated from the mantle during its passage, i.e. successively less dense material, or if the plume is chemically bouyant, i.e. with a high volatile content, then propogation could take as little as 15 Ma. In practice, an equilibrium must be struck between incorporation of local material *speeding* the rising plume and resulting cooling increasing viscosity and *slowing* ascent. Given the rapid passage of kimberlitic magmatism, the minimum possible age for time of ascent of São Luiz and Guinean diamonds transported through the mantle by the preferred mechanism of a mantle plume can be considered to be 10-15 Ma.

In comparison to plume upwelling, rates of normal mantle convection although, highly dependent on the poorly constrained property of mantle viscosity, are liable to be far slower. For two layer convection, Olson et al. (1990) presents a time constant for upper mantle circulation of 1-2 Ga. In other words, on average, subducting material will take 1-2 Ga to reach the surface again by normal mantle convection. Diamonds travelling directly from the the upper mantle / lower mantle boundary to the base of the lithosphere, may be expected to take, on average, therefore, 250 - 500 Ma. Such

---

[1] The hotspots considered by Richards et al. (1989), are all of different ages, any variation in eruption rate and thus, plume travel velocity may, therefore, be a function of the age of the hotspot.

[2] Taken from Réunion data

long timescales can be considered to be especially relevent to lower mantle material which can be considered by mass balance to have entered the upper mantle at the same rate as penetration into the lower mantle of the particular subducting plates which achieve such depths.

Inferences on ascent rate by São Luiz and Guinean diamonds:

Theory: The single body of information which can be considered to best tackle the question of the rate of exhumation of São Luiz and Guinean diamonds is the relative equilibration of touching and non-touching inclusions. Given the constraints discussed in section 5.3.1, included material can be regarded as being chemically unaltered from the time of incorporation within diamond to break-out and analysis. It can, therefore, be assumed that groups of isolated inclusions will record the equilibrium conditions of partitioning of elements in the region of formation. Subject to thermodynamic and kinetic controls and the influence of temperature (such as closure temperature) and time, touching grains, although retaining a *gross* chemical sanctity, may be expected to re-equilibrate during exhumation. Any re-equilibration can be expected to adopt a range of forms.

- Temperature remained too low, diffusion rates were too slow, or rate of exhumation was so fast, that no significant opportunity for re-equilibration occurred. Such a framework would be identifiable by partition coefficients between touching phases being the same as those between non-touching phases from the same diamond.
- An intermediary scenario of partial re-equilibration where temperature was low, diffusion rates small or exhumation rate rapid, but all significant, would be manifest by compositional gradients across grain boundaries of touching grains (as distribution of elements attempts to adjust to new equilibria).
- The end-member scenario where touching grains remain, within each phase, compositionally homogeneous but record low P,T partitioning values whereas non-touching grains record different, high P, T partitioning. In such a scenario, either temperature was high enough, diffusion rates fast enough and / or exhumation rate slow enough, to allow total re-equilibration between phases.

The three scenarios discussed above could be considered powerful tools for quantifying exhumation rate however, it should be kept in mind that for such material as involved in the present study, any comments can only be qualitative. Coefficients of diffussion are not know for any element in TAPP or aluminous MgSi-Pvk. Additionally, given the uncertainties of the details of pressure and temperature histories of São Luiz inclusions, any *estimate* of diffusion rates would be subject to large error.

Discussion of results: It has been the conclusion of section 4.5.1 that the partition coefficients of coexisting inclusions released from São Luiz diamonds are, in general, consistent with equilibrium growth (e.g. figure 4.4_38). There are only slight differences between the partitioning of non-touching compared to touching inclusions, even amongst grains for which compositional re-equilibration may be expected. Additionally, the two EPMA transects and three EPMA maps (section 2.2.2) show little evidence for a compositional gradient across the grain boundaries of touching grains (section 4.5.2). Furthermore, it is important to note that, although exsolution features are in evidence for isolated majoritic garnets (section 2.2.1.3.2) none appear to have gone to completion whereby non-majoritic garnet coexists with pyroxene. The volume expansion of inclusions due to adoption of low pressure polymorphs, will be opposed by the diamond hosts. However, this cannot be considered to be an insurmountable factor. After all, what are believed to originally have been perovkite structured pyroxenes seen as inclusions in São Luiz stones, have undergone inversion to clinopyroxene structure with a subsequent expansion of cell volume.

It is not questionable that the temperature of the mantle is high, throughout (section 4.2) so observations of only partial re-equilibration are indicative of rapid exhumation. In particular, the lack of evidence for upper mantle reactions such as the full exsolution of majoritic garnets[3] may be indicative of particularly rapid exhumation as would be associated with kimberlitic eruption. It is not possible to say over what timescale such rapid exhumation would have to occur over. As mentioned before, diffusion rates are not known and the effect of diamond constriction is unclear. What can be said, however, is that, in addition to the negative points raised in section 7.3.2, the slow exhumation invoked by normal mantle convection are inconsistent with the compostional evidence from inclusion compositions. Furthermore, the 28Ma passage from the D’’ layer for a non-entraining plume (section 7.3.1) is also likely to be too slow. It would appear from inclusion compositional evidence that, at least, a rapidly rising partially entraining plume model, followed by kimberlite magmatism (section 7.3.1), must be invoked for the exhumation of São Luiz and Guinean diamonds.

---

[3] It should be noted, however, that in such regions the lower temperature and higher volume expansion on reaction would also act to prevent re-equilibration.

Chapter 8 Summary and Conclusions

The present study has confirmed an origin within the deep mantle transition zone and lower mantle for diamonds from the São Luiz alluvial deposit, Brazil, in addition to a more restricted suite from Guinea, West Africa. Summarised in the following are both the means by which a conclusion of a deep mantle source has been attained, in addition to the inferences on sub-lithospheric mantle composition which are inferred. The present study has provided indications of the oxidation state, bulk composition and phase assemblages of regions of the deep mantle transition zone and lower mantle. In addition, study of São Luiz diamond inclusions has provided constraints on both the thermal state of the upper mantle / lower mantle boundary and the nature of mantle convection.

Evidence for a deep mantle source for São Luiz and Guinean diamonds:

Inclusions have been recovered with a broadly garnet composition but also with a significant pyroxene component in solution (majoritic garnet). Si cation concentrations lie in the range of 3.08 - 3.18 (3.36 for a sub-grain in a Guinean inclusion) per 12 O anions and are representative of formation in the transition zone (Akaogi and Akimoto, 1977). Specifically, trends in major elements with varying Si-content are more consistent with the loss of majoritic component with depth on the crystallisation of perovskite structured $MgSiO_3$ and $CaSiO_3$ (Irifune and Ringwood, 1987), and indicates formation in the pressure range of 20 - 25 GPa (~560 - 690 km). Indeed trace element characteristics of one low-Ca partially majoritic garnet are transitional between the majoritic garnets in general (which show maximum REE concentrations of ~10 - 50 x C1) and garnet composition inclusions of lower mantle association. This is particularly diagnostic of crystallisation with CaSi-Pvk which shows a propensity to accommodate large concentrations (up to ~400 x C1 for LREE) in its structure.

Inclusions of $(Mg,Fe)SiO_3$ composition have been recovered from the same diamonds as (Mg,Fe)O (fPer) inclusions. Such an association is only believed to be stable under pressures of over 24 GPa (Yagi et al., 1978), within the lower mantle, where it is stabilised by the breakdown of $(Mg,Fe)_2SiO_4$ ringwoodite. Under such conditions, $(Mg,Fe)SiO_3$ adopts a perovskite structure, and, although no such structure has been found to be retained by São Luiz grains, the activation energy of back transformation to pyroxene structure is believed to be particularly low (Knittle and Jeanloz, 1987c).

The assemblage of aluminous-$MgSiO_3$ with ruby has also been recovered. Under lower mantle conditions, such an association is indicative of pressures of formation in excess of 26 GPa (Irifune et al., 1996) in relatively aluminous bulk compositions.

A single diamond has yielded an assemblage of olivine composition and fPer. Such an association (termed UM/LM) has a stability field lying between 16 and 26 GPa (Jeanloz and Thompson, 1983) dependent on bulk composition and is thus indicative of formation close to the upper mantle / lower mantle boundary.

Phases of a broadly pyrope - almandine composition and with very low CaO contents (<0.15 wt%), have been recovered from São Luiz inclusions. These grains have been shown to adopt a tetragonal $I\bar{4}2d$ structure and are previously unrecorded. They are referred to by the acronym TAPP (tetragonal almandine - pyrope phase). As garnet is a dominant phase throughout the upper mantle and has only been understood to break down in favour of an alternative (perovskite) structure under lower mantle conditions (e.g. Kesson et al., 1995) it is believed that TAPP is an intermediary phase stable close to the upper mantle - lower mantle boundary. The association of TAPP with olivine composition and fPer inclusions from a single diamond in addition to depleted trace element characteristics consistent with a coexistence with CaSi-Pvk, is consistent with such an interpretation.

Mössbauer spectroscopy of fPer inclusions has shown that they contain very low concentrations of Fe^{3+} (0.01 - 0.07 Fe^{3+}/Total Fe). McCammon (1995a) has shown that unless fO_2 is exceedingly low, such a deficiency of Fe^{3+} in fPer is indicative of formation pressures of over 18 GPa. Furthermore, SEM, EPMA and TEM analysis has shown that many fPer inclusions contain sub-micron inclusions of magnesioferrite which is consistent with conditions more oxidised than Fe-FeO, thus refuting a low pressure origin. Additional Mössbauer analyses on aluminous and non-aluminous $(Mg,Fe)SiO_3$ has yielded very large concentrations of Fe^{3+} (Fe^{3+}/Total Fe of 0.20 for 2 wt% Al_2O_3 $(Mg,Fe)SiO_3$ and 0.75 for 10 wt% Al_2O_3 $(Mg,Fe)SiO_3$). Such large concentrations are indicative of formation with a perovskite structure MgSi-Pvk (McCammon, 1997) and thus within the lower mantle.

The change in cell parameters for two fPer inclusions, one from Guinea and one from São Luiz, have been measured by XRD. On the basis of thermoelastic modelling and using published physical constants for diamond and fPer, minimum possible formation depths of ~ 300 km (depending on the geotherm used) are inferred. The diamonds however, are observed to have deformed both plastically and under brittle conditions. This deformation has been estimated and a subsequent correction to the thermoelastic models yields true formation depths within the lower mantle and up to in excess of 760 km.

Although not evidence in themselves for a deep mantle origin, features of the diamonds are consistent with high temperatures, long residence times and extreme conditions of shear. Transition zone diamonds have highly aggregated nitrogen compositions (IaB >58%), and for the few lower mantle stones which contain any nitrogen, aggregation is even more extreme (IaB >95%). Such characteristics are evidence for long residence at high temperature (Evans and Harris, 1989). Evidence for high shear stress, as would, perhaps, be encountered along the upper mantle / lower mantle boundary, comes from the observation that some diamonds showing the existence of platelets are also plastically deformed. Diamonds from other localities (e. g. Chinn et al., 1995) have consistently shown that the two features are mutually exclusive; platelets act in a similar fashion to work-hardening in metals by acting as barriers to the propagation of micro-dislocations. Work by Evans and Wild (1965) suggests that for platelet containing diamond to be deformed plastically, extreme conditions of shear are required. Furthermore, cathodoluminescence characteristics of lower mantle diamonds show complex features of growth and resorption consistent with age.

Evidence for the bulk composition of mantle regions:

Transition zone (TZ) sourced diamonds contain associations of majoritic garnet, pyrrhotite and diopside. Compositions of individual phase in addition to the phase fields they define are consistent with an eclogitic (Kushiro and Aoki, 1989) or primitive MORB composition (Green et al., 1979). The range of $\delta^{13}C$ compositions of transition zone diamonds are either indicative of two separate suites (one suite with $\delta^{13}C$ of ~ -12‰ and a less depleted suite ranging over ~ -3‰ to -8%) or else a single distribution with a negative skew. The sample population is too small to be certain, however, if the latter is the case, precipitation from a CO_2-rich fluid is envisaged. The presence of large quantities of Fe^{3+} in majoritic garnet (McCammon et al., 1995b) may also be consistent with such an interpretation.

The UM/LM association implies a bulk composition most consistent with some combination of Anderson (1989)'s solar model and a Ca-poor component such as harzburgite. It is clearly an aluminous system.

The association of fPer and Al-free $(Mg,Fe)SiO_3$ (Type I MgSi-Pvk) also involves TAPP and is termed the LM I association. The phase field defined by these three phase is consistent with a bulk composition transitional between those of a solar composition (Anderson, 1989) and a peridotitic composition. As discussed above, the oxidation state is probably reasonably high (due to the presence of 'blebs' in fPer). In terms of diamond compositional inferences for fO_2, the $\delta^{13}C$ distribution for the population as a whole is highly restricted to values around $\delta^{13}C$ = -5‰. This implies a particularly homogeneous reservoir of $\delta^{13}C$ for the lower mantle as distinct from the upper mantle. Some individual diamonds show a variation of $\delta^{13}C$ across them with a negative skew which, supports observation of high fO_2 from fPer by implying precipitation by CO_2.

The LM II association contains fPer, ruby and aluminous $(Mg,Fe)SiO_3$ (Type II MgSi-Pvk) and is consistent with a solar bulk composition but is significantly more aluminous than the LM I association.

The LM III association involves fPer, TAPP or the low Ca-majoritic garnet described above, and a previously unrecorded unrecorded C2/c structured Al-Ca-Na-Fe^{3+}-rich magnesium silicate (with 11, 5 and 6 wt% Al_2O_3, CaO and Na_2O respectively). Bulk composition has strongest affinities to eclogite or primitive MORB and Na is clearly a dominant additional component.

Although it cannot be said to what degree the São Luiz associations are representative of deep mantle compositions, they are the only material available for study. It is noteworthy that there are distinct compositional differences between associations and, in particular, a gradation from eclogitic affinity compositions for associations with transition zone or lower mantle / upper mantle boundary origins to affinities with a solar composition inferred from lower mantle associations. Furthermore, there is strong evidence to suggest that there exists a density contrast of the order of 10 % between TZ association source rock and LM I association source rock at a depth of 670 km. These observations support sufficient compositional and density differences existing between the upper and lower mantle to sustain layered convection.

Evidence for temperature:

Partitioning of Ni, Fe and Mg between fPer and Type I MgSi-Pvk yield low values of $(Fe/Mg)_{fPer}$ / $(Fe/Mg)_{MgSi\text{-}Pvk}$ of ~ 2.17 to 2.73 and $(Ni/Mg)_{fPer}$ / $(Ni/Mg)_{MgSi\text{-}Pvk}$ of ~ 6 to 17 comparison with experimental work by Malavergne et al. (1995 and 1997) and Kesson and Fitz Gerald (1991). These values, in addition to the partitioning of Fe and Mg between olivine composition and $(Mg,Fe)SiO_3$ are most consistent with formation at significantly higher temperature than 2000K and supports a steep thermal gradient between the upper and lower mantle.

Evidence for exhumation speed:

Lack of re-equilibration of major elements in composite grains, the full exsolution of majoritic garnet and the lack of dissolution of magnesioferrite into fPer is considered to be indicative of relatively rapid exhumation. The high internal pressures of occluding diamonds are also believed to play an important part in these observations. Although a timescale cannot be put on ascent from the deep mantle to the base of the lithosphere, it would seem more likely that ascent within a mantle plume of ~ 15 Ma (Richards et al., 1989) is more likely than ascent by ‘normal’ upper mantle convection over 250 - 500 Ma (Olson et al., 1990).

Other notable points:

São Luiz has revealed the first recorded sapphire inclusion in diamond from a stone with a $\delta^{13}C$ composition of -4.41 to -4.99 ‰ and $\delta^{15}N$ composition of -0.3 ‰.

Blebs of up to 5 µm in a highly Fe-rich (Mg/(Mg+Fe) = 0.36) fPer have been shown to have be Fe_4Ni alloy. Their interpretation is unclear although it may be possible that they are sourced according to the reaction: $Mg_xFe_{1-x}SiO_3 + 3[(1-x)-s]Fe = xMgSiO_3 + sSiO_2 + [3(1-x)-2s]FeO + [(1-x)-s]FeSi$ in the D’’ layer between core and lower mantle. Experimental evidence may, however, be inconsistent with such an interpretation as Ni is believed to become increasingly less siderophile with depth in the lower mantle (Malavergne et al., 1997).

Thermoelastic modelling has suggested that, particularly for diamond, and with a thermal boundary layer between the upper and lower mantle, an *increase* in density occurs with ascent in the depth region of 710 - 670 km. What this means is that diamond reaching the upper / lower mantle boundary from below will tend to accumulate in this region.

The occurrence of deep mantle diamonds within off-craton and mobile belt settings is interpreted on the basis that, in such regions fO_2 at shallow depth is still favourable for the stability of diamond (unlike oceanic and non-cratonic continental crust) but is sufficiently distinct from regions of deep lithospheric diamond source which would otherwise vastly outnumber deep mantle diamonds.

Chapter 9 Suggestions for further work

While every attempt has been made to undertake a comprehensive study of the diamonds available, due to timescales, risks and/or availability of precision analytical methodology, a number of interesting facets of study of São Luiz inclusions reside in the future domain. Additionally, details of composition of São Luiz and Guinean inclusions have prompted questions relating to deep mantle mineralogy which could be addressed by experimental petrology at high pressure and temperature.

Inclusion dating: Notwithstanding the important conclusions regarding mantle state which study of São Luiz material has so far supplied, one crucial detail remains to be addressed: that of time. As it is expected that regional variations in composition and physical conditions have evolved significantly since the earth's formation, in order for conclusions of deep mantle state from study of São Luiz material to be discussed in the context of planetary evolution, it is crucial that the age of these diamonds be determined.

The kimberlites which are believed to have hosted São Luiz diamonds are of Cretaceous age: any inferences made on deep mantle state must, therefore, relate to the Cretaceous or older. Furthermore, a number of factors *suggest* that São Luiz and Guinean diamonds are significantly older than this:

- The preferred exhumation mechanism for São Luiz diamonds is within an upwelling body of mantle elevated above ambient temperature: a mantle plume. Modelling of plume ascent rates (Richards et al., 1989) suggests exhumation over a period of ~20 Ma.
- Cathodoluminescence studies have revealed that São Luiz diamonds have undergone multiple growth and resorption events, indicative of a long history of formation.
- Although not *directly* comparable, it is noteworthy that many diamonds from *other* sources have been proven to be xenocrysts of exceptional age within their magmatic hosts (e.g. Richardson et al., 1993; Richardson et al., 1984).
- Calculations based on the thermoelastic properties of lower mantle mineral phases, suggest that, with a thermal boundary layer between the upper and lower mantles, there exists a small depth region where diamond density *decreases* with depth. Such a region would promote gravitational accumulation of diamond fed by mantle convection. As the timescales involved in mantle convection are large, diamonds, such as those from São Luiz, which are sourced from this region, are likely, on average, to be of significant age.

Indications exists, therefore, to support a pre-Cretaceous age for São Luiz diamonds, however *evidence* of inclusion age can only be supplied by direct dating methods.

Of the useful radiogenic elements, Sm, Nd, Rb, Sr and K have been measured in the present study. The most significant quantities have been found within $CaSiO_3$ composition inclusions (20 ppm K, 150 ppm Nd, 50 ppm Sm, 600 ppm Sr) with 20 ppm K also being located in $MgSiO_3$. Any dating work involves a necessity for closed-system material. As such, diamond inclusions are particularly useful as it has been shown for São Luiz material, that closed system protection on inclusion material is usually afforded by occluding diamond. Furthermore, it is not believed that the observation of compositional gradients in diamond inclusions such as found by Shimizu and Sobolev (1995) presents a problem here as this is believed to be an artefact of release by combustion (or a secondary grain boundary phase). The material, itself, therefore, is regarded as being suitable. Whether such techniques as are available at present are applicable to the material available, however, is questionable. Most isotopic techniques (e.g. Richardson et al., 1993) require significantly larger quantities of material than are practically available. São Luiz inclusions are both small in number, and in size (at most 500 μm in diameter but typically ~80 μm), indeed only a single $CaSiO_3$ is available for study. Dating which *has* been attempted (Harris, 1993 *personal communication*), involved a very significant proportion of the inclusion population (majoritic garnets) and concluded in ambiguous results. It is hoped that with the ongoing development of milliprobe techniques such as by Burgess et al. (1992 and 1995) results may be attainable without a heavy burden on the sample population in the future.

Helium isotope determination: It is a matter of extensive debate whether the lower mantle convects separately from the upper mantle and, additionally, at what time in relation to mantle degassing and crust formation, any separation occurred. An important means to answer these questions lies in identifying whether compositional differences exist between the upper and lower mantle. Major element compositions of inclusions from the present study have suggested that such a compositional difference does exist (section 4.4.2). Another useful indicator would be measurement of He in diamond hosts. Some authors believe that there is evidence to suggest that He, an element whose isotopes will have been fractionated on degassing, yields a different value in upper mantle rocks compared to lower mantle rocks (Verchovsky and Begemann, 1993). Indeed, study of OIB (assumed to be lower mantle material) yields $^4He/^3He$ values of ~25000 compared to high values of ~86000 from MORB (Allègre et al., 1993). It is questionable, however, whether measurements on OIB are particularly reliable as an indicator of lower mantle He isotopic composition because of the unknown factor of an upper mantle component in OIB. A better means to determining lower mantle He isotopic composition lies in measuring its composition in unaltered lower mantle material such as São Luiz diamonds.

He is a common component in diamond and can be measured with accuracy. Furthermore, because it is also believed to diffuse very slowly (Ozima, 1989), measurement of the He composition of São Luiz diamonds is expected to yield a reliable lower mantle composition. There exist, however, a number of potential problems.

The isotopic content of He in diamond is subject to significant readjustment by interaction of cosmogenic influx. This means that the He isotopic content of alluvial diamonds, or diamonds associated with the first ~20m of kimberlite host, of which São Luiz diamonds are representative, cannot be considered 'uncontaminated'. After extensive discussion with Burgess, R. (1995, *personal communication*), especially as He isotopic fractionation between diamond and melt is unconstrained, analysis was not considered practical under the present framework. It is, however, considered possible that any cosmogenic component can be separated from the mantle component. Cosmogenic He will be associated with significant defects and thus is likely to be released first, on graphitisation step-heating (Harper, 1996 *personal communication*). Because of the multiple growth histories of deep mantle diamonds, care would be required to use only lower mantle precipitated diamond. The most suitable material, thus, would be diamond of the deepest possible association (LM II) with homogeneous cathodoluminescence characteristics. Isotopic analysis is envisaged to proceed by step heating gas mass spectrometry although milliprobe techniques may be appropriate. It is expected that this project will involve techniques at the forefront of the science; its feasibility, being, therefore, dependent on discussion and feedback from suitable laboratories.

Identification of blebs in fPer: Significant inroads have been made into the identification of blebs in fPer inclusions as magnesioferrite. One particular important question still remains; whether or not fPer which *don't* show blebs under BS-SEM *do* contain blebs but at sub-SEM resolution. The presence of magnesioferrite provides an insight into lower mantle oxidation state (more so than the ferric iron content of fPer and MgSi-Pvk, which are largely independent of fO_2 conditions at high pressure, McCammon et al., 1997). Furthermore, with fPer being such an important lower mantle phase, the presence of significant inclusion material within it has important implications for the conductivity of the lower mantle (Duba and Wanamaker, 1994). It is believed, therefore, that this is a question which merits resolving. Indeed an attempt was instigated but met with organisational boundaries.

Further internal pressure measurement: A framework now exists (chapter 7) for assessing the significance of internal pressures imposed by diamond on all included transition zone and lower mantle phases (with the exception of TAPP), in addition to their low pressure polymorphs. Although the expansion of fPer inclusions (sections 3.3 and 7.1.5) represents a cornerstone of proof for a deep origin for some São Luiz and Guinean diamonds, it is expected that this can be consolidated by study of, as-yet, unbroken stones.

Search for perovskite-structured inclusions in lower mantle diamonds: It is believed that one of the unique characteristics of the lower mantle is that a significant number of its dominant mineral species exist as high-pressure perovksite structured polymorphs of pyroxenes (e. g. Liu, 1976). Identification of perovskite structured $MgSiO_3$, for example, therefore, would be irrefutable evidence for a lower mantle origin. The back transformation of perovskite structured pyroxenes to low pressure polymorphs, however, has a small activation energy (Knittle and Jeanloz, 1987) and so discovery of perovskite structured material in most mantle material is expected to be exceptionally unlikely. The elevated pressures which can be imposed by diamond make diamond inclusions the most likely source of perovskite-structure retaining lower mantle material. Although extensive structural study during the present work has kept the possibility of discovering perovskite structures in mind, none have been forthcoming. It is believed, however, that opportunity does still exist for such a discovery, particularly amongst colourless inclusions with a large diamond to inclusion volume ratio.

TEM studies of reverted high pressure phases: X-Ray studies of a number of São Luiz inclusions have shown that they are polycrystalline (section 3.2): a crystallographic arrangement which is consistent with regression from high pressure polymorphs. Furthermore, partitioning of Fe and Mg with fPer is consistent with olivine composition and MgSi-Pvk composition inclusions having initially crystallised as ringwoodite and perovskite structures respectively. Additionally, the amorphous nature of SiO_2 inclusions (section 2.2.1.2) may also be cited as evidence for regression from a high pressure phase (in this case, stishovite). TEM represents a further technique for the searching for evidence of polymorphic regression. Grains having undergone regression will show small scale textures which can imaged by TEM. This technique has been utilised in the identification of regressed MgSi-Pvk (Sharp et al., 1997) and could equally be applied to São Luiz inclusions. At the present stage, the rareity of, in particular olivine composition inclusions, combined with the risks involved in TEM preparation make such a project unfeasible. On recovery of further samples, however, such study would be an important additional means to investigate original high pressure origins for São Luiz and Guinean inclusions.

Thermoelastic properties of TAPP: The determination of thermoelastic properties of deep mantle phases has allowed for significant advances to be made in the prediction of the bulk properties of deep mantle material (e.g. Ringwood and Irifune, 1988). Additionally, comparison can be made with lithospheric material taken to depth, in an attempt to predict the behaviour of subducted slabs. A significant gap in present knowledge is the thermoelastic properties of TAPP, which remains the only known lower mantle phase for which first order thermoelastic properties are unconstrained. Given that indications from São Luiz material suggest that TAPP is an important phase in, at least, some regions of the lower mantle close to the upper mantle boundary, its presence has an important bearing on the behaviour of subducted material. Determination of the physical constants of TAPP can, therefore, be considered to be essential in future modelling of the physical properties of the deep mantle. Additionally, values for the bulk modulus of TAPP and its pressure derivative would provide central components to arguments relating to the relative stability of TAPP and garnet in the deep earth.

Attempt is being made to investigate the thermoelastic properties of TAPP (BZ244B) by Brouillon scattering (Conrad, P., Carnegie Institution). At the time of writing, however, results have not been forthcoming.

Synthsesis of TAPP: Given the question of the role of Al in the lower mantle and the importance of TAPP within lower mantle assemblages from São Luiz inclusions (section 2.2.1.3.3), it would seem imperative to attempt a synthesis of TAPP. Its synthesis would allow for quantitative constraint of its stability within the deep earth, which has important implications for all the physical and chemical properties of this region. It is notable that care would be taken during synthesis to emulate the high ferric iron content which is observed in São Luiz TAPP inclusions (section 2.5.1.2). Depending on the success of synthesis of TAPP using a TAPP bulk composition, a natural progression would be an attempt to reproduce the lower mantle association of TAPP with fPer and / or perovskite-structured $MgSiO_3$.

Determination of phase relations in the system FMNACS (Na_2O-CaO-Al_2O_3-SiO_2-MgO-FeO): The role of Na and Ca under conditions of the lower mantle have, not so far, been addressed by experimental petrology. The existence of unique pyroxene compositions amongst São Luiz inclusions (Type III pyroxene, section 2.2.1.5), indicates that at least in some regions of the lower mantle, most likely near the lower mantle / upper mantle boundary, Na_2O and CaO are important components. Experimental petrology could be expected to answer questions regarding the stability of Type III pyroxene as well as the partitioning of Na_2O and CaO with other phases.

Investigation of structural control over a Eu anomaly in CaSi-Pvk: The positive Eu anomaly detected in São Luiz inclusions (section 2.2.1.6) can be considered to be indicative either of a Eu excess in the host rock or a particular effect of the structure of CaSi-Pvk and oxidation conditions of the lower mantle (section 4.4.2.4). This question could be resolved by the synthesis of CaSi-Pvk from appropriate mantle compositions (e.g. MORB or pyrolite) doped with REE and under a range of fO_2 conditions.

Guinean diamonds: Results from the present study have shown the Guinean suite of diamonds to have many factors in common with São Luiz stones. Further study of Guinean diamonds is clearly merited and is presently being undertaken by Stachel (Institut fuer Mineralogie, Frankfurt).

References

A B C D E F G H I J K L M N O P Q R S T U V W X Y Z

Ackermann R. and Sorrell, C. (1974) Thermal expansion and the high-low transformation in quartz I. High-temperature X-Ray studies *J. Appl. Crystallog.* **7**, 461-467

Ahmed-Zaïd, I. and Madon, M. (1995) Electron microscopy of high-pressure phases synthesised from natural garnets in a diamond anvil cell: implications for the mineralogy of the lower mantle *Earth Planet. Sci. Lett.* **129**, 233-247

Ahrens, T. and Graham, E. (1972) A shock-induced phase change in iron-silicate garnet *Earth Planet. Sci. Lett.* **14**, 87-90

Akaogi, M and Akimoto, S. (1977) Pyroxene - garnet solid solution equilibria in the systems $Mg_4Si_4O_{12}$ - $Mg_3Al_2Si_4O_{12}$ and $Fe_4Si_4O_{12}$ - $Fe_3Al_2Si_4O_{12}$ at high pressures and temperatures *Phys. Earth Planetary Interiors* **15**, 90-106

Akaogi, M., Ross, N. L., McMillan, P. and Navrotsky, A. (1984) The Mg_2SiO_4 polymorphs (olivine, modified spinel and spinel)-Thermodynamic properties from oxide melt solution calorimetry, phase relation and models of lattice vibrations *Amer. Mineral.* **69**, 499-512

Akaogi, M., Navrotsky, A., Yagi, T. and Akimoto, S. (1987) Pyroxene-garnet transformation: thermochemistry and elasticity of garnet solid solutions and applications to a pyrolite mantle *High Pressure Research in Mineral Physics (Ed.. Manghnani, M. H. and Syono, Y. TERRAPUB, Tokyo)* 251-260

Akimoto, S. (1972) The system MgO-FeO-SiO_2 at high pressures and temperatures: Phase equilibrium and elastic properties *Tectonophys.* **13**, 161-187

Akimoto, S. and Syono, Y. (1972) High pressure transformations in $MnSiO_3$ *Amer. Mineral.* **57**, 76-84

Akimoto, S., Matsui, Y. and Syono, Y. (1976) High pressure crystal chemistry of orthosilicates and formation of the mantle transition zone *Physics and Chemistry of Minerals. and Rocks (Ed.. Strens, R. J. D. Wiley, New York)* 327-363

Aldebert, P. and Traverse, J. (1984) αAl_2O_3: A high-temperature thermal expansion standard *High Temperature-High Pressure* **16**, 127-135

Allègre, C. J., Sarda, P. and Staudacher, T. (1993) Speculations about the cosmic origin of He and Ne in the interior of the Earth *Earth Planet. Sci. Lett.* **117**, 229-233

Allègre, C. J., Poirier, J-P., Humler, E. and Hofmann, A. W. (1995) The chemical composition of the Earth *Earth Planet. Sci. Lett.* **134**, 515-526

Anastasiou, P. and Seifert, F. (1972) Solid solubility of Al_2O_3 in enstatite at high temperatures and 1-5 kb water pressure *Contrib. Mineral. Petrol.* **34**, 272-287

Anderson, D. L. (1977) Composition of the mantle and core *Annual Rev. Earth Planetary Sci.* **5**, 179-202

Anderson, D. (1981) Hotspots, basalts and the evolution of the mantle *Science* **213**, 82-89

Anderson, D. (1982) The earth's core and phase diagram of iron *Phil. Trans. Roy. Soc. London* **A306**, 21-35

Anderson, D. (1989) Composition of the earth *Science* **243**, 367-370

Anderson, D. and Bass, J. (1986) Transition Region of the Earth’s Upper Mantle *Nature* **320**, 321-328

Anderson, O. (1967) Equation for thermal expansivity in planetary interiors *J. Geophys. Res.* **72**, 3661-3668

Anderson, O. L. and Isaak, D. G. (1995) Elastic constants of mantle minerals at high temperatures *AGU Ref. 2 Mineral Physics and Crystallography: A Handbook of Physical Constants (Ed.. Ahrens, T. J. AGU, Washington)* 64-97

Anderson, O. and Masuda, K. (1994) A thermodynamic method for computing thermal expansivity, α, versus T along isobars for silicate perovskite *Phys. Earth Planetary Interiors* **85**, 227-236

Anderson, O. L., Masuda, K. and Guo, D. (1995) Pure silicate perovskite and the PREM lower mantle model: a thermodynamic analysis *Phys. Earth Planetary Interiors* **89**, 35-49

Angel, R. (1992) Order-disorder and the high-pressure P1-I1 transition in anorthite *Amer. Mineral.* **77**, 923-929

Angel, R. J., Chopelas, A. and Ross, N. L. (1992a) Stability of high-density clinoenstatite at upper-mantle pressures *Nature* **358**, 322-324

Angel, R. J., Ross, N. L., Wood, I. G. and Woods, P. A. (1992b) Single-crystal X-Ray diffraction at high pressures with diamond-anvil cells *Phase Transitions* **39**, 13-32

Angus, J. and Hayman, C. (1988) Low-pressure, metastable growth of diamond and ‘diamond-like’ phases *Science* **241**, 913-921

Arculus, R. J. and Delano, J. W. (1987) Oxidation state of the upper mantle: present conditions, evolution and controls *Mantle Xenoliths (Ed.. Nixon Wiley, Chichester)* 589-598

Arima, M., Nakayama, K., Akaishi, M., Yamaoka, S. and Kanda, H. (1993) Crystallisation of diamond from a silicate melt of kimberlite composition in high-pressure and high-temperature *Geology* **21**, 968-970

Armbruster, T., Geiger, C. A. and Lager, G. A. (1992) Single crystal X-ray structure study of synthetic pyrope almandine garnets at 100 and 293K *Amer. Mineral.* **77**, 512-521

Arndt, N. T. (1977) Ultrabasic Magmas and High-Degree Melting of the Mantle *Contrib. Mineral. Petrol.* **64**, 205-221

Ashida, T., Kume, S., Ito, E. and Navrotsky, A. (1988) $MgSiO_3$ Ilmenite: heat capacity, thermal expansivity and enthalpy of transformation *Phys. Chem. Mineral.* **16**, 239-245

Azbel, I., Tolstikhin, I. N., Kramers, J. D., Pechernikova, G. V. and Vityazev, A. V. (1993) Core growth and siderophile element depletion of the mantle during homogeneous earth accretion *Geochim. Cosmochim. Acta* **57**, 2889-2898

Babuska V., Fiala, J., Kumazawa, M. and Ohno, I. (1978) Elastic properties of garnet solid solution series *Phys. Earth Planetary Interiors* **16**, 157-176

Bachmann, P. K., Leers, D. and Lydtin, H. (1991) Towards a general concept of diamond chemical vapour deposition *Diamond and Related Materials* **1**, 1

Bai, Q. and Kohlstedt, D. (1993) Effects of chemical environments on the solubility and incorporation mechanisms for hydrogen in olivine *Phys. Chem. Mineral.* **19**, 460-471

Bajt, S., Sutton, S. R. and Delaney, J. S. (1994) X-ray microprobe analysis of iron oxidation-states in silicates and oxides using x-ray-absorption near-edge structure (XANES) *Geochim. Cosmochim. Acta* **58**, 5209-5214

Baker, M. B., Hirschmann, M. M., Ghiorso, M. S. and Stolper, E. M. (1995) Composition of near-solidus peridotite melts from experiments and thermodynamic calculations *Nature* **375**, 308-311

Ballhaus, C. (1993) Redox states of lithospheric and asthenospheric upper mantle *Contrib. Mineral. Petrol.* **114**, 331-348

Ballhaus, C. and Ellis, D. (1996) Mobility of core melts during Earth’s accretion *Earth Planet. Sci. Lett.* **143**, 1-4

Ballhaus, C., Berry, R. F. and Green, D. H. (1990) Oxygen fugacity controls in the earth's upper mantle *Nature* **348**, 437-440

Ballhaus, C., Berry, R. F. and Green, D. H. (1991) High pressure experimental calibration of the olivine-orthopyroxene-spinel oxygen geobarometer: implications for the oxidation state of the upper mantle *Contrib. Mineral. Petrol.* **107**, 27-40

Bashir, N., Beckett, J., Hutcheon, I and Stolper E. (1996) Carbon in the metal of iron meteorites *Abstracts of papers submitted to the Lunar and Planetary Science Conference* **27**, 63-64

Bass, J. (1995) Elasticity of Minerals, Glasses and Melts *AGU Ref. 2 Mineral Physics and Crystallography: A Handbook of Physical Constants (Ed.. Ahrens, T. J. AGU, Washington)* 45-63

Bass, J. and Kanzaki, M. (1990) Elasticity of a majorite-pyrope solid solution *Geophys. Res. Lett.* **17**, 1989-1992

Bassett, W. and Barnett, J. (1970) Isothermal compression of Stishovite and coesite up to 85 kilobars at room temperature by x-ray diffraction *Phys. Earth Planetary Interiors* **3**, 45-60

Beattie, P. (1993a) Uranium thorium disequilibria and partitioning on melting of garnet peridotite *Nature* **363**, 63-65

Beattie, P. (1993b) On the occurrence of apparent non-Henry's Law behaviour in experimental partitioning studies *Geochim. Cosmochim. Acta* **57**, 47-55

Bell, P. M., Yagi, T. and Mao, H. K. (1979) Iron-Magnesium distribution coefficients between spinel [$(Mg,Fe)_2SiO_4$], magnesiowüstite [(Mg,Fe)O] and perovskite [$(Mg,Fe)SiO_3$] *Carnegie Institution of Washington Year Book* **78**, 618-621

Berger, J., Berthon, J., Revcolevschi, A. and Jolles, E. (1981) Elastic constants of $Fe_{1-x}O$ single crystals *J. Amer. Ceramic Soc.* **64**, 153-154

Bibby, D. (1982) Impurities in Natural Diamond *Chemistry and Physics of Carbon (Ed.. Thrower, P. A. Marcel Dekker, Inc. New York)* 1-91

Bickle, M. J. (1986) Implications of melting for stabilisation of the lithosphere and heat-loss in the Archean *Earth Planet. Sci. Lett.* **80**, 314-324

Binns, R., Davis, R. and Reed, S. (1969) Ringwoodite, natural $(Mg,Fe)_2SiO_4$ spinel in the Tenham meteorite *Nature* **221**, 943-944

Birch, A. F. (1952) Elasticity and constitution of the earth’s interior *J. Geophys. Res.* **57**, 227-286

Birch, A. F. (1961) Composition of the earth’s mantle *Geophys. J. Roy. Astronom. Soc.* **48**, 295-311

Bishop, F., Smith, J. and Dawson, B. (1978) Na, K, P and Ti in garnet, pyroxene and olivine from peridotite and eclogite xenoliths from African kimberlites *Lithos* **11**, 155-173

Blacic, J. D., Mathez, E. A., Maggiore, C., Mitchell, T. E. and Fogel, R. (1991) Oxygen in diamond by the nuclear microprobe: analytical technique and initial results *Extended abstracts of the fifth international kimberlite conference, Brazil, (1991) CPRM, Rio de Janeiro* 20-22

Blundy, J. and Wood, B. (1994) Prediction of crystal-melt partition coefficients from elastic moduli *Nature* **372**, 452-454

Boctor, N. and Boyd, F. (1979) Distribution of rare earth elements in perovskite from kimberlites *Carnegie Institution of Washington Year Book* **78**, 372-374

Boehler, R. (1992) Melting of the Fe-FeO and the Fe-FeS systems at high pressure - constraints on core temperatures *Earth Planet. Sci. Lett.* **111**, 217-227

Boehler, R. (1993) Temperatures in the Earth's core form melting-point measurements of iron at high static pressures *Nature* **363**, 534-536

Boehler, R., Vonbargen, N. and Chopelas, A. (1990) Melting, thermal-expansion, and phase-transitions of iron at high-pressures *J. Geophys. Res.* **95**, 21731-21736

Bonczar, L. and Graham, E. (1982) The pressure dependence of the elastic properties of polycrystal magnesiowüstite *J. Geophys. Res.* **87**, 1061-1078

Bonczar, L. and Graham, E. (1997) The pressure and temperature dependence of the elastic constants of pyrope garnet *J. Geophys. Res.* **82**, 2529-2534

Bouaziz, S. and D’Arco, Ph. (1993) Pseudopotential periodic Hartree-Fock study of Mg_2SiO_4 polymorphs: olivine, modified spinel, spinel *Phys. Chem. Mineral.* **20**, 333-340

Boyd, F. (1970) Garnet peridotites and the system $CaSiO_3$-$MgSiO_3$-Al_2O_3 *Mineralogical Society of America Spec. Paper* **3**, 63-75

Boyd, F. R. and England, J. L. (1964) The system enstatite-pyrope *Carnegie Institution of Washington Year Book* **63**, 157-161

Boyd, F. and Finnerty, A. (1980) Conditions of origin of natural diamonds of peridotite affinity *J. Geophys. Res.* **85,** 6911-6918

Boyd, S. and Pillinger, C. (1994) A preliminary study of $^{15}N/^{14}N$ in octahedral growth form diamonds *Chem. Geol.* **116**, 43-59

Boyd, S., Mattey, D., Pillinger, C., Milledge, H., Mendelssohn, M. and Seal, M. (1987) Multiple growth events during diamond genesis: an integrated study of carbon and nitrogen isotopes and nitrogen aggregation state in coated stones *Earth Planet. Sci. Lett.* **86**, 341-353

Boyd, S. R., Pillinger, H. J., Milledge, H. J., Mendelssohn, M. J. and Seal, M. (1988) Fractionation of nitrogen isotopes in a synthetic diamond of mixed crystal habit *Nat*ure **331**, 604-607

Boyd, S. R., Pillinger, H. J., Milledge, H. J., Mendelssohn, M. J. and Seal, M. (1992) C and N isotopic composition and the infrared absorption spectra of coated diamonds: evidence for the regional uniformity of CO_2-H_2O rich fluids in lithosphere mantle *Earth Planet. Sci. Lett.* **109**, 633-644

Boyd, S. R., Kiflawi, I. and Woods, G. S. (1994a) The relationship between infrared absorption and the A defect concentration in diamond *Phil. Mag.* **B 69**, 1149-1153

Boyd, S. R., Pineau, F. and Javoy, M. (1994b) Modelling the growth of natural diamonds *Chem. Geol.* **116**, 29-42

Boyd, S. R., Kiflawi, I. and Woods, G. S. (1995a) Infrared absorption by the B nitrogen aggregate in diamond *Phil. Mag.* **B 72**, 351-361

Boyd, S., Rejou-Michel, A. and Javoy, M. (1995b) Improved techniques for the extraction, purification and quantification of nanomole quantities of nitrogen gas: the nitrogen content of diamond. *Meas. Sci. Technol.* **6**, 297-305

Brey, G., Dovoslev, A. and Koganko, L. (1991) The join pyrope-knorringite: experimental constraints for a new geothermobarometer for coexisting garnet and spinel *Extended abstracts of the fifth international kimberlite conference, Brazil, (1991) CPRM, Rio de Janeiro* 26-28

Brovkin, A. A., Novoselov, Y. M. and Kitsul, V. I. (1975) Distribution of aluminium in the crystal structure of high-alumina hypersthene *Dokl. Akad. Nauk SSSR* **223**, 148-150

Brown, J. and Shankland, T. (1981) Thermodynamic parameters in the earth as determined from seismic profiles *Geophys. J. Roy. Astronom. Soc.* **6**, 579-596

Bundy, F. P., Hall, H. T., Strong, H. M. and Wentorf, R. H. (1955) Man-made diamonds *Nature* **176**, 51-55

Bunge, H-P., Richards, M. and Baumgardner, J. (1996) Effect of depth-dependent viscosity on the planform of mantle convection *Nature* **379**, 436-438

Burgess, R., Turner, G. and Harris, J. W. (1992) ^{40}Ar-^{39}Ar laser probe studies of clinopyroxene inclusions in eclogitic diamonds *Geochim. Cosmochim. Acta* **56**, 389-402

Burgess, R., Turner, G. and Harris, J. W. (1997) ^{40}Ar^{39}Ar dating of diamonds *Mineral Deposits Studies Group A. G. M. Programme with Abstracts (Eds., Hall, A. J. et al., University of Glasgow, Glasgow)* 14-15

Burns, R. and Solberg, T. (1990) ^{57}Fe-bearing oxide, silicate and aluminosilicate minerals *Spectroscopic characterisation of minerals and their surfaces (Ed. Coyne et al. American Chemical Society, Washington DC)* 262-283

Burton, K. W., Matthew, K. J., Cohen, A. S. and O'Nions, R. K. (1995) The relative diffusion of Pb, Nd, Sr and O in garnet *Earth Planet. Sci. Lett.* **133**, 199-211

Cadek, O., Yuen, D., Steinbach, V., Chopelas, A. and Matayska, C. (1994) Lower mantle thermal structure deduced from seismic tomography, mineral physics and numerical modelling *Earth Planet. Sci. Lett.* **121**, 385-402

Campbell, I. H. and Griffiths, R. W. (1990) Implications of mantle plume structure for the evolution of flood basalts *Earth Planet. Sci. Lett.* **99**, 79-93

Campbell, I. H., Griffiths, R. W. and Hill, R. I. (1989) Melting in an Archean mantle plume: heads its basalts, tails its komatiites *Nature* **339**, 697-699

Campbell, L. S., Henderson, P., Wall, F. and Nielsen, T. F. D. (1997) Rare earth chemistry of perovskite group minerals from the Gardiner Complex, East Greenland *Mineral. Mag.* **61**, 197-212

Canil, D. (1990) Experimental study bearing on the absence of carbonate in mantle-derived xenoliths *Geology* **18**, 1011-1013

Caporuscio, F. and Smyth, J. (1990) Trace element crystal chemistry of mantle eclogites *Contrib. Mineral. Petrol.* **105**, 550-561

Carlson, R.W. (1991) Physical and Chemical evidence on the cause and source characteristics of flood basalt vulcanism *Austral. J. Earth Sci.* **38**, 525-544

Carlson, W. and Lindsley, D. (1988) Thermochemistry of pyroxenes on the join $Mg_2Si_2O_6$ - $CaMgSi_2O_6$ *Amer. Mineral.* **73**, 242-252

Carter, R. (1959) Thermal expansion of $MgFe_2O_4$, FeO and $Mg_{0.2}FeO$ *J. Amer. Ceram. Soc.* **42**, 324-327

Cartigny, P., Boyd, S., Harris, J. W. and Javoy, M. (1996) Nitrogen isotopic composition of diamonds from Fuxian, China *J. Conf. Abs.* **1**, 97

Cassé, M., Lehoucq, R. and Vangioniflam, E. (1995) Production and evolution of light-elements in active star-forming regions *Nature*, **373,** 318-319

Chang, Z. and Barsch, G. (1977) Elastic properties of oxides in the NaCl structure *J. Geophys. Res.* **74**, 3291-3294

Chen, M., Sharp, T. G., Elgoresy, A., Wopenka, B. and Xie, X. D. (1996) The majorite-pyrope + magnesiowüstite assemblage: constraints on the history of shock veins in chondrites *Science* **271**, 1570-1573

Chinn, I., Gurney, J. J., Milledge, H. J., Taylor, W. R. and Woods, P. A. (1995) Cathodoluminescence of CO_2-bearing and CO_2-free diamonds from the George Creek kimberlite dyke, Colorado-Wyoming State Line District *Extended Abstracts of the 6th International Kimberlite Conference, UIGMM, Novosibirsk*, 116-117

Chopelas A., Boehler, R. and Ko, T. (1994) Thermodynamics and behaviour of γ-Mg_2SiO_4 at high pressure: Implications for Mg_2SiO_4 phase equilibrium *Phys. Chem. Mineral.* **21**, 351-359

Chung, D. (1970) Effects of iron/magnesium ratio on P and S wave velocities in olivine *J. Geophys. Res.* **75**, 7353-7361

Chung, D. (1974) General relationships among sound speeds: I New experimental information *Phys. Earth Planetary Interiors* **8**, 113-120

Clark, J. R., Appleman, D. E. and Papike, J. J. (1969) Crystal-chemical characterization of clinopyroxene based on eight new structure refinements *Geol. Soc. Amer. Spec. Paper* **2**, 31-50.

Clarke, L. B. and Le Bas, M. J. (1990) Magma mixing and metasomatic reaction in silicate carbonate liquids at the Kruidfontein carbonatitic volcanic complex, Transvaal *Mineral. Mag.* **54**, 45-56

Clayton, R. N. and Mayeda, T. K. (1984) Oxygen isotopic compositions of Enstatite chondrites and Aubrites *J. Geophys. Res.* **89,** 245-249

Clemens, J. (1993) Experimental evidence against CO_2-promoted deep crustal melting *Nature* **363**, 336-338

Cohen, R., E. (1987) Elasticity and equation of state $MgSiO_3$ perovskite *Geophys. Res. Lett.* **14**, 1053-1056

Cohen, R. (1991) Bonding and elasticity of stishovite SiO_2 at high pressure: Linearised augmented plane wave calculations *Amer. Mineral.* **76**, 733-742

Comodi, P., Princivalle, F., Tirone, M. and Zanazzi, P. F. (1995) Comparative compressibility of clinopyroxenes from mantle nodules *Eur. J. Mineral.* **7**, 141-149

Cordier, P., Liebermann, R. C., Raterron, P. and Wang, Y. (1996) T.E.M. study of silicate garnet deformed in a multi-anvil high-pressure apparatus *EMPG-VI Abs. Suppl. 1 to TERRA Nova* **8**, 14

Craig, H. (1957) Isotopic standards for carbon and oxygen and correction factors for mass-spectrometric analysis of carbon dioxide *Geochim. Cosmochim. Acta* **12**, 133-149

Creager, K., C. and Jordan, T., H. (1984) Slab penetration into the lower mantle *J. Geophys. Res.* **89**, 3031-3049

Cynn, H., Isaak, D. G., Cohen, R. E., Nicol, M. F. and Anderson, O. L. (1990) A high-pressure phase transition of corundum predicted by the potential induced breathing model *Amer. Mineral.* **75**, 439-442

D'Amour, H., Schiferl, D., Denner, W., Schultz, H. and Holzapfel, W. B. (1978) High pressure single-crystal structure determinations for ruby up to 90 kbar using an automatic diffractometer *J. Appl. Phys.* **49**, 4411-4416

D'Arco P., Silvi, B., Roetti, C. and Orlndo, R. (1991) Comparative study of spinel compounds: a pseudopotential periodic Hartree-Fock calculation of Mg_2SiO_4, Mg_2GeO_4, Al_2MgO_4, Ga_2MgO_4 *J. Geophys. Res.* **96**, 6107-6112

D’Arco, Ph., Sandrone, G., Dovesi, R., Aprà, E. and Saunders, V. R. (1993) A quantum mechanical study of the perovskite structure type of $MgSiO_3$ *Phys. Chem. Mineral.* **20**, 407-414

D'Arco, Ph, Sandrone, G., Aprà, E. and Saunders, V. R. (1994) A quantum-mechanical study of the relative stability under pressure of $MgSiO_3$-ilmenite, $MgSiO_3$-perovskite and MgO-periclase + SiO_2-stishovite assemblage *Phys. Chem. Mineral.* **21**, 285-293

Dalton, J. and Wood, B. (1993) The partitioning of Fe and Mg between olivine and carbonate and the stability of carbonate under mantle conditions *Contrib. Mineral. Petrol.* **114**, 501-509

Dalton, J. and Wood, B. (1995) The stability of carbonate under upper-mantle conditions as a function of temperature and oxygen fugacity *Eur. J. Mineral.* **7**, 883-891

Daniels, L. R. M. (1991) Diamonds and related minerals from the Dokolwayo kimberlite, Swaziland *Unpublished PhD thesis, University of Cape Town*

Daniels, L. R. M. and Gurney, J. J. (1991) Oxygen fugacity constraints on the southern African lithosphere *Contrib. Mineral. Petrol.* **108**, 154-161

Daniels, L. R. M., Richardson, S. H., Menzies, A. H., de Bruin, D. and Gurney, J. J. (1995) Diamondiferous garnet macrocrysts in the Newlands kimberlite, South Africa - Rosetta stones from the Kaapvaal craton keel *Extended Abstracts of the 6th International Kimberlite Conference, UIGMM, Novosibirsk*, 121-123

Daniels, L. R. M., Gurney, J. J. and Harte, B. (1996) A crustal mineral in a mantle diamond *Nature* **379**, 153-156

Davies, G. (1976) The A nitrogen aggregate in diamond - its symmetry and possible structure *J. Phys.* **C9**, L537-L542

Davies, G. (1979) Cathodoluminescence *The properties of diamond (Ed.. Field, J. E. Academic Press, London)* 165-181

Davies, G. and Richards, M (1992) Mantle Convection *J. Geol.* **100**, 151-206

Davies, G., Nixon, P., Pearson, D. and Obata, M. (1993) Tectonic implications of graphitised diamonds from the Ronda peridotite massif, southern Spain *Geology* **21**, 471-474

Davy, H. (1814) Some experiments on the combustion of the diamond and other carbonaceous substances *Phil. Trans.* **104**, 557-570

Dawson, J. B. (1980) Kimberlites and their xenoliths *Springer-Verlag, Berlin*

De Vita, A., Galli, G., Canning, A. and Car, R. (1996) A microscopic model for surface-induced diamond to graphite transitions *Nature* **379**, 523-526

De Vries, R. C. (1975) Plastic deformation and "work hardening" of diamond *Materials Res. Bull.* **10**, 1193-1200

Deer, W., Howie, R. and Zussman, J. (1983) An introduction to the Rock Forming Minerals *Longman, Harlow*

Deines, P. (1980) The carbon isotopic composition of diamonds: relationships to diamond shape, colour, occurrence and vapour composition *Geochim. Cosmochim. Acta* **44**, 943-961

Deines, P. and Harris, J. W. (1995) Sulfide inclusion chemistry and carbon isotopes of African diamonds *Geochim. Cosmochim. Acta* **59**, 3173-3188

Deines, P. and Wickman, F. (1973) The isotopic composition of 'graphitic' carbon from iron meteorites and some remarks on the troilitic sulfur of iron meteorites *Geochim. Cosmochim. Acta* **37**, 1295-1319

Deines, P. and Wickman, F. (1975) A contribution to the stable carbon isotope geochemistry of iron meteorites *Geochim. Cosmochim. Acta* **39**, 547-557

Deines, P., Gurney, J. J. and Harris, J. W. (1984) Associated chemical and carbon isotopic composition variations in diamonds from Finsch and Premier kimberlites, South Africa *Geochim. Cosmochim. Acta* **48**, 325-342

Deines, P., Harris, J. W. and Gurney, J. J. (1987) Carbon isotopic composition, nitrogen content and inclusion composition of diamonds from the Roberts Victor kimberlite, South Africa: evidence for ^{13}C depletion in the mantle *Geochim. Cosmochim. Acta* **51**, 1227-1243

Deines, P., Harris, J., Spear, P. and Gurney, J. (1989) Nitrogen and ^{13}C content of Finsch and Premier diamonds and their implications *Geochim. Cosmochim. Acta* **53**, 1367-1378

Deines, P., Harris, J. W. and Gurney, J. J. (1991) The carbon isotopic composition and nitrogen content of lithospheric and asthenospheric diamonds from the Jagersfontein and Koffiefontein kimberlite, South Africa *Geochim. Cosmochim. Acta* **55**, 2615-2625

Deines, P. D., Harris, J. W. and Gurney, J. J. (1993) Depth-related carbon isotope and nitrogen concentration variability in the mantle below the Orapa kimberlite, Botswana, Africa *Geochim. Cosmochim. Acta* **57**, 2781-2796

Ding, X-Y and Grand, S. (1994) Seismic structure of the deep Kurile subduction zone *J. Geophys. Res.* **99**, 23767-23786

Downes, H. (1990) Shear zones in the upper mantle - relation between geochemical enrichment and deformation in mantle peridotites *Geology* **18,** 374-377

Downs, R. T., Bartelmehs, K. B., Gibbs, G. V. and Boisen, M. B. Jr. (1993) Interactive Software for Calculating and Displaying X-Ray or Neutron Powder Diffraction Patterns of Crystalline Materials *Amer. Mineral.* **78**, 1104-1107

Dowty, E. and Lindlsey, D. H. (1973) Mössbauer spectral study of synthetic hedenbergite - ferosilite pyroxenes *Amer. Mineral.* **71**, 955-965

Duba, A. (1992) Earth's core not so hot *Nature* **359**, 197-198

Duba, A. (1994a) Comment on change of electrical conductivity of olivine associated with the olivine-spinel transformation *Phys. Earth Planetary Interiors* **82**, 75-77

Duba, A. (1994b) Iron - What is melt? *High Pressure Science and Technology-1993 (Eds. Schmidt, S. C. et al., AIP Press, New York)* 923-926

Duba, A. and Vondergönna, J. (1994) Comment on change of electrical-conductivity of olivine associated with the olivine spinel transition *Phys. Earth Planetary Interiors* **82,** 75-77

Duba, A. and Wanamaker, B. (1994) DAC measurement of perovskite conductivity and implications for the distribution of mineral phases in the lower mantle *Geophys. Res. Lett.* **21**, 1643-1646

Duffy, T. and Anderson, D. (1989) Seismic velocities in mantle minerals and the mineralogy of the upper mantle *J. Geophys. Res.* **94**, 1895-1912

Duffy, T. S., Zha, C-s., Downs, R. T., Mao, H-k. and Hemley, R. J. (1995) Elasticity of forsterite to 16 GPa and the composition of the upper mantle *Nature* **378**, 170-173

Dumas, J. and Stas, J. (1840) Recherches sur le véritable poids atomique du carbone *Comptes Rendus Paris* **11**, 991-1020

Duncan, R. A. and Richards, M. A. (1991) Hotspots, mantle plumes, flood basalts and true polar wander *Rev. Geophys.* **29**, 31-50

Dupré, B. and Allègre, C. J. (1980) Pb-Sr-Nd isotopic correlation and the chemistry of the North Atlantic mantle *Nature* **286**, 17-22

Dziewonski, A. M. and Anderson, D. L. (1981) Prelimenary reference earth model *Phys. Earth Planetary Interiors* **25**, 297-356

Dziewonski, A. M., Hales, A. L. and Lapwood, E. R. (1975) Parametrically simple Earth models consistent with geophysical data *Phys. Earth Planetary Interiors* **10**, 12-48

Eggler, D. H. (1987) Solubility of major and trace elements in mantle metasomatic fluids: experimental constraints *Mantle Metasomatism (Eds. Menzies, M. A. and Hawkesworth, C. J. Academic Press, London)* 21-41

Eggler, D. H. (1989) Kimberlites: how do they form? *Kimberlites and Related Rocks Vol. 2 (Eds. Ross, J. et al., Blackwell Science Publications, Carlton)* 489-504

Eggler, D. and Lorand, P. (1994) Sulfides, diamonds and mantle fO_2 *Proceedings of the fifth international kimberlite conference, Brazil: Diamonds: Characterisation, Genesis and Exploration (Volume 2) CPRM, Rio de Janeiro* 160-169

Eggler, D. H., Lorand, J. P. and Meyer, H. O. A. (1991) Sulphides, diamonds, mantle fO_2 and recycling *Extended abstracts of the fifth international kimberlite conference, Brazil, (1991) CPRM, Rio de Janeiro* 88-91

Eldridge, C. S., Compston, W., Williams, I. S., Harris, J. W. and Bristow, J. W. (1991) Isotope evidence for the involvement of recycled sediments in diamond formation *Nature* **353**, 649-653

Ellam, R. M. (1992) Lithospheric thickness as a control on basalt geochemistry *Geology* **20**, 153-156

Ellam, R. N. and Cox, K. G. (1989) A Proterozoic lithospheric source for Karoo magmatism; evidence from the Nuanetsi picrites *Earth Planet. Sci. Lett.* **92**, 207-218

Ellis, D. and Green D. (1979) An experimental study of the effect of Ca upon garnet-clinopyroxene Fe-Mg exchange equilibria *Contrib. Mineral. Petrol.* **71**, 13-22

Ellsworth, K. and Schubert, G. (1988) Numerical models of thermally and mechanically coupled two-layer convection in highly viscous fluids *Geophys. J. Int.* **93**, 347-363

Elsasser, W. M., Olson, P. and Marsh, B. D. (1979) The depth of mantle convection *J. Geophys. Res.* **84**, 147-155

England, P. and Houseman, G. (1984) On the geodynamic setting of kimberlite genesis *Earth Planet. Sci. Lett.* **67,** 109-122

England, P. and Jackson, J. (1987) Migration of the seismic - aseismic transition during uniform and nonuniform extension of the continental lithosphere *Geology* **15**, 291-294

Evans, T. (1976) Diamonds *Contemporary Phys.* **17**, 45-70

Evans, T. and Harris, J. W. (1989) Nitrogen aggregation, inclusion equilibrium temperatures and the age of diamonds *Kimberlites and Related Rocks Vol. 2 (Eds. Ross, J. et al., Blackwell Science Publications, Carlton)* 1001-1006

Evans, T. and Phaal, C. (1962) Imperfections in Type I and Type II diamonds *Proc. Roy. Soc. London* **A270**, 538-552

Evans, T. and Wild, R. K. (1965) Plastic bending in diamond plates *Phil. Mag.* **12**, 479-489

Farber, D. L., Williams, Q. and Ryerson, F. J. (1994) Diffusion in Mg_2SiO_4 polymorphs and chemical heterogeneity in the mantle transition zone *Nature* **371**, 693-695

Farges, F., Guyot, F., Andrault, D. and Wang, Y. (1994) Local structure around Fe in $Mg_{0.9}Fe_{0.1}SiO_3$ perovskite: An X-Ray absorption spectroscopy study at Fe-K edge *Eur. J. Mineral.* **6**, 303-312

Farquar, J. and Chacko, T. (1994) Exsolution-enhanced oxygen exchange: implications for oxygen isotope closure temperatures in minerals *Geology* **22**, 751-754

Fei, Y. and Mao, H-k. (1994) In-situ determination of the NiAs phase of FeO at high pressure and temperature *Science* **266**, 1678-1680

Fei, Y. and Saxena, S. (1986) A thermochemical database for phase equilibria in the system Fe-Mg-Si-O at high-pressure and temperature *Phys. Chem. Mineral.* **13**, 311-324

Fei, Y., Saxena, S. K. and Navrotsky, A. (1990) Internally consistent thermodynamic data and equilibrium phase relations in the system $MgO-SiO_2$ at high pressure and temperature *J. Geophys. Res.* **95**, 6915-6928

Fei, Y., Mao, H-K. and Mysen, B. O. (1991) Experimental determination of element partitioning and calculation of phase relations in the $MgO-FeO-SiO_2$ system at high pressure and high temperature *J. Geophys. Res.* **96, B2**, 2157-2169

Fei, Y., Mao, H-K., Shu, J. and Hu, J. (1992) P-V-T Equation of state of magnesiowüstite $(Mg_{0.6}Fe_{0.4})O$ *Phys. Chem. Mineral.* **18**, 416-422

Fei, Y., Virgo, D., Mysen, B. O., Wang, Y. and Mao, H. K. (1994) Temperature-dependent electron delocalisation on $(Mg,Fe)SiO_3$ perovskite *Amer. Mineral.* **79**, 826-837

Field, J. (1979) Strength and fracture properties of diamond *Properties of Diamond (Ed.. Field, Academic Press, London)* 281-324

Field, S. and Haggerty, S. (1994) Symplectites in upper mantle peridotites: development and implications for the growth of subsolidus garnet, pyroxene and spinel *Contrib. Mineral. Petrol.* **118**, 138-156

Finger, L. W., Hazen, R. M., Zhang, J., Ko, J. and Navrotsky, A. (1993) The effect of Fe on the crystal structure of wadsleyite β-$(Mg_{1-x}Fe_x)SiO_4$, $0.00 \leq x \leq 0.4$ *Phys. Chem. Mineral.* **20**,361-368

Finnerty, A. and Boyd, F. (1987) Thermobarometry from garnet peridotites: basis for the determination of thermal and compositional structure of the upper mantle *Mantle Xenoliths (Ed.. Nixon Wiley, Chichester)* 381-402

Fipke, C. E., Dummett, H. T., Moore, R. O., Carlson, J. A., Ashley, R. M., Gurney, J. J. and Kirkley, M. B. (1995) History of the discovery of diamondiferous kimberlites in the Northwest Territories, Canada *Extended Abstracts of the 6th International Kimberlite Conference, UIGMM, Novosibirsk,* 158-160

Fitton, J. G. and James, D. (1986) Basic volcanism associated with intraplate linear features *Phil. Trans. Roy. Soc. London* **A317**, 253-266

Foster, P. and Welch, A. (1956) Metal oxide solutions: I. Lattice constants and phase relations in ferrous oxide (wüstite) and in solid solutions of ferrous oxide and manganous oxide *Trans. Faraday Soc.* **52**, 1626-1634

Frenklach, M., Skokov, S. and Weiner, B. (1994) An atomistic model for stepped diamond growth *Nature* **372**, 535-537

Friedman, I. and O'Neill, J. R. (1977) Compilation of the stable isotope formation factors of geochemical interest *Data of Geochemistry Sixth Edition (Ed.. Fleischer, M. Geol. Survey Prof. Paper)* **440**

Frisillo, A. and Barsch, G. (1972) Measurement of single-crystal elastic constants of bronzite as a function of pressure and temperature *J. Geophys. Res.* **77**, 6360-6384

Frondel, C. and Marvin, U. (1967) Londsdaleite, a hexagonal polymorph of diamond *Nature* **214**, 587-589

Frost, D. J. and Wood, B. (1997) Experimental measurements of the fugacity of CO_2 and graphite/diamond stability from 35 to 77 kbar at 925 - 1650ºC *Geochim. Cosmochim. Acta* **61**, 1565-1574

Fujino, K., Sasaki, S., Takeuchi, Y. and Sadanaga, R. (1981) X-Ray determination of electron distributions in forsterite, fayalite and tephroite *Acta Crystallog.* **B37**, 513-518

Fujino, K., Momoi, H., Sawamoto, H. and Kumazawa, M. (1986) Crystal structure and chemistry of $MnSiO_3$ tetragonal garnet *Amer. Mineral.* **71**, 781-785

Fukunaga, K., Matsuda, J., Nagao, K., Miyamoto, M and Ito, K. (1987) Noble gas enrichment in vapour-growth diamonds and the origin of diamonds in ureilites *Nature* **328**, 141-143

Funamori, N., Yagi, T., Utsumi, W., Kondo, T. and Uchida, T. (1996) Thermoelastic properties of $MgSiO_3$ perovskite determined by in-situ X-Ray observations up to 30 GPa and 2000 K *J. Geophys. Res.* **101**, 8257-8269

Fung, A. and Haggerty, S. (1995) Petrography and mineral compositions of eclogites from the Koidu kimberlite complex, Sierra Leone *J. Geophys. Res.* **100 B10**, 20451-20473

Gandolfi, G. (1967) Discussion upon methods to obtain x-ray 'powder patterns' from a single crystal *Miner. Petrogr. Acta* **13**, 67-74

Garzanti, E. (1993) Himalayan ironstones, "superplumes," and the breakup of Gondwana *Geology* **21**, 105-108

Gasparik, T. (1989) Transformation of enstatite-diopside-jadeite pyroxenes to garnet *Contrib. Mineral. Petrol.* **102**, 389-405

Gasparik, T. (1990) Phase relations in the transition zone *J. Geophys. Res.* **95 B10**, 15751-15769

Gasparik, T. and Drake, M. (1995) Partitioning of elements among two silicate perovskites, superphase B and volatile-bearing melt at 23 GPa and 1500-1600°C *Earth Planet. Sci. Lett.* **134**, 307-318

Gasparik, T., Wolf, K. and Smith, C. M. (1994) Experimental determination of phase relations in the $CaSiO_3$ system from 8 to 15 GPa *Amer. Mineral.* **79**, 1219-1222

Gautron, L. and Madon, M. (1994) A study of the stability of anorthite in the PT conditions of earth's transition zone *Earth Planet. Sci. Lett.* **125**, 281-291

Giardini, A. A. and Tydings, J. E. (1962) Diamond synthesis: observations on the mechanism of formation *Amer. Mineral.* **47**, 1393-1421

Girnis, A. V., Brey, G. P. and Ryabchikov, I. D. (1995) Origin of group 1A kimberlites: Fluid-saturated melting experiments at 45-55 kbar *Earth Planet. Sci. Lett.* **134**, 283-296

Gong, Z., Cohen, R. E. and Boyer, L. L. (1991) Molecular dynamics simulations of melting of MgO at high pressures *Carnegie Institution of Washington Year Book,* **90,** 129-134

Goresy, A., Zinner, E. and Martl, K. (1995) Survival of isotopically heterogeneous graphite in a differentiated meteorite *Nature* **373**, 496-499

Goto, T., Anderson, O. L., Ohno, I. and Yamamoto, S. (1989) Elastic constants of corundum up to 1825K, single crystal aluminium oxide *J. Geophys. Res.* **94**, 7588-7602

Graham, E. and Ahrens, T. (1973) Shock wave compression of iron-silicate garnet *J. Geophys. Res.* **78**, 375-392

Graham, E. and Barsch, G. (1969) Elastic constants of single crystal forsterite as a function of temperature and pressure *J. Geophys. Res.* **74**, 5949-5960

Graham E. K., Schwab, J. A., Sopkin, S. M. and Takei, H. (1988) The pressure and temperature dependence of the elastic properties of single crystal fayalite Fe_2SiO_4 *Phys. Chem. Mineral.* **16**, 186-198

Grand, S. (1994) Mantle shear structure beneath the Americas and surrounding oceans *J. Geophys. Res.* **99**, 11591-11621

Green, D., Hibberson, W., and Jaques, A. (1979) Petrogenesis of mid-ocean ridge basalts *The Earth: its origin, structure and evolution (Ed. McElhinny Academic Press, London)* 265-299

Green, H. II and Gueguen, Y. (1974) Origin of kimberlite pipes by diapiric upwelling in the upper mantle *Nature* **249**, 617-620

Green, T. (1996) Experimental versus natural two-mineral partition coefficients - a 'high-tech' controversy *J. Conf. Abs.* **1**, 213

Griffen, D. T., Hatch, D. M., Phillips, W. R. and Kulaksiz, S. (1992) Crystal chemistry and symmetry of a birefringent tetragonal pyralspite$_{75}$-grandite$_{25}$ garnet *Amer. Mineral.* **77**, 399-406

Griffin, W., Jaques, A., Sie, S., Ryan, C., Cousens, D. and Suter, G. (1988) Conditions of diamond growth: a proton microprobe study of inclusions in West Australia diamonds *Contrib. Mineral. Petrol.* **99**, 143-158

Griffin, W. L., Gurney, J. J. and Ryan, C. G. (1992) Variation in trapping temperatures and trace elements in peridotite-suite inclusions from African diamonds: evidence for two inclusion suites and implications for lithosphere stratigraphy *Contrib. Mineral. Petrol.* **110**, 1-15

Griffiths, R.W., Gurnis, M. and Eitelberg, G. (1989) Holographic measurements of surface topography on laboratory models of mantle hotspots *Geophys. J.* **96**, 477-495

Gromet, P., Dymek, R., Haskine, L. and Korotev, L. (1984) The 'North American Shale composite': Its compilation, major and trace element characteristics *Geochim. Cosmochim. Acta* **48**, 2469-2482

Grover, R., Getting, I. C. and Kennedy, G. C. (1973) Simple compressibility relation for solids *Phys. Rev. B Cond. Matter* **7**, 567

Gundmundsson, G. and Wood, B. (1995) Experimental tests of garnet peridotite oxygen barometry *Contrib. Mineral. Petrol.* **119**, 56-67

Gurney, J. J. (1984) A correlation between garnets and diamonds in kimberlite *Kimberlite Occurrence and Origin (Eds. Glover and Harris, P. G., Publication No. 8, University of Western Australia, Perth)* 143-166

Gurney, J. J. (1989) Diamonds *Kimberlites and Related Rocks Vol. 2 (Eds. Ross, J. et al., Blackwell Science Publications, Carlton)* 935-965

Gurney, J. J. (1990) The diamondiferous roots of our wandering continent *S. Afr. J. Geol.* **93**, 423-437

Gurney, J. J., Harris, J. W. and Rickard, R. S. (1984) Silicate and oxide inclusions in diamonds from the Orapa Mine, Botswana *Kimberlites II, The mantle and crust-mantle relationships (Ed.. Kornprobst, J., Elsevier, Amsterdam)* 3-9

Guyot, F., Madon, M., Peyronneau, J. and Poirier, J P. (1988) X-ray microanalysis of high pressure / high temperature phases synthesised from natural olivine in a diamond anvil cell *Earth Planet. Sci. Lett.* **90**, 52-64

Gwanmesia, G. D., Ridgen, S., Jackson, I. and Liebermann, R.(1990) Pressure dependence of elastic wave velocity for β-Mg_2SiO_4 and the composition of the earth's mantle *Science* **250**, 794-797

Hager, B. H. and Richards, M. A. (1989) Long wave-length variations in earth's geoid - physical models and dynamical implications *Phil. Trans. Roy. Soc. London* **A328**, 309-327

Haggerty, S. (1976) Opaque mineral oxides in terrestrial igneous rocks *Oxide Minerals (Ed.. Rumble III Mineralogical Society of America Southern Publishing Company, Blacksburg)* 101, 300

Haggerty, S. (1986) Diamond genesis in a multi-constrained model *Nature* **320**, 34-38

Haggerty, S. (1990) Redox state of the continental lithosphere *Continental Mantle (Ed.. Menzies Clarendon Press, Oxford)* 87-109

Haggerty, S. (1994) Superkimberlites: a geodynamic window to the earth's core *Earth Planet. Sci. Lett.* **122**, 57-69

Haggerty, S. and Sautter, V. (1990) Ultradeep (Greater than 300 kilometres), ultramafic upper mantle xenoliths *Science* **248**, 993-996

Haggerty, S. E., Fung, A. T. and Burt, D. M. (1994) Apatite, phosphorus and titanium in eclogitic garnet from the upper mantle *Geophys. Res. Lett.* **21**, 1699-1702

Hamilton, W. B. (1993) Evolution of Archean mantle and crust *The Geology of North America v.C-2 Precambrian: Coterminous U.S. (Eds. Reed Jr. et al., Geol. Soc. Amer., Boulder)* 597-614

Harmon, R. S. (1987) $^{18}O/^{16}O$ Ratios in anhydrous spinel lherzolite xenoliths from the Shavaryn-Tasman volcano, Mongolia *Earth Planet. Sci. Lett.* **81,** 193-202

Harris, J. W. (1992) Diamond Geology *The properties of natural and synthetic diamond (Ed. Field, Academic Press, London)* 325-393

Harris, J. W. and Gurney, J. (1979) Inclusions in diamond *Properties of diamond (Ed.. Field, Academic Press, London)* 555-594

Harris, J. W., Milledge, H. J., Barron, T. H. K. and Munn, R. W. (1970) Thermal expansion of garnets included in diamond *J. Geophys. Res.* **75**, 5775-5794

Harris, J. W., Hutchison, M., Hursthouse, M., Light, M. and Harte, B. (1997) A new tetragonal silicate mineral from the lower mantle *Nature* **387**, 486-488

Harris, P. G. and Middlemost, E. A. K. (1969) The evolution of kimberlites *Lithos* **3**, 77-88

Harry, D. L. and Sawyer, D. S. (1992) Basaltic volcanism, mantle plumes, and the mechanisms of rifting: The Paraná flood basalt province of South America *Geology* **20**, 207-210

Hart R., Damarupurshad, A., Sellschopp, J., Meyer, H., McCallum, M. and Koeberi, C. (1993) The trace element analysis of single diamond crystal by neutron activation analysis *Extended Abs EUG* **(1993)**, 163-166

Hart, S. and Zindler, A. (1988) Constraints on the nature and development of chemical heterogeneities in the mantle *Mantle convection: plate tectonics and global dynamics (Ed.. Peltier, W. R., Gordon and Bread Science Publishers, London)* 262-387

Harte, B. (1992) Trace element characteristics of deep-seated eclogitic parageneses - an ion microprobe study of inclusions in diamonds *V. M. Goldschmidt Conference: Programme and Abstracts (The Geochemical Society, U.S.A.)* A-48

Harte, B. and Harris, J. W. (1993), Lower mantle inclusions from diamonds *Terra Nova* **5** *Abstract Supplement* **1**, 101

Harte, B. and Harris, J. (1994) Lower mantle mineral associations preserved in diamonds *Mineral. Mag.* **58A**, 384-385

Harte, B. and Hawkesworth, C. (1987) Mantle domains and mantle xenoliths *Kimberlites and Related Rocks Vol. 2 (Eds. Ross, J. et al., Blackwell Science Publications, Carlton)* 649-683

Harte, B. and Kirkley, M. B. (1997) Partitioning of trace elements between clinopyroxene and garnet: data from mantle eclogites *Chem. Geol.* **136**, 1-24

Harte, B. and Otter, M. (1992) Carbon isotope measurements on diamonds *Chem. Geol.* **101**, 177-183

Harte, B., Gurney, J. J. and Harris, J. W. (1980) The formation of peridotitic suite inclusions in diamond *Contrib. Mineral. Petrol.* **72**, 181-190

Harte, B., Mathews, B., Winterburn, P. and Gurney, J. (1991) Aspects of melt composition, crystallisation, metasomatism and distribution shown by mantle xenoliths from the Matsoku kimberlite pipe *Extended abstracts of the fifth international kimberlite conference, Brazil, (1991) CPRM, Rio de Janeiro* 167-169

Harte, B., Hutchison, M. T. and Harris, J. W. (1994) Trace element characteristics of the lower mantle: an ion probe study of inclusions in diamonds from São Luiz, Brazil *Mineral. Mag.* **58A**, 386-387

Harte, B., Fitzsimons, I. C. W. and Kinny, P. D. (1996a) Clinopyroxene-garnet trace element partition coefficients for mantle peridotite and melt assemblages *J. Conf. Abs.* **1**, 235

Harte, B., Harris, J. W. and Hutchison, M. T. (1996b) Mineral associations in diamonds from across the mantle transition zone *Advanced Materials '96: New trends in High Pressure Research (National Institute for High Pressure Research in Inorganic Materials, Tsukuba)* 81-86

Hauri, E. H., Zhang, J., Herzberg, C. and Fei, Y. (1996) Trace element partitioning at high pressures: New ion probe results and implications for differentiation of a terrestrial magma ocean *J. Conf. Abs.* **1**, 241

Hawkins, J. W., Bloomer, S. H., Evans, C. A. and Melchoir, J. T. (1983) Evolution of intra-oceanic arc-trench systems *Tectonophys.* **102**, 175-205

Hawthorne, F. C. (1988) Mössbauer Spectroscopy *Spectroscopic Methods in Mineralogy and Geology (Ed. Hawthorne, F. C. Mineral. Soc. Amer., Washington)* 255-340

Hazen, R. (1976a) Effect of temperature and pressure on the crystal structure of forsterite *Amer. Mineral.* **61**, 1280-1293

Hazen, R. (1976b) Effects of temperature and pressure on the cell dimension and X-Ray temperature factors of periclase *Amer. Mineral.* **61**, 266-271

Hazen, R. and Finger, L. (1978) Crystal structure and compressibilities of pyrope and grossular to 60kbar *Amer. Mineral.* **63**, 297-303

Hazen, R. M., Downs, R. T., Finger, L., Conrad, P. G. and Gasparik, T. (1994) Crystal chemistry of Ca-bearing majorite *Amer. Mineral.* **79**, 581-584

Hearman, R. (1979) The elastic constants of crystal and other anisotropic material *Landolt-Börnstein Tables III/11 (Ed.. Hellwege and Hellwege Springer-Verlag, Berlin)* 1-244

Hearman, R. (1984) The elastic constants of crystal and other anisotropic material *Landolt-Börnstein Tables III/18 (Eds. Hellwege and Hellwege, Springer-Verlag, Berlin)* 1-154

Heinz, D. and Jeanloz, R. (1987) Measurement of the melting curve of $Mg_{0.9}Fe_{0.1}SiO_3$ at lower mantle conditions and its geophysical implications *J. Geophys. Res.* **92, B11**, 11437-11444

Hemley, R. J., Jackson, M. D. and Gordon, R. G. (1987) Theoretical study of the structure, lattice dynamics and equation of state of perovskite-type $MgSiO_3$ and $CaSiO_3$ *Phys. Chem. Mineral.* **14**, 2-12

Hemley, R J., Strixude, L., Fei, Y. and Mao, H. K. (1992) Constraints on lower mantle composition from P, V, T measurements of $(Fe,Mg)SiO_3$-perovskite and (Fe,Mg)O *High pressure research: Application to Earth and Planetary sciences (Eds. Syono, Y. and Manghnani, M. H., Terra Scientific, Tokyo)* 183-189

Hentschel, B. (1970) Stoichiometric FeO as metastable intermediate of decomposition of wüstite at 225°C *Z. Naturforsch* **25a**, 1996-1997

Hervig, R. L., Smith, J. V., Steele, I. M., Gurney, J. J., Meyer, H. O. A. and Harris, J. W. (1980) Diamonds: Minor elements in silicate inclusions: Pressure-Temperature implications *J. Geophys. Res.* **85 B12**, 6919-6929

Hervig, R., Smith, J. and Dawson, B. (1986) Lherzolite xenoliths in kimberlites and basalts: petrogenetic and crystallochemical significance of some minor and trace elements in olivine, pyroxenes, garnet and spinel *Trans. Roy. Soc., Edinburgh: Earth Sci.* **77**, 181-201

Herzberg, C. (1984) Chemical stratification in the silicate earth *Earth Planet. Sci. Lett.* **67**, 249-260

Herzberg, C. and Zhang, J. (1996) Melting experiments on anhydrous peridotite KLB-1: Compositions of magmas in the upper mantle and transition zone *J. Geophys. Res.* **101**, 8271-8295

Hildebrand, P. R. and Gurney, J. J. (1995) Lithosphere evolution in rifted, craton and mobile belt environments from Zimbabwe and implications for diamond prospectivity *Extended Abstracts of the 6th International Kimberlite Conference, UIGMM, Novosibirsk*, 236-238

Hill, R. I. (1991) Starting plumes and continental break-up *Earth Planet. Sci. Lett.* **104**, 398-416

Hill, S. (1989) A study of diamonds from the Star kimberlite, Orange Free State, South Africa *Unpublished M. S. Thesis, University of Cape Town*

Hirsch, P. B., Hutchison, J. L. and Titmarsh, J. (1986) Voidites in diamond Evidence for a crystalline phase containing nitrogen *Phil. Mag. A* **54**, L49-L54

Hoal, B., Hoal, K., Boyd, F. and Pearson D. G. (1995) Tectonic settings and mantle composition inferred from peridotitic xenoliths, Gibeon kimberlite field, Namibia *Extended Abstracts of the 6th International*

Kimberlite Conference, UIGMM, Novosibirsk, 239-241

Hoal, K., Hoal, B., Erlank, A. J. and Shimizu, N. (1994) Metasomatism of the mantle lithosphere recorded by rare earth elements in garnets *Earth Planet. Sci. Lett.* **126**, 303-313

Hoernle, K., Zhang, Y-S. and Graham, D. (1995) Seismic and geochemical evidence for large-scale mantle upwelling beneath the eastern Atlantic and western and central Europe *Nature* **374**, 34-39

Höfer, H. E., Schulz-Dobrik, B., Brey, G. and Oberhänsli (1993) The determination of the oxidation state of iron by electron microprobe analysis *Abs. Suppl. 1 to TERRA Nova* **5,** 508

Höfer, H. E., Brey, G. P., Schulz-Dobrick, B. and Oberhänsli, R. (1994), The determination of oxidation state of iron by the electron microprobe *Eur J. Min.* **6**, 407-418

Hofmann, A. (1997) Mantle geochemistry: the message from oceanic volcanism *Nature* **385**, 219-229

Hofmann, A. W. and White, W. N. (1982) Mantle plumes from ancient oceanic-crust *Earth Planet. Sci. Lett.* **57**, 421

Hofmann, A. W., Jochum, K. P., Seufert, M. and White, W. M. (1986) Nd and Pb in oceanic basalts: new constraints on mantle evolution *Earth Planet. Sci. Lett.* **79**, 33-45

Holland, T. and Powell, R. (1990) An enlarged and updated internally consistent thermodynamic dataset with uncertainties and correlations: The system K_2O-Na_2O-CaO-MgO-MnO-FeO-Fe_2O_3-Al_2O_3-TiO_2-SiO_2-C-H_2-O_2 *Journal of Metamorphic Geology* **8**, 89-124

Honda, M., McDougall, I., Patterson, D. B., Doulgeris, A. and Clague, D. A. (1993) Noble gases in submarine pillow basalt glasses from Loihi and Killauea, Hawaii: A solar component in the earth *Geochim. Cosmochim. Acta* **57**, 859-874

Horiuchi, H. and Sawamoto, H. (1981) β-Mg_2SiO_4: single crystal X-Ray diffraction study *Amer. Mineral.* **66**, 568-575

Horiuchi, H., Hirano, M., Ito, E. and Matsui, Y. (1982) $MgSiO_3$ (ilmenite-type): Single crystal X-Ray diffraction study *Amer. Mineral.* **67**, 788-793

Horiuchi, H., Ito, E. and Weidner, D. J. (1987) Perovskite-type $MgSiO_3$: Single crystal X-Ray diffraction study *Amer. Mineral.* **72**, 357-360

Hough, R., Gilmour, I., Pillinger, C., Arden, J., Gilkes, K., Yuan, J. and Milledge, H. (1995) Diamond and silicon carbide in impact melt rock from the Reis impact crater *Nature* **378**, 41-44

Hugh-Jones, D. and Angel, R. (1994) A compressional study of $MgSiO_3$ orthoenstatite up to 8.5 GPa *Amer. Mineral.* **79**, 405-410

Hurley, P. M., Leo, G. W., White, R. W. and Fairbairn, H. W. (1971) Liberian Age Province (about 2,700 m. y.) and adjacent provinces in Liberia and Sierra Leone *Bull. Geol. Soc. Amer.* **82**, 3483-3490

Huss, G. and Lewis, R. (1995) Presolar diamond, SiC and graphite in primitive chondrites: abundances as a function of meteorite class and petrographic type *Geochim. Cosmochim. Acta* **59**, 115-160

Hutchison, M. T., Harte, B., Harris, J. W. and Fitsimons, I. (1995a) Inferences on the exhumation history of lower mantle inclusions in diamonds *Extended Abstracts of the 6th International Kimberlite Conference, UIGMM, Novosibirsk,* 242-244

Hutchison, M., Harte, B., Moore, R. and Gurney, J. (1995b) A REE study of Megacrysts from the Monastery Diatreme *Terra Abs. Suppl. 1 to Terra Nova* **7**, 334

Hutchison, M. T., Harris, J. W. and Harte, B. (1997) Deep diamonds and inferences on the role of aluminium in the transition zone and lower mantle *Abstracts of the AGM Mineral Deposits Studies Group (Eds., Hall, et al., University of Glasgow, Glasgow)* 34-35

Hynes, A., Francis, D. and Legault, F. (1994) Basalt petrochemistry as a probe of crustal thickness in the Hudson Bay Arc, Quebec *Earth Planet. Sci. Lett.* **127**, 11-24

Iidaka, T. and Suetsugu, D. (1992) Seismological evidence for metastable olivine inside a subducting slab *Nature* **356**, 593-595

Ireland, T. R., Rudnick, R. L. and Spetsius, Z. (1994) Trace elements in diamond inclusions from eclogites reveal link to Archean granites *Earth Planet. Sci. Lett.* **128**, 199-213

Irifune, T. (1994) Absence of an aluminous phase in the upper part of the earth's lower mantle *Nature* **370**, 131-133

Irifune, T. and Ringwood, A. E. (1987) Phase transformations in primitive MORB and pyrolite compositions to 25 GPa and some geophysical implications *High Pressure Research in Mineral Physics (Ed.. Manghnani, M. H. and Syono, Y. TERRAPUB, Tokyo)* 231-242

Irifune, T. and Ringwood, A. E. (1993) Phase transformations in subducted oceanic crust and buoyancy relationships at depths of 600-800 km in the mantle *Earth Planet. Sci. Lett.* **117**, 101-110

Irifune, T., Adachi, Y., Fujino, K., Ohtani, E., Yoneda, A. and Sawamoto, H. (1992) A performance test for WC anvils for multianvil apparatus and phase transformations in some aluminous minerals up to 28 GPa *High Pressure Research: Applications to Earth and Planetary Sciences (Eds. Syono, Y. and Manghnani, M. H. TERRAPUB, Tokyo)* 43-50

Irifune, T., Ringwood, A. E. and Hibberson, W. O. (1994) Subduction of continental crust and terrigenous and pelagic sediments: an experimental study *Earth Planet. Sci. Lett.* **126**, 351-368

Irifune, T., Koizumi, T. and Ando, J-i (1996) An experimental study of the garnet-perovskite transformation in the system $MgSiO_3$-$Mg_3Al_2Si_3O_{12}$ *Phys. Earth Planetary Interiors* **96**, 147-157

Isaak, D. (1992) High temperature elasticity of iron bearing olivines *J. Geophys. Res.* **97**, 1871-1885

Isacks, B. and Molnar, P. (1971) Distribution of stresses in the descending lithosphere from a global survey of focal mechanism solutions of mantle earthquakes *Rev. Geophys. Space Phys.* **9**, 103-174

Ito, E. and Katsura, T. (1989) A temperature profile of the mantle transition zone *Geophys. Res. Lett.* **16**, 425-428

Ito, E. and Matsui, Y. (1978) Synthesis and crystal chemical characterisation of $MgSiO_3$ perovskite *Earth Planet. Sci. Lett.* **38**, 43-450

Ito, E. and Navrotsky, A. (1985) $MgSiO_3$ ilmenite: Calorimetry, phase equilibria and decomposition at atmospheric pressure *Amer. Mineral.* **70**, 1020-1026

Ito, E. and Takahashi, E. (1987a) Melting of peridotite at uppermost lower-mantle conditions *Nature* **328**, 514-517

Ito, E. and Takahashi, E. (1987b) Ultra-high-pressure phase transformations and the constitution of the deep mantle *High Pressure Research in Mineral Physics (Ed.. Manghnani, M. H. and Syono, Y. TERRAPUB, Tokyo)* 221-229

Ito, E., Kawada, K. and Akimoto, S-i. (1974) Thermal expansion of stishovite *Phys. Earth Planetary Interiors* **8**, 277-281

Ito, E., Takahashi, E and Matsui, Y. (1984) The mineralogy and chemistry of the lower mantle: an implication of the ultrahigh-pressure phase relations in the system MgO-FeO-SiO_2 *Earth Planet. Sci. Lett.* **67**, 238-248

Iwamori, H. (1993) A model for disequilibrium mantle melting incorporating melt transport by porous and channel flows *Nature* **366**, 734-737

Jackson, I. (1977) Phase relations in the system LiF-MgF_2 at elevated pressures: implications for the proposed mixed-oxide zone of the earth's mantle *Phys. Earth Planetary Interiors* **14**, 86-94

Jackson, I. and Niesler, H. (1982) The elasticity of periclase to 3 GPa and some geophysical implications *High Pressure Research in Geophysics, Advances in Earth and Planetary Sciences*, **v. 12** *(Eds. Akimoto, S. and Manghnani, M. H. Centre for Academic Publications, Tokyo)* 93-113

Jackson, I., Liebermann, R. and Ringwood, A. (1978) The elastic properties of $(Mg_xFe_{1-x})O$ solid solutions *Phys. Chem. Mineral.* **3**, 11-31

Jackson, I., Khanna, S., Revcolevschi, A. and Berthon, J. (1990) Elasticity, shear mode softening and high pressure polymorphism of wüstite $(Fe_{1-x}O)$ *J. Geophys. Res.* **95 B10**, 21671-21685

Jackson, J. (1996) Diamonds, is their lustre fading? *Time* **March 4 (1996)**, 38-44

Jacobsen, S. (1988) Isotopic and chemical constraints on mantle-crust evolution *Geochim. Cosmochim. Acta* **52**, 1341-1350

Jagoutz, E., Palme, H., Baddenhausen, K., Blum, M., Cendales, G., Dreibus, B., Spettel, V., Lorenz, V. and Wanke, H. (1979) The abundances of major, minor and trace elements in the earth's mantle as derived from primitive ultramafic nodules *Proc. 10th Lunar Sci. Conf.* **2**, 2031-2050

Jakobsson, S. and Oskarsson, N. (1990) Experimental determination of fluid compositions in the system C-O-H at high P and T and low fO_2 *Geochim. Cosmochim. Acta* **54**, 355-362

Jaques, A., Hall, A., Sheraton, J., Smith, C., Sun, S-s., Drew, R., Foudoulis, C. and Ellingsen, C. (1989) Composition of crystalline inclusions and C isotope composition of Argyle and Ellendale Diamonds *Kimberlites and Related Rocks Vol. 2 (Eds.. Ross, J. Blackwell Scientific, Carlton)* 1029-1041

Jaques, A., O'Neill, H., Smith, C. B., Moon, J. and Chappell, B. W. (1990) Diamondiferous peridotitic xenoliths from the Argyle (AK1) lamproite pipe, Western Australia *Contrib. Mineral. Petrol.* **104**, 255-276

Javoy, M. (1995) The integral enstatite chondrite model of the earth *Geophys. Res. Lett.* **22**, 2219-2222

Javoy, M., Pineau, F. and Demaiffe, D. (1984) Nitrogen and carbon isotopic composition in the diamonds of Mbuji Mayi (Zaïre) *Earth Planet. Sci. Lett.* **68**, 399-412

Javoy, M., Pineau, F. and Delorme, H. (1986) Carbon and nitrogen isotopes in the mantle *Chem. Geol.* **57**, 41-62

Jeanloz, R. (1988) Majorite: Vibrational and compressional properties of a high-pressure phase *J. Geophys. Res.* **86**, 6171-6179

Jeanloz, R. and Ahrens, T. (1980) Equations of state of FeO and CaO *Geophys. J. Roy. Astronom. Soc.* **62**, 505-528

Jeanloz, R. and Hazen, R. (1993) Composition limits of Fe_xO and the earth's lower mantle *Science* **261**, 923-925

Jeanloz, R. and Knittle, E. (1989) Density and composition of the lower mantle *Phil. Trans. Roy. Soc. London* **A 328**, 377-389

Jeanloz, R. and Richter, F. (1979) Convection, composition and the thermal state of the lower mantle *J. Geophys. Res.* **84 B10**, 5497-5504

Jeanloz, R. and Sato-Sorensen, Y. (1986) Hydrostatic compression of $Fe_{1-x}O$ wüstite *J. Geophys. Res.* **91**, 4665-4672

Jeanloz, R. and Thompson, A. (1983) Phase transitions and mantle discontinuities *Rev. Geophys. Space Phys.* **21**, 51-74

Jeffreys, H. (1937) A further study of near earthquakes *Monthly Notices Roy. Astronom. Soc., Geophys. Suppl.* **4**, 196-225

Jerde, E. A., Taylor, L. A., Crozaz, G., Sobolev, N. V. and Sobolev, V. N. (1993) Exsolution of garnet within clinopyroxene of mantle eclogites: major- and trace- element chemistry *Contrib. Mineral. Petrol.* **114**, 148-159

Johnson, L. R. (1967) Array measurements of P velocities in the upper mantle *J. Geophys. Res.* **72**, 6309-6325

Jones, J. and Drake, M. (1993) Rubidium and caesium in the earth and the moon *Geochim. Cosmochim. Acta* **57**, 3785-3792

Kagi, H., Takahashi, K, Hidaka, H. and Masuda, A. (1994) Chemical properties of Central African carbonado and its genetic implications *Geochim. Cosmochim. Acta* **58**, 2629-2638

Kaiser, W. and Bond, W. L. (1959) Nitrogen, a major impurity in common type I diamond *Phys. Rev.* **115**, 857-863

Kaminskii, F. V. (1987) Genesis of carbonado: polycrystalline aggregate of diamond (In Russian) *Dokl. Akad.. Nauk SSSR* **291**, 439-440

Kaminsky, F, Chernaya, I. P. and Cherny, A. V. (1986) Occurrence of diamond in alkaline picrites and alkaline ultrabasic rocks (In Russian) *Mineral. Zh.* **8**, 39-45

Karato, S-i, Wang, Z., Liu, B. and Fujino, K. (1995) Plastic deformation of garnets: systematics and implications for the rheology of the mantle transition zone *Earth Planet. Sci. Lett.* **130**, 13-30

Karig, D. E. and Sharman, G. F. III (1975) Subduction and accretion in trenches *Bull. Geol. Soc. Amer.* **86**, 377

Kato, T. (1986) Stability relation of $(Mg,Fe)SiO_3$ garnets, major constituents in the Earth's interior *Earth Planet. Sci. Lett.* **77**, 399-408

Kato, T. and Kumazawa, M. (1985) Garnet phase of $MgSiO_3$ filling the pyroxene-ilmenite gap at very high temperature *Nature* **316**, 803-805

Kato, T., Ringwood, A. E. and Irifune, T. (1988) Experimental determination of element partitioning between silicate perovskites, garnet and liquids: constraints on early differentiation of the mantle *Earth Planet. Sci. Lett.* **89**, 123-145

Kato, T., Ohtani, E., Morishima, H., Yamazaki, D., Suzuki, A., Suto, M., Kubo, T., Kikegawa, T. and Shimomura, O. (1995) In-situ X ray observation of high-pressure phase transitions of $MgSiO_3$ and thermal expansion of $MgSiO_3$ perovskite at 25 GPa by double-stage multianvil system *J. Geophys. Res.* **100** 20475-20481

Katsura, T. and Ito, E. (1989) The system Mg_2SiO_4 - Fe_2SiO_4 at high pressures and temperatures: Precise determination of stabilities of olivine, modified spinel and spinel *J. Geophys. Res.* **94**, 15663-15670

Kawakatsu, H. and Niu, F. (1994) Seismic evidence for a 920-km discontinuity in the mantle *Nature* **371**, 301-305

Kendall, J-M and Silver, P. (1996) Constraints from seismic anisotropy on the nature of the lowermost mantle *Nature* **381**, 409-412

Kennedy, C. and Kennedy, G. (1976) The equilibrium boundary between graphite and diamond *J. Geophys. Res.* **81**, 2467-2470

Kent, R. W., Storey, M. and Saunders, A. D. (1992) Large igneous provinces: Sites of plume impact or plume incubation *Geology* **20**, 891-894

Keppler, H. (1996) Constraints from partitioning experiments on the composition of subduction-zone fluids *Nature* **380**, 237-240

Keppler, H., McCammon, C. A. and Rubie, D. C. (1994) Crystal-field and charge-transfer spectra of (Mg,Fe)SiO_3 perovskite *Amer. Mineral.* **79**, 1215-1218

Kerr, R. A. (1993) Earth-Science - bits of the lower mantle found in Brazillian diamonds *Science* **261**, 1391

Kerrich, R., Fyfe, W. S., Barnett, R. L., Blair, B. B. and Willmore, L. M. (1987) Corundum, Cr-muscovite rocks at O'Briens, Zimbabwe: the conjunction of hydrothermal desilicification and LIL-element enrichment - geochemical and isotopic evidence *Contrib. Mineral. Petrol.* **95**, 481-498

Keskar, N. R., Trouiller, N., Martins, J. L. and Chelikowsky, J. (1991) Structural properties of SiO_2 in the stishovite structure *Phys. Rev. B Cond. Matter* **44**, 4081-4088

Kesson, S. and Fitz Gerald, J. (1991) Partitioning of MgO, FeO, NiO, MnO and Cr_2O_3 between magnesian silicate perovskite and magnesiowüstite: implications for the origin of inclusions in diamond and the composition of the lower mantle *Earth Planet. Sci. Lett.* **111**, 259-240

Kesson, S. and Ringwood, A. E. (1989) Slab-mantle interactions 2: The formation of diamonds *Chem. Geol.* **78**, 97-118

Kesson, S. E., Fitz Gerald, J. D. and Shelley, J. M. G. (1994) Mineral chemistry and density of subducted basaltic crust at lower-mantle pressures *Nature* **372**, 767-769

Kesson, S. E., Fitz Gerald, J. D., Shelley, J. M. G. and Withers, R. L. (1995a) Phase relations of aluminous Mg,Fe silicate perovskites *Plume 2, Terra Nostra, (Ed. Anderson, Hart and Hofmann Alfred-Wegener-Stiftung, Bonn)* 72-74.

Kesson, S. E., Fitz Gerald, J. D., Shelley, J. M. G. and Withers, R. L. (1995b) Phase relations, structure and crystal chemistry of some aluminous silicate perovskites *Earth Planet. Sci. Lett.* **134**, 187-201

Kesson S. E., Fitz Gerald, J. and Shelley, J. M. (1996) Diagnostic phase chemistry of syngenetic inclusions in diamonds from the transition zone and lower mantle *Abstract of the RSES Diamond Workshop, ANU Canberra (1996)*

Kiflawi, I., Fisher, D., Kanda, H. and Sittas, G. (1996) The creation of the 3107 cm^{-1} hydrogen absorption peak in synthetic diamond single crystals *Diamond and related materials* **5**, 1516-1518

King, S. D. and Masters, G. *Geophys. Res. Lett.* **19**, 1551-1552

Kingma, K. J., Cohen, R. E., Hemley, R. and Mao, H. (1995) Transformations of stishovite to a denser phase at lower-mantle pressures *Nature* **374**, 243-245

Kirkley, M., Gurney, J., Otter, M., Hill, S. and Daniels, L. (1991) The application of C isotope measurements to the identification of the sources of C in diamonds: a review *Appl. Geochem.* **6**, 477-494

Klages, C-P. (1995) Metastable diamond synthesis - principles and applications *Eur. J. Mineral.* **7**, 767-774

Knittle, E. and Jeanloz, R. (1987a) Synthesis and equation of state of (Mg,Fe)SiO_3

perovskite to over 100 gigapascals *Science* **235**, 668-670

Knittle, E. and Jeanloz, R. (1987b) Synthesis and equation of state of (Mg,Fe)SiO_3 to over 100 GPa *Science* **235**, 668-670

Knittle, E. and Jeanloz, R. (1987c) The activation energy of the back transformation of silicate perovskite to enstatite *High Pressure Research in Mineral Physics (Ed.. Manghnani, M. H. and Syono, Y. TERRAPUB, Tokyo)* 243-250

Knittle, E. and Jeanloz, R. (1991a) Earth's core-mantle boundary: results of experiments at high pressures and temperatures *Science* **251**, 1438-1443

Knittle, E. and Jeanloz, R. (1991b) The high-pressure phase-diagram $Fe_{0.94}O$ - a possible constituent of the earth’s core *J. Geophys. Res.* **96**, 16169-16180

Knittle, E., Jeanloz, R. and Smith, G. L. (1987) Thermal expansion of silicate perovskite and stratification of the earth's mantle *Nature* **319**, 214-216

Kopylova, M. G., Gurney, J. J. and Daniels, L. R. M. (1995) Mineral inclusions in diamond from the River Ranch Kimberlite *Extended Abstracts of the 6th International Kimberlite Conference, UIGMM, Novosibirsk*, 289-291

Krogh, E. J. (1988) The garnet-clinopyroxene Fe-Mg geothermometer - a reinterpretation of existing experimental data *Contrib. Mineral. Petrol.* **99**, 44-48

Krot, A., Posukhova, T. V., Guseva, Ye, V., Galimov, E. M., Botkunov, A. I., Ramenskaya, M. Ye. and Oglobina, A. I. (1994) Origin of garnets containing hydrocarbon inclusions in the Mir kimberlite pipe *Geochem. Int.* **31**, 122-130

Krupka, K. M., Robie, R. A. and Hemingway, B. S. (1979) High temperature heat capacities of corundum, periclase, anorthite, $CaAl_2Si_2O_8$ glass, muscovite, pyrophyllite, $KAlSi_3O_8$ glass, grossular and $NaAlSi_3O_8$ glass *Amer. Mineral.* **64**, 86-101

Kudoh, Y., Ito, E. and Takeda, H. (1987) Effect of pressure on the crystal structure of perovskite-type $MgSiO_3$ *Phys. Chem. Mineral.* **14**, 350-354

Kudoh, Y., Prewitt, C. T. and Finger, L. W. (1990) Effect of iron on the crystal structure of (Mg,Fe)SiO_3 perovskite *Geophys. Res. Lett.* **17**, 1481-1484

Kumazawa, M. and Anderson, O. (1969) Elastic moduli, pressure derivatives and temperature derivatives of single-crystal olivine and single crystal forsterite *J. Geophys. Res.* **74**, 5961-5972

Kushiro, I. and Aoki, K. (1968) Origin of some eclogite inclusions in kimberlite *Amer. Mineral.* **53**, 1347-1367

Lander, J. J. and Morrison, J. (1963) *J. Chem. Phys.* **34**, 1403-

Lang, A. R. (1979) Internal Structure *The Properties of Diamond (Ed. Field, J. E. Academic Press, London)* 425-469

Lang, A. (1994) Comments on 'An unusual octahedral diamond' by A. Yacoot and M. Moore *Mineral. Mag.* **58**, 508-512

Larsen, R.L. (1991) Latest pulse of Earth: Evidence for a mid-Cretaceous superplume *Geology* **19**, 547-550

Latin, D. and Waters, F. (1991) Melt generation during rifting in the North Sea *Nature* **351**, 559-562

Lawn, B. R. and Wilshaw, T. R. (1975) Fracture of Brittle Solids *Cambridge University Press, Cambridge*

Le Page, Y., Calvert, L. D. and Gabe, E. J. (1980) Parameter variation in low quartz between 94 and 298K *J. Phys. Chem. Solids* **41**, 721-725

Lee, D-C. and Halliday, A. (1995) Hafnium-tungsten chronometry and the timing of terrestrial core formation *Nature* **378**, 771-774

Leinenweber, K., Wang, Y., Yagi, T. and Yusa, H. (1994) An unquenchable perovskite phase of $MgGeO_3$ and comparison with $MgSiO_3$ perovskite *Amer. Mineral.* **79**, 197-199

Leitner, B. J., Weidner, D. J. and Liebermann, R. C. (1980) Elasticity of single crystal pyrope and implications for garnet solid solution series *Phys. Earth Planetary Interiors* **22**, 111-121

Lenardic, A. and Kaula, W. (1995) Mantle dynamics and the heat flow into the earth's continents *Nature* **378**, 709-711

Li, J. and Agee, C. (1996) Geochemistry of mantle-core differentiation at high pressure *Nature* **381**, 686-689

Li, X. and Jeanloz, R. (1991) Phases and electrical conductivity of a hydrous silicate assemblage at lower-mantle conditions *Nature* **350**, 332-334

Li, X. and Mao H-K (1994) Solid carbon at high pressure: electrical resistivity and phase transition *Phys. Chem. Mineral.* **21**, 1-5

Liang, Y., Richter, F. M. and Watson, E. B. (1994) Convection in multicomponent silicate melts driven by coupled diffusion *Nature* **369,** 390-392

Lindsley, D. H. and Dixon, S. A. (1976) Diopside-enstatite equilibria at 850° to 1400°C, 5 to 35 kb *Amer. J. Sci.* **276**, 1285-1301

Lindsley, D. H., Grover, J. E. and Davidson, P. M. (1981) The thermodynamics of the $Mg_2Si_2O_6$ - $CaMgSi_2O_6$ join: a review and an improved model *Advances in Physical Geochemistry Vol. 1: Thermodynamics of minerals and melts (Eds. Newton, R. C. et al., Springer-Verlag, New York)* 149-175

Liu, L-G. (1975) High Pressure reconnaissance investigation in the system $Mg_3Al_2Si_3O_{12}$-$Fe_3Al_2Si_3O_{12}$ *Earth Planet. Sci. Lett.* **26**, 425-433

Liu, L-G. (1976a) First occurrence of garnet-ilmenite transition in silicates *Science* **195**, 990-991

Liu, L-G. (1976b) Orthorhombic perovskite phases observed in olivine, pyroxene and garnet at high pressures and temperatures *Phys. Earth Planetary Interiors* **11**, 289-298

Liu, L-G. (1978) A new high-pressure phase of $Ca_2Al_2SiO_7$ and implications or the earth's interior *Earth Planet. Sci. Lett.* **40**, 401-406

Liu, L-G. (1979a) On the 650 km seismic discontinuity *Earth Planet. Sci. Lett.* **42**, 202-208

Liu, L-G. (1979b) High-pressure phase transitions in the system $CaSiO_3$-Al_2O_3 *Earth Planet. Sci. Lett.* **43**, 331-335

Liu, L-G. (1984) Compression and phase behaviour of solid CO_2 to half a megabar *Earth Planet. Sci. Lett.* **71**, 104-110

Liu, L-G. and Lin, C-C (1995) High-pressure phase transformations of carbonates in the system CaO-MgO-SiO_2-CO_2 *Earth Planet. Sci. Lett.* **134**, 297-305

Liu, L-G. and Ringwood, A. E. (1975) Synthesis of a perovskite-type polymorph of $CaSiO_3$ *Earth Planet. Sci. Lett.* **28**, 209-211

Liu, L-G., Bassett, W. A. and Takahashi, T. (1974) Effect of pressure on the lattice parameters of stishovite *J. Geophys. Res.* **79**, 1160-1164

Liu, L-G. Mernagh, T. P. and Jaques, A. L. (1990) A mineralogical Raman spectroscopy study on eclogitic garnet inclusions in diamonds from Argyle *Contrib. Mineral. Petrol.* **105**, 156-161

Loubeyre, P. and LeToullec, R. (1995) Stability of O_2 /H_2 mixtures at high pressure *Nature* **378**, 44-46

Loubser, J. H. N. and van Wyk, J. A. (1981) Models for H3 and H4 centres based on ESR measurements *Diamond Conference Abstracts 1981, Readin*g *(Unpublished)* 13/35-40

Luth, R. W., Virgo, D., Boyd, F. R. and Wood, B. J. (1990) Ferric iron in mantle-derived garnets: implications for thermobarometry and the oxidation state of the mantle *Contrib. Mineral. Petrol.* **104**, 56-72

Luther, L. C. and Moore, W. J. (1964) Diffusion of helium in silicon, germanium and diamond *J. Chem. Phys.* **41**, 1018-1026

Maaloe, S. and Aoki, K-i. (1977)The major element composition of the upper mantle estimated from the composition of lherzolites *Contrib. Mineral. Petrol.* **63**, 161

Macgregor, I. (1974) The system MgO-Al_2O_3-SiO_2: solubility of Al_2O_3 in enstatite for spinel and garnet peridotite compositions *Amer. Mineral.* **59**, 110-119

Mackwell, S. and Kohlstedt, D. (1990) Diffusion of hydrogen in olivine: implications for water in the mantle *J. Geophys. Res.* **95, B4**, 5079-5088

Maeno, Y., Hashimoto, H., Yoshida, K., Nishizaki, S., Fujita, T., Bednorz, J. G. and Lichtenberg, F. (1994) Superconductivity in a layered perovskite without copper *Nature* **372,** 532-534

Malavergne, V., Guyot, F., Peyronneau, J. and Poirier, J-P. (1995) Distribution du fer, du cobalt et du nickel entre minéraux du manteau inférieur terrestre à haute pression et haute témperature *C. R. Academie des Sciences de Paris* **320 série IIa**, 455-462

Malavergne, V., Guyot, F., Wang, Y. and Martinez, I. (1997) Partitioning of nickel, cobalt and manganese between silicate perovskite and periclase: a test of crystal field theory at high pressure *Earth Planet. Sci. Lett.* **146**, 499-509.

Mao, H. K, and Hemley, R. J. (1996) Energy dispersive X-Ray diffraction of micro-crystals at ultrahigh pressures *High Pressure Research* **14**, 257-267

Mao, H-K., Takahashi, T., Bassett, W., Weaver, J. and Akimoto, S. (1969) Effect of pressure and temperature on the molar volumes of wüstite and of three $(Fe,Mg)_2SiO_4$ spinel solid solutions *J. Geophys. Res.* **74**, 1061-1069

Mao, H. K., Bell, P. M. and Yagi, T. (1979) Iron-Magnesium fractionation model for the earth *Carnegie Institution of Washington Year Book* **78**, 621-625

Mao, H. K., Chien, L. C., Hemley, R. J., Jephcoat, A. P. and Wu, Y. (1989) Stability and equation of state of $CaSiO_3$-perovskite to 134 GPa *J. Geophys. Res.* **94,** 17889-17894

Mao, H. K., Hemley, R. J., Fei, Y., Shu, J. F., Chen, L. C., Jephcoat, A. P. and Wu, Y. (1991) Effect of pressure, temperature and composition on lattice parameters and density of $(Fe,Mg)SiO_3$-perovskite to 30 GPa *J. Geophys. Res.* **96**, 8069-8079

Mao, H-k, Shu, J., Fie, Y., Hu, J. and Hemley, R. (1996) The wüstite enigma *Phys. Earth Planetary Interiors* **96**, 135-145

Martin, H. (1986) Effect of steeper Archean geothermal gradient on geochemistry on subduction-zone magmas *Geology* **14**, 753-756

Marton, F. and Cohen, R. (1994) Prediction of a high-pressure phase transition in Al_2O_3 *Amer. Mineral.* **79**, 789-792

Marumo, F., Isobe, M. and Akimoto, S. (1977) Electron density distributions in crystals for γ-Fe_2SiO_4 and γ-Co_2SiO_4 *Acta Crystallog.* **B33** 713-716

Marx, P. C. (1972) Pyrrhotine and the origin of terrestrial diamonds *Mineral. Mag.* **38**, 636-638

Mathez, E., Blacic, J., Maggiore, C., Mitchell, T. and Fogel, R. (1993) The determination of the O content of diamond by microactivation *Amer. Mineral.* **78**, 753-761

Matsubara, R., Toraya, H., Tanaka, S. and Sawamoto, H. (1990) Precision lattice-parameter determination of $(Mg,Fe)SiO_3$ tetragonal garnets *Science* **247**, 697-699

Mattey, D., Taylor, W., Green, D. and Pillinger, C. (1990) Carbon isotopic fractionation between CO_2 vapour, silicate and carbonate melts: an experimental study to 30 kbar *Contrib. Mineral. Petrol.* **104**, 492-505

Matthews, M., Harte, B. and Prior, D. (1992) Mantle garnets: a cracking yarn *Geochim. Cosmochim. Acta* **56**, 2633-2642

Matyska, C., Moser, J. and Yuen, D. A. (1994) The potential influence of radiative heat transfer on the formation of megaplumes in the lower mantle *Earth Planet. Sci. Lett.* **125**, 255-266

McCammon, C. (1993) Effect of pressure on the composition of the lower mantle end member Fe_xO *Science* **259**, 66-68

McCammon, C. (1994) A Mössbauer milliprobe: Practical considerations *Hyperfine Interactions* **92**, 1235-1239

McCammon, C. A. (1995) Mössbauer spectroscopy of minerals *Mineral Physics and Crystallography: A Handbook of Physical Constants (Ed. Ahrens, T. J., AGU, Washington)* 332-347

McCammon, C. (1996) Crystal Chemistry of iron containing perovskites *Phase Transitions* **58,** 1-26

McCammon, C. (1997) Perovskite as a possible sink for ferric iron in the lower mantle *Nature* **387**, 694-696

McCammon, C., Chaskar, V. and Richards, G. G. (1991) A technique for spatially resolved Mössbauer spectroscopy applied to quenched metallurgical slags *Meas. Sci. Technol.* **2**, 657-662

McCammon, C., Rubie, D., Ross II, C., Seifert, F. and O'Neill, H. (1992) Mössbauer spectra of $^{57}Fe_{0.05}Mg_{0.95}SiO_3$ perovskite at 80 and 298K *Amer. Mineral.* **77**, 894-897

McCammon, C. A., Harris, J. W., Harte, B. and Hutchison, M. T. (1995a) Ferric iron content of (Fe,Mg)O from lower mantle inclusions *Plume 2, Terra Nostra, (Eds. Anderson, Hart and Hofmann, Alfred-Wegener-Stiftung, Bonn)* **3**, 91-94

McCammon, C. A., Harris, J. W., Harte, B. and Hutchison, M. T. (1995b) Fe^{3+} content of diamond inclusions from the transition zone and lower mantle *Annual Report of the Bayerisches Geoinstitut, (Universität Bayreuth, Bayreuth)* 43-44

McCammon, C., Harris, J. W., Harte, B. and Hutchison, M. T. (1996a) Partitioning of ferric iron between lower mantle phases: results from natural and synthetic samples *J. Conf. Abs.* **1**, 390

McCammon, C. A., Hutchison, M. T., Harte, B. and Harris, J. W. (1996b) Ferric Iron and the electrical conductivity of the lower mantle *Eos Trans. AGU Fall Meet. Suppl.* **77(46)** F167

McCammon, C., Hutchison, M. T. and Harris, J. W. (1997) Oxidation of mineral inclusions in diamonds from São Luiz: A view into the lower mantle *Science* **278**, 434-436

McCandless, T. and Gurney, J. (1989) Criteria for classifying mantle eclogites *Kimberlites and Related Rocks Vol. 2 (Eds. Ross, J. et al., Blackwell Science Publications, Carlton)* 827-832

McCandless, T. E., Kirkley, M. B., Robinson, D. N., Gurney, J. J., Griffen, W. L., Cousens, D. R. and Boyd, F. R. (1989) Some initial observations on polycrystalline diamonds mainly from Orapa (Abstr.) *Workshop on Diamonds. 28th International Geological Congress, Washington* 47-51

McDade, P. and Harris, J. W. (1996) Multiple diamond sources at the Kalahari craton margin: Letseng-la-terai, Lesotho *J. Conf. Abs.* **1**, 391

McKenzie, D. (1984) The generation and compaction of partially molten rock *J. Petrol.* **25**, 713-765

McKenzie, D. (1989) Some remarks on the movement of small melt fractions in the mantle *Earth Planet. Sci. Lett.* **95,** 53-72

McKenzie, D. and Jarvis, G. (1980) The conversion of heat into mechanical work by mantle convection *J. Geophys. Res.* **85**, 6093-6096

McKenzie, D. and O'Nions, R. (1991) Partial melt distribution from inversion of rare earth element concentration *J. Petrol.* **32**, 1021-1091

McKenzie, D. and O'Nions, R. (1995) The source regions of ocean island basalts *J. Petrol.* **36**, 133-159

McLennan, S. (1994) Rare earth element geochemistry and the 'tetrad' effect *Geochim. Cosmochim. Acta* **58**, 2025-2033

McMahon, B. and Haggerty, S. (1984) The Benfontein kimberlite sills: Magmatic reactions and high intrusion temperatures *Amer. J. Sci.* **84**, 893-911

Mehta, S., Novotny, P., Williams, D. and Goldstein, J. (1980) Electron optical observations of ordered Fe-Ni in the Estherville meteorite *Nature* **284**, 151-153

Meng, Y., Fei, Y., Weidner, D. J., Gwanmesia, G. D. and Hu, J. (1994) Hydrostatic compression of γ-Mg_2SiO_4 to mantle pressures and 700K: Thermal equation of state and related elastic properties *Phys. Chem. Mineral.* **21**, 407-412

Menzies, M. A. (1992) The lower lithosphere as a major source for continental flood basalts: a re-appraisal *Magmatism and the causes of continental break-up (Eds. Storey, B. C. et al., Geol. Soc. Spec. Pub., London)* **68**, 31-39

Meyer, H. O. A. (1987) Inclusions in Diamond *Mantle Xenoliths (Ed.. Nixon, P. Wiley, Chichester)* 501-522

Meyer, H. and Boyd, F. (1972) Composition and origin of crystalline inclusions in natural diamonds *Geochim. Cosmochim. Acta* **36**, 1255-1273

Meyer, H. and Gübelin, E. (1981) Ruby in Diamond *Gems and Gemology* **Fall (1981)**, 153-156

Meyer, H. and McCallum, M. (1985) Mineral inclusions in diamonds from the Sloan kimberlites, Colorado *J. Geol.* **94**, 600-612

Michael, P. and Bonatti, E. (1985) Peridotite composition from the North Atlantic: regional and tectonic variations and implications for partial melting *Earth Planet. Sci. Lett.* **73**, 91-104

Milashev, V., Krutoyarski, M., Rabkhin, M. and Zirlich, A. (1963) Kimberlitic rocks and picritic porphyres of the north-eastern part of the Siberian Platform *Trudy Naushno-Issledovatelskoga Institut Geologiya Arktiki* **126**, 1-215

Mitchell, R. and Reed, S. (1988) Ion microprobe determination of rare earth elements in perovskite from kimberlites and alnöites *Mineral. Mag.* **52**, 331-339

Miyajima, N., Fujino, K., Yagi, T. and Kondo, T. (1996) Analytical electron microscopy of garnet-perovskite transformations in a laser-heated diamond anvil cell. *Advanced Materials '96: Proceedings of the 3rd NIRIM International Symposium on Advanced Materials, Tsukuba, (1996) (Ed. Akaishi, M. et al. NIRIM, Tsukuba)* 341-344

Moore, M. (1990) X-Ray topography and lattice parameter mapping of synthetic diamonds *Diamond Conference Abstracts 1990, Reading (Unpublished)* 33/1-2

Moore, R. O. and Gurney, J. J. (1985) Pyroxene solid solution in garnets included in diamond *Nature* **318**, 553-555

Moore, R. O. and Gurney, J. J. (1986) Mineral inclusions in diamonds from the Monastery Kimberlite, South Africa *Abs. Geol. Soc. Austral.* **16**, 406-408

Moore, R. O. and Gurney, J. J. (1989) Mineral inclusions in diamond from the Monastery kimberlite, South Africa *Kimberlites and Related Rocks Vol. 2 (Eds. Ross, J. et al., Blackwell Science Publications, Carlton)* 1029-1041

Moore, R. O., Otter, M. L., Rickard, R. S., Harris, J. W. and Gurney, J. J. (1986) The occurrence of moissanite and ferro-periclase as inclusions in diamond *Abs. Geol. Soc. Austral.* **16** Sydney 409-411

Moore, R. O., Gurney, J. J., Griffin, W. L. and Shimizu, N. (1991) Ultra-high pressure garnet inclusions in Monastery diamonds: trace element abundance patterns and conditions of origin *Eur. J. Mineral.* **3**, 213-230

Morgan, J. and Shearer, P. (1993) Seismic constraints on mantle flow and topography of the 660-km discontinuity: evidence for whole mantle convection *Nature* **365**, 506-511

Mori, T. and Green, D. H. (1985) Laboratory duplication of phase equilibria observed in natural garnet lherzolites *J. Geol.* **86**, 83-97

Moxon, T. J. (1991) On the origin of agate with particular reference to foritification agate found in the Midland Valley, Scotland *Chemie der Erde* **51**, 251-260

Nakakuki, T., Sato, H. and Fujimoto, H. (1994) Interaction of the upwelling plume with the phase and chemical boundary at the 670km discontinuity: effects of temperature-dependent viscosity *Earth Planet. Sci. Lett.* **121**, 369-384

Navon, O. (1991a) Pressure-temperature-volume path of micro inclusion bearing diamonds *Extended abstracts of the fifth international kimberlite conference, Brazil, (1991) CPRM, Rio de Janeiro* 304-306

Navon, O. (1991b) High internal pressures in diamond fluid inclusions determined by infrared absorption *Nature* **353**, 746-748

Navrotsky, A. (1987) Silicate and germanate garnets, ilmenites and perovskites: thermochemistry, lattice vibrations and spectroscopy *High Pressure Research in Mineral Physics (Ed.. Manghnani, M. H. and Syono, Y. TERRAPUB, Tokyo)* 261-268

Navrotsky, A. and Weidner, D. (1989) (Editors) Perovskite: a structure of great interest to Geophysics and materials science *American Geophysical Union, Washington*

Newnham, R. E. and deHaan, Y. M. (1962) Refinement of the alpha Al_2O_3, Ti_2O_3, V_2O_3 and Cr_2O_3 structures *Z. Krist* **117**, 235-237

Nickel, K. and Green, D. (1985) Empirical geothermobarometry for garnet peridotites and implications for the nature of the lithosphere, kimberlites and diamonds *Earth Planet. Sci. Lett.* **73**, 158-170

Nier, A. O. (1950) A redetermination of the relative abundances of the isotopes of carbon, nitrogen, oxygen, argon and potassium *Phys. Rev.* **77**, 789-793

Nier, A. and Gulbransen, E.(1939) Variations in the relative abundance of carbon isotopes *J. Amer. Chem. Soc.* **61**, 697-698

Nixon, P. (1979) (Editor) Mantle Xenoltihs *Wiley, Chichester*

O'Neill, B. and Jeanloz, R. (1994) $MgSiO_3$-$FeSiO_3$-Al_2O_3 in the Earth's lower mantle: Perovskite and garnet at 1200 km depth *J. Geophys. Res.* **99, B10**, 19901-19915

O'Neill, B., Bass, J. D., Smyth, J. and Vaughan, M. T. (1991) Elasticity of a grossular-pyrope-almandine garnet *J. Geophys. Res.* **94**, 17819-17824

O'Neill, H. StC. and Wood, B. J. (1979) An experimental study of Fe-Mg partitioning between garnet and olivine and its calibration as a geothermometer *Contrib. Mineral. Petrol.* **70**, 59-70

O'Neill, H. StC., Rubie, D. C., Canil, D., Geiger, C. A., Ross II, C. R., Seifert, F. and Woodland, A. B. (1993) Ferric iron in the upper mantle and in transition zone assemblages: implications for relative oxygen fugacities in the mantle *Evolution of the Earth and Planets Geophys. Mono. 74 IUGG* **14**, 73-88

O'Nions, R. K. and Tolstikhin, I. (1994) Behaviour and residence times of lithophile and rare gas tracers in the upper mantle *Earth Planet. Sci. Lett.* **124**, 131-138

O'Nions, R. K., Hamilton, P. J. and Evensen, N. M. (1977) Variations in ^{143}Nd/^{144}Nd and ^{87}Sr/^{86}Sr ratios in oceanic basalts *Earth Planet. Sci. Lett.* **34**, 13-22

O'Nions, R. K., Evensen, N. M. and Hamilton, P. J. (1979) Geochemical modelling of mantle differentiation and crustal growth *J. Geophys. Res.* **64,** 6091-6101

Odling, N. W. A. (1995) An experimental replication of upper-mantle metasomatism *Nature* **373**, 58-60

Ohtani, E. (1983) Melting temperature distribution and fractionation in the lower mantle *Phys. Earth Planetary Interiors* **33**, 12-25

Ohtani, E. (1987) Ultrahigh-pressure melting of a model chondritic mantle and pyrolite compositions *High Pressure Research in Mineral Physics (Ed.. Manghnani, M. H. and Syono, Y. TERRAPUB, Tokyo)* 87-93

Olson, P., Silver, P. G. and Carlson, R.W. (1990) The large-scale structure of convection in the earth's mantle *Nature* **344**, 209-215

Otter, M. (1989) Diamonds and their mineral inclusions from the Sloan diatremes of the Colorado-Wyoming State Line kimberlite district, North America *Unpublished PhD thesis, University of Cape Town*

Otter, M. and Gurney, J. (1989) Mineral inclusions in diamonds from the Sloan diatremes, Colorado-Wyoming State-line district, North America *Kimberlites and Related Rocks Vol. 2 (Eds. Ross, J. et al., Blackwell Science Publications, Carlton)* 1042-1053

Otter, M., Gerneke, D., Harte, B., Gurney, J., Harris, J. and Wilding, M. (1991) Diamond growth histories revealed by cathodoluminescence and carbon isotope studies *Extended abstracts of the fifth international kimberlite conference, Brazil, (1991) CPRM, Rio de Janeiro* 318-319

Ozima, M. (1989) Gases in diamonds *Annual Review of Earth and Planetary Science* **17**, 361-384

Park, K. T., Terakura, K. and Matsui, Y. (1988) Theoretical evidence for a new ultra-high-pressure phase of SiO_2 *Nature* **336**, 670-672

Pearson, D., Davies, G., Nixon, P. and Milledge, H. J. (1989) Graphitised diamond from a peridotitic massif in Morocco and implications for anomalous diamond occurrences *Nature* **338**, 60-62

Pearson, D. G., Davies, G. R. and Nixon, P. H. (1993) Geochemical constraints on the petrogenesis of diamond facies pyroxenites from the Beni Bousera peridotite massif, North Morocco *J. Petrol.* **34**, 125-172

Peter, F. (1923) *Z. Phys.* **15**, 358-368

Plymate, T. and Stout, J. (1994) Pressure-Temperature-Volume behaviour of γ-Fe_2SiO_4 (spinel) based on static compression measurements at 400°C *Phys. Chem. Mineral.* **21**, 413-420

Pollack, H. N. and Chapman, D. S. (1977) On the regional variation of heat flow, geotherms and lithospheric thickness *Tectonophys.* **38**, 279-296

Polyakov, V. and Kharlashina, N. (1995) The use of heat capacity data to calculate carbon isotope fractionation between graphite, diamond and carbon dioxide: a new approach *Geochim. Cosmochim. Acta* **59**, 2561-2572

Poe, B., Seifert, F., Sharp, T. and Wu, Z. (1997) ELNES spectroscopy of mixed Si coordination minerals *Phys. Chem. Mineral.* **24**, 477-487

Powell, R. (1985) Regression diagnostics and robust regression in geothermometer / geobarometer calibration: the garnet-clinopyroxene geothermometer revisited *J. Metamorphic Geol.* **3**, 231-243

Price, G. D., Wall, A. and Parker, S. C. (1989) The properties and behaviour of mantle minerals: a computer simulation approach *Phil. Trans. Roy. Soc. London* **A 328**, 391-407

Pyle, J. and Haggerty, S. (1994) Silicate-carbonate liquid immiscibility in upper-mantle eclogites implications for natrosilicate an carbonatitic conjugate melts *Geochim. Cosmochim. Acta* **58**, 2997-3001

Raeburn, S. P., Ilton, E., Veblen, D. and Kerrick, D (1995) Microbeam determination of Fe(II)/Fe(III) in biotites in situ in pelitic rocks using X-Ray spectroscopy (XPS) *Terra Abs. Suppl. 1 to Terra Nova* **7**, 320

Ramsden, A. R. and Cameron, E. N. (1966) Kamacite and taenite superstructures and a metastable tetragonal phase in iron meteorites *Amer. Mineral.* **51**, 37-55

Rancourt, D. (1994) Mössbauer Spectroscopy of minerals I. Inadequacy of Lorentzian-line doublets in fitting spectra arising from quadrupole splitting distributions *Phys. Chem. Mineral.* **21**, 244-249

Rancourt, D., Christie, I., Royer, M., Kodama, H., Robert, J.-L., Lalonde, A. and Murad, E. (1994) Determination of accurate [4]Fe^{3+}, [6]Fe^{3+} and [6]Fe^{2+} site populations in synthetic annite by Mössbauer spectroscopy *Amer. Mineral.* **79**, 51-62

Rayleigh, C. B. and Paterson, M. S. (1965) Experimental deformation of serpentinite and its tectonic implications *J. Geophys. Res.* **70**, 3965-3985

Reeber, R., Goessel, K. and Wang, K. (1995) Thermal expansion and molar volume of MgO, periclase, from 5 to 2900 K *Eur. J. Mineral.* **7**, 1039-1047

Reed, J. C. Jr., Ball, T. T., Farmer, G. L. and Hamilton, W. B. (1993) A broader view *The Geology of North America v.C-2 Precambrian: Coterminous U.S. (Eds. Reed Jr. et al., Geol. Soc. Amer., Boulder)* 597-636

Reid, A., Brown, R., Dawson, B., Whitfield, G. and Siebert, J. (1973) Diamond-bearing eclogites *Abstracts of the International Conference on Kimberlites, Cape Town, R. S. A.*, 271

Richards, M. A., Duncan, R. A. and Courtillot, V. E. (1989) Flood Basalts and Hot-Spot Tracks: Plume Heads and Tails *Science* **246**, 103-107

Richardson, S. H., Gurney, J. J., Erlank, A. J. and Harris, J. W. (1984) Origin of diamonds in old enriched mantle *Nature* **310**, 198-202

Richardson, S. H., Erlank, A. J., Harris, J. W. and Hart, S. R. (1990) Eclogitic diamonds of Proterozoic age fom Cretaceous Kimberlites *Nature* **346**, 54-56

Richardson, S. H., Harris, J. W. and Gurney, J. J. (1993) Three generations of diamonds from old continental mantle *Nature* **366**, 256-258

Richet, P. Mao, H-K. and Bell, P. M. (1988) Bulk moduli of magnesiowüstites from static compression measurements *J. Geophys. Res.* **B93**, 15279-15288

Richet, P., Mao, H-K. and Bell, P. (1989) Bulk moduli of magnesiowüstites from static compression measurements *J. Geophys. Res.* **94**, 3073-3045

Richet, P., Ingrin, J., Mysen, B. O., Courtial, P. and Gillet, P. (1994) Premelting effects in minerals: an experimental study *Earth Planet. Sci. Lett.* **121**, 589-600

Richter, F. and McKenzie, D. (1981) On some consequences and possible causes of layered mantle convection *J. Geophys. Res.* **86 B7**, 6133-6142

Rickard, R., Gurney, J. and Cardaso, P. (1989) Mineral inclusions in diamonds form the Koffiefontein mine *Kimberlites and Related Rocks Vol. 2. (Eds.. Ross, J. et al. Blackwell, Victoria)* 121-142

Ringwood, A. (1967) The pyroxene-garnet transformation in the earth's mantle *Earth Planet. Sci. Lett.* **2**, 255-263

Ringwood, A. E. (1970) Phase transformations and the constitution of the mantle *Phys. Earth Planetary Interiors* **3**, 109-155

Ringwood, A. (1989) Constitution and evolution of the mantle *Kimberlites and Related Rocks Vol. 1 (Eds. Ross, J. et al., Blackwell Science Publications, Carlton)* 457-485

Ringwood, A. and Irifune, T. (1988) Nature of the 670-km seismic discontinuity: implications for mantle dynamics and differentiation *Nature* **331**, 131-136

Ringwood, A. E., Kesson , S. E., Hibberson, W. and Ware, N. (1993) Origin of kimberlites and related magmas *Earth Planet. Sci. Lett.* **113**, 521-538

Ringwood, A. and Major, A. (1966) Synthesis of Mg_2SiO_4 - Fe_2SiO_4 spinel solid solutions *Earth Planet. Sci. Lett.* **1**, 241-245

Robie, R. A., Hemingway, B. S. and Fisher, J. R. (1979) Thermodynamic properties of minerals and related substances at 298.15°K and 1 bar (10^5 pascals) pressure and at higher temperatures *U.S. Geol. Survey Bull.* **1452**, 1-456

Robinson, D. N. (1978) The characteristics of natural diamond and their interpretation *Mineral Sci. Engineering* **10** 55-72

Rombouts, L. (1987) Geology and evaluation of the Guinea diamond deposits *Annal. Soc. Geol. Belgium* **110**, 241-259

Rosenbaum, J. M., Walker, D. and Kyser, T. K. (1994) Oxygen isotope fractionation in the mantle *Geochim. Cosmochim. Acta* **58**, 4767-4777

Rosenhauer, M., Mao., H-K., Woermann, E. (1976) Compressibility of magnesiowüstite ($Fe_{0.4}Mg_{0.6}$)O to 264 kbar *Carnegie Institution of Washington Year Book* **75**, 513-515

Ross, M., Young, D. A. and Grover, R. (1990) Theory of the iron phase diagram at earth core conditions *J. Geophys. Res.* **95**, 21713-21716

Ross, N. and Hazen, R. (1989) Single crystal X-Ray diffraction study of $MgSiO_3$ perovskite from 77 to 400 K *Phys. Chem. Mineral.* **16**, 415-420

Ross, N. and Hazen, R. (1990) High-pressure crystal chemistry of $MgSiO_3$ perovskite *Phys. Chem. Mineral.* **17**, 228-237

Ross, N. L., Shu, J-F. and Hazen, R. M. (1990) High-pressure crystal chemistry of stishovite *Amer. Mineral.* **75**, 739-747

Rudnick, R. L., Eldridge, C. S. and Bulanova, G. P. (1993) Diamond growth history from in situ measurement of Pb and S isotopic compositions of sulphide inclusions *Geology* **21**, 13-16

Rye, R., Kuo, P. H. and Holland, H. D. (1995) Atmospheric carbon-dioxide concentrations before 2.2-billion years ago *Nature* **378**, 603-605

Ryburn, R., Råheim, A. and Green, D. H. (1976) Determination of the P, T paths of natural eclogites during metamorphism-record of subduction *Lithos* **9**, 161-164

Salviulo, G., Secco, L., Antonini, P. and Piccirillo, E. M. (1997) C2/c pyroxene from two alkaline sodic suites (Western Ross Embayment - Antarctica): crystal chemical characterization and its petrologic significance *Mineral. Mag.* **61**, 423-439

Sasaki, S., Takeuchi, Y., Fujino, K. and Akimoto, S. (1982a) Electron density distributions of three orthopyroxenes, $Mg_2Si_2O_6$, $Co_2Si_2O_6$ and $Fe_2Si_2O_6$ *Z. Krist.* **156**, 279-297

Sasaki, S., Prewit, C. T., Sato, Y. and Ito, E. (1982b) Single-crystal X-Ray study of gamma-Mg_2SiO_4 *J. Geophys. Res.* **87**, 7829-7832

Sato, Y. (1977a) Equation of state of mantle minerals determined through high-pressure x-ray study *High Pressure Research: Application to Geophysics (Eds. Manghnani, M. H. and Akimoto, S. Academic Press, San Diego)* 307-323

Sato, Y. (1977b) Pressure-volume relationship of stishovite under hydrostatic compression *Earth Planet. Sci. Lett.* **34**, 307-312

Saunders, A. D., Storey, M., Kent, R. W. and Norry, M. J. (1992) Consequences of plume-lithosphere interactions *Magmatism and the causes of continental break-up (Eds. Storey, B. C. et al., Geol. Soc. Spec. Pub., London)* **68**, 41-60

Sautter, V., Haggerty, S. E. and Field, S. (1991) Ultradeep (>300 kilometres) ultramafic xenoliths: petrological evidence from the transition zone *Science* **252**, 827-830

Sawamoto, H. (1977) Orthorhombic perovskite (Mg,Fe)SiO_3 and the constitution of the lower mantle *High Pressure Research (Eds. Manghnani, M. H. and Akimoto, S. Academic Press, San Diego)* 219-244

Sawamoto, H., Weidner, D. J., Sasaki, S. and Kumazawa, M. (1984) Single crystal elastic properties of the modified spinel (Beta) phase of magnesium orthosilicate *Science* **224**, 749-751

Sawamoto, H. (1987) Phase study of $MgSiO_3$ at pressures up to 24 GPa and temperatures up to 2200°C: phase stability and properties of tetragonal garnet *High Pressure Research in Mineral Physics (Ed.. Manghnani, M. H. and Syono, Y. TERRAPUB, Tokyo)* 209-219

Saxena, S. K. and Fei, Y. (1987) High pressure and high temperature fluid fugacities *Geochim. Cosmochim. Acta* **51**, 783-791

Scacchi, A. (1941) *Mem. Min. Geol.*, 23

Schiano, P., Allègre, C. J., Dupré, B., Lewin, E. and Joron, J-L. (1993) Variability of trace elements in basaltic suites *Earth Planet. Sci. Lett.* **119**, 37-51

Schrauder, M. and Navon, O. (1993) Solid carbon dioxide in a natural diamond *Nature* **365**, 42-44

Schrauder, M. and Navon, O. (1994) Hydrous and carbonatitic fluids in fibrous diamonds from Jwaneng, Botswana *Geochim. Cosmochim. Acta* **58**, 761-771

Schreyer, W., Werding, G. and Abraham, K. (1981) Corundum-Fuchsite rocks in greenstone belts of southern africa: petrology, geochemistry, and possible origin *J. Petrol.* **22**, 191-231

Schubert, G., Yuen, D. and Turotte, D. (1975) Role of phase transitions in a dynamic mantle *Geophys. J. Roy. Astronom. Soc.* **42**, 705-735

Scott-Smith, B., Danchin, R., Harris, J. and Stracke, K. (1984) Kimberites near Orrorroo, South Australia *Kimberlites I: Kimberlites and Related Rocks (Ed.. Kornprobst, J., Elsevier, Amsterdam)* 121-142

Shannon, (1976) *Acta. Cryst.* **A32** 751

Sharp, T. G., Lingemann, C. M., Dupas, C. and Stöffler, D. (1997) Natural occurrence of $MgSiO_3$-Ilmenite and evidence for $MgSiO_3$-Perovskite in a shocked L Chondrite *Science* **277**, 352-355

Shen, G., Fei, Y., Hålenius, U. and Wang, Y. (1994) Optical absorption spectra of $(Mg,Fe)SiO_3$ silicate perovskites *Phys. Chem. Mineral.* **20**, 478-482

Shenck, V. R. and Dingmann, T. (1927) Gleichgewichtsuntersuchungen über die Reduktions Oxydations und Kohlungsvorgänge beim Eisen. III *Zeitanorg. Chem.* **166**, 113-154

Sherman, D. (1993a) Equation of state and high pressure phase transitions of stishovite (SiO_2): ab initio (Peridioc Hartree-Fock) results *J. Geophys. Res.* **98, B7**, 11865-11873

Sherman, D. (1993b) Equation of state, elastic properties and stability of $CaSiO_3$ perovskite: First principles (Periodic Hartree-Fock) results *J. Geophys. Res.* **98, B11**, 19795-19805

Shimizu, N (1975) Rare earth elements in garnets and clinopyroxenes from garnet lherzolite nodules in kimberlites *Earth Planet. Sci. Lett.* **25**, 26-32

Shimizu, N. and Sobolev, N. (1995) Young peridotitic diamonds from the Mir kimberlite pipe *Nature* **375**, 394-397

Shutong, X., Okay, A. I., Shouyuan, J., Sengör, A. M. C., Wen, S., Yican, L. and Laili, J. (1992) Diamond from the Dabie Shan metamorphic rocks and its implications for tectonic setting *Science* **256**, 80-82

Silver, P. G., Beck, S. L., Wallace, T. C., Meade, C., Myers, S. C., James, D. E. and Kuehnel, R. (1995) Rupture characteristics of the deep Bolivian earthquake of 9 June 1994 and the mechanisms of deep focus earthquakes *Science* **268**, 69-73

Simmons, G. and Wang, H. (1971) Single crystal elastic constants and calculated aggregate properties: a handbook *MIT Press, Cambridge MA*

Simons, B. and Seifert, F. (1978) High-pressure wüstite: cell parameters and Mössbauer spectra *Carnegie Institute of Washington Year Book* **77**, 625-626

Sinogeikin, S., Bass. J., O'Neill, B. and Gasparik, T. (1997) Elasticity of tetragonal end-member majorite and solid solutions in the system $Mg_4Si_4O_{12}$-$Mg_3Al_2Si_3O_{12}$ *Phys. Chem. Mineral.* **24**, 115-121

Skinner, B. (1956) The thermal expansions of thoria, periclase and diamond *Amer. Mineral.* **41**, 39-55

Skinner, B. (1966) Thermal Expansion *Handbook of Physical Constants (Ed.. Clark J. Geol. Soc. Amer., Boulder)* 75-95

Skinner, B. J. and Boyd, F. R. (1964) Aluminous enstatites *Carnegie Institution of Washington Year Book* **63**, 163-165

Smirnov, G., Mofolo, M., Lerotholi, P., Kaminsky, F., Galimov, E. and Ivanovskaya, I. (1979) Isotopically light carbon in diamonds from some kimberlite pipes in Lesotho *Nature* **278**, 630

Smith, J. V. and Dawson, J. B. (1985) Carbonados: Diamond aggregates from early impact of crustal rocks? *Geology* **13**, 342-343

Smith, J. V. and Mason, B. (1970) Pyroxene-garnet transformations in Coorara meteorite *Science* **168**, 832-833

Smyth, J. (1987) β-Mg_2SiO_4: a potential host for water in the mantle? *Amer. Mineral.* **72**, 1051-1055

Smyth, J. (1994) A crystallographic model for hydrous wadsleyite (β-Mg_2SiO_4): An ocean in the earth's interior? *Amer. Mineral.* **79**, 1021-1024

Smyth, J. R. and McCormick, T. C. (1995) Crystallographic data for minerals *AGU Ref. 2 Mineral Physics and Crystallography: A Handbook of Physical Constants (Ed.. Ahrens, T. J. AGU, Washington)* 1-17

Smyth, J. R., Artioli, G., Smith, J. V. and Kvick, A. (1987) Crystal structure of coesite, a high pressure form of SiO_2, at 15 and 298 K from single crystal neutron and X-Ray diffraction data: test of bonding models *J. Phys. Chem.* **91**, 988-992

Snyder, G., Jerde, E., Taylor, L., Halliday, A., Sobolev, V. and Sobolev, N. (1993) Nd and Sr isotopes from diamondiferous eclogites, Udachnaya kimberlite pipe, Yakutia, Siberia: evidence of differentiation in the early earth? *Earth Planet. Sci. Lett.* **118**, 91-100

Sobolev, N. and Shatsky, V. (1990) Diamond inclusions in garnets from metamorphic rocks: a new environment for diamond formation *Nature* **343**, 742-746

Sobolev, N., Galimov, E., Ivanovskaya, I. and Yefimova, E. (1979) Isotope composition of carbon of diamonds containing crystalline inclusions (translated from Russian) *Dokl. Akad.. Nauk SSSR* **249**, 1217-1220

Sobolev, N. V., Yefimova, E. S. and Pospelova, L. N. (1981) Native iron in Yakutian diamonds and its paragenesis *Geologika i Geofizica* **12**, 25-29

Solheim, L. and Petltier, W. (1992) Mantle phase transitions and layered convection *Can. J. Earth Sci.* **30**, 881-892

Song, X. and Richards, P. (1996) Seismological evidence for differential rotation of the Earth's inner core *Nature* **382**, 221-224

Speidel, D. (1966) Phase equilibria in the system MgO-FeO-Fe_2O_3: The 1300°C isothermal section and extrapolations to other temperatures *Proc. 68th Annual Meeting Amer. Ceram. Soc.* **48,** B-66, 243-247

Spetsius, (1996) Trace elements in mafic and ultramafic xenoliths from kimberlies of Yakutia *J. Conf. Abs.* **1**, 587

Spetzler, H. (1970) Equation of state of polycrystalline and single crystal MgO to 8 kbar and 800 K *J. Geophys. Res.* **75**, 2073-2087

Spiliopoulos, S. and Stacey, F. (1984) The earth's thermal profile: Is there a mid-mantle thermal boundary layer? *J. Geodynamics* **1**, 61-77

Srecec, I., Ender, A., Woermann, E., Gans, W., Jaconsson, E., Eriksson, G and Rosén, E. (1987) Activity-composition relations of the magnesiowüstite solid solution series in equilibrium with metallic iron in the temperature range 1050-1400 K *Phys. Chem. Mineral.* **14**, 492498

Stacey, F. (1995) Theory of thermal and elastic properties of the lower mantle and core *Phys. Earth Planetary Interiors* **89**, 219-245

Stachel, T. and Harris, J. W. (1996) Syngenetic mineral inclusions in diamonds from Ghana-unique samples from the base of the peridotitic mantle lithosphere *J. Conf. Abs.* **1**, 588

Stachel, T., Harris, J. W. and Cartigny, P. (1995) Diamonds and their syngenetic mineral inclusions from the Birimian deposits, Ghana, West-Africa *Extended Abstracts of the 6th International Kimberlite Conference, UIGMM, Novosibirsk*, 578-580

Steinbach, V. and Yuen, D. (1994) Melting instabilities in the transition zone *Earth Planet. Sci. Lett.* **127**, 67-75

Stephens, W. and Dawson, B. (1977) Statistical comparison between pyroxenes from kimberlites and their associated xenoliths *J. Geol.* **85,** 433-449

Stevenson, D. J. (1981) Models of the earth’s core *Science* **214,** 611-619

Stewart, D. N., Busse, F. H., Whaler, K. A. and Gubbins, D. (1995) Geomagnetism, earth rotation and the chemical conductivity of the lower mantle *Phys. Earth Planetary Interiors* **92**, 199-214

Storey, B. (1995) The role of mantle plumes in continental breakup: case histories from Gondwanaland *Nature* **377**, 301-308

Storey B. C., Alabaster, T., Hole, M. J., Pankhurst, R. J. and Wever, H. E. (1992) Role of subduction-plate boundary forces during the initial stages of Gondwana break-up: evidence from the proto-Pacific margin of Antarctica *Magmatism and the causes of continental break-up* (*Eds. Storey, B. C. et al., Geol. Soc. Spec. Pub., London)* **68**, 149

Strixude, L. and Cohen, R. (1993) Stability of orthorhombic $MgSiO_3$ perovskite in the Earth's lower mantle *Nature* **364**, 613-616

Sugiyama, M., Endo, S. and Koto, K. (1987) The crystal structure of stishovite under pressure to 6 GPa *Miner. J.* **13**, 455-466

Sumino, Y. (1979) The elastic constants of Mn_2SiO_4, Fe_2SiO_4 and Co_2SiO_4 and elastic properties of the olivine group minerals at high temperature *J. Phys. Earth* **27**, 209-238

Sumino, Y. and Anderson, O. (1984a) Elastic constants of minerals *Handbook of Physical properties III (Ed.. Carmichael, CRC Press, Boca Raton)*

Sumino, Y. and Anderson O. (1984b) Temperature coefficients of elastic constants of single crystal MgO between 80 and 1300 K *Phys. Chem. Mineral.* **9**, 38-47

Sumino, Y., Kumazawa, M., Nishizawa, O. and Pluschkell, W. (1980) The elastic constants of single crystal $Fe_{1-x}O$, MnO and CoO and the elasticity of stoichiometric magnesiowüstite *J. Phys. Earth* **28**, 475-495

Sumino, Y., Anderson, O. and Suzuki, I (1983) Temperature coefficients of elastic constants of single crystal MgO between 80 and 1300K *Phys. Chem. Mineral.* **9**, 38-47

Sun, S-s. (1982) Chemical composition and origin of the earth's primitive mantle *Geochim. Cosmochim. Acta* **46**, 179-192

Sun S-s. and McDonough W. F. (1989) Chemical and isotopic systematics of oceanic basalts: implications for mantle composition and processes *Magmatism in Ocean Basins (Eds. Saunders, A. D. and Norry, M. J.) Spec. Pub. Geol. Soc.* **42**, 313

Sutherland, D. (1993) The diamond deposits of the Mandala Basin, SE Guinea, West Africa *Trans. Roy. Soc. Edinburgh Earth Sci.* **84**, 137-149

Sutton, S. R., Jones, K. W., Gordon, B., Rivers, M. L., Bajt, S. and Smith, J. V. (1993) Reduced chromium in olivine grains from lunar basalt 15555: X-Ray absorption near edge structure (XANES) *Geochim. Cosmochim. Acta* **57**, 461-468

Suzuki, A., Ohtani, E. and Kato, T. (1995) Flotation of diamond in mantle melt at high pressure *Science* **269**, 216-218

Suzuki, I and Anderson, O. (1983) Elasticity and thermal expansion of a natural garnet up to 1000K *J. Phys. Earth* **31**, 125-138

Suzuki, I., Ohtani, E. and Kumazawa, M. (1979) Thermal expansion of γ-Mg_2SiO_4 *J. Phys. Earth* **27**, 53-61

Suzuki, I., Seya, K., Takei, H. and Sumino, Y. (1981) Thermal expansion of fayalite, Fe_2SiO_4 *Phys. Chem. Mineral.* **7**, 60-63

Svisero, D. P. (1995) Distribution and origin of diamonds in Brazil: an overview *J. Geodynamics* **20**, 493-514

Syono, Y., Akimoto, S. and Matsui, Y. (1971) High pressure transformation in zinc silicates *J. Solid State Chem.* **3**, 369-380

Takahashi, E. and Ito, E. (1987) Mineralogy of mantle peridotite along a model geotherm up to 700 km depth *High Pressure Research in Mineral Physics (Ed.. Manghnani, M. H. and Syono, Y. TERRAPUB, Tokyo)* 427-437

Takahashi, T. Bassett, W. and Mao, H-W (1966) Isothermal compression of the alloys of iron up to 300 kilobars at room temperature: iron-nickel alloys *J. Geophys. Res.* **73**, 4717-4725

Takaoka, N. and Ozima, M. (1978) Rare gas isotopic compositions in diamonds *Nature* **271**, 45-46

Tamai, H. and Yagi, T. (1989) High-pressure and high-temperature phase relations in $CaSiO_3$ and $CaMgSi_2O_6$ and elasticity of perovskite-type $CaSiO_3$ *Phys. Earth Planetary Interiors* **54**, 370-377

Tarduno, J. and Gee, J. (1995) Large-scale motion between Pacific and Atlantic hotspots *Nature* **378**, 477-480

Tarrida, M. and Richet, P. (1989) Equation of state of $CaSiO_3$-perovskite to 96 GPa *Geophys. Res. Lett.* **16**, 1351-1354

Taylor, L. A. and Neal, C. R. (1989) Eclogites with oceanic crustal and mantle signatures from the Bellsbank kimberlite, South Africa, Part I: mineralogy, petrology and whole rock chemistry *J. Geol.* **97**, 551-567

Taylor, W. R., Tompkins, L. A. and Haggerty, S. E. (1994) Comparative geochemistry of West African kimberlites: Evidence for a micaceous kimberlite endmember of sublithospheric origin *Geochim. Cosmochim. Acta* **58**, 4017-4037

Taylor, W. R., Bulanova, G. and Milledge, H. J. (1995a) Quantitative nitrogen aggregation study of some Yakutian diamonds: constraints on the growth, thermal and deformation history of peridotitic and eclogitic diamonds *Extended Abstracts of the 6th International Kimberlite Conference, UIGMM, Novosibirsk*, 608-610

Taylor, W. R., Kiviets, G., Gurney, J. J., Milledge, H. J., Woods, P. A. and Harte, B. (1995b) Growth history of an eclogitic diamond from the Kaal Vallei kimberlite, South Africa - an infrared, cathodoluminescence and carbon isotope study *Extended Abstracts of the 6th International Kimberlite Conference, UIGMM, Novosibirsk*, 617-619

Thompson, A. B. (1992) Water in the Earth's upper mantle *Nature* **358**, 295-302

Thompson, R. N. and Gibson, S. A. (1991) Subcontinental mantle plumes, hotspots and pre-existing thinspots *J. Geol. Soc. London* **148**, 973-977

Thoraval, C., Machetel, P. and Cazenave, A. (1995) Locally layered convection inferred from dynamic models of the earth's mantle *Nature* **375**, 777-780

Tolansky, S. (1973) Distribution of Type I and Type II in South African diamonds *Diamond Research (1973): Supplement to The Industrial Diamond Review*, 28-31

Tomioka, N. and Fujino, K. (1997) Natural (Mg,Fe)SiO_3-Ilmenite and -Perovskite in the Tenham meteorite *Science* **277**, 1084-1086

Tompkins, L. (1992) Kimberlite structural environments and diamond productivity of Brazil *Russian Geology and Geophysics* **33**, 91-98

Trønnes, R. G., Canil, D. and Wei, K. J. (1992) Element partitioning between silicate minerals and coexisting melts at pressures of 1-27 GPa and implications for mantle evolution *Earth Planet. Sci. Lett.* **111**, 241-255

Tsukida, Y. and Yagi, T. (1989) A new post-stishovite high pressure polymorph of silica *Nature* **340**, 217-220

Urakawa, S. (1991) Partitioning of Ni between magnesiowüstite and metal at high pressure: implications for core-mantle equilibrium *Earth Planet. Sci. Lett.* **105**, 293-313

Urakawa, S., Kondo, T., Igawa, N., Shimomura, O. and Ohno, H. (1994) Synchrotron radiation study on the high-pressure and high-temperature phase relations of $KAlSi_3O_8$ *Phys. Chem. Mineral.* **21**, 387-391

van der Hilst, R. (1995) Complex morphology of subducted lithosphere in the mantle beneath the Tonga trench *Nature* **374**, 154-157

van der Hilst, R. and Seno, T. (1993) Effects of relative plate motion on the deep-structure and penetration depth of slabs below the Izu-Bonin and Mariana island arcs *Earth Planet. Sci. Lett.* **120**, 395-407

van Heerden, L. (1993) A nitrogen and carbon stable isotope study of some Western Australian diamonds *Unpublished PhD thesis (The Open University, Milton Keynes)*

van Heerden, L. A., Gurney, J. J. and Deines, P. (1995) The carbon isotopic composition of harzburgitic, lherzolitic, websteritic and eclogitic paragenesis diamonds from southern Africa: a comparison of genetic models *S. Afr. J. Geol.* **98**, 119-125

van Vechten, J. A. (1973) Quantum dielectric theory of electronegativity in covalent systems III Pressure-temperature phase diagrams, heats of mixing and distribution coefficients *Phys. Rev. B Cond. Matter* **7**, 1479-1494

Verchovsky, A., Ott, U. and Begemann, F. (1993) Implanted radiogenic and other noble gases in crustal diamonds from northern Kazakhstan *Earth Planet. Sci. Lett.* **120**, 87-102

Verhoogen, J. (1980) Energetics of the Earth *National Academy of Sciences, Washington*

Vinogradov, A., Vdovykin, G., Il, in-P. and Loseva, L (1968) Structure of diamond-graphite aggregates in meteorites (ureylites) in connection with their origin *Geokhimiya* **8**, 891-905

Wakatsuki, M. and Takano, K. (1987) Suppression of spontaneous nucleation and seeded growth of diamond *High Pressure Research in Mineral Physics (Ed.. Manghnani, M. H. and Syono, Y. TERRAPUB, Tokyo)* 203-207

Wang, A. I., Wang, W. Y. and Zhang, A. D. (1991) Microstructural variations of a pyrope inclusion in diamond, as revealed by micro-

Raman spectroscopic study *Canad. Mineral.* **29**, 517-524

Wang, A., Dhamelincourt, P., Meyer, H. O. A., Guo, L. and Zhang, A. (1994) A carbon-rich multiphase inclusion in a Chinese diamond and its geochemical implications *Contrib. Mineral. Petrol.* **117**, 15-24

Wang, C-y (1972) Temperature in the Lower Mantle *Geophys. J. Roy. Astronom. Soc.* **27**, 29-36

Wang, Y. B., Weidner, D. J., Liebermann, R. C., Liu, X., Ko, J., Vaughan, M. T., Zhao, Y., Yeganeh-Haeri, A. and Pacalo, R. E. (1991) Phase transformations and thermal expansion of $MgSiO_3$ perovskite *Science* **251**, 410-413

Wang, Y. B., Gasparik, T. and Liebermann, R. C. (1993) Modulated microstructure in synthetic majorite *Amer. Mineral.* **78**, 1165-1173

Wang, Y. B., Weidner, D. J., Liebermann, R. C. and Zhao, Y. (1994) P-V-T equation of state of $(Mg,Fe)SiO_3$ perovskite: Constraints on the composition of the lower mantle *Phys. Earth Planetary Interiors* **83**, 13-40

Watanabe, H. Thermochemical properties of synthetic high-pressure compounds relevant to the earth's mantle *High-Pressure Research in Geophysics (Eds. Syono, Y. and Manghnani, M. H. Centre for Academic Publishing, Tokyo)* 411-464

Watson, E. and Green, T. (1981) Apatite / liquid partition coefficients for the rare earth elements and strontium *Earth Planet. Sci. Lett.* **56**, 405-421

Watt, G., Harris, J., Harte, B., and Boyd, S. (1994) A high-chromium corundum (ruby) inclusion in diamond from the São Luiz alluvial mine, Brazil *Mineral. Mag.* **58**, 490-492

Waychunas, G., Dollase, W. and Ross, C. (1994) Short-range order measurements in Mg)-FeO and $MgO-LiFeO_2$ solid solutions by DLS simulation-assisted EXAFS analysis *Amer. Mineral.* **79**, 274-288

Webb, S. (1989) The elasticity of the upper mantle orthosilicates olivine and garnet to 3 GPa *Phys. Chem. Mineral.* **16**, 684-692

Wedlake, R. J. (1974) The three allotropes of carbon *Diamond Res.* **1974**, 2-6

Weidner D. and Carleton, H. (1977) Elasticity of coesite *J. Geophys. Res.* **82**, 1334-1346

Weidner, D. and Ito, E. (1985) Elasticity of $MgSiO_3$ in the ilmenite phase *Phys. Earth Planetary Interiors* **40**, 65-70

Weidner, D., Wang, H. and Ito, J. (1977) Elasticity of enstatite (abstract) *EOS Trans. AGU* **58**, T-15 491

Weidner, D. J., Bass, J. D., Ringwood A. E. and Sinclair, W. (1982) The single crystal elastic moduli of stishovite *J. Geophys. Res.* **87**, 4740-4746

Weidner, D. J., Sawamoto, H., Sasaki, S. and Kumazawa, M. (1984) Single crystal elastic properties of the spinel phase of Mg_2SiO_4 *J. Geophys. Res.* **89**, 7852-7860

Weidner, D. J., Wang, Y. B. and Vaughan, M. T. (1994) Strength of diamond *Science* **266**, 419-422

Wentzcovitch, R. M., Ross, N. L. and Price D. G. (1995) Ab initio study of $MgSiO_3$ and $CaSiO_3$ perovskites at lower-mantle pressures *Phys. Earth Planetary Interiors* **90**, 101-112

Wessel, P. and Smith, W. H. F. (1995) The Generic Mapping Tools - GMT - Technical Reference and Cookbook *School of Ocean and Earth Science and Technology (SOEST), University of Hawaii at Manoa*

Wetherill, G. (1994) Provenance of the terrestrial planets *Geochim. Cosmochim. Acta* **58**, 4513-4520

White, R and McKenzie, D. (1989) Magmatism at rift zones: The generation of volcanic continental margins *J. Geophys. Res.* **94**, 7685-7729

Whitehead, J. A. and Luther, D. S. (1975) Dynamics of laboratory fluid and plume models *J. Geophys. Res.* **80**, 705-717

Wiens, D. A., Mcguire, D. J., Shore, P. J., Bevis, M. G., Draunidalo, K., Prasad, M. G. and Helu, S. P. (1994) A deep earthquake aftershock sequence and implications for the rupture mechanism of deep earthquakes *Nature* **372**, 540-543

Wiens, R. C., Lal, D., Rison, W. and Wacker, J. F. (1994) Helium isotope diffusion in natural diamonds *Geochim. Cosmochim. Acta* **58**, 1747-1757

Wilding, M. (1991) Untitled *PhD Thesis of University of Edinburgh, U. K.*

Wilding M. C., Harte, B. and Harris, J. W. (1991) Evidence for a deep origin for São Luiz diamonds *Extended abstracts of the fifth international kimberlite conference, Brazil, (1991) CPRM, Rio de Janeiro* 456-458

Wilks, J. and Wilks, E. (1991) Properties and applications of diamond *Butterworth Heinemann, Oxford*

Williams, Q., Jeanloz, R., Bass, J., Svendsen, B. and Ahrens, T. J. (1987) The melting curve of iron to 250 gigapascals - a constraint on the temperature at earth's centre *Science* **236**, 181-182

Winkler, B., Milman, V. and Payne, M. C. (1995) Ab initio total energy studies of minerals using density functional theory and the local density approximation *Mineral. Mag.* **59**, 589-596

Wolf, G. and Bukowinski, M. (1987), Theoretical study of the structural properties and equations of state of $MgSiO_3$ and $CaSiO_3$ perovskites: implications for lower mantle composition *High Pressure Research in Mineral Physics (Ed.. Manghnani, M. H. and Syono, Y. TERRAPUB, Tokyo)* 313-331

Wolf, G. and Jeanloz, R. (1985) Lattice dynamics and structural distortion of $CaSiO_3$ and $MgSiO_3$ perovskites *Geophys. Res. Lett.* **12**, 413-416

Wood, B. (1993) Carbon in the core *Earth Planet. Sci. Lett.* **117**, 593-607

Woodland, A. and O'Neill, H. (1993) Synthesis and stability of $Fe_3^{2+}Fe_2^{3+}Si_3O_{12}$ garnet and phase relations with $Fe_3Al_2Si_3O_{12}$-$Fe_3^{2+}Fe_2^{3+}Si_3O_{12}$ solutions *Amer. Mineral.* **78**, 1002-1015

Woods, G. S. (1985) Platelets and infrared absorption in type Ia diamonds *Diamond Conference Abstracts 1985, Reading (Unpublished)* 95-102

Woods, G. S. and Collins, A. T. (1983) Infrared-absorption spectra of hydrogen complexes in type-1 diamonds *J. Phys. Chem. Solids* **44**, 471-475

Wyckoff, R. W. G. (1963) Crystal structures *Wiley, New York*

Wyllie, P. (1980) The origin of kimberlite *J. Geophys. Res.* **85, B12**, 6902-6910

Wyllie, P. J. (1989) The genesis of kimberlites and some low SiO_2, high-alkali magmas *Kimberlites and Related Rocks Vol. 2 (Eds. Ross, J. et al., Blackwell Science Publications, Carlton)* 603-615

Wysession, M. (1996) Large-scale structure at the core-mantle boundary from diffracted waves *Nature* **382**, 244-248

Xie, Q. and Kerrich, R. (1994) Silicate-perovskite and majorite signature komatiites from the Archean Abitibi greenstone belt: Implications for early mantle differentiation and stratification *J. Geophys. Res.* **99 B8,** 15799-15812

Yagi, A., Suzuki, T. and Akaogi, M. (1994) High pressure transitions in the system $KAlSi_3O_8$-$NaAlSi_3O_8$ *Phys. Chem. Mineral.* **21**, 12-17

Yagi, T. and Akimoto, S. (1976) Direct determination of coesite-stishovite transition by in-situ X-Ray measurements *Tectonophys.* **35**, 259-270

Yagi, T., Marumo, F. and Akimoto, S. (1974) Crystal structures of spinel polymorphs of Fe_2SiO_4 and Ni_2SiO_4 *Amer. Mineral.* **59**, 486-490

Yagi, T., Mao, H-k. and Bell, P. M. (1978) Structure and chemistry of perovskite-type $MgSiO_3$ *Phys. Chem. Mineral.* **3**, 97-110

Yagi, T., Mao, H. K. and Bell, P. M. (1979a) Lattice parameters and specific volume for the perovskite phase of orthopyroxene composition, (Mg,Fe)SiO_3 *Carnegie Institution of Washington Year Book* **77**, 612-613

Yagi, T., Mao, H. K. and Bell, P. M. (1979b) Hydrostatic compression of $MgSiO_3$ of perovskite structure *Carnegie Institution of Washington Year Book* **78**, 613-614

Yagi, T., Bell, P. and Mao. H. (1979c) Phase relations in the system MgO-FeO-SiO_2 between 150 and 700 kbar at 1000°C *Carnegie Institution of Washington Year Book* **78**, 614-618

Yagi, T., Mao, H-k. and Bell, P. M. (1982) Hydrostatic compression of perovskite-type $MgSiO_3$ *Advances in Physical Geochemistry (Ed.. Saxena, S. K., Springer, Berlin)* 317-325

Yagi, T., Suzuki, T. and Akimoto, S. (1985) Static compression of wüstite ($Fe_{0.98}O$) to 120 GPa *J. Geophys. Res.* **90**, 8784-8788

Yagi, T., Kusanagi, S., Tsuchida, Y. and Fukai, Y. (1989) Isothermal compression and stability of perovskite-type $CaSiO_3$ *Proc. Japanese Academic Service* **B65**, 129-132

Yagi, T., Uchiyama, Y., Akaogi, M. and Ito, E. (1992) Isothermal decompression curve of $MgSiO_3$ tetragonal garnet *Phys. Earth Planetary Interiors* **74**, 1-7

Yagi, T., Kondo, T. and O'Neill, B. (1996) Phase transformations of pyrope under lower mantle conditions and the crystal chemistry of Al-containing silicate perovskite *EMPG-VI Abs. Suppl. 1 to TERRA Nova* **8**, 69

Yamaoka, F., Kanda, H. and Setaka, N. (1980) Etching of diamond octahedra at high temperatures and pressures with controlled oxygen partial pressure *J. Materials Sci.* **15**, 332-334

Yang, H. and Ghose, S. (1994) Thermal expansion, Debye temperature and Grüneisen parameter of synthetic $(Fe,Mg)SiO_3$ orthopyroxenes *Phys. Chem. Mineral.* **20**, 575-586

Yang, H. and Ghose, S. (1995) A transitional structural state and anomalous Fe-Mg order-disorder in Mg-rich orthopyroxene, $(Mg_{0.75}Fe_{0.25})_2Si_2O_6$ *Amer. Mineral.* **80**, 9-20

Yeganeh-Haeri, A. and Weidner, D. J. (1989) Elasticity of $MgSiO_3$ in the perovskite structure *Science* **243**, 787-789

Yeganeh-Haeri, A., Weidner, D. J. and Ito, E. (1989) Single-crystal elastic moduli of magnesium metasilicate perovskite *Perovskite: a structure of great interest to Geophysics and materials science (Eds. Navrotsky, A. and Weidner, D., American Geophysical Union, Washington)* **45**, 13-23

Yeganeh-Haeri, A., Weidner, D. J. and Ito, E. (1990) Elastic properties of the pyrope-majorite solid solution series *Geophys. Res. Lett.* **17**, 2453-2456

Yoneda, A. (1990) Pressure derivatives of elastic constants of single crystal MgO and $MgAl_2O_4$ *J. Phys. Earth* **38**, 19-55

Yoo, C. S., Holmes, N. C., Ross, M., Webb, D. J. and Pike, C. (1993) Shock temperatures and melting of iron at earth core conditions *Phys. Rev. Letters* **70**, 3931-3934

Young, T. E., Green, H. W., Hofmeister, A. M. and Walker, D. (1993) Infrared spectroscopic investigation of hydroxyl in β-$(Mg,Fe)_2SiO_4$ and coexisting olivine: implications for mantle evolution and dynamics *Phys. Chem. Mineral.* **19**, 409-422

Yusa, H., Yagi, T. and Shimobayashi, N. (1995) A new unquenchable high-pressure polymorph of $Ca_3Al_2Si_3O_{12}$ *Phys. Earth Planetary Interiors* **92**, 25-31

Zashu, S. and Hiyagon, H. (1995) Degassing mechanisms of noble gases from carbonado diamonds *Geochim. Cosmochim. Acta* **59**, 1321-1328

Zerr, A. and Boehler, R. (1994) Constraints on the melting temperature of the lower mantle from high pressure experiments on MgO and magnesiowüstite *Nature* **371**, 506-508

Zhang, Y. and Zindler, A. (1993) Distribution and evolution of carbon and nitrogen in earth *Earth Planet. Sci. Lett.* **117**, 331-345

Zhao, J. X. and McCulloch, M. T. (1993) Melting of a subduction-modified continental lithosphere mantle - evidence from late Proterozoic mafic dike swarms in central Australia *Geology* **21**, 463-466

Zhao, Y. S., Weidner, D. J., Ko, J. D., Leinenweber, K., Liu, X., Li, B. S., Meng, Y., Pacalo, R. E. G., Vaughan, M. T., Wang, Y. B. and Yeganeh-Haeri, A. (1994) Perovskite at high P-T conditions: An in-situ synchrotron X-Ray diffraction study of $NaMgF_3$ perovskite *J. Geophys. Res.* **99,** 2871-2885

Zheng, Y-F. (1996) Oxygen isotope layering of the mantle as deduced from isotopic partitioning in mantle minerals *J. Conf. Abs.* **1**, 695

Zhu, H., Newton, R. C. and Kleppa, O. J. (1994) Enthalpy of formation of wollastonite ($CaSiO_3$) and anorthite ($CaAl_2Si_2O_8$) by experimental phase equilibrium measurements and high-pressure solution calorimetry *Amer. Mineral.* **79**, 134-144

Appendix 1 Inclusion breakout

Appendix 1.1 Apparatus and Methodology

The crusher employed was manufactured following a design of Harris (1993, *personal communication*) (figure A1_1), similar models being employed in the work of Wilding (1991), Stachel and Harris (1995) and McDade and Harris (1995).

A flat base and two cylindrical holes were milled into a 80/80 stainless steel disc: the base being for stability in a vertical aspect, the lateral hole for mounting and viewing of the diamond and the axial hole for housing of the moveable anvil. Diamonds for crushing are placed on the static anvil (made of hardened silver steel) in an orientation such that the included material is as far from either anvil face as possible and that the most likely fracture surface is at 45° to the anvil axis. Such an orientation allows for the least catastrophic breaking of the stone and the greatest likelihood of preservation of unbroken inclusion material. In practice, however, suitable fractures are not always readily observable and, even if they are, occasionally stones can prove very hard to break. This makes explosive fracturing difficult to avoid; the result being that occasionally only a little strain energy is required for the stone to explode (particularly if internal pressure of inclusions on diamond host is high). An additional result of such a breakage often tends to be the fracturing of the glass viewing plates, hence the possibility of glass contamination of fracture products. The risk of such an eventuality can be reduced by a coating of nail varnish being applied to the viewing disks (Stachel, 1996 *personal communication*). With the inclusion mounted, the viewing plates are secured by friction applied by rubber O-rings against their cusps in the steel crushing block. The movable anvil is then screwed down to finger tightness to hold the stone in place. The anvil apparatus is subsequently moved to a comfortable viewing position under an optical macroscope. Fracturing is induced by tightening of the anvil with an allen key in a step-wise fashion; tightening and then relaxing slightly to induce micro-fracturing and final fracture as delicately as possible. A ball bearing is used between the allen screw and the anvil to avoid any rotational movement of the anvil which could induce loss of diamond positioning. In some cases it is clear that the stone is close to final fracture as energy is released in the form of high pitched sound waves and an irridescent interference pattern due to strain can be seen throughout the stone.

After fracturing, the broken material is brushed into a flat-based petri-dish for examination and removal of included material, subject to the conditions previously outlined. The breaking process often has to be repeated to release all visible inclusion material. Potential inclusion grains are transferred by needle onto a graticule in order to estimate their dimensions. Transferral tends to be easy for some inclusions which show slight magnetic properties although this poses problems for the removal of the grain from the needle. In this case, a wooden needle is used to brush the sample onto the graticule. In cases where the included material could not easily be picked up, the addition of finger grease or silica grease to the needle aids transferral. After measurement, the inclusions are moved to a lightly greased glass slide inside a circle of ink adopted for ease of subsequent location for mounting in Araldite®. A ring of Araldite® is smeared around the inclusion with a little cusp being taken over the inclusion itself to aid adhesion to subsequent Araldite® and to avoid the formation of air bubbles around the inclusion. A brass pip[1] is then coated internally with Araldite® to improve subsequent flow down the inside edge and to, again, reduce the risk of air bubbles forming. The pip is subsequently placed over the inclusion and small amounts of Araldite® bled down the inside surface of the pip. At this stage, care is taken to observe the behaviour of the inclusion under the deluge of Araldite®. Any extreme movement being addressed at this stage. Once a reasonable thickness of Araldite® (a few mm) covers the inclusion, the pip can be filled more speedily. Pips prepared in this fashion are allowed to harden on a hotplate over night in preparation for polishing.

Depending on the shape of termination of the pip, thickness of grease on the slide, depth of inclusion into the first cusp of Araldite® and the degree to which the inclusion is lifted into a meniscus of Araldite® inside the pip, the grain will reside at different levels with reference to the top surface of the pip. At this stage, in order to bring the inclusion to the surface, the pip is ground with 600 grit adopting only a few rotations at a time. As some form of meniscus always occurs, grounding can be monitored by observing a ground edge appearing inwards from the edge of the pip. In this way, it can be ensured that the process is adopted even more carefully as the inclusion is approached. Once the inclusion is on the surface, it will be observable in reflected light in addition to transmitted light through the Araldite®. At this stage, the pip can be taken and polished using diamond grit. For this study, grades of 6 µm, 1 µm and 1/4 µm diamond grit have generally been adopted with 6 inclusions being polished at a time in an automatic lap designed for this purpose. The head of the lap consists of six pip-sized holes in an aluminium disk, each pip being weighed down on the back surface by a brass block. The head is then lowered onto a lap and the polish achieved by movement throughout 360° providing, in theory, a flat and even polish. In practice, however, a number of problems were encountered. All non-cruddy inclusions are significantly harder than the Araldite® surrounding them and so rounding at the edges is unavoidable. For larger inclusion, this presented no significant problem but it was found that for small inclusions (<50 µm in diameter) very little flat area was obtained by this method. This problem was compounded by the problem that, with time, wear of the

---

[1] ~ 4.8 mm depth with an inside diameter of ~ 2.6 mm

brass against the holes in the lap head caused an increasingly poor fit; samples began to rock within their holes. It was found that ommiting the 1/4µm stage avoided rounding becoming too severe but it could not be wholly avoided. This meant that care had to be exercised in choosing points for electron and ion probe analysis although, at least for the former technique, a poor choice of analysis point could be identified by poor totals. It should be noted that some workers utilise denture fixative rather than Araldite® which, being harder, causes less of a rounding effect on the grains (Stachel, 1995 *personal communication*). This technique has the alternative problem, however, of behaving less fluidly than Araldite® thus is therefore more difficult to manipulate into the pip and ensure that the positioning of the inclusion is not disturbed. With practice, however, it may be a technique which would produce better results.

Aside from the mechanisms of the break-out process, careful consideration of each individual stone and inclusion is considered an integral part of the process and can yield invaluable information as to the history of the diamond and reliability of the inclusions as primary included phases. In view of this, as described in appendix 1.2, the following methodology was adopted for each stone:

- Observation was made of colour, morphology, state of plastic deformation and resorption of the stone in addition to any obvious fracturing.
- Observation was also made of position, distribution and abundance of inclusion material and their relationship to features of the diamond host. An initial identification of possible inclusion type was made at this stage bearing in mind the difficulties of being conclusive with such identification due to surface feature obstruction, imposed morphology and internal reflection and refraction.
- The stones were then broken, notes being made on how this proceeded, eg. if along particular fracture systems etc.
- Observation was then made of the look of the diamond after breaking, in addition to number, colour and morphology of inclusions recovered: this was found to be particularly useful in comparing with observations in-situ and for noting the common features that some inclusions appearing colourless turned out not to be so, due to internal reflection. Additionally, some which appeared to have diffuse colour, appeared homogeneous, for the same reason whilst others, which appeared black in colour proved not to be, this due to inclusion / diamond boundary graphitisation. Where particular observations of this nature appeared to be pertinent to aspects of this study, these are tackled, where appropriate, in the text. A particular example is the high proportion of plastically deformed stones, section 5.3.2.

Figures A2_1 to A2_9 show what some of the released inclusions look like.

Appendix 1.2 *Summary of visual observations on diamonds BZ215 - BZ272, JH7 - JH17 and GU4 with details of breakage where applicable*

Stone	**Packet**	**Diamond observations**	**Inclusion Observations**	**Breakout**	**Notes**
JH2	Unknown	Colourless stone showing plastic deformation	Elongate octahedral light-medium brown inclusion showing some additional facets. Showed slight magnetism	Inclusion recovered whole	
JH6	Unknown	Stepped octahedral stone with terminations showing a crude cubic morphology due to stepped growth of octahedral faces. Colourless. Partial resorption and no obvious plastic deformation	Large dark brown coloured inclusion surrounded (predominately to the opposite side of laser cut) by brown coloration possibly due to oxidation along fractures	The inclusion broke in two and showed a red oxidation	
JH7	Unknown	Highly resorbed colourless stone exhibiting a circular surficial pit filled with graphite (opposite laser cut face)	Two inclusions observed; one light brown coloured and a minute colourless inclusion towards the apex of the stone	Brown inclusion broke into two large tabular pieces and a few small fragments	

JH11	Unknown	Part of an aggregate stone (large octahedral portion with an formless neighbour). The octahedral portion exhibits rounded edges and shows plastic deformation features.	Inclusion occupied octahedral portion and seemed close to the surface. A fracture plane seems to extend to the surface of the stone. The inclusion shows an iridescence and exhibits a hexagonal form in section. It lies below a pit showing concentric rings of black coloration (possibly graphite).	Breakout resulted in seven inclusion fragments	Fragments kept in two bottles (JH11a(dfa) & JH11a(dfb))
JH12	Unknown	Brown stone with rounding (dodecahedral side) and shield lamellae (non-dodecahedral side). Plastic deformation is in evidence.	Black inclusion with octahedral morphology.	The inclusion broke into two main pieces one of which has a half octahedral morphology.	
JH17	Unknown	Colourless highly resorbed stone with corrosion sculpture observed near surface. Its morphology is that of a flat and rounded octahedron.	Large intensely iridescent inclusion with elongate octahedral morphology	The inclusion broke into 3 pieces with one fragment showing octahedral termination.	
BZ215	JH3/86 Pkt 11	Dodecahedral aggregate of two inclusions showing plastic deformation features.	A black inclusion with a corona of black material surrounding it (perhaps suitable itself for analysis) was identified. Additionally a little orange grain was found.	The black inclusion broke into primarily two grains one of which showed an iridescence and both appeared to be non-magnetic.	Two additional grains of black material remain in BZ215(df).

BZ216	JH3/86 Pkt 11	Colourless stepped octahedral stone.	Two inclusions appearing to be black in colour were identified with one showing iridescence and the larger exhibiting a marked corona. There is evidence of hazy brown material near to the surface separate from the larger inclusion which is possibly contaminant.	On breaking the stone one fragment appeared which was colourless and had a single crystal type morphology. It appeared to be isotropic. Two halves were found to fit together to an elongate cuboctahedron[2].
BZ217	JH3/86 Pkt 11	Colourless stepped octahedral stone.	What appears to be a planar occurrence of black material within the stone was noted. At the centre of this lies a cubic inclusion showing a silvering due to internal reflections but was thought to be ferropericlase.	On breaking no obvious inclusion material was identified either in PPL or XPL. Some material was recovered which appeared to be contaminant from the brush and a v. slightly orange 'inclusion' was finally mounted.
BZ218	JH3/86 Pkt 11	Brown dodecahedral and slightly elongate stone showing plastic deformation.	Minor areas of oxidised looking material and black flecks appear throughout the stone in addition to an oxidised looking fracture and an isolated black fracture system with a clear 'eye'.	On breaking the stone a single orangey brown inclusion was recovered in addition to a highly birefringent slightly green inclusion with a 120 degree edge and a further highly birefringent grain.
BZ219	JH3/86 Pkt 11	Brown irregular stone with prominent hexagonal pitting on pseudo-octahedral faces. The stone is plastically deformed.	A large disc shaped fracture with one or two eyes was noted with a small amount of iridescence around one possibly associated with a few colourless inclusions on the edge of the fracture system. Because of surface pitting it is very difficult to see into the stone.	Two pieces of brown cruddy looking material were recovered, one of which appears reasonably crystalline. In addition a paper thin highly birefringent fragment was obtained (possibly diamond) and a crystalline black half octahedral grain.

---

[2] Cubo-octahedral morphologies often arise in mineral inclusions in diamonds because the diamond imposes its own morphology on the inclusions during a period of mutual growth (Harris and Gurney, 1979).

BZ220	JH3/86 Pkt 11	Brown dodecahedral stone showing plastic deformation. A dark fracture system showing an occasional iridescence and a separate small pseudo-cubic colourless 'inclusion' were observed in situ.	No inclusions were recovered on breaking the stone.	
BZ221	JH3/86 Pkt 11	Brown dodecahedral stone with hexagonal pitting and plastic deformation.	An internal black fracture plane with a dark 'inclusion' within was identified. In addition a second black/brown coloration with an internal fracture was observed but no obvious inclusion appeared throughout. Surface characteristics especially secondary external coloration prevent a clear view into the stone however.	One cuboctahedral dirty metallic yellow magnetic inclusion (possibly sulphide) was recovered in three pieces.
BZ222	JH3/86 Pkt 11	Brown macle octahedron with stepped faces, trigons, hexagonal pitting on octahedral faces and plastic deformation features.	Exclusively in the one half of the macle some brown material was identified on the surface and a zone of black material under one face showed on or perhaps two small iridescent inclusions.	Four fragments of inclusions were recovered.

BZ223	JH9/88 Pkt 25	Colourless aggregate of two pseudo-dodecahedral stones with intensive step resorption and plastic deformation.	Two clear inclusions possibly close to one face and a large sulphide looking inclusion close to the centre of the stone were identified. One small fracture away from any inclusion appears to be clear of infilled material.	Two brown crystalline inclusions were recovered, one showing a tabular morphology and the other a mottled appearance. In addition a ferropericlase looking inclusion a half octahedral iron or ferropericlase inclusion and a green fragment which seemed possibly to be a diamond fragment were recovered.	
BZ224	JH9/88 Pkt 125	Colourless dodecahedral stone with rings of aggregate almost star shaped diamond. It is resorbed and plastically deformed.	Centrally located is a black mass whose form is obscured by surface features. It shows characteristics of a sulphide inclusion. It shows an iridescence. A couple of small black flecks surround the central form one of which is tabular in morphology and iridescent.	No inclusion material was recovered, only extensive graphitised material.	
BZ225	JH9/88 Pkt 125	Brown octahedral approaching dodecahedral stone showing slight resorption and plastic deformation features.	A large black patch showing iridescence towards one side and an 'eye' appearance was noted. This inclusion appears near to the surface. Distinct from this area, a small patch of possible graphitisation was observed although surface features make observation difficult.	Two large inclusions appearing to be too metallic for ferropericlase and too black for sulphide were recovered. One of these looked octahedral but they may be crushing steel. Additionally a tabular emerald green inclusion was recovered.	
BZ226	JH3/86 Pkt 47	Colourless elongate showing at one end a slightly rounded clear dodecahedral face the other being more irregular. Plastic deformation is in evidence.	A deep blue coloured inclusion with a metallic sheen occupies the dodecahedral end. Associated with this are a few blebs of black material and another small cubic blue inclusion. The main inclusion is elongate but orthogonal to the elongation of the host. A few brown specks are distributed thoughout the rest of the stone.	On breaking the stone an emerald green isotropic inclusion with an olivine-type morphology was recovered. This was thought to be a green garnet. In addition a small brown isotropic grain and a tabular deep red/brown anisotropic grain and a number of ferropericlase looking grains were recovered.	Some inclusion fragments of 'ferropericlase' were left in BZ226(df).

BZ227	JH9/88 Pkt 57	Cloudy irregular elongate stone with evidence of plastic deformation.	An intense sky-blue diffuse coloration was observed deep in the stone in addition to an 'eye' inclusion marginally nearer to the surface. This 'eye' inclusion exhibits a black border surrounding a colourless core. Occasional black/brown flecks occur in other parts of the stone.	A single blue rounded crystal with a vitreous lustre was recovered in addition to a possible ferropericlase which resembled crusher material. Furthermore a piece of greeny material was obtained.
BZ228	JH3/86 Pkt 17	Brown fairly irregular pseudo-cubic stone showing plastic deformation.	A large black internal mass was observed but surface irregularities make it difficult to view internal features.	A number of green flecks were picked out, which looked like contaminant. In addition a goldy metallic grain a brown single crystal and a large white isotropic and spherical grain were recovered. Lastly, a second very small brown grain was obtained again resembling contaminant.
BZ229	JH3/86 Pkt 17	Slightly brown stepped octahedral stone showing plastic deformation. A deep negative trigon occupies on face.	No obvious internal fracturing was observed. A large black winged area of included material occupies an off-centre position and surrounds a white 'eye'. The trigon shows an orangey coloration.	Brown orange material was observed on fracturing and a small fragment resembling ferropericlase was obtained. In addition two shards of a deep blue material were obtained which seemed anisotropic but did not look convincingly crystalline.
BZ230	JH3/86 Pkt 17	Colourless stepped dodecahedral stone exhibiting plastic deformation.	Two black areas of internal coloration are apparent one encompassing an 'eye'.	Four grains were recovered: two halves of an octahedral magnetic and silvery crystal (possibly sulphide): a small fragment of metallic blue/grey non-metallic 'ferropericlase' and a single blue grain.

BZ231	JH3/86 Pkt 17	Brown macle showing stepped and resorbed faces. One side has a slight dodecahedral form the other being irregular. Plastic deformation is apparent.	The dodecahedral half incorporates a black area and the other side incorporates a small copper brown inclusion. Brown coloration is apparent on the surface of the stone.	One half octahedral metallic grey/black grain was obtained in addition to two more mottled looking versions (these may be graphitised diamond). Furthermore an irregular blue mottled grain was recovered.
BZ232	JH3/86 Pkt 15	Brown dodecahedral stone showing plastic deformation.	A fracture surface is filled with light brown material but appears not to penetrate too deeply into the stone. A colourless inclusion with irregular form and a black rim is apparent.	Three grains were recovered: a friable grain showing a black metallic lustre and a strong red coloration in transmitted light: a sky-blue grain and a dark metallic grain which although showed good faces could be crushing material.
BZ233	JH3/86 Pkt 15	Brown irregular stone with a mottled surface.	A colourless 'eye' inclusion is apparent with a black outline. In addition, brown surface coloration is in evidence.	On breaking the stone a brown coloured fracture appeared to penetrate towards the centre of the stone but seemed distinct from the inclusion area. Two grains of possibly oxidised brown green material were obtained as well as a prismatic dark metallic non magnetic grain resembling ferropericlase and a larger half octahedral dark metallic grain (again possible ferropericlase).

BZ234	JH3/86 Pkt 15	Colourless irregular stone with much surface pitting. Plastic deformation is not seen.	Brown surface staining is dominant and internally some black coloured areas can be identified despite obscuring surface effects. One patch includes a colourless 'eye'.	Breakage was very easy, implying internal fracturing. A large number of sapphire blue 'inclusions' were recovered which appeared to vary in intensity of colour perhaps due to thickness. The fragments seem crystalline but have poor form and are thin but not too friable. These are possibly contaminant.	Some pieces of blue material are left in BZ234(df).
BZ235	JH3/86 Pkt 15	Brown irregular slightly octahedral stone showing plastic deformation. There is extensive surface pitting.	A large fracture cuts across one side and into the middle of the stone. A colourless 'eye' surrounded by black material was observed.	On breaking the stone fractured along the crack and exhibited an intense brown coloration (oxidation) throughout the fracture system. This area was distinct however from the main inclusion but on the first break some black crystalline fragments resembling ferropericlase were recovered. A very friable brown inclusion appeared from the hole surrounded by black material from what appeared to be the colourless 'eye'. In addition a grey, metallic, tabular grain was recovered, a blue grain resembling carborundum and a birefringent milky grain.	
BZ236	JH3/86 Pkt 15	Irregular stone with one flat face suggesting previous fracture along this plane. There is evidence of plastic deformation.	Severe brown staining occurs along three large fractures and at one end a colourless 'eye' 'inclusion' was seen.	No inclusion material was recovered.	

BZ237	JH9/88 Pkt 35 (10/10)	Brown irregular partially resorbed stone showing plastic deformation.	A large irregular shaped inclusion surrounded by a disk-shaped fracture filled with black material was observed. The inclusion appears dichromic from bright green to reddy orange with no obvious boundary between colours. Close by there are three relatively small inclusions of what look like similar material.	Only green inclusion fragments were obtained in addition to what appeared to be a ferropericlase and a green/white inclusion.
BZ238	JH12/87 Pkt 16	Colourless dodecahedral plastically deformed stone.	An iridescent inclusion surrounded by black flecks of what look like graphite was observed in addition to another black fleck towards the centre of the stone.	Recovered was a small green grain and what looked like a ferropericlase.
BZ239	JH6/86 Pkt 31	Brown elongate dodecahedral stone with an intense area of trigons and hexagons on half of one side. The stone appears to be plastically deformed.	Much included material was observed. Surface coloration is yellow and included material involves a number of black flecks and a small green inclusion surrounded by black coloration. In addition a colourless inclusion with black bordering an 'eye' inclusion (possibly ferropericlase) and a dark inclusion surrounded by brown material near to the surface were observed.	On breaking the stone a single black slightly metallic and irregular ferropericlase-type inclusion was recovered. In addition three small shards of slightly green anisotropic material was recovered as well as a small irregular brown black inclusion which looked secondary. Furthermore a small spherical black grain, a very light green grain, a milky anisotropic grain (this resembled diamond) and a goldy metallic grain were recovered.

BZ240	JH3/86 Pkt 19	Light brown elongate irregular macle. One end exhibits a dodecahedral termination. This stone is pitted and shows evidence of plastic deformation.	No major fracture planes were observed and the stone includes numerous black flecks, some of which are apparent on the surface of the stone. A small green inclusion appears to occupy the dodecahedral end and has some black material surrounding it. In the centre there appears to be a colourless inclusion surrounded by some dark material.	One birefringent cloudy irregular grain was recovered which looked rather contaminated. In addition a green inclusion was also recovered.
BZ241	JH6/86 Pkt 49	Brown highly irregular stone. A hexagonal window appears on one area.	One end of the stone shows intense black coloration on the surface as well as some brown oxidised looking material in this area. A dark inclusion is apparent in the opposite end of the stone which appears to be surrounded by undisturbed clear diamond. This inclusion resembles a ferropericlase. In addition through the hexagonal pit can be seen a dichromic inclusion which appears to be predominantly green with a red tip.	On breaking a light brown isotropic grain was recovered which resembled either ferropericlase or oxidised material. In addition two birefringent grains were recovered one of which was green and paper thin and the other was green with a red tip.
BZ242	JH6/86 Pkt 49	Brown highly irregular aggregate stone.	Some surface brown coloration is apparent. Close to the surface resides a black and iridescent inclusion which resembles ferropericlase and again towards the surface of the stone appears a green elongate inclusion with a small purplish end. This is surrounded by a small internal fracture system filled with black material.	An elongate cubo-octahedral grain resembling ferropericlase were recovered whole in addition to a piece of green material.

BZ243	JH3/86 Pkt 32	Brown macle stone with evidence of dodecahedral faces and many shallow surface striations. Plastic deformation is evident.	Included material involves one dark speck with some surrounding black coloration (possibly graphitisation). This could be a ferropericlase. Next to this inclusion appears an 'eye' which appears colourless but again could be a ferropericlase. Both these inclusions occur towards one end of the stone but fairly deep. At the other end a brown elongate mass surrounds a milky inclusion next to a small colourless inclusion surrounded by some small internal fracturing and graphitisation. Associated with this is an equant emerald green inclusion. Both these latter inclusions are relatively near to the surface but show no evidence of contamination.	On breaking, a green anisotropic grain, three grains of material resembling ferropericlase and a colourless anisotropic grain were recovered. The 'ferropericlase' appears to be a distinctly cubic cubo-octahedra in parts.

BZ244	JH12/87 Pkt 28	Brown irregular stone with surface pitting and negative trigons. There is also evidence of plastic deformation.	There appears to be a green inclusion surrounded by some graphite-free internal fracturing. Nearby an elongate octahedral 'eye' inclusion is apparent with some internal fracturing emanating from the inclusion terminations.	On breaking the stone two large fragments were obtained: one containing a black octahedral grain resembling ferropericlase and the other exhibiting a green crystal an 'eye' inclusion and a small colourless inclusion surrounded by internal fracturing. Obtained from these pieces was a half octahedral metallic black grain leaving some graphitisation in the hole. The green inclusion came out whole and seemed to exhibit a gradation in intensity of colour. Turquoise material which resembled contaminant and a small black fragment which resembled crushing material were also recovered. No colourless inclusion was retrieved.	The other half octahedron of 'ferropericlase' was left in BZ244(df).
BZ245	JH3/86 Pkt 13	Slightly brown irregular stone showing areas of fine surface pitting and more intense surface pitting and negative trigons.	An inclusion which appears to be near to the surface shows a gradational blue coloration and a slightly dusky appearance. This inclusion occurs towards one end of the stone. Additionally a reddy brown inclusion appears close to the surface and resembles oxidised material.	Fracturing proved extremely difficult but eventually yielded a single tabular monoclinic looking black inclusion resembling ferropericlase. Additionally one similar fragment was recovered. It seemed that a fragment of diamond exhibited a sulphide inclusion but this was obtained as an amorphous brown grain looking oxidised.	Additional 'ferropericlase' was left in BZ245(df).
BZ246	JH3/86 Pkt 51	Colourless irregular slightly octahedral stone with intense fine resorption on one side and clear on the other.	A number of black specks occur throughout the stone and towards one end a cluster of clear inclusions are surrounded by coronas of black material (probably graphite).	A rather altered looking mottled and anisotropic green grain was recovered.	

BZ247	JH3/86 Pkt 13	Brown slightly irregular dodecahedral stone showing evidence for plastic deformations.	A colourless 'inclusion' appears close to the surface but could be a feature of internal reflection. Additionally a large greeny brown inclusion with an amorphous lustre appears deeper into the stone as well as a number of smaller dark specks and more brown material. No obvious fractures appear down to these inclusions.	Some greeny brown material was recovered which proved to be very friable and obviously secondary. This was not mounted. Additionally a rather altered looking isotropic light brown grain was recovered as well as a tabular anisotropic and slightly green inclusion. This however resembles a fragment of diamond.
BZ248	JH3/86 Pkt 13	Intensely brown roughly dodecahedral stone with a finely pitted surface. The stone exhibits evidence of plastic deformation.	The stone is filled with brown coloration towards one end and generally looks contaminated close to the surface throughout. Deep in the stone is an indication of a large tabular colourless inclusion with a black corona: i.e. an 'eye' inclusion.	A large number of black fragments of material were recovered and were obviously altered. Nothing of value was found.
BZ249	JH9/88 Pkt 59 (9/10)	Colourless dodecahedral stone with evidence of slight resorption and pitting on the long axis. The ends are cloudy due to mild surface pitting. The stone exhibits some evidence of surface trigons and plastic deformation.	An area of black corona surrounds a colourless core and nearby appears a green inclusion with some black material surrounding it. The green coloration could be due to internal refraction and reflection. The stone appears to be generally clean and free from alteration.	

BZ250	ZIL1/90 Pkt 19 Lot 9 (3/10)	Brown slightly irregular dodecahedral stone with a generally pit free surface although it is slightly cloudy and evidence for plastic deformation.	An 'eye' inclusion appears towards one end of the stone which has an obvious platy graphitic fabric. The inclusion seems colourless but in some orientations has a slightly green coloration possibly due to internal reflection and refraction. Elsewhere in the stone there appears a deep black gash up to the surface far from any inclusion. Throughout are a few black specks and next to the eye appears a small green inclusion which seems to be part of the 'eye' fracture system.	On breaking a brown mottled looking tabular crystal was removed and looked rather altered. Additionally a slight brown isotropic tabular grain was removed along with a black non-metallic looking grain which may be ferropericlase or crushing material. The 'eye' remains showed extensive black coloration.
BZ251	(1/8)	Brown irregular? plastically deformed and mottled stone	Two main inclusions appear on one polished face of this stone: one is black and octahedral with a little black corona, the other is colourless with two small internal fractures. Throughout many small colourless inclusions with small black fracture systems occur. At one end is a cluster of one tabular colourless and a small tabular green inclusion.	
BZ252	(2/8)	Deeply brown and plastically deformed irregular stone with much surface obscuration	One large fracture system runs through the stone although perhaps not to the edges of the stone. Along this fracture is much black colouration and a small single, colourless inclusion occupies the centre on the polished surface. Deeper in the stone there appears to be a pseudo-octahedral colourless inclusion with a dark brown internal fracture system. Occasional black flecks occur throughout.	

BZ254	JH9/88 Pkt 129 (4/8)	Irregular brown plastically deformed stone with a mottled surface.	Four main inclusions can be identified all with small internal fracturing: one strongly brass coloured elongate inclusion, a lozenge shaped black inclusion and a cluster of two pseudo-octahedral colourless inclusions		
BZ255	ZIL1/90 Pkt 64(5/8)	Irregular brown highly plastically deformed stone with some graphitisation on the surface.	A single colourless looking inclusion occupying a small fracture system with a little internal graphitisation. Even on the exposed surface, this inclusion looks colourless but otherwise has irridescence consistent with fPer.		
BZ257	ZIL1/90 Pkt 54 (7/8)	Irregular, possibly macled colourless stone with a mottled surface and plastic deformation	Through the single window can be seen a large single black irridescent inclusion with coign fractures extending partly into the diamond. Grey graphitisation is seen on the octahedral surfaces of the inclusion in addition to a more graphitised corona. A possible very small green inclusion is seen on the apex of the main inclusion. In addition there exists a small tabular colourless inclusion near the window surface and some small black flecks occur throughout.	The stone broke catastrophically with the main inclusion being released as a large fragment in addition to a number of smaller fragments. The inclusion is black to watery brown on very thin edges and shows a strong irridescence on irregular surfaces. The largest fragment shows a conchoidal fracture and striations and an irregular morphology. Four other fragments, one looking perhaps metallic were recovered in addition to a tabular black crystal.	Other pieces from the main inclusion were left in phial BZ257(df) in addition to a single mottled orange grain and a smaller, slightly orange crystal. Both appear to be secondary.
BZ258	ZIL1/90 Pkt 44 (8/8)	Brown irregular plastically deformed stone.	One large irregular colourless looking inclusion with some surface graphitisation, black corona and some irridescence. A possible small red inclusion lies near the apex of this inclusion. In addition a small graphitised tabular inclusion lies in a single internal fracture plane.		

BZ259	ZIL1/90 Pkt 33 (1/10)	Brown irregular stone showing extensive resorption negative trigons and evidence for plastic deformation. One face appears to be relatively unresorbed.	Through the unresorbed face can be seen a colourless inclusion partly surrounded by black material. Next to this is a further 'colourless' inclusion with a more extensive black corona. Additionally there appears to be a small green inclusion near to the surface.	An altered looking green inclusion was recovered which has a mottled surface similar to that of diamond shard. Indeed a fragment of diamond seemed to be attached to this inclusion which proved difficult to remove. An additional smaller apple green grain was recovered. The edges of this grain appear to be a little mottled but it looked crystalline.
BZ260	ZIL1/90 Pkt 66 (2/10)	Brown rounded dodecahedral stone with evidence for plastic deformation. One of the windows intensely scored and pitted.	The pitted window is speckled with black material which is probably steel from the polishing lap. Inside the stone is a corona surrounding an 'eye'. The fractures do not however appear to reach the surface. Nearby is a black slightly metallic looking tabular inclusion.	The stone initially broke easily down the middle but no inclusion or secondary material was revealed. One fragment contained a large spherical looking black area possibly a ferropericlase inclusion or part of the corona. A brown orange shard was also recovered. Furthermore an altered looking light green brown inclusion with a mottled appearance but reasonably good shape was recovered. Additionally a little black sphere lacking an obvious metallic lustre was recovered. After further breaking a single crystal ferropericlase was recovered showing a black coloration.
BZ261	ZIL1/90 Pkt 18 (4/10)	Brown irregular plastically deformed with much surface graphitisation	One distinctly orange tabular inclusion with a small internal fracture system appears close to a clear surface of the stone. A single colourless very elongate tabular inclusion occurs deeper in the stone and, throughout are small black flecks.	

BZ262	ZIL1/90 Pkt 19 (5/10)	Irregular colourless plastically deformed stone with areas of large surface pitting and some mottling and surface graphitisation.	One small colourless inclusion occurs deep within the stone. Nearer the surface, a larger orange inclusion lies within a extensive black internal fracture system. A cluster of small octahedral black inclusions lie within the stone.
BZ263	ZIL1/90 Pkt 18 (6/10)	Dodecahedral broken mottled colourless stone with plastic deformation.	One small fPer-looking inclusion lies close to the surface at one end. It appears colourless with some irridescence and a little black corona. A number of additional small inclusions occur throughout all with very small isolated fractures. One is irridescent blue and another exhibits a tabular morphology and grey-brown colour.
BZ264	ZIL1/90 Pkt 13 (7/10)	Large irregular colourless stone with some surface graphitisation, mottled surface in places and plastic deformation lines.	A single octahedral inclusion lies at the tapered end of the stone. It has a small coign fracture system with a little black graphitisation and some grey graphitisation on octahedral faces. There is some irridescence, otherwise the inclusion looks colourless: indicative of fPer.
BZ266	JH3/86 Pkt 11 (S1)	Stepped octahedral colourless stone with a little orange surface colouration.	A large sulphide coloured mass resides in the centre of the stone with black fractures extending towards the surface.
BZ267	JH3/86 Pkt 11 (S2)	Stepped and etched octahedral colourless stone.	A large sulphide coloured mass resides in the centre of the stone with small black fractures extending towards the surface.

BZ268	JH3/86 Pkt 11 (S3)	Irregular brown macle-octahedral stone with plastic deformation lines and some surface orange colouration.	Two main inclusion centres occur within the stone, both with a sulphide colouration and black internal fracture systems.
BZ269	JH3/86 Pkt 11 (S4)	Colourless, stepped octahedral stone with trigons.	A single sulphide coloured mass occurs towards one end deep in the stone. It has extensive black colouration in small fracture systems throughout. Its morphology is indistinct.
BZ270	JH9/88 Pkt 96	Irregular brown broken stone showing plastic deformation.	A number of black flecks occur throughout including, in particular a generally colourless looking near surface inclusion with some black surface colouration and a small internal fracture system (probably fPer).
BZ271	JH3/86 Pkt 14	Colourless irregular stone with mottled surface and plastic deformation.	Small colourless inclusion with black corona appears deep in the stone towards one end. It has the appearence of a fPer. In addition a larger black fracture occurs internally elsewhere in the stone.
BZ272	JH3/86 Pkt 14	Brown slightly irregular dodecahedral stone with a mottled surface and some plastic deformation	A small octahedral black inclusion occurs near to the surface on one side. Deeper in the stone are to clean looking inclusions, one colourless and the other purple.

GU4	JH04/93 DG0393 4/93	Colourless irregular resorbed cuboctahedron with vestiges of dodecahedral faces and strong plastic deformation.	A twin fracture plane was identified within the stone at the centre of which is a large iridescent clear octahedral inclusion. This shows all the characteristics typical of a ferropericlase inclusion.	On breaking the 'ferropericlase' came out in one half octahedron and a number (at least four) of additional fragments. The thinner fragments showed a slightly dark green coloration and an additional single green crystal was also located. In addition an emerald green fragment and a highly birefringent colourless fragment was recovered. On further breaking of the diamond fragments a tabular ferropericlase looking single crystal was recovered in addition to more greeny octahedral fragments and a very slightly red large tabular inclusion.	A few of the 'ferropericlase' and dark green inclusions were left in GU4(df)

Appendix 2 Summary of EPMA study and inclusion release from São Luiz diamonds for the present study including Guinean inclusions and unbroken stones assigned BZ- numbers

---

Inclusion	**Identity**	**Chemistry**	**Colour**	**Packet**	**InSitu Iden.**
207A,C *	**TAPP/I px**		**grn/cless**	**XXX**	**XXX**
215A	**Pyrrhotite**		**Blk**	**JH3/86,11**	**Sulphide**
215B	-		Blk	"	
215C	**CMF Maj.**		**Orange**	**"**	
216A1	**CMF Maj.**		**c/less iso.**	**JH3/86,11**	**Sulphide**
216A2	-		c/less iso.	"	
217A	**MFC Maj.**		**sl. orange**	**JH3/86,11**	**Sulphide**
218A	**MFC Maj.**		**sl. or/brn**	**JH3/86,11**	**Sulphide**
218B	**CMF Cpx**		**green**	**"**	
218C	-		c/less aniso.	"	
219A	-		crud aniso.	JH3/86,11	Sulphide
219B	-		brown crud	"	
219C	Moissanite		black	"	
221A1	-		mt. yll (mg)	JH3/86,11	Sulphide
221A2	**Pyrrhotite**		**mt. yll (mg)**	**"**	
222A	**Pyrrhotite**		**black yll.**	**JH3/86,11**	
222B	**Pyrrhotite**		**black yll.**	**"**	
222C	**Pyrrhotite**		**black yll.**	**"**	
223A	**CFM Maj**		**brown**	**JH9/88,25**	**Sulphide**
223B	**CFM Maj**		**sl. cr. brown**	**"**	
223C	Fe contam		mt. yll black	"	
223D	Moissanite		black	"	
223E	-		green	"	
225A	Fe contam		mt. black	JH9/88,125	Sulphide
225B	-		em. grn.	"	
226A	-		green	JH3/86,47	Kyanite
226B	-		brown aniso.	"	
226C	-		brown/red	"	
226D1 (CD)	-		black	"	
226D2,3	**fPer,-**	**MF=0.568**	**black,black**	**"**	
227A	**Sapphire**		**blue**	**JH9/88,57**	**Kyanite**
227B	Fe contam		mt. black	"	
227C	-		greeny	"	
228A	Cor,-,-		green	JH3/86,17	Sulphide
228B	-		mt. gold	"	
228C	Brass		brown	"	
228D (XR)	Amorph		amorph white	"	
228E	-		brown	"	
229A	-		black	JH3/86,17	Sulphide
229B	Cor,-		blue,blue	"	
230A	Fe contam		silv. mag	JH3/86,17	

Inclusion	**Identity**	**Chemistry**	**Colour**	**Packet**	**InSitu Iden.**
230B	Moissanite		black/grey	"	
230C	Fe contam		gold mag	"	
230D	Moissanite		blue	"	
231A	**Pyrrhotite**		**grn. blck mt.**	**JH3/86,17**	
231B	-		mt.	"	
231C	-		blue	"	
232A	-		deep red	JH3/86,15	colourless
232B	Moissanite		sky blue	"	
232C	Fe		mt. black	"	
233A	**???,-**		**grn, grn**	**JH3/86,15**	**colourless**
233B	-		mt. black	"	
233C	**fPer**	**MF=0.805**	**mt. black**	**"**	
234A	CF Grt?x2		blue,blue	JH3/86,15	colourless
235A	Fe contam		black	JH3/86,15	colourless
235B	**S?**		**mt. grey**	**"**	
235C	Moissanite		blue	"	
235D	**Silica**		**white aniso.**	**"**	
237A1	**III px**		**green**	**JH9/88,35**	
237A2	**III px**		**green**	**"**	
237A3,4,5	**III px**		**green**	**"**	
237B	-		black	"	
237A6,C	**III px/Maj.**		**grn/white**	**"**	
237A7,8	**III px**		**Green**	**"**	
238A	**TAPP**		**Green**	**JH12/87**	
238B	**fPer**	**MF=0.829**	**Black**	**"**	
239A	**fPer**	**MF=0.817**	**Black**	**JH6/86,31**	**grt,c/less,fPer**
239B	-		Black	"	
239C	-		sl. grn.	"	
239D	**Biot/Silica**		**brown black**	**"**	
239E	**Alb/Plag**		**v. sl. Grn.**	**"**	
239F	**Silica**		**aniso. Milky**	**"**	
239G	**fPer**	**MF=0.81**	**gold mt.**	**"**	
239H	-		Green	"	
240A	-		aniso. Cloudy	JH3/86,19	grt,colourless
240B	**TAPP**		**Green**	**"**	
241A	**fPer (Cor)**	**MF=0.810**	**brown black**	**JH6/86,49**	**fPer,grt,cpx**
241B1,C	**II px/Ruby**		**green & red**	**"**	
241B2	**II px**		**grn. Aniso**	**"**	
242A	**fPer**	**MF=0.829**	**Black**	**JH6/86,49**	**fPer,cpx**
242B	**III px**		**Green**	**"**	
243A	**TAPP**		**grn aniso.**	**JH3/86,32**	**fPer,grt,c/less**
243B	**fPer**	**MF=0.796**	**Black**	**"**	
243C	**Olivine**		**c/less aniso.**	**"**	
244A	Fe contam		Black	JH12/87,28	colourless,grt
244B	**TAPP**		**grn. to c/less**	**"**	
244C	-		black mt.	"	
245A	**fPer**	**MF=0.65**	**Black**	**JH3/86,3**	**altered kyanite**
245B	**fPer**	**MF=0.677**	**Black**	**"**	
246A	**III px**		**grn aniso.?**	**JH3/86,51**	**grt/red ?**

Inclusion	**Identity**	**Chemistry**	**Colour**	**Packet**	**InSitu Iden.**
247A	Si EDS?		l. brown crud	JH3/86,13	colourless
247B	-		sl. Grn	"	
249A (XR) (LO)	Cpx		em. Grn	JH9/88,59	em.grn. cpx
249B	-		l. grn iso.	"	
249C	??CaSi		Red	"	
249D	-		v. l. grn	"	
249E	Cd contam		c/less grn	"	
249F	-		iso. Grn	"	
250A	-		brown mott	ZIL1/90,19 (58)	olivine
250B	-		sl. Brown iso	"	
250C	**fPer**		**Black**	**"**	
251A	**fPer**		**Black**	**1 of 8**	
251B	**I px**		**c/less**	**"**	
252A	**$CaSiO_3$**		**c/less**	**JH6/86,27**	
253(UB)				3 of 8	
254A	$MgSiO_3$		c/less	JH9/99 ZIL 1/88,129	
255A	**fPer**		**Black**	**ZIL1/90,64**	
256(UB)				6 of 8	
257A1 (XR)	**fPer**		**Black**	**ZIL1/90,54 7 of 8**	**fPer**
257A2	**fPer**		**Black**	**"**	
257A3 (CD)	-		Black	"	
257A4 (CD)	-		Black	"	
257A5 (CD)	-		Black	"	
257B (CD)	-		Black	"	
258 (UB)				ZIL1/90,44 8 of 8	
259A1	**TAPP**		**grn.**	**ZIL1/90**	**cpx/colourless**
259A2,B	**TAPP/III Px**		**grn./cless**	**"**	
259C	-		grn.	"	
260A	MgFeSi crud		l.grn./brown	ZIL1/90	orange grt
260B	-		Black	"	
260C	CaSi crud		l. grn.	"	
260D	**fPer**	**MF=0.794**	**Black**	**"**	
260E	**fPer**	**MF=0.791**	**Black**	**"**	
261 (UB)				ZIL1/90,19(55)4/10	orange grt
262 (UB)				ZIL1/90,18(53)5/10	orange grt
263 (UB)				ZIL1/90,18(52) 6 of 10	
264 (UB)				ZIL1/90,13 7 of 10	
265 (UB)				8 of 10	
266 (UB)				JH3/86,11 (S1)	Sulphide?
267 (UB)				JH3/86,11 (S2)	Sulphide?
268 (UB)				JH3/86,11 (S3)	Sulphide?
269 (UB)				JH3/86,11 (S4)	Sulphide?
270 (UB)				JH9/88,96	fPer
271 (UB)				JH3/86,14	
272 (UB)				JH3/86,14	Purple Grt + cpx
JH2 !!	**fPer**	**MF=0.72**	**Black**	**XXX**	**fPer**
JH6A1 !!	cruddy fPer		**Black**	**XXX**	fPer
JH6A2 !! (LO)	-		Black	"	

Inclusion	**Identity**	**Chemistry**	**Colour**	**Packet**	**InSitu Iden.**
JH6A3 !!	diamond		Black	"	
JH6A4 !!	diamond		Black	"	
JH7A1 !!	**fPer**	**MF=0.74**	**Black**	**XXX**	**fPer**
JH7A2 !! (LO)	-		Black	"	
JH7A3 !! (XR)	**fPer**		**Black**	**"**	
JH11A1 !!	**fPer**	**MF=0.52**	**Black**	**XXX**	**fPer**
JH11A2 !! (XR)	**fPer**		**Black**	**"**	
JH11A3 !! (CD)	-		Black	"	
JH11A4 !! (CD)	-		Black	"	
JH12A1 !!	**fPer**	**MF=0.73**	**Black**	**XXX**	**fPer**
JH12A2 !! (XR)	**fPer**		**Black**	**"**	
JH17A1 !!	**fPer**	**MF=0.70**	**Black**	**XXX**	**fPer**
JH17A2 !! (CD)	-		Black	"	
JH17A3 !! (XR)	**fPer**		**Black**	**"**	
JH17A4 !! (CD)	-		Black	“	
GU2A	**fPer**	**MF=0.82**	**Black**	**XXX**	
GU3B	**FCM Maj**			**XXX**	
GU3C	**Cpx**			**"**	
GU4A1	**fPer**	**MF=0.87**	**black/grn.**	**XXX**	**fPer**
GU4A2-5	-		black/grn.	"	
GU4B	-		c/less	"	
GU4C	-		em. grn.	"	
GU4D	-		grn.	"	
GU4E	-		black/red	"	
GU4F	fPer		grn.		
GU4G	-		em. grn.	"	

Inclusion	**Init. Iden**	**Mk5**	**Camebax**	**Total av.**	**Size**
207A,C *	**XXX**	**0,0**	**7,9**	**6,9**	**XXX**
215A	**fPer**	**1**	**0**	**1**	**200,100,50**
215B	fPer	0	0	0	120,80,20
215C	**Garnet**	**3**	**5**	**6**	**100,80,20**
216A1	**-**	**5**	**5**	**7**	**100,100,100**
216A2	-	0	0	0	120,70,70
217A	**Garnet**	**3**	**2**	**5**	**200,200,100**
218A	**Garnet**	**3**	**3**	**5**	**125,90,45**
218B	**Cpx**	**3**	**3**	**6**	**200,90,90**
218C	-	0	0	0	50,50,50
219A	crud	0	0	0	40,40/45,20
219B	crud	0	0	0	90,90,90
219C	fPer	3	0	0	300,190,190
221A1	Sulphide	0	0	0	
221A2	**Sulphide**	**1**	**0**	**1**	
222A	**Sulphide**	**1**	**0**	**1**	**90,60,60**
222B	**Sulphide**	**1**	**0**	**1**	**90,60,60**
222C	**Sulphide**	**2**	**0**	**1**	**45,45,45**
223A	**-**	**3**	**4**	**4**	**90,60,60**
223B	**-**	**3**	**5**	**6**	**60,60,45**
223C	Fe	1	0	0	60,60,60
223D	fPer	1	0	0	130,90,45
223E	Diamond	0	0	0	60,60,45
225A	Fe	1	0	0	300/150.200.150
225B	Fe	0	0	0	130,50,50
226A	olivine	0	0	0	40,120,40
226B	crud	0	0	0	50,40,30
226C	-	0	0	0	180,50,40
226D1 (CD)	fPer	-	-	-	80,80,80
226D2,3	**fPer,fPer**	**3,0**	**1**	**4**	**60/160,60/40,60/40**
227A	**kyanite**	**4**	**3**	**6**	**300,200,150**
227B	Fe	1	0	0	100,50,60
227C	crud	0	0	0	60,60,60
228A	-	3,0,0	0	3	60/30/40,60/20/30,40/20/30
228B	Sulphide	0	0	0	40,50,10
228C	-	0	0	0	50,50,40
228D (XR)	amorphous	-	-	0	200,200,160
228E	crud	0	0	0	50,40,30
229A	fPer	0	0	0	40,40,30
229B	-	3	1	4	120/80,50/60,40
230A	Sulphide	1	0	0	160/100,120/100,120/80
230B	fPer	1	0	0	60,60,40
230C	Sulphide	1	0	0	80,60,40
230D	-	0	0	0	40,40,30
231A	**fPer**	**0**	**0**	**0**	**70,60,50**
231B	Diamond	0	0	0	120/160,60/120,40/40
231C	-	0	0	0	60,60,40
232A	crud	0	0	0	60,30,30
232B	-	1	0	0	90,70,70

Inclusion	**Init. Iden**	**Mk5**	**Camebax**	**Total av.**	**Size**
232C	fper	1	0	0	80,40,40
233A	**crud**	**5**	**1**	**1**	**160/80,100/80,100/80**
233B	fPer	0	0	0	30,30,80
233C	**fPer**	**3**	**2**	**3**	**80,60,80**
234A	-	2	0	0	200/120,200/120,60/40
235A	fPer	1	0	0	50/60,80/60,50/40
235B	**-**	**2,1**	**0**	**0**	**60/50,40/30, 40/30**
235C	Moissanite	1	0	0	50,30,30
235D	**-**	**4**	**2**	**5**	**200,120,120**
237A1	**-**	**3**	**2**	**see A7**	**80,40,40**
237A2	**-**	**1**	**4**	**see A7**	**120,90,60**
237A3,4,5	**-**	**1,2,1**	**5,2,2**	**see A7**	**60,60,60**
237B	fPer	1	1	**see A7**	150,80,80
237A6,C	**-**	**2,4**	**9,6**	**see A7, 5**	**80,40,60**
237A7,8	**-**	**3,1**	**2,1**	**30**	**60/50,60/50, 40/40**
238A	**-**	**2**	**3**	**4**	**40,40,30**
238B	**fPer**	**3**	**4**	**4**	**120,80,80**
239A	**fPer**	**0**	**4**	**3**	**120,120,120**
239B	fPer	0	1	0	60,60,40
239C	-	0	0	0	50/50/40,40/30/40,10/10/30
239D	**crud**	**0**	**4**	**1,1**	**80,40,40**
239E	**-**	**0**	**3,4**	**2,2**	**80,40,30**
239F	**Diamond**	**0**	**1**	**1**	**80,80,80**
239G	**Fe**	**0**	**2**	**1**	**120,100,30**
239H	-	0	0	0	80,40,30
240A	crud	0	0	0	80,45,30
240B	**-**	**0**	**3**	**3**	
241A	**fPer?**	**0**	**3,1**	**3**	**100,100,80**
241B1,C	**cpx/garnet**	**0**	**11,6**	**3,4**	**60,40,30**
241B2	**cpx**	**0**	**3**	**3**	**100,100,50**
242A	**fPer**	**0**	**3**	**1**	**80,50,50**
242B	**cpx**	**0**	**3**	**3**	**60,30,30**
243A	**cpx**	**0**	**3**	**3**	**70,60,40**
243B	**fPer**	**0**	**4**	**1**	**50,60,40+ smaller**
243C	**-**	**0**	**4**	**3**	**60,40,30**
244A	fPer	0	0	0	120,80,80
244B	**-**	**0**	**2**	**2**	**50,50,50**
244C	Fe	0	0	0	20,40,20
245A	**fPer ?**	**0**	**5**	**5**	**200,80,80**
245B	**fPer**	**0**	**3**	**2**	**80,80,60**
246A	**-**	**0**	**5**	**3**	**80,70,30**
247A	crud	0	0	0	40,30,20
247B	-	0	0	0	50,30,20
249A (XR) (LO)	cpx	-	-	0	120,30,30
249B	garnet	0	0	0	30,30,10
249C	crud	0	0	0	30,30,10
249D	-	0	0	0	50,40,40
249E	Cd	0	0	0	60,50,40

Inclusion	Init. Iden	Mk5	Camebax	Total av.	Size
249F	-	0	0	0	60,60,40
250A	amorphous	0	0	0	40,30,20
250B	-	0	0	0	80,60,40
250C	**fPer**	**0**	**2**	**2**	**80,40,40**
251A	**fPer**	**0**	**5**	**4**	**160,120,??? ♥**
251B	**-**	**0**	**4**	**3**	**130,80,??? ♥**
252A	**-**	**0**	**3**	**3**	**120,120,??? ♥**
254A	fPer	0	5	0	20,20,??? ♥
255A	**-**	**0**	**6**	**4**	**75,25,??? ♥**
257A1 (XR)	**fPer**				**200,120,120**
257A2	**fPer**				**120,80,20**
257A3 (CD)	fPer				120,120,20
257A4 (CD)	fPer				140,40,10
257A5 (CD)	fPer or Fe?				80,60,60
257B (CD)	fPer				80,20,10
258 (UB)					
259A1	**grn garnet**	**0**	**5**	**2**	**40,40,30**
259A2,B	**garnet/ -**	**0**	**26,25**	**7,14**	**140,60,40**
259C	grn garnet	0	0	0	60,40,20
260A	-	0	3	0	80,60,60
260B	-	0	0	0	40,40,40
260C	-	0	1	0	40,50,40
260D	**fPer**	**0**	**4**	**3**	**160,160,160**
260E	**fPer**	**0**	**5**	**2**	**40,30,30**
261 (UB)					N/A
262 (UB)					N/A
263 (UB)					N/A
264 (UB)					N/A
265 (UB)					N/A
266 (UB)					N/A
267 (UB)					N/A
268 (UB)					N/A
269 (UB)					N/A
270 (UB)					N/A
271 (UB)					N/A
272 (UB)					N/A
JH2 !!	**fPer**	**3**	**0**	**3**	**500,300,300**
JH6A1 !!	fPer	6	0	0	400,200,100
JH6A2 !! (LO)	fPer				500,150,100
JH6A3 !!	fPer				700,300,200
JH6A4 !!	fPer				600,400,400
JH7A1 !!	**fPer**	**4**	**0**	**4**	**380,150,100**
JH7A2 !! (LO)	fPer				300,200,200
JH7A3 !! (XR)	**fPer**				**400,100,100**
JH11A1 !!	**fPer**	**8**	**0**	**4**	**200,100,100**
JH11A2 !! (XR)	**fPer**				**200,100,100**
JH11A3 !! (CD)	fPer				200,100,50
JH11A4 !! (CD)	fPer				100,80,10
JH12A1 !!	**fPer**	**6**	**0**	**5**	**200,150,100**

Inclusion	Init. Iden	Mk5	Camebax	Total av.	Size
JH12A2 !! (XR)	**fPer**				**150,150,75**
JH17A1 !!	**fPer**	**3**	**0**	**3**	**150,100,100**
JH17A2 !! (CD)	fPer				**150,150,100**
JH17A3 !! (XR)	**fPer**				**150,150,100**
GU2A		**4**	**0**	**4**	
GU3B		**6**	**0**	**5**	
GU3C		**8**	**0**	**5**	
GU4A1	**fPer**	**4**	**0**	**4**	**180,180,130**
GU4A2-5	-				130/130/90/130,45/130/45/90, 45/90/45/45
GU4B	-				45,45,45
GU4C	-				130,45,45
GU4D	-				45,45,45
GU4E	fPer				100,60,60
GU4F	-				90,90,90
GU4G	-				60,60,45

* BZ207 previously analysed by Gordon Watt. NB. no. for av (number for average) includes his data. Analyses considered here carried out by M. Hutchison on 31/1/96 on ion-probed remains.

Grt- Garnet; Maj.- Majoritic garnet; fPer- ferropericlase (Mg,Fe)O

I px- Type I MgSi-Pvk; II px- Type II MgSi-Pvk; III px- Type III MgSi-Pvk

mt.- metallic; yll.- yellow; (em.)grn.- (emerald) green; c/less- colourless

(an)iso.- (an)isotropic; v.- very; sl.- slightly; cr.- cruddy

CD- Sample mounted on card after release from diamond; UB- Sample unbroken

XR- Sample identified by XRD and not analysed by EPMA; LO- Sample lost before EPMA analysis

?- Possibly; XXX, ???- Unknown

Camebax- Number of analyses undertaken on the Cameca Camebax, University of Edinburgh

MkV- Number of analyses undertaken on the Cambridge Instruments MkV, University of Edinburgh

In situ iden- Initial identification of the inclusion types before breaking the stone

Init Iden.- Initial identification of released inclusion material before EPMA or XRD analysis

Av.- Number of good analyses incorporated into the average analysis for each inclusion or fragment.

Size- Dimensions of released inclusions in μm. Where more than one inclusion is present in a pip, dimensions are separated by a / as in: $x_A/x_B/x_C$,$y_A/y_B/y_C$,$z_A/z_B/z_C$ where x,y,z are measurement axes and A,B,C are inclusion fragments

♥ Area exposed on diamond surface

Appendix 3 Major and minor element compositions of inclusions

Appendix 3.1 Single point electron microprobe analyses

Analyses in bold are incorporated into the average analyses presented in appendix 3.2. Each analysis name is prefixed with BZ-, JH or GU; representing the source locality (see glossary). The following number refers to the diamond which is then followed by a letter identifying the inclusion (except for BZ66 and BZ83) and, occasionally, a subsequent number for the inclusion fragment (some inclusions broke on release). Dark-BS areas, dark BS-blebs or light BS-areas are referred to by BS, Dk and L. Each inclusion name is sufficed by a dash followed by a number which refers to the analysis point.

Analyses of São Luiz phases as silicates

	BZ66L-1	BZ66L-2	BZ66L-3	BZ66L-4	BZ66-1	**BZ83DkBl-1**	**BZ83Dk-1**
	Fe:Ni	Fe:Ni	Fe:Ni	Fe:Ni:fPer	fPer	**Magnetite**	**Magnetite**
SiO_2	0.03	0.01	0.02	0.04	0.03	**0.08**	**0.07**
TiO_2	0.02	0.05	0.03	0.04	0.03	**1.02**	**1.46**
Al_2O_3	0.01	0.56	0.13	0.01	0.06	**0.77**	**1.18**
Cr_2O_3	0.29	0.41	0.45	0.71	0.97	**0.01**	**0.02**
FeO	96.21	84.32	81.37	75.64	74.04	**90.87**	**89.31**
MnO	0.10	0.16	0.24	0.53	0.78	**0.59**	**0.52**
NiO	25.38	28.35	28.74	16.10	0.07	**0.00**	**0.00**
Na_2O	0.00	0.08	0.00	0.59	0.83	**0.01**	**0.00**
MgO	0.06	2.23	1.44	13.91	17.11	**0.88**	**0.76**
CaO	0.00	0.01	0.01	0.01	0.00	**0.02**	**0.01**
K_2O	0.00	0.02	0.00	0.00	0.00	**0.00**	**0.00**
Total	122.09	116.20	112.44	107.57	93.93	**94.26**	**93.33**

	BZ83Dk-2	**BZ83L-1**	**BZ83L-2**	BZ207A-1	BZ207A-2	BZ207A-3	BZ207A-4
	Magnetite	**Magnetite**	**Magnetite**	MF Grt	MF Grt	MF Grt	MF Grt
SiO_2	**0.05**	**0.04**	**0.06**	42.65	41.04	42.20	41.34
TiO_2	**1.43**	**0.12**	**0.13**	4.06	4.07	4.21	4.26
Al_2O_3	**1.13**	**0.07**	**0.08**	19.63	20.44	20.57	20.31
Cr_2O_3	**0.01**	**0.04**	**0.04**	1.33	1.35	1.37	1.37
FeO	**89.12**	**94.52**	**94.22**	9.22	9.37	9.62	9.58
MnO	**0.50**	**0.85**	**0.88**	0.27	0.25	0.26	0.25
NiO	**0.02**	**0.03**	**0.01**	0.00	0.04	0.03	0.05
Na_2O	**0.00**	**0.00**	**0.00**	0.02	0.01	0.00	0.01
MgO	**0.70**	**1.83**	**1.87**	25.85	25.48	26.46	26.08
CaO	**0.00**	**0.02**	**0.01**	0.03	0.04	0.04	0.02
K_2O	**0.00**	**0.00**	**0.00**	0.01	0.00	0.01	0.00
Total	**92.97**	**97.51**	**97.31**	103.31	102.17	104.91	103.41

	BZ207A-5	**BZ207A-6**	BZ207A-7	BZ207C-1	BZ207C-2	BZ207C-3	**BZ207C-4**
	MF Grt	**MF Grt**	MF Grt	Opx	Opx	Opx	**Opx**
SiO_2	**40.24**	**40.33**	41.19	56.45	56.88	57.86	**55.35**
TiO_2	**4.25**	**4.26**	4.26	0.21	0.19	0.18	**0.22**
Al_2O_3	**19.81**	**19.90**	20.37	2.65	2.66	2.76	**2.60**
Cr_2O_3	**1.29**	**1.29**	1.38	0.16	0.17	0.17	**0.14**
FeO	**9.46**	**9.75**	9.51	8.96	9.21	9.21	**9.00**
MnO	**0.26**	**0.29**	0.27	0.34	0.32	0.32	**0.30**
NiO	**0.00**	**0.02**	0.03	0.01	0.00	0.03	**0.03**
Na_2O	**0.02**	**0.02**	0.00	0.09	0.07	0.06	**0.07**
MgO	**25.41**	**25.53**	26.22	32.42	33.07	33.24	**32.20**
CaO	**0.03**	**0.03**	0.02	0.05	0.05	0.05	**0.05**
K_2O	**0.00**	**0.01**	0.01	0.00	0.00	0.00	**0.01**
Total	**100.90**	**101.56**	103.36	101.33	102.60	103.88	**99.97**

	BZ207-5	**BZ207C-6**	**BZ207C-7**	BZ207C-8	BZ207C-9	BZ215A-2	**BZ215C-1**
	Opx	**Opx**	**Opx**	Opx	Opx	Pyrrhotite	**CMF Maj**
SiO_2	**55.72**	**55.47**	**55.56**	57.76	57.47	0.07	**41.30**
TiO_2	**0.21**	**0.19**	**0.20**	0.19	0.22	0.00	**1.56**
Al_2O_3	**2.60**	**2.55**	**2.54**	2.72	2.74	0.01	**18.39**
Cr_2O_3	**0.16**	**0.14**	**0.17**	0.19	0.17	0.06	**0.06**
FeO	**9.01**	**9.14**	**9.05**	9.07	8.95	73.89	**11.94**
MnO	**0.27**	**0.31**	**0.33**	0.33	0.32	0.04	**0.24**
NiO	**0.03**	**0.04**	**0.03**	0.03	0.00	5.26	**0.02**
Na_2O	**0.06**	**0.08**	**0.07**	0.09	0.08	0.01	**0.82**
MgO	**31.97**	**31.80**	**31.84**	33.24	33.03	0.02	**9.64**
CaO	**0.04**	**0.06**	**0.05**	0.06	0.06	0.00	**14.66**
K_2O	**0.01**	**0.00**	**0.01**	0.01	0.00	0.00	
Total	**100.08**	**99.79**	**99.83**	103.69	103.04	79.35	**98.63**

	BZ215C-2	**BZ215C-3**	BZ215C-4	BZ215C-5	**BZ215C-6**	**BZ215C-7**	**BZ215C-8**
	CMF Maj	**CMF Maj**	CMF Maj	CMF Maj	**CMF Maj**	**CMF Maj**	**CMF Maj**
SiO_2	**41.00**	**40.67**	38.09	39.35	**41.02**	**42.10**	**41.13**
TiO_2	**1.49**	**1.47**	1.41	1.49	**1.47**	**1.44**	**1.44**
Al_2O_3	**18.44**	**18.54**	17.10	17.71	**18.57**	**19.09**	**18.49**
Cr_2O_3	**0.08**	**0.08**	0.10	0.11	**0.10**	**0.12**	**0.08**
FeO	**12.00**	**11.94**	12.00	12.06	**12.05**	**12.02**	**11.96**
MnO	**0.25**	**0.23**	0.24	0.25	**0.26**	**0.26**	**0.25**
NiO	**0.01**	**0.00**	0.01	0.01	**0.01**	**0.01**	**0.00**
Na_2O	**0.83**	**0.89**	0.89	0.87	**0.85**	**0.85**	**0.04**
MgO	**9.69**	**9.56**	10.18	10.00	**9.87**	**9.85**	**9.51**
CaO	**14.75**	**14.84**	14.44	14.51	**14.67**	**14.73**	**14.73**
K_2O			0.00	0.00	**0.01**	**0.00**	**0.00**
Total	**98.54**	**98.22**	94.44	96.36	**98.87**	**100.46**	**97.62**

	BZ215CDk-1 CFM Maj	BZ215CDk-2 CFM Maj	**BZ216A1-1** **CMF Grt**	**BZ216A1-2** **CMF Grt**	**BZ216A1-3** **CMF Grt**	**BZ216A1-4** **CMF Grt**	**BZ216A1-5** **CMF Grt**
SiO_2	39.26	35.97	**43.28**	**42.92**	**43.62**	**43.21**	**43.19**
TiO_2	1.26	1.38	**0.13**	**0.15**	**0.17**	**0.18**	**0.18**
Al_2O_3	12.10	16.79	**20.68**	**20.81**	**20.75**	**20.77**	**20.79**
Cr_2O_3	0.10	0.07	**0.17**	**0.18**	**0.17**	**0.15**	**0.15**
FeO	9.98	12.19	**7.53**	**7.55**	**8.25**	**8.12**	**8.05**
MnO	0.17	0.25	**0.18**	**0.17**	**0.16**	**0.16**	**0.18**
NiO	0.02	0.01	**0.03**	**0.02**	**0.02**	**0.03**	**0.00**
Na_2O	4.52	0.75	**1.11**	**1.07**	**1.09**	**1.14**	**1.06**
MgO	7.38	8.55	**12.81**	**12.79**	**12.87**	**12.85**	**12.83**
CaO	11.99	14.18	**12.31**	**12.22**	**13.27**	**13.04**	**13.03**
K_2O	0.00	0.00					
Total	86.80	90.15	**98.23**	**97.88**	**100.37**	**99.65**	**99.46**

	BZ216A1-6 CMF Grt	**BZ216A1-7** **CMF Grt**	**BZ216A1-8** **CMF Grt**	BZ216A1-9 CMF Grt	BZ216A1-10 CMF Grt	BZ216A1Dk-1 Jadeite	BZ216A1Dk-2 Jadeite
SiO_2	40.87	**41.78**	**42.20**	40.97	39.85	54.31	47.77
TiO_2	0.17	**0.20**	**0.17**	0.17	0.16	0.18	0.18
Al_2O_3	19.93	**20.08**	**20.35**	19.67	19.12	12.13	12.76
Cr_2O_3	0.16	**0.18**	**0.18**	0.16	0.17	0.06	0.13
FeO	8.24	**8.20**	**8.14**	8.32	8.31	5.42	4.39
MnO	0.19	**0.21**	**0.17**	0.18	0.17	0.10	0.10
NiO	0.04	**0.02**	**0.01**	0.02	0.04	0.02	0.00
Na_2O	1.02	**1.04**	**1.02**	1.07	1.04	6.16	4.99
MgO	12.66	**12.73**	**12.73**	12.40	12.43	6.07	9.73
CaO	12.99	**13.02**	**13.01**	13.09	13.13	8.92	13.77
K_2O	0.00	**0.01**	**0.01**	0.00	0.01	0.01	0.01
	0.00	**0.00**	**0.00**	0.00	0.00		
Total	96.26	**97.45**	**98.00**	96.02	94.42	93.37	93.83

	BZ217A-1 **MFC Maj**	**BZ217A-2** **MFC Maj**	**BZ217A-3** **MFC Maj**	**BZ217A-4** **MFC Maj**	**BZ217A-5** **MFC Maj**	BZ217ADk-1 Jadeite	BZ217ADk-2 Jadeite
SiO_2	**44.09**	**43.45**	**44.13**	**44.06**	**43.41**	56.01	54.60
TiO_2	**0.08**	**0.08**	**0.09**	**0.08**	**0.09**	0.10	0.07
Al_2O_3	**20.67**	**20.58**	**20.86**	**20.75**	**20.46**	13.00	13.14
Cr_2O_3	**0.05**	**0.07**	**0.07**	**0.00**	**0.06**	0.07	0.03
FeO	**12.63**	**12.77**	**12.81**	**12.80**	**12.62**	5.99	5.80
MnO	**0.30**	**0.32**	**0.33**	**0.33**	**0.30**	0.13	0.12
NiO	**0.00**	**0.00**	**0.03**	**0.00**	**0.00**	0.01	0.01
Na_2O	**1.12**	**1.09**	**1.03**	**1.00**	**1.10**	6.53	6.52
MgO	**17.72**	**17.60**	**17.38**	**16.93**	**17.58**	8.69	8.31
CaO	**3.08**	**3.06**	**3.05**	**3.02**	**3.07**	4.16	4.17
K_2O			**0.00**	**0.00**		0.01	0.00
Total	**99.74**	**99.02**	**99.79**	**98.98**	**98.69**	94.70	92.77

	BZ217ADk-3	BZ217ADk-4	**BZ218A-1**	**BZ218A-2**	BZ218A-3	**BZ218A-4**	**BZ218A-5**
	Jadeite	Jadeite	**MFC Maj**	**MFC Maj**	MFC Maj	**MFC Maj**	**MFC Maj**
SiO_2	49.49	56.19	**42.43**	**42.34**	43.75	**41.58**	**43.35**
TiO_2	0.08	0.09	**0.26**	**0.24**	0.27	**0.30**	**0.30**
Al_2O_3	12.28	13.71	**20.13**	**20.14**	21.06	**20.12**	**20.87**
Cr_2O_3	0.04	0.03	**0.10**	**0.11**	0.11	**0.10**	**0.10**
FeO	5.76	5.76	**15.69**	**15.76**	16.00	**15.89**	**15.88**
MnO	0.11	0.12	**0.29**	**0.31**	0.31	**0.30**	**0.32**
NiO	0.00	0.00	**0.03**	**0.01**	0.05	**0.00**	**0.03**
Na_2O	6.95	6.36	**1.18**	**1.19**	1.20	**1.10**	**1.18**
MgO	8.39	8.04	**12.53**	**12.36**	12.99	**12.37**	**13.10**
CaO	4.30	4.50	**6.78**	**6.80**	6.74	**6.82**	**6.72**
K_2O	0.00	0.00			0.01	**0.00**	**0.00**
Total	87.41	94.81	**99.42**	**99.26**	102.47	**98.58**	**101.85**

	BZ218A-6	BZ218ADk-1	**BZ218B-1**	**BZ218B-2**	**BZ218B-3**	**BZ218B-4**	**BZ218B-5**
	MFC Maj	Jadeite	**CMF Cpx**	**CMF Cpx**	**CMF Cpx**	**CMF Cpx**	**CMF Cpx**
SiO_2	**41.83**	47.14	**53.91**	**54.41**	**54.67**	**54.20**	**53.80**
TiO_2	**0.28**	0.30	**0.54**	**0.54**	**0.54**	**0.52**	**0.59**
Al_2O_3	**19.91**	6.89	**6.59**	**6.58**	**5.73**	**6.45**	**6.34**
Cr_2O_3	**0.09**	0.13	**0.03**	**0.02**	**0.07**	**0.04**	**0.06**
FeO	**15.58**	15.13	**4.97**	**5.05**	**5.52**	**5.21**	**5.17**
MnO	**0.30**	0.29	**0.05**	**0.06**	**0.06**	**0.06**	**0.07**
NiO	**0.02**	0.03	**0.04**	**0.06**	**0.07**	**0.05**	**0.05**
Na_2O	**1.14**	1.83	**4.92**	**5.00**	**3.61**	**4.79**	**4.88**
MgO	**12.28**	11.20	**11.07**	**11.12**	**12.10**	**11.26**	**11.36**
CaO	**6.83**	7.86	**15.68**	**15.72**	**16.73**	**15.55**	**15.54**
K_2O		0.01			**0.04**	**0.05**	**0.05**
Total	**98.26**	90.80	**97.80**	**98.56**	**99.15**	**98.17**	**97.90**

	BZ218B-6	BZ219C-1	BZ219C-2	BZ219C-3	**BZ223A-1**	BZ223A-2	**BZ223A-3**
	CMF Cpx	Moissanite	Moissanite	Moissanite	**CFM Maj**	CFM Maj	**CFM Maj**
SiO_2	**54.91**	155.30	153.58	154.99	**41.63**	43.07	**41.87**
TiO_2	**0.53**	0.00	0.02	0.00	**1.59**	1.34	**1.44**
Al_2O_3	**6.52**	0.46	0.38	0.45	**18.01**	17.73	**17.91**
Cr_2O_3	**0.04**	0.02	0.01	0.00	**0.04**	0.03	**0.05**
FeO	**5.01**	0.02	0.00	0.00	**12.14**	12.21	**12.27**
MnO	**0.05**	0.00	0.03	0.01	**0.27**	0.31	**0.27**
NiO	**0.04**	0.03	0.01	0.00	**0.02**	0.02	**0.00**
Na_2O	**4.95**	0.03	0.00	0.00	**1.18**	0.95	**1.12**
MgO	**11.05**	0.01	0.02	0.02	**9.30**	7.94	**9.27**
CaO	**15.66**	0.00	0.02	0.01	**14.88**	13.87	**14.58**
K_2O							
Total	**98.76**	155.87	154.07	155.48	**99.06**	97.47	**98.78**

	BZ223A-4	**BZ223A-5**	BZ223A-6	**BZ223A-7**	BZ223ADk-1	BZ223ADk-2	BZ223AL-1
	CFM Maj	**CFM Maj**	CFM Maj	**CFM Maj**	CFMMaj	CFMMaj	???
SiO_2	40.71	**42.06**	37.66	**43.23**	39.36	36.18	29.61
TiO_2	1.48	**1.48**	1.41	**1.46**	1.24	1.35	1.25
Al_2O_3	17.47	**18.12**	16.24	**18.56**	12.69	16.63	22.81
Cr_2O_3	0.07	**0.04**	0.09	**0.06**	0.04	0.04	0.12
FeO	12.55	**12.42**	12.41	**12.26**	8.66	12.52	15.91
MnO	0.24	**0.27**	0.28	**0.27**	0.14	0.23	0.26
NiO	0.01	**0.02**	0.04	**0.03**	0.00	0.00	0.02
Na_2O	1.07	**0.97**	1.21	**0.99**	3.78	1.04	0.31
MgO	8.92	**8.49**	9.86	**8.67**	6.55	8.35	10.33
CaO	14.70	**14.83**	14.31	**14.77**	13.41	13.53	10.78
K_2O	0.01	**0.01**	0.01	**0.01**	0.00	0.00	0.00
			0.00				
Total	97.22	**98.70**	93.52	**100.31**	85.88	89.86	91.39

	BZ223AL-2	**BZ223B-1**	**BZ223B-2**	**BZ223B-3**	**BZ223B-4**	BZ223B-5	**BZ223B-6**
	???	**CFM Maj**	**CFM Maj**	**CFM Maj**	**CFM Maj**	CFM Maj	**CFM Maj**
SiO_2	25.91	**41.79**	**42.35**	**41.75**	**41.66**	40.74	**40.89**
TiO_2	1.19	**1.52**	**1.50**	**1.50**	**1.49**	1.48	**1.46**
Al_2O_3	29.06	**17.73**	**17.97**	**17.86**	**17.83**	17.54	**17.64**
Cr_2O_3	0.09	**0.04**	**0.05**	**0.04**	**0.08**	0.08	**0.06**
FeO	16.53	**12.24**	**12.33**	**12.37**	**12.63**	12.48	**12.61**
MnO	0.25	**0.26**	**0.26**	**0.27**	**0.27**	0.25	**0.22**
NiO	0.02	**0.02**	**0.04**	**0.01**	**0.03**	0.03	**0.00**
Na_2O	0.27	**1.13**	**1.17**	**1.19**	**1.06**	0.87	**1.14**
MgO	9.70	**9.32**	**9.42**	**9.36**	**9.17**	7.51	**9.40**
CaO	9.98	**14.64**	**14.78**	**14.81**	**14.66**	14.99	**14.56**
K_2O	0.00				**0.01**	0.01	**0.00**
Total	93.00	**98.69**	**99.87**	**99.16**	**98.88**	95.96	**97.97**

	BZ223B-7	**BZ223B-8**	BZ223C-1	BZ223D-1	BZ225A-1	**BZ226D2-1**	**BZ226D2-2**
	CFM Maj	**CFM Maj**	Fe	Moissanite	Fe	**fPer**	**fPer**
SiO_2	48.31	**43.00**	0.51	157.49	0.55	**0.00**	**0.00**
TiO_2	1.42	**1.52**	0.00	0.00	0.01	**0.00**	**0.00**
Al_2O_3	20.47	**18.49**	0.08	0.09	0.09	**0.07**	**0.08**
Cr_2O_3	0.05	**0.04**	0.79	0.01	0.71	**0.17**	**0.17**
FeO	11.47	**12.52**	123.43	0.00	123.15	**56.54**	**56.08**
MnO	0.28	**0.25**	0.44	0.00	0.42	**0.30**	**0.32**
NiO	0.01	**0.02**	0.09	0.00	0.11	**0.34**	**0.35**
Na_2O	1.18	**1.02**	0.02	0.01	0.01	**0.19**	**0.18**
MgO	10.70	**8.67**	0.03	0.02	0.01	**42.17**	**42.19**
CaO	15.13	**14.71**	0.01	0.01	0.00	**0.00**	**0.00**
K_2O	0.00	**0.01**					
Total	109.02	**100.23**	125.40	157.63	125.06	**99.78**	**99.37**

	BZ226D2-3	**BZ226D2-4**	BZ227A-1	**BZ227A-2**	**BZ227A-3**	**BZ227A-4**	**BZ227A-5**
	fPer	**fPer**	Sapphire	**Sapphire**	**Sapphire**	**Sapphire**	**Sapphire**
SiO_2	**0.01**	**0.03**	0.22	**0.22**	**0.20**	**0.22**	**0.58**
TiO_2	**0.00**	**0.02**	0.08	**0.09**	**0.11**	**0.09**	**0.10**
Al_2O_3	**0.09**	**0.04**	102.24	**98.55**	**99.34**	**99.32**	**98.62**
Cr_2O_3	**0.16**	**0.20**	0.02	**0.00**	**0.00**	**0.01**	**0.01**
FeO	**56.41**	**57.87**	0.60	**0.57**	**0.61**	**0.59**	**0.63**
MnO	**0.29**	**0.30**	0.00	**0.01**	**0.00**	**0.01**	**0.00**
NiO	**0.30**	**0.43**	0.00	**0.00**	**0.00**	**0.00**	**0.02**
Na_2O	**0.14**	**0.11**	0.00	**0.01**	**0.02**	**0.02**	**0.01**
MgO	**42.17**	**40.80**	0.18	**0.14**	**0.16**	**0.16**	**0.16**
CaO	**0.00**	**0.01**	0.00	**0.01**	**0.02**	**0.02**	**0.00**
K_2O		**0.00**					**0.00**
Total	**99.57**	**99.80**	103.34	**99.60**	**100.46**	**100.44**	**100.13**

	BZ227A-6	**BZ227A-7**	BZ227B-1	**BZ228A-1**	**BZ228A-2**	**BZ228A-3**	**BZ229B-1**
	Sapphire	**Sapphire**	Fe	**Corundum**	**Corundum**	**Corundum**	**Corundum**
SiO_2	**0.49**	**0.59**	0.59	**0.00**	**0.00**	**0.00**	**0.03**
TiO_2	**0.11**	**0.11**	0.00	**0.12**	**0.15**	**0.14**	**0.73**
Al_2O_3	**97.40**	**96.61**	0.04	**99.70**	**99.73**	**99.11**	**98.62**
Cr_2O_3	**0.01**	**0.04**	0.71	**0.00**	**0.00**	**0.00**	**0.02**
FeO	**0.60**	**0.62**	124.38	**0.01**	**0.00**	**0.00**	**0.00**
MnO	**0.00**	**0.00**	0.40	**0.01**	**0.00**	**0.01**	**0.00**
NiO	**0.03**	**0.00**	0.11	**0.00**	**0.00**	**0.02**	**0.00**
Na_2O	**0.01**	**0.00**	0.01	**0.01**	**0.00**	**0.01**	**0.01**
MgO	**0.12**	**0.12**	0.02	**0.03**	**0.03**	**0.04**	**0.08**
CaO	**0.02**	**0.01**	0.00	**0.00**	**0.01**	**0.01**	**0.00**
K_2O	**0.00**	**0.00**					
Total	**98.77**	**98.12**	126.26	**99.88**	**99.92**	**99.34**	**99.49**

	BZ229B-2	**BZ229B-3**	**BZ229B-4**	BZ230A-1	BZ230B-1	BZ230C-1	BZ232B-1
	Corundum	**Corundum**	**Corundum**	Fe	Moissanite	Fe	Moissanite
SiO_2	**0.01**	**0.05**	**0.12**	0.54	158.36	0.58	157.28
TiO_2	**0.41**	**1.13**	**0.75**	0.00	0.00	0.01	0.00
Al_2O_3	**98.62**	**98.55**	**98.24**	0.09	0.18	0.08	0.11
Cr_2O_3	**0.00**	**0.03**	**0.03**	0.70	0.00	0.70	0.01
FeO	**0.01**	**0.00**	**0.02**	124.17	0.00	123.27	0.00
MnO	**0.01**	**0.01**	**0.00**	0.41	0.00	0.40	0.03
NiO	**0.00**	**0.00**	**0.00**	0.12	0.01	0.16	0.04
Na_2O	**0.01**	**0.01**	**0.01**	0.02	0.01	0.04	0.01
MgO	**0.04**	**0.23**	**0.06**	0.02	0.01	0.00	0.01
CaO	**0.00**	**0.01**	**0.00**	0.01	0.00	0.00	0.02
K_2O			**0.00**				
Total	**99.11**	**100.02**	**99.24**	126.08	158.57	125.24	157.51

	BZ232C-1	BZ233A-1	BZ233A-2	BZ233A-3	BZ233A-4	BZ233A-5	BZ233A-6
	Fe	????	SiO2	TiO2	????	????	????
SiO_2	0.51	34.30	95.05	7.25	39.82	29.14	20.80
TiO_2	0.00	0.29	0.00	73.80	1.19	6.04	31.37
Al_2O_3	0.04	30.20	0.27	7.24	34.96	28.04	18.18
Cr_2O_3	0.79	0.16	0.00	0.05	0.19	0.09	0.17
FeO	124.15	21.31	0.74	8.33	11.15	27.06	21.28
MnO	0.43	0.03	0.02	0.03	0.02	0.04	0.39
NiO	0.12	0.02	0.00	0.01	0.02	0.04	0.00
Na_2O	0.07	0.10	0.01	0.06	0.00	0.11	0.12
MgO	0.01	0.36	0.01	0.12	0.10	0.08	0.05
CaO	0.00	0.05	0.00	0.05	0.05	0.06	0.03
K_2O							
Total	126.12	86.82	96.10	96.94	87.50	90.70	92.39

	BZ233C-1	**BZ233C-2**	**BZ233C-3**	BZ233C-4	BZ233C-5	BZ234A-1	BZ234A-2
	fPer	**fPer**	**fPer**	fPer	fPer	CF Grt (blue)	CF Grt (blue)
SiO_2	**0.01**	**0.00**	**0.01**	0.02	0.05	5.57	8.70
TiO_2	**0.01**	**0.02**	**0.00**	0.02	0.00	0.13	0.19
Al_2O_3	**0.02**	**0.05**	**0.07**	0.02	0.04	4.36	7.49
Cr_2O_3	**0.58**	**0.53**	**0.60**	0.56	0.59	0.01	0.01
FeO	**29.53**	**29.43**	**29.09**	29.63	29.80	7.09	0.16
MnO	**0.43**	**0.43**	**0.43**	0.47	0.45	0.03	0.01
NiO	**1.30**	**1.28**	**1.28**	1.35	1.32	0.04	0.00
Na_2O	**0.07**	**0.10**	**0.10**	0.08	0.07	0.13	0.06
MgO	**68.11**	**67.93**	**67.56**	62.63	61.87	0.26	0.33
CaO	**0.00**	**0.00**	**0.00**	0.00	0.01	13.55	13.78
K_2O				0.00	0.01		
Total	**100.06**	**99.77**	**99.14**	94.80	94.19	31.17	30.73

	BZ235A-1	BZ235B1-1	BZ235C-1	**BZ235D-1**	**BZ235D-2**	BZ235D-3	**BZ235D-4**
	Fe	S??	Moissanite	**SiO2**	**SiO2**	SiO2	**SiO2**
SiO_2	3.15	0.00	157.84	**97.35**	**97.22**	96.47	**98.95**
TiO_2	0.50	0.00	0.02	**0.01**	**0.01**	0.04	**0.03**
Al_2O_3	8.61	0.05	0.14	**0.02**	**0.03**	0.06	**0.03**
Cr_2O_3	1.49	0.00	0.00	**0.01**	**0.00**	0.00	**0.00**
FeO	62.83	0.03	0.00	**0.00**	**0.01**	0.01	**0.00**
MnO	0.24	0.04	0.00	**0.00**	**0.00**	0.00	**0.02**
NiO	0.00	0.03	0.01	**0.00**	**0.00**	0.00	**0.02**
Na_2O	0.02	0.03	0.01	**0.01**	**0.00**	0.01	**0.02**
MgO	0.09	0.00	0.01	**0.00**	**0.00**	0.00	**0.01**
CaO	0.10	0.00	0.00	**0.01**	**0.00**	0.00	**0.00**
K_2O							
Total	77.03	0.18	158.03	**97.41**	**97.27**	96.59	**99.08**

	BZ235D-5	**BZ235D-6**	**BZ237A1-1**	BZ237A1-2	**BZ237A1-3**	**BZ237A1-4**	**BZ237A1-5**
	SiO2	**SiO2**	**Cpx**	Cpx	**Cpx**	**Cpx**	**Cpx**
SiO_2	**101.62**	**101.50**	**55.78**	55.33	**55.74**	**57.72**	**57.95**
TiO_2	**0.01**	**0.03**	**0.01**	0.00	**0.01**	**0.02**	**0.02**
Al_2O_3	**0.01**	**0.03**	**8.02**	8.01	**7.95**	**8.26**	**8.37**
Cr_2O_3	**0.02**	**0.02**	**3.24**	3.09	**3.11**	**3.12**	**3.14**
FeO	**0.07**	**0.08**	**3.13**	3.11	**3.11**	**3.17**	**3.25**
MnO	**0.00**	**0.01**	**0.43**	0.47	**0.46**	**0.46**	**0.47**
NiO	**0.02**	**0.01**	**0.01**	0.00	**0.02**	**0.00**	**0.02**
Na_2O	**0.00**	**0.00**	**6.72**	6.78	**6.95**	**5.96**	**6.10**
MgO	**0.02**	**0.01**	**15.84**	15.94	**15.80**	**16.31**	**16.70**
CaO	**0.00**	**0.00**	**5.22**	5.18	**5.18**	**5.05**	**5.02**
K_2O	**0.00**	**0.03**				**0.00**	**0.00**
Total	**101.77**	**101.72**	**98.40**	97.91	**98.33**	**100.06**	**101.05**

	BZ237A2-1	**BZ237A2-2**	**BZ237A2-3**	**BZ237A2-4**	**BZ237A2-5**	**BZ237A3-1**	BZ237A3-2
	Cpx	**Cpx**	**Cpx**	**Cpx**	**Cpx**	**Cpx**	Cpx
SiO_2	**56.02**	**58.06**	**57.56**	**58.32**	**56.85**	**56.81**	55.40
TiO_2	**0.01**	**0.01**	**0.01**	**0.02**	**0.02**	**0.03**	0.00
Al_2O_3	**8.07**	**8.31**	**8.23**	**8.39**	**8.16**	**8.21**	7.93
Cr_2O_3	**3.15**	**3.11**	**3.23**	**3.24**	**3.21**	**3.14**	3.23
FeO	**3.19**	**3.25**	**3.23**	**3.12**	**3.23**	**3.11**	3.19
MnO	**0.43**	**0.51**	**0.47**	**0.48**	**0.50**	**0.44**	0.48
NiO	**0.02**	**0.00**	**0.01**	**0.01**	**0.02**	**0.00**	0.01
Na_2O	**6.88**	**6.16**	**6.01**	**6.15**	**5.73**	**6.98**	6.21
MgO	**16.02**	**16.75**	**16.12**	**16.35**	**15.41**	**16.07**	16.28
CaO	**5.27**	**5.04**	**5.03**	**5.08**	**5.16**	**5.17**	5.07
K_2O		**0.01**	**0.00**	**0.00**	**0.00**		0.01
Total	**99.06**	**101.22**	**99.88**	**101.15**	**98.28**	**99.96**	97.82

	BZ237A3-3	BZ237A3-4	**BZ237A3-5**	**BZ237A3-6**	BZ237A4-1	**BZ237A4-2**	**BZ237A4-3**
	Cpx	Cpx	**Cpx**	**Cpx**	Cpx	**Cpx**	**Cpx**
SiO_2	**56.66**	55.92	**57.62**	**57.05**	54.33	**56.11**	**56.93**
TiO_2	**0.01**	0.00	**0.01**	**0.00**	0.01	**0.00**	**0.03**
Al_2O_3	**8.14**	8.02	**8.31**	**8.22**	7.69	**8.03**	**8.18**
Cr_2O_3	**3.18**	3.14	**3.11**	**3.15**	3.07	**3.20**	**3.09**
FeO	**3.16**	3.18	**3.13**	**3.17**	2.97	**3.11**	**3.21**
MnO	**0.48**	0.47	**0.46**	**0.47**	0.44	**0.47**	**0.46**
NiO	**0.02**	0.01	**0.01**	**0.02**	0.03	**0.01**	**0.02**
Na_2O	**6.05**	6.15	**6.47**	**6.22**	6.72	**6.96**	**6.19**
MgO	**15.88**	16.04	**16.70**	**16.33**	15.28	**15.89**	**16.39**
CaO	**5.09**	5.03	**5.06**	**5.03**	4.97	**5.19**	**4.99**
K_2O	**0.00**	0.01	**0.01**	**0.02**			**0.00**
Total	**98.68**	97.96	**100.90**	**99.67**	95.51	**98.97**	**99.49**

	BZ237A4-4	**BZ237A5-1**	**BZ237A5-2**	**BZ237A5-3**	**BZ237A6-1**	**BZ237A6-2**	BZ237A6-3
	Cpx	**Cpx**	**Cpx**	**Cpx**	**Cpx**	**Cpx**	Cpx
SiO_2	**57.96**	**56.08**	**58.08**	**56.86**	**51.86**	**56.17**	55.62
TiO_2	**0.01**	**0.01**	**0.01**	**0.00**	**0.00**	**0.01**	0.01
Al_2O_3	**8.37**	**8.01**	**8.41**	**8.20**	**12.05**	**7.91**	7.90
Cr_2O_3	**3.14**	**3.14**	**3.17**	**3.20**	**3.08**	**3.07**	3.10
FeO	**3.19**	**3.07**	**3.12**	**3.26**	**3.82**	**3.10**	3.25
MnO	**0.47**	**0.43**	**0.47**	**0.51**	**0.62**	**0.45**	0.47
NiO	**0.02**	**0.00**	**0.01**	**0.02**	**0.00**	**0.02**	0.01
Na_2O	**6.35**	**6.98**	**6.30**	**6.17**	**4.45**	**6.78**	5.76
MgO	**16.77**	**15.94**	**16.39**	**16.18**	**18.58**	**15.85**	15.76
CaO	**5.04**	**5.19**	**5.07**	**5.07**	**4.02**	**5.17**	5.08
K_2O	**0.01**		**0.00**	**0.01**			0.00
Total	**101.30**	**98.85**	**101.02**	**99.45**	**98.48**	**98.53**	96.96

	BZ237A6-4	**BZ237A6-5**	BZ237A6-6	BZ237A6-7	**BZ237A6-8**	**BZ237A6-9**	**BZ237A6-10**
	Cpx	**Cpx**	Cpx	Cpx	**Cpx**	**Cpx**	**Cpx**
SiO_2	56.06	**57.06**	55.79	59.74	**57.76**	**57.80**	**57.58**
TiO_2	0.02	**0.01**	0.00	0.01	**0.02**	**0.02**	**0.01**
Al_2O_3	8.02	**8.18**	8.05	8.63	**8.30**	**8.27**	**8.27**
Cr_2O_3	3.04	**3.18**	3.17	3.11	**3.12**	**3.03**	**3.15**
FeO	3.19	**3.19**	3.09	3.11	**3.04**	**3.17**	**3.07**
MnO	0.47	**0.47**	0.46	0.46	**0.46**	**0.47**	**0.45**
NiO	0.02	**0.03**	0.01	0.03	**0.02**	**0.01**	**0.01**
Na_2O	5.81	**5.70**	5.82	6.09	**5.87**	**5.78**	**5.84**
MgO	15.66	**15.64**	15.75	16.43	**15.71**	**15.60**	**15.84**
CaO	5.07	**5.07**	5.01	5.06	**5.08**	**5.06**	**5.06**
K_2O	0.00	**0.01**	0.00	0.00	**0.01**	**0.01**	**0.00**
Total	97.36	**98.53**	97.14	102.65	**99.39**	**99.23**	**99.26**

	BZ237A6-11	**BZ237A7-1**	BZ237A7-2	BZ237A7-3	**BZ237A7-4**	**BZ237A7-5**	BZ237A8-1
	Cpx	**Cpx**	Cpx	Cpx	**Cpx**	**Cpx**	Cpx
SiO_2	**58.70**	**57.00**	7.66	55.61	**57.50**	**57.49**	55.46
TiO_2	**0.01**	**0.00**	0.01	0.00	**0.02**	**0.02**	0.00
Al_2O_3	**8.41**	**8.04**	0.76	7.76	**8.18**	**8.21**	7.86
Cr_2O_3	**3.05**	**3.20**	0.32	3.06	**3.13**	**3.05**	3.08
FeO	**3.17**	**3.09**	0.50	3.03	**3.16**	**3.14**	3.03
MnO	**0.47**	**0.47**	0.04	0.46	**0.46**	**0.48**	0.45
NiO	**0.01**	**0.00**	0.01	0.03	**0.01**	**0.00**	0.00
Na_2O	**5.96**	**6.89**	0.41	6.90	**5.90**	**5.86**	6.79
MgO	**16.05**	**15.95**	1.42	15.71	**15.77**	**15.41**	15.82
CaO	**5.06**	**5.25**	0.25	5.15	**5.10**	**5.13**	5.25
K_2O	**0.01**				**0.00**	**0.00**	
Total	**100.91**	**99.89**	11.38	97.71	**99.24**	**98.79**	97.74

	BZ237A8-2	BZ237B-1	BZ237B-2	**BZ237C-1**	BZ237C-2	BZ237C-3	BZ237C-4
	Cpx	???	???	**MF Grt**	MF Grt	MF Grt	MF Grt
SiO_2	**59.04**	0.05	134.86	**41.81**	40.90	39.84	31.10
TiO_2	**0.02**	0.02	0.01	**0.00**	0.00	0.00	0.00
Al_2O_3	**8.47**	0.03	0.06	**20.89**	20.10	19.18	14.75
Cr_2O_3	**3.01**	0.02	0.01	**2.91**	2.88	2.72	2.03
FeO	**3.16**	0.05	0.09	**5.87**	6.02	5.76	4.59
MnO	**0.46**	0.00	0.01	**0.86**	0.92	0.86	0.67
NiO	**0.02**	0.02	0.01	**0.00**	0.03	0.00	0.00
Na_2O	**5.98**	0.20	0.01	**0.31**	0.31	0.30	0.22
MgO	**15.78**	0.02	0.00	**23.47**	22.99	21.23	17.31
CaO	**5.04**	0.27	0.01	**1.69**	1.70	1.53	1.12
K_2O	**0.00**						
H_2O							
Total	**100.97**	0.68	135.08	**97.81**	95.85	91.42	71.79

	BZ237C-5	BZ237C-6	**BZ237C-7**	**BZ237C-8**	**BZ237C-9**	**BZ237C-10**	**BZ238A-1**
	MF Grt	MF Grt	**MF Grt**	**MF Grt**	**MF Grt**	**MF Grt**	**MF Grt**
SiO_2	51.65	37.74	**44.43**	**43.58**	**43.35**	**43.68**	**40.75**
TiO_2	0.02	0.02	**0.01**	**0.02**	**0.02**	**0.02**	**0.00**
Al_2O_3	25.60	18.97	**21.47**	**21.67**	**21.51**	**21.81**	**22.91**
Cr_2O_3	2.86	3.12	**2.97**	**2.99**	**3.00**	**2.96**	**3.04**
FeO	5.96	6.09	**6.00**	**6.09**	**6.08**	**6.08**	**5.01**
MnO	0.89	0.92	**0.90**	**0.89**	**0.91**	**0.91**	**0.92**
NiO	0.02	0.02	**0.03**	**0.03**	**0.01**	**0.02**	**0.02**
Na_2O	0.30	0.24	**0.34**	**0.24**	**0.23**	**0.23**	**0.13**
MgO	27.07	22.50	**22.32**	**21.95**	**21.41**	**21.87**	**25.07**
CaO	1.55	1.68	**1.82**	**1.72**	**1.69**	**1.69**	**0.14**
K_2O	0.01	0.00	**0.01**	**0.02**	**0.01**	**0.01**	
Total	115.93	91.30	**100.29**	**99.19**	**98.21**	**99.26**	**97.99**

	BZ238A-2	BZ238A-3	**BZ238A-4**	**BZ238A-5**	**BZ238B-1**	**BZ238B-2**	**BZ238B-3**
	MF Grt	MF Grt	**MF Grt**	**MF Grt**	**fPer**	**fPer**	**fPer**
SiO_2	**40.40**	38.78	**42.04**	**42.44**	**0.20**	**0.02**	**0.01**
TiO_2	**0.03**	0.04	**0.04**	**0.03**	**0.03**	**0.02**	**0.08**
Al_2O_3	**22.65**	22.05	**23.80**	**24.02**	**0.13**	**0.12**	**0.11**
Cr_2O_3	**3.01**	3.00	**3.00**	**2.94**	**0.66**	**0.65**	**0.65**
FeO	**4.88**	5.07	**5.12**	**4.91**	**26.38**	**26.36**	**26.32**
MnO	**0.92**	0.94	**0.93**	**0.91**	**0.37**	**0.34**	**0.36**
NiO	**0.00**	0.01	**0.02**	**0.02**	**1.36**	**1.41**	**1.37**
Na_2O	**0.13**	0.12	**0.12**	**0.25**	**0.10**	**0.16**	**0.11**
MgO	**24.93**	24.04	**25.10**	**24.68**	**71.88**	**71.94**	**72.34**
CaO	**0.13**	0.13	**0.13**	**0.11**	**0.00**	**0.00**	**0.00**
K_2O		0.00	**0.02**	**0.02**			
Total	**97.08**	94.16	**100.31**	**100.33**	**100.93**	**101.02**	**101.35**

	BZ238B-4	BZ238B-5	**BZ238B-6**	BZ238B-7	**BZ239A-1**	**BZ239A-2**	BZ239A-3
	fPer	fPer	**fPer**	fPer	**fPer**	**fPer**	fPer
SiO_2	0.06	0.02	**0.06**	0.08	**0.03**	**0.04**	0.03
TiO_2	0.06	0.07	**0.05**	0.07	**0.00**	**0.01**	0.02
Al_2O_3	0.10	0.11	**0.12**	0.10	**0.06**	**0.06**	0.06
Cr_2O_3	0.65	0.75	**0.70**	0.66	**0.87**	**0.83**	0.85
FeO	26.57	26.55	**26.41**	26.31	**27.73**	**27.63**	28.07
MnO	0.37	0.36	**0.38**	0.33	**0.35**	**0.34**	0.32
NiO	1.44	1.43	**1.45**	1.41	**1.42**	**1.37**	1.39
Na_2O	0.07	0.10	**0.10**	0.08	**0.18**	**0.22**	0.20
MgO	65.70	67.45	**69.08**	67.38	**68.22**	**69.78**	66.38
CaO	0.00	0.00	**0.01**	0.01	**0.01**	**0.01**	0.00
K_2O	0.00	0.00	**0.00**	0.00	**0.02**	**0.01**	0.00
Total	95.01	96.85	**98.35**	96.42	**98.88**	**100.30**	97.33

	BZ239A-4	BZ239AL-1	BZ239AL-2	**BZ239D-1**	BZ239D-2	**BZ239D-3**	BZ239D-4
	fPer	fPer	fPer	**SiO2**	Plag	**Biotite**	Biotite
SiO_2	**0.03**	0.03	0.06	**100.84**	36.46	**55.00**	49.99
TiO_2	**0.03**	0.03	0.03	**0.01**	0.16	**0.75**	0.47
Al_2O_3	**0.08**	0.07	0.07	**0.10**	12.47	**16.94**	15.76
Cr_2O_3	**0.83**	0.90	0.83	**0.02**	0.04	**0.01**	0.01
FeO	**27.72**	28.13	27.84	**0.14**	17.55	**9.90**	8.16
MnO	**0.32**	0.33	0.34	**0.00**	0.16	**0.06**	0.06
NiO	**1.41**	1.09	1.10	**0.02**	0.05	**0.04**	0.03
Na_2O	**0.19**	0.24	0.19	**0.01**	0.32	**0.24**	0.20
MgO	**68.95**	65.41	64.41	**0.03**	14.72	**5.59**	3.78
CaO	**0.00**	0.00	0.01	**0.02**	2.16	**1.30**	1.05
K_2O	**0.01**	0.00	0.00	**0.03**	0.20	**6.71**	9.00
						4.46	4.03
Total	**99.57**	96.22	94.85	**101.20**	84.29	**101.01**	92.53

	BZ239E-1	BZ239E-2	BZ239E-3	**BZ239E-4**	**BZ239E-5**	BZ239E-6	**BZ239E-7**
	Plag	Plag	Plag	**Plag**	**Alb**	Alb	**Alb**
SiO_2	**59.45**	53.58	63.33	**60.00**	**68.07**	69.14	**77.27**
TiO_2	**0.04**	0.01	0.03	**0.05**	**0.01**	0.01	**0.02**
Al_2O_3	**25.37**	28.51	22.57	**25.83**	**19.51**	18.86	**21.20**
Cr_2O_3	**0.00**	0.02	0.02	**0.00**	**0.00**	0.01	**0.02**
FeO	**0.37**	0.29	0.34	**0.41**	**0.01**	0.13	**0.08**
MnO	**0.02**	0.00	0.00	**0.03**	**0.01**	0.02	**0.01**
NiO	**0.00**	0.02	0.01	**0.02**	**0.02**	0.01	**0.02**
Na_2O	**5.73**	3.82	5.64	**5.03**	**6.93**	5.87	**3.32**
MgO	**0.05**	0.03	0.03	**0.06**	**0.01**	0.01	**0.02**
CaO	**7.52**	8.14	4.72	**8.02**	**0.85**	0.40	**0.82**
K_2O	**0.43**	0.21	0.73	**0.45**	**0.09**	0.62	**0.18**
Total	**98.98**	94.63	97.40	**99.87**	**95.51**	95.08	**102.96**

	BZ239F-1	**BZ239G-1**	BZ239G-2	**BZ240B-1**	**BZ240-2**	**BZ240B-3**	**BZ241A-1**
	SiO2	**fPer**	fPer	**MF Grt**	**MF Grt**	**MF Grt**	**fPer**
SiO_2	**100.84**	**0.00**	0.01	**43.31**	**42.28**	**42.37**	**0.03**
TiO_2	**0.02**	**0.00**	0.00	**0.01**	**0.02**	**0.02**	**0.04**
Al_2O_3	**0.01**	**0.05**	0.05	**24.27**	**23.62**	**23.85**	**0.11**
Cr_2O_3	**0.05**	**0.80**	0.82	**2.32**	**2.36**	**2.33**	**0.96**
FeO	**0.25**	**27.75**	27.77	**4.71**	**4.77**	**4.79**	**28.54**
MnO	**0.03**	**0.33**	0.33	**0.73**	**0.73**	**0.76**	**0.44**
NiO	**0.02**	**1.43**	1.40	**0.00**	**0.01**	**0.01**	**1.48**
Na_2O	**0.00**	**0.15**	0.17	**0.12**	**0.13**	**0.13**	**0.10**
MgO	**0.00**	**66.40**	66.19	**25.78**	**25.77**	**25.97**	**69.01**
CaO	**0.01**	**0.01**	0.00	**0.10**	**0.11**	**0.12**	**0.01**
K_2O	**0.00**	**0.01**	0.00	**0.00**	**0.00**	**0.01**	**0.00**
Total	**101.23**	**96.92**	96.75	**101.35**	**99.80**	**100.35**	**100.73**

	BZ241A-2	**BZ241A-3**	BZ241B1-1	**BZ241B1-2**	**BZ241B1-3**	BZ241B1-4	BZ241B1-5
	fPer	**fPer**	Cpx	**Cpx**	**Cpx**	Cpx	Cpx
SiO_2	**0.09**	**0.03**	55.97	**55.71**	**55.63**	56.67	56.76
TiO_2	**0.04**	**0.05**	0.04	**0.02**	**0.02**	0.02	0.01
Al_2O_3	**0.12**	**0.10**	10.57	**10.69**	**10.50**	10.09	10.72
Cr_2O_3	**1.04**	**0.99**	1.23	**1.19**	**1.15**	2.22	1.25
FeO	**28.53**	**28.81**	5.40	**5.41**	**5.29**	5.38	5.30
MnO	**0.42**	**0.42**	1.24	**1.24**	**1.23**	1.91	1.23
NiO	**1.50**	**1.50**	0.01	**0.05**	**0.01**	0.00	0.01
Na_2O	**0.12**	**0.13**	0.85	**0.85**	**0.82**	0.50	0.83
MgO	**68.21**	**67.41**	27.57	**27.02**	**26.73**	28.46	27.70
CaO	**0.01**	**0.01**	0.64	**0.64**	**0.66**	1.88	0.63
K_2O	**0.00**	**0.00**	0.00	**0.00**	**0.00**	0.00	0.00
Total	**100.07**	**99.44**	103.52	**102.82**	**102.04**	107.12	104.43

	BZ241B1-6	BZ241B1-7	BZ241B1-8	BZ241B1-9	BZ241B1-10	BZ241B1-11	**BZ241B2-1**
	Cpx	Cpx	Cpx	Cpx	Cpx	Cpx	**Px**
SiO_2	**56.34**	41.26	45.49	38.01	39.54	45.43	**52.77**
TiO_2	**0.03**	0.01	0.02	0.02	0.02	0.01	**0.01**
Al_2O_3	**10.67**	9.34	10.18	8.83	8.76	10.04	**10.04**
Cr_2O_3	**1.23**	1.71	1.71	1.76	1.67	1.77	**1.12**
FeO	**5.36**	3.96	3.96	3.08	3.79	4.01	**5.37**
MnO	**1.22**	1.52	1.51	1.62	1.59	1.47	**1.23**
NiO	**0.00**	0.02	0.00	0.04	0.01	0.01	**0.01**
Na_2O	**0.78**	5.09	5.13	2.32	3.53	5.05	**0.83**
MgO	**26.49**	17.90	17.67	17.12	16.08	17.63	**27.14**
CaO	**0.63**	5.01	5.05	7.59	5.35	5.06	**0.65**
K_2O	**0.01**	0.02	0.01	0.05	0.02	0.00	**0.00**
Total	**102.77**	85.86	90.72	80.44	80.32	90.47	**99.17**

	BZ241B2-2	**BZ241B2-3**	**BZ241C-1**	BZ241C-2	**BZ241C-3**	**BZ241C-4**	**BZ241C-5**
	Px	**Px**	**Ruby**	Ruby	**Ruby**	**Ruby**	**Ruby**
SiO_2	**53.28**	**51.82**	**0.76**	0.78	**0.79**	**0.79**	**0.79**
TiO_2	**0.02**	**0.00**	**0.05**	0.06	**0.06**	**0.06**	**0.04**
Al_2O_3	**9.94**	**9.61**	**89.70**	92.03	**89.52**	**89.96**	**90.60**
Cr_2O_3	**1.21**	**1.16**	**8.54**	8.69	**8.68**	**8.73**	**8.68**
FeO	**5.27**	**5.48**	**0.70**	0.71	**0.71**	**0.72**	**0.73**
MnO	**1.28**	**1.26**	**0.05**	0.07	**0.05**	**0.07**	**0.07**
NiO	**0.02**	**0.02**	**0.01**	0.00	**0.03**	**0.00**	**0.01**
Na_2O	**0.97**	**0.83**	**0.00**	0.01	**0.01**	**0.00**	**0.01**
MgO	**28.26**	**27.21**	**0.46**	0.42	**0.43**	**0.43**	**0.43**
CaO	**0.81**	**0.65**	**0.00**	0.02	**0.02**	**0.00**	**0.02**
K_2O	**0.00**	**0.00**	**0.01**	0.01	**0.01**	**0.02**	**0.01**
Total	**101.04**	**98.05**	**100.28**	102.80	**100.30**	**100.77**	**101.38**

	BZ241C-6	BZ242A-1	**BZ242A-2**	BZ242A-3	**BZ242B-1**	**BZ242B-2**	**BZ242B-3**
	Ruby	fPer	**fPer**	fPer	**Cpx**	**Cpx**	**Cpx**
SiO_2	0.78	0.03	**0.01**	0.02	**55.12**	**54.46**	**55.31**
TiO_2	0.04	0.02	**0.03**	0.01	**0.02**	**0.04**	**0.04**
Al_2O_3	92.04	0.09	**0.09**	0.08	**12.64**	**12.44**	**12.65**
Cr_2O_3	8.66	0.85	**0.81**	0.87	**1.71**	**1.77**	**1.77**
FeO	0.77	25.45	**25.50**	25.48	**3.97**	**4.00**	**3.89**
MnO	0.04	0.32	**0.33**	0.36	**1.30**	**1.26**	**1.30**
NiO	0.01	1.38	**1.41**	1.42	**0.00**	**0.01**	**0.03**
Na_2O	0.00	0.50	**0.50**	0.52	**4.68**	**4.55**	**4.67**
MgO	0.43	67.78	**69.30**	68.94	**16.47**	**16.01**	**16.58**
CaO	0.00	0.01	**0.01**	0.01	**4.40**	**4.39**	**4.36**
K_2O	0.01	0.00	**0.00**	0.00	**0.01**	**0.00**	**0.01**
Total	102.78	96.42	**97.99**	97.70	**100.31**	**98.93**	**100.60**

	BZ243A-1	**BZ243A-2**	**BZ243A-3**	BZ243B-1	BZ243B-2	BZ243B-3	**BZ243B-4**
	MF Grt	**MF Grt**	**MF Grt**	fPer	fPer	fPer	**fPer**
SiO_2	**43.04**	**41.34**	**42.33**	0.03	0.04	0.05	**0.03**
TiO_2	**0.04**	**0.04**	**0.04**	0.01	0.03	0.01	**0.01**
Al_2O_3	**24.57**	**23.72**	**24.21**	0.09	0.10	0.12	**0.08**
Cr_2O_3	**2.39**	**2.42**	**2.43**	1.11	1.16	1.07	**1.14**
FeO	**5.15**	**5.21**	**5.21**	29.72	29.93	30.24	**29.43**
MnO	**0.90**	**0.92**	**0.88**	0.37	0.38	0.37	**0.40**
NiO	**0.03**	**0.03**	**0.02**	0.90	0.97	1.22	**1.01**
Na_2O	**0.10**	**0.09**	**0.09**	0.51	0.57	0.68	**0.52**
MgO	**24.63**	**24.18**	**24.27**	62.44	62.92	62.39	**64.57**
CaO	**0.12**	**0.11**	**0.11**	0.00	0.00	0.00	**0.01**
K_2O	**0.00**	**0.00**	**0.01**	0.01	0.00	0.00	**0.01**
Total	**100.96**	**98.06**	**99.60**	95.19	96.08	96.16	**97.20**

	BZ243C-1	BZ243C-2	BZ243C-3	BZ243C-4	BZ244B-1	BZ244B-2	BZ245A-1
	Olivine	Olivine	Olivine	Olivine	MF Grt	MF Grt	fPer
SiO_2	40.09	43.47	39.79	41.62	42.10	42.14	0.05
TiO_2	0.02	0.02	0.01	0.02	0.06	0.06	0.03
Al_2O_3	0.05	0.05	0.05	0.03	23.82	23.84	0.04
Cr_2O_3	0.20	0.21	0.19	0.19	2.81	2.79	0.72
FeO	11.89	11.83	11.96	11.80	4.59	4.62	45.69
MnO	0.10	0.08	0.10	0.10	0.96	0.97	0.39
NiO	0.42	0.42	0.41	0.41	0.00	0.02	0.95
Na_2O	0.06	0.06	0.05	0.05	0.08	0.10	0.23
MgO	46.26	47.23	45.78	47.15	25.44	25.82	50.78
CaO	0.00	0.01	0.00	0.01	0.09	0.09	0.00
K_2O	0.01	0.01	0.00	0.00	0.00	0.00	0.00
Total	99.10	103.37	98.33	101.37	99.94	100.46	98.86

	BZ245A-2	BZ245A-3	BZ245A-4	BZ245A-5	BZ245B-1	BZ245B-2	BZ245B-3
	fPer	fPer	fPer	fPer	fPer	fPer	fPer
SiO_2	0.03	0.05	0.05	0.04	0.01	0.02	0.02
TiO_2	0.02	0.04	0.02	0.02	0.01	0.02	0.01
Al_2O_3	0.05	0.03	0.04	0.04	0.06	0.04	0.04
Cr_2O_3	0.68	0.71	0.72	0.72	0.72	0.74	0.71
FeO	45.78	46.85	46.97	46.54	45.37	45.64	45.63
MnO	0.38	0.39	0.37	0.36	0.37	0.40	0.36
NiO	0.96	1.00	0.95	0.93	0.91	0.95	0.96
Na_2O	0.25	0.29	0.32	0.30	0.26	0.27	0.27
MgO	51.18	48.01	48.75	49.65	54.49	53.69	53.84
CaO	0.00	0.00	0.01	0.01	0.01	0.01	0.00
K_2O	0.00	0.00	0.00	0.00	0.00	0.00	0.01
Total	99.34	97.37	98.21	98.61	102.19	101.79	101.85

	BZ246A-1	BZ246A-2	BZ246A-3	BZ246A-4	BZ246A-5	BZ250C-1	BZ250C-2
	Cpx	Cpx	Cpx	Cpx	Cpx	fPer	fPer
SiO_2	51.96	51.69	51.59	52.69	53.96	0.05	0.04
TiO_2	0.04	0.03	0.04	0.04	0.03	0.01	0.02
Al_2O_3	11.70	11.56	11.48	11.50	11.75	0.07	0.09
Cr_2O_3	2.02	1.96	2.00	1.92	2.02	0.24	0.26
FeO	4.37	4.41	4.37	4.41	4.38	66.04	66.51
MnO	1.95	1.95	1.94	1.88	1.90	0.82	0.80
NiO	0.02	0.00	0.01	0.01	0.02	1.15	1.17
Na_2O	3.87	3.84	3.84	4.69	4.77	0.09	0.09
MgO	16.85	16.44	16.06	16.34	16.72	31.59	31.97
CaO	4.52	4.54	4.49	4.61	4.53	0.00	0.00
K_2O	0.01	0.00	0.00	0.00	0.00	0.00	0.01
Total	97.31	96.40	95.81	98.09	100.09	100.05	100.96

	BZ251A-1	**BZ251A-2**	**BZ251A-3**	BZ251A-4	**BZ251A-5**	**BZ251B-1**	**BZ251B-2**
	fPer	**fPer**	**fPer**	fPer	**fPer**	**MgSiPvk**	**MgSiPvk**
SiO_2	**0.01**	**0.05**	**0.04**	0.02	**0.06**	**57.35**	**57.27**
TiO_2	**0.01**	**0.02**	**0.00**	0.02	**0.00**	**0.15**	**0.15**
Al_2O_3	**0.01**	**0.04**	**0.05**	0.02	**0.05**	**1.35**	**1.32**
Cr_2O_3	**0.36**	**0.32**	**0.35**	0.32	**0.34**	**0.43**	**0.40**
FeO	**23.32**	**23.48**	**23.79**	23.26	**23.48**	**3.83**	**3.84**
MnO	**0.20**	**0.23**	**0.25**	0.23	**0.21**	**0.14**	**0.12**
NiO	**1.31**	**1.27**	**1.19**	1.23	**1.22**	**0.00**	**0.00**
Na_2O	**0.17**	**0.16**	**0.18**	0.19	**0.20**	**0.02**	**0.02**
MgO	**76.20**	**75.62**	**71.73**	77.07	**75.52**	**37.12**	**35.62**
CaO	**0.01**	**0.01**	**0.05**	0.02	**0.01**	**0.05**	**0.05**
K_2O	**0.00**	**0.01**	**0.02**	0.01	**0.01**	**0.01**	**0.03**
Total	**101.58**	**101.20**	**97.65**	102.37	**101.10**	**100.45**	**98.82**

	BZ251B-3	**BZ251B-4**	**BZ252A-1**	**BZ252A-2**	**BZ252A-3**	BZ254A-1	BZ254A-2
	MgSiPvk	**MgSiPvk**	**CaSiPvk**	**CaSiPvk**	**CaSiPvk**	MgSiPvk	MgSiPvk
SiO_2	56.60	**56.50**	**51.15**	**51.30**	**51.07**	47.91	28.50
TiO_2	0.15	**0.14**	**0.06**	**0.06**	**0.05**	0.11	0.08
Al_2O_3	1.31	**1.31**	**0.06**	**0.07**	**0.07**	1.44	0.78
Cr_2O_3	0.40	**0.38**	**0.02**	**0.05**	**0.01**	0.36	0.26
FeO	3.68	**3.73**	**0.19**	**0.20**	**0.09**	7.38	11.07
MnO	0.11	**0.16**	**0.05**	**0.07**	**0.07**	0.13	0.11
NiO	0.00	**0.01**	**0.04**	**0.03**	**0.00**	0.02	0.03
Na_2O	0.04	**0.04**	**0.02**	**0.00**	**0.02**	0.53	0.95
MgO	35.27	**36.00**	**0.15**	**0.12**	**0.14**	26.26	13.77
CaO	0.08	**0.07**	**48.49**	**48.37**	**48.42**	0.11	0.12
K_2O	0.02	**0.03**	**0.02**	**0.01**	**0.03**	0.18	0.36
Total	97.66	**98.37**	**100.26**	**100.28**	**99.97**	84.43	56.02

	BZ254A-3	BZ254A-4	BZ254A-5	**BZ255A-1**	**BZ255A-2**	**BZ255A-3**	**BZ255A-4**
	MgSiPvk	MgSiPvk	MgSiPvk	**fPer**	**fPer**	**fPer**	**fPer**
SiO_2	38.08	32.84	35.21	**0.12**	**0.12**	**0.10**	**0.14**
TiO_2	0.08	0.08	0.10	**0.02**	**0.02**	**0.02**	**0.02**
Al_2O_3	1.14	1.07	1.03	**0.04**	**0.02**	**0.03**	**0.04**
Cr_2O_3	0.27	0.21	0.25	**0.18**	**0.21**	**0.18**	**0.19**
FeO	8.43	11.30	9.48	**52.51**	**52.11**	**51.15**	**52.62**
MnO	0.16	0.11	0.14	**0.22**	**0.21**	**0.22**	**0.23**
NiO	0.06	0.06	0.04	**0.43**	**0.41**	**0.43**	**0.41**
Na_2O	1.04	1.08	1.04	**0.06**	**0.04**	**0.05**	**0.05**
MgO	22.24	17.21	19.99	**45.49**	**44.94**	**45.64**	**44.83**
CaO	0.13	0.14	0.13	**0.02**	**0.01**	**0.00**	**0.01**
K_2O	0.36	0.41	0.36	**0.00**	**0.01**	**0.00**	**0.00**
Total	71.97	64.51	67.76	**99.09**	**98.81**	**97.81**	**98.53**

	BZ255A-5	BZ255A-6	**BZ257A3-1**	**BZ257A3-2**	BZ257A3-3	**BZ257A3-4**	**BZ257A3L-1**
	fPer	fPer	**fPer**	**fPer**	fPer	**fPer**	**fPer**
SiO_2	0.25	0.14	**0.02**	**0.02**	0.02	**0.02**	**0.02**
TiO_2	0.05	0.03	**0.02**	**0.01**	0.02	**0.04**	**0.03**
Al_2O_3	0.04	0.06	**0.04**	**0.02**	0.01	**0.00**	**0.08**
Cr_2O_3	0.16	0.19	**0.60**	**0.58**	0.59	**0.63**	**0.64**
FeO	37.83	52.93	**38.37**	**38.32**	38.39	**38.50**	**42.90**
MnO	0.12	0.20	**0.08**	**0.06**	0.05	**0.08**	**0.06**
NiO	0.29	0.39	**0.30**	**0.29**	0.29	**0.32**	**0.29**
Na_2O	0.04	0.03	**0.01**	**0.00**	0.02	**0.03**	**0.01**
MgO	18.95	43.63	**62.28**	**62.51**	56.52	**62.41**	**57.63**
CaO	0.01	0.00	**0.00**	**0.01**	0.00	**0.01**	**0.02**
K_2O	0.00	0.00	**0.01**	**0.00**	0.00	**0.02**	**0.00**
Total	57.73	97.60	**101.73**	**101.81**	95.91	**102.05**	**101.67**

	BZ259A1-1	BZ259A1-2	BZ259A1-3	**BZ259A1-4**	**BZ259A1-5**	BZ259A2-1	BZ259A2-2
	MF Grt	MF Grt	MF Grt	**MF Grt**	**MF Grt**	MF Grt	MF Grt
SiO_2	**42.21**	41.28	41.33	**42.27**	**42.22**	40.00	39.34
TiO_2	**0.03**	0.03	0.02	**0.03**	**0.03**	0.02	0.02
Al_2O_3	**23.15**	22.76	22.58	**23.08**	**23.22**	21.96	21.71
Cr_2O_3	**2.39**	2.41	2.34	**2.36**	**2.32**	2.46	2.45
FeO	**4.48**	4.41	4.45	**4.42**	**4.44**	4.55	4.52
MnO	**0.67**	0.68	0.66	**0.67**	**0.66**	0.68	0.63
NiO	**0.01**	0.02	0.02	**0.03**	**0.01**	0.00	0.01
Na_2O	**0.15**	0.14	0.17	**0.14**	**0.13**	0.16	0.14
MgO	**26.08**	25.77	25.59	**25.93**	**26.01**	25.18	25.25
CaO	**0.10**	0.11	0.10	**0.11**	**0.11**	0.11	0.12
K_2O	**0.00**	0.00	0.00	**0.01**	**0.00**	0.02	0.02
Total	**99.28**	97.59	97.26	**99.05**	**99.15**	95.12	94.19

	BZ259A2-3	BZ259A2-4	BZ259A2-5	**BZ259A2-6**	**BZ258A2-7**	**BZ258A2-8**	BZ259A2-9
	MF Grt	MF Grt	MF Grt	**MF Grt**	**MF Grt**	**MF Grt**	MF Grt
SiO_2	38.79	40.99	38.46	**41.01**	**41.59**	**41.22**	40.65
TiO_2	0.02	0.01	0.01	**0.02**	**0.03**	**0.01**	0.02
Al_2O_3	21.41	22.58	21.25	**22.69**	**22.87**	**22.70**	22.86
Cr_2O_3	2.38	2.43	2.43	**2.39**	**2.39**	**2.40**	2.37
FeO	4.42	4.44	4.42	**4.38**	**4.39**	**4.42**	4.32
MnO	0.69	0.61	0.62	**0.67**	**0.65**	**0.65**	0.64
NiO	0.01	0.02	0.03	**0.03**	**0.01**	**0.02**	0.03
Na_2O	0.14	0.15	0.13	**0.15**	**0.13**	**0.22**	0.18
MgO	24.73	25.29	24.34	**26.26**	**26.12**	**25.89**	30.86
CaO	0.12	0.12	0.11	**0.11**	**0.11**	**0.11**	0.09
K_2O	0.00	0.00	0.02	**0.02**	**0.01**	**0.02**	0.00
Total	92.71	96.63	91.80	**97.73**	**98.29**	**97.64**	102.18

	BZ259A2-10	BZ259A2-11	BZ259A2-12	BZ259A2-13	**BZ259A2-14**	**BZ259A2-15**	**BZ259A2-16**
	MF Grt	MF Grt	MF Grt	MF Grt	**MF Grt**	**MF Grt**	**MF Grt**
SiO_2	43.81	43.07	44.32	46.15	**41.88**	**41.40**	**40.26**
TiO_2	0.03	0.03	0.03	0.03	**0.03**	**0.03**	**0.03**
Al_2O_3	24.26	23.79	24.50	25.47	**23.24**	**23.24**	**22.45**
Cr_2O_3	2.45	2.40	2.44	2.33	**2.42**	**2.43**	**2.43**
FeO	4.43	4.53	4.32	4.34	**4.47**	**4.42**	**4.42**
MnO	0.62	0.65	0.66	0.67	**0.69**	**0.67**	**0.66**
NiO	0.01	0.04	0.00	0.02	**0.00**	**0.02**	**0.01**
Na_2O	0.16	0.15	0.15	0.16	**0.16**	**0.17**	**0.14**
MgO	28.92	28.35	28.29	28.97	**28.29**	**28.78**	**28.01**
CaO	0.10	0.11	0.12	0.10	**0.12**	**0.12**	**0.11**
K_2O	0.01	0.01	0.01	0.00	**0.01**	**0.01**	**0.01**
Total	104.79	103.15	104.82	108.25	**101.34**	**101.32**	**98.56**

	BZ259A2-17	**BZ259A2-18**	**BZ259A2-19**	**BZ259A2-20**	**BZ259A2-21**	**BZ259A2-22**	BZ259A2-23
	MF Grt	**MF Grt**	**MF Grt**	**MF Grt**	**MF Grt**	**MF Grt**	MF Grt
SiO_2	**42.16**	**42.12**	**41.62**	**41.10**	**42.17**	**42.28**	40.29
TiO_2	**0.02**	**0.03**	**0.01**	**0.02**	**0.02**	**0.03**	0.01
Al_2O_3	**23.37**	**23.29**	**23.10**	**22.81**	**23.23**	**23.38**	22.44
Cr_2O_3	**2.41**	**2.41**	**2.37**	**2.34**	**2.49**	**2.35**	2.36
FeO	**4.44**	**4.48**	**4.48**	**4.39**	**4.46**	**4.36**	4.30
MnO	**0.65**	**0.65**	**0.69**	**0.64**	**0.65**	**0.67**	0.66
NiO	**0.03**	**0.01**	**0.01**	**0.00**	**0.01**	**0.01**	0.00
Na_2O	**0.16**	**0.16**	**0.16**	**0.15**	**0.16**	**0.14**	0.14
MgO	**27.37**	**27.06**	**26.83**	**26.37**	**26.65**	**26.47**	26.25
CaO	**0.11**	**0.11**	**0.11**	**0.11**	**0.12**	**0.12**	0.12
K_2O	**0.01**	**0.00**	**0.02**	**0.01**	**0.01**	**0.01**	0.01
Total	**100.73**	**100.33**	**99.39**	**97.92**	**99.98**	**99.80**	96.57

	BZ259A2-24	**BZ259A2-25**	BZ259A2-26	BZ259B-1	BZ259B-2	BZ259B-3	BZ259B-4
	MF Grt	**MF Grt**	MF Grt	AlCaPx	AlCaPx	AlCaPx	AlCaPx
SiO_2	46.15	**41.33**	47.25	54.89	54.41	54.13	53.93
TiO_2	0.03	**0.02**	0.02	0.02	0.02	0.02	0.01
Al_2O_3	25.74	**22.86**	26.04	9.81	9.74	9.70	9.79
Cr_2O_3	2.44	**2.41**	2.37	1.27	1.30	1.30	1.25
FeO	4.30	**4.43**	4.29	3.50	3.62	3.57	3.63
MnO	0.64	**0.65**	0.63	1.11	1.16	1.10	1.15
NiO	0.00	**0.01**	0.04	0.01	0.04	0.05	0.01
Na_2O	0.17	**0.14**	0.19	5.54	5.52	5.70	5.54
MgO	29.58	**27.64**	29.61	15.64	15.56	15.67	15.32
CaO	0.11	**0.11**	0.11	5.35	5.31	5.30	5.38
K_2O	0.01	**0.00**	0.01	0.04	0.02	0.04	0.04
Total	109.17	**99.63**	110.55	97.17	96.69	96.58	96.06

	BZ259B-5	BZ259B-6	BZ259B-7	BZ259B-8	**BZ259B-9**	BZ259B-10	**BZ259B-11**
	AlCaPx	AlCaPx	AlCaPx	AlCaPx	**AlCaPx**	AlCaPx	**AlCaPx**
SiO$_2$	53.53	54.29	54.51	54.28	**55.88**	57.78	**55.44**
TiO$_2$	0.02	0.02	0.01	0.01	**0.00**	0.04	**0.01**
Al$_2$O$_3$	9.59	9.71	9.76	9.73	**10.05**	10.49	**10.09**
Cr$_2$O$_3$	1.29	1.27	1.24	1.30	**1.22**	1.26	**1.28**
FeO	3.65	3.63	3.61	3.62	**3.60**	3.54	**3.61**
MnO	1.18	1.14	1.12	1.09	**1.10**	1.14	**1.16**
NiO	0.02	0.02	0.03	0.00	**0.01**	0.01	**0.01**
Na$_2$O	5.37	5.81	5.71	5.77	**5.87**	5.92	**5.78**
MgO	15.27	16.10	15.76	15.78	**16.15**	16.37	**15.90**
CaO	5.40	5.29	5.33	5.25	**5.32**	5.30	**5.31**
K$_2$O	0.03	0.02	0.03	0.02	**0.03**	0.02	**0.03**
Total	95.34	97.31	97.11	96.84	**99.23**	101.87	**98.62**

	BZ259B-12	BZ259B-13	**BZ259B-14**	**BZ259B-15**	**BZ259B-16**	BZ259B-17	**BZ259B-18**
	AlCaPx	AlCaPx	**AlCaPx**	**AlCaPx**	**AlCaPx**	AlCaPx	**AlCaPx**
SiO$_2$	57.17	56.74	**56.40**	**55.79**	**56.42**	57.69	**55.84**
TiO$_2$	0.04	0.01	**0.02**	**0.00**	**0.03**	0.01	**0.03**
Al$_2$O$_3$	10.42	10.24	**10.29**	**10.17**	**10.23**	10.48	**10.08**
Cr$_2$O$_3$	1.32	1.29	**1.33**	**1.31**	**1.31**	1.30	**1.33**
FeO	3.61	3.67	**3.61**	**3.49**	**3.54**	3.65	**3.67**
MnO	1.10	1.10	**1.13**	**1.15**	**1.16**	1.11	**1.07**
NiO	0.00	0.05	**0.01**	**0.01**	**0.04**	0.04	**0.01**
Na$_2$O	6.19	6.10	**6.02**	**5.96**	**5.98**	6.13	**6.06**
MgO	16.68	16.74	**16.62**	**16.51**	**16.38**	16.86	**16.64**
CaO	5.31	5.37	**5.31**	**5.35**	**5.29**	5.33	**5.32**
K$_2$O	0.03	0.03	**0.03**	**0.04**	**0.02**	0.03	**0.03**
Total	101.86	101.33	**100.77**	**99.75**	**100.40**	102.62	**100.07**

	BZ259B-19	**BZ259B-20**	**BZ259B-21**	**BZ259B-22**	**BZ259B-23**	**BZ259B-24**	**BZ259B-25**
	AlCaPx	**AlCaPx**	**AlCaPx**	**AlCaPx**	**AlCaPx**	**AlCaPx**	**AlCaPx**
SiO$_2$	**55.87**	**55.24**	**55.27**	**55.52**	**55.72**	**55.56**	**55.84**
TiO$_2$	**0.01**	**0.01**	**0.01**	**0.04**	**0.01**	**0.01**	**0.02**
Al$_2$O$_3$	**10.11**	**10.02**	**9.97**	**10.05**	**10.15**	**10.08**	**10.20**
Cr$_2$O$_3$	**1.24**	**1.29**	**1.32**	**1.28**	**1.30**	**1.29**	**1.31**
FeO	**3.62**	**3.58**	**3.67**	**3.60**	**3.69**	**3.69**	**3.65**
MnO	**1.13**	**1.15**	**1.08**	**1.17**	**1.11**	**1.11**	**1.12**
NiO	**0.03**	**0.01**	**0.02**	**0.04**	**0.05**	**0.05**	**0.00**
Na$_2$O	**6.00**	**5.82**	**5.92**	**6.01**	**5.95**	**5.93**	**5.98**
MgO	**16.55**	**16.28**	**16.67**	**16.60**	**16.61**	**16.55**	**16.59**
CaO	**5.37**	**5.26**	**5.35**	**5.35**	**5.32**	**5.33**	**5.35**
K$_2$O	**0.04**	**0.03**	**0.03**	**0.03**	**0.01**	**0.03**	**0.03**
Total	**99.97**	**98.69**	**99.30**	**99.69**	**99.92**	**99.61**	**100.08**

	BZ260D-1	**BZ260D-2**	BZ260D-3	**BZ260D-4**	BZ260E-1	BZ260E-2	BZ260E-3
	fPer	**fPer**	fPer	**fPer**	fPer	fPer	fPer
SiO_2	**0.04**	**0.05**	0.05	**0.05**	0.06	0.05	0.08
TiO_2	**0.01**	**0.03**	0.02	**0.00**	0.04	0.02	0.01
Al_2O_3	**0.11**	**0.07**	0.09	**0.09**	0.08	0.08	0.08
Cr_2O_3	**0.62**	**0.61**	0.60	**0.63**	0.60	0.64	0.61
FeO	**30.74**	**30.82**	30.65	**30.70**	30.88	30.78	30.79
MnO	**0.47**	**0.46**	0.46	**0.42**	0.43	0.50	0.47
NiO	**1.12**	**1.17**	1.13	**1.15**	1.22	1.16	1.21
Na_2O	**0.11**	**0.11**	0.12	**0.12**	0.15	0.15	0.15
MgO	**66.48**	**66.14**	63.25	**66.10**	63.20	62.27	64.19
CaO	**0.01**	**0.00**	0.00	**0.01**	0.00	0.00	0.00
K_2O	**0.02**	**0.01**	0.00	**0.00**	0.00	0.01	0.01
Total	**99.74**	**99.47**	96.37	**99.28**	96.66	95.65	97.60

	BZ260E-4	**BZ260E-5**	**JH2-1**	**JH2-2**	**JH2-3**	JH6A1-1	JH6A1-2
	fPer	**fPer**	**fPer**	**fPer**	**fPer**	fPer	fPer
SiO_2	**0.08**	**0.13**	**0.00**			5.70	5.64
TiO_2	**0.01**	**0.02**				0.02	0.03
Al_2O_3	**0.09**	**0.11**	**0.03**	**0.06**	**0.04**	0.22	0.54
Cr_2O_3	**0.60**	**0.60**	**0.13**	**0.17**	**0.16**	0.80	0.79
FeO	**30.46**	**30.59**	**35.91**	**35.71**	**35.81**	72.04	71.75
MnO	**0.39**	**0.46**	**0.23**	**0.23**	**0.25**	0.28	0.23
NiO	**1.23**	**1.18**	**1.08**	**1.07**	**1.06**	1.14	1.12
Na_2O	**0.12**	**0.11**				0.10	0.15
MgO	**65.65**	**65.83**	**63.86**	**63.89**	**63.80**	3.41	3.31
CaO	**0.00**	**0.00**				0.11	0.10
K_2O	**0.01**	**0.00**					
Total	**98.64**	**99.02**	**101.25**	**101.14**	**101.12**	83.82	83.66

	JH6A1-3	JH6A1-4	JH6A1-5	JH6A1-6	**JH7A1-1**	**JH7A1-2**	**JH7A1-3**
	fPer	fPer	fPer	fPer	**fPer**	**fPer**	**fPer**
SiO_2	6.80	6.15	1.71	3.84	**0.02**	**0.00**	**0.00**
TiO_2	0.03	0.05	0.00	0.06	**0.01**	**0.00**	**0.00**
Al_2O_3	0.41	0.16	0.21	0.29	**0.01**	**0.05**	**0.07**
Cr_2O_3	0.83	0.77	0.43	0.70	**0.50**	**0.55**	**0.52**
FeO	68.20	70.93	59.73	75.33	**38.18**	**38.22**	**38.15**
MnO	0.24	0.25	0.23	0.26	**0.34**	**0.36**	**0.34**
NiO	0.90	1.17	0.38	0.61	**1.07**	**1.03**	**1.05**
Na_2O	0.17	0.08	0.00	0.08	**0.51**	**0.43**	**0.41**
MgO	2.02	3.31	0.85	1.73	**61.10**	**61.17**	**61.14**
CaO	0.08	0.13	0.00	0.10	**0.00**	**0.00**	**0.00**
K_2O							
Total	79.68	83.00	63.69	83.00	**101.74**	**101.81**	**101.68**

	JH7A1-4	**JH11A1-1**	**JH11A1-2**	**JH11A1-3**	JH11A1-4	JH11A1-5	JH11A1-6
	fPer	**fPer**	**fPer**	**fPer**	fPer	fPer	fPer
SiO_2	**0.00**	**0.04**	**0.03**	**0.05**	0.09	0.76	0.39
TiO_2	**0.00**	**0.03**	**0.05**	**0.04**	0.03	0.00	0.03
Al_2O_3	**0.06**	**0.15**	**0.13**	**0.11**	0.13	0.13	0.14
Cr_2O_3	**0.51**	**0.87**	**0.90**	**0.84**	0.82	0.16	0.82
FeO	**38.16**	**61.16**	**61.10**	**60.68**	59.90	12.10	58.78
MnO	**0.31**	**0.53**	**0.53**	**0.52**	0.50	0.07	0.52
NiO	**1.08**	**0.42**	**0.47**	**0.45**	0.47	0.09	0.36
Na_2O	**0.41**	**0.26**	**0.26**	**0.26**	0.17	0.01	0.17
MgO	**60.49**	**36.61**	**36.44**	**36.12**	34.81	5.28	26.93
CaO	**0.00**	**0.00**	**0.00**	**0.00**	0.00	0.01	0.02
K_2O							
Total	**101.02**	**100.07**	**99.91**	**99.07**	96.92	18.61	88.16

	JH11A1-7	**JH11A1-8**	**JH12A1-1**	**JH12A1-2**	**JH12A1-3**	JH12A1-4	**JH12A1-5**
	fPer	**fPer**	**fPer**	**fPer**	**fPer**	fPer	**fPer**
SiO_2	0.48	**0.03**	**0.00**	**0.00**	**0.00**	0.10	**0.00**
TiO_2	0.03	**0.03**	**0.00**	**0.00**	**0.01**	0.02	**0.00**
Al_2O_3	0.12	**0.12**	**0.02**	**0.05**	**0.04**	0.05	**0.05**
Cr_2O_3	0.52	**0.87**	**0.40**	**0.37**	**0.37**	0.38	**0.36**
FeO	46.13	**61.78**	**39.72**	**39.69**	**39.77**	39.02	**39.30**
MnO	0.35	**0.47**	**0.33**	**0.30**	**0.33**	0.28	**0.29**
NiO	0.32	**0.44**	**0.92**	**0.90**	**0.88**	0.94	**0.93**
Na_2O	0.03	**0.27**	**0.29**	**0.34**	**0.28**	0.26	**0.29**
MgO	20.77	**36.71**	**59.05**	**59.20**	**59.78**	55.23	**58.61**
CaO	0.02	**0.01**	**0.00**	**0.00**	**0.00**	0.09	**0.00**
K_2O							
Total	68.77	**100.73**	**100.73**	**100.85**	**101.46**	96.37	**99.83**

	JH12A1-6	**JH17A1-1**	**JH17A1-2**	**JH17A1-3**
	fPer	**fPer**	**fPer**	**fPer**
SiO_2	**0.00**	**0.00**	**0.02**	**0.04**
TiO_2	**0.00**	**0.03**	**0.02**	**0.02**
Al_2O_3	**0.06**	**0.10**	**0.08**	**0.10**
Cr_2O_3	**0.39**	**0.76**	**0.77**	**0.76**
FeO	**39.65**	**43.31**	**43.28**	**42.97**
MnO	**0.32**	**0.22**	**0.21**	**0.23**
NiO	**0.87**	**0.62**	**0.61**	**0.60**
Na_2O	**0.32**	**0.05**	**0.06**	**0.06**
MgO	**59.00**	**56.68**	**55.70**	**55.56**
CaO	**0.00**	**0.00**	**0.00**	**0.00**
K_2O				
Total	**100.61**	**101.77**	**100.75**	**100.34**

Analyses of Guinean phases as silicates

	GU2A-1	**GU2A-2**	**GU2A-3**	**GU2A-4**	**GU3B-1**	GU3B-2	**GU3B-3**
	fPer	**fPer**	**fPer**	**fPer**	**FCM Maj**	FCM Maj	**FCM Maj**
SiO_2	**0.01**	**0.00**	**0.02**	**0.00**	**40.83**	38.36	**41.29**
TiO_2	**0.00**	**0.00**	**0.00**	**0.00**	**1.73**	1.67	**1.70**
Al_2O_3	**0.00**	**0.00**	**0.04**	**0.02**	**18.54**	17.60	**18.57**
Cr_2O_3	**0.38**	**0.38**	**0.39**	**0.37**	**0.07**	0.05	**0.04**
FeO	**20.52**	**20.67**	**20.26**	**20.11**	**13.13**	12.77	**13.06**
MnO	**0.13**	**0.14**	**0.15**	**0.12**	**0.33**	0.34	**0.35**
NiO	**1.38**	**1.36**	**1.38**	**1.39**			
Na_2O	**0.21**	**0.21**	**0.20**	**0.22**			
MgO	**77.84**	**77.69**	**77.32**	**77.61**	**11.78**	11.06	**11.95**
CaO	**0.00**	**0.00**	**0.04**	**0.00**	**12.60**	12.31	**12.62**
K_2O							
Total	**100.47**	**100.45**	**99.80**	**99.84**	**99.01**	94.16	**99.58**

	GU3B-4	**GU3B-5**	**GU3B-6**	**GU3BDk-1**	GU3BDk-2	GU3C-1	**GU3C-2**
	FCM Maj	**FCM Maj**	**FCM Maj**	**CMF Maj**	CMF Maj	Cpx	**Cpx**
SiO_2	**40.60**	**40.77**	**40.98**	**45.05**	40.91	52.91	**54.68**
TiO_2	**1.62**	**1.57**	**1.68**	**1.66**	1.83	0.39	**0.45**
Al_2O_3	**18.52**	**18.48**	**18.51**	**13.64**	15.34	4.10	**4.28**
Cr_2O_3	**0.07**	**0.06**	**0.04**	**0.06**	0.10	0.05	**0.04**
FeO	**12.87**	**13.02**	**13.09**	**11.42**	10.45	4.70	**4.82**
MnO	**0.30**	**0.31**	**0.33**	**0.31**	0.23	0.05	**0.04**
NiO				**0.00**	0.01		
Na_2O				**0.43**	0.55	2.33	**2.29**
MgO	**11.65**	**11.63**	**11.88**	**12.42**	12.10	12.64	**13.33**
CaO	**12.34**	**12.39**	**12.60**	**14.48**	15.05	17.29	**18.28**
K_2O				**0.02**	0.01		
Total	**97.97**	**98.23**	**99.11**	**99.50**	96.60	94.46	**98.21**

	GU3C-3	GU3C-4	**GU3C-5**	**GU3C-6**	GU3C-7	**GU3C-8**	**GU4A1-1**
	Cpx	Cpx	**Cpx**	**Cpx**	Cpx	**Cpx**	**fPer**
SiO_2	**54.11**	51.55	**54.79**	**53.59**	53.44	**54.37**	
TiO_2	**0.43**	0.39	**0.42**	**0.42**	0.44	**0.45**	
Al_2O_3	**4.29**	3.97	**4.27**	**4.33**	4.22	**4.24**	**0.07**
Cr_2O_3	**0.02**	0.01	**0.03**	**0.02**	0.01	**0.05**	**0.75**
FeO	**4.98**	4.79	**4.96**	**4.92**	4.87	**4.88**	**20.75**
MnO	**0.06**	0.07	**0.08**	**0.10**	0.10	**0.09**	**0.19**
NiO							**1.44**
Na_2O	**2.31**	2.07	**2.34**	**2.34**	2.32	**2.26**	
MgO	**13.21**	12.14	**13.42**	**13.32**	13.14	**12.99**	**76.88**
CaO	**18.23**	17.73	**18.65**	**18.58**	18.30	**19.27**	
K_2O							
Total	**97.64**	92.72	**98.96**	**97.62**	96.84	**98.60**	**100.08**

	GU4A1-2	**GU4A1-3**	**GU4A1-4**
	fPer	**fPer**	**fPer**
SiO_2	**0.00**	**0.00**	**0.01**
TiO_2			
Al_2O_3	**0.03**	**0.06**	**0.08**
Cr_2O_3	**0.73**	**0.78**	**0.74**
FeO	**20.82**	**20.94**	**20.88**
MnO	**0.19**	**0.22**	**0.17**
NiO	**1.42**	**1.44**	**1.34**
Na_2O			
MgO	**76.95**	**77.45**	**75.95**
CaO			
K_2O			
Total	**100.14**	**100.89**	**99.17**

Analyses of São Luiz phases as sulphide

	BZ215A-1	**BZ221A2-1**	**BZ222A-1**	**BZ222B-1**	**BZ222C-1**	BZ222C-2	**BZ231A-1**
	Pyrrhotite	**Pyrrhotite**	**Pyrrhotite**	**Pyrrhotite**	**Pyrrhotite**	Pyrrhotite	**Pyrrhotite**
Fe	**57.37**	**56.48**	**60.39**	**60.54**	**58.06**	57.01	**62.69**
Co	**0.43**	**0.37**	**0.30**	**0.32**	**0.28**	0.10	**0.00**
Ni	**3.38**	**4.33**	**1.61**	**1.61**	**1.38**	0.31	**0.22**
Cu	**1.93**	**0.61**	**0.97**	**1.28**	**1.43**	0.45	**0.20**
Zn	**0.07**	**0.00**	**0.03**	**0.03**	**0.06**	0.08	**0.00**
S	**36.14**	**36.46**	**35.69**	**35.33**	**35.32**	31.83	**36.45**
Total	**99.33**	**98.26**	**98.98**	**99.10**	**96.54**	89.78	**99.55**

	BZ231A-2	**BZ231A-3**	BZ235B1-2	BZ235B2-1
	Pyrrhotite	**Pyrrhotite**	Sulphur	Sulphur
Fe	**62.79**	**62.90**	0.00	0.00
Co	**0.00**	**0.00**	0.00	0.00
Ni	**0.08**	**0.12**	0.05	0.01
Cu	**0.12**	**0.08**	0.11	0.12
Zn	**0.04**	**0.04**	0.00	0.00
S	**36.47**	**36.58**	114.61	111.43

Appendix 3.2 Averaged electron microprobe analyses including cation concentrations

fPer **

Number	BZ66	BZ67	BZ70	BZ73	BZ74	BZ76	BZ103	BZ116A	BZ120A	BZ201A	BZ205B	BZ205C
Phase	fPer	fPer	fPer	fPer	fPer	fPer	fPer	fPer	fPer	fPer	fPer	fPer
Av *	3	5	2	3	3	4	3	5	2	4	5	4
SiO$_2$	0.01	0.00	0.05	0.02	0.00	0.03	0.01	0.02	0.00	0.02	0.02	0.05
TiO$_2$	0.01	0.01	0.00	0.02	0.00	0.01	0.01	0.00	0.00	0.03	0.01	0.02
Al$_2$O$_3$	0.13	0.06	0.13	0.04	0.05	0.08	0.03	0.03	0.04	0.04	0.07	0.23
Cr$_2$O$_3$	1.06	0.03	0.79	0.38	0.30	0.81	0.37	0.75	0.75	0.15	0.77	2.56
FeO	73.56	59.80	41.51	43.35	50.04	32.08	43.47	28.77	42.81	49.95	27.72	49.26
MnO	0.80	0.28	0.21	0.10	0.22	0.34	0.10	0.18	0.41	0.16	0.35	0.30
NiO	0.10	0.28	0.49	0.40	0.53	1.21	0.36	1.33	0.77	0.34	1.25	0.70
Na$_2$O	1.05	0.11	0.07	0.06	0.06	0.82	0.05	0.39	0.54	0.02	0.49	0.05
MgO	23.13	39.75	57.33	56.37	50.00	65.25	55.38	67.94	55.25	48.91	69.14	46.84
CaO	0.01	0.00	0.00	0.00	0.02	0.00	0.01	0.00	0.00	0.01	0.02	0.00
K$_2$O												
Total	99.87	100.32	100.55	100.73	101.21	100.60	99.79	99.54	100.55	99.63	99.86	100.02
Si	0.001	0.000	0.004	0.001	0.000	0.002	0.001	0.002	0.000	0.001	0.002	0.005
Ti	0.001	0.001	0.000	0.001	0.000	0.000	0.001	0.000	0.000	0.002	0.001	0.001
Al	0.016	0.006	0.012	0.004	0.005	0.007	0.003	0.003	0.004	0.004	0.007	0.023
Cr	0.084	0.002	0.051	0.025	0.020	0.050	0.024	0.046	0.049	0.010	0.047	0.175
Fe^{2+}	5.768	4.456	2.773	2.914	3.472	2.055	2.957	1.834	2.895	3.529	1.750	3.479
Fe^{3+}	0.427	0.091	0.071	0.075	0.089	0.053	0.076	0.047	0.074	0.090	0.045	0.089
Mn	0.068	0.021	0.014	0.007	0.016	0.023	0.007	0.012	0.028	0.012	0.023	0.022
Ni	0.008	0.021	0.032	0.026	0.036	0.076	0.024	0.084	0.051	0.024	0.078	0.049
Na	0.206	0.019	0.010	0.010	0.009	0.125	0.009	0.059	0.086	0.003	0.074	0.008
Mg	3.471	5.386	7.002	6.926	6.342	7.641	6.887	7.916	6.829	6.316	7.980	6.047
Ca	0.001	0.000	0.000	0.000	0.002	0.000	0.001	0.000	0.000	0.001	0.001	0.000
K	0.000	0.000	0.000	0.000	0.000	0.000	0.000	0.000	0.000	0.000	0.000	0.000
Total	10.051	10.004	9.970	9.988	9.992	10.031	9.989	10.003	10.017	9.991	10.008	9.899

fPer **

Number	BZ206A	BZ207B	BZ210A	BZ226D2	BZ233C	BZ238B	BZ239A	BZ239G	BZ241A	BZ242A	BZ243B	BZ245A
Phase	fPer	fPer	fPer	fPer	fPer	fPer	fPer	fPer	fPer	fPer	fPer	fPer
Av *	3	4	3	4	3	4	3	1	3	1	1	5
SiO_2	0.05	0.03	0.05	0.01	0.01	0.07	0.03	0.00	0.05	0.01	0.03	0.04
TiO_2	0.02	0.02	0.01	0.01	0.01	0.04	0.01	0.00	0.04	0.03	0.01	0.03
Al_2O_3	0.14	0.11	0.13	0.07	0.05	0.12	0.07	0.05	0.11	0.09	0.08	0.04
Cr_2O_3	1.41	0.51	1.33	0.18	0.57	0.66	0.84	0.80	1.00	0.81	1.14	0.71
FeO	27.34	43.14	27.20	56.73	29.35	26.37	27.69	27.75	28.63	25.50	29.43	46.37
MnO	0.35	0.43	0.29	0.30	0.43	0.36	0.33	0.33	0.42	0.33	0.40	0.38
NiO	1.23	0.90	1.27	0.35	1.29	1.40	1.40	1.43	1.49	1.41	1.01	0.96
Na_2O	1.25	0.14	0.87	0.15	0.09	0.12	0.20	0.15	0.12	0.50	0.52	0.28
MgO	69.01	54.84	69.22	41.83	67.87	71.31	68.98	66.40	68.21	69.30	64.57	49.67
CaO	0.00	0.01	0.01	0.00	0.00	0.00	0.00	0.01	0.01	0.01	0.01	0.01
K_2O	0.01	0.01	0.51	0.00		0.00	0.01	0.01	0.00	0.00	0.01	0.00
Total	100.80	100.13	100.38	99.63	99.66	100.41	99.58	96.92	100.08	97.99	97.20	98.48
Si	0.004	0.003	0.004	0.001	0.001	0.006	0.003	0.000	0.004	0.001	0.002	0.004
Ti	0.001	0.001	0.000	0.000	0.001	0.003	0.001	0.000	0.002	0.002	0.000	0.002
Al	0.013	0.011	0.012	0.007	0.004	0.011	0.006	0.004	0.010	0.008	0.008	0.004
Cr	0.086	0.034	0.081	0.013	0.035	0.040	0.052	0.051	0.061	0.050	0.073	0.049
Fe^{2+}	1.711	2.933	1.702	4.194	1.870	1.598	1.753	1.814	1.812	1.628	1.934	3.281
Fe^{3+}	0.044	0.075	0.044	0.086	0.048	0.084	0.045	0.047	0.046	0.042	0.050	0.084
Mn	0.023	0.030	0.019	0.023	0.028	0.023	0.022	0.022	0.028	0.022	0.027	0.028
Ni	0.076	0.060	0.079	0.026	0.081	0.086	0.087	0.092	0.093	0.089	0.066	0.067
Na	0.186	0.023	0.129	0.027	0.014	0.017	0.030	0.023	0.018	0.076	0.082	0.046
Mg	7.896	6.815	7.919	5.625	7.904	8.108	7.983	7.930	7.891	8.088	7.756	6.426
Ca	0.000	0.001	0.001	0.000	0.000	0.000	0.000	0.001	0.001	0.001	0.001	0.000
K	0.001	0.001	0.050	0.000	0.000	0.000	0.001	0.001	0.000	0.000	0.001	0.000
Total	10.040	9.986	10.039	10.002	9.986	9.975	9.983	9.984	9.967	10.006	9.999	9.991

fPer **

Number	BZ245B	BZ250C	BZ251A	BZ255A	BZ257A3	BZ260D	BZ260E	JH2	JH7A1	JH11A1	JH12A1	JH17A1
Phase	fPer	fPer	fPer	fPer	fPer	fPer	fPer	fPer	fPer	fPer	fPer	fPer
Av *	2	2	4	4	3	3	2	3	4	4	5	3
SiO_2	0.02	0.05	0.04	0.12	0.020	0.05	0.11	0.00	0.01	0.04	0.00	0.02
TiO_2	0.02	0.02	0.01	0.02	0.02	0.01	0.01		0.00	0.04	0.00	0.02
Al_2O_3	0.04	0.08	0.03	0.03	0.02	0.09	0.10	0.04	0.05	0.13	0.04	0.09
Cr_2O_3	0.73	0.25	0.34	0.19	0.60	0.62	0.60	0.16	0.52	0.87	0.38	0.76
FeO	45.63	66.27	23.52	52.10	38.40	30.75	30.53	35.81	38.18	61.18	39.63	43.19
MnO	0.38	0.81	0.22	0.22	0.07	0.45	0.43	0.24	0.34	0.51	0.31	0.22
NiO	0.96	1.16	1.25	0.42	0.30	1.15	1.20	1.07	1.06	0.45	0.90	0.61
Na_2O	0.27	0.09	0.18	0.05	0.01	0.11	0.11		0.44	0.26	0.30	0.06
MgO	53.77	31.78	74.77	45.22	62.40	66.24	65.74	63.85	60.98	36.47	59.13	55.98
CaO	0.00	0.00	0.02	0.01	0.01	0.01	0.00		0.00	0.00	0.00	0.00
K_2O	0.00	0.01	0.01	0.01	0.01	0.01	0.01					
Total	101.82	100.50	100.38	98.56	101.86	99.50	98.83	101.17	101.56	99.95	100.70	100.95
Si	0.002	0.004	0.003	0.011	0.002	0.004	0.008	0.000	0.000	0.003	0.000	0.002
Ti	0.001	0.001	0.000	0.001	0.001	0.001	0.001	0.000	0.000	0.003	0.000	0.001
Al	0.004	0.009	0.003	0.003	0.002	0.008	0.009	0.004	0.004	0.014	0.004	0.009
Cr	0.048	0.019	0.020	0.013	0.038	0.039	0.037	0.010	0.033	0.064	0.024	0.050
Fe^{2+}	3.084	5.170	1.441	3.808	2.479	1.976	1.974	2.310	2.488	4.644	2.625	2.900
Fe^{3+}	0.079	0.106	0.037	0.078	0.064	0.051	0.051	0.059	0.064	0.095	0.067	0.074
Mn	0.027	0.065	0.014	0.017	0.005	0.030	0.029	0.016	0.023	0.040	0.022	0.015
Ni	0.064	0.089	0.076	0.030	0.019	0.073	0.077	0.068	0.068	0.033	0.059	0.040
Na	0.043	0.017	0.026	0.008	0.002	0.017	0.017	0.000	0.068	0.047	0.048	0.009
Mg	6.642	4.509	8.376	6.013	7.365	7.781	7.772	7.526	7.266	5.035	7.160	6.871
Ca	0.000	0.000	0.002	0.001	0.001	0.001	0.000	0.000	0.000	0.000	0.000	0.000
K	0.000	0.001	0.001	0.001	0.001	0.001	0.001	0.000	0.000	0.000	0.000	0.000
Total	9.994	9.989	9.998	9.984	9.979	9.981	9.976	9.993	10.015	9.979	10.010	9.972

	fPer (Guinea) **		Corundum				
Number	GU2A	GU4A1	BZ214A	BZ227A	BZ228A	BZ229B	BZ241C
Phase	fPer	fPer	Ruby	Sapphire	Corundum	Corundum	Ruby
Av *	4	4	8	6	3	4	4
SiO_2	0.01	0.01	0.58	0.38	0.00	0.05	0.78
TiO_2	0.00		0.10	0.10	0.14	0.75	0.05
Al_2O_3	0.02	0.06	90.37	98.31	99.51	98.51	89.94
Cr_2O_3	0.38	0.75	8.58	0.01	0.00	0.02	8.66
FeO	20.39	20.85	0.28	0.60	0.00	0.01	0.71
MnO	0.14	0.19	0.04	0.00	0.01	0.01	0.06
NiO	1.38	1.41	0.02	0.01	0.01	0.00	0.01
Na_2O	0.21		0.01	0.01	0.01	0.01	0.00
MgO	77.62	76.81	0.40	0.14	0.03	0.10	0.44
CaO	0.01		0.01	0.01	0.01	0.00	0.01
K_2O				0.00		0.00	0.01
Total	100.14	100.07	100.39	99.59	99.71	99.46	100.68
Si	0.001	0.001	0.010	0.007	0.000	0.001	0.014
Ti	0.000	0.000	0.001	0.001	0.002	0.010	0.001
Al	0.001	0.005	1.855	1.981	1.997	1.984	1.846
Cr	0.022	0.044	0.118	0.000	0.000	0.000	0.119
Fe^{2+}	1.234	1.267	0.000	0.009	0.000	0.000	0.010
Fe^{3+}	0.032	0.032	0.005				
Mn	0.008	0.012	0.001	0.000	0.000	0.000	0.001
Ni	0.082	0.084	0.000	0.000	0.000	0.000	0.000
Na	0.030	0.000	0.000	0.000	0.000	0.000	0.000
Mg	8.591	8.529	0.010	0.004	0.001	0.003	0.011
Ca	0.001	0.000	0.000	0.000	0.000	0.000	0.000
K	0.000	0.000	0.000	0.000	0.000	0.000	0.000
Total	10.003	9.975	2.000	2.001	2.000	1.997	2.003

	Diopside (Sao Luiz) £				**Diopside (Guinea) £**	**CaSiPvk**		
Number	BZ209A	BZ209B	BZ218B	BZ213A	GU3C	BZ97	BZ115	BZ252A
Phase	Na-Diopside	Na-Diopside	Na-Diopside	Diopside	Na-Diopside	CaSiPvk	CaSiPvk	CaSiPvk
Av *	4	4	6	4	5	2	3	3
SiO_2	55.38	55.55	54.32	54.68	54.31	50.80	50.59	51.18
TiO_2	0.88	0.80	0.54	0.23	0.43	0.00	0.01	0.06
Al_2O_3	6.09	6.43	6.37	1.15	4.28	0.11	0.08	0.07
Cr_2O_3	0.12	0.12	0.04	0.73	0.03	0.00	0.01	0.03
FeO	6.06	5.71	5.15	3.62	4.91	0.08	0.16	0.16
MnO	0.09	0.09	0.06	0.12	0.07	0.04	0.02	0.06
NiO	0.03	0.04	0.05	0.09		0.00	0.00	0.02
Na_2O	4.52	4.51	4.69	0.72	2.31	0.02	0.02	0.01
MgO	11.50	11.43	11.33	19.51	13.25	0.09	0.14	0.14
CaO	14.80	15.23	15.81	18.67	18.60	48.71	48.49	48.43
K_2O	0.00	0.00	0.05	0.00				0.02
Total	99.98	100.16	98.39	99.53	98.21	99.83	99.51	100.17
Si	1.997	1.999	1.981	1.980	2.011	0.983	0.982	0.991
Ti	0.024	0.022	0.015	0.006	0.012	0.000	0.000	0.001
Al	0.259	0.273	0.274	0.049	0.187	0.003	0.002	0.002
Cr	0.003	0.003	0.001	0.020	0.001	0.000	0.000	0.000
Fe^{2+}	0.148	0.163	0.091	0.100	0.152	-0.032	-0.032	0.003
Fe^{3+}	0.035	0.009	0.067	0.009	0.000	0.033	0.035	
Mn	0.003	0.003	0.002	0.004	0.002	0.001	0.000	0.001
Ni	0.001	0.001	0.001	0.003	0.000	0.000	0.000	0.000
Na	0.316	0.315	0.332	0.051	0.166	0.001	0.001	0.001
Mg	0.618	0.613	0.616	1.053	0.731	0.002	0.004	0.004
Ca	0.572	0.587	0.618	0.724	0.738	1.010	1.008	1.005
K	0.023	0.012	0.002	0.000				0.000
Total	4.000	4.000	4.000	4.000	4.000	2.000	2.000	2.008

	Type I MgSi-Pvk ^			**Type II MgSi-Pvk $**			**Type III MgSi-Pvk !**			
Number	BZ120C	BZ207C	BZ251B	BZ210B	BZ241B1	BZ241B2	BZ237A	BZ242B	BZ246A	BZ259B
Phase	Type I	Type I	Type I	Type II	Type II	Type II	Type III	Type III	Type III	Type III
Av *	3	9	3	4	3	3	30	3	3	14
SiO_2	56.64	55.43	57.04	51.41	55.89	52.63	57.07	54.96	52.87	55.75
TiO_2	0.22	0.20	0.15	0.02	0.02	0.01	0.01	0.03	0.04	0.01
Al_2O_3	1.23	2.66	1.33	10.04	10.62	9.86	8.34	12.58	11.65	10.11
Cr_2O_3	0.45	0.15	0.40	1.19	1.19	1.16	3.14	1.75	1.99	1.29
FeO	4.63	9.02	3.80	5.14	5.35	5.37	3.18	3.95	4.39	3.62
MnO	0.16	0.30	0.14	0.93	1.23	1.26	0.47	1.29	1.91	1.13
NiO	0.01	0.03	0.00	0.02	0.02	0.01	0.01	0.01	0.02	0.02
Na_2O	0.06	0.07	0.03	1.05	0.82	0.87	6.21	4.63	4.44	5.95
MgO	35.39	32.03	36.25	30.21	26.75	27.54	16.13	16.35	16.64	16.46
CaO	0.04	0.05	0.06	0.65	0.64	0.70	5.07	4.38	4.55	5.32
K_2O	0.01	0.00	0.02	0.26	0.01	0.00	0.00	0.01	0.00	0.03
Total	98.75	99.96	99.21	100.66	102.54	99.42	99.63	99.95	98.50	99.70
Si	1.961	1.935	1.961	1.757	1.875	1.832	2.000	1.914	1.888	1.957
Ti	0.006	0.005	0.004	0.001	0.000	0.000	0.000	0.001	0.001	0.000
Al	0.050	0.109	0.054	0.404	0.420	0.404	0.345	0.516	0.490	0.418
Cr	0.012	0.004	0.011	0.031	0.031	0.032	0.087	0.048	0.056	0.036
Fe^{2+}	0.107	0.218	0.087	0.037	0.038	0.039	0.023	0.029	0.033	0.027
Fe^{3+}	0.027	0.055	0.022	0.110	0.113	0.118	0.070	0.086	0.098	0.080
Mn	0.005	0.009	0.004	0.027	0.035	0.037	0.014	0.038	0.058	0.033
Ni	0.000	0.001	0.003	0.000	0.000	0.000	0.000	0.000	0.000	0.000
Na	0.004	0.005	0.002	0.070	0.053	0.059	0.422	0.313	0.307	0.405
Mg	1.827	1.667	1.857	1.539	1.337	1.429	0.843	0.849	0.885	0.861
Ca	0.002	0.002	0.002	0.024	0.023	0.026	0.190	0.164	0.174	0.200
K	0.000	0.000	0.001	0.000	0.000	0.000	0.000	0.000	0.000	0.001
Total	4.000	4.001	4.004	4.000	3.926	3.978	3.995	3.959	3.991	4.018

Majoritic Garnet (Sao Luiz)

Majoritic Garnet (Guinea)

Number	BZ215C	BZ216A1	BZ217A	BZ218A	BZ223A	BZ223B	BZ237C	GU3B	GU3BDk
Phase	CMF Maj	MCF Maj	MFC Maj	MFC Maj	CMF Maj	CMF Maj	MF Maj	MCF Maj	MCF Maj
Av *	6	7	5	5	4	6	5	5	1
SiO_2	41.20	42.45	43.83	42.31	42.20	41.91	43.37	40.89	45.05
TiO_2	1.48	0.17	0.08	0.28	1.49	1.50	0.01	1.66	1.66
Al_2O_3	18.59	20.42	20.66	20.23	18.15	17.92	21.47	18.52	13.64
Cr_2O_3	0.09	0.17	0.05	0.10	0.05	0.05	2.96	0.06	0.06
FeO	11.99	8.04	12.73	15.76	12.27	12.45	6.02	13.03	11.42
MnO	0.25	0.18	0.32	0.30	0.27	0.25	0.89	0.32	0.31
NiO	0.01	0.02	0.01	0.02	0.02	0.02	0.02		0.00
Na_2O	0.71	1.07	1.07	1.16	1.06	1.12	0.27		0.43
MgO	9.69	12.74	17.44	12.53	8.93	9.22	22.20	11.78	12.42
CaO	14.73	12.89	3.06	6.79	14.77	14.69	1.72	12.51	14.48
K_2O	0.00	0.01	0.00	0.00	0.01	0.00	0.01		0.02
	0.00	0.00	0.00	0.00	0.00	0.00	0.00		
Total	98.72	98.15	99.24	99.47	99.21	99.13	98.95	98.78	99.50
Si	6.229	6.281	6.351	6.290	6.350	6.323	6.150	6.164	6.714
Ti	0.169	0.019	0.010	0.031	0.168	0.170	0.001	0.188	0.186
Al	3.313	3.563	3.530	3.546	3.220	3.188	3.587	3.290	2.394
Cr	0.011	0.020	0.008	0.011	0.006	0.006	0.332	0.006	0.008
Fe^{2+}	1.515	0.997	1.541	1.958	1.544	1.570	0.715	1.642	1.424
Fe^{3+}									
Mn	0.031	0.022	0.040	0.039	0.032	0.031	0.106	0.040	0.040
Ni	0.000	0.001	0.001	0.001	0.002	0.001	0.002		0.000
Na	0.207	0.308	0.300	0.333	0.312	0.327	0.074		0.126
Mg	2.182	2.809	3.767	2.776	2.003	2.075	4.693	2.646	2.760
Ca	2.387	2.045	0.476	1.082	2.381	2.377	0.261	2.020	2.312
K	0.001	0.001	0.001	0.000	0.002	0.001	0.002		0.004
Total	16.045	16.063	16.020	16.068	16.025	16.073	15.926	16.000	15.964

	TAPP #									**Magnetite**	
Number	BZ205A	BZ206B	BZ207A	BZ238A	BZ240B	BZ243A	BZ244B	BZ259A1	BZ259A2	BZ83Dark	BZ83Light
Phase	TAPP	TAPP	TAPP	TAPP	TAPP	TAPP	TAPP	TAPP	TAPP	Magnetite	Magnetite
Av *	4	5	6	4	3	3	2	2	7	3	2
SiO_2	42.54	42.43	39.93	41.41	42.65	42.24	42.12	42.24	41.83	0.07	0.05
TiO_2	0.02	0.01	4.23	0.03	0.01	0.04	0.06	0.03	0.02	1.30	0.13
Al_2O_3	23.88	23.48	20.01	23.34	23.91	24.17	23.83	23.12	23.15	1.03	0.08
Cr_2O_3	2.47	2.22	1.34	3.00	2.34	2.41	2.80	2.38	2.40	0.01	0.04
FeO	4.96	4.64	9.51	4.98	4.76	5.19	4.60	4.45	4.43	89.77	94.37
MnO	0.84	0.47	0.27	0.92	0.74	0.90	0.96	0.67	0.65	0.54	0.87
NiO	0.01	0.07	0.02	0.01	0.01	0.02	0.01	0.02	0.01	0.01	0.02
Na_2O	0.16	0.15	0.02	0.16	0.12	0.09	0.09	0.15	0.15	0.00	0.00
MgO	25.43	26.66	25.16	24.95	25.84	24.36	25.63	26.01	26.91	0.78	1.85
CaO	0.11	0.12	0.03	0.13	0.11	0.11	0.09	0.10	0.11	0.01	0.02
K_2O	0.00	0.01	0.01	0.02	0.00	0.00	0.00	0.00	0.01	0.00	0.00
Total	100.44	100.24	100.57	98.93	100.50	99.54	100.20	99.16	99.68	93.52	97.41
Si	5.874	5.835	5.628	5.840	5.892	5.901	5.849	5.910	5.832	0.003	0.002
Ti	0.002	0.001	0.448	0.002	0.002	0.004	0.006	0.003	0.002	0.037	0.003
Al	3.887	3.805	3.323	3.880	3.893	3.979	3.900	3.812	3.804	0.046	0.003
Cr	0.270	0.242	0.149	0.333	0.255	0.266	0.308	0.263	0.264	0.000	0.001
Fe^{2+}	0.149	0.139	0.291	0.153	0.143	0.206	0.139	0.135	0.134	0.975	0.876
Fe^{3+}	0.424	0.394	0.829	0.435	0.406	0.401	0.396	0.386	0.383	1.877	1.987
Mn	0.098	0.054	0.032	0.109	0.087	0.106	0.114	0.080	0.077	0.017	0.027
Ni	0.001	0.008	0.002	0.001	0.001	0.003	0.001	0.003	0.001	0.000	0.001
Na	0.044	0.039	0.006	0.045	0.033	0.026	0.024	0.041	0.041	0.000	0.000
Mg	5.233	5.464	5.286	5.247	5.320	5.073	5.305	5.423	5.593	0.044	0.100
Ca	0.017	0.018	0.004	0.019	0.016	0.017	0.013	0.016	0.017	0.000	0.001
K	0.000	0.002	0.001	0.004	0.001	0.001	0.001	0.001	0.001	0.000	0.000
Total	16.000	16.000	16.000	16.071	16.049	15.984	16.053	16.069	16.151	3.000	3.000

Olivine

Number	BZ111	BZ117B	BZ243C
Phase	Olivine	Olivine	Olivine
Av *	3	4	3
SiO_2	40.90	40.07	40.50
TiO_2	0.00	0.00	0.01
Al_2O_3	0.04	0.02	0.04
Cr_2O_3	0.01	0.04	0.19
FeO	9.11	10.59	11.88
MnO	0.10	0.15	0.10
NiO	0.38	0.30	0.41
Na_2O	0.05	0.03	0.05
MgO	50.98	49.57	46.40
CaO	0.05	0.08	0.00
K_2O			0.00
Total	101.62	100.85	99.60
Si	0.981	0.974	1.007
Ti	0.000	0.000	0.000
Al	0.001	0.001	0.001
Cr	0.000	0.001	0.004
Fe^{2+}	0.143	0.164	0.247
Fe^{3+}	0.039	0.051	0.000
Mn	0.002	0.003	0.002
Ni	0.007	0.006	0.008
Na	0.002	0.001	0.003
Mg	1.822	1.797	1.719
Ca	0.001	0.002	0.000
K			0.000
Total	3.000	3.000	2.991

Pyrrhotite

Number	BZ215A	BZ221A2	BZ222A	BZ222B	BZ222C	BZ231A
Phase	Pyrrhotite	Pyrrhotite	Pyrrhotite	Pyrrhotite	Pyrrhotite	Pyrrhotite
Av *	1	1	1	1	1	3
Fe	57.37	56.48	60.39	60.54	58.06	62.79
Co	0.43	0.37	0.30	0.32	0.28	0.00
Ni	3.38	4.33	1.61	1.61	1.38	0.14
Cu	1.93	0.61	0.97	1.28	1.43	0.13
Zn	0.07	0.00	0.03	0.03	0.06	0.03
S	36.14	36.46	35.69	35.33	35.32	36.50
Total	99.33	98.26	98.98	99.10	96.54	99.59
Fe	0.911	0.889	0.972	0.984	0.944	0.988
Co	0.006	0.006	0.005	0.005	0.004	0.000
Ni	0.051	0.065	0.025	0.025	0.021	0.002
Cu	0.027	0.008	0.014	0.018	0.020	0.002
Zn	0.001	0.000	0.000	0.000	0.001	0.000
S	1.000	1.000	1.000	1.000	1.000	1.000
Total	0.996	0.968	1.014	1.032	0.990	0.992

** Fe^{3+} calculated using values of $Fe^{3+}/\Sigma Fe = 0.025$ for high Mg-fPer and 0.02 from low Mg-fPer; £ Fe^{3+} calculated on the basis of charge balance: ^ Fe^{3+} calculated using $Fe^{3+}/\Sigma Fe = 0.20$, section 2.5.3: $ Fe^{3+} calculated using $Fe^{3+}/\Sigma Fe = 0.75$, section 2.5.3: ! Fe^{3+} calculated using $Fe^{3+}/\Sigma Fe = 0.75$, section 2.5.3: # Fe^{3+} calculated using $Fe^{3+}/\Sigma Fe = 0.74$, section 2.5.1.2 except for BZ243A where $Fe^{3+}/\Sigma Fe = 0.66$. * Number of analyses incorporated into calculation of the average analysis. Averaged compositions for grains BZ66 - BZ120C calculated from Wilding (1990) except for BZ83 and light areas of BZ66. Compositions for grains BZ201A - BZ214A from Harris and Watt (1990, *personal communication*). BZ207A and BZ207C involve analyses undertaken during the present study.

Appendix 4.1 Ion Microprobe analyses

	fPer												
Analysis	**BZ76-1**	**BZ103-1**	**BZ103-2**	**BZ116B-1**	**BZ116B-2**	**BZ205B-1**	BZ205C-1	BZ205C-2	**BZ206A-1**	**BZ207B-1**	**BZ207B-2**	**BZ210A-1**	**BZ210A-2**
Rb		3.89E-1	4.23E-1	1.63E+0	1.79E+0	4.11E+0	6.82E+2	1.15E+3	2.88E+0	1.58E+0	1.51E+0	2.07E+0	2.81E+0
K													
Ba		1.38E+0	7.60E-1	8.48E-1	n.d.	2.00E+0	3.32E+3	3.01E+3	4.11E-2	1.59E-1	2.25E-1	1.81E-1	2.03E+0
Sr		2.89E-1	1.50E-1	2.27E+1	n.d.	1.45E+0	1.54E+3	1.48E+3	6.36E-1	4.42E-1	4.92E-1	5.04E-1	1.74E+0
La		1.16E-2		8.57E-2	n.d.	7.28E-1				2.15E-2	n.d.	n.d.	1.37E-1
Ce		2.67E-2	1.21E-2	1.97E-2	n.d.	7.09E-1	9.82E+1	2.85E+2	n.d.	2.48E-2	n.d.	n.d.	1.75E-1
Pr		n.d.	n.d.	2.36E-2	n.d.	2.46E-1	2.78E+1	5.66E+1	n.d.	6.57E-3	n.d.	n.d.	2.42E-2
Nd		n.d.	n.d.	1.26E-7	4.33E+0	6.80E-1	1.74E+2	n.d.	n.d.	n.d.	n.d.	n.d.	1.16E-1
Pm													
Sm		n.d.	n.d.	1.04E-7	n.d.	3.30E-1	n.d.	n.d.	n.d.	8.45E-2	7.62E-2	n.d.	n.d.
Eu		7.09E-3	n.d.	5.44E-3	n.d.	1.48E-1	9.92E+0	n.d.	n.d.	8.69E-3	3.55E-2	n.d.	n.d.
Gd		n.d.	n.d.	n.d.	n.d.	2.93E-1	4.24E+1	n.d.	n.d.	n.d.	n.d.	n.d.	6.60E-3
Tb										n.d.	n.d.	n.d.	
Dy		n.d.	n.d.	9.39E-8	n.d.	5.55E-1	5.87E+1	n.d.	n.d.	8.45E-2	n.d.	n.d.	5.50E-2
Ho		1.31E-2	1.19E-2	1.81E-8	n.d.	2.48E-1	6.79E+0	3.45E+1	n.d.	n.d.	n.d.	n.d.	5.93E-3
Er										n.d.	n.d.	n.d.	
Tm						1.80E-1							
Yb		n.d.	n.d.	1.50E-1	n.d.	1.05E+0	n.d.	8.00E+0	n.d.	9.14E-4	n.d.	n.d.	n.d.
Lu			n.d.			3.12E-1	1.75E+1	n.d.	n.d.				
Hf	n.d.		1.36E-1			3.20E+0	3.20E+1	n.d.	6.31E-2				
Ta	n.d.	n.d.	n.d.	7.08E-8	n.d.								n.d.
Pb	5.44E+1		9.87E+0				1.11E+4	6.29E+4	n.d.				
Th	n.d.		1.94E-2				2.93E+1	4.96E+1	n.d.				
U	1.34E-1		2.00E-2				1.02E+1	5.21E+1	n.d.				
Y		2.49E-2	1.62E-2	1.35E-1	2.11E-1	2.61E-1	1.70E+2		6.17E-2	4.33E-2	3.67E-2	2.44E-2	2.07E-1
Zr		3.62E-1	1.58E-1	1.97E+0	n.d.	9.67E-1	8.80E+2	6.01E+2	2.10E-1	2.98E-1	4.39E-1	2.26E-1	1.60E+0
Nb		2.24E-2	n.d.	4.63E-1	n.d.	7.81E-1	n.d.	n.d.	n.d.	n.d.	1.34E-2	n.d.	4.06E-1

	fPer								**Diopside**			
Analysis	**BZ241A-1**	**BZ241A-2**	**BZ243B-1**	**BZ243B-2**	**JH11A1-1**	**JH7A1-1**	**JH7A1-2**	**JH17A1-1**	**BZ213A-1**	**BZ213A-2**	**BZ213A-3**	**BZ213A-4**
Rb	**4.53E+0**	**4.73E+0**	**1.01E+0**	**7.24E+0**	**4.85E-1**	**1.57E+0**	**1.71E+0**	**6.23E-1**	**n.d.**	**n.d.**		
K									**6.97E+1**	**5.68E+1**		
Ba	**3.16E+0**	**1.40E+0**	**2.77E+0**	**2.30E+1**	**5.01E-2**	**1.66E-2**	**4.63E-1**	**1.55E-2**	**6.24E-2**	**5.54E-2**	**2.59E-2**	**1.03E-1**
Sr	**4.63E+0**	**1.74E+0**	**6.49E-1**	**6.49E+0**	**1.23E-1**	**5.11E-1**	**6.84E-1**	**2.25E-1**	**3.20E+2**	**3.22E+2**		
La	**1.40E-1**	**3.04E-2**	**n.d.**	**2.59E-1**					**2.86E+0**	**2.77E+0**		
Ce	**3.27E-1**	**1.41E-1**	**n.d.**	**5.46E-1**	**n.d.**	**1.29E-2**	**n.d.**	**n.d.**	**1.30E+1**	**1.33E+1**	**1.41E+1**	**1.24E+1**
Pr	**7.78E-2**	**7.01E-3**	**n.d.**	**1.50E-2**	**n.d.**	**n.d.**	**n.d.**	**n.d.**	**2.39E+0**	**2.40E+0**	**2.42E+0**	**2.39E+0**
Nd	**n.d.**	**5.83E-1**	**n.d.**	**n.d.**	**n.d.**	**8.28E-2**	**n.d.**	**n.d.**	**1.39E+1**	**1.25E+1**	**1.49E+1**	**1.32E+1**
Pm												
Sm	**n.d.**	**9.82E-2**	**n.d.**	**n.d.**	**1.15E-1**	**n.d.**	**1.48E-1**	**n.d.**	**2.82E+0**	**3.20E+0**	**3.13E+0**	**2.54E+0**
Eu	**n.d.**	**n.d.**	**5.81E-1**	**5.40E-2**	**9.70E-3**	**n.d.**	**5.31E-3**	**n.d.**	**8.03E-1**	**7.59E-1**	**8.32E-1**	**6.12E-1**
Gd	**n.d.**		**n.d.**	**n.d.**	**n.d.**	**n.d.**	**n.d.**	**n.d.**	**2.06E+0**	**1.12E+0**	**1.33E+0**	**1.21E+0**
Tb	**n.d.**	**n.d.**	**n.d.**	**1.01E-1**					**2.79E-1**	**2.16E-1**	**2.38E-1**	**1.98E-1**
Dy	**n.d.**	**7.84E-3**	**7.62E-1**	**n.d.**	**n.d.**	**n.d.**	**n.d.**	**n.d.**			**5.22E-1**	**1.01E+0**
Ho	**n.d.**	**n.d.**	**n.d.**	**1.74E-2**	**n.d.**	**1.27E-2**	**n.d.**	**n.d.**	**1.18E-1**	**4.63E-2**		
Er	**4.69E-3**	**4.07E-2**	**4.11E-3**	**2.17E-2**					**2.77E-1**	**1.67E-1**		
Tm												
Yb	**1.06E-2**	**1.29E-1**	**n.d.**	**9.39E-2**	**n.d.**			**n.d.**	**6.50E-1**	**1.05E+0**		
Lu					**n.d.**	**3.67E-3**	**n.d.**	**n.d.**				
Hf					**4.13E-4**	**9.23E-4**	**n.d.**	**n.d.**				
Ta					**n.d.**	**4.49E-2**	**5.34E-4**					
Pb					**4.17E+0**	**7.27E+0**	**n.d.**	**3.40E-1**				
Th					**n.d.**	**n.d.**	**n.d.**	**8.03E-3**				
U					**n.d.**	**n.d.**	**n.d.**	**8.44E-3**				
Y	**1.62E-1**	**1.29E-1**	**2.42E-1**	**2.40E-1**	**1.85E-2**	**3.44E-2**	**6.68E-2**	**2.45E-2**	**2.06E+0**	**2.22E+0**		
Zr	**1.24E+1**	**1.02E+1**	**5.90E+0**	**3.23E+0**	**2.06E-1**	**1.68E-1**	**2.67E-1**	**8.66E-2**	**1.24E+1**	**1.30E+1**		
Nb	**n.d.**	**n.d.**	**2.83E-1**	**n.d.**	**3.56E-1**	**n.d.**	**n.d.**	**n.d.**	**2.30E-1**	**2.19E-1**		

TAPP

Analysis	BZ205A-1	BZ205A-2	BZ205A-3	BZ206B-1	BZ206B-2	BZ206B-3	BZ206B-4	BZ206B-5	BZ206B-6	BZ206B-7	BZ206B-8	BZ207A-1	BZ207A-2
Rb	2.81E-1	2.51E-1	7.32E-2	n.d.	6.17E-1	n.d.				4.83E+1	4.97E+1	n.d.	
K				6.16E+1	2.65E+1	9.78E+0						6.29E+1	
Ba	5.52E-1	9.71E-2	1.18E+0	7.24E-1	5.35E-1	4.67E-2	4.39E-1	6.89E-2	3.85E-2	4.87E+2	1.53E+3	1.80E-1	5.20E-2
Sr	1.12E-1	5.48E-2	4.05E-2	5.55E-1	2.03E-1	6.94E-2				7.87E+2	5.15E+2	1.03E-1	
La	8.99E-3	n.d.		2.38E-2	1.36E-2	n.d.						1.29E-2	
Ce	1.72E-2	4.89E-5	4.33E-3	1.63E-2	6.62E-11	4.71E-3	3.30E-10	n.d.	3.27E-2	1.55E+2	3.19E+1	3.91E-2	1.38E-2
Pr	2.74E-3	n.d.	8.56E-4	8.64E-3	8.23E-3	3.75E-3	1.64E-1	3.87E-2	4.34E-3	2.47E+1	1.27E+1	1.94E-2	1.46E-2
Nd	n.d.	3.16E-4	n.d.	1.86E-1	n.d.	4.14E-10	7.08E-1	3.34E-1	1.12E-1	n.d.	n.d.	1.01E-1	n.d.
Pm													
Sm	n.d.	n.d.	1.12E-2	3.19E-2	n.d.	2.76E-2	1.94E-9	2.85E-1	9.59E-2	n.d.	n.d.	4.01E-1	2.15E-1
Eu	3.68E-3	n.d.	6.66E-4	1.68E-2	1.24E-2	1.85E-3	1.23E-1	6.67E-2	3.86E-2	n.d.	n.d.		5.40E-2
Gd	n.d.	n.d.	2.04E-2	5.76E-2	2.23E-2	2.50E-2	4.44E-1	n.d.	n.d.	n.d.	n.d.	n.d.	n.d.
Tb	n.d.	n.d.		1.28E-2	1.07E-2	n.d.	8.87E-2	4.18E-2	1.41E-2			3.06E-3	5.56E-3
Dy	n.d.	n.d.	1.12E-2				n.d.	3.24E-1	7.11E-2	n.d.	1.56E+2		3.12E+1
Ho	n.d.	n.d.	n.d.	1.67E-2	n.d.	n.d.				n.d.	n.d.	n.d.	
Er	1.09E-4	n.d.		n.d.	1.75E-2	n.d.						2.94E-2	
Tm													
Yb	3.70E-4	n.d.	n.d.	8.40E-2	n.d.	n.d.				1.50E+2	1.68E+0	8.52E-2	
Lu			1.23E-3							n.d.	n.d.		
Hf			1.07E-1							n.d.	n.d.		
Ta			1.63E-2							n.d.	n.d.		
Pb			9.48E-1							6.20E+3	2.12E+3		
Th			n.d.							8.22E+1	n.d.		
U			n.d.							n.d.	n.d.		
Y	1.45E-2	1.41E-3	2.16E-3	4.32E-2	2.13E-2	1.67E-2				n.d.	n.d.	5.33E-2	
Zr	3.31E+0	3.00E+0	3.03E+0	1.36E+0	1.01E+0	7.78E-1				3.16E+2	2.36E+2	8.76E+2	
Nb	2.76E-2	n.d.	5.71E-3	6.80E-2	2.02E-2	n.d.				5.41E+1	2.23E+2	7.12E+2	

	TAPP					**Majorite**	**Corundum**		**Olivine**
Analysis	**BZ207A-3**	**BZ207A-4**	**BZ207A-5**	**BZ243A-1**	**BZ259A1-1**	**BZ237C-1**	**BZ214A-1**	**BZ214A-2**	**BZ243C-1**
Rb	**n.d.**	**5.63E-1**			**n.d.**	**9.87E-1**	**7.42E-2**		**n.d.**
K									
Ba	**7.27E-1**	**2.85E+0**		**1.51E+0**	**2.34E-1**	**1.39E-1**	**n.d.**		**2.55E-1**
Sr	**2.27E-1**	**6.13E-1**		**1.14E+0**	**1.89E-1**	**8.34E-2**	**5.60E-3**		**5.99E-1**
La	**2.82E-3**	**3.94E-2**		**6.67E+0**	**5.59E-2**	**5.34E-2**	**n.d.**		**5.75E-2**
Ce	**2.75E-2**	**7.45E-2**		**7.89E-1**	**1.76E-1**	**9.55E-2**	**n.d.**		**2.27E-1**
Pr	**7.74E-3**	**3.62E-2**		**6.02E-1**	**n.d.**	**8.71E-2**	**n.d.**		**1.06E-2**
Nd	**1.56E-8**	**3.48E-2**		**4.57E+0**	**9.06E-2**	**6.82E-1**	**n.d.**		**8.70E-2**
Pm									
Sm	**6.09E-2**	**3.98E-1**		**5.17E+0**	**2.01E-1**	**4.57E-1**	**n.d.**		**n.d.**
Eu	**4.93E-3**	**2.33E-2**		**1.30E+0**	**1.33E-3**	**2.20E-1**	**n.d.**		**3.51E-2**
Gd	**4.44E-4**	**n.d.**		**2.33E+0**	**4.65E-2**	**4.53E-1**	**n.d.**		**n.d.**
Tb	**1.96E-9**			**2.30E-1**	**n.d.**				**1.05E-2**
Dy	**1.09E-8**	**n.d.**		**2.15E+0**	**1.74E-1**	**3.43E-1**	**n.d.**		**5.29E-2**
Ho	**n.d.**	**6.21E-4**		**4.02E-1**	**n.d.**	**4.19E-2**	**n.d.**		**n.d.**
Er	**n.d.**				**n.d.**				**n.d.**
Tm				**5.44E-1**		**1.37E-2**			
Yb	**1.56E-2**	**n.d.**		**2.99E+0**	**1.61E-2**	**n.d.**	**1.48E-2**		**7.76E-1**
Lu				**4.95E-1**		**2.40E-2**			
Hf			**1.10E+1**	**4.44E+0**		**1.13E-1**		**n.d.**	
Ta		**6.23E+1**	**2.49E+1**				**n.d.**	**n.d.**	
Pb			**2.45E+0**					**1.56E+0**	
Th			**1.14E-2**					**n.d.**	
U			**1.03E-2**					**n.d.**	
Y	**9.62E-3**	**1.26E-1**		**3.35E-1**	**1.73E-2**	**1.31E-2**	**1.86E-3**		**5.39E-2**
Zr	**4.17E+1**	**1.16E+3**		**3.77E+0**	**1.09E+0**	**1.39E-1**	**2.51E-2**		**4.01E-1**
Nb	**4.00E+1**	**1.07E+3**		**4.01E-1**	**3.36E-2**	**8.91E-2**	**n.d.**		**2.42E-2**

	Type I MgSiPvk			Type II MgSiPvk				Type III MgSiPvk			
Analysis	**BZ207C-1**	**BZ207C-2**	**BZ207C-3**	**BZ210B-1**	**BZ210B-2**	**BZ210B-3**	**BZ241B2-1**	**BZ237A2-1**	**BZ246A-1**	**BZ259B-1**	**BZ259B-2**
Rb	n.d.	n.d.		n.d.	n.d.	8.38E-2	2.69E-1	n.d.	3.57E-2	2.70E-1	6.98E-1
K		3.00E+1									
Ba	4.33E-1	2.03E-1	7.27E-2	2.97E-2	5.84E-2	4.30E-2	5.83E-2	3.34E-1	3.11E-1	2.34E-1	4.58E-1
Sr	3.08E-1	1.83E-1		7.95E-2	4.36E-1	1.86E-1	1.00E-1	4.81E-1	5.85E-1	2.54E+1	2.79E+1
La		8.37E-3		6.41E-3			3.67E-3	1.08E-2	1.59E-2	2.80E-1	2.35E-1
Ce	8.96E-3	1.43E-2	1.93E-2	1.47E-2	n.d.	n.d.	n.d.	4.40E-2	6.77E-2	2.71E-1	2.30E-1
Pr	7.08E-3	n.d.	2.04E-2	n.d.	n.d.		6.79E-3	n.d.	n.d.	6.75E-2	2.59E-1
Nd	n.d.	6.55E-2	n.d.	n.d.	n.d.		5.55E-2	4.09E-2	5.60E-1	1.86E-1	9.42E-1
Pm											
Sm	n.d.	n.d.	3.01E-1	n.d.	n.d.		n.d.	n.d.	n.d.	2.26E-1	4.50E-1
Eu	4.68E-3		5.36E-2	5.57E-3	4.84E-3	n.d.	2.78E-3	n.d.	2.16E-3	n.d.	7.79E-2
Gd	n.d.	n.d.	n.d.	n.d.	n.d.	n.d.	n.d.	3.15E-2	n.d.	n.d.	n.d.
Tb		n.d.	7.78E-3				2.90E-3	n.d.	n.d.		
Dy	n.d.		4.37E+1	n.d.	n.d.		n.d.	n.d.	n.d.	5.68E-2	1.31E-1
Ho	4.43E-3	6.50E-4		7.21E-3	n.d.		n.d.	1.18E-2	n.d.	1.07E-2	2.53E-2
Er		1.59E-2					8.59E-5	4.93E-4	4.58E-4		
Tm										5.17E-5	7.91E-2
Yb	9.71E-4	n.d.		n.d.	1.84E-2	5.75E+0	2.15E-2	n.d.	2.97E-2	7.64E-2	3.93E-1
Lu					2.43E-3	n.d.				6.57E-2	6.79E-2
Hf	2.01E-1				n.d.					5.86E-1	9.37E-1
Ta	2.19E-1			n.d.	n.d.						
Pb	8.96E+0				3.62E+0	2.51E+0					
Th	7.16E-3				n.d.						
U	n.d.				n.d.						
Y		9.84E-3		2.29E-3	5.89E-3	3.82E-3	9.27E-3	5.85E-3	2.29E-2	3.13E-2	4.93E-2
Zr	3.78E+0	2.68E+0		3.58E-1	7.84E-1	5.82E-1	2.49E+0	2.98E-1	6.34E+0	4.51E-1	6.15E-1
Nb	2.66E+0	1.22E+0		n.d.	n.d.	n.d.	n.d.	1.55E-10	n.d.	1.22E-1	1.79E-1

CaSiPvk

Analysis	**BZ97-1**	**BZ115-1**	**BZ97-2**	**BZ115-2**
Rb	**n.d.**	**n.d.**	**n.d.**	**n.d.**
K				
Ba	**4.01E-1**	**8.62E-2**	**1.45E+0**	**1.42E-1**
Sr	**7.09E+2**	**4.28E+2**	**7.68E+2**	**4.35E+2**
La				
Ce	**2.71E+2**	**1.51E+2**	**2.91E+2**	**1.61E+2**
Pr	**3.66E+1**	**2.11E+1**	**3.84E+1**	**2.30E+1**
Nd	**1.91E+2**	**1.22E+2**	**1.98E+2**	**1.31E+2**
Pm				
Sm	**5.24E+1**	**3.92E+1**	**5.76E+1**	**4.42E+1**
Eu	**2.35E+1**	**2.03E+1**	**2.55E+1**	**2.20E+1**
Gd	**5.99E+1**	**4.74E+1**	**6.60E+1**	**5.23E+1**
Tb				
Dy	**4.77E+1**	**3.68E+1**	**4.60E+1**	**4.44E+1**
Ho	**6.79E+0**	**6.23E+0**	**7.75E+0**	**7.14E+0**
Er				
Tm				
Yb	**9.72E+0**	**9.17E+0**	**9.94E+0**	**1.05E+1**
Lu	**2.33E+0**	**1.85E+0**	**2.66E+0**	**1.99E+0**
Hf	**1.08E+0**	**1.60E-1**	**3.25E+0**	**1.14E-1**
Ta	**3.06E-1**	**n.d.**	**1.47E-1**	**n.d.**
Pb	**7.01E+0**	**4.79E+0**	**1.88E+1**	**3.16E+0**
Th	**n.d.**	**8.66E-3**	**n.d.**	**n.d.**
U	**8.12E-3**	**9.08E-3**	**n.d.**	**n.d.**
Y	**1.41E+2**	**1.30E+2**	**1.56E+2**	**1.40E+2**
Zr	**1.72E+2**	**8.45E+1**	**1.91E+2**	**9.48E+1**
Nb	**n.d.**	**n.d.**	**n.d.**	**n.d.**

Corundum

	BZ227A-1	BZ214A-3	BZ241Acor-1	BZ228A-1	BZ228A-2	BZ229B-1	BZ227A-2	BZ241C-1
Al	2.60E+4	2.39E+4	2.62E+4	2.63E+4	2.63E+4	2.61E+4	2.60E+4	2.38E+4
Ca	1.60E-1	4.76E-1	4.67E+0	7.69E+1	3.71E+0	1.34E+2	3.94E-2	4.29E+0
Ti	4.90E+0	4.46E+0	5.76E-1	1.97E+1	9.70E+0	1.40E+2	5.42E+0	4.13E+0
Cr	2.33E-2	1.25E+2	1.41E+1	2.45E+0	2.08E-1	3.36E-1	2.55E-2	2.32E+2
Fe	1.08E+1	5.81E+0	6.53E-1	1.17E+1	1.10E+0	1.55E+0	1.23E+1	3.56E+1
Ni	5.13E-3	6.35E-3	2.61E-3	4.51E-2	4.11E-3	5.85E-3	5.42E-3	1.47E-2
Ga	1.12E-1	2.71E-2	8.51E-3	1.39E-3	1.24E-4	1.88E-2	1.21E-1	4.05E-2
Ge	2.58E-4	2.48E-4	4.45E-6	7.83E-5	4.58E-5	1.02E-3	2.89E-4	2.12E-4
Rb	3.20E-5	4.19E-5	9.62E-5	1.47E-3	7.38E-5	3.03E-3	5.00E-5	1.56E-4
Sr	5.36E-5	2.70E-4	1.39E-3	2.81E-2	3.43E-3	1.65E+0	7.86E-5	2.01E-4
Y	3.00E-4	1.14E-5	1.44E-4	5.77E-3	1.42E-3	7.52E-1	1.53E-5	2.04E-4
Zr	6.36E-5	2.23E-4	3.13E-3	1.68E-1	6.66E-2	1.59E+1	3.73E-5	1.95E-3
Nb	4.99E-6	2.62E-5	1.76E-4	1.01E-2	9.79E-4	1.10E-3	5.85E-6	1.76E-4
Pb	1.46E-6	2.19E-6	3.27E-6	1.07E-4	6.25E-6	7.08E-6	2.44E-7	5.53E-6

n.d. Counts per second recorded for this element were equal to or below background. Blank spaces represent elemental compositions not measured.

Appendix 4.2 Averaged Chondrite Normalised Ion Microprobe Analyses

	fPer												
	BZ76	BZ103	BZ116B	BZ205B	BZ206A	BZ207B	BZ210A	BZ241A	BZ243B	JH7A1	JH11A1	JH17A1	**fPer**
Rb		0.175	0.736	1.772	1.240	0.667	1.050	1.996	1.778	0.706	0.209	0.269	**0.855**
K													**0.029**
Ba		0.445	0.352	0.830	0.017	0.080	0.459	0.946	5.346	0.100	0.021	0.006	**0.764**
Sr		0.030	3.127	0.200	0.088	0.064	0.155	0.439	0.492	0.082	0.017	0.031	**0.268**
La		0.049	0.362	3.072		0.091	0.577	0.359	1.093				**0.564**
Ce		0.032	0.032	1.158		0.041	0.286	0.382	0.892	0.021			**0.255**
Pr			0.248	2.589		0.069	0.255	0.446	0.158				**0.602**
Nd			4.639	1.456			0.248	1.248		0.177			**1.640**
Sm				2.157		0.525		0.642		0.967	0.748		**0.795**
Eu		0.122	0.094	2.552		0.381		0.299	12.491	0.091	0.167		**2.550**
Gd				1.426			0.032						**0.729**
Tb									2.701				**1.397**
Dy				2.185		0.333	0.217	0.031	3.000				**0.869**
Ho		0.221		4.382			0.105		0.307	0.224			**0.780**
Er								0.137	0.078				**0.108**
Tm				7.059									**7.059**
Yb			0.882	6.176		0.005		0.411	0.552				**1.406**
Lu				12.283						0.144			**6.214**
Hf		1.276		30.019	0.592					0.009	0.004		**6.380**
Ta										1.622			**1.081**
Pb	22.024	3.998								2.943	1.687	0.138	**6.158**
Th		0.669										0.277	**0.473**
U	16.750	2.503										1.055	**6.769**
Y		0.013	0.110	0.166	0.039	0.025	0.074	0.093	0.154	0.032	0.012	0.016	**0.056**
Zr		0.067	0.509	0.250	0.054	0.095	0.236	2.920	1.180	0.056	0.053	0.022	**0.445**
Nb		0.091	1.882	3.175		0.055	1.650		1.150		1.446		**1.196**

	TAPP						**Majorite**		**Corundum**	
	BZ205A	BZ206B	*BZ207A*	*BZ243A*	BZ259A1	**TAPP**	BZ237C	**Majorite**	BZ214A	**Cor**
Rb	0.087	0.266	*0.243*			**0.132**	0.425	**0.425**	0.032	**0.032**
K		0.060	*0.115*			**0.041**				
Ba	0.253	0.128	*0.395*	*0.627*	0.097	**0.141**	0.058	**0.058**		
Sr	0.010	0.038	*0.043*	*0.157*	0.026	**0.020**	0.011	**0.011**	0.001	**0.001**
La	0.038	0.079	*0.078*	*28.143*	0.236	**0.148**	0.225	**0.225**		
Ce	0.012	0.029	*0.063*	*1.289*	0.288	**0.075**	0.156	**0.156**		
Pr	0.019	0.399	*0.205*	*6.337*		**0.315**	0.917	**0.917**		
Nd	0.001	0.717	*0.097*	*9.786*	0.194	**0.585**	1.460	**1.460**		
Sm	0.073	0.720	*1.756*	*33.791*	1.314	**0.915**	2.987	**2.987**		
Eu	0.037	0.748	*0.472*	*22.414*		**0.570**	3.793	**3.793**		
Gd	0.099	0.668	*0.002*	*11.338*	0.226	**0.644**	2.204	**2.204**		
Tb		0.899	*0.077*	*6.150*		**1.005**				
Dy	0.044	0.778	*0.000*	*8.465*	0.685	**0.673**	1.350	**1.350**		
Ho		0.295	*0.011*	*7.102*		**0.776**	0.740	**0.740**		
Er	0.001	0.106	*0.178*			**0.532**				
Tm				*21.333*			0.537	**0.537**		
Yb	0.002	0.494	*0.296*	*17.588*	0.095	**0.652**			0.087	**0.087**
Lu	0.048			*19.488*		**0.048**	0.945	**0.945**		
Hf	1.007		*103.002*	*41.651*		**1.007**	1.060	**1.060**		
Ta	1.166		*3112.500*			**1.166**				
Pb	0.384		*0.990*			**0.384**			0.632	**0.632**
Th			*0.392*							
U			*1.288*							
Y	0.004	0.017	*0.040*	*0.213*	0.011	**0.011**	0.008	**0.008**	0.001	**0.001**
Zr	0.804	0.271	*178.958*	*0.974*	0.282	**0.567**	0.036	**0.036**	0.006	**0.006**
Nb	0.068	0.179	*2468.835*	*1.630*	0.137	**0.120**	0.362	**0.362**		

	Type I MgSiPvk		**Type II MgSiPvk**			**Type III MgSiPvk**			
	BZ207C	**Type I**	BZ210B	BZ241B2	**Type II**	BZ237A2	BZ246A	BZ259B	**Type III**
Rb			0.036	0.116	**0.076**		0.015	0.209	**0.144**
K	0.055	**0.043**							
Ba	0.098	**0.078**	0.018	0.024	**0.020**	0.139	0.129	0.144	**0.139**
Sr	0.034	**0.025**	0.032	0.014	**0.028**	0.066	0.081	3.671	**1.872**
La	0.035	**0.036**	0.027	0.015	**0.021**	0.046	0.067	1.086	**0.571**
Ce	0.023	**0.022**	0.024		**0.024**	0.072	0.111	0.409	**0.250**
Pr	0.145	**0.145**		0.071	**0.071**			1.718	**1.718**
Nd	0.140	**0.140**		0.119	**0.119**	0.088	1.199	1.208	**0.926**
Sm	1.967	**1.967**						2.209	**2.209**
Eu	0.081	**0.081**	0.090	0.106	**0.095**		0.127	1.343	**0.735**
Gd						0.153			**0.153**
Tb	0.208	**0.208**		0.078	**0.078**				
Dy								0.370	**0.370**
Ho	0.045	**0.055**	0.127		**0.127**	0.208		0.318	**0.282**
Er	0.096	**0.156**		0.001	**0.001**	0.003	0.003		**0.003**
Tm								1.552	**1.552**
Yb	0.006	**0.006**	16.966	0.126	**11.353**		0.175	1.381	**0.979**
Lu		**0.843**	0.096		**0.096**			2.630	**2.630**
Hf	1.882	**1.882**						7.144	**7.144**
Ta	15.636	**15.636**							
Pb	3.628	**3.628**	1.241		**1.241**				
Th	0.247	**0.247**							
U									
Y	0.006	**0.015**	0.003	0.006	**0.003**	0.004	0.015	0.026	**0.017**
Zr	0.835	**0.816**	0.148	0.643	**0.272**	0.077	1.638	0.138	**0.498**
Nb	7.894	**7.894**			**1.454**			0.612	**0.612**

	CaSiPvk			**Olivine**		**Diopside**	
	BZ97	BZ115	**CaSiPvk**	BZ243C	**Olivine**	BZ213A	**Diopside**
Rb					**0.031**		
K			**0.050**		**0.003**	0.116	**0.116**
Ba	0.384	0.047	**0.193**	0.106	**0.053**	0.026	**0.026**
Sr	101.722	59.435	**75.128**	0.083	**0.060**	44.215	**44.215**
La			**196.343**	0.243	**0.127**	11.878	**11.878**
Ce	459.150	254.902	**315.126**	0.371	**0.371**	21.569	**21.569**
Pr	394.737	232.105	**284.842**	0.112	**0.112**	25.263	**25.263**
Nd	416.488	270.878	**310.829**	0.186	**0.124**	29.176	**29.176**
Sm	359.477	272.549	**282.540**		**0.154**	19.101	**19.101**
Eu	422.554	364.253	**358.546**		**0.080**	12.952	**12.952**
Gd	306.326	242.579	**253.917**			6.959	**6.959**
Tb			**154.545**	0.281	**0.155**	6.223	**6.223**
Dy	184.449	159.843	**153.825**	0.208	**0.208**	3.016	**3.016**
Ho	128.445	118.110	**111.686**			1.451	**1.451**
Er			**70.272**		**0.041**	1.341	**1.341**
Tm			**30.235**				
Yb	57.824	57.853	**51.929**	*4.565*		5.000	**5.000**
Lu	98.228	75.591	**63.313**		**0.083**		
Hf	20.310	1.285	**10.797**				
Ta	16.179		**16.179**				
Pb	5.225	1.609	**3.417**				
Th		0.299	**0.299**				
U	1.015	1.135	**1.075**				
Y	94.586	85.987	**85.987**	0.034	**0.026**	1.363	**1.363**
Zr	46.899	23.165	**33.583**	0.104	**0.064**	3.282	**3.282**
Nb				0.098	**0.208**	0.913	**0.913**

Analyses in italics are not included in the final average. Analyses in bold are averaged values including data from Harte et al. (1994).

Chondrite normalising values in ppm were obtained from Sun and McDonough (1989).

Appendix 5 Ion Microprobe analyses of $\delta^{13}C$ and nitrogen content of polished slabs, BZ251, BZ252, BZ254 and BZ255

δ^{13}C analyses undertaken on Cameca ims-4f of the Department of Geology and Geophysics, University of Edinburgh / NERC

Sample	δ^{13}C	Sample	δ^{13}C	Sample	δ^{13}C	Sample	δ^{13}C
BZ251-1	-4.41	BZ252-1	-4.75	BZ254-1	-3.92	BZ255-1	-5.69
BZ251-2	-3.92	BZ252-2	-3.33	BZ254-2	-5.51	BZ255-2	-4.77
BZ251-3	-4.16	BZ252-3	-2.30	BZ254-3	-7.08	BZ255-3	-7.23
BZ251-4	-4.03	BZ252-4	-4.98	BZ254-4	-3.65	BZ255-4	-6.76
BZ251-5	-4.11	BZ252-5	-5.10	BZ254-5	-5.32	BZ255-5	-4.03
BZ251-6	-3.23	BZ252-6	-9.57	BZ254-6	-3.18	BZ255-6	-3.08
BZ251-7	-3.99	BZ252-7	-1.51	BZ254-7	-4.03	BZ255-7	-4.37
BZ251-8	-5.86	BZ252-8	-1.34	BZ254-8	-3.56	BZ255-8	-3.26
BZ251-9	-4.78	BZ252-9	-3.66	BZ254-9	-4.50	BZ255-9	-3.82
BZ251-10	-5.47	BZ252-10	-1.82	BZ254-10	-1.30		
BZ251-11	-6.29	BZ252-11	-3.51	BZ254-11	-7.90		
BZ251-12	-3.11	BZ252-12	-2.04	BZ254-12	-10.24		
BZ251-13	-2.82	BZ252-13	-2.05	BZ254-13	-5.46		
BZ251-14	-3.16	BZ252-14	-3.64	BZ254-14	-5.42		
BZ251-15	-3.15	BZ252-15	-3.03	BZ254-15	-6.57		
BZ251-16	-2.95	BZ252-16	-2.85	BZ254-16	-3.18		
BZ251-17	-2.25						
BZ251-18	-6.60						
BZ251-19	-2.48						
BZ251-20	-5.11						

Numerical suffices to sample numbers refer to the analysis point the location of which can be determined with reference to figures 5.5_1 - 5.5_4.

Nitrogen analyses undertaken on Cameca ims4f of the Department of Geology and Geophysics, University of Edinburgh / NERC

Sample	N (ppm)	+/-	Sample	N (ppm)	+/-	Sample	N (ppm)	+/-
BZ251-1	226.96	16.47	BZ251-14	8.36	0.69	BZ251-27	34.44	2.67
BZ251-2	204.00	13.84	BZ251-15	12.82	1.49	BZ251-28	199.96	14.13
BZ251-3	1.53	0.15	BZ251-16	151.90	10.54	BZ251-29	6.95	0.78
BZ251-4	142.61	10.02	BZ251-17	10.92	0.74	BZ251-30	9.21	0.68
BZ251-5	0.32	0.02	BZ251-18	106.72	7.33	BZ251-31	96.92	7.05
BZ251-6	0.10	0.01	BZ251-19	4.05	0.31	BZ251-32	38.56	3.18
BZ251-7	239.98	17.76	BZ251-20	174.51	12.55	BZ251-33	0.10	0.01
BZ251-8	199.06	15.91	BZ251-21	260.00	17.89	BZ251-34	81.35	5.98
BZ251-9	189.58	12.73	BZ251-22	76.87	6.26	BZ251-35	0.25	0.02
BZ251-10	203.43	13.52	BZ251-23	6.18	0.46	BZ251-36	10.18	0.71
BZ251-11	13.81	1.01	BZ251-24	190.23	13.11	BZ251-37	8.32	0.58
BZ251-12	218.55	14.99	BZ251-25	183.76	13.26	BZ251-38	14.34	1.00
BZ251-13	38.41	3.41	BZ251-26	59.05	4.29			

Sample	N (ppm)	+ / -	Sample	N (ppm)	+ /-
BZ252N-1	32.19	3.16	BZ252-18	1.49	0.16
BZ252N-2	40.14	3.89	BZ252-19	49.92	4.74
BZ252N-3	0.43	0.06	BZ252-20	5.54	0.57
BZ252N-4	10.20	1.06	BZ252-21	29.42	2.82
BZ252N-6	217.22	21.35	BZ252-22	0.07	0.00
BZ252N-7	5.05	0.53	BZ252-23	2.02	0.06
BZ252N-8	635.37	60.39	BZ252-24	10.61	0.31
BZ252N-9	0.96	0.12	BZ252-25	82.57	1.84
BZ252-10	1.59	0.19	BZ252-26	1.43	0.04
BZ252-11	42.99	4.18	BZ252-27	12.60	0.27
BZ252-12	0.61	0.09	BZ252-28	4.08	0.11
BZ252-13	22.30	2.23	BZ252-29	0.40	0.01
BZ252-14	1.54	0.17	BZ252-30	182.24	3.72
BZ252-15	3.21	0.34	BZ252-31	3.38	0.25
BZ252-16	140.51	13.37	BZ252-32	3.65	0.27
BZ252-17	0.20	0.03	BZ252-33	0.14	0.01

Sample	N (ppm)	+ / -	Sample	N (ppm)	+ /-
BZ255N-1	0.29	0.02	BZ255-12	0.64	0.04
BZ255N-2	0.34	0.02	BZ255-13	2.24	0.12
BZ255N-3	0.92	0.06	BZ255-14	0.07	0.01
BZ255N-4	3.58	0.18	BZ255-15	4.30	0.23
BZ255N-5	0.52	0.04	BZ255-16	9.89	0.63
BZ255N-6	2.45	0.13	BZ255-17	0.06	0.01
BZ255N-7	0.78	0.05	BZ255-18	0.05	0.00
BZ255N-8	0.19	0.03	BZ255-19	0.87	0.05
BZ255N-9	2.75	0.15	BZ255-20	5.61	0.31
BZ255-10	0.11	0.01	BZ255-21	3.85	0.20
BZ255-11	2.02	0.11	BZ255-22	0.06	0.01

Sample	**N (ppm)**	**+ / -**	**Sample**	**N (ppm)**	**+ /-**
BZ254N-1	0.17	0.02	BZ254-15	0.16	0.01
BZ254N-2	0.16	0.01	BZ254-16	0.17	0.01
BZ254N-3	0.85	0.06	BZ254-17	1.59	0.11
BZ254N-4	0.14	0.01	BZ254-18	0.11	0.01
BZ254N-5	149.36	14.98	BZ254-19	1.26	0.11
BZ254N-6	0.17	0.01	BZ254-20	0.49	0.04
BZ254N-7	1.40	0.10	BZ254-21	1.07	0.08
BZ254N-8	0.11	0.01	BZ254-22	1.05	0.08
BZ254N-9	2.78	0.21	BZ254-23	0.23	0.02
BZ254-10	4.31	0.40	BZ254-24	2.91	0.22
BZ254-11	0.07	0.01	BZ254-25	2.49	0.19
BZ254-12	3.26	0.26	BZ254-26	0.18	0.02
BZ254-13	0.11	0.01	BZ254-27	0.70	0.05
BZ254-14	0.11	0.01	BZ254-28	0.05	0.00

Nitrogen abundance in wt% ppm and calculated against SYNAL standard for BZ252, BZ254 and BZ255 and against SYNAT standard for BZ251

Appendix 6 Fourier Transform Infra Red (FTIR) analyses of São Luiz and Guinean diamond

---

Spectra collected at the Laboratoire de Geochimie et des Isotopes Stables, Universitaire de Paris VII:

FTIR spectra were collected using a Nicolet magna Bench 550 coupled with an IR Plan Spectratech microscope equipped with MCT(A) detector apparatus. Fragments from all stones yielding syngenetic inclusions from the suites BZ215-BZ260 and JH2 - JH17 were analysed in addition to fragments from: the single broken Guinean stone, GU4; ten stones from the Wilding (1990) suite; fourteen stones from the series BZ201 - BZ214. With the exception of a single analysis of a fragment from BZ207, FTIR spectra from the series BZ201-BZ214 were collected by Boyd; deconvolution of these spectra in addition to all other analyses and deconvolution was undertaken by myself.

Spectra collected at Diamond Trading Company Research Centre in Maidenhead:

Analyses were undertaken with a Nicolet Magna-IR™ 750 Spectrometer with samples located either within the main sample compartment or under a Nic-Plan I.R. microscope.

- Six points were analysed on BZ251 within the main sample compartment masked by a 100μm metal aperture. Due to the small nature of the aperture, analyses were collected in 4 cm^{-1} steps[1]. In order to incorporate the data into the deconvolution programme ABD1400.XLW, between each step, a single linearly interpolated data point was added.
- Analyses were undertaken on BZ251, BZ252 and BZ254 using the Nic-Plan I.R. microscope and a 48 μm aperture in steps of 2 cm^{-1}. The parallel sided nature of the sample meant that fringing occurred in the spectra at wavenumbers below 1000 cm^{-1}. This caused problems in baseline correction and so, as all N containing analyses exhibited pure IaB aggregated N, spectra were deconvoluted simply by fitting a standard IaB spectrum to the *collected* spectrum.
- Spectra from fourteen unbroken stones[2] from the series BZ215-BZ272 were collected using steps of 2cm^{-1} over the range 400 cm^{-1} to 4000 cm^{-1}.

The detection limit for nitrogen content for the FTIR apparatus employed depends on a number of factors including the sample quality and thickness and is of the order of 10 - 20 ppm.

---

[1] Absorption bands in the one-phonon region due to N are relatively wide. Adopting a 4cm^{-1} step rather than the more commonly adopted 2 cm^{-1} step-size, represents, therefore, no significant reduction in the quality of data.

[2] These represent all the remaining unbroken stones from the BZ215-BZ272 series with the exception of BZ253. BZ256 and BZ265 which were residing at the Carnegie Institution during analysis.

Deconvolution of FTIR Spectra: Spectra are corrected for background by removing a baseline from spectra obtained, usually in the range of 4000 to 400 cm^{-1}. This baseline will, not necessarily, be a straight line, but may be distorted depending on machine conditions. The corrected spectra should show a smooth tail-off from carbon absorption in the two-phonon region through the one-phonon region. Any N absorption should merely be observed as absorption peaks from this smooth tail. The absolute absorption of the baseline corrected spectra must subsequently be calculated. This is done by multiplying the entire spectral absorption obtained[3] by a scaling factor. The scaling factor is determined commonly as the ratio of 11.94 to measured absorption for the dip in lattice carbon absorption at 1995 cm^{-1}. The one-phonon region of the corrected absolute absorption spectra of the sample can then be fitted to standard spectra of A, B and D absorption for which absolute absorption is directly proportional to N content of each aggregation type. Spectra obtained in Maidenhead were deconvoluted using the programme ABD1400.XLW developed by David Fisher at the Diamond Research Laboratories (1997, *personal communication*). Spectra obtained in Paris were deconvoluted using software developed by Boyd, Cartigny and Stachel (1995, *personal communication*). Absorption for each aggregation type is measured at 1282 cm^{-1} and corresponds to 16.5 ±1 atomic ppm N / cm^{-1} for IaA (Boyd et al., 1994) and 79.4 ±8 atomic ppm N / cm^{-1} for IaB (Boyd et al., 1995).

---

[3] Absorption depends on the thickness of the sample, internal fracturing, reflection, refraction and impurities in the stone.

Appendix 6.1 One phonon region of FTIR spectra

Spectra of diamond fragments obtained in Paris: The following spectra represent the region of 1000 - 1400 cm^{-1}. Graphs presented here are of absorbance relative to the standard diamond absorption at 1995 cm-1 for each spectra. The following spectra are not those used in the calculation of values for ppm N, %A and %B presented herein; they do not involve a correction of baseline *gradient*. A correction such that the lowest absorbance in the one-phonon region was set to a value of zero and all other absorbance scaled appropriately. The following are all the spectra obtained which showed the slightest presence of nitrogen for which deconvolution was attempted. Quantitative data was not, necessarily obtained from each spectra, for these details, the reader should refer to Appendix 6.2.

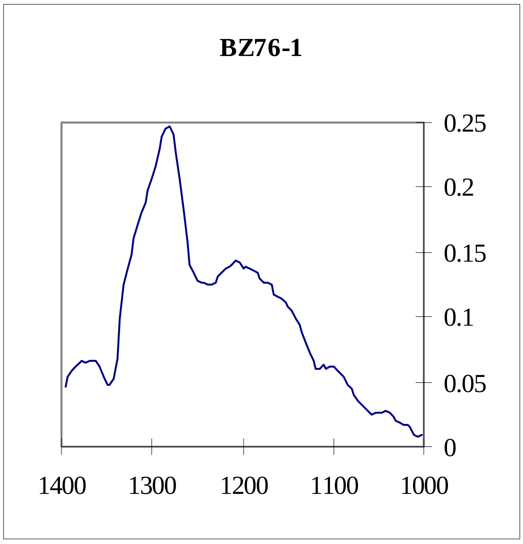

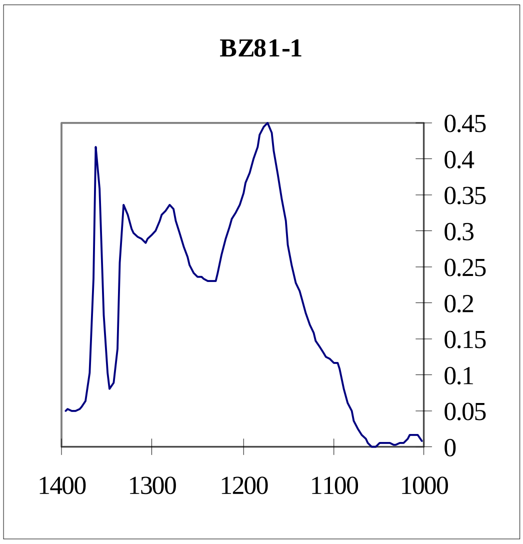

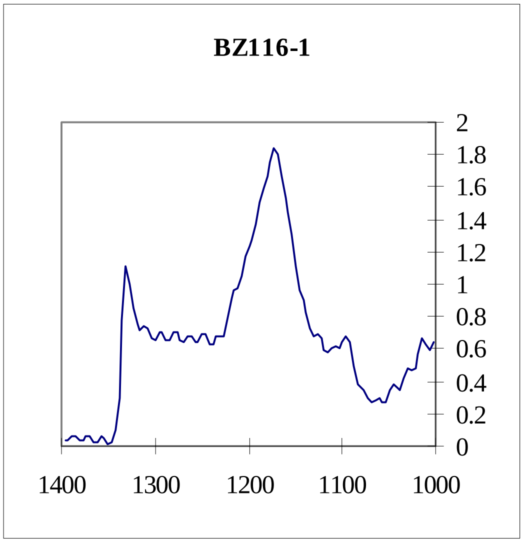

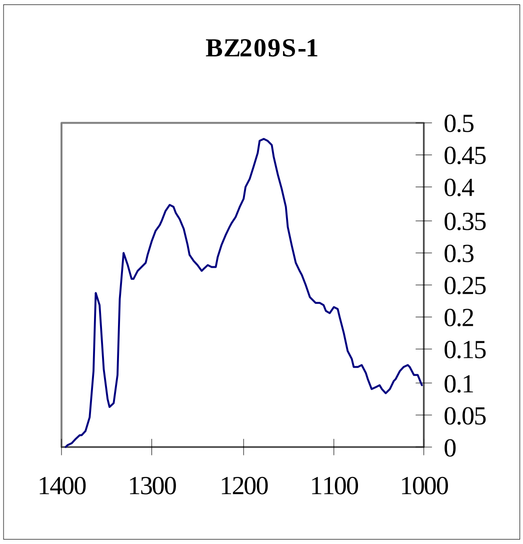

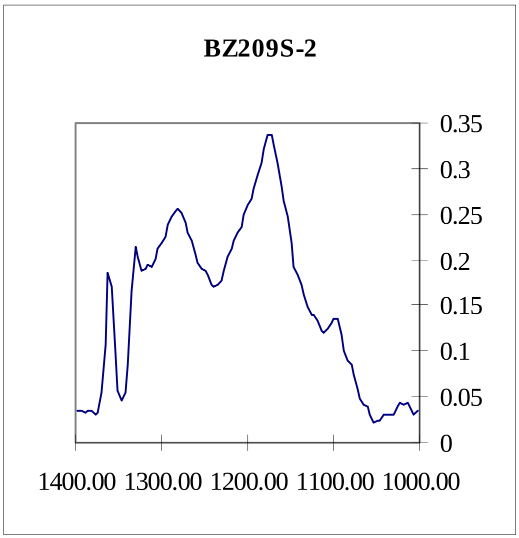
BZ209S-2
0.35
0.3
0.25
0.2
0.15
0.1
0.05
0
1400.00 1300.00 1200.00 1100.00 1000.00

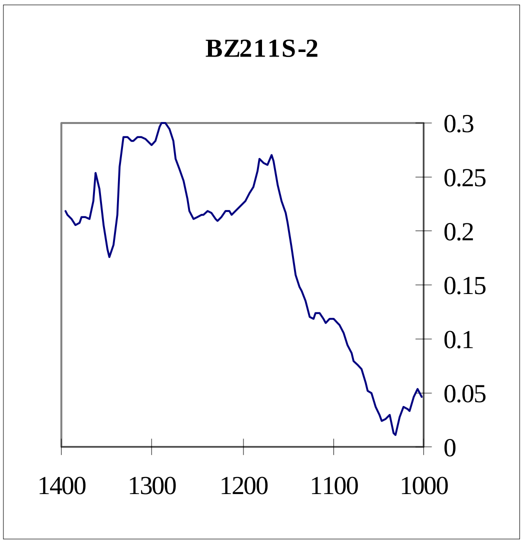
BZ211S-2
0.3
0.25
0.2
0.15
0.1
0.05
0
1400
1300
1200
1100
1000

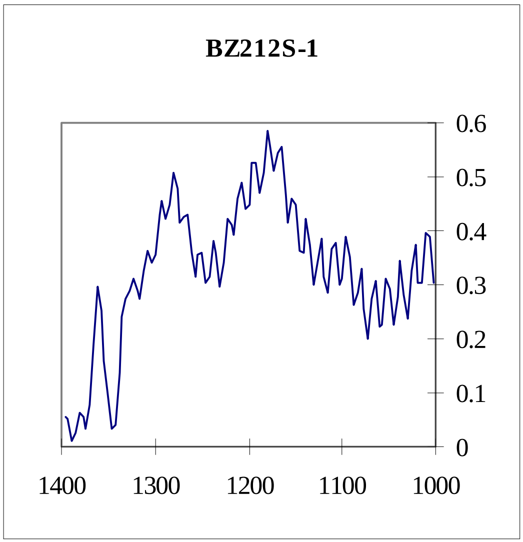
BZ212S-1
0.6
0.5
0.4
0.3
0.2
0.1
0
1400
1300
1200
1100
1000

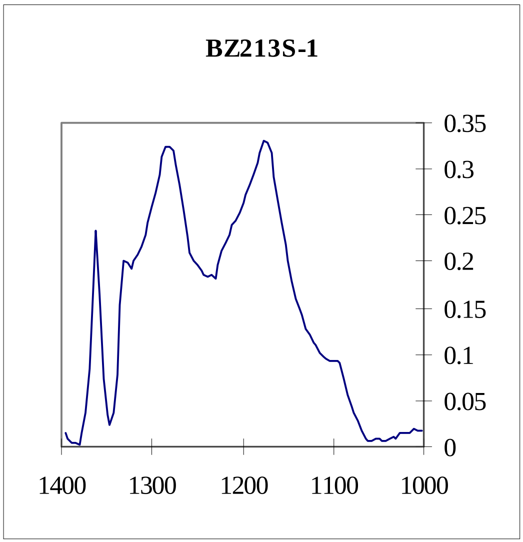
BZ213S-1
0.35
0.3
0.25
0.2
0.15
0.1
0.05
0
1400
1300
1200
1100
1000

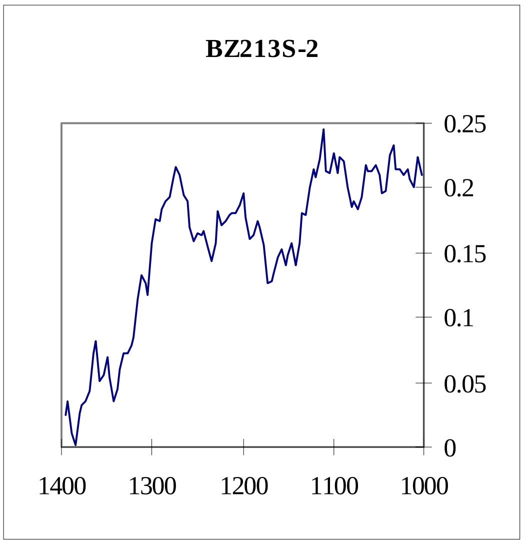
BZ213S-2
0.25
0.2
0.15
0.1
0.05
0
1400
1300
1200
1100
1000

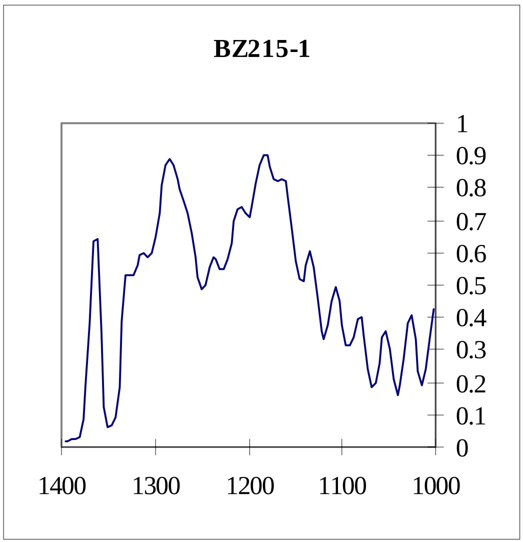
BZ215-1
1
0.9
0.8
0.7
0.6
0.5
0.4
0.3
0.2
0.1
0
1400
1300
1200
1100
1000

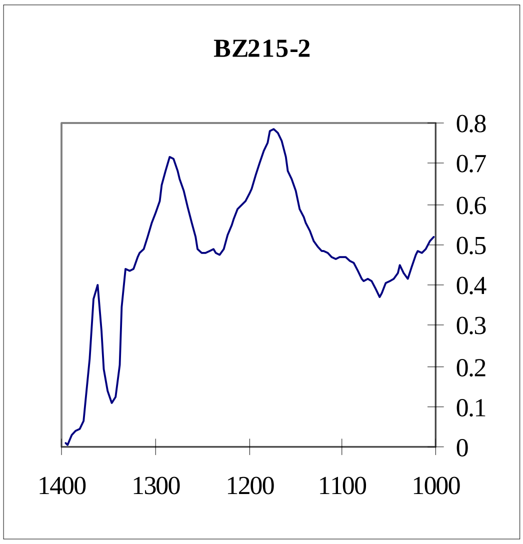
BZ215-2

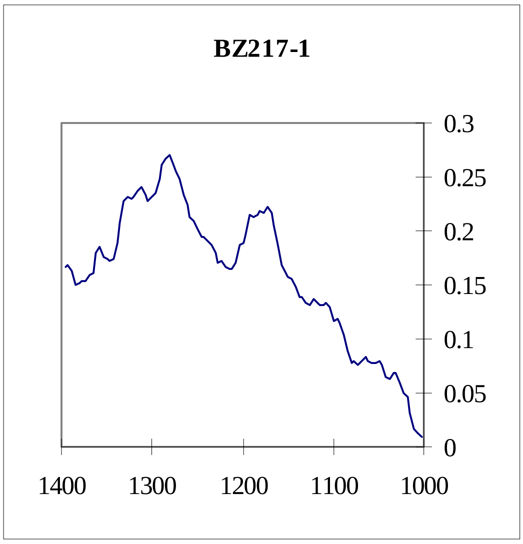
BZ217-1

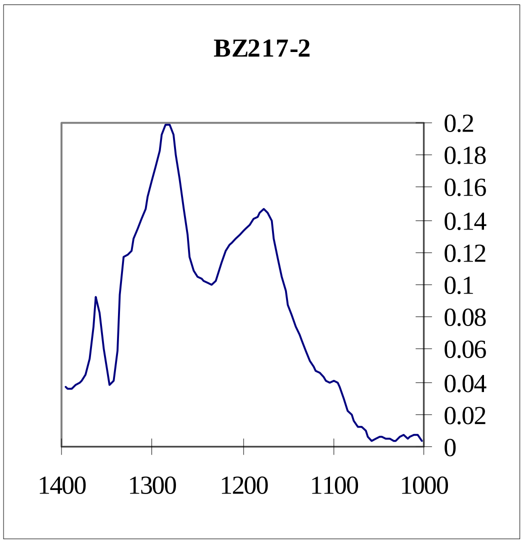
BZ217-2

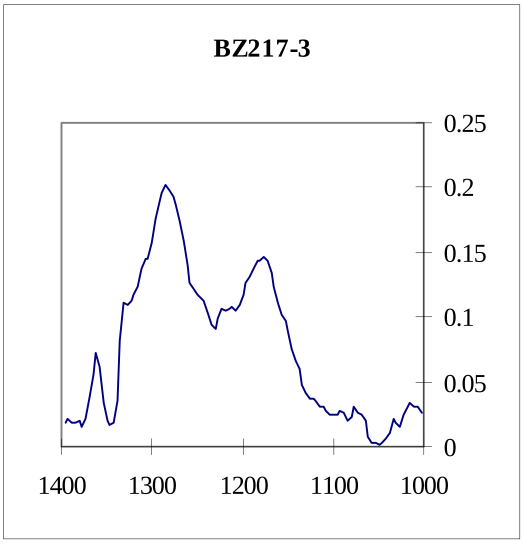
BZ217-3

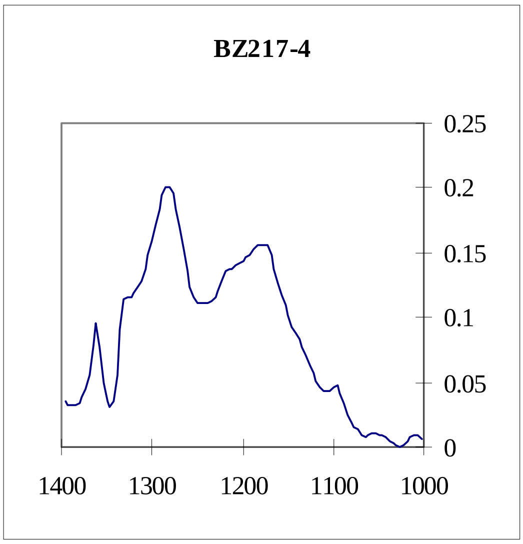
BZ217-4

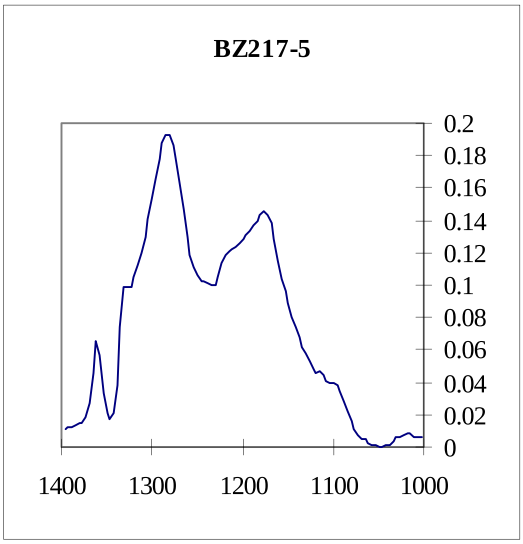
BZ217-5

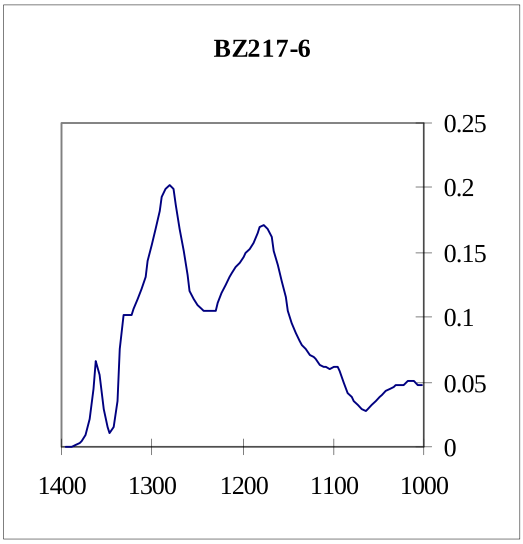
BZ217-6

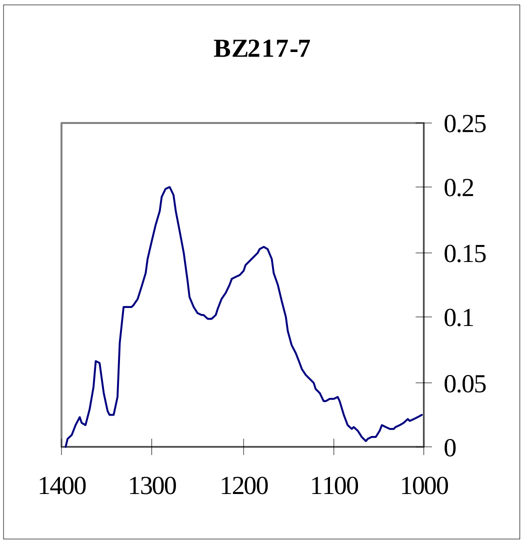
BZ217-7

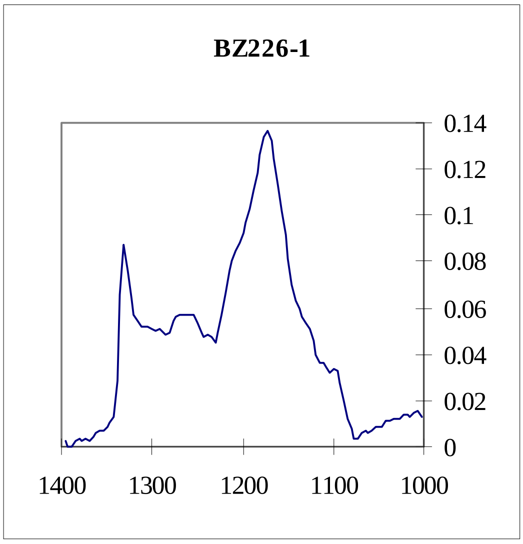
BZ226-1

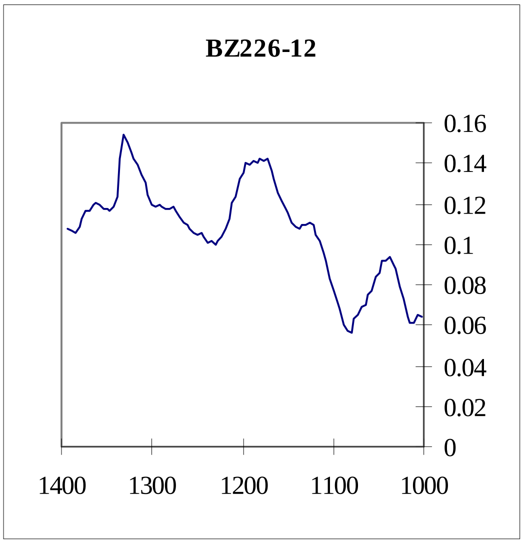
BZ226-12

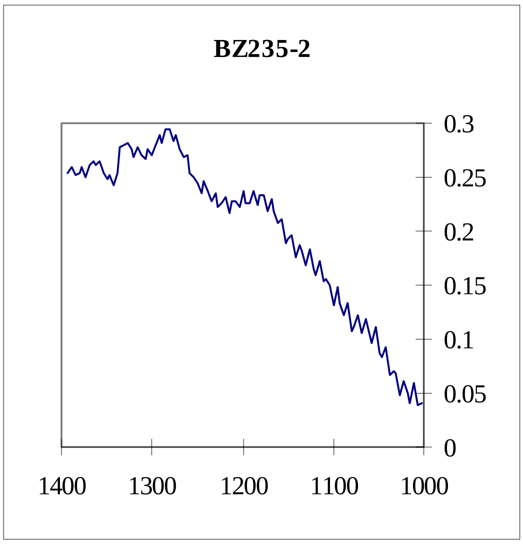
BZ235-2

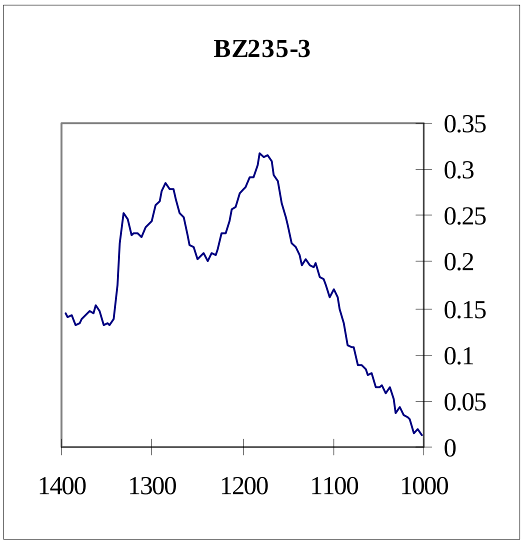
BZ235-3

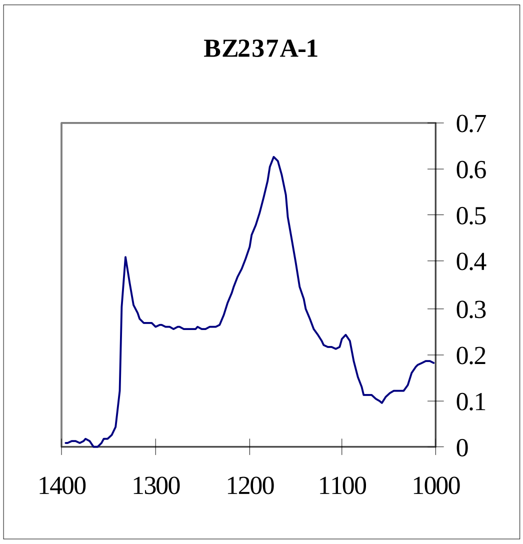

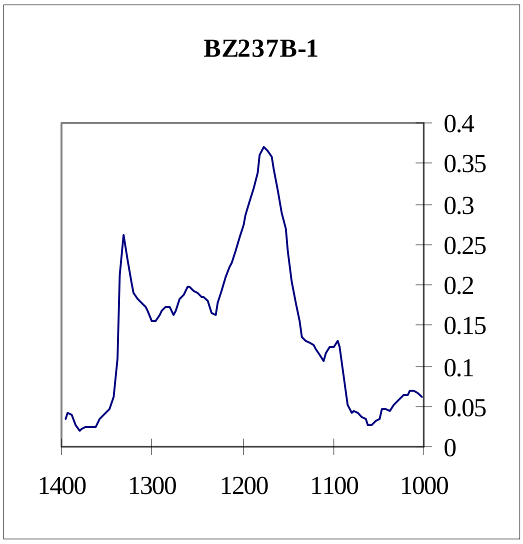

Spectra of diamond fragments obtained in Maidenhead using a 1 mm aperture: The following spectra represent the region of 1000 - 1400 cm-1. Graphs presented here include raw data subjected to baseline correction and absorption relative to the standard diamond absorption at 1995 cm^{-1}, following the procedure outlined previously. Deconvoluted components A, B and D in addition to the data fit are also presented having been calculated using the programme ABD1400.XLS. Data included below each spectra refer to % A absorption, % B absorption and total N ppm wt. The following are all the spectra obtained which showed the slightest presence of nitrogen for which deconvolution was attempted; analysis points BZ257-1, BZ264-1 to BZ264-3 and BZ258-1 to BZ258-3, showed no nitrogen absoprtion and are characteristic of Type II diamond. Points BZ263-1 and BZ266-1 yielded noisy spectra which could not be devconvoluted and point BZ271-1, although clearly a IaB spectra yielded an irregular spectra which could not be deconvoluted. The reader should refer to table 10.6_1 for details of all analyses.

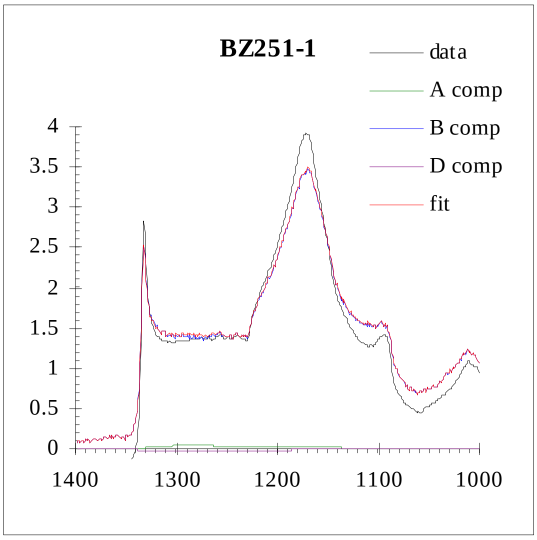

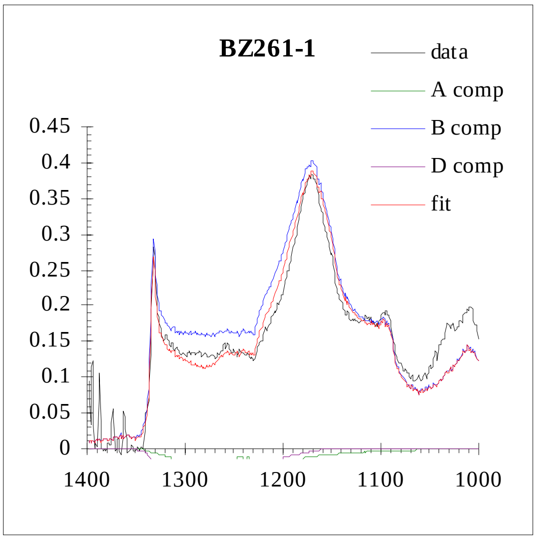

0.9	99.1	107.98	0	100	11.89

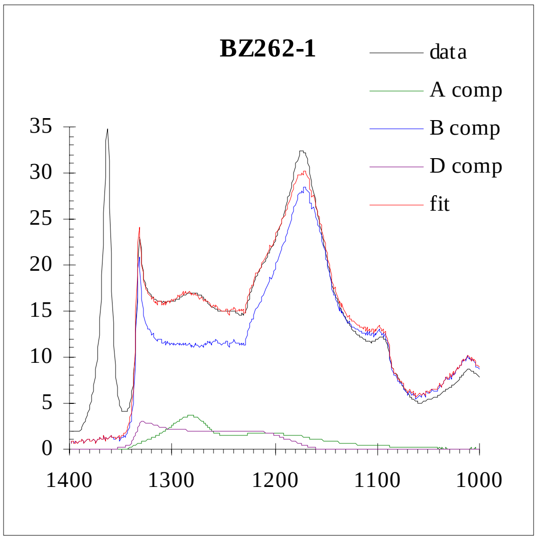

6.4 93.6 935.16

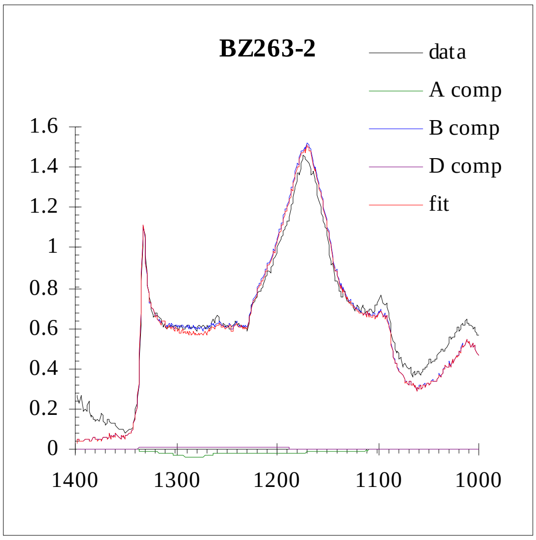

0 100 46.06

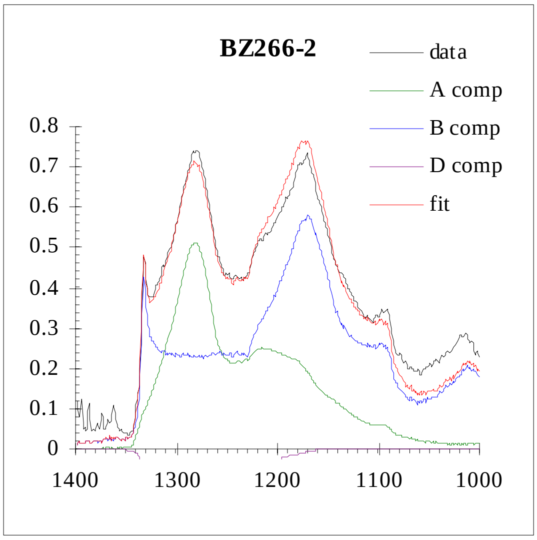

32.1 67.9 26.31

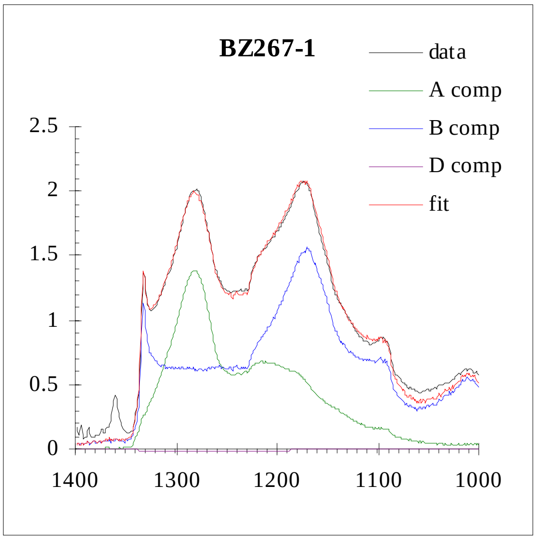

32.3 67.7 70.78

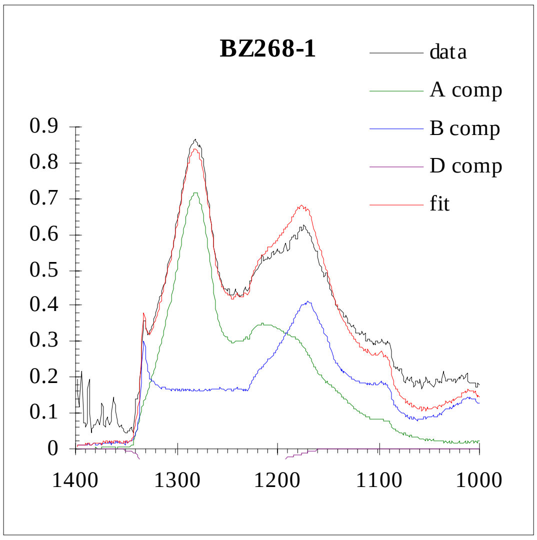

48.2 51.8 24.48

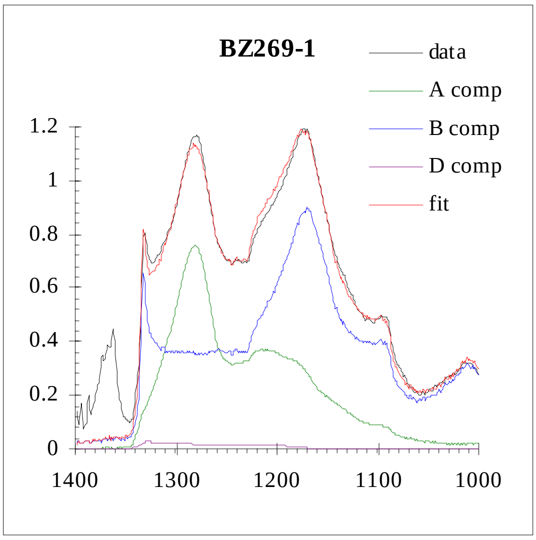

31.2 68.8 40.12

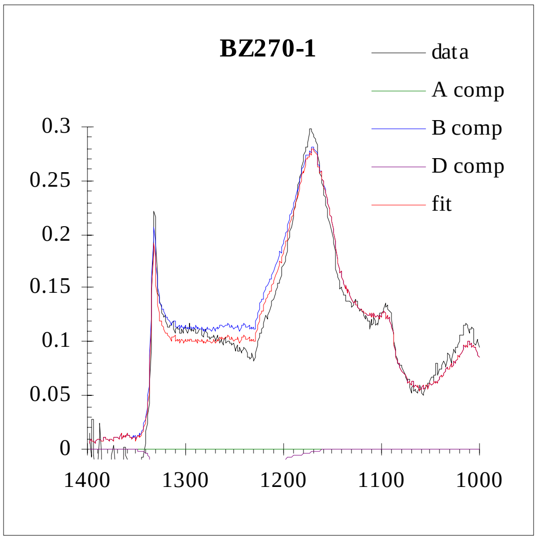

0 100 8.66

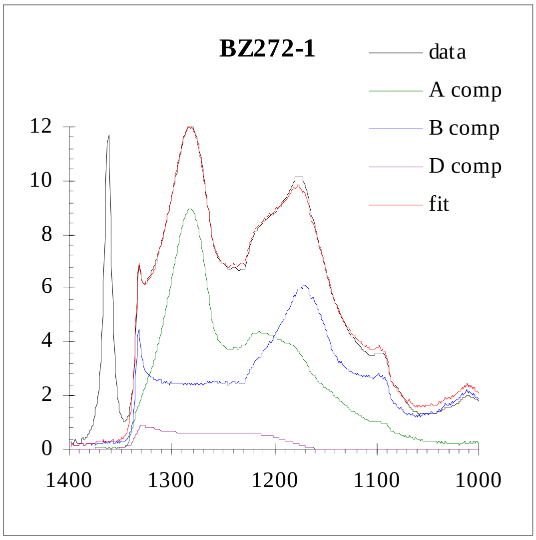

43.9 56.1 335.67

Spectra of diamond plates obtained at Maidenhead using 0.048 mm aperture: The following spectra represent the region of 1000 - 1400 cm-1. Graphs presented here include raw data subjected to baseline correction and absorption relative to the standard diamond absorption at 1995 cm^{-1}, following the procedure outlined previously. Deconvoluted components A, B and D in addition to the data fit are also presented having been calculated using the programme ABD1400.XLS. Data included below each spectra refer to % A absorption, % B absorption and total N ppm wt. The following are all the spectra obtained which showed the slightest presence of nitrogen for which deconvolution was attempted; analysis points 251pp-8, 252pp-4 and 254pp-1 showed no nitrogen absoprtion and are characteristic of Type II diamond. The reader should refer to table 10.6_1 for details of all analyses.

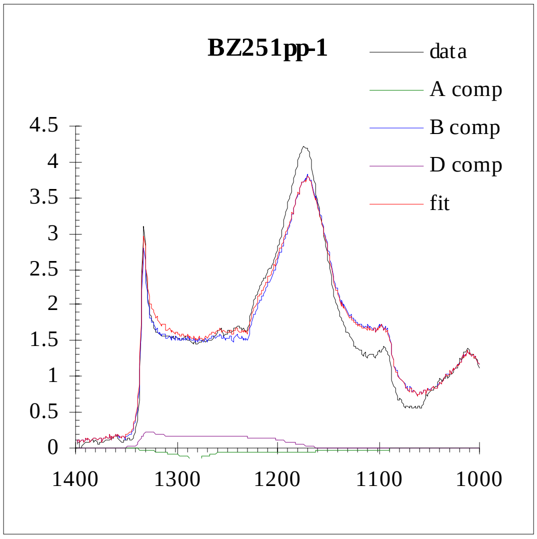

0 100 115.03

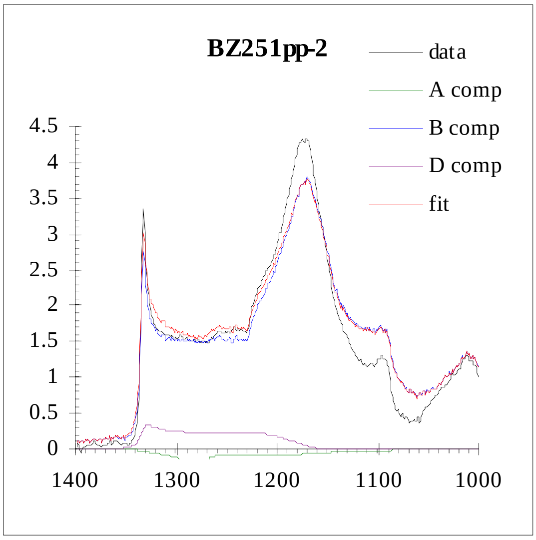

0 100 113.7

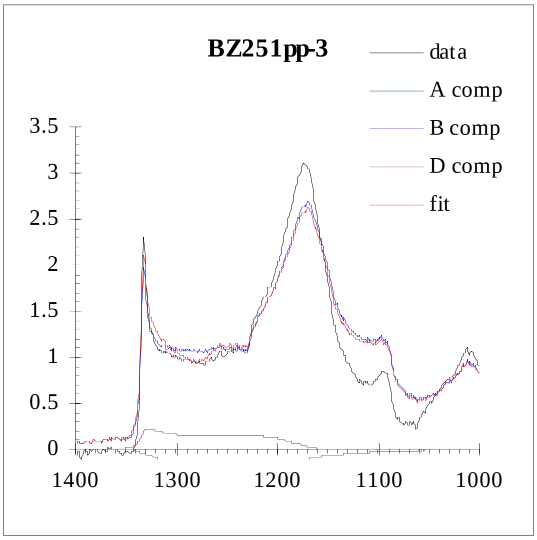
BZ251pp-3

0 100 78.37

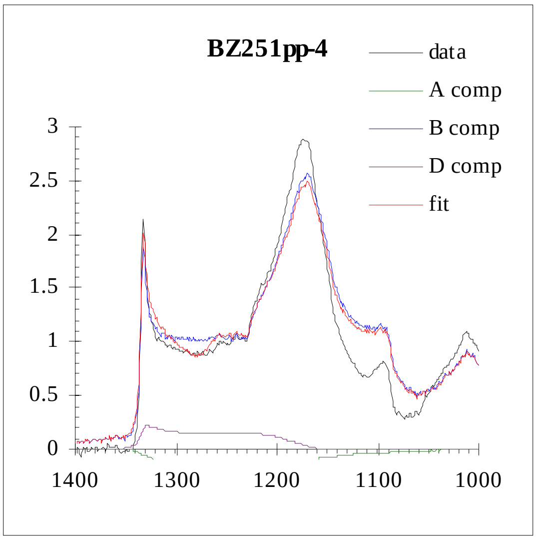
BZ251pp-4

0 100 74.19

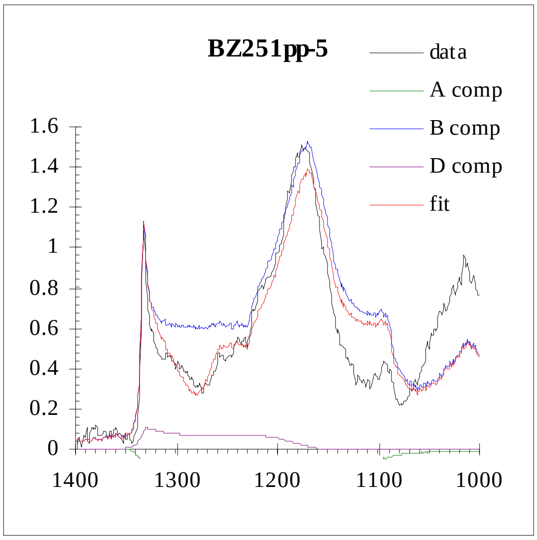
BZ251pp-5

0 100 40.26

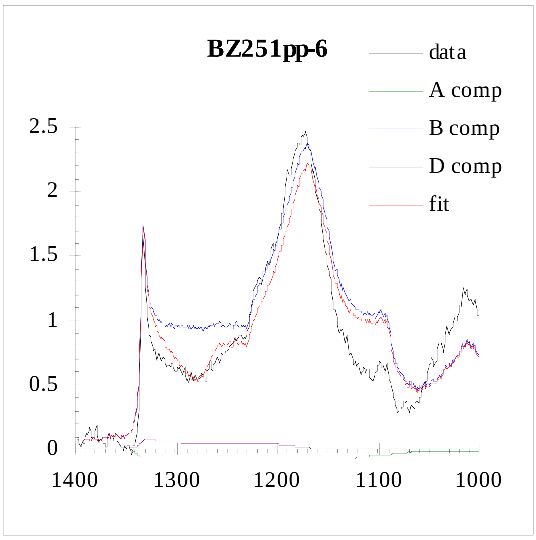
BZ251pp-6

0 100 65.54

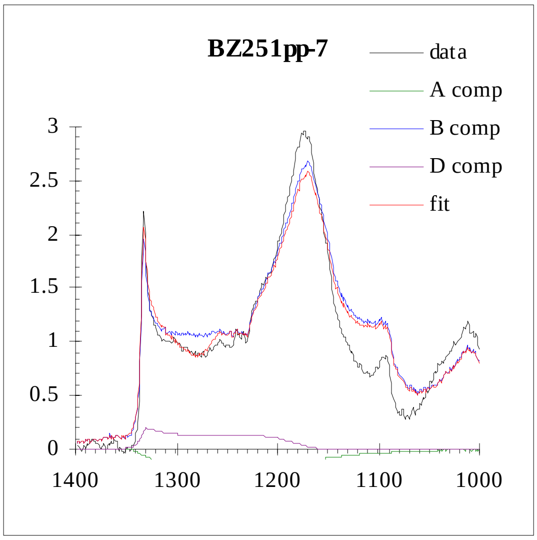
BZ251pp-7

0 100 77.10

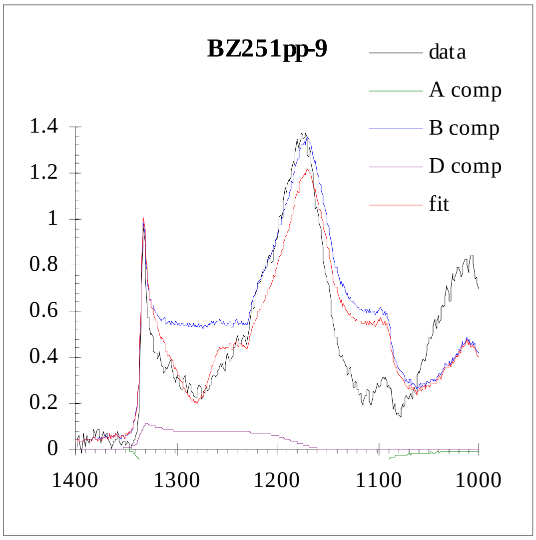
BZ251pp-9

0 100 34.93

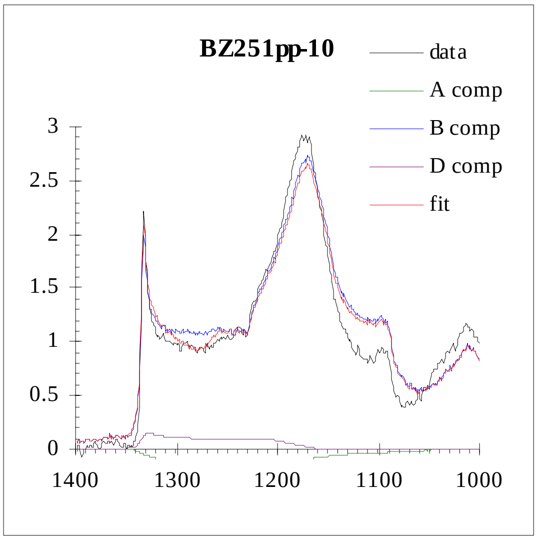

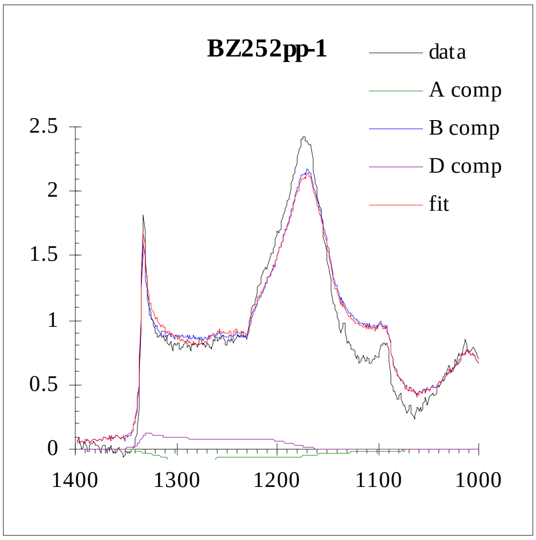

0 100 79.75

0 100 64.75

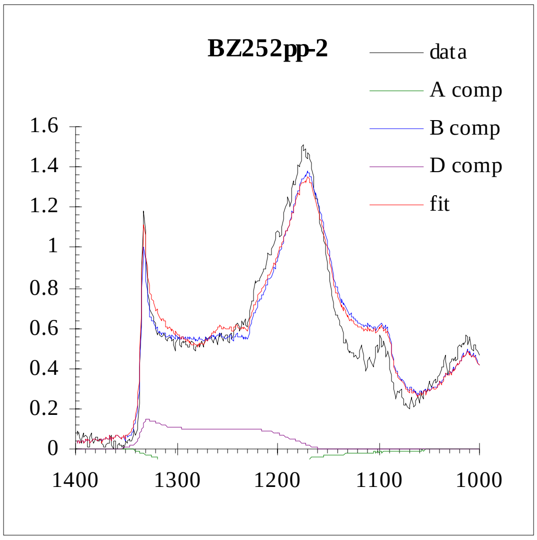

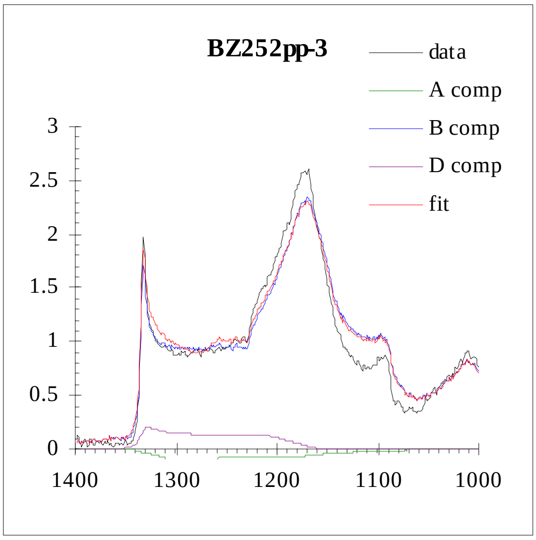

0 100 40.22

0 100 69.4

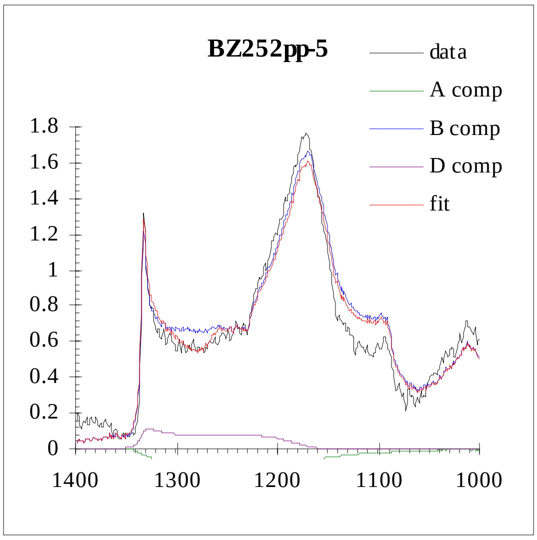

0 100 48.15

Appendix 6.2 Tabulation of results of deconvolution of FTIR spectra

FTIR Spectra of diamond fragments obtained in Paris

Sample	Weight ¥	Agg *	% IaA	% IaB	ppm	Comments
BZ76-1	0.4345	IaA	45	55	160	sl. C-H_s sl. C-H_b
BZ76-2	1.3839	n. d.			114.4	For N analysis
BZ81	0.7582	IaAB	9	92	334	C-H_s
BZ82	0.3853	II				sl. C-H_b
BZ88	1.037	II				C-H_b + CO_2?
BZ90	0.5979	II				
BZ96	1.2722	II				
BZ99	0.3373	II				
BZ111	0.2597	II	‡	‡		v. sl. C-H_b
BZ116-1	0.1212	IaB	0	100	204	C-H_s Poor spectrum
BZ116-2	1.1814	n. d.			388.1	For N analysis
BZ117	0.3803	II				
BZ 201S	?	II				
BZ 202S-1	?	II				
BZ 202S-2	?	II				
BZ 203S	?	II				
BZ 204S-1	?	II				
BZ 204S-2	?	II				
BZ 205S-1	?	II				
BZ 205S-2	?	II				
BZ 206S	?	II				sl. C-H_b CO_2?
BZ 207S	?	II			15	sl. C-H_s sl. C-H_b
BZ207	0.3829	~ II				
BZ 208S-1	?	¤	‡	‡	25	C-H_b CO_2?
BZ 208S-2	?	¤	‡	‡	av	C-H_b
BZ 209S-1	?	IaAB	11	89	311	C-H_s
BZ 209S-2	?	IaAB	11	89	252	C-H_s
BZ 210S	?	II				C-H_b
BZ 211S-1	?	IaA ?	‡	‡	311	C-H_b?
BZ 211S-2	?	IaA	‡	‡	av	C-H_s sl. C-H_b
BZ 212S-1	?	IaAB	‡	‡	47	C-H_s CO_2?
BZ 213S-1	?	IaAB	22	78	252	C-H_s
BZ 213S-2	?	II	‡	‡		CO_2?
BZ 214S	?	II				v. sl. C-H_b
BZ215-1	0.517	IaAB	‡	‡		C-H_s sl. C-H_b
		IaAB	29	71	289	C-H_s
BZ216	0.3238	XXX				
BZ217-1	1.2789	IaB	‡	‡	76	C-H_b
BZ217-2	1.611	n. d.				Replaced in BZ217(df)
BZ217-3	0.627	IaAB	47	53	99	sl. C-H_s sl. C-H_b
		IaAB	‡	‡		C-H_s and C-H_b
		IaAB	34	66	127	C-H_s and sl. C-H_b
		IaAB	35	65	125	sl. C-H_s and sl. C-H_b
		IaAB	‡	‡		C-H_s and sl. C-H_b
		IaAB	58	42	90	C-H_s sl. C-H_b Poor spectrum

Sample	Weight ¥	Agg *	% IaA	% IaB	ppm	Comments
BZ217-4	0.7026	IaAB	‡	‡		sl. C-H$_b$
		IaAB	‡	‡		
		IaAB	‡	‡		
		IaAB	‡	‡		
		IaAB	‡	‡		sl. C-H$_b$
		IaAB	‡	‡		
BZ218-1	0.3177	II				
BZ218-2	0.596	II				
BZ221	2.3288	II				
BZ222	1.9876	II				poss CO$_2$?
BZ223	1.1094	II	‡	‡		C-H$_s$
BZ226-1	3.824	IaB	2	98	67	C-H$_s$ Fragment lost
BZ226-2	2.2331	II IaAB	‡	‡		
		II IaAB	‡	‡		
BZ226-3	2.6797	IaAB IaB	‡	‡		
		IaAB IaB	‡	‡		
		IaAB IaB	‡	‡		
		IaAB IaB	‡	‡		
BZ226-4	0.7184	IaB II	‡	‡		
		IaB	6	94	222	v. sl. C-H$_s$
		IaB II	‡	‡		sl. C-H$_s$ sl. C-H$_b$
		IaB II	‡	‡		sl. C-H$_s$ sl. C-H$_b$ CO$_2$?
		IaB II	‡	‡		
BZ226-5	0.8542	II	‡	‡		
		II	‡	‡		
BZ227-1	1.7089	II			71	
BZ227-2	1.2727	~ II				
BZ227-3	0.9312	n. d.				For extra carbon
BZ231	0.1507	II				CO$_2$?
BZ233-1	0.4308	II				
BZ233-2	0.06	II				
BZ235-1	0.4762	IaAB	‡	‡		C-H$_s$ sl. CO$_2$?
		IaAB	8	92	178	
		IaAB	7	93	212	sl. C-H$_s$ sl. C-H$_b$ sl. CO$_2$?
BZ235-2	2.0985	n. d.				For extra carbon
BZ237a-1	1.9764	IaB	0	100	152	C-H$_s$ / % IaB estimated
BZ237b-1	1.2194	IaAB	5	95	145	C-H$_s$ / Lost in attempting δ^{13}C
BZ237b-2	1.9725	n. d.				
BZ238	0.8001	n. d.				
BZ239	0.2988	II				C-H$_s$ CO$_2$?
BZ240	1.218	II				
BZ241	0.3216	II				
BZ242-1	0.1295	II				
BZ242-2	0.6344	II				
BZ243-1	0.1327	II				
BZ243-2	0.3104	II				
BZ244	0.3214	II				
BZ245a	0.1474	Glass				Discarded
BZ245b	0.3715	II				
BZ246	1.4266	II				
BZ250-1	0.7403	II				
BZ250-2	0.7424	II	‡	‡		

Sample	Weight ¥	Agg *	% IaA	% IaB	ppm	Comments
BZ259	0.2298	II				
BZ260	1.7338	II	‡	‡		
JH2	1.1281	II				
JH6	2.5542	II				
JH7	1.8193	II				
JH11	0.0525	II				
JH12	0.5546	II				
JH17	1.7487	II				
GU4	2.1003	II				

Numerical suffices to sample numbers refer to individual fragments used in each analysis and taken from the (df) bottles comprising broken material from each diamond. For the Wilding (1990) material, BZ76 - BZ117, the diamond fragments cannot, necessarily, be relied upon to be the diamonds associated with inclusions bearing the same number, as discussed in section 5.4.1. All other diamond fragments are entirely reliable. The suffix ‘S’ to sample numbers implies that spectra were collected by Stuart Boyd; the weight of these samples is unknown as represented by ‘?’. For each fragment, often, more than one FTIR spectrum was collected.
¥ - Weight in mg; * - Aggregation state, where two spectral types are indicated for a single analysis, the spectra were interpreted as being transitional between the two types; ‡ - Spectra, although showing an indication of the presence of nitrogen, could not be deconvoluted; ¤ - Spectra not observed in graphical form; n. d. - not determined, fragment was chosen for δ^{15}N or δ^{13}C analysis only.
Abbreviations in the ‘comments’ collumn: sl. - slightl(y), v. - very, sm. - small, ? - possibly, C-H$_s$ - C-H stretching absorption at 3107 cm^{-1}, C-Hb - C-H bending absorption at 2840 and 2905 cm^{-1}, CO$_2$ - Atmospheric CO$_2$ absorption at 2376 cm^{-1}

Results from FTIR spectra from unbroken stones obtained in Maidenhead

Sample	Agg *	% IaA	% IaB	ppm N
BZ251	IaB	0.9	99.1	107.98
BZ257	II	-	-	< 20
BZ258	II	-	-	< 20
	II	-	-	< 20
	II	-	-	< 20
BZ261	IaB (sm)	0	100	11.89
BZ262	IaAB (huge)	6.4	93.6	935.16
BZ263	IaB	‡	‡	‡
	IaB	0	100	46.06
BZ264	II	-	-	< 20
	II	-	-	< 20
	II	-	-	< 20
BZ266	Crud	‡	‡	‡
	IaAB	32.1	67.9	26.31
BZ267	IaAB	32.3	67.7	70.78
BZ268	IaA (sm.)	48.2	51.8	24.48
BZ269	IaAB	31.2	68.8	40.12
BZ270	IaB (sm.)	0	100	8.66
BZ271	IaB shoulder	‡	‡	‡
BZ272	IaAB (big)	43.9	56.1	335.67

* - Aggregation state; ‡ - Spectra, although showing an indication of the presence of nitrogen, could not be deconvoluted; sm. - small; Crud - poor spectrum; shoulder - the spectrum included an anomalous shoulder on the IaB absorption which resulted in the spectrum being un-deconvolutable.

Results from FTIR spectra from diamond flats obtained in Maidenhead

Sample	Agg	% IaA	% IaB	ppm N
BZ251pp-1	IaB	0	100	115.03
BZ251pp-2	IaB	0	100	113.7
BZ251pp-3	IaB	0	100	78.37
BZ251pp-4	IaB	0	100	74.19
BZ251pp-5	IaB	0	100	40.26
BZ251pp-6	IaB	0	100	65.54
BZ251pp-7	IaB	0	100	77.1
BZ251pp-8	II	-	-	< 20
BZ251pp-9	IaB	0	100	34.93
BZ251pp-10	IaB	0	100	79.75
BZ252pp-1	IaB	0	100	64.75
BZ252pp-2	IaB	0	100	40.22
BZ252pp-3	IaB	0	100	69.4
BZ252pp-4	II	-	-	<20
BZ252pp-5	IaB	0	100	48.15
BZ254pp-1	II	-	-	<20

Suffices pp-x refer to the analysis point on each slab; these can be located with reference to figures 5.5_9 - 5.5_11.

Appendix 7 Compositional analyses of bulk diamond

Total nitrogen and nitrogen isotopic content of bulk diamond

Sample	**$\delta^{15}N$**	**min**	**max**	**ppm wt N**
BZ76-2	0.2	-0.6	1	118
BZ81	3.1	2.3	4.2	145
BZ116-2	-10.6	-11.3	-10.1	392
BZ207	n.d.	-	-	-
BZ215-1	1.3	0.4	2.4	193
BZ217-1	1.2	0.2	2.3	72
BZ226-2	n.d.	-	-	-
BZ227-1	-0.3	-1.2	0.6	74
BZ227-2	n.d.	-	-	-
BZ235-2	-1.2	-2.1	-0.4	63
BZ237a-1	-6	-6.6	-5.5	305
BZ237b-2	-5.2	-6.2	-4.6	82

Carbon isotopic content of bulk diamond

Sample	**$\delta^{13}C$**	**Sample**	**$\delta^{13}C$**	**Sample**	**$\delta^{13}C$**
BZ76-2	-7.74	BZ 209S-1	-12.42	BZ239	-5.25
BZ81	-10.66	BZ 210S	-4.90	BZ240	-5.43
BZ82	-8.31	BZ 211S-1	-12.96	BZ241	-5.30
BZ88	-14.78	BZ 212S-1	-8.54	BZ242-2	-5.24
BZ90	-4.68	BZ 213S-1	-5.27	BZ243-1	-5.34
BZ96	-5.07	BZ 214S	-11.56	BZ244	-4.82
BZ99	-4.20	BZ215-1	-8.85	BZ245b	-4.58
BZ111	-7.59	BZ216	-6.23	BZ246	-8.31
BZ116-2	-7.88	BZ217-1	-8.64	BZ250-1	-5.28
BZ117	-3.81	BZ218-1	-7.90	BZ251	-4.09
BZ 201S	-5.53	BZ221	-4.95	BZ252	-3.47
BZ 202S-1	-4.71	BZ222	-12.12	BZ254	-5.05
BZ 202S-2	-4.73	BZ223	-4.63	BZ255	-4.78
BZ 203S	-4.46	BZ226-2	-4.02	BZ259	-4.70
BZ 204S-1	-4.22	BZ227-1	-4.99	BZ260	-4.84
BZ 204S-2	-4.56	BZ227-2	-4.41	JH2	-4.83
BZ 205S-1	-5.57	BZ231	-7.77	JH6-1	-4.57
BZ 205S-2	-4.99	BZ233-1	-5.45	JH7	-4.57
BZ 206S	-5.00	BZ235-1	-10.83	JH11	-5.09
BZ 207S	-4.85	BZ235-2	-10.62	JH12	-4.89
BZ207	-5.00	BZ237a-1	-4.93	JH17	-5.22
BZ 208S-1	-5.22	BZ237b-2	-5.25	GU4	-5.11

All analyses carried out at the Laboratoire de Geochimie et des Isotopes Stables, Universitaire de Paris VII by Pierre Cartigny.
Suffices represent the fragment number used for the analysis from the appropriate (df) bottle containing broken material from each stone. Weights and FTIR results for each fragment number are presented in appendix 6.
n.d. - no nitrogen was detected on combustion of the diamond

Appendix 8 Electron probe principles and calculations

Inclusions were analysed for major and minor element compositions using the Cambridge Instruments MkV and Cameca Camebax electron microprobe apparatus (EPMA) of the University of Edinburgh Department of Geology and Geophysics. A beam current of 20nA was employed with an accelerating voltage of 20kV for all analyses with the exception of elemental mapping analyses of BZ237A6,C, BZ241B1,C and BZ259A2,B (section 2.2.2.1). These analyses were carried out on a 128 x 128 micron grid in steps of 1 micron, with operating conditions of 20kV and 80nA. Counts were collected for 0.3 s on each point. Table A8_1 summarises the standards employed. Initial concentrations were corrected automatically according to the ZAF procedure (correcting for average atomic number, matrix absorption and fluorescence) and cation concentrations were calculated according to standard methods. Detection limit and precision for elements measured on specific phases were calculated following equations A8_1 and A8_2 and are presented in table A8_2.

$$\text{Detection limit} = \frac{3}{m}\sqrt{\frac{R_b}{T_b}} \qquad \text{Equation A8\_1}$$

$$\text{Precision}(\sigma) = \frac{100}{\sqrt{T}\sqrt{\left(R_p - R_b\right)}} \qquad \text{Equation A8\_2}$$

where *Rp* is the peak count rate (counts s^{-1}), *Rb* is the background count rate, *Tp* is the time on peak (s), *Tb* is the time on background (s) and m is the count rate per wt% of element

Mössbauer analysis where obtained (section 5.5), are applied to all similar phases for the estimation of Fe^{3+} concentration rather than using methods based on EPMA data such as Ryburn et al. (1976). As outlined in section 2.5, Mössbauer analysis represents a significantly more accurate method for the determination of iron oxidation state. Indeed, as figure A8_1 shows, plotting Fe^{3+}/Total Fe cations calculated from EPMA analysis against Mössbauer analysis of inclusions in the present study shows nothing like the ideal 1:1 relationship.

Table A8_1 Standards employed in EPMA analysis of inclusions

Element	**Standard**	**Element**	**Standard**	**Element**	**Standard**
Si	Wollastonite	Mn	Mn-metal	K	Orthoclase
Ti	Rutile	Ni	Ni-metal	S	Pyrite
Al	Corundum	Na	Jadeite	Co	Co-metal
Cr	Cr-Metal	Mg	Periclase	Cu	Cu-metal
Fe	Fe-metal	Ca	Wollastonite	Zn	Zn-metal

Table A8_2 Detection limits and precision for electron microprobe analyses

	Detection Limit	Precision	Detection Limit	Precision	Detection Limit	Precision
	TAPP		**Olivine**		**fPer**	
Ca	0.015	0.069	0.019	0.073		
Mg	0.012	0.007	0.018	0.004	0.002	0.004
Mn	0.019	0.017	0.036	0.426	0.040	0.157
Al	0.011	0.008	0.012	4.591	0.011	0.492
Fe	0.021	0.021	0.036	0.022	0.058	0.011
Si	0.016	0.002	0.018	0.005	0.015	
Ni	0.028	1.478	0.044	0.144	0.043	0.050
Cr	0.020	0.025	0.024	0.686	0.042	0.117
Ti			0.019	1.670	0.022	
	Maj. garnet		**Type I,II,III**		**Diopside**	
Ca	0.026	0.010	0.019	0.075	0.027	0.009
Mg	0.016	0.012	0.017	0.005	0.016	0.012
Mn	0.034	0.147	0.034	0.359	0.034	0.025
Al	0.016	0.008	0.013	0.044	0.013	0.012
Fe			0.038	0.029	0.034	0.025
Si	0.017	0.006	0.018	0.004	0.018	0.046
Ni	0.048		0.042	0.365	0.040	1.199
Cr	0.027	0.459	0.024	0.053	0.035	0.770
Na	0.025	0.244	0.028	0.726	0.028	0.025
Ti	0.021	0.042	0.020	0.498	0.020	0.069
K	0.025					

Data from Wilding (1990). Detection limits in wt% and precision as a percentage.

Appendix 9 Ion microprobe operating conditions and calculations

The Ion Microprobe: The University of Edinburgh / N.E.R.C. Cameca ims-4f ion microprobe facility was employed for analyses conducted in this study. In brief, the ion microprobe allows for the measurement of concentrations of trace elements down to levels of the order of 0.1 ppm. Practically, whether an element can be precisely measured depends on its propensity to ionise and the degree of interference its isotopes have with isotopes and molecular species of other elements. Essentially the ion microprobe generates a beam of ions, generally either O_2^+ or Cs^+ ions (O^- or Cs^+ in the case of the Edinburgh ims-4f), which are focused on the target. This sputters a portion of the specimen from the surface, which is measured by an electron multiplier subsequent to separation through a mass spectrometer. The apparatus can be operated at varying degrees of mass resolution:

- Low mass resolution (appendix 9.1) has been adopted for measurement of trace elemental concentrations in inclusions and uses the O^- beam of the duo-plasmatron. Here, isotopes of the ‘same’ mass from different elements are not separated, correction being made via other means (e. g. see the following notes on the calculation of Eu counts per second (cps)).
- High mass resolution (appendix 9.2) is generally adopted for the measurement of isotopic ratios of certain species and for the determination of concentrations of elemental species where low mass resolution is inappropriate. Here the technique has been employed for the determination of N and $\delta^{13}C$ in diamond flats and uses the Cs^+ ion beam as it gives higher yields for negative ions and is smaller and more stable than the O^- beam. The ion microprobe has the advantage over the commonly used technique of bulk analysis of laser sectioned sample for N and $\delta^{13}C$ (e. g. Boyd et al., 1987 and van Heerden, 1993) in that spacial resolution is much higher and analyses can truly be said to be constrained within a particular zone of cathodoluminescence if desired. The disadvantage, however, is that larger errors are involved and, occasionally, such as in the search for diamonds in voidites (section 5.4.2.2), bulk, rather than spot determinations are required. The ims-4f facility is currently pioneering work on the measurement of carbon and oxygen isotopes and nitrogen concentration in a variety of crystalline materials. Details of the technique employed here are given in Harte and Otter (1992).

Values of counts per second (cps) for each mass of interest are collected in cycles throughout an analysis. These are statistically analysed and converted to a single cps value for each mass for each analysis. Cps values can subsequently be converted to absolute concentrations using the techniques outlined in appendices 9.1 and 9.2.

Appendix 9.1 Analysis of diamond inclusions for trace elements

Operating conditions employed: The duo-plasmatron gun was employed using O^- ions. Beam currents of 6nA or 8nA were used with an accelarating voltage of -10.68 kV. The secondary column optics were set with a contrast diaphragm (CD) of = 150µm, field aperture (FA) of 1 with an energy offset of 75 or 80 keV. Background was measured at mass 130.5 and reference masses employed were ^{30}Si for silicates and ^{26}Mg for fPer. For samples with low trace element concentrations, gold was measured at mass 197 in order to calibrate the magnet. A number of molecular peaks were measured in order to correct for overlap with atomic peaks. A total of 26 masses could be measured for each analysis. In addition to reference masses, molecular peaks, background and ^{197}Au, the remaining masses were chosen to represent elements from amongst what is termed herein the 'standard set'. This standard set comprises: large ion lithophile elements (LILE) Rb, K, Ba and Sr; rare earth elements (REE) La, Ce, Pr, Nd, Sm, Eu, Gd, Tb, Dy, Ho, Er, Tm, Yb and Lu; high field strength elements (HFSE) Hf, Ta, Y, Zr and Nb; in addition to the heavy elements Pb, Th and U.

Practicalities of analysing inclusion material: The small size of inclusion material merits close attention being applied to beam positioning before collection of counts. This is particularly true for composite grains. In general, beam / sample coincidence was determined by careful centring of the beam and viewing optics immediately prior to analysis. However, for more difficult grains, alignment was achieved by moving the sample under the beam and trying to identify the area with appropriate counts from key elements (such as Si or Al).

Conversion of cps to concentration: Each element will ionise to a differing degree and so the cps obtained on each isotope will reflect only a proportion of the isotope present in the sample. This proportion is termed the ion yield and depends, additionally, on instrumental conditions. The relative ion yield (RIY) is independent of instrumental conditions and is defined as follows:

$$RIY = \left({}^{cps}\!/_{conc}\right)_X \Big/ \left({}^{cps}\!/_{conc}\right)_{REF}$$

Equation A9_1

where *conc* refers to the concentration in ppm of element *X* or the reference (REF) element and cps used are deadtime, background, isotopic interference nd isotopic abundance corrected.

Any element which occurs in significant quantities in the sample can be chosen as the reference element providing four qualities are satisfied:

- The element has a suitable isotope which will not produce so many counts as to flood the electron multiplier[1].
- This suitable mass is not subject to unreasonable interferences.
- The element in question will ionise.
- The concentration of the element in the unknown is known (usually this will be due to previous electron microprobe analysis).

For silicates, Si is measured on mass 30 and for fPer, Mg is measured on mass 26.

In order to convert from wt% oxide concentration, as presented in electron probe analyses to the ppm values required for ion microprobe calculation, the following formula is adopted:

$$ppm_X = \frac{1000 wt\%_{Xoxide} \, mass_X}{A mass_X \, B mass_O} \qquad \text{Equation A9\_2}$$

Where ppm_X is the concentration of element X expressed as parts per million (wt), mass is the atomic mass, A is the number of cations in the oxide of element X and B is the number of oxygen anions. For example, for Al_2O_3, A will be equal to 2 and B will be equal to 3.

Masses are measured for isotopes of element X so cps_X must be obtained from $cps^A{}_X$. This is done simply by dividing $cps^A{}_X$ by the relative abundance of the isotope ^AX and subtracting from this any contribution of interfering molecular or elemental species (see section on calculation of Eu).

So far, therefore, values for cps_X, cps_{REF}, $conc_{REF}$ in equation A9_1 are known: $conc_X$ can simply be calculated, therefore, if it is assumed that the RIY of the sample is equal to the RIY of standard[2] material.

From equation A9_1 and the definition of ion yield highlighted previously:

$$conc_X = \left(\frac{1}{RIY}\right)_{STD} \left(\frac{cps_X}{IY_{REF}}\right)_{UN} \qquad \text{Equation A9\_3}$$

where RIY_{STD} is the relative ion yield of element X against the reference element in the standard material, IY_{REF} is the ion yield of the reference element.

---

[1] This poses a problem for the measurement of trace elements in corundums. The only suitably abundant element (except for Cr in the case of rubies) is Al. Al has only one naturally occuring isotope, however, ^{27}Al, which if measured, would produce cps in sufficient quantities as to damage the electron multiplier. This problem is overcome by measuring either doubly charged ^{27}Al on mass 13.5 or the molecular species $^{27}Al^{27}Al$ on mass 54. See section 2.3.7 for details.

[2] RIY will vary from matrix to matrix and so it is always preferable to take measurements from standard material which is of a similar type to the unknown. Generally, garnet standards will be measured for garnet unknowns etc. In the case of material in this study, for which, generally, standard material is unavailable, measurement is made, commonly from SRM glasss standard SRM610. It is not thought that the difference in matrix effects should affect the quality of analyses presented herein to a significant degree.

Calculation of true values of cps for Eu: Because of the importance of any possible anomaly in the relative concentration of Eu to other REE, as discussed in section 4.4.2.4, particular care has been exercised for relevent[3] São Luiz inclusions in correcting for all possible interferences with Eu. Counts measured on both Eu masses, 151 and 153 are subject to interference with Ba oxides which, in turn, are subject to their own interferences. In order to make suitable corrections, two procedures can be adopted:

- The measurement of Eu on mass 153 and subsequent correction for ^{138}BaO using calculated values for BaO / Ba.
- The measurement of Eu on masses 151 and 153 followed by calculation of Eu by adopting the method of solution of simultaneous equations.

The two methods are explained as follows:

Calculation of BaO / Ba using mass 154: Mass 154 comprises contributions from a number of isotopes and oxides:

$$\sum cps_{154} = cps_{^{138}\mathrm{BaO}} + cps_{^{138}\mathrm{LaO}} + cps_{^{138}\mathrm{CeO}} + cps_{^{154}\mathrm{Sm}} + cps_{^{154}\mathrm{Gd}} \qquad \text{Equation A9\_4}$$

where *cps* is the counts per second measured on mass 154.

The contribution to measurement on mass 154 is assessed by counting on convenient masses of the elements[4] in question. Cps contributions are then predicted using known isotopic abundance values and, where relevent, known oxide / element ratios. For example, in order to calculate the contribution of ^{138}LaO, counts are measured on mass 139, which involves a contribution from ^{139}La only. Total La is then calculated using the known relative abundance of ^{139}La, in this case 0.99911. From this figure, a value for cps for LaO is then calculated using the known ratio of LaO / La, in this case, 0.176. Finally, a value for cps for ^{138}LaO can be calculated using the relative abundance of ^{138}La to total La, in this case 0.00089. Table A9_1 summarises the isotopic ratios, oxide ratios and masses adopted for the elements used in equation A9_4.

---

[3] CaSi-Pvk is the only phase involved in the present study which has significant contents of Eu and neighbouring REE. All trace element analyses of CaSi-Pvk grains were, therefore, subjected to this correction procedure. Analyses were: BZ97-1, BZ97-2, BZ115-1 and BZ115-2. Furthermore, a number of analyses on additional phases were undertaken in this fashion, particularly towards the beginning of the present study, in order to increase certainty regarding the quality of analyses. Such analyses were: BZ103-1, BZ103-2,BZ116B-1, BZ116B-2, BZ205A-1, BZ205A-2, BZ205A-3, BZ205C-1, BZ205C-2, BZ206A-1, BZ206B-7, BZ206B-8, BZ207A-5, BZ207A-6, BZ207B-1, BZ207B-2, BZ210A-1, BZ210A-2, BZ210B-1, BZ210B-2, BZ210B-3, BZ214A-1, JH7A1-1, JH7A1-2, JH11A1-1, JH17A1-1.

[4] Theoretically, the oxides of these elements could be counted on but the abundances of oxides are far lower than those of their equivalent non-oxides and are swamped by elemental counts.

Table A9_1 Data applicable to the calculation of non-^{138}BaO contributions on mass 154.

Element	**Mass counted on**	**Ratio (XO / X)**	**Isotopic ratio**	**Isotopic ratio**
La	139	0.176	0.9911 (mass 139)	0.00089 (mass 138)
Ce	140	0.21	0.88 (mass 140)	0.00254 (mass 138)
Sm	149	not relevent	0.13 (mass 149)	0.2275 (mass 154)
Gd	157	not relevent	0.15 (mass 157)	0.2181 (mass 154)

An additional complication arises for measurement of ^{157}Gd in that mass 157, additionally, involves a contribution from ^{141}PrO. ^{141}Pr is the sole isotope of Pr so no isotopic correction is necessitated: estimate of the ^{141}PrO contribution merely, therefore, requires counting on mass 141 (solely involving ^{141}PrO) and converting to an oxide value using a value of 0.158 for PrO / Pr.

From the data in Table A9_1, counting on masses, 139, 140, 141, 149, 154 and 157, and invoking equation A9_4, a value for ^{138}BaO can be readily calculated. Equation A9_5 summarises this procedure.

$$cps_{154_{\mathrm{BaO}}} = cps_{154} - \mathrm{La}abn_{La}rat_{La} - \mathrm{Ce}abn_{Ce}rat_{La} - \mathrm{Sm}abn_{Sm} - \mathrm{Gd}abn_{Gd} \qquad \text{Equation A9\_5}$$

where abn_x is the relative abundance of the measured isotope of x, rat_x is the oxide ratio of La or Ce as outlined above and the elemental symbols, La, Ce, Sm, Gd refer, in this case to cps values obtained for the isotopes of each of these elements.

A value for BaO / Ba can subsequently be calculated from ^{138}BaO using the abundance ratio of 0.71 for ^{138}Ba / Ba to give BaO, and, by measuring on mass 138 and correcting for the interference of ^{138}La (the abundance of ^{138}Ce is considered negligible) in a similar fashion to that highlighted above.

Calculation of Eu using BaO / Ba: Eu cps are determined by counting on mass 153 and correcting for the contribution of ^{137}BaO: the ^{137}BaO component being calculated using mass 138, corrected for interference by 138La and the previously determined ratio of BaO / Ba. Such procedure is summarised in Equation A9_6.

$$cps_{Eu} = \frac{cps_{153} - \left(cps_{138} - La_{138}\right)\left(\frac{0.1122}{0.71}\right)\left(\frac{\mathrm{BaO}}{\mathrm{Ba}}\right)}{0.5223} \qquad \text{Equation A9\_6}$$

where La_{138} is the contribution of ^{138}La (measured from mass 139), 0.5223 is the ratio of ^{153}Eu / Eu and 0.1122 and 0.71 are the relative abundances of ^{137}Ba and ^{138}Ba respectively.

Calculation of Eu via simultaneous equations: Masses 151 and 153 comprise contributions from Eu and BaO:

$$cps_{151} = cps_{^{135}BaO} + cps_{^{151}Eu}$$ Equation A9_7

$$cps_{153} = cps_{^{137}BaO} + cps_{^{153}Eu}$$ Equation A9_8

^{135}Ba comprises 6.593% of Ba so:

$$^{137}\mathrm{Ba} = \frac{11.22^{135}\mathrm{Ba}}{6.593}$$ Equation A9_9

These relationships will be the same for the oxides of Ba. The oxide equivalent of equation A9_9 can be substituted into equation A9_8 and, by rearranging equation A9_7 in terms of ^{135}BaO, this can be substituted into the new version of equation A9_8. This procedure essentially eliminates the BaO component from equations A9_7 and 8 which can then be solved simultaneously. The solution can be expressed as:

$$^{151}\mathrm{Eu} = \left[\left(1.70236 cps_{151}\right) - cps_{153}\right] \Big/ 0.557$$ Equation A9_10

Counts for ^{151}Eu can simply be converted to Eu counts by dividing by the relative proportion of ^{151}Eu, ie. 0.5223.

In practice, for the calculation of absolute abundance of Eu for São Luiz material, an average from $\mathrm{cps_{Eu}}$ calculated by both methods was adopted. The conversion of $\mathrm{cps_{Eu}}$ to Eu concentration adopted follows the methodology for element X as detailed previously in Appendix 9.1.

Errors: Average errors for analysed trace elements are presented in table A9_2 and are calculated from output for each analysis from the ins-4f software.

Table A9_2 Average percentage errors for selected trace elements measured on inclusion phases in the present study

	fPer	TAPP/Maj.	Corundum	MgSi-Pvk	CaSi-Pvk	Olivine	Diopside
Rb	11.7	3.7	22.4	5.4		2.8	
K	14.7	1.1		2.2	3.0	5.6	0.8
Ba	33.2	26.3		26.7	7.3	4.5	30.9
Sr	14.1	14.5	50.0	14.6	0.2	6.8	0.4
La	48.1	44.8		67.2	0.8	40.8	5.4
Ce	61.9	45.5		58.8	0.5	57.7	2.7
Pr	67.1	54.5		49.8	1.1		5.7
Nd	59.5	56.9			1.4	37.8	7.0
Sm	84.9	48.3		25.0	2.1		13.8
Eu	76.7	59.2		63.7	1.2		13.8
Gd	99.0	59.9			2.2		11.7
Tb	57.7	54.5		33.3	0.8		14.2
Dy	50.0	46.2		2.3	1.9		15.7
Ho	84.9	39.4		66.0	1.7		27.5
Er		58.8			1.3		28.4
Tm					5.6		
Yb	78.4	59.1	99.0	82.7	4.8		21.1
Lu	99.0	70.7		49.5	3.7		
Hf	91.9	17.7		50.0	7.3		
Ta	84.9	17.4		20.0	8.8		
Pb	45.0	26.5	40.8	36.5	24.5		
Th	99.0	35.4		99.0	99.0		
U	89.9	37.8			99.0		
Y	35.3	26.9	70.7	65.2	0.4	17.1	3.6
Zr	21.4	3.6	33.3	8.6	0.7	16.4	2.6
Nb	22.6	11.0		3.5		11.0	15.0

Errors apply as +/- percentage to chondrite normalised values.
Maj.- Majoritic garnet

Procedure for calculation of relative proportions of trace elements in corundums: From the values for counts per second obtained for each mass collected for each analysis, predicted counts per second for each element, irrespective of mass can be calculated:

$$cps_{{}^{M_o}Z} = \frac{100\,cps_{{}^{M_x}Z}}{\Psi} \qquad \text{Equation A9\_11}$$

where cps is counts per second, M_o refers to all isotopes of the element Z, M_x refers to the isotope measured and ψ is the natural percentage of the measured isotope.

In the case of the reference element Al, because only one isotope occurs naturally, namely ^{27}Al, this means that $\psi = 1$. Because of the high abundance of Al in corundum, however, the counts per second which would be encountered on measuring ^{27}Al would flood the electron multiplier. For this study, therefore, the lower concentration $^{27}Al^{2+}$ ion was collected, its relative abundance to $^{27}Al^{3+}$ being 0.0911.

Using values for the concentration of Al (taken here as the reference element) in ppm where:

$$Al_{ppm} = \frac{1000 Al_{wt\%} m_{Al}}{\left(2m_{Al} + 3m_{O}\right)}$$ Equation A9_12

where m is mass of the subscripted element, and Al_{ppm} and $Al_{wt\%}$ refer to the concentration of Al in units of ppm and wt% respectively.

and given that the counts per second for each element reflect only the proportion of that element which will ionise, counts per second values can be converted to absolute concentration (ppm):

$$ppm_{M_0\,Z} = \frac{cps_{Mo\,Z}\, ppm_{M_o\,Al}}{cps_{M_o\,Al}\, RIY_{M_o\,Z}}$$ Equation A9_13

where RIY is the proportion of a particular element which will ionise under the ion microprobe beam at the particular operating conditions relative to Al.

Due to a lack of standard material, appropriate ion yield data for Al_2O_3 matrices were unobtainable. Estimated values were employed (table A9_3) but this means that only an estimate of absolute concentration could be obtained. For the purposes of comparison of the São Luiz inclusions, this presents no problem, but the reader should be aware that the absolute values have an uncertain error.

Table A9_3 Relative Ion Yield values adopted for analysis of São Luiz corundum grains

Element	Al	Ca	Ti	Cr	Fe	Ni	Ga	Ge	Rb	Sr	Y	Zr	Nb	Pb
RIY	1	0.998	0.656	0.288	0.608	0.059	0.074	0.038	0.141	0.406	0.479	0.3	0.183	0.004

Appendix 9.2 Analysis of diamond flats for δ^{13}C and N

Preparation: Samples BZ251, BZ252, BZ254 and BZ255 were cleaned ultrasonically in petroleum spirit to remove surface deposits. An aluminium holder suitable for receipt by the ion microprobe was prepared with a central reservoir of indium metal. The stones were then placed inclusion side upwards onto the indium and pressed into the metal by means of a hydraulic ram thus obtaining level surfaces flush with the steel holder[1]. The samples were subsequently gold coated and a strip of silver-dag was taken to the edge of each stone in order to allow for the earthing of any beam induced charging.

Operating conditions for δ^{13}C analysis: Analyses were carried out using a 14.5 keV $^{133}Cs^{+}$ pimary beam with a 8nA beam current. Field aperture 3, 150 µm contrast aperture, 150 µm image field and ± 12.5 eV energy slits were selected. Counts were collected on masses corresponding to ^{13}C and ^{12}C in 100 cycles collecting times being 5s on ^{13}C and 1s on ^{12}C. The minimum mass resolving power (MRP) required to separate these masses is 1207. No energy off-set was employed. At the start of each analysis the time was recorded and, both before and after each analysis, the primary beam spot was imaged to check for constancy of primary beam shape and centring within the field aperture. Additionally, primary beam current was monitored. For all analyses, beam and beam current drift were found to be minimal. Mass calibration was checked at the beginning of each analysis, being measured by the Hall probe, and was found to vary minimally between analyses. A burn-in time of 5 minutes were followed for each analysis to ensure removal of surface contaminant. Machine output using ims-4f software was collected corresponding to ^{13}C / ^{12}C ratios for each cycle + error. Reference was made throughout to synthetic standard SYNAT supplied by Harris and characterised by Boyd for δ^{13}C using mass spectrometry at the Laboratoire de Geochimie et des Isotopes Stables of the Universitaire de Paris VII. Generally, two standard measurements were made for every three unknowns with standards being read on commencement and completion of each analysis block.

Calculation of δ^{13}C composition: Data was processed firstly by removing obviously anomalous cycles due to surface contamination (particularly within fractures) or machine instability and then data from any further cycles lying more than 3σ from the mean for each analysis[2]. Adjusted ratios and errors were subsequently calculated.

---

[1] In order to facilitate viewing with the optics, the sample is required to be flat in the sample holder.

[2] Few were found to deviate by more than 3σ from the mean of their respective analyses thus demonstrating the reliability of the measurements obtained.

Investigation of machine drift during analysis was then undertaken. Alteration of certain beam conditions (such as beam shape) or processes such as close-down and re-start, will cause the counts per second obtained for a particular ^{13}C concentration to vary. Relating counts per second to absolute concentration must, therefore, be undertaken within blocks of the same broad machine conditions. For the standards, assumed to be homogeneous, ratios were plotted against time from the start of the analysis period. Such a plot is shown in figure A9_1. Blocks of differing machine conditions are clearly visible. A drift in the standard ratio occurs through each block and to correct for this drift, regression curves were fitted to each block and values for unknowns were calculated using a time dependent value for the standard ratio rather than a mean. Thus from these regression curves, a standard ratio could be assigned to any particular time and thus for each unknown analysis. Ratios between unknown ^{13}C / ^{12}C and standard value for each unknown were then calculated. These ratios were subsequently multiplied by a δ^{13}C value[3] for the standard obtained by independent methods thus giving ppm values of unknown points. A value of -23.924 determined by Boyd was used for SYNAT. This calculation can be summarised by the following formula:

$$d^{13}C_{UN} = d^{13}C_{STD}\left(\frac{{}^{13}C/{}^{12}C(t)_{UN}}{{}^{13}C/{}^{12}C(t)_{STD}}\right) \qquad \text{Equation A9\_14}$$

where ${}^{13}C/{}^{12}C(t)_{STD} = mt + c$; values for m and c being given for each block in table A9_4

Table A9_4 Regression lines for blocks of analyses undertaken on SYNAT standard

Block	Intercept (c) ^{13}C/^{12}C	Gradient (m) ^{13}C/^{12}C per minute
Block 1	1.05681×10^{-2}	-1.2351×10^{-7}
Block 2	1.06458×10^{-2}	-1.9384×10^{-7}
Block 3	1.11371×10^{-2}	-2.6399×10^{-7}
Block 4	1.03589×10^{-2}	1.4057×10^{-8}

Errors were calculated initially as a percentage error by summing the ims-4f calculated error as a percentage of the unknown with the percentage standard deviation of the average value for each block of analyses. This percentage error was found to be close to δ^{13}C = 1 ‰ at 1σ (2 ‰ at 2σ) throughout. Data for δ^{13}C thus calculated are presented in appendix 5.

Operating conditions for N analysis: A beam current of 8nA was used and contrast aperture 3 selected. Analysis pits were slightly larger (40 μm) and more irregular than those of the δ^{13}C study due to machine conditions and Cs^{+} ioniser age. This did not pose a problem for analyses obtained as,

---

[3] δ^{13}C values used here refer to the standard notation against Pee Dee belemnite following equation 1.3_1 of section 1.3.2.1

by using a small field aperture (aperture 2) and narrow energy slits (+/- 25 eV), counts were only collected from the central portion of each sampled area. Counts were collected on masses corresponding to ^{13}C and ^{14}N + ^{12}C in 50 cycles; collecting times being 1s on ^{13}C and 5s on ^{12}C + ^{14}N for the first nine analyses of BZ251. For all subsequent analyses, this time was reduced to 1s on ^{13}C and 2s on ^{12}C + ^{14}N for the remaining analyses as sufficient counts were still observed at this level. In order to separate the molecular species ^{12}C + ^{14}N from ^{13}C + ^{13}C a mass resolution of 7500 is required. These particular masses were chosen in order to minimise switching distance between masses. The time for the start of each analysis was recorded. Before and after each analysis the primary beam spot was imaged to check for constancy of primary beam shape and centring within the field aperture. In addition primary beam current was measured. For all analyses, beam and beam current drift were found to be minimal. Mass calibration was checked at the beginning of each analysis, being measured by Hall probe, and was found to vary by less than 0.002% between analyses. Burn-in time of generally 2 minutes was followed for each analysis to ensure removal of surface contaminant. Machine output using ims-4f software was collected corresponding to (^{14}N + ^{12}C) / ^{13}C ratios for each cycle including a caclulation of error. Reference was made throughout to synthetic diamond standards SYNAL and SYNAT from the same stone supplied by Harris and characterised by Boyd for N using the nitrogen line of the Laboratoire de Geochimie et des Isotopes Stables of the Universitaire de Paris VII. Generally, two standard measurements were made for every six unknowns with standards read on commencement and finishing of each analysis block.

Calculation of N content: Data was processed for anomalous cycles in the same fashion as for $\delta^{13}C$ analysis. Of 9582 cycles used, only 43 deviated by more than 3σ from the mean of their respective analyses thus demonstrating the reliability of the measurements obtained.

For the standards, assumed to be homogeneous, ratios were plotted against time from the start of each analysis period. where work was completed during one period for BZ251 and one period for BZ252, BZ254 and BZ255 (figures A9_2 and A9_3). Blocks of differing machine conditions are clearly visible but no machine drift is evident within each block[4]. Mean and standard deviation was calculated for each block for all standards used. Ratios between unknown ^{14}N+ ^{12}C / ^{13}C and standard value for each block (using SYNAL for BZ252, BZ254 and BZ255 and SYNAT for BZ251) were then calculated. These ratios were subsequently multiplied by a N ppm value for each standard obtained independently (Boyd, S., 1994 *personal communication*) thus giving ppm values or unknown points following from equation 5.5_2. A value of 230.4 ppm N (wt) determined by Boyd was used for SYNAT. From this, a value of 132.7 ppm N (wt) was for SYNAL using 12 analyses

---

[4] Regression curves based on rather poor correlations were fitted initially to each of blocks 1-4 and values for unknowns were calculated using a time dependent value for the standard ratio rather than a mean (in a similar fashion to the method outlined in section 5.5.1). The results obtained in this way, however, were found not to differ significantly (<1‰) from values calculated by the above method.

determined in Block 4 and 20 by Harte (1996 *personal communication*) calculated according to the formula:

$$N_{ppm(wt)_{UN}} = N_{ppm(wt)_{STD}} \left(\frac{\left({}^{12}C + {}^{14}N \right) \Big/ {}^{13}C_{UN}}{\left({}^{12}C + {}^{14}N \right) \Big/ {}^{13}C_{STD}} \right) \qquad \text{Equation A9\_15}$$

Appendix 10 X-Ray theory and operating conditions employed

Aparatus and operating conditions:

UCL FTIR: A Bruker IFS45 FTIR spectrometer equipped with an MCT detector was used. Analyses were conducted by collecting reference spectra in air, diamond spectra and spectra from around the area of in-situ inclusion material; inclusion spectra being calculated by difference. Apertures of 40 - 120 μm in diameter were employed depending on the size of the included material and, typically, 500 scans were collected for each spectra.. Samples analysed were BZ251, BZ252, BZ253, BZ254, BZ255, BZ256, BZ257, BZ258.

UCL XRD: Initial analyses employed a Laue diffractometer fitted with a low light TV phosphor system as a means for screening stones. Detailed analyses were conducted on BZ251, BZ253 and BZ255 using a Picket four circle X-Ray diffractometer with sealed tube MoKα source operated at 40kV and 30mA. Collimation was such that inclusions greater than 100 μm in diameter, only, could be measured. Signal to noise ratio was improved by removing unnecessary diamond absorption by means of a metal aperture.

Edinburgh Gandolfi-XRD: A Philips PW1130/90 generator was operated at 50 kV and 20 mA. Radiation used was Ni filtered[1] CuKα and Zr filtered MoKα. Film employed was 3M Rontgen film developed in AGFA Structurix G128 and fixed in AGFA Structurix G328[2]. Films were measured using a micro-ruler.

Use of a Gandolfi camera (Gandolfi, 1967) is a convenient method for single crystal structural determination. Unlike the other single crystal techniques employed herein, it requires no alignment more complex than simply ensuring that the material to be analysed coincides with the path of the X-Ray beam. Additionally, it provides the means to determine structural infomation of included cystalline material whilst occluded by diamond (in-situ)[3]. The camera itself is a Debye Scherrer camera with a mount which rotates the sample on two axes throughout the analysis. The incident X-Ray diffracts off different planes as the sample rotates and produces what is, essentially, a powder diffraction pattern. The methodology, therefore, for calculating d-spacings for diffraction lines follows that for powder patterns.

---

[1] Filtration acts to remove Kβ radiation.

[2] Expansion of film during the development process was found to be minimal. Strips of film whose lengths were measured before and after development were found to expand by a factor of between 1.00024 and 1.00073. Such values are within error of the original measurement and so measured values for 2θ from developed film can be considered to reflect their true values.

To familiarise with alignment procedures and exposure times, the first 15 analyses were conducted using CuKα radiation, simply because of the sole availability of this radiation at the time. A single crystal of $NH_4O_2.H_2O$ was initially analysed as a means of calibrating the sample holder positioning. Due to its low symmetry, this material produces a large number of diffraction lines which, using CuKα, are distributed over a wide range of 2θ. Substantially longer exposure times than those employed for Debye Scherrer camera analysis were required; the Gandolfi camera differs significantly from the Debye Scherrer camera in that, with the Gandolfi camera, the X-Ray beam only 'sees' each plane of diffraction for a small proportion of the analysis. For example, an exposure time of 18 hours was required for $NH_4O_2.H_2O$[4], compared to a recommended exposure of one hour by Debye Scherrer methods). It was found that, in general, 100 μm fPer grains gave good diffraction lines with 24 hour exposures and the single large (1000 μm) diamond chip, JH2(df) required 4 hours. Fe does, however, fluoresce under CuKα radiation which resulted in little contrast in iron-bearing samples. This problem was circumvented by the employment of MoKα radiation, when it became available, for further analyses.

A total of 45 exposures were conducted using MoKα radiation. In-situ analysis showed that even with exposure times of a number of days, useable results were often not forthcoming. It was thus decided to abandon the study of *in-situ* material using this technique as, although. it was concluded that results *could* be obtained, the extensive use of machine time was better be employed in determining powder information from single grains. Emphasis was, therefore placed on sructural determination of green 'garnets', subsequently identified as TAPP, section 3.3.1, an on fPer inclusions.

All single crystal fPer grains analysed using CuKα were repeated successfully with MoKα. In comparison with fPer single crystals, required exposure times were found to be long. Additionally, TAPP inclusions subjected to analysis are small and, more importantly, being of lower symmetry than fPer, distribute diffracted radiation over a significantly larger number of angles of 2θ. This results in a far lower intensity for even the strongest lines of TAPP compared to fPer and thus longer exposure times. For example, JH12A2, an fPer grain of approximately 16 x 10^5 μm^3, yielded strong lines after 72 hours of exposure. If exposure time can be regarded as being inversely proportional to volume, and BZ240B was of the same composition as JH12A2, being 2 x 10^5 μm^3 in size, appropriate exposure would be completed after 336 hours. However, with 408 hours of exposure only two lines were obtained.

---

[3] Diamond represents an ideal host for included material in the application of the X-Ray techniques. Being cubic, it produces few diffraction lines and thus leaves a large area of diffraction 'space' within which any inclusion lines can be searched for.

[4] Given constant operating conditions, the actual value of exposure time depends on a variety of factors, namely, size of sample, crystallinity of sample, symmetry of sample. Some single crystals required extremely long exposure times, eg. analysis of BZ240B, the first identification that a green 'garnet' did not yield a garnet structure, required exposure of 408 hours. Estimate of suitable exposure time is further complicated by the fact that exposure should be long enough to produce lines from the included material but not too long to result in these lines being obscured by general fogging of the film from background scattering from the host and atmospheric debris.

Edinburgh XRD: BZ249A and BZ257A1 were analysed using a Siemens Stoe Stadi-4A 4-circle diffractometer. Operating conditions were 50kV with a beam current of 50 mA using graphite monochromated MoKα radiation (λ=0.71069 Å). Analyses were collected at 298(2) K and structures were determined by Siemens refinement programme SHELXTL 5.03.

ESPRC XRD: Samples BZ227A, BZ241B2, BZ242B, BZ243C and BZ244B were measured using a Delft Instruments Fast TV area detector at 293(2) K using graphite monochromated MoKα radiation (λ=0.71069 Å). The use of a high intensity, well collimated beam has the particular advantage of permitting detailed structural analyses of very small (30μm) samples without necesitating the employment of expensive and time consuming synchrotron source. Structures were determined via direct methods (SHELX-86; Sheldrick, 1990) for all samples bar BZ243C which gave no significant diffraction. Refinement was carried out by the least-squares program SHELX-93 (Shelrick, 1993).

Carnegie XRD: Analyses were undertaken on BZ253, BZ256, BZ257 and BZ265 and released inclusion BZ257A5 using a micro X-Ray diffraction technique developed by workers at the Carnegie Institution of Washington (Mao and Hemley, 1996). The technique is energy dispersive and analyses were conducted using beamline X17C of the National Synchrotron Light Source at Brookhaven National Laboratory. The synchrotron radiation is polychromatic with energy dispersive analyses being conducted over 2000 channels with an energy window between 5 and 75 keV. Diamonds containing included material are mounted on a chi circle, the physical dimensions of this circle constrain the omega values (similar to 2θ values) which can be searched. Rotating the angles c and w of the apparatus produce energy dispersive spectra (EDS) at orientations where the diffraction condition (equation A10_1) is satisfied. The sample can be aligned using this information and, by compensating for the index of refraction of diamond[5], structural determination of included material can be obtained. The beam is highly collimated and very intense; by focussing with two Kirkpatrick-Baez mirrors a very small beam size, approximately 11 x 15 μm, can be obtained making the technique particularly useful for small material such as involved in the present study. As results discussed in section 3.3 show, the technique allows for the determination of included material within inclusions themselves.

X-Ray diffraction theory: The principles of X-Ray diffraction are expressed by an equation in terms of plane spacing, X-Ray wavelength and diffraction angle (equation A10_1). This relationship is termed the Bragg equation:

$$n\lambda = 2d\sin\theta$$ Equation A10_1

---

[5] Correction for refractive index of diamond in this EDS technique is easy as, being cubic, the refractive index is unaffected by orientation.

where n is the natural number pertaining to the order of the plane measured, eg. (111) corresponds to $n = 1$, whereas (222) corresponds to $n = 2$. θ is the angle of incidence of the X-Ray wave direction to the crystallographic plane of the material being analysed, d is the d-spacing of the crystallographic plane and λ is the wavelength of radiation employed (table A10_1).

Table A10_1 X-Ray wavelengths in Å relevent to the present structural study.

Source / Radiation	$K\alpha_1$	$K\alpha_2$	$K\alpha$
Mo	0.70926	0.71354	0.71070
Cu	1.54050	1.54434	1.5418

For X-Ray techniques which involve either a large number of randomly orientated grains (powder techniques) or else single crystal samples which are rotated (e.g. Gandolfi analysis), the net diffraction for each crystal plane is conical in shape. The angle 2θ corresponds to the angle between the X-Ray beam and the cone of diffracted X-Rays, the greater the value of θ, therefore, the greater the distance between the central hole of the film and the exposed line[6]. X-Ray cameras utilising this phenomenum are often manufactured such that the internal circumference, against which the film is taped, is 360mm (including the Gandolfi camera used in this study). This means that on the film, 1mm corresponds to 1° 2θ. The significance of equation A10_1 is that, providing the wavelength of incident radiation is known, the d-spacing corresponding to each diffraction line can simply be obtained from its position on the photographic film.

In order to calculate the unit cell d-spacing for the unknown, the diffraction lines must be indexed. As all deconvolutable analyses obtained by Gandolfi camera in this study have been from cubic phases, indexing is a simple process.

For a cubic crystal:

$$d = a \Big/ \sqrt{h^2 + k^2 + l^2} \qquad \text{Equation A10\_2}$$

where a is the unit cell edge and h, k and l are the Miller indices of the plane of interest.

Combining equation A10_1 and A10_2 gives:

$$N = \left(4a^2 \big/ \lambda^2\right) \sin^2 \theta \qquad \text{Equation A10\_3}$$

where:

---

[6] Standard procedure involves measurement of the distance between the exposed line and its counterpart at the other end of the film, yielding a value of 4θ.

$$N = h^2 + k^2 + l^2$$ Equation A10_4

Plotting N against $\sin^2\theta$ for a cubic crystal should (depending on the quality of the analysis), therefore, produce a straight line plot. At this stage N for each diffraction line is not known, however, it can be ascertained by determining the line through the origin for which each value of $\sin^2\theta$ is an integer. A value for *a* is thus determined using the gradient of the line, $4a^2/\lambda^2$. Additionally, the cubic space group is determinable by the unique pattern of values of N.

Kα radiation is a combination of two distinct wavelengths, Kα_1 and Kα_2, which means that at large values of 2θ, two lines for each plane will be discernable. Calculation of *a* can, therefore, be measured on the basis of each wavelength individually or, by using a weighted value for Kα if splitting is indistinct or uncommon.

Appendix 11 Gas extraction and the determination of bulk $\delta^{13}C$ and $\delta^{15}N$ composition of diamond

---

Sample preparation: Bulk samples of between 0.05 μg and 2.5 μg were weighed using a microbalance and cleaned by heating to 873 K in air for at least 60 minutes.

Method for the determination of $\delta^{15}N$ composition and N content: Twelve fragments from ten broken stones from São Luiz were analysed for $\delta^{15}N$ and absolute N content. Measurement was carried out at the Laboratoire de Geochimie et des Isotopes Stables of the Universitaire de Paris VII under the auspices of Prof. Marc Javoy on apparatus set-up by Dr. Stuart Boyd. Operation was carried out by Pierre Cartigny. The technique for producing sub-nanometer quantities of gas from diamond for $\delta^{15}N$ and N content analysis adopted follows the same methology described in detail by Boyd et al. (1995b). Up to three samples at a time are introduced into the sample chambers which are then evacuated. Each diamond is dropped into the reaction vessel (a platinum crucible) which is heated by resistence wire to 1100 °C. Samples are initially pyrolised over a period of 5 minutes to release adsorbed atmospheric gases. Oxygen is then supplied for combustion by a separate CuO furnace maintained at 920 °C. Combustion proceeds over ~ 15 minutes with oxygen fed directly to the diamond, resulting CO_2 being removed by a liquid nitrogen trap. Subsequently, excess oxygen is removed by reducing the temperature of the CuO furnace to 450 °C. The liquid nitrogen trap is then removed and released gas passed through a Cu **-** CaO furnace maintained at 600 °C. In this furnace CaO traps any CO_2 (after the temperature is lowered to 100 °C) and Cu reduces any oxides of nitrogen to N_2. The quantity of resulting nitrogen is measured as ppm wt using a ‘Baratron’ 315B MKS Instruments capacitance manometer with an accuracy of +/- 2.5%. The minimum quantitiy of nitrogen which can be measured is ~50 ng which corresponds to 25 wt ppm for a fragment of weight 2mg. Nitrogen isotopic content is subsequently determined by mass spectrometry with an accuracy for $\delta^{15}N$ of ~ 1‰ standardised against International Standard IAEA N1 internally and International Standard IAEA N2 once every 12 analyses.

Method for the determination of $\delta^{13}C$: Combustion follows the procedure for the extraction and purification of N_2 detailed previously. Subsequent to the removal of N_2 from the CaO **-** Cu furnace, the temperature of the furnace is raised from 100 °C to 850 °C and maintained for 20 minutes. Released CO_2 is channelled into removable aliquots[1] for $\delta^{13}C$ dermination. Aliquots are transferred to a VG Optima / Finnigan δE mass spectrometer and analysed for $\delta^{13}C$ against a Prolabo carbonate standard (Cartigny, 1997 *personal communication*) according to the method described by Boyd et al. (1995).

---

[1] Some aliquots result from the same combustion run used to separate N_2 for $d^{15}N$ measurement

Appendix 12 Database of experiments aimed at elucidating the state of the deep mantle

Information is split into two tables, both of which are subdivided in terms of components and then by date and author. The first table deals with starting compositions, apparatus and physical conditions of temperature and pressure employed (with errors where available). The second table presents details of run products and methods of determining run products. It is not intended for this list to be a comprehensive description of all experimental work undertaken under deep mantle conditions. Instead, it is purposed to be a summary of the experimental work used for the construction and discussion of phase diagrams in section 4.2 in addition to some of the works used for the construction of the database of thermoelastic constants presented in appendix 13 and employed in section 7.1.

Table A12_1 Starting materials, apparatus and physical conditions of deep mantle-emulating experiments

Field (referred to)	Reference	Starting Material	Apparatus	Temperature	+/-	Pressure	+/-
C							
C	Kennedy and Kennedy (1976)	Diamond (synth) Graphite and Invar equal vols.	Piston cylinder	1100-1625 C	?	43 - 63 kbar	?
C-H-O							
C-H-O	Deines (1980)	C-H-O	Theoretical	600-1600 C	?	30-60 kbar	?
Fe-C-S							
Fe-C-S	Wood (1993)	Fe-C-S alloys (synth and theretical)	Review	2400 K	?	1.7-5 GPa	?
FeO							
FeO	Jackson and Khanna (1990)	Fe0.945O (synth by floating zone tecnique)	Calc fr meas sonic	298K	?	0-3GPa	?
FeO	Fei and Mao (1994)	FeO (synth)	DAC YAG	300-1100K	?	16-100 GPa	?
Fe-FeO							
Fe-FeO	Boehler (1993)	Fe and FeO mixtures	DAC YAG	2000-3750 K	250 K	0.5-2 Mbar	0.05 Mbar
(Fe-FeO)	Duba (1994)	N / A	N / A	N / A	N / A	N / A	N / A
	Duba (1994)	N / A	N / A	N / A	N / A	N / A	N / A

FeO-Fe2O3

FeO-Fe2O3	McCammon (1993)	Fe0.952O + Fe	Piston and m'anvil	1000 C	?	1.5-18 GPa	?

CO2

CO2	Liu (1984)	CO2 (synth)	DAC	289K ??	?	5-515 kbar	?

Al2O3

Al2O3	Marton and Cohen (1994)	Al2O3 (theoretical)	Theoretical	0K	0K	0-200GPa	?

SiO2

SiO2	Sherman (1993)	SiO2 (theoretical)	Theoretical	0K	N/A	0-108 GPa	N/A
SiO2	Kingma et al. (1995)	SiO2 (nat)	DAC	0-2500 K	?	0-65 GPa	?

MgO-FeO

MgO-FeO	Zerr and Boehler (1994)	MgO (synth ?)	DAC CO2	3000 - 4000 K	150 - 400 K	0-315 kbar	10kbar
(MgO-FeO-SiO2)	Zerr and Boehler (1994)	Mg0.85Fe0.15O (synth ?)	DAC CO2	3400 K	100 K	190 kbar	?

MgO-SiO2

MgO-SiO2	Horiuchi et al. (1987)	MgSiO3 (synth)	Multi anvil	1830 C	?	27GPa	?
MgO-SiO2	Navrotsky (1987)	MgSiO3 (???)	? Review	800 -2200 K	?	13-21 GPa	?
MgO-SiO2	Sawamoto (1987)	MgSiO3 (?)	Multi anvil	1100-2100 C	50 C ?	15.5-24 GPa	>0.5>22GPa
MgO-SiO2	Wolf and Bukowinski (1987)	MgSiO3 (theoretical)	Theoretical	500-4000K	N/A	0-125 GPa	N/A
MgO-SiO2	Angel et al. (1992)	MgSiO3 (synth)	DAC	298 K	?	to 7.93 GPa	?
MgO-SiO2	Yagi et al. (1992)	MgSiO3 (synth)	DAC	298 K	?	1.43-9.72 GPa	?
MgO-SiO2	D'Arco et al. (1993)	MgSiO3 (theoretical)	N/A	0K, 298 K	N/A	Var+atm	N/A
MgO-SiO2	Strixude and Cohen (1993)	MgSiO3 (theoretical)	Theoretical	6000-30000K	N/A	0-180 GPa	N/A
MgO-SiO2	Wang et al. (1993)	MgSiO3 maj (synth)	Multi anvil	2050-2500 C	?	21.9-22.6 GPa	?
MgO-SiO2	D'Arco et al. (1994)	MgSiO3 (theoretical)	Theoretical	0K	N/A	0-60 GPa	N/A
MgO-SiO2	Hugh-Jones and Angel (1994)	MgSiO3 (synth)	DAC	298 K	?	0-8.51 GPa	?
MgO-SiO2	Kato et al. (1995)	MgSiO3	x2 multi anvil	25-1200 C	?	20-30 GPa	?
MgO-SiO2	Funamori et al. (1996)	MgSiO3 (synth)	MA8 multi anvil	300-2000K	?	21-29 GPa	?
MgO-SiO2	Silvi et al. (1993)	Mg2SiO4	Theoretical	0 K	N/A	0-26 GPa	?
MgO-SiO2	Chopelas et al. (1994)	Mg2SiO4 (synth)	Calc + DAC	295 K	1 K	0-200 kbar	?
MgO-SiO2	Meng et al. (1994)	Mg2SiO4 (synth)	DAC Wire	573-973 K	?	0-30.8 GPa	?
MgO-SiO2	Duffy et al. (1995)	Mg2SiO4 (synth)	DAC	298 K	?	3-16 GPa	?

FeO-SiO2

FeO-SiO2	Plymate and Stout (1994)	Fe2SiO4 (synth)	DAC	673K	plus/-2%	0-24 GPa	plus/-2.3%

MgO-FeO-Fe2O3

MgO-FeO-Fe2O3	Speidel (1966)	Various compostions (synth)	Heating	1300-1400 C	?	1 bar	?
MgO-FeO-Fe2O3	Srecec et al. (1987)	Various compositions (synth)	YSZ tube	1050-1400 K	?	1 bar	?
MgO-FeO-Fe2O3	McCammon et al. (1995)	Mg0.8Fe0.2O+Re-reO2 or Fe (synth)	Multi anvil	1000 C	?	18 GPa	?

MgO-FeO-SiO2-Fe-FeSi

MgO-FeO-SiO2-Fe-FeSi	Knittle and Jeanloz (1991)	MgSiO3 + Fe mix (synth)	DAC YAG	3500 K	?	20-75 GPa	15%

MgO-FeO-SiO2

MgO-FeO-SiO2	Bell et al. (1979)	Various	DAC YAG	1000 C	?	175-255 kbar	
MgO-FeO-SiO2	Mao et al. (1979)	N/A	DAC YAG	1000 C	?	200-450 kbar	
MgO-FeO-SiO2	Yagi et al. (1979c)	MgFeSiO3 (?)	DAC YAG	?	?	?	?
MgO-FeO-SiO2	Yagi et al. (1979c)	Fo-Cpx (?)	DAC YAG	1000 C	?	400 kbar	?
MgO-FeO-SiO2	Yagi et al. (1979c)	En (?)	DAC YAG	1000 C	?	160 kbar +	?
MgO-FeO-SiO2	Jeanloz and Thompson (1983)	Fo-Fa, En-Fs + various	N/A (review)	1000,1100 C	?	0-80 GPa	?
MgO-FeO-SiO2	Ito et al. (1984)	Olivine and Pyroxene (synth)	Split sphere	1600 C	?	26 GPa	?
MgO-FeO-SiO2	Kato (1986)	MgSiO3 and FeSiO3 (synth)	Multi anvil	1800-1220 C	?	20 GPa	?
MgO-FeO-SiO2	Heinz and Jeanloz (1987)	Mg0.9Fe0.1SiO3 (nat)	DAC	2500-3000K	300 K	18-65 GPa	?
MgO-FeO-SiO2	Ito and Takahashi (1987b)	Various synth	Multi anvil	1100-1600 C	10 C	19-26 GPa	0.5 GPa
MgO-FeO-Cr2O3-SiO2	Kudoh et al. (1990)	Mg0.9Fe0.1SiO3 (synth)	Multi anvil	2173 K	?	26GPa	?
MgO-FeO-SiO2	Matsubara et al. (1990)	Mg1-0.81Fe0-0.19SiO3	Multi anvil	2000 C	?	20 GPa	?
MgO-FeO-SiO2	Farges et al. (1994)	Mg0.9Fe0.1SiO3 (nat)	Multi anvil	1973 K	?	260 kbar	?
MgO-FeO-SiO2	Anderson et al. (1995)	MgFeSiO3 (theoretical)	N/A	0-140 GPa	N/A	0-2000 K	N/A
MgO-FeO-SiO2	Yang and Ghose (1995)	Mg0.75Fe0.25SiO3 (synth)	Heating	296-1300 K	?	1 bar	?
MgO-FeO-SiO2	Yagi et al. (1979c)	Fo-Fa (?)	DAC YAG	1000 C	?	150-700 kbar	?
MgO-FeO-SiO2	Guyot et al. (1988)	Mg0.83Fe0.17SiO4 (nat)	DAC YAG	2500 K	750 K	25-75 GPa	?
MgO-FeO-SiO2	Guyot et al. (1988)	Mg0.83Fe0.17SiO4 (nat)	DAC YAG	2500 K	750 K	50 GPa	?
MgO-FeO-SiO2	Fei et al. (1991)	Ol and fPer (synth)	Piston	1472 1723 K	?	2-4GPA	?
MgO-FeO-SiO2	Fei et al. (1991)	Ol and fPer (synth)	Multi anvil	1723-1773 K	?	9-15GPa	?
MgO-FeO-SiO2	Fei et al. (1991)	Ol and fPer (synth)	DAC YAG	1673 K	?	26 GPa	?
MgO-FeO-SiO2	Fei et al. (1991)	Olivine	Theoretical	1373-1873 K	N /A	5-30 GPa	N /A
MgO-FeO-SiO2	Kesson and Fitz Gerald (1991)	Olivine (synth)	DAC YAG	? Subsolidus	Big	25-30 GPa	2.5 GPa
[+ NiO MnO Cr2O3]							
MgO-FeO-NiO-CoO-SiO2	Malavergne et al. (1995)	(Mg0.71Fe0.2Co0.09)2SiO4	DAC YAG	1500 C	grain size	15, 40 GPa	?
MgO-FeO-NiO-CoO-SiO2	Malavergne et al. (1995)	(Mg0.78Fe0.2Ni0.02)2SiO4	DAC YAG	1500 C	grain size	15, 40 GPa	?

MgO-FeO-SiO2-H2O

MgO-FeO-SiO2-H2O	Li and Jeanloz (1991)	(Mg0.88Fe0.12)SiO3 + H2O (nat)	DAC YAG	2000 K	50-300 K	40-60 GPa	5 GPa

MgO-FeO-Fe2O3-SiO2

MgO-FeO-Fe2O3-SiO2	McCammon et al. (1992)	Mg0.95Fe0.05SiO3 (synth)	Multi anvil	1650 C	?	25 GPa	?
MgO-FeO-Fe2O3-SiO2	Finger et al. (1993)	(MgxFe1-x)2SiO4 (x<0.4) (synth)	Multi anvil	1400-1800 C	?	15.2-16 GPa	?
MgO-FeO-Fe2O3-SiO2	Fei et al. (1994)	Mg0.95Fe0.05SiO3 (synth)	Multi anvil	1273 K	?	1.5GPa	?
MgO-FeO-Fe2O3-SiO2	Keppler et al. (1994)	Mg0.94Fe0.06SiO3 synth)	Multi anvil	1650 C	?	24GPa	?
MgO-FeO-Fe2O3-SiO2	McCammon et al. (1996)	Mg0.8Fe0.2O	Muliti anvil	1000 C	?	18 GPa	?
MgO-FeO-Fe2O3-SiO2	McCammon et al. (1996)	Mg0.95Fe0.05SiO3	Muliti anvil	1650 C	?	24-25 GPa	?

MgO-FeO-CaO-SiO2

CaO-FeO-MgO-SiO2	Liu (1976)	(Mg-Fe)2SiO4 (synth)	DAC YAG	1200-1600 C	200K	265-300 kbar	10 percent
CaO-FeO-MgO-SiO2	Liu (1976)	Mg-FeSiO3 (synth)	DAC YAG	1200-1600 C	200K	265-300 kbar	10 percent
CaO-FeO-MgO-SiO2	Liu (1976)	(Mg-Fe)3Al2Si3O12 (synth)	DAC YAG	1000-1600 C	200K	250-+300 kbar	10 percent

MgO-FeO-Fe2O3-CaO-SiO2

MgO-FeO-Fe2O3-CaO-SiO2 *[+Al2O3-TiO2-Cr2O3]*	Comodi et al. (1995)	Cpx (nat)	DAC	298 K	?	1bar-46 kbar	?

MgO-FeO-Al2O3-SiO2

MgO-FeO-Al2O3-SiO2 *[+MnO-CaO]*	Graham and Ahrens (1973)	Almandine (nat)	Shock wave	298K ??	??	93-663 kbar	5-10 kbar
MgO-FeO-Al2O3-SiO2	Liu (1975)	Mg and Fe garnet (synth)	DAC YAG	1200 K	200K	120-270 kbar	?
MgO-FeO-Al2O3-SiO2 *[+CaO-MnO-Cr2O3-TiO2-Na2O}*	O'Neill and Jeanloz (1994)	Bronzite, En, Py (nat)	DAC	1100-2100 K	300K	to 65 GPa	?
MgO-FeO-Al2O3-SiO2	Karato et al. (1995)	Py, al, gross (?)	H.Press + M.anv	Various	?	Various	?
MgO-FeO-Al2O3-SiO2	Kesson et al. (1995a)	Py-Alm (synth?)	DAC IRlas	Over Gtherm	Big	55-75 GPa	?
MgO-FeO-Al2O3-SiO2	Kesson et al. (1995b)	Py-Alm or En +/-MgAl2O4 (synth)	DAC IRlas	?	large	55-70 GPa	5 Gpa

MgO-FeO-CaO-Al2O3-SiO2

MgO-FeO-CaO-Al2O3-SiO2	Ringwood (1967)	Qtz tholleiite and Ol tholeiite glass (synth)	Multi anvil	~1673K	?	10-17 GPa	?
CaO-MgO-Al2O3-FeO-SiO2	Ahrens and Graham (1972)	Garnet (natural)	Shock	273 K	N/A	0-66 GPa	plus/- 10%
[+ MnO]							
MgO-FeO-CaO-Al2O3-SiO2	Irifune and Ringwood (1987)	MORB (nat)	Multi anvil	1200-1300 C	?	4.6-24.5 GPa	?
[+Na2O+TiO2]							
MgO-FeO-CaO-Al2O3-SiO2	Irifune and Ringwood (1987)	Pyrolite-Ol (synth)	Multi anvil	1200-1400 C	?	4-24.5 GPa	?
[+Na2O+TiO2+Cr2O3]							
CaO-MgO-Al2O3-FeO-SiO2	Ito and Takahashi (1987a)	Peridotite (shr. lherz)	Multi anvil	1700-2300 C	?	17-25GPa	?
CaO-MgO-Al2O3-FeO-SiO2	Ohtani (1987)	CI (synth)	Multi anvil	1750-2150 K	?	120-200 kbar	?
CaO-MgO-Al2O3-FeO-SiO2	Ohtani (1987)	Pyrolite (synth)	Multi anvil	1720-2175 K	?	80 -200 kbar	?
CaO-MgO-Al2O3-FeO-SiO2	Takahashi and Ito (1987)	Peridotite (garnet peridotite)	Multi anvil	1500-1650 C	?	9 -26 GPa	?
CaO-MgO-Al2O3-FeO-SiO2	Kato et al. (1988)	Komatiite doped (synth)	Multi anvil	1900-2150 C	?	12-18 GPa	?
[+Cr2O3 and TiO2]	Kato et al. (1988)	Pyrolite doped (synth)	Multi anvil	2000-2280 C	?	16-24.5 GPa	?
	Kato et al. (1988)	Pyrolite doped (synth)	Multi anvil	1400-1900 C	?	25 GPa	?
	Kato et al. (1988)	Chondrite doped (synth)	Multi anvil	2100-2280 C	?	16 GPa	?
	Kato et al. (1988)	Basalt doped (synth)	Multi anvil	1400-2200 C	?	20-25 GPa	?
CaO-MgO-Al2O3-FeO-SiO2	Tronnes et al. (1992)	Komatiite (Al-poor) (nat)	Multi anvil	1650-1950 C	?	4-11 GPa	?
[+Cr2O3]	Tronnes et al. (1992)	C1 (nat)	Multi anvil	2030-2170 C	?	20-27 GPa	?
MgO-FeO-CaO-Al2O3-SiO2	Irifuneand Ringwood (1993)	MORB (nat)	Multi anvil	1200-1500 C	?	24.5-28 GPa	?
[+Na2O+TiO2]							
CaO-MgO-Al2O3-FeO-SiO2	Irifune (1994)	Pyrolite (synth)	Multi anvil	1550 C	50 C	23-28 GPa	1 GPa
MgO-FeO-CaO-Al2O3-SiO2	Irifune et al. (1994)	Cc (synth)	Multi anvil	1200-1900 C	20 C	6-24GPa	>0.5GPa
[+Na2O+TiO2+K2O]							
MgO-FeO-CaO-Al2O3-SiO2	Kesson et al. (1994)	MORB (synth)	DAC IRlas	to 3000 C??	Big	45, 80 100 GPa	?
[+Na2O]							
CaO-MgO-Al2O3-FeO-SiO2	Ahmed-Zaid and Madon (1995)	Pyrope, Grossular (nat)	DAC YAG	1000-2500 K	500 K	40, 50 GPa	?
CaO-MgO-Al2O3-FeO-SiO2	Ahmed-Zaid and Madon (1995)	Fe-rich garnet (nat)	DAC YAG	1000-2500 K	500 K	50 GPa	?
CaO-MgO-Al2O3-FeO-SiO2	Baker et al. (1995)	Peridotite (fused seps.)	DAggC	1150-1330 C	?	2-10 GPa	?
[+ Cr2O3 TiO2 Na2O]	Baker et al. (1995)	Peridotite (fused seps.)	Theortetical	1150-1330 C	?	2-10 GPa	?

MgO-CaO-SiO2

MgO-CaO-SiO2	Ito and Takahashi (1987b)	0.725,0.64En+0.2,0.18Wo+0.075,0.18Cor (synth)	Multi anvil	1600 C	10 C	10-27 GPa	0.5 GPa
MgO-CaO-SiO2	Hazen et al. (1994)	Not specified !	Split-Sphere	2050C	N/A	18.2GPa	N/A
MgO-CaO-SiO2	Wentzcovitch et al. (1995)	Mg/CaSiO3 (theoretical)	Theoretical	0K ?	N/A	0-150GPa	N/A
MgO-CaO-SiO2	Gasparik and Drake (1995)	0.7En0.2Fo0.1Wo+dopes (synth)	Split sphere	1500-1600 C	?	23 GPa	?
[+Al2O3, TiO2, H2O, F]							

MgO-CaO-SiO2-CO2

MgO-CaO-SiO2-CO2	Liu and Lin (1995)	Dolomite	DAC	1273 K	?	0-7 GPa	plus/-10%
MgO-CaO-SiO2-CO2	Liu and Lin (1995)	Huntite	DAC	1273 K	?	0-6 GPa	plus/-10%
MgO-CaO-SiO2-CO2	Liu and Lin (1995)	Spurrite and tilleyite	DAC	1273 K	?	0-4 GPa	plus/-10%

CaO-Al2O3-SiO2

CaO-Al2O3-SiO2	Liu (1978)	Ca2Al2SiO7 (synth)	DAC YAG	1000 C	?	150 kbar	plus 30 kbar
CaO-Al2O3-SiO2	Liu (1979)	Ca3Al2Si3O12 (synth)	DAC YAG	c1000C	large	100-300 kbar	c10%
CaO-Al2O3-SiO2	Angel (1992)	CaAl2Si2O6 (nat)	DAC	298 K	?	0-7.8 GPa	?
CaO-Al2O3-SiO2	Gautron and Madon (1994)	24.79 wt%CaO An (synth)	DAC YAG	1100-2500 K	500 K	12.5-22.5 GPa	?
CaO-Al2O3-SiO2	Yusa et al. (1995)	Ca3Al2Si3O12 (synth)	DAC YAG	1250 C	250 C	30.2GPa	?

CaO-SiO2

CaO-SiO2	Liu and Ringwood (1975)	CaSiO3 (synth)	DAC YAG	1600 C	200 C	160 kbar	?
CaO-SiO2	Mao et al. (1989)	CaSiO3 (synth)	DAC	300 K	?	0-41GPa	?
CaO-SiO2	Sherman (1993)	CaSiO3 (theoretical)	Theoretical	0K	N/A	0-106 GPa	N/A
CaO-SiO2	Gasparik et al. (1994)	CaSiO3	Multi anvil	1000-2510 C	50 C	8-15.2 GPa	?

MgO-Al2O3-SiO2

MgO-Al2O3-SiO2	Ringwood (1967)	0.9 MgSiO3 - 0.1 Al2O3 wt% glass (synth)	Multi anvil	1173K	?	25 GPa	?
MgO-Al2O3-SiO2	Liu (1977)	3MgSiO3.Al2O3 glass (pyrope) (synth)	DAC YAG	1000-1400 C	?	100-290 kbar	?
MgO-Al2O3-SiO2	Liu (1978)	Mg2Al2SiO7 (theoretical)	Theoretical	N/A	N/A	N/A	N/A
MgO-Al2O3-SiO2 *[+CaO]*	Akaogi et al. (1987)	En-Py (synth)	Multi anvil	900-1000 C	?	4-17GPa	?
MgO-Al2O3-SiO2	Irifune et al. (1996)	MgSiO3xAl2O3 glass garnet and amphibolite (synth)	Multi anvil	1500 C	?	22-28 GPa	1 GPa
MgO-Al2O3-SiO2	Irifune et al. (1996)	MgSiO3xAl2O3 glass garnet and amphibolite (synth)	Multi anvil	1500-1800C	?	27 GPa	1 GPa
MgO-Al2O3-SiO2	Sinogeikin et al. (1997)	En100, En80Py20, En50Py50 (synth)	Brouillon	298 K	?	0 GPa	?

FeO-Fe2O3-Al2O3-SiO2

FeO-Fe2O3-Al2O3-SiO2	Woodland and O'Neill (1993)	And-Almandine (synth)	Multi anvil	1080-1200 C	?	1.5-10.5 GPa	?

MgO-CaO-Na2O-Al2O3-SiO2

MgO-CaO-Na2O-Al2O3-SiO2	Gasparik (1989)	Many oxide mixes c. En,Jd (synth)	Split sphere	1250-1750 C	?	100-165 kbar	?
MgO-CaO-Na2O-Al2O3-SiO2	Gasparik (1990)	Many oxide mixes c. En,Jd (synth)	Split sphere	1350-2450 C	?	166-226 kbar	?

K2O-Na2O-Al2O3-SiO2

K2O-NaO-Al2O3-SiO2	Yagi et al. (1994)	(K1-xNax)AlSi3O8 (synth)	Bridg and multi	700-1200 C	?	5-23 GPa	?

K2O-Al2O3-SiO2

K2O-Al2O3-SiO2	Urawaka et al. (1994)	Sanidine (synth) + sanidine gel	Multi anvil + Cg	760-1800 C	?	5-11 GPa	?

Table A12_2 Run products obtained and identification techniques used in deep mantle emulating experiments

Reference	Run products	Quenching?	Phase identification
C			
Kennedy and Kennedy (1976)	Diamond and grapjite (reversed)	Yes	Binoc microscope and SEM
C-H-O			
Deines (1980)	Various gaseous phases	N/A	Thermodynamics
Fe-C-S			
Wood (1993)	Alloy and L	N/A	Birch-Murnaghan
FeO			
Jackson and Khanna (1990)	Elastic modes det and calc phase transition to CsCl or NiAs found at c100GPa	No for sonic	N/A
Fei and Mao (1994)	NiAs structure adopted above 96GPa from NaCl struct and Rhomb at low T mid P	No	Pow XRD
Fe-FeO			
Boehler (1993)	Melt	No	Visual
Duba (1994)	N / A	N / A	N / A
Duba (1994)	N / A	N / A	N / A
FeO-Fe2O3			
McCammon (1993)	FexO	Yes	Mossbuer at 80K and XRD
CO2			
Liu (1984)	Dry ice CO2 exc at low P	No	Pow XRD
Al2O3			
Marton and Cohen (1994)	Corundum to Rh2O3 Pbna structure above ???90GPa	N/A	LAPW
SiO2			
Sherman (1993)	Stishovite then poss alpha PbO2 transition	N/A	Hartree-Fock
Kingma et al. (1995)	Stishovite below 60GPa CaCl2 structure above	No	Raman spec

MgO-FeO

Zerr and Boehler (1994)	Melt	No	Visual obs. of large T inc.
Zerr and Boehler (1994)	Melt	No	Visual obs. of large T inc.

MgO-SiO2

Horiuchi et al. (1987)	MgSiPvk	Yes	Single xst XRD
Navrotsky (1987)	Pyroxenoid, Garnet, Ilmenite and Pvk structures of MgSiO3	Yes	?
Sawamoto (1987)	T>1800 C opx to cpx to tet grt to il to pvk T<1800 C same exc with mod sp+st then sp+st before pvk	Yes	Pow XRD
Wolf and Bukowinski (1987)	MgSiPvk - enstatite	N/A	N/A
Angel et al. (1992)	P21/c - C2/c	No	Single xst XRD
Yagi et al. (1992)	Garnet structured MgSiO3	No	Synch XRD
D'Arco et al. (1993)	MgSiPvk	N/A	Hartree-Fock
Strixude and Cohen (1993)	Pbnm MgSiPvk	N/A	LAPW
Wang et al. (1993)	Majorite+ilmenite+Pvk+/-Melt	Yes	TEM
D'Arco et al. (1994)	Il - Pvk at 29.4 GPa and MgO+Stisshovite has higher entropy than both end members	N/A	Hartree-Fock
Hugh-Jones and Angel (1994)	Orthoenstatite	No	Single xst XRD
Kato et al. (1995)	Sp+ St to 20 GPa 800 C then Il to 24GPa 800C or 25GPa 1200C then Pvk	No	Pow XRD
Funamori et al. (1996)	MgSiPvk	No	XRD
Silvi et al. (1993)	Olivine, Wadsleyite, Ringwoodite	N/A	Hartree-Fock
Chopelas et al. (1994)	Wadsleyite to Ringwoodite transition calc from vibrational modes	No	Raman
Meng et al. (1994)	Ringwoodite	No	Synch XRD
Duffy et al. (1995)	alpha-Olivine	No	Brillouin scattering + Pow XRD

FeO-SiO2

Plymate and Stout (1994)	Ringwoodite	No	ED XRD

MgO-FeO-Fe2O3

Speidel (1966)	fPer, fPer+Mg Ferrite, fPer+Spinel	No	Thermogravimetry
Srecec et al. (1987)	fPer	No	Wet chemical
McCammon et al. (1995)	fPer of diff. Fe2O3 contnents	Yes	Mossbauer

MgO-FeO-SiO2-Fe-FeSi

Knittle and Jeanloz (1991)	Melted iron and reaction products MgFeSiPvk+Fe=MgSiPvk+FeO+FeSi	Yes	E-probe

MgO-FeO-SiO2

Bell et al. (1979)	Various St always around dep on comp	Yes	Pow XRD
Mao et al. (1979)	2 Phase fPer with phase change of wustite above 700kbar	N/A	N/A
Yagi et al. (1979c)	MgSiPvk	?	?
Yagi et al. (1979c)	MgSiPvk	Yes	XRD
Yagi et al. (1979c)	Sp then MgSiPvk(or St) +fPer	Yes	Pow XRD
Jeanloz and Thompson (1983)	Various	N/A	N/A
Ito et al. (1984)	Pvk+fPer +/- St dep on comp	Yes	Pow XRD SEM EPMA
Kato (1986)	L, Ilmenite, Spinel, Stishovite, Garnet, MnSiO3 tet-struct garnet, Cpx dep on comp and T	Yes	Pow XRD EPMA
Heinz and Jeanloz (1987)	Melted pvk	No	Emmisivity measurement
Ito and Takahashi (1987b)	MgSiPvk above 15GPa fPer throughout	Yes	E-probe Pow XRD
Kudoh et al. (1990)	MgFeCrSiPvk	Yes	E-probe Synch XRD
Matsubara et al. (1990)	Garnet structured MgFeSiO3	Yes	Pow XRD
Farges et al. (1994)	MgFeSiPvk	Yes	XAFS
Anderson et al. (1995)	MgFeSiPvk	N/A	Thermodynamic
Yang and Ghose (1995)	Pbca-Pbcn	No	XRD
Yagi et al. (1979c)	Sp then MgSiPvk(or St) +fPer	Yes	Pow XRD
Guyot et al. (1988)	fPer, Sp, MgFeSiPvk	Yes	TEM (mixing line for small grains)
Guyot et al. (1988)	Mg0.91Fe0.09Si2O5 ('High Si Phase')+ fPer (Mg0.75Fe0.25O)	Yes	TEM (mixing line for small grains)
Fei et al. (1991)	fPer + Ol	Yes	E-probe
Fei et al. (1991)	fPer + Ol, beta or spinel	Yes	E-probe
Fei et al. (1991)	fPer + Mg,FeSiPvk	Yes No	E-probe (mixing line) Pow XRD
Fei et al. (1991)	Pv, Sp, beta, Ol, St, fPer	N / A	N / A
Kesson and Fitz Gerald (1991)	fPer + MgSiPvk	Yes	TEM EDS
Malavergne et al. (1995)	Sp, fPer, MgFeSiPvk	Yes	TEM (mixing line for small grains)
Malavergne et al. (1995)	Sp + Fe,Ni at low P and fPer, FeNi + Amorph Silicate at high (40Gpa) press	Yes	TEM (mixing line for small grains)

MgO-FeO-SiO2-H2O

Li and Jeanloz (1991)	Pvk of same Fe/Mg as starting material + Hydrous phase D [(Mg,Fe)SiH2O4]	Yes	Pow XRD

MgO-FeO-Fe2O3-SiO2

McCammon et al. (1992)	MgFeSiPvk (+St and Fe from preparation)	Yes	micro XRD and Pow XRD
Finger et al. (1993)	Wadsleyite	Yes	Single Xst XRD E-probe Mossbauer
Fei et al. (1994)	MgFeSiPvk	Yes	Pow XRD E-probe
Keppler et al. (1994)	MgFeSiPvk (+ St from preparation)	Yes	XRD FTIR
McCammon et al. (1996)	fPer	Yes	Mossbauer
McCammon et al. (1996)	MgFeSiPvk	Yes	Mossbauer

MgO-FeO-CaO-SiO2

Liu (1976)	fPer + Pvk (sometimes stishovite + spinel (on increasing Fe))	Yes	Pow XRD
Liu (1976)	Pvk (sometimes stishovite or fPer (on increasing Fe))	Yes	Pow XRD
Liu (1976)	Garnet or fPer + Pvk (the latter on increasing Fe)	Yes	Pow XRD

MgO-FeO-Fe2O3-CaO-SiO2

Comodi et al. (1995)	Cpx	No	Single xst XRD

MgO-FeO-Al2O3-SiO2

Graham and Ahrens (1973)	Garnet then hpp garnet (ilmenite type) above 200kbar	Yes	Pow XRD + Hugoniot data
Liu (1975)	High P grt then fPer + unknown then fPer + unknown	Yes	Pow XRD
O'Neill and Jeanloz (1994)	Garnet then Pvk (FeO and Al2O3 stabilises garnet)	Yes	Pow XRD
Karato et al. (1995)	Garnet structure	No	Review
Kesson et al. (1995a)	Al is accomodated in Pvk struct and precludes Grt and fPer	Yes	TEM
Kesson et al. (1995b)	Al increases stability range of MgFe sil pvk (alm is not found as pvk however). Al Pvk are R-3c (not Pbnm)	Yes	TEM

MgO-FeO-CaO-Al2O3-SiO2

Ringwood (1967)	Majoritic garnet	Yes	Pow XRD
Ahrens and Graham (1972)	Garnet up to 20.5 GPa then orthorhombic hpp (not ilmenite structured)	Yes	Pow XRD
Irifune and Ringwood (1987)	Maj+Cpx then Maj+St+Cpx then Maj+St then Grt+St+CaSiPvk	Yes	E-probe Pow XRD
Irifune and Ringwood (1987)	Grt+Cpx+Opx then Maj+Cpx then Maj then Grt+CaSiPvk then Grt+CaSiPvk+Il then Grt+CaSiPvk+MgSiPvk	Yes	E-probe Pow XRD
Ito and Takahashi (1987a)	Sub-liquidus and liquid products Pv solidus above 25GPa below Maj + beta	Yes	E-probe
Ohtani (1987)	Sub-liquidus products Ol Grt Cpx MS L	Yes	Pow XRD and SEM for melt
Ohtani (1987)	Sub-liquidus products Ol Grt Cpx MS L	Yes	Pow XRD and SEM for melt
Takahashi and Ito (1987)	Ol+en+Di+grt, 9GPa; Ol p'morphs+grt+Di to 20GPa; 20GPa Ca-P phase; 24GPa+fPer+MgPvk+Ca-P+Al-P	Yes	Pow XRD EPMA and SEM
Kato et al. (1988)	Ol, Grt, Cpx, L	Yes	XRD E-probe
Kato et al. (1988)	Grt, Ol, L	Yes	XRD E-probe
Kato et al. (1988)	Grt, MgPvk, SiPvk	Yes	XRD E-probe
Kato et al. (1988)	Grt, Ol, L	Yes	XRD E-probe
Kato et al. (1988)	Grt, St, CaSiPvk, L	Yes	XRD E-probe
Tronnes et al. (1992)	Melt + Ol + Grt + Px	Yes	EPMA
Tronnes et al. (1992)	Melt + Majorite or Majorite + 5wt% Al MgFeSiPvk	Yes	EPMA
Irifuneand Ringwood (1993)	Maj+CaSiPvk+Stishovite (Al-phase CaFerrite structure)	Yes	E-probe Pow XRD
Irifune (1994)	Ringw.+CaSiPvk+Maj at 23GPa then CaSiPvk+MgSiPvk+fPer+Grt at 25GPa then loss of Grt	Yes	Pow XRD E-probe
Irifune et al. (1994)	KalSi3O8 hollandite CAS CaSiPvk Ca Ferrite St at high P	Yes	E-probe
Kesson et al. (1994)	MgAlPvk+st+CaSiPvk+Ca Ferrite phase	Yes	TEM
Ahmed-Zaid and Madon (1995)	CaSiPvk+(Ca,Mg)Al2SiO6 (mod T) CaSiPvk+Al2SiO5 V3O5 struct (high T)	Yes	ATEM
Ahmed-Zaid and Madon (1995)	(Ca,Mg,Fe)Al2Si2O5 hollandite struct	Yes	ATEM
Baker et al. (1995)	Melt	Yes	SEM

Baker et al. (1995)	Melt	N / A	N / A

MgO-CaO-SiO2

Ito and Takahashi (1987b)	CaSiPvk above 20 GPa Maj throughout exc. at 27 GPa Al-rich phase	Yes	E-probe Pow XRD
Hazen et al. (1994)	Ca0.49Mg2.51MgSiSi3O12 Majoritic garnet (sl. tetragonal)	Yes	Single xst XRD EPMA
Wentzcovitch et al. (1995)	MgSiPvk CaSiPvk	N/A	ab initio molecular dynamics
Gasparik and Drake (1995)	MgPvk CaPvk + L for F poor system with lowering of MP and intro of hy-B for F rich	Yes	EPMA

MgO-CaO-SiO2-CO2

Liu and Lin (1995)	Aragonite + Magnesite at 60-70kbar 1273 K	Yes	Pow XRD
Liu and Lin (1995)	New orthorhombic phase below 40kbar then dolomite + magnesite at 60kbar	Yes	Pow XRD
Liu and Lin (1995)	Component carbonates and silicates from 40kbar 1273K	Yes	Pow XRD

CaO-Al2O3-SiO2

Liu (1978)	Ca Ferrite Pvk structure above 100kbar 900 C	Yes	Pow XRD
Liu (1979)	Ca-end goes through IIGrossular to Pvk around 150 kbar otherwise Garnet ss through or + Cor if >25%Al	Yes	Pow XRD
Angel (1992)	P-1 - I-1	No	Single xst XRD
Gautron and Madon (1994)	An below 17.5 GPa+Ca1.33Al1.33Si2.33O8 (holl struct)+Ky+CaAlSiPvk	Yes	Pow XRD ATEM
Yusa et al. (1995)	Pvk garnet	No at 5.4GPa	Pow XRD

CaO-SiO2

Liu and Ringwood (1975)	CaSiPvk	T Yes P No	XRD
Mao et al. (1989)	CaSiPvk (metastable down to 0.1GPa (100bar))	No	Synch XRD and normal XRD
Sherman (1993)	CaSiPvk Cubic	N/A	Hartree-Fock
Gasparik et al. (1994)	Wollastromite to Ca2SiO4 + CaSi2O5 to CaSiPvk +/- L	Yes	E-probe Pvk struct assumed

MgO-Al2O3-SiO2

Ringwood (1967)	Majorite	Yes	Pow XRD
Liu (1977)	Ilmenite structure (R-3) (Mg0.75Al0.25)(Si0.75Al0.25)O3 appears above 250kbar	Yes	Pow XRD
Liu (1978)	Ca ferrite structure	N/A	N/A
Akaogi et al. (1987)	Majorite	Yes	Pow XRD Calorimetry
Irifune et al. (1996)	Maj goes to AlPvk at 24-27GPa (Al inc with P) but pyrope goes to sub-Al Pvk + corundum s.s.	Yes	Pow XRD TEM E-Probe
Irifune et al. (1996)	Al in Pvk increases from 11wt% to 17wt% with T	Yes	Pow XRD TEM E-Probe
Sinogeikin et al. (1997)	Majoritic garnets	N/A	XRD and Brouilln scattering

FeO-Fe2O3-Al2O3-SiO2

Woodland and O'Neill (1993)	Grt +/- spinel + stishovite/coesite + opx	Yes	Pow XRD E-probe Mossbauer

MgO-CaO-Na2O-Al2O3-SiO2

Gasparik (1989)	En-Py solubility NA restricts stability of garnet com slightly	Yes	EPMA?
Gasparik (1990)	Extensive phase diagram determination	Yes	EPMA?

K2O-Na2O-Al2O3-SiO2

Yagi et al. (1994)	Sanidine-Wadeite+Ky+Co-Holl for K-end: Jd+St-Ca-Ferrite struct + St for Na	Yes	Pow XRD EPMA

K2O-Al2O3-SiO2

Urawaka et al. (1994)	Sanidine < 6GPa then Wadeite+Kyanite+Coesite below 9 GPa then Holandite structure, melting at 1600 C	No	In situ synch XRD

Appendix 13 Thermoelastic properties of mantle mineral phases

Conditions refer to atmospheric pressure and temperature unless otherwise stated. References are indicated by single numbers in italics in columns after each value.

Structure	**GRAPHITE**		**DIAMOND**			
Composition	C		C			
Ks	161	*1*	443	*2*	584.8	*3*
dKs/dP			4	*2*		
dKs/dT (MPa/K)			-0.0087	*2*		
μ	109.3	*1*	535.7	*2*	346.3	*3*
dμ/dP			2.3	*2*		
dμ/dT (MPa/K)			-5.7	*2*		
Debye Temp (K)			1839	*3*		
α_1 x $10^{-4}K^{-1}$			0.02844	*4*		
α_2 x $10^{-8}K^{-2}$			1.06	*4*		
α_3 K			-0.00267	*4*		
Vo ($Å^3$)			45.38	*5*		
ρ (gcm^{-3})	2.26	*1*	3.512	*2*	3.51	*3*
Molar V (cm^3/mol)			3.4168	*4*		

1	see Bass (1995)
2	McSkimin and Bond (1972)
3	Simmons and Wang (1971)
4	Skinner (1956)
5	Wyckoff (1963)

Structure	**CORUNDUM**						**Rh_2O_3 (II)**					
Composition	Al_2O_3						Al_2O_3					
Ko (GPa)	262	*1*	257	*1*	254	*6*	262	*1*	261	*1*	359	*7*
	262	*1*	257	*1*	356	*7*	260	*1*	262	*1*		
dKo/dP	3.87	*1*	4.01	*1*	4.3	*6*	4.03	*1*	3.97	*1*	4.01	*7*
	4.29	*1*	4.05	*1*	3.93	*7*	4.48	*1*	3.88	*1*		
$d^2Ko/dP^2(GPa^{-1})$	-0.03	*1*	-0.016	*1*			-0.036	*1*	-0.011	*1*		
Ks	251.7	*2*	251.9	*3*								
dKs/dP	4.3	*11*										
dKs/dT (GPa/K)	-0.015	*11*										
μ	162.5	*2*	162	*3*								
Debye Temp (K)	1030	*3*										
δ	5	*12*										
α(/K)	2.60E-05	*9*										
α_1 x $10^{-4}K^{-1}$	0.2276	*13*										
α_2 x $10^{-8}K^{-2}$	0.4198	*13*										
α_3 K	-0.0897	*13*										
Vo ($Å^3$)	41.79	*1*	41.74	*1*	42.65	*6*	40.8	*1*	40.84	*1*	40.56	*7*
	41.8	*1*	41.79	*1*	41.56	*7*	40.78	*1*	40.84	*1*		
alpha V	6.40E+05	*4*										
beta V	9.00E+05	*4*										
ρ (gcm^{-3})	3.999	*5*	3.99	*3*								
Molar V (cm^3/mol)	2.558	*8*										

1	Marton and Cohen (1994)
2	Hearman (1979)
3	Sumino and Anderson (1984)
4	Robie et al. (1979)
5	Bass (1995)
6	d'Amour et al. (1978)
7	Cynn et al. (1990)
8	Holland and Powell (1990)
9	Skinner (1966)
10	Aldebert and Traverse (1984)
11	Goto et al. (1989)
12	Anderson and Isaak (1995)
13	Alexandrov and Ryzhova (1961)

Structure	**OLIVINE**											
Composition	Olivine		Mg_2SiO_4		$Fo_{91}Fa_9$		$Fo_{90}Fa_{10}$				Fe_2SiO_4	
Press (GPa)	0		0		0		0				0	
Temp (K)	300		298		298		298				298	
Ko (GPa)			129	*2*							137.9	*11*
			128	*3*								
dKo/dP			5.2	*2*							4	*11*
			5.37	*3*								
d^2Ko/dP^2			-0.15	*7*								
(dKT/dT)P GPa/K			-0.0224	*3*							-0.0258	*12*
Ks	129.1+8xFe	*1*	128.2	*4*	129.5	*7*	129	*8*			134	*13*
			128.6	*33*							132	*35*
			129.1	*34*							122	*36*
dKs/dP	5.2	*1*	4.8	*5*	4.6	*7*	4.2	*9*			5.2	*14*
dKs/dT (MPa/K)							-18	*10*	-0.017	*8*		
μ			80.5	*4*	77.6	*7*	79	*9*	79	*8*	50.7	*13*
			81.6	*34*							51	*35*
			81.1	*33*							54	*36*
$d\mu/dP$					1.9	*7*	1.4	*9*				
$d\mu/dT$ (MPa/K)							-13.6	*10*	-14	*8*		
Debye Temp (K)			757	*4*								
Gruneisen	1.25	*1*	1.25	*2*								
δ	4+1.5xFe	*1*	4	*2*								
α(/K)			3.72E-05	*2*								
			3.50E-05	*31*								
			2.50E-05	*6*								
$\alpha_1 \times 10^{-4}K^{-1}$			0.3052	*3*							0.266	*15*
$\alpha_2 \times 10^{-8}K^{-2}$			0.8504	*3*							0.8736	*15*
α_3 K			-0.5824	*3*							-0.2487	*15*
Vo ($Å^3$)			289.56	*39*							307.42	*39*
ρ (gcm^{-3})			3.21	*4*	3.325	*7*					4.38	*13*
Molar V $(cm)^3/mol$	43.67+2.6xFe	*1*	43.79	*2*							46.28	*16*
			43.67	*3*								

Structure	**WADSLEYITE**									
Composition	Mg_2SiO_4				$Fo_{92}Fa_8$		$Fo_{90}Fa_{10}$		Fe_2SiO_4	
Ko (GPa)	174	*2*	172	*3*					166	*21*
	172	*25*								
dKo/dP	4	*2*	4.3	*3*					4	*21*
(dKT/dT)P GPa/K	-0.0323	*3*							-0.0215	*21*
Ks	167	*1*	174	*18*			174	*18*		
dKs/dP	4	*1*	4.8	*17*			4.8	*17*		
dKs/dT (MPa/K)							-0.018	*20*		
μ	114	*18*					110	*18*		
$d\mu/dP$	1.7	*17*					1.7	*17*		
$d\mu/dT$ (MPa/K)							-0.02	*9*		
Debye Temp (K)	888	*18*								
Gruneisen	1.3	*2*	1.3	*1*						
δ	3	*2*								
α(/K)	3.07	*2*	3.2	*30*						
$\alpha_1 \times 10^{-4}K^{-1}$	0.2711	*3*							0.2319	*21*
$\alpha_2 \times 10^{-8}K^{-2}$	0.6885	*3*							0.7117	*21*
α_3 K	-0.5767	*3*							-0.243	*21*
Vo ($Å^3$)	538.14	*40*								
ρ (gcm^{-3})	3.474	*18*	3.472	*19*	3.585	*19*				
Molar V (cm^3/mol)	40.52+2.7xFe	*1*	40.51	*2*					43.15	*21*
	40.54	*3*								

Structure	**RINGWOODITE**											
Composition	Olivine		Mg_2SiO_4						Fe_2SiO_4			
Pressure (GPa)	0		0				0		0		0	
Temperature (K)	300		298				700		298		673	
Ko (GPa)			184	*2*	259	*23*	171	*37*	197	*26*	177	*38*
			183	*3*	239	*23*						
			241	*22*	184	*25*						
dKo/dP			4	*2*	4	*23*	4.4	*37*	4	*26*	5.4	*38*
			4.3	*3*	4.6	*22*						
			4	*24*	5	*32*						
(dKT/dT)P GPa/K			-0.0348	*3*	-0.027	*37*			-0.0357	*27*	-0.04	*38*
Ks	213-16xFe	*1*	184	*25*								
dKs/dP	4.8	*1*										
μ			119	*25*								
Debye Temp (K)			904	*25*								
Gruneisen	1.35	*1*	1.35	*2*								
δ			3	*2*								
α(/K)			2.55	*2*					2.14	*29*	2.62	*38*
			2.6	*30*								
α_1 x $10^{-4}K^{-1}$			0.2367	*3*	0.187	*37*			0.2455	*29*		
α_2 x $10^{-8}K^{-2}$			0.5298	*3*	0.421	*37*			0.3591	*29*		
α_3 K			-0.5702	*3*	-0.6537	*37*			-0.3703	*29*		
Vo (A^3)			524.56	*41*					558.26	*42*		
ρ (gcm^{-3})			3.559	*25*					4.848	*42*		
Molar V (cm^3/mol)	39.65+2.37xFe	*1*	39.49	*2*					42.02	*28*		
			39.65	*3*								

1 see Jeanloz and Thompson (1983)
2 see Akaogi et al. (1987)
3 Fei et al. (1990)
4 Sumino and Anderson (1984)
5 Graham and Barsch (1969)
6 Poirier (1991)
7 Webb (1989)
8 Isaak et al. (1989)
9 Duffy et al. (1995)
10 Isaak (1990)
11 Sumino (1979)
12 Watanabe (1982)
13 Isaak (1992)
14 Graham et al. (1988)
15 Suzuki et al. (1981)
16 Akimoto et al. (1976)
17 Gwanmesia et al. (1990)
18 Sawamoto et al. (1984)
19 Finger et al. (1992)
20 Fei et al. (1992)
21 Fei and Saxena (1986)
22 D'Arco et al. (1991)
23 Bouaziz and D'Arco (1993)
24 Sawamoto (1977)
25 Weidner et al. (1984)
26 Sato (1977)
27 Watanabe (1982)
28 Marumo et al. (1977)
29 Suzuki et al. (1979)
30 Akaogi et al. (1984)
31 Hazen (1976)
32 Gasparik (1990)
33 Kumuzawa and Anderson (1969)
34 Graham and Barsch (1969)
35 Akimoto (1972)
36 Chung (1970)
37 Meng et al. (1994)
38 Plymate and Stout (1994)
39 Fugino et al. (1981)
40 Horiuchi and Sawamoto (1981)
41 Sasaki et al. (1982)
42 Yagi et al. (1974)

Structure	**PEROVSKITE**									
Composition	$CaSiO_3$									
Ko (GPa)	280	*1*	247	*9*	288	*11*	288	*12*	325	*8*
	274	*2*	281	*4*	281	*4*	281	*4*		
	254	*3*	275	*10*	290	*6*	263	*7*		
dK_o/dP	4	*1*	3.85	*2*	4	*11*	4	*12*	4	*8*
	4.4	*3*	5.3	*9*	4	*4*	4.13	*7*		
	4	*4*	4	*10*	5.6	*6*	4	*4*		
$d^2K_o/dP^2(GPa^{-1})$					-0.077	*6*				
K_s	177	*5*								
μ	209	*6*	104	*5*						
Debye Temp (K)	917	*1*	750	*5*						
Gruneisen	1.96	*1*								
α(/K)	1.40E-05	*7*								
V_o (Å^3)	45.37	*4*	44.87	*6*						
	45.58	*8*	45.58	*11*						
ρ (gcm^{-3})	4.252	*4*	4.04	*5*						

1	see Kesson et al. (1994)	5	Sumino and Anderson (1984)	9	Hemley et al. (1987)
2	Wolf and Jeanloz (1985)	6	Sherman (1993)	10	Tarrida and Richet (1989)
3	Wentzcovitch et al. (1995)	7	Wolf and Bukowinski (1987)	11	Yagi et al. (1989)
4	Mao et al. (1989)	8	Yagi (1989)	12	Yagi et al. (1982)

Structure	**OPX**								**CPX**	
Composition	$MgSiO_3$						$FeSiO_3$		Cpx	
Press (GPa)	0		<4 GPa		4-8 GPa		0		0	
Temp (K)	298		298		298		298		300	
Ko (GPa)	108	*1*	95.8	*6*	122.8	*6*				
	107	*2*								
dKo/dP	7	*1*	14.9	*6*	5.6	*6*				
	4.2	*2*								
d^2Ko/dP^2	-1.6	*52*								
$(dKT/dT)_P$ (GPa/K)	-0.02	*2*								
Ks	107.5	*3*					116	*47*	108-10xFe	*5*
	108-10xFe	*5*								
	107.5	*46*					102	*48*		
dKs/dP	7	*5*							7	*5*
dKs/dT (MPa/K)	-0.0268	*51*								
μ	75.4	*3*					55	*47*		
	75.5	*46*					61	*48*		
Debye Temp (K)	731	*3*								
Gruneisen	1.1	*1*							1.1	*5*
δ	6	*1,5*							6	*5*
α(/K)	2.92E-05	*1*							3.20E-05	*43*
	2.30E-05	*4*								
	3.20E-05	*36*								
α_1 x $10^{-4}K^{-1}$	0.2947	*2*								
α_2 x $10^{-8}K^{-2}$	0.2694	*2*								
α_3 K	-0.5588	*2*								
Vo (Å^3)	832.49	*53*								
ρ (gcm^{-3})	3.2	*3*								
Molar V (cm^3/mol)	31.2875	*1*							31.29+1.69xFe	*5*
	31.33	*2*								
	31.33+1.63xFe	*5*								

Structure	**ILMENITE**		**GARNET**				**Ca-FERRITE**			
Composition	$MgSiO_3$		$MgSiO_3$		Diopside		¥		¥	
Pressure (GPa)	0		0		0		130		0	
Temperature (K)	298		298		298		2650		298	
Ko (GPa)			154	*1*	156	*1*			225	*38*
			171.8-0.11xEn	*39*						
dKo/dP	4	*45*	4.5	*1*	4.5	*1*			4	*38*
			assume 4	*39*						
Ks	212	*7*	177	*40*						
dKs/dP			4.5	*40*						
μ	132	*7*	101	*40*						
dμ/dP			1.45	*40*						
dμ/dT (MPa/K)			-10.1	*40*						
Debye Temp (K)	943	*7*							900	*38*
Gruneisen			1.1	*1*	1.1	*1*			1.3	*38*
δ			3.5	*40*	6	*1*				
			6	*1*						
α(/K)	2.50E-05	*44*	2.40E-05	*40*	2.46	*1*				
			2.57	*1*						
dα/dT (K)			3.90E-09	*40*						
α_1 x $10^{-4}K^{-1}$	0.244	*50*								
α_2 x $10^{-8}K^{-2}$	0	*50*								
Vo (A^3)	262.54	*54*	1513.1	*39*					236.4	*38*
			1516.6	*41*						
ρ (gcm^{-3})	3.795	*7*	3.556	*40*			5.51	*38*		
Molar V (cm^3/mol)	26.35+0.5xFe ¤	*5*	114	*1*	123.18	*1*				

Structure	**PEROVSKITE**							
Composition	$MgSiO_3$							
Ko (GPa)	262	*8*	309 at 0K	*13*	254	*16*	259	*21*
	258	*8*	246	*15*	266	*20*	272	*22*
	245	*19*	260	*10*	258	*10*	254	*16*
	247	*9*	247	*2*	266	*17*	266	*24*
	255	*8*	247	*9*	260	*25*	261	*49*
dKo/dP	3	*8*	4	*9*	3.9	*21*	4.5	*19*
	3 to 5	*10*	4	*10*	4	*9*	4	*16*
	4	*8*	4	*16*	3.9	*20*	4.2	*24*
	5	*8*	4.2	*17*	4	*22*	4.01	*25*
	4	*49*	4	*2*				
(dKT/dT)P GPa/K	-0.055	*2*	-0.028	*49*				
Ks	246.4	*11*						
μ	184.2	*11*	184	*15*	178	*21*		
Debye Temp (K)	1094	*12*						
α(/K)	1.80E-05	*25*	2.2E-05 <381K	*18*	4.4E-05	*45*		
	0.00002 *	42	4E-05 298<x<840K	*23*				
α_1 x $10^{-4}K^{-1}$	0.2627	*2*	0.00001982	*49*	0.2947	*36*		
α_2 x $10^{-8}K^{-2}$	1.5198	*2*	8.18E-09	*49*	0.2694	*36*		
α_3 K	-0.0429	*2*	0.474	*49*	-0.5588	*36*		
Vo (Å^3)	162.12	*13*	162.36	*15*	162.8	*9*	162.4	*16*
	162.352	*14*	162.752	*8*	162.8	*22*	162.75	*8*
ρ (gcm^{-3})	4.108	*11*	4.11	*12*				
Molar V (cm^3/mol)	24.5	*2*	24.5	*19*				

* - 298 to 1498K, ¥ - Na, Al, Mg silicate, ¤ - (Mg,Fe)SiO_3 with Fe<0.15

Structure	**PEROVSKITE**							
Composition	$(Mg,Fe)SiO_3$		$FeSiO_3$				MgAlSiPvk £	
Ko (GPa)	263	*26*	101	*33*			254	*38*
	261	*27*	287.2	*34*				
	263	*28*	230	*19*				
	260	*29*						
dKo/dP	3.9	*26*	3.6	*19*			4	*38*
	4	*27*	4.2	*33*				
	3.9	*28*	4	*34*				
	4	*29*						
(dKT/dT)P GPa/K			-0.02	*35*	-0.0596	*34*		
Ks	262	*5*						
dKs/dP	4	*5*						
Debye Temp (K)	1017	*26*					957	*38*
	825	*29*						
	1094	*27*						
	1060	*28*						
Gruneisen	1.96	*26*					1.96	*38*
	2.2	*29*						
	1.3	*27*						
	1.5	*28*						
δ	7	*26*						
	4.3	*27*						
	5	*28*						
Alpha (/K)	2.00E-05	*30*						
	5.00E-05	*32*						
α_1 x $10^{-4}K^{-1}$			0.2627	*34*				
α_2 x $10^{-8}K^{-2}$			1.5198	*34*				
α_3 K			-0.0429	*34*				
Vo ($Å^3$)							166.9	*38*
ρ (gcm^{-3})							5.73 $	*38*
Molar V (cm^3/mol)	24.46	*26*	32.95	*37*	25.2	*19*		
	24.46+1.03xFe	*5*						
	24.46	*28*						
	24.46	*27*	25.599	*34*				
	24.39	*29*						

£ - 16-24 wt% Al_2O_3, $ - 130 GPa, 2650K

1	Akaogi et al. (1987)	*19*	Guyot et al. (1988)	*37*	Syono et al. (1971)
2	Fei et al. (1990)	*20*	Knittle and Jeanloz (1987)	*38*	see Kesson et al. (1994)
3	Sumino and Anderson (1984)	*21*	Wentzcovitch et al. (1995)	*39*	Yagi et al. (1992)
4	Poirier (1991)	*22*	Horiuchi et al. (1987)	*40*	Sawamoto (1987)
5	see Jeanloz and Thompson (1983)	*23*	Knittle et al. (1987)	*41*	Matsubara et al. (1990)
6	Hugh-Jones and Angel (1994)	*24*	Mao et al. (1989)	*42*	Kato et al. (1995)
7	Weidner and Ito (1985)	*25*	Wolf and Bukowinski (1987)	*43*	Gasparik (1990)
8	Yagi et al. (1978)	*26*	Hemley et al. (1992)	*44*	Ashida et al. (1988)
9	Kudoh et al. (1987)	*27*	Wang et al. (1994)	*45*	Gasparik (1990)
10	Yagi et al. (1982)	*28*	Anderson and Matsuda (1994)	*46*	Weidner et al. (1977)
11	Yeganegh-Haeri et al. (1989)	*29*	Knittle et al. (1986)	*47*	Akimoto (1972)
12	Haeri et al. (1988)	*30*	Wang et al. (1991)	*48*	Chung (1974)
13	D'Arco et al. (1993)	*31*	Anderson et al. (1995)	*49*	Funamori et al. (1996)
14	Ito and Matsui (1978)	*32*	Mao et al. (1991)	*50*	Ashida et al. (1988)
15	Yeganeh-Haeri et al. (1990)	*33*	Akimoto (1972)	*51*	Frisilo and Barsch (1972)
16	Ross and Hazen (1990)	*34*	Fei and Saxena (1986)	52	Webb and Jackson (1994)
17	Strixude and Cohen (1993)	*35*	Watanabe (1982)	*53*	Sasaki et al. (1982)
18	Ross and Hazen (1989)	*36*	Skinner (1966)	*54*	Horiuchi et al. (1982)

Structure	**QUARTZ**		**COESITE**		**STISHOVITE**											
Composition	SiO_2		SiO_2		SiO_2										2.8wt% Al_2O_3	
Ko (GPa)					314	*2*	292	*9*	306	*12*	277.4	*8*	300	*16*	314	*17*
					313	*3*	288	*10*	344	*13*	298	*15*	306	*5*		
					328	*4*	313	*11*	324	*14*	376	*6*				
dKo/dP					4	*5*	6	*3*	5.86	*9*	4	*16*			5	*17*
					4	*4*	3.14	*10*	0.7	*15*	2 to 7	*13*				
					4	*6*	2.8	*4*	4.04	*14*	2.8	*11*				
					6	*2*										
(dKT/dT)P (GPa/K)					-0.047	*2*										
Ks	37.8	*21*	98	*1*	316	*1*	316	*7*								
dKs/dP	6.4	*23*	7	*1*	4	*1*										
dKs/dT (GPa/K)	-0.0085	*23*														
μ	44.3	*21*	61.6	*24*	220	*7*	232.2	*8*								
Debye Temp (K)					1217	*8*									1192	*17*
Gruneisen			0.35	*1*	1.7	*1*	1.7	*5*							1.7	*17*
δ					3	*5*										
α(/K)					2.00E-05	*5*	2.30E-05	*19*								
α_1 x $10^{-4}K^{-1}$	0.1417	*22*	0.0597	*20*	0.1023	*2*										
α_2 x $10^{-8}K^{-2}$	9.6581	*22*	0.7697	*20*	1.35	*2*										
α_3 K	-1.6973	*22*	-0.1231	*20*	0	*2*										
Vo (A^3)	113.01	*25*	548.76		46.1	*4*	46.615	*11*	45.64	*9*	14.01	*2*	14.01	*5*		
					46.591	*3*	47.5	*10*	46.16	*14*						
ρ (gcm^{-3})	2.648	*21*	2.911	*24*	4.29	*7*	4.29	*8*							5.22*	*18*
Molar V (cm)	22.688	*25*	20.568	*1*	14.01	*1*										

* 2650K, 130 Gpa

1 See Jeanloz and Thompson (1983)
2 Fei et al. (1990)
3 Sugiyama et al. (1987)
4 Sherman (1993)
5 See Akaogi et al. (1987)
6 Tsuchida and Yagi (1989)
7 Weidner et al. (1982)
8 Sumino and Anderson (1984)
9 Keskar et al. (1991)
10 Park et al. (1988)
11 Ross et al. (1990)
12 Weidner et al. (1989)
13 Liu et al. (1974)
14 Cohen (1991)
15 Sato (1977)
16 Basset and Barnet(1970)
17 See Kesson et al. (1994)
18 Kesson et al. (1994)
19 Ito et al. (1974)
20 Skinner (1966)
21 Hearmon (1979)
22 Ackermann and Sorrell (1974)
23 Sumino and Anderson (1984)
24 Weidner and Carlton (1977)
25 LePage et al. (1980)
26 Smyth et al. (1987)

Structure	**PERICLASE**																	
Composition	fPer		MgO						Fe$_{0.943}$O		Fe$_{0.95}$O		FeO					
Ko (GPa)			160.3	*2*	162.1	*24*							154.5	*3*	178	*19*	154	*26*
			160	*3*	162.5	*4*							180	*14*	181.4	*11*	169	*27*
			162.3	*23*	162.8	*29*							153	*22*	185	*25*	157	*28*
dKo/dP			4.85	*3*	3.11	*24*							2.75	*3*	4	*27*		
			4.27	*23*	4.13	*4*							4	*26*	4	*28*		
d^2Ko/dP^2			-0.03	*4*														
KT			4.13	*2*									4	*14*				
(dKT/dT)P GPa/K			-0.0272	*2*									-0.02	*14*				
Ks	162.7+17xFe	*1*	79.16	*5*	162.5	*4*	162.8	*20*	154.8	*12*	153	*13*						
			162.7	*6*	162.8	*7*	163	*19*					182	*19*				
dKs/dP	4.1-0.5xFe	*1*	4.13	*4*					5.1	*12*			4.9	*15*				
dKs/dT (MPa/K)			-14.5	*4*														
μ			130.3	*5*	130.8	*4*	131	*19*	46.4	*12*	46.8	*13*	59	*19*				
dμ/dP			2.5	*4*					0.71	*12*								
dμ/dT (MPa/K)			-24	*4*														
Debye Temp (K)			936	*7*														
Gruneisen	1.5+0.07xFe	*1*											1.63	*16*				
δ	3.03	*1*																
dα/dT (K)													0	*17*				
α_1 x $10^{-4}K^{-1}$			0.3681	*2*	0.4232	*8*	0.31	*9*					0.1688	*14*				
α_2 x $10^{-8}K^{-2}$			0.9283	*2*	0.363	*8*	0.42	*18*					0.204	*14*				
α_3 K			-0.7445	*2*	-0.01756	*8*							0.019	*14*				
Vo (A^3)			74.71	*8*									81.35	*30*				
ρ (gcm^{-3})			3.584	*5*	3.584	*6*	3.58	*10*	5.708	*12*	5.73	*13*						
Molar V (cm^3/mol)	11.25+1xFe	*1*	11.25	*8*	11.25	*3*	12.848	*21*					12.25	*3*				
			11.25	*2*	11.247	*21*							12.25	*14*				

1	see Jeanloz and Thompson (1983)
2	Fei et al. (1990)
3	Richet et al. (1988)
4	Jackson and Neisler (1982)
5	Hearmon (1979)
6	Yoneda (1990)
7	Sumino and Anderson (1984)
8	Skinner (1956)
9	Poirier (1991)
10	Simmons and Wang (1971)
11	Sumino et al. (1980)
12	Jackson and Khanna (1990)
13	Berger et al. (1981)
14	Fei and Saxena (1986)
15	Jackson et al. (1990)
16	Jeanloz and Ahrens (1980)
17	Carter (1959)
18	Hazen (1976b)
19	Jackson et al. (1978)
20	Spetzler (1970)
21	Reeber et al. (1995)
22	Berger et al. (1981)
23	Chang and Barsch (1969)
24	Bonczar and Graham (1982)
25	Jeanloz and Ahrens (1980)
26	Mao et al. (1969)
27	Yagi et al. (1985)
28	Jeanloz and Sato-Sorensen (1986)
29	Sumino et al. (1983)
30	Hentschel (1970)

Structure	**GARNET**																**PEROVSKITE**			
Composition	Pyrope				*Garnet		Gr_1Py_1		(yMj, 1-yPy)		$Mj_{41}Py_{59}$		$Mj_{33}Py_{67}$		Al		Pyrope		Grossular	
Ko (GPa)	166	*1*					167	*1*									216	*10*	283	*11*
dKo/dP	4.5	*1*					4.5	*1*									4	*10*	assume 4	*11*
d^2Ko/dP^2	-0.28	*21*																		
Ks	170	*2*	177	*4*							164	*9*	170	*8*	180.1	*13*				
	172.8	*3*	176.6	*5*											177.9	*14*				
	165.8	*13*	173.6	*14*																
dKs/dP	4.74	*16*							4.5	*7*										
dKs/dT (MPa/K)	-0.0188	*16*																		
μ	92.6	*2*	89	*4*	98	*6*					89	*9*	92	*8*	94.7	*13*				
	92	*3*	89.6	*5*											98.3	*14*				
	91.4	*13*	91.7	*14*																
Debye Temp (K)	788	*5*																		
Gruneisen	1.1	*1*					1.1	*1*	1.1	*7*										
δ	6	*1*					6	*1*	6.3	*7*										
α (/K)	2.57E-05	*1*					2.46	*1*												
	2.70E-05	*12*																		
α_1 x $10^{-4}K^{-1}$	0.288	*15*																		
α_2 x $10^{-8}K^{-2}$	0.2787	*15*																		
α_3 K	-0.5221	*15*																		
Vo ($Å^3$)	1501.9	*18*															163.78	*10*	183.96	*11*
ρ (gcm^{-3})	3.704	*2*	3.567	*3*							3.555	*9*	3.545	*8*						
	3.563	*4*	3.56	*5*																
Molar V (cm^3/mol)	115.6	*2*	113.21	*1*			119.45	*1*	¥	*7*										

* - $(Mg_{0.46}Mn_{0.25}Fe_{0.22}Ca_{0.07})_3Al_2Si_3O_{12}$, ¥ - 113.19+2.04xFe+y(0.94+1.32xFe), Gr - grossular, Py - pyrope, Mj - majorite ($MgSiO_3$)

1 see Akaogi et al. (1987)
2 Babuska et al. (1978)
3 O'Neill et al. (1991)
4 Leitner et al. (1980)
5 Sumino and Anderson (1984)
6 Karato et al. (1995)
7 see Jeanloz and Thompson (1987)
8 Yeganeh-Haeri et al. (1990)
9 Bass and Kanzaki (1990)
10 Irifune et al. (1992)
11 Yusa et al (1995)
12 Hazen and Finger (1978)
13 Izaak and Graham (1976)
14 Babuska et al. (1978)
15 Suzuki and Anderson (1983)
16 Bonczar and Graham (1977)
17 Webb (1989)
18 Armbruster et al. (1992)

Appendix 14 Seismologically based models of the mantle and PREM

The variation of seismic velocities, S and P-waves, with depth is one of the best constrained relationships in the Earth's mantle. It represents a powerful tool for calculation of other mantle properties through simple physical identities and ultimately provides a framework for the fitting of compositional models. The most commonly used Earth model based on seismic constraints is the PREM model (Dziewonski and Anderson, 1981)[1]. It predicts the distribution of density, bulk and shear modulii through the Earth. Two simple expressions govern the relationship between S and P wave velocity with elastic constants:

$$\alpha = \sqrt{\frac{K + \frac{4}{3}\mu}{\rho}}$$ Equation A14_1

$$\beta = \sqrt{\frac{\mu}{\rho}}$$ Equation A14_2

Where α is P-wave velocity (ms^{-1}), β is S-wave velocity (ms^{-1}), ρ is density in (gm^{-3}), μ is shear modulus (Pa) and K is bulk modulus (Pa).

In order to solve for the three unknown variables, however, a third equation is required. This relies upon the variation of density with pressure of a spherical object. Assuming that the Earth is made of an infinite series of homogeneous shells, the increase in pressure (δP) from a depth $r+\delta r$ to r is simply determined by the weight of the shell of thickness δr.

$$\delta P=-g(r)\rho(r)$$ Equation A14_3

or, in differential form

$$\frac{dP}{dr} = -g(r)\rho(r)$$ Equation A14_4

---

[1] Stacey (1995) subjected PREM to a rigorous test on the basis of thermodynamic derivation of the elastic properties of crystalline material. He asserts the relationship: dK/dP against P/K must show a monotonous decrease of dK/dP with increasing P/K. Both for the outer core and lower mantle, values of dK/dP, K and P from PREM do not fit this observation. Stacey (1995) attests that the reason that PREM appears to predict μ, K and P well is that it affects μ and K in the same way. It should be noted that suspect values may not, however, be due to limitations of the mathematics employed but due to inhomogeneity in the earth. This, as section 4.4.2 discusses, can be considered to be a most reasonable explanation. Furthermore, despite any criticisms of PREM for the purposes of this study it can be considered satisfactory because it is applied only in order to predicte P with depth for use in section 7.1.2.

The acceleration due to gravity at radius r is simply due to the mass towards the centre of the sphere from radius r inwards: the mass of outer shells has a zero net gravitational attraction. Therefore g(r) can be expressed as

$$g(r) = \frac{GM_r}{r^2}$$ Equation A14_4

So Equation A14_4 becomes

$$\frac{dP}{dr} = -\frac{GM_r \rho(r)}{r^2}$$ Equation A14_5

Determination of density with depth i.e. δρ/δr, is required which can be expressed as

$$\frac{d\rho}{dr} = \frac{dP}{dr}\frac{d\rho}{dP}$$ Equation A14_6

Using Equation A14_6 this distribution can be expressed as

$$\frac{d\rho}{dr} = -\frac{GM_r \rho(r)}{r^2}\frac{d\rho}{dP}$$ Equation A14_7

At this stage it is useful to express dρ/dP in terms of the bulk modulus, K:

$$K = \frac{dP}{dv / V}$$ Equation A14_8

Where dv/V is the fractional change in volume (unitless)

Since density is the ratio of mass to volume:

$$\frac{d\rho}{dV} = -\frac{m}{V^2} = -\frac{\rho}{V}$$ Equation A14_9

Where m is mass (g) and V is volume (m^3).

Substituting into Equation A14_8 gives:

$$K = \rho\frac{dP}{d\rho}$$ Equation A14_10

So Equation A14_7 thus becomes:

$$\frac{d\rho}{dr} = -\frac{GM_r \rho(r)}{r^2}\frac{\rho(r)}{K}$$ Equation A14_11

Now, combining Equations A14_1 amd A14_2 gives:

$$\frac{K}{\rho} = \alpha^2 - \frac{4}{3}\beta^2$$ Equation A14_12

So substituting into Equation A14_11, gives an expression of density distribution with radius as a function of measurable seismic parameters:

Adams-Williamson Equation $$\frac{d\rho}{dr} = -\frac{GM_r\rho(r)}{r^2(\alpha^2 - {}^4\!/_3\beta^2)}$$ Equation A14_13

This is termed the Adams-Williamson equation.

Calculating density with depth directly from Equation A14_13, however, gives an unrealistic density distribution for the Earth, principally because the main assumptions underlying the equation are false: that the Earth has a homogeneous composition, no phase changes and the temperature gradient is adiabatic. These assumptions can, however, be corrected for to some degree. Because the mantle is assumed to convect, heat flow is likely to be superadaibatic. Equation A14_13 can thus be modified by adding a correction term of $a\rho(r)\tau$ to the right hand side to give equation A14_14, where α is the coefficient of thermal expansion (K^{-1}) and τ is the difference between actual temperature and adiabatic temperature at a given depth.

$$M_r = M_E - 4\pi\int_{a=r}^{a=R} \rho(a)a^2\,da$$ Equation A14_14

Where M_E is the mass of the Earth (g), M_r is the mass within radius r and R is the radius of the Earth (m)

To solve the problem of compositional variation and phase changes with depth, Equation A14_14 is solved in successive parts with the Earth split into crust, upper and lower mantle, outer and inner core and estimates of density jump at each boundary incorporated. Only certain combinations of density jump will satisfy the criteria that the total mass of all the shells must equal the mass of the Earth. In order to further constrain which combination is correct a further independent observations are required. These come in the form of measurement of the Earth's moment of inertia which can be determined by observations of orbit and is sensitive to the distribution of mass in the Earth; and experimental determination of the density changes resulting from phase transitions expected through the Earth.

A number of models (e. g. PREM) follow from such a procedure, results varying principally due to application of differing interpretations of the results of experimental work on phase relations. From PREM, the variation of depth with pressure (Table A14_1) is employed in section 7.1 and follows the relationship of equation A14_15 constructed as a best fit (R^2 =0.9997) of data taken from a tabulation of PREM values in Poirier (1991). Equation A14_15 is presented graphically in figure 7.1_6.

$$depth = 30.799P - 0.1345P^2 + 0.0005P^3$$ Equation A14_15

where depth is expressed in km and pressure, *P*, is expressed in GPa

Table A14_1 Summary of PREM model data

Pressure (GPa)	Depth (km)	Pressure (GPa)	Depth (km)
0	0	21	592
1	31	22	618
2	61	23	643
3	91	24	669
4	121	25	694
5	151	26	719
6	180	27	743
7	209	28	768
8	238	29	792
9	267	30	816
10	295	31	840
11	323	32	864
12	351	33	888
13	379	34	911
14	406	35	935
15	433	36	958
16	460	37	981
17	487	38	1004
18	514	39	1026
19	540	40	1049
20	566		

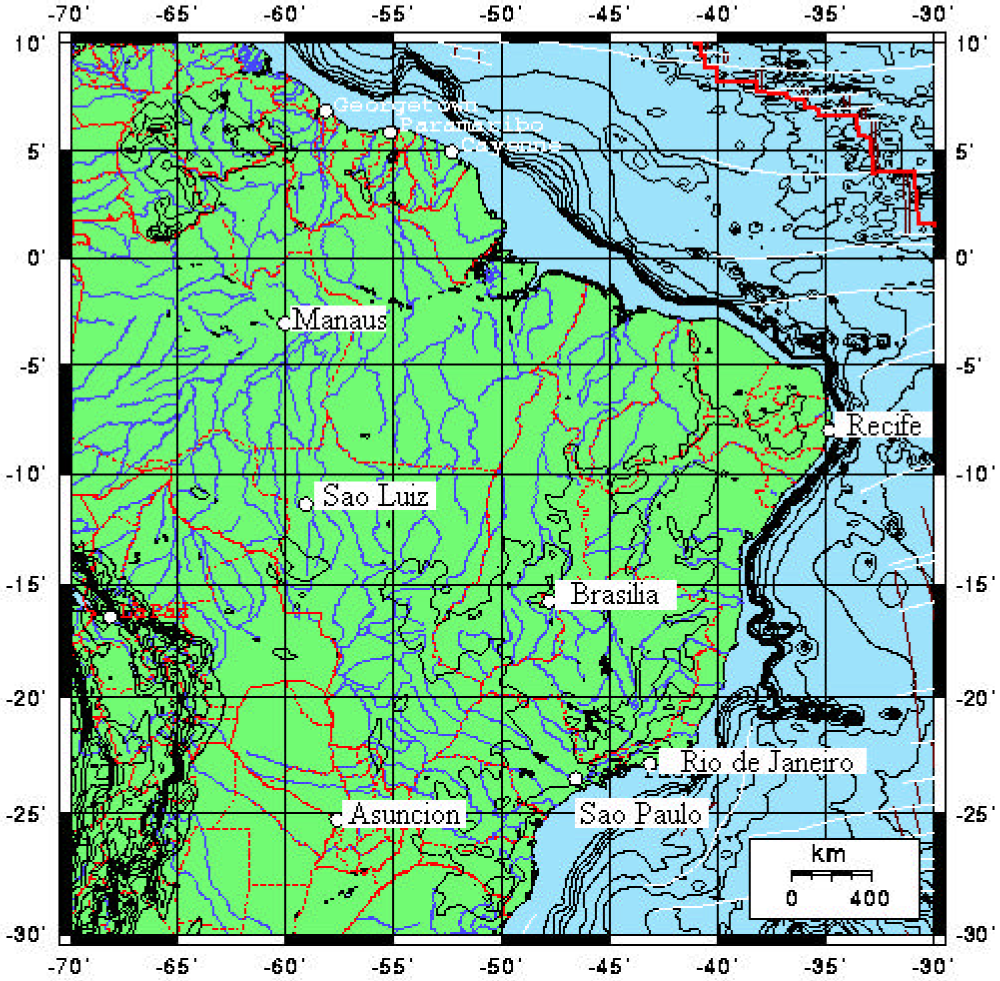

Figure 1.2_1 Location of the São Luiz alluvial diamond deposit within Brazil

Map created at the Online Map Creation facility, Kiel (http://www.aquarius.geomar.de/omc/), Wessel and Smith (1995)

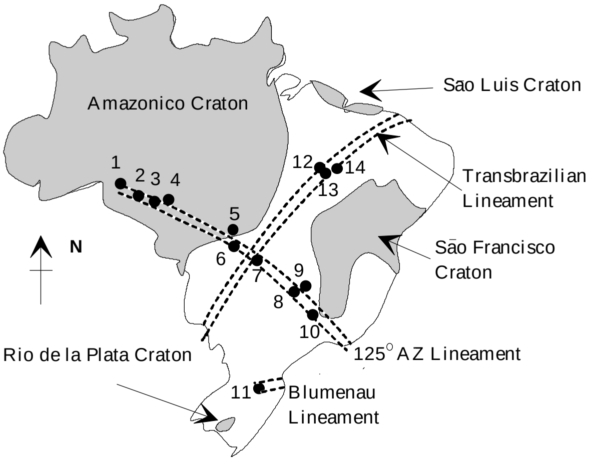

Figure 1.2_2 Principal Structural features of the Geology of Brazil

Kimberlite / lamproite provinces: 1 - Ariquimes, 2 - Pimenta Buemo, 3 - Vilheno, 4 - Aripuana Juina (São Luiz), 5 - Paranatinga, 6 - Poxoreu, 7 - Amorinopolis, 8 - Alto Paranaiba, 9 - Presidente Olegario, 10 - Bambui, 11 - Lajes, 12 - Redondao, 13 - Santa Filomena-Bom Jesus, 14 - Picus. After Tompkins (1992)

Figure 1.2_3 Reconstruction of the African and S. American plates at 144 Ma.

Reconstruction shows that the Amazonica, São Luis and W. African Cratons appear to have been initially part of a single body. The locations of São Luiz and S. E. Guinean alluvial diamond deposits are indicated by black dots on the Amazonica and W. African Cratons respectively.
Craton locations from Dawson (1980) and Tompkins (1992). Construction by the computer programme GLG-Plates (Ford, C. E., University of Edinburgh, 1995) using an orthorhombic projection and viewing down -50° Latitude, -5° Longitude.

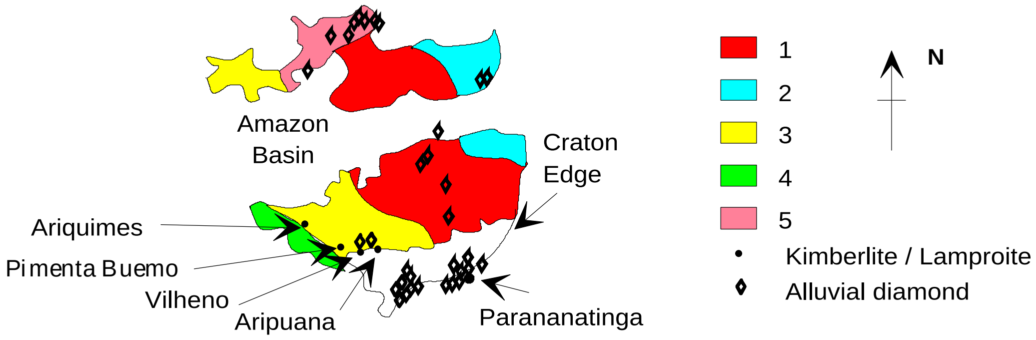

Figure 1.2_4 Detail of the Amazonica Craton within Brazil

The São Luiz deposit, although lying within the limits of the Amazonico Craton, is not located over an area of craton root, but within the 1.75 - 1.5 Ga Rio Negro Juruena Mobile Belt.
1 - Central Amazonico Province, 2 - Maroni Mobile Belt, 3 - Rio Negro Juruena Mobile Belt, 4 - Rondoman Mobile Belt, 5 - Phanerozoic Cover, 6 - Alluvial Diamond Occurrences 7 - Juina diamond deposits (São Luiz). After Tompkins (1992)

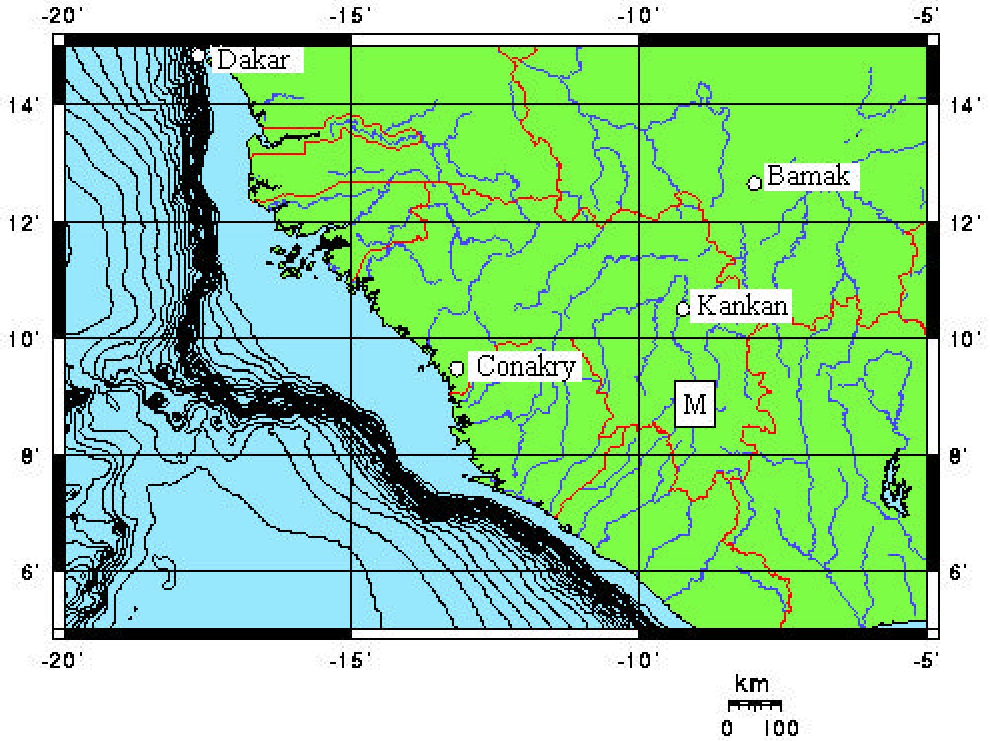

Figure 1.3_1 Geographical location map of Guinea and some of the diamond deposits of the S.E.

M - The drainage area of the Mandala Basin and source of diamonds described by Sutherland (1993).
Map created at the Online Map facility, Kiel (http://www.aquarius.geomar.de/omc/), Wessel and Smith (1995)

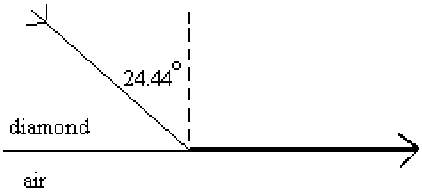

Figure 1.4_1 Total internal reflection

Light incident on a diamond / air interface at any angle > 24.44° will be completely reflected back into the diamond.

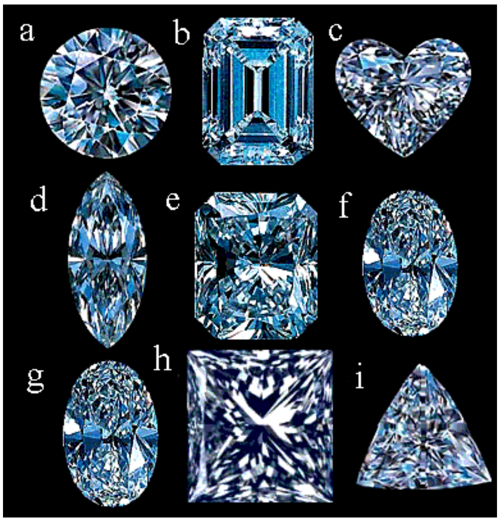

Figure 1.4_2 Diamond Shapes

a - Brilliant, b - Emerald, c - Heart, d - Marquise, e - Radiant, f - Oval, g - Pear, h - Princess, i - Trillions

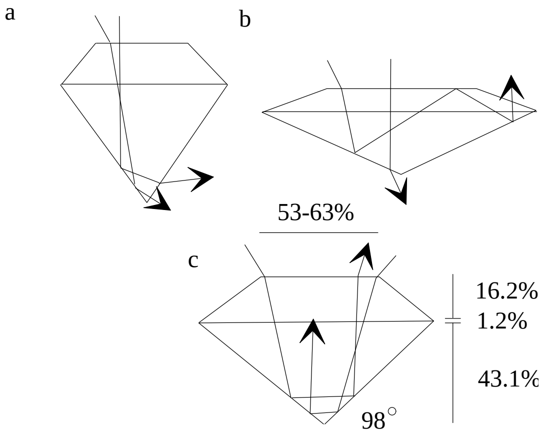

Figure 1.4_3 Light refraction in diamond in terms of table and depth

a - The stone is cut too deep, producing a dull stone, b - The stone is cut too shallow, producing a light by lifeless stone, c - A well cut stone produces the diamond’s characteristic brilliance.

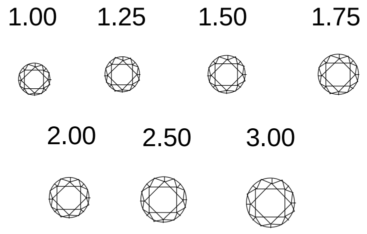

Figure 1.4_4 Scale diagram of 1 - 3 carat brilliant cut stones

Sizes in carats

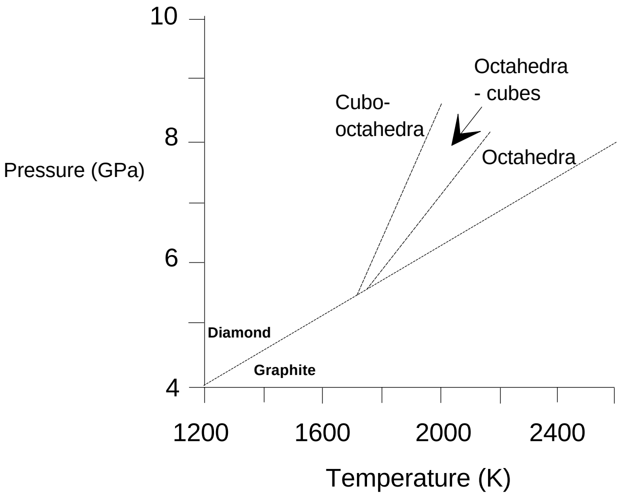

Figure 1.5_1 Regions of cubic and octahedral growth of diamond

From Giardini and Tydings (1962).

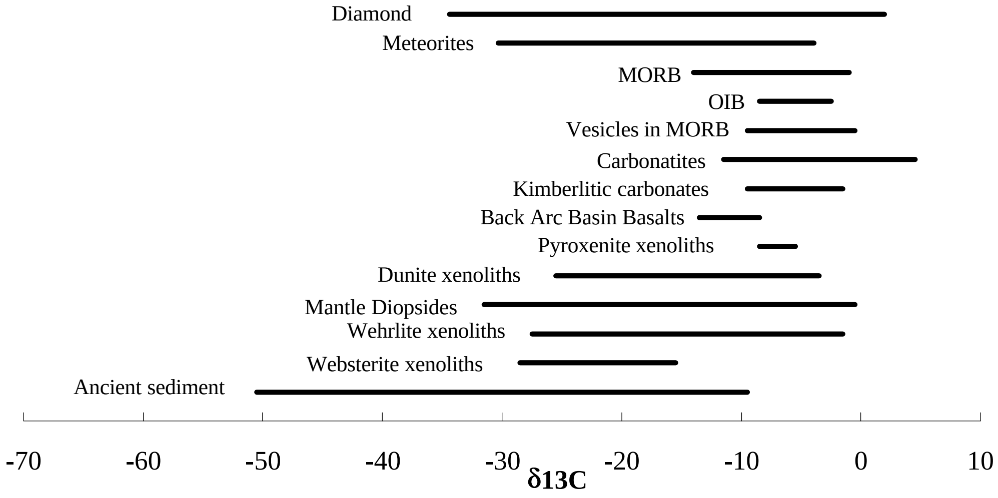

Figure 1.5_2 Ranges in $\delta^{13}C$ composition of mantle rocks and ancient sediment

Diamond exhibits a greater range in $\delta^{13}C$ composition than other mantle samples and is particularly coincident with the range found in meterorites.
From van Heerden (1993) and Deines and Wickman (1973)

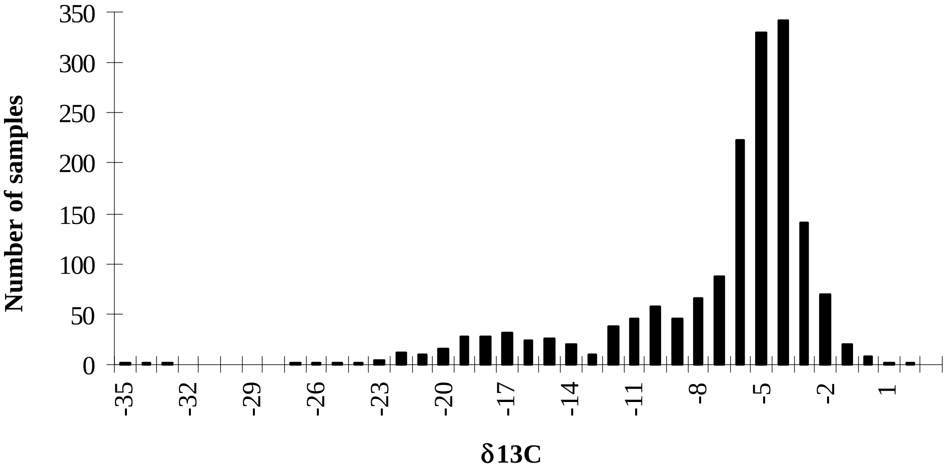

Figure 1.5_3 Distribution of $\delta^{13}C$ composition of natural diamonds

Data from van Heerden (1993), Hill (1989), Daniels (1991), Deines et al. (1987, 1989, 1991, 1993), Cartigny et al. (1996), Wilding (1990), Otter (1989), Jaques et al. (1989), Harte and Otter (1992), Deines and Harris (1995), Boyd and Pillinger (1994), Boyd et al. (1987, 1992, 1994), Smirnov et al. (1979), Javoy et al. (1984), Sobolev et al. (1979), McDade and Harris (1997, *personal communication*) and the present study.

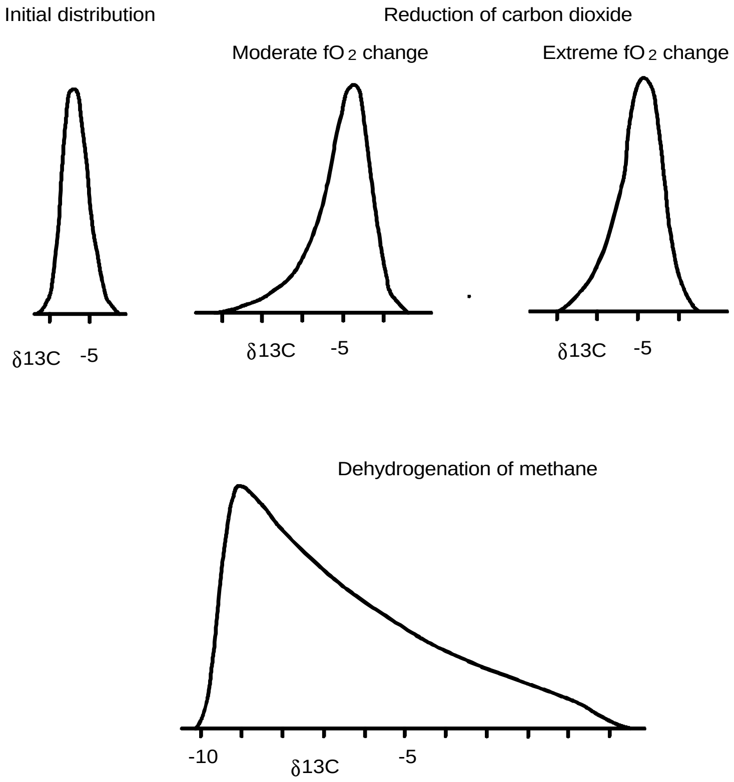

Figure 1.5_4 Carbon isotopic distribution expected of diamond precipitated from a $\delta^{13}C$ = -5‰ by reduction of CO_2 or dehydrogenation of CH_4

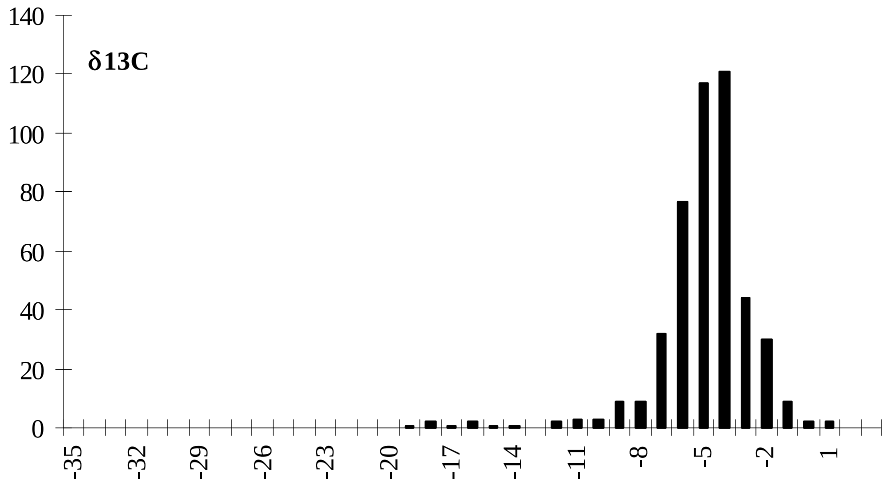

Figure 1.5_5 $\delta^{13}C$ distribution of peridotitic inclusion - bearing diamonds from worldwide localities

References, see figure 1.5_3

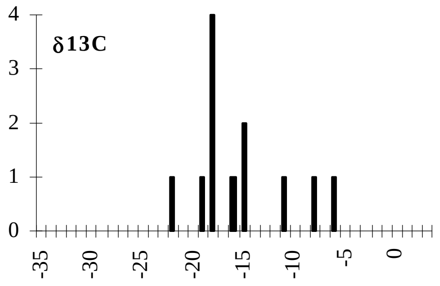

Figure 1.5_6 $\delta^{13}C$ of websteritic diamonds

Data from Deines et al. (1993) and McDade and Harris (1997, *personal communication*)

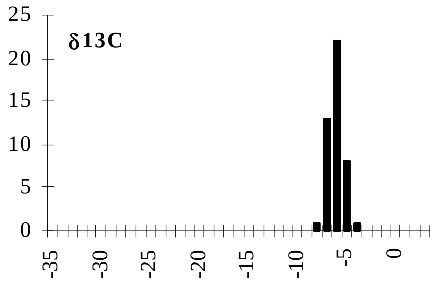

Figure 1.5_7 δ^{13}C of coated diamonds

Data from Boyd et al. (1987, 1992 and 1994)

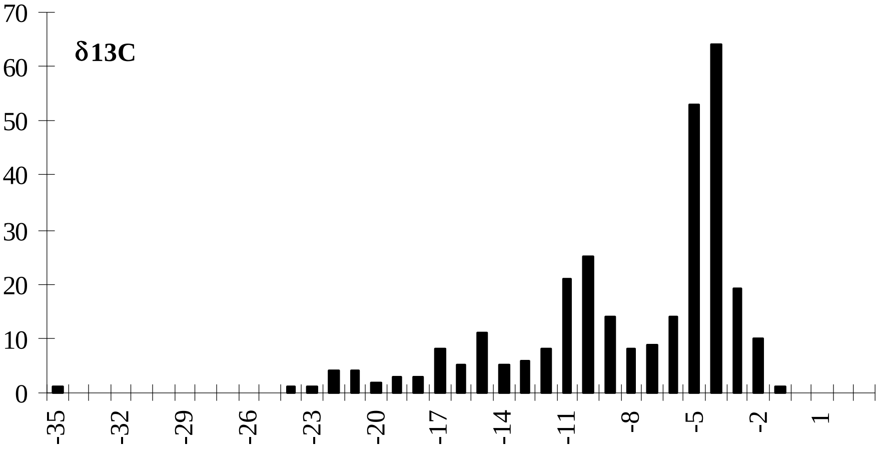

Figure 1.5_8 $\delta^{13}C$ composition of eclogitic inclusion - bearing diamonds from worldwide localities

Data sources, see figure 1.5_3

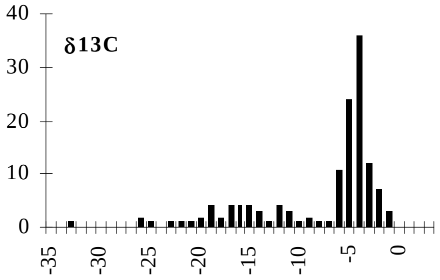

Figure 1.5_9 δ^{13}C composition of sulphide - bearing diamonds

Data from Deines and Harris (1995)

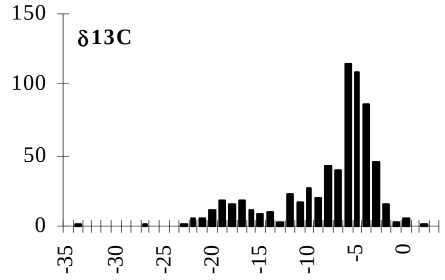

Figure 1.5_10 $\delta^{13}C$ composition of diamonds of unknown paragenesis

Data sources, see figure 1.5_3

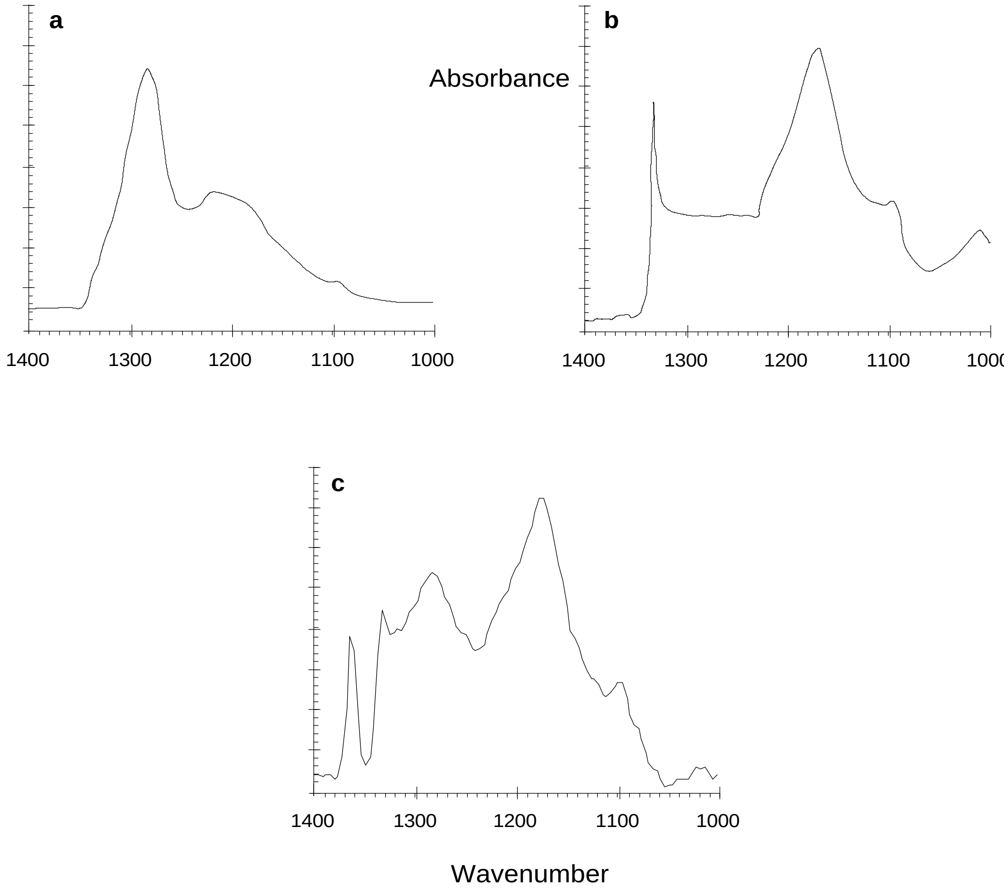

Figure 1.5_11 Summary of FTIR characteristics of natural diamonds in the one phonon region

a - IaA spectrum, b - IaB spectrum, c - IaAB spectrum showing platelet absorption. Wavenumbers in cm^{-1}

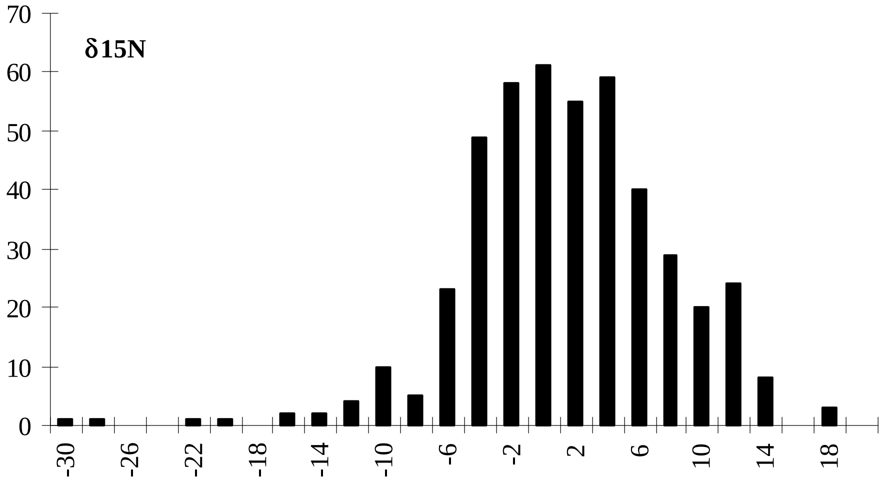

Figure 1.5_12 Distribution of $\delta^{15}N$ composition of natural diamonds

Data from Boyd and Pillinger (1994), Boyd et al. (1987, 1992 and 1994), Javoy et al. (1984), van Heerden (1993) and the present study.

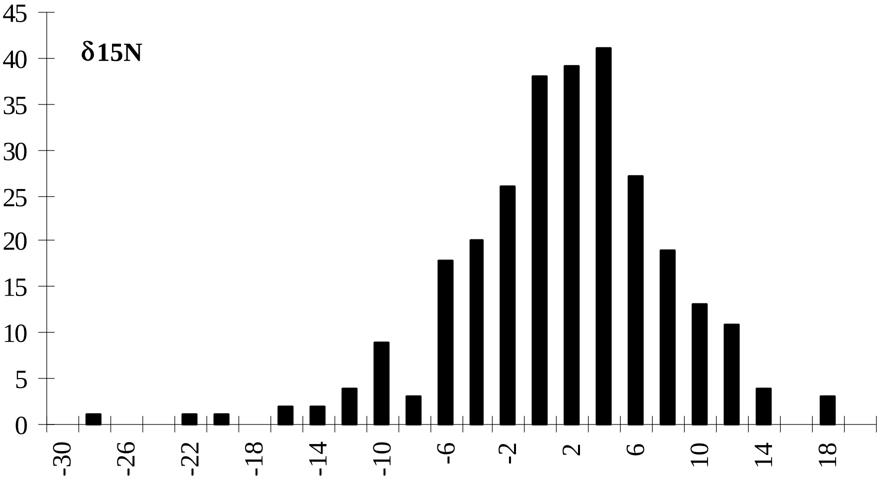

Figure 1.5_13 $\delta^{15}N$ composition of diamonds of unknown paragenesis

Data from Boyd and Pillinger (1994), Boyd et al. (1987, 1992 and 1994), Javoy et al. (1984), van Heerden (1993) and the present study.

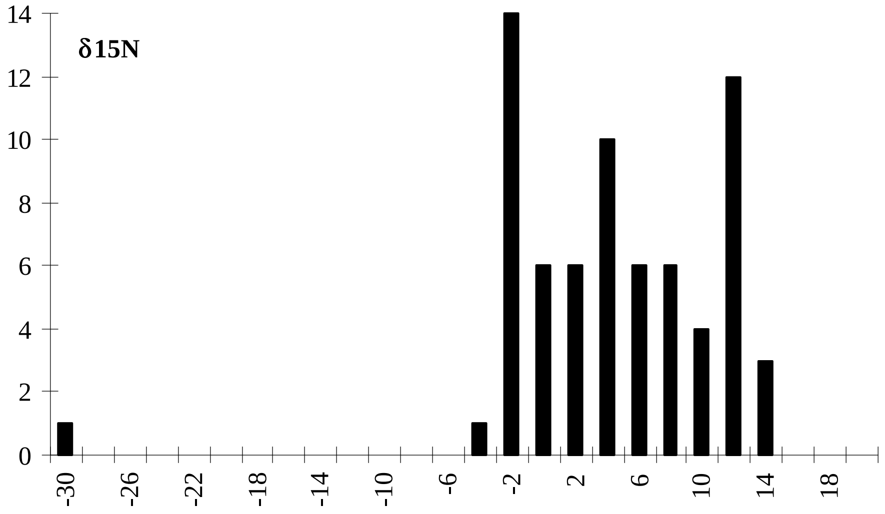

Figure 1.5_14 δ^{15}N composition of diamonds of eclogitic paragenesis

Data from van Heerden (1993).

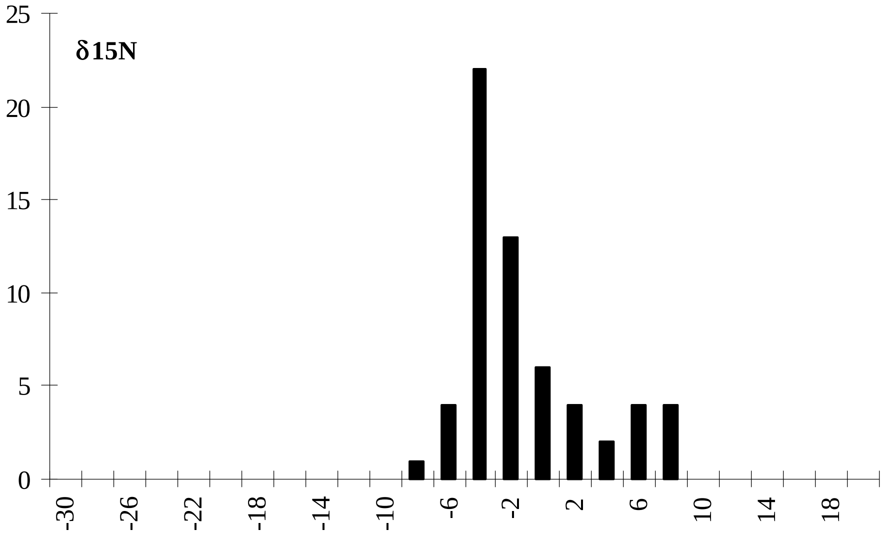

Figure 1.5_15 δ^{15}N composition of coats of coated diamonds

Data from Boyd et al. (1987, 1992, 1994) and Boyd and Pillinger (1994).

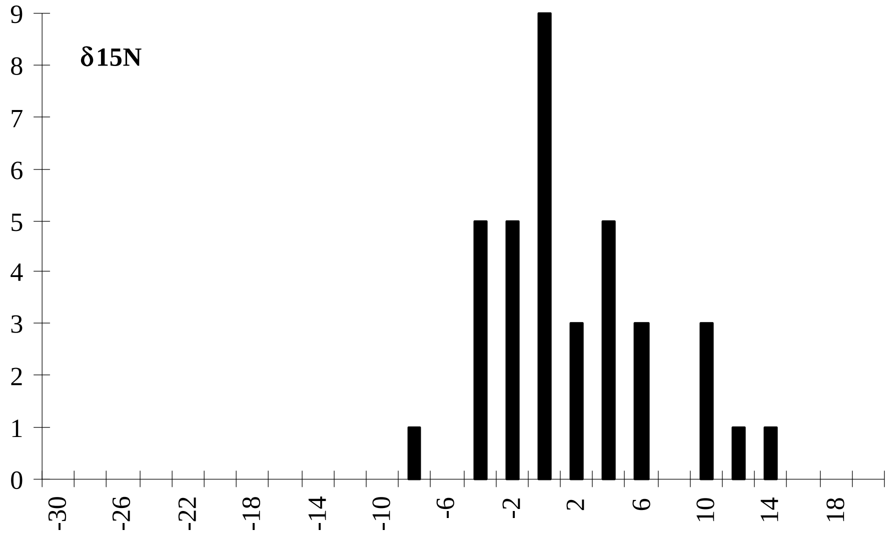

Figure 1.5_16 $\delta^{15}N$ composition of diamonds of peridotitic paragenesis

Data from van Heerden (1993).

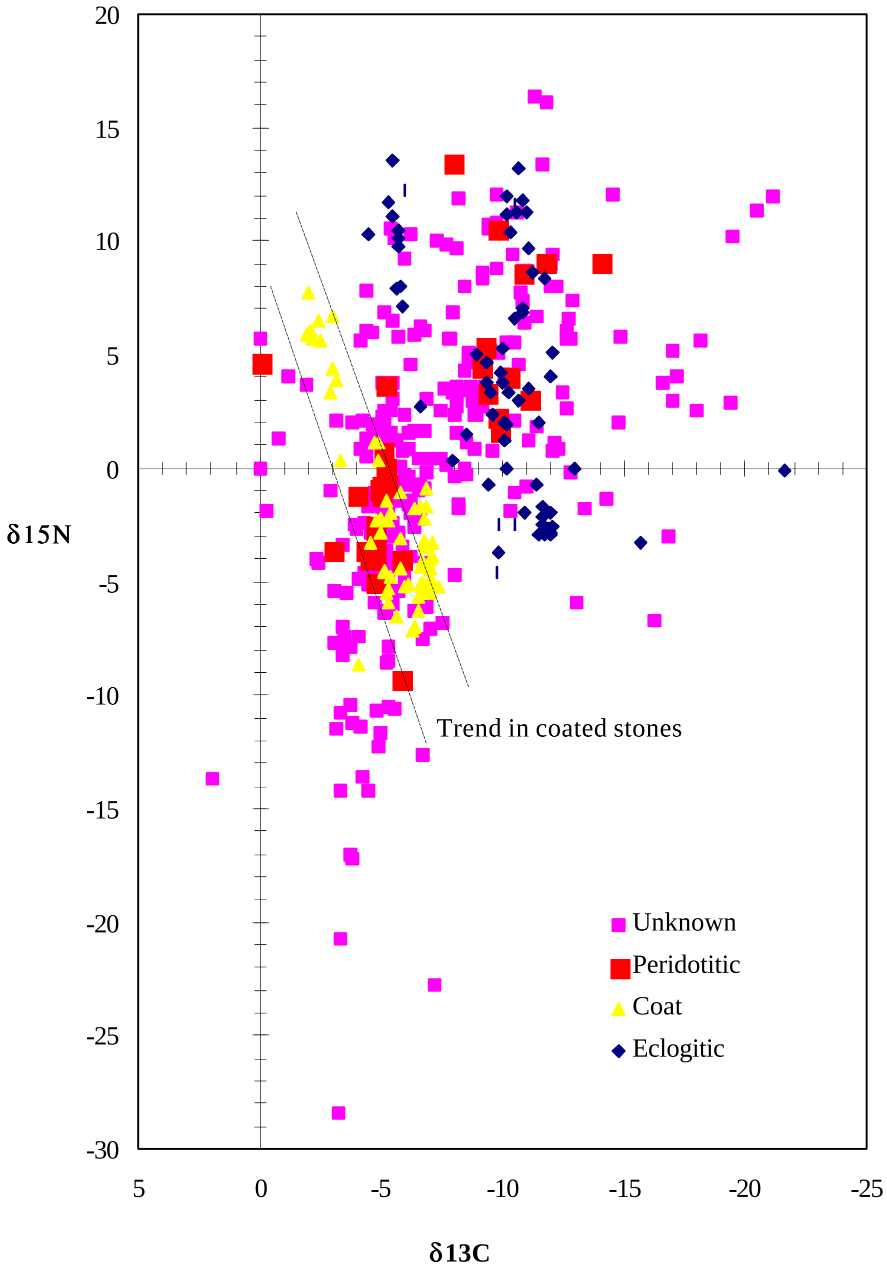

Figure 1.5_17 Distribution of δ^{15}N against δ^{13}C for natural diamonds

Data from Boyd and Pillinger (1994), Boyd et al. (1987, 1992 and 1994), Javoy et al. (1984), van Heerden (1993) and the present study.

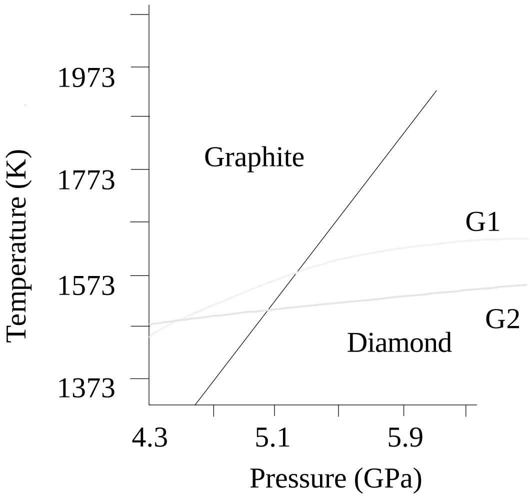

Figure 1.5_18 Phase transition of graphite to diamond in terms of pressure and temperature

From Kennedy and Kennedy (1976), G1 and G2 refer to standard geotherms discussed in section 4.2.

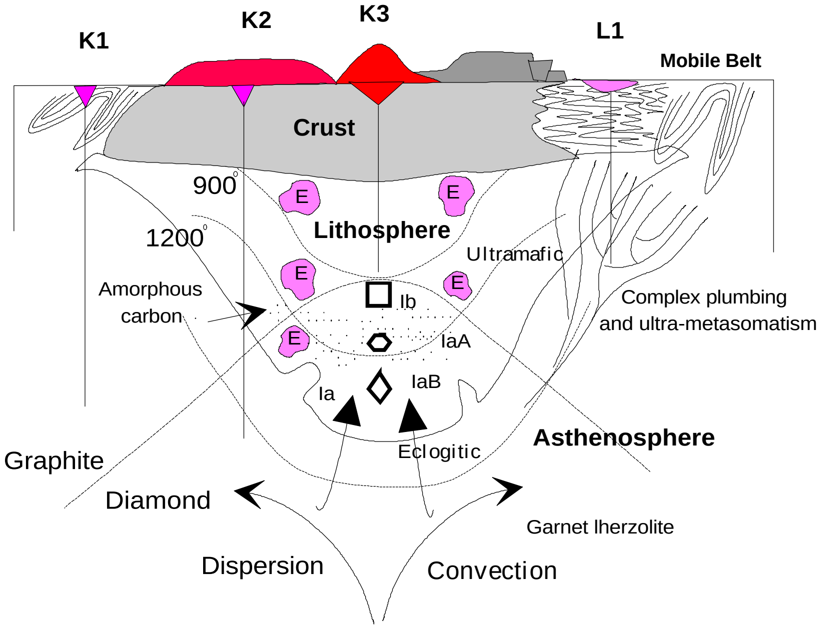

Figure 1.5_19 Formation of diamond in the cratonic lithosphere

From Figure 2 of Haggerty (1986). K1 - K3 and L1 are typical kimberlite (K) and lamproite (L) sampling profiles. The range of diamond shapes and aggregation state with depth of formation are indicated by square, hexagon and diamond shapes and the terms Ib, Ia, IaA and IaB are as described in the text. Geotherm temperatures are in °C. The diagram is scaled to a lithosphere thickness of approximately 200 km.

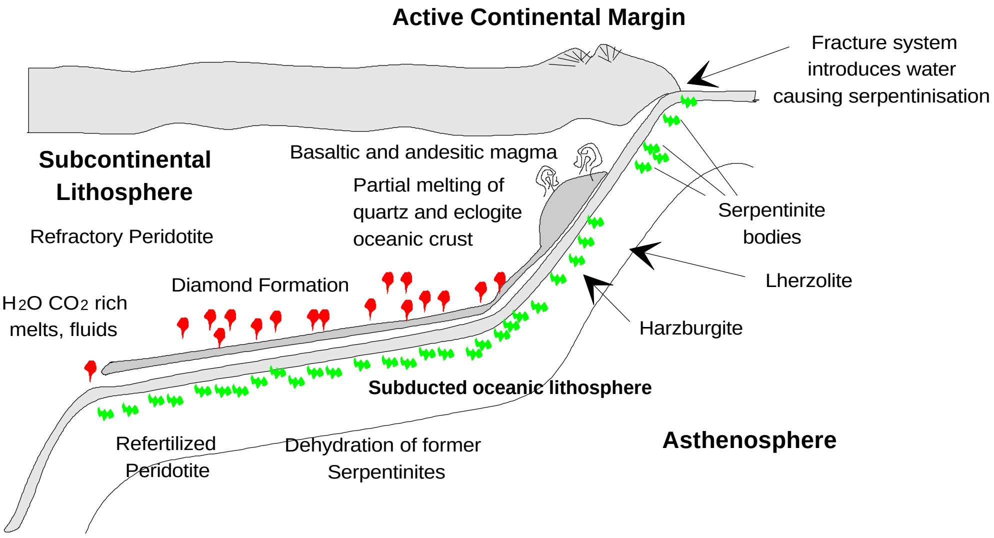

Figure 1.5_20 Diamond formation via melt from dehydrating slab

From Kesson and Ringwood (1989)

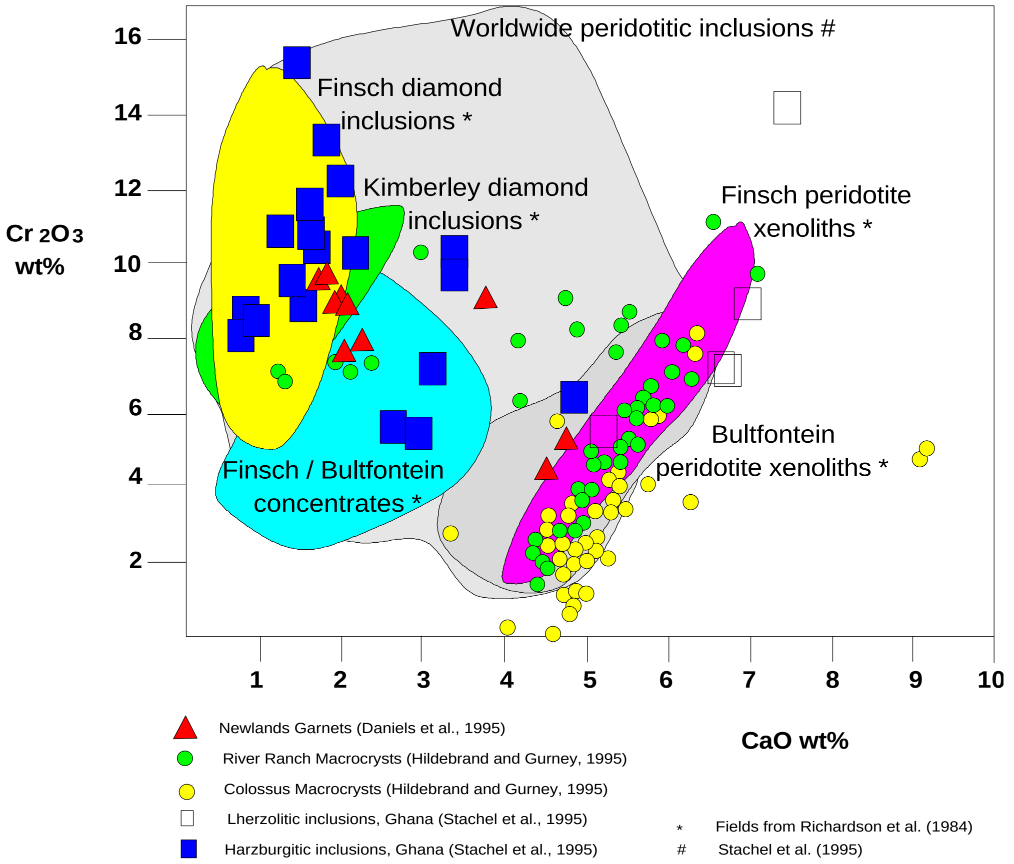

Figure 1.6_1 CaO / Cr_2O_3 wt% distribution for peridotitic garnet inclusions obtained from diamonds and garnets in mantle xenoliths and kimberlite sourced megacrysts.

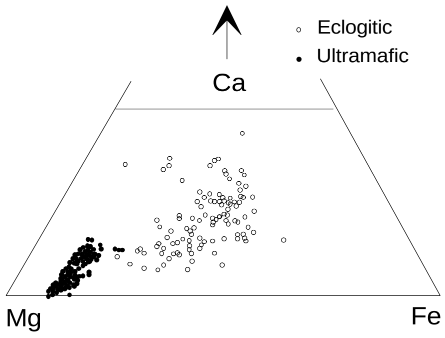

Figure 1.6_2 Garnet inclusions in diamonds from worldwide localities in terms of Ca, Mg and Fe cations.

From Meyer (1987)

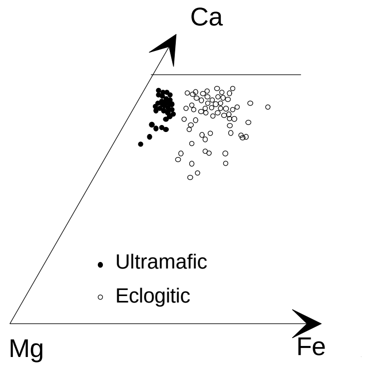

Figure 1.6_3 Clinopyroxene inclusions in diamonds from worldwide localities in terms of Ca, Mg and Fe cations.

From Meyer (1987)

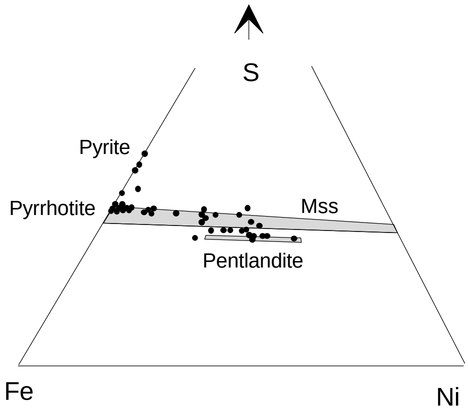

Figure 1.6_4 Composition of sulphide inclusions in diamonds from worldwide localities.

From Meyer (1987)

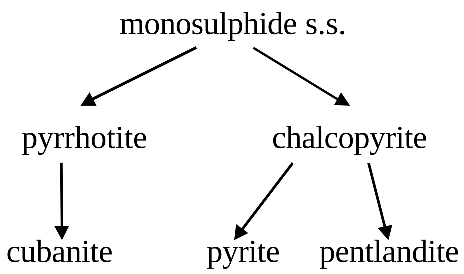

Figure 1.6_5 Exsolution of monosulphide solid solution.

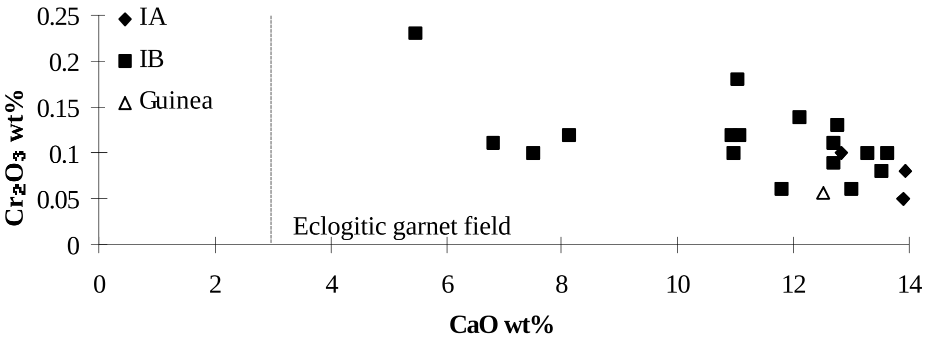

Figure 2.2_1 CaO / Cr_2O_3 plot of Grosspaldite (Group I) garnets from Wilding (1990) and GU3B

IA and IB refer follow Wilding's (1990) terminology where IB coexist with pyroxene.

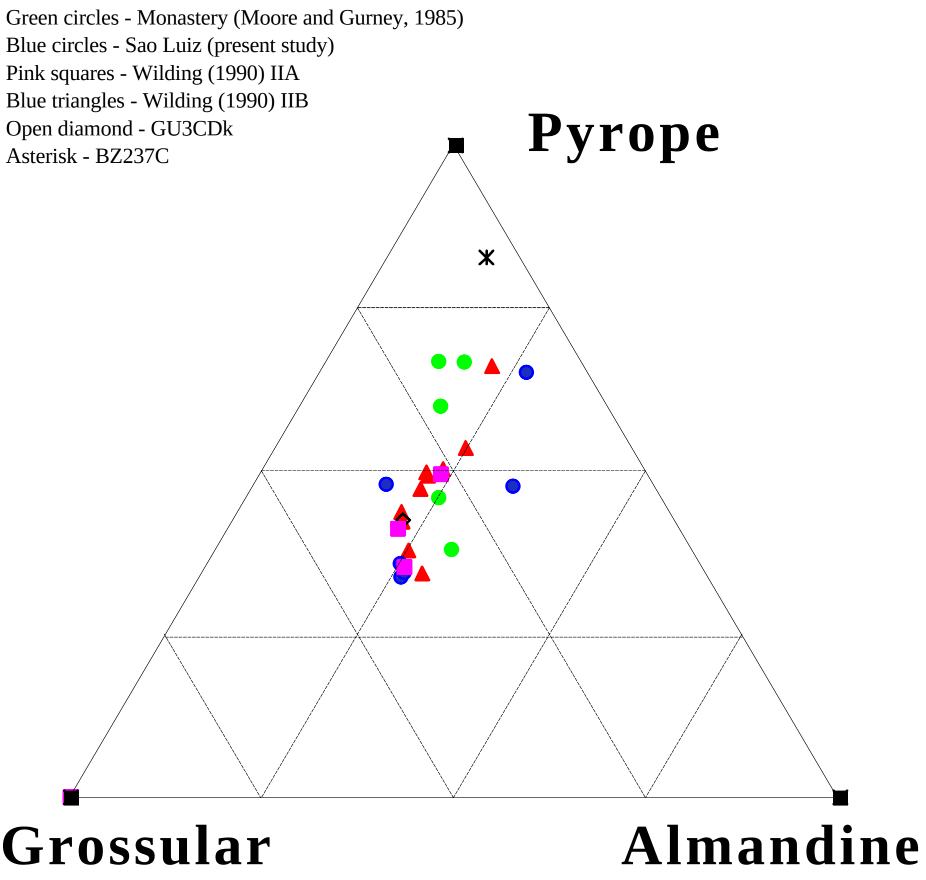

Figure 2.2_2 Fields of majoritic garnet in terms of pyrope - almandine - grossular

The São Luiz majoritic garnet from the present study closely bounds the range of Wilding (1990) compositions from São Luiz as do majoritic garnet inclusions in Monastery diamonds. LM III association low Ca, slightly majoritic garnet BZ237C is clearly on a different compositional field.

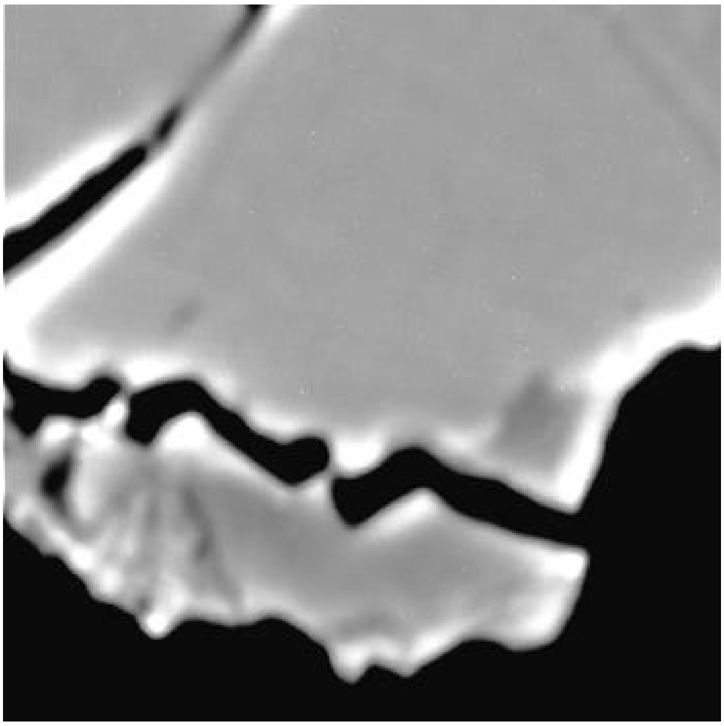

Figure 2.2_3 BSE image of majoritic garnet BZ216A1

EPMA analysis of the area of low BS-intensity on the bottom right hand corner of the grain suggests it has a jadeite composition. The field of view is approximately 20µm across.

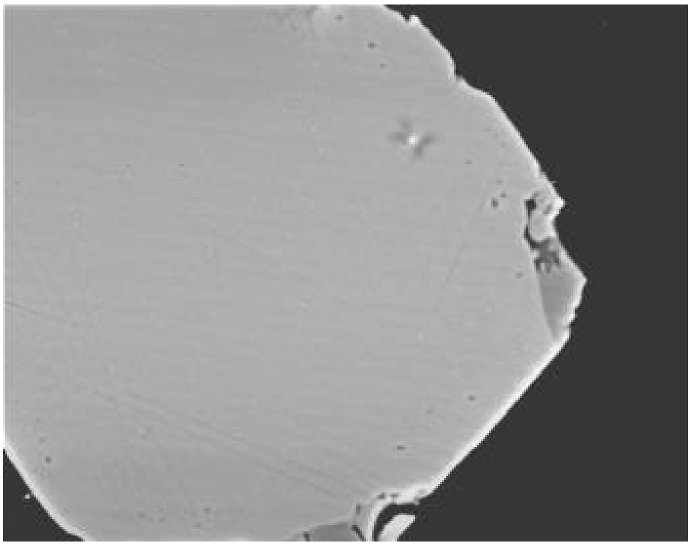

Figure 2.2_4 BSE image of majoritic garnet BZ217A

Areas of low BS-intensity at the corners of the grain are of jadeitic diopside composition. The field of view is approximately 150 µm across.

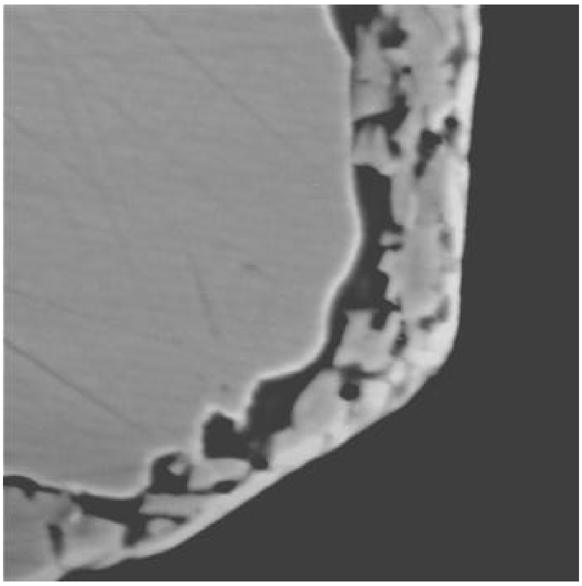

Figure 2.2_5 BSE image of majoritic garnet BZ218A

The partially broken off edge of this grain gives an EDS spectra with significant Na, it is likely that this area is jadeitic diopside. The field of view is approximately 90 µm across.

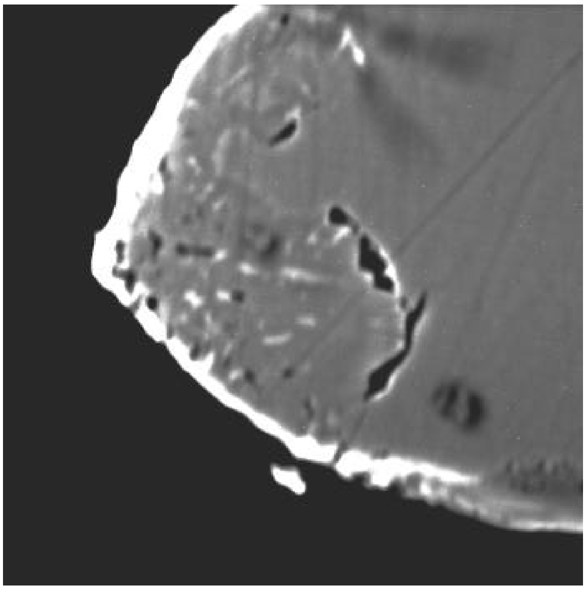

Figure 2.2_6 BSE image of majoritic garnet BZ223A

The small dark specks towards the lower portion of the inclusion appear to have a jadeitic diopside composition. The identity of the bright flecks is more puzzling. The average atomic mass must be greater than majoritic garnet. EPMA analysis suggests that Al, Mg and Fe are significant components. The phase could either be an Al, Fe, Mg spinel, gehlenite or, less likely, an Fe-rich hydrated phase. The field of view is approximately 60 µm across.

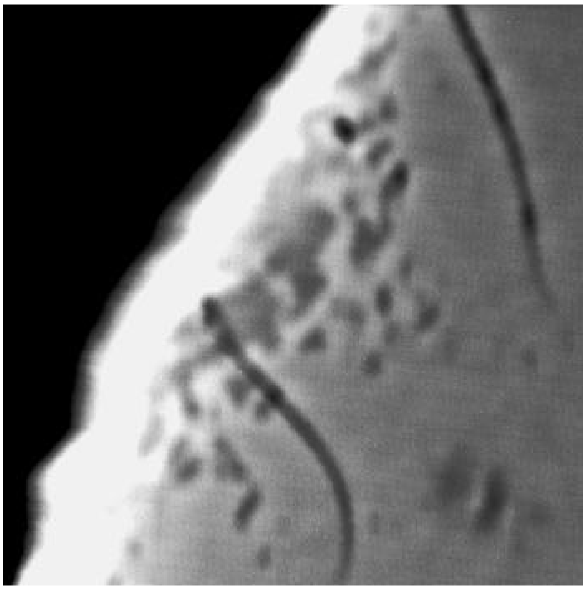

Figure 2.2_7 BSE image of majoritic garnet GU3B

The dark circular features towards the edge of the grain are highly majoritic garnet (3.36 Si cations per 12 O anions). The field of view is approximately 20μm across.

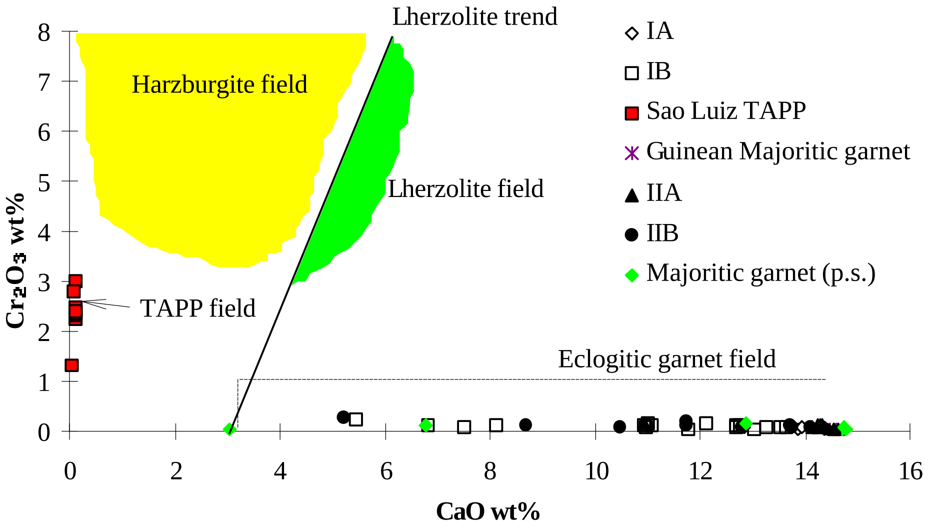

Figure 2.2_8 The location of TAPP grains in terms of a Cr_2O_3 / CaO plot showing, for comparison, fields of eclogitic, peridotitic and majoritic association garnets (p. s. = present study)

TAPP clearly lies in a compositional field of its own.

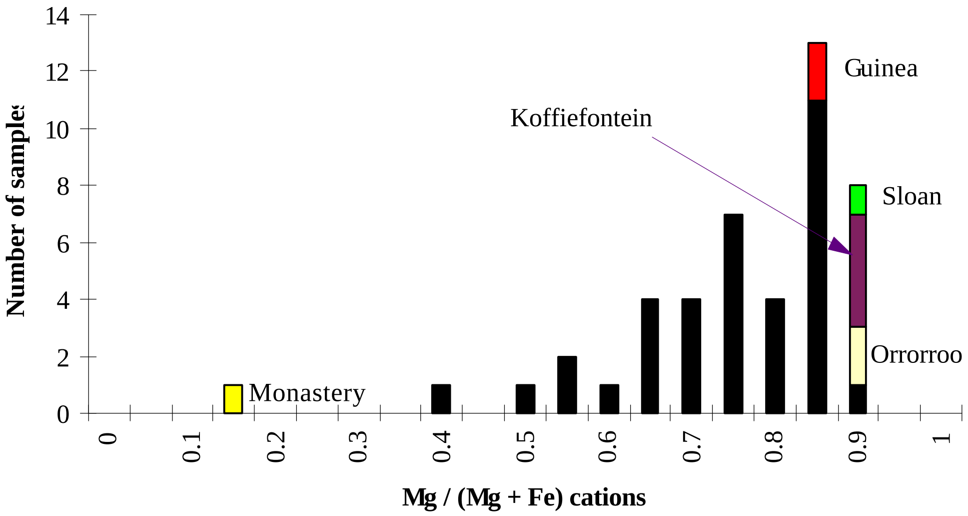

Figure 2.2_9 Histogram of Mg/(Mg+Fe) cation content of São Luiz fPer inclusions in addition to grains from other localities

Inclusion data from other localities: Guinea (this study), Monastery, Sloan and Koffiefontein (Moore et al., 1985), Orrorroo (Scott-Smith et al.., 1984). São Luiz samples fill most of the gap between the particularly Mg-rich compositions of Koffiefontein, Sloan and Guinea fPer and the very Fe-rich Monastery sample. The distribution has a pronounced skew to Fe-rich compositions.

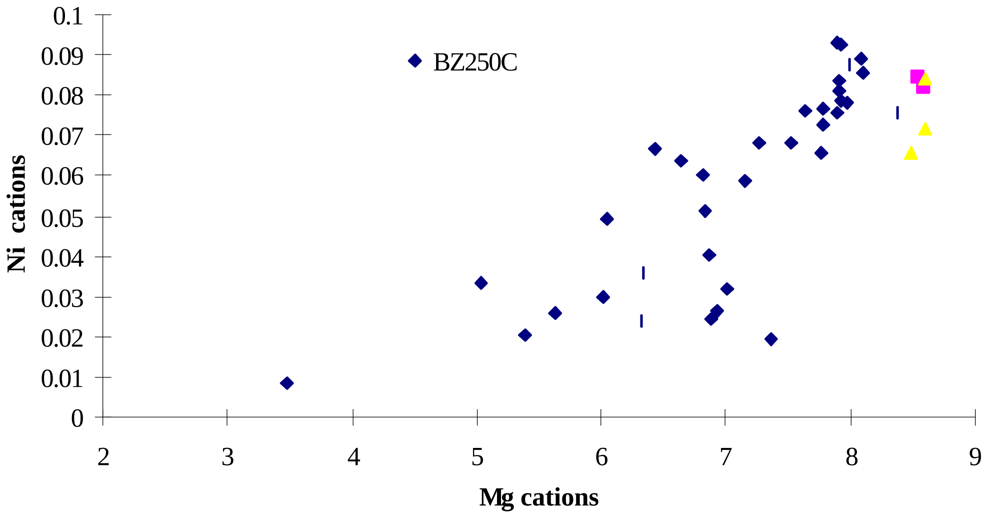

Figure 2.2_10 Composition of São Luiz and Guinean fPer inclusions in terms of Ni / Mg cations

BZ250C has a significantly different compositions from the general population. Triangles represent data from literature fPer (Moore et al., 1985 and Scott-Smith et al., 1984). Squares represent Guinea fPer from the present study.

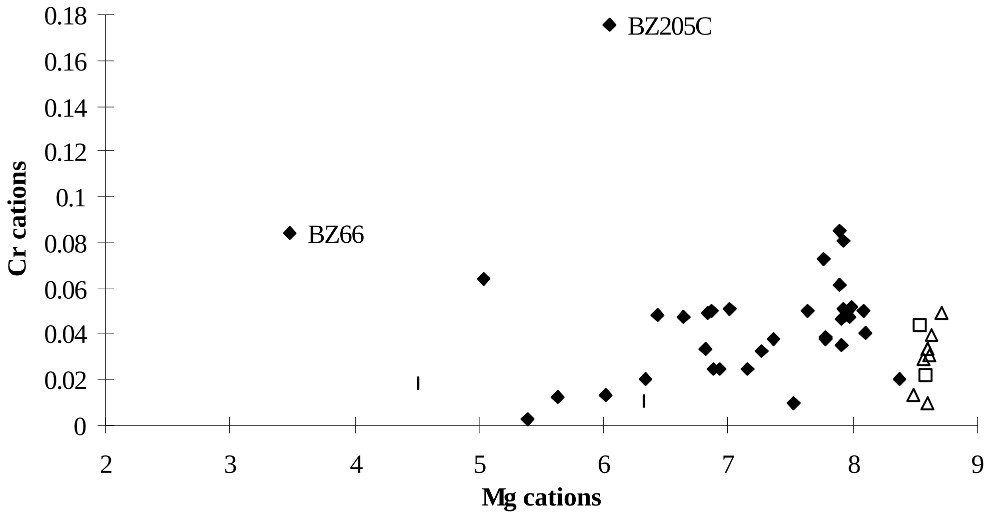

Figure 2.2_11 Composition of São Luiz and Guinean fPer inclusions in terms of Cr / Mg cations

BZ66 and BZ250C lie outwith the general compositional field. Triangles represent data from literature fPer (Moore et al., 1985 and Scott-Smith et al. 1984). Squares represent Guinea fPer from the present study.

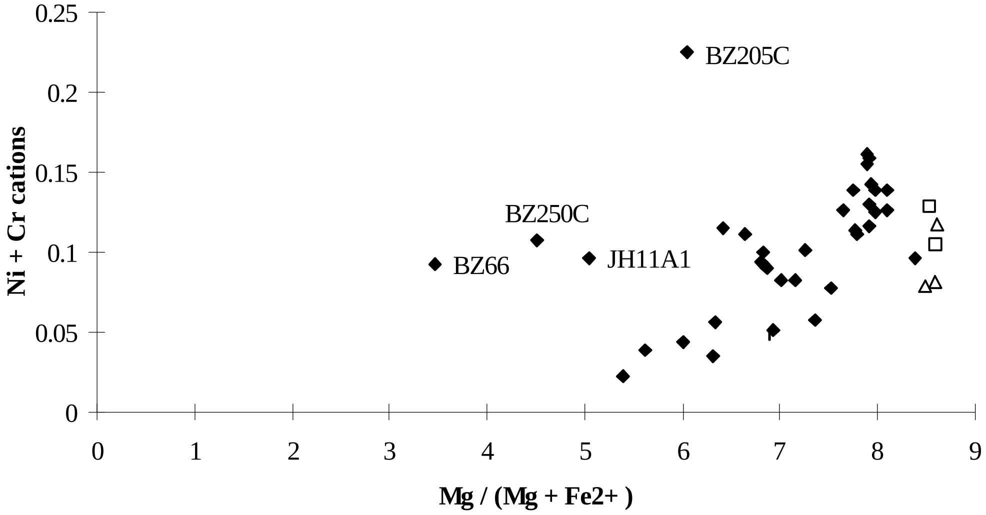

Figure 2.2_12 Composition of São Luiz and Guinean fPer inclusions in terms of Ni+Cr / Mg/(Mg+Fe) cations

BZ66 and BZ250C, in addition to BZ205C (the disequilibrium inclusion in terms of associated TAPP from diamond BZ205) and JH11A1 lie outwith the general compositional field. Triangles represent data from literature fPer (Moore et al., 1985 and Scott-Smith et al. 1984). Squares represent Guinea fPer from the present study.

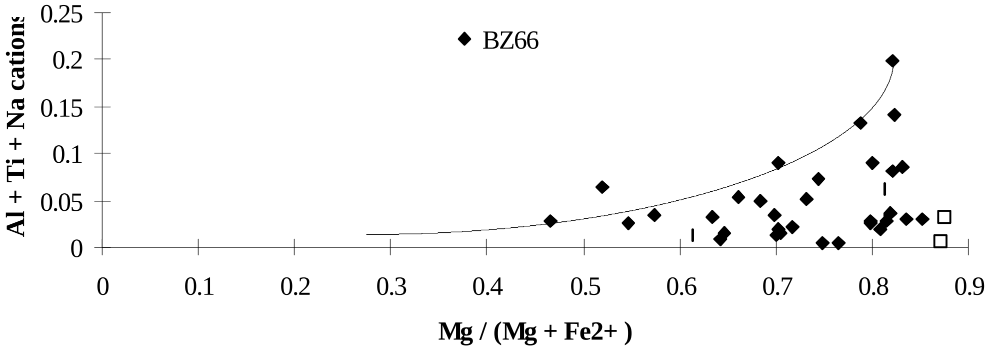

Figure 2.2_13 Composition of São Luiz and Guinean fPer inclusions in terms of Al+Ti+Na / Mg/(Mg+Fe^{2+}) cations

BZ66 shows a composition inconsistent with the general field. Squares represent Guinea fPer from the present study.

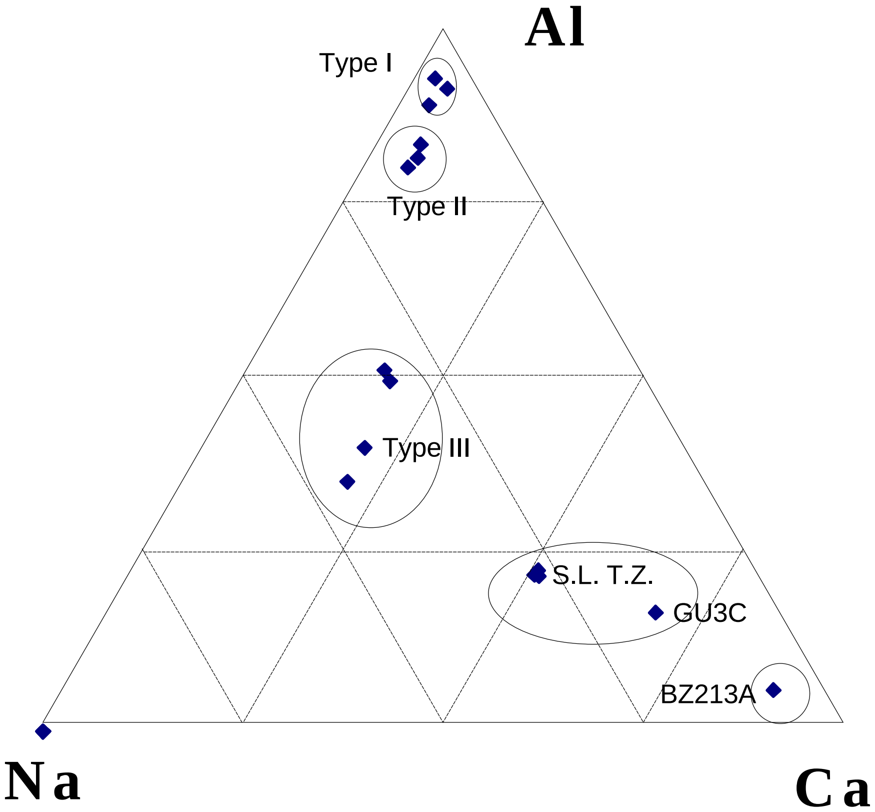

Figure 2.2_14 Delineation of compositional fields of grains of general pyroxene-type composition from São Luiz and Guinea

Type I, Mg-silicate, Type II Mg-Al-silicate, significant, yet small Na and Ca, Type III (Na and Ca-rich Mg-Al-silicate), TZ association (Ca-rich) and upper mantle association (BZ213A) lie within distinct compositional fields.

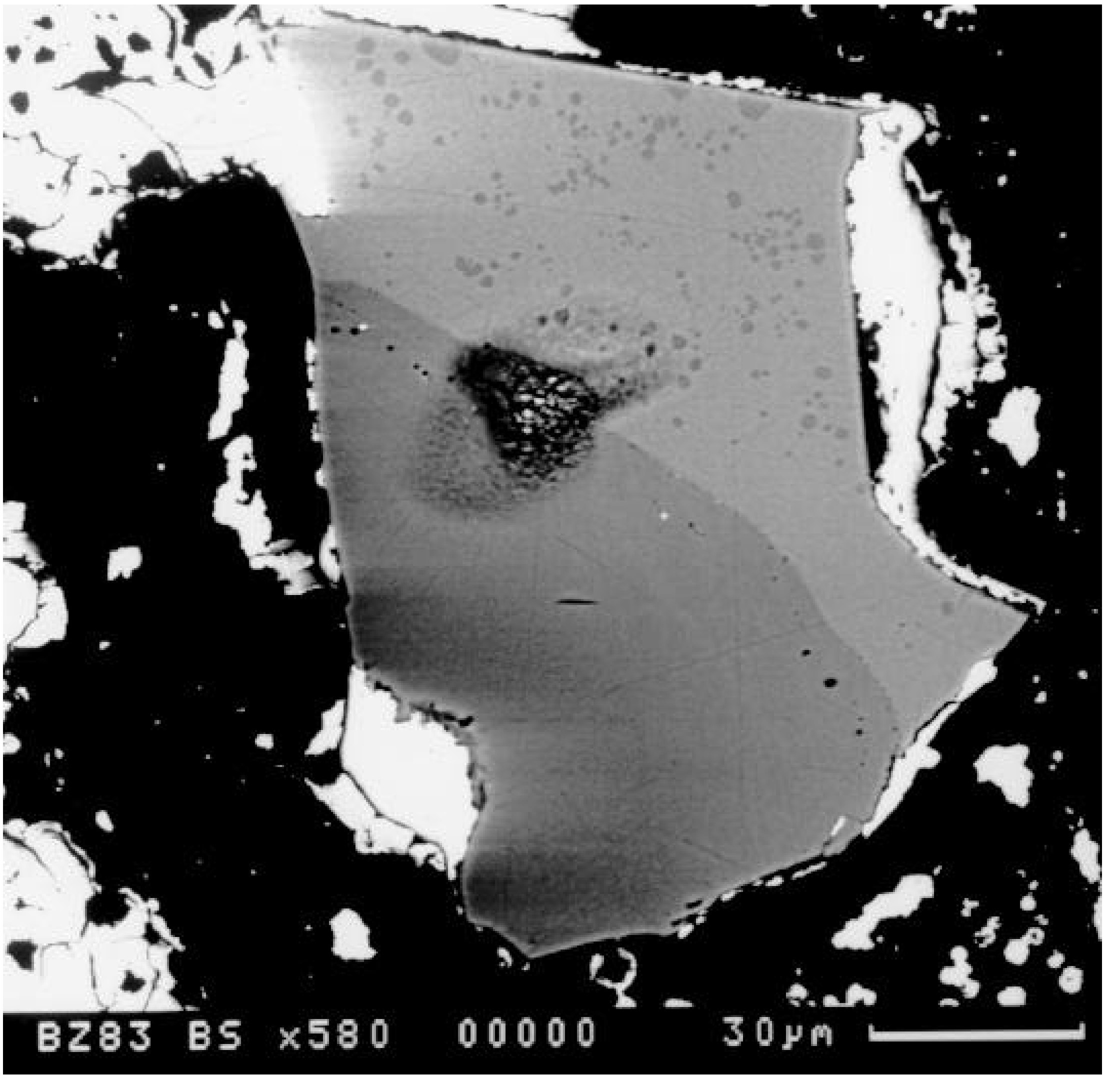

Figure 2.2_15 BS-SEM image of magnetite composite grain BZ83

The dark portion and dark circular patches have a magnetite composition where the A-site is occupied by Fe^{3+} and Al^{3+}. The B-site comprises Fe^{2+}, Ti^{4+}, Mn^{2+} and Mg^{2+}. The light portion of the grain has a full A-site occupancy by Fe^{3+}, the B-site comprises Fe^{2+}, Fe^{3+}, Mg^{2+} and a small amount of Mn^{2+}.

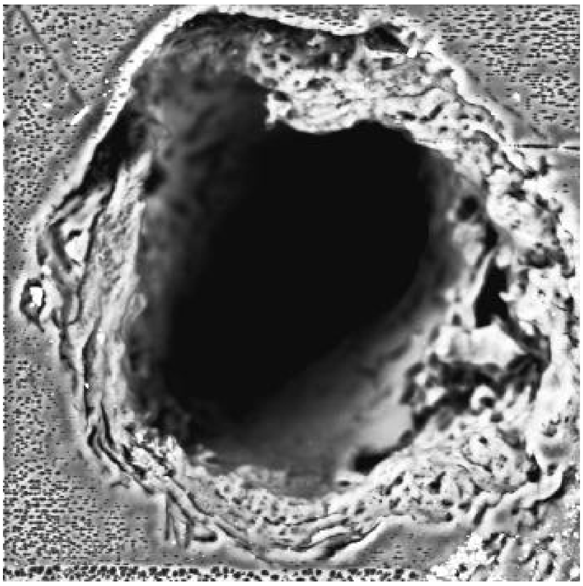

Figure 2.2_16 High resolution electron probe image of epigenetic inclusion BZ228D

This image serves to demonstrate the contrast between BZ228D and syngenetic inclusions. The grain is hollow with growth inwards from the diamond surface characteristic of precipitation from a fluid phase. EDS analysis suggests that the inclusion is composed of a mixture of sulphide and silicate (probably quartz). The field of view is approximately 200µm across.

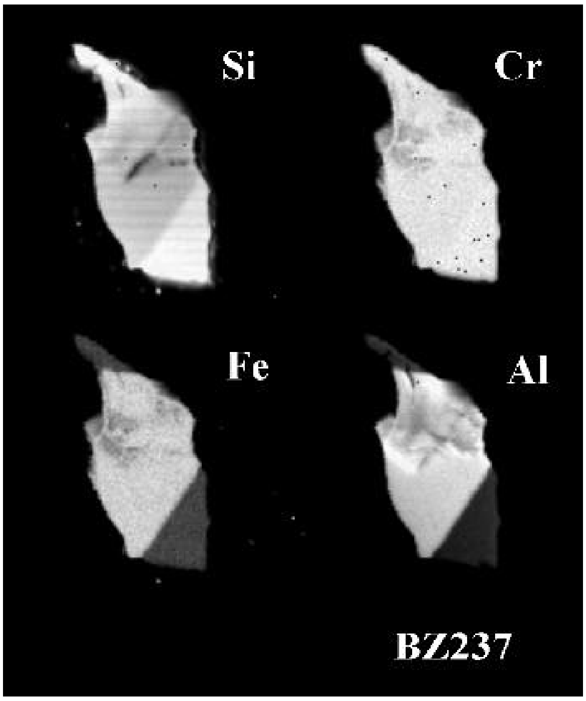

Figure 2.2_17 EPMA map of composite grain BZ237A6,C

The central band (BZ237C) is of low Ca majoritic garnet composition, the rest of the grain being Type III pyroxene composition (BZ237A6). No compositional variation is observed across the boundaries. The grain is 80 µm long.

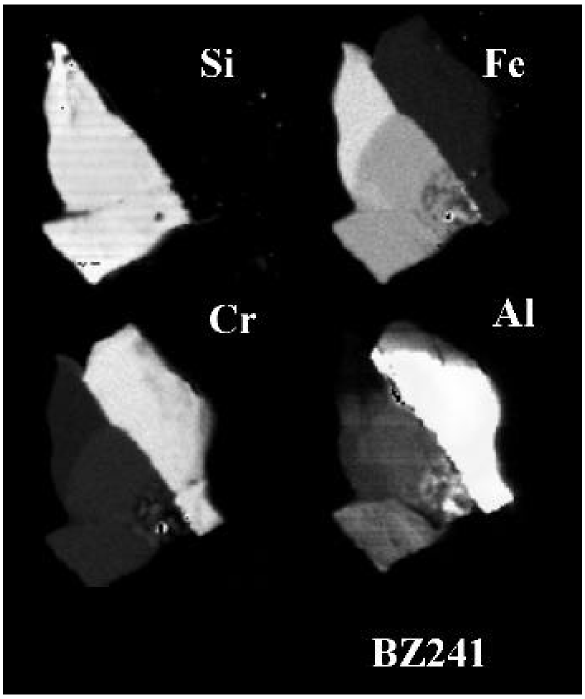

Figure 2.2_18 EPMA map of composite grain BZ241B1,C

The right hand side of the image is of ruby, BZ241C, whereas the left hand is Type II MgSi-Pvk, BZ241B1. No compositional variation is observed across the boundary. The grain is grain is 60 µm in longest axis.

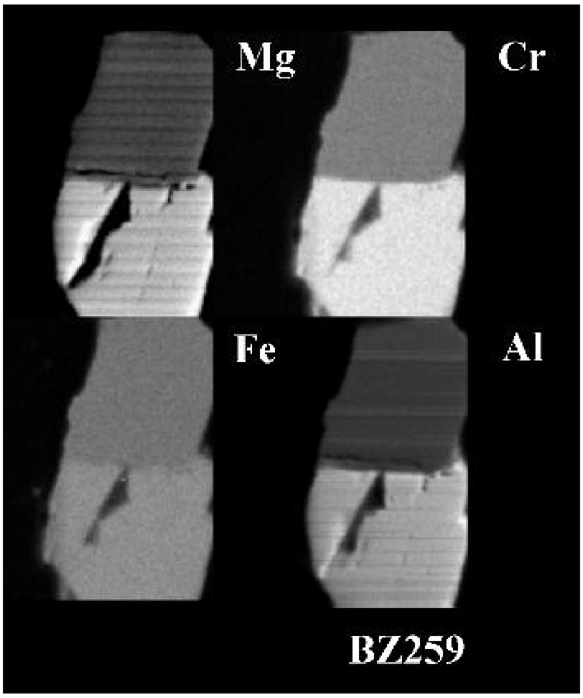

Figure 2.2_19 EPMA map of composite grain BZ259A2,B

Upper portion is BZ259B (Type III-px) the lower portion is BZ259A2 (TAPP). No compositional variation is observed. The grain is 140 µm long.

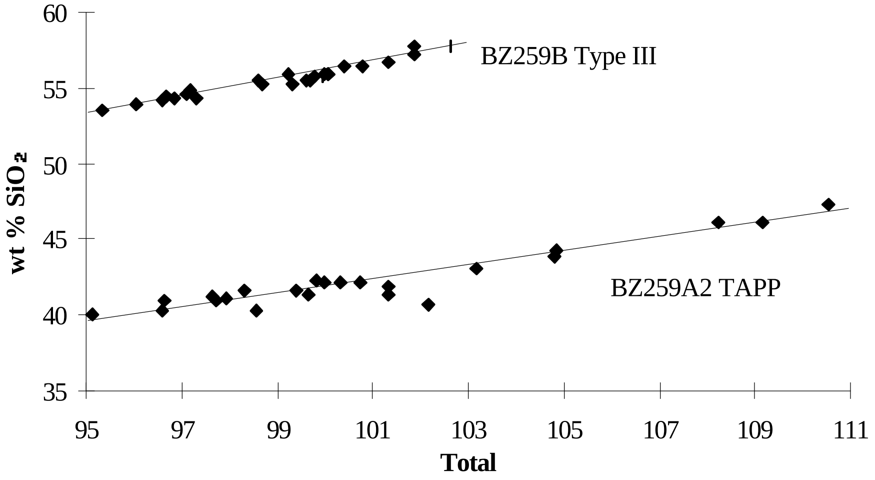

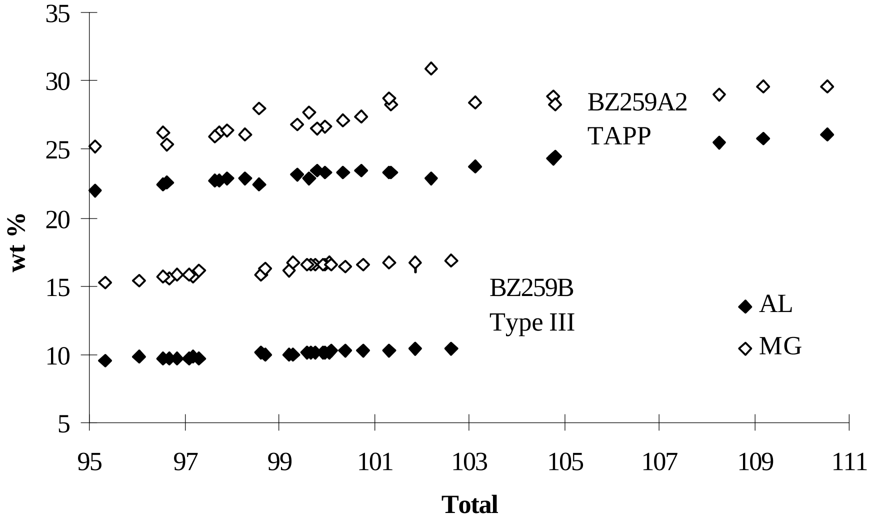

Figure 2.2_20 Relationship of SiO_2 wt% (top diagram) and Al_2O_3 and MgO wt% (bottom diagram) against analysis total for BZ259A2 and BZ259B

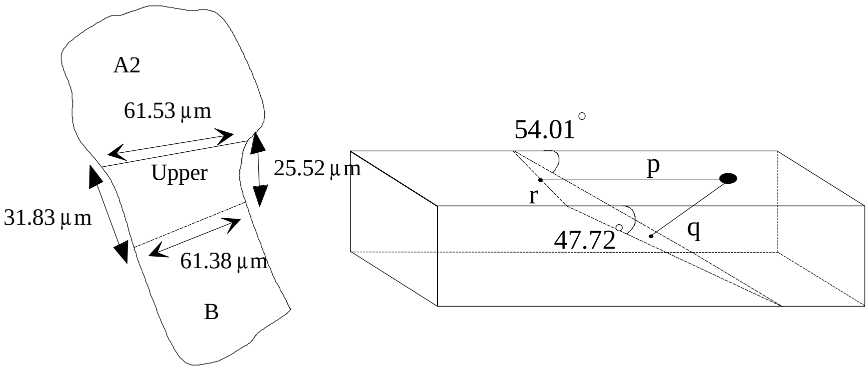

Figure 2.2_21 Representation of suture line in BZ259A2,B and calculation of distance from analysis point grain boundary.

The dotted line on the plan view represents the grain boundary on the base of the inclusion. The diagram is not to scale.

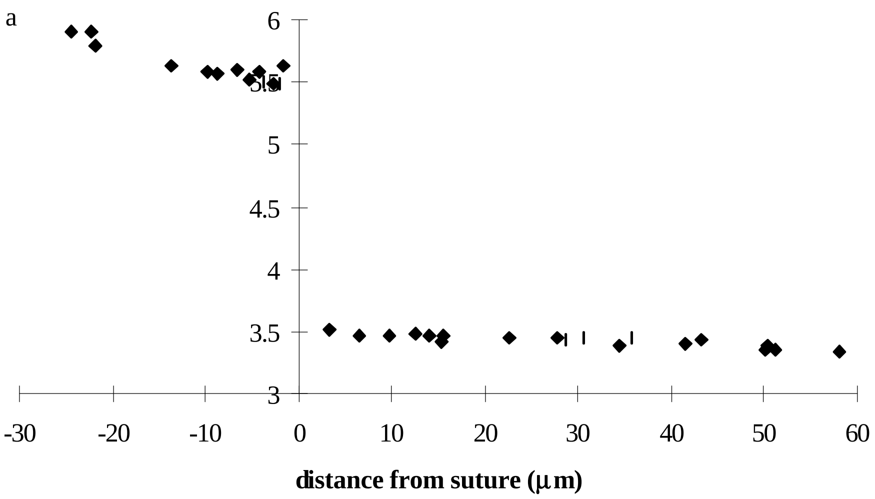

Fig. 2.2_22a Cation values for Mg against distance in microns for analyses lying between totals of 97% and 101%

Points for BZ259B, Type III pyroxene lie to the right side whereas BZ259A2, TAPP lie to the left.

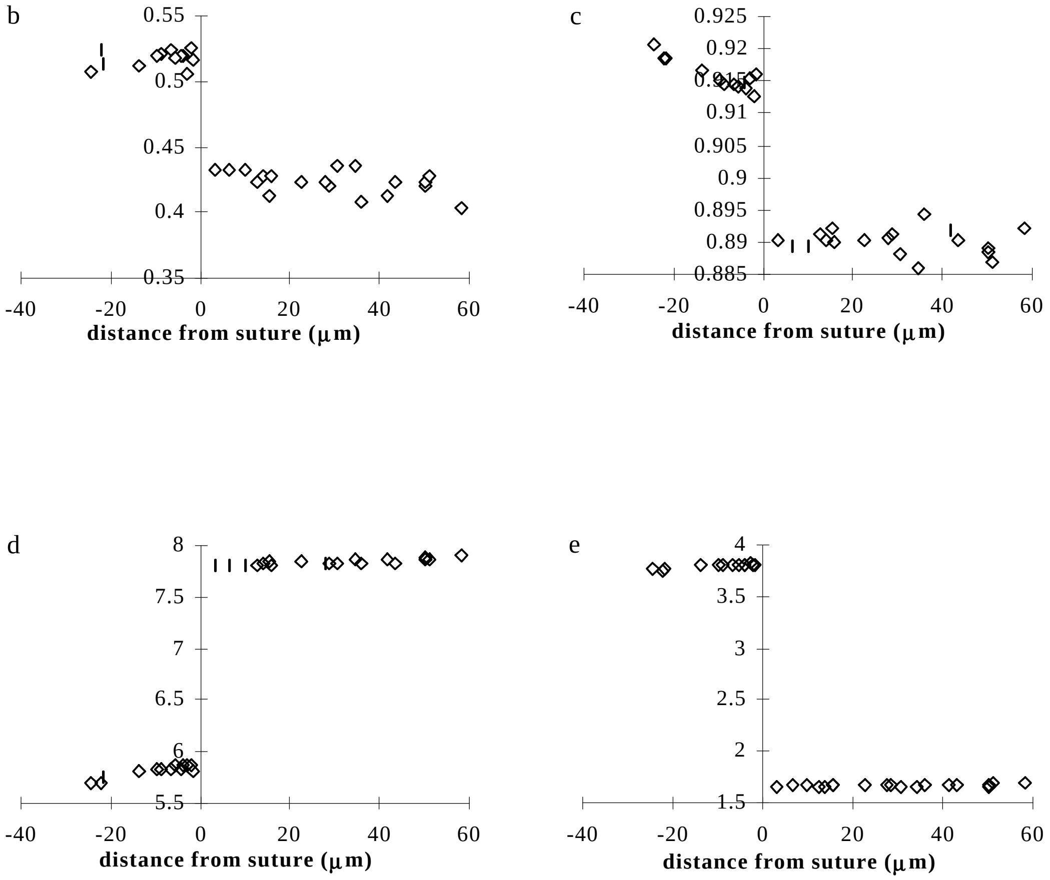

Fig. 2.2_22 b, c, d and e Cation values for Fe, Mg/(Mg+Fe), Si and Al against distance in microns for analyses lying between totals of 97% and 101%

b - Fe, c - Mg/(Mg+Fe), d - Si, e - Al. Points for BZ259B, Type III pyroxene lie to the right side whereas BZ259A2, TAPP lie to the left.

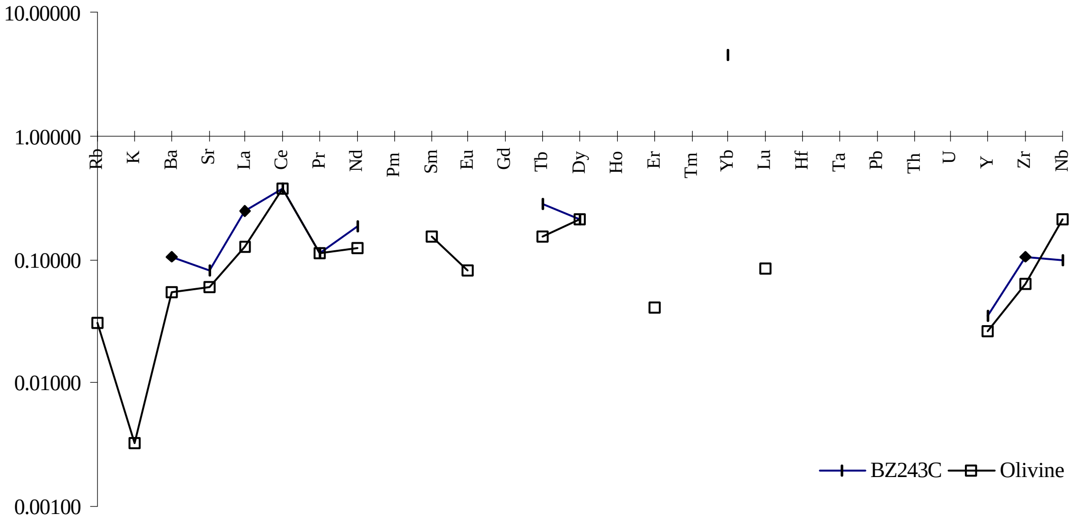

Figure 2.4_1 Trace element composition of olivine BZ243C and averaged olivine.

Data is normalised against C1 chondrite using data from Sun and McDonough (1989). Averaged olivine includes data from BZ111 (*Harte, 1993 personal communication*).

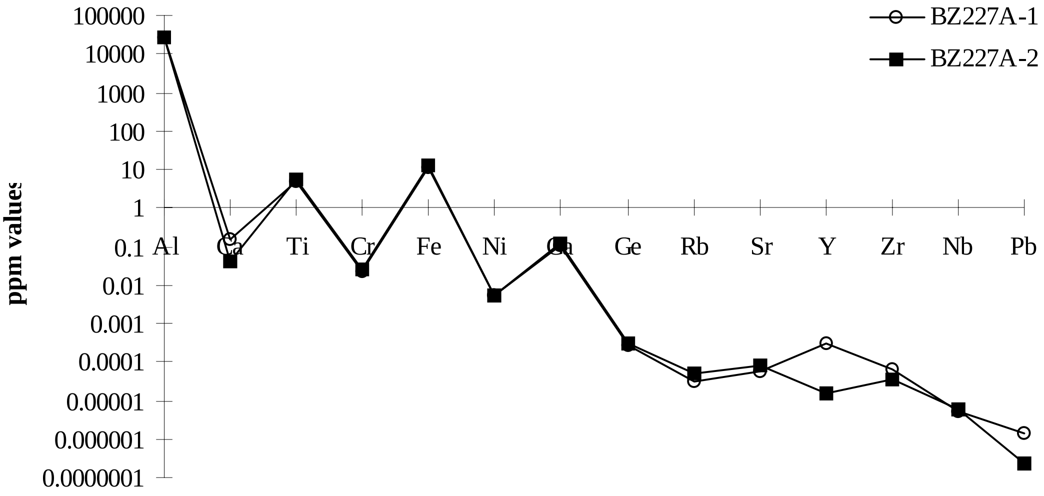

Figure 2.4_2 Trace element composition of sapphire grain BZ227A (2 analyses).

ppm values are estimates as ion yield values for Al_2O_3 are not known.

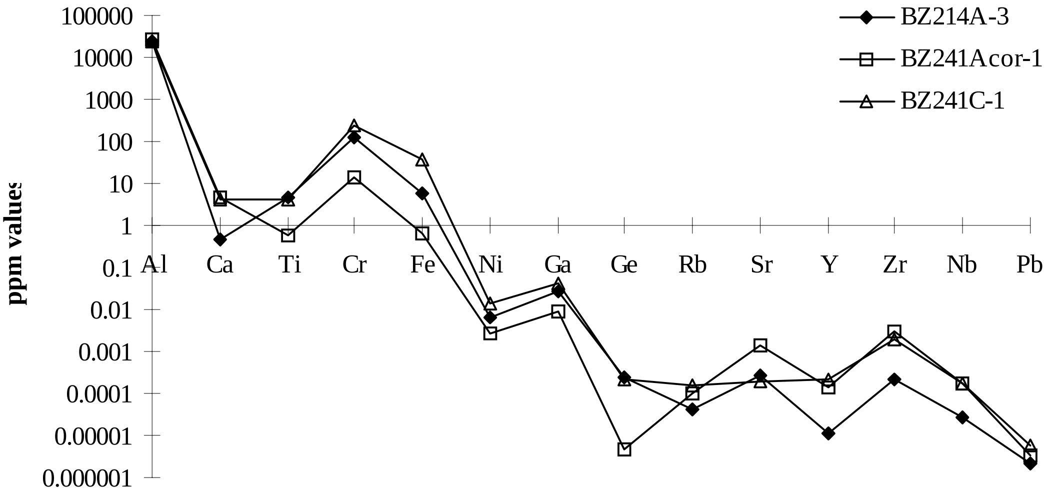

Figure 2.4_3 Trace element composition of ruby grains BZ214A, BZ241C and BZ241Acor.

ppm values are estimates as ion yield values for Al_2O_3 are not known.

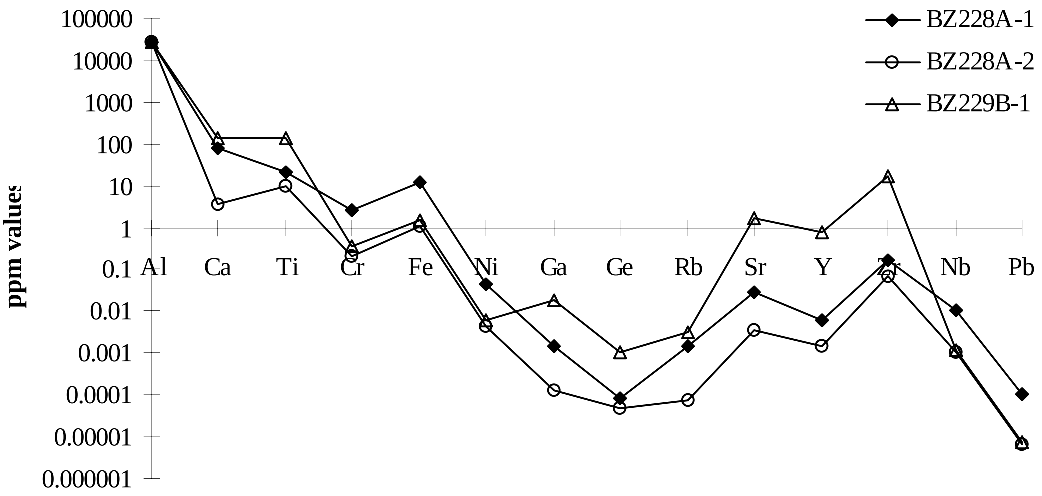

Figure 2.4_4 Trace element composition of corundum grains BZ228A (2 analyses) and BZ229B.

ppm values are estimates as ion yield values for Al_2O_3 are not known.

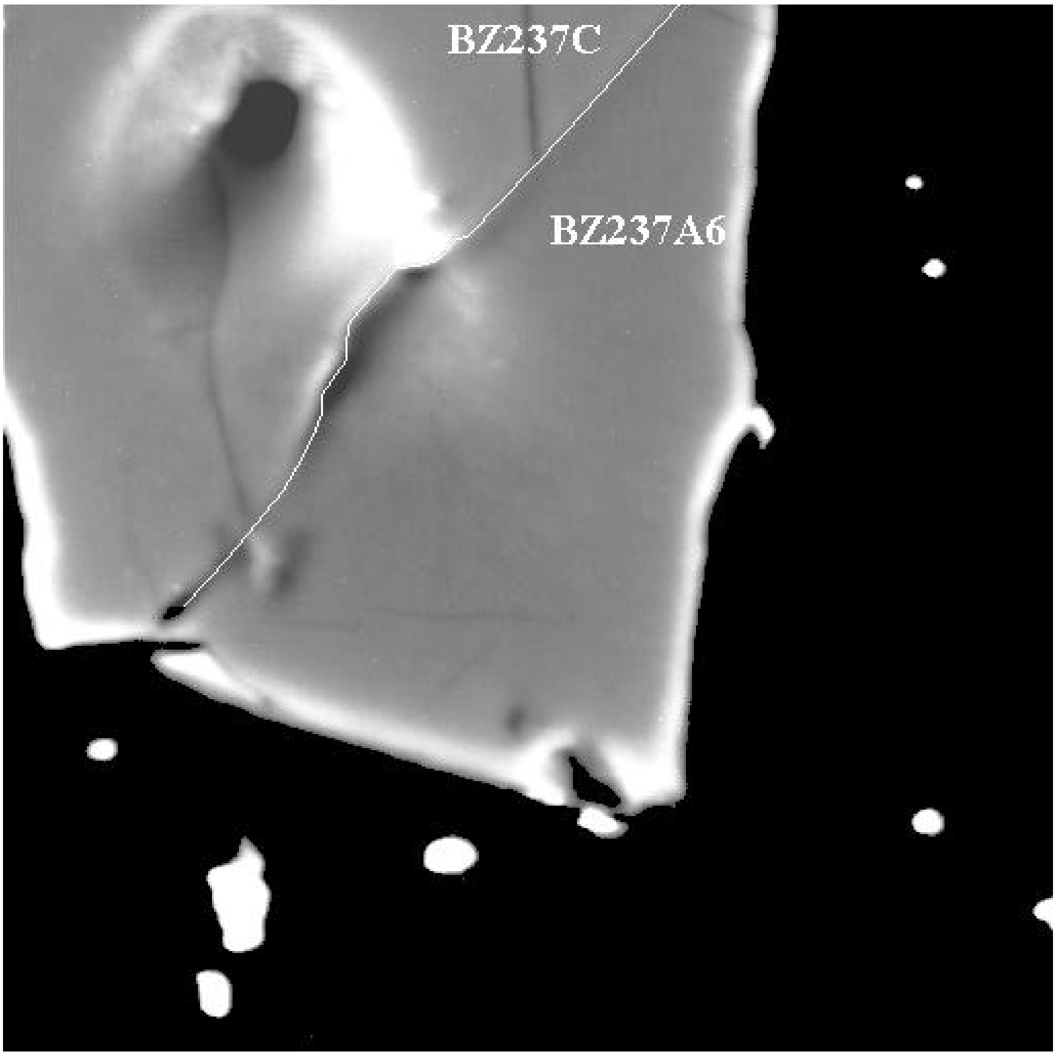

Figure 2.4_5 BS-SEM image of composite grain BZ237A6,C showing the ion microprobe placement wholly within BZ237C (TAPP).

The grain is approximately 60 µm across and the grain boundary is annotated by a thin white line.

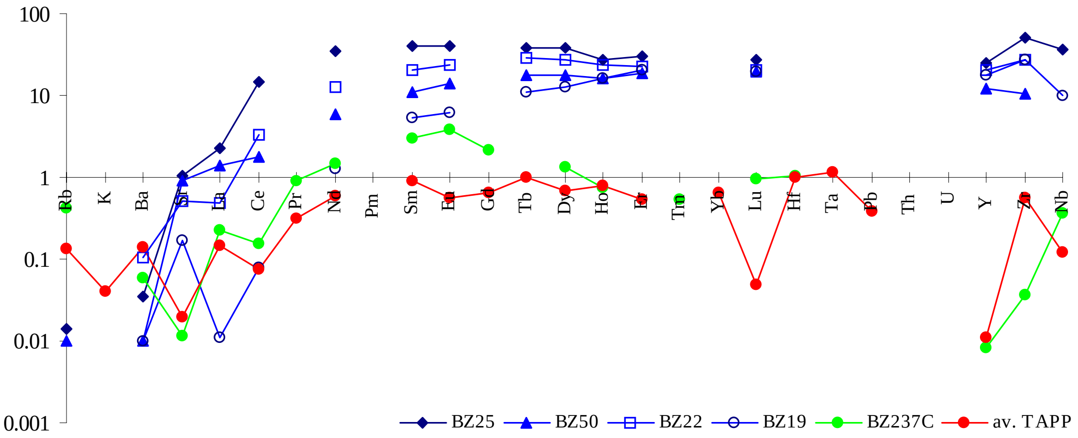

Figure 2.4_6 Trace element composition of LM III low Si and Ca- majoritic garnet (BZ237C) in comparison with São Luiz majoritic garnet from Harte (1992) and TAPP.

Data is normalised against C1 chondrite using data from Sun and McDonough (1989). BZ237C shows trace element concentrations intermediary between TAPP and majoritic garnet.

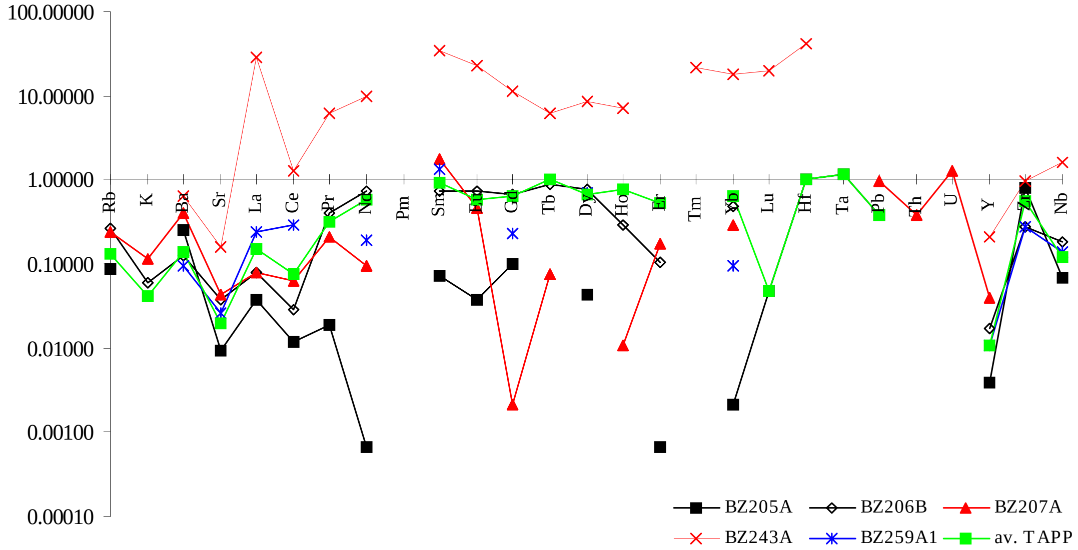

Figure 2.4_7 Trace element composition of TAPP grains.

Data is normalised against C1 chondrite using data from Sun and McDonough (1989). Averaged TAPP analysis does not include BZ243A (which has a composition inconsistent with other TAPPs), or BZ207A (which gave spurious results and a large scatter). Due to the very large values obtained for Hf, Ta, Zr and Nb on BZ207A, they are omitted from the figure.

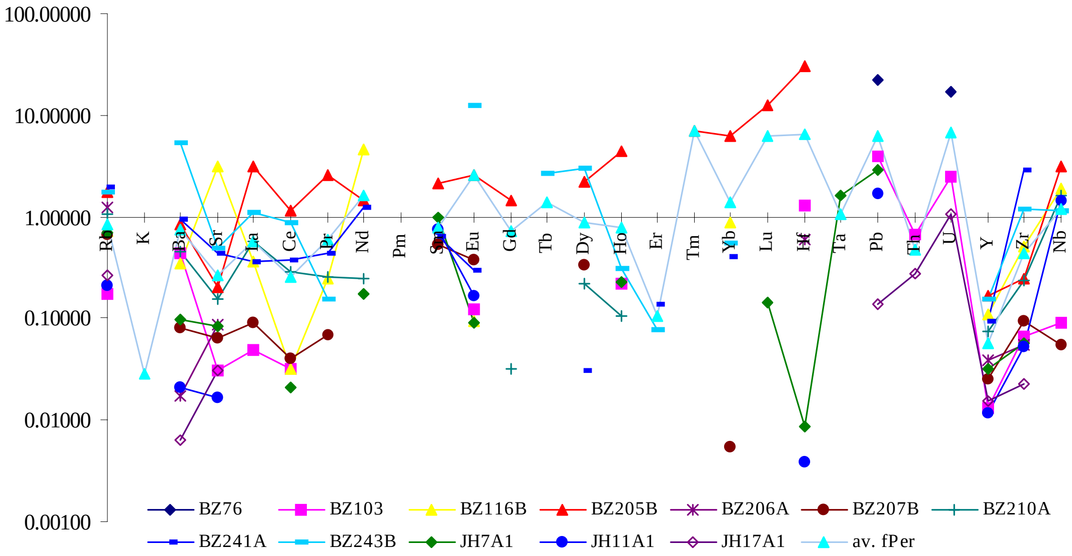

Figure 2.4_8 Trace element composition of fPer inclusions

Data is normalised against C1 chondrite using data from Sun and McDonough (1989).

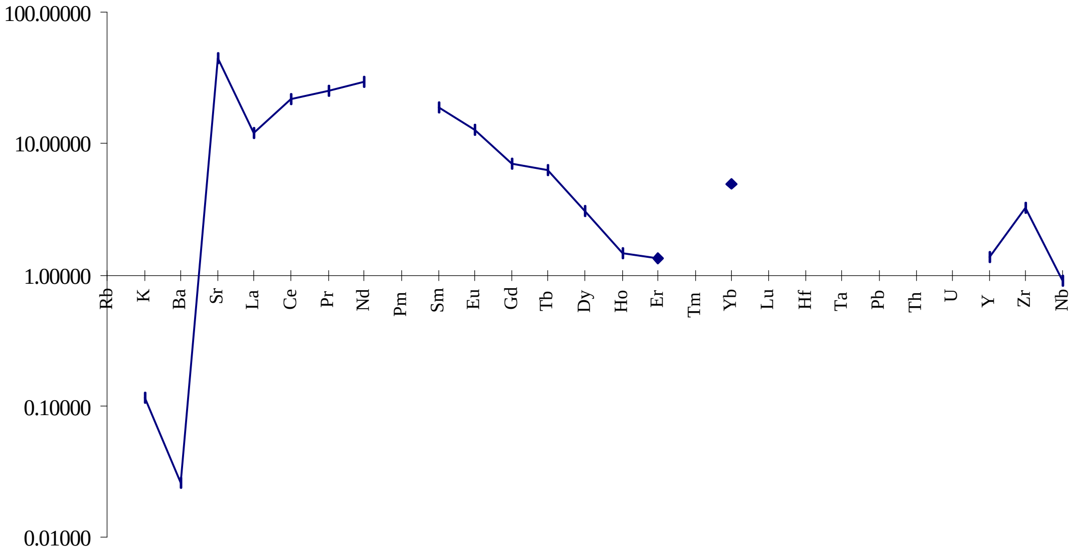

Figure 2.4_9 Trace element composition of UM association pyroxene, BZ213A.

Data is normalised against C1 chondrite using data from Sun and McDonough (1989).

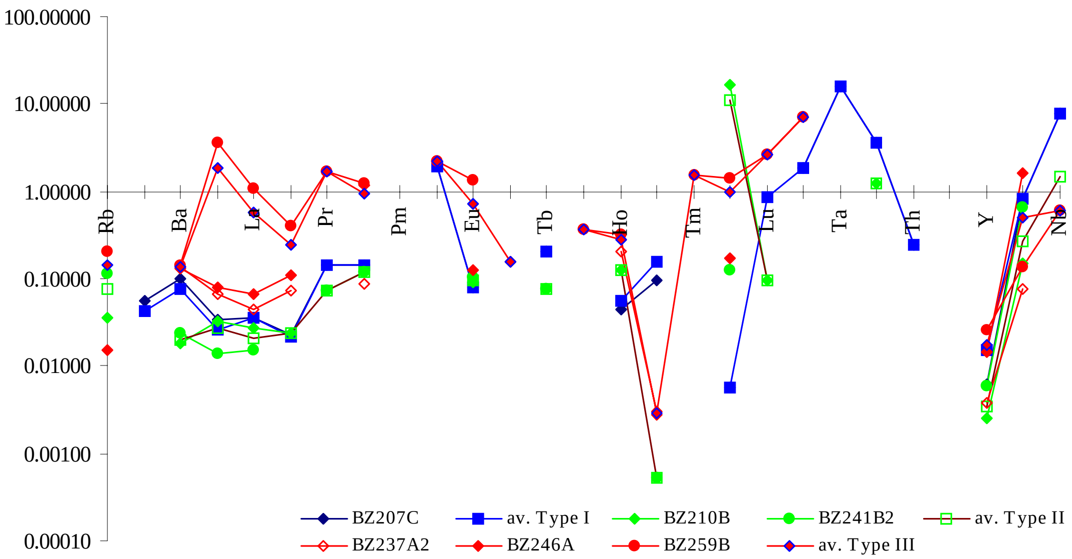

Figure 2.4_10 Trace element composition of Type I, II and III MgSi-Pvk.

Data is normalised against C1 chondrite using data from Sun and McDonough (1989). Included in the averages for Type I and Type II pyroxene are data from Harte (1993, *personal communication*).

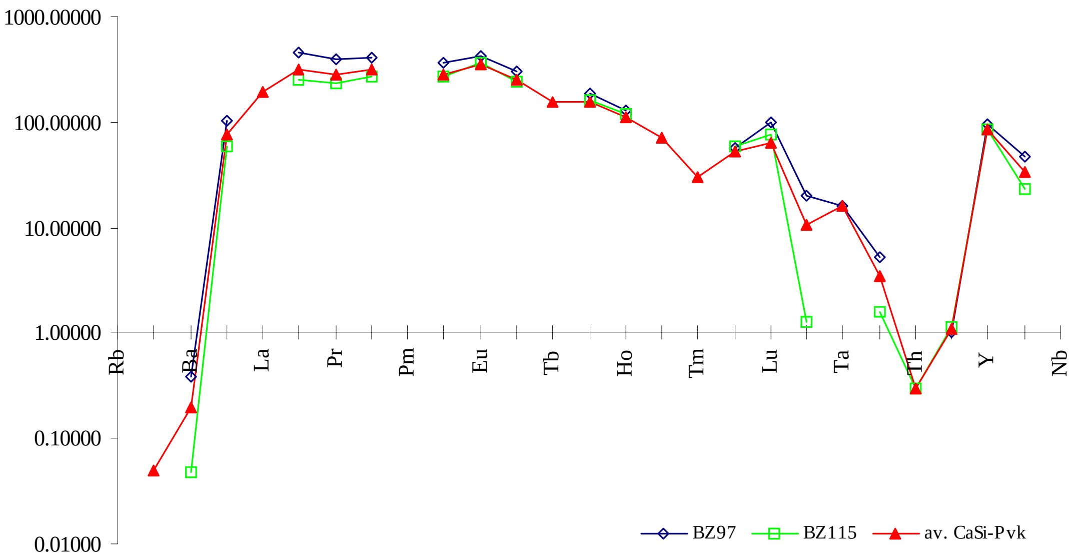

Figure 2.4_11 Trace element composition of CaSi-Pvk.

Data is normalised against C1 chondrite using data from Sun and McDonough (1989). Included in the average composition are two analyses, one on each of BZ97 and BZ115 by Harte (1993, *personal communication*).

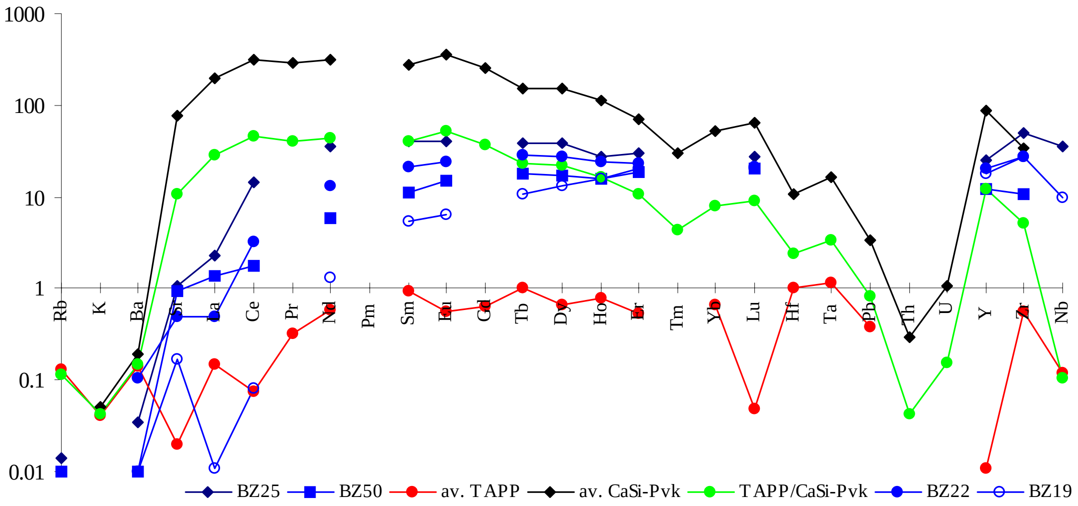

Figure 2.4_12 Comparison of majoritic garnet trace element composition with a 1:6 mixture of CaSi-Pvk against TAPP.

Majoritic garnet data from Harte (1992). The slight discrepency between the fit can be accounted for by expected trace element composition of diopside associated with the majoritic garnets.

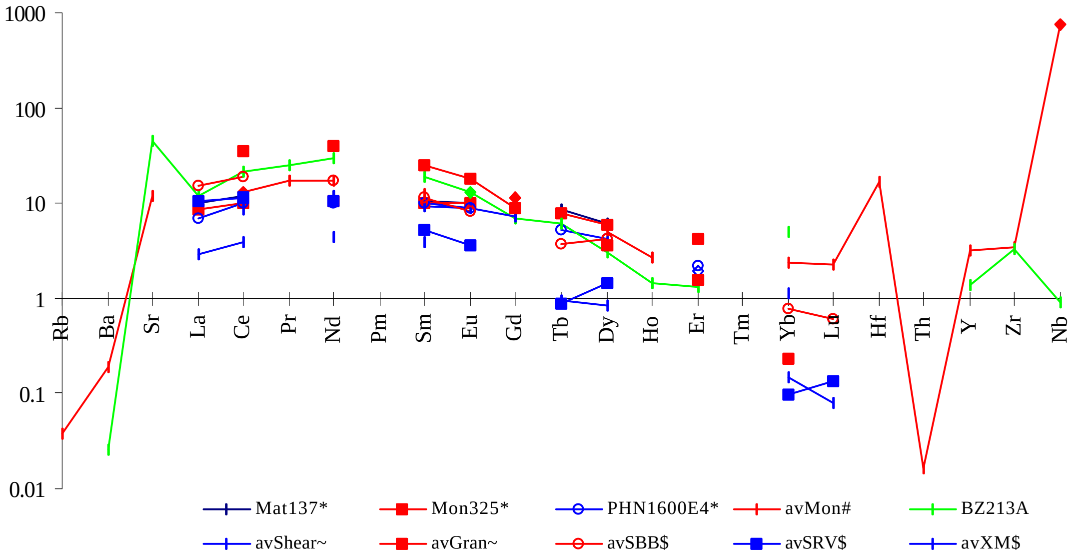

Figure 2.4_13 Comparison of trace element composition of UM association pyroxene BZ213A with literature data.

Data from # - Hutchison et al. (1995), * - Harte et al. (1991), $ - Caporuscio and Smyth (1990) and ~ - Shimizu (1975). BZ213A mirrors more closely the trend of granular lherzolite trend from Liquobong (av Gran, Shimizu, 1975), Bultfontein (av Gran, Shimizu, 1975), Bobejaan (av SBB, Caporuscio and Smyth, 1990) and Roberts Victor (av SRV, av XM, Caporuscio and Smyth, 1990).

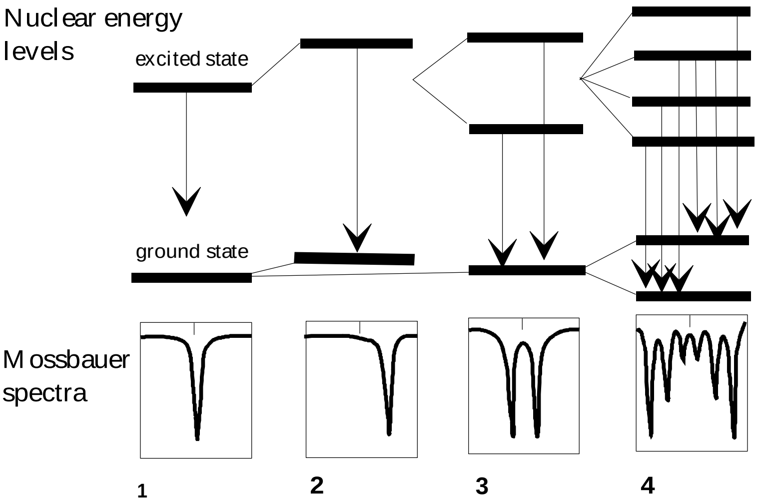

Figure 2.5_1 Hyperfine interactions characteristic of Mössbauer spectroscopy for ^{57}Fe.

1 - Spectra for a bare nucleus of ^{57}Fe. 2 - Isomer shift due to oxidation, 3 - Quadrupole splitting due to external electron environmental influence (such as neighbouring atoms in a crystal lattice), 4 - Magnetic dipole interaction. From McCammon (1995).

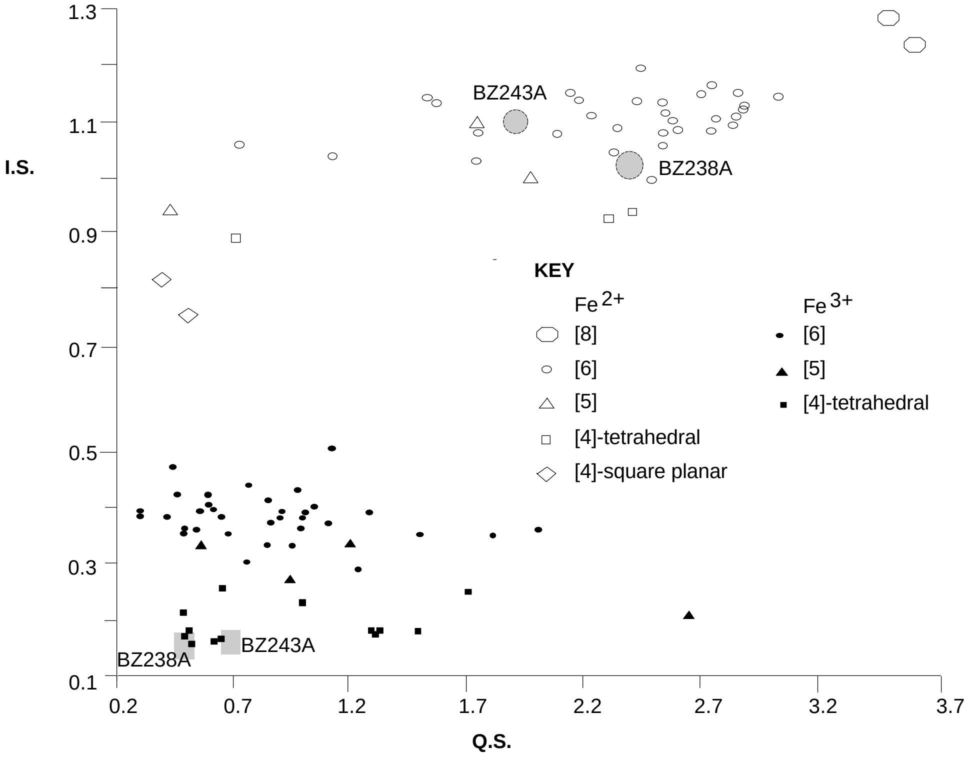

Figure 2.5_2 Fields of Fe^{3+} and Fe^{2+} in various coordinations in terms of I. S. / Q. S.

From Burns and Solberg (1990) The location of TAPP Fe^{2+} and Fe^{3+} is also plotted.

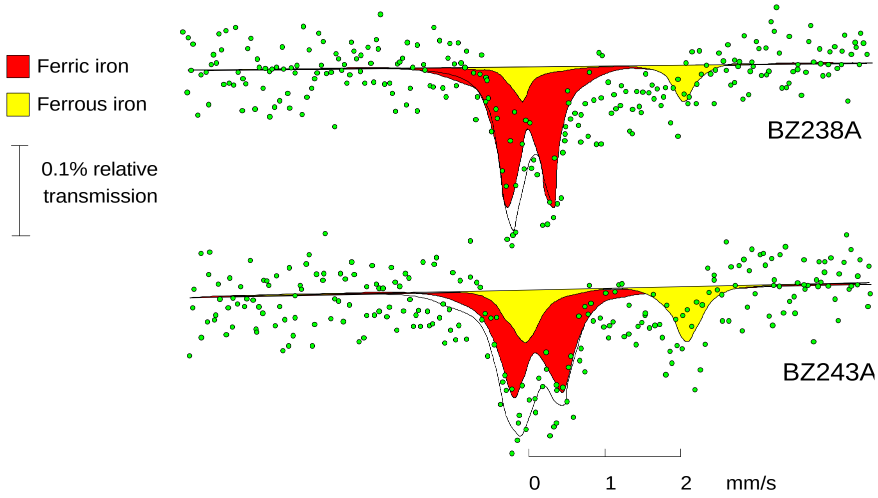

Figure 2.5_3 Mössbauer spectra of TAPP grains BZ238A and BZ243A.

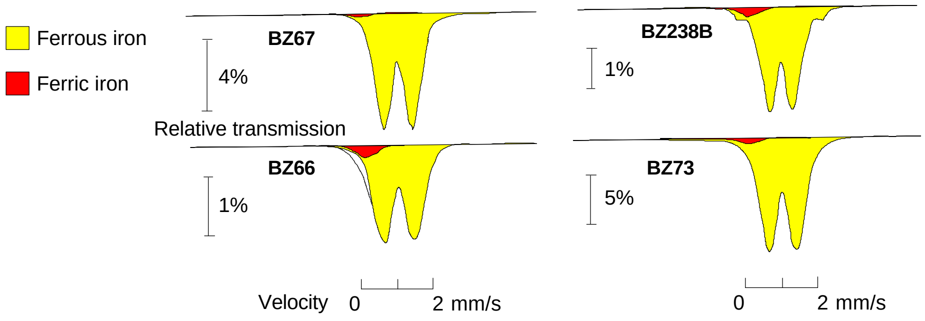

Figure 2.5_4 Mössbauer spectra of fPer grains BZ66, BZ67, BZ73, BZ238B.

Scatter of analytical points are approximately an order of magnitude less than for non-fPer samples (figures 2.5_3 and 2.5_7)

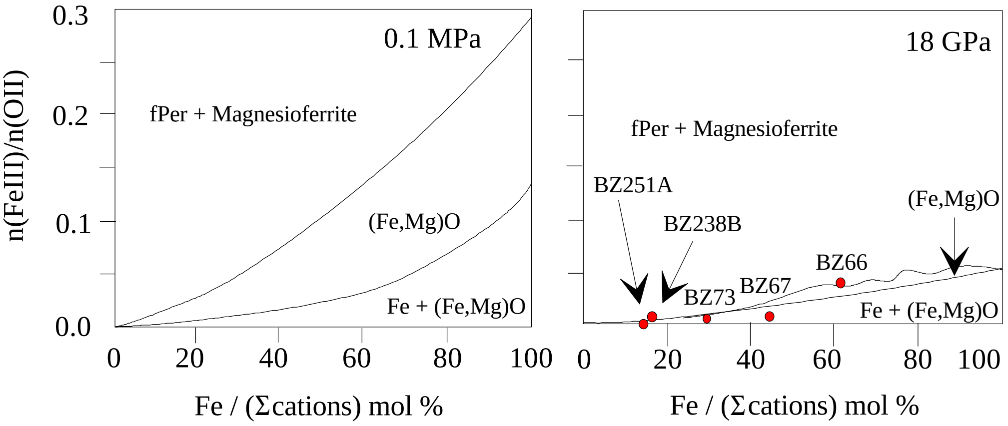

Figure 2.5_5 Minimum solubility of Fe^{3+} in fPer at 0.1 MPa and 18 GPa.

From McCammon et al. (1995) Fe^{3+} content of São Luiz fPer are plotted and show that they are consistent with formation at high pressure.

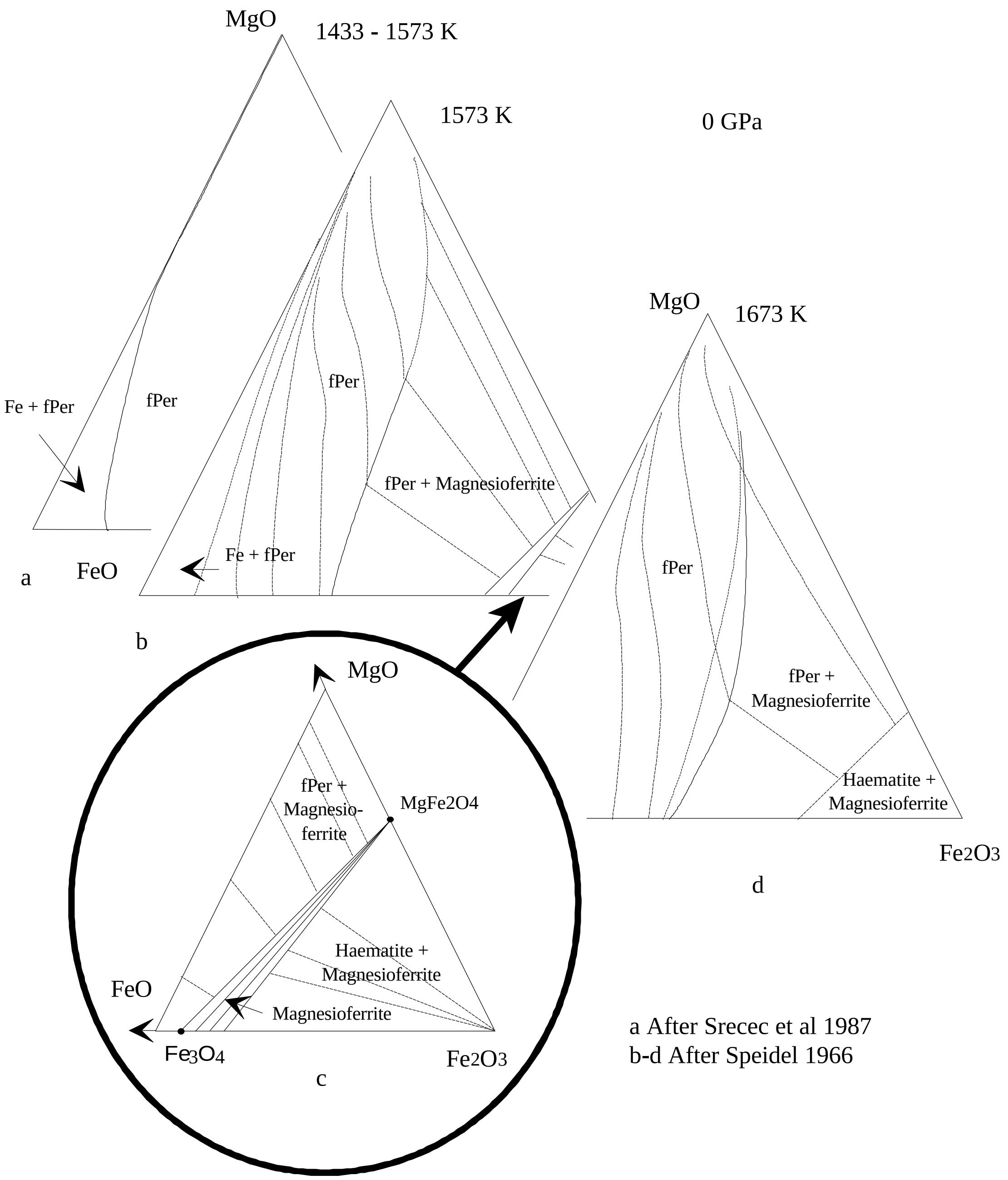

a After Srecec et al 1987
b-d After Speidel 1966

Figure 2.5_6 Phase relations in the FeO - Fe_2O_3 - MgO system with varying temperature.

With increasing temperature, the stability of fPer expands slightly towards higher oxygen content. However, as figure 2.5_5 shows, with increasing pressure, the phase field of fPer shrinks to lower values of Fe^{3+}. This is believed to be due to the stabilisation of a high pressure phase of magnesioferrite.

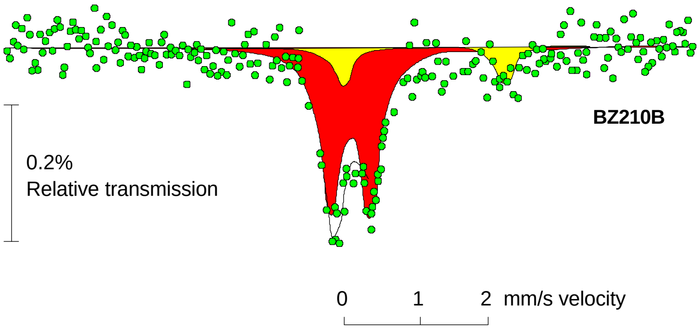

Figure 2.5_7 Mössbauer spectra of Type II MgSi-Pvk, BZ210B.

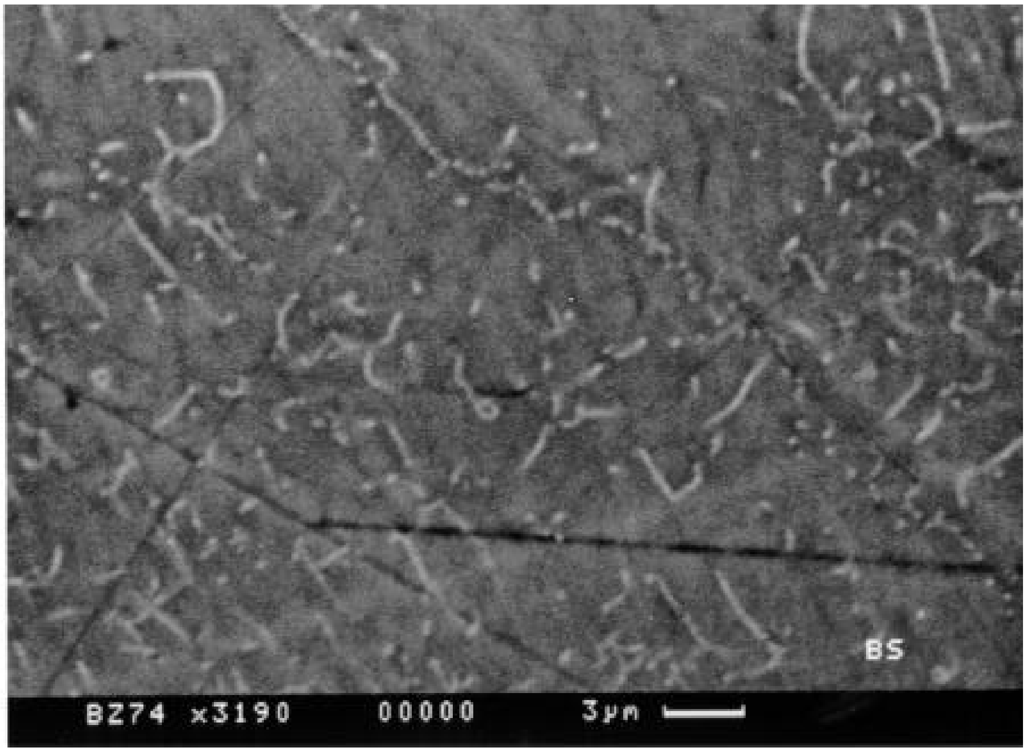

Figure 2.6_1 BS-SEM image of BZ74 showing elongate and spot 'blebs' of high BS-reflectivity.

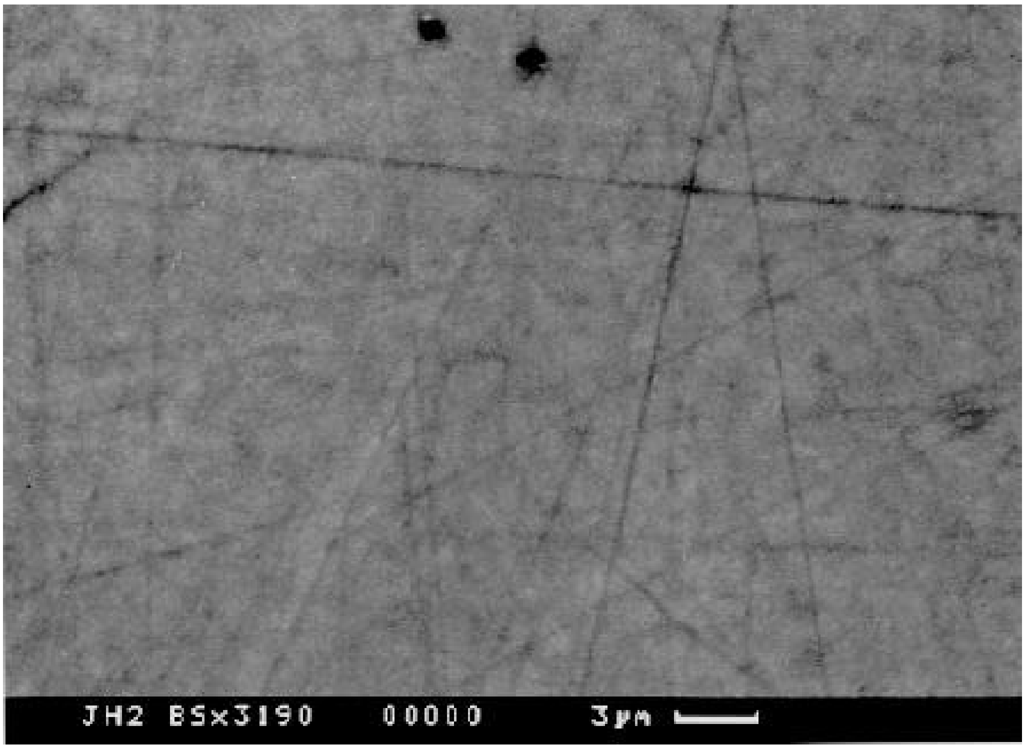

Figure 2.6_2 BS-SEM image of JH2 showing no 'blebs' only scratches due to the polishing process.

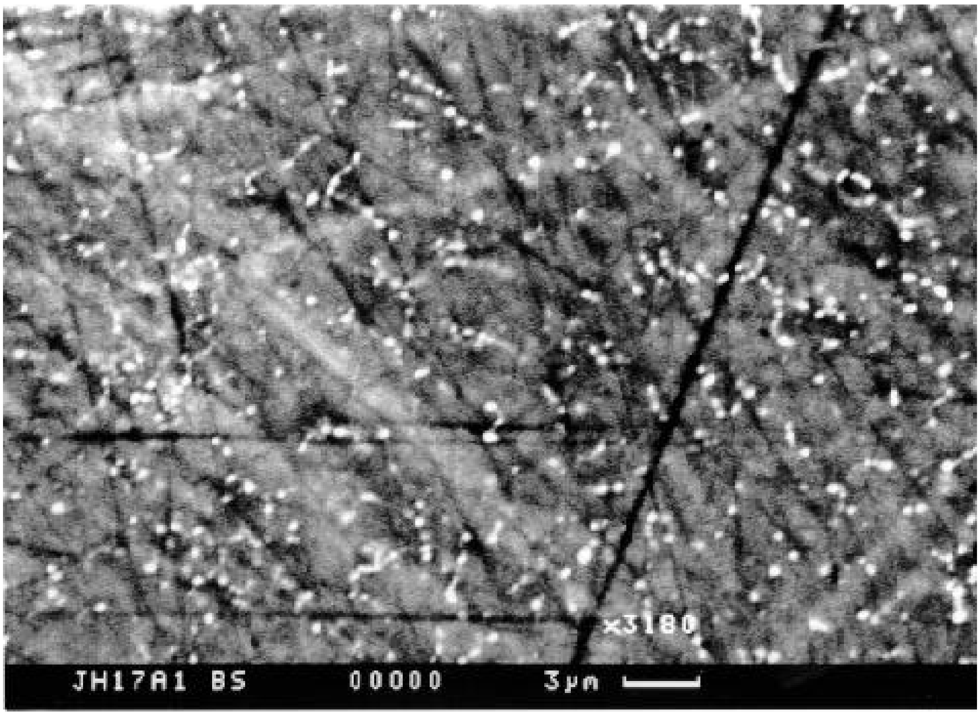

Figure 2.6_3 BS-SEM of 'blebs' in JH17A1 showing spots congregating into linear features.

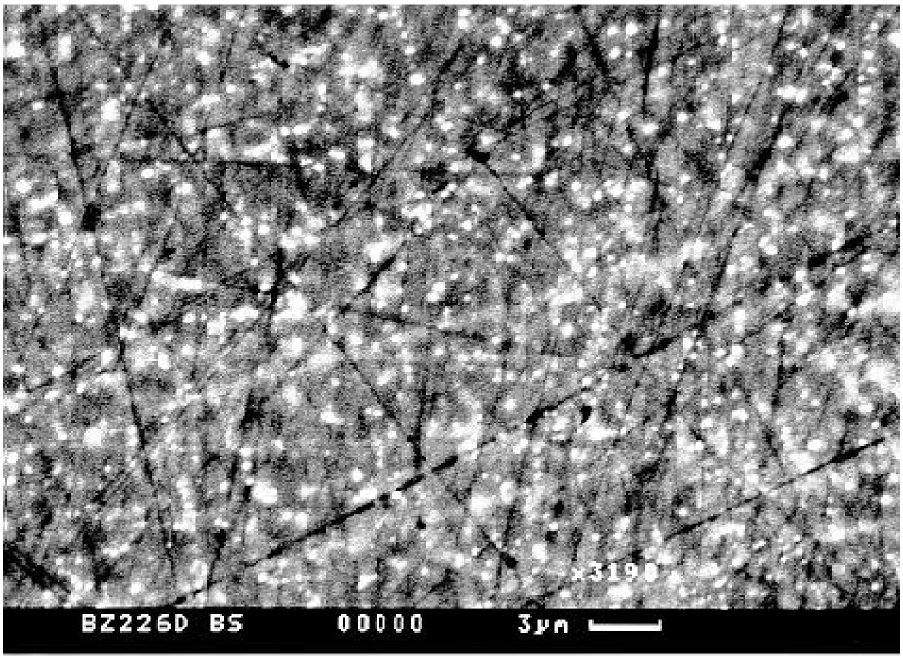

Figure 2.6_4 BS-SEM image of BZ226B showing a dominance of spots ($\Sigma_{\text{linear blebs}}$ / Σ_{spots}= 0.0451).

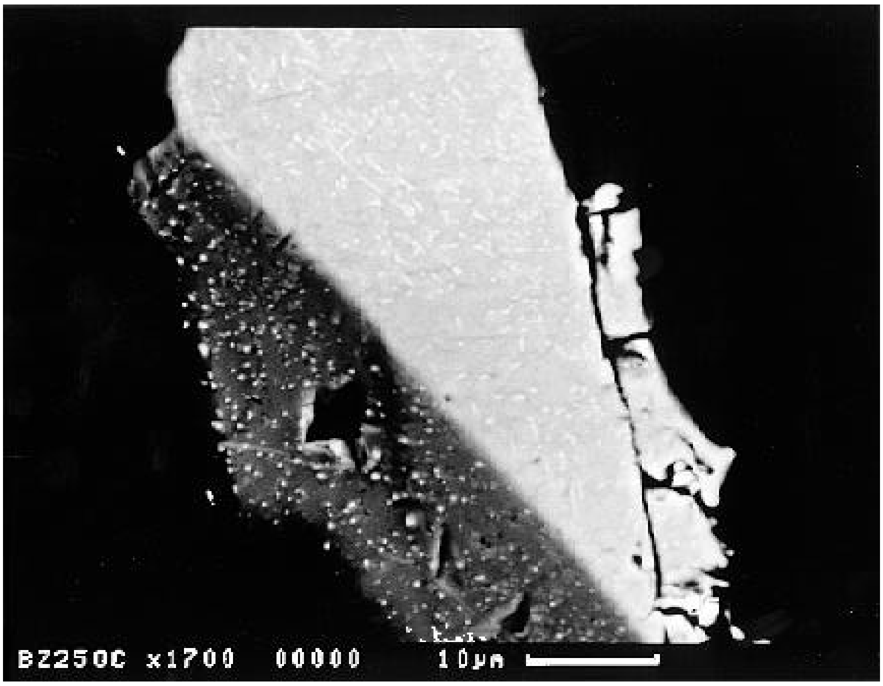

Figure 2.6_5 BS-SEM image of BZ250C showing the contrast between large rounded dust grains occupying the depression on the grain surface into the araldite with the 'blebs' on the flat grain surface.

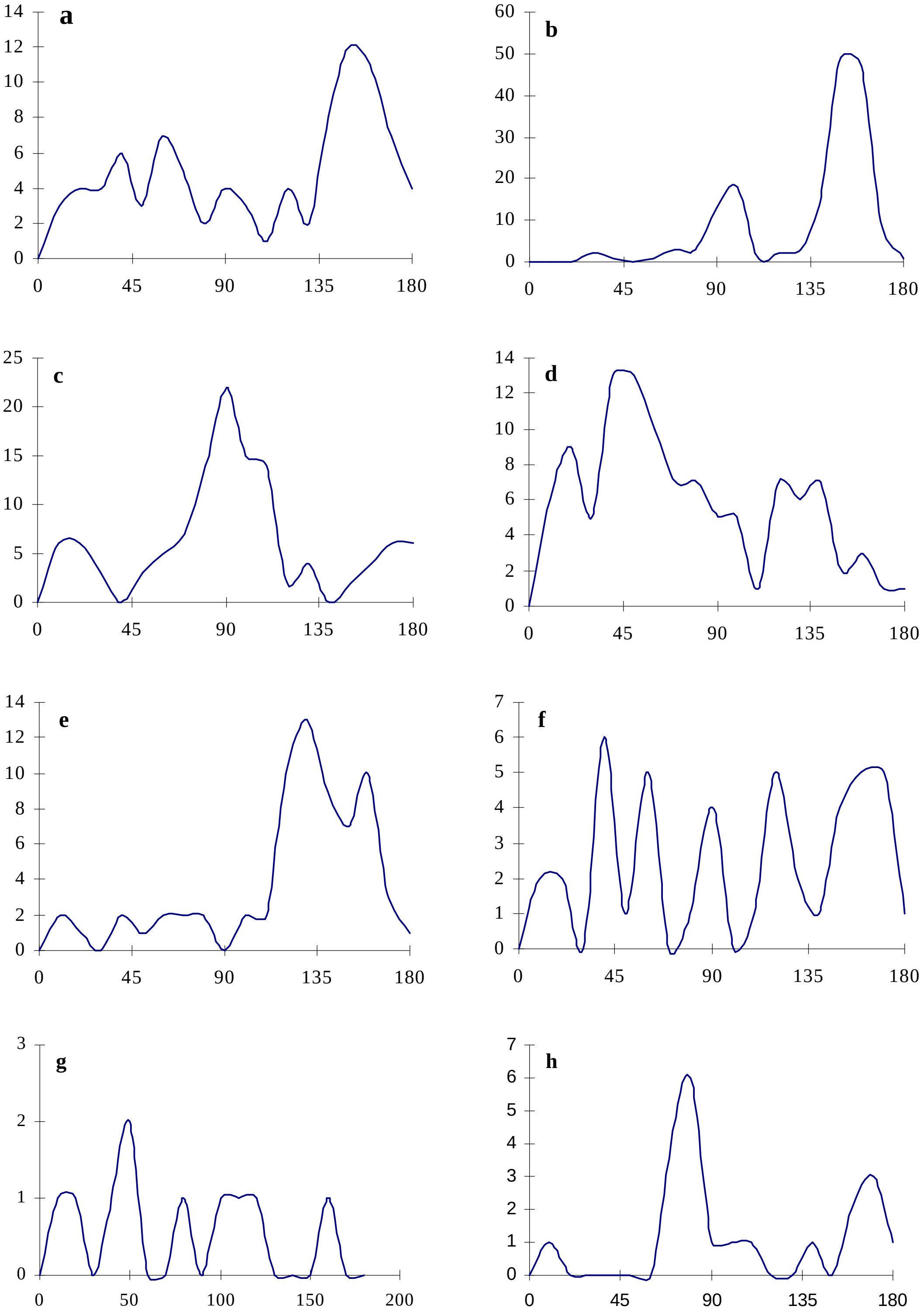

Figure 2.6_6 Histograms of frequency against angle (°) of elongate bleb orientation.

Data is weighted such that longer 'blebs' have more influence, however, the same conclusions are reached from unbiased data Generally inclusion surfaces with large ratios of $\Sigma_{\text{linear blebs}}$ / Σ_{spots} (σ) show two preferred orientations at ~ 90° to each other. a - BZ74 x3190 (image magnification) $\sigma = 1.26$, b - BZ74 x1500 $\sigma = 1.14$, c - BZ70 x2970 $\sigma = 1.08$, d - BZ201A x3180 $\sigma = 0.76$, e - BZ250C x3500 $\sigma = 0.61$, f - JH17A1 x3180 $\sigma = 0.18$, g - BZ205C x3180 $\sigma = 0.05$, h - BZ226B x3190 $\sigma = 0.05$.

Figure 2.6_7 TEM image of a 0.4 μm 'bleb' within fPer grain BZ67 showing a further 0.1 μm inclusion within.

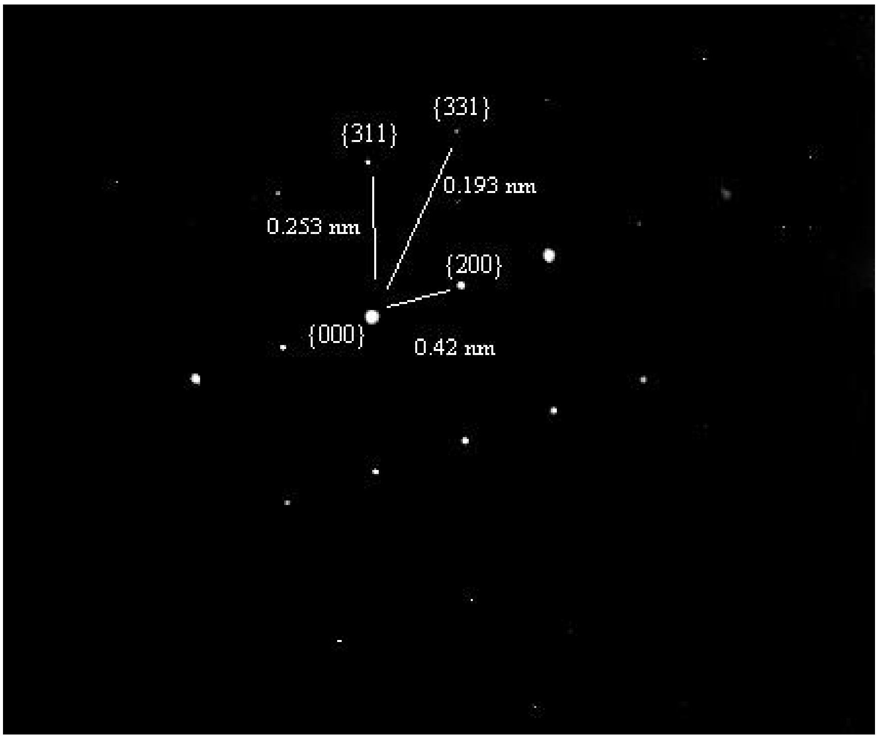

Figure 2.6_8 TEM diffraction pattern of a 'bleb' within BZ67 indexed as magnetite.

As table 2.6_2 shows, the 'bleb' proves to fit a standard magnetite (end member in the magnesioferrite s.s.) pattern very well.

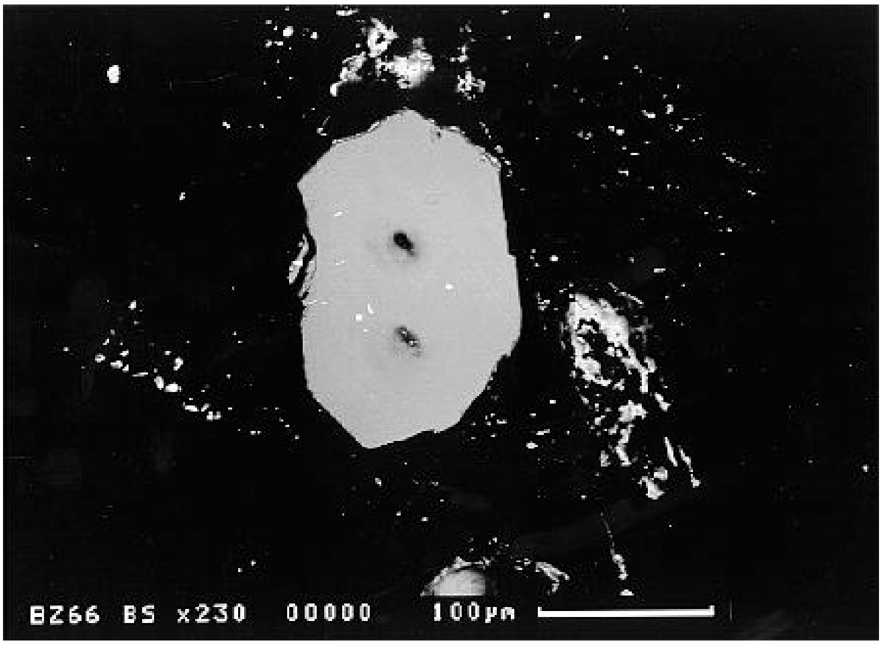

Figure 2.6_9 BS-SEM image of BZ66 showing a number of large, bright ~ 1-4 μm features.

EPMA analyses shows the composition of bright BS areas in BZ66 to be FeNi alloy.

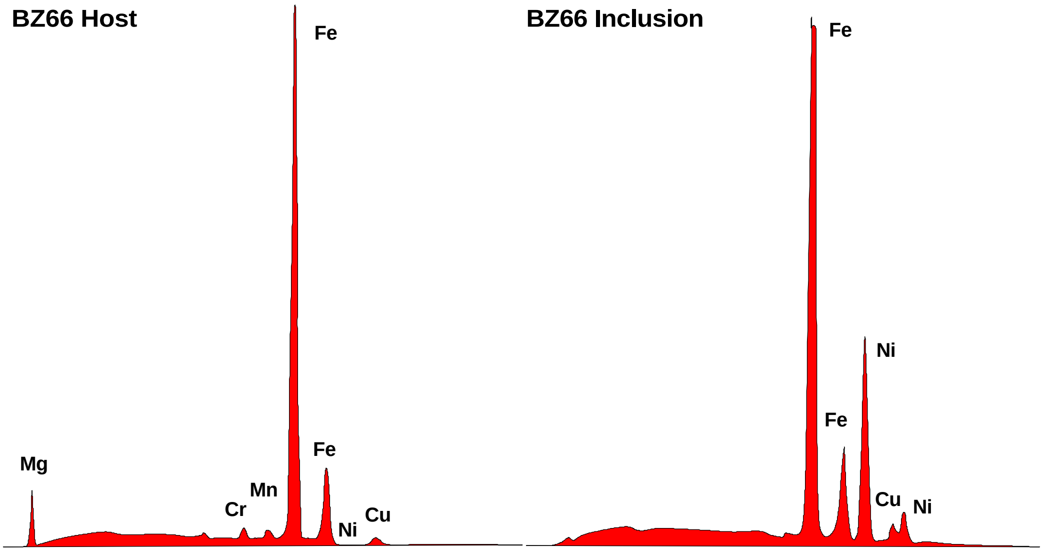
BZ66 Host

BZ66 Inclusion

Figure 2.6_10 EDS spectra of BZ66 host compared to the large bright BS area.

The bright area is markedly enriched in Ni and exhibits an even larger Fe / Mg ratio.

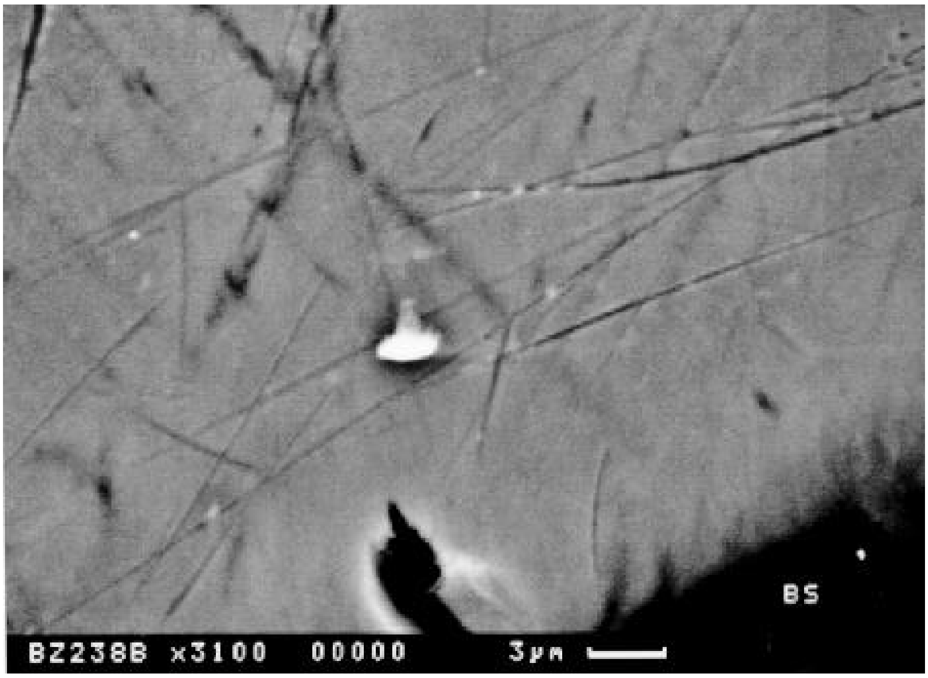

Figure 2.6_11 BS-SEM image of BZ238B showing a single bright area ~ 2μm in width.

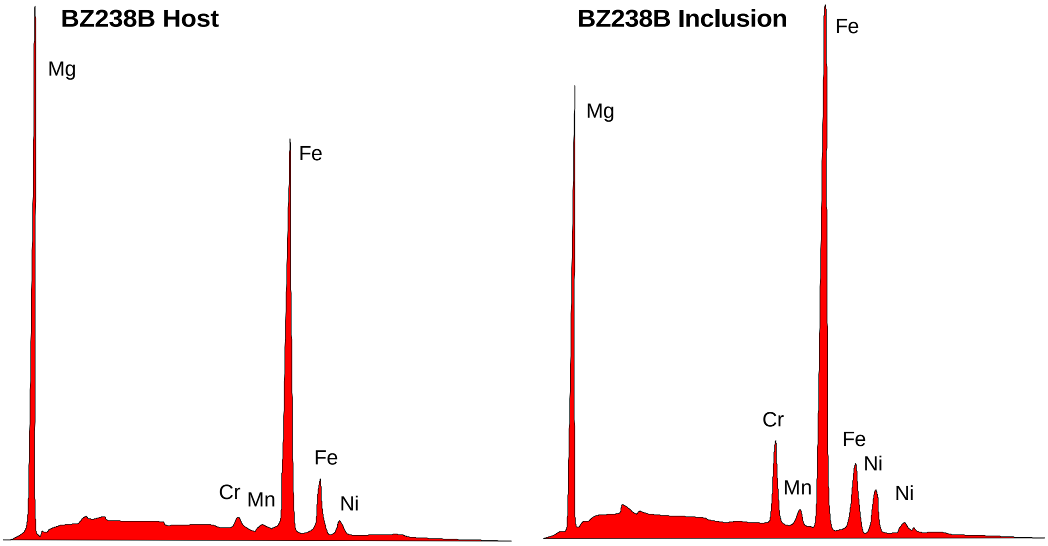

Figure 2.6_12 EDS spectra of BZ238B host compared to the bright BS area.

The bright area has a larger Fe / Mg ratio, significantly higher Cr content and more Mn and Ni.

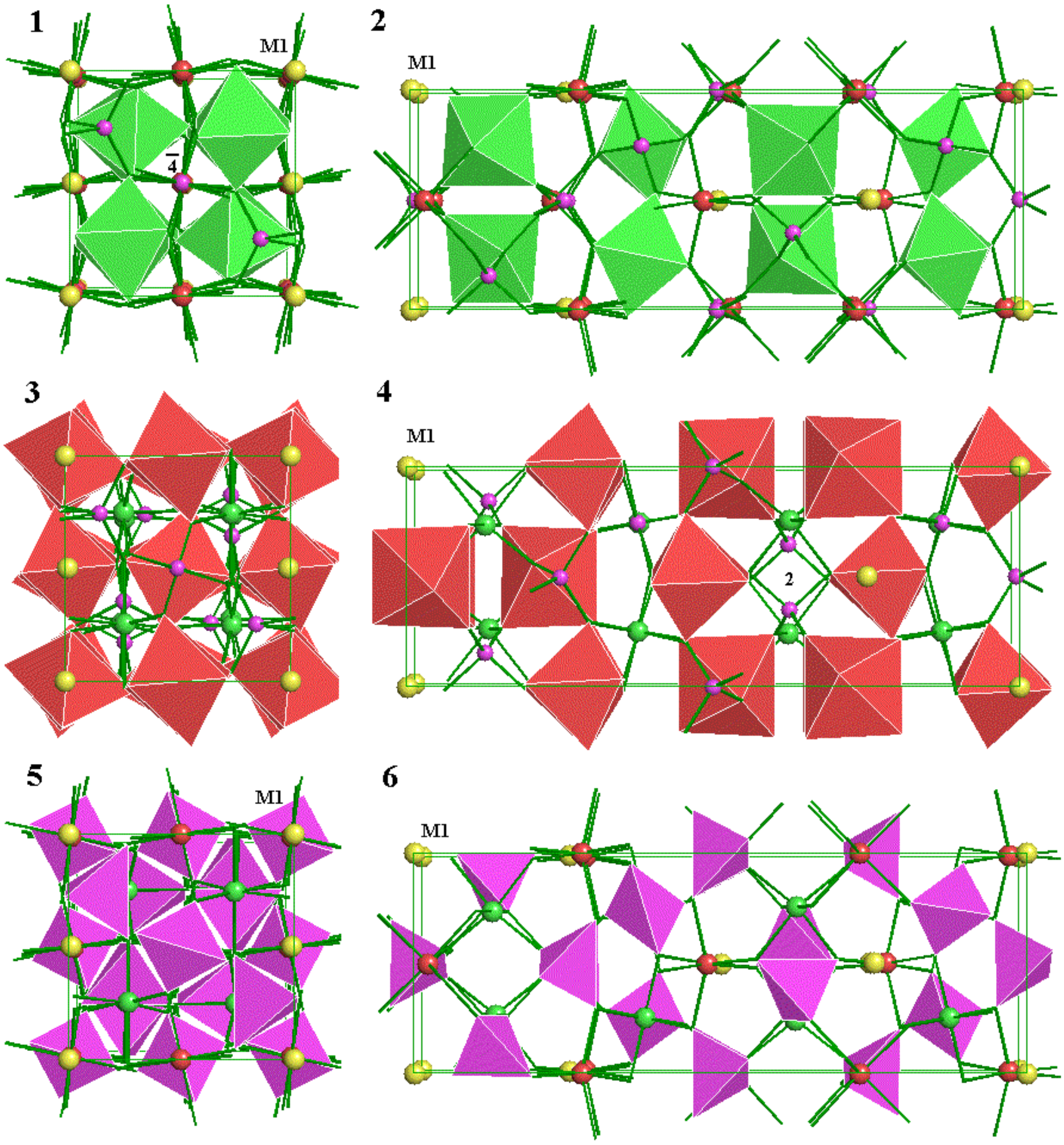

Figure 3.3_1 The structure of TAPP onto (001) and (010) with Si-tetrahedra, M2 and M3 octahedra emphasised.

The tetragonal nature of the structure and the independent Si-tetrahedra are particularly notable aspects of TAPP.
1 - M2 Octahedra looking onto (001), 2 - M2 Octahedra looking onto (010), 3 - M3 Octahedra looking onto (001), 4 - M3 Octahedra looking onto (010), 5 - Si Tetrahedra looking onto (001), 6 - Si Tetrahedra looking onto (010).

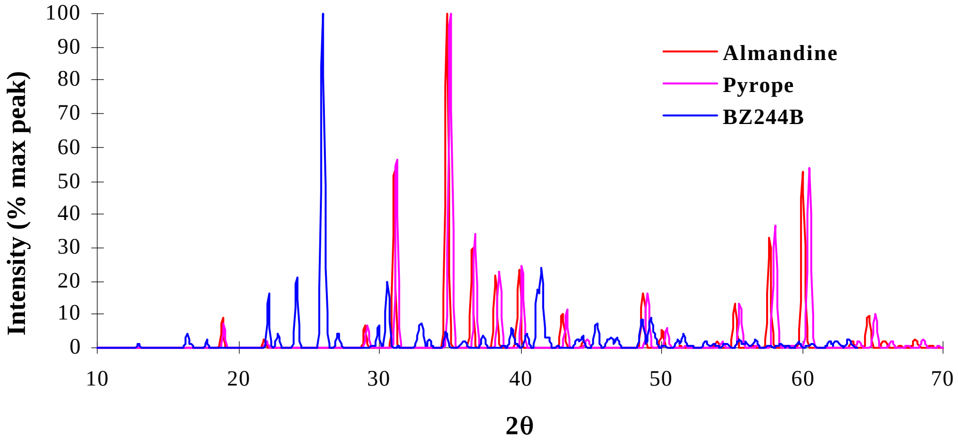

Figure 3.3_2 Comparison of predicted powder patterns for TAPP, garnet structured pyrope and almandine.

Calculated from pyrope and almandine crystallographic data from Armbruster et al. (1992) and for BZ244B, section 3.3.1.2.

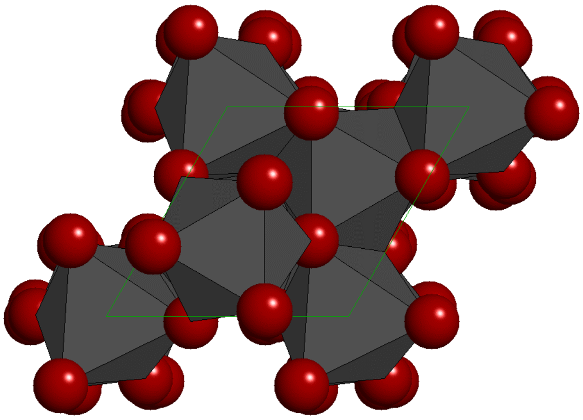

Figure 3.3_3 A single unit cell of BZ227A sapphire showing Al - O polyhedra.

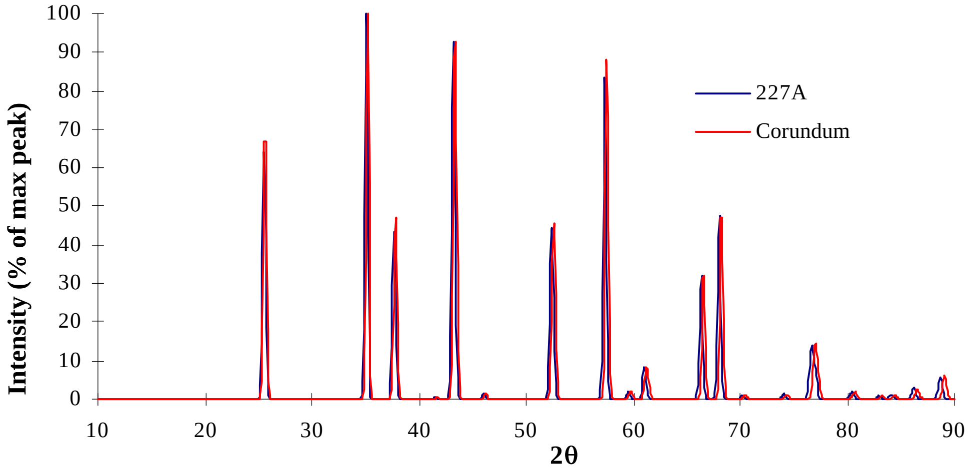

Figure 3.3_4 Comparison of calculated powder pattern of BZ227A sapphire and natural Al_2O_3.

Calculated from alumina data from Newnham and De Haan (1962) and for BZ227A, section 3.3.2.1.

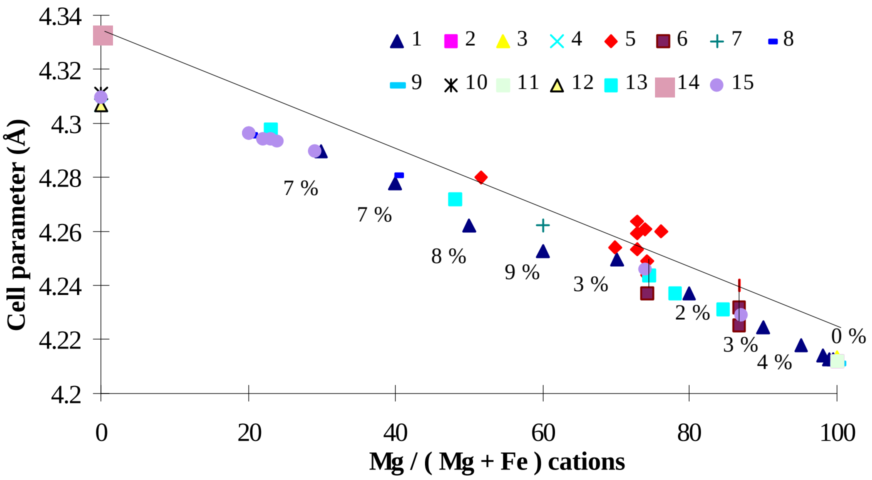

Figure 3.3_5 Cell parameter values for natural and synthetic Periclase - Wüstite.

The deviation from a linear relationship amongst low pressure synthetic samples from the literature towards the FeO end member is attributed to the presence of significant Fe^{3+}. Concentrations of % $Fe^{3+}/\Sigma Fe$ from Waychunas et al. (1994).
1 - Waychunas et al. (1994), 2 - Skinner (1956), 3 - Scacchi (1841), 4 - Shenk and Dingmann (1927), 5 - This study (released), 6 - This study (in-situ), 7 - Rosenhauer et al. (1976), 8 - Richet et al. (1989), 9 - Hazen (1976), 10 - Foster et al. (1956), 11 - Reeber et al. (1995), 12 - Jackson et al. (1990), 13 - Jackson et al . (1978), 14 - Hentschel (1970), 15 - Bell et al. (1979)

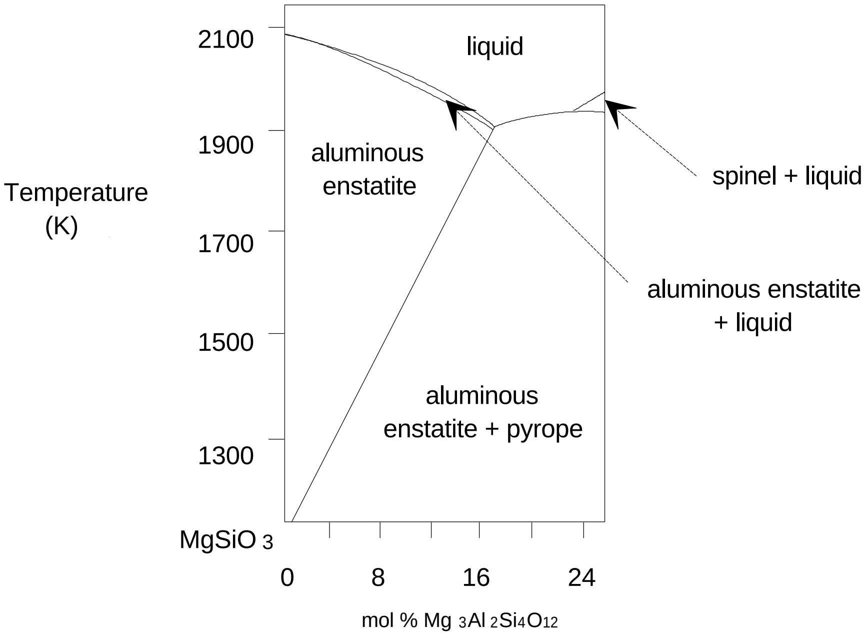

Figure 3.3_6 Phase relations in the $MgSiO_3$ - $Mg_3Al_2Si_4O_{12}$ system at 3 GPa and variable temperature.

After Boyd and England (1964).

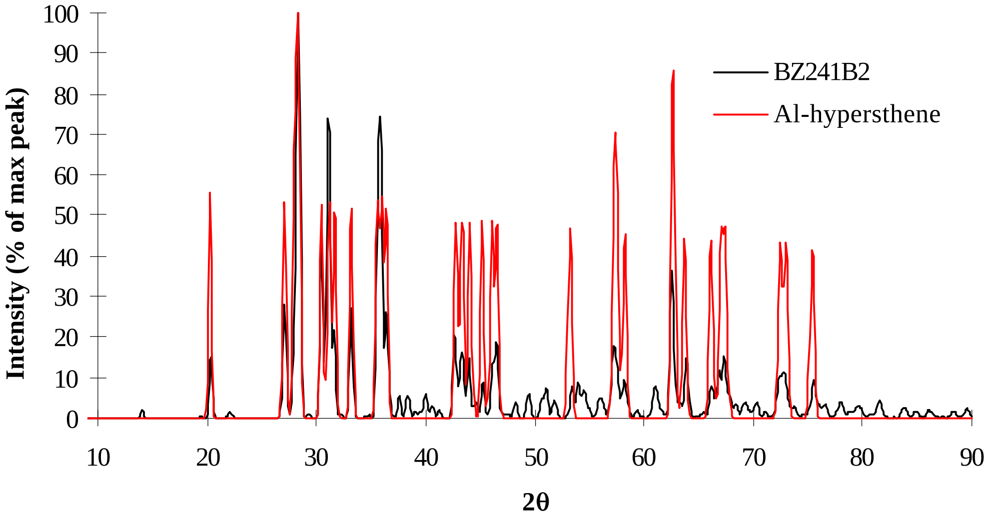

Figure 3.3_7 Comparison of calculated diffraction of aluminous hypersthene from the Sutam River and Type II pyroxene, BZ241B2.

Calculated from data in Brovkin et al. (1975) and for BZ241B2 from section 3.3.5.2

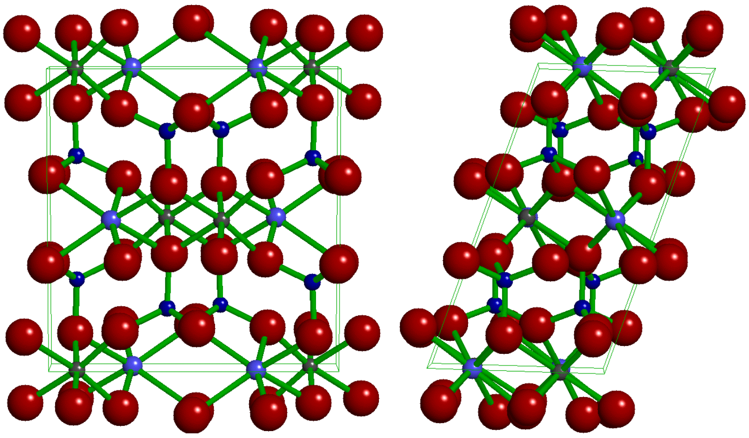

Figure 3.3_8 Crystal structure of BZ242B, Type III aluminous Ca, Na pyroxene.

BZ242B adopts a C2/c monoclinic structure as is apparent from the non-orthogonal nature of the unit cell axes (β = 108.33°).

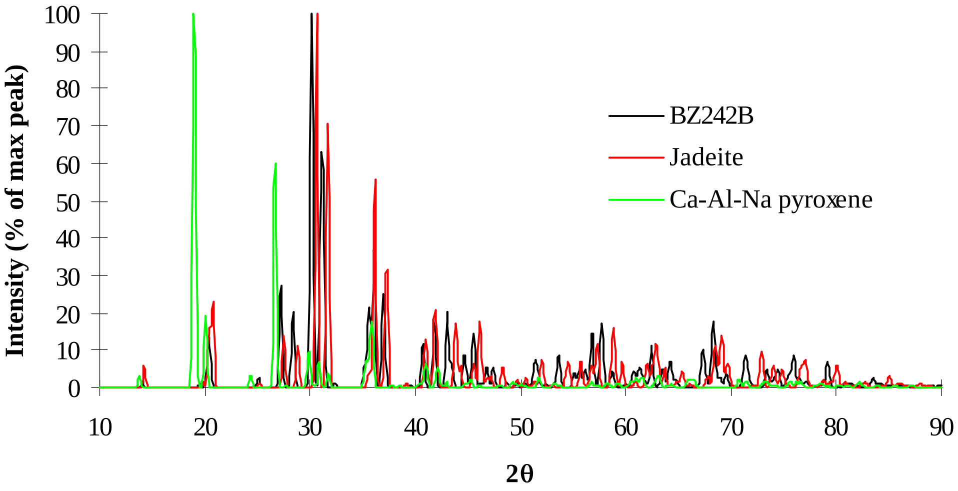

Figure 3.3_9 Comparison of principal diffraction lines of natural jadeite, aluminous Ca, pyroxene from the Western Ross Embayment and Type III pyroxene, BZ242B.

Calculated from data in Salviulo et al. (1997) and Clark et al. (1969) and for BZ242B in section 3.3.5.2.

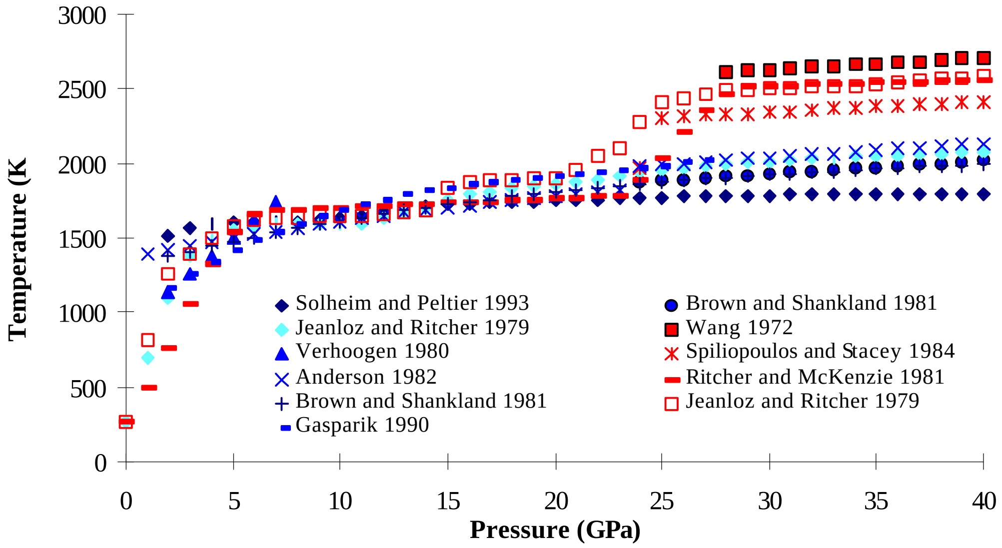

Figure 4.2_1 Mantle geotherms.

Postulated mantle geotherms cluster into two distinct groups, one involving a sharp increase in temperature into the lower mantle (termed the thermal boundary), the other showing a relatively constant rise in temperature throughout the transition zone and lower mantle.

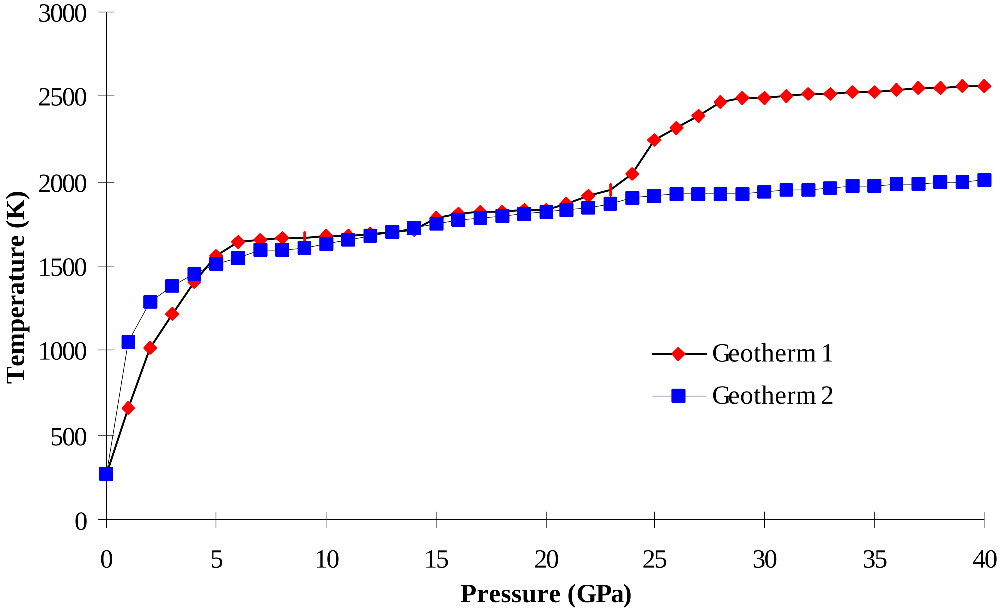

Figure 4.2_2 Averaged mantle geotherms.

Geotherm 1- involving a thermal boundary between upper and lower mantle and a typical cratonic lithosphere geotherm. Geotherm 2 - involving no thermal boundary between upper and lower mantle and a relatively slow final temperature fall with decreaing pressure characteristic of rapid exhumation.

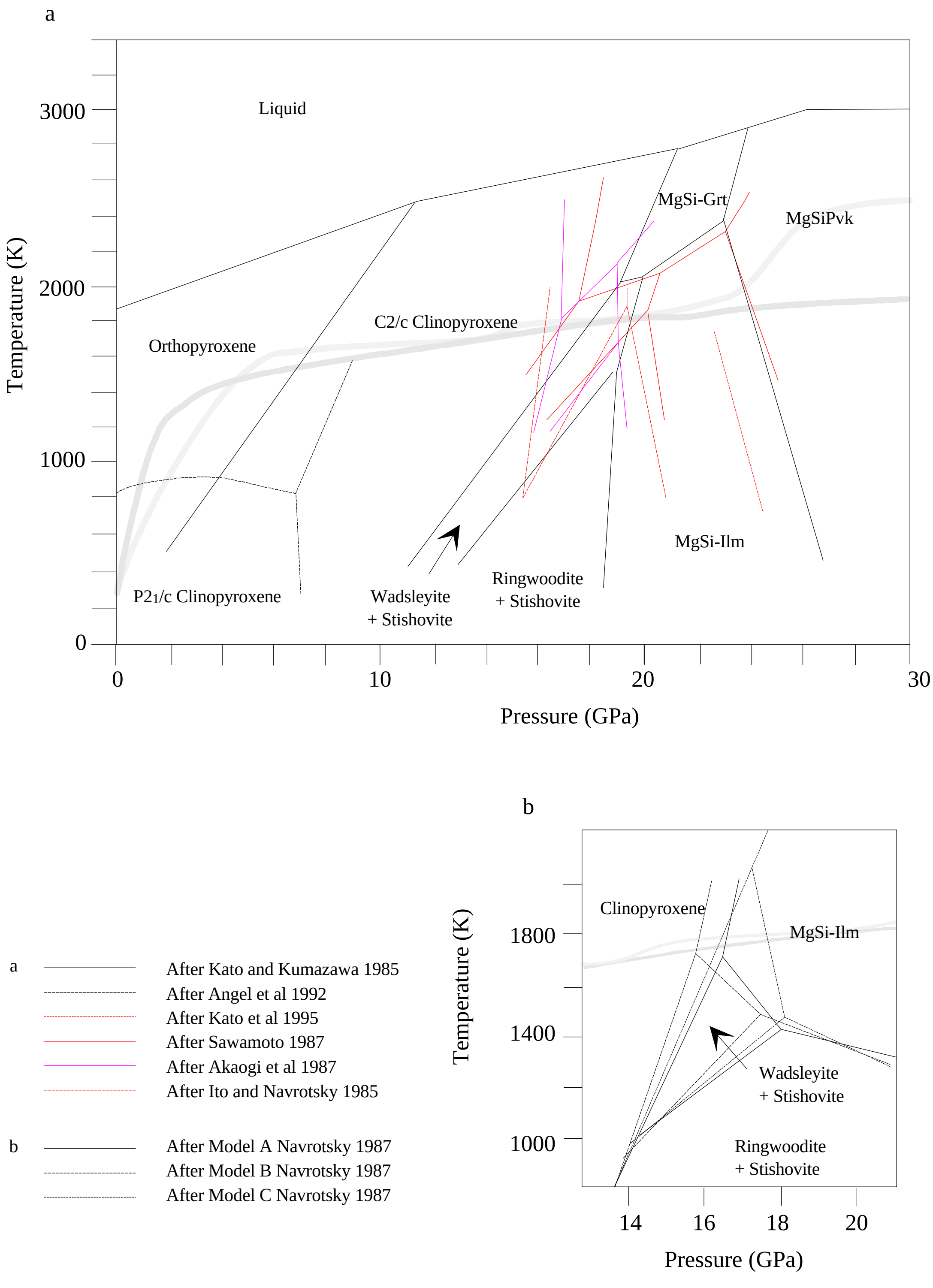

Figure 4.4_1 Phase relations in the $MgSiO_3$ system in terms of pressure and temperature.

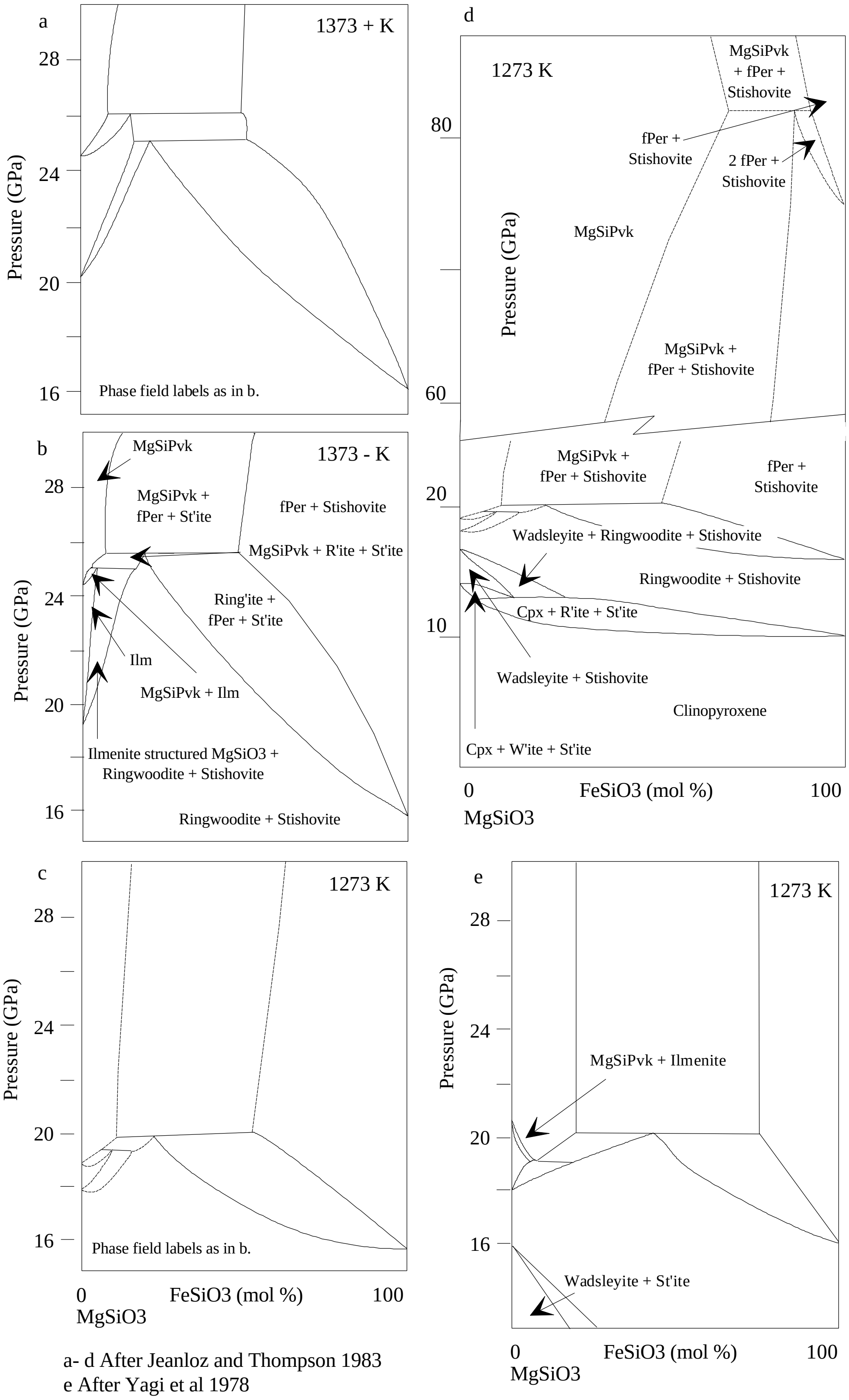

a- d After Jeanloz and Thompson 1983
e After Yagi et al 1978

Figure 4.4_2 Phase relations in the $MgSiO_3$ - $FeSiO_3$ system in terms of pressure and at different temperatures.

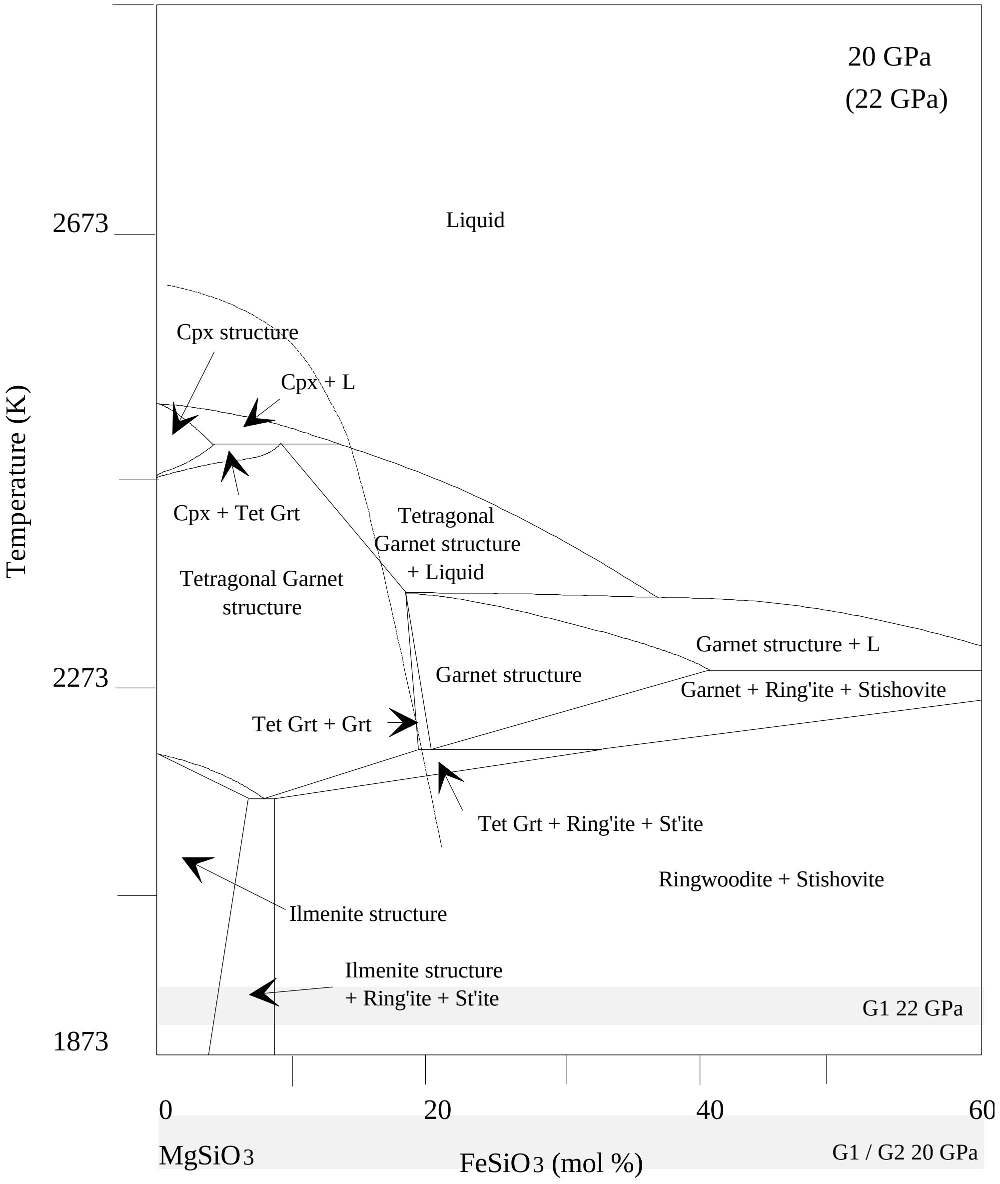

After Kato 1986

------- After Wang et al 1993, dotted line denotes phase boundary between tetragonal and normal (cubic) garnet structure to higher T (22 GPa)

Figure 4.4_3 Phase relations in the $MgSiO_3$ - $FeSiO_3$ system in terms of temperature and at deep transition zone pressures.

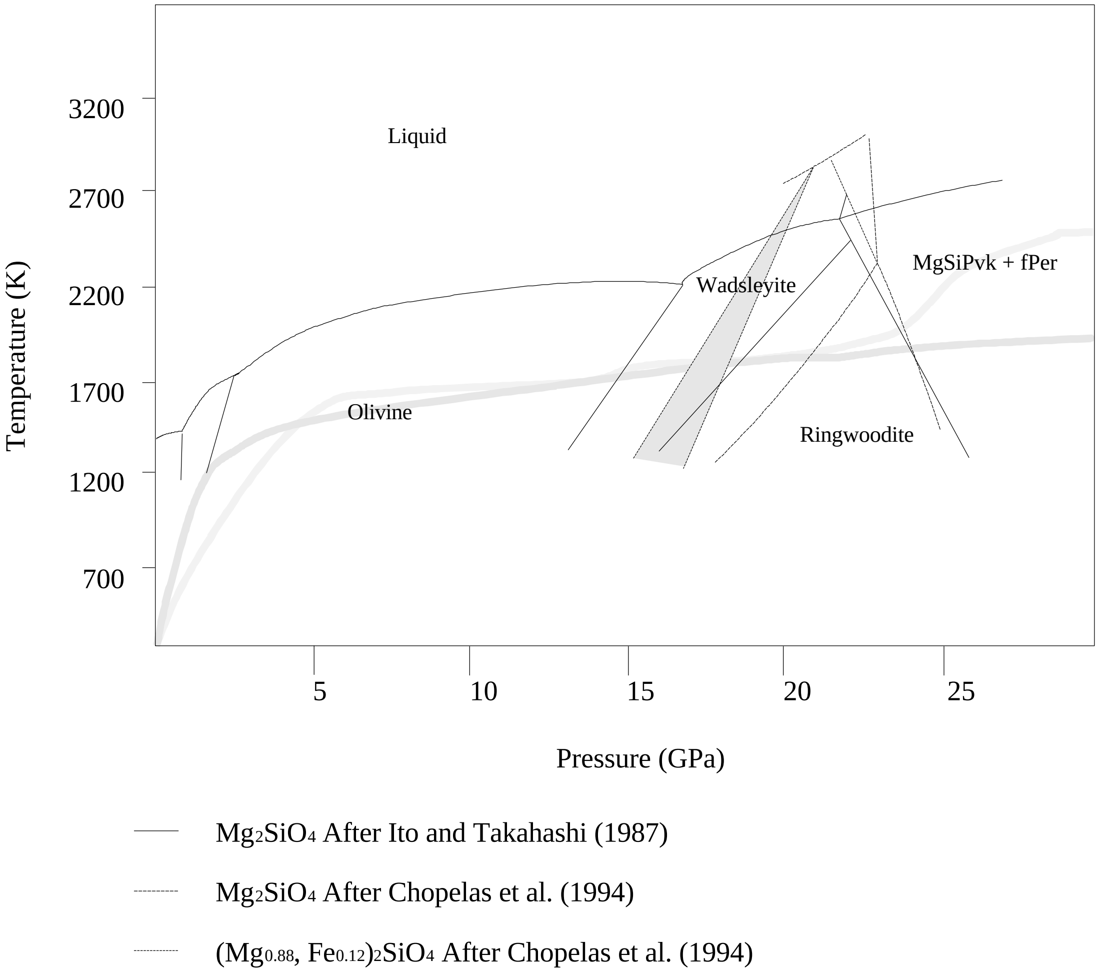

Figure 4.4_4 Phase relations in the $(Mg,Fe)_2SiO_4$ system in terms of temperature and pressure.

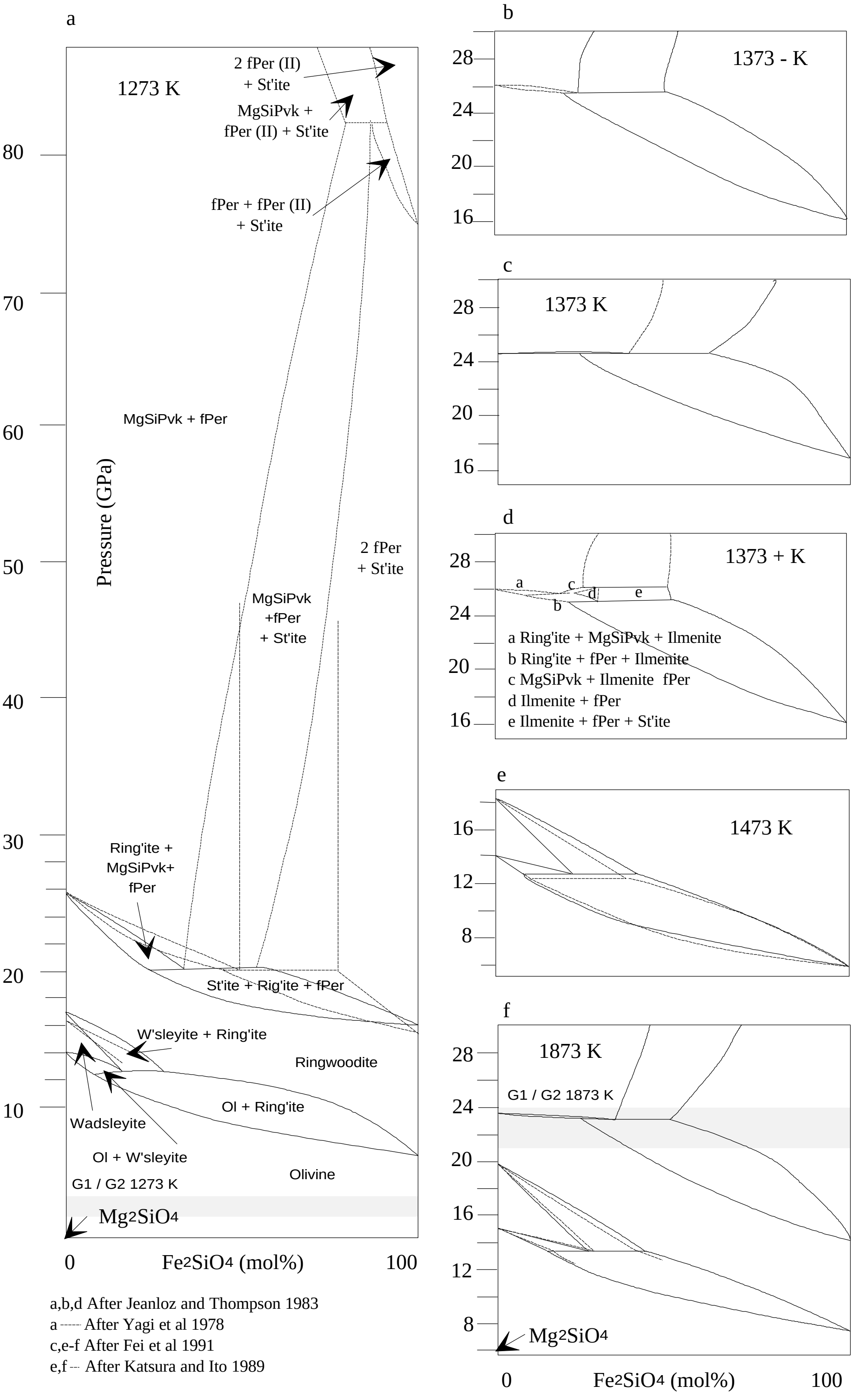

Figure 4.4_5 Phase relations in the Mg_2SiO_4 - Fe_2SiO_4 system in terms of pressure and at different temperatures.

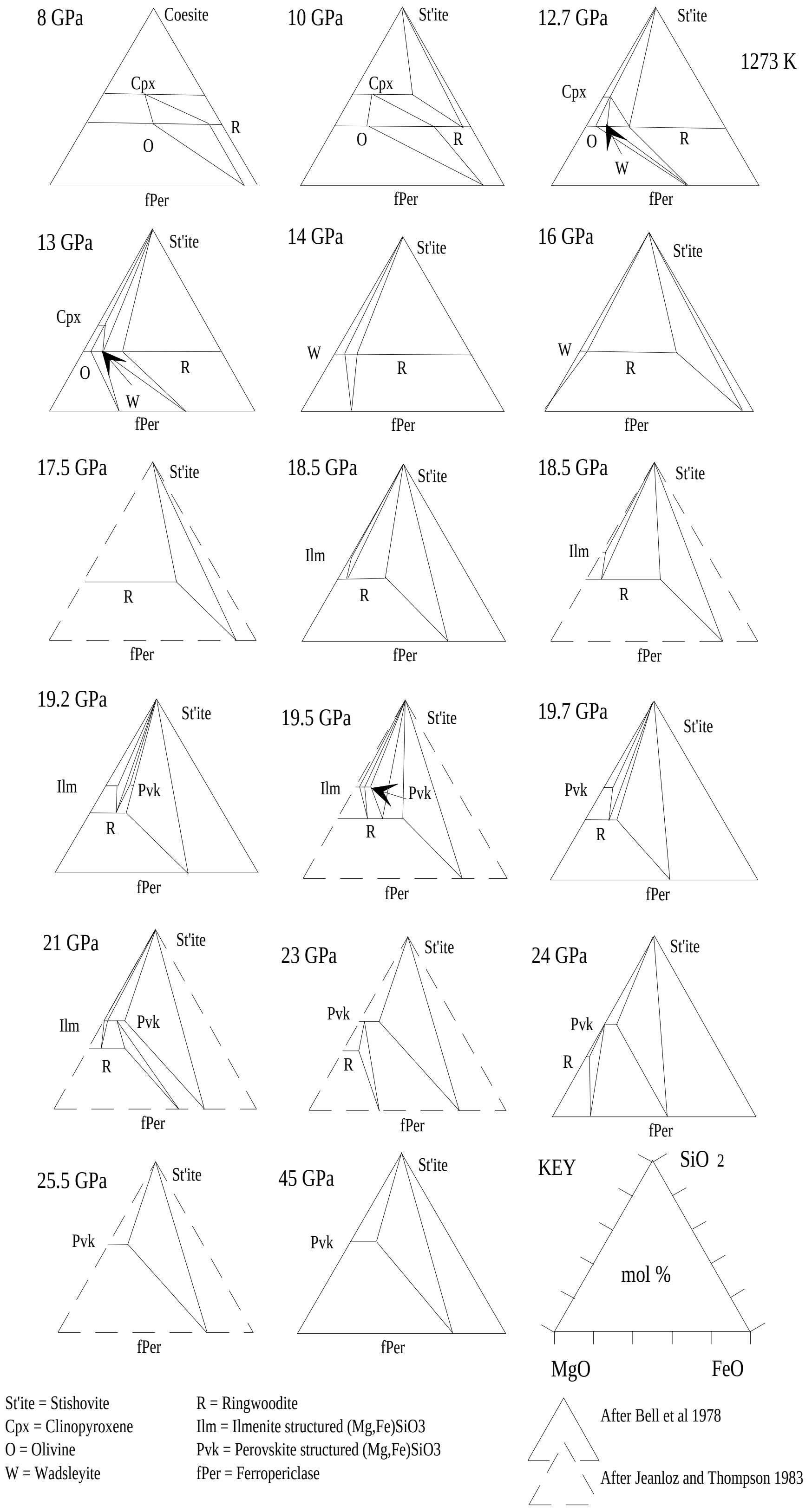

Figure 4.4_6 Phase relations in the ternary system MgO- FeO - SiO_2 in terms of pressure and at constant temperature 1273K.

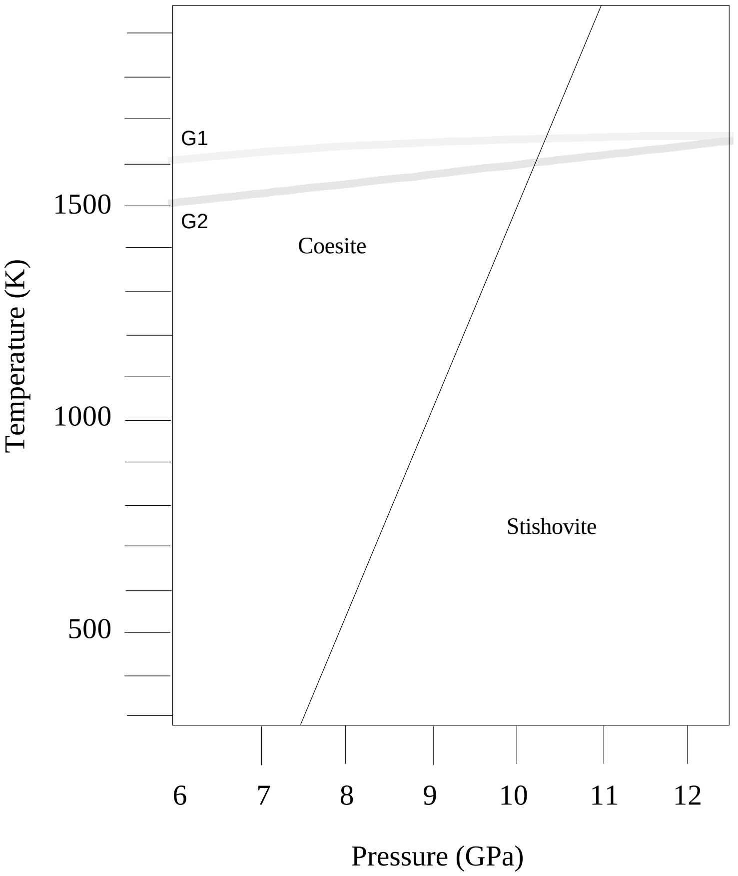

After Yagi and Akimoto 1976

Figure 4.4_7 Phase relations in the SiO_2 system in terms of pressure and temperature.

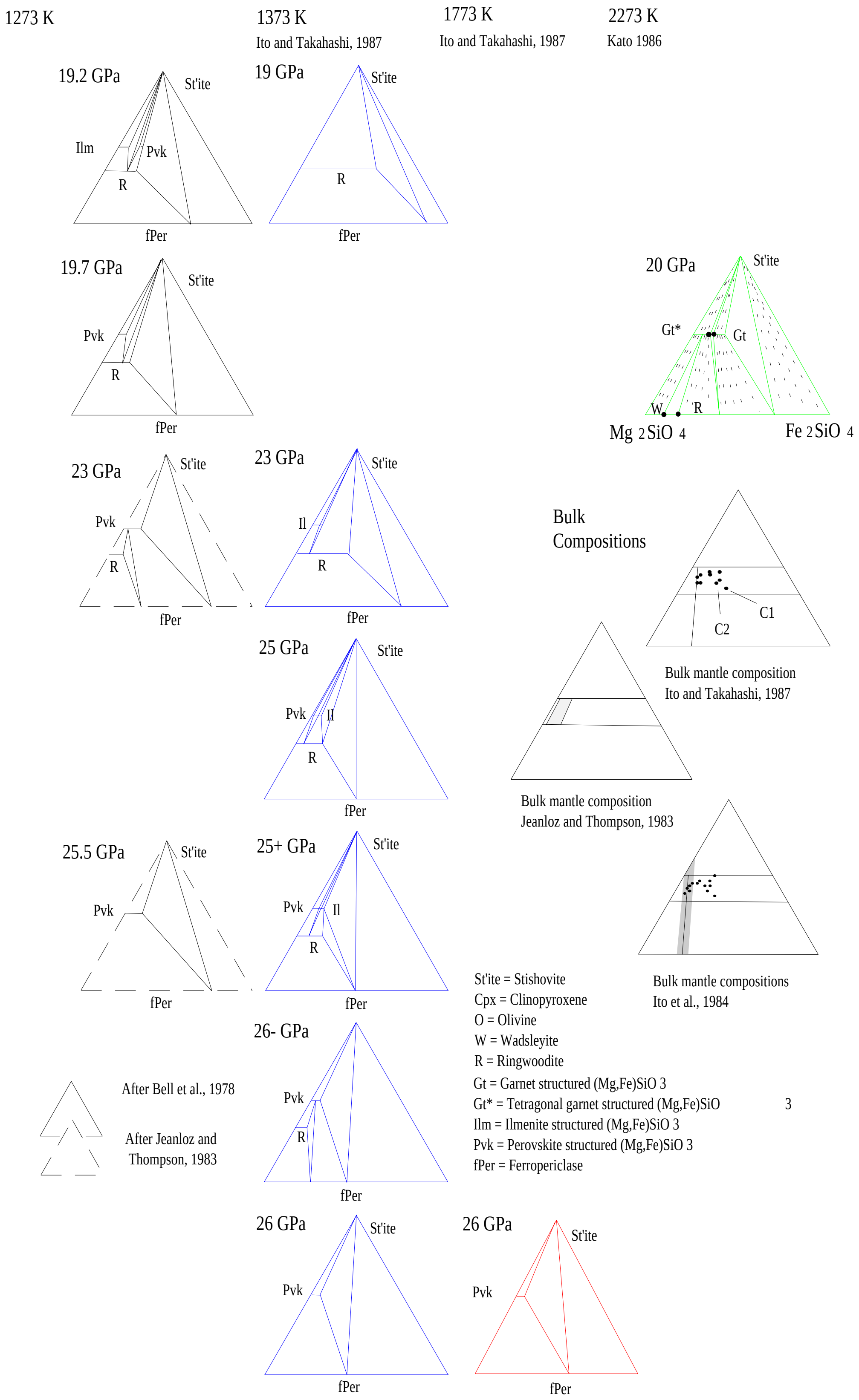

Figure 4.4_8 Phase relations in the ternary system MgO - FeO - SiO_2 in terms of pressures and temperatures relevent to the the mantle transition zone and lower mantle.

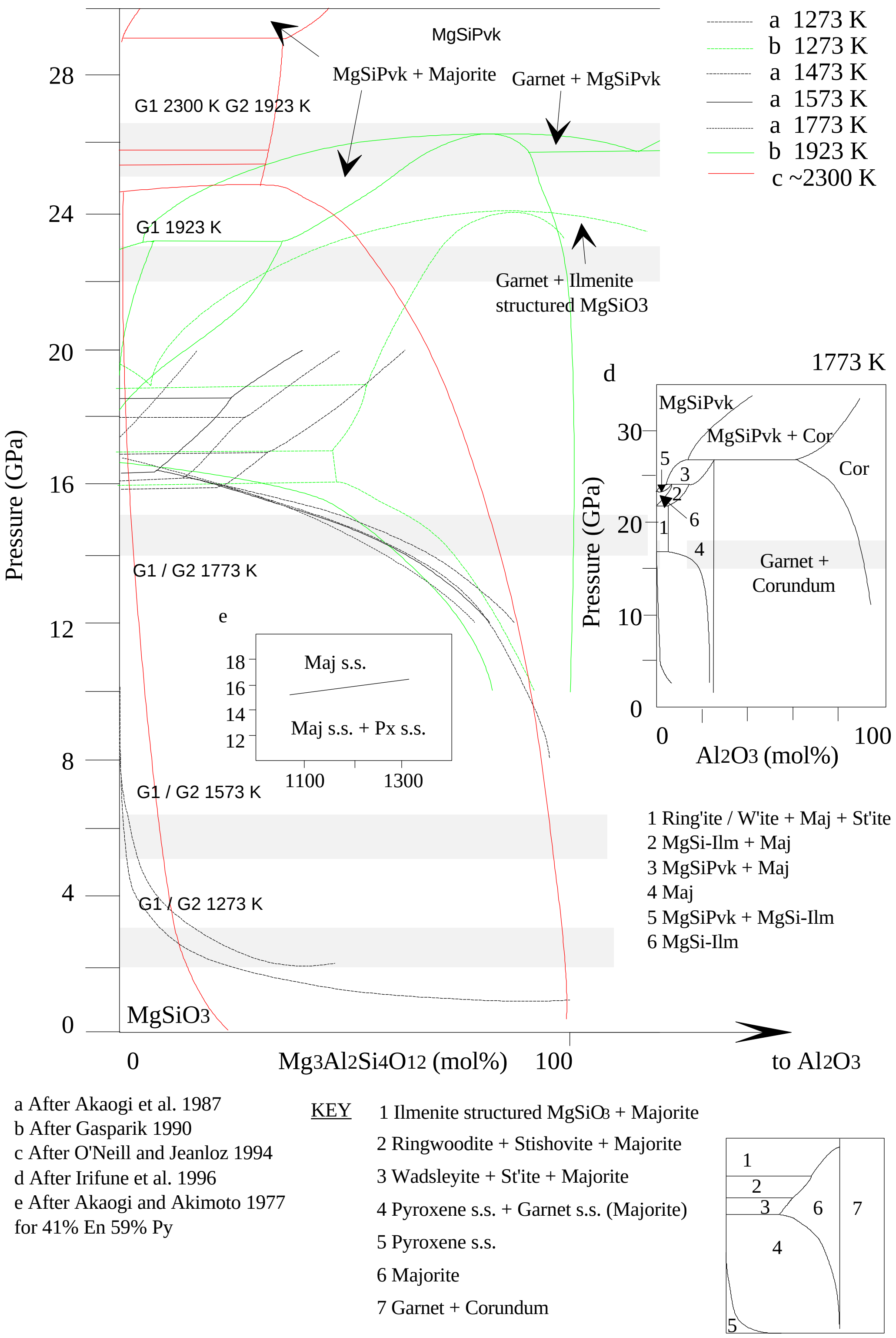

a After Akaogi et al. 1987
b After Gasparik 1990
c After O'Neill and Jeanloz 1994
d After Irifune et al. 1996
e After Akaogi and Akimoto 1977
for 41% En 59% Py

<u>KEY</u>

1 Ilmenite structured $MgSiO_3$ + Majorite
2 Ringwoodite + Stishovite + Majorite
3 Wadsleyite + St'ite + Majorite
4 Pyroxene s.s. + Garnet s.s. (Majorite)
5 Pyroxene s.s.
6 Majorite
7 Garnet + Corundum

Figure 4.4_9 Phase relations in the $MgSiO_3$ - $Mg_3Al_2Si_4O_{12}$ system in terms of pressure and at different temperatures.

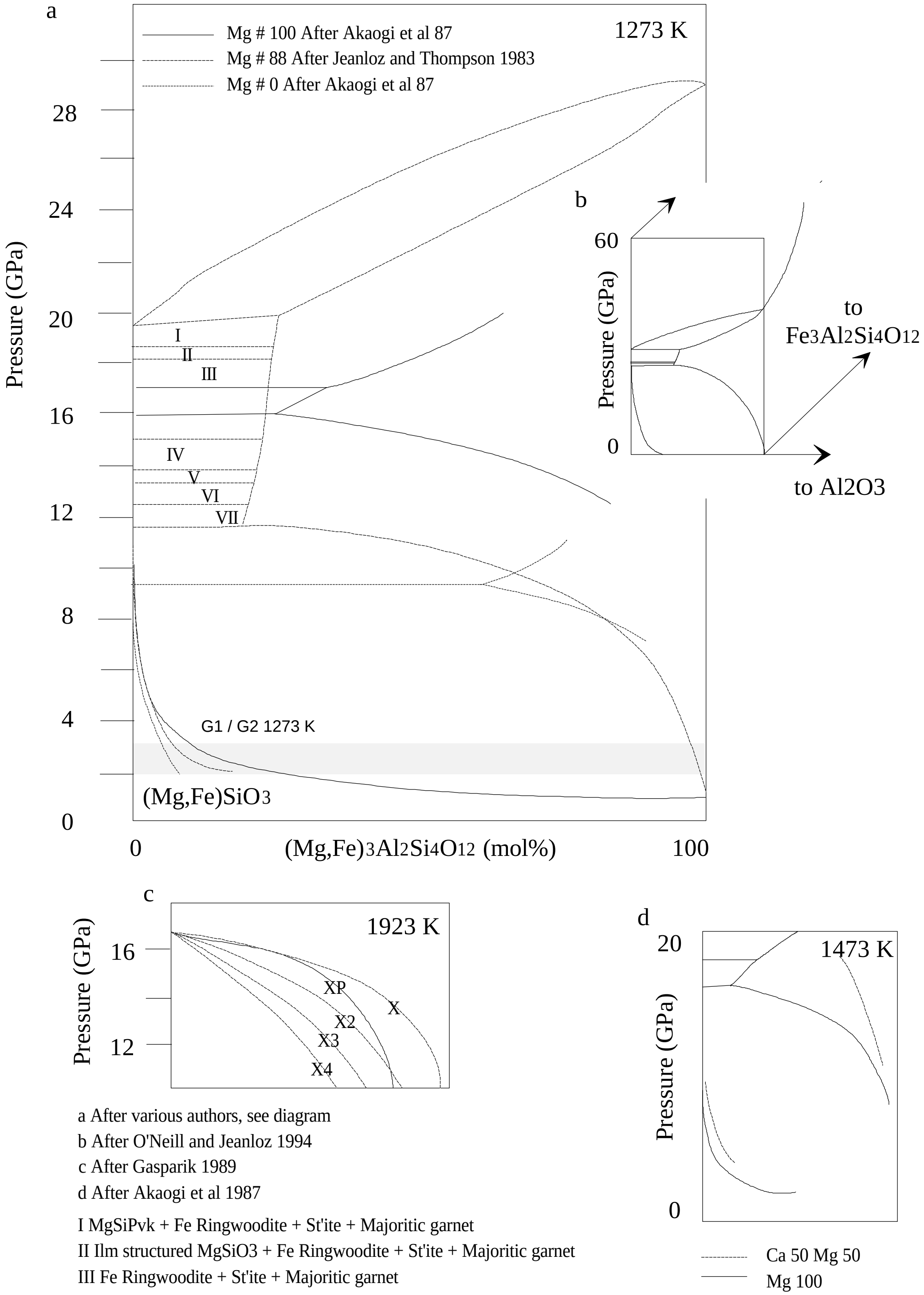

a After various authors, see diagram
b After O'Neill and Jeanloz 1994
c After Gasparik 1989
d After Akaogi et al 1987

I MgSiPvk + Fe Ringwoodite + St'ite + Majoritic garnet
II Ilm structured $MgSiO_3$ + Fe Ringwoodite + St'ite + Majoritic garnet
III Fe Ringwoodite + St'ite + Majoritic garnet
IV Mg Wadsleyite + Fe Ringwoodite + St'ite + Majoritic garnet
V Mg Wadsleyite + St'ite + Majoritic garnet
VI Mg Cpx + Wadsleyite + St'ite + Majoritic garnet
VII Mg Cpx + St'ite + Majoritic garnet

Figure 4.4_10 The effect of Fe and Ca on phase relations in the $MgSiO_3$ - $Mg_3Al_2Si_4O_{12}$ system in terms of pressure and under different temperature conditions.

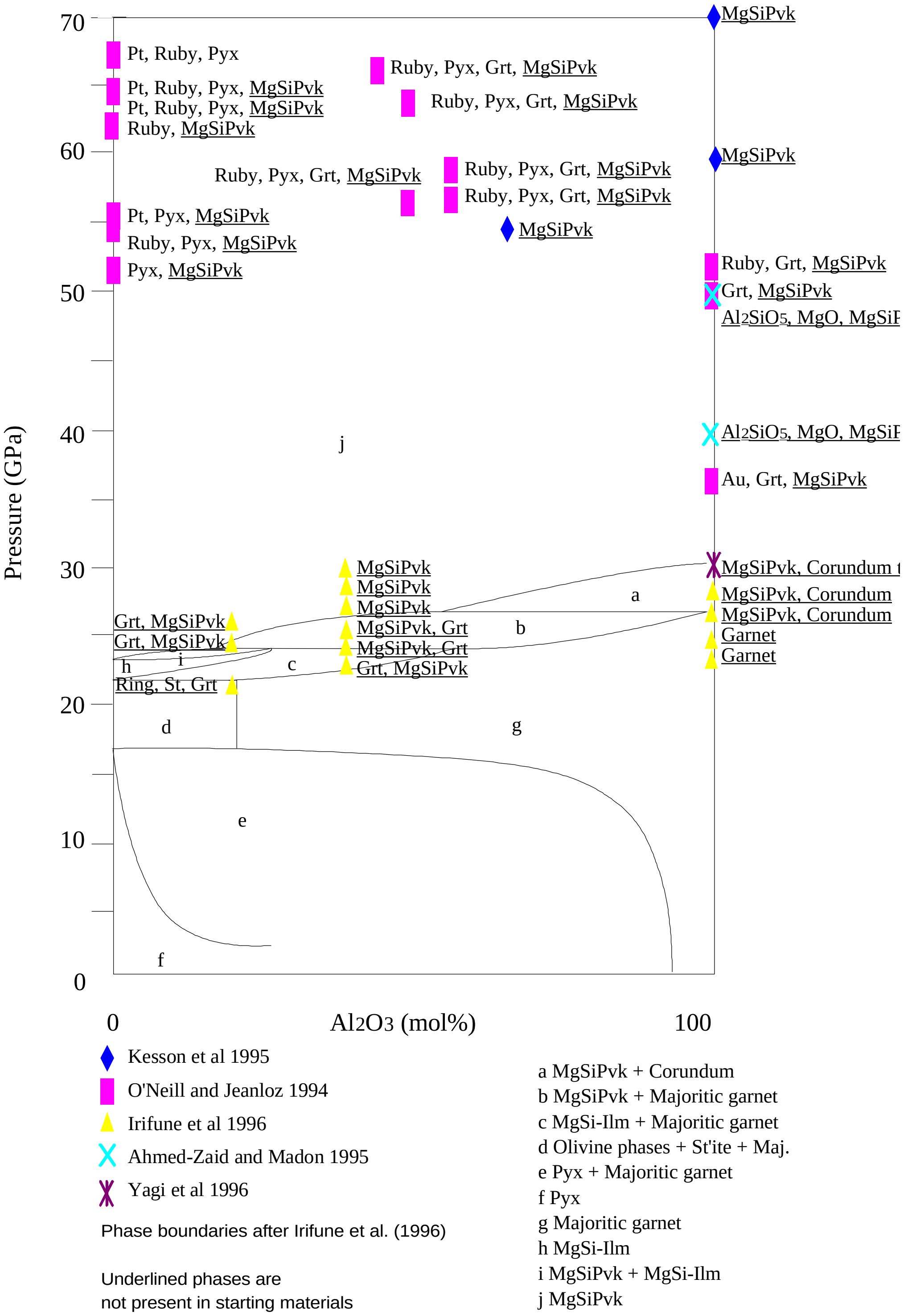

Figure 4.4_11 Run products of experiments in the $MgSiO_3$ - $Mg_3Al_2Si_4O_{12}$ system under conditions of lower mantle pressure and temperature.

It is concluded that phase relations determined by Irifune et al. (1996) and Kesson et al. (1995) truly reflect the behaviour of the system at high pressure. The presence of ruby and garnets in the run products of O'Neill and Jeanloz (1994) over 50GPa are interpreted as being metastable relicts of starting materials. In this region of pressure, all Al can be accommodated within perovskite structured $MgSiO_3$.

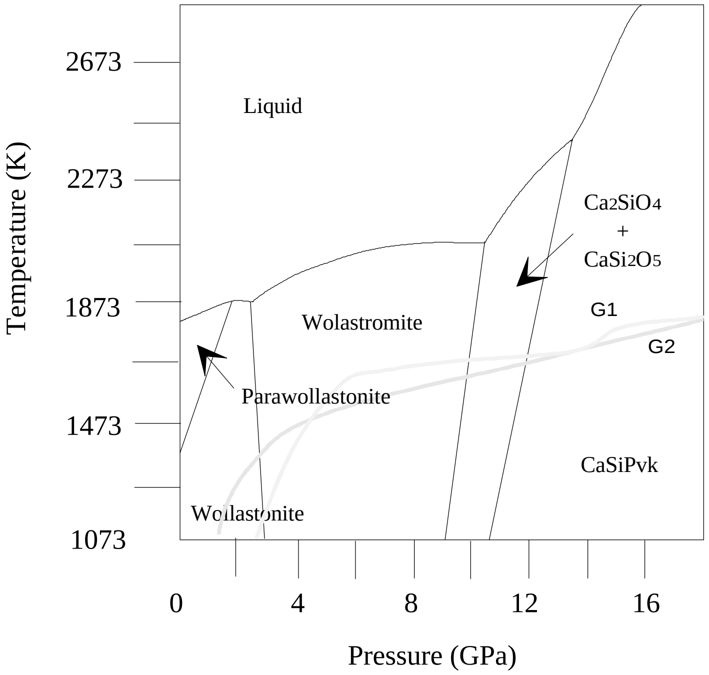

After Gasparik et al 1994

Figure 4.4_12 Phase relations in the $CaSiO_3$ system in terms of pressure and temperature.

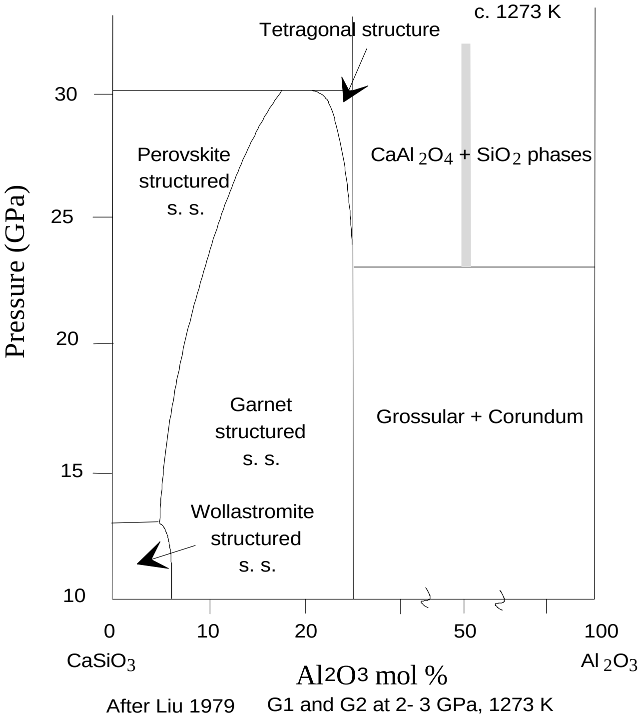

Figure 4.4_13 Phase relations in the $CaSiO_3$ - Al_2O_3 system in terms of pressure at ~1273K.

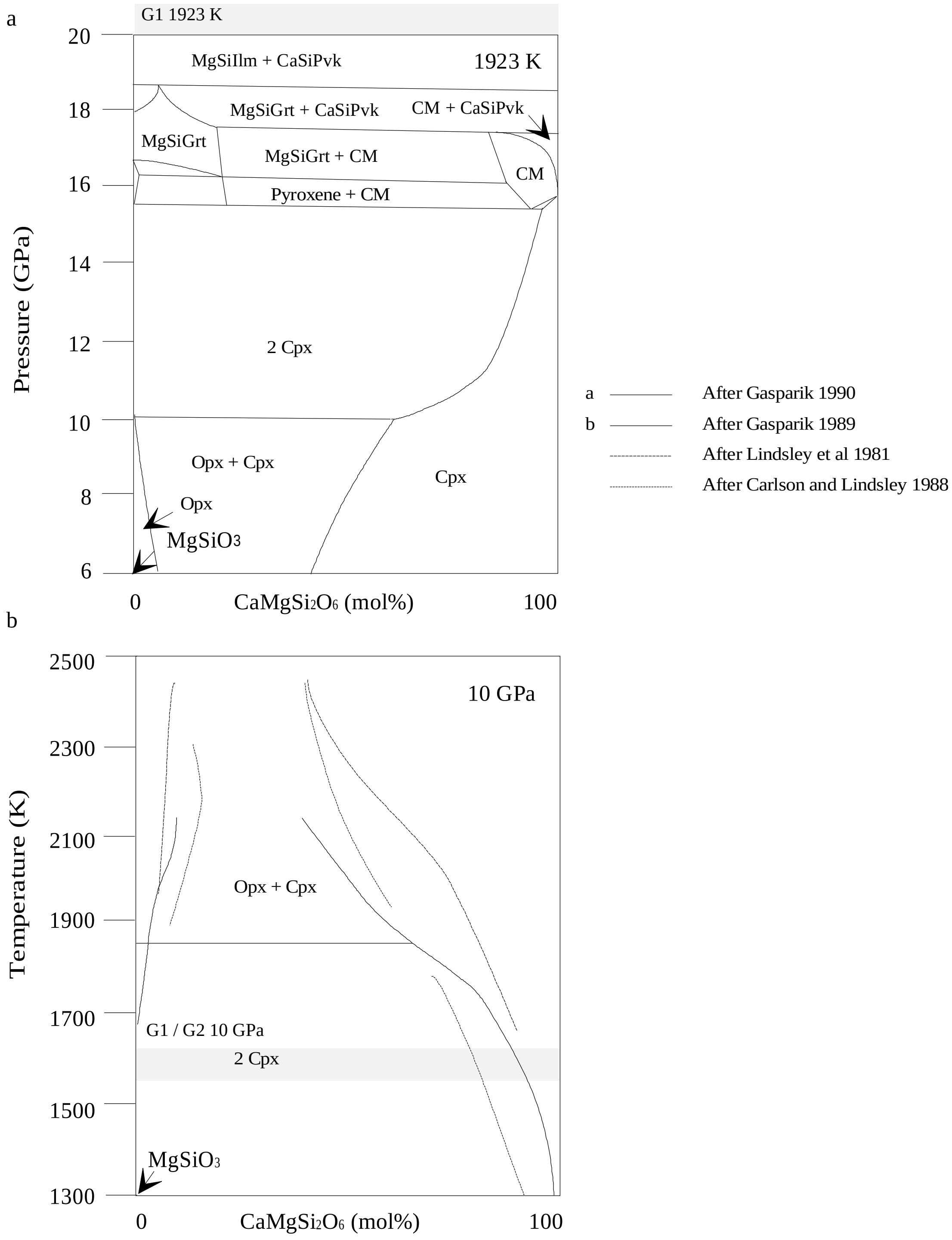

Figure 4.4_14 Phase relations in the $MgSiO_3$ - $CaMgSi_2O_6$ system in terms of pressure at 1923K and in terms of temperature at 10 GPa.

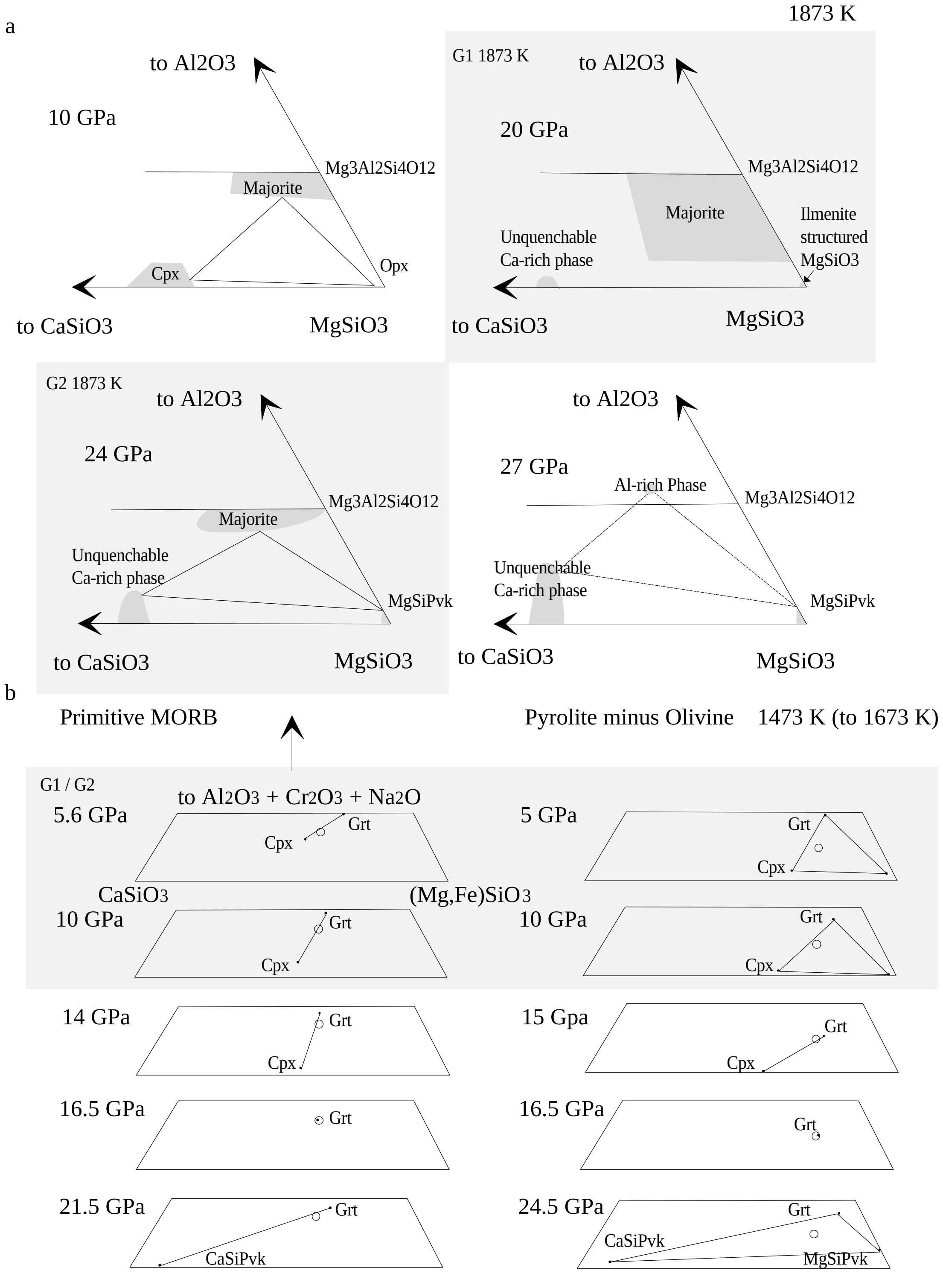

a After Ito and Takahashi 1987a
b After Irifune and Ringwood 1987

Figure 4.4_15 Phase relations in the ternary system Al_2O_3 - $CaSiO_3$ - $MgSiO_3$ in terms of pressure and at varying temperature and with additional minor components.

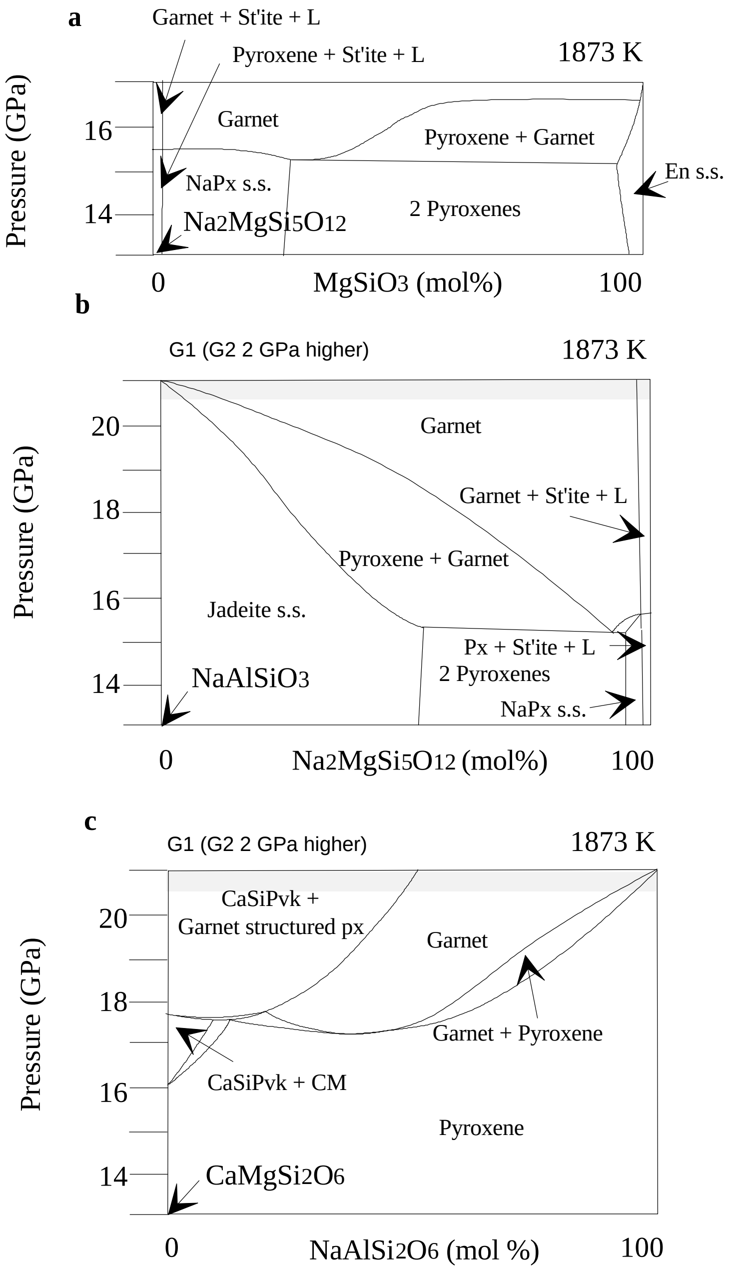

After Gasparik 1990

Figure 4.4_16 Phase relations in the Ca, Na, Mg, Al bearing pyroxene composition system in terms of pressure at 1873K.

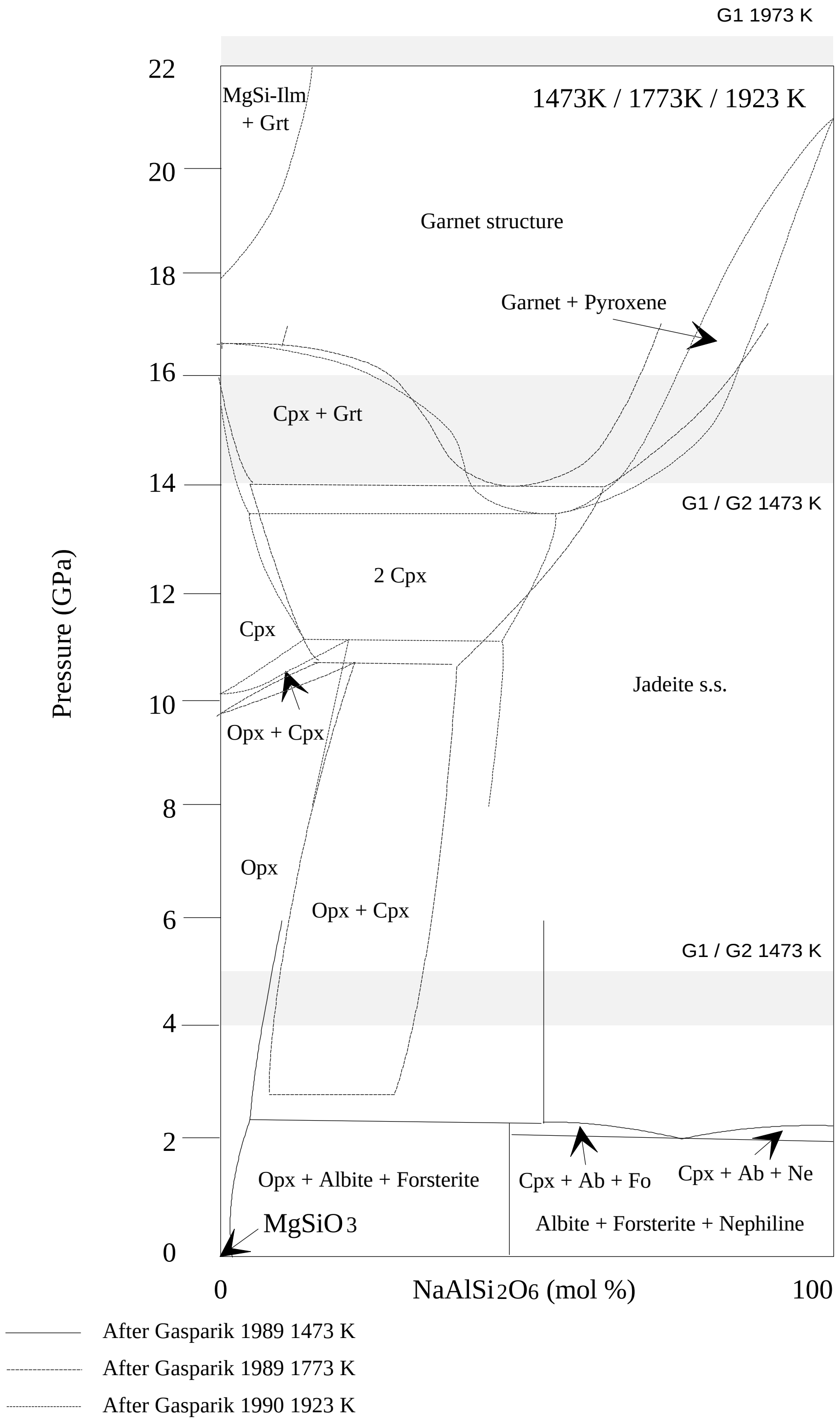

Figure 4.4_17 Phase relations in the $MgSiO_3$ - $NaAlSi_2O_6$ system in terms of pressure and under varying conditions of temperature.

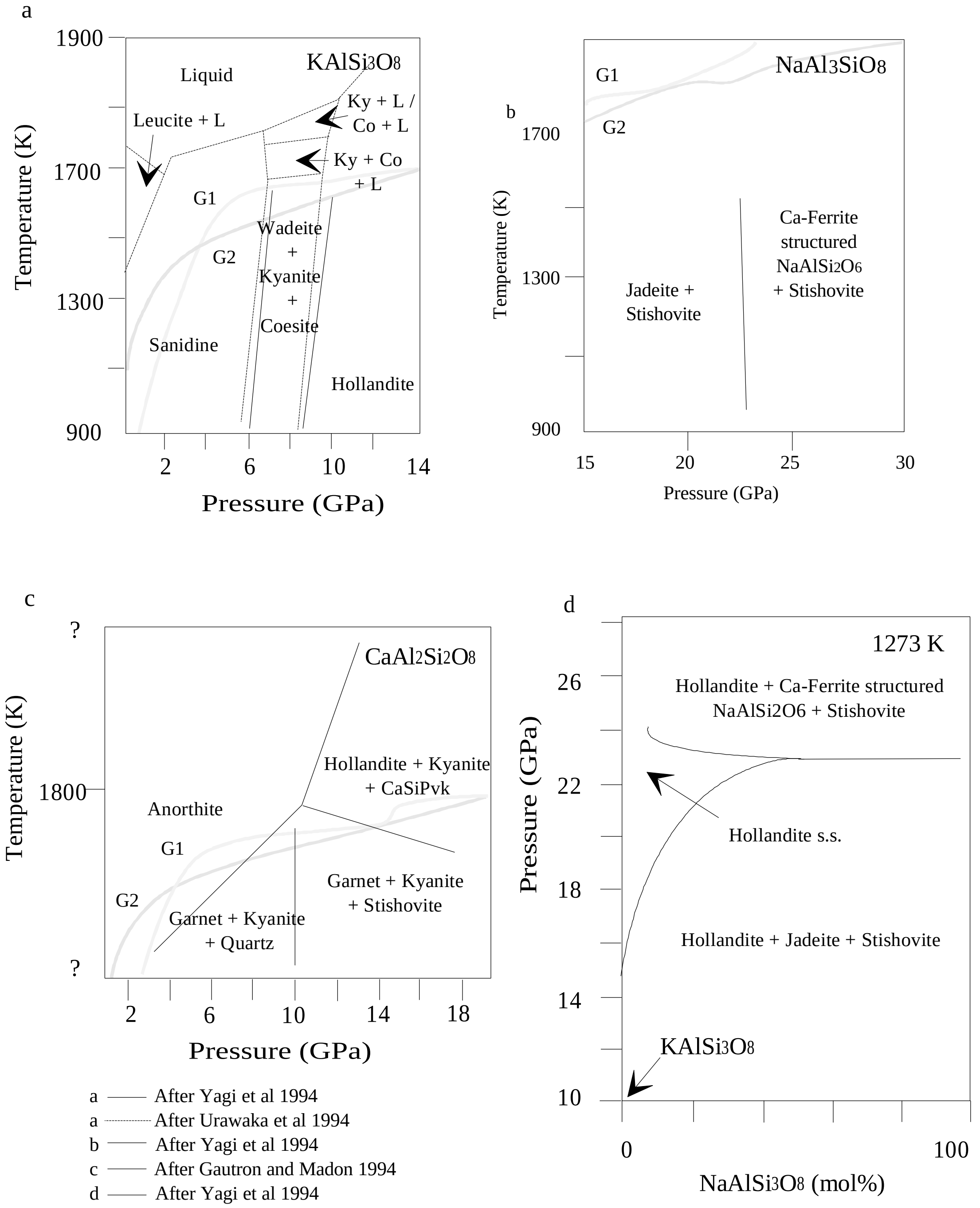

Figure 4.4_18 Phase relations in the systems $KAlSi_3O_8$, $NaAlSi_3O_8$ and $CaAl_2Si_2O_8$ in terms of pressure and temperature.

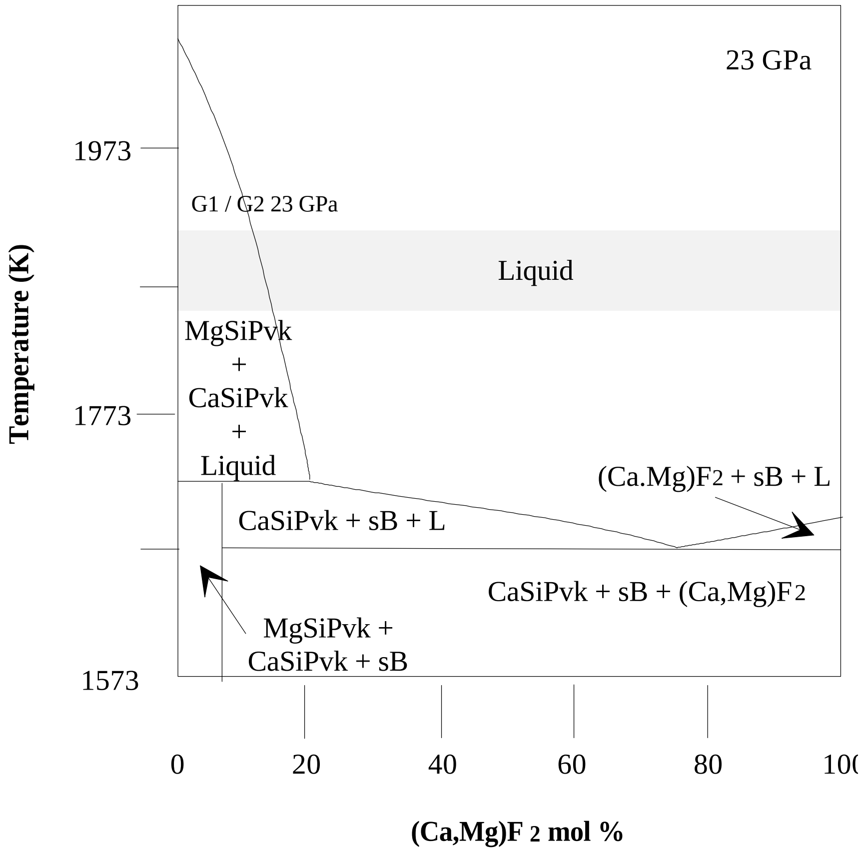

After Gasparik and Drake 1995

Figure 4.4_19 Phase relations involving pyrolite bulk composition with hydrous fluid content modelled by fluorine in terms of pressure and temperature.

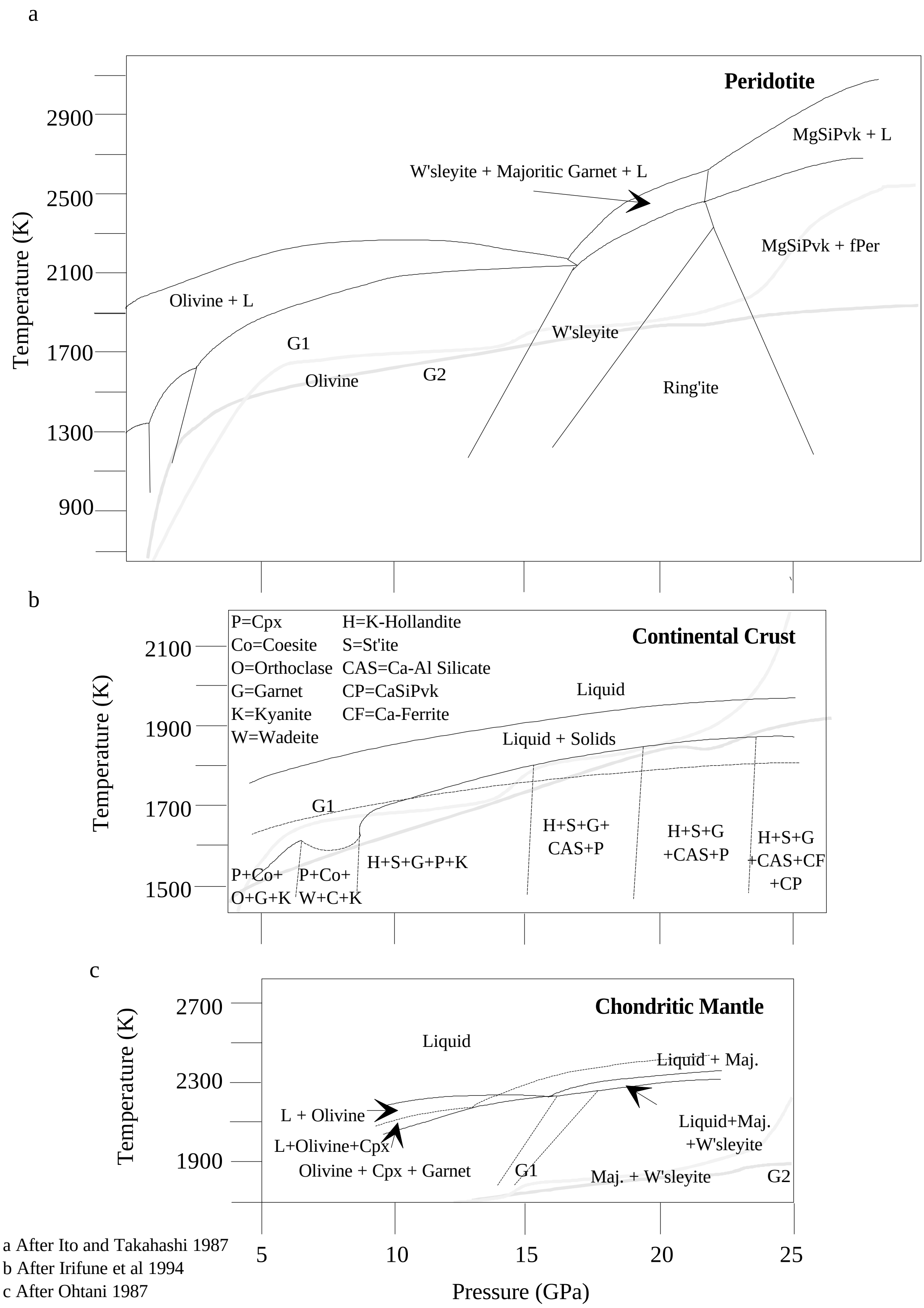

a After Ito and Takahashi 1987
b After Irifune et al 1994
c After Ohtani 1987

Figure 4.4_20 Phase relations in terms of pressure and temperature for peridotite, continental crust and chondritic mantle bulk compositions.

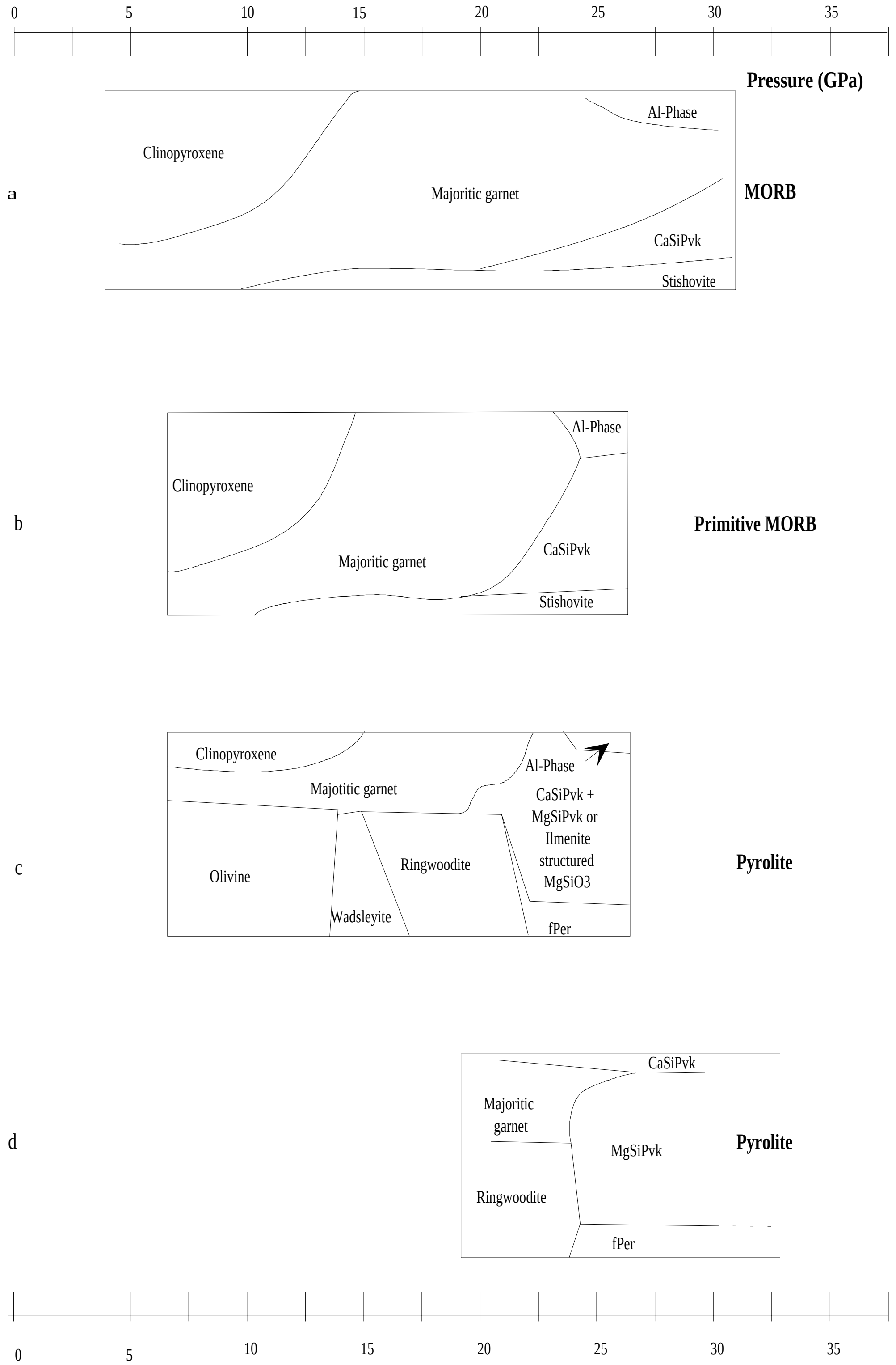

a After Irifune and Ringwood 1993, b and c After Irifune and Ringwood 1987, d After Irifune 1994

Figure 4.4_21 a - d Proportions of phases present over varying pressure into the lower mantle for MORB, primitive MORB and pyrolite.

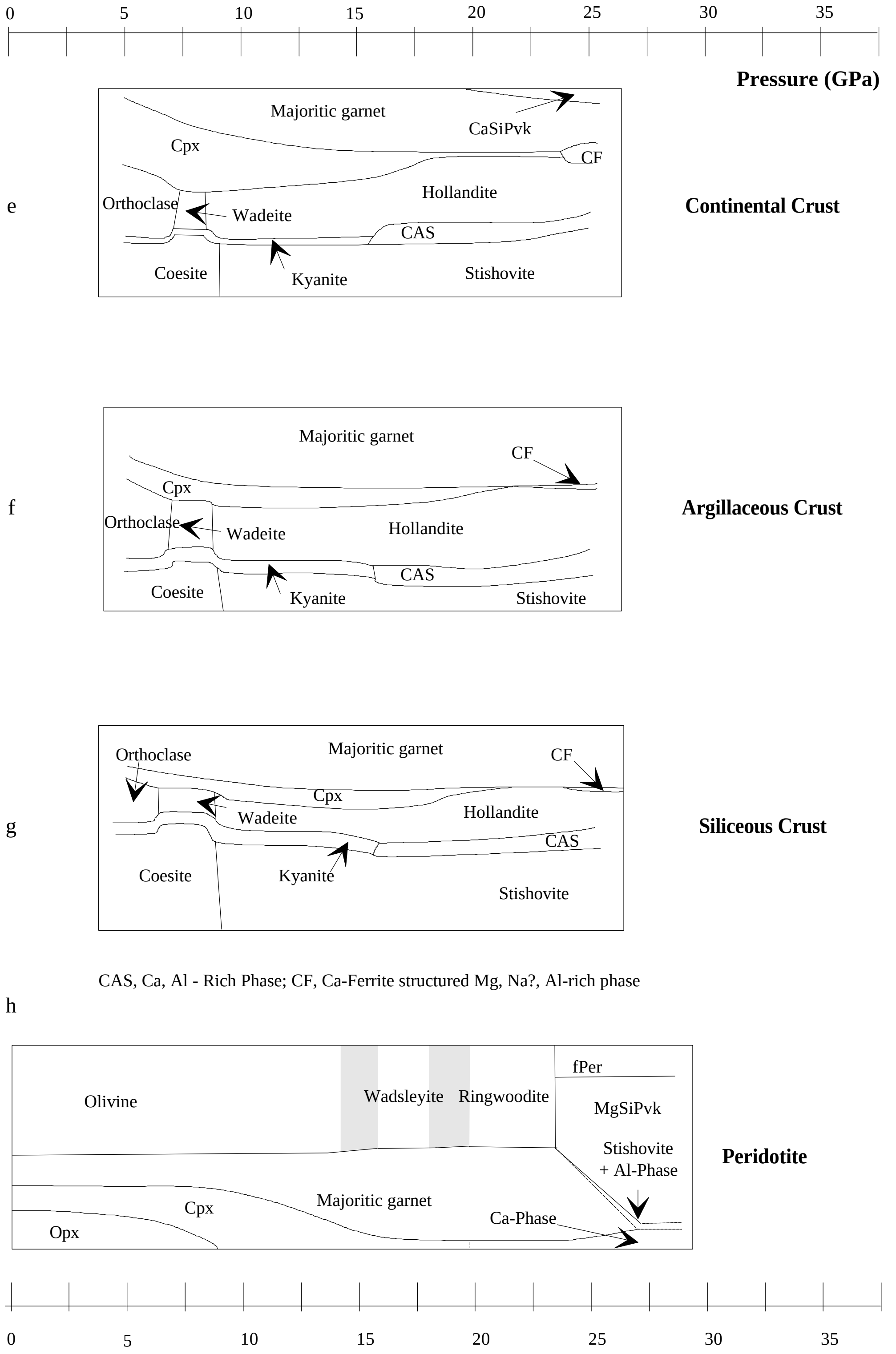

CAS, Ca, Al - Rich Phase; CF, Ca-Ferrite structured Mg, Na?, Al-rich phase

e, f and g After Irifune et al 1994, h After Ito and Takahashi 1987

Figure 4.4_21 e - h Proportions of phases present over varying pressure into the lower mantle for continental crust, argillaceous crust, siliceous crust and peridotite bulk compostions.

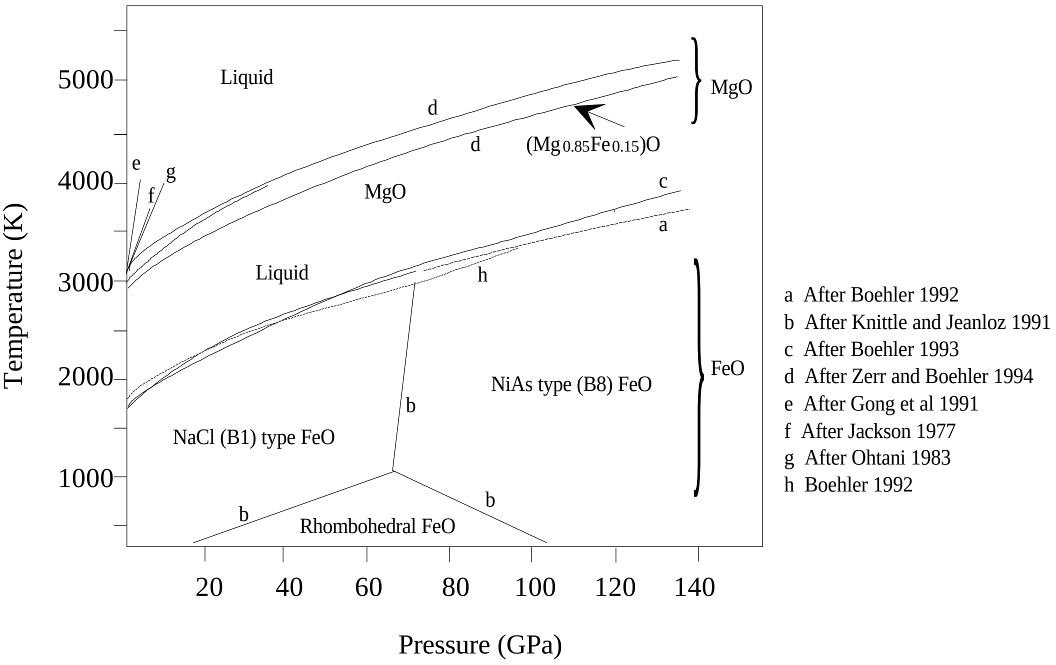

Figure 4.4_22 Phase relations in the MgO - FeO system in terms of pressure and temperature

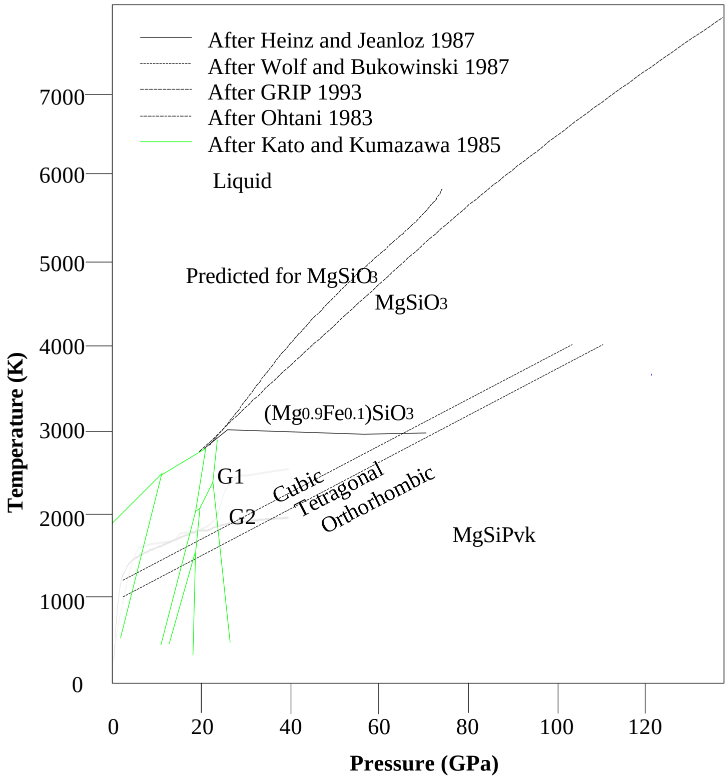

Figure 4.4_23 Melting behaviour in the (Mg,Fe)SiO$_3$ system in terms of pressure and temperature with Geotherms 1 and 2 plotted for comparison.

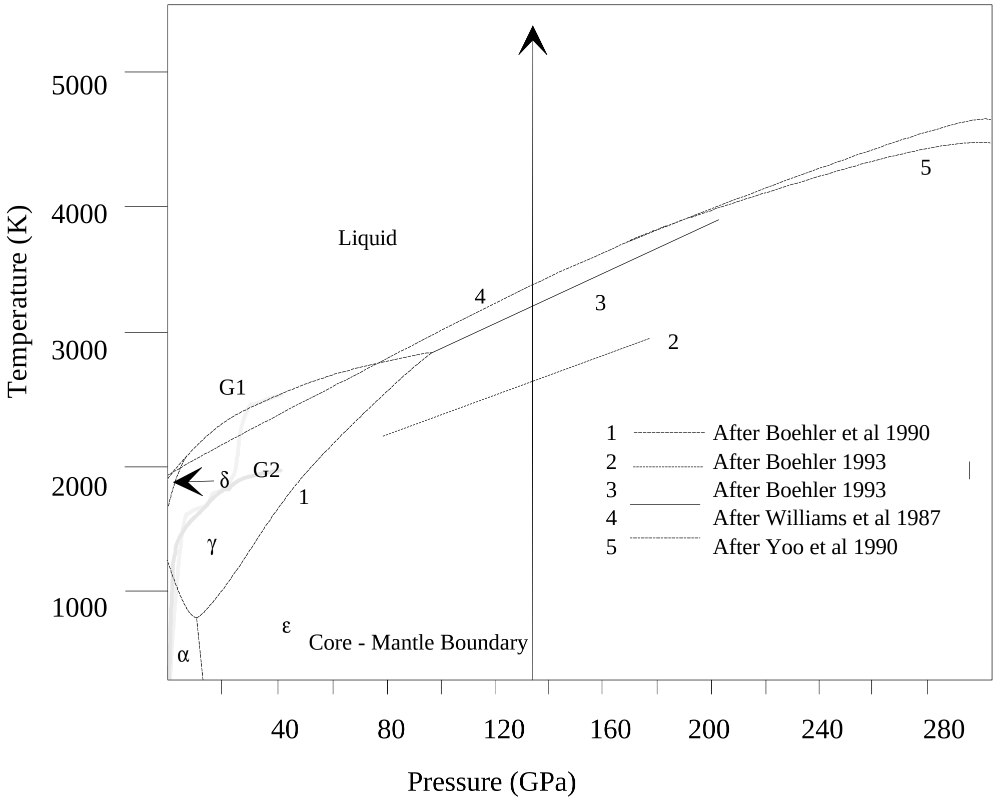

Figure 4.4_24 Phase transitions of Fe in terms of pressure and temperature.

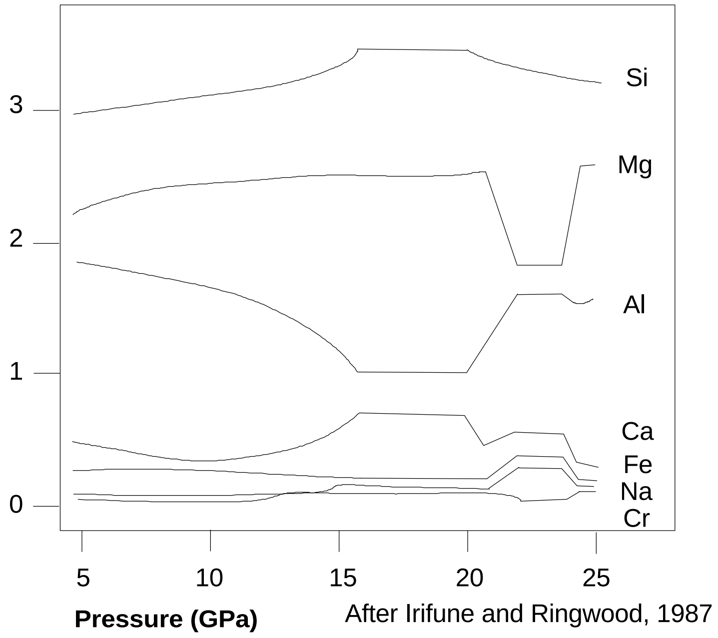

Figure 4.4_25 Variations of cation values per 12 O anions for majoritic garnet in a pyrolitic bulk composition in terms of pressure.

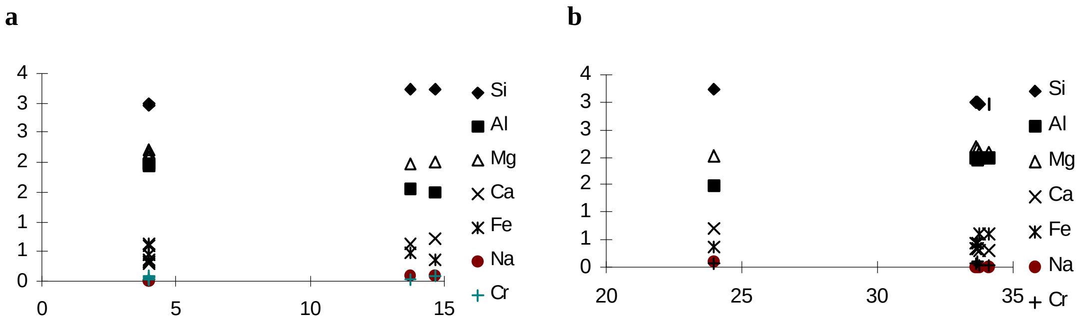

Figure 4.4_26 Cation concentration per 12 O anions against pressure (GPa) for majoritic garnets in xenoliths from Jagersfontein.

Calculated from data in Haggerty and Sauter (1990). Pressure assigned on the basis of Si-content following figure 4.4_25. a- Low pressure solid solution, b - High pressure solid solution.

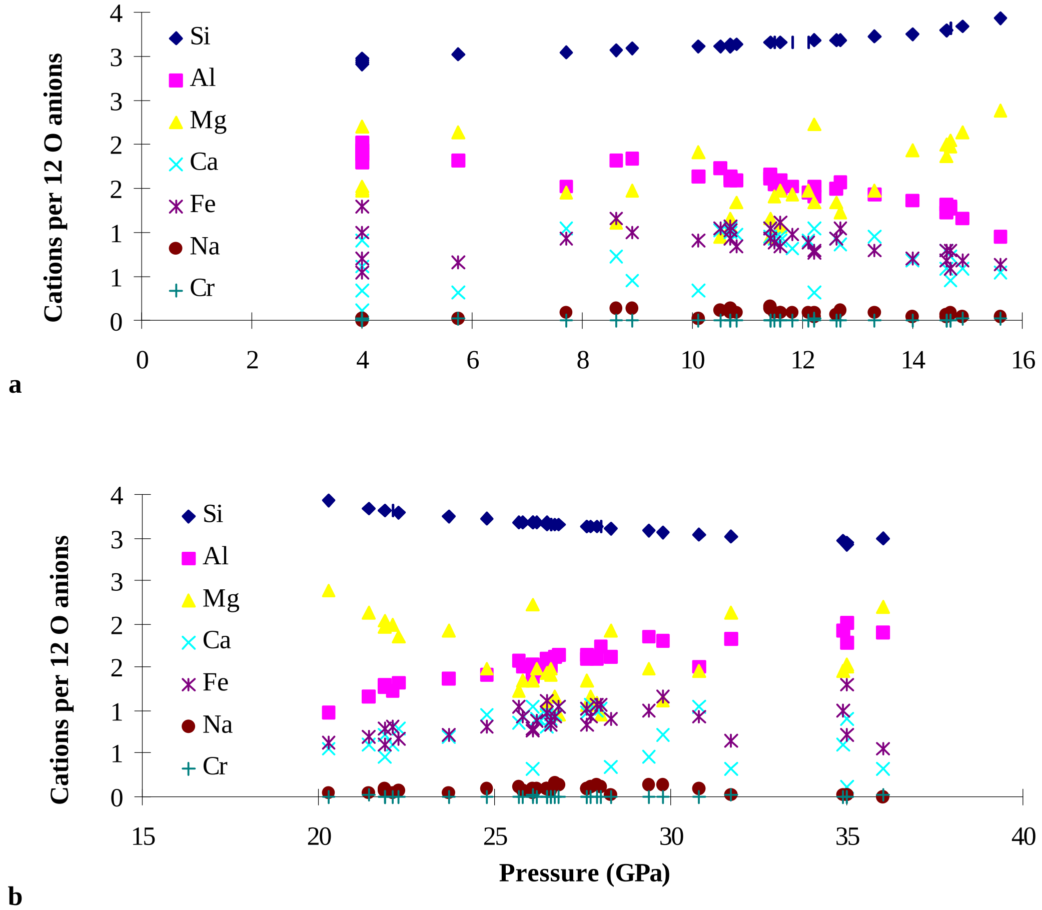

Figure 4.4_27 Cation concentration per 12 O anions against pressure for majoritic garnets in diamonds from Monastery.

Calculated from data in Moore et al. (1991) and Moore and Gurney (1985). Pressure assigned on the basis of Si-content over the low pressure solid solution range (a) and high pressure solid solution range (b) and following figure 4.4_25.

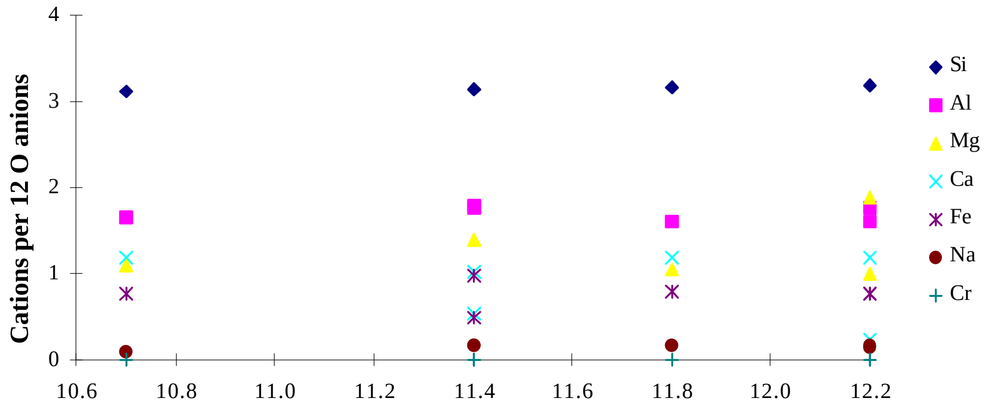

a

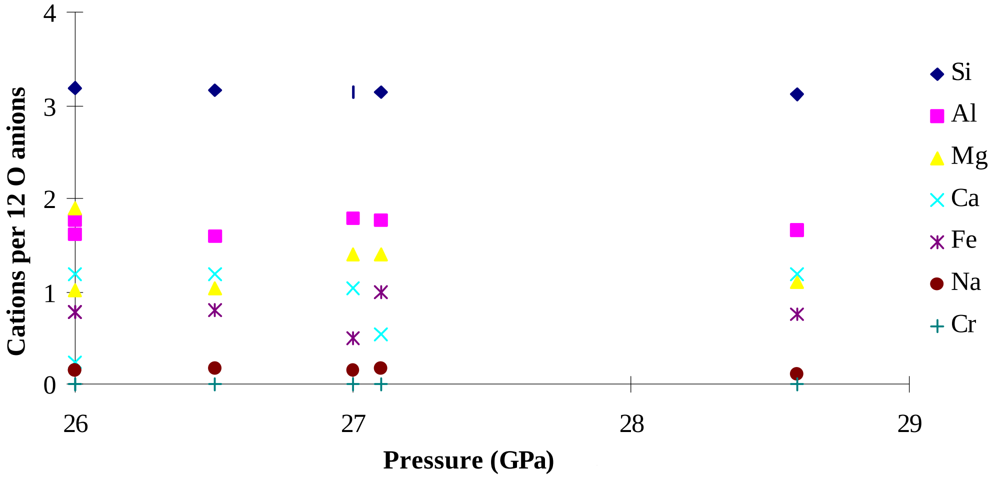

b

Figure 4.4_28 Cation concentration per 12 O anions against pressure for majoritic garnets in diamonds from the present study of São Luiz

Pressure assigned on the basis of Si-content over the low pressure solid solution range (a) and high pressure solid solution range (b) and following figure 4.4_25.

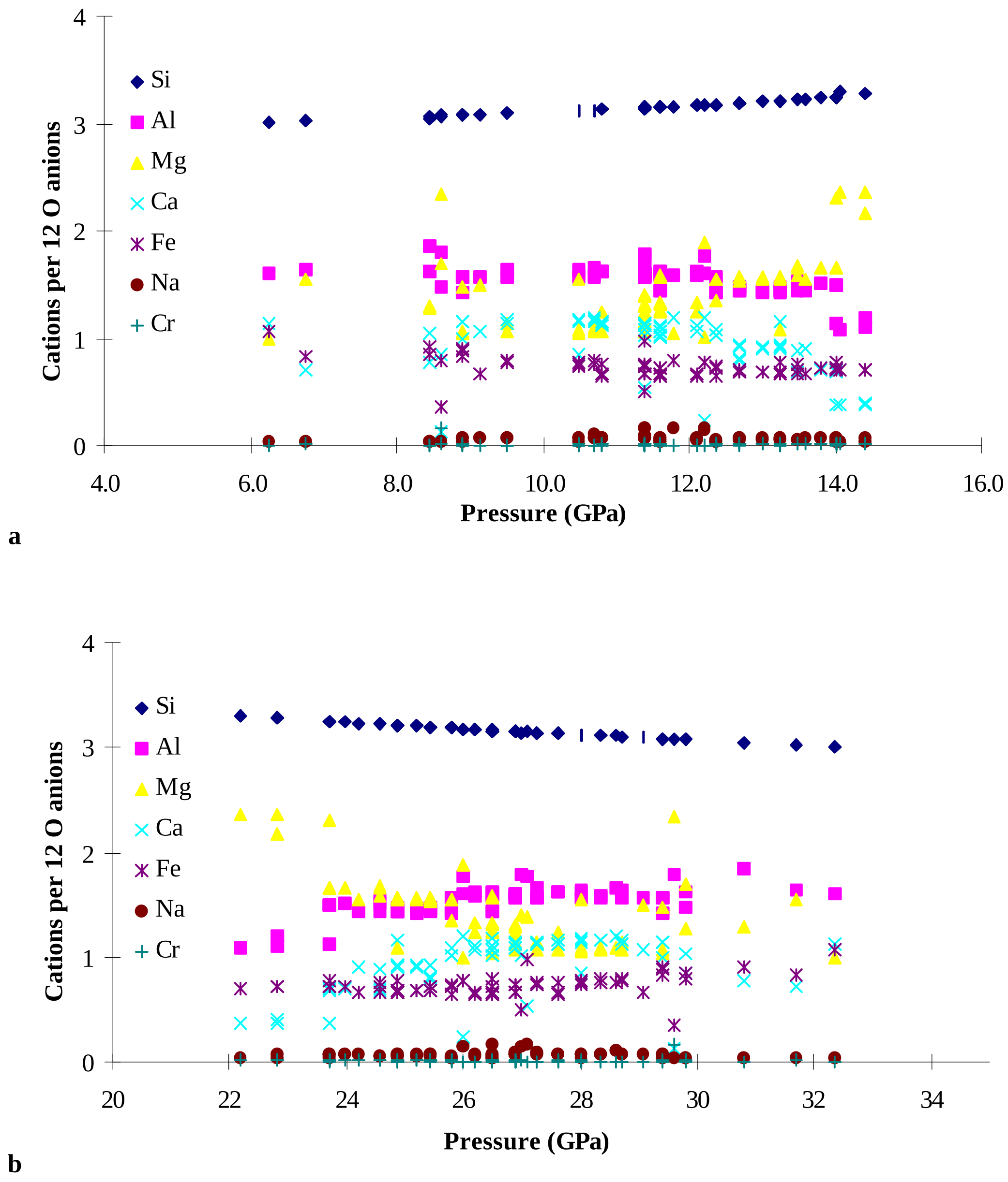

Figure 4.4_29 Cation concentration per 12 O anions against pressure for majoritic garnets in diamonds from São Luiz.

Pressure assigned on the basis of Si-content over the low pressure solid solution range (a) and high pressure solid solution range (b) and following figure 4.4_25.

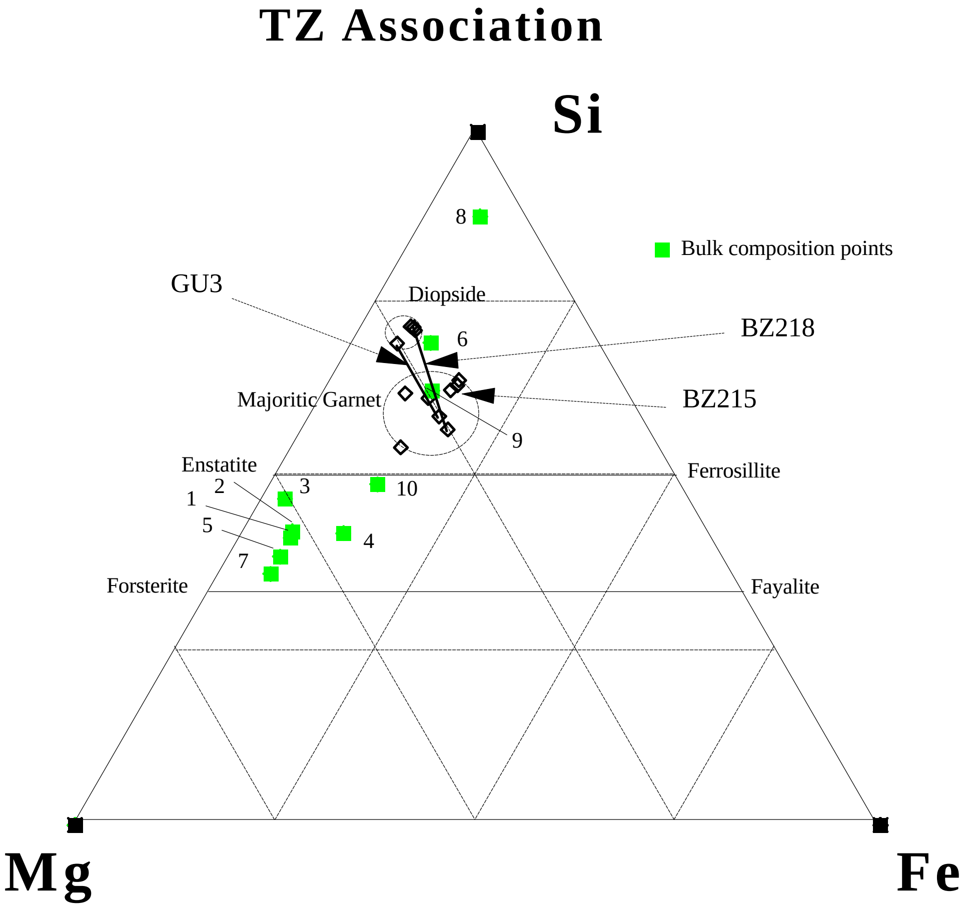

Figure 4.4_30 Cation compositions of inclusions of the TZ association from São Luiz and Guinean diamonds in the ternary system Si - Fe - Mg.

Bulk composition points 1 - 10 correspond to possible mantle compositions discussed in section 4.1: 1 - Pyrolite (Jagoutz et al., 1979), 2 - PRIMA (Allègre et al., 1995), 3 - C1 chondrites (Anderson and Bass, 1986), 4 - Solar mantle (Anderson, 1989), 5 - Lherzolite (Maaole and Aoki, 1977), 6 - primitive MORB (Green et al., 1979), 7 - Harzburgite (Michael and Bonatti, 1985), 8 - Average sediment (Gromet et al., 1984), 9 - Eclogite (Kushiro and Aoki, 1968), 10 - Lower mantle (Javoy, 1995)

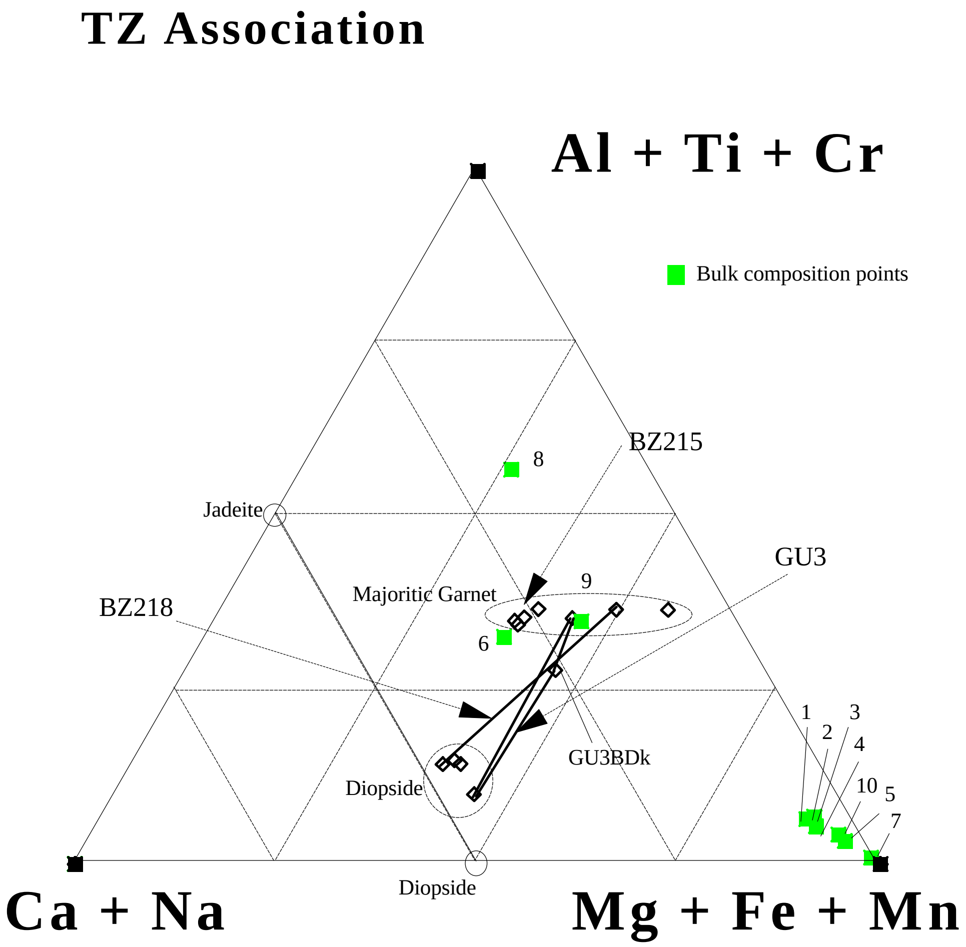

Figure 4.4_31 Cation compositions of inclusions of the TZ association from São Luiz and Guinean diamonds in the ternary system Al+Ti+Cr - Mg+Fe+Mn - Ca+Na.

For bulk composition sources see figure 4.4_30.

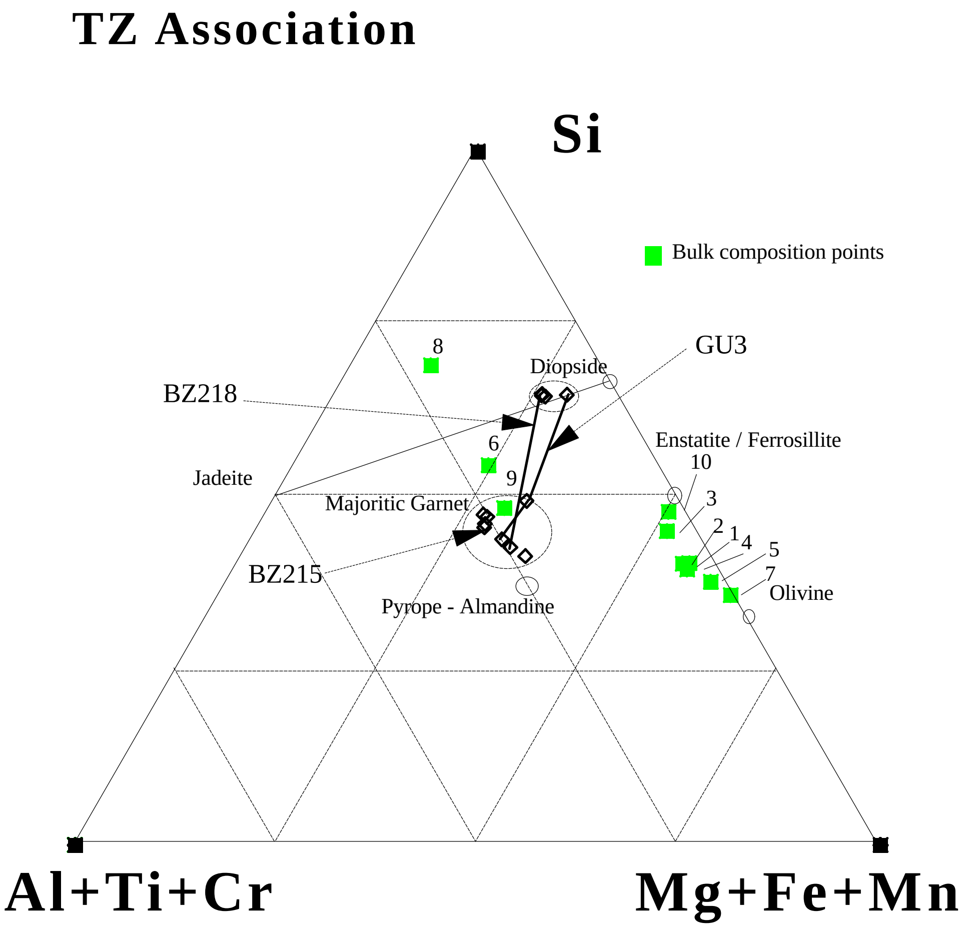

Figure 4.4_32 Cation compositions of inclusions of the TZ association from São Luiz and Guinean diamonds in the ternary system Si - Mg+Fe+Mn - Al+Ti+Cr.

For bulk composition sources see figure 4.4_30.

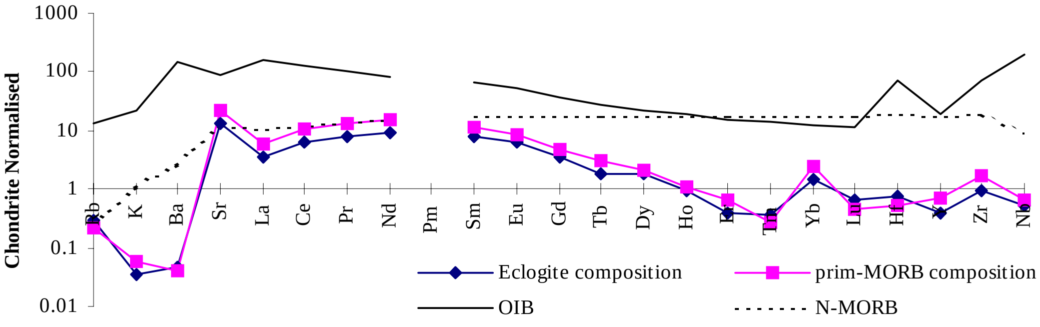

Figure 4.4_33 Trace element characteristics of the TZ association reconstructed to eclogitic and primitive MORB bulk compositions with N-MORB and OIB for comparison.

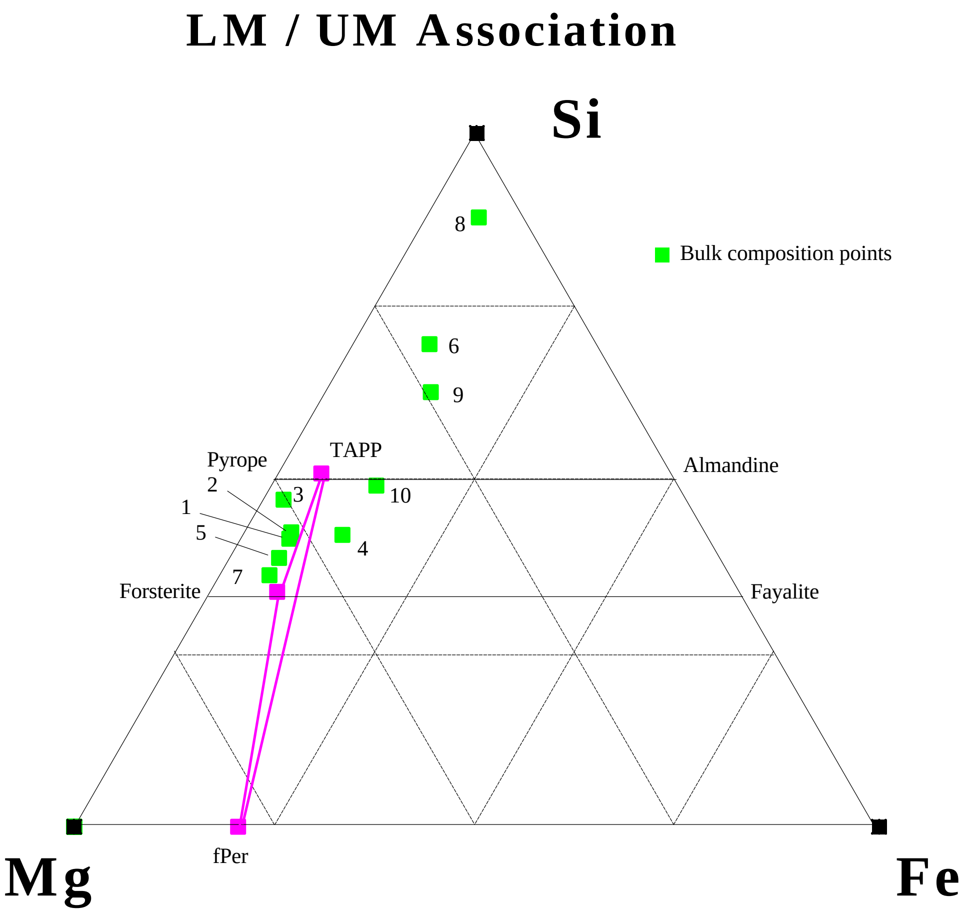

Figure 4.4_34 Cation compositions of inclusions of the UM/LM association from São Luiz diamond BZ243 in the ternary system Si - Fe - Mg.

For bulk composition sources see figure 4.4_30.

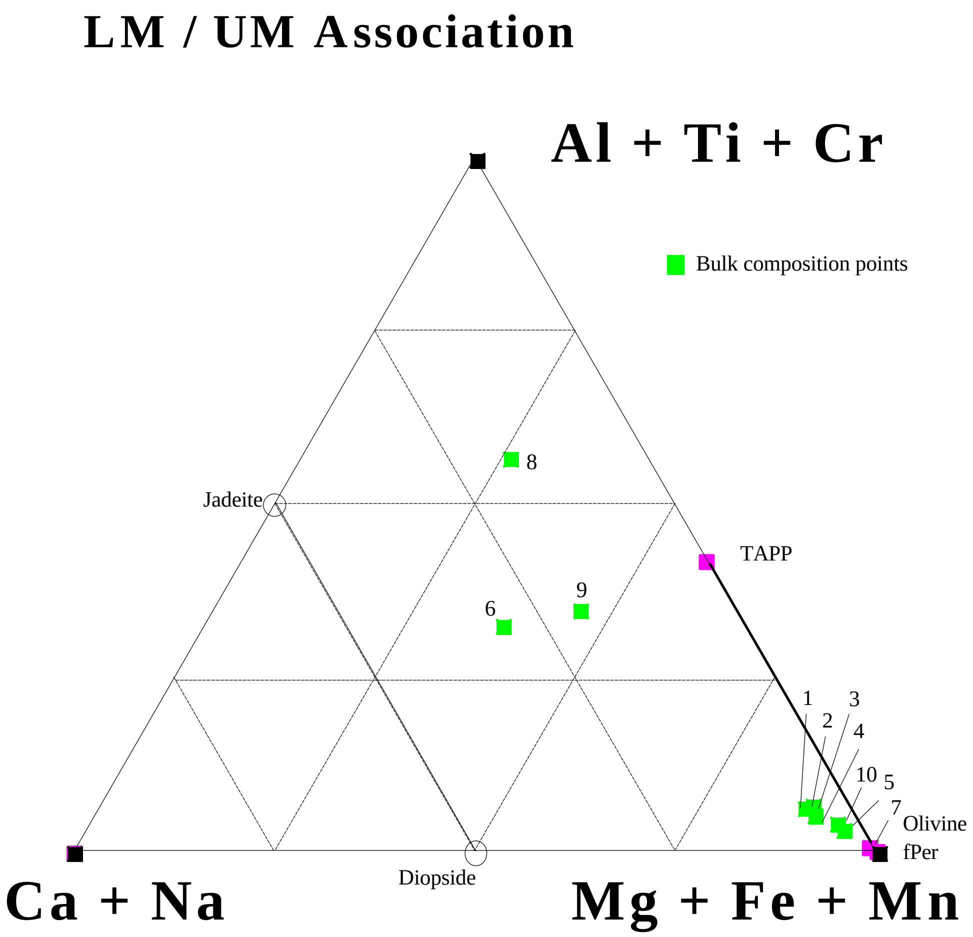

Figure 4.4_35 Cation compositions of inclusions of the UM/LM association from São Luiz diamond BZ243 in the ternary system Al+Ti+Cr - Mg+Fe+Mn - Ca+Na.

For bulk composition sources see figure 4.4_30.

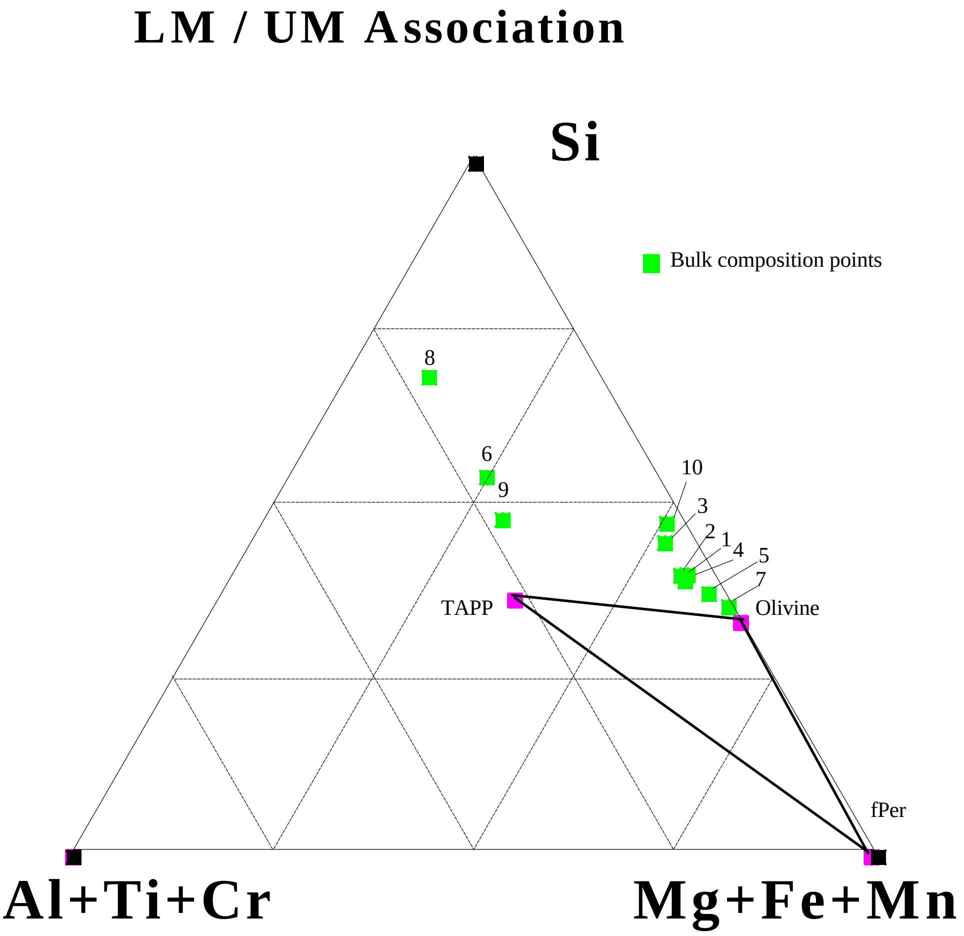

Figure 4.4_36 Cation compositions of inclusions of the UM/LM association from São Luiz diamond BZ243 in the ternary system Si - Mg+Fe+Mn - Al+Ti+Cr.

For bulk composition sources see figure 4.4_30.

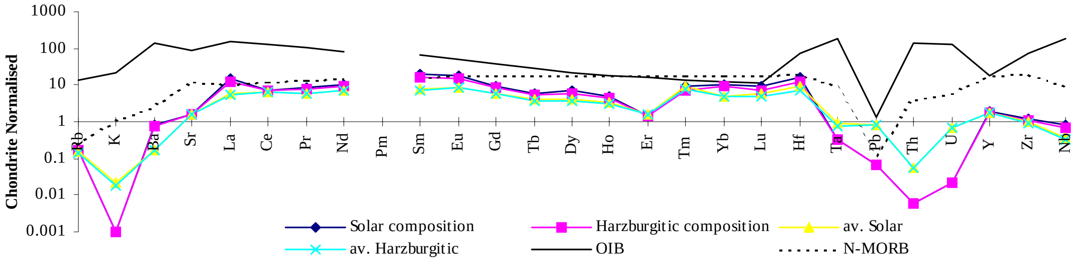

Figure 4.4_37 Trace element characteristics of the UM/LM association reconstructed to harzburgite and solar bulk compositions with N-MORB and OIB for comparison.

av. Averaged values for TAPP, CaSi-Pvk, fPer and olivine composition are employed.

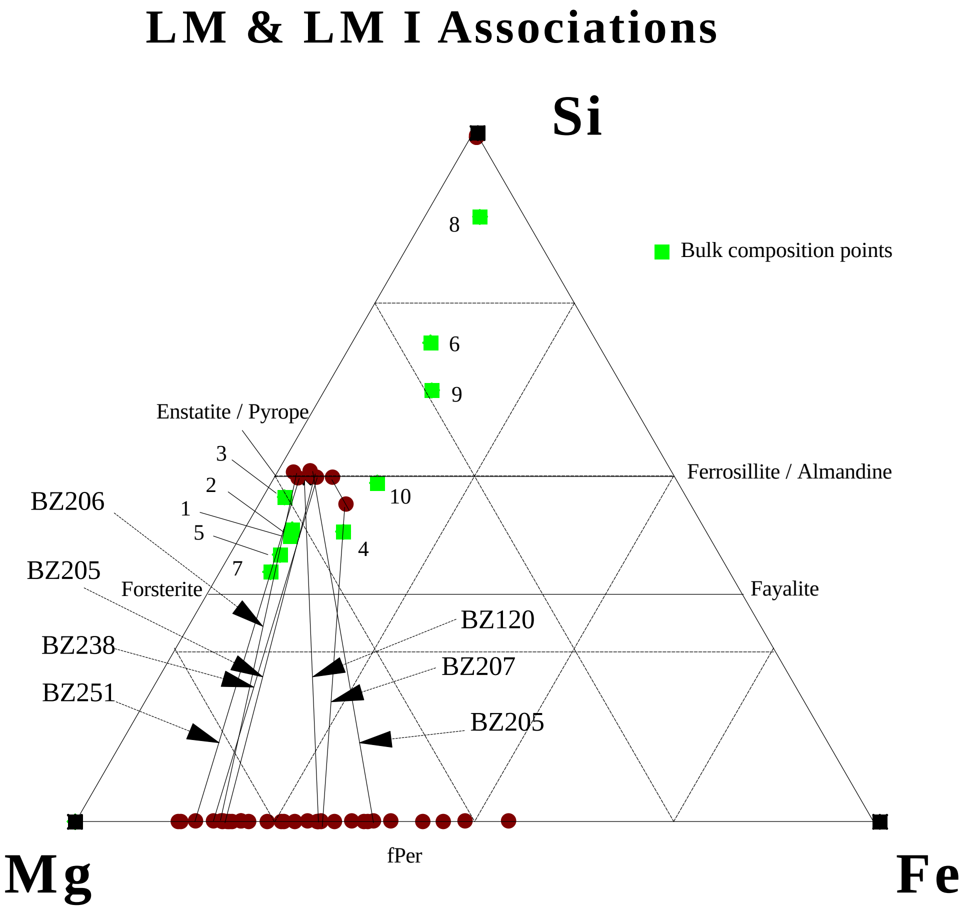

Figure 4.4_38 Cation compositions of inclusions of the LM and LM I associations from São Luiz diamonds in the ternary system Si - Fe - Mg.

For bulk composition sources see figure 4.4_30.

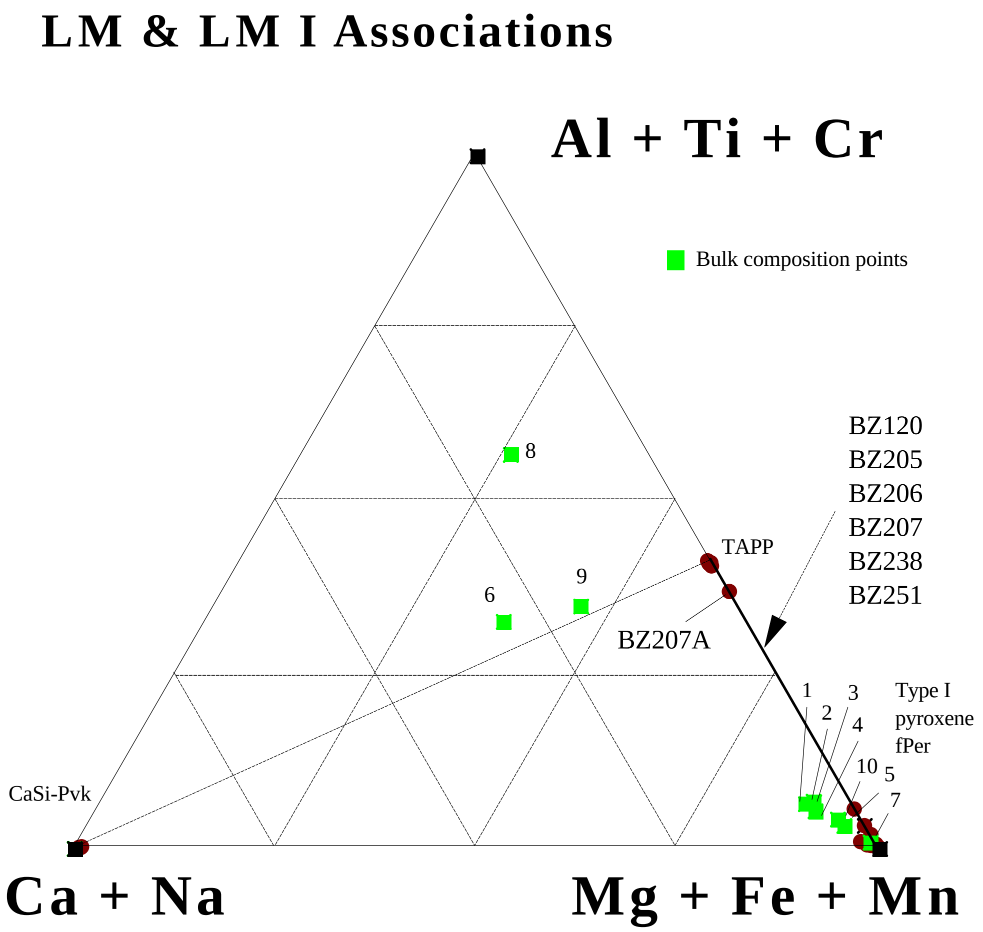

Figure 4.4_39 Cation compositions of inclusions of the LM and LM I associations from São Luiz diamonds in the ternary system Al+Ti+Cr - Mg+Fe+Mn - Ca+Na.

For bulk composition sources see figure 4.4_30.

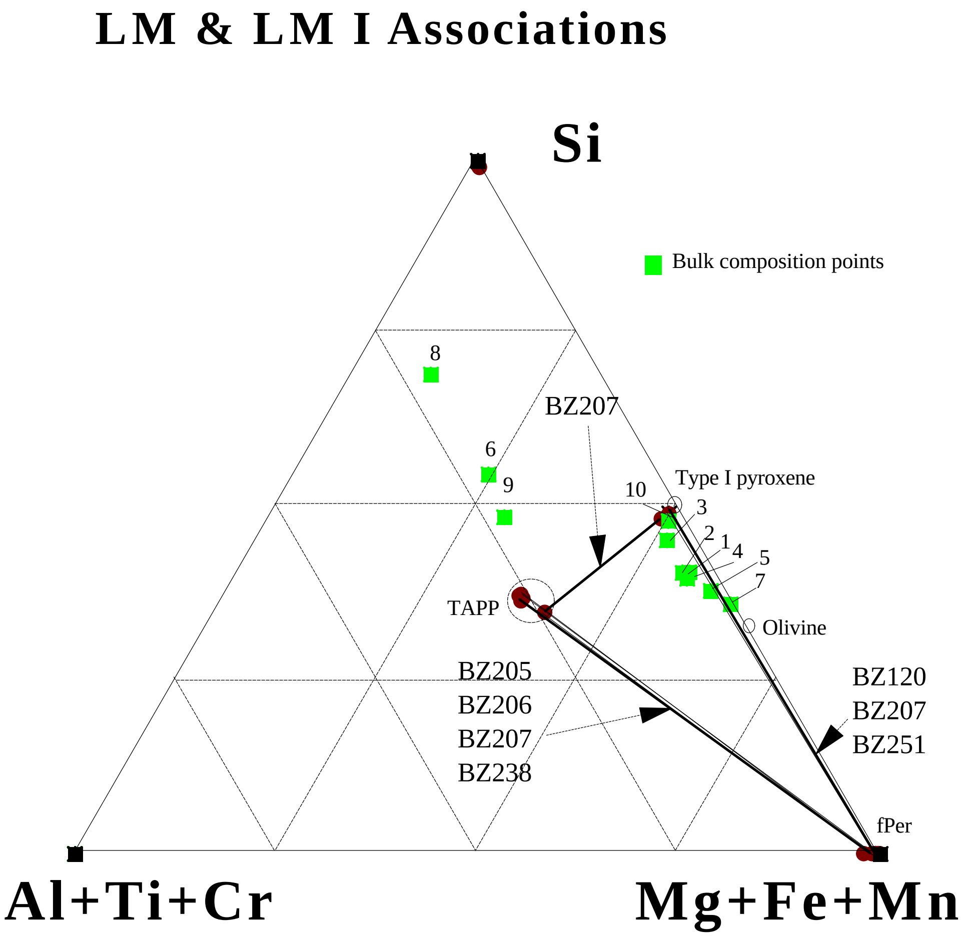

Figure 4.4_40 Cation compositions of inclusions of the LM and LM I associations from São Luiz diamonds in the ternary system Si - Mg+Fe+Mn - Al+Ti+Cr.

For bulk composition sources see figure 4.4_30.

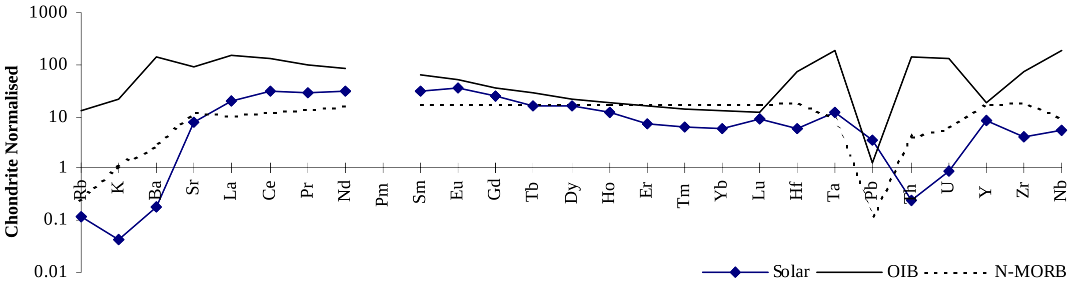

Figure 4.4_41 Trace element characteristics of the LM I association reconstructed to a solar bulk composition with N-MORB and OIB for comparison.

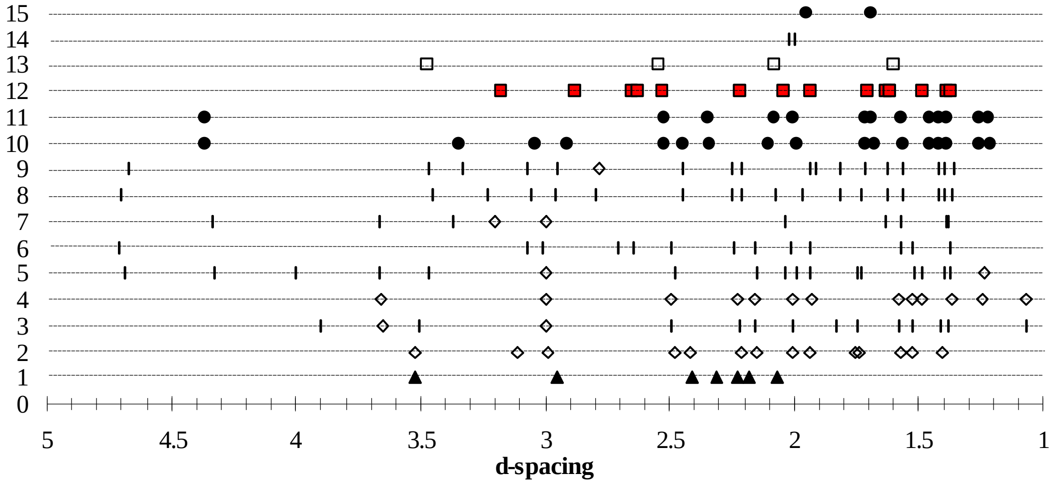

Figure 4.4_42 Comparison of d-spacings of TAPP with unknown aluminous phases from the literature.

1 - Ahrens and Graham (1972), 2 to 9 - Liu (1975), 10, 11 - Irifune and Ringwood (1993), 12 - TAPP, 13 - Ito et al. (1996), 14 - Takahashi and Ito (1987), 15 - Irifune and Ringwood (1993).

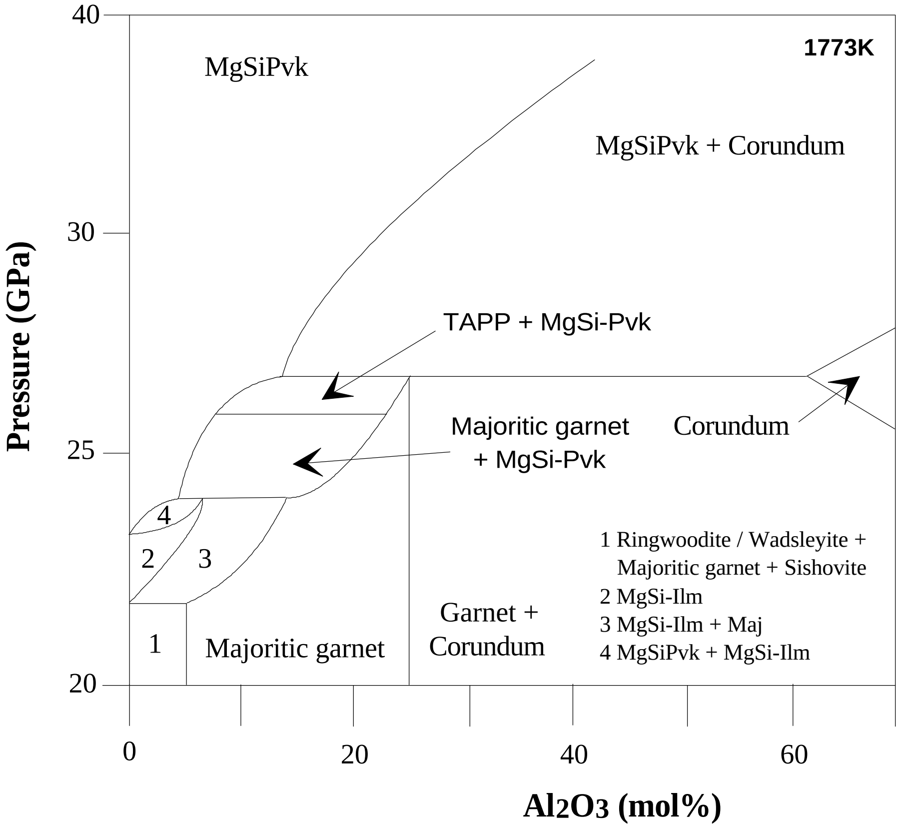

Figure 4.4_43 Prediction of the stability of TAPP within phase relations in the $(Mg,Fe)SiO_3$ - $(Mg,Fe)_3Al_2Si_4O_{12}$ system.

Phase boundaries not involving TAPP after Irifune et al. (1996).

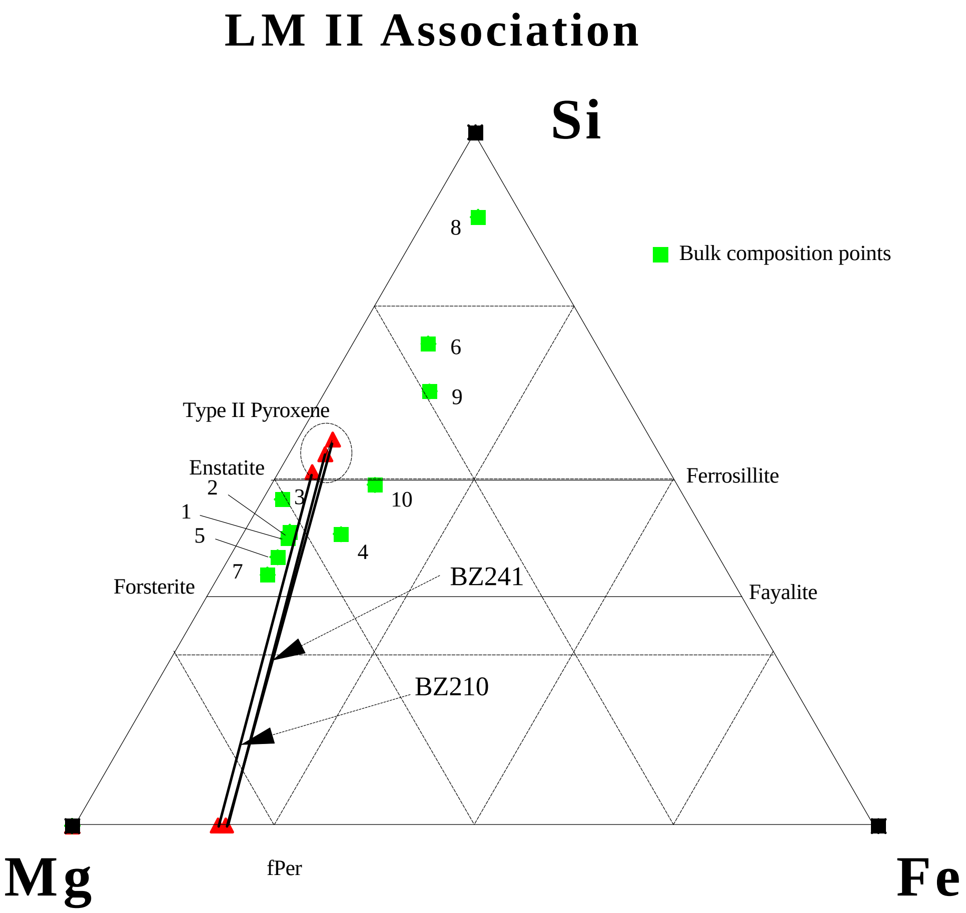

Figure 4.4_44 Cation compositions of inclusions of the LM II association from São Luiz diamonds in the ternary system Si - Fe - Mg.

For bulk composition sources see figure 4.4_30.

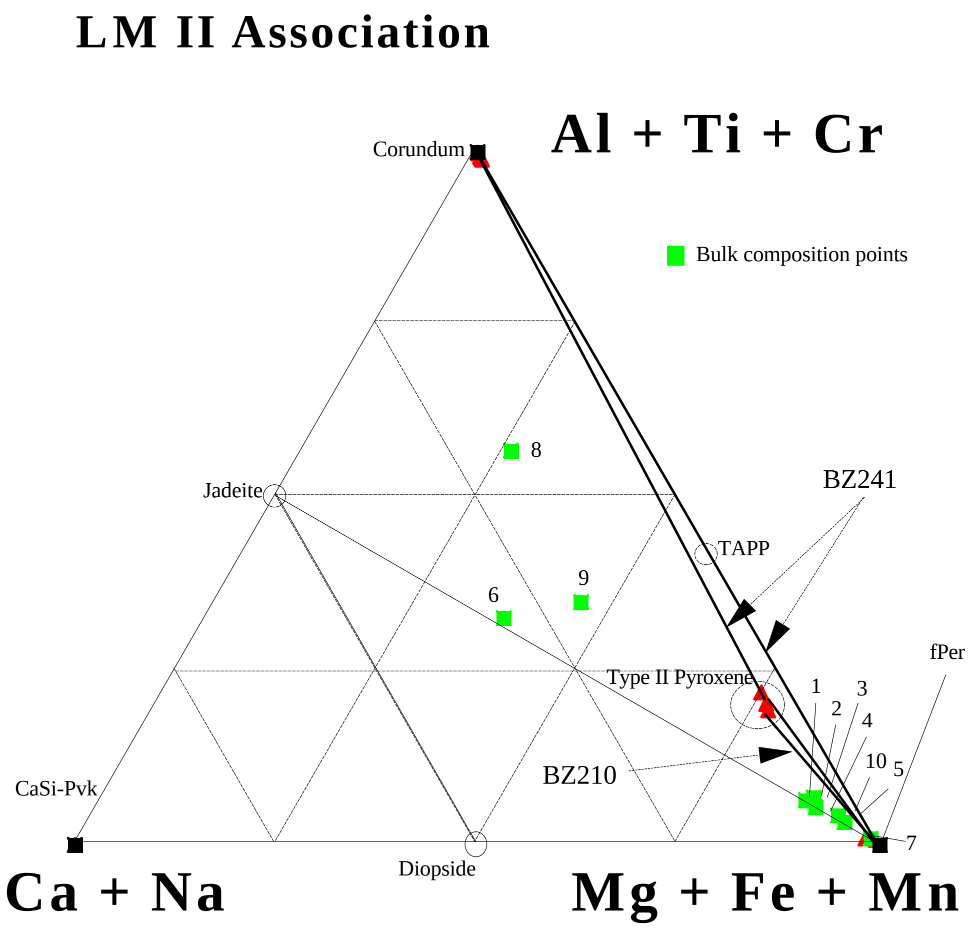

Figure 4.4_45 Cation compositions of inclusions of the LM II association from São Luiz diamonds in the ternary system Al+Ti+Cr - Mg+Fe+Mn - Ca+Na.

For bulk composition sources see figure 4.4_30.

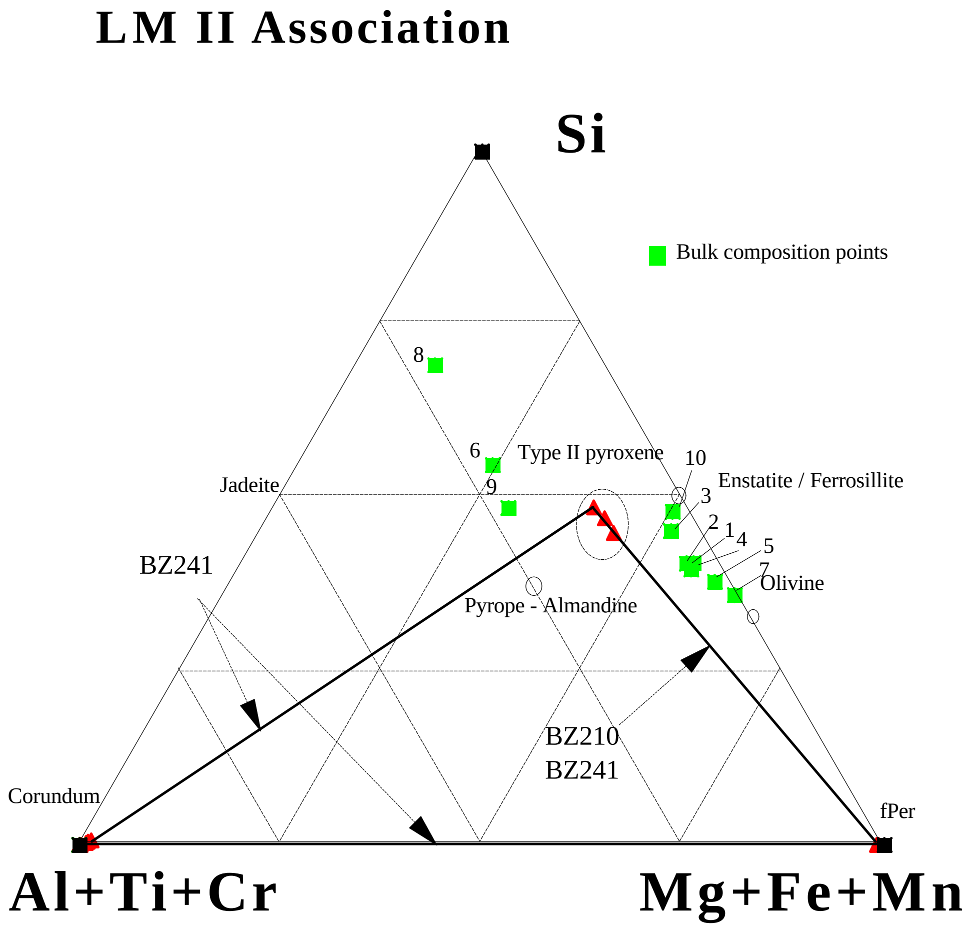

Figure 4.4_46 Cation compositions of inclusions of the LM II association from São Luiz diamonds in the ternary system Si - Mg+Fe+Mn - Al+Ti+Cr.

For bulk composition sources see figure 4.4_30.

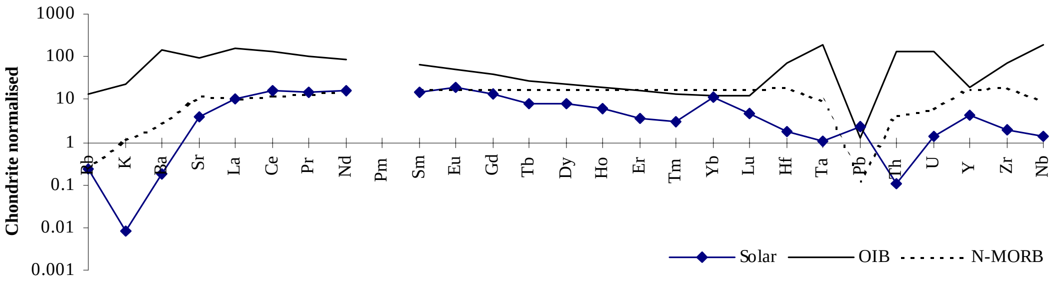

Figure 4.4_47 Trace element characteristics of the LM II association reconstructed to a solar bulk composition with N-MORB and OIB for comparison.

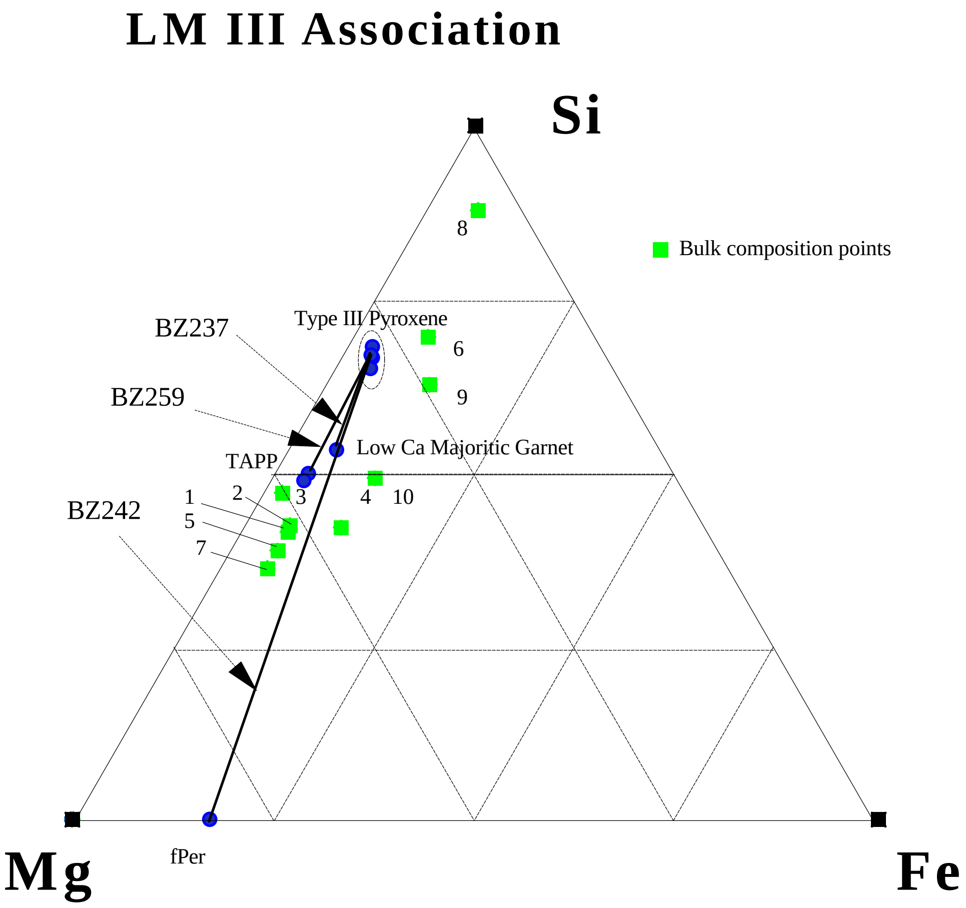

Figure 4.4_48 Cation compositions of inclusions of the LM III association from São Luiz diamonds in the ternary system Si - Fe - Mg.

For bulk composition sources see figure 4.4_30.

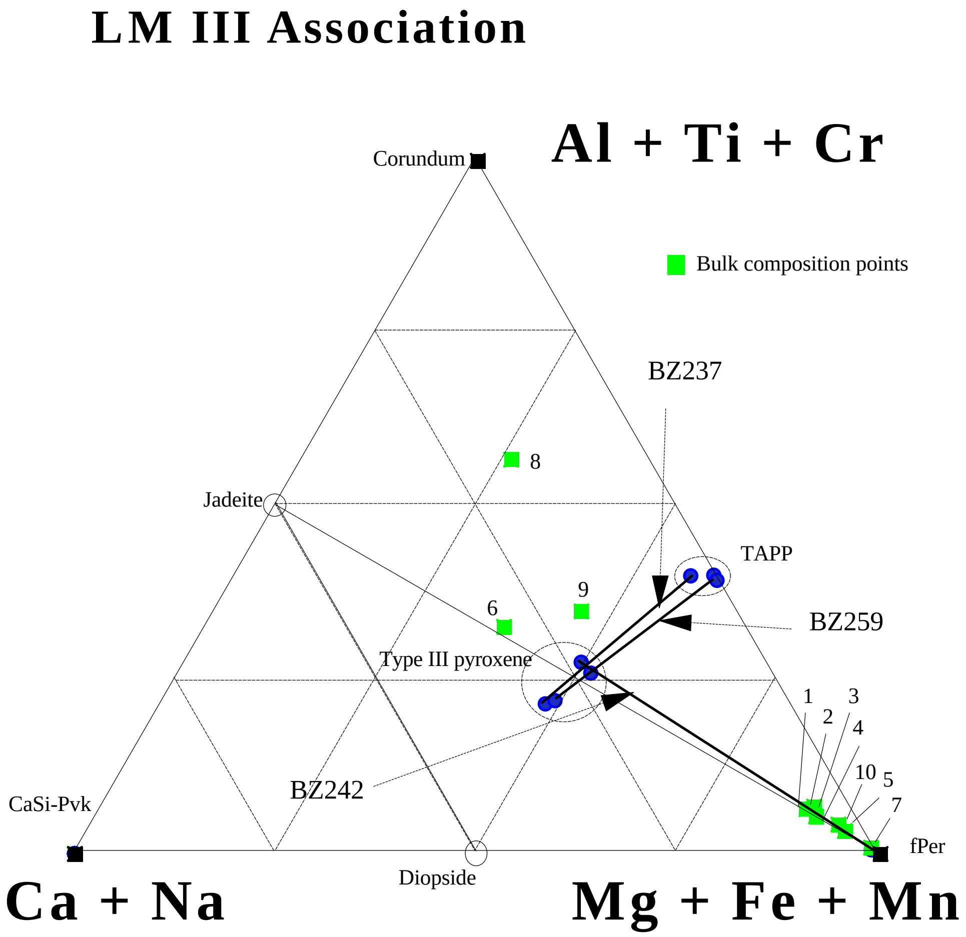

Figure 4.4_49 Cation compositions of inclusions of the LM III association from São Luiz diamonds in the ternary system Al+Ti+Cr - Mg+Fe+Mn - Ca+Na.

For bulk composition sources see figure 4.4_30.

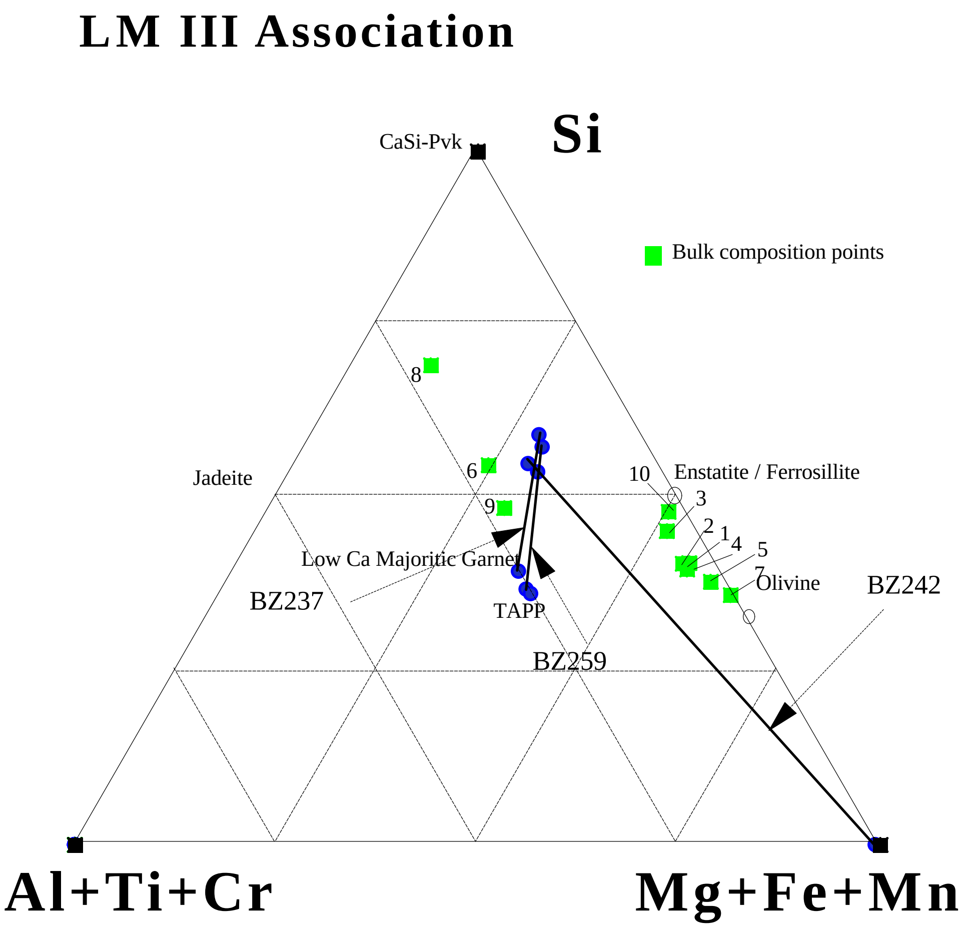

Figure 4.4_50 Cation compositions of inclusions of the LM III association from São Luiz diamonds in the ternary system Si - Mg+Fe+Mn - Al+Ti+Cr.

For bulk composition sources see figure 4.4_30.

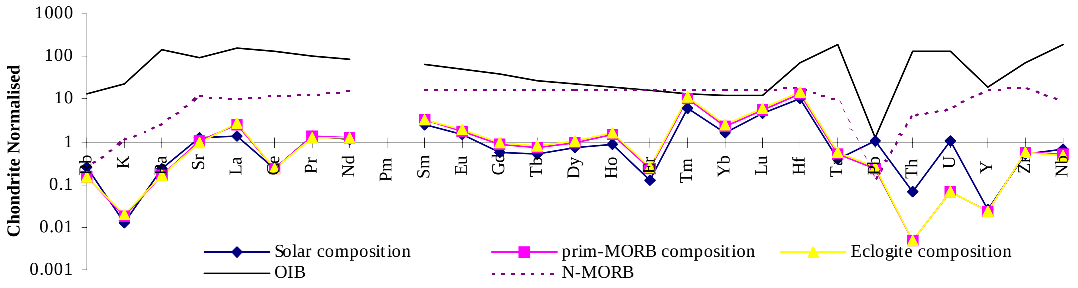

Figure 4.4_51 Trace element characteristics of the LM III association reconstructed to a solar bulk composition with N-MORB and OIB for comparison.

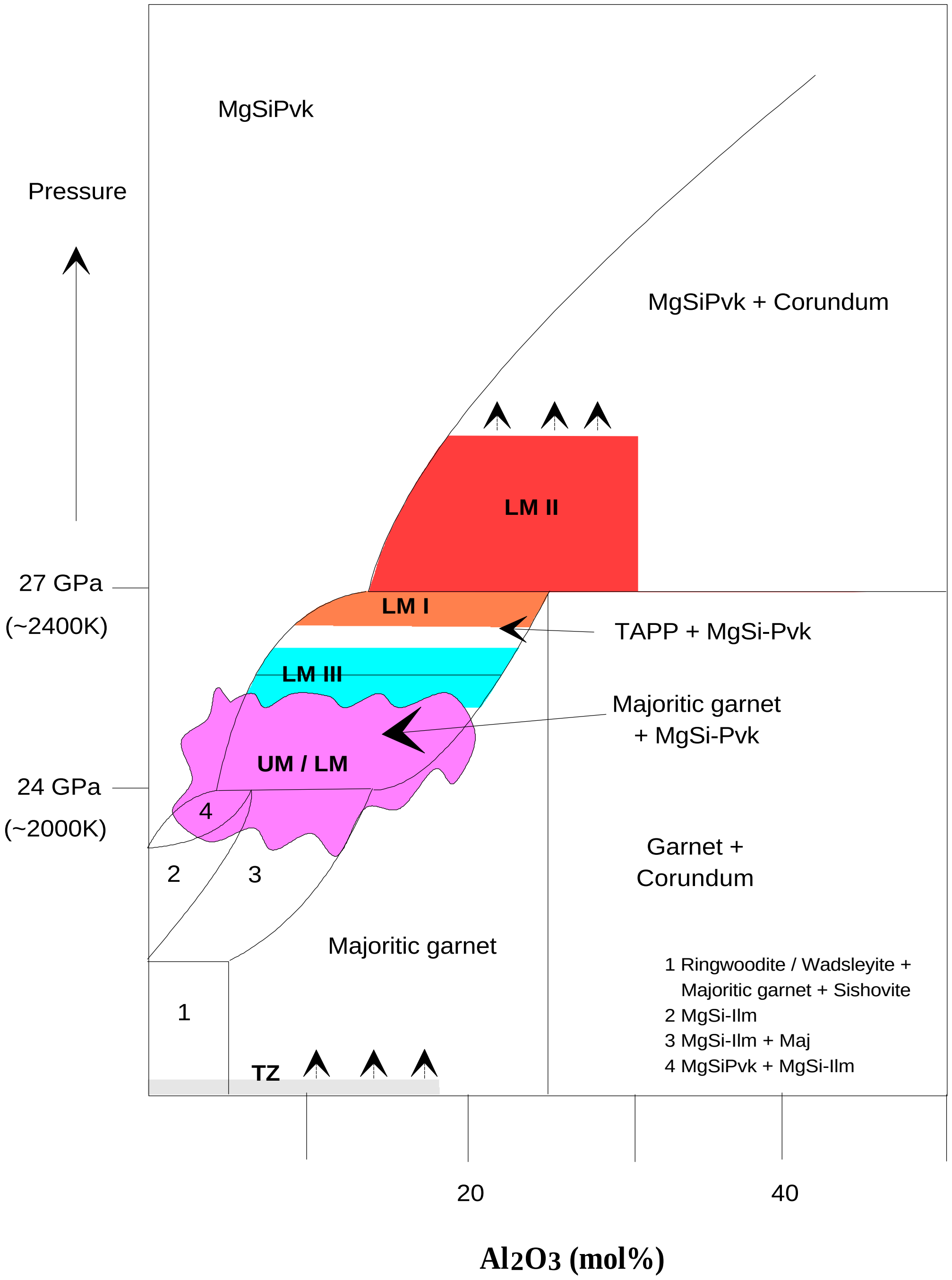

Figure 4.4_52 Summary of São Luiz and Guinean deep mantle associations projected onto a phase diagram in the $MgSiO_3$ - Al_2O_3 system.

Non-TAPP phase boundaries after Irifune et al. (1996). All associations relate well to the phase relations in the $MgSiO_3$ - $Mg_3Al_2Si_4O_{12}$ system with the exception of the UM/LM association which shows olivine composition in coexistence with TAPP. Ilmenite structured MgSi-Pvk is not stable in compositions with significant Fe-content so it is believed that the phase fields of TAPP and olivine will converge on the addition of Fe and other components in the depths range indicated by the UM/LM field presented.

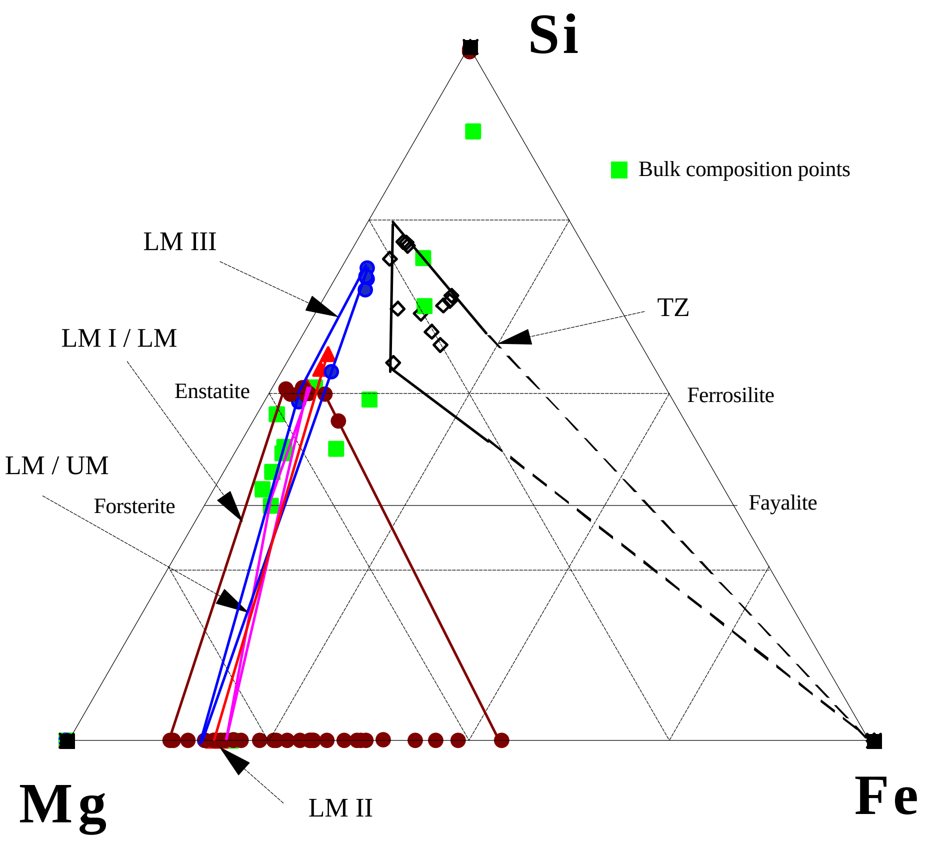

Sao Luiz and FEG Associations

Figure 4.4_53 Summary of cation compositions of inclusions of deep mantle associations from São Luiz diamonds in the ternary system Si - Fe - Mg.

For bulk composition sources see figure 4.4_30.

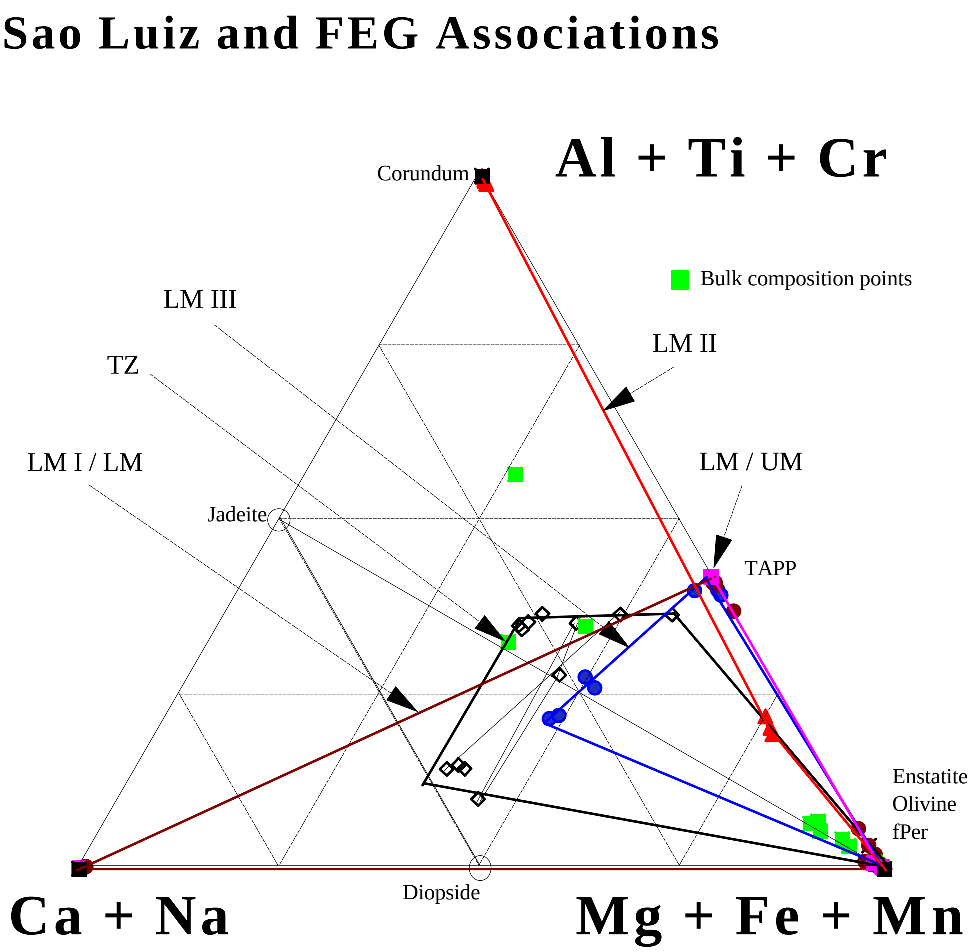

Figure 4.4_54 Summary of cation compositions of inclusions of deep mantle associations from São Luiz diamonds in the ternary system Al+Ti+Cr - Mg+Fe+Mn - Ca+Na.

For bulk composition sources see figure 4.4_30.

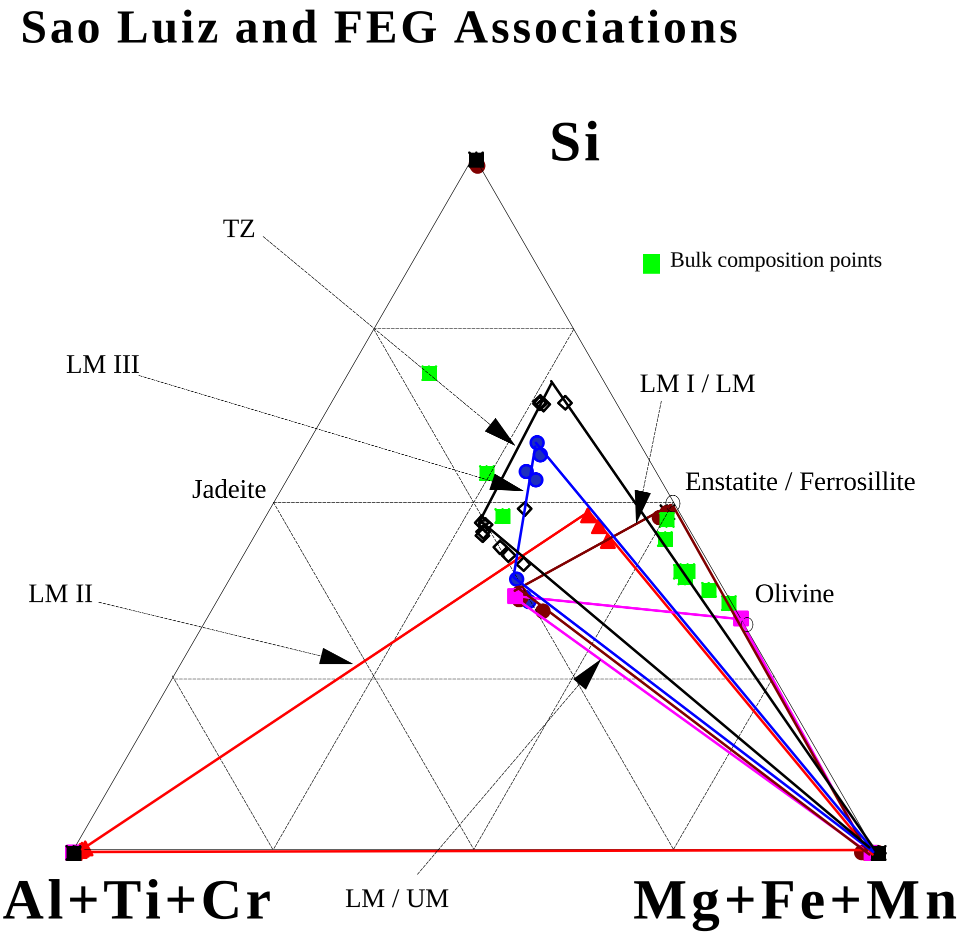

Figure 4.4_55 Summary of cation compositions of inclusions of deep mantle associations from São Luiz diamonds in the ternary system Si - Mg+Fe+Mn - Al+Ti+Cr.

For bulk composition sources see figure 4.4_30.

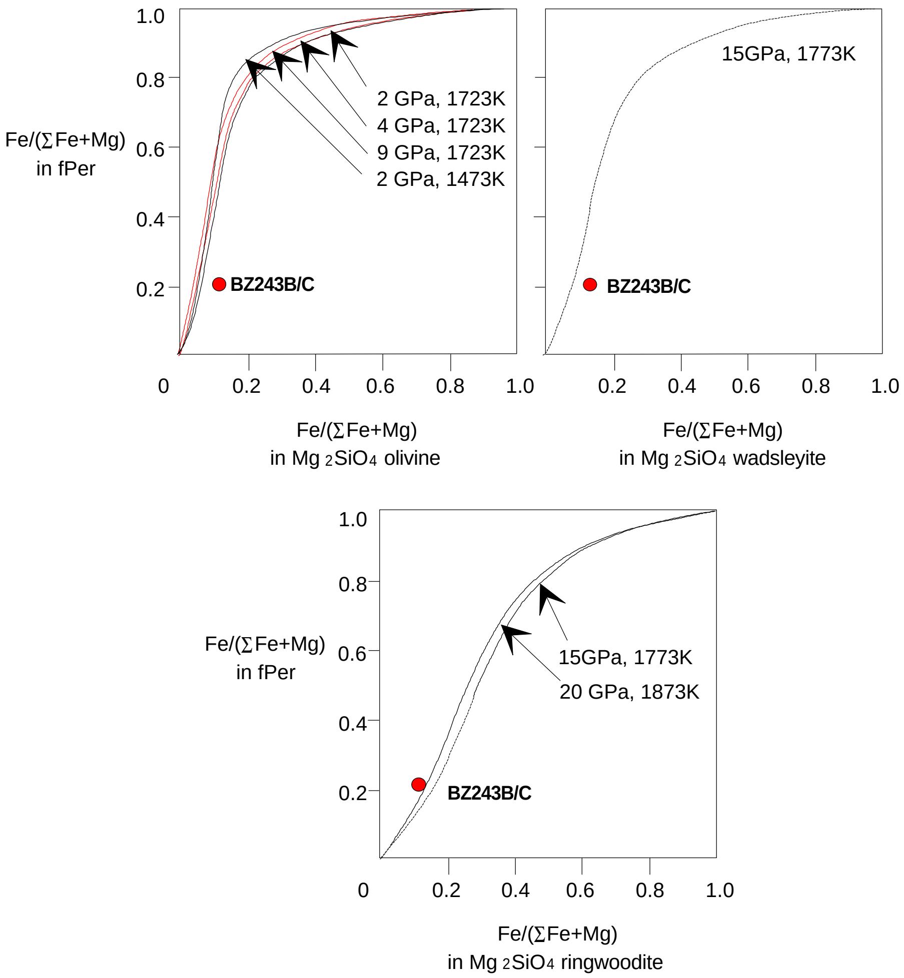

Figure 4.5_1 Partitioning of Fe and Mg between (Mg,Fe)$_2$SiO$_4$ polymorphs and fPer.

Interpretation of partitioning data in terms of olivine (a) and wadsleyite (b) polymorphs is not consistent with formation under likely conditions of mantle pressure and temperature. In terms of Fe/(Fe+Mg)cations for fPer against ringwoodite (c), inclusions from

(Mg,Fe)$_2$SiO is not stable at pressures of over 24GPa, partitioning behaviour of BZ243 inclusions suggests that the upper regions

and suggests a thermal boundary exists between upper and lower mantle.

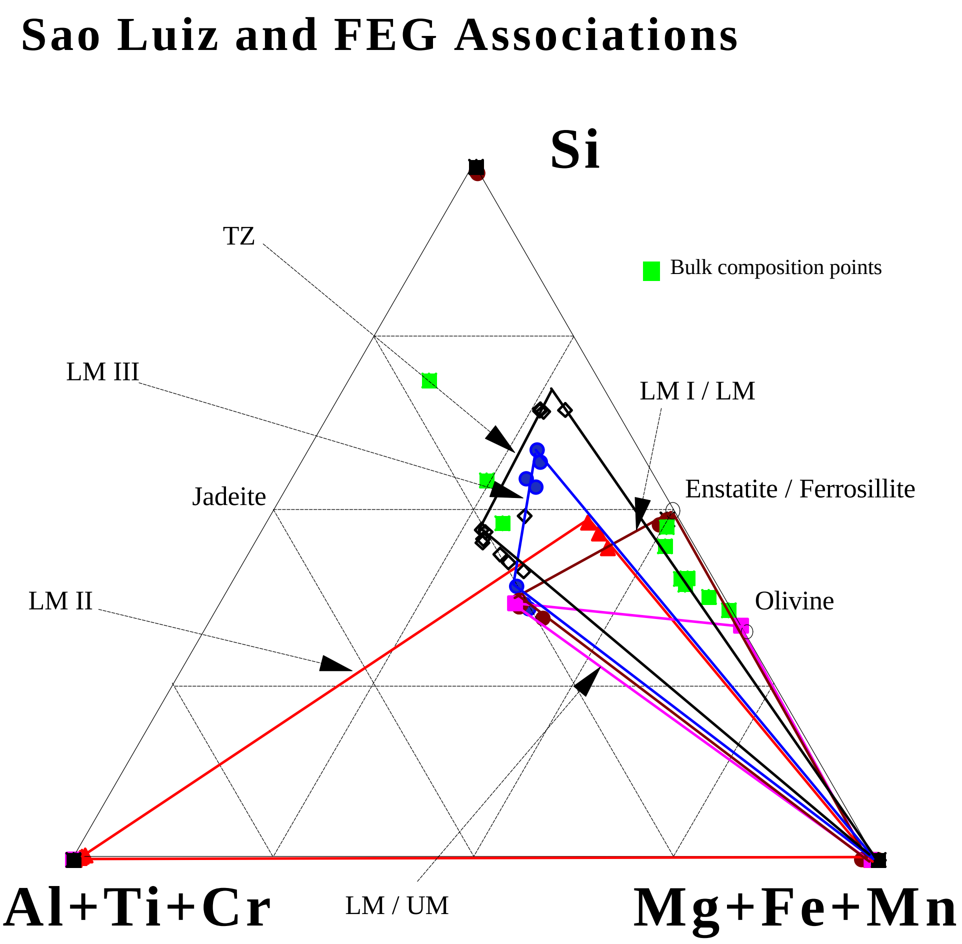

Figure 4.4_55 Summary of cation compositions of inclusions of deep mantle associations from São Luiz diamonds in the ternary system Si - Mg+Fe+Mn - Al+Ti+Cr.

For bulk composition sources see figure 4.4_30.

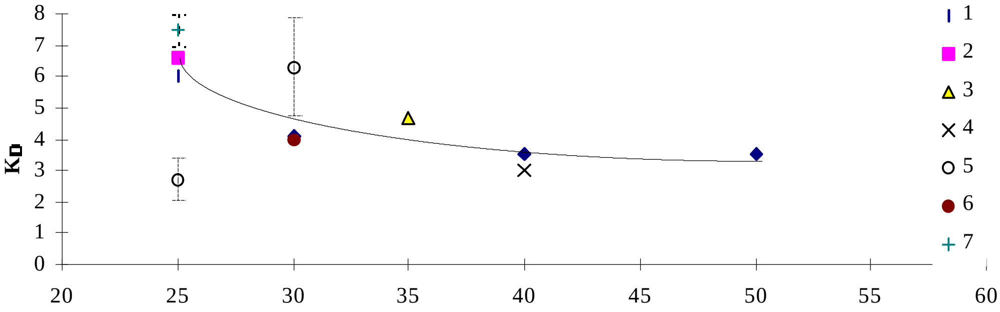

Figure 4.5_2 The dependence of K_D for Fe and Mg partitioning between fPer and MgSi-Pvk against pressure (GPa).

From 1 - Guyot et al. (1988), 2 - Ito et al. (1984), 3 - Bell et al. (1979), 4 - Malavergne et al. (1995), 5 - Kesson and Fitzgerald (1991), 6 - Yagi et al. (1979) 1173 K, and 7 - calculated from Fei et al. (1991) where $K_D = (Fe/Mg)_{fPer} / (Fe/Mg)_{MgSi\text{-}Pvk}$.

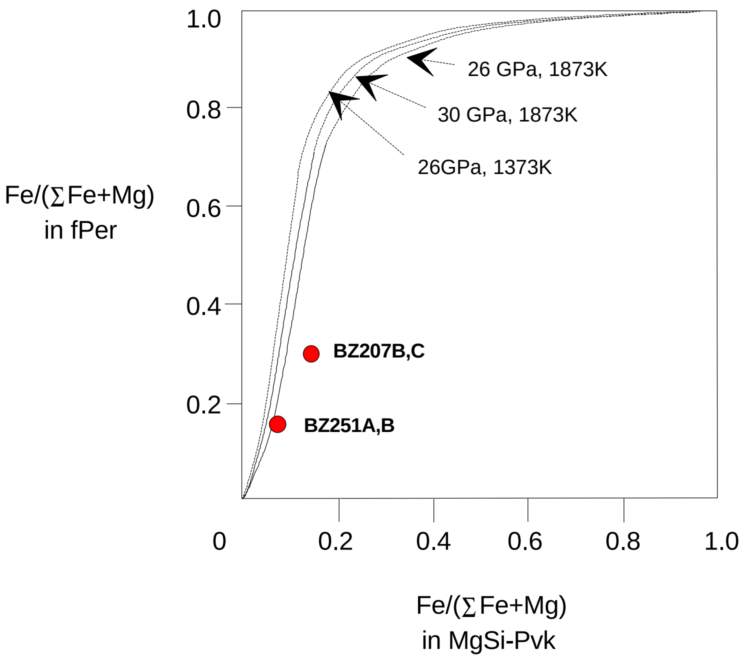

Figure 4.5_3 Partitioning of Fe and Mg between MgSi-Pvk and fPer.

Partitioning data from Fei et al. (1995) in comparison with LM I association inclusions from BZ207 and BZ251.

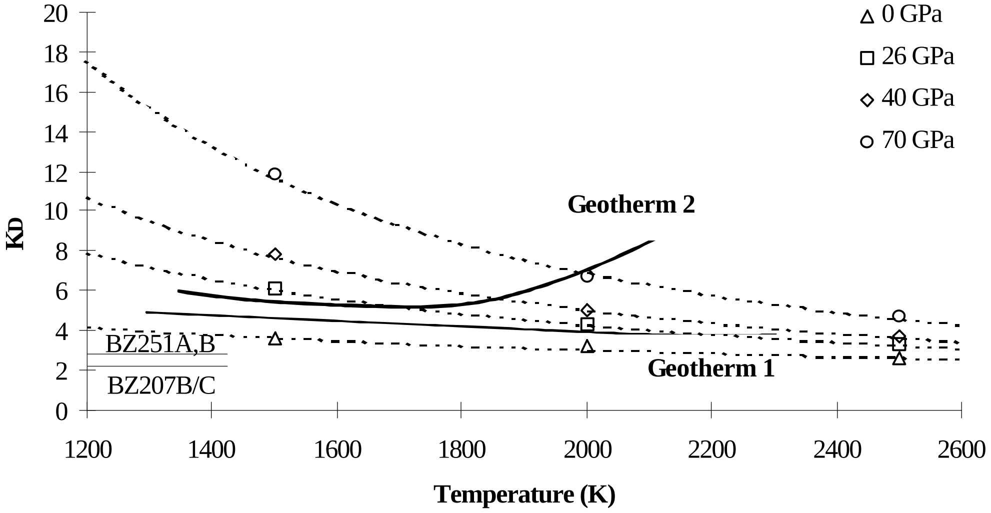

Figure 4.5_4 K_D Fe - Mg partitioning between fPer and MgSi-Pvk against temperature for 0, 26, 40 and 70 GPa.

From Malavergne et al. (1997) Model 1, where $K_D = (Fe/Mg)_{fPer} / (Fe/Mg)_{MgSi\text{-}Pvk}$. Plotted are Geotherms 1 and 2 and compositional data for inclusions in BZ207 and BZ251. Partitioning of São Luiz inclusions is most consistent with a high temperature geotherm.

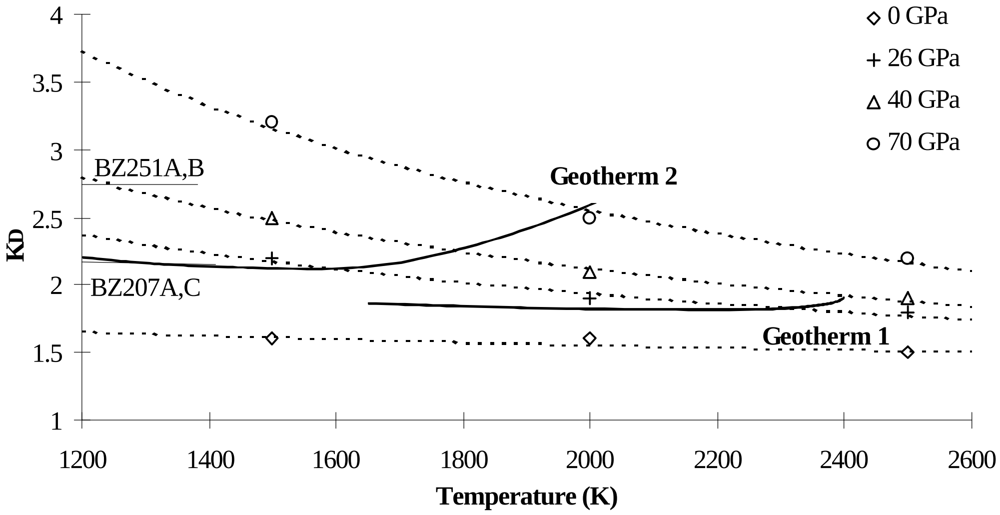

Figure 4.5_5 K_D Fe - Mg partitioning between fPer and MgSi-Pvk against temperature for 0, 26, 40 and 70 GPa.

From Malavergne et al. (1997) Model 2, where $K_D = (Fe/Mg)_{fPer} / (Fe/Mg)_{MgSi\text{-}Pvk}$. Plotted are Geotherms 1 and 2 and compositional data for inclusions in BZ207 and BZ251. Compared to this model, partitioning of São Luiz inclusions is most consistent with a low temperature geotherm.

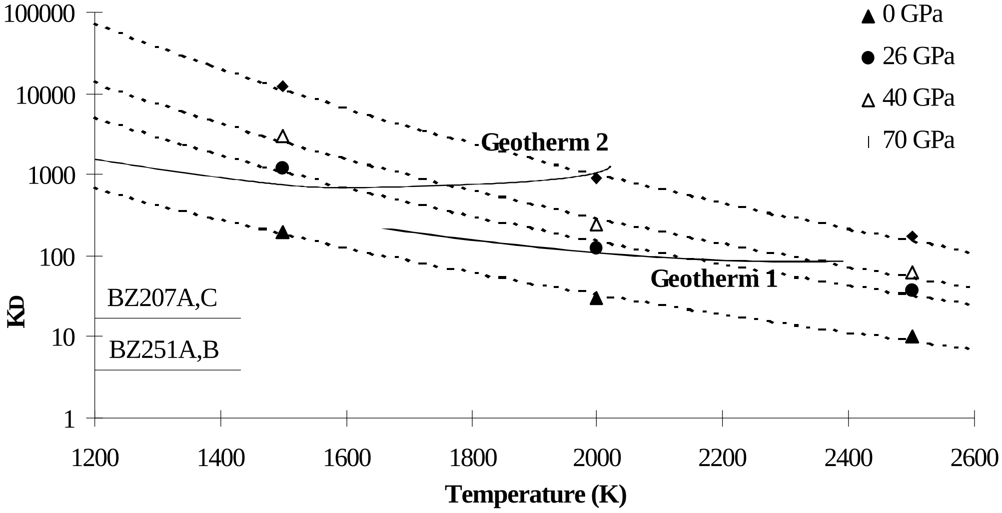

Figure 4.5_6 K_D Ni - Mg partitioning between fPer and MgSi-Pvk against temperature for 0, 26, 40 and 70 GPa.

From Malavergne et al. (1997) Model 1, where $K_D = (Ni/Mg)_{fPer} / (Ni/Mg)_{MgSi\text{-}Pvk}$. Plotted are Geotherms 1 and 2 and compositional data for inclusions in BZ207 and BZ251. Partitioning of São Luiz inclusions is most consistent with a high temperature geotherm.

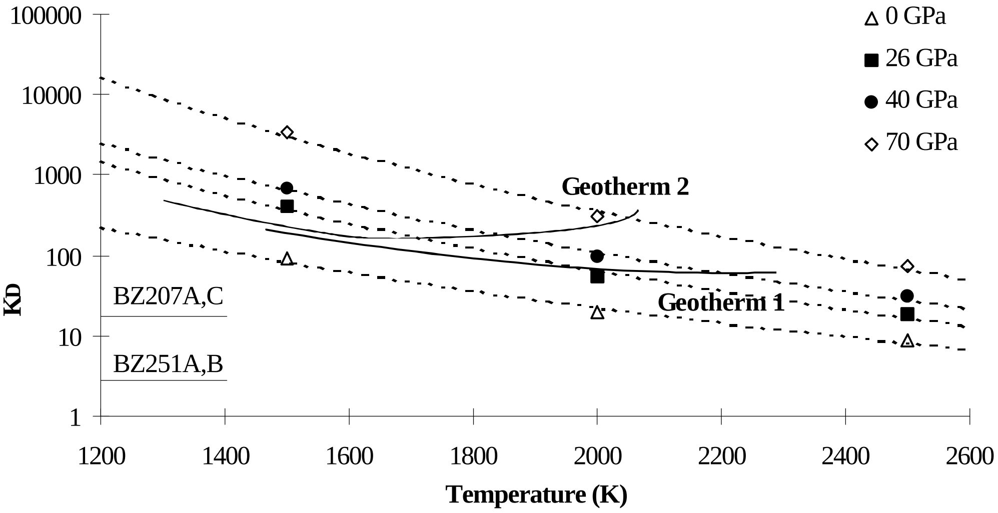

Figure 4.5_7 K_D Ni - Mg partitioning between fPer and MgSi-Pvk against temperature for 0, 26, 40 and 70 GPa.

From Malavergne et al. (1997) Model 2, where $K_D = (Ni/Mg)_{fPer} / (Ni/Mg)_{MgSi\text{-}Pvk}$. Plotted are Geotherms 1 and 2 and compositional data for inclusions in BZ207 and BZ251. Partitioning of São Luiz inclusions is most consistent with a high temperature geotherm.

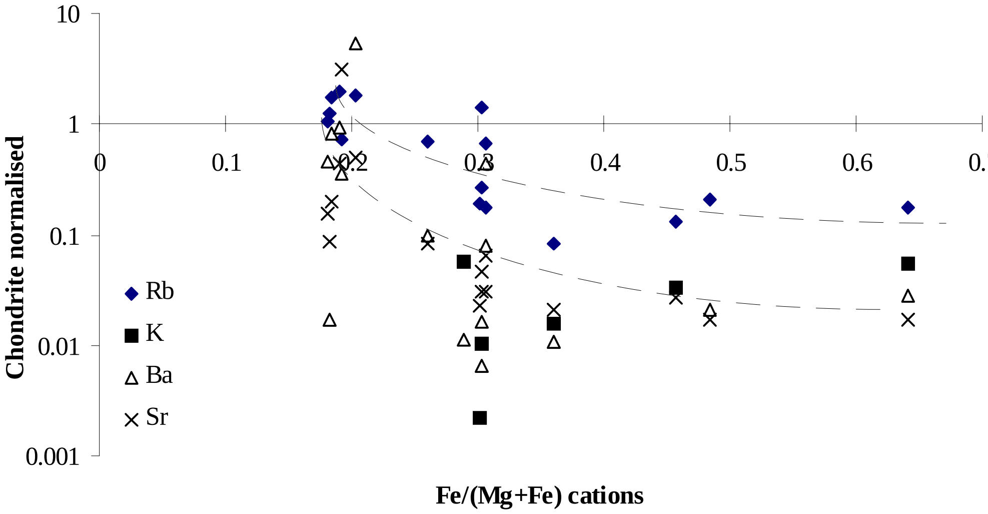

Figure 4.5_8 fPer LILE compositional variation with Fe/(Fe+Mg) composition.

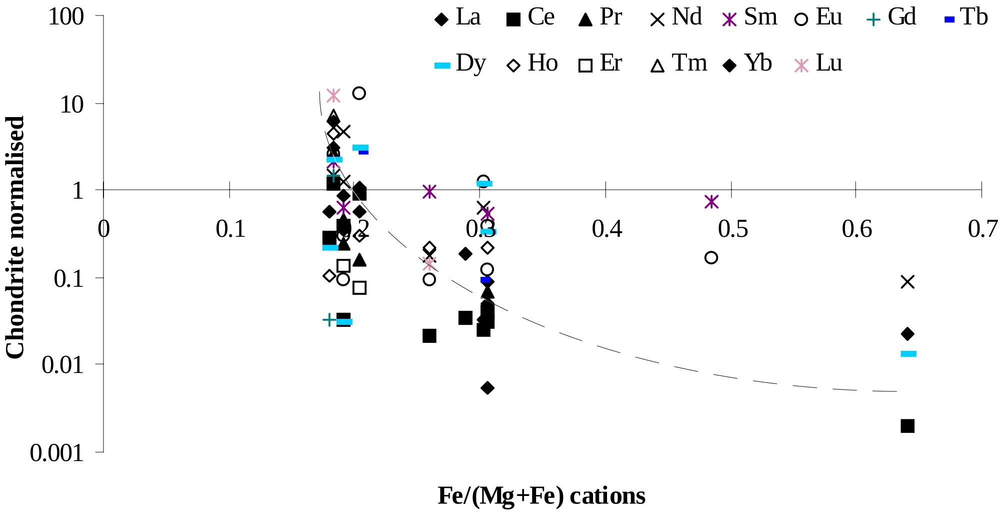

Figure 4.5_9 fPer REE compositional variation with Fe/(Fe+Mg) composition.

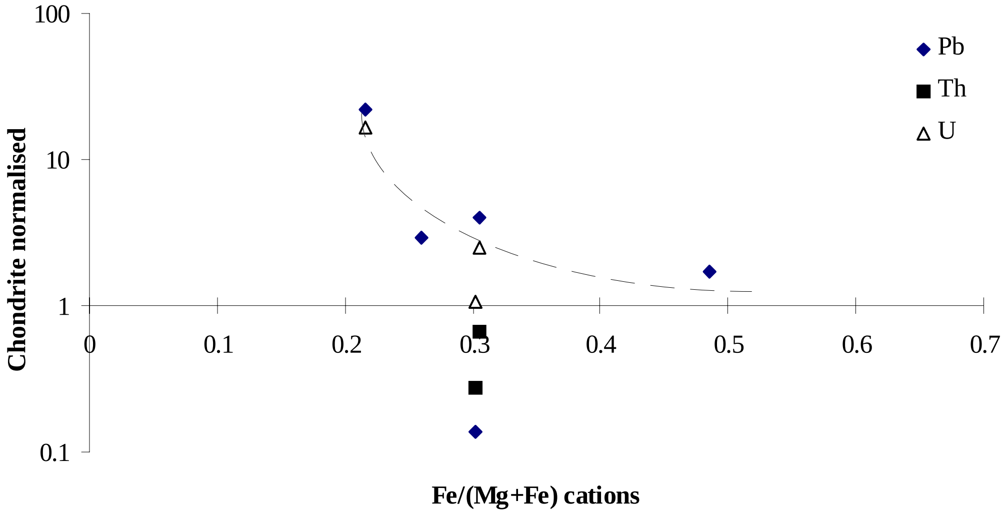

Figure 4.5_10 fPer heavy element compositional variation with Fe/(Fe+Mg) composition.

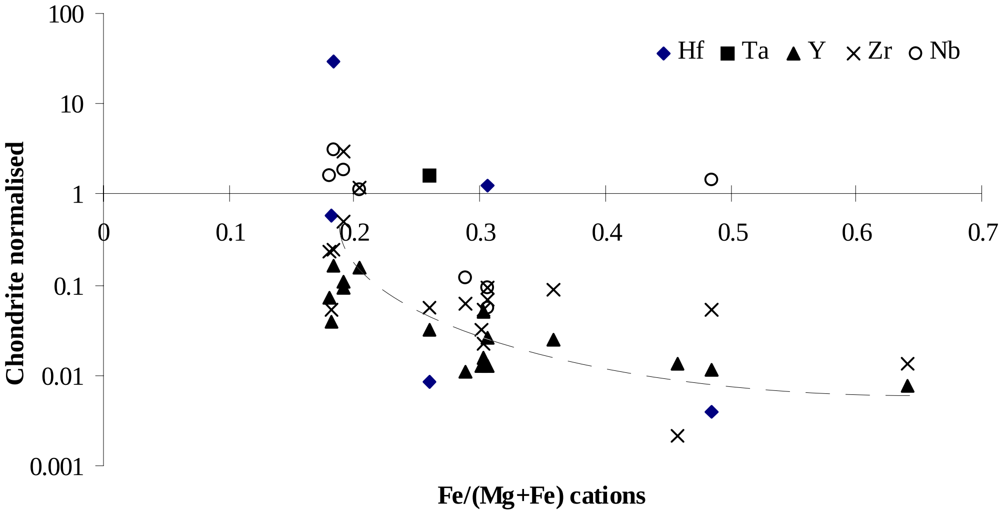

Figure 4.5_11 fPer HFSE compositional variation with Fe/(Fe+Mg) composition.

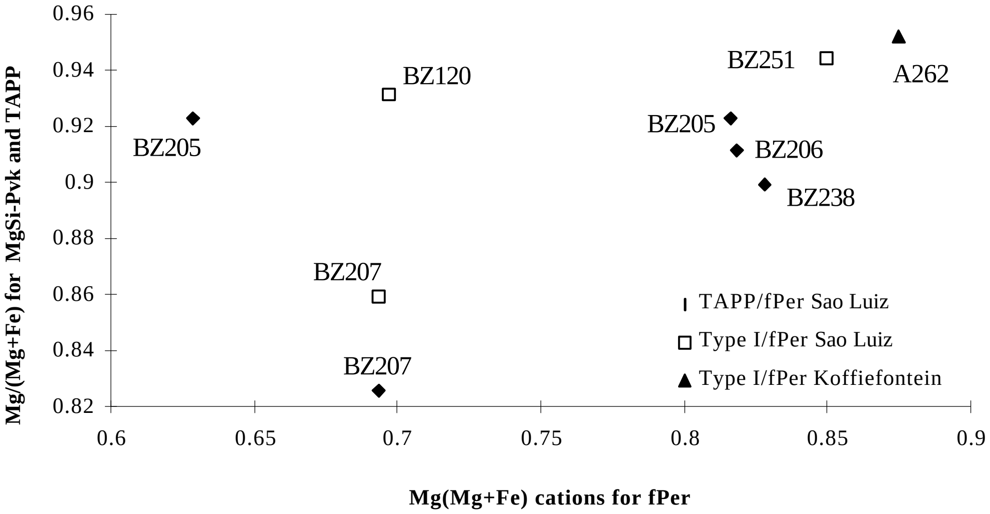

Figure 4.5_12 Mg/(Mg+Fe) for TAPP and Type I MgSi-Pvk against fPer for coexisting grains from São Luiz and Koffiefontein.

Koffiefontein data from Moore et al. (1985).

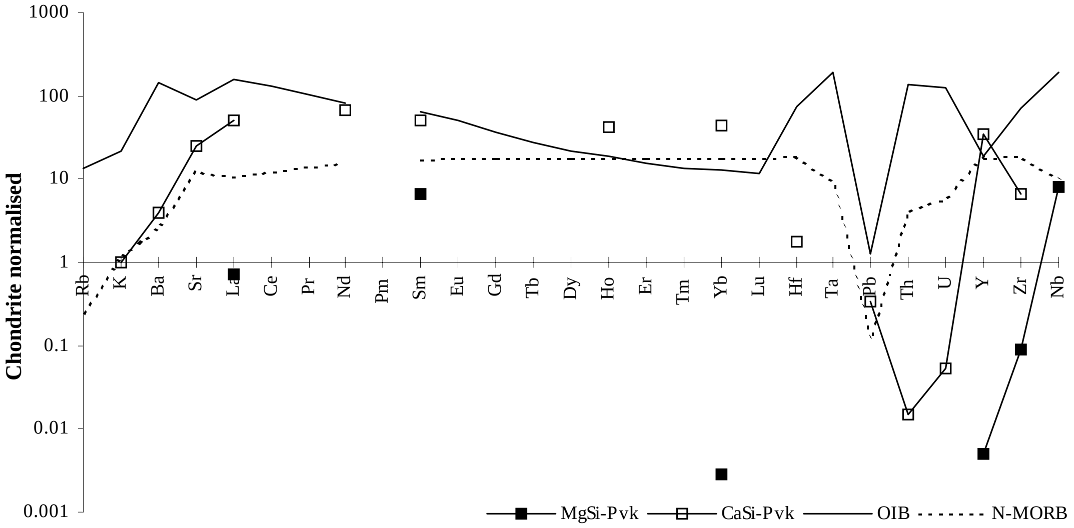

Figure 4.6_1 Liquids in equilibrium with phases from the LM I association in comparison with MORB and OIB.

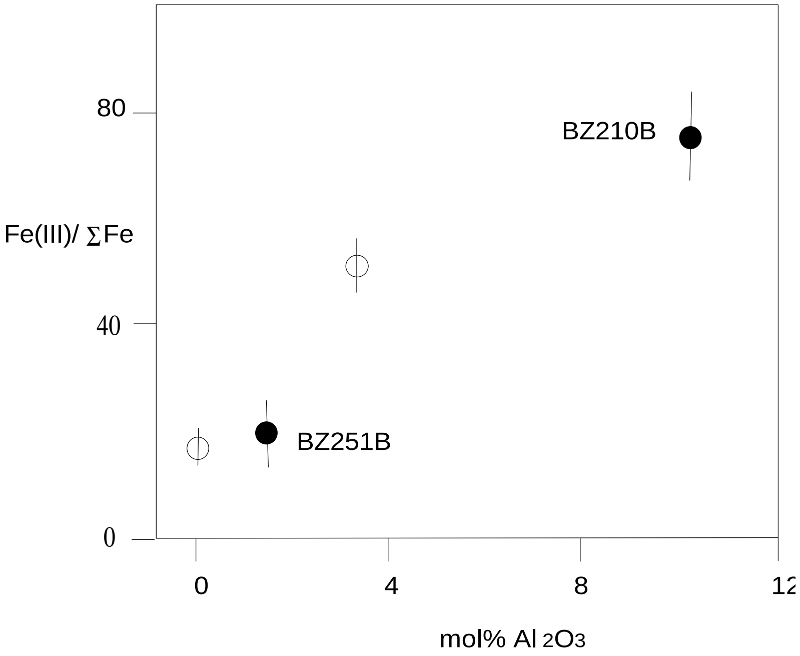

Figure 4.7_1 The relationship of Fe^{3+} content against mol% Al_2O_3 in aluminous MgSi-Pvk for experimental and São Luiz samples.

After McCammon et al. (submitted). Experimental data (open circles) from McCammon (1997).

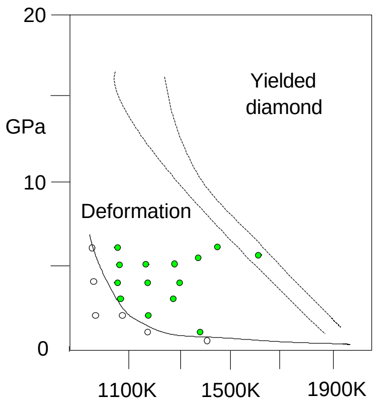

Figure 5.3_1 Yield strength in diamond as a function of temperature

Solid line, solid circles (where deformation lamellae are observed) and empty circle (no deformation) after De Vries (1975), dashed line after Weidner et al. (1994).

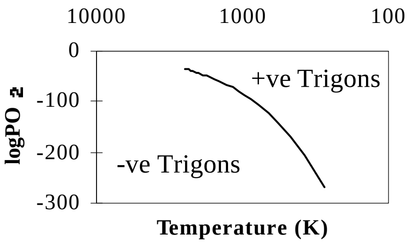

Figure 5.3_2 Régimes of positive and negative trigon formation in diamond

Calculated from Yamaoka et al. (1980) where oxygen pressure (PO_2) is in kbar and temperature in kelvin. Under natural conditions of diamond formation, negative trigons will be formed.

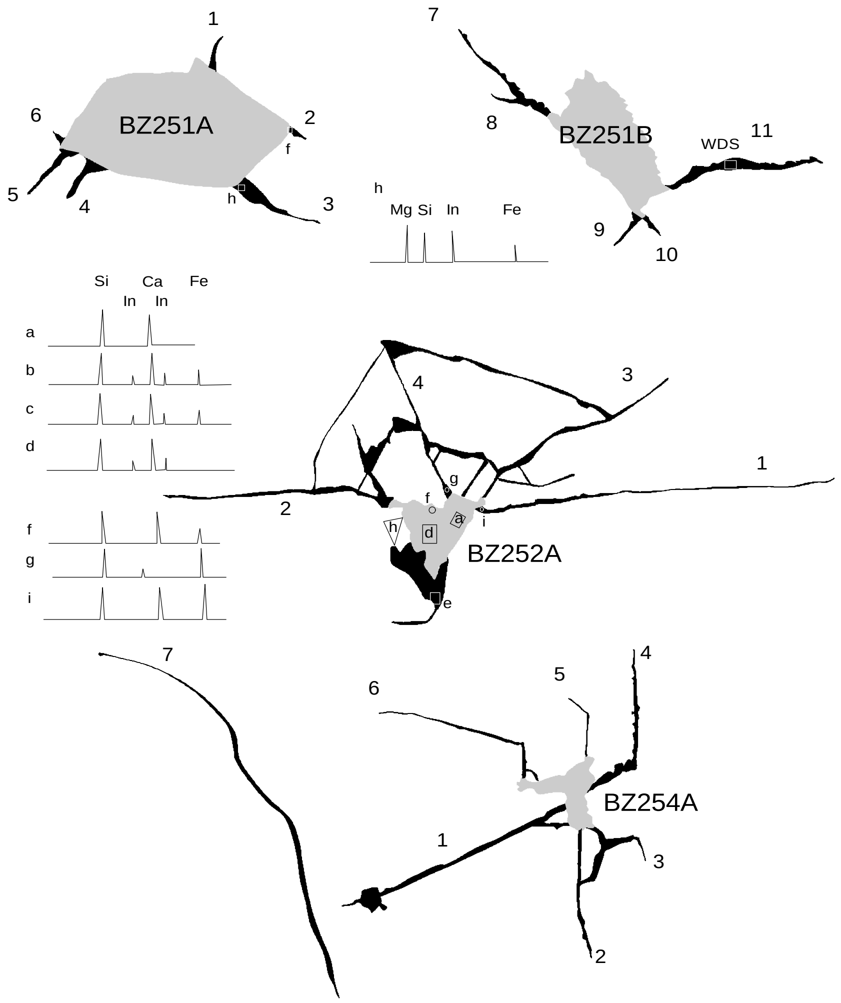

Figure 5.3_3 Nomenclature adopted for fractures on polished slabs with EDS spectra for selected areas

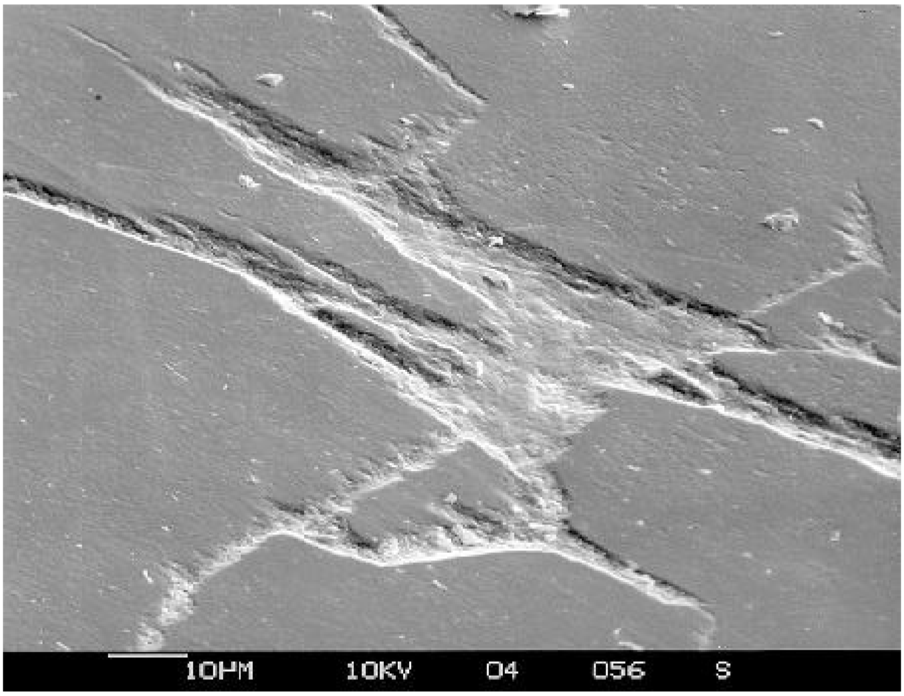

Figure 5.3_4 SEM image of Type I MgSi-Pvk inclusion, BZ254A and associated fracture.

Due to the hardness contrast between diamond and BZ254A, the inclusion lies significantly below the diamond surface. The image shows the diamond surface inclined at 70º.

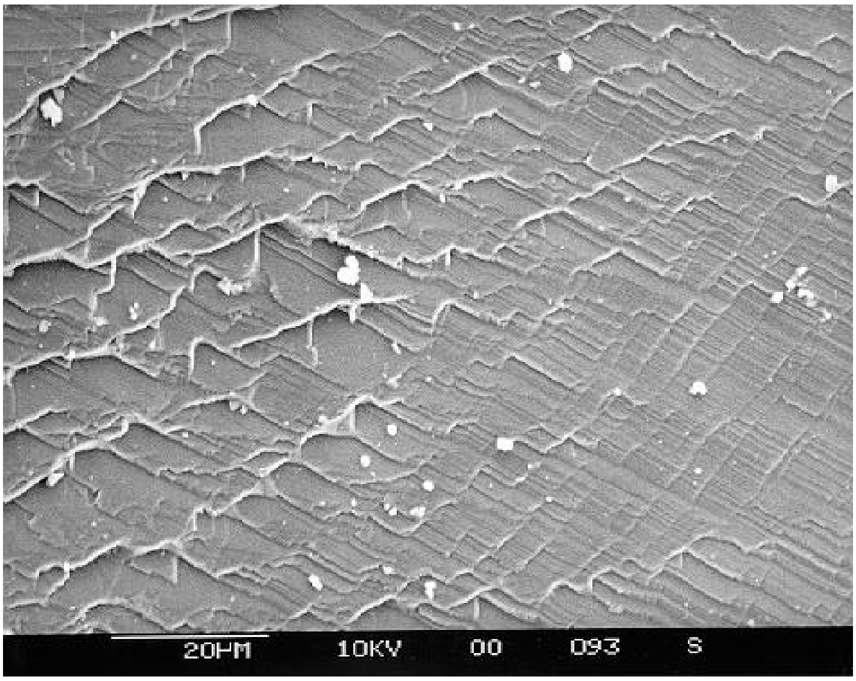

Figure 5.3_5 Step fractures in the surface of diamond cleaved under atmospheric conditions.

Cleavage traces of (111) at 65º are clearly picked out under such conditions of brittle fracture.

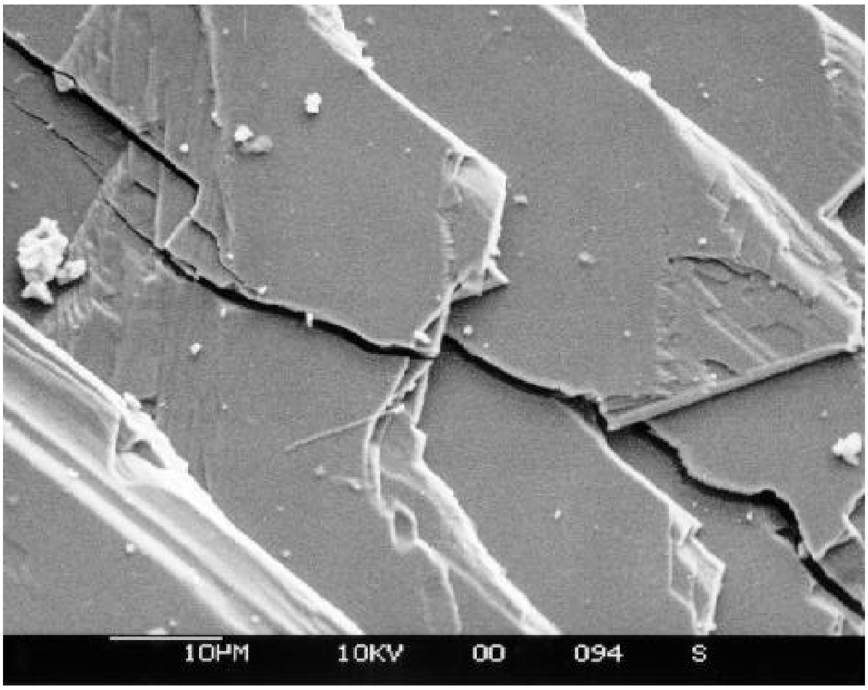

Figure 5.3_6 Cleavage of diamond JH2 under atmospheric conditions.

The sharp boundaries and imperceptibly terminating fractures visible contrast strongly with the blunt termination of fractures affected by plastic deformation under higher temperature, c.f. figure 5.3_7

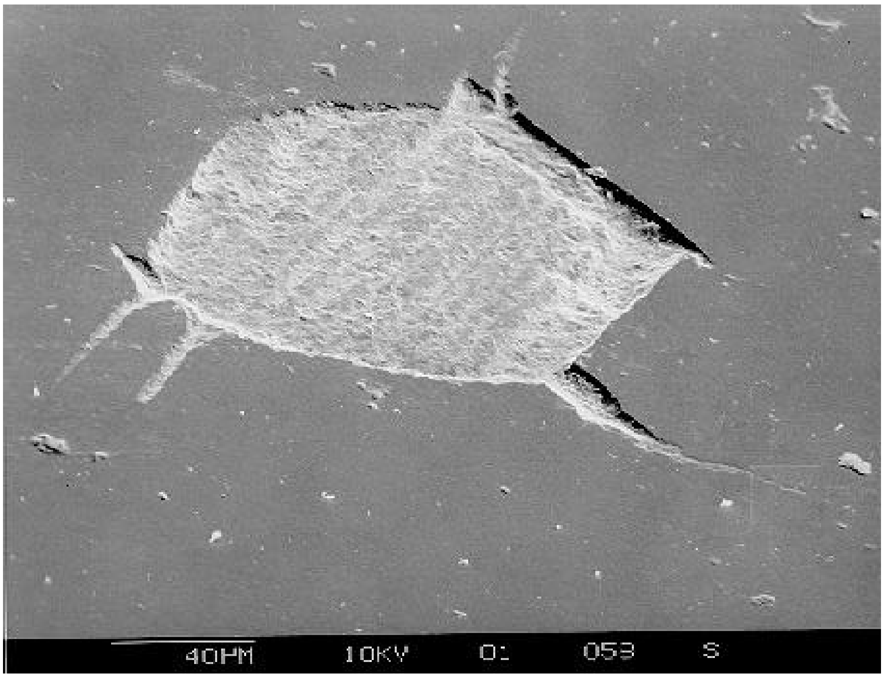

Figure 5.3_7 Fractures associated with fPer inclusion BZ251A.

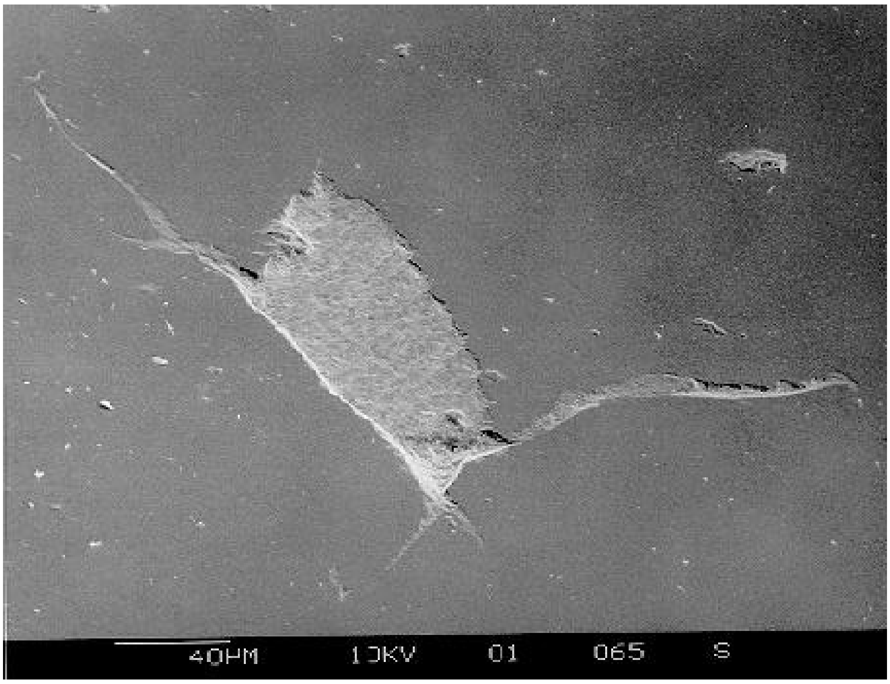

Figure 5.3_8 Fractures associated with Type I MgSi-Pvk inclusion BZ251B.

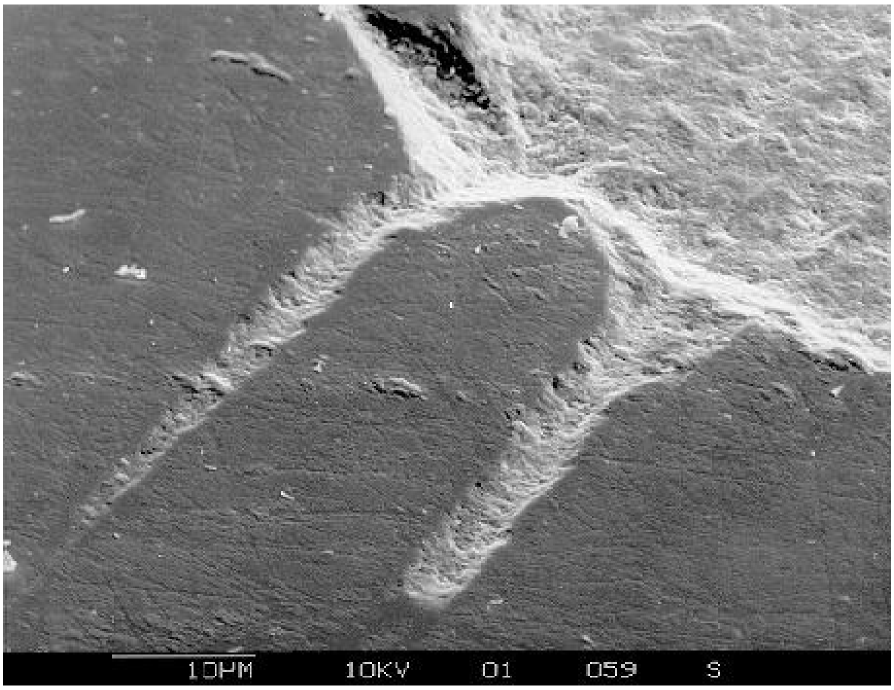

Figure 5.3_9 Blunt and sharp termination of fractures associated with BZ251A.

Being in the same general direction and growth zone (as determined by CL), there is no crystallographic control to explain the differences in fracture termination. It is concluded that the two fractures occurred within different fracturing events, the sharper under a régime dominated by brittle failure, and the blunter within a more plastic régime.

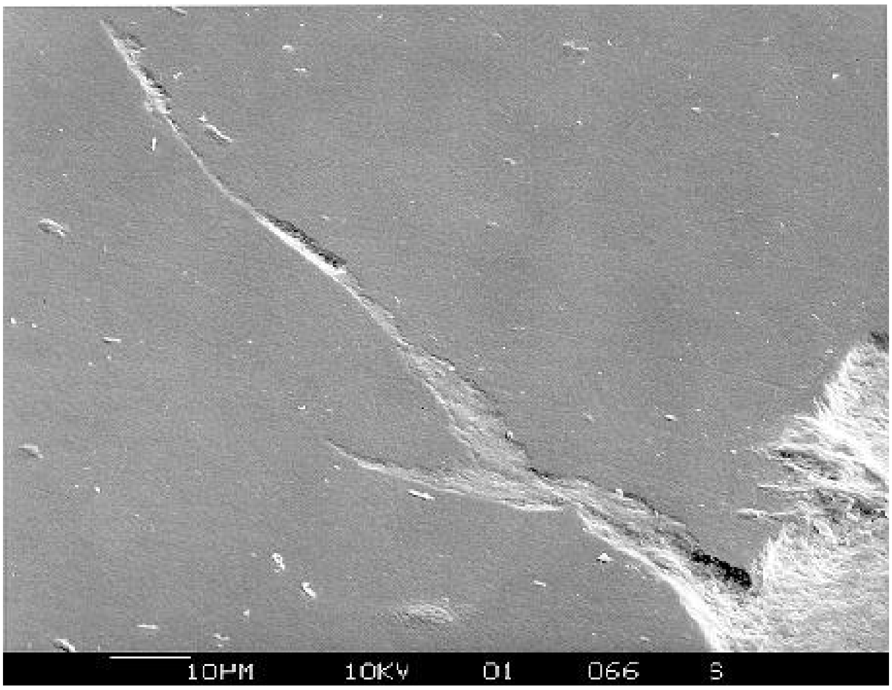

Figure 5.3_10 ‘Augen’ fracture emanating from inclusion BZ251B.

The morphology of the fracture is indicative of partial healing by a mechanism of rezipping; neither CL nor $\delta^{13}C$ analysis support healing by diamond re-precipitation.

Figure 5.3_11 'Augen' termination of fracture 3 of BZ252A.

The fracture can be followed by discrete depressions separated by completely rehealed diamond.

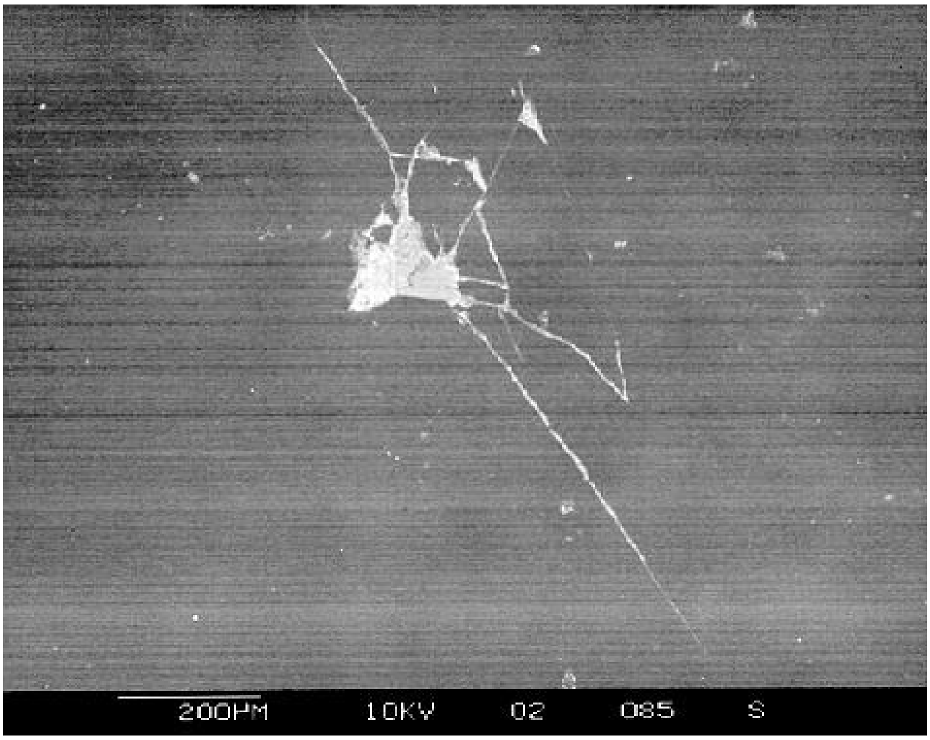

Figure 5.3_12 Spiders web of sinuous fractures surrounding BZ252 CaSi-Pvk inclusion.

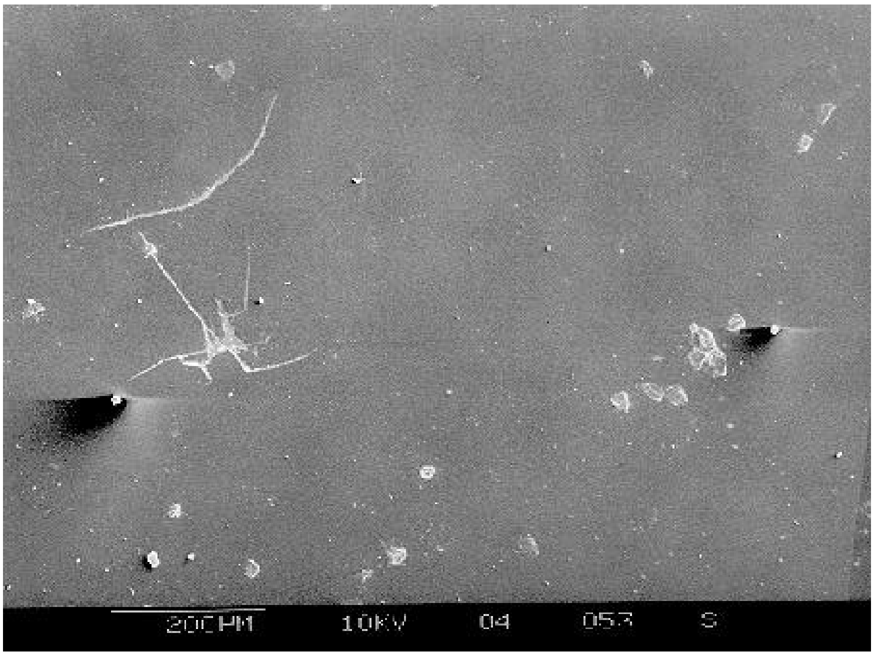

Figure 5.3_13 Penetration of BZ254A inclusion in context with the diamond surface.

The separate fracture system is probably also associated with the inclusion at depth. Note also the cluster of roughly hexagonal positive surface features to the right of the inclusion.

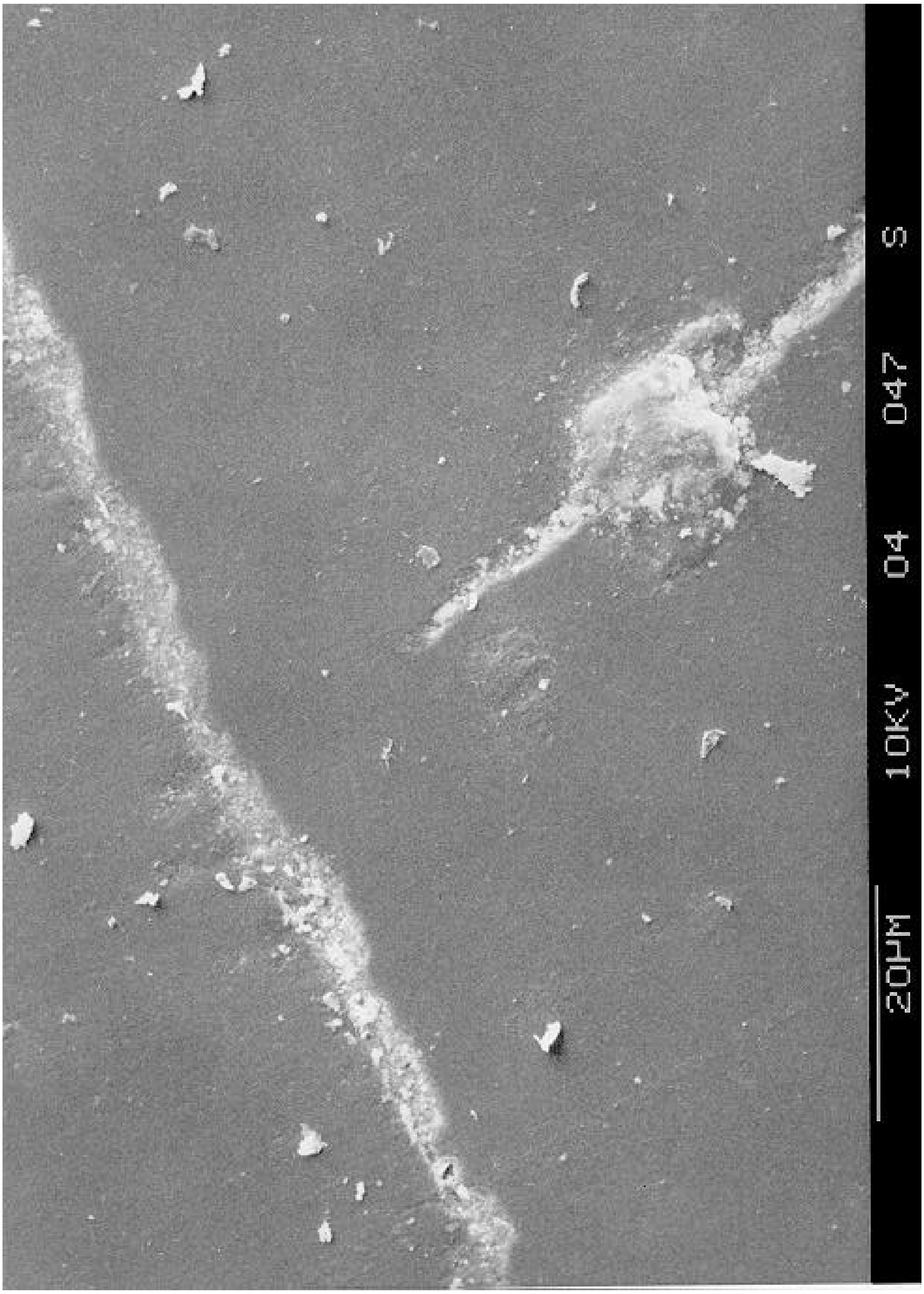

Figure 5.3_14 Blunt termination of fracture 1, 20µm from isolated fracture 7 in BZ254.

Fracture 1 propogated to this stage subsequent to the formation of fracture 7 stopping abruptly as its damage zone met with the 90° oriented fracture 7.

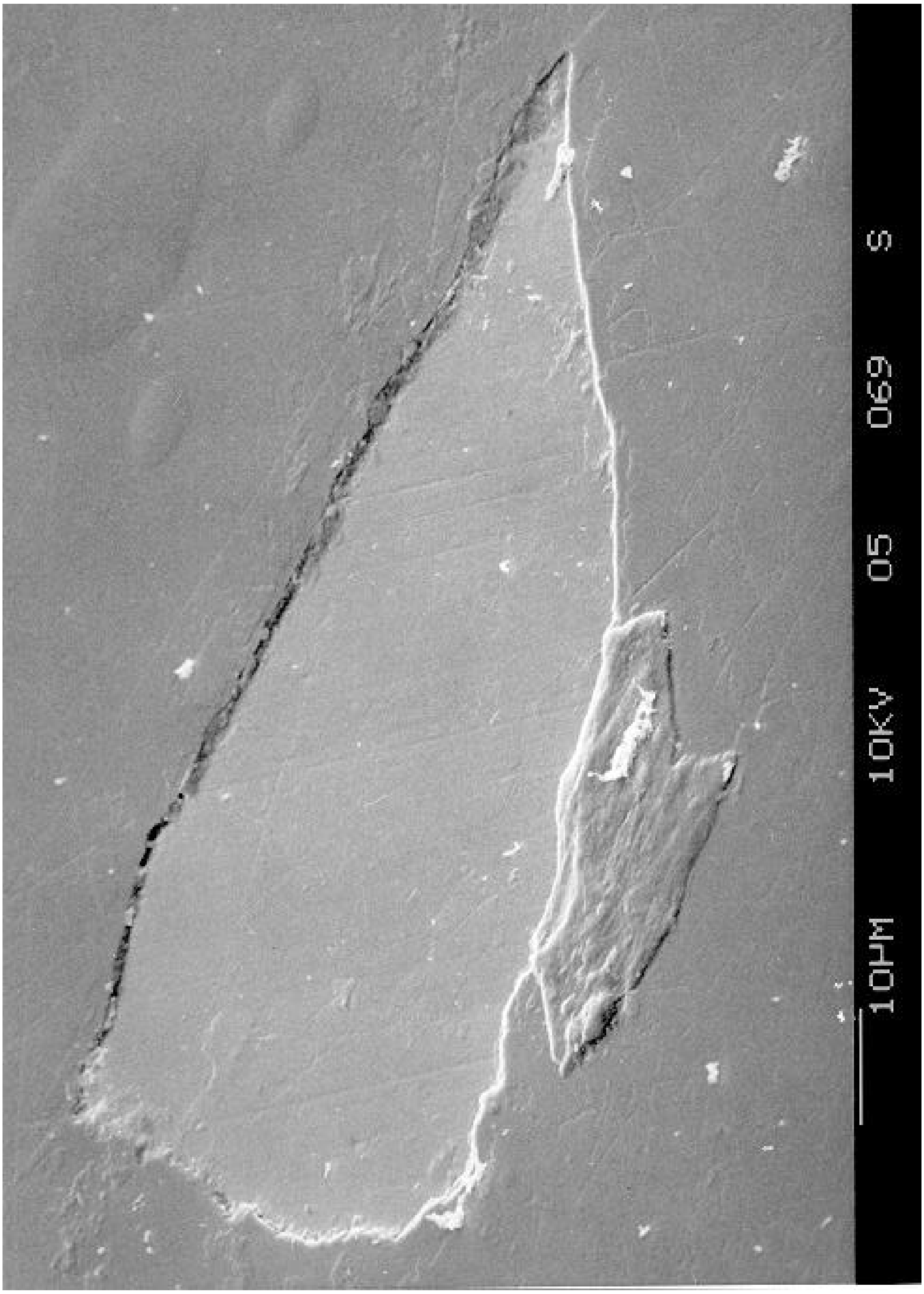

Figure 5.3_15 fPer inclusion BZ255A showing a remarkably well polished surface.

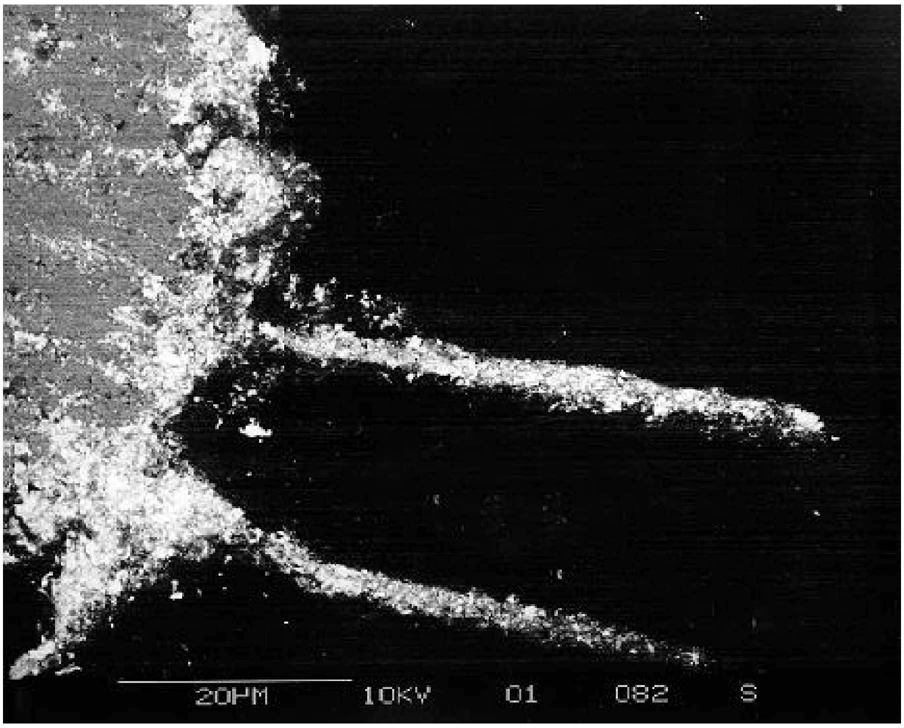

Figure 5.3_16 BS-SEM image of blunt and sharp terminations from BZ251A

The degree of BS- contrast is consistent with the fracture filling material being Fe or In from the polishing process and is consistent with EDS analysis.

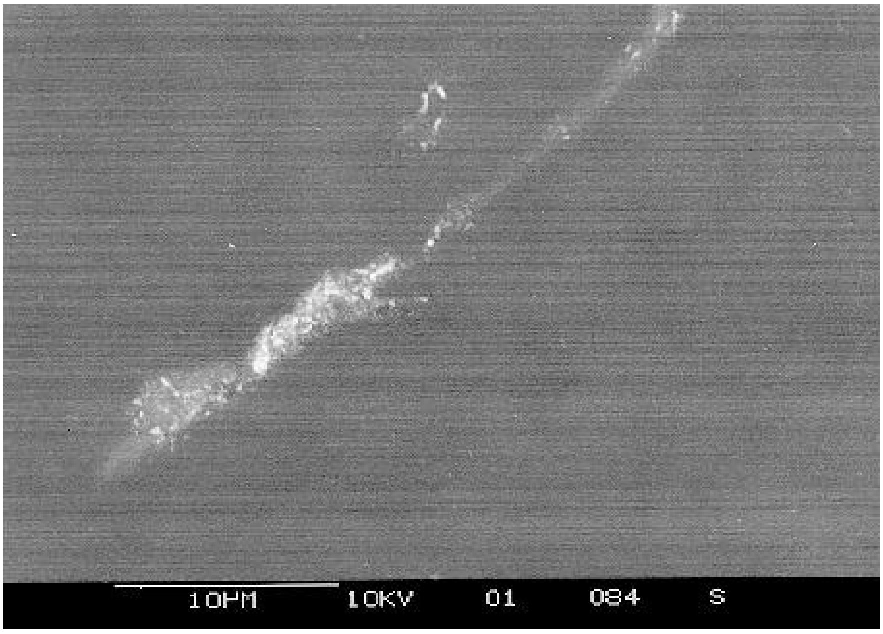

Figure 5.3_17 High magnification (x7500) BS-SEM image of fracture 7 from BZ251B.

Even at high magnification fractures appear free of material other than Fe and In, c.f. figure 5.3_10.

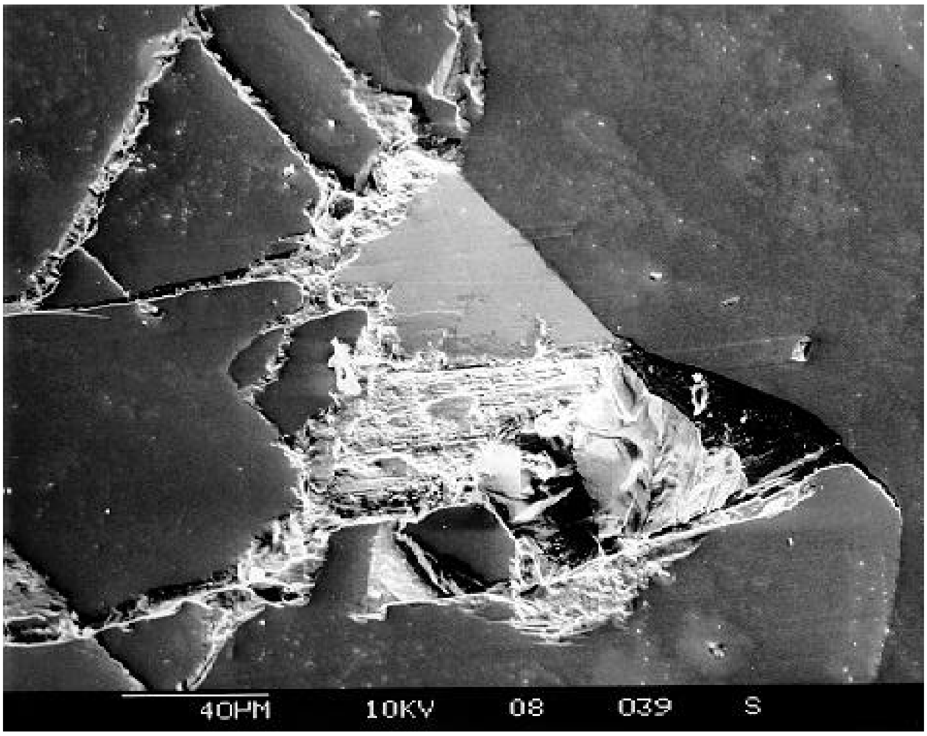

Figure 5.3_18 BS-SEM image of inclusion BZ252A.

The extent of exposed CaSi-Pvk inclusion is difficult to assess, particularly due to the inclined topography of part of the inclusion surface. WDS imagery in Si showed that the inclusion material has a triangular shape, additional BS features to the bottom of the image being due to polishing Fe and In in cusps in the diamond host.

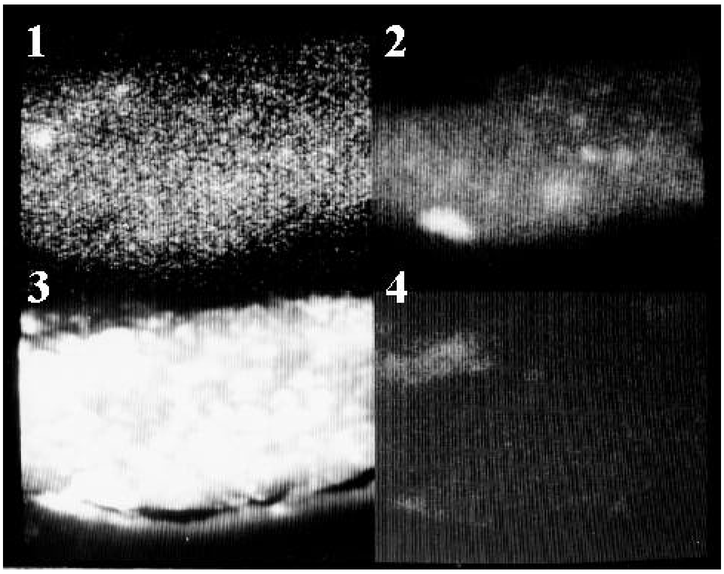

Figure 5.3_19 WDS images collected for 'augen'fracture 11 of BZ251B

1 - Si, 2 - Fe, 3 -BS-image, 4 - In. The back scattered image show that the high BS-SEM features correspond either to Fe or In. There is also a dusting of Si in the fracture, however, intensity of the Si image is not directly comparable with the other elements measured as Si Kα diffraction lies on the high of the background spectra. Furthermore as Si is a feature of the diamond surface in general, this is interpreted as being due to surface contaminant. Each image is approximately 10 µm across.

Figure 5.3_20 AFM image of BZ251B showing a regular lineation in surface topography.

The image inclusion is 150 µm lengthways.

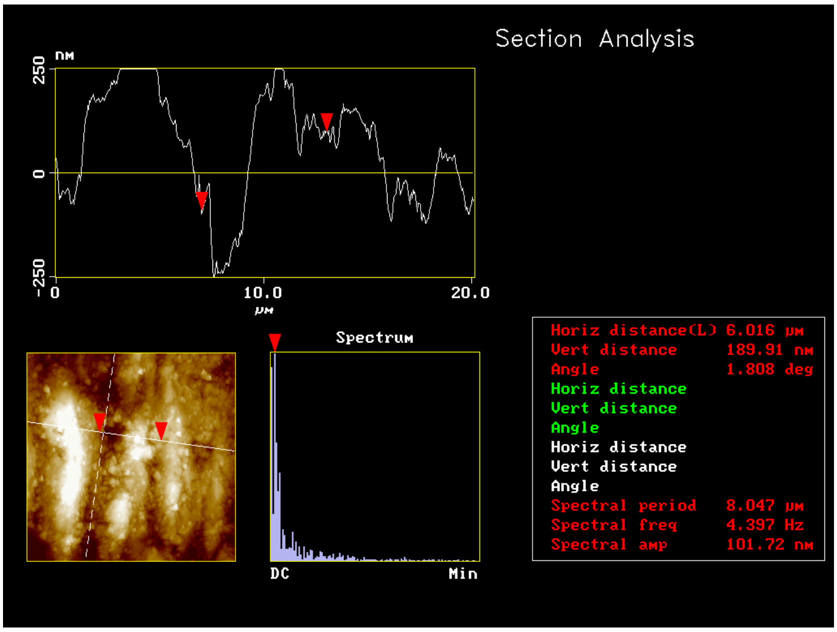

```
Horiz distance(L) 6.016 µm
Vert distance     189.91 nm
Angle             1.808 deg
Horiz distance
Vert distance
Angle
Horiz distance
Vert distance
Angle
Spectral period   8.047 µm
Spectral freq     4.397 Hz
Spectral amp      101.72 nm
```

Figure 5.3_21 AFM spectral deconvolution of lineation in the surface of BZ251B

A sharp peak in the periodicity spectrum apears at 8.05 µm. Either the polishing grit was remarkably evenly spaced on the last stages of polishing or else these features are an due to cleavage planes in the inclusion.

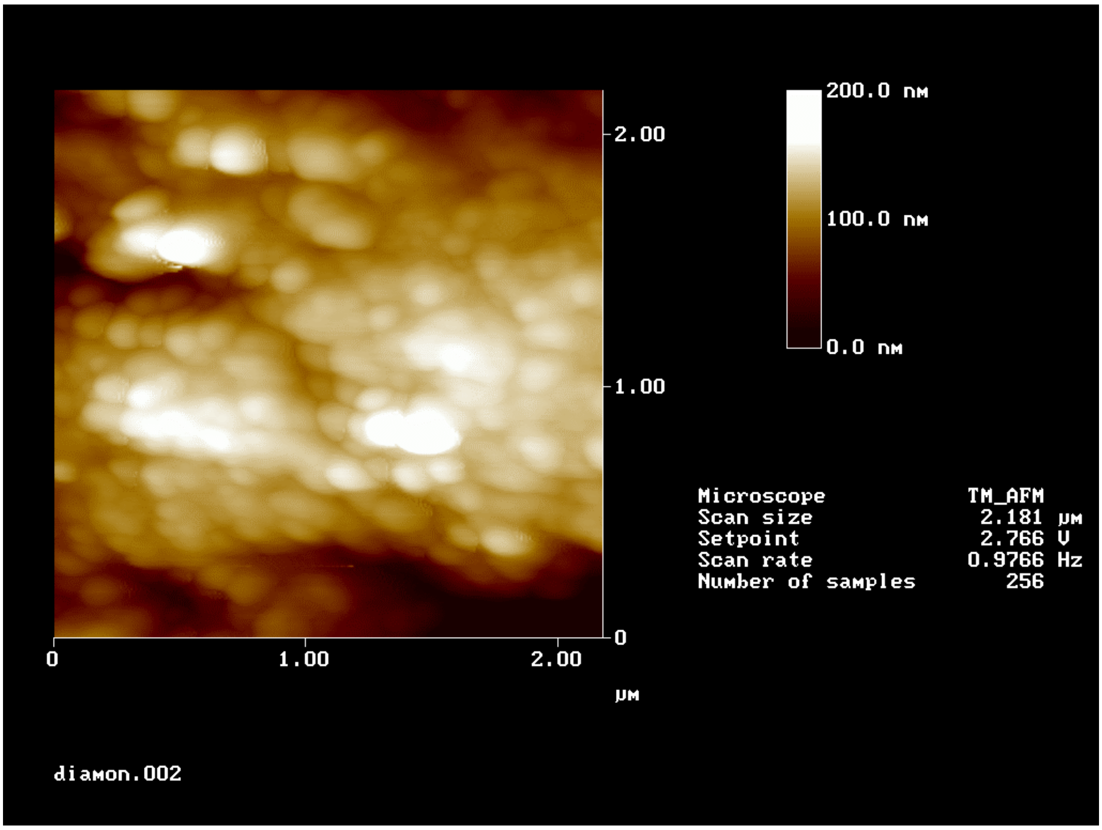

Figure 5.3_22 AFM image of 1/4 µm diamond polishing grit in a fracture of BZ251B.

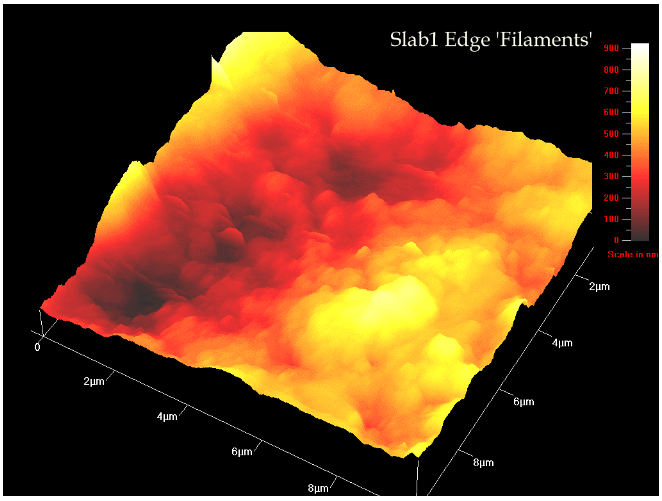

Figure 5.3_23 SPM image of area h within fracture from BZ251A.

As in figure 5.3_22, polishing material of approximately1/4 µm is evident.

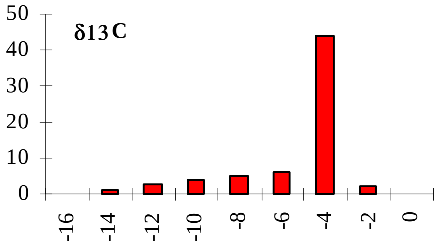

Figure 5.4_1 $\delta^{13}C$ Distribution of $\delta^{13}C$ content of all São Luiz diamonds.

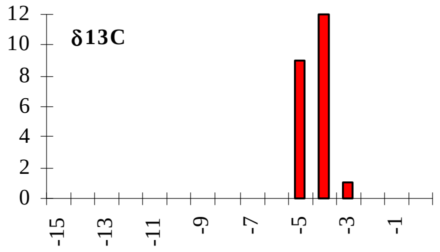

Figure 5.4_2 LM association diamond δ^{13}C.

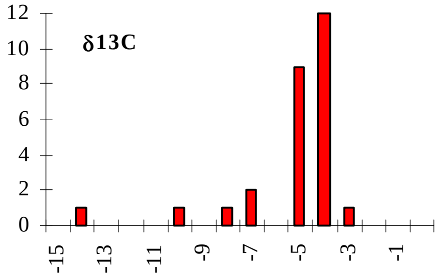

Figure 5.4_3 LM association diamond δ^{13}C compositions in addition to Wilding (1990) 'fPer association diamonds'.

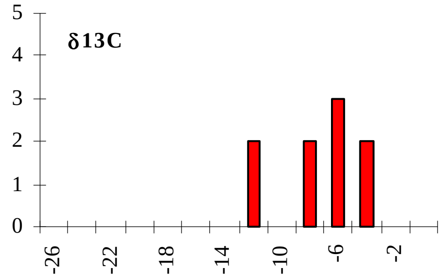

Figure 5.4_4 LM III association diamond $\delta^{13}C$ composition.

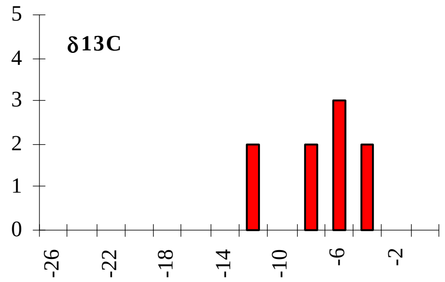

Figure 5.4_5 TZ association diamond $\delta^{13}C$ composition.

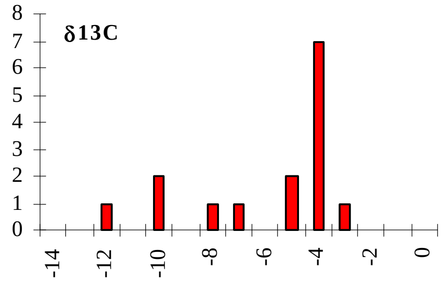

Figure 5.4_6 $\delta^{13}C$ composition of diamonds of unknown paragenesis.

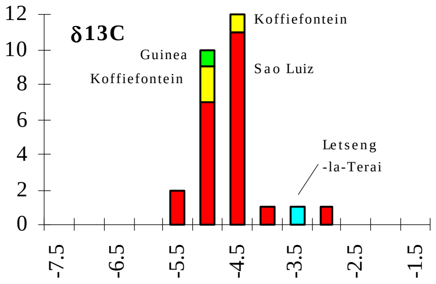

Figure 5.4_7 δ^{13}C composition of worldwide lower mantle sourced diamonds.

Koffiefontein data from Deines et al. (1991), Letseng-la-terai data from McDade and Harris (1997, personal communication), Guinea and São Luiz data from the present study plus Wilding (1990) and Boyd (1993, personal communication).

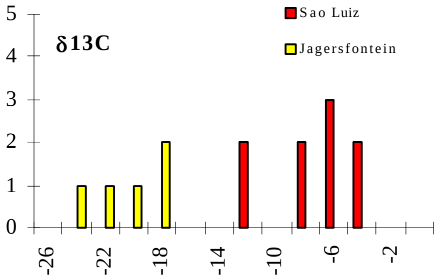

Figure 5.4_8 δ^{13}C composition of majoritic garnet association diamonds from worldwide sources.

Jagersfontein data from Deines et al. (1991), São Luiz data from the present study.

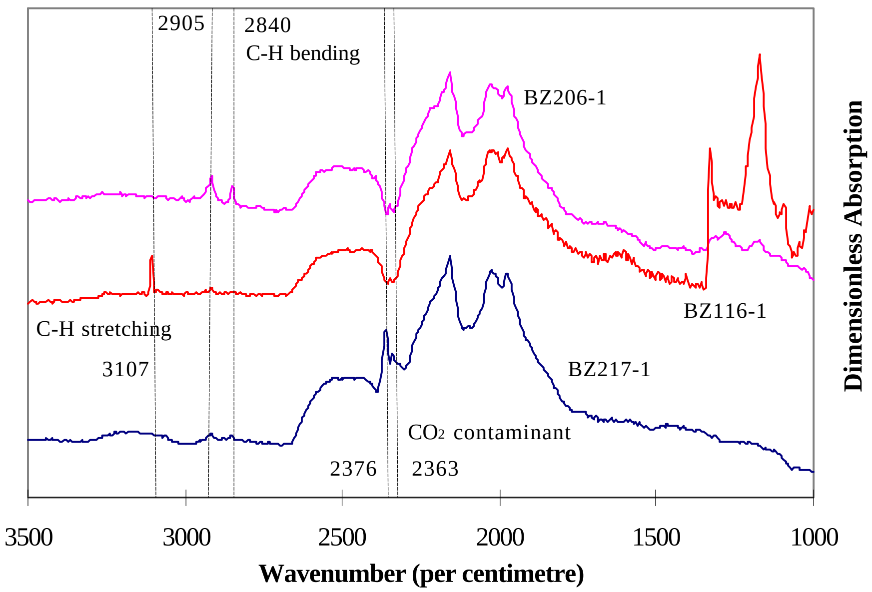

Figure 5.4_9 FTIR spectra showing typical diamond absorption due to lattice C, H and N in addition to atmospheric CO_2 contaminant evident on some FTIR spectra.

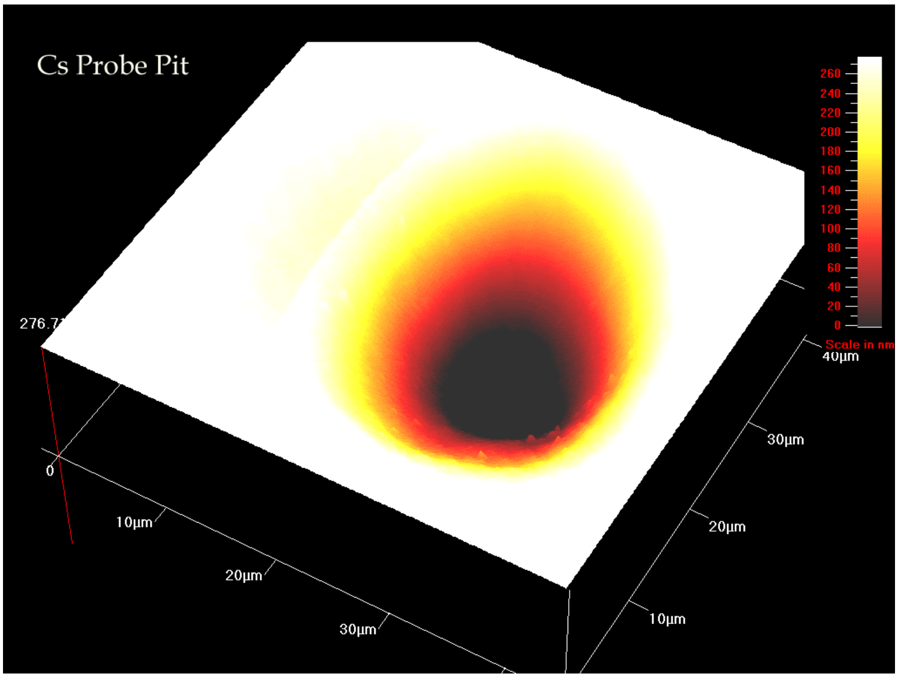

Figure 5.5_1 Cs$^+$ ion probe pit for the measurment of $\delta^{13}C$ on the surface of diamond BZ251.

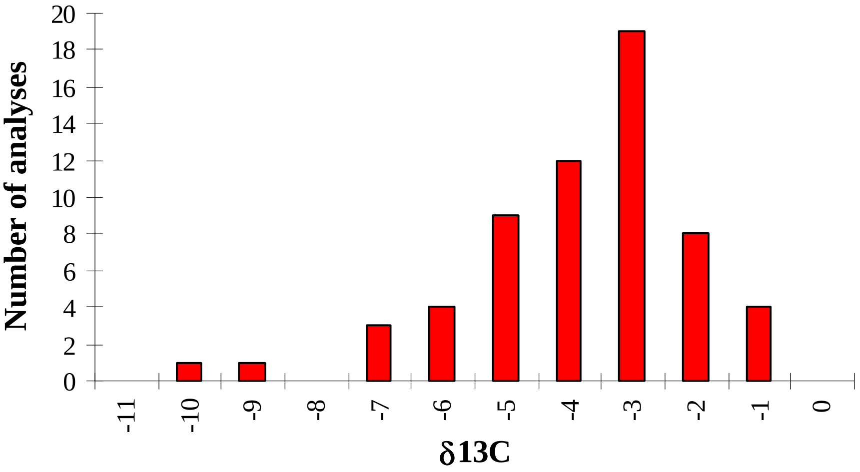

Figure 5.5_2 Distribution of δ^{13}C composition for four diamond 'flats', BZ251, BZ252, BZ245 and BZ255.

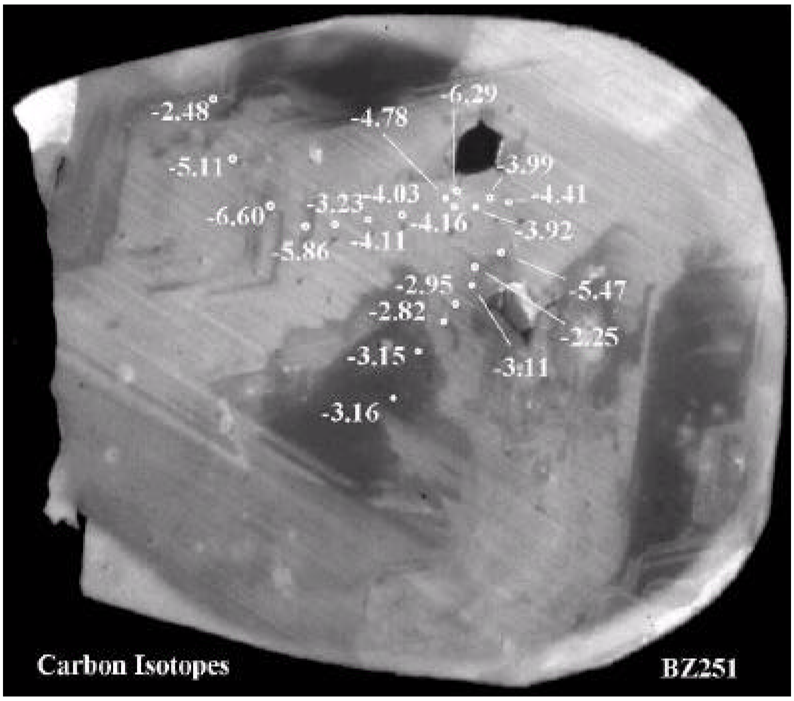

Figure 5.5_3 Distribution of δ^{13}C on diamond BZ251 showing CL features.

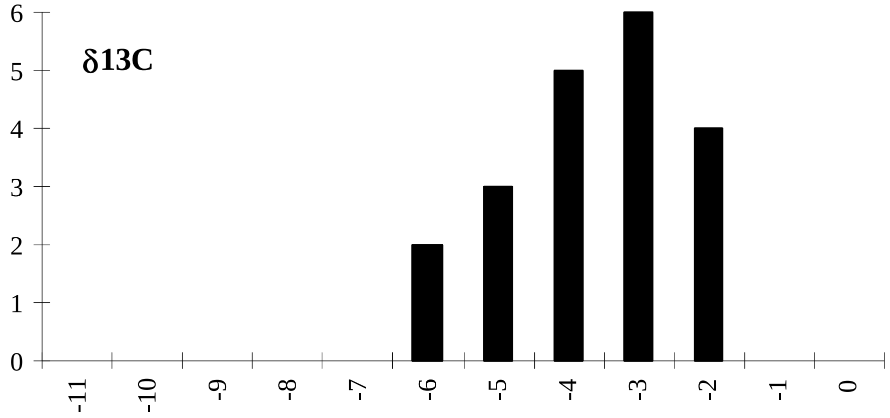

Figure 5.5_4 Histogram of $\delta^{13}C$ point analyses of diamond BZ251.

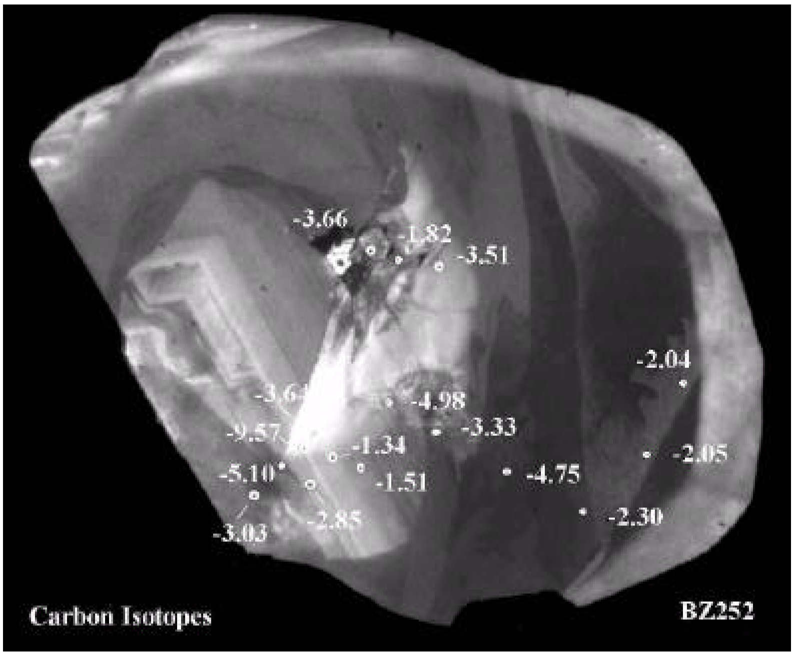

Figure 5.5_5 Distribution of $\delta^{13}C$ on diamond BZ252 showing CL features.

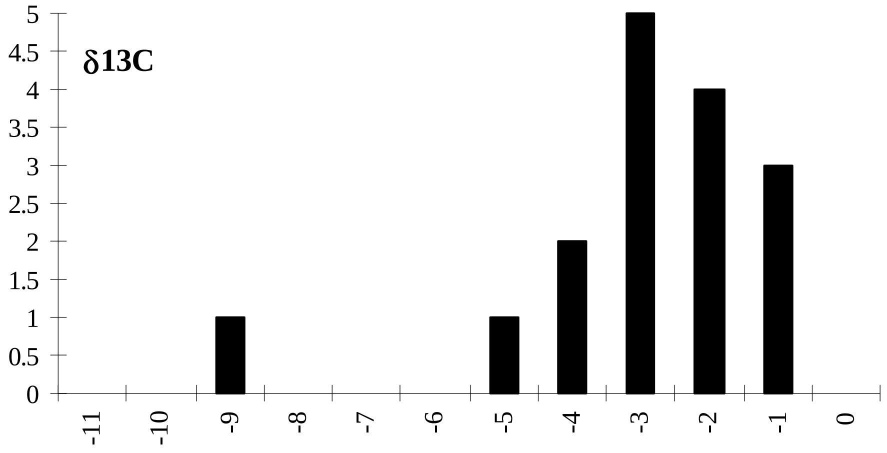

Figure 5.5_6 Histogram of $\delta^{13}C$ point analyses of diamond BZ252.

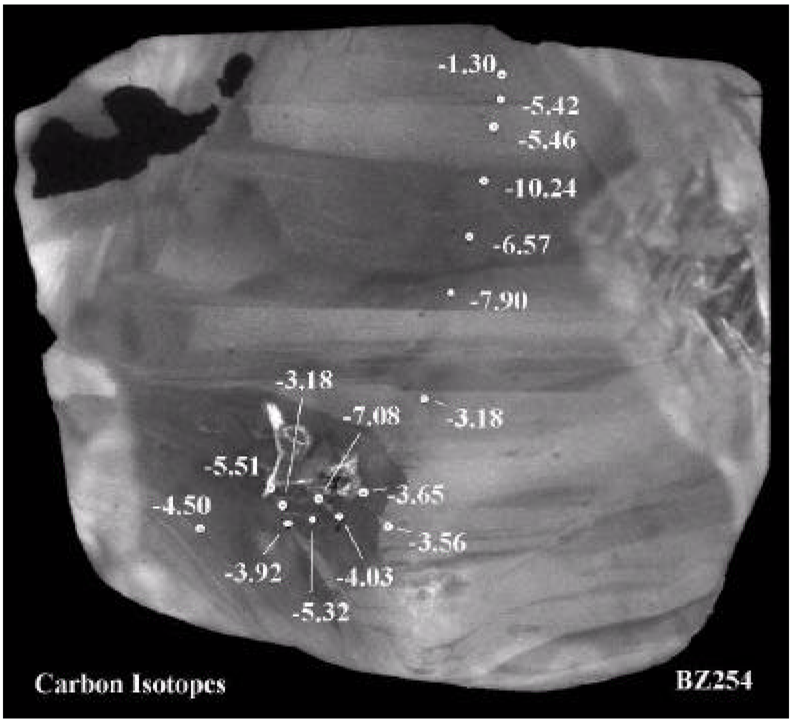

Figure 5.5_7 Distribution of $\delta^{13}C$ on diamond BZ254 showing CL features.

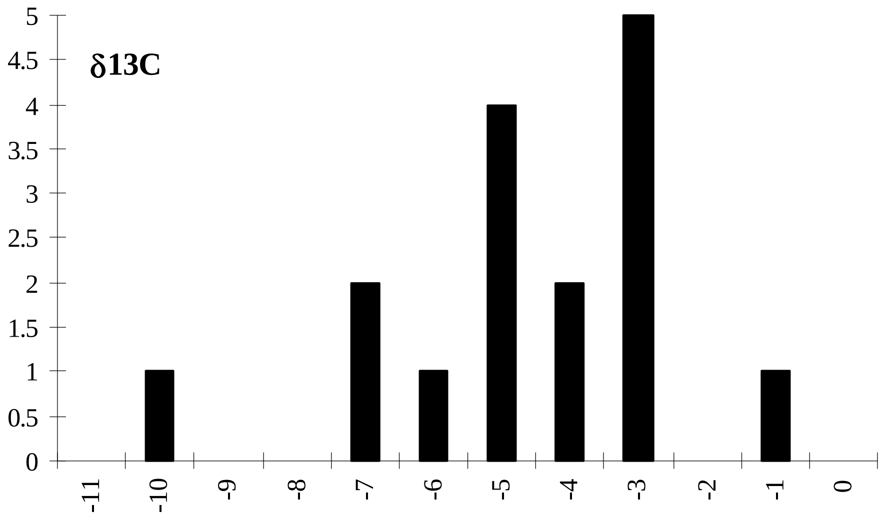

Figure 5.5_8 Histogram of $\delta^{13}C$ point analyses of diamond BZ254.

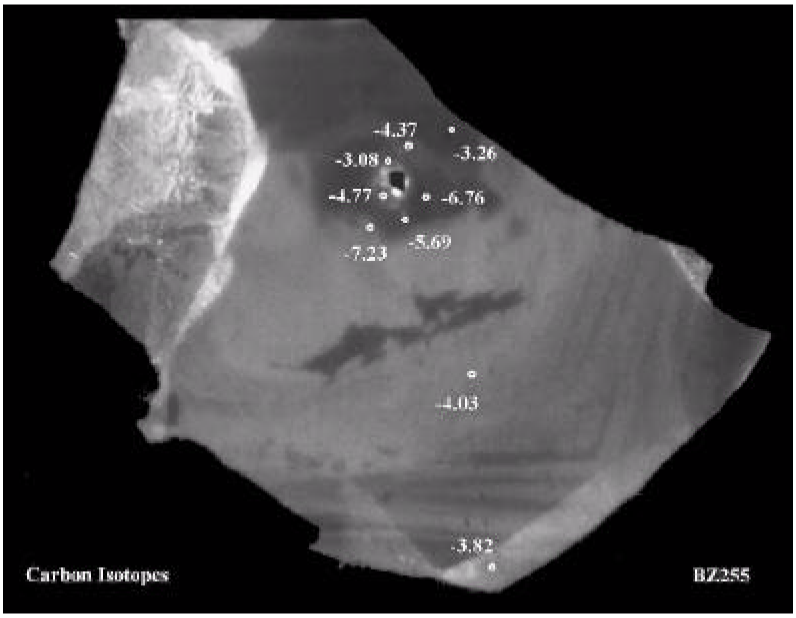

Figure 5.5_9 Distribution of $\delta^{13}C$ on diamond BZ255 showing CL features.

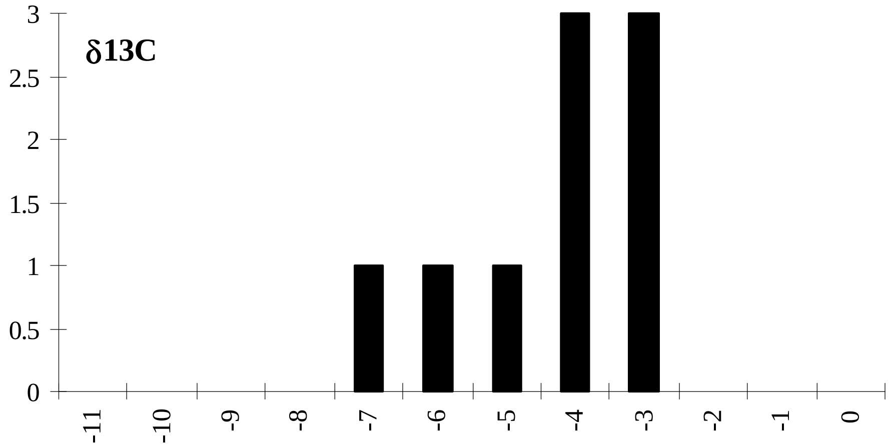

Figure 5.5_10 Histogram of δ^{13}C point analyses of diamond BZ255.

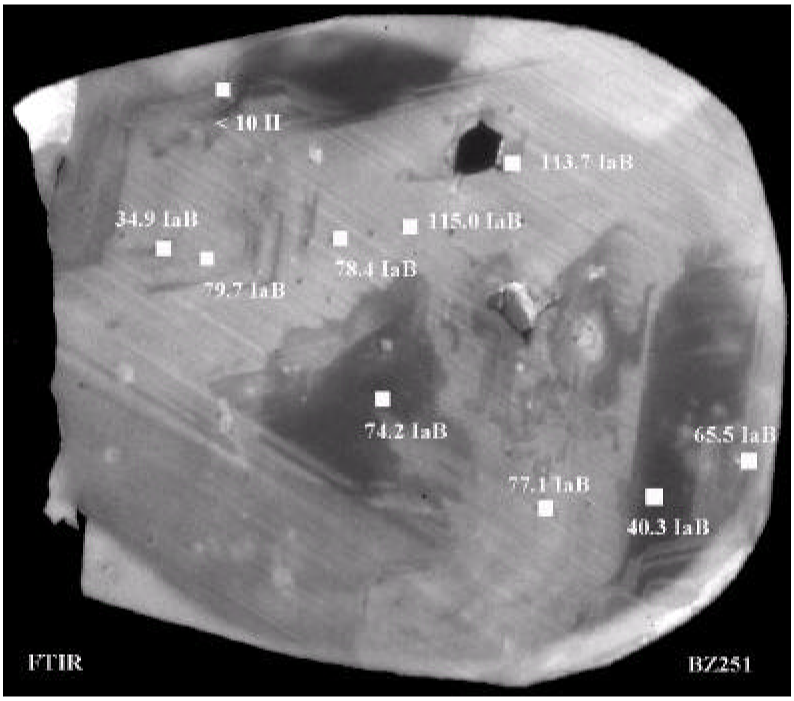

Figure 5.5_11 Concentration and aggregation of N obtained by FTIR on diamond ‘flat’ BZ251.

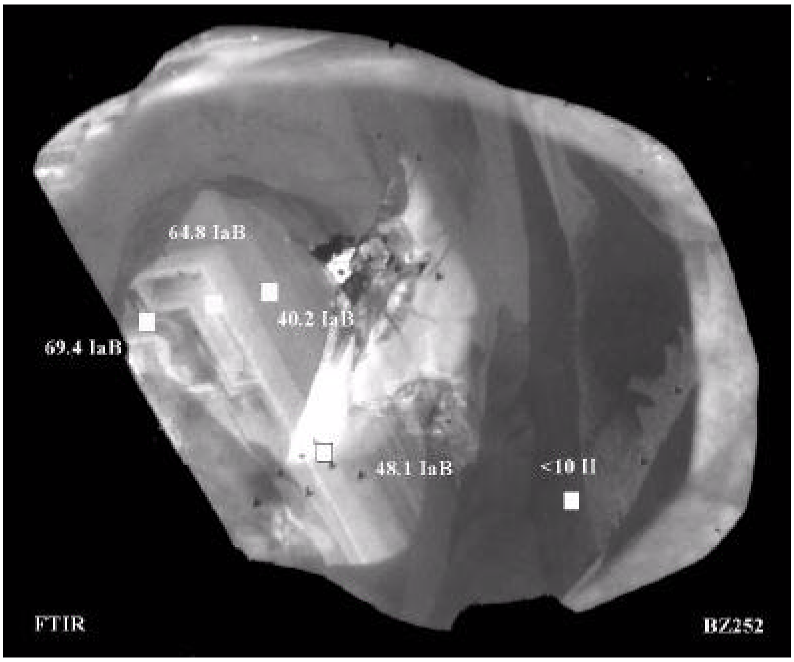

Figure 5.5_12 Concentration and aggregation of N obtained by FTIR on diamond 'flat' BZ252.

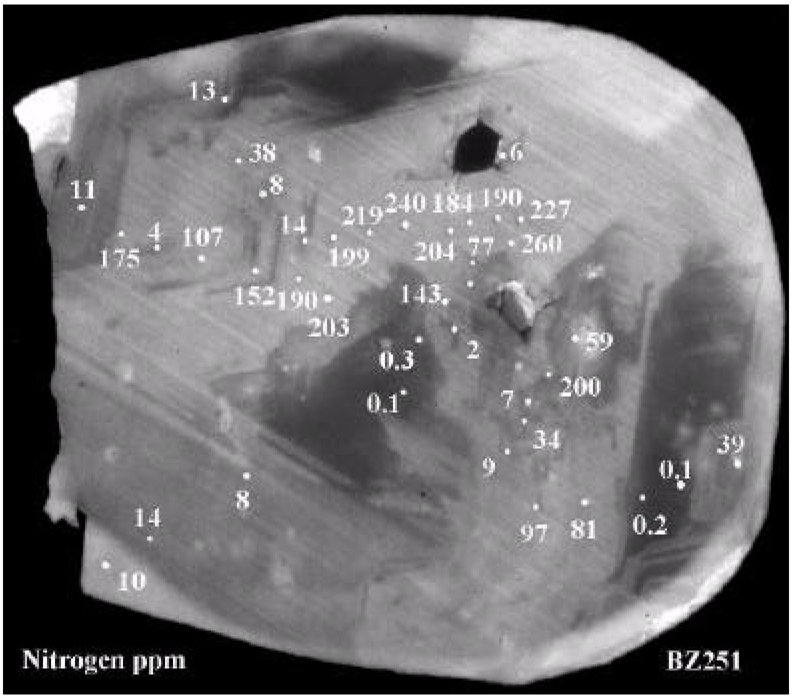

Figure 5.5_13 Concentration of nitrogen as determined by ion microprobe across BZ251.

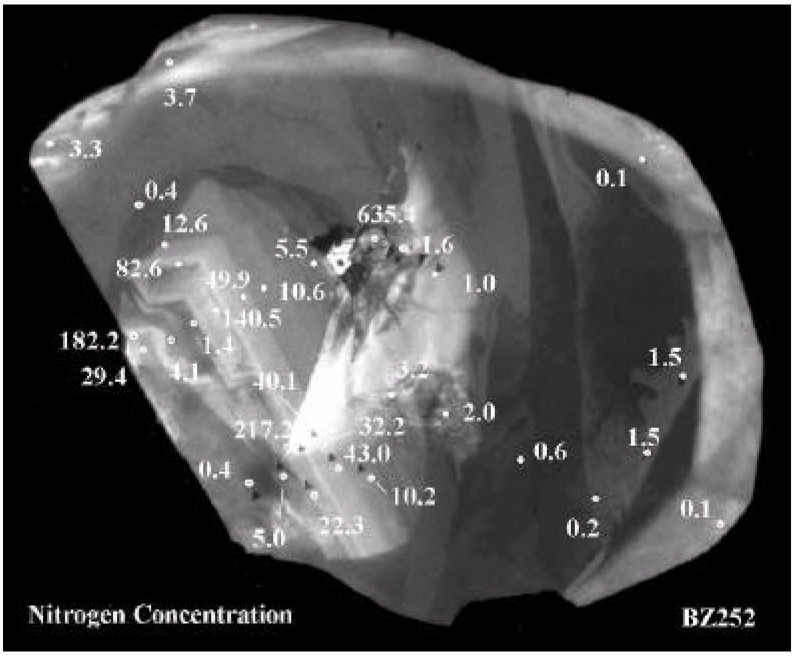

Figure 5.5_14 Concentration of nitrogen as determined by ion microprobe across BZ252.

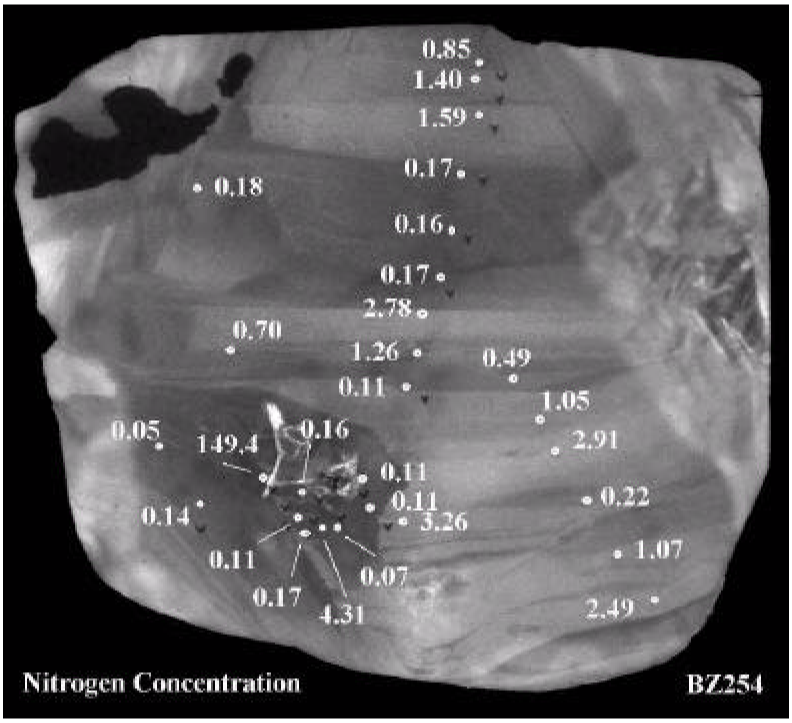

Figure 5.5_15 Concentration of nitrogen as determined by ion microprobe across BZ254.

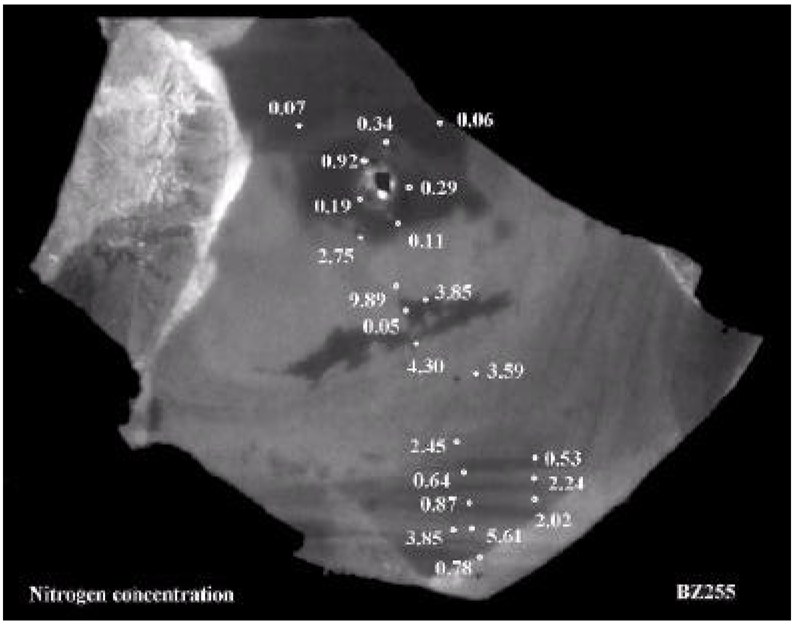

Figure 5.5_16 Concentration of nitrogen as determined by ion microprobe across BZ255.

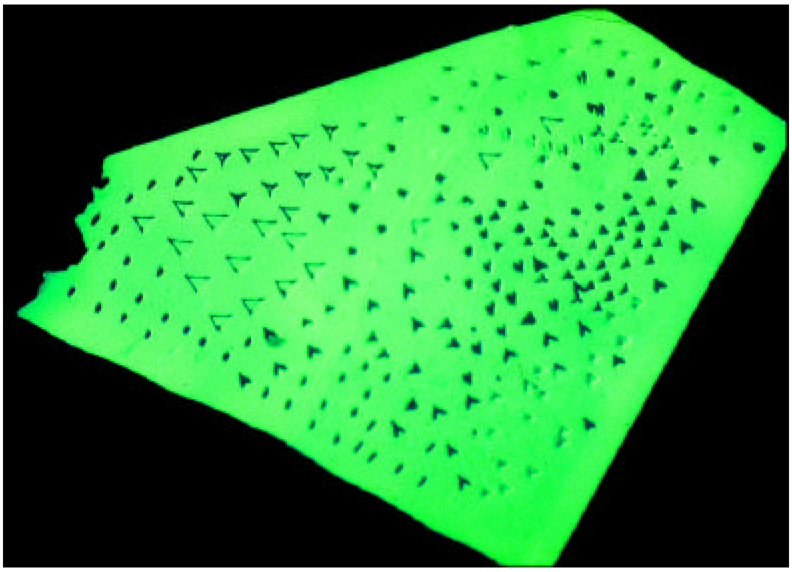

Figure 5.6_1 Green cathodoluminescence typical of synthetic diamond.

Fragment of synthetic stone, SYNAT, shows ion microprobe pits for $\delta^{13}C$ determination (ovals, ~30 μm across) and N concentration measurement (triangles).

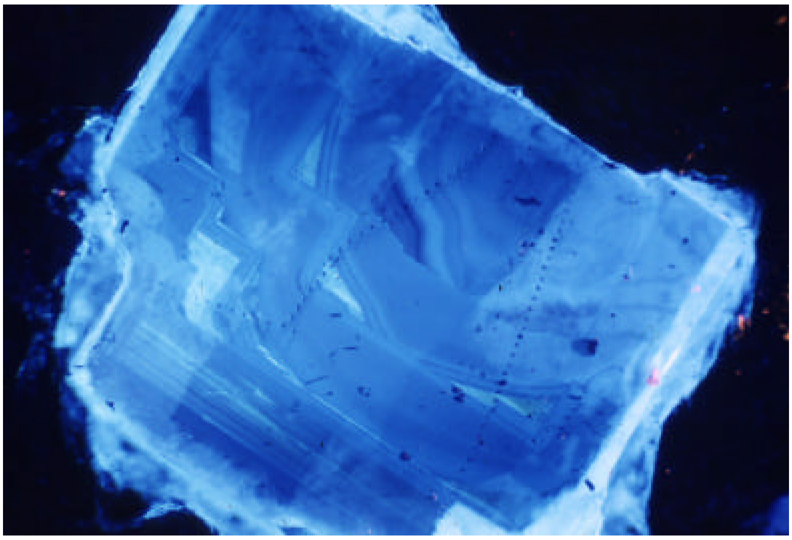

Figure 5.6_2 Cathodoluminescence image of Bultfontein stone 1064.2 showing concentric growth zonation and ion microprobe pits.

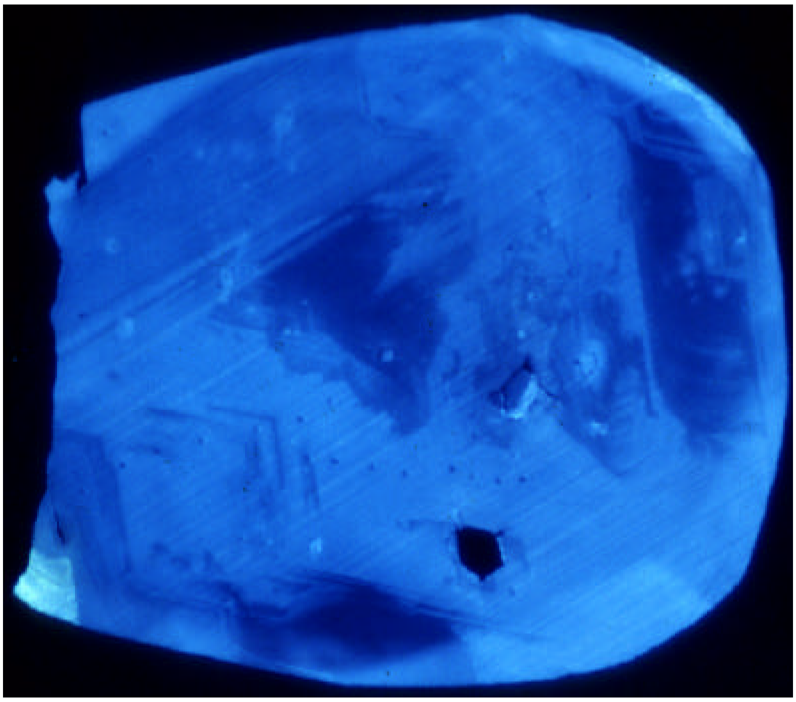

Figure 5.6_3 Cathodoluminescence image of BZ251 showing complex growth and resorption-related zonation.

Superimposed are parallel bands due to sample preparation and a band of light CL surrounding the stone is an artefact of internal reflection.

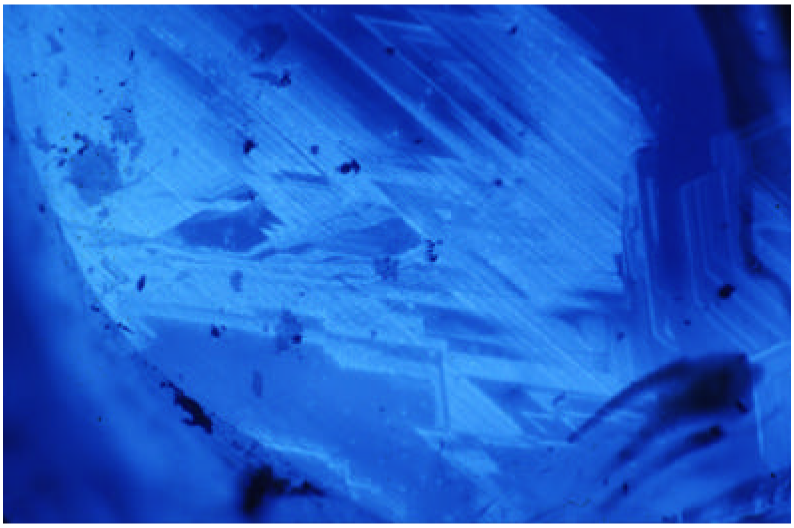

Figure 5.6_4 Cathodoluminescence close-up of 'zig-zag' patterns in BZ251 indicative of plastic deformation.

Figure 5.6_5 Cathodoluminescence of BZ252 showing a region of complex stepped growth.

The bright semi-circle across the inclusion is a result of internal reflection of an inclined fracture.

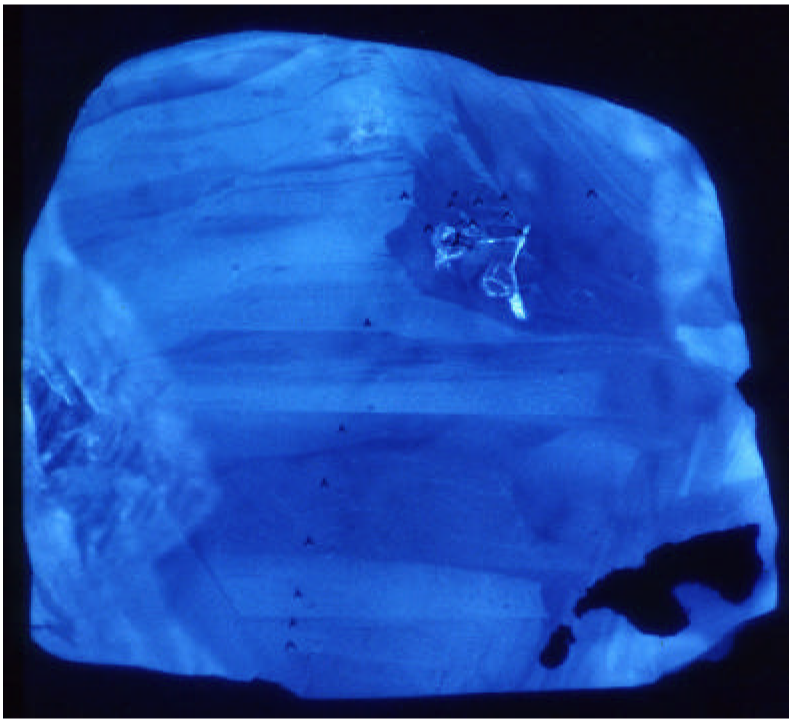

Figure 5.6_6 Cathodoluminescence of BZ254 showing an indistinct concentric zonation centred off the stone.

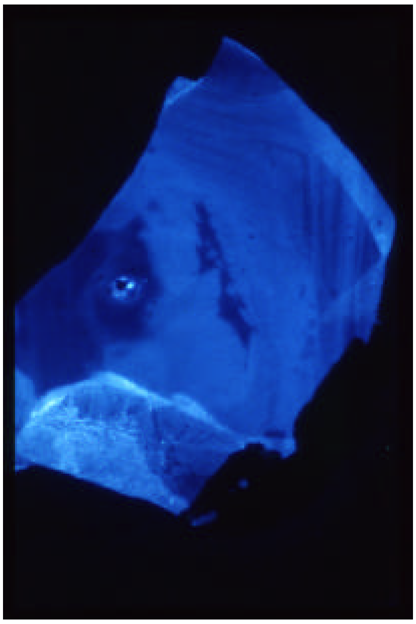

Figure 5.6_7 CL image of BZ255 showing inclusion-centred concentric zonation.

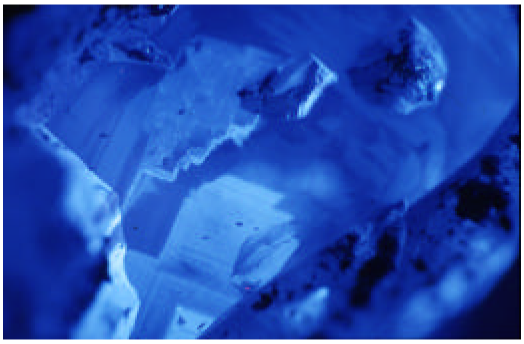

Figure 5.6_8 CL image of BZ253 showing complex zonation.

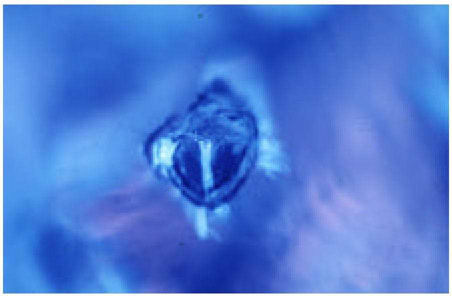

Figure 5.6_9 CL image of diamond surounding fPer inclusion BZ257A and associated fracture system.

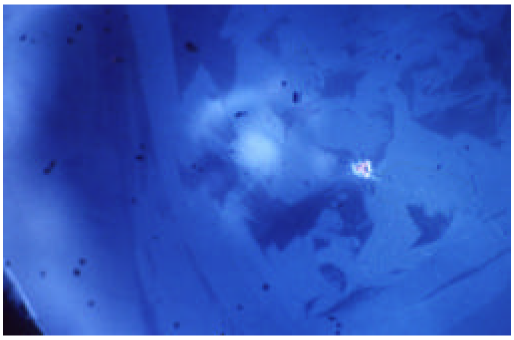

Figure 5.6_10 CL image of BZ258 with inclusions and dark 'flecks' evident.

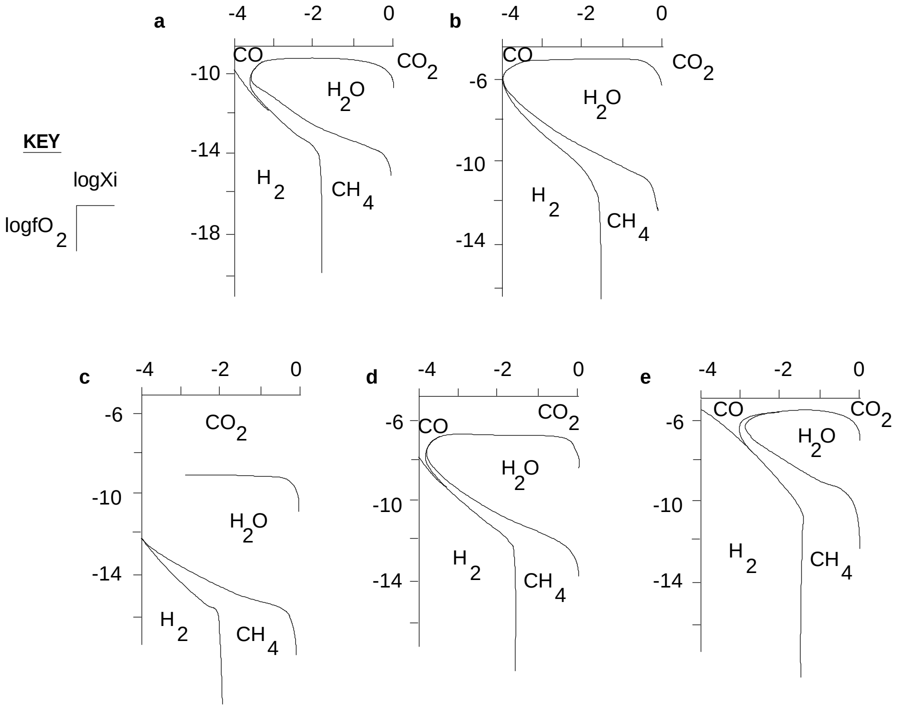

Figure 6.1_1 Phase relations in the C-O-H system saturated with elemental carbon in terms of oxygen fugacity and under varying conditions of pressure and temperature relevent to the mantle lithsophere.

From Deines (1980). a - 1173K 3.5 GPa, b - 1373K 5.5 GPa, c - 1073K 4.5 GPa, d - 1273K 4.5 GPa, e - 1473K 4.5 GPa. By far the most dominant fluid species to coexist with diamond are CH_4, CO_2 and H_2O.

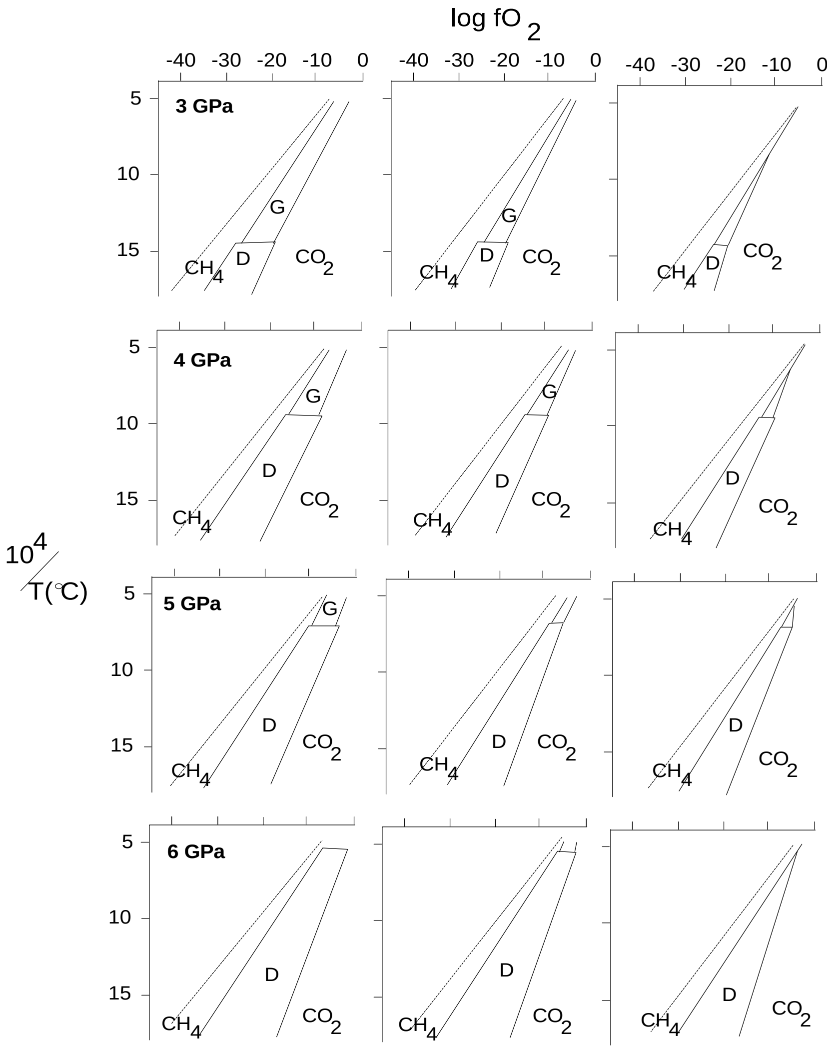

Figure 6.1_2 The stability of elemental carbon in the C-O-H system in terms of XH_2O, temperature and pressure.

From Deines (1980). First column, 10 mol% H_2O content in vapour, second column, 50 mol% H_2O in vapour, third column, 90 mol% H_2O in vapour. With increasing pressure and temperature, the stability field of diamond is seen to move to more oxidised conditions in preference to CH_4 and at the expense of CO_2. Although the errors in extrapolating such observations to conditions of the lower mantle are likely to be very large, and the influence of additional components is not known, it is interesting to note the consistency between this observation and the fact that significant Fe^{3+} content in magnesioferrite in fPer inclusions, is indicative of diamond stability in the lower mantle within relatively oxidised conditions.

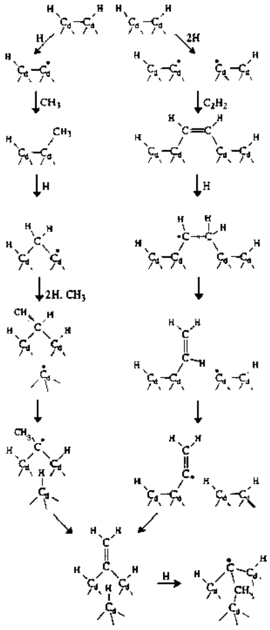

Figure 6.1_3 Surface reactions for the hydrogen catalysed growth of diamond.

From Frenklaech et al. (1994). The high concentration of free radicals in CVD diamond growth for which the mechanism is proposed is not a geologically viable scenario. Similar mechanisms may occur, however, in nature over longer timescales and may explain the presence of H and N within the lattice of natural stones such as São Luiz. Where diamond growth is relatively rapid, catalytic species will be expected to be unable to escape the growth environment and be entrapped and ultimately combined as lattice components.

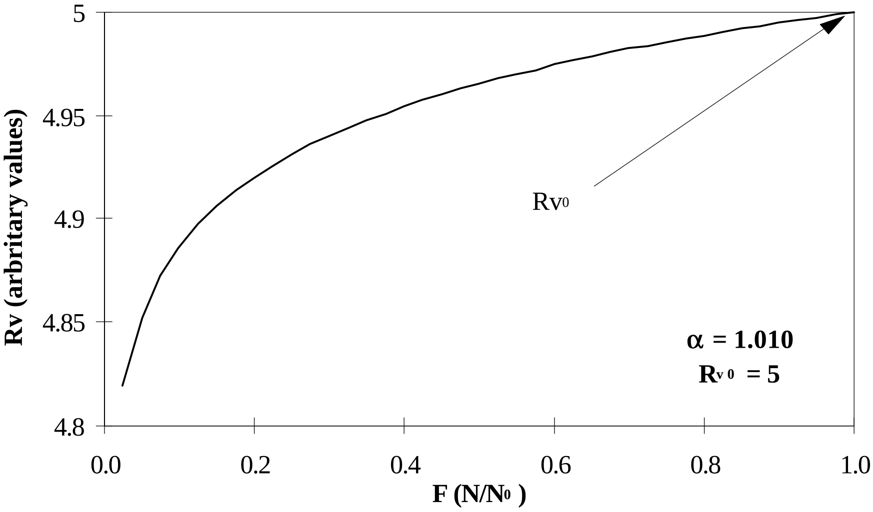

Figure 6.3_1 The effect on composition of fractionation in a system of growth following Rayleigh condensation.

Constructed following equation 6.3_1 where where R_v and R_{v0} are the isotopic ratios in the source and residue respectively, F is the degree of fractionation, and α is the fractionation factor constant. Initial isotopic composition R_{v0} is taken to be equal to 5 for the purposes of demonstration.

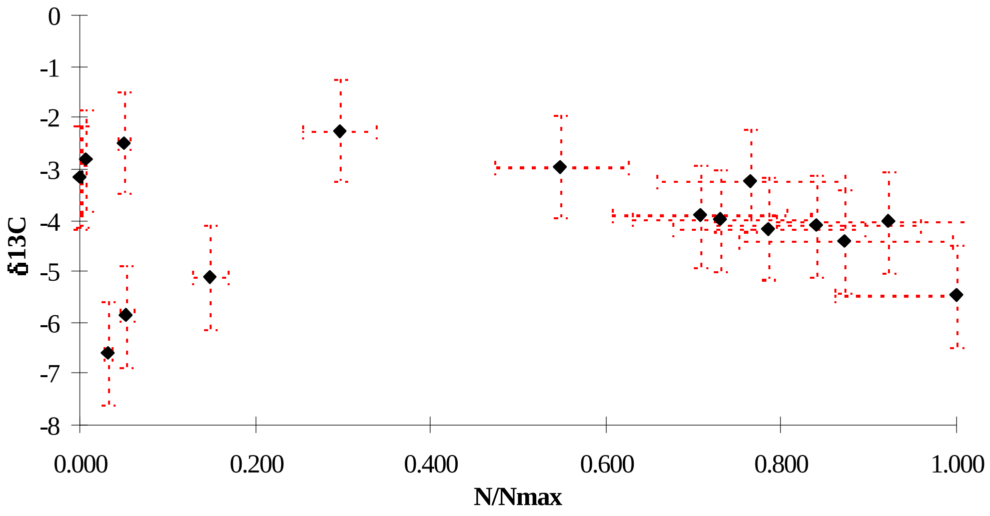

Figure 6.3_2 Investigation of the likelihood of precipitation of diamond BZ251 via Rayleigh condensation by $\delta^{13}C$ composition against fractionation as (N/N_{max}).

The wide scatter in the data shows no similarity with the distribution expected for Rayleigh condensation (as presented in figure 6.3_1). If anything, the trend shows a break in slope at mid-nitrogen concentration suggestive of a change in growth style. Error bars for $\delta^{13}C$ are based on an average value of +/- 1 ‰ at 1σ for $\delta^{13}C$ and for N/N_{max} of 14% (combination of a 10% error on each analysis).

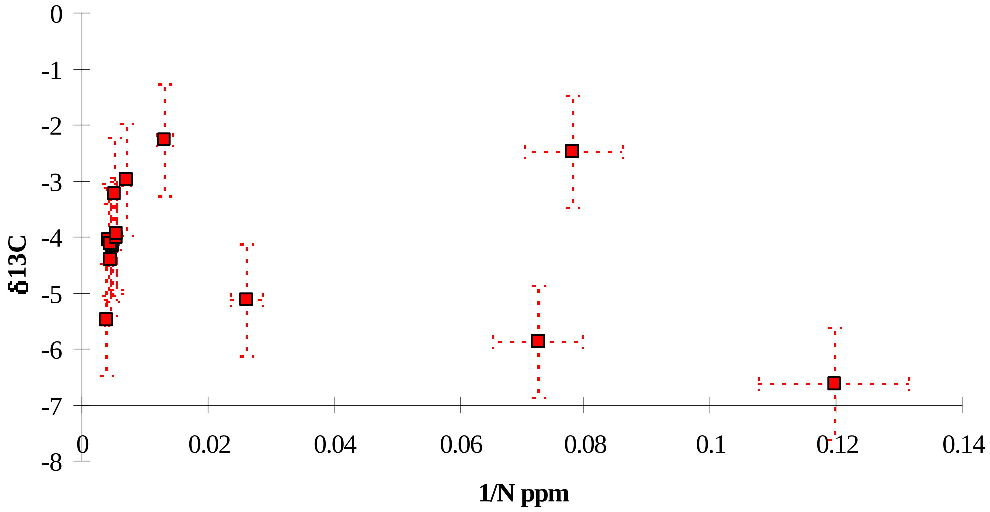

Figure 6.3_3 Investigation of the likelihood of precipitation of diamond BZ251 from two-component mixing by δ^{13}C composition against 1/N.

Even on omission of low N data (as for this graph), no linear trend is seen as would be expected for simple two component mixing. Error bars for δ^{13}C are based on an average value of +/- 1 ‰ at 1σ for δ^{13}C and for N/N_{max} of 10%.

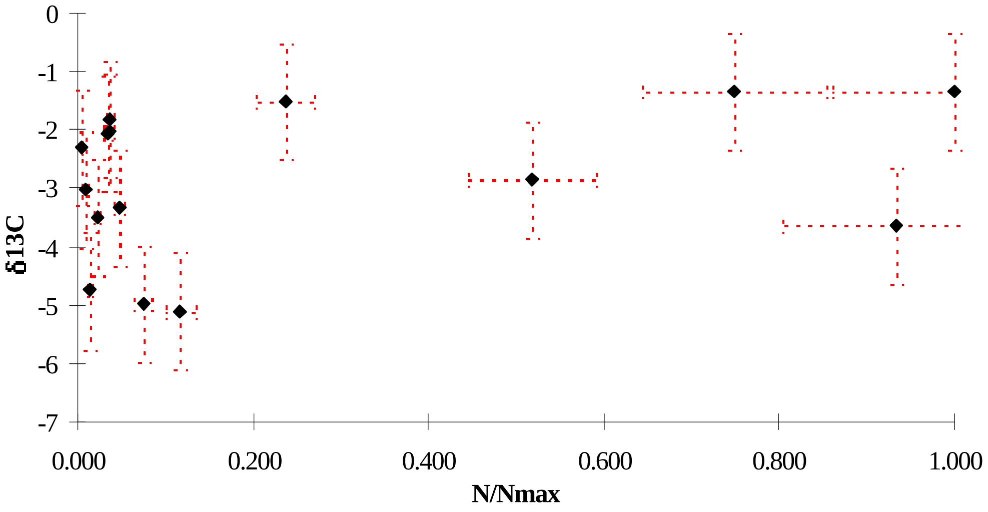

Figure 6.3_4 Investigation of the likelihood of precipitation of diamond BZ252 via Rayleigh condensation by $\delta^{13}C$ composition against fractionation as (N/N_{max}).

Even with the omission of the single spurious nitrogen value of 635 ppm, the wide scatter in the data shows no similarity with the distribution expected for Rayleigh condensation (as presented in figure 6.3_1). Low $\delta^{13}C$ compositions do, very crudely, occur in regions of low nitrogen. Error bars for $\delta^{13}C$ are based on an average value of +/- 1 ‰ at 1σ for $\delta^{13}C$ and for N/N_{max} of 14% (combination of a 10% error on each analysis).

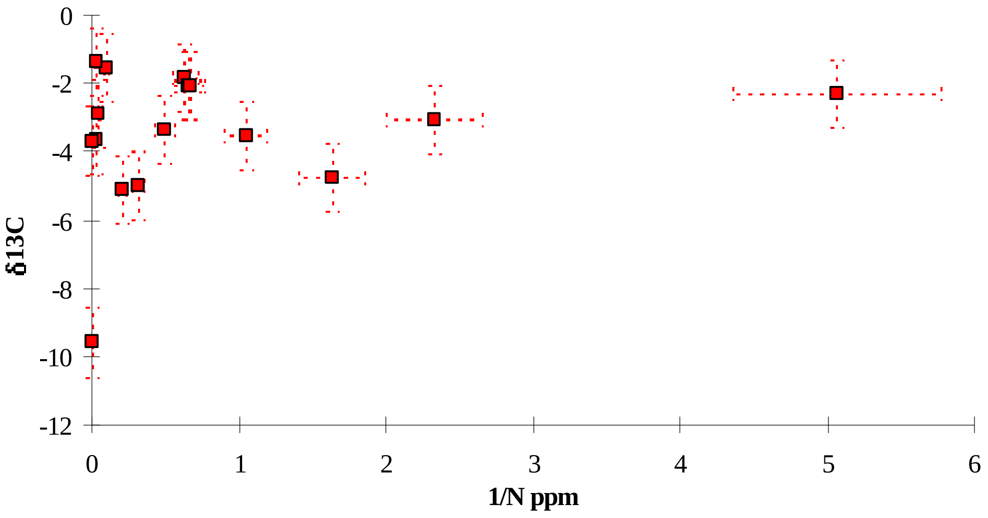

Figure 6.3_5 Investigation of the likelihood of precipitation of diamond BZ252 from two-component mixing by $\delta^{13}C$ composition against 1/N.

No linear trend is seen as would be expected for simple two component mixing. Error bars for $\delta^{13}C$ are based on an average value of +/- 1 ‰ at 1σ for $\delta^{13}C$ and for N/N_{max} of 10%.

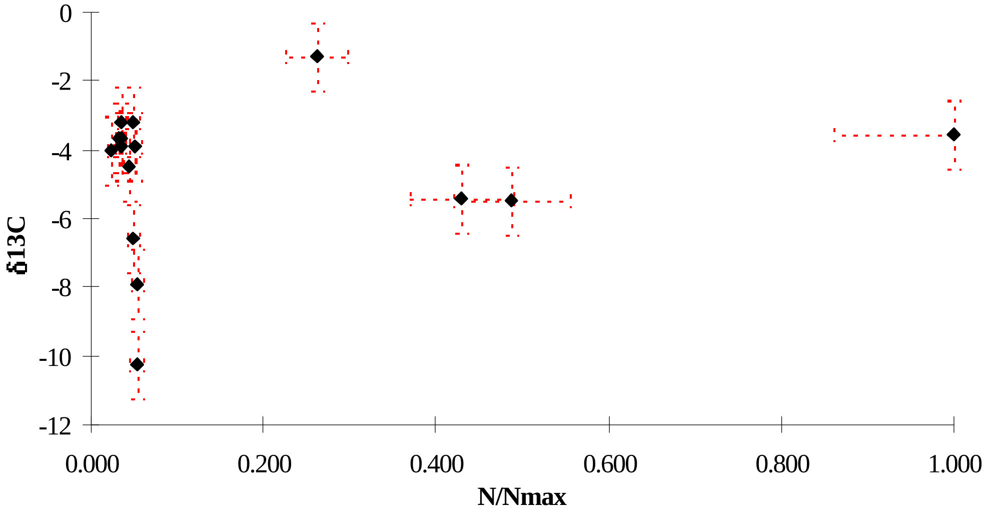

Figure 6.3_6 Investigation of the likelihood of precipitation of diamond BZ254 via Rayleigh condensation by $\delta^{13}C$ composition against fractionation as (N/N_{max}).

Despite the omission of the high nitrogen value of 149.4 ppm obtained within a fracture, the wide scatter in the data shows only a similarity with the distribution expected for Rayleigh condensation (as presented in figure 6.3_1) to the extent that depleted $\delta^{13}C$ occurs in areas of low nitrogen. Error bars for $\delta^{13}C$ are based on an average value of +/- 1 ‰ at 1σ for $\delta^{13}C$ and for N/N_{max} of 14% (combination of a 10% error on each analysis).

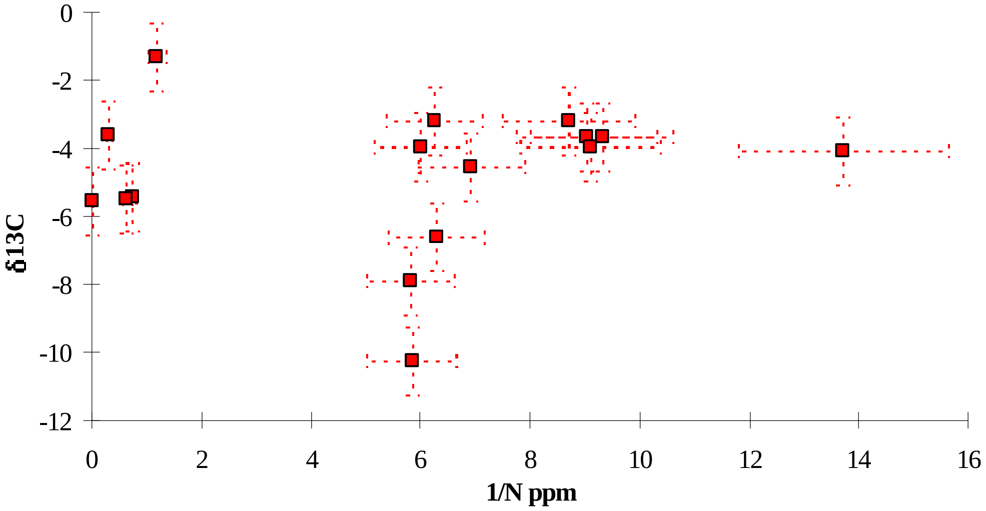

Figure 6.3_7 Investigation of the likelihood of precipitation of diamond BZ254 from two-component mixing by $\delta^{13}C$ composition against 1/N.

No linear trend is seen as would be expected for simple two component mixing. Error bars for $\delta^{13}C$ are based on an average value of +/- 1 ‰ at 1σ for $\delta^{13}C$ and for N/N_{max} of 10%.

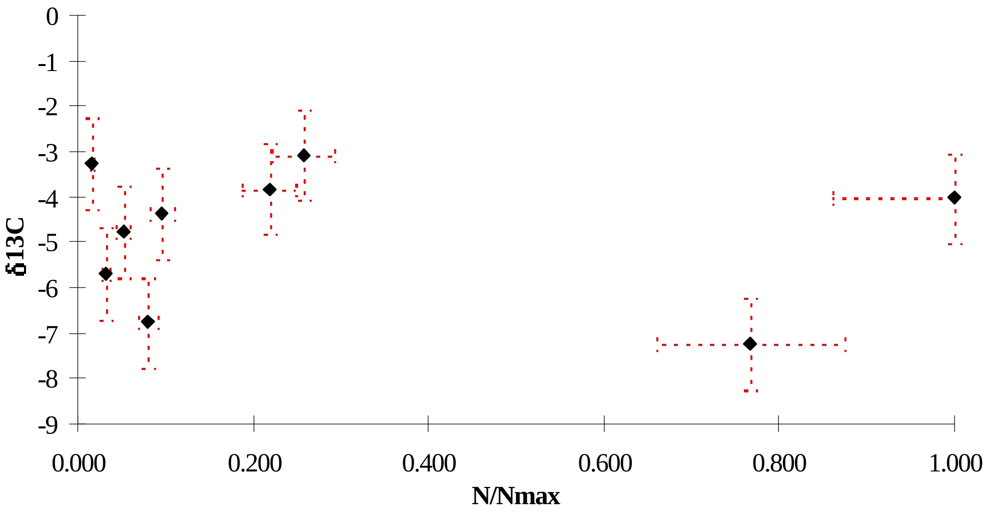

Figure 6.3_8 Investigation of the likelihood of precipitation of diamond BZ255 via Rayleigh condensation by $\delta^{13}C$ composition against fractionation as (N/N_{max}).

The wide scatter in the data shows no similarity with the distribution expected for Rayleigh condensation (as presented in figure 6.3_1). Error bars for $\delta^{13}C$ are based on an average value of +/- 1 ‰ at 1σ for $\delta^{13}C$ and for N/N_{max} of 14% (combination of a 10% error on each analysis).

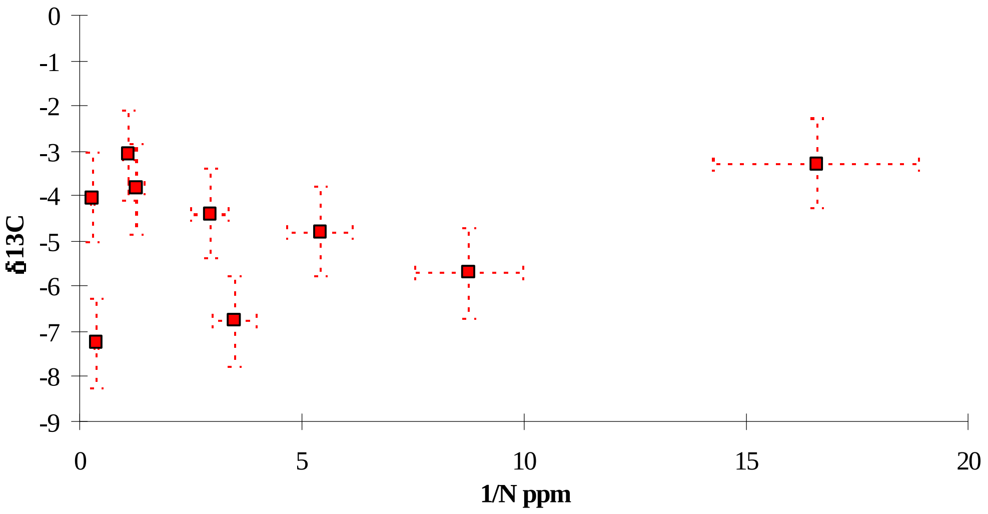

Figure 6.3_9 Investigation of the likelihood of precipitation of diamond BZ255 from two-component mixing by δ^{13}C composition against 1/N.

No linear trend is seen as would be expected for simple two component mixing. Error bars for δ^{13}C are based on an average value of +/- 1 ‰ at 1σ for δ^{13}C and for N/N_{max} of 10%.

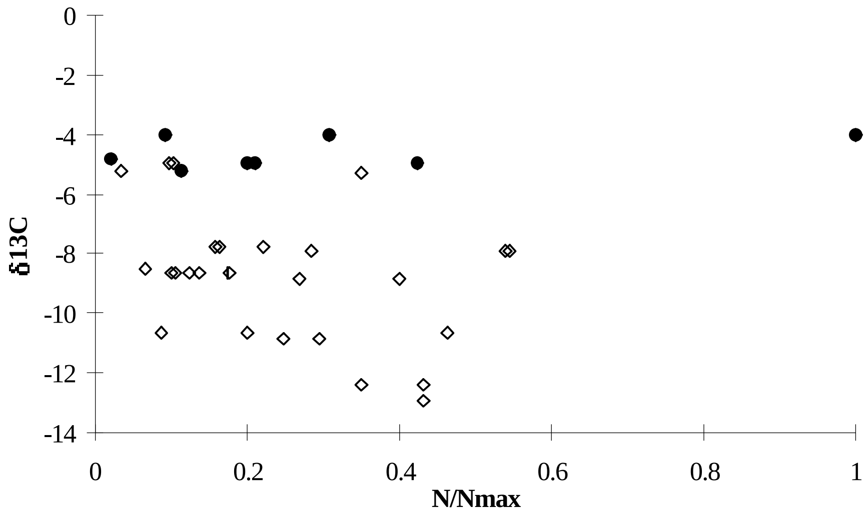

Figure 6.3_10 Investigation of the likelihood of precipitation of lower mantle and upper mantle diamond suites via Rayleigh condensation by $\delta^{13}C$ composition against fractionation as (N/N_{max}).

The whole data set of bulk analyses are combined in terms of upper mantle and lower mantle sourced stones. Black circles - lower mantle stones, open diamonds - upper mantle stones. As for single diamonds, the wide scatter in the data shows no similarity with the distribution expected for Rayleigh condensation (as presented in figure 6.3_1).

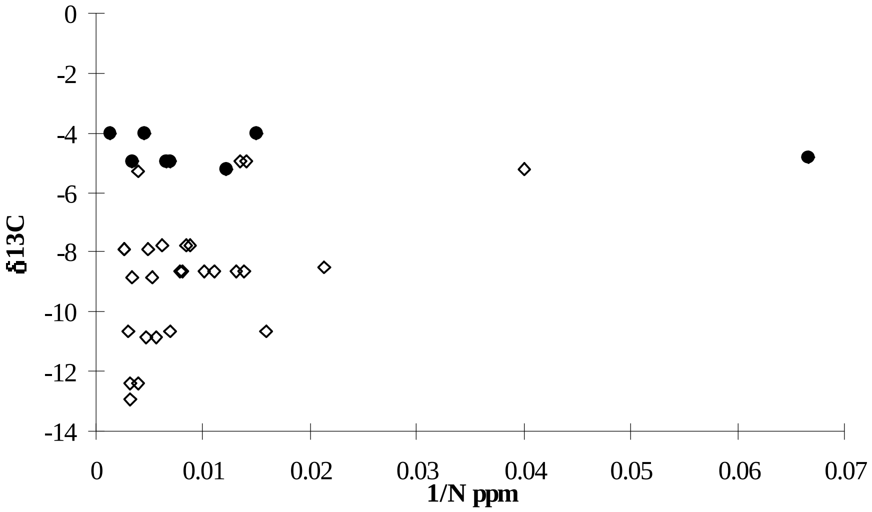

Figure 6.3_11 Investigation of the likelihood of precipitation of lower mantle and upper mantle suites from two-component mixing by $\delta^{13}C$ composition against 1/N.

The whole data set of bulk analyses are combined in terms of upper mantle and lower mantle sourced stones. Black circles - lower mantle stones, open diamonds - upper mantle stones. As for single diamonds, no linear trend is seen as would be expected for simple two component mixing.

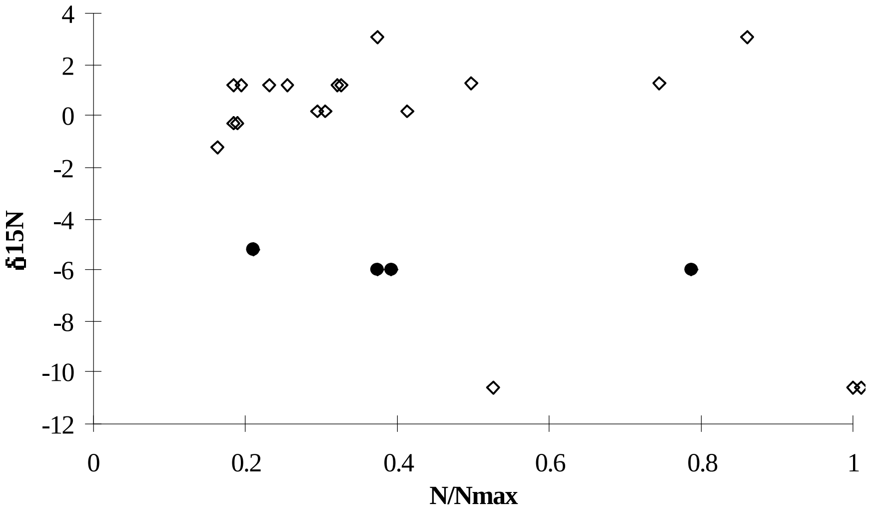

Figure 6.3_12 Investigation of the likelihood of precipitation of lower mantle and upper mantle diamond suites via Rayleigh condensation by $\delta^{15}N$ composition against fractionation as (N/N_{max}).

The whole data set of bulk analyses are combined in terms of upper mantle and lower mantle sourced stones. Black circles - lower mantle stones, open diamonds - upper mantle stones. The three lower mantle points lying at $\delta^{15}N$ = -6‰ are for three determinations of nitrogen content for fragments of BZ237. As for $\delta^{13}C$ analysis, the wide scatter in the data shows no similarity with the distribution expected for Rayleigh condensation (as presented in figure 6.3_1).

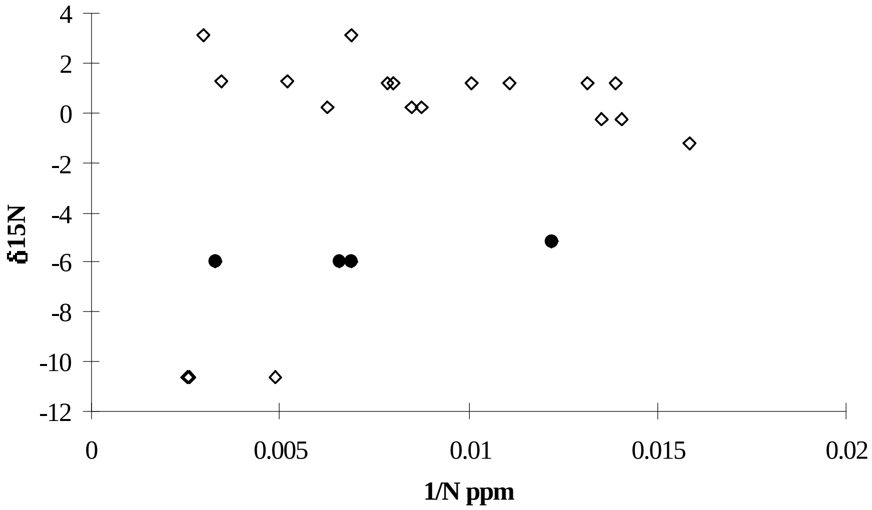

Figure 6.3_13 Investigation of the likelihood of precipitation of lower mantle and upper mantle suites from two-component mixing by δ^{15}N composition against 1/N.

The whole data set of bulk analyses are combined in terms of upper mantle and lower mantle sourced stones. Black circles - lower mantle stones, open diamonds - upper mantle stones. The three lower mantle points lying at δ^{15}N = -6‰ are for three determinations of nitrogen content for fragments of BZ237. As for δ^{13}C analysis, no linear trend is seen as would be expected for simple two component mixing.

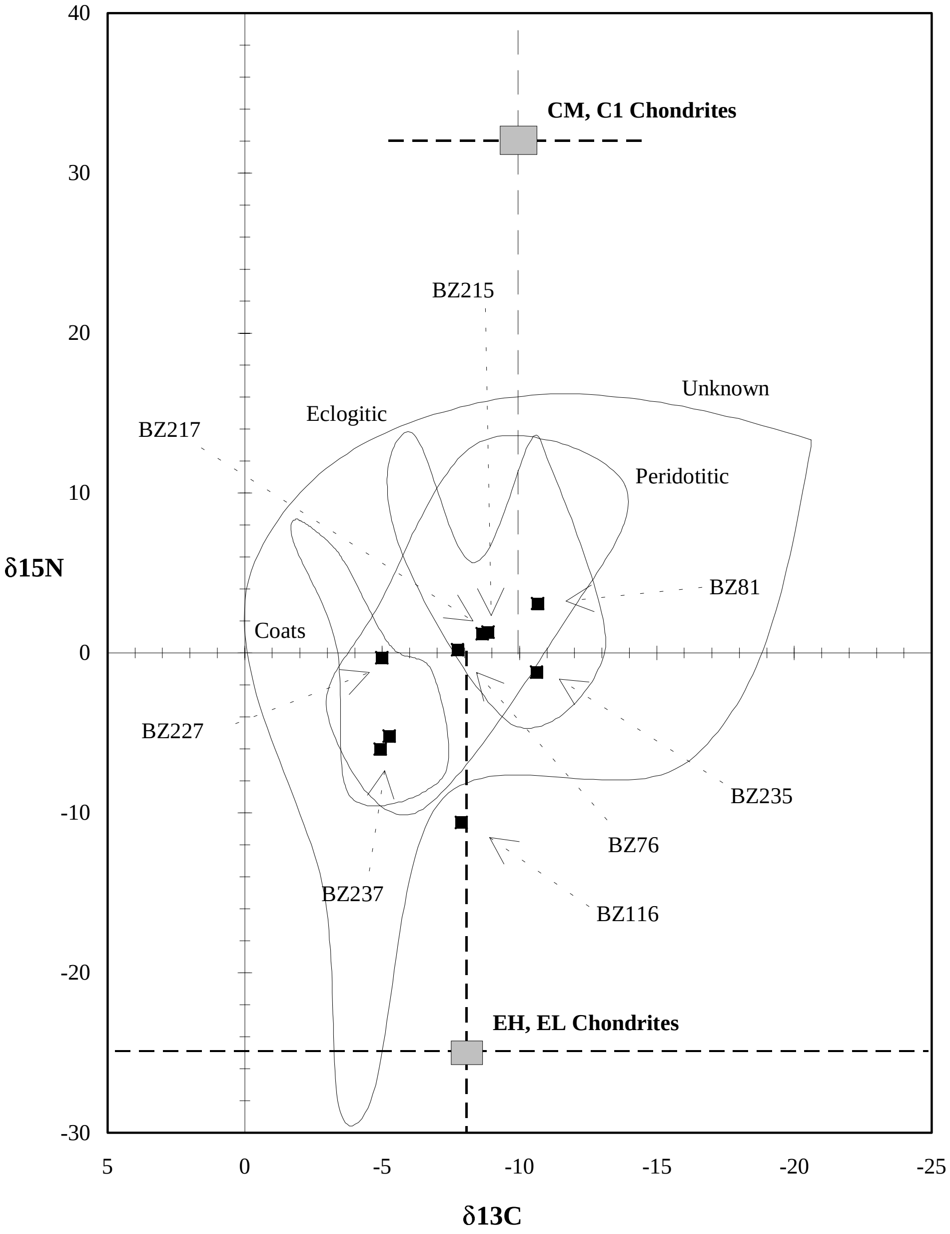

Figure 6.3_14 The distribution of δ^{13}C composition against δ^{15}N composition of São Luiz diamonds in comparison with fields of diamond composition from other sources and ranges of enstatite and carbonaceous chondrites.

Although only based on two data points from a single diamond believed to have formed close to the upper mantle / lower mantle boundary, it is worthy of note that BZ237 indicates a negative δ^{15}N composition with δ^{13}C of -5 ‰ for the lower mantle. This compsition lies outwith the compositional range of carbonaceous chondrites but within the range of enstatite chondrites proposed by Javoy (1995) as a suitable lower mantle protolith.

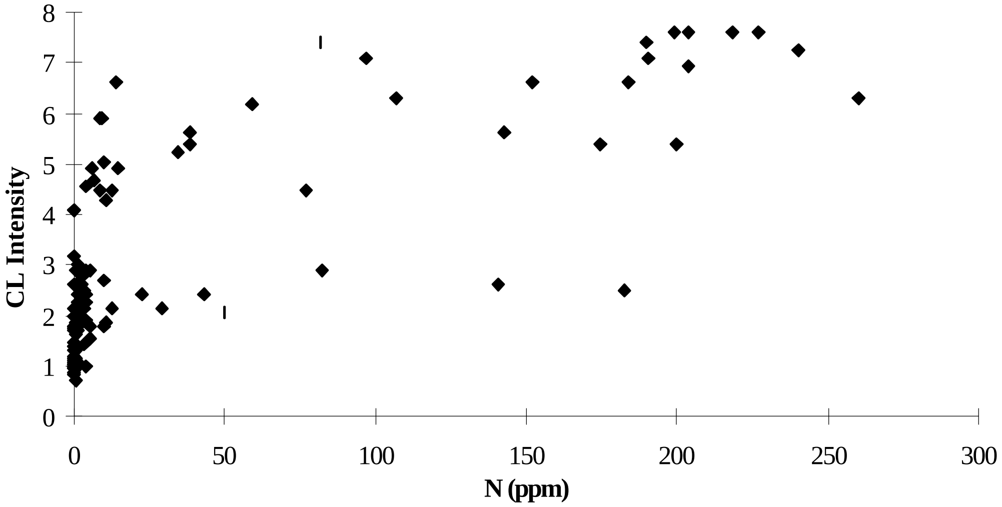

Figure 6.3_15 Variation of cathodoluminescence intensity against nitrogen concentration for all diamond flats.

A general trend of increasing cathodoluminescence intensity with increasing nitrogen content is observed.

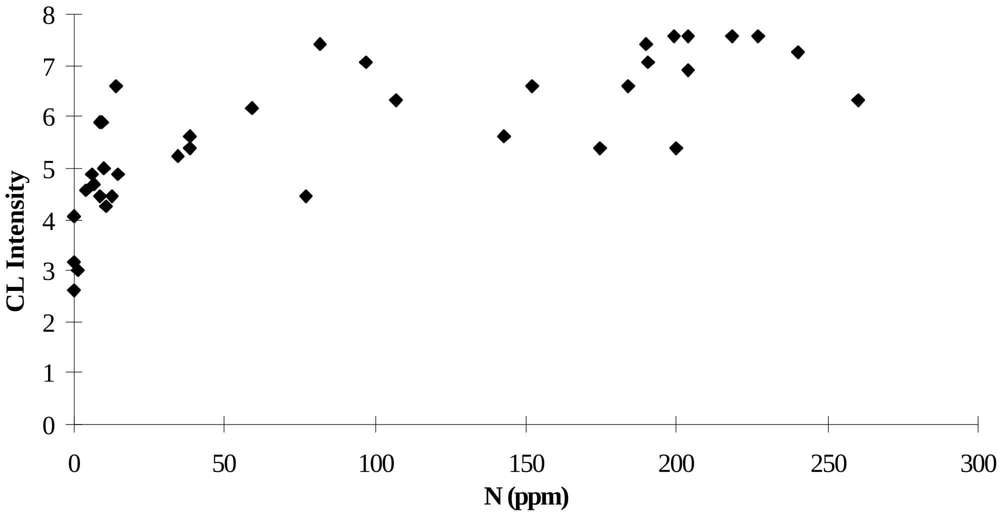

Figure 6.3_16 Variation of cathodoluminescence intensity against nitrogen concentration for BZ251.

A general trend of increasing cathodoluminescence intensity with increasing nitrogen content is observed.

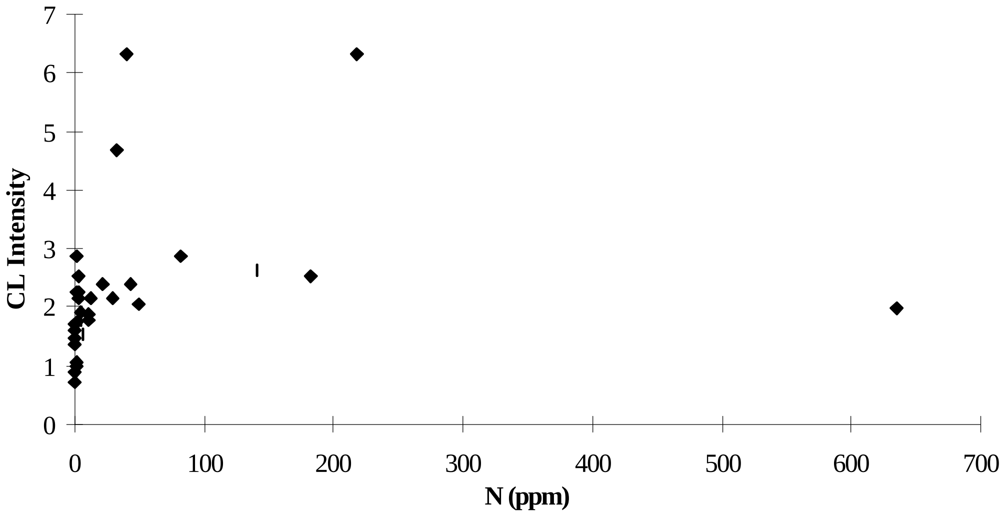

Figure 6.3_17 Variation of cathodoluminescence intensity against nitrogen concentration for BZ252.

On ignoring three particulary high values for CL intensity (from internal relection from fractures) and the single point of unusually high N concentration, it would appear that there is a correlation. CL intensity appears to increase rapidly with nitrogen concentraiton for low nitrogen values, subsequently flattening off to a weaker dependence on concentration.

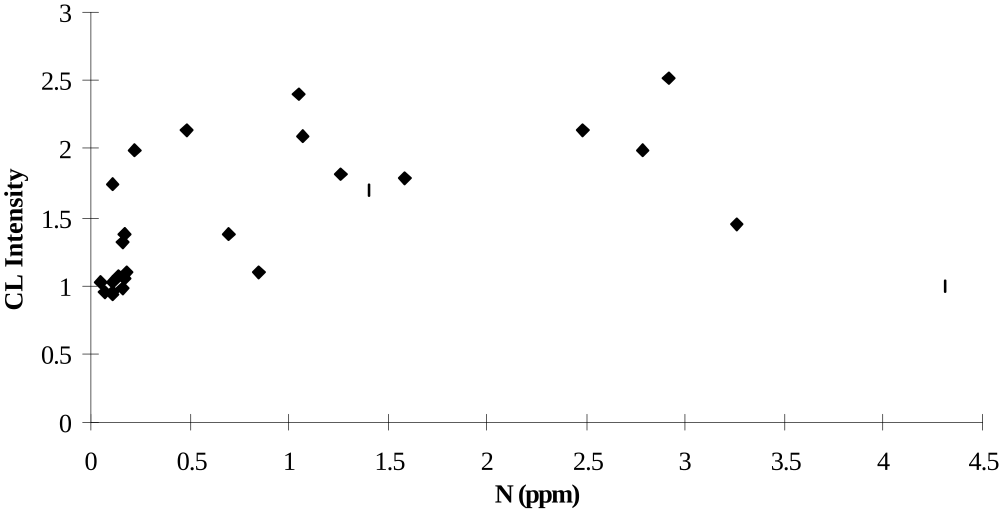

Figure 6.3_18 Variation of cathodoluminescence intensity against nitrogen concentration for BZ254.

CL intensity appears to increase rapidly with nitrogen concentration for low nitrogen values, subsequently flattening off to a weaker dependence on concentration.

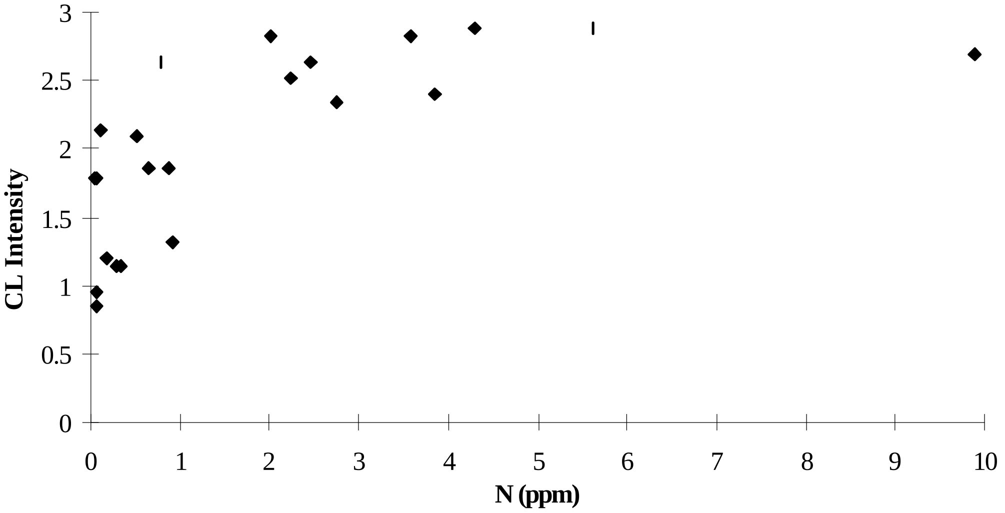

Figure 6.3_19 Variation of cathodoluminescence intensity against nitrogen concentration for BZ255.

CL intensity appears to increase rapidly with nitrogen concentration for low nitrogen values, subsequently flattening off to a weaker dependence on concentration.

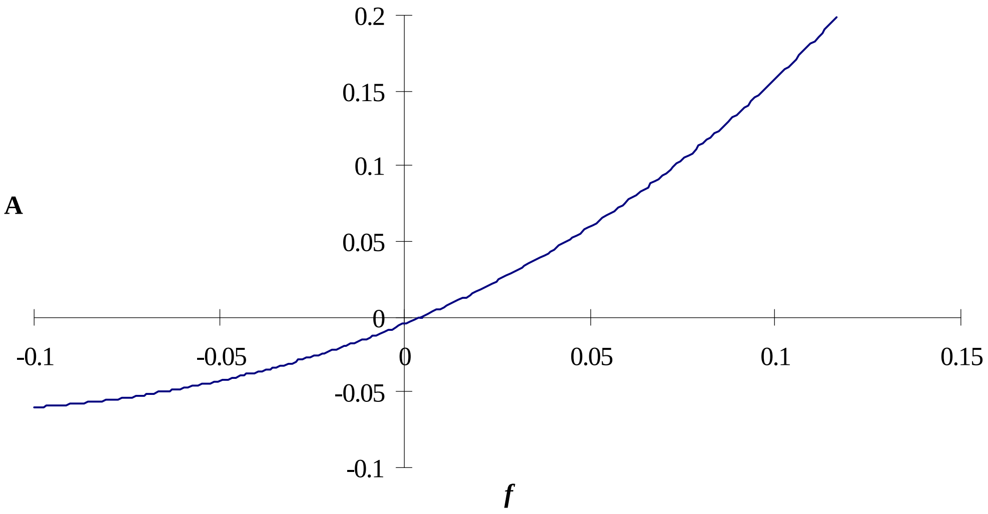

Figure 7.1_1 Investigation of the function A in terms of *f* (function of volume change).

where A = $f(1+2f)^{5/2}(1-\zeta_1 f)$-X and X and *f* are as defined in the text and in figure 7.1_5.
The graph is plotted for a range of *f* corresponding to geologically relevent volume change and shows that there is a unique solution for the point of interest at A = 0.

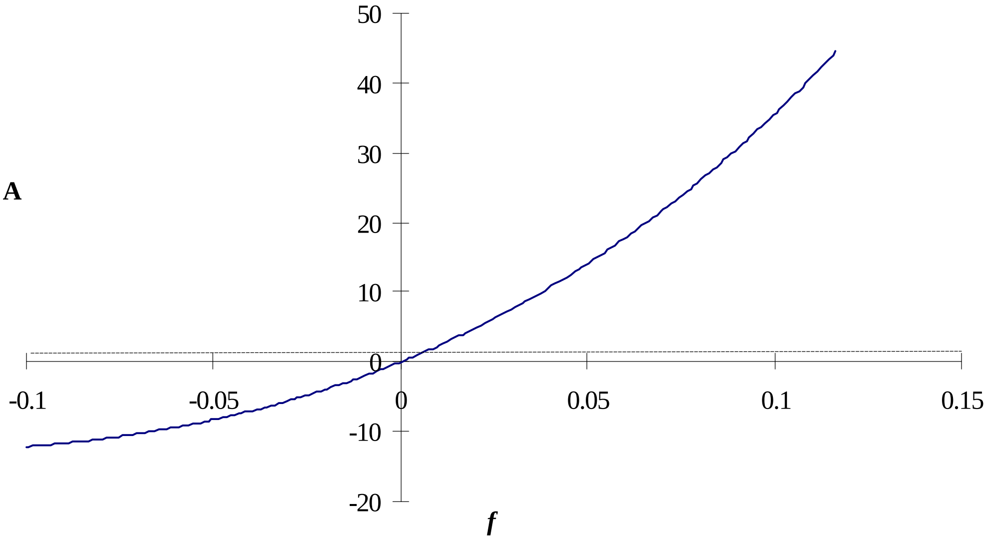

Figure 7.1_2 Investigation of the function A in terms of *f* (function of volume change).

where A = $f(1+2f)^{5/2}(1-\zeta_1 f)/X$ and X and *f* are as defined in the text and in figure 7.1_5.
The graph is plotted for a range of *f* corresponding to geologically relevent volume change and shows that there is a unique solution for the point of interest at A = 1.

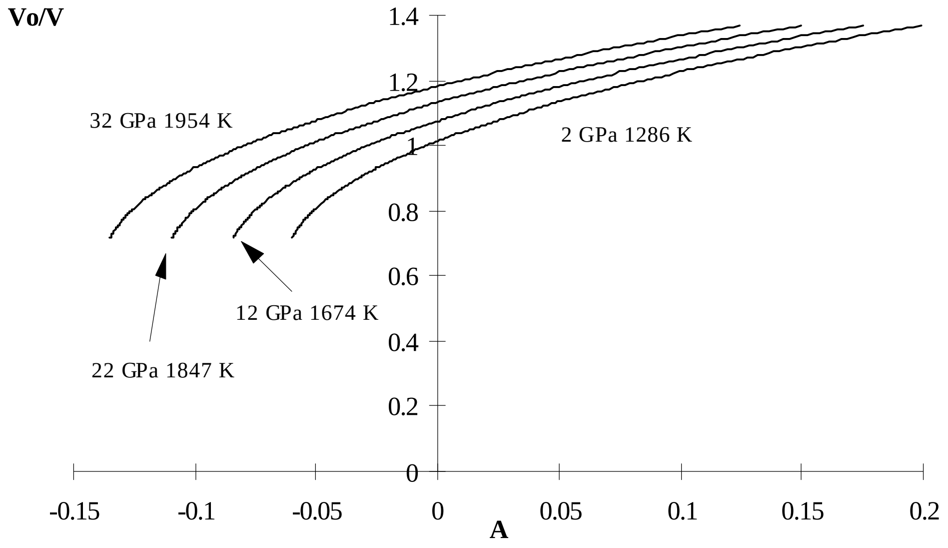

Figure 7.1_3 Graph of volume change against A for varying pressure and temperature conditions.

where A = $f(1+2f)^{5/2}(1-\zeta_1 f)$-X and X and *f* are as defined in the text and in figure 7.1_5.
Relative change in volume (V_0/V) is seen to compress with increasing P and temperature (values taken from Geotherm 2)

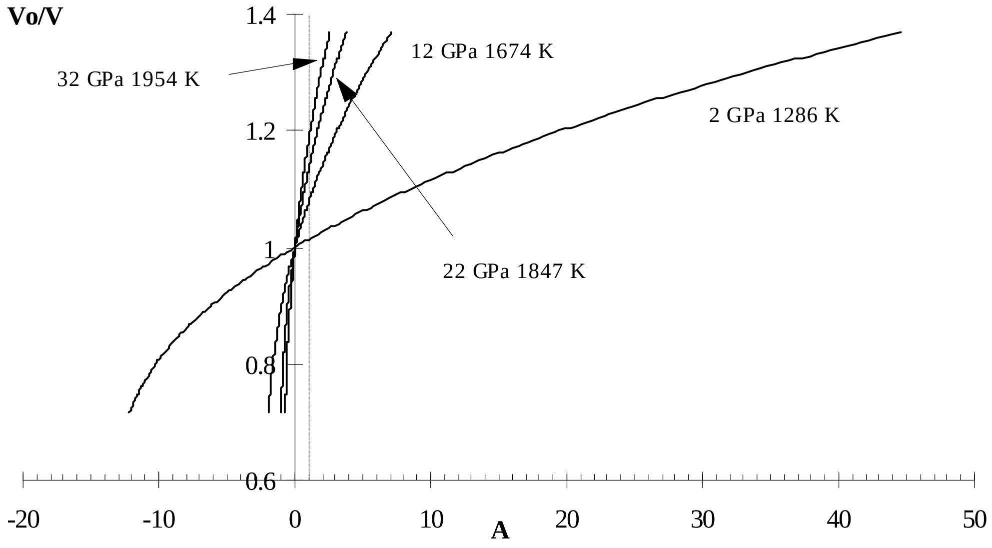

Figure 7.1_4 Graph of volume change against A for varying pressure and temperature conditions.

where $A = f(1+2f)^{5/2}(1-\zeta_1 f)/X$ and X and f are as defined in the text and in figure 7.1_5.
Relative change in volume (V_0/V) is seen to compress with increasing P and temperature (values taken from Geotherm 2)

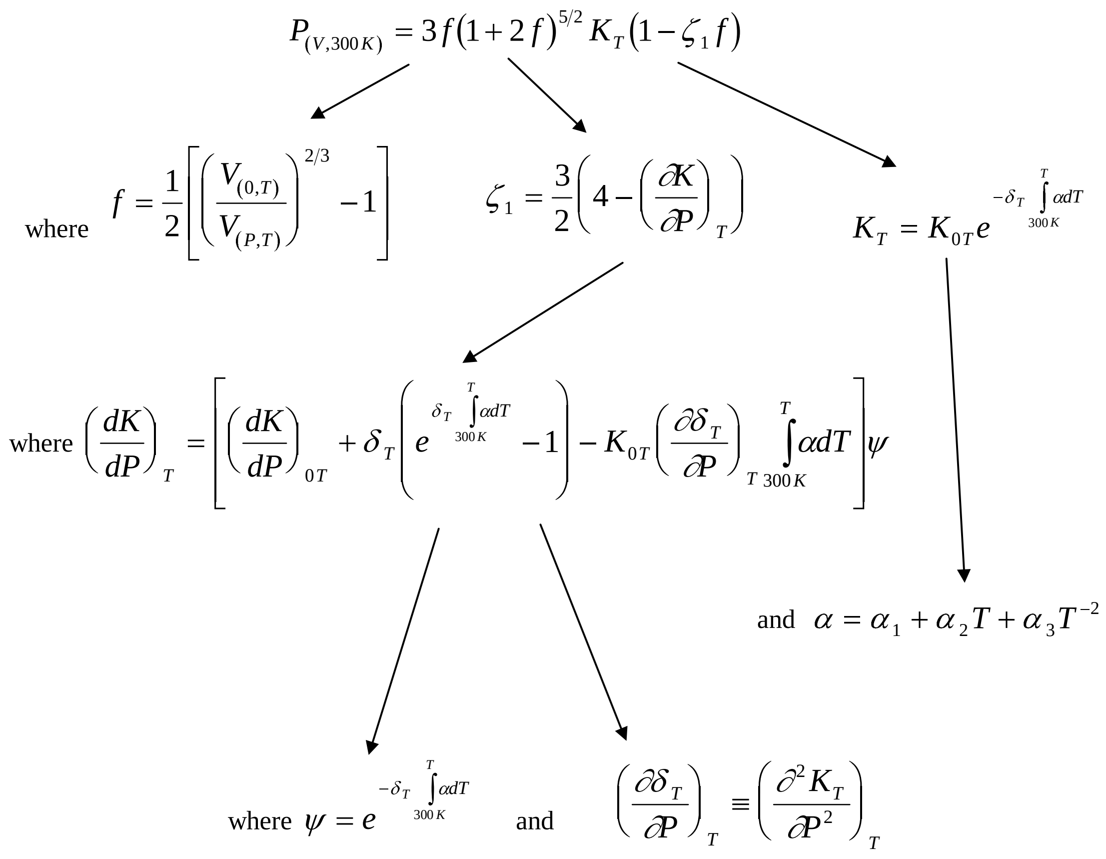

$$P_{(V,300K)} = 3f(1+2f)^{5/2} K_T (1-\zeta_1 f)$$

where $$f = \frac{1}{2}\left[\left(\frac{V_{(0,T)}}{V_{(P,T)}}\right)^{2/3} - 1\right]$$

$$\zeta_1 = \frac{3}{2}\left(4 - \left(\frac{\partial K}{\partial P}\right)_T\right)$$

$$K_T = K_{0T} e^{-\delta_T \int_{300K}^{T} \alpha dT}$$

where $$\left(\frac{dK}{dP}\right)_T = \left[\left(\frac{dK}{dP}\right)_{0T} + \delta_T\left(e^{\delta_T \int_{300K}^{T} \alpha dT} - 1\right) - K_{0T}\left(\frac{\partial \delta_T}{\partial P}\right)_T \int_{300K}^{T} \alpha dT\right]\psi$$

and $\alpha = \alpha_1 + \alpha_2 T + \alpha_3 T^{-2}$

where $\psi = e^{-\delta_T \int_{300K}^{T} \alpha dT}$ and $\left(\frac{\partial \delta_T}{\partial P}\right)_T \equiv \left(\frac{\partial^2 K_T}{\partial P^2}\right)_T$

variables ψ, α, K_T, ξ, $3K_T$, δK/δPare solved for each value of P (GPa) and T(K): the only unknown being f

The dimensionless equation to solve, therefore is: $$f(1+2f)^{5/2}(1-\zeta_1 f) - X = 0$$

where $$X = \frac{P}{3K_T}$$

Finally: $\dfrac{V_{(P,T)}}{V_{(0,300)}}$ is obtained by using: $$V_{(0,T)} = V_{(0,300)} e^{\int_{300}^{T} \alpha dT}$$

Figure 7.1_5 Flow chart for the construction of the solution of volume change in terms of pressure / temperature and physical properties of mantle minerals.

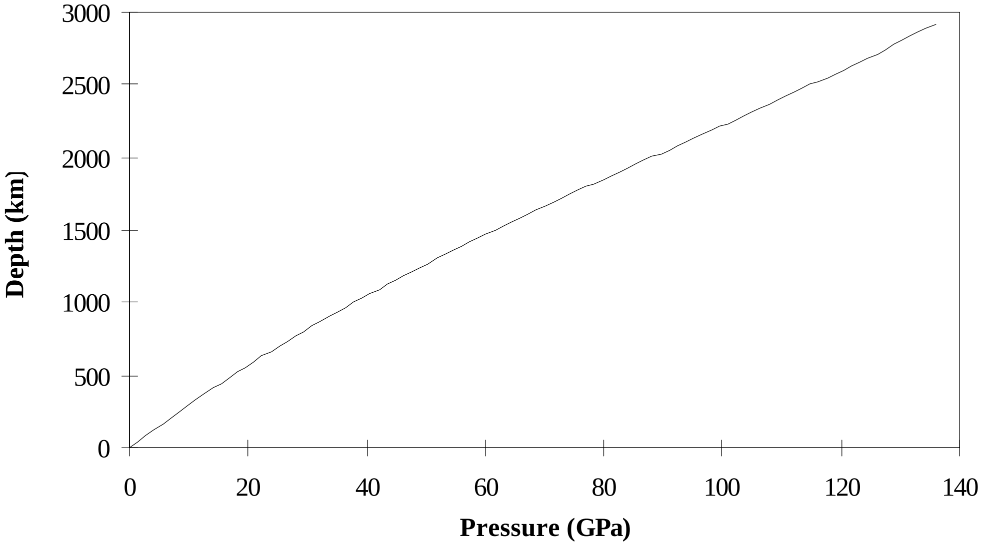

Figure 7.1_6 Relationship of depth (km) against pressure (GPa) as predicted by the PREM model.

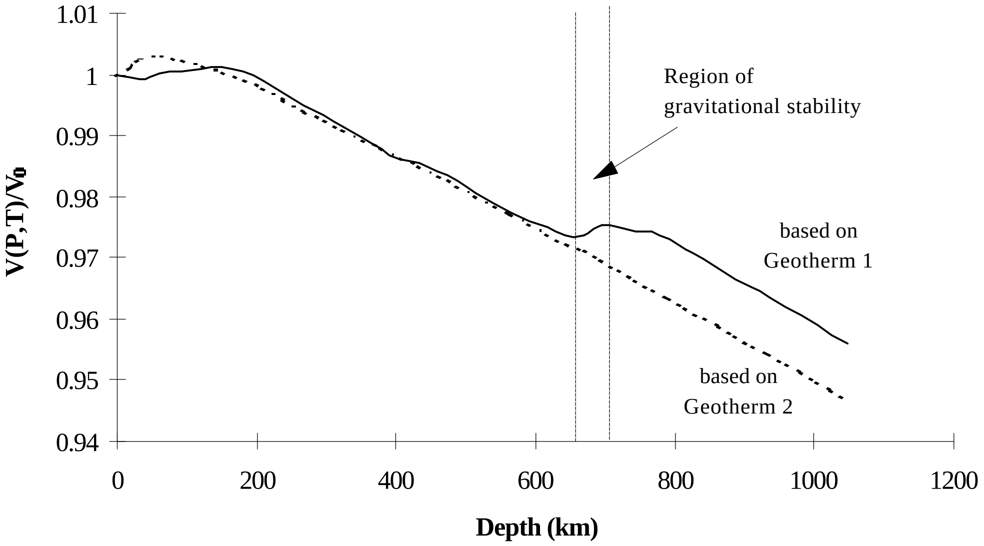

Figure 7.1_7 Relative volume change with depth along Geotherms 1 and 2 for diamond.

V_0 is defined as volume at conditions of atmospheric temperature and pressure (ATP). Comparison with the following figures will show the overall small compressibility of diamond. Additionally of note is the region of ~ 700 - 750 km where, along Geotherm 1 (with a thermal boundary between upper and lower mantle) diamond will be subjected to little volume (and thus density) change. Furthermore, on decrease in depth, the rapid drop in temperature will cause a relative contraction and thus increase in density, thus gravitationally stabilising diamond below the boundary with the upper mantle.

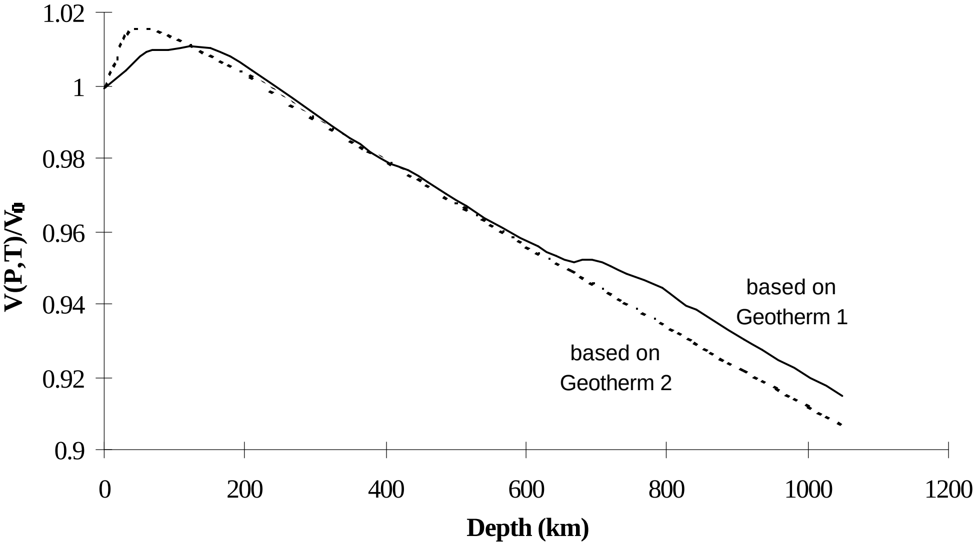

Figure 7.1_8 Relative volume change with depth along Geotherms 1 and 2 of corundum.

V_0 is defined as volume at conditions of atmospheric temperature and pressure (ATP). Comapred to diamond, contraction with depth is greater and the gravitational stability on the upper / lower mantle boundary is less evident. The large expansion over ATP volume under conditions of volcanic exhumation (i. e. rapid decompression at high teperature and demonstrated along the low depth region of Geotherm 2) is particularly noteworthy, corundum occluding diamonds will be subjected to large internal pressure on volcanic exhumation.

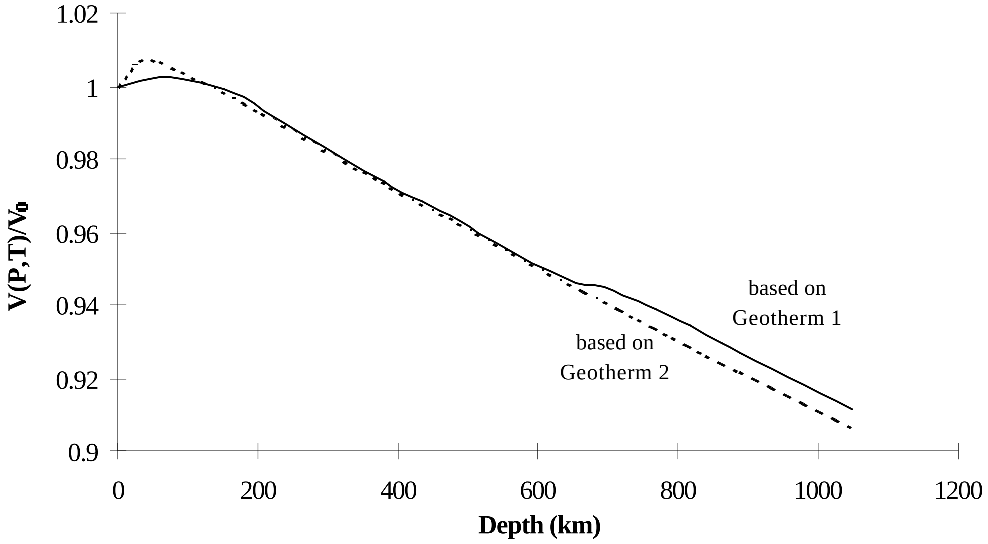

Figure 7.1_9 Relative volume change with depth along Geotherms 1 and 2 of perovskite structured $CaSiO_3$ (CaSi-Pvk).

V_0 is defined as volume at conditions of atmospheric temperature and pressure (ATP). The low thermal expansivity of CaSi-Pvk is reflected in the absence of a region of gravitational stability on the upper / lower mantle boundary along Geotherm 1. Note that regions of the diagram involve CaSi-Pvk being metastable, encapsulation in diamond, for example, may offer an opportunity for retaining metastable structure.

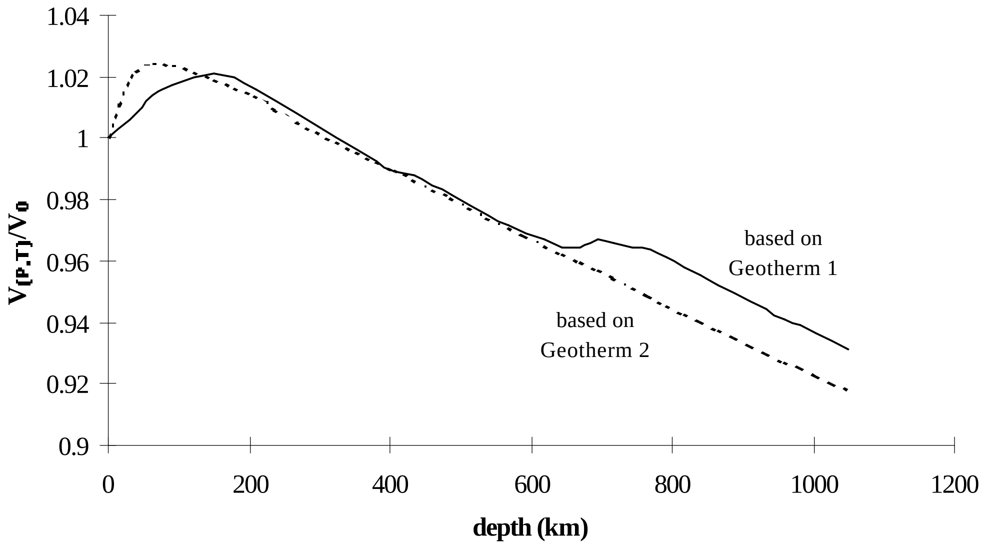

Figure 7.1_10 Relative volume change with depth along Geotherms 1 and 2 of perovskite structured $Mg_{0.9}Fe_{0.1}SiO_3$ (MgSi-Pvk) of similar composition to Type I MgSi-Pvk.

V_0 is defined as volume at conditions of atmospheric temperature and pressure (ATP). The extremely large expansion over ATP volume under conditions of volcanic exhumation (i. e. rapid decompression at high temperature and demonstrated along the low depth region of Geotherm 2) is particularly noteworthy, MgSi-Pvk occluding diamonds will be subjected to very large internal pressure on volcanic exhumation. Note that regions of the diagram involve MgSi-Pvk being metastable, encapsulation in diamond, for example, may offer an opportunity for retaining metastable structure. The effect of phase transition on volume change is shown in figure 7.1_17.

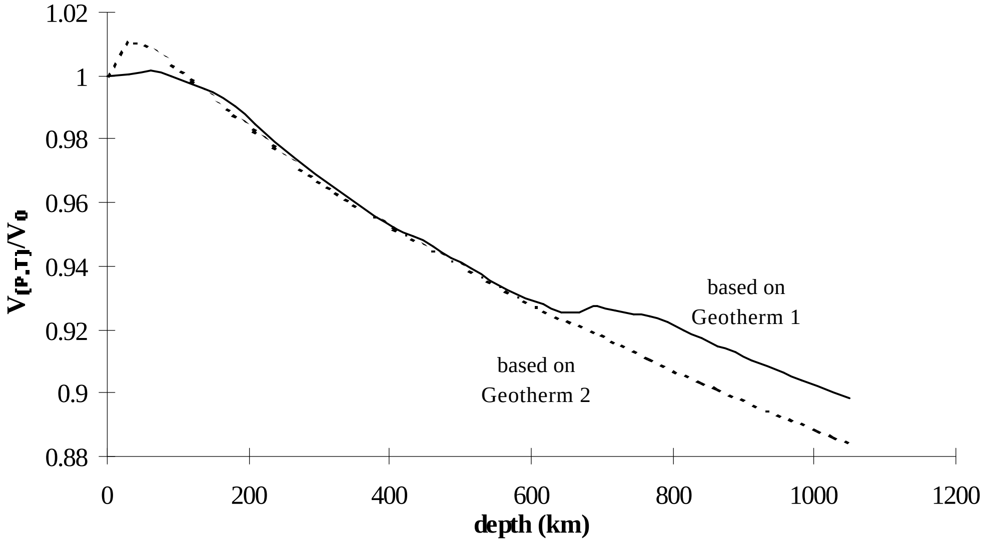

Figure 7.1_11 Relative volume change with depth along Geotherms 1 and 2 of orthorhombic structured $Mg_{0.9}Fe_{0.1}SiO_3$ (MgSi-Opx).

V_0 is defined as volume at conditions of atmospheric temperature and pressure (ATP). Note that regions of the diagram involve MgSi-Opx being metastable, encapsulation in diamond, for example, may offer an opportunity for retaining metastable structure, the effect of phase transition on volume change is shown in figure 7.1_17.

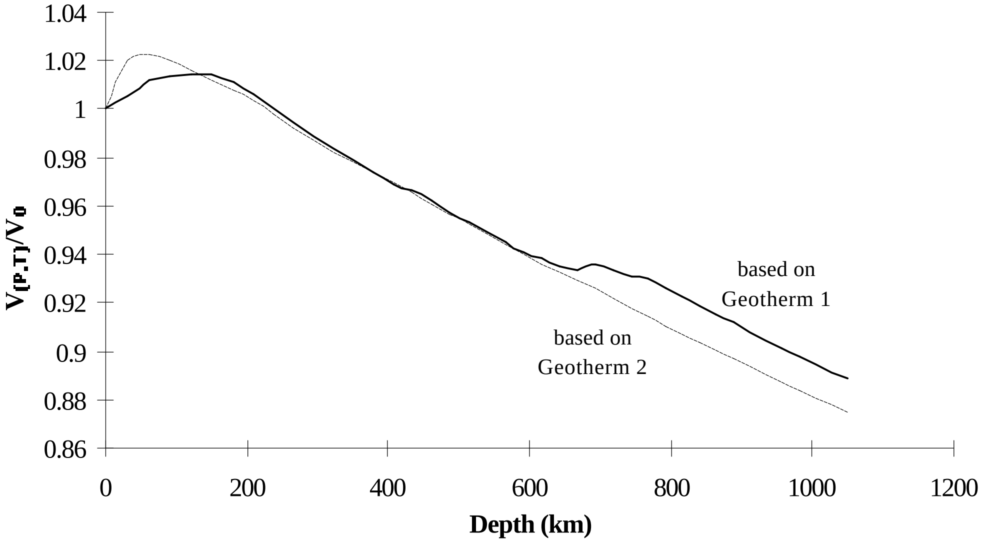

Figure 7.1_12 Relative volume change with depth along Geotherms 1 and 2 of $(Mg_{0.868}Fe_{0.132})O$ fPer (GU4A composition).

V_0 is defined as volume at conditions of atmospheric temperature and pressure (ATP).

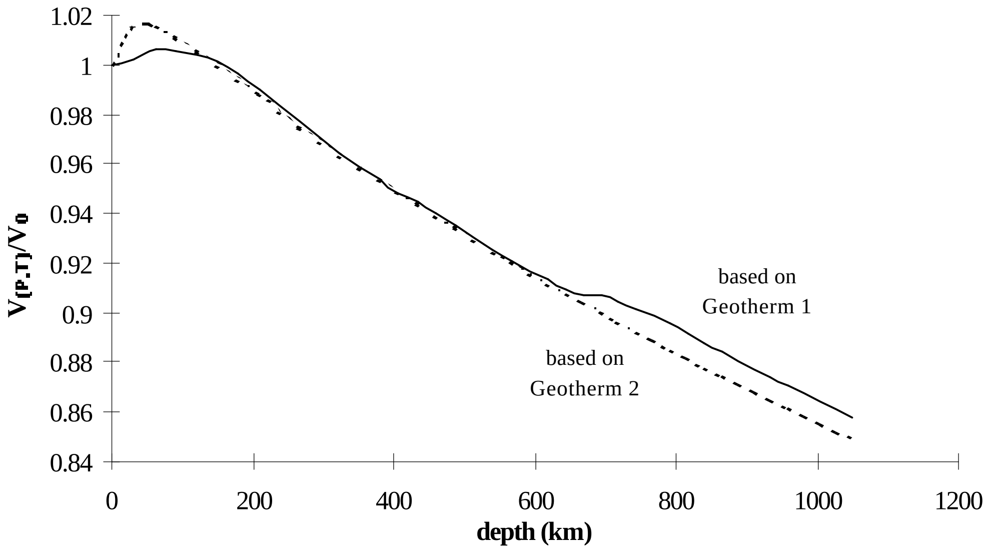

Figure 7.1_13 Relative volume change with depth along Geotherms 1 and 2 of olivine structured $(Mg_{0.87}Fe_{0.13})_2SiO_4$ (of São Luiz olivine inclusion composition).

V_0 is defined as volume at conditions of atmospheric temperature and pressure (ATP). Note that regions of the diagram involve $(Mg,Fe)_2SiO_4$ being metastable, encapsulation in diamond, for example, may offer an opportunity for retaining metastable structure, the effect of phase transition on volume change is shown in figure 7.1_16.

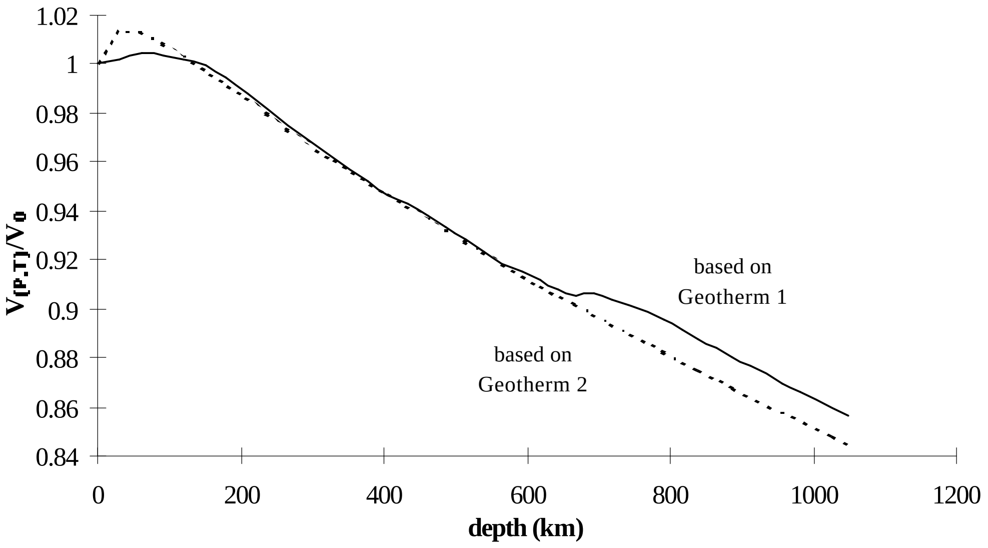

Figure 7.1_14 Relative volume change with depth along Geotherms 1 and 2 of wadsleyite structured $(Mg_{0.87}Fe_{0.13})_2SiO_4$ (of São Luiz olivine inclusion composition).

V_0 is defined as volume at conditions of atmospheric temperature and pressure (ATP). Note that regions of the diagram involve $(Mg,Fe)_2SiO_4$ being metastable, encapsulation in diamond, for example, may offer an opportunity for retaining metastable structure, the effect of phase transition on volume change is shown in figure 7.1_16.

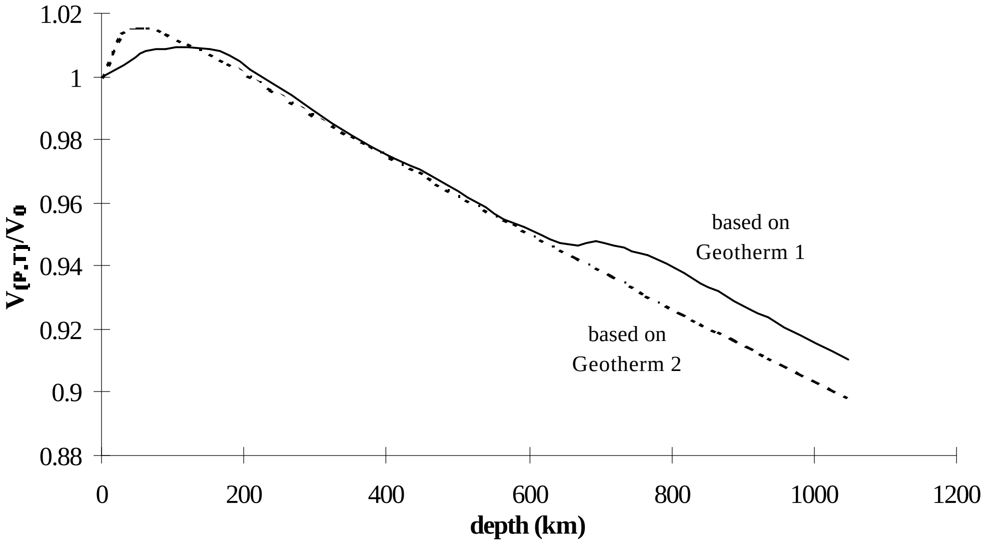

Figure 7.1_15 Relative volume change with depth along Geotherms 1 and 2 of ringwoodite structured $(Mg_{0.87}Fe_{0.13})_2SiO_4$ (of São Luiz olivine inclusion composition).

V_0 is defined as volume at conditions of atmospheric temperature and pressure (ATP). Note that regions of the diagram involve $(Mg,Fe)_2SiO_4$ being metastable, encapsulation in diamond, for example, may offer an opportunity for retaining metastable structure, the effect of phase transition on volume change is shown in figure 7.1_16.

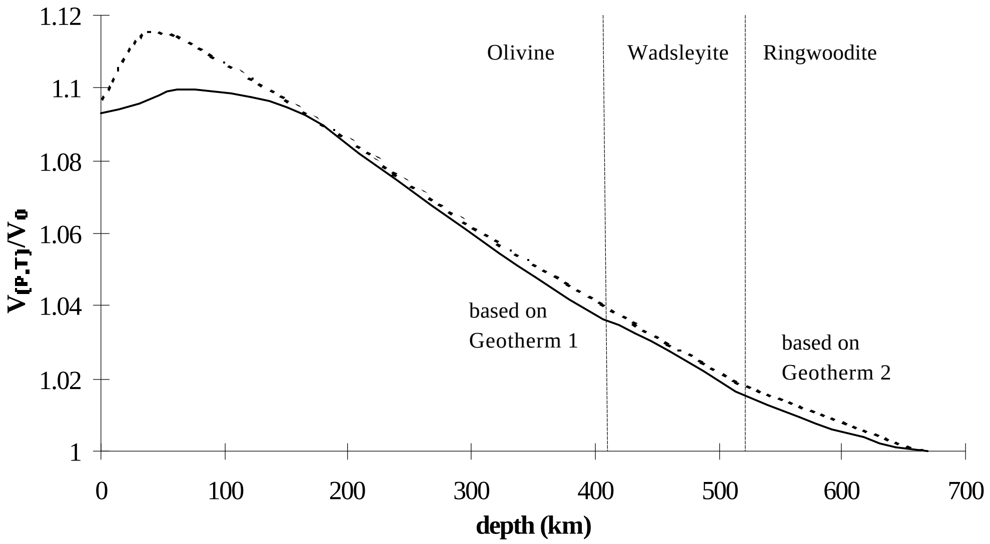

Figure 7.1_16 Relative volume change of a $(Mg_{0.87}Fe_{0.13})_2SiO_4$ phase forming at 670 km and rising to the Earth's surface.

V_0 is defined as volume at conditions of pressure and temperature relevent to Geotherms 1 and 2 at a depth of 670km. Phase transitions from ringwoodite to wadsleyite to olivine stuctures are modelled at depths corresponding to pressure and temperature conditions from figure 4.4_4. The slight changes in slope in addition to pressure and temperature effects are indicative of the change in thermoelastic properties.

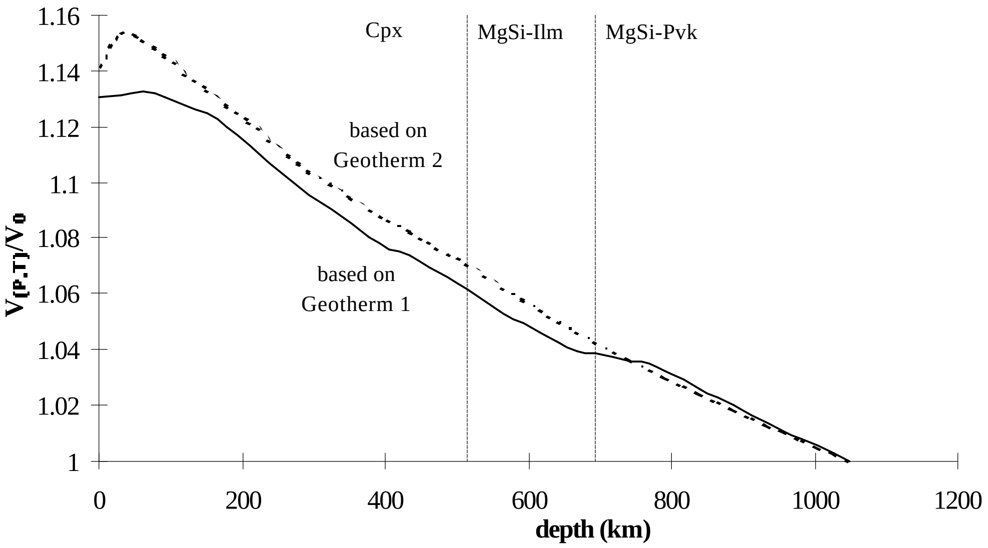

Figure 7.1_17 Relative volume change of a $Mg_{0.9}Fe_{0.1}SiO_3$ phase forming at 1050 km and rising to the Earth's surface.

V_0 is defined as volume at conditions of pressure and temperature relevent to Geotherms 1 and 2 at a depth of 670km. Phase transitions from perovskite to ilmenite to clinopyroxene stucture are modelled at depths corresponding to pressure and temperature conditions from figure 4.4_1. The slight changes in slope in addition to pressure and temperature effects are indicative of the change in thermoelastic properties.

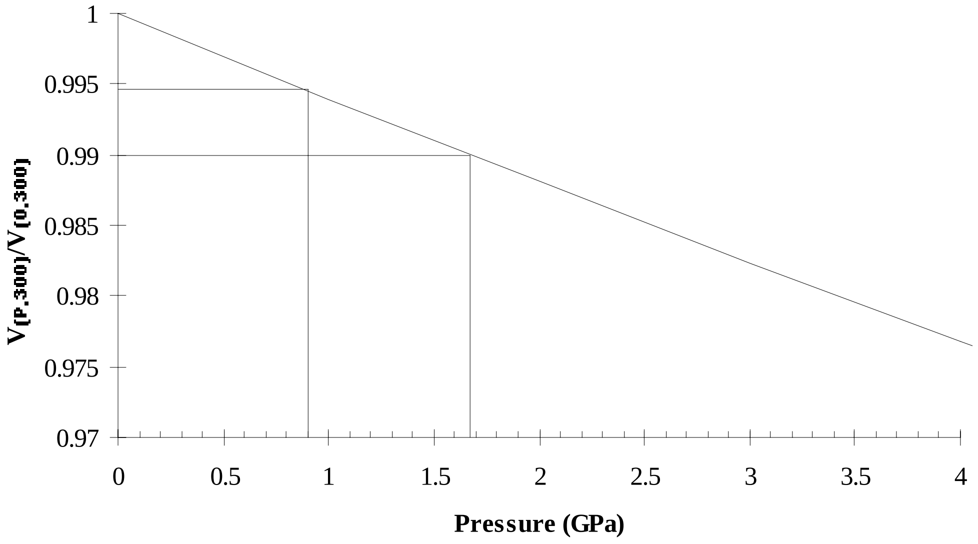

Figure 7.1_18 Relative volume change for constant temperature (300K) against pressure for fPer of composition ($(Mg_{0.868}Fe_{0.132})O$) (GU4A).

V_0 is defined as volume at conditions of atmospheric temperature and pressure (ATP). The two relative volume changes for released against in-situ GU4A indicate an internal pressure on the diamond host (GU4) of 0.91- 1.67 GPa.

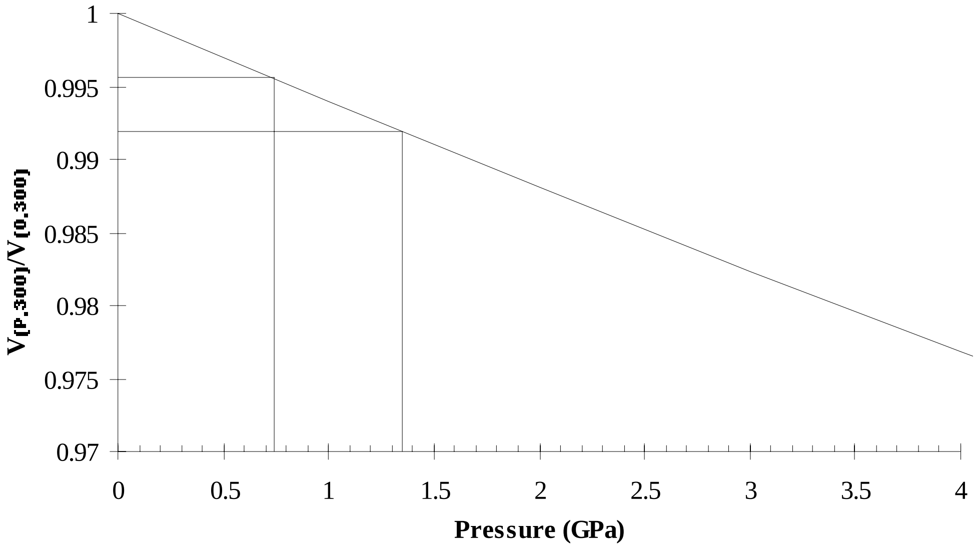

Figure 7.1_19 Relative volume change for constant temperature (300K) against pressure for fPer of composition ($(Mg_{0.743}Fe_{0.257})O$ (BZ257A).

V_0 is defined as volume at conditions of atmospheric temperature and pressure (ATP). The two relative volume changes for released against in-situ BZ257A indicate an internal pressure on the diamond host (GU4) of 0.75 - 1.35 GPa.

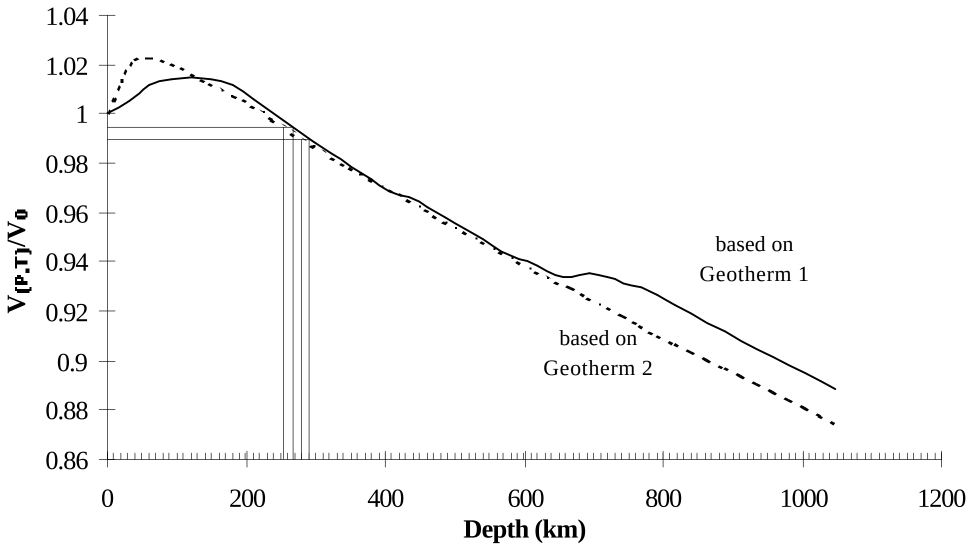

Figure 7.1_20 Relative volume change along Geotherms 1 and 2 for fPer of composition ($Mg_{0.868}Fe_{0.132}$)O (GU4A).

V_0 is defined as volume at conditions of atmospheric temperature and pressure (ATP). Without correcting for the relative expansion of the diamond host on exhumation, cell parameter change for GU4A indicates depths of formation of 280 +/- 12 km (Geotherm 1) and 266 +/- 13 km (Geotherm 2).

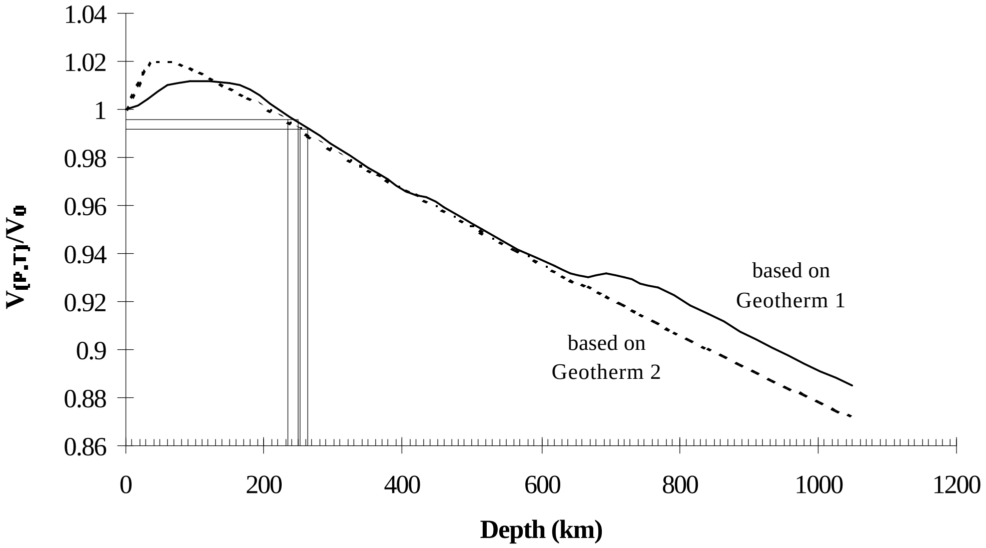

Figure 7.1_21 Relative volume change for constant temperature (300K) against pressure for fPer of composition ($(Mg_{0.743}Fe_{0.257})O$) (BZ257A).

V_0 is defined as volume at conditions of atmospheric temperature and pressure (ATP). Without correcting for the relative expansion of the diamond host on exhumation, cell parameter change for BZ257A indicates depths of formation of 256 +/- 8 km (Geotherm 1) and 243 +/- 8 km (Geotherm 2).

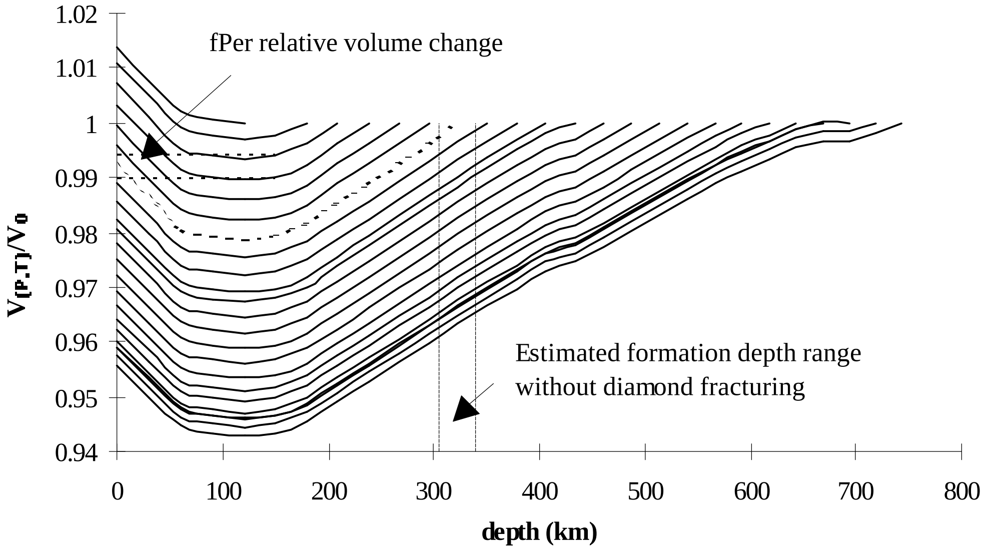

Figure 7.1_22 Models of the relative change in cell parameters expected for fPer of GU4A composition included in diamond at a range of depths from 750km assuming change in temperature and pressure along Geotherm 1.

V_0 is defined as volume on encapsulation of fPer in diamond. Intersection of observed cell parameter change indicates a formation depth of 324 +/- 18 km. This depth range represents the minimum possible depth of formation for GU4A in terms of structural observation but makes no correction for additional diamond expansion due to deformation.

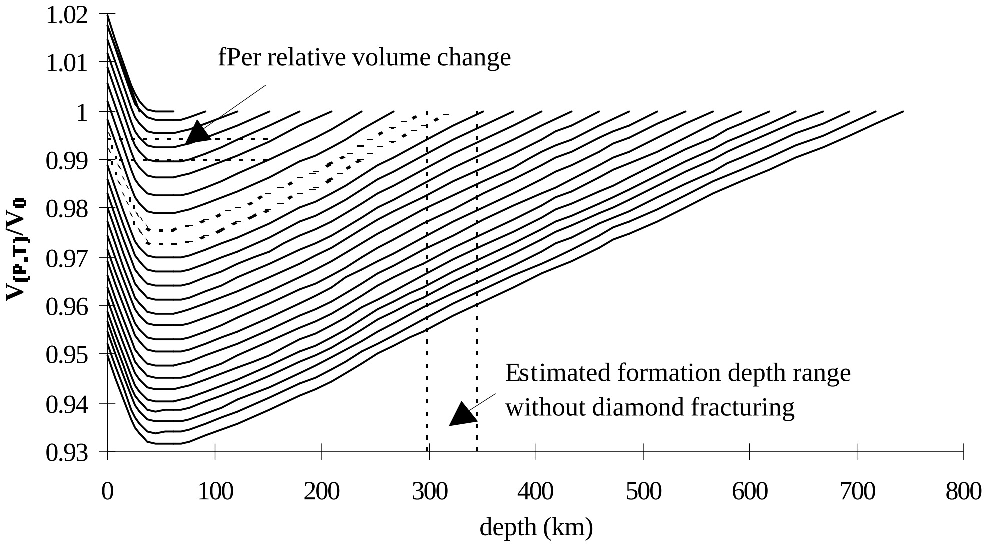

Figure 7.1_23 Models of the relative change in cell parameters expected for fPer of GU4A composition included in diamond at a range of depths from 750km assuming change in temperature and pressure along Geotherm 2.

V_0 is defined as volume on encapsulation of fPer in diamond. Intersection of observed cell parameter change indicates a formation depth of 318 +/- 21 km. This depth range represents the minimum possible depth of formation for GU4A in terms of structural observation but makes no correction for additional diamond expansion due to deformation.

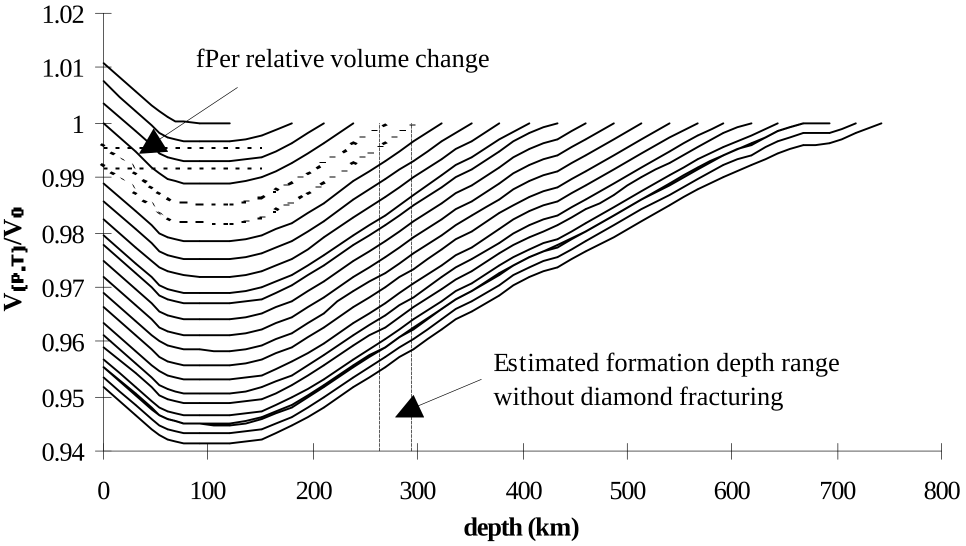

Figure 7.1_24 Models of the relative change in cell parameters expected for fPer of BZ257A composition included in diamond at a range of depths from 750km assuming change in temperature and pressure along Geotherm 1.

V_0 is defined as volume on encapsulation of fPer in diamond. Intersection of observed cell parameter change indicates a formation depth of 286 +/- 15 km. This depth range represents the minimum possible depth of formation for BZ257A in terms of structural observation but makes no correction for additional diamond expansion due to deformation.

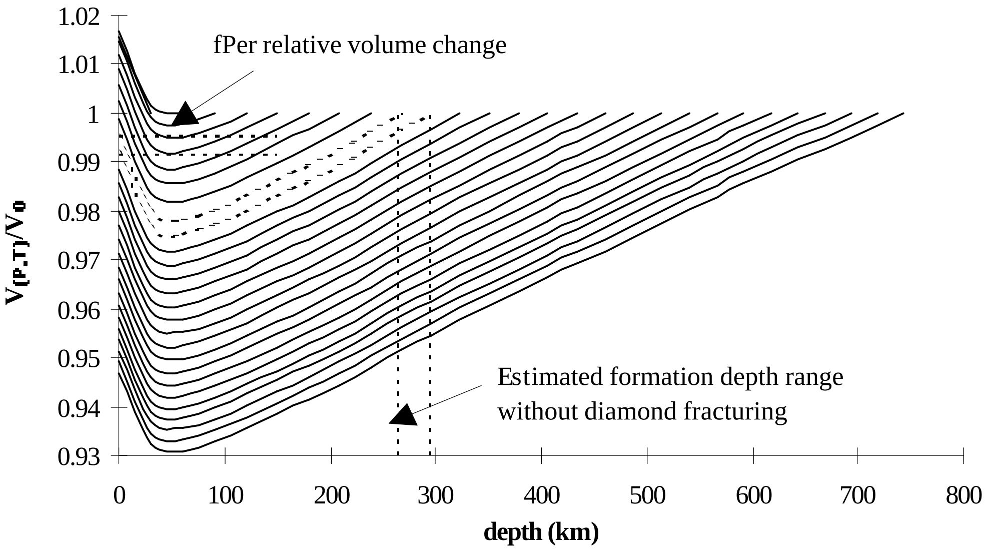

Figure 7.1_25 Models of the relative change in cell parameters expected for fPer of BZ257A composition included in diamond at a range of depths from 750km assuming change in temperature and pressure along Geotherm 2.

V_0 is defined as volume on encapsulation of fPer in diamond. Intersection of observed cell parameter change indicates a formation depth of 278 +/- 15 km. This depth range represents the minimum possible depth of formation for BZ257A in terms of structural observation but makes no correction for additional diamond expansion due to deformation.

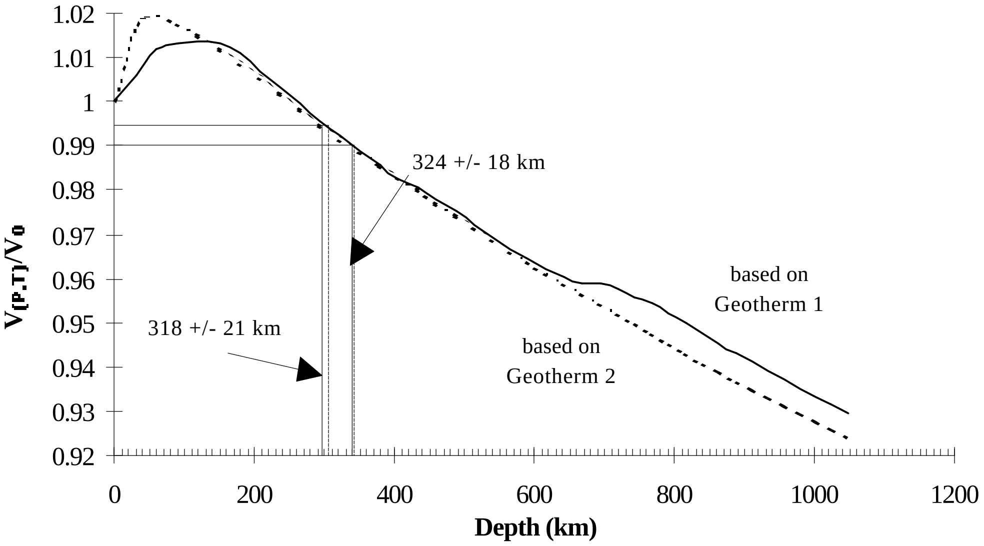

Figure 7.1_26 Alternative approach to the calculation of minimum depth of formation for GU4A by relative volume change of fPer / diamond against depth.

V_0 is defined as volume at conditions of atmospheric temperature and pressure (ATP). Depth ranges are the same as concluded from figures 7.1_22 and 7.1_23.

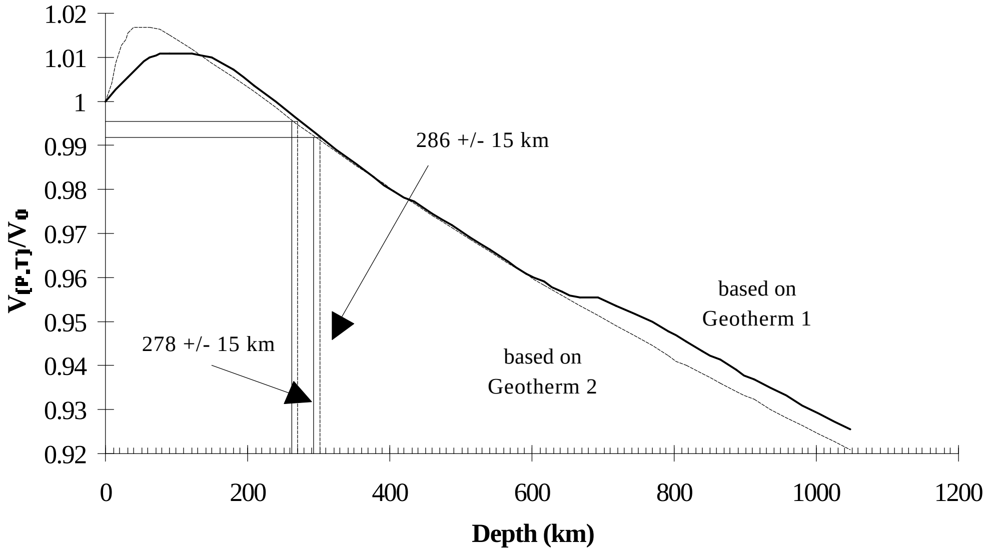

Figure 7.1_27 Alternative approach to the calculation of minimum depth of formation for BZ257A by relative volume change of fPer / diamond against depth.

V_0 is defined as volume at conditions of atmospheric temperature and pressure (ATP). Depth ranges are the same as concluded from figures 7.1_24 and 7.1_25.

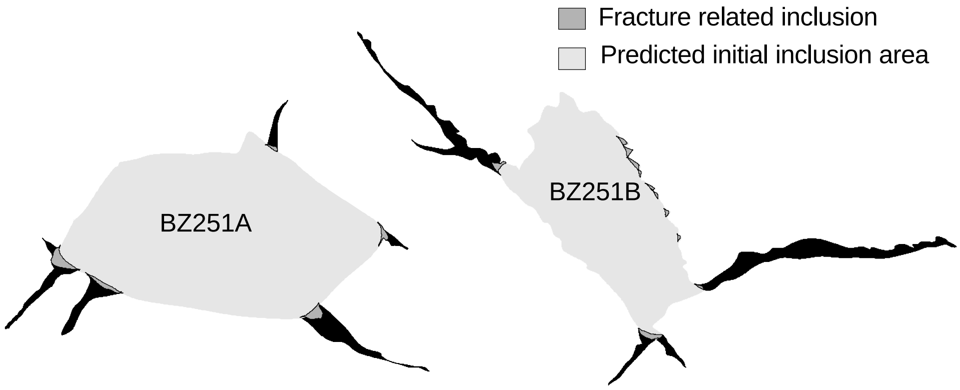

Figure 7.1_28 Estimation of the relative volume expansion due to deformation using inclusions in diamond BZ251

Assuming expansion of inclusion material into regions of fractures described in section 5.3.1.2, diamond fracture expansion is estimated to have been x 1.037 by volume. This is believed to be a conservative estimate of diamond expansion due to deformation.

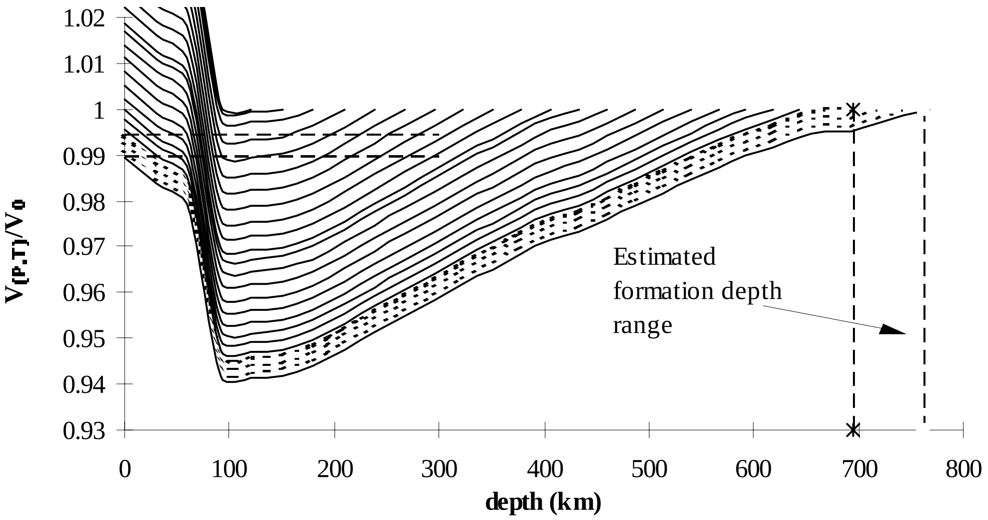

Figure 7.1_29 Models of the relative change in cell parameters expected for fPer of GU4A composition included in diamond at a range of depths from 750km involving shallow diamond fracture.

V_0 is defined as volume on encapsulation of fPer in diamond. Change in temperature and pressure follows Geotherm 1 and a single diamond fracturing event at 91 km depth (the depth of greatest internal pressure on diamond, c. f. figure 7.1_22) is modelled resulting in an extra diamond expansion of x 1.037 by volume. Application of measured inclusion expansion on release from diamond implies a formation depth of 728 +/- 34 km.

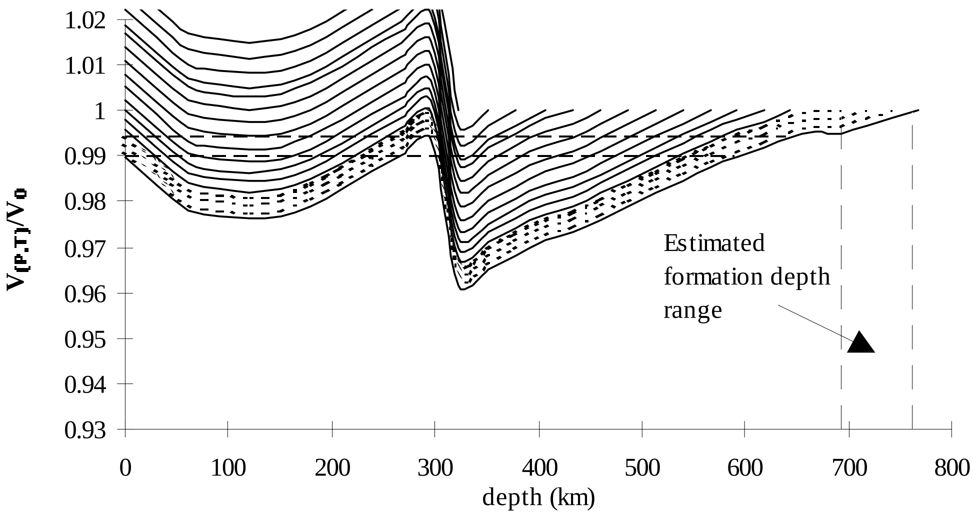

Figure 7.1_30 Models of the relative change in cell parameters expected for fPer of GU4A composition included in diamond at a range of depths from 750km involving deep diamond fracture.

V_0 is defined as volume on encapsulation of fPer in diamond. Change in temperature and pressure follows Geotherm 1 and a single diamond fracturing event at 295 km depth is modelled resulting in an extra diamond expansion of x 1.037 by volume. Application of measured inclusion expansion on release from diamond implies a formation depth of 728 +/- 34 km, the same as for deformation at 91 km in depth.

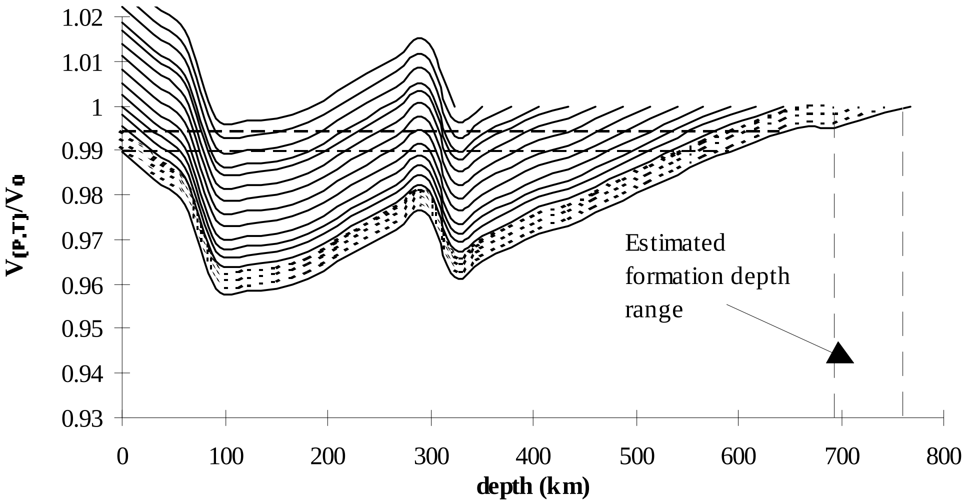

Figure 7.1_31 Models of the relative change in cell parameters expected for fPer of GU4A composition included in diamond at a range of depths from 750km involving multiple diamond fracture

V_0 is defined as volume on encapsulation of fPer in diamond. Change in temperature and pressure follows Geotherm 1 and a single diamond fracturing event at 91 km and 295 km depth is modelled resulting in a total extra diamond expansion of x 1.037 by volume. Application of measured inclusion expansion on release from diamond implies a formation depth of 728 +/- 34 km, the same as for all deformation occurring at 91 km or 295 km in depth. What this shows is that the depth of any diamond deformation will not affect any conclusions relating to inclusion encapsulation depth.

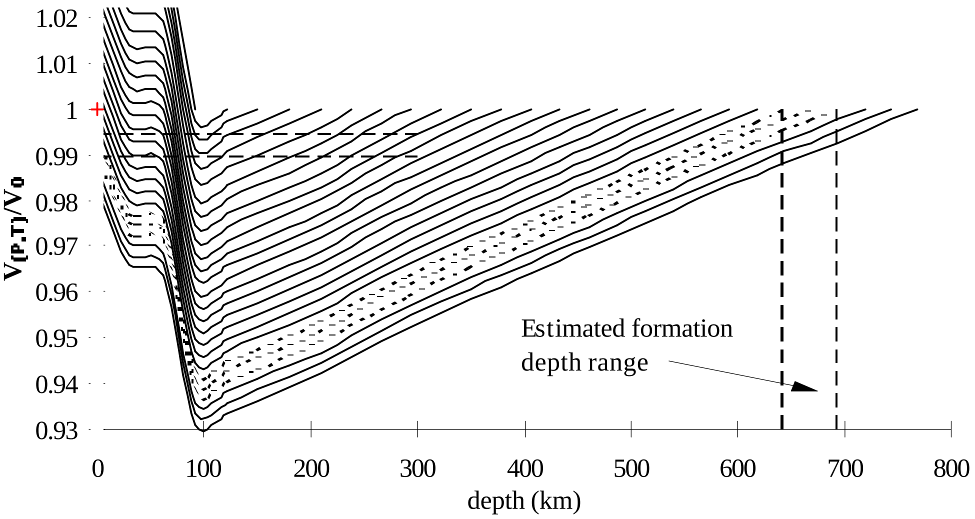

Figure 7.1_32 Models of the relative change in cell parameters expected for fPer of GU4A composition included in diamond at a range of depths from 750km involving shallow diamond fracture.

V_0 is defined as volume on encapsulation of fPer in diamond. Change in temperature and pressure follows Geotherm 2 and a single diamond fracturing event at 91 km depth is modelled resulting in an extra diamond expansion of x 1.037 by volume. Application of measured inclusion expansion on release from diamond implies a formation depth of 666 +/- 26 km. As diamond deformation - related expansion of x 1.037 is believed to be a conservative estimate, the true depth of formation can be confidently placed within the lower mantle.

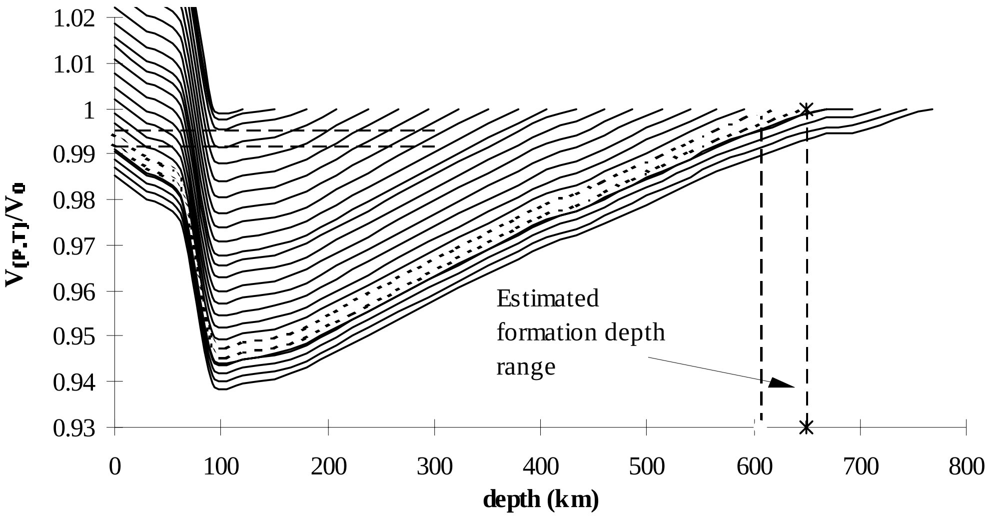

Figure 7.1_33 Models of the relative change in cell parameters expected for fPer of BZ57A composition included in diamond at a range of depths from 750km involving shallow diamond fracture

V_0 is defined as volume on encapsulation of fPer in diamond. Change in temperature and pressure follows Geotherm 1 and a single diamond fracturing event at 91 km depth is modelled resulting in an extra diamond expansion of x 1.037 by volume. Application of measured inclusion expansion on release from diamond implies a formation depth of 628 +/- 22 km. As diamond deformation - related expansion of x 1.037 is believed to be a conservative estimate, the true depth of formation can be confidently placed within the lower mantle.

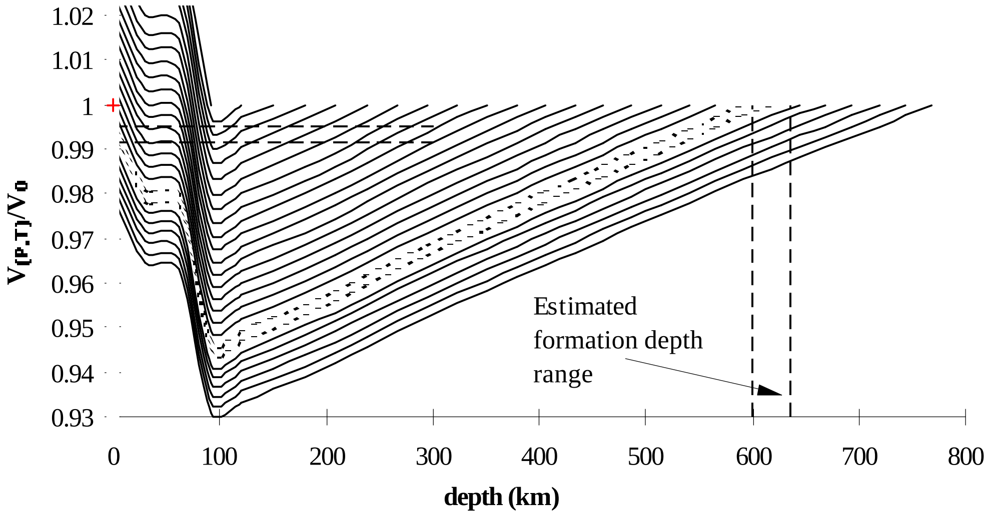

Figure 7.1_34 Models of the relative change in cell parameters expected for fPer of BZ257A composition included in diamond at a range of depths from 750km involving shallow diamond fracture.

V_0 is defined as volume on encapsulation of fPer in diamond. Change in temperature and pressure follows Geotherm 2 and a single diamond fracturing event at 91 km depth is modelled resulting in an extra diamond expansion of x 1.037 by volume. Application of measured inclusion expansion on release from diamond implies a formation depth of 617 +/- 18 km. As diamond deformation - related expansion of x 1.037 is believed to be a conservative estimate, the true depth of formation can be confidently placed within the lower mantle.

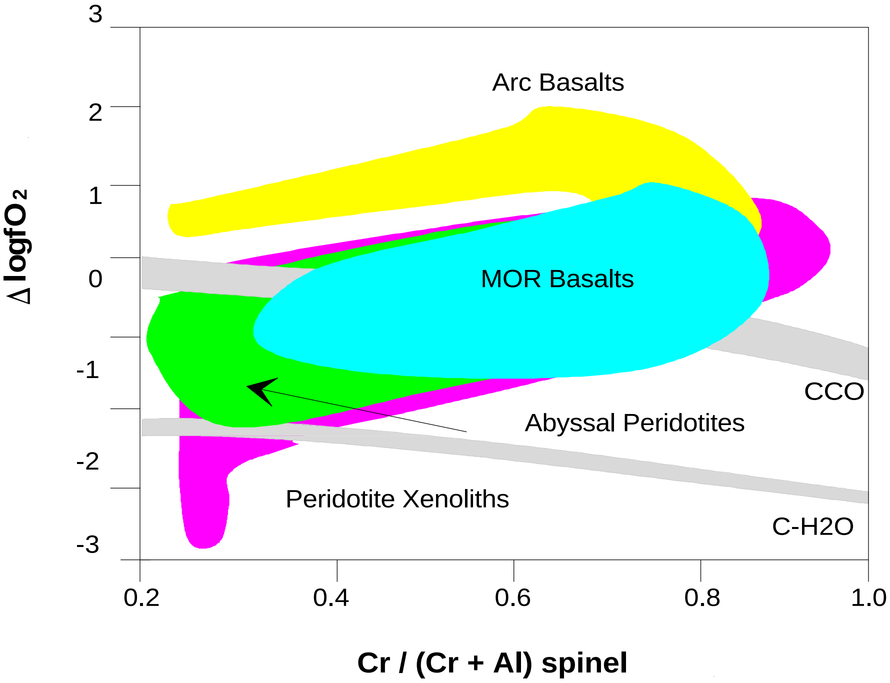

Figure 7.2_1 fO_2 relative to FMQ against Cr/(Cr+Al) showing fields of mantle related rocks.

Cr/(Cr+Al) is measured on Cr-spinel and increases with the degree of melt removal (which is roughly proportional to temperature). The general locations of CCO and C-H_2O reaction boundaries determining the stability of diamond are shown. Arc basalts are clearly significantly more oxidised than will stabilise diamond due, presumably to a signifcant slab-related H_2O component. Even at significant pressure, therefore, diamond will not be stable in such a régime. Adapted from Ballhaus (1993).

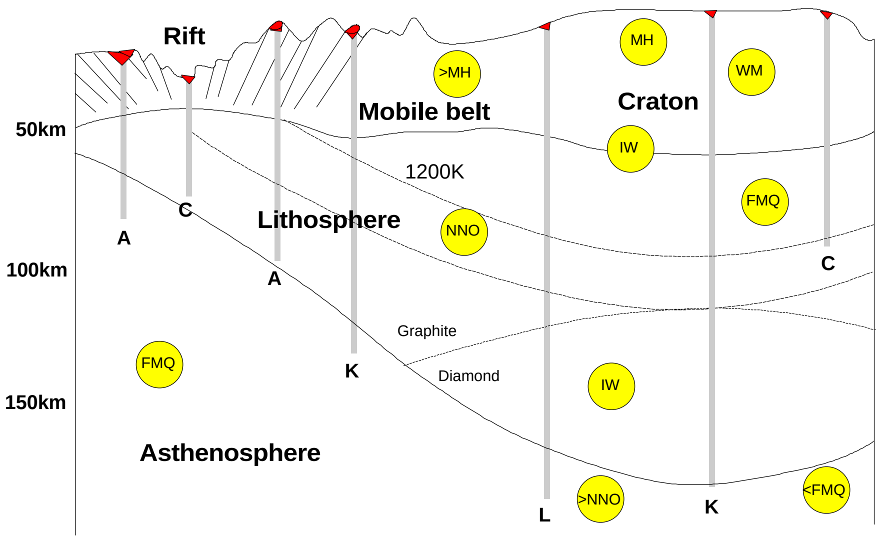

Figure 7.2_2 Oxidation state of cratonic lithosphere and related asthenosphere.

From Haggerty (1990). A - Alkali-rich melt, K - Kimberlite, C - Carbonatite, L - Lamproite. Buffers in order of increasing fO_2: IW - iron wüstite, WM - wüstite-magnetite, FMQ - fayalite-magnetite-quartz, NNO - nickel-nickel-oxide, MH - manganosite-hausmanite. Even on a summary diagram such as this, it is clear that the upper mantle shows a significant range in oxidation state. In cratonic régimes, however, there exists significant opportunity for diamond to remain within oxidation conditions appropriate to preserving its stability which, broadly speaking, is below FMQ.

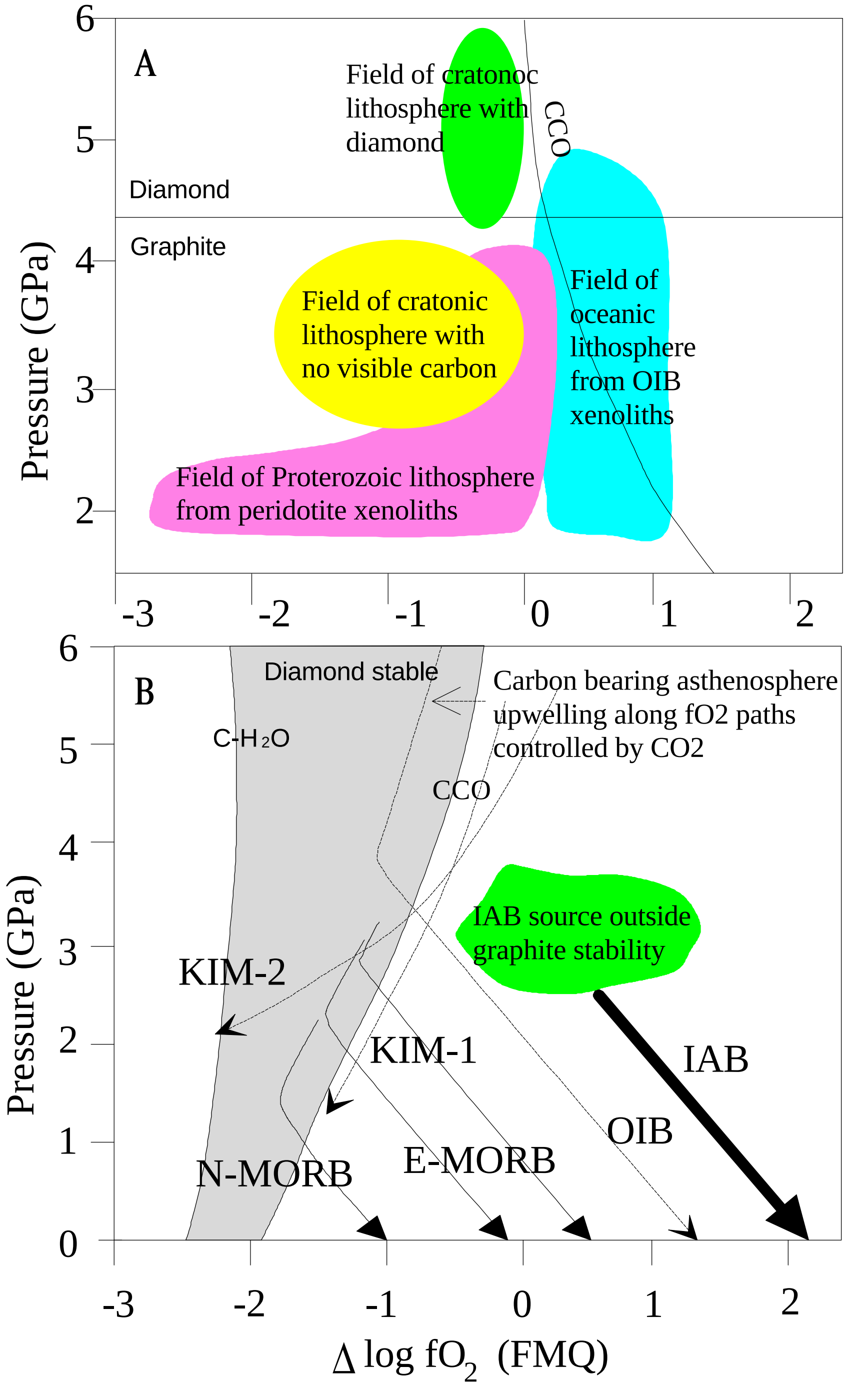

Figure 7.2_3 Pressure against fO_2 relative to FMQ.

A - CCO is calculated on the basis of a cratonic geotherm of $40 mWm^{-2}$. Fields of mantle lithospheric material are generally lie on the diamond stability side of CCO even at relatively shallow depth (~60 km), whereas by these shallow depths oceanic lithosphere is becoming inappropriate to stabilise atomic carbon. After Ballhaus (1993).

B - CCO is calculated for an eruptive geotherm. On the final stages of magmatism, all oceanic basalts, N-MORB, E-MORB and OIB rapidly become too oxidised for diamond to remain stable. Indeed, the *source* of IAB magma is believed to be too oxidised to stabilise diamond. It is only kimberlite magma which, on ascent, remains predominantly within the stability field of diamond. This is particularly true for Type II kimberlites in contrast to some Type I kimberlites which occasionally contain partially oxidised diamond. This diagram summarises why any deep diamond entrained into the upper mantle lithosphere will not survive final exhumation by oceanic basalts.

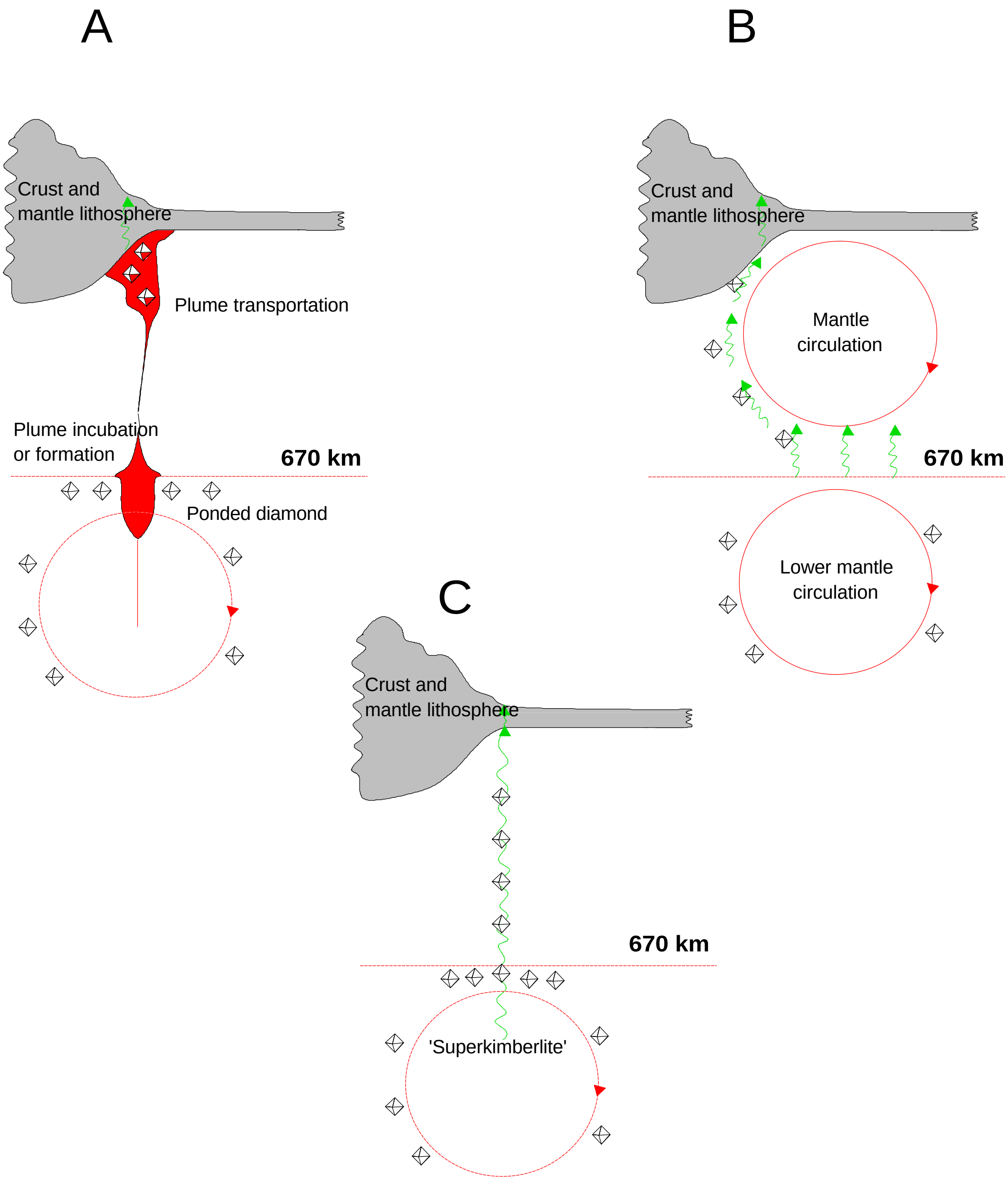

Figure 7.3_1 Possible models for the exhumation of deep diamonds.

Due to the lack of re-equilibration of diamond inclusions, a model of rapid exhumation is preferred, of the type of Model A. Transport to the base of the lithosphere by a mantle plume exhumation would be envisaged to take a total of ~ 10 - 15 Ma. Such a timescale contrasts strongly with exhumation via Model B of 'normal' mantle convection of ~ 250 - 500 Ma. It is not believed necessary to invoke Model C of superkimberlite transportation from formation depths (aka Haggerty, 1994). Although features of São Luiz diamonds are not inconsistent with such exhumation, the large range of depths sampled would more likely suggest a partially entraining rather than explosive mechanism of exhumation through the upper mantle.

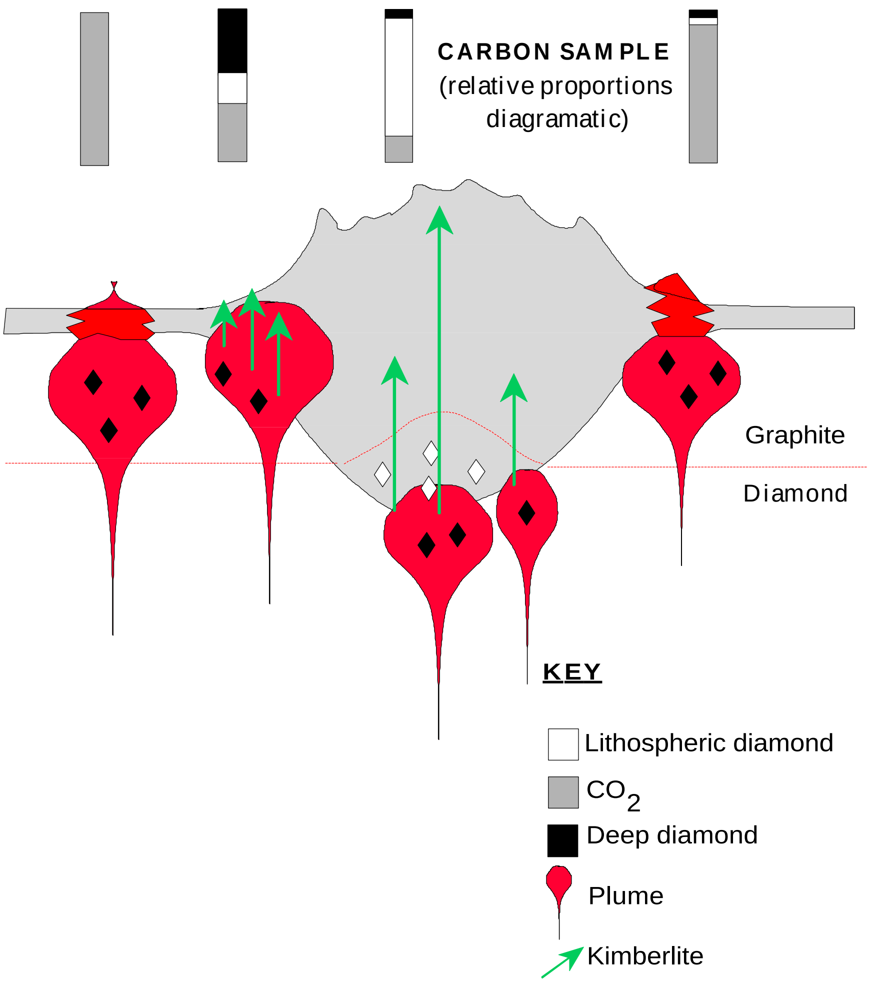

Figure 7.3_2 Predicted relative abundance of deep mantle diamond, lithospheric diamond and CO2 by exhumation through a range of crustal settings.

It is predicted that areas of thin craton represent the best opportunity for sampling deep mantle diamonds. Thin craton regions, such as mobile belts, are believed to preserve oxidation states suitable for diamond stability and are sufficiently removed from regions of lithospheric diamond production to avoid flooding of diamond population by shallow sourced stones. Additionally, it is expected that relatively weak plumes (perhaps sourced in the 670 km region and hence the dominance of upper mantle / lower mantle sourced diamonds from São Luiz) are required to transport deep diamonds to such a régime. Such weak plumes allow heat percolation into the mantle lithosphere with subsequent kimberlite production without causing continental rupture and subsequent whole scale melting and loss of diamond stability.

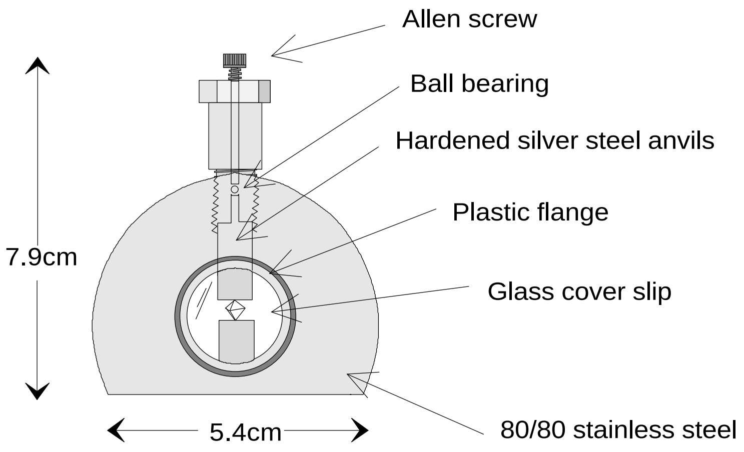

Figure A1_1 Design of the steel crusher used in the present study for the fracturing of diamonds for the release of inclusions

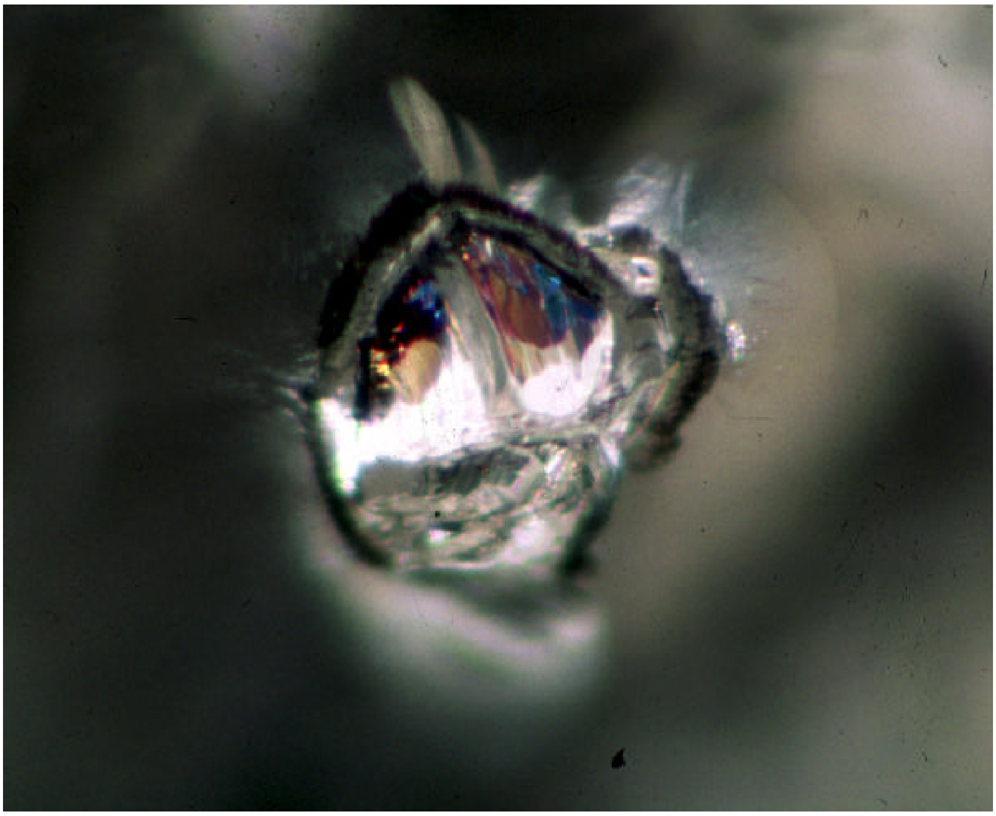

Figure A2_1 In-situ fPer inclusion BZ257A showing characteristic iridescence

The imposed diamond morphology is apparent as are the fracture systems emanating from the inclusion apices. The additional brown colouration to the fPer / diamond interface is due to a film of graphite (confirmed by XRD, Conrad, 1997 *personal communication*). The inclusion is ~200 µm across.

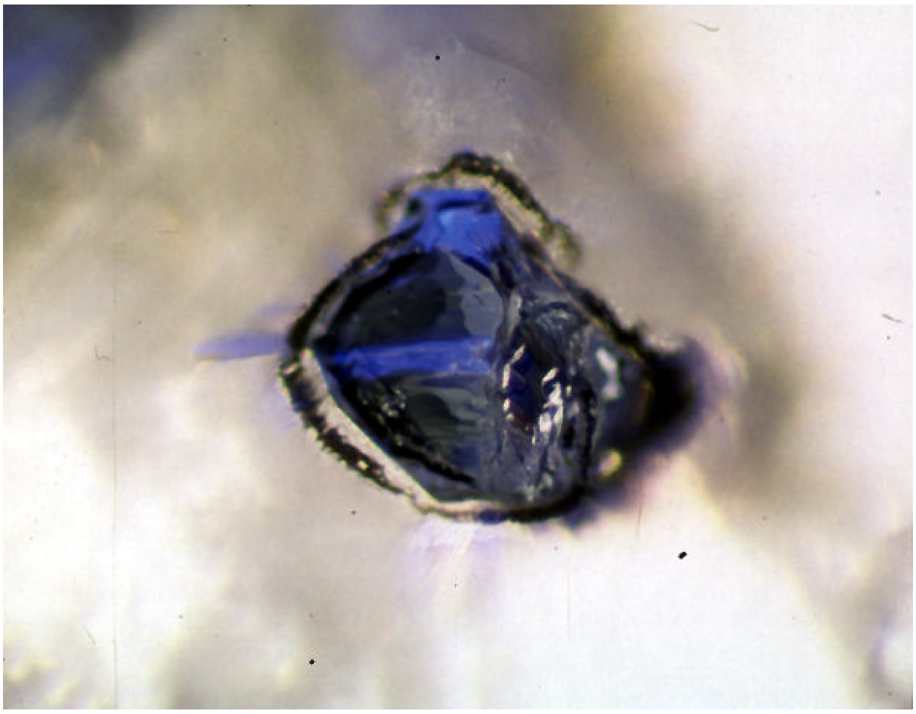

Figure A2_2 In-situ fPer inclusion BZ257A showing grey black colouration characteristic of fPer

In contrast to figure A2_1 of the same inclusion, the true dark colouration of the grain is evident. Variation of the angle of incident light often causes profound differences in the appearance of inclusions. The effect is particularly marked because of the high refractive index of diamond and its tendency to cause total internal reflection. In some cases, fPer can look colourless in all orientations, making visual identification as fPer difficult. The inclusion is ~200µm across.

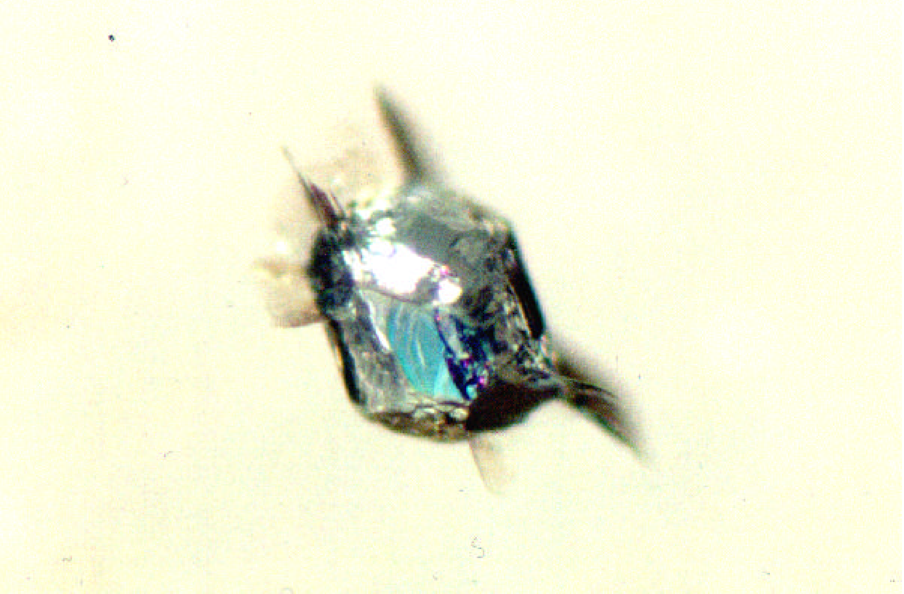

Figure A2_3 In-situ fPer inclusion BZ255

Orientation of the fPer in this manner suggest that the inclusion is colourless, where, in fact it is black. The inclusion is estimated to be ~75 µm in maximum dimension.

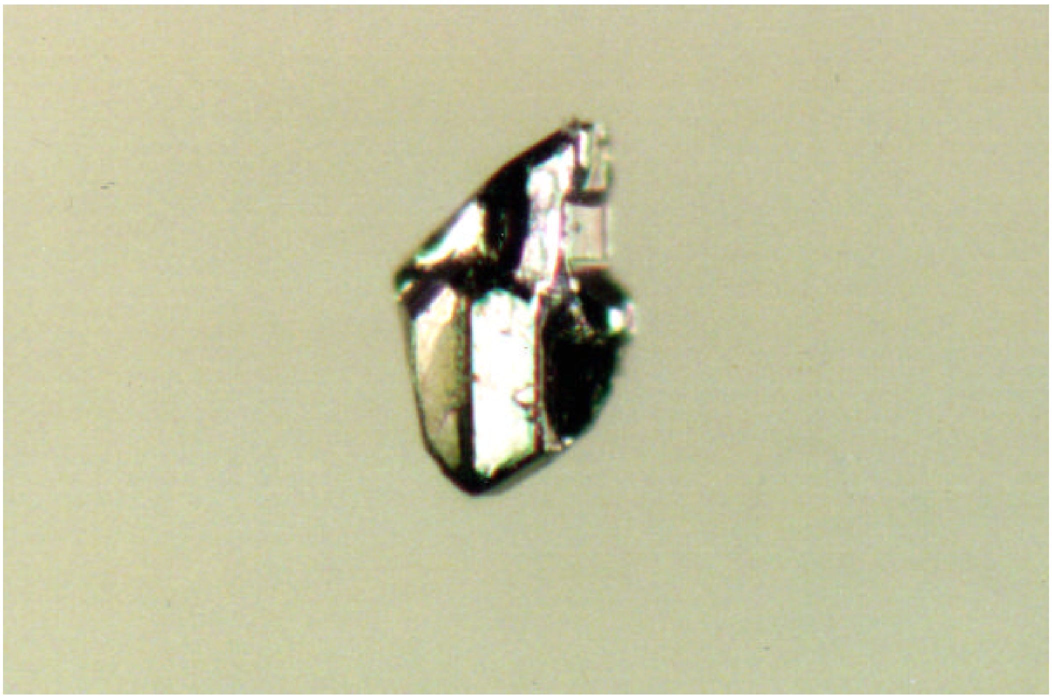

Figure A2_4 Released fPer inclusion JH2

Without the occluding diamond, the characteristic black colouration and imposed morphology is evident. The inclusion is ~500 x 300 x 300 µm in size.

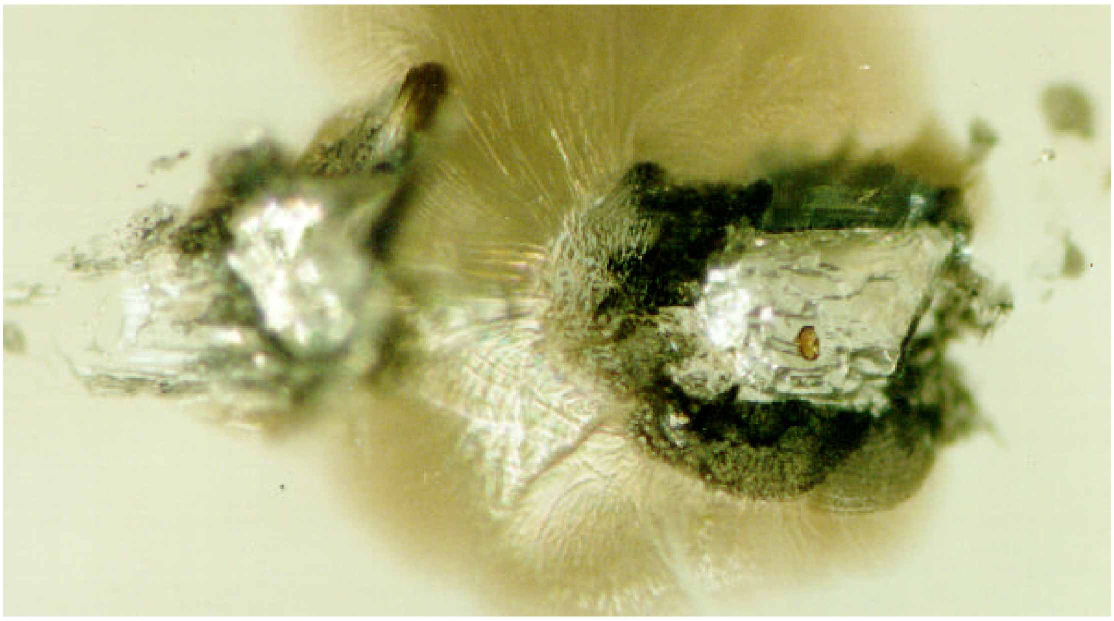

Figure A2_5 CaSi-Pvk inclusion BZ252A

The fracture corona surrounding the inclusion is particularly striking. Not only is it picked out by internal reflection but also by a film of black graphitisation. The inclusion (~ 120μm across), rather looking colourless has an opaque appearance due to reflection from the diamond / inclusion interface. As small unidentified inclusion is visible on the CaSi-Pvk / diamond grain boundary. Its orange colouration suggests that it may be a majoritic garnet.

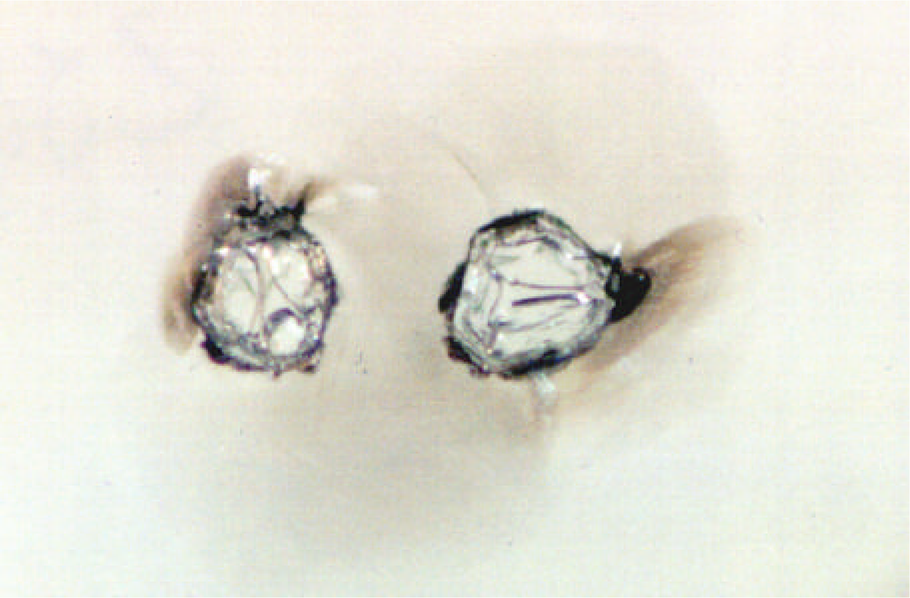

Figure A2_6 Twin colourless inclusions of Type I MgSi-Pvk in BZ254

EDS analysis of a minute portion of the left-hand inclusion exposed on the diamond surface suggests that this grain is a Al-free Mg silicate consistent with an identification as Type I MgSi-Pvk. As is common for São Luiz inclusions, fractures appear from the inclusion apices into the diamond. The grains are ~80 µm across.

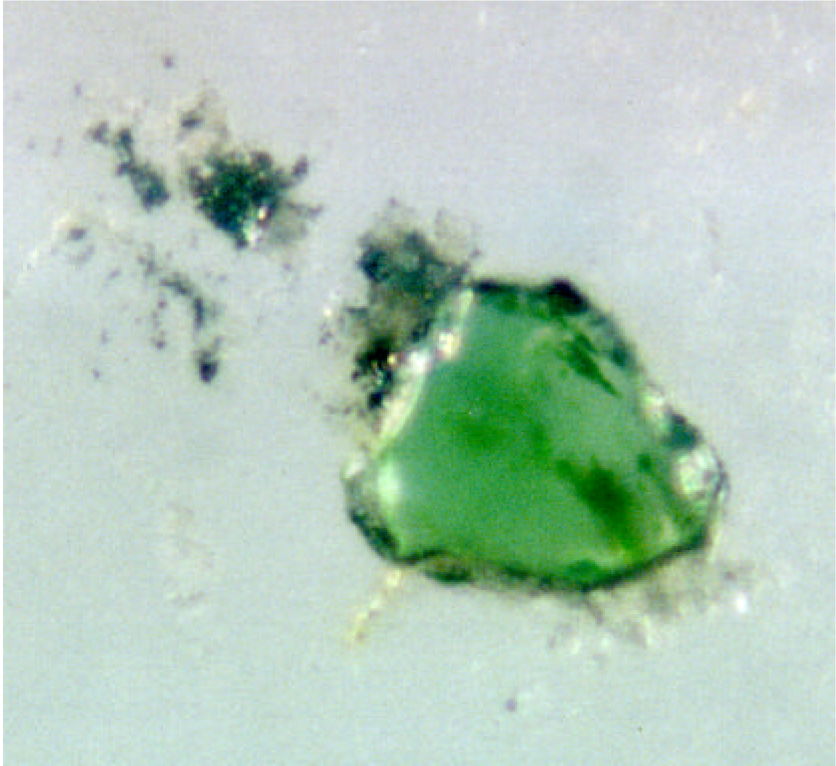

Figure A2_7 TAPP grain BZ238A showing the characteristic green colouration

The grain is ~40 μm across and is shown polished and mounted in araldite.

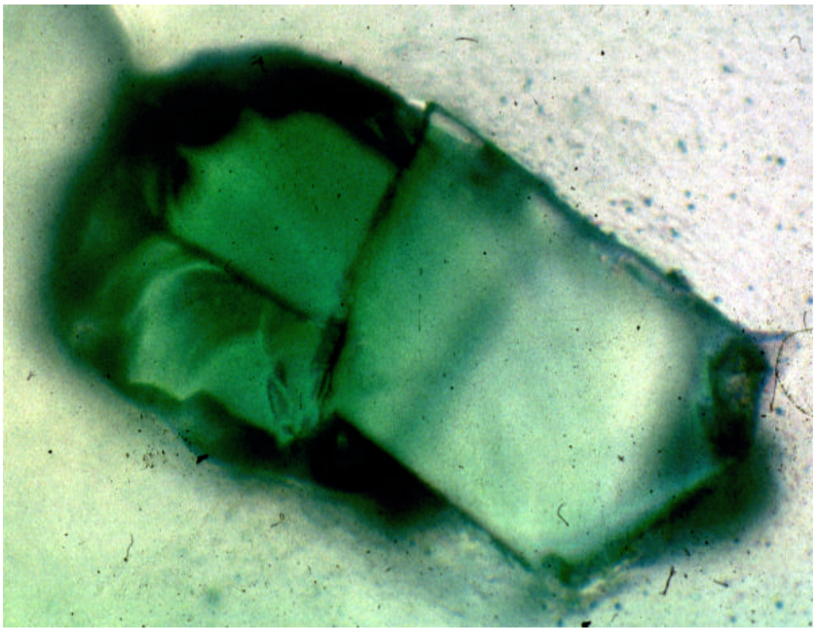

Figure A2_8 Composite inclusion BZ259A2,B

The colourless portion (BZ259B) is a Type III MgSi-Pvk and the green portion (BZ259A2) is a TAPP. The entire composite grain is ~140µm long and is shown polished and mounted in araldite.

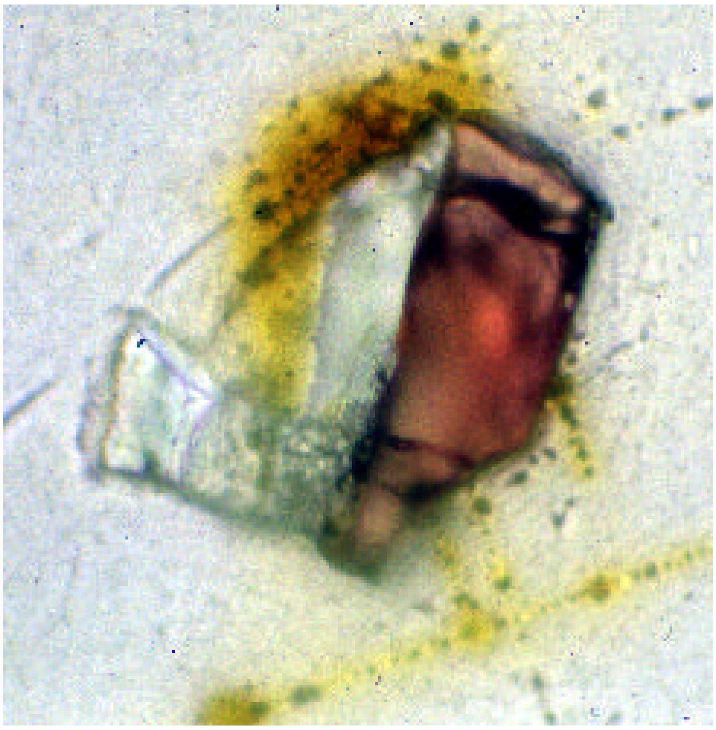

Figure A2_9 Composite inclusion BZ241B1,C

The red portion (BZ241C) is a ruby and the colourless potion (BZ241B1) is a Type II MgSi-Pvk. The grain is polished and mounted in araldite and is ~60 µm across.

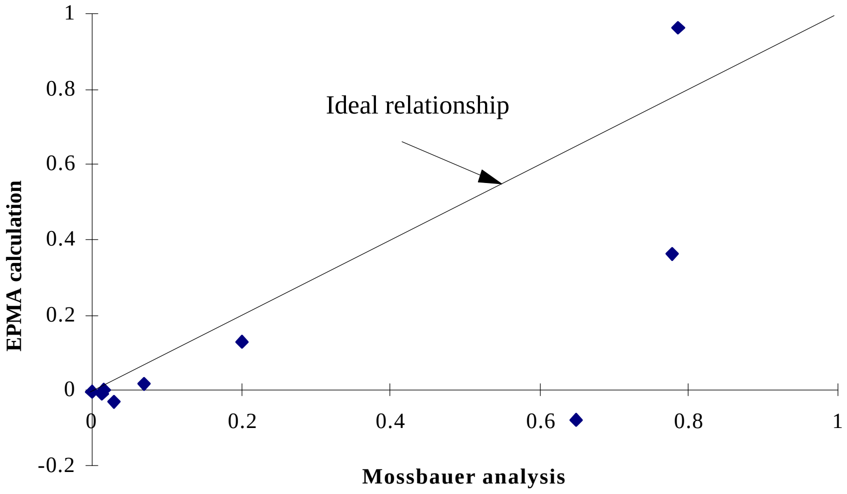

Figure A8_1 The relationship of (Fe^{3+}/Total Fe)$_{\text{cations}}$ determined by EPMA against Mössbauer analysis

The lack of coincidence of Fe^{3+} calculation by via EPMA with that of Mössbauer analysis is interpreted as being due to cumulative errors and uncertainty in EPMA Fe^{3+} determination. Wherever possible, inclusion Fe^{3+} concentration is calculated from Mössbauer data from related grains.

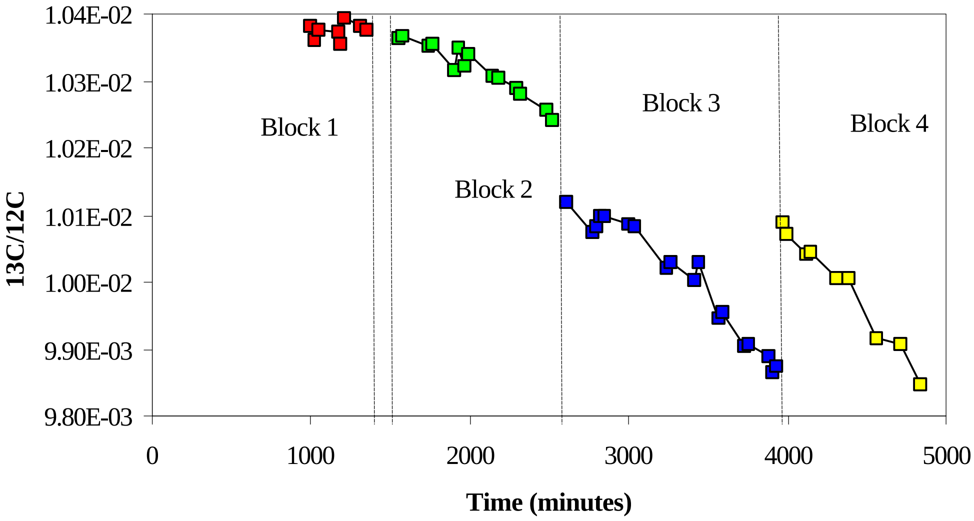

Figure A9_1 $^{13}C/^{12}C$ against time for analyses of SYNAT standard

The determined $^{13}C/^{12}C$ ratio exhibits a pronounced drift throughout and a marked hiatus between, analysis sessions. Correction for absolute concentration of unknown is thus carried out using a standard calibration dependent on time and analysis session.

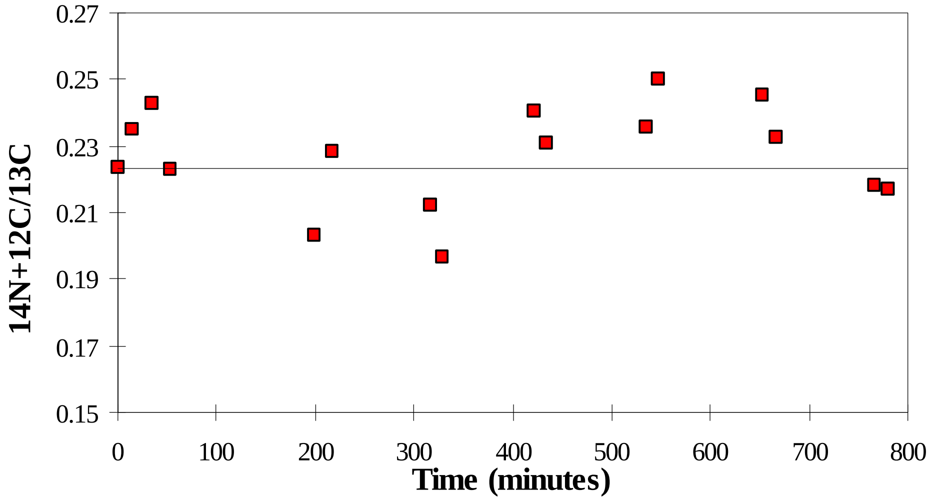

Figure A9_2 The variation of ^{14}N+^{12}C/^{13}C observed against time on SYNAT standard during analysis of diamond flat BZ251

No significant drift was observed throughout the course of the analysis session. An averaged value for standard counts was, therefore, employed for determination of N concentration in the unknown.

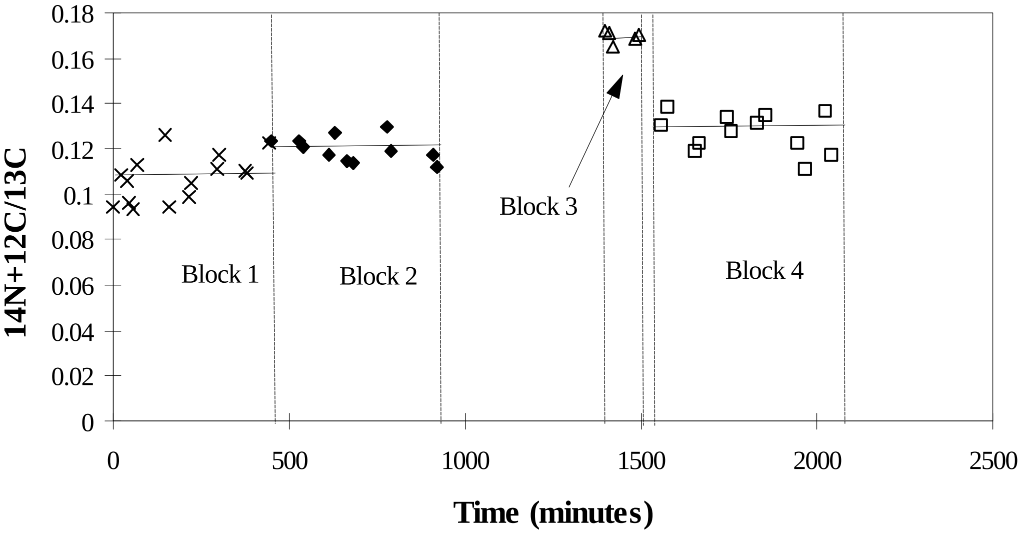

Figure A9_3 Blocks of analysis of $^{14}N+^{12}C/^{13}C$ against time for SYNAL standard measured during analysis of diamond flats BZ252, BZ254 and BZ255

No significant drift in isotopic ratio is observed within each sessions. Significant variation was, however, observed between sessions. Nitrogen concentrations in the unknowns were calculated, therefore, using an averaged standard count ratio for each block of analyses.